BEILSTEIN JOURNAL OF ORGANIC CHEMISTRY

Advances in photoredox catalysis

Edited by Timothy Noël

Generated on 08 April 2026, 14:41

Imprint

Beilstein Journal of Organic Chemistry
www.bjoc.org
ISSN 1860-5397
Email: journals-support@beilstein-institut.de

The *Beilstein Journal of Organic Chemistry* is published by the Beilstein-Institut zur Förderung der Chemischen Wissenschaften.

Beilstein-Institut zur Förderung der Chemischen Wissenschaften
Trakehner Straße 7–9
60487 Frankfurt am Main
Germany
www.beilstein-institut.de

The copyright to this document as a whole, which is published in the *Beilstein Journal of Organic Chemistry*, is held by the Beilstein-Institut zur Förderung der Chemischen Wissenschaften. The copyright to the individual articles in this document is held by the respective authors, subject to a Creative Commons Attribution license.

BEILSTEIN JOURNAL OF ORGANIC CHEMISTRY

Visible-light-induced addition of carboxymethanide to styrene from monochloroacetic acid

Kaj M. van Vliet, Nicole S. van Leeuwen, Albert M. Brouwer and Bas de Bruin*

Full Research Paper

Open Access

Address:
Van 't Hoff Institute for Molecular Sciences, Faculty of Science, University of Amsterdam, Science Park 904, 1098 XH Amsterdam, Netherlands

Email:
Bas de Bruin* - b.debruin@uva.nl

* Corresponding author

Keywords:
ATRA; catalysis; chloroacetic acid; lactone; photoredox

Beilstein J. Org. Chem. **2020,** *16,* 398–408.
doi:10.3762/bjoc.16.38

Received: 10 January 2020
Accepted: 05 March 2020
Published: 16 March 2020

This article is part of the thematic issue "Advances in photoredox catalysis".

Guest Editor: T. Noël

© 2020 van Vliet et al.; licensee Beilstein-Institut.
License and terms: see end of document.

Abstract

Where monochloroacetic acid is widely used as a starting material for the synthesis of relevant groups of compounds, many of these synthetic procedures are based on nucleophilic substitution of the carbon chlorine bond. Oxidative or reductive activation of monochloroacetic acid results in radical intermediates, leading to reactivity different from the traditional reactivity of this compound. Here, we investigated the possibility of applying monochloroacetic acid as a substrate for photoredox catalysis with styrene to directly produce γ-phenyl-γ-butyrolactone. Instead of using nucleophilic substitution, we cleaved the carbon chlorine bond by single-electron reduction, creating a radical species. We observed that the reaction works best in nonpolar solvents. The reaction does not go to full conversion, but selectively forms γ-phenyl-γ-butyrolactone and 4-chloro-4-phenylbutanoic acid. Over time the catalyst precipitates from solution (perhaps in a decomposed form in case of *fac*-[Ir(ppy)$_3$]), which was proven by mass spectrometry and EPR spectroscopy for one of the catalysts (*N*,*N*-5,10-di(2-naphthalene)-5,10-dihydrophenazine) used in this work. The generation of HCl resulting from lactone formation could be an additional problem for organometallic photoredox catalysts used in this reaction. In an attempt to trap one of the radical intermediates with TEMPO, we observed a compound indicating the generation of a chloromethyl radical.

Introduction

Monochloroacetic acid is an industrially important compound, with applications ranging from thickening agents (carboxymethyl cellulose, E466) [1,2], herbicides (2,4-dichlorophenoxyacetic acid), cosmetics (cocamidopropyl betaine), dyes (indigo vat dye) [3], to pharmaceuticals (ibuprofen, glycine, malonates) [4] (see Figure 1). Many reactions with monochloroacetic acid have been published. The production of basic building blocks like glycine [5] (>600 000 tons/year in China in 2015) and

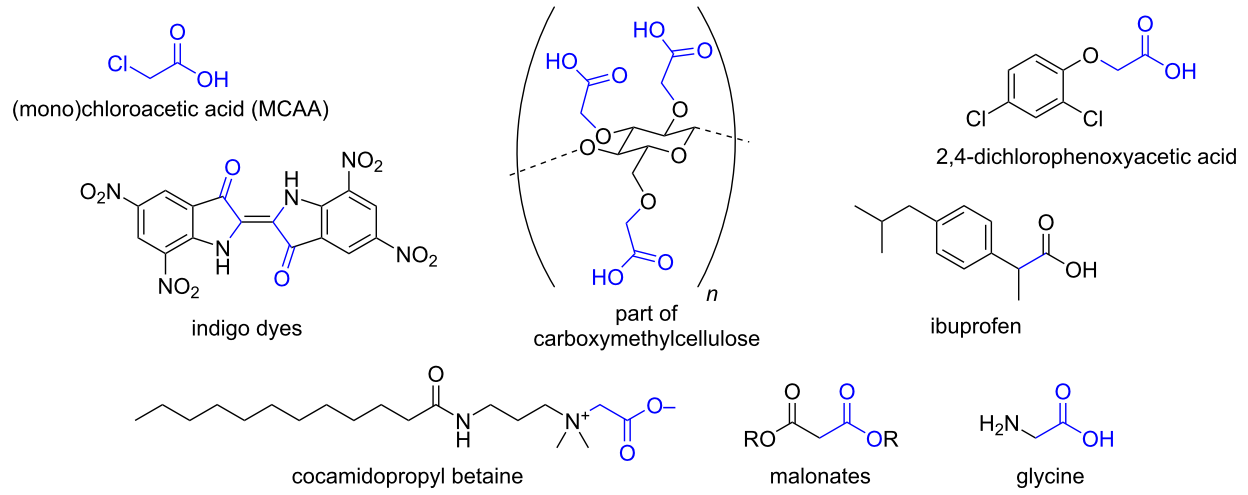

Figure 1: A part of the industry around monochloroacetic acid.

diethyl malonate from monochloroacetic acid show the value of this compound as a starting material. Many reactions with monochloroacetic acid, including the synthesis of glycine and diethyl malonate, are based on nucleophilic substitution of the chlorine [6-10].

In an attempt to find new synthetic applications of monochloroacetic acid we turned our attention to photoredox catalysis. We were inspired by the rebirth of visible light photoredox catalysis, induced by the work of Yoon, Stephenson and MacMillan [11]. By selective excitation of an organic or organometallic dye by visible light a species is formed that can act as a single-electron oxidant and single-electron reductant. In this way reactive radical intermediates can be formed catalytically in situ, resulting in reactivity different from common two-electron pathways. Photoredox catalysis reactivity is very different from traditional redox reactions, and the same reactivity cannot be achieved by stoichiometric addition of both a reductant and an oxidant to a reaction mixture (as that would lead to a rapid redox reaction between the oxidant and the reducing agent instead of converting the substrate). Excitation of the photocatalyst, on the other hand, allows continuous formation of low concentrations of both oxidized and reduced radical forms of the substrate(s), and the excited catalysts (and/or their oxidized/reduced forms) can perform both opposed redox events before returning to their original oxidation state for re-excitation. If no substrate is encountered during the lifetime of the excited state the ground state is typically regenerated.

Such photogenerated radical intermediates can be useful for the formation of new C–C bonds. Previous works from our group presented cobalt-catalyzed radical cyclization and carbonylation reactions [12-16]. Photoredox catalysis provides a way to generate radical intermediates from simple organic molecules by single-electron redox processes. Single-electron oxidation can produce carbon-centered radicals from substrates such as amines [17], alkenes [18], and carboxylates [19], or by hydrogen-atom transfer to an oxidatively formed thiolate radical [20]. Single-electron reduction produces carbon-centered radicals from, for example, aryl nitriles [21], carbonyl or imine species [22], iodonium or diazonium salts [23], or halide species [24].

The formation of radicals from halide species by photoredox catalysis has been widely studied. It has been applied as a mild method for the dehalogenation of several compounds [25-27]. In the light of photoredox catalytic C–C bond formation, its application in the field of atom transfer radical addition (ATRA) reactions is very important. Remarkably, this type of C–C bond formation became only popular in 2011, while the first example was already published by Barton in 1994 [28].

Recently, Kokotos and co-workers published a visible light photoredox catalyzed lactone formation from iodoacetic acid and alkenes [29] (Scheme 1). In addition, it has been shown that monochloroacetic acid can be reduced by hydrated electrons [30,31]. The group of Goez developed a strategy for the photoredox generation of hydrated electrons and applied that for the dehalogenation of monochloroacetic acid [32,33]. However, to the best of our knowledge, a photoredox catalyzed application of monochloroacetic acid without using a sacrificial electron donor is not known. Interestingly, monochloroacetic acid also contains a carboxyl group that could perhaps be oxidatively decarboxylated to generate a chloromethyl radical. In this

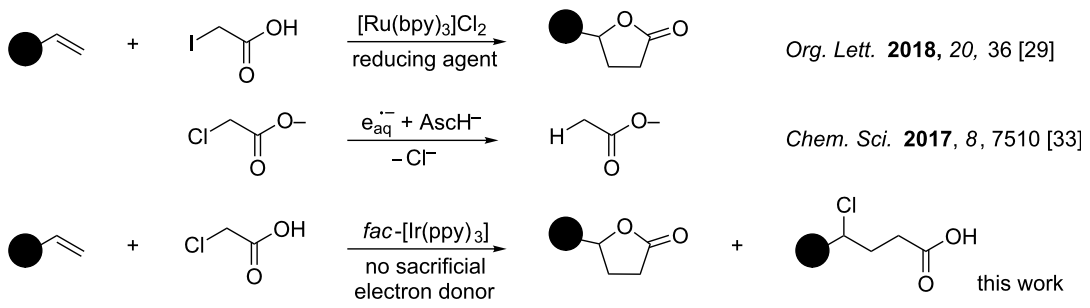

Scheme 1: Redox based activation of haloacetic acid.

study, we investigated the possibility of redox neutral, visible light photoredox catalyzed C–C bond formation with monochloroacetic acid.

Results and Discussion

First, we used cyclic voltammetry to determine the oxidation potential (E_{Ox}) of monochloroacetic acid in acetonitrile (Figure 2). This way it could be verified, if monochloroacetic acid can quench the excited state of one of the common photoredox catalysts. In Figure 1 the cyclic voltammogram of monochloroacetic acid is shown. One can see the onset potential for the reduction of monochloroacetic acid at −1.5 V vs Fc/Fc^+. The two photoredox catalysts, *fac*-$Ir(ppy)_3$ (E^*_{ox} = −2.1 V vs Fc/Fc^+) [34] and $[Cu(dap)_2]Cl$ (E^*_{ox}= −1.8 V vs Fc/Fc^+) are strong enough reducing agents in their excited states to be oxidatively quenched by monochloroacetic acid. Based on these data, we concluded that the visible-light-promoted reductive photoredox C–C bond coupling reaction with monochloroacetic acid should be possible.

As such, we chose *fac*-$[Ir(ppy)_3]$ and $[Cu(dap)_2]Cl$ for the photoredox reaction between monochloroacetic acid and styrene in acetonitrile under an atmosphere of N_2 to form the lactone 5-phenyldihydrofuran-2(3*H*)-one (and HCl) or the acid 4-chloro-4-phenylbutanoic acid via an ATRA reaction (Scheme 2). The photoredox catalysts are excited by using blue

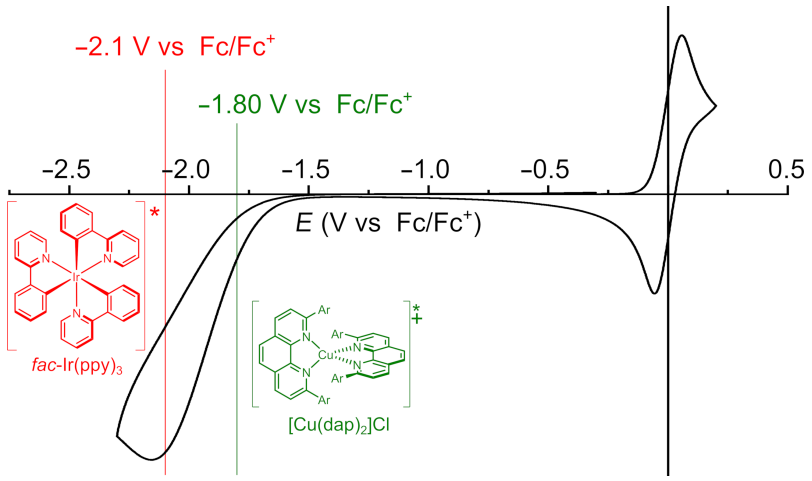

Figure 2: Cyclic voltammogram of monochloroacetic acid and ferrocene with 0.1 M [TBA][PF_6] in MeCN. The potential is referenced to the Fc/Fc^+ redox couple (0 V). The excited state reduction potentials of two different reducing photoredox catalysts (in red and green) are shown in the figure.

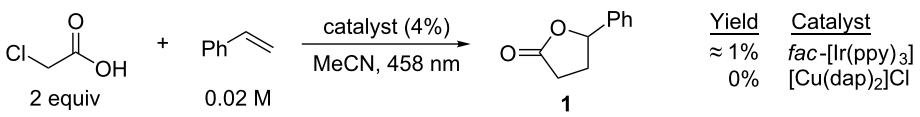

Scheme 2: Initial attempts for lactone formation by photoredox catalysis.

LEDs with a peak excitation of 458 nm (see the experimental section for a detailed description) which is sufficient for the excitation of both complexes. For $[Cu(dap)_2]Cl$, no product was observed, but with *fac*-$[Ir(ppy)_3]$ we could observe the desired lactone, albeit in small amounts.

After these unsatisfying results we focused on the formation of the carboxymethanide radical. We attempted trapping the radical by replacing styrene with TEMPO (2,2,6,6-tetramethylpiperidin-1-yl)oxyl). However, GC–MS analysis indicated full conversion of TEMPO to the adduct resulting from a radical coupling between a cyanomethanide radical and TEMPO (Scheme 3) for the highly reducing $[Ir(ppy)_3]$ (−1.73 V vs SCE in its excited state [35]). The weak C–H bond of acetonitrile (93.0 kcal mol^{-1}) compared to the C–H bond strength of a carbonyl α-C–H bond (94.1 kcal mol^{-1}) resulted in formation of **2** (2,2,6,6-tetramethylpiperidin-1-yl)oxyacetonitrile (compound **2**; Scheme 3) [36].

Hence, to avoid the reaction with the solvent, we applied solvents with stronger C–H bonds (see Table 1). DMF and DMSO are used frequently in the field of photoredox catalysis, but the use of these solvents did not lead to formation of the desired product either (Table 1, entries 2 and 3), using *fac*-$[Ir(ppy)_3]$ or $[Cu(dap)_2]Cl$ as the photosensitizer. Because the use of polar solvents did not lead to the desired reactivity, we turned to non-

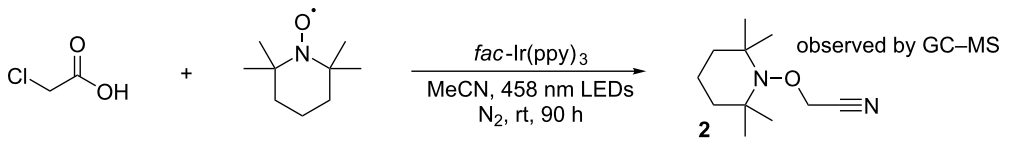

Scheme 3: The photoredox reaction of TEMPO with monochloroacetic acid catalyzed by fac-$[Ir(ppy)_3]$.

Table 1: Conditions screening for the photoredox catalyzed reaction between monochloroacetic acid and styrene.[a]

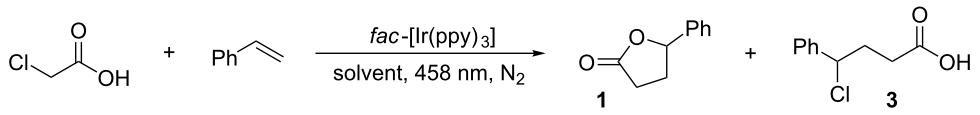

Exp.	Cat. loading	Solvent	ClAcOH (equiv)	Yield (**1**:**3**)
1	4%	MeCN	2	≈1% (1:0)
2	4%	DMF	2	<1%
3	4%	DMSO	2	<1%
4	**4%**	**benzene**	**2**	**49% (1:3.0)**
5	4%	trifluoromethylbenzene	2	13% (1:4.4)
6	4%	chlorobenzene	2	22% (1:3.3)
8	4%	toluene	2	27% (1:4.7)
9	4%	DCE	2	11% (1:1.3)
10	**10%**	**benzene**	**2**	**84% (1:4.3)**
11	3%	benzene	2	34% (1:2.8)
12	2%	benzene	2	32% (1:2.2)
13	1%	benzene	2	18% (1:1.3)
14	0.5%	benzene	2	<1%
15	4%	benzene	0.5	46% (1:2.8)
16	4%	benzene	3	43% (1:3.3)
17	4%	benzene	4	45% (1:3.1)
18	4%	benzene	5	46% (1:2.8)
19[b]	4%	benzene	2	11% (1:1.2)
20	0%	benzene	2	–
21[c]	4%	benzene	2	–

[a]A mixture of styrene (0.02 M), monochloroacetic acid and *fac*-$[Ir(ppy)_3]$ in solvent (2 mL) was irradiated overnight under a N_2 atmosphere with 458 nm LEDs. The yield was determined by ^1H NMR spectroscopy with trimethoxybenzene as external standard. [b]60 W fluorescent light bulb. [c]In the dark.

polar solvents. Since $[Cu(dap)_2]Cl$ is insoluble in nonpolar solvents, we continued with the more reducing *fac*-$[Ir(ppy)_3]$ photocatalyst. The choice of benzene as a solvent led to a significant formation of the desired lactone, according to GC–MS analysis. The ^{1}H NMR and mass spectra of the crude reaction mixture also demonstrated the formation of the ATRA product 4-chloro-4-phenylbutanoic acid. The two products were obtained in a combined yield of 49% (Table 1, entry 4). A further screening of nonpolar solvents did not lead to any significant increase of the yield or selectivity (Table 1, entries 5–9).

The reduction of catalyst loading resulted in a lower yield and a lower selectivity for the acid compound **3** (Table 1, entries 10–14). The products indicate an oxidative quenching of the photoredox catalyst by reduction of the carbon chlorine bond of monochloroacetic acid. Varying the stoichiometry of substrates also did not lead to any improvement of the yield (Table 1, entries 15–18), most likely because the *fac*-$[Ir(ppy)_3]^+$ complex (+0.77 V vs SCE) is unable to oxidize styrene sufficiently. In the absence of the photoredox catalyst or light, the reaction does not take place (Table 1, entries 19 and 20).

Notably, during the reaction, the bright yellow color of the solution resulting from the absorption of the catalyst disappears and an insoluble precipitate is formed. The use of C_6D_6 as a solvent allowed us to directly measure the ^{1}H NMR spectrum of the crude reaction mixture. The presence of both monochloroacetic acid and styrene in this mixture is another indication that the catalyst had decomposed or precipitated from the solution before consumption of all substrate. Unfortunately, because of a lack of solubility, we were unable to analyze the precipitate. We also applied organic photoredox catalysts [37]. Miyake and co-workers have introduced highly reducing organic photoredox catalysts [38-43]. The use of 5,10-di(naphthalen-2-yl)-5,10-dihydrophenazine or 3,7-di(biphenyl-4-yl)-10-(naphthalen-1-yl)-10*H*-phenoxazine instead of $[Ir(ppy)_3]$ as the photoredox catalyst had no beneficial effect on the yield or conversion, and also led to the formation of a precipitate. However, the precipitate that was formed when the organic dye 5,10-di(naphthalene-2-yl)-5,10-dihydrophenazine was used proved to be soluble in DMSO, allowing us to characterize the material. After we discovered that the redissolved precipitate was NMR-silent, a room temperature EPR spectrum was recorded (Figure 3). The multiplicity in this spectrum is in agreement with formation of the 1e-oxidized form of the organic photocatalyst, showing hyperfine interactions with two equivalent nitrogen nuclei (g_{iso} = 2.0032; A^N_{iso} = 18.6 MHz). The HRMS of this species showed the mass of the catalyst, thus confirming that the oxidized catalyst precipitates as a salt from solution when using benzene as a solvent.

Based on the formation of the cation of the photoredox catalyst, we believe that after oxidative quenching the catalyst is not fully reduced back to the neutral complex, accumulates in solution and as a result precipitates as chloride salt (with Cl^- stemming from the substrate). We assume that the same happens when using the *fac*-$[Ir(ppy)_3]$ photocatalyst (vide supra; although for the precipitate generated from this catalyst we were

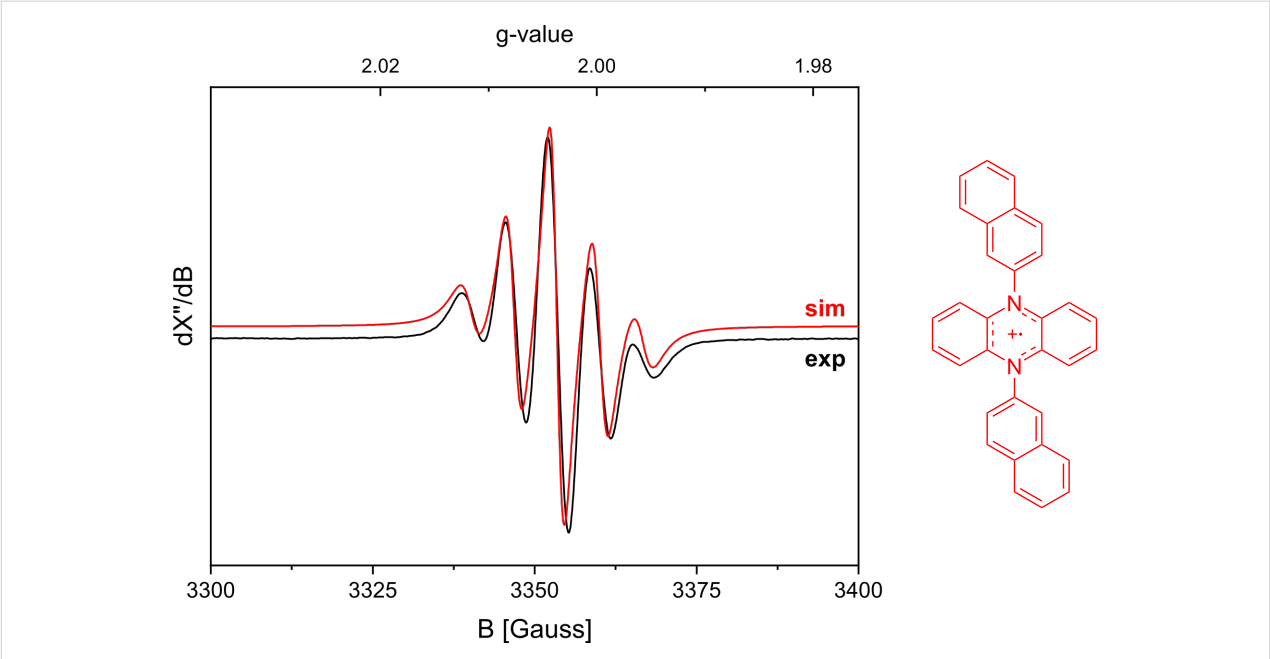

Figure 3: EPR spectra measured (black) and simulated (red) based on the structure of the oxidized photoredox catalyst shown on the right.

unable to redissolve the solids for characterization). Also here the catalyst is likely to precipitate as $[Ir(ppy)_3]Cl$, but for this photocatalyst additional deactivation pathways could also play a role. For every lactone product that is formed, HCl is generated and in the case of *fac*-$[Ir(ppy)_3]$, the acid could potentially cause protodemetalation. This protodemetalation could be even more pronounced in the excited state (which is after all a metal-to-ligand charge-transfer state). Therefore, we focused on methods to trap the HCl from solution (see Table 2). An addition of 2,6-lutidine as a base leads to a lower conversion. Although the addition of a base is an efficient method to remove HCl, deprotonation of monochloroacetic acid leads to an anionic species that is harder to reduce. However, the use of 2,6-lutidine gave a 32% yield. This could be caused by the reduced Brønsted base strength in apolar solvents. Thus, to avoid using a base that deprotonates monochloroacetic acid, we added sodium chloroacetate to capture HCl from the reaction. However, under these conditions the desired product was not formed at all. Addition of $[Ag]PF_6$ to remove the chloride and solubilize the oxidized photocatalyst also did not lead to any product formation. $[Ag]PF_6$ is poorly soluble in benzene and the Ag^+ ion is likely to act as an oxidizing agent quenching the excited state of the photocatalyst. Another additive we tried was tetrabutylammonium hexafluorophosphate, thought to precipitate [TBA]Cl and to keep $[Ir(ppy)_3]^+$ in solution as the PF_6^- salt. However, performing the reaction in the presence of $[TBA]PF_6$ led to a decreased yield. The use of diphenylurea to trap Cl^- did not lead to a significant increase of the reaction yield either. In addition, sodium iodide and tetrabutylammonium iodide were tested in an attempt to form an iodo intermediate which was expected to cyclize more easily to the lactone [44]. However, the lack of solubility of these reagents in benzene likely hampered nucleophilic substitution and resulted in very low yields. Sodium ascorbate was also added to investigate whether a sacrificial electron donor could increase the yields, but this was not observed. Interestingly, the reaction with sodium ascorbate favored the formation of lactone **1** over linear acid **3**. The exact reason for this behavior is not clear, but perhaps ascorbate acts as a weak base favoring lactone formation without deprotonating monochloroacetic acid.

In another attempt to avoid the formation of HCl we applied methyl chloroacetate. Hereby the formation of the lactone is inaccessible and HCl cannot be formed. However, when using this substrate only 13% of the ATRA product were observed. Hence, there thus seems to be a positive effect of the acid on the activation of the C–Cl bond. The precise mechanism of this reductive cleavage is currently unclear. Besides the direct reduction of a carbon chlorine bond by electron transfer into the C–Cl antibonding orbital (Scheme 4A), the same intermediate can be formed by fragmentation of an α-haloketyl radical (Scheme 4B). The acidic environment could lead to easier formation of this ketyl radical. Intuitively, pathway B seems most probable.

The reaction in benzene forms mainly the acid product **3** originating from an ATRA reaction. We propose that this product is formed by radical propagation followed by a mechanism first

Table 2: Additive screening for the photoredox reaction between styrene and monochloroacetic acid.[a]

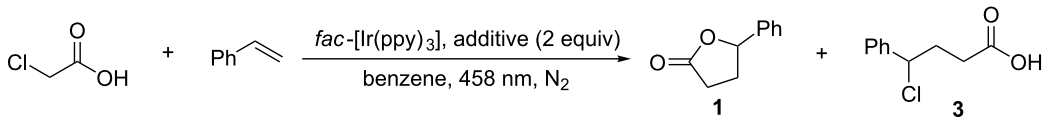

Exp	Additive	Yield (**1**:**3**)
1[b]	2,6-lutidine	32% (1:2.2)
2	$[Ag]PF_6$	<1%
3	$[TBA]PF_6$	29% (1:3.8)
4	sodium chloroacetate	<1%
5	diphenylurea	50% (1:5)
6	sodium iodide	3% (1:0)
7	tetrabutylammonium iodide	≈1% (1:0)
8	sodium ascorbate	39% (1:0.75)
9[c]	MeOH	12% (1: 0.75)
10[c]	acetic acid	31% (1:2.5)

[a]A mixture of styrene (0.02 M), monochloroacetic acid (2 equiv), fac-$[Ir(ppy)_3]$ and an additive (2 equiv) in benzene (2 mL) was irradiated overnight under an N_2 atmosphere with 458 nm LEDs. The yield was determined by ^1H NMR spectroscopy with trimethoxybenzene as external standard. [b]0.5 equiv of monochloroacetic acid were used. [c]Additive as a cosolvent (10%).

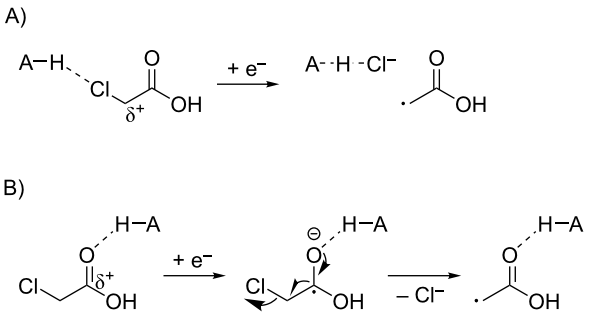

Scheme 4: Two possible acid-assisted, reductive activation pathways of monochloroacetic acid (A–H = acid).

found by Kharasch and co-workers, where the benzyl radical formed after addition of the generated α-carbonyl radical abstracts a chloride from monochloroacetic acid to obtain the product and propagates the reaction [45]. In situ IR experiments show an exponential grow for product formation, which is indeed indicative of a radical propagation mechanism (see Supporting Information File 1). In acetonitrile, a small amount of lactone was formed and no desired acid. Therefore, we investigated the effect of polarity on the selectivity of the reaction by mixing acetonitrile with benzene (Table 3). Based on the result with pure acetonitrile as a solvent (Scheme 2 and Scheme 3), we expected a lower yield with higher concentrations of acetonitrile. Indeed, the yield decreased with increasing amounts of acetonitrile. On the other hand, the selectivity for the formation of the lactone increased by adding more acetonitrile [46].

To evaluate if γ-phenyl-γ-butyrolactone (**1**) can be formed from 4-chloro-4-phenylbutanoic acid (**3**) in benzene we reacted irradiated mixtures of **3** with either the photoredox catalyst, monochloroacetic acid or both. We did not see any formation of the lactone (**1**) after irradiating the mixtures overnight with 458 nm LEDs. Therefore, it is unlikely that in benzene direct conversion from **3** to **1** plays any significant role under the applied reaction conditions. The photoredox activation of monochloroacetic acid leads to the formation of precipitate during the reaction (see Figure 4), again indicating catalyst precipitation/deactivation.

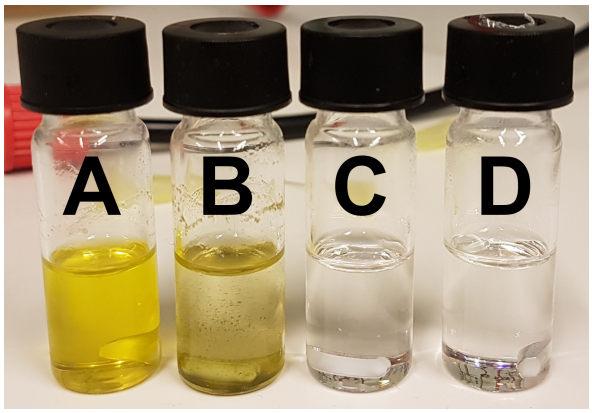

Figure 4: Reaction mixtures after overnight irradiation of (A) 4-chloro-4-phenylbutanoic acid (**3**) and *fac*-[Ir(ppy)$_3$]; (B) **3**, *fac*-[Ir(ppy)$_3$] and monochloroacetic acid; (C) **3**; (D) **3** and monochloroacetic acid. In none of the vials lactone **1** was formed.

Works in the group of Noël and others have revealed that flow chemistry can increase the rate and yield of photoredox reactions significantly [47-53]. According to the law of Lambert–Beer, only the outer shell of a batch reactor (vial or Schlenk flask) is excited efficiently. Hence, radical formation (and propagation) is only efficient within this illuminated shell.

Table 3: Screening of the effect of mixing acetonitrile in benzene on the photoredox reaction.[a]

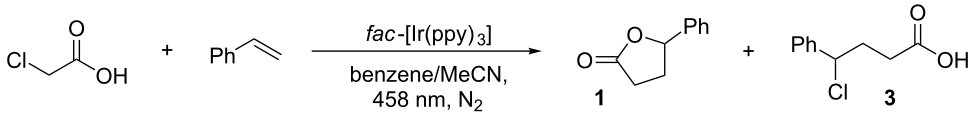

Entry	% MeCN	Yield (**1**:**3**)
1	0	49 (1:3)
2	5	26 (1:1)
3	10	25 (1:0.79)
4	15	22 (1:0.46)
5	20	18 (1:0.28)
6	50	11 (1:0)

[a]A mixture of styrene (0.02 M), monochloroacetic acid (5 equiv), fac-[Ir(ppy)$_3$] in a mixture of benzene and acetonitrile (2 mL) was irradiated overnight under an N_2 atmosphere with 458 nm LEDs. The yield was determined by ^{1}H NMR spectroscopy with trimethoxybenzene as external standard.

We anticipated that in a flow setup using tubing with a small internal diameter (0.71 mm) the photocatalyzed reaction pathways could be more efficient. However, in this case, performing the reaction under flow conditions did not lead to better results. The reaction performed in a flow reactor led to a combined yield of 32% within 1 hour. Furthermore, as in a normal reactor, we also observed formation of precipitate in the flow setup, forming clusters of solids. These solids presumably consist of the oxidized or otherwise deactivated photocatalyst.

More insight into the selectivity for either the formation of the lactone or the ATRA reaction was obtained by screening a small substrate scope of *para*-substituted styrene derivatives in the photocatalyzed reaction with monochloroacetic acid using *fac*-[Ir(ppy)$_3$] as the photocatalyst (Scheme 5). For electron-poor *p*-halogenated and *p*-trifluoromethylated styrenes no lactone formation took place in these reactions, and only the Kharasch-addition product was observed. The benzylic radical resulting from radical addition to these styrene derivatives seems to be too electron poor for efficient oxidation induced cyclization, thus resulting in a Kharasch-type radical propagation reaction as the main pathway. Upon increasing the electron density by using 4-vinylanisole, we did see formation of the lactone product. When we used *p*-nitrostyrene, no formation of the desired products was observed at all.

Based on the results described above we propose the mechanism shown in Scheme 6, in which monochloroacetic acid oxidatively quenches the excited photocatalyst (*fac*-[Ir(ppy)$_3$]*). The thus obtained reduced monochloroacetic acid loses Cl^- to give the carboxymethanide radical intermediate **A**. Addition of this species to styrene results in benzyl radical intermediate **B**. From here two pathways are considered. Species **B** can be oxidized by the $[Ir(ppy)_3]^+$ species that is formed after oxida-

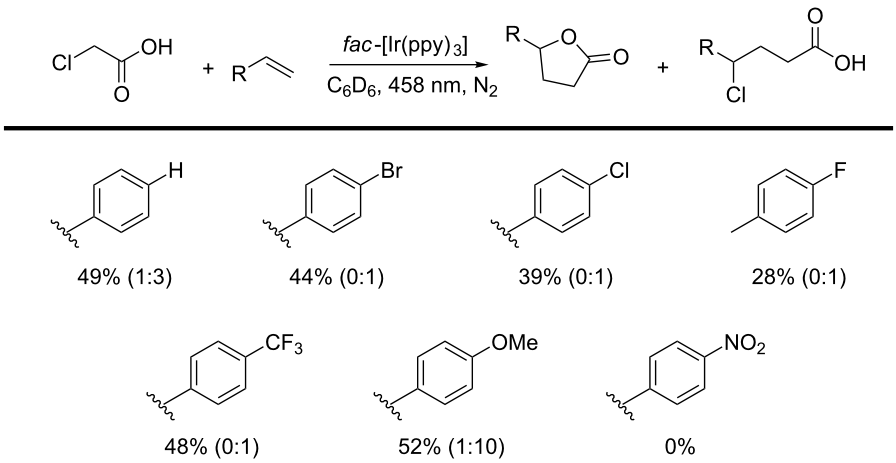

Scheme 5: Substrate scope of styrene derivatives in the photoredox reaction with monochloroacetic acid. Yields have been determined by ^{1}H NMR spectroscopy of the crude reaction mixture, using 1,3,5-trimethoxybenzene as the external standard.

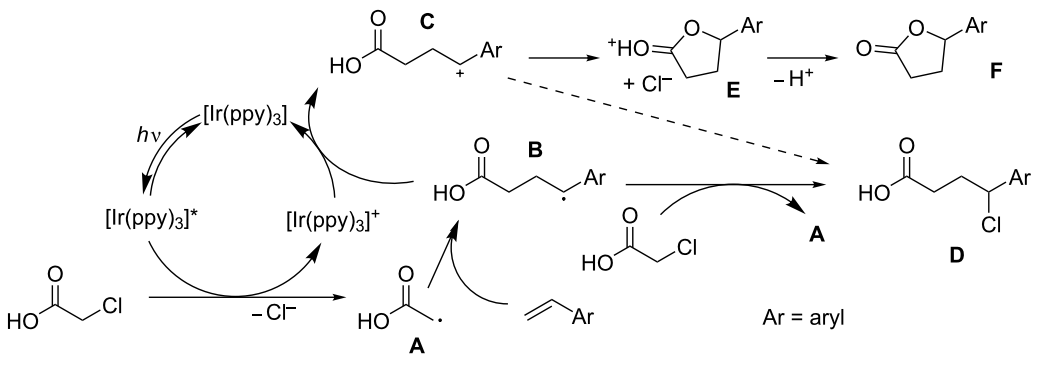

Scheme 6: Proposed reaction mechanism.

tive quenching to regenerate the ground-state photocatalyst together with the formation of the benzyl cation intermediate **C**. Species **C** then cyclizes to give intermediate **E**, which releases H^+ to form the lactone product **F**. Alternatively, **B** forms the Kharasch-addition product **D** by chlorine atom abstraction from another monochloroacetic acid molecule, thus forming a new radical species **A**. Capture of Cl^- by intermediate **C** (dashed arrow) cannot be fully ruled out, but seems unlikely to compete with ring closure to **F** for entropic reasons.

All attempts to trap intermediate **C** using methanol or acetic acid as co-solvent (see Table 2) were unsuccessful and resulted in lower yields, especially in the case of methanol, likely due to the increased polarity of the reaction mixture. Additionally, to provide evidence for oxidative quenching, we tried trapping the carboxymethanide radical with TEMPO in benzene. We were surprised to see that instead we trapped the chloromethyl radical (Scheme 7) which was not expected in the absence of any base and with a relatively poorly oxidizing photoredox catalyst such as *fac*-[Ir(ppy)$_3$]. It is known that under acidic conditions TEMPO can disproportionate into $[TEMPO]^+$ and TEMPO–H [54-56]. $[TEMPO]^+$ (+0.25 V vs Fc/Fc^+ [56]) is a strong enough oxidant to oxidatively quench [Ir(ppy)$_3$]* (−0.30 V vs Fc/Fc^+ [34]). However, the oxidizing power of $[Ir(ppy)_3]^+$ (+0.77 V vs SCE) is insufficient to oxidatively decarboxylate an acetate intermediate (≈ +1.2 V vs SCE). Unexpected electron transfer pathways can be considered, such as the self-decarboxylation that was previously observed for a $[Cl_3CCO_2H][O_2CCl_3]$ mixture [57].

Inspired by the result above on decarboxylative activation we anticipated its possibilities in cyclopropanation. The chloromethyl radical generation by photoredox catalysis is a useful strategy for cyclopropanation [58]. Most photoredox catalyzed, decarboxylative generations of carbon-centered radicals are based on the formation of "stabilized" α-amino [59-65] or benzyl [66-70] radical species. However, the generation of unstabilized alkyl radical species is also known [71-74]. Based on these observations and considerations, we attempted to use monochloroacetic acid as a precursor for cyclopropanation. We have screened a series of strongly oxidizing photoredox catalysts and various alkenes, but unfortunately we were thus far unsuccessful in obtaining cyclopropane derivatives (see experimental section).

Conclusion

We have shown that it is possible to use monochloroacetic acid to form two types of radicals with visible light photoredox catalysis. The reductive formation of the carboxymethanide radical could be used for lactone formation with styrene. Benzene was found to be the best solvent for this reaction. However, the reaction is associated with some unsolved problems. The carboxylic acid group seems to be advantageous for the activation of monochloroacetic acid, but the apolar solvent in combination with formation of HCl is likely to cause catalyst deactivation/precipitation. This effect is more pronounced if electron-poor styrenes are used. We also found indications that a chloromethyl radical can be formed with photoredox catalysis from monochloroacetic acid, but we were not yet able to apply such reactions in a productive manner, such as in cyclopropanation reactions.

Supporting Information

Supporting Information File 1

Experimental details.
[https://www.beilstein-journals.org/bjoc/content/supplementary/1860-5397-16-38-S1.pdf]

Acknowledgements

We would like to thank Ed Zuidinga for measuring mass spectra and Tijmen Bakker for recording the emission spectra of the light sources used in this work. We would like to thank Paul Kuijpers and Sander Woutersen for useful discussions regarding the IR spectroscopy measurements.

Funding

This research was supported by The Netherlands Organization for Scientific Research (NWO), the Holland Research School of Molecular Chemistry (HRSMC), the UvA Research Priority Area "Sustainable Chemistry" and the Advanced Research Center Chemical Building Blocks Consortium (ARC-CBBC project number 2019.021.A).

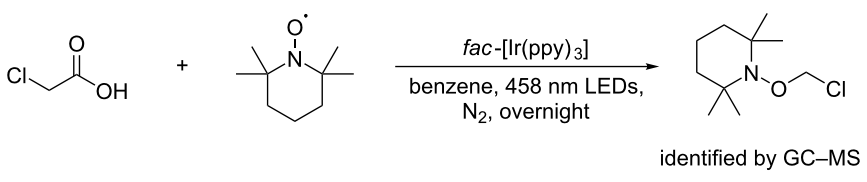

Scheme 7: The photoredox formation of 1-(chloromethoxy)-2,2,6,6-tetramethylpiperidine.

ORCID® iDs

Albert M. Brouwer - https://orcid.org/0000-0002-1731-3869
Bas de Bruin - https://orcid.org/0000-0002-3482-7669

References

1. Toğrul, H.; Arslan, N. *Carbohydr. Polym.* **2003,** *54,* 73–82. doi:10.1016/s0144-8617(03)00147-4
2. Joshi, G.; Naithani, S.; Varshney, V. K.; Bisht, S. S.; Rana, V.; Gupta, P. K. *Waste Manage. (Oxford, U. K.)* **2015,** *38,* 33–40. doi:10.1016/j.wasman.2014.11.015
3. Nwokonkwo, D. C.; Okafor, C. O. *Int. J. Appl. Chem.* **2016,** *12,* 67–74.
4. Product essay monochloroacetic acid, Kat Chem. http://www.kat-chem.hu/en/prod-bulletins/monoklorecetsav (accessed Nov 6, 2019).
5. Zeng, Y.; Li, Z.; Asselin, E. *Ind. Eng. Chem. Res.* **2015,** *54,* 3488–3497. doi:10.1021/acs.iecr.5b00320
6. Yang, L. M.; Jiang, N. N.; Zhao, Z. Y. *Adv. Mater. Res.* **2011,** *396–398,* 1711–1715. doi:10.4028/www.scientific.net/amr.396-398.1711
7. Li, W.; Chang, S.; Chen, X.; Qi, X.; Sun, H.-B. *Asian J. Chem.* **2014,** *26,* 3404–3406. doi:10.14233/ajchem.2014.17537
8. Maisonial, A.; Serafin, P.; Traïkia, M.; Debiton, E.; Théry, V.; Aitken, D. J.; Lemoine, P.; Viossat, B.; Gautier, A. *Eur. J. Inorg. Chem.* **2008,** 298–305. doi:10.1002/ejic.200700849
9. Islamgulova, V. R.; Shitova, E. N.; Akhmerova, S. G.; Tomilov, A. P. *Russ. J. Appl. Chem.* **2002,** *75,* 1438–1440. doi:10.1023/a:1022276812235
10. Weiner, N. *Org. Synth.* **1938,** *18,* 50. doi:10.15227/orgsyn.018.0050
11. Stephenson, C.; Yoon, T.; MacMillan, D. W. C. *Visible Light Photocatalysis in Organic Chemistry;* Wiley-VCH: Weinheim, Germany, 2018. doi:10.1002/9783527674145
12. Chirila, A.; van Vliet, K. M.; Paul, N. D.; de Bruin, B. *Eur. J. Inorg. Chem.* **2018,** 2251–2258. doi:10.1002/ejic.201800101
13. Chirila, A.; Brands, M. B.; de Bruin, B. *J. Catal.* **2018,** *361,* 347–360. doi:10.1016/j.jcat.2018.02.013
14. Chirila, A.; Gopal Das, B.; Paul, N. D.; de Bruin, B. *ChemCatChem* **2017,** *9,* 1413–1421. doi:10.1002/cctc.201601568
15. Otte, M.; Kuijpers, P. F.; Troeppner, O.; Ivanović-Burmazović, I.; Reek, J. N. H.; de Bruin, B. *Chem. – Eur. J.* **2014,** *20,* 4880–4884. doi:10.1002/chem.201400055
16. Paul, N. D.; Chirila, A.; Lu, H.; Zhang, X. P.; de Bruin, B. *Chem. – Eur. J.* **2013,** *19,* 12953–12958. doi:10.1002/chem.201301731
17. Hu, J.; Wang, J.; Nguyen, T. H.; Zheng, N. *Beilstein J. Org. Chem.* **2013,** *9,* 1977–2001. doi:10.3762/bjoc.9.234
18. Margrey, K. A.; Nicewicz, D. A. *Acc. Chem. Res.* **2016,** *49,* 1997–2006. doi:10.1021/acs.accounts.6b00304
19. Jin, Y.; Fu, H. *Asian J. Org. Chem.* **2017,** *6,* 368–385. doi:10.1002/ajoc.201600513
20. Cuthbertson, J. D.; MacMillan, D. W. C. *Nature* **2015,** *519,* 74–77. doi:10.1038/nature14255
21. Zhu, S.; Qin, J.; Wang, F.; Li, H.; Chu, L. *Nat. Commun.* **2019,** *10,* No. 749. doi:10.1038/s41467-019-08669-1
22. Wang, R.; Ma, M.; Gong, X.; Fan, X.; Walsh, P. J. *Org. Lett.* **2019,** *21,* 27–31. doi:10.1021/acs.orglett.8b03394
23. Ghosh, I.; Marzo, L.; Das, A.; Shaikh, R.; König, B. *Acc. Chem. Res.* **2016,** *49,* 1566–1577. doi:10.1021/acs.accounts.6b00229
24. Ye, S.; Zheng, D.; Wu, J.; Qiu, G. *Chem. Commun.* **2019,** *55,* 2214–2217. doi:10.1039/c9cc00347a
25. Fukuzumi, S.; Mochizuki, S.; Tanaka, T. *J. Phys. Chem.* **1990,** *94,* 722–726. doi:10.1021/j100365a039
26. Narayanam, J. M. R.; Tucker, J. W.; Stephenson, C. R. J. *J. Am. Chem. Soc.* **2009,** *131,* 8756–8757. doi:10.1021/ja9033582
27. Poelma, S. O.; Burnett, G. L.; Discekici, E. H.; Mattson, K. M.; Treat, N. J.; Luo, Y.; Hudson, Z. M.; Shankel, S. L.; Clark, P. G.; Kramer, J. W.; Hawker, C. J.; Read de Alaniz, J. *J. Org. Chem.* **2016,** *81,* 7155–7160. doi:10.1021/acs.joc.6b01034
28. Barton, D. H. R.; Csiba, M. A.; Jaszberenyi, J. C. *Tetrahedron Lett.* **1994,** *35,* 2869–2872. doi:10.1016/s0040-4039(00)76646-9
29. Triandafillidi, I.; Kokotou, M. G.; Kokotos, C. G. *Org. Lett.* **2018,** *20,* 36–39. doi:10.1021/acs.orglett.7b03256
30. Li, X.; Ma, J.; Liu, G.; Fang, J.; Yue, S.; Guan, Y.; Chen, L.; Liu, X. *Environ. Sci. Technol.* **2012,** *46,* 7342–7349. doi:10.1021/es3008535
31. Brautzsch, M.; Kerzig, C.; Goez, M. *Green Chem.* **2016,** *18,* 4761–4771. doi:10.1039/c6gc01113f
32. Goez, M.; Kerzig, C.; Naumann, R. *Angew. Chem., Int. Ed.* **2014,** *53,* 9914–9916. doi:10.1002/anie.201405693
33. Naumann, R.; Kerzig, C.; Goez, M. *Chem. Sci.* **2017,** *8,* 7510–7520. doi:10.1039/c7sc03514d
34. Doeven, E. H.; Zammit, E. M.; Barbante, G. J.; Francis, P. S.; Barnett, N. W.; Hogan, C. F. *Chem. Sci.* **2013,** *4,* 977–982. doi:10.1039/c2sc21707d
35. Prier, C. K.; Rankic, D. A.; MacMillan, D. W. C. *Chem. Rev.* **2013,** *113,* 5322–5363. doi:10.1021/cr300503r
36. Speight, J. *Lange's Handbook Of Chemistry,* 16th ed.; McGraw-Hill Education: New York, NY, USA, 2005.
37. Sideri, I. K.; Voutyritsa, E.; Kokotos, C. G. *Org. Biomol. Chem.* **2018,** *16,* 4596–4614. doi:10.1039/c8ob00725j
38. Theriot, J. C.; Lim, C.-H.; Yang, H.; Ryan, M. D.; Musgrave, C. B.; Miyake, G. M. *Science* **2016,** *352,* 1082–1086. doi:10.1126/science.aaf3935
39. Lim, C.-H.; Ryan, M. D.; McCarthy, B. G.; Theriot, J. C.; Sartor, S. M.; Damrauer, N. H.; Musgrave, C. B.; Miyake, G. M. *J. Am. Chem. Soc.* **2017,** *139,* 348–355. doi:10.1021/jacs.6b11022
40. Pearson, R. M.; Lim, C.-H.; McCarthy, B. G.; Musgrave, C. B.; Miyake, G. M. *J. Am. Chem. Soc.* **2016,** *138,* 11399–11407. doi:10.1021/jacs.6b08068
41. Ramsey, B. L.; Pearson, R. M.; Beck, L. R.; Miyake, G. M. *Macromolecules* **2017,** *50,* 2668–2674. doi:10.1021/acs.macromol.6b02791
42. Ryan, M. D.; Pearson, R. M.; French, T. A.; Miyake, G. M. *Macromolecules* **2017,** *50,* 4616–4622. doi:10.1021/acs.macromol.7b00502
43. Du, Y.; Pearson, R. M.; Lim, C.-H.; Sartor, S. M.; Ryan, M. D.; Yang, H.; Damrauer, N. H.; Miyake, G. M. *Chem. – Eur. J.* **2017,** *23,* 10962–10968. doi:10.1002/chem.201702926
44. Zhang, M.; Li, W.; Duan, Y.; Xu, P.; Zhang, S.; Zhu, C. *Org. Lett.* **2016,** *18,* 3266–3269. doi:10.1021/acs.orglett.6b01515
45. Kharasch, M. S.; Skell, P. S.; Fisher, P. *J. Am. Chem. Soc.* **1948,** *70,* 1055–1059. doi:10.1021/ja01183a053
46. The change in product ratio in polar solvents in favor of lactone product **1** could be due to nucleophilic substitution of Cl by the carboxylic acid of product **3**. This does not occur in benzene (vide infra).
47. Wei, X.-J.; Boon, W.; Hessel, V.; Noël, T. *ACS Catal.* **2017,** *7,* 7136–7140. doi:10.1021/acscatal.7b03019
48. Sharma, U. K.; Gemoets, H. P. L.; Schröder, F.; Noël, T.; Van der Eycken, E. V. *ACS Catal.* **2017,** *7,* 3818–3823. doi:10.1021/acscatal.7b00840
49. Straathof, N. J. W.; Tegelbeckers, B. J. P.; Hessel, V.; Wang, X.; Noël, T. *Chem. Sci.* **2014,** *5,* 4768–4773. doi:10.1039/c4sc01982b

50. Straathof, N. J. W.; Gemoets, H. P. L.; Wang, X.; Schouten, J. C.; Hessel, V.; Noël, T. *ChemSusChem* **2014,** *7,* 1612–1617. doi:10.1002/cssc.201301282
51. Tucker, J. W.; Zhang, Y.; Jamison, T. F.; Stephenson, C. R. J. *Angew. Chem., Int. Ed.* **2012,** *51,* 4144–4147. doi:10.1002/anie.201200961
52. Garlets, Z. J.; Nguyen, J. D.; Stephenson, C. R. J. *Isr. J. Chem.* **2014,** *54,* 351–360. doi:10.1002/ijch.201300136
53. Anselmo, M.; Basso, A.; Protti, S.; Ravelli, D. *ACS Catal.* **2019,** *9,* 2493–2500. doi:10.1021/acscatal.8b03875
54. Janiszewska, A. M.; Grzeszczuk, M. *Electroanalysis* **2004,** *16,* 1673–1681. doi:10.1002/elan.200303011
55. Israeli, A.; Patt, M.; Oron, M.; Samuni, A.; Kohen, R.; Goldstein, S. *Free Radical Biol. Med.* **2005,** *38,* 317–324. doi:10.1016/j.freeradbiomed.2004.09.037
56. Gerken, J. B.; Stahl, S. S. *ACS Cent. Sci.* **2015,** *1,* 234–243. doi:10.1021/acscentsci.5b00163
57. Valencia, D. P.; Astudillo, P. D.; Galano, A.; González, F. J. *Org. Biomol. Chem.* **2013,** *11,* 318–325. doi:10.1039/c2ob26961a
58. Guo, T.; Zhang, L.; Liu, X.; Fang, Y.; Jin, X.; Yang, Y.; Li, Y.; Chen, B.; Ouyang, M. *Adv. Synth. Catal.* **2018,** *360,* 4459–4463. doi:10.1002/adsc.201800761
59. Chen, Y.; Lu, P.; Wang, Y. *Org. Lett.* **2019,** *21,* 2130–2133. doi:10.1021/acs.orglett.9b00443
60. Rahman, M.; Mukherjee, A.; Kovalev, I. S.; Kopchuk, D. S.; Zyryanov, G. V.; Tsurkan, M. V.; Majee, A.; Ranu, B. C.; Charushin, V. N.; Chupakhin, O. N.; Santra, S. *Adv. Synth. Catal.* **2019,** *361,* 2161–2214. doi:10.1002/adsc.201801331
61. Garreau, M.; Le Vaillant, F.; Waser, J. *Angew. Chem., Int. Ed.* **2019,** *58,* 8182–8186. doi:10.1002/anie.201901922
62. Kammer, L. M.; Lipp, B.; Opatz, T. *J. Org. Chem.* **2019,** *84,* 2379–2392. doi:10.1021/acs.joc.8b02759
63. Cartwright, K. C.; Tunge, J. A. *ACS Catal.* **2018,** *8,* 11801–11806. doi:10.1021/acscatal.8b03282
64. Shu, C.; Mega, R. S.; Andreassen, B. J.; Noble, A.; Aggarwal, V. K. *Angew. Chem., Int. Ed.* **2018,** *57,* 15430–15434. doi:10.1002/anie.201808598
65. Hsieh, H.-W.; Coley, C. W.; Baumgartner, L. M.; Jensen, K. F.; Robinson, R. I. *Org. Process Res. Dev.* **2018,** *22,* 542–550. doi:10.1021/acs.oprd.8b00018
66. Guo, J.; Huang, G.-B.; Wu, Q.-L.; Xie, Y.; Weng, J.; Lu, G. *Org. Chem. Front.* **2019,** *6,* 1955–1960. doi:10.1039/c9qo00380k
67. Sakakibara, Y.; Ito, E.; Fukushima, T.; Murakami, K.; Itami, K. *Chem. – Eur. J.* **2018,** *24,* 9254–9258. doi:10.1002/chem.201802143
68. Chen, H.; He, Y.; Zhou, L. *Org. Chem. Front.* **2018,** *5,* 3240–3244. doi:10.1039/c8qo00970h
69. Guo, J.; Wu, Q.-L.; Xie, Y.; Weng, J.; Lu, G. *J. Org. Chem.* **2018,** *83,* 12559–12567. doi:10.1021/acs.joc.8b01849
70. Song, H.-T.; Ding, W.; Zhou, Q.-Q.; Liu, J.; Lu, L.-Q.; Xiao, W.-J. *J. Org. Chem.* **2016,** *81,* 7250–7255. doi:10.1021/acs.joc.6b01360
71. Tian, W.-F.; Hu, C.-H.; He, K.-H.; He, X.-Y.; Li, Y. *Org. Lett.* **2019,** *21,* 6930–6935. doi:10.1021/acs.orglett.9b02539
72. Sherwood, T. C.; Li, N.; Yazdani, A. N.; Dhar, T. G. M. *J. Org. Chem.* **2018,** *83,* 3000–3012. doi:10.1021/acs.joc.8b00205
73. Ramirez, N. P.; Gonzalez-Gomez, J. C. *Eur. J. Org. Chem.* **2017,** 2154–2163. doi:10.1002/ejoc.201601478
74. Johnston, C. P.; Smith, R. T.; Allmendinger, S.; MacMillan, D. W. C. *Nature* **2016,** *536,* 322–325. doi:10.1038/nature19056

License and Terms

This is an Open Access article under the terms of the Creative Commons Attribution License (https://creativecommons.org/licenses/by/4.0). Please note that the reuse, redistribution and reproduction in particular requires that the authors and source are credited.

The license is subject to the *Beilstein Journal of Organic Chemistry* terms and conditions: (https://www.beilstein-journals.org/bjoc)

The definitive version of this article is the electronic one which can be found at:
doi:10.3762/bjoc.16.38

BEILSTEIN JOURNAL OF ORGANIC CHEMISTRY

Photocatalytic deaminative benzylation and alkylation of tetrahydroisoquinolines with *N*-alkylpyrydinium salts

David Schönbauer[1], Carlo Sambiagio[2], Timothy Noël[2] and Michael Schnürch[*1]

Full Research Paper

Open Access

Address:
[1]Institute of Applied Synthetic Chemistry, TU Wien, Getreidemarkt 9/163, 1060 Vienna, Austria and [2]Department of Chemical Engineering and Chemistry, Micro Flow Chemistry and Synthetic Methodology, Eindhoven University of Technology, Den Dolech 2, 5612 AZ Eindhoven, The Netherlands

Email:
Michael Schnürch[*] - michael.schnuerch@tuwien.ac.at

* Corresponding author

Keywords:
C–H functionalization; C(sp^3)–C(sp^3) coupling; deaminative coupling; Katritzky salt; photoredox catalysis

Beilstein J. Org. Chem. **2020,** *16,* 809–817.
doi:10.3762/bjoc.16.74

Received: 04 February 2020
Accepted: 04 April 2020
Published: 21 April 2020

This article is part of the thematic issue "Advances in photoredox catalysis" and is dedicated to Professor Marko D. Mihovilovic on the occasion of his 50th birthday.

Associate Editor: J. A. Murphy

© 2020 Schönbauer et al.; licensee Beilstein-Institut.
License and terms: see end of document.

Abstract

A ruthenium-catalyzed photoredox coupling of substituted *N*-aryltetrahydroisoquinolines (THIQs) and different bench-stable pyridinium salts was successfully developed to give fast access to 1-benzyl-THIQs. Furthermore, secondary alkyl and allyl groups were also successfully introduced via the same method. Additionally, the typically applied *N*-phenyl group in the THIQ substrate could be replaced by the cleavable *p*-methoxyphenyl (PMP) group and successful N-deprotection was demonstrated.

Introduction

The selective formation of new carbon–carbon bonds via direct C–H functionalization bears the potential of being a process of high efficiency [1-3]. Since C–H bonds are omnipresent in organic compounds it is very appealing to exploit them as "functional groups", avoiding tedious prefunctionalization. However, the ubiquity of C–H bonds gives rise to another problem, namely selectivity. Since the bond strength of C–H bonds in a typical organic compound varies only by a few kcal/mol, it is difficult to address a single C–H bond selectively without compromising the others. To circumvent this problem, directing groups can be installed, which guide a metal catalyst to a specific C–H bond [4,5]. In case the directing group is not needed in the final product, this strategy accounts for additional reaction steps for the installation and removal of the directing group. However, there is also a good number of substrates containing C–H bonds that are inherently more reactive than others in the same molecule, and in such cases a selective C–H functionalization can be achieved in the absence of any directing group [2,6,7]. For example, in tetrahydroisoquinolines (THIQs) the benzylic C1-position is significantly more reactive compared to the others and its selective functionalization has been reported [8]. The THIQ moiety is of special interest due to its presence in several different natural products [9] and pharmaceuticals [10,11]. Consequently, the direct functionalization of this scaf-

fold has attracted significant interest in recent years. Even though many transformations have been realized via a cross-dehydrogenative coupling approach [12,13] (e.g., arylations [14,15], cyanomethylation [16], alkynation [17,18], or allylation [19]), this method has certain drawbacks, most importantly the frequent requirement of superstoichiometric amounts of an oxidant. Hence, alternative methods were investigated and photoredox catalysis proved to be a viable option [20-22].

By now, several different methods for C–C bond formation at the α position of these amines have been studied under photoredox catalysis (Scheme 1) [23-26].

Among the functionalized THIQs, 1-benzyl-substituted analogues were shown to be able to modulate Ca/K channels, and the synthesis of these compounds is therefore of interest [27]. In our continuing quest to develop methods for the introduction of pure hydrocarbon residues avoiding volatile reagents [28,29], our attention was drawn to stable *N*-alkyl-(2,4,6-triphenyl)pyridinium salts (Katritzky salts) as alkylation reagents in the context of non-directed C–H functionalization. These salts are known since the late 1970s [30], but only in the last few years they have found application in a wide variety of radical processes, initiated by a single-electron reduction of the pyridinium salts, and subsequent generation of alkyl radicals [31-34]. Among these, electrophilic alkyl radicals were used in several transformations, such as electrophilic cross couplings under nickel catalysis, either with boronic acids [35] or different (aryl)halides [36-38]. Furthermore, visible light-promoted uncatalyzed electron transfer via the formation of electron donor–acceptor (EDA) complexes [39] was established between Hantzsch esters and pyridinium salts generating radicals, which were coupled with several substrates [40]. Later, methods without sacrificial reductant were also established, forming an EDA complex between the used substrates. Examples of this strategy are borylations [41,42], heteroarylations [43], and thioesterifications [44]. Additionally, several methods using photoredox chemistry were also published. For instance, the alkylation of isoquinolines under iridium catalysis and alkynylation with eosin Y as the catalyst [45,46].

In this contribution, we demonstrate the deaminative coupling of *N*-benzylpyridinium Katritzky salts with THIQs under ruthenium photoredox catalysis. During the preparation of this

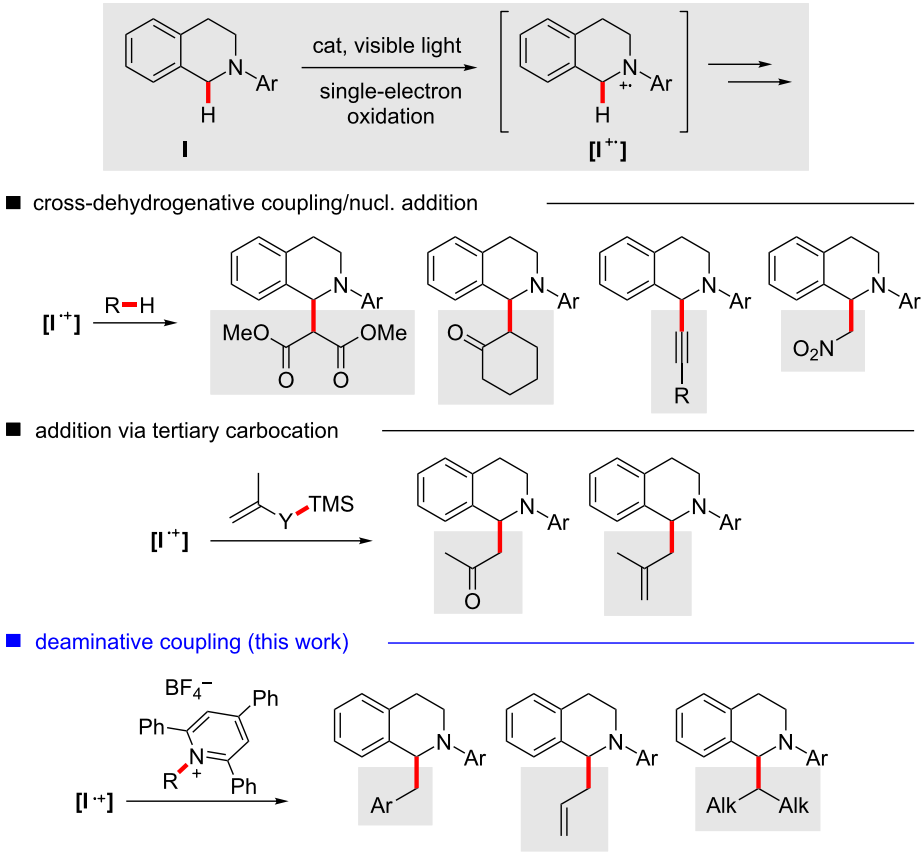

Scheme 1: Examples of photocatalytic C–C bond formation by nucleophilic trapping of a reactive THIQ intermediate.

article, a similar transformation was disclosed using an iridium photoredox catalyst [47].

Results and Discussion

We started our investigations by screening the coupling between *N*-phenyl-THIQ (**1**) with *N*-benzyl-(2,4,6-triphenyl)pyridinium tetrafluoroborate (**2**, Table 1; the complete optimization table can be found in Supporting Information File 1). First, a screening of different photocatalysts was performed (Table 1, entries 1–4). The best results were obtained with $[Ru(bpy)_3]Cl_2$, albeit the reaction was still low-yielding (29%, Table 1, entry 1) and was accompanied with substantial decomposition of the starting material. Eosin Y, fluorescein, and $[Ir(dtbbpy)(ppy)_2]PF_6$ gave lower yields in comparison (Table 1, entries 2, 3 and 4). Applying strictly inert conditions did not improve the yield, but decomposition of **1** was significantly reduced (Table 1, entry 5). Next, a solvent screening (Table 1, entries 6–12) was performed, showing that reactions in DMSO, DMA, DMF, or DMA/ACN 1:1 improved the yield to >50%, with mass balances of 78–91%. DCE and DCM had no beneficial effects on the yield. Different ratios of substrate and salt had also no impact on the yield (Table 1, entries 13 and

Table 1: Selected optimization of the reaction conditions.[a]

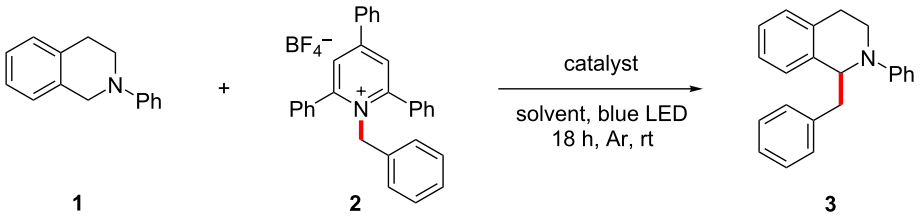

1 0.2 mmol + **2** 1.05 equiv → **3**

entry	catalyst [5 mol %]	solvent	**1**	**3**
1[b]	$[Ru(bpy)_3]Cl_2$	ACN (0.1 M)	14%	29%
2[b]	eosin Y	ACN (0.1 M)	36%	21%
3[b]	fluorescein	ACN (0.1 M)	74%	13%
4	$[Ir(dtbbpy)(ppy)_2]PF_6$	ACN (0.1 M)	9%	21%
5[c]	$[Ru(bpy)_3]Cl_2$	ACN (0.1 M)	54%	30%
6[d]	$[Ru(bpy)_3]Cl_2$	ACN (0.1 M)	6%	33%
7	$[Ru(bpy)_3]Cl_2$	DCE (0.1 M)	63%	22%
8	$[Ru(bpy)_3]Cl_2$	DCM (0.1 M)	55%	25%
9	$[Ru(bpy)_3]Cl_2$	DMSO (0.1 M)	27%	55%
10	$[Ru(bpy)_3]Cl_2$	DMA (0.1 M)	27%	51%
11	$[Ru(bpy)_3]Cl_2$	DMF (0.1 M)	37%	54%
12	$[Ru(bpy)_3]Cl_2$	DMA/ACN (0.1 M)	24%	58%
13[e]	$[Ru(bpy)_3]Cl_2$	DMF (0.1 M)	34%	56%
14[f]	$[Ru(bpy)_3]Cl_2$	DMF (0.1 M)	41%	56%
15	$[Ru(bpy)_3]Cl_2$	DMA/ACN (0.05 M)	14%	67%
16[g]	$[Ru(bpy)_3]Cl_2$	DMA/ACN (0.05 M)	21%	64%
17[b,g]	$[Ru(bpy)_3]Cl_2$	DMA/ACN (0.05 M)	12%	73% (64%)
18[g]	$[Ru(bpy)_3](PF_6)_2$	DMA/ACN (0.05 M)	33%	57%
19[g]	$[Ir(dtbbpy)(ppy)_2]PF_6$	DMA/ACN (0.05 M)	18%	69%
20[g]	eosin Y	DMA/ACN (0.05 M)	77%	12%
21[g,h]	$[Ru(bpy)_3]Cl_2$	DMA/ACN (0.05 M)	19%	33%
22[g,i]	$[Ru(bpy)_3]Cl_2$	DMA/ACN (0.05 M)	15%	67%
23[g,j]	$[Ru(bpy)_3]Cl_2$	DMA/ACN (0.05 M)	27%	32%
24[b]	–	DMA/ACN (0.05 M)	73%	18%
25[b,g,k]	$[Ru(bpy)_3]Cl_2$	DMA/ACN (0.05 M)	91%	9%

[a]Yields refer to calibrated GC yields. Numbers in parentheses are isolated yields. If not otherwise noted, 5 mol % catalyst and a 6 W LED were used; [b]18 W LED; [c]degassed solvent; [d]ambient atmosphere; [e]**1a**/**2a** 1.0:1.3; [f]**1a**/**2a** 1.3:1.0; [g]2 mol % catalyst; [h]K_2CO_3 (1.5 equiv) was added; [i]lutidine (1.5 equiv) was added; [j]DIPEA (1.5 equiv) was added; [k]no light.

14). However, the isolated yield was increased to 67% when using a 1:1 mixture of DMA/ACN and a concentration of 0.05 M instead of 0.10 M (Table 1, entry 15). Additionally, the catalyst loading could be decreased to 2 mol % without negative effects (cf. entries 15 and 16 in Table 1). Further dilution gave no further improvement in the yield (see Supporting Information File 1). Next, increasing the power of the LEDs from 6 to 18 W gave 73% GC yield and a 64% isolated yield of **3** (Table 1, entry 17; see also Scheme 2). Different catalysts were then reinvestigated using the DMA/ACN solvent mixture at 0.05 M concentration. $[Ru(bpy)_3](PF_6)_2$ led to a decreased yield of 57% (Table 1, entry 18), whereas $[Ir(dtbbpy)(ppy)_2]PF_6$ showed a comparable efficiency (69%, Table 1, entry 19). Eosin Y was inefficient under these conditions (Table 1, entry 20). Since $[Ru(bpy)_3]Cl_2$ is significantly cheaper than the iridium catalyst, the former was used in further reactions. Regarding the addition of different bases, the yield remained unchanged, when lutidine was added. Potassium carbonate and DIPEA reduced the yield substantially (Table 1, entries 21–23). Separate control experiments without catalyst (Table 1, entry 24) or in the dark (Table 1, entry 25) gave no or little conversion to the product, indicating the catalytic role of the ruthenium complex.

With the optimized reaction conditions in hand, we looked at the kinetic profile of the transformation in order to determine the ideal reaction time. The kinetic profile clearly showed that the product formation stopped after approximately 5–6 hours, with further reaction time only resulting in lower mass balance, suggesting possible decomposition of the reaction components (Figure 1).

Then, the substrate scope of the transformation was investigated, reacting different benzylic pyridinium salts with *N*-phenyl-THIQ (**1**, Scheme 2). Initially, steric effects were investigated using *ortho*, *meta*, and *para*-methylated benzylpyridinium salts. The *para*-substituted product **6** was isolated in 64% yield, and the two sterically more congested products **4** and **5** gave about 10% lower yields (Scheme 2). This went in line with the similarly sterically demanding 2-methylnaphthyl product **7**, which was obtained in 50% yield. Halides, such as bromo and fluoro substituents were also well tolerated. Especially the *para*-bromo compound **8** was interesting, since the bromine provides a handle for further functionalization. The electron-withdrawing CF_3 group gave a good yield of **10** (61%), whereas the electron-donating methoxy group led to a decrease in yield (**11**, 44%). The α- and β-picolinylpyridinium salts gave significantly lower yields for **12** and **13** in comparison. In four examples, **3**, **9**, **10**, and **11**, the effect of longer reaction times was also investigated, and experiments with 18 h reaction time were carried out. It was found that the yields were within the experimental error for three of the examples, while for compound **10**, a longer reaction time gave a significantly lower yield (50% vs 61%).

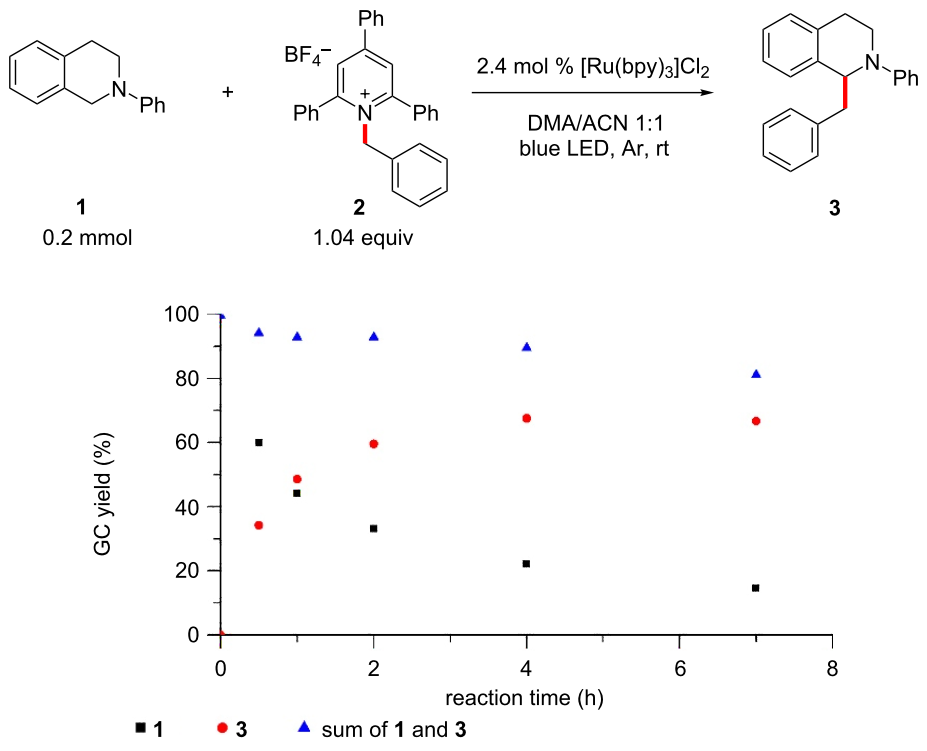

Figure 1: Kinetic profile for the benzylation of **1** to **3**.

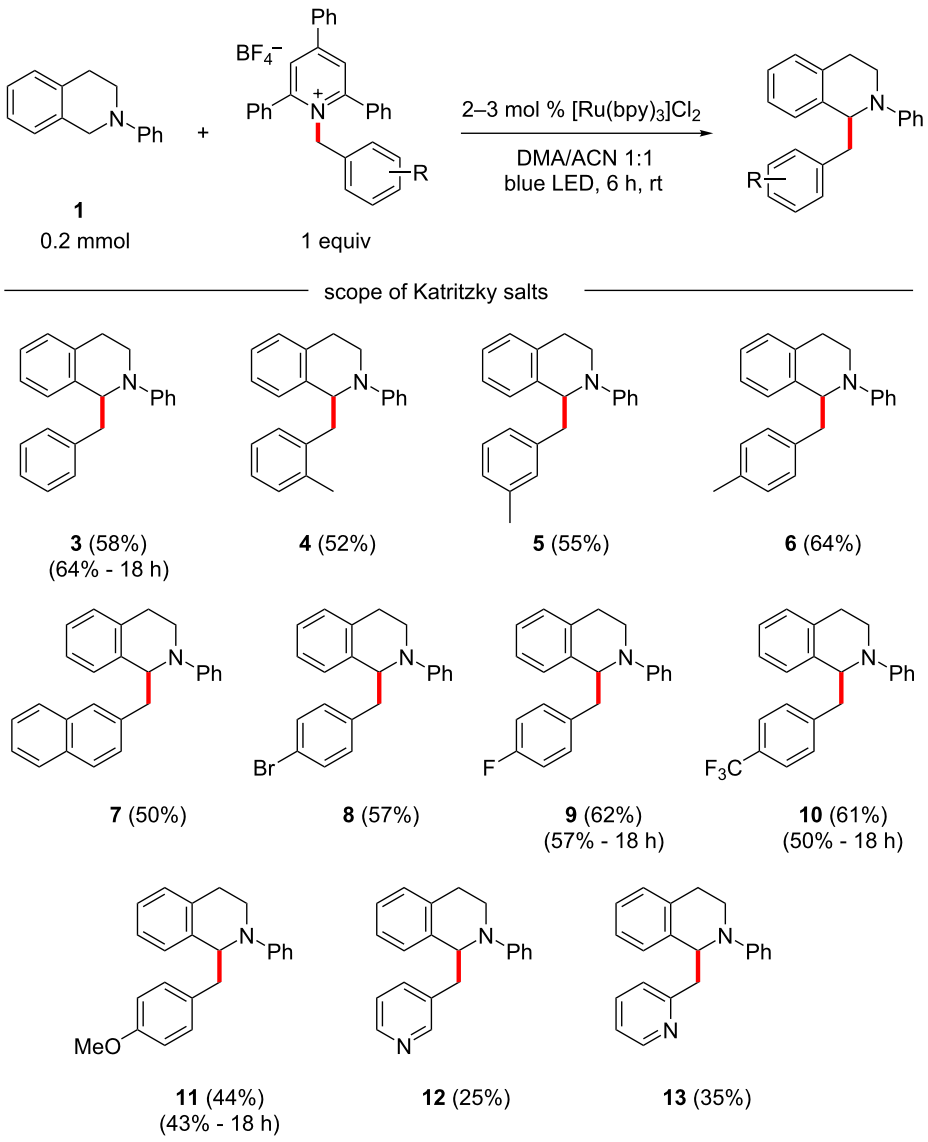

Scheme 2: Benzylation of *N*-phenyl-THIQ.

Next, differently substituted THIQs were tested with (substituted) benzylpyridinium salts as reaction partners (Scheme 3). Initially, different substituents on the *N*-phenyl group were investigated. Instead of the *N*-phenyl group, other protecting groups such as acetyl, benzoyl, or carbamates were tested, but the corresponding starting materials proved to be unreactive in the desired transformation. The use of substituted *N*-phenyl groups revealed that almost all of the substituents had a negative effect on the efficiency of the transformation, independently of their electronic effects (Scheme 3, **21**–**25**). Still, halides, nitriles, and ester substituents were tolerated, giving a possible handle for further manipulation. However, the presence of a nitro group impeded the reaction completely (not shown). Notably, PMP-protected THIQ was found to give a good yield of 61% (compound **24**), which was specifically important since this group is relatively easily removed, contrarily to the unsubstituted phenyl group. The benzylation of THIQ **14** was accompanied by small amounts (3%) of the bisbenzylated side product **21a**. According to NMR analysis (COSY, HSQC and HMBC, see Supporting Information File 1), this second benzyl group was attached to position 7 of the THIQ scaffold.

Additionally, the effect of different substituents on the THIQ core was investigated. A fluoro substituent in position 7 (in **19**) gave **26** in 44% yield after 6 h (Scheme 3). A more relevant substrate was the 6,7-dimethoxy-THIQ (**20**), since this struc-

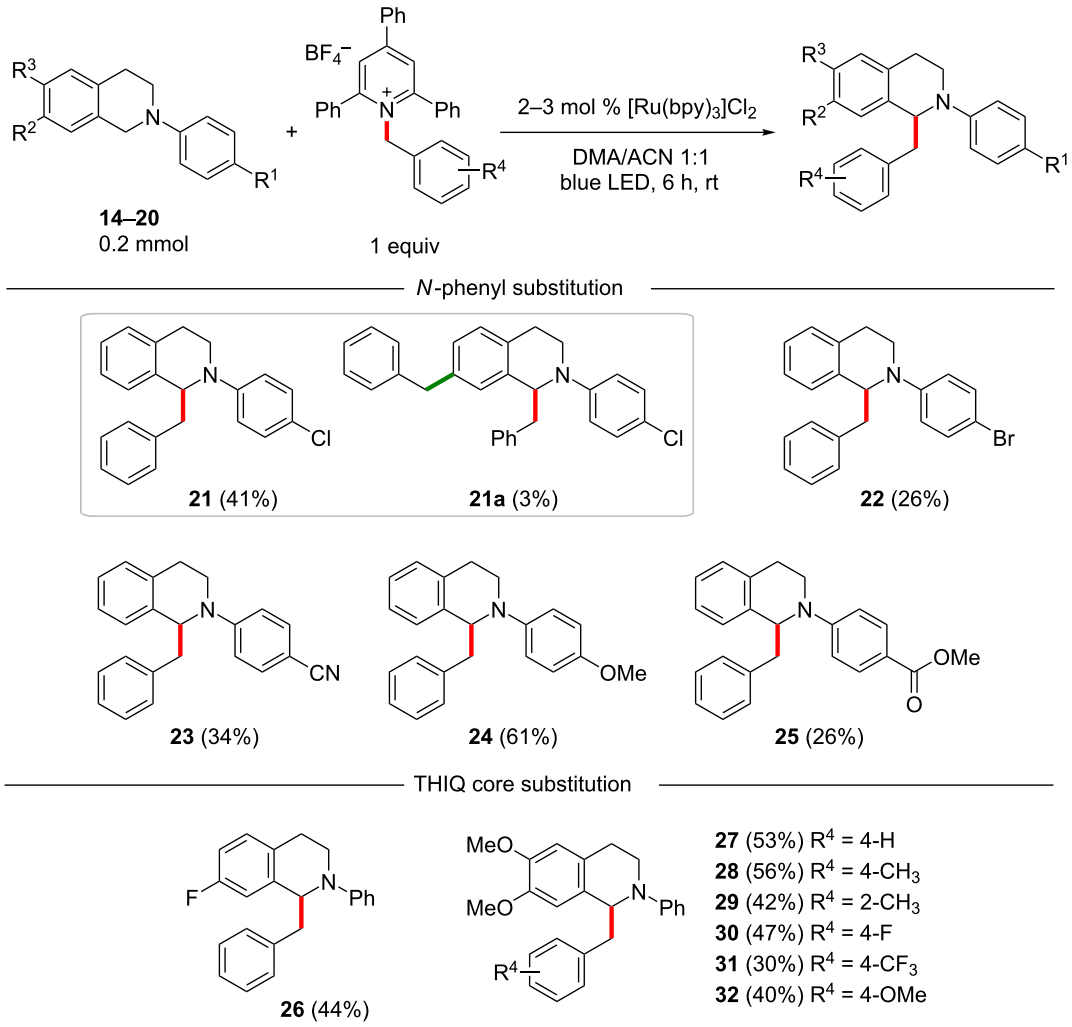

Scheme 3: Benzylation of substituted *N*-arylTHIQs.

tural motif occurs in many natural products. The yields were slightly lower as compared to the transformations on substrate **1**. The unsubstituted benzyl residue was incorporated to give **27** in 53% yield (vs 58% in 6 h for **3**). Again, a *p*-methylbenzyl substituent led to higher yields as compared to an *o*-methylbenzyl group (cf. Scheme 3, compounds **28** and **29**). Also, the *p*-F and *p*-CF_3-substituted products **30** and **31** were obtained in 47% and 30% yields, respectively. Interestingly, the *p*-OMe-substituted product **32** was obtained in only slightly lower yield as compared to the corresponding unsubstituted THIQ product **11**.

For better application in the synthesis of bioactive compounds or natural products, the removal of the aryl moiety on the nitrogen is necessary as most of these compounds are either free amines or N-alkylated [48,49]. Hence, we tested the oxidative cleavage of the PMP group of compound **24** (Scheme 4), with ceric ammonium nitrate (CAN) [50,51]. After column chromatography, 50% of the desired free amine were isolated, which made this method a viable route towards desired bioactive compounds.

At last, we turned our interest towards non-benzylic Katritzky salts, showcasing that also the reaction with unactivated secondary alkyl and allyl radicals takes place (Scheme 5). For the less reactive secondary alkyls the more expensive catalyst $[Ir(dtbbpy)(ppy)_2]PF_6$ had to be employed instead of $[Ru(bpy)_3]Cl_2$ [45,47]. Considerably lower conversion rates were observed in comparison to the benzylic radicals, which translated to longer reaction times for all the substrates tested. For the isoproplyation and *sec*-butylation, moderate yields of about 40% were observed after 60 h reaction time (**34** and **35**). For the cyclohexylation the yield was even lower and conversion stopped after 48 h (26%, **36**). When $[Ru(bpy)_3]Cl_2$ was

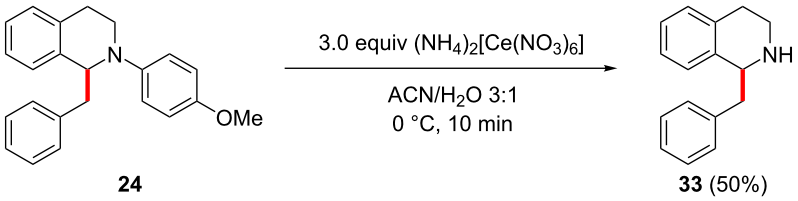

Scheme 4: Removal of the PMP protecting group.

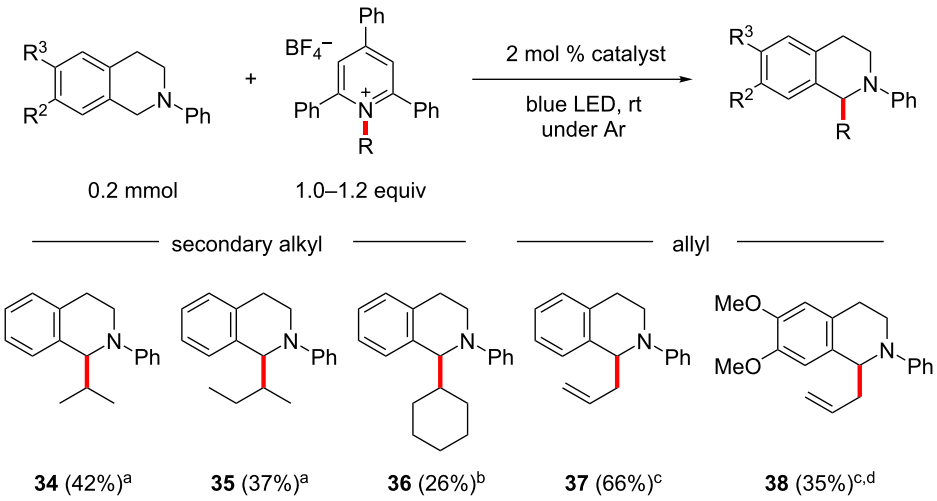

Scheme 5: Alkylation of *N*-phenyl-THIQ derivatives. Conditions: [a]2 mol % $[Ir(dtbbpy)(ppy)_2]PF_6$, DMA, 60 h; [b]2 mol % $[Ir(dtbbpy)(ppy)_2]PF_6$, DMA, 48 h; [c]2 mol % $[Ru(bpy)_3]Cl_2$, DMA/ACN 1:1, 6 h; [d]2 mol % $[Ru(bpy)_3]Cl_2$, DMA/ACN 1:1, 3 h.

used as the catalyst, GC–MS analysis of the crude material showed considerably less conversion in comparison. We found that Katritzky salts deriving from amino acids gave a complex reaction mixture, and the desired products could not be isolated. Additionally, alkyl salts derived from primary amines were unreactive.

For the more stable allyl radicals, our initially optimized conditions with $[Ru(bpy)_3]Cl_2$ in DMA/ACN were again applicable and the reaction time was kept at 6 h, or was even shortened to 3 h for 6,7-dimethoxy-*N*-phenyl-THIQ (products **37** and **38**). Allylation of the unsubstituted phenyl-THIQ was again more efficient compared to the dimethoxylated substrate.

Based on previous reports [45,47,52], we propose the following mechanism for the benzylation of *N*-aryl-THIQs [47]: After excitation of the catalyst, the Katritzky salt is reduced via SET, giving a Ru(III) species and intermediate **III**, followed by C–N cleavage to give benzylic radical **IV** and triphenylpyridine [45]. The Ru(II) catalyst is regenerated by another SET from the THIQ derivative. The now positively charged THIQ radical **I** is deprotonated to give neutral radical **II** [52]. Combination of **II** and **IV** finally furnishes the benzylated (alkylated) THIQ derivative (Scheme 6). The product formation by radical–radical coupling might explain why high yields were difficult to achieve.

Conclusion

In summary, we developed a photoredox-catalyzed C(sp^3)–H alkylation of *N*-aryltetrahydroisoquinolines under mild conditions. Easily accessible and bench-stable pyridinium salts were used as precursors for the required alkyl radicals. The transformation gives good to moderate yields using benzyl and allyl pyridinium salts. The introduction of secondary alkyl chains was also proved possible. Additionally, the crucial removal of a PMP protecting group to furnish unprotected THIQ was demonstrated, which enables this method to be used for the synthesis of natural products and bioactive substances. Further investigations in this direction are ongoing in our labaratories.

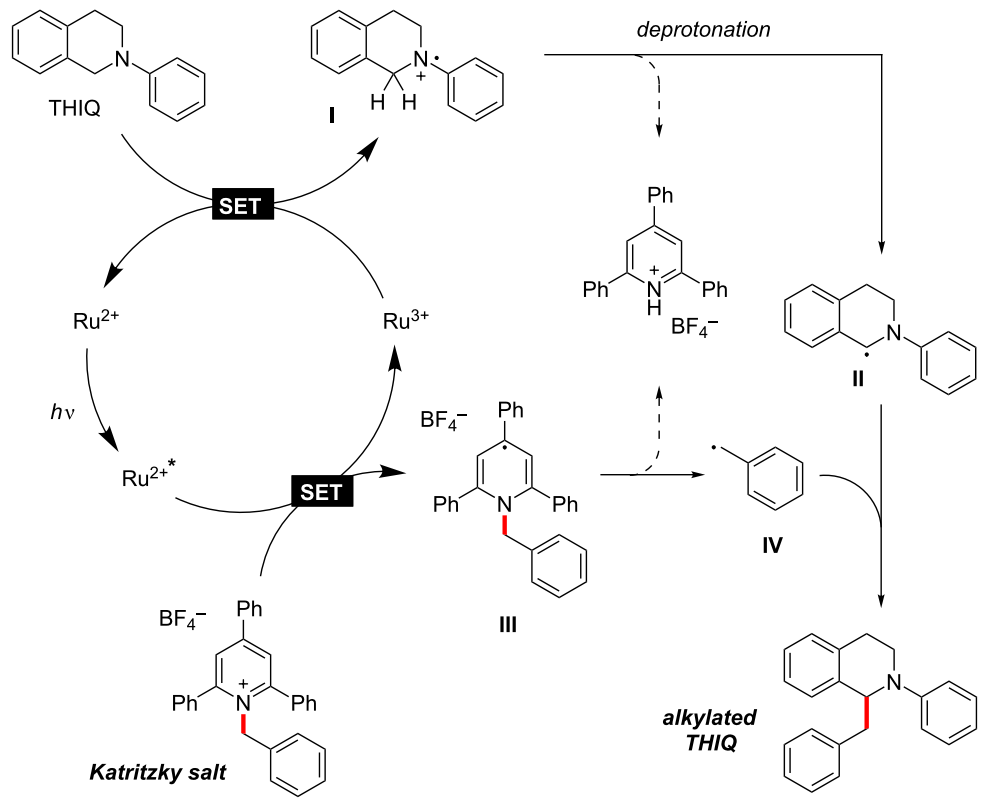

Scheme 6: Proposed mechanism.

Supporting Information

Supporting Information File 1

Experimental procedures, characterization data and copies of spectra.
[https://www.beilstein-journals.org/bjoc/content/supplementary/1860-5397-16-74-S1.pdf]

Funding

D.S. acknowledges CHAOS COST Action CA15106 for financial support of a STSM at Eindhoven University of Technology. C.S. acknowledges the European Union for a Marie Curie European Fellowship (FlowAct, Grant No.794072)

ORCID® iDs

David Schönbauer - https://orcid.org/0000-0001-7559-0787
Carlo Sambiagio - https://orcid.org/0000-0001-8536-103X
Michael Schnürch - https://orcid.org/0000-0003-2946-9294

References

1. Yi, H.; Zhang, G.; Wang, H.; Huang, Z.; Wang, J.; Singh, A. K.; Lei, A. *Chem. Rev.* **2017,** *117,* 9016–9085. doi:10.1021/acs.chemrev.6b00620
2. Liu, C.; Yuan, J.; Gao, M.; Tang, S.; Li, W.; Shi, R.; Lei, A. *Chem. Rev.* **2015,** *115,* 12138–12204. doi:10.1021/cr500431s
3. Hashiguchi, B. G.; Bischof, S. M.; Konnick, M. M.; Periana, R. A. *Acc. Chem. Res.* **2012,** *45,* 885–898. doi:10.1021/ar200250r
4. Chen, Z.; Wang, B.; Zhang, J.; Yu, W.; Liu, Z.; Zhang, Y. *Org. Chem. Front.* **2015,** *2,* 1107–1295. doi:10.1039/c5qo00004a
5. Sambiagio, C.; Schönbauer, D.; Blieck, R.; Dao-Huy, T.; Pototschnig, G.; Schaaf, P.; Wiesinger, T.; Zia, M. F.; Wencel-Delord, J.; Besset, T.; Maes, B. U. W.; Schnürch, M. *Chem. Soc. Rev.* **2018,** *47,* 6603–6743. doi:10.1039/c8cs00201k
6. Hartwig, J. F.; Larsen, M. A. *ACS Cent. Sci.* **2016,** *2,* 281–292. doi:10.1021/acscentsci.6b00032
7. Davies, H. M. L.; Morton, D. *J. Org. Chem.* **2016,** *81,* 343–350. doi:10.1021/acs.joc.5b02818
8. Li, Z.; Li, C.-J. *J. Am. Chem. Soc.* **2005,** *127,* 3672–3673. doi:10.1021/ja050058j
9. Bentley, K. W. *Nat. Prod. Rep.* **2005,** *22,* 249–268. doi:10.1039/b316108k
10. Scott, J. D.; Williams, R. M. *Chem. Rev.* **2002,** *102,* 1669–1730. doi:10.1021/cr010212u
11. Le, V. H.; Inai, M.; Williams, R. M.; Kan, T. *Nat. Prod. Rep.* **2015,** *32,* 328–347. doi:10.1039/c4np00051j
12. Li, Z.; Bohle, D. S.; Li, C.-J. *Proc. Natl. Acad. Sci. U. S. A.* **2006,** *103,* 8928–8933. doi:10.1073/pnas.0601687103
13. Boess, E.; Schmitz, C.; Klussmann, M. *J. Am. Chem. Soc.* **2012,** *134,* 5317–5325. doi:10.1021/ja211697s
14. Basle, O.; Li, C.-J. *Org. Lett.* **2008,** *10,* 3661–3663. doi:10.1021/ol8012588

15. Li, Z.; Li, C.-J. *J. Am. Chem. Soc.* **2005,** *127,* 6968–6969. doi:10.1021/ja0516054
16. Zhang, W.; Yang, S.; Shen, Z. *Adv. Synth. Catal.* **2016,** *358,* 2392–2397. doi:10.1002/adsc.201600050
17. Li, Z.; Li, C.-J. *Org. Lett.* **2004,** *6,* 4997–4999. doi:10.1021/ol047814v
18. Huang, T.; Liu, X.; Lang, J.; Xu, J.; Lin, L.; Feng, X. *ACS Catal.* **2017,** *7,* 5654–5660. doi:10.1021/acscatal.7b01912
19. Yan, C.; Liu, Y.; Wang, Q. *Org. Lett.* **2015,** *17,* 5714–5717. doi:10.1021/acs.orglett.5b03042
20. Sambiagio, C.; Noël, T. *Trends Chem.* **2020,** *2,* 92–106. doi:10.1016/j.trechm.2019.09.003
21. McAtee, R. C.; McClain, E. J.; Stephenson, C. R. J. *Trends Chem.* **2019,** *1,* 111–125. doi:10.1016/j.trechm.2019.01.008
22. Marzo, L.; Pagire, S. K.; Reiser, O.; König, B. *Angew. Chem., Int. Ed.* **2018,** *57,* 10034–10072. doi:10.1002/anie.201709766
23. Condie, A. G.; Gonzalez-Gomez, J. C.; Stephenson, C. R. J. *J. Am. Chem. Soc.* **2010,** *132,* 1464–1465. doi:10.1021/ja909145y
24. Freeman, D. B.; Furst, L.; Condie, A. G.; Stephenson, C. R. J. *Org. Lett.* **2012,** *14,* 94–97. doi:10.1021/ol202883v
25. Nakajima, K.; Miyake, Y.; Nishibayashi, Y. *Acc. Chem. Res.* **2016,** *49,* 1946–1956. doi:10.1021/acs.accounts.6b00251
26. Hou, H.; Zhu, S.; Atodiresei, I.; Rueping, M. *Eur. J. Org. Chem.* **2018,** 1277–1280. doi:10.1002/ejoc.201800117
27. Graulich, A.; Scuvée-Moreau, J.; Alleva, L.; Lamy, C.; Waroux, O.; Seutin, V.; Liégeois, J.-F. *J. Med. Chem.* **2006,** *49,* 7208–7214. doi:10.1021/jm0607395
28. Schönbauer, D.; Spettel, M.; Pollice, R.; Pittenauer, E.; Schnürch, M. *Org. Biomol. Chem.* **2019,** *17,* 4024–4030. doi:10.1039/c9ob00243j
29. Spettel, M.; Pollice, R.; Schnürch, M. *Org. Lett.* **2017,** *19,* 4287–4290. doi:10.1021/acs.orglett.7b01946
30. Bapat, J. B.; Blade, R. J.; Boulton, A. J.; Epsztajn, J.; Katritzky, A. R.; Lewis, J.; Molina-Buendia, P.; Nie, P.-L.; Ramsden, C. A. *Tetrahedron Lett.* **1976,** *17,* 2691–2694. doi:10.1016/s0040-4039(00)77797-5
31. Sowmiah, S.; Esperança, J. M. S. S.; Rebelo, L. P. N.; Afonso, C. A. M. *Org. Chem. Front.* **2018,** *5,* 453–493. doi:10.1039/c7qo00836h
32. He, F.-S.; Ye, S.; Wu, J. *ACS Catal.* **2019,** *9,* 8943–8960. doi:10.1021/acscatal.9b03084
33. Correia, J. T. M.; Fernandes, V. A.; Matsuo, B. T.; Delgado, J. A. C.; de Souza, W. C.; Paixão, M. W. *Chem. Commun.* **2020,** *56,* 503–514. doi:10.1039/c9cc08348k
34. Pang, Y.; Moser, D.; Cornella, J. *Synthesis* **2020,** *52,* 489–503. doi:10.1055/s-0039-1690703
35. Liao, J.; Guan, W.; Boscoe, B. P.; Tucker, J. W.; Tomlin, J. W.; Garnsey, M. R.; Watson, M. P. *Org. Lett.* **2018,** *20,* 3030–3033. doi:10.1021/acs.orglett.8b01062
36. Martin-Montero, R.; Yatham, V. R.; Yin, H.; Davies, J.; Martin, R. *Org. Lett.* **2019,** *21,* 2947–2951. doi:10.1021/acs.orglett.9b01016
37. Yue, H.; Zhu, C.; Shen, L.; Geng, Q.; Hock, K. J.; Yuan, T.; Cavallo, L.; Rueping, M. *Chem. Sci.* **2019,** *10,* 4430–4435. doi:10.1039/c9sc00783k
38. Ni, S.; Li, C.-X.; Mao, Y.; Han, J.; Wang, Y.; Yan, H.; Pan, Y. *Sci. Adv.* **2019,** *5,* eaaw9516. doi:10.1126/sciadv.aaw9516
39. Lima, C. G. S.; de M. Lima, T.; Duarte, M.; Jurberg, I. D.; Paixão, M. W. *ACS Catal.* **2016,** *6,* 1389–1407. doi:10.1021/acscatal.5b02386
40. Wu, J.; He, L.; Noble, A.; Aggarwal, V. K. *J. Am. Chem. Soc.* **2018,** *140,* 10700–10704. doi:10.1021/jacs.8b07103
41. Wu, J.; Grant, P. S.; Li, X.; Noble, A.; Aggarwal, V. K. *Angew. Chem., Int. Ed.* **2019,** *58,* 5697–5701. doi:10.1002/anie.201814452
42. Sandfort, F.; Strieth-Kalthoff, F.; Klauck, F. J. R.; James, M. J.; Glorius, F. *Chem. – Eur. J.* **2018,** *24,* 17210–17214. doi:10.1002/chem.201804246
43. James, M. J.; Strieth-Kalthoff, F.; Sandfort, F.; Klauck, F. J. R.; Wagener, F.; Glorius, F. *Chem. – Eur. J.* **2019,** *25,* 8240–8244. doi:10.1002/chem.201901397
44. Yang, M.; Cao, T.; Xu, T.; Liao, S. *Org. Lett.* **2019,** *21,* 8673–8678. doi:10.1021/acs.orglett.9b03284
45. Klauck, F. J. R.; James, M. J.; Glorius, F. *Angew. Chem., Int. Ed.* **2017,** *56,* 12336–12339. doi:10.1002/anie.201706896
46. Ociepa, M.; Turkowska, J.; Gryko, D. *ACS Catal.* **2018,** *8,* 11362–11367. doi:10.1021/acscatal.8b03437
47. Xu, Y.; Xu, Z.-J.; Liu, Z.-P.; Lou, H. *Org. Chem. Front.* **2019,** *6,* 3902–3905. doi:10.1039/c9qo01175g
48. Menachery, M. D.; Lavanier, G. L.; Wetherly, M. L.; Guinaudeau, H.; Shamma, M. *J. Nat. Prod.* **1986,** *49,* 745–778. doi:10.1021/np50047a001
49. Jangir, R.; Argade, N. P. *Synthesis* **2017,** *49,* 1655–1663. doi:10.1055/s-0036-1588920
50. Wuts, P. G. M.; Greene, T. W. Protection for the Amino Group. *Greene's Protective Groups in Organic Synthesis;* John Wiley & Sons: Hoboken, NJ, USA, 2006; pp 696–926. doi:10.1002/9780470053485.ch7
51. Wang, T.; Schrempp, M.; Berndhäuser, A.; Schiemann, O.; Menche, D. *Org. Lett.* **2015,** *17,* 3982–3985. doi:10.1021/acs.orglett.5b01845
52. Bartling, H.; Eisenhofer, A.; König, B.; Gschwind, R. M. *J. Am. Chem. Soc.* **2016,** *138,* 11860–11871. doi:10.1021/jacs.6b06658

License and Terms

This is an Open Access article under the terms of the Creative Commons Attribution License (http://creativecommons.org/licenses/by/4.0). Please note that the reuse, redistribution and reproduction in particular requires that the authors and source are credited.

The license is subject to the *Beilstein Journal of Organic Chemistry* terms and conditions: (https://www.beilstein-journals.org/bjoc)

The definitive version of this article is the electronic one which can be found at: doi:10.3762/bjoc.16.74

BEILSTEIN JOURNAL OF ORGANIC CHEMISTRY

Aldehydes as powerful initiators for photochemical transformations

Maria A. Theodoropoulou, Nikolaos F. Nikitas and Christoforos G. Kokotos*

Review

Open Access

Address:
Laboratory of Organic Chemistry, Department of Chemistry, National and Kapodistrian University of Athens, Athens 15784, Greece

Email:
Christoforos G. Kokotos* - ckokotos@chem.uoa.gr

* Corresponding author

Keywords:
aldehyde; green chemistry; photochemistry; photoinitiation; sustainable chemistry

Beilstein J. Org. Chem. **2020,** *16,* 833–857.
doi:10.3762/bjoc.16.76

Received: 16 February 2020
Accepted: 09 April 2020
Published: 23 April 2020

This article is part of the thematic issue "Advances in photoredox catalysis".

Guest Editor: T. Noël

© 2020 Theodoropoulou et al.; licensee Beilstein-Institut.
License and terms: see end of document.

Abstract

Photochemistry, the use of light to promote organic transformations, has been known for more than a century but only recently has revolutionized the way modern chemists are thinking. Except from transition metal-based complexes, small organic molecules have been introduced as catalysts or initiators. In this review, we summarize the potential that (aromatic or aliphatic) aldehydes have as photoinitiators. The photophysical properties and photoreactivity of benzaldehyde are initially provided, followed by applications of aldehydes as initiators for polymerization reactions. Finally, the applications to date regarding aldehydes as photoinitiators in organic synthesis are presented.

Introduction

Photochemistry, and especially photoredox catalysis have altered the way that modern researchers treat radical species [1-4]. In most cases, a metal-based photocatalyst is employed, having multiple advantages since ligand manipulation can lead to optimized photoredox properties. Unfortunately, the use of metals can pose some critical disadvantages in an organic process. Especially since the natural abundance of various noble metals that are used as photocatalysts is limited and since any pharmaceutically relevant compounds must not contain any metal contamination [5], the use of organic dyes is quite popular and can substitute the use of metal-based photocatalysts [6]. An alternative solution is the use of organic molecules as photocatalysts. There are already many reviews highlighting organocatalytically-mediated reactions [7-10] with potential in the field of photoorganocatalysis. The power of metal-based photocatalysts is indisputable and can be pinpointed through the ease that they can catalyze difficult photocatalytic reactions, such as the decarboxylation of aliphatic acids and the coupling of the residual chain with various electrophiles. Metal-based catalysts are common in reactions that require a high redox

potential for a single electron transfer (SET) procedure to take place. On the other hand, even if organocatalysts have lower redox potentials, they are capable to induce other types of reactions, such as hydrogen atom abstraction (HAT) processes or triplet state energy transfer processes (EnT). Carbonyl compounds, especially diaryl ketones, have shown great potential as far as their catalytic scope is concerned. Benzophenone or acetophenone (**64**) and similar derivatives have already been used in a plethora of chemical transformations, and their photochemical properties have been studied extensively [11]. In an attempt to mimic the potential of ketones, various aldehydes have been employed as photocatalysts or photoinitiators. Even if aromatic ketones are useful photocatalysts, the corresponding aldehydes are not so widely utilized to promote chemical reactions. In this review, our goal was to summarize the photophysical properties of aromatic aldehydes, highlight the use of aldehydes as photoinitiators in polymerization reactions, and provide all examples where aldehydes were employed as photoinitiators in organic synthesis.

Review

Photophysical properties of carbonyl compounds

The interest in the interaction of aldehydes with light to promote reactions can be traced many years back. In 1966, Davies and co-worker studied the energy transfer from aliphatic ketones and aldehydes to olefins upon excitation of the carbonyl compound [12]. More specifically, aliphatic ketones and aldehydes can absorb irradiation in the long-wavelength region (240–340 nm), which is then transformed into electronic excitation through the S_1 (n,π*) transition, excitation of a nonbonding electron on the oxygen atom to the first excited singlet state. This singlet state can lead to the corresponding triplet state T_1 (n,π*) through intersystem crossing. This triplet state can be quenched through various chemical transformations, like Norrish type I and Norrish type II dissociations (Scheme 1). However, when a possible energy acceptor is present, the triplet state energy can be transferred from the carbonyl compound to the acceptor, returning the carbonyl compound to the ground electronic state. For example, in reaction (1) of Scheme 1, the β-bond dissociation of methyl *n*-butyl ketone (**1**) yields acetone (**4**) and propylene (**3**). Reaction (2) of Scheme 1 refers to a type II intramolecular rearrangement of crotonaldehyde (**5**) to 3-butenal (**7**). The triplet state energy donors were quenched by diacetyl and *cis*-2-butene.

In 1970, Cocivera and Trozzollo studied the photolysis of benzaldehyde (**8**) in solution by NMR [13]. After recording the NMR spectra of ground-state benzaldehyde (**8**) and the derived products after irradiation, they were able to detect short-living paramagnetic intermediates, species with unpaired electrons, which, although existing in low concentration, could be detected because the unpaired electrons strongly polarized the nuclear spins. This type of polarization is retained when the intermediates return to their ground state. In order to account for the recorded spectrum, a radical pair formation between an excited molecule of benzaldehyde (**9**) and a ground-state molecule of benzaldehyde (**8**) was proposed. The excited molecule of benzaldehyde (**9**) could dissociate to a benzoyl radical (**10**) and a hydrogen atom or to a radical pair of a benzoyl radical (**10**) and an α-hydroxybenzyl radical (**11**), yielding a molecule of benzoin (**12**), which could be cleaved again upon irradiation, reforming the radical pair (Scheme 2).

At the same time, Closs and Paulson came to the same conclusions via chemically induced dynamic nuclear spin polarization (CIDNP) NMR studies of an irradiated solution of benzaldehyde (**8**) [14]. Interestingly, around the same time, Yang and co-workers showed that aldehydes can transfer their triplet state energy to an acceptor, inducing changes in the reactivity of the acceptor. Accordingly, the aldehyde can react with the higher-

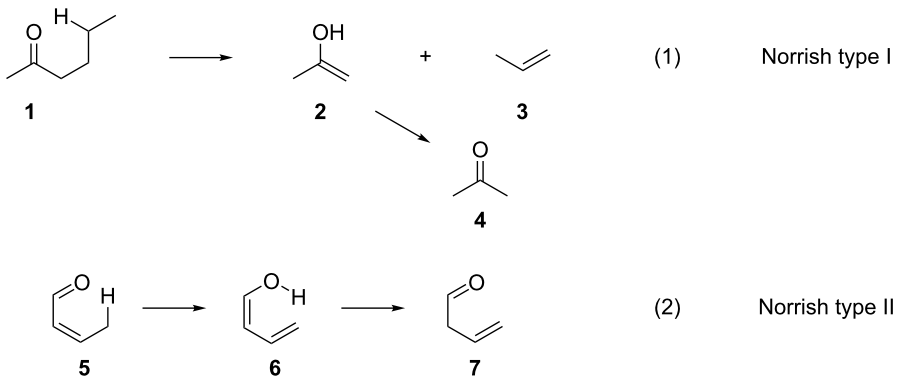

Scheme 1: Norrish type I and II dissociations.

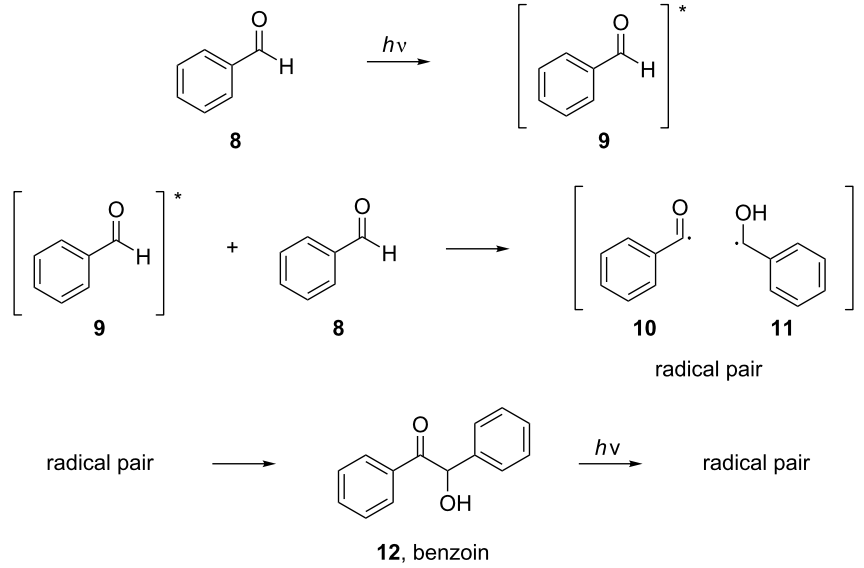

Scheme 2: Proposed radical pair formation after the photolysis of benzaldehyde (**8**).

energy-state olefin via a Paterno–Büchi reaction, indicating that benzaldehyde (**8**) can have an EnT ability comparable to that of known photocatalysts, such as aryl ketones (Scheme 3) [15-17].

Later, Steel and co-workers examined the photochemical properties of benzaldehyde (**8**), studying the EnT from **8** to azo compounds [18]. Upon the irradiation and excitation of benzaldehyde (**8**), the phosphorescence was quenched either by the formation of the radical pair mentioned in Scheme 2 or by a triplet state-energy acceptor, such as 2,3-diazabicyclo[2.2.1]hept-2-ene (DBH, **18**, Scheme 4).

Trying to shed more light on the photolysis of benzaldehyde, Atkins and co-workers studied the photolysis of benzaldehyde (**8**) with electron spin resonance flash photolysis (ESRFP) and CIDNP in various solvents, depending on the efficiency of the solvents as hydrogen donors [19]. More specifically, triplet state

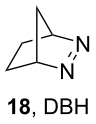

Scheme 4: 2,3-Diazabicyclo[2.2.1]hept-2-ene (DBH).

benzaldehyde (**9**) dissolved in an efficient hydrogen donor solvent can lead to an α-hydroxybenzyl radical (**11**) as the only detectable species, which will rapidly react with the solvent. In nondonating solvents, such as hexane, triplet state benzaldehyde (**9**) reacts with ground state benzaldehyde (**8**) to form a radical pair of a benzoyl radical (**10**) and an α-hydroxybenzyl radical (**11**). The formation of benzoin (**12**) was also detected in solvents that did not react with the excited benzaldehyde (**9**, Scheme 2).

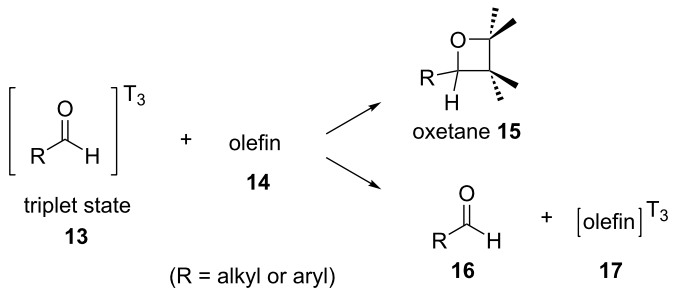

Scheme 3: Aldehydes in the Paterno–Büchi reaction.

Photoorganocatalysts are known for their ability to abstract hydrogen atoms from various substrates, furnishing radical species. Benzophenone is a very well-studied example of this category. Alongside with benzophenone and acetophenone, benzaldehyde (**8**) has also been studied for the ability to carry out HAT processes. In 1975, Obi and co-worker studied the photochemistry of excited benzaldehyde (**9**) with the use of electron paramagnetic resonance (EPR) [20]. They detected that the generated radicals from this process were the α-hydroxybenzyl (**11**) and the benzoyl radical (**10**). Also, their relative abundance showed that the α-hydroxybenzyl radical (**11**) was formed faster than the benzoyl radical (**10**), with the latter being probably a product of the direct dissociation of **9**. They suggested that benzaldehyde (**8**) and related compounds, such as aryl ketones, could participate in HAT processes as hydrogen atom abstractors [20]. More specifically, aldehydes can absorb irradiation at 300 nm and be excited from their ground state S_0 to their singlet state S_1 (n,π*), Then, through intersystem crossing (ISC), they can transition to a lower energy state T_2 (π,π*), which will subsequently drive them to a lower triplet state T_1 (n,π*), with the latter one being responsible for the specific reactivity of the carbonyl compounds [21,22]. During the photoexcitation of a carbonyl compound, and after they reach the T_2 excited triplet state, there are three possible dissociation pathways that can be followed (Scheme 5). Moreover, Reilly and co-workers observed the decomposition of benzaldehyde (**8**) into benzene (**21**) and carbon monoxide (**22**) (reaction (3) in Scheme 5) after the irradiation at 258.9 nm via laser ionization mass spectrometry and photoelectron spectroscopy [23].

In 1975, MacLauchlan and co-worker carried out a quantitative CIDNP study on the photolysis of benzaldehyde (**8**) in solution. They presented a possible pathway for the formation of the various radical species (Scheme 6) [24].

It was suggested that the triplet state of benzaldehyde (**9**) can abstract a hydrogen atom from a molecule of the solvent, furnishing a solvent molecule radical, which can propagate the radical chain route.

The photophysical properties of benzaldehyde (**8**) were thoroughly examined, allowing the researchers to better understand the source of this specific reactivity [25]. The triplet state energy of carbonyl compounds can also be transferred to halogen-containing compounds, leading to the homolytic dissociation of the carbon–halogen bond. This interaction has been studied for *tert*-butyl chloride, where the descendant radical is quite stabilized [26]. The electronic distribution and the spectroscopy of the excited states of benzaldehyde (**8**) have been examined. These studies illuminate the ways that the various excited states of benzaldehyde (**8**) decay, either through phosphorescence or through the dissociation to benzene (**21**) and carbon monoxide (**22**) or to a benzoyl radical (**10**) and a hydrogen atom (reactions (2) and (3) in Scheme 5). A practical application of these studies can be seen in the work of Kuhn et al., who demonstrated the use of the dissociation properties of benzaldehyde (**8**) and phenylglyoxylic acid in order to achieve highly deuterated products, which were more stable than the undeuterated ones upon irradiation and subsequent excitation [27,28]. The excited triplet state T_1 (n,π*) of carbonyl compounds tends to be the most reactive state (compared to the singlet state). Furthermore, this excited state is easily accessible, as the quantum yield for the formation of the triplet state is close to unity, as measured by Itoh [29].

The dissociation route depends on the reaction conditions. Recently, Zhu and Cronin studied the dissociation of benzaldehyde after photoexcitation at 280–320 nm. The most efficient wavelength was found to be 285 nm, and the followed pathway

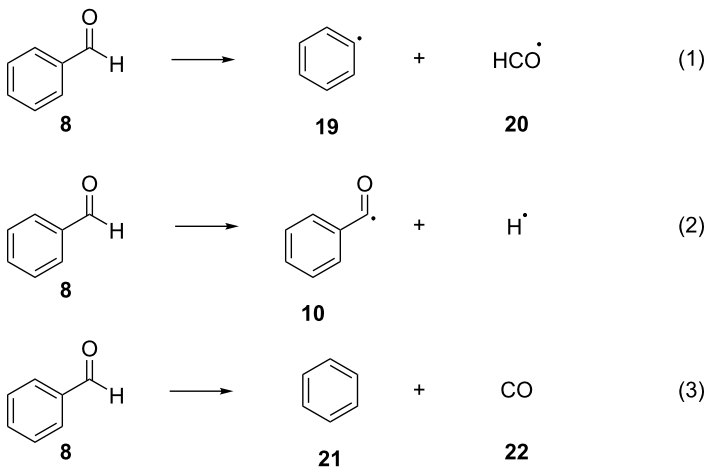

Scheme 5: Dissociation pathways of benzaldehyde.

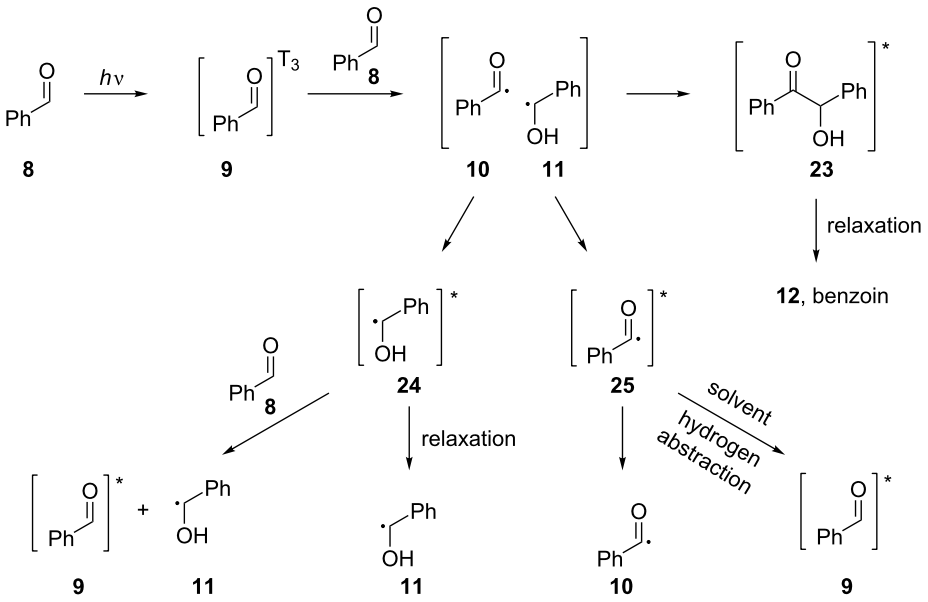

Scheme 6: Reactions that lead to polarized products detectable by CIDNP.

was the pathway described in reaction (1) of Scheme 5 [30]. In another study on the photochemical dissociation of benzaldehyde (**8**), Bagchi et al. detected two major routes, furnishing either a formyl radical (**20**, reaction (1) of Scheme 5) or carbon monoxide (**22**, reaction (3) of Scheme 5) upon photolysis at 248 nm and 265 nm, respectively, while upon irradiation at 193 nm, reaction (1) from Scheme 5 was the main pathway [31]. The main reason for not observing the reaction (2) from Scheme 5 was that the product, the benzoyl radical (**10**), could decompose rapidly upon irradiation, supporting the other two pathways. Also, mechanistic studies by Cui et al. showed that the energy levels of the reactions (1) and (2) in Scheme 5 were closely tied, so distinguishing them is not always trivial [32].

The triplet state quenching of **8** and related compounds, such as aryl ketones, has been studied and mentioned numerous times. More specifically, Turro and co-workers studied them with time-resolved electron spin resonance and laser flash spectroscopy. The photolysis of **8** showed that the fate of the triplet state of **8** was also dependent on the concentration of **8** and on the type of the solvent [33]. Where the concentration of the aldehyde **8** is relatively high and the solvent is a poor hydrogen donor, such as acetonitrile, the HAT process from the solvent will not occur. In this case, a self-reduction of the excited benzaldehyde (**9**) will occur, leading to the formation of a radical pair of an α-hydroxybenzyl radical (**11**) and a benzoyl radical (**10**). This upper statement shows the potential of benzaldehyde (**8**) compared to the related aryl ketones, which are known to be capable of HAT.

Until recently, the quenching of the fluorescence of excited benzaldehyde (**9**) was unreasonably thought to originate from the basicity of the aldehyde. A recent publication though came to empower the statement that the HAT properties of benzaldehyde (**8**) are responsible for the observed quenching of the fluorescence [34].

Aldehydes as photoinitiators for photochemical polymerizations

A number of carbonyl compounds, including aliphatic or aromatic ketones and aldehydes, have been employed as photoinitiators in polymerization reactions. The first studies reported in the literature where carbonyl compounds were used as initiators inspired researchers to study the use of aldehydes as well. In 1978, McGinniss and co-workers reported the polymerization of methyl methacrylate (**26**, MMA) by employing 4,4'-bis(*N*,*N*-diethylamino)benzophenone (**27**, DEABP) as the photoinitiator (Scheme 7) [35]. It was already well-accepted that aminoaromatic compounds, such as Michler's ketone (**28**) and DEABP (**27**), present large extinction coefficients and charge transfer states as well as relatively long-lived triplet states in solution, making them suitable as photoinitiators [36,37].

The irradiation and excitation of DEABP (**27**) to the singlet state is followed by intersystem crossing to the triplet state **29**, which then leads to two different types of free radical intermediates, **30** and **31** (Scheme 8). The species **31** was shown to be the primary initiating radical compound.

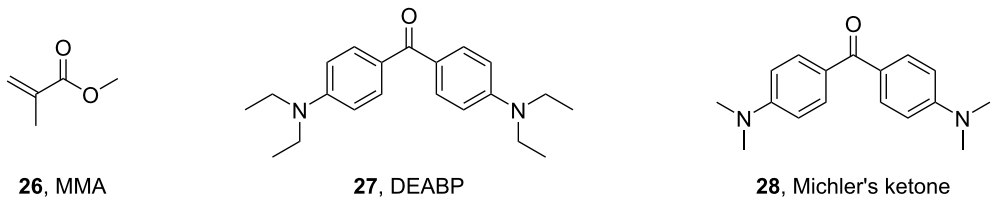

Scheme 7: MMA (**26**), DEABP (**27**), and Michler's ketone (**28**).

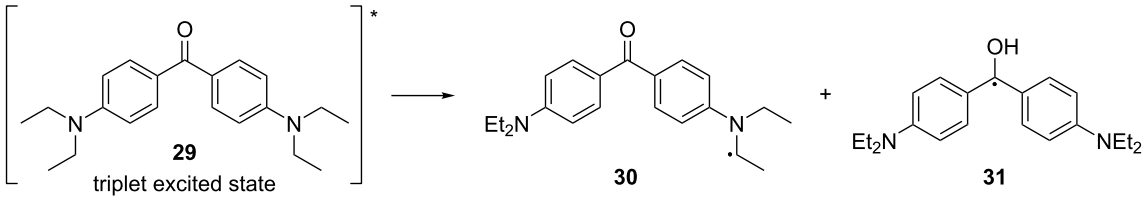

Scheme 8: Radical intermediates of DEABP.

In 2006, Aydin and Arsu employed benzaldehyde (**8**) as the coinitiator for the photoinitiated free radical polymerization of multifunctional MMA (**26**) [38]. Benzaldehyde (**8**) was tested as an alternative to tertiary amines, which are commonly employed in radical-mediated reactions due to their ability to bind to atmospheric oxygen, which inhibits such reactions. The quinoxalines **32** were used as the prime photoinitiators, and the reaction was placed in a photoreactor equipped with a cooling fan and lamps emitting at 350 nm at room temperature. The polymerization reaction led to good results. As depicted in Scheme 9, the postulated reason for the successful polymerization was that after the irradiation of benzaldehyde (**8**) with the quinoxalines **32**, the benzoyl radical (**10**) was formed from **8**. This was thought to be the initiating radical for the photoinitiated polymerization of monomeric MMA (**26**).

The photochemical properties of aliphatic aldehydes have also been employed in photografting. Even if they are not the most efficient photoinitiators, aliphatic aldehydes and ketones were studied in the photografting of acrylic acids. In 1988, Allméar and co-workers, while studying the grafting of acrylic acid (**34**) onto high- or low-density polyethylene and polystyrene using benzophenone as the photoinitiator and acetone (**4**) as the solvent, observed that the grafting was possible even in the absence of benzophenone due to acetone (**4**), but at a slower rate [39]. Later, Kubota and co-workers found that acetone (**4**) could act as an efficient photoinitiator for photografting, in contrast to other aliphatic ketones [40]. In 2004, Wang and co-workers also observed that acetone (**4**) could efficiently initiate photografting under UV irradiation when mixed with water [41] and performed a theoretical study on the matter a few years later [42]. The same research group later studied other aliphatic ketones for their efficiency in initiating photografting [43,44]. Recently, they reported that formaldehyde (**35**) could also act as a photoinitiator when employed for photografting even though it was not as efficient as acetone (**4**) (Scheme 10) [45].

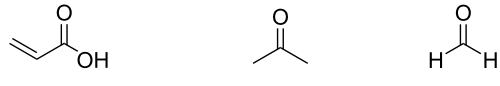

Scheme 10: Acetone (**4**) and formaldehyde (**35**) as photografting initiators.

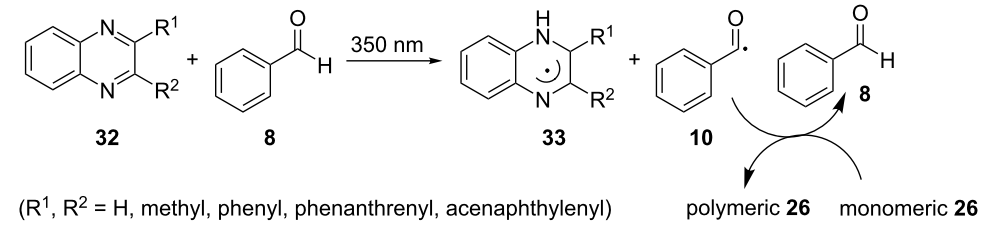

Scheme 9: Photoinitiated polymerization of monomeric MMA (**26**) using the quinoxalines **32** and benzaldehyde (**8**).

The proposed mechanism of action is depicted in Scheme 11. The same research group extended their study and found that acetaldehyde (**36**) was also capable of initiating the photografting of methacrylic acid (MAA, **42**) onto HDPE, highlighting that acetaldehyde (**36**) is a better initiator that outperformed formaldehyde (**35**) and acetone (**4**) [46].

In more detail, in 2011, Wang and co-workers studied the efficiency of acetaldehyde (**36**) as the photoinitiator for the photografting of MAA (**42**) onto high-density polyethylene (**39**) in an aqueous solution [46]. The light source was a high-pressure mercury UV lamp (2 kW), and a cooling fan was used in order to maintain ambient temperature. Acetaldehyde (**36**) proved to be more efficient than acetone (**4**) and formaldehyde (**35**) in initiating the photografting in an aqueous solution. The maximum extent of grafting was observed for 10 wt % of **36**. The concentration of **42** also affected the extent of photografting. The extent of grafting increased with the increase of the monomer up to 2 mol/L and then kept constant or slightly decreased. The possible initiation of the polymerization is presented in Scheme 11, where hydrogen bonding of **36** with water is crucial.

In 2013, Wang and co-workers also reported the use of aliphatic ketones and aldehydes as photoinitiators for the photopolymerization of **42** in aqueous solutions [47]. For the cases where the ketones or the aldehydes were not soluble in, or miscible with water, an amount of ethanol was added. The light source employed was a UV high-pressure mercury lamp (2 kW). All aliphatic ketones tested, including acetone (**4**), butanone, and pentan-2-one, as well as formaldehyde (**35**), efficiently initiated the polymerization of MAA (**42**), and butanone was the most efficient compound. Since acrylates and methacrylates can be photopolymerized by self-initiation, a blank experiment without the use of any aliphatic ketone **44** or formaldehyde (**35**) was carried out, indicating that the polymerization of MAA (**42**) was mainly induced by photoinitiation by the aliphatic ketones **44** or formaldehyde (**35**), rather than by self-initiation of the monomer. Furthermore, oxygen was shown to strongly inhibit the photopolymerization, and an increase in the UV intensity increased the percentage of conversion and the polymerization rate. Finally, the percentage of conversion decreased, whereas the polymerization rate increased with an increase of the initial monomer concentration since an increase in the concentration of the monomer led to MAA (**42**) absorbing more energy than acetone (**4**). The authors proposed that the photoinitiation mechanism for the photopolymerization of aliphatic ketones or aldehydes was similar to the one concerning photografting, and the mechanism is presented in Scheme 12 [42,44]. While the aliphatic ketones **44** did not exhibit photoinitiation when they were alone present in an aqueous solution, they tended to form hydrates **45** with water via hydrogen bonding. The hydrogen bonding increased the energy levels of the excited states of **45**, permitting the formation of radicals after UV light absorption [48]. These radicals either dissociated via Norrish type I reactions, forming two radicals, **47** and **48** (reaction (1) in Scheme 12), or abstracted a hydrogen atom from a ketone/aldehyde monomer, forming a monomeric radical and an alcohol radical **49** (reaction (2) in Scheme 12). The excited state of the hydrates **45** and **46**, in an aqueous solution may prefer to abstract a hydrogen atom from a ketone/aldehyde monomer molecule rather than to decompose, forming a monomeric radical, which can initiate the polymerization.

In 2017, Ma and co-workers performed a photoinduced controlled radical polymerization of methacrylates using perfluoro-1-iodohexane (**50**) as the polymerization initiator and benzaldehyde derivatives as organic photocatalysts [49]. 23 W compact fluorescent lamps were employed as the light source and *N,N*-dimethylaniline (**51**) was used as a potential reductant. The

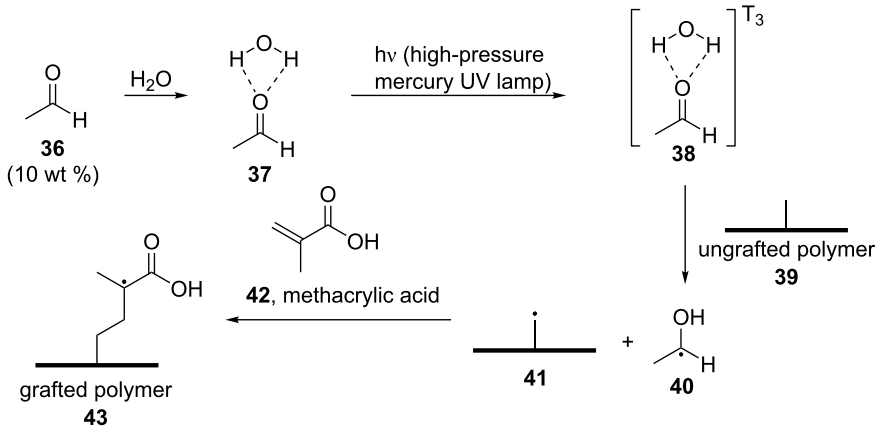

Scheme 11: Photografting by employing acetaldehyde (**36**) as the photoinitiator.

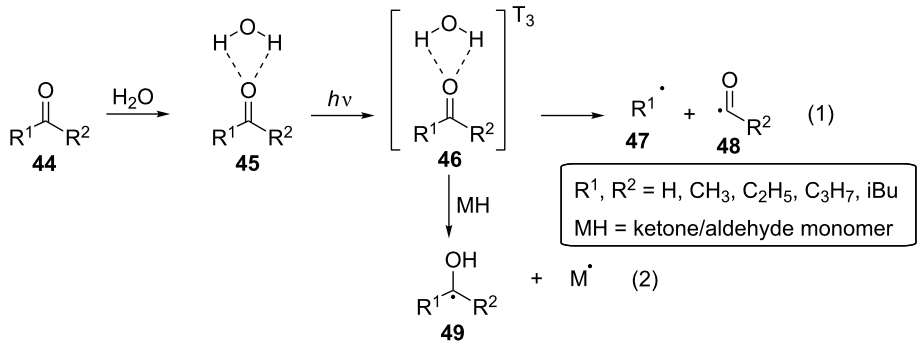

Scheme 12: Proposed photolysis mechanism for aliphatic ketones **44** and formaldehyde (**35**).

benzaldehyde derivatives tested are presented in Scheme 13 and included 4-anisaldehyde (**52**), 4-cyanobenzaldehyde (**53**), and 2,4-dimethoxybenzaldehyde (**54**), all three of which showed strong absorption bands below 340 nm.

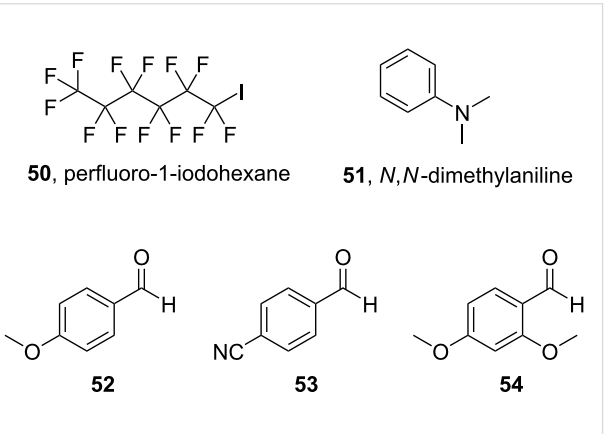

Scheme 13: Initiator **50**, reductant **51**, and benzaldehyde derivatives **52**–**54** for the polymerization of the methacrylates **59**.

As shown in Scheme 14, the excited state **55** of the benzaldehyde derivatives **52**–**54**, respectively, that occurred after irradiation could reduce perfluoro-1-iodohexane (**50**), generating a benzaldehyde radical cation (**56**) and the radical of the alkyl group C_6F_{13}, **58**, which was proposed to initiate the radical polymerization of a methacrylate monomer **59**. *N*,*N*-Dimethylaniline (**51**) acted as the reducing agent, regenerating the ground state of the benzaldehyde catalysts **52**–**54**, respectively, establishing an equilibrium between the dormant species and the active radicals, which was required for a controlled radical polymerization.

No polymerization product was detected in the absence of the benzaldehyde derivatives **52**–**54**, respectively, as well as when the polymerization was performed in darkness. Furthermore, the authors studied the effect of the concentration of the benzaldehyde derivative, the initiator, and *N*,*N*-dimethylaniline (**51**) and the molar ratio of the compounds.

Aldehydes as photoinitiators in organic synthesis

The knowledge of the photophysical properties of aldehydes and the ability of aldehydes to initiate chemical transformations after irradiation was the first milestone in using them as initiators in organic synthesis. In the meantime, the use of aldehydes as reagents in some chemical transformations that employ a light source for photoexcitation shed more light on some mechanistic pathways and set the key foundation for the further use as photoinitiators or photocatalysts.

In 1961, Hammond and co-workers studied the *cis*/*trans* isomerization of the piperylenes (1,3-pentadienes) **61** and **62** in the presence of carbonyl compounds as photosensitizers (Scheme 15) [50]. Among the compounds tested, 1-naphthaldehyde (**63**) provided a photostationary mixture rich in the *trans*-diene (*trans*/*cis* ratio ≈ 13). A year later, the same group further studied the *cis*/*trans* isomerization of the piperylenes **61** and **62** utilizing energy transfer from the triplet states of various aldehydes and ketones that were used as photosensitizers (Scheme 15) [51].

In more detail, a solution of *cis*-piperylene (**61**) in benzene in the presence of various carbonyl compounds was irradiated using a Hanovia quartz immersion reactor. It was shown that compounds that had a triplet state energy of 70 kcal/mol or more produced photostationary mixtures of a *trans*/*cis* ratio of ≈1.25. Such compounds were acetophenone (**64**), benzaldehyde (**8**), 4-hydroxybenzaldehyde (**65**), and 2-methoxybenzaldehyde (**66**). However, 9-anthraldehyde (**67**), which has a very low-lying triplet state below 50 kcal/mol, proved to be completely inactive as the photosensitizer. Also, no reaction was observed

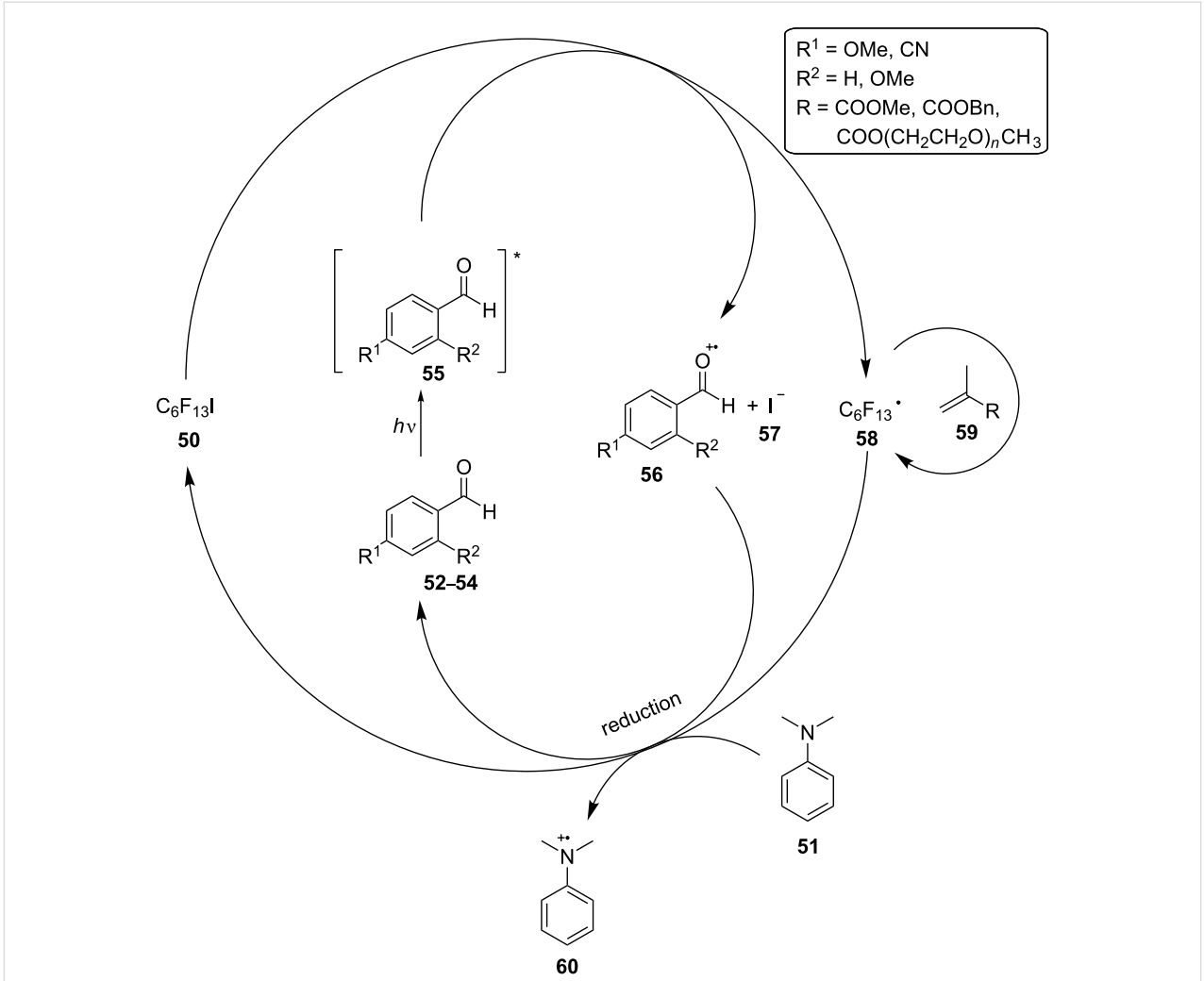

Scheme 14: Proposed mechanism of the photomediated atom transfer radical polymerization employing the benzaldehyde derivatives **52**–**54**, respectively, as the photocatalysts.

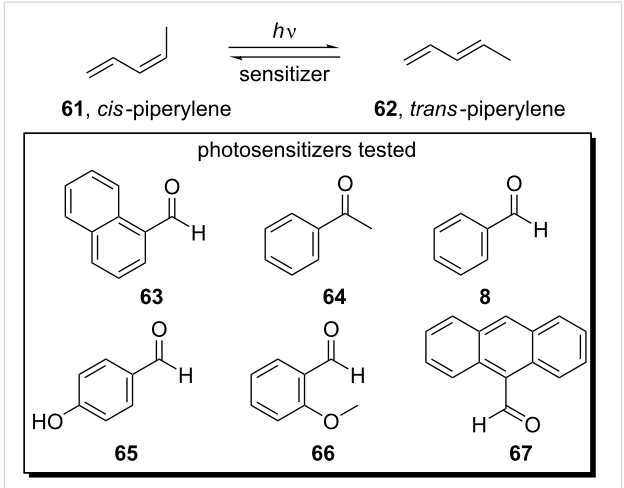

Scheme 15: *cis*/*trans* isomerization employing triplet states of photosensitizers.

when salicylaldehyde (**68**) was employed as a photosensitizer, despite of a triplet state energy of ≈70 kcal/mol, most probably due to an internal hydrogen bond (Scheme 16).

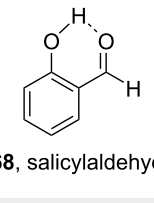

Scheme 16: Salicylaldehyde (**68**) forms an internal hydrogen bond.

As mentioned before, in the section on the photophysical properties of aldehydes, in 1968, Yang and co-workers investigated the mechanism of energy transfer from the triplet states of carbonyl compounds to simple olefins [15,16]. In more detail, in

order to find out if the excitation energy of the triplet state of the carbonyl compounds could be transferred to the olefins in the Paterno–Büchi reaction, they performed a photochemical reaction between benzaldehyde (**8**) or benzophenone and the 3-methyl-2-pentenes **69** and **70**, respectively. The isomerization of the starting olefins indicated a bimolecular energy transfer mechanism (Scheme 17).

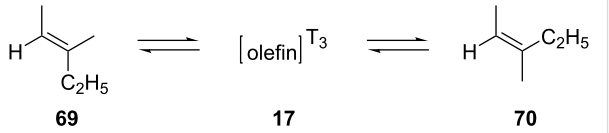

69 **17** **70**

Scheme 17: Olefin isomerization via energy transfer from a carbonyl compound.

Benzophenone proved to transfer the triplet state energy more efficiently than benzaldehyde (**8**). Furthermore, the triplet state of the carbonyl compound was thought to be the intermediate for both the Paterno–Büchi oxetane formation and the olefin isomerization. Two possible mechanistic pathways for the Paterno–Büchi reaction were described. The first one included an attack on the π-system of the olefin by the oxygen atom of the excited carbonyl compound, forming a biradical intermediate **72**. Then, the biradical intermediate **72** could either cyclize to produce an oxetane **73** or dissociate to form again the carbonyl compound **44** and a triplet state olefin molecule **17** in a nonplanar configuration. Both processes, oxetane formation and isomerization, were thought to proceed via the triplet state of benzaldehyde. The alternative pathway includes a polarization of the π-system of the olefin, forming a transition state intermediate **74** where the olefin moiety is no longer planar (Scheme 18).

In 1973, the same group investigated the photochemical addition of benzaldehyde (**8**), 4-methoxybenzaldehyde, 3-methoxybenzaldehyde, 3,4-dimethylenedioxybenzaldehyde, and 2-naphthaldehyde to isomeric 2-butenes after irradiation using a Hanovia 450 W mercury arc [17]. If the reaction proceeded stereospecifically, *cis*-2-butene would have led to the formation of the oxetanes **75a** and **75b**, while *trans*-2-butene would have led to the oxetanes **75c** and **75d** (Scheme 19). It was suggested that the reaction proceeded through a long-lived biradical intermediate and rotation of the C3–C4 bond could in principle lead

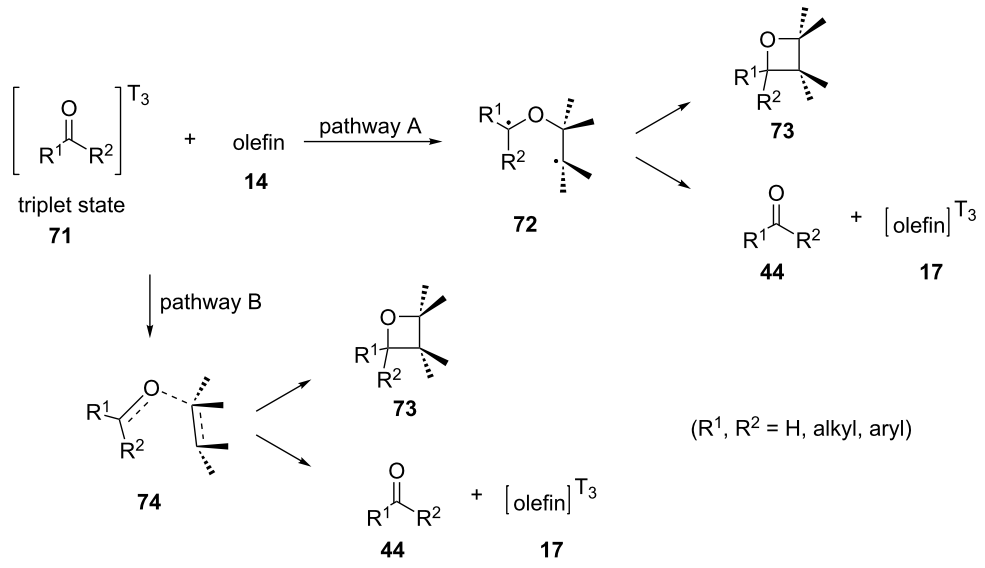

Scheme 18: Mechanistic pathways for the Paterno–Büchi reaction.

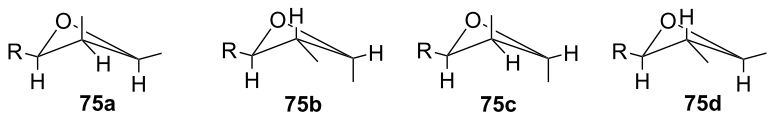

R = phenyl, 4-methoxyphenyl, 3-methoxyphenyl, 3,4-methylenedioxyphenyl, 2-naphthyl

Scheme 19: Isomeric oxetanes formed after photochemical addition of aryl aldehydes to 2-butenes.

to all four possible oxetanes (Scheme 20). However, the formation of the oxetanes **75a** and **75d** was favored over that of the oxetanes **75b** and **75c**, probably because the intermediates for the products **75a** and **75d** contained the residue group and the 4-methyl group at the favorable pseudoequatorial position.

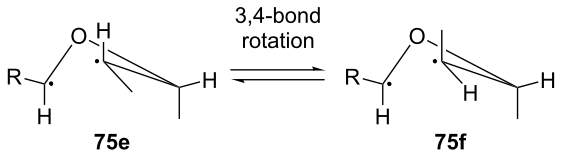

Scheme 20: Rotation of the C3–C4 bond of the biradical intermediate may lead to all four conformations.

In 1972, Bradshaw and co-workers studied the photolysis products of benzaldehyde (**8**) in different solvents [52]. The irradiation of benzaldehyde (**8**) in a benzene solution initially led to benzoin (**12**) formation, but after 14 hours of irradiation, the compounds **12**, **76**, and **77** were obtained in equal amounts. The irradiation of benzaldehyde (**8**) in ethanol yielded mostly compound **77** and traces of **12** (Scheme 21a). When benzaldehyde (**8**) was mixed with hex-1-yne (**78**), after a short irradiation time, the main products that were obtained were **80**, **81**, and **82**, as shown in Scheme 21b. The authors claimed that the compounds **80** and **81** could have formed by the addition of a benzoyl radical (**10**) to hex-1-yne (**78**). The compound **79** could have occurred as a reduction product of **80** and **81**. Finally, the compound **82** could have resulted from the addition of the benzoyl radical (**10**) to **80** and **81**.

In 1976, Davidson and co-workers reported the formation of *N-tert*-butylbenzamides, such as **83**, from *tert*-butylamine (**84**) and substituted aromatic aldehydes, such as **8** [53]. The reaction between the substituted benzaldehydes and *tert*-butylamine (**84**) took place in a benzene solution by being irradiated for 16 h using a 100 W Hanovia medium-pressure mercury lamp. The aromatic aldehydes tested included benzaldehyde (**8**), 4-chlorobenzaldehyde, 2,4-dichlorobenzaldehyde, and 4-fluorobenzaldehyde, which gave the corresponding benzamides in moderate to low yield. The reaction mechanism was thought to proceed via the benzoyl radical (**10**) formed after the irradiation of **8**. The benzoyl π-radical **85** formed could then react with the nucleophilic *tert*-butylamine (**84**), and the radical intermediate **86** could be rapidly oxidized, either by other radicals or by oxygen, to the amide **83**, as shown in Scheme 22.

The low yield of the amide formation was attributed mainly to a concurrent imine formation, which was catalyzed by benzoic acid formed as a result of benzaldehyde (**8**) oxidation during the photoreaction. There was also a competition between two bimolecular processes, the attack of a triplet state aldehyde molecule on a ground state aldehyde molecule and the reaction of a triplet state aldehyde molecule with the amine.

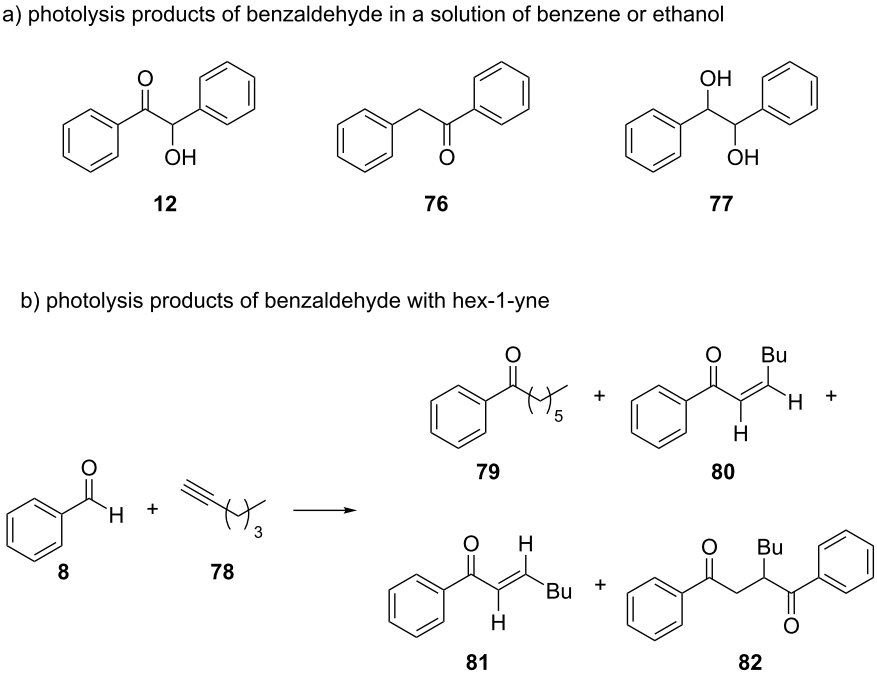

Scheme 21: Photolysis products of benzaldehyde (**8**) in different solvents. a) In benzene or ethanol. b) In hex-1-yne.

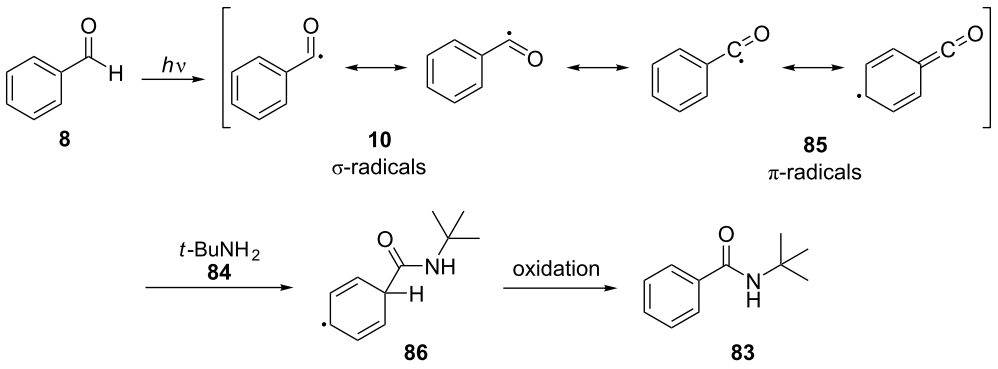

Scheme 22: *N-tert*-Butylbenzamide formation proceeds via a benzoyl radical.

In 2003, Li and co-workers developed a novel method for the pinacol reaction, the coupling of aromatic aldehydes and ketones, using solar energy [54]. The aromatic carbonyl compounds were dissolved in isopropanol and exposed to direct sunlight for 7–10 days to give the corresponding 1,2-diols **92** in high to moderate yield. The excitation of the carbonyl compound **87** was followed by hydrogen atom abstraction from the solvent **89**, affording the α-hydroxybenzyl radical **90**, which then coupled, forming the 1,2-diol **92** (Scheme 23).

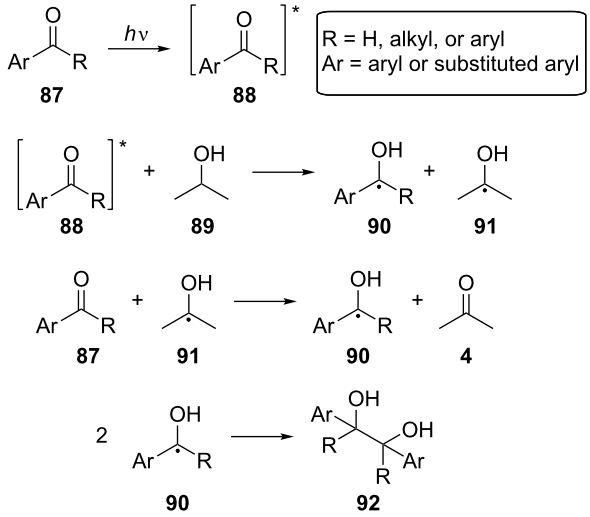

Scheme 23: Photochemical pinacol coupling.

In 2014, Melchiorre and co-workers found that 4-anisaldehyde (**52**) could efficiently catalyze the intermolecular atom transfer radical addition (ATRA) of the haloalkanes **93** to the olefins **94** under irradiation with a household 23 W compact fluorescent light (CFL) bulb at ambient temperature [55]. A base, 2,6-lutidine, was used to neutralize traces of HX (X = halogen), which formed by the homolytic cleavage of the C–X bond of the haloalkanes **93** (Scheme 24).

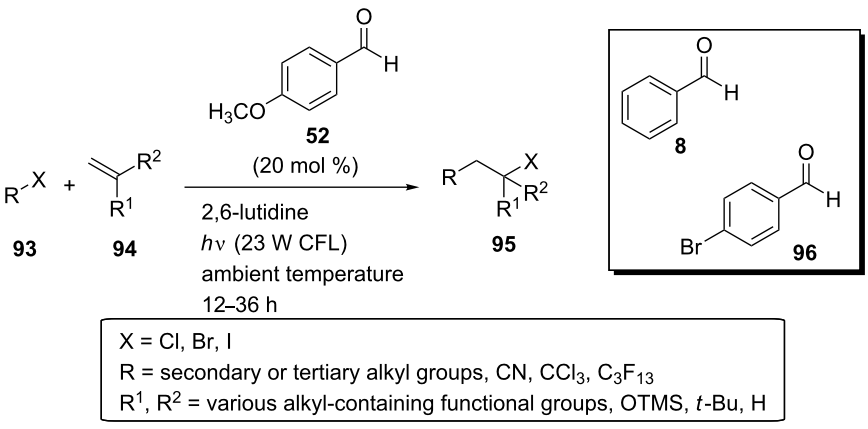

Scheme 24: Photochemical ATRA catalyzed by 4-anisaldehyde (**52**).

Among the aldehydes tested, benzaldehyde (**8**) and 4-bromobenzaldehyde (**96**) were also effective as photocatalysts, providing, however, a lower product yield. On the contrary to aromatic aldehydes, benzophenone, which was also tested as a photocatalyst, could promote the reaction only when used in superstoichiometric amounts. This way, 4-anisaldehyde (**52**) was found to be the most effective organocatalyst. In the absence of light or 4-anisaldehyde (**52**), no transformation was observed. No transformation was observed either in the presence of 2,2,6,6-tetramethylpiperidine-1-oxyl, 2,6-di-*tert*-butyl-4-methylphenol or air, indicating a radical mechanism. The reaction proceeded efficiently for a wide range of substrates in moderate to excellent yield, including various alkyl halides **93**, carbon tetrachloride, 2-norbornene, cyclic alkenes, a terminal disubstituted olefin, and a terminal alkyne. The reaction mechanism was thought to proceed via energy transfer from the aldehyde catalyst to the haloalkanes. Using cutoff filters for certain wavelengths, the authors found that the near-UV part of the CFL emission was necessary for the excitation of 4-anisaldehyde (**52**) through a n→π* transition. No ground state association between the reaction components was detected. Moreover, the excited 4-anisaldehyde (**98**) underwent energy transfer over the addition to the double bond of the alkene, as no Paterno–Büchi cycloadducts were observed. Furthermore, the detection of the photolysis products of the alkyl halides mentioned above indicated the presence of triplet state 4-anisaldehyde (**98**), which possessed a relatively long lifetime and an energetic value sufficient for C–X bond cleavage. The participation of the triplet state 4-anisaldehyde (**98**) in the reaction mechanism was also confirmed by the complete inhibition of the ATRA reaction in the presence of oxygen, a triplet state quencher, as well as by the lowered rate of the reaction in the presence of the triplet energy quencher 2,5-dimethylhexa-2,4-diene or pyridazines, additives with lower triplet state energies than 4-anisaldehyde (**52**). The fact that the solvent polarity did not affect the sensitivity of the process supported the energy transfer pathway. Thus, the proposed triplet sensitization mechanism of the photocatalytic ATRA reaction is depicted in Scheme 25.

In 2016, Ji and co-workers developed a new photoredox cross-dehydrogenative coupling (CDC) method for the α-heteroarylation of amides (α to nitrogen, e.g., formamide) and ethers through C–H activation using various five- and six-membered heteroarenes (e.g., benzothiazole) and employing benzaldehyde (**8**) as the photoinitiator [56]. This protocol was compatible with both C(sp^3)–H activation (*N*-alkyl C–H bonds of amides or C_α–H bonds of ethers) and C(sp^2)–H activation (carbonyl C–H bonds of formamides). Some of the amides or ethers found to be compatible with this method are shown in Scheme 26.

A wide range of heteroarenes **114** was also found compatible with this method, including substituted benzothiazole substrates, substituted benzimidazoles, and thiazoles, giving selectively the C-2-substituted product in moderate to excellent yield (Scheme 27a). However, only traces of the product were detected employing benzoxazole. Six-membered heteroaromatic compounds, such as pyridine, pyrazine, quinazoline, and even carboline, in some cases fused to a benzene ring, were also found to be compatible. 23 W CFL bulbs were used as the light source for the excitation of benzaldehyde. $(NH_4)_2S_2O_8$ (**116**)

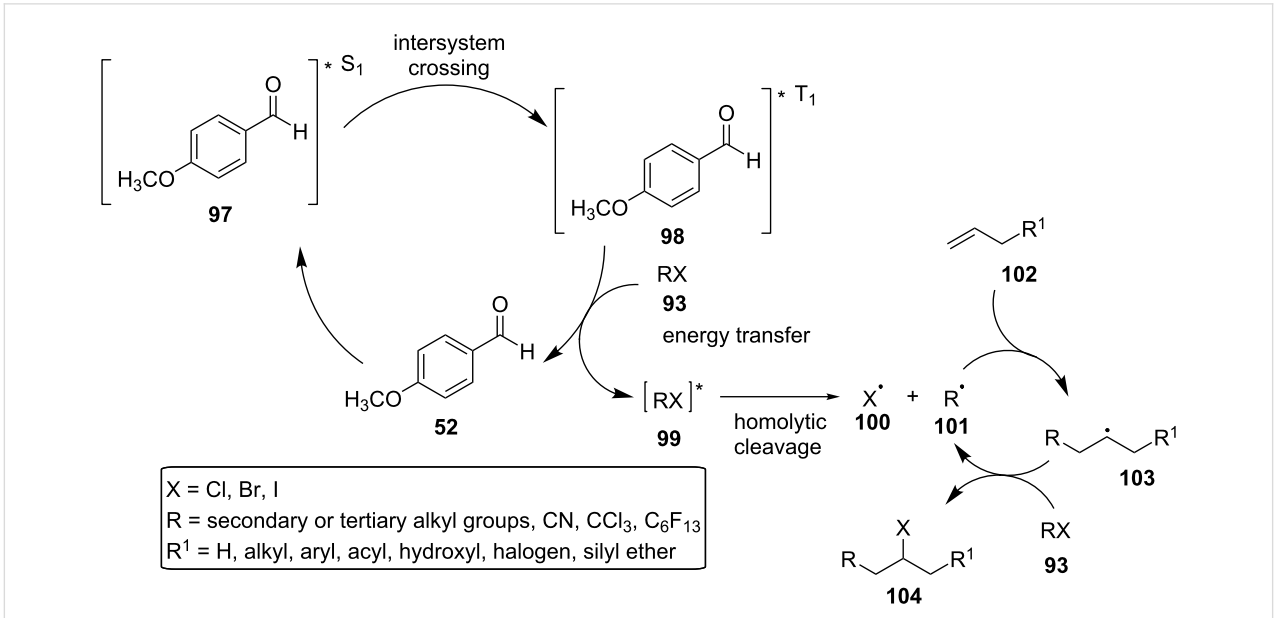

Scheme 25: Proposed triplet sensitization mechanism of the ATRA reaction in the presence of 4-anisaldehyde (**52**).

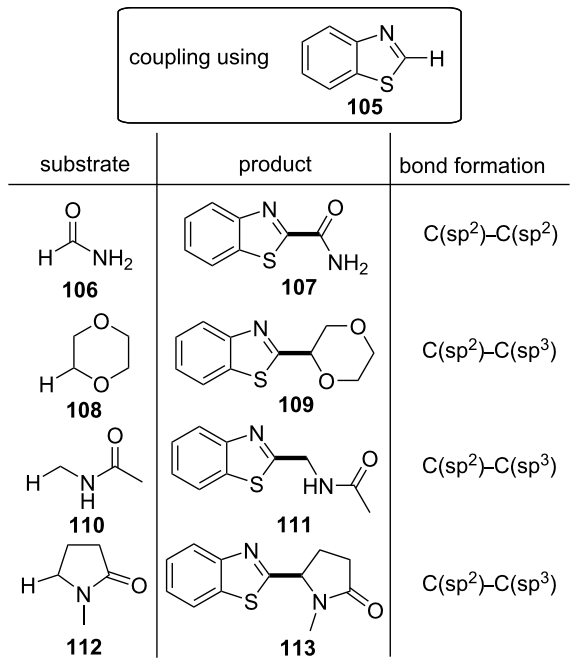

Scheme 26: Benzaldehyde-mediated photoredox CDC reaction: compatible amides and ethers.

was used as the radical initiator. Photoexcited benzaldehyde (**8**) enhanced the $(NH_4)_2S_2O_8$ (**116**) decomposition, accompanied by the generation of the sulfate radical **123** (Scheme 27b). The sulfate radical then reacted with formamide (**106**) to produce the carbamoyl radical **125**, which could perform a nucleophilic addition to the C-2 position of the protonated benzothiazole **126**. A deprotonation, followed by an oxidation, most probably by the intermediates **121** and **122**, could lead to the formation of the desired product and the regeneration of benzaldehyde (**8**). In most cases, *p*-toluenesulfonic acid (TsOH) was also used in order to improve the yield through the protonation and activation of benzothiazole. The proposed reaction mechanism, as explained above, is depicted in Scheme 27b.

Even 0.5 equivalents of benzaldehyde were able to promote the reaction. Furthermore, atmospheric oxygen and TEMPO inhibited the reaction. These facts suggest a radical mechanism. A very low yield was observed in the absence of irradiation. No product was detected in the absence of $(NH_4)_2S_2O_8$ (**116**), indicating the necessity of the benzaldehyde (**8**)-mediated decomposition of $(NH_4)_2S_2O_8$ (**116**) to generate carbamoyl radicals **125**. Varying the light wavelength, the authors observed that it was the near-UV region that was required for the reaction.

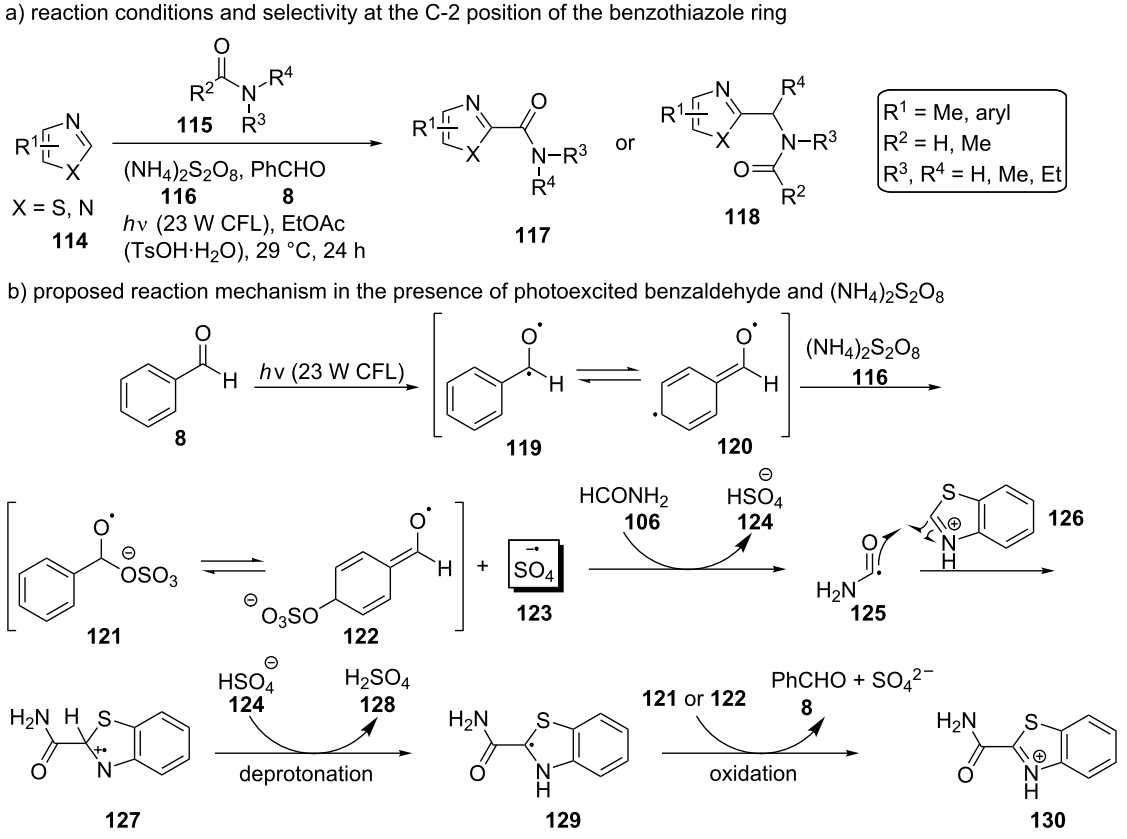

Scheme 27: Photoredox cross-dehydrogenative coupling (CDC) conditions and proposed reaction mechanism.

There was no ground state association observed between the reaction components. Although the authors found that **8** went through an excited n→π* transition, it was indicated that the triplet state of benzaldehyde, **9**, was not involved since it would have been quenched by the acid. Thus, the excited state of benzaldehyde directly promoted the $(NH_4)_2S_2O_8$ (**116**) decomposition, initiating the radical chain reaction. Other substituted benzaldehydes were also investigated. Finally, experiments employing benzaldehyde-α-d_1, showing no hydrogen/deuterium exchange, indicated no formation of a benzoyl radical (**10**) in this reaction.

In 2019, Hashmi and co-workers reported a selective photoredox merger C(sp^3)–H alkylation/arylation of ethers using benzaldehyde as the photoorganocatalyst and nickel as the transition metal catalyst [57]. For the coupling between (3-bromopropyl)benzene (**132**) and THF (**131**), presented in Scheme 28, $NiBr_2$·glyme (**134**) was employed as the precatalyst, 4,4'-di-*tert*-butyl-2,2'-bipyridyl (dtbbpy) as the ligand for the nickel catalyst, benzaldehyde (**8**) as the photosensitizer and hydrogen abstractor, K_2HPO_4 as the base, and UV-A light for the excitation of **8**. The reaction mixture was placed under a N_2 atmosphere and irradiated for 72 h.

Their hypothesis was that the excitation of benzaldehyde (**8**) to the singlet state followed by ISC to the triplet state could lead to a HAT process from the THF solvent molecule, resulting in the α-hydroxybenzyl radicals **10** or **11** and solvent radicals, which could then undergo coupling with an alkyl bromide in the presence of the nickel catalyst and a base via a typical oxidative addition, insertion, and reductive elimination sequence to afford the desired product (Scheme 29).

In the absence of K_2HPO_4, only traces of the desired product were detected. Other known photosensitizers, such as acetone (**4**), acetophenone (**64**), benzophenone, as well as substituted benzaldehydes were not as efficient as benzaldehyde (**8**). Using 4-anisaldehyde (**52**) and irradiation with CFL bulbs, no product was obtained. The reaction could also take place in acetone as the solvent using 10 equivalents of THF and applying irradiation for 96 h. The aryl (i.e., **133**), ether (i.e., **140a**), ester (i.e., **140b**), *tert*-butyldimethylsilyloxy (i.e., **140c**), boronic ester (i.e.,

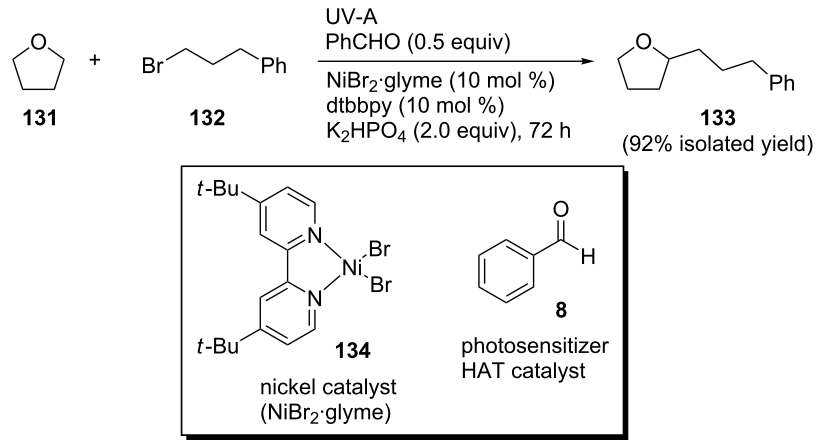

Scheme 28: Optimized conditions for the photoredox merger reaction.

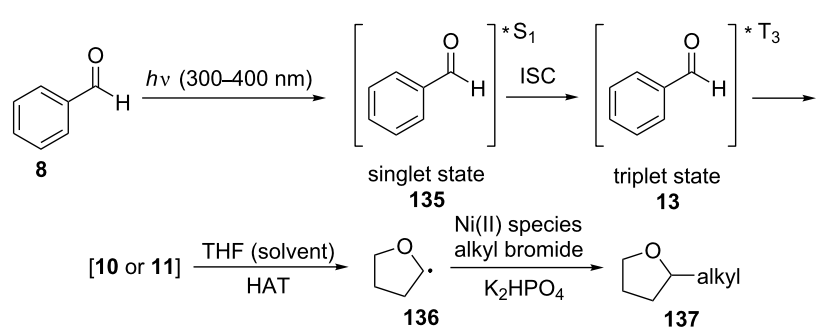

Scheme 29: Proposed mechanism for the C(sp^3)–H alkylation/arylation of ethers.

140d), acetal (i.e., **140e**), and indol products (i.e., **140h**) of various bromo-substituted starting materials were successfully obtained. For 1-bromo-3-chloropropane, the coupling occurred selectively at the carbon atom bearing the bromine atom, yielding **140f**. The products **140g**, **140i**, and **140j–m** of cyclic, aryl, and heteroaryl bromides, respectively, were also found compatible with this methodology. All bromides mentioned above afforded the desired products in good to excellent yields. However, benzyl and vinyl bromides did not prove efficient for this coupling reaction. Common cyclic and acyclic ethers, symmetric or nonsymmetric, such as oxetane, tetrahydropyran, dioxane, 2-methyltetrahydrofuran, and 2-methoxy-2-methylpropane, were found compatible, affording the desired products **140n–t** in moderate to good yields (Scheme 30).

A few months later, the same research group extended this methodology to an α-C(sp^3)–H bond functionalization of nitrogen-containing molecules and thioethers [58]. In order to achieve the highest yield, an optimum concentration of acetone (**4**) was necessary since at higher concentrations, the nickel catalyst would not dissolve completely. By increasing the amount of **141**, the yield gradually increased, so that 5 equivalents of *N*-Boc-pyrrolidine (**141**) were used, prolonging the irradiation time to 60 h, to achieve a yield of 88%. Other nickel salts were also tested, but they did not prove to be more efficient than the one already used. The optimized reaction conditions are presented in Scheme 31.

A wide variety of aryl bromides, containing either electron-donating or electron-withdrawing substituents, was found to be compatible with this methodology, affording the products **143** and **145a–d** in good yield. The N-substituted pyrrolidines **144a**/**d–g** were also compatible, providing the desired products in good yields, except from the *N*-acetyl (**144e**) and *N*-pival-

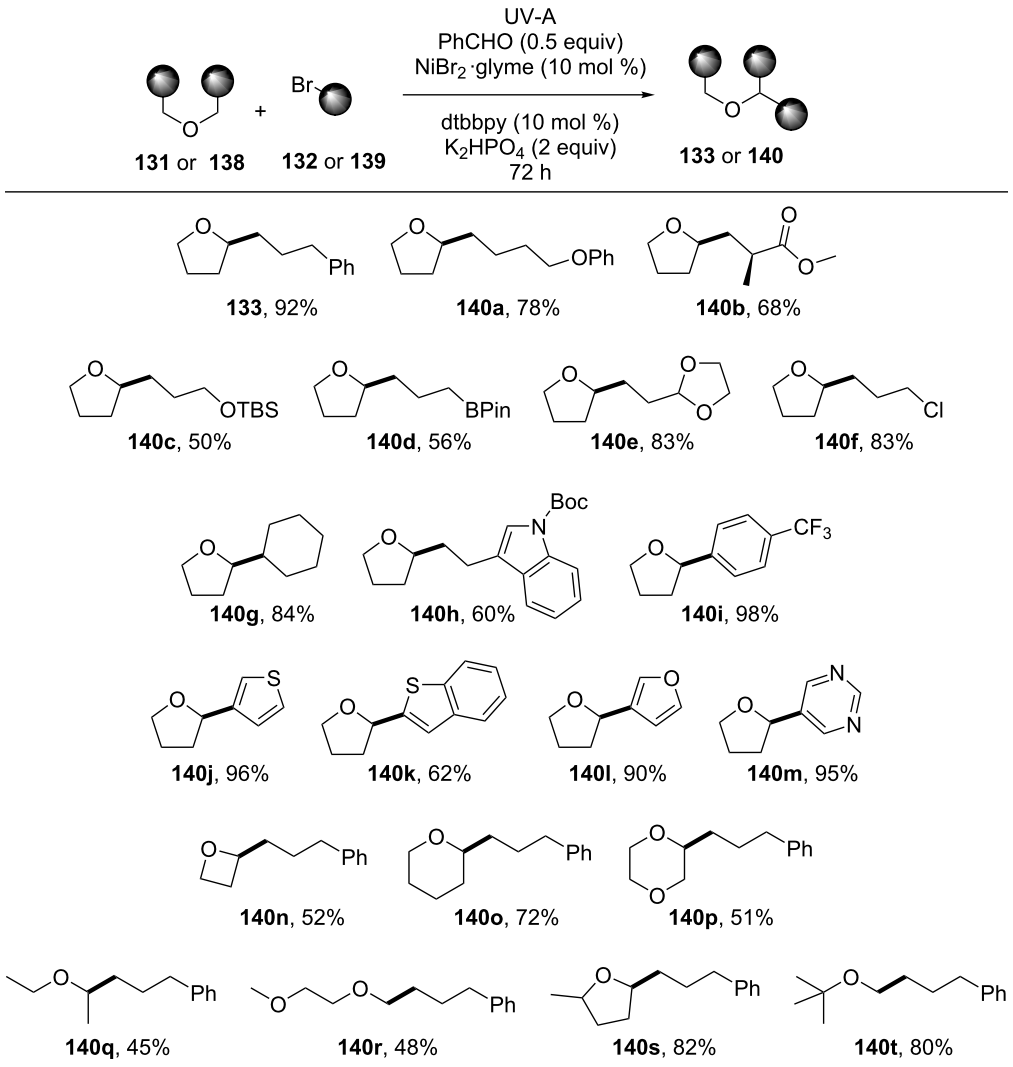

Scheme 30: Substrate scope for the photochemical alkylation of ethers.

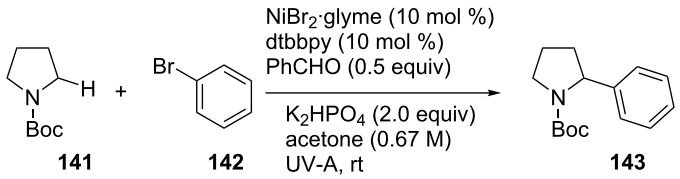

Scheme 31: C(sp^3)–H Functionalization of N-containing molecules.

oylpyrrolidines (**144f**), for which the yields dropped considerably. The alkylation of the pyrrolidine **141** was also possible employing a variety of alkyl bromides, including cyclic and acyclic secondary alkyl bromides as well as alkyl bromides carrying functional groups such as organosilyl and boronate moieties. However, the solvent had to be changed from acetone to acetonitrile in order to achieve good yields of **145h–l** (Scheme 32). Additionally, products derived from ureas (i.e., **146**), *N*,*N*-dimethylaniline (i.e., **147**), amides (i.e., **148**), and lactams (i.e., **149a**) were obtained. Moreover, for *N*-methylpyrrolidinone, α-arylation was achieved in a good yield and regioselectivity for the substitution of the 2-position, yielding **149a**, rather than for the *N*-methyl group, which would yield **149b** (Scheme 33).

In the same manner, thioethers were also susceptible to α-arylations or alkylations, using bromides containing a variety of functional groups, giving moderate to good yields (Scheme 34).

The proposed mechanism for the C(sp^3)–H functionalization of N-containing molecules and thioethers is in accordance with the one described previously for ether functionalizations and is presented in Scheme 35.

In 2019, Kokotos and co-workers employed 4-cyanobenzaldehyde (**53**) as the photoinitiator for the hydroacylation of Michael acceptors under irradiation with 80 W household bulbs [59]. 4-Cyanobenzaldehyde (**53**) exhibited the highest yield

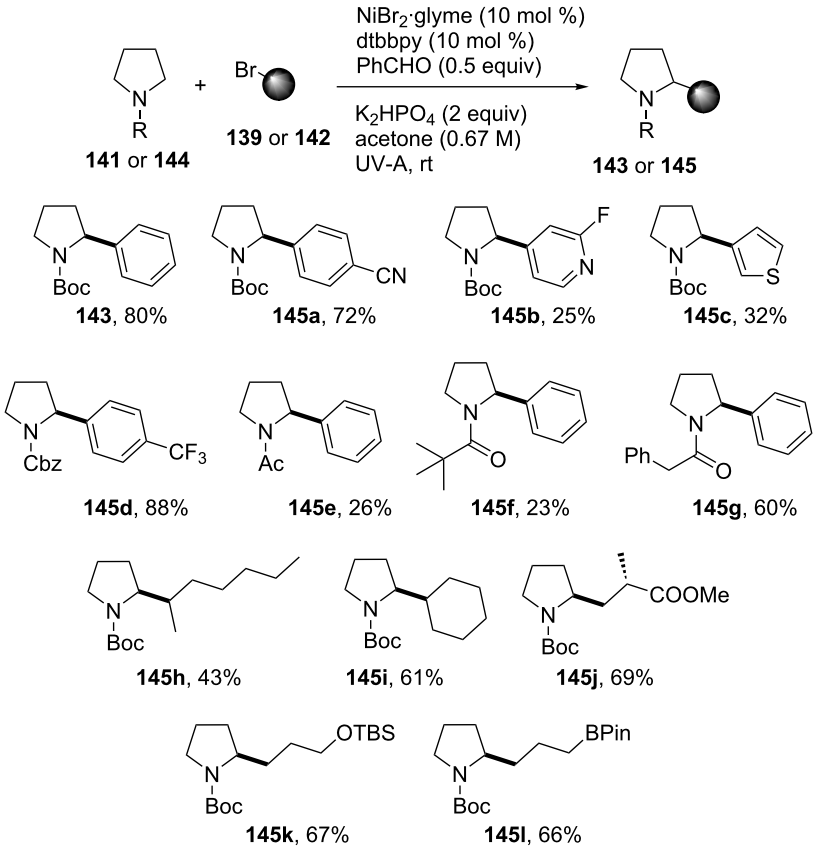

Scheme 32: Substrate scope for the photochemical alkylation of N-containing molecules.

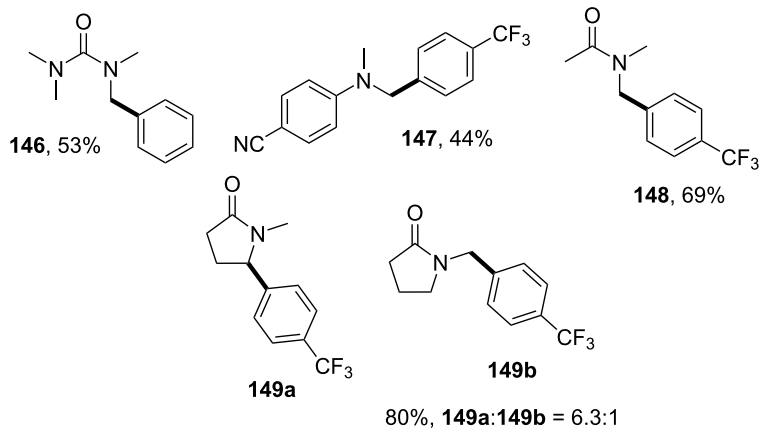

Scheme 33: Additional products yielded by the photochemical alkylation reaction of N-containing molecules.

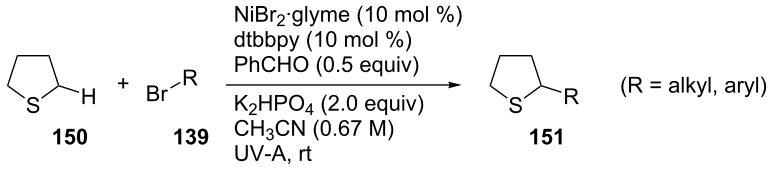

Scheme 34: C(sp^3)–H functionalization of thioethers.

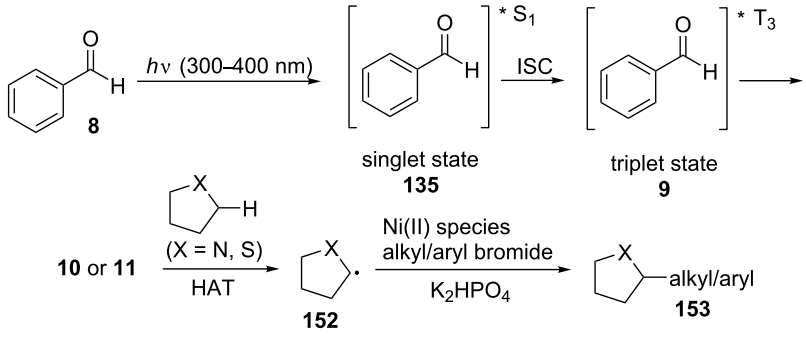

Scheme 35: Proposed mechanism for the C(sp^3)–H alkylation/arylation of N-containing molecules and thioethers.

(86%) among 25 substituted benzaldehydes in the reaction between diethyl maleate (**154**) and octanal (**155**) (Scheme 36). During the optimization, different solvents, catalyst loadings, and aldehyde equivalents were tested. Petroleum ether (bp 40–60 °C) afforded a high yield even at 10 mol % catalyst loading. In the absence of light or a catalyst or when the reac-

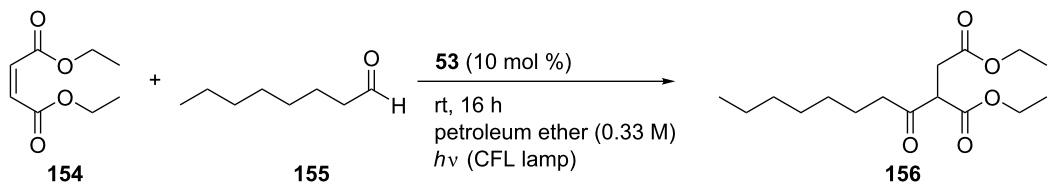

Scheme 36: Hydroacylation using 4-cyanobenzaldehyde (**53**) as the photoinitiator.

tion was placed in the dark at 60 °C, the reaction did not proceed.

When α,α-disubstituted aldehydes, e.g., cyclohexyl carboxaldehyde (**157**) are used in this type of reaction, the acyl radicals formed can easily be decarbonylated due to the rather stable secondary radical formed, so the selectivity of the reaction was studied. For this, the authors studied the reaction between diethyl maleate (**154**) and cyclohexyl carboxaldehyde (**157**) to find that 4-cyanobenzaldehyde (**53**) again proved to be the best photoinitiator in terms of the yield and selectivity, affording the desired carbonylated product **158** in a selectivity ratio of >20:1 (Scheme 37).

Primary alkyl aldehydes, aldehydes containing branched alkyl chains or cyclic aliphatic moieties, amide bonds, triple bonds, or ether moieties afforded the desired products in moderate to good yield (**156**, **158**, **162a–e**). α,α-Disubstituted aldehydes also afforded the products in good yield and moderate to good selectivity (**162f–k**). Benzyl diesters and aliphatic diesters were compatible with this methodology, affording the products **162l** and **162m** in moderate to good yield, while the products deriving from α,β-unsaturated carbonyl compounds, the products **163a–c** were obtained in moderate yield (Scheme 38).

Next, the authors conducted various mechanistic experiments, including fluorescence quenching studies, UV–vis spectroscopy experiments, calculation of the quantum yield, a cutoff experiment below 400 nm, GC–MS analysis, and NMR spectroscopic mechanistic experiments. They also concluded that an energy transfer mechanism could not be possible since the solvent employed affected the yield. The drop in the yield was insignificant in the absence of oxygen. An insignificant drop in the yield was also noticed when an electron scavenger, $CuCl_2$, was added to the reaction mixture, excluding a single electron transfer process. When a triplet state quencher, anthracene, was added, the reaction did not proceed, indicating that the triplet state of 4-cyanobenzaldehyde (**53**) was involved. Radical traps also inhibited the reaction, indicating a radical propagation mechanism. Based on these observations, they proposed a possible mechanistic pathway (Scheme 39). Under irradiation, 4-cyanobenzaldehyde (**53**) could transit to the excited singlet state **164** and then to the triplet state **165** through intersystem crossing. The interaction with a ground state molecule of **53** may lead to the radical pair of the hydroxybenzyl and benzoyl radicals **166** and **167**. The interaction of the benzoyl radical **167** with the aldehyde **161** could afford the acyl radical **168** through a HAT process, which then could add to diethyl maleate (**154**) and afford the desired product **162** through a propagation mechanism.

In 2019, König and co-workers presented a catalytic arylation of aromatic aldehydes **170** by aryl bromides **171** using UV as the light source and a nickel catalyst [60]. The authors suggested that the product **172**, a substituted benzophenone, could act as the photocatalyst and the hydrogen atom transfer agent in this reaction (Scheme 40). They optimized the reaction conditions with regard to the nickel catalyst, the solvent, the base, and the irradiation wavelength. Next, they investigated the reaction potential, with most aryl bromides and benzaldehydes tested being compatible to this transformation, affording the products in moderate to excellent yield.

The proposed photocatalytic cycle starts with the excitation of the benzophenone **172** to the triplet state **173** by UV irradiation, followed by HAT from the aldehyde **170** to **173** and the formation of the acyl radical **175**. At the same time, the nickel(0) complex **176** performs an oxidative addition reaction to the aryl bromide **171**, and the nickel(II) complex **177** formed reacts with an acyl radical **175** to give the nickel(III) complex **178**, which could then undergo a reductive elimination reaction to furnish the desired ground state benzophenone product **172**. The nickel(0) catalyst can then be regenerated by SET (Scheme 41). However, they suggested that the first photocatalytically active species can be initiated by the reaction mixture, containing traces of different benzaldehyde photolysis products together with benzaldehyde.

In 2020, Landais and co-workers developed a photosensitized sulfonylcyanation of chiral cyclobutenes [61]. Although cyclobutanes are substrates of significant pharmaceutical use, the unsaturated analogs, cyclobutenes, are characterized by a

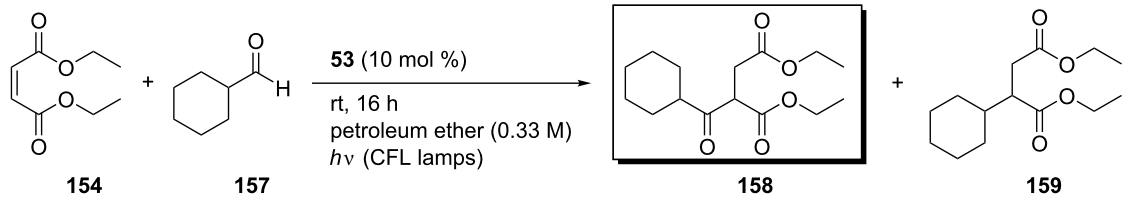

Scheme 37: Selectivity for the formation of the α,α-disubstituted aldehydes.

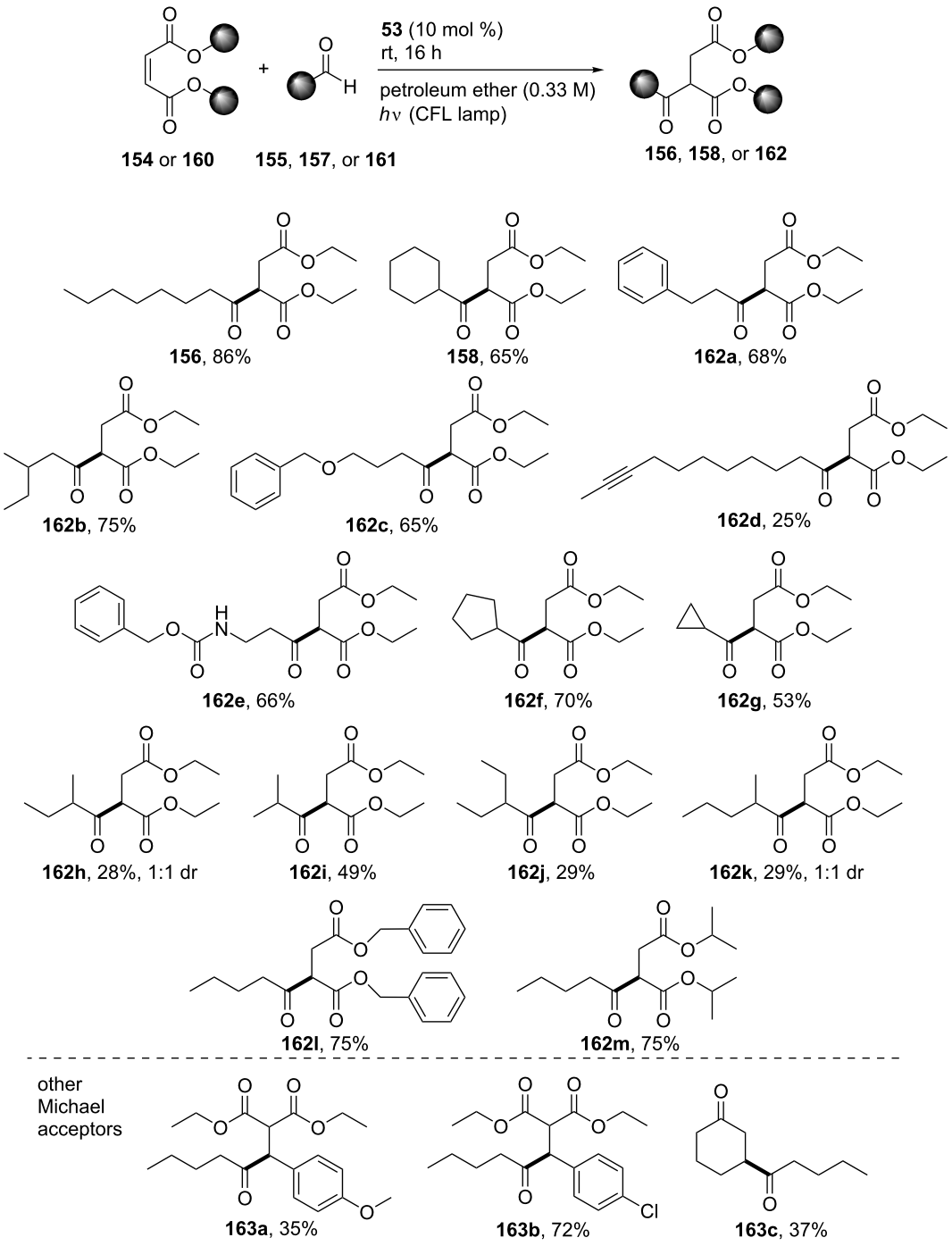

Scheme 38: Substrate scope for the photochemical addition of aldehydes to Michael acceptors.

poor reactivity of the π-bond, restricting the access to chiral cyclobutanes. This research group worked on a photocatalyzed addition of an electrophilic sulfonyl radical and a cyanide group across the π-bond of a chiral cyclobutene **180**, providing highly functionalized cyclobutanes **182** and an access to the enantio-enriched cyanosulfones **183**, resulting from cyclobutane ring opening, or the new tetrasubstituted cyclobutanes **184** (Scheme 42).

The cyclobutenes **180** were subjected to a photocatalyzed radical addition, and upon optimization, 4-anisaldehyde (**52**) proved to be a better photocatalyst under UV-A irradiation than

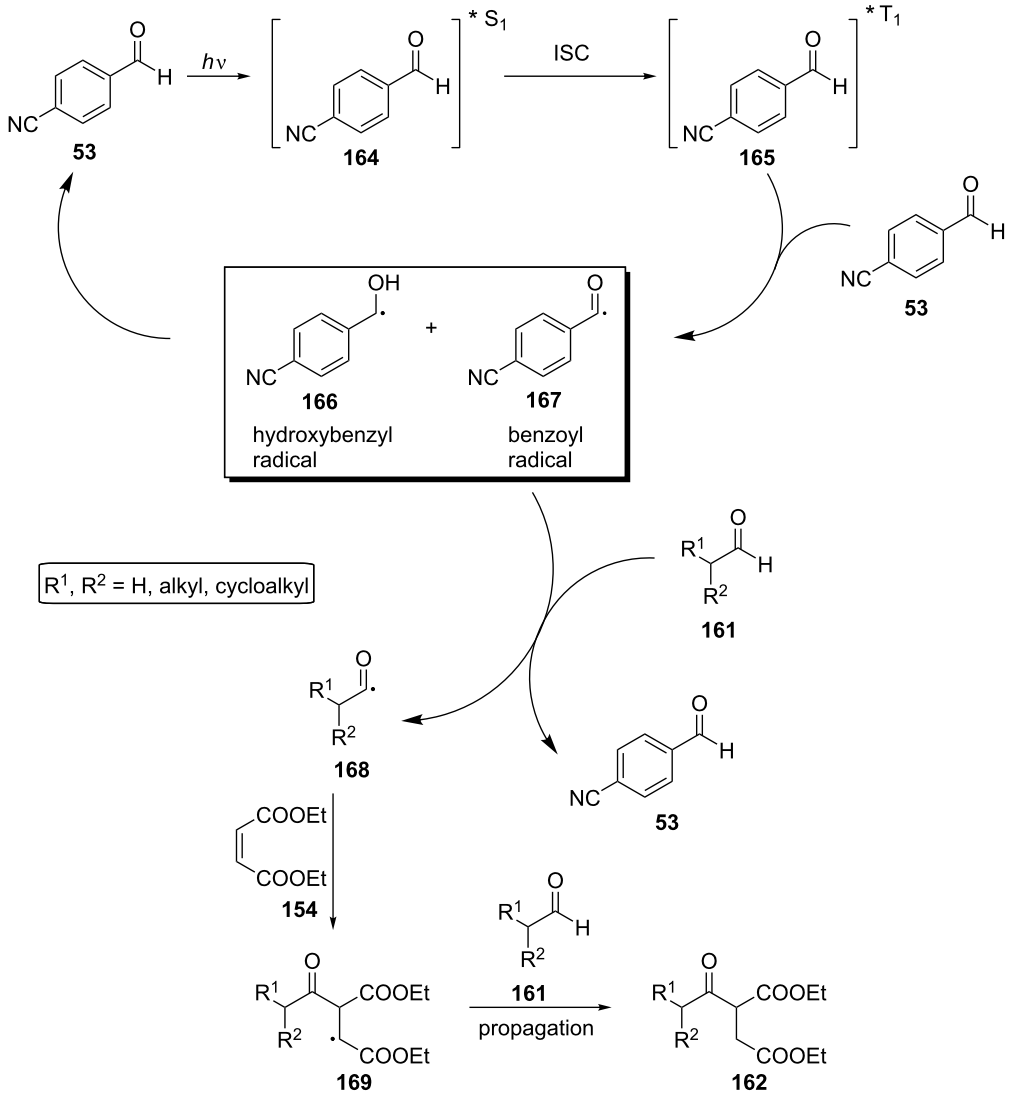

Scheme 39: Proposed mechanism for the hydroacylation of Michael acceptors using 4-cyanobenzaldehyde (**53**) as the photoinitiator.

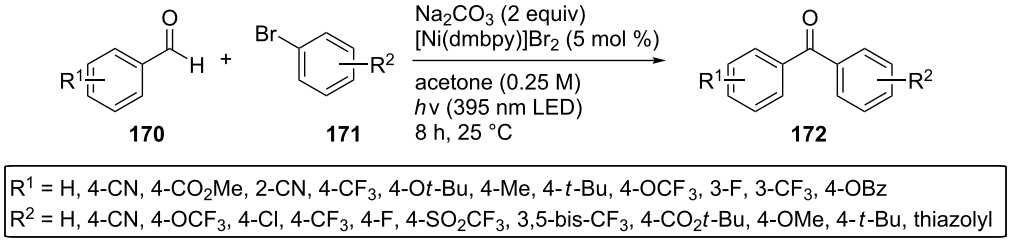

Scheme 40: Catalytic arylation of aromatic aldehydes by aryl bromides in which the reaction product acts as the photocatalyst.

the initially used eosin Y. Compound **182**, the all-*trans*-isomer, was the major product. The optimized conditions are presented in Scheme 43a. Conducting several control experiments and noticing that the presence of 4-anisaldehyde (**52**), UV-A light, and the absence of a triplet state quencher were essential for this transformation, they proposed a possible reaction mechanism (Scheme 43b): Energy transfer from triplet-excited-state 4-anisaldehyde (**98**) to the sulfonyl cyanide **181** can lead to a

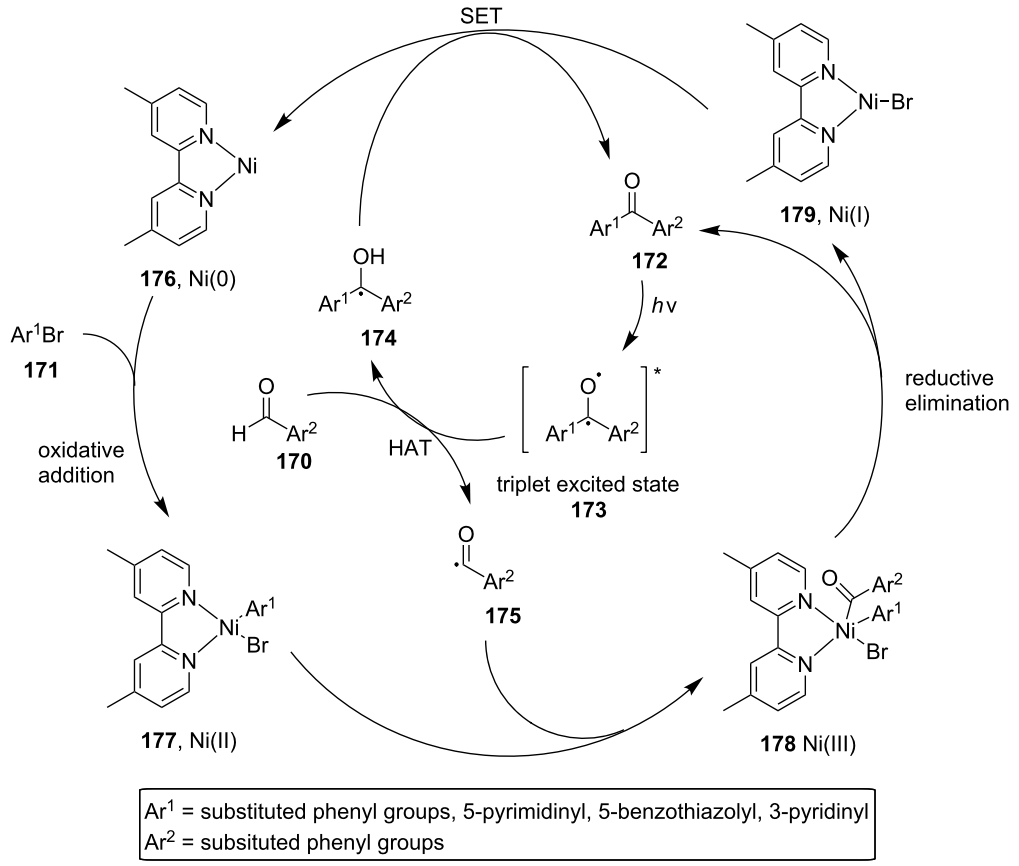

Scheme 41: Proposed mechanism for the catalytic arylation of benzaldehydes by aryl bromides in which the reaction product acts as a photocatalyst.

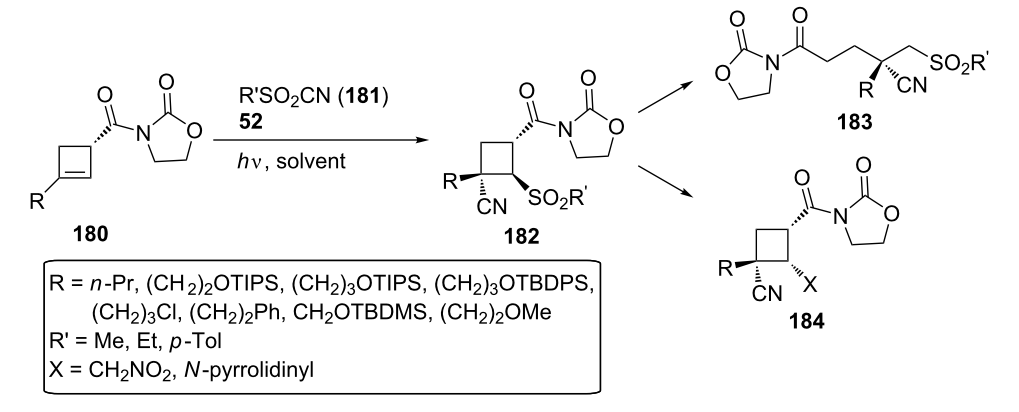

Scheme 42: Functionalization of the chiral cyclobutanes **180**.

homolytic cleavage of the C–S bond, providing the sulfonyl radical **186**. The sulfonyl radical **186** can then approach *anti* to the oxazolidinone moiety in **180**, generating a β-sulfonyl radical **187**, which, once trapped by another sulfonyl cyanide molecule **181**, affords the desired product **182**, and the sulfonyl radical reenters the catalytic cycle.

Various alkyl substituents on the cyclobutene ring, such as substituents bearing a chlorine atom, or silyl ethers were well-tolerated. However, bulky groups (e.g., TBDMS) led to lower yields. Methyl, ethyl, or aryl sulfones were all compatible with this methodology, and could even be extended to functionalized sulfonyl cyanides, though providing lower yields. In every

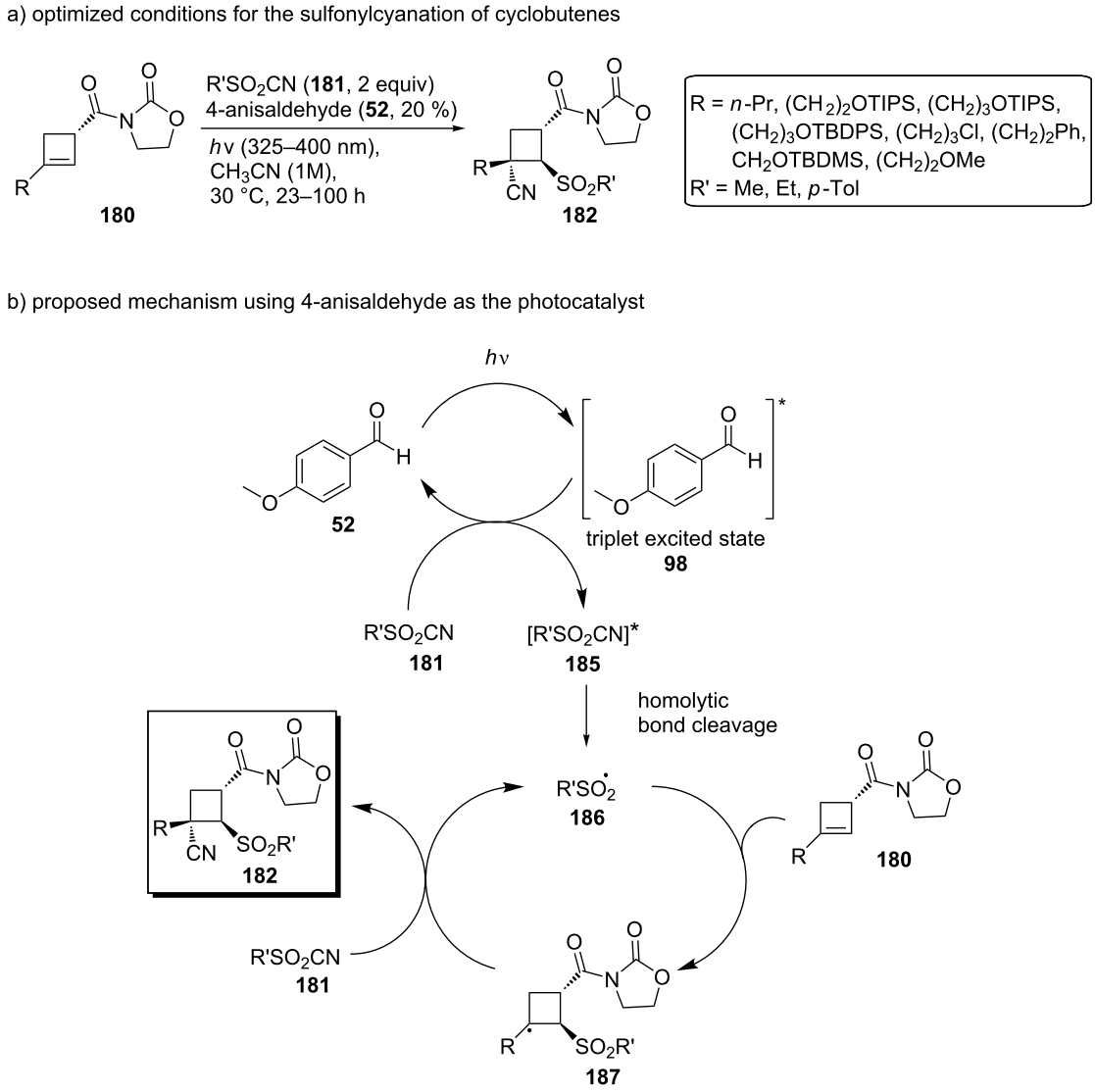

Scheme 43: Optimized reaction conditions and proposed mechanism for the sulfonylcyanation of cyclobutenes.

case, the diastereoselectivity was high (dr > 19:1:1) and in favor of the all-*trans*-product.

Conclusion

In this review, we summarized the photophysical properties of aromatic aldehydes and the potential that (aromatic and aliphatic) aldehydes have as photoinitiators. In more detail, we cited their use as initiators in polymerization and photografting reactions and finally, we provided the applications of aldehydes as photoinitiators in organic synthesis. We strongly believe that as researchers seek greener and sustainable processes to advance chemistry, the use of aldehydes in conjunction with light irradiation, even sunlight, will become more popular, providing a vast array of applications.

Funding

The authors gratefully acknowledge the Laboratory of Organic Chemistry of the Department of Chemistry of the National and Kapodistrian University of Athens for financial support. C. G. K. would like to thank the John Latsis Foundation for financial support through the programme "EPISTHMONIKES MELETES 2015" (PhotoOrganocatalysis: Development of new environmentally-friendly methods for the synthesis of compounds for the pharmaceutical and chemical industry). N. F. N. would like to thank the State Scholarship Foundation (IKY) for financial support through a doctoral fellowship, which is cofinanced by Greece and the European Union (European Social Fund, (ESF)) through the Operational Programme "Human Resources Development, Education and Lifelong Learning" in

the context of the project “Strengthening Human Resources Research Potential via Doctorate Research” (MIS-5000432), implemented by the State Scholarships Foundation (IKY). C. G. K. would like to thank the Hellenic Foundation for Research and Innovation (HFRI) for financial support through a grant that is financed by 1st Call for HFRI Research Projects to Support Faculty Members & Researchers and Procure High-Value Research Equipment (grant number 655).

ORCID® iDs

Maria A. Theodoropoulou - https://orcid.org/0000-0002-6552-5217
Christoforos G. Kokotos - https://orcid.org/0000-0002-4762-7682

References

1. Prier, C. K.; Rankic, D. A.; MacMillan, D. W. C. *Chem. Rev.* **2013,** *113,* 5322–5363. doi:10.1021/cr300503r
2. Skubi, K. L.; Blum, T. R.; Yoon, T. P. *Chem. Rev.* **2016,** *116,* 10035–10074. doi:10.1021/acs.chemrev.6b00018
3. Cambié, D.; Bottecchia, C.; Straathof, N. J. W.; Hessel, V.; Noël, T. *Chem. Rev.* **2016,** *116,* 10276–10341. doi:10.1021/acs.chemrev.5b00707
4. Kärkäs, M. D.; Porco, J. A., Jr.; Stephenson, C. R. J. *Chem. Rev.* **2016,** *116,* 9683–9747. doi:10.1021/acs.chemrev.5b00760
5. Gad, S. C. *Device Safety Evaluation;* Safety Evaluation of Pharmaceuticals and Medical Devices; Springer US: Boston, MA, U.S.A., 2011; pp 91–112. doi:10.1007/978-1-4419-7449-5_7
6. Nicewicz, D. A.; Nguyen, T. M. *ACS Catal.* **2014,** *4,* 355–360. doi:10.1021/cs400956a
7. Ravelli, D.; Fagnoni, M.; Albini, A. *Chem. Soc. Rev.* **2013,** *42,* 97–113. doi:10.1039/c2cs35250h
8. Romero, N. A.; Nicewicz, D. A. *Chem. Rev.* **2016,** *116,* 10075–10166. doi:10.1021/acs.chemrev.6b00057
9. Ravelli, D.; Protti, S.; Fagnoni, M. *Chem. Rev.* **2016,** *116,* 9850–9913. doi:10.1021/acs.chemrev.5b00662
10. Sideri, I. K.; Voutyritsa, E.; Kokotos, C. G. *Org. Biomol. Chem.* **2018,** *16,* 4596–4614. doi:10.1039/c8ob00725j
11. Capaldo, L.; Ravelli, D. *Eur. J. Org. Chem.* **2017,** 2056–2071. doi:10.1002/ejoc.201601485
12. Cundall, R. B.; Davies, A. S. *Trans. Faraday Soc.* **1966,** *62,* 2444–2451. doi:10.1039/tf9666202444
13. Cocivera, M.; Trozzolo, A. M. *J. Am. Chem. Soc.* **1970,** *92,* 1772–1774. doi:10.1021/ja00709a066
14. Closs, G. L.; Paulson, D. R. *J. Am. Chem. Soc.* **1970,** *92,* 7229–7231. doi:10.1021/ja00727a051
15. Yang, N. C.; Cohen, J. I.; Shani, A. *J. Am. Chem. Soc.* **1968,** *90,* 3264–3266. doi:10.1021/ja01014a066
16. Yang, N. C. *Photochem. Photobiol.* **1968,** *7,* 767–773. doi:10.1111/j.1751-1097.1968.tb08062.x
17. Yang, N. C.; Kimura, M.; Eisenhardt, W. *J. Am. Chem. Soc.* **1973,** *95,* 5058–5060. doi:10.1021/ja00796a054
18. Berger, M.; Goldblatt, I. L.; Steel, C. *J. Am. Chem. Soc.* **1973,** *95,* 1717–1725. doi:10.1021/ja00787a004
19. Atkins, P. W.; Frimston, J. M.; Frith, P. G.; Gurd, R. C.; McLauchlan, K. A. *J. Chem. Soc., Faraday Trans. 2* **1973,** *69,* 1542–1557. doi:10.1039/f29736901542
20. Murai, H.; Obi, K. *J. Phys. Chem.* **1975,** *79,* 2446–2450. doi:10.1021/j100589a022
21. Ohmori, N.; Suzuki, T.; Ito, M. *J. Phys. Chem.* **1988,** *92,* 1086–1093. doi:10.1021/j100316a019
22. Silva, C. R.; Reilly, J. P. *J. Phys. Chem.* **1996,** *100,* 17111–17123. doi:10.1021/jp961282l
23. Long, S. R.; Meek, J. T.; Harrington, P. J.; Reilly, J. P. *J. Chem. Phys.* **1983,** *78,* 3341–3343. doi:10.1063/1.445204
24. Frith, P. G.; McLauchlan, K. A. *J. Chem. Soc., Faraday Trans. 2* **1975,** *71,* 1984–1993. doi:10.1039/f29757101984
25. Metcalfe, J.; Brown, R. G.; Phillips, D. *J. Chem. Soc., Faraday Trans. 2* **1975,** *71,* 409–413. doi:10.1039/f29757100409
26. Harriman, A.; Rockett, B. W.; Poyner, W. R. *J. Chem. Soc., Perkin Trans. 2* **1974,** 485–489. doi:10.1039/p29740000485
27. Defoin, A.; Defoin-Straatmann, R.; Kuhn, H. J. *J. Labelled Compd. Radiopharm.* **1982,** *19,* 891–898. doi:10.1002/jlcr.2580190709
28. Defoin, A.; Defoin-Straatmann, R.; Kuhn, H. J. *Tetrahedron* **1984,** *40,* 2651–2662. doi:10.1016/s0040-4020(01)96882-6
29. Itoh, T. *Chem. Phys. Lett.* **1988,** *151,* 166–168. doi:10.1016/0009-2614(88)80089-7
30. Zhu, L.; Cronin, T. J. *Chem. Phys. Lett.* **2000,** *317,* 227–231. doi:10.1016/s0009-2614(99)01375-5
31. Bagchi, A.; Huang, Y.-H.; Xu, Z. F.; Raghunath, P.; Lee, Y. T.; Ni, C.-K.; Lin, M. C.; Lee, Y.-P. *Chem. – Asian J.* **2011,** *6,* 2961–2976. doi:10.1002/asia.201100483
32. Cui, G.; Lu, Y.; Thiel, W. *Chem. Phys. Lett.* **2012,** *537,* 21–26. doi:10.1016/j.cplett.2012.04.008
33. Khudyakov, I. V.; McGarry, P. F.; Turro, N. J. *J. Phys. Chem.* **1993,** *97,* 13234–13242. doi:10.1021/j100152a030
34. Fletcher, K.; Bunz, U. H. F.; Dreuw, A. *ChemPhysChem* **2016,** *17,* 2650–2653. doi:10.1002/cphc.201501059
35. McGinniss, V. D.; Provder, T.; Kuo, C.; Gallopo, A. *Macromolecules* **1978,** *11,* 393–404. doi:10.1021/ma60062a022
36. Suppan, P. *J. Chem. Soc., Faraday Trans. 1* **1975,** *71,* 539–547. doi:10.1039/f19757100539
37. Schuster, D. I.; Goldstein, M. D.; Bane, P. *J. Am. Chem. Soc.* **1977,** *99,* 187–193. doi:10.1021/ja00443a034
38. Aydın, M.; Arsu, N. *Prog. Org. Coat.* **2006,** *56,* 338–342. doi:10.1016/j.porgcoat.2006.06.006
39. Allméar, K.; Hult, A.; Rårnby, B. *J. Polym. Sci., Part A: Polym. Chem.* **1988,** *26,* 2099–2111. doi:10.1002/pola.1988.080260809
40. Liqun, Z.; Irwan, G. S.; Kondo, T.; Kubota, H. *Eur. Polym. J.* **2000,** *36,* 1591–1595. doi:10.1016/s0014-3057(99)00222-0
41. Wang, H.; Brown, H. R. *J. Polym. Sci., Part A: Polym. Chem.* **2004,** *42,* 253–262. doi:10.1002/pola.11022
42. Zhao, A.; Li, Z.; Wang, H. *Polymer* **2010,** *51,* 2099–2105. doi:10.1016/j.polymer.2010.02.050
43. Wang, H.; Brown, H. R. *Macromol. Rapid Commun.* **2004,** *25,* 1257–1262. doi:10.1002/marc.200400145
44. Wang, H.; Brown, H. R.; Li, Z. *Polymer* **2007,** *48,* 939–948. doi:10.1016/j.polymer.2006.12.058
45. Han, J.; Wang, H. *J. Appl. Polym. Sci.* **2009,** *113,* 2062–2071. doi:10.1002/app.29938
46. Song, A.; Zhao, D.; Rong, R.; Zhang, L.; Wang, H. *J. Appl. Polym. Sci.* **2011,** *119,* 629–635. doi:10.1002/app.32683
47. Guo, R.; Gao, Y.; Wu, M.; Wang, H. *Polymer* **2013,** *54,* 4940–4947. doi:10.1016/j.polymer.2013.07.006
48. Coutinho, K.; Saavedra, N.; Canuto, S. *J. Mol. Struct.: THEOCHEM* **1999,** *466,* 69–75. doi:10.1016/s0166-1280(98)00338-8

49. Ma, W.; Zhang, X.; Ma, Y.; Chen, D.; Wang, L.; Zhao, C.; Yang, W. *Polym. Chem.* **2017,** *8,* 3574–3585. doi:10.1039/c7py00408g
50. Hammond, G. S.; Leermakers, P. A.; Turro, N. J. *J. Am. Chem. Soc.* **1961,** *83,* 2396–2397. doi:10.1021/ja01471a045
51. Hammond, G. S.; Turro, N. J.; Leermakers, P. A. *J. Phys. Chem.* **1962,** *66,* 1144–1147. doi:10.1021/j100812a041
52. Bradshaw, J. S.; Knudsen, R. D.; Parish, W. W. *J. Chem. Soc., Chem. Commun.* **1972,** 1321–1322. doi:10.1039/c39720001321
53. Davidson, R. S.; Edwards, J.; Warburton, S. K. *J. Chem. Soc., Perkin Trans. 1* **1976,** 1511–1514. doi:10.1039/p19760001511
54. Li, J.-T.; Yang, J.-H.; Han, J.-F.; Li, T.-S. *Green Chem.* **2003,** *5,* 433–435. doi:10.1039/b300150b
55. Arceo, E.; Montroni, E.; Melchiorre, P. *Angew. Chem., Int. Ed.* **2014,** *53,* 12064–12068. doi:10.1002/anie.201406450
56. Zhang, Y.; Teuscher, K. B.; Ji, H. *Chem. Sci.* **2016,** *7,* 2111–2118. doi:10.1039/c5sc03640b
57. Zhang, L.; Si, X.; Yang, Y.; Zimmer, M.; Witzel, S.; Sekine, K.; Rudolph, M.; Hashmi, A. S. K. *Angew. Chem., Int. Ed.* **2019,** *58,* 1823–1827. doi:10.1002/anie.201810526
Angew. Chem. **2019,** *131,* 1837-1841. doi:10.1002/ange.201810526
58. Si, X.; Zhang, L.; Hashmi, A. S. K. *Org. Lett.* **2019,** *21,* 6329–6332. doi:10.1021/acs.orglett.9b02226
59. Sideri, I. K.; Voutyritsa, E.; Kokotos, C. G. *ChemSusChem* **2019,** *12,* 4194–4201. doi:10.1002/cssc.201901725
60. Schirmer, T. E.; Wimmer, A.; Weinzierl, F. W. C.; König, B. *Chem. Commun.* **2019,** *55,* 10796–10799. doi:10.1039/c9cc04726c
61. Pirenne, V.; Traboulsi, I.; Rouvière, L.; Lusseau, J.; Massip, S.; Bassani, D. M.; Robert, F.; Landais, Y. *Org. Lett.* **2020,** *22,* 575–579. doi:10.1021/acs.orglett.9b04345

License and Terms

This is an Open Access article under the terms of the Creative Commons Attribution License (http://creativecommons.org/licenses/by/4.0). Please note that the reuse, redistribution and reproduction in particular requires that the authors and source are credited.

The license is subject to the *Beilstein Journal of Organic Chemistry* terms and conditions: (https://www.beilstein-journals.org/bjoc)

The definitive version of this article is the electronic one which can be found at: doi:10.3762/bjoc.16.76

BEILSTEIN JOURNAL OF ORGANIC CHEMISTRY

A method to determine the correct photocatalyst concentration for photooxidation reactions conducted in continuous flow reactors

Clemens R. Horn* and Sylvain Gremetz

Letter

Open Access

Address:
Corning European Technology Center, 7 Bis Avenue de Valvins, F-77215 Avon Cedex, France

Email:
Clemens R. Horn* - Clemens.R.Horn@gmail.com

* Corresponding author

Keywords:
catalyst concentration; channel height; flow chemistry; photooxidation

Beilstein J. Org. Chem. **2020,** *16,* 871–879.
doi:10.3762/bjoc.16.78

Received: 26 February 2020
Accepted: 16 April 2020
Published: 27 April 2020

This article is part of the thematic issue "Advances in photoredox catalysis".

Guest Editor: T. Noël

© 2020 Horn and Gremetz; licensee Beilstein-Institut.
License and terms: see end of document.

Abstract

When conducting a photooxidation reaction, the key question is what is the best amount of photocatalyst to be used in the reaction? This work demonstrates a fast and simple method to calculate a reliable concentration of the photocatalyst that will ensure an efficient reaction. The determination is based on shifting the calculation away from the concentration of the compound to be oxidized to utilizing the limitations on the total light dose that can be delivered to the catalyst. These limitations are defined by the photoflow setup, specifically the channel height and the emission peak of the light source. This method was tested and shown to work well for three catalysts with different absorption properties through using LEDs with emission maxima close to the absorption maximum of each catalyst.

Introduction

The renaissance of photochemistry that occurred over the last decade has been described as “old light through new windows”, and much of this work centered on the combination of light with continuous flow reactors [1-6]. The reason for this increased interest is that continuous flow photochemical reactors can overcome various limitations that occur when the same reaction run in batch reactors [7]. For example, the flow reactor can overcome the difficulties that occur upon scale-up. The most desirable approach for industrial-scale reactions is described by the quote “the best approach to the scale-up of a photoreaction seems to be the enlarging of a laboratory-type prototype reactor, with the important parameters being changed as little as possible” [8]. This phrase describes the approach used to scale up flow reactors to an industrial scale [9,10]. This is particularly true when it comes to biphasic reactions, like a gas/liquid reaction as is the case for photooxidations [11]. An inter-

esting aspect of photooxidations is that the combination of light, the "greenest reagent" oxygen, and a catalyst as well as applying mild process conditions under process-intensified conditions can be considered a very sustainable setup [12-14].

The scaling-up of photoflow reactors has also been affected by the increased use of LED sources over mercury arcs and other light sources commonly used in industry and classical synthetic organic photochemistry. LEDs typically have much narrower emission spectra when compared to these light sources, all of which have broad emission spectra except for low-pressure sodium vapor lamps [15,16]. These broad emission spectra pose some further complications as they are ultimately a rather inefficient way to use the energy and provide wavelengths that can effectively increase the risk of side reactions [17]. The fact that only a portion of the emitted light is used in the reaction can further complicate the scale-up of the light source and design of the reactor. LED sources have continuously been evolving and will continue to do so because when being employed, the light source is no longer a limiting factor in the design of a larger-scale photoreactor setup [18]. Since an LED provides a narrower emission wavelength, the appropriate wavelength above 365 nm can be selected for every reaction, and the scale-up can be achieved by simply increasing the number of the LEDs applied [19]. The narrower spectra, while providing many benefits and likely reducing the occurrence of side reactions, also facilitate that other factors become more important. Notably, an exact description of the photoflow setup is now crucial to ensure reproducible experiments [20,21].

Results and Discussion

The effect of 1 mol % photocatalyst

This work was accomplished using the Corning® AdvancedFlow™ Lab Photo Reactor, providing a robust platform for a rapid screening of the reaction conditions (e.g., the wavelength) and, for photooxidation reactions, the catalysts. For a schematic reaction setup see Figure 1, and further details can be found in Supporting Information File 1 [22]. As a test reaction, we rapidly screened 9 photocatalysts for the oxidation of citronellol (Scheme 1), using the conditions described by Lévesque and Seeberger [23].

The reaction conditions used for the experiments shown in Scheme 1 are detailed in Figure 2 below, and the best results are highlighted in grey.

The conversions of the photooxidation reactions were determined under similar reaction conditions using 11 different wavelengths (10 sources with defined wavelength and 1 white light source with a color temperature of 4000 K). At the same time, the transmission spectra of all starting solutions were recorded using a cuvette with a path length of 0.5 mm, which is close to that of the fluidic module in the reactor (0.4 mm). The lower-right value in each field of Figure 2 corresponds to the transmission recorded at the LED emission maximum. In about 30% of the tests, a complete conversion was obtained (highlighted in grey in Figure 2), but only in 15% of the cases, the catalyst concentration was high enough to absorb all the light at the given wavelength (highlighted with a bold frame, transmission < 1%).

Overall, the results show that 1 mol % of the catalyst was not the ideal concentration for the various initiators. For example, in the extreme case of using tetraphenylporphyrin (TPP, **H**), the concentration was so high that a complete conversion was obtained at any wavelength. This included a case where the reaction was performed at 624 nm, with the measured transmission for the solution being 100% (Figure 3). There was still enough

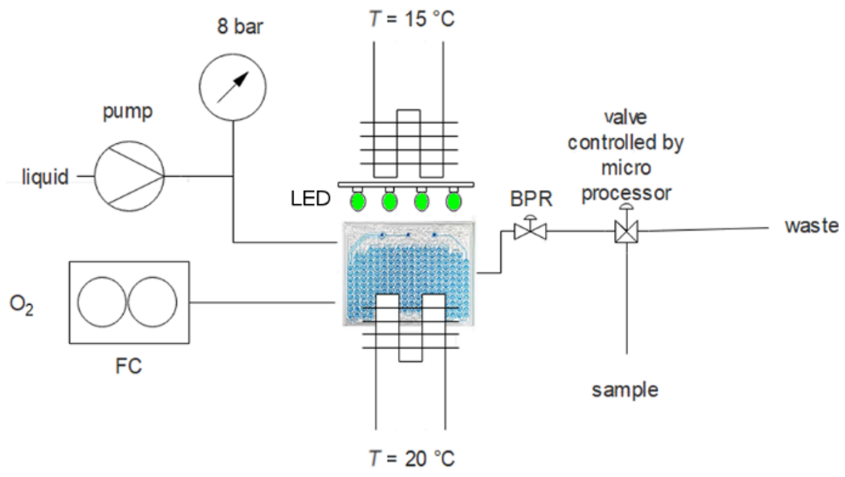

Figure 1: Reaction setup (FC: flow controller, BPR: back pressure regulator).

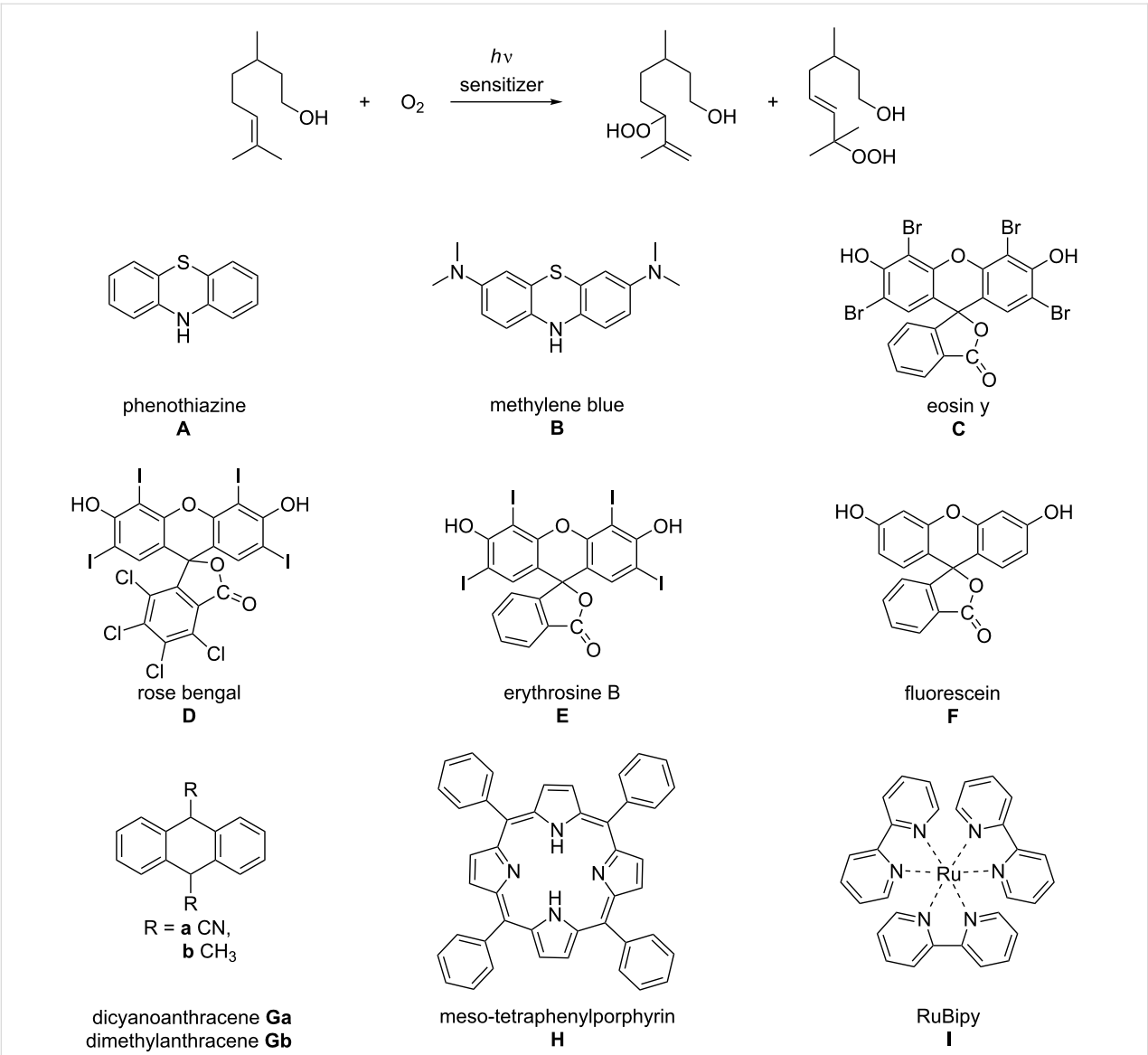

Scheme 1: Photocatalysts **A**–**I** screened for the oxidation of citronellol.

overlap with the Q bands of **H** at 593 and 649 nm to provide a high enough light intensity for the reaction, and thus causing the complete conversion.

A method to obtain an estimation of the required photocatalyst

As the photooxidation reaction has been shown to be dependent on the photocatalyst concentration, a simple method to determine the required amount in a reaction mixture is necessary. Further, when considering an industrial process, the concentration of the photocatalyst will have not only an economic impact but could also impact the downstream process or subsequent synthetic steps. It may be noted that in typical studies on photooxidation reactions, the concentration of the reactants is usually varied, while the catalyst concentration is rarely addressed [24-26].

To study the required photocatalyst concentration, we pursued a different approach based on the realization that in a photochemical reaction, the often overlooked key reagent is, in fact, the light, and through the subsequent interaction between light and the photocatalyst, the light is transformed. Following this logic led to the observation that one needs to more carefully consider not only the concentration of the catalyst but the details of how and to what extent the light interacts with the catalyst in the region where it is exposed to the light. A good starting point for this analysis was the Bunsen–Roscoe law of reciprocity, which states that a photochemical effect is directly proportional to the

Conv[a] / Trans[b]	365	375	383	396	407	424	443	467	524	624	4000k
A	2 71	3 88	2 99	1 100	1 100	0 100	1 100	0 100	0 100	0 100	0 n.a.
B	33 49	53 53	46 53	59 64	28 96	30 100	63 93	66 61	65 29	>96 0	85 n.a.
C	62 45	81 39	84 37	>96 37	89 45	>96 68	88 35	62 20	55 26	0 100	36 n.a.
D	92 21	94 46	91 59	>96 59	>96 57	>96 69	>96 62	>96 33	>96 1	4 100	90 n.a.
E	72 29	78 47	80 49	>96 43	93 44	93 72	>96 53	>96 5	95 1	0 100	64 n.a.
F	3 50	8 53	5 57	2 61	9 68	17 91	35 73	35 77	35 94	5 100	26 n.a.
Ga	>96 7	>96 1	>96 3	>96 1	>96 3	>96 1	>96 100	46 100	0 100	0 100	21 n.a.
H	>96 0	>96 0	96 0	>96 0	>96 0	>96 0	>96 28	>96 55	>96 1	>96 100	>96 n.a.
I[c]	23 80	26 86	31 92	48 91	49 95	61 100	85 100	59 100	0 100	0 100	12 n.a.

Figure 2: Conversion and transmission at fixed reaction conditions (0.5 N citronellol, 1 mL/min,1 mol % catalyst, 2 equiv oxygen, 8 bar, 20 °C, reactor volume: 2.7 mL, solvent: ethanol (**B**, **C**, **D**, **E**, and **F**) or dichloromethane (**A**, **G**, **H**, and **I**)). [a]The conversion was determined by GC after quenching with PPh_3. [b]Transmission (in %) of the starting solution at 0.5 mm pathlength. [c]Catalyst concentration: 0.1 mol %.

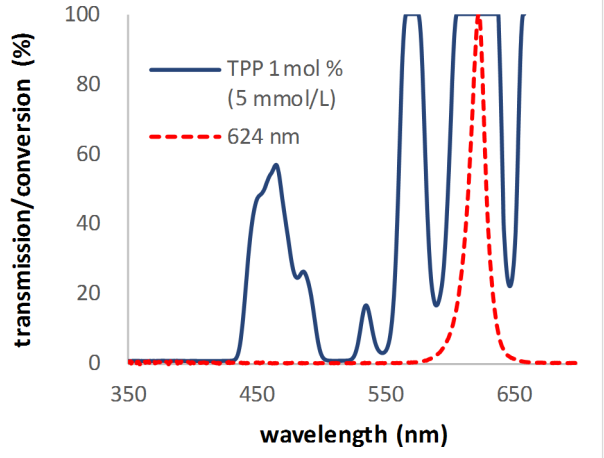

Figure 3: Measured transmission spectrum of a 5 mmol/L (1 mol %) solution of TPP (**H**) in dichloromethane with 0.5 N citronellol and the emission spectrum of the LED with an emission maximum at 624 nm.

total energy dose, which, for a flow reactor, is the product of the light intensity and time [27-29]. The light intensity can be considered as the limiting factor in a flow setup as the space around the reaction channel is limited, as is the power of the light source. The exposure time has less limitations as it is controlled by the flow rate. This implies that in order to conduct an efficient reaction, the use of the light has to be optimized such that the quantity of light reaching the reaction mixture in the channel is large enough to be totally absorbed.

Our approach to considering light more conspicuously as a reagent uses the Bouguer–Lambert–Beer law as a starting point to estimate a concentration close to the optimum. The law in its basic definition is not entirely applicable to a flow reactor but will nevertheless provide a convenient starting point [30,31]. The analysis of the required concentration of the catalyst begins with recognizing how the law is applied and what the differences from the batch approach that it describes are [32]. A flow reactor has a channel height that is a well-defined rectangle, allowing it to be used synonymously to the path length of the light. However, since the path length of the channel is much shorter than the path length used in a classical cuvette measurement, the values obtained from the Beer's law plot may be less accurate. A second contribution to the approximation is that to use all the light, the transmission through the channel needs to be below 1%, which corresponds to an absorption of >2. This condition also limits the use of the Bouguer–Lambert–Beer law since at these high absorption values, the extinction coefficient may exhibit a nonlinear behavior with respect to the concentration of the catalyst [33]. Taking note of the facts above but pressing on and applying Beer's law using a path length fixed at 0.04 cm and an extinction of 2, the molar extinction coefficient still needs to be calculated. Therefore, the molar extinction coefficient needs to be measured separately in a UV–vis spectrometer as the emission maximum of the LED source does, in most cases, not correspond to the absorption maximum of the catalyst. Furthermore, the spectra need to be obtained under the

same conditions under which the reactions take place, i.e., in the same reaction medium, at the same temperature and, if possible, at the same path length. The first two parameters are extremely important as the absorption peak will shift in both height and wavelength depending on the reaction medium and temperature [34]. The path length should be as close as practical to that of the reactor as this will reduce the error imparted by the limitations of the Bouguer–Lambert–Beer law. Table 1 shows the values measured for the extinction coefficient, the LED peak, and the absorption maximum based on the measured values and the predicted concentration for the catalyst using the channel height of 0.04 cm.

Figures 4–6 serve to illustrate three possible examples. For rose bengal (**D**, Figure 4), the emission maximum of the used LED fits nearly to a secondary peak. Dimethylanthracene (DMA, **Gb**, Figure 5), with three absorption peaks, covers a wide range of possible LEDs. TPP (**H**, Figure 6) is the opposite of DMA (**Gb**). It has a very high absorption in a very narrow peak range (that is, a Soret band). As can be seen in Figure 6, the absorption maximum (here transmission 0%) is close to the emission spectra of two of the LEDs, with only 5 and 12 nm difference, respectively. Nevertheless, the calculated concentrations were nearly two or three times higher when compared to the lowest concentration, which would be required for a perfect fit between the absorption maximum and the LED emission. This highlights why it is so important to measure the absorption in the intended reaction medium. A solvent change could shift the maximum by a few nm (TPP: 416 nm in chloroform [37], 418 nm in benzene [38], and 419 nm in toluene [35]).

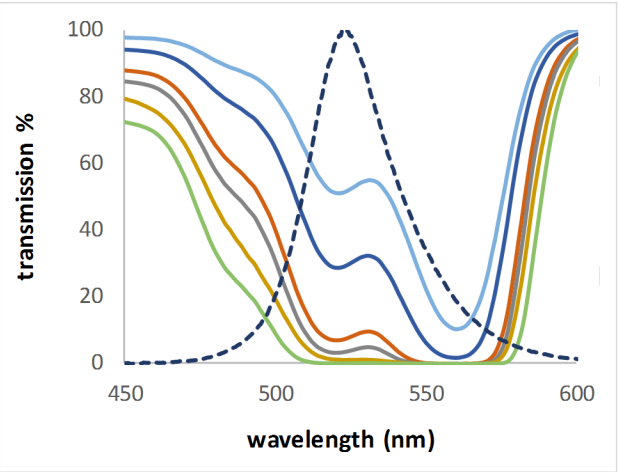

Figure 4: Transmission spectra of rose bengal (**D**) and the emission spectrum of an LED with a maximum at 524 nm (scaled to 100%).

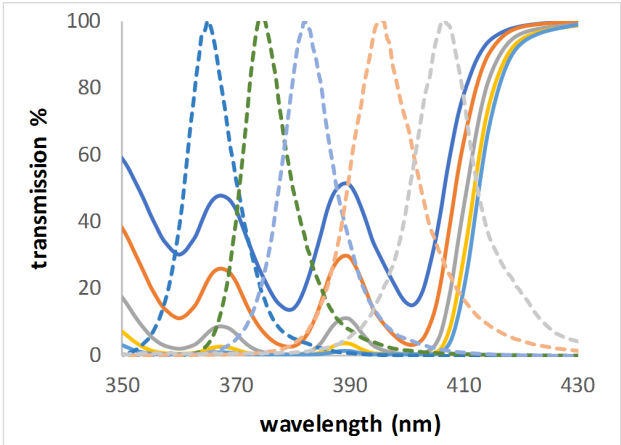

Figure 5: Transmission spectra of dimethylanthracene (**Gb**) and emission spectra of LEDs with maxima at 365, 375, 383, 394, and 407 nm, respectively (all scaled to 100%).

Table 1: Measured extinction coefficients and estimated ideal catalyst concentrations.

sensitizer	wavelength [nm]	extinction coefficient [L/(mol·cm)]	literature reference	calculated sensitizer concentration [mmol/L]
rose bengal (**D**)	**560**	**90000**	**90400** [35]	**0.56**
	524[a]	37400		1.34
	524[b]	38100		1.31
TPP (**H**)	424	349000		0.20
	419	**401000**	**443000** [35]	**0.12**
	407	158000		0.32
DMA (**Gb**)	407	2800		17.86
	398	**7300**	**7500** [36]	**6.85**
	396	6000		8.33
	383	6900		7.25
	375	6500		7.69
	365	3800		13.16

Rose bengal (**D**) was measured in [a]ethanol or [b]acetonitrile, with 0.5 N citronellol; TPP (**H**) was measured in toluene with 1 N alpha-terpinene; DMA (**Gb**) was measured in toluene with 0.5 N alpha-terpinene.

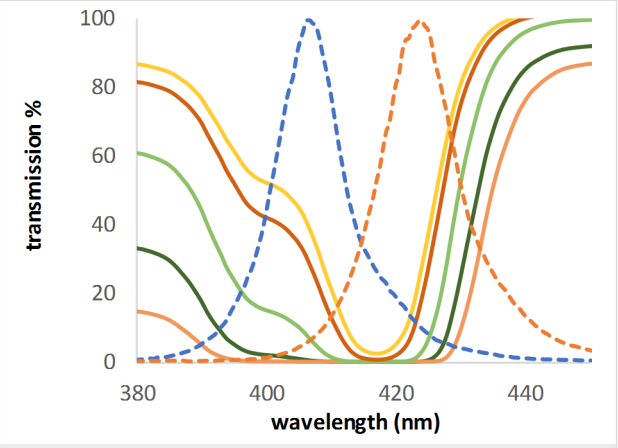

Figure 6: Transmission spectra of TPP (**H**) and emission spectra of LEDs with maxima at 407 and 424 nm, respectively (both scaled to 100%).

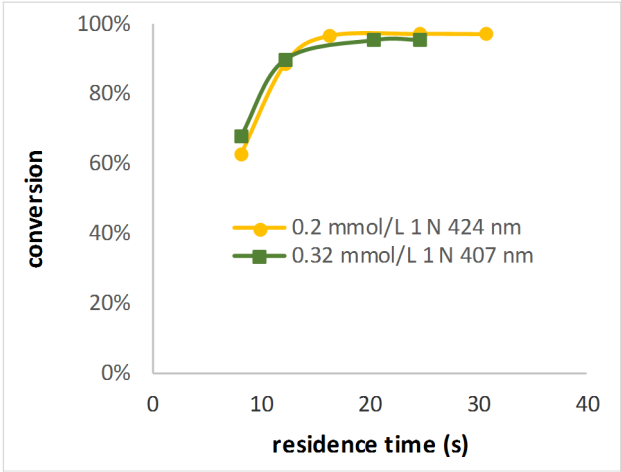

Figure 7: Conversion of alpha-terpinene using the wavelength-adapted TPP (**H**) concentrations.

Reactions using calculated photocatalyst concentrations

The concentrations calculated for the catalyst were tested using the oxidation of alpha-terpinene (Scheme 2) and the oxidation of citronellol (Scheme 1). All reactions were conducted with 2 equiv of oxygen at 8 bar and 20 °C. The temperature of the light source was kept constant at 15 °C. It is very important to control the temperature of the reaction and the LEDs as the emission and absorption maxima are dependent on the temperature. The (minimum) exposure times were calculated using the liquid flow rate and the flow rate of the gas at the entrance. The results (Figure 7) show that similar results were obtained for the photooxidation of alpha-terpinene using TPP (**H**) at different wavelengths with the corresponding calculated amount of the catalyst.

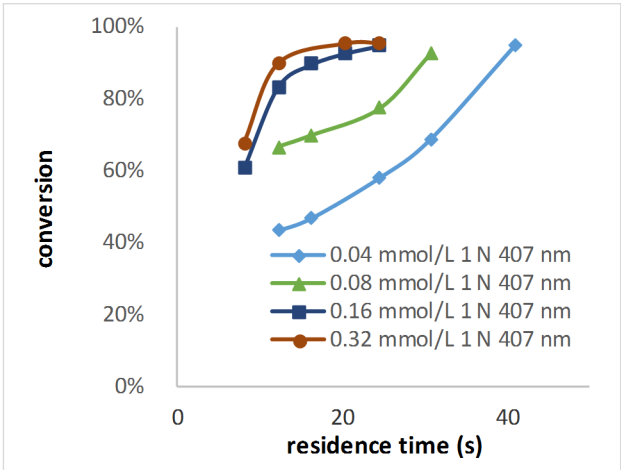

Figure 8: Conversion of alpha-terpinene at different TPP (**H**) concentrations.

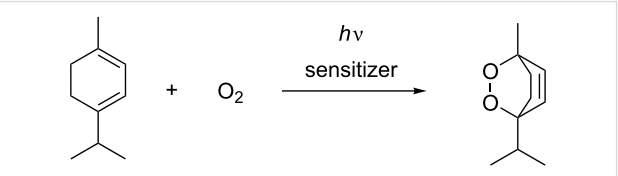

Scheme 2: Photooxidation of alpha-terpinene.

The reduction of the catalyst concentration to half of the calculated value led to a small decrease in the conversion. This decrease became much larger when the catalyst concentration was further decreased by half again (Figure 8). This exponential decrease can be explained by the fact that the transmission of the light increased exponentially with a decreasing amount of the catalyst.

When DMA (**Gb**) was used and short exposure times were applied, the expected difference in conversion for the wavelengths 365 nm and 407 nm was seen: the reaction was not complete for any of the used wavelengths (Figure 9). This is completely in line with the observations made for TPP catalyst (**H**) concentrations.

Rose bengal (**D**) gave similar results: increasing the amount of the catalyst by 50% provided a slightly higher conversion for high flow rates, and the change of the solvent from ethanol to acetonitrile had the same impact (Figure 10). This can be attributed to the higher absorption of **D** in acetonitrile [39]. Those two results show the limitation of our approach because if the Bouguer–Lambert–Beer law would have been valid, the conversion should have been the same for the three conditions.

Our approach was to provide a simple means to optimize the catalyst used in conjunction with the maximum amount of light. As such, the question concerning the effect obtained upon varia-

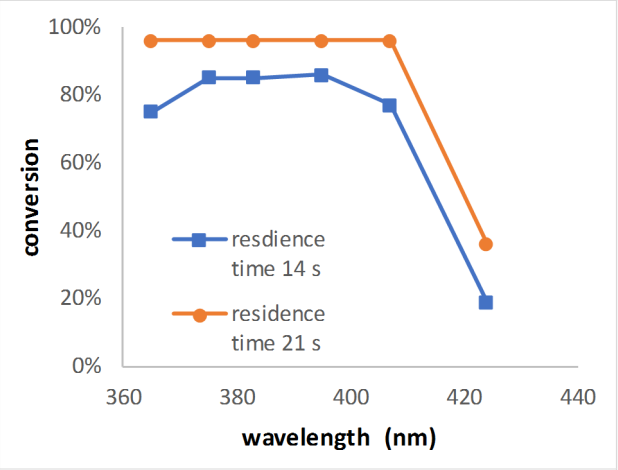

Figure 9: Conversion of alpha-terpinene (0.5 N) as a function of the wavelength using DMA (**Gb**) as the catalyst (7.25 mmol/L).

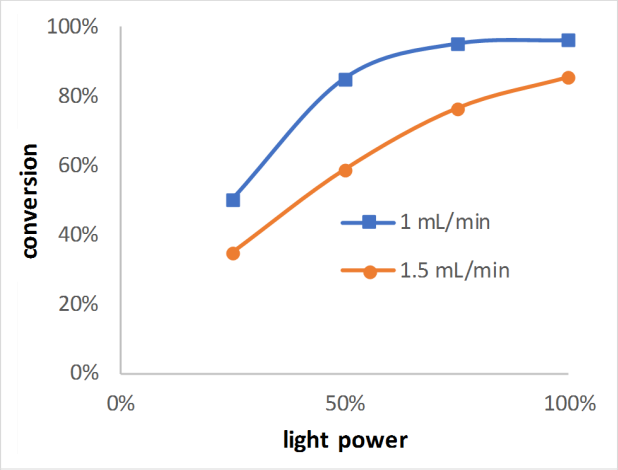

Figure 11: Conversion of citronellol as a function of the light power (0.5 mol/L of citronellol, 1.34 mmol/L rose bengal (**D**).

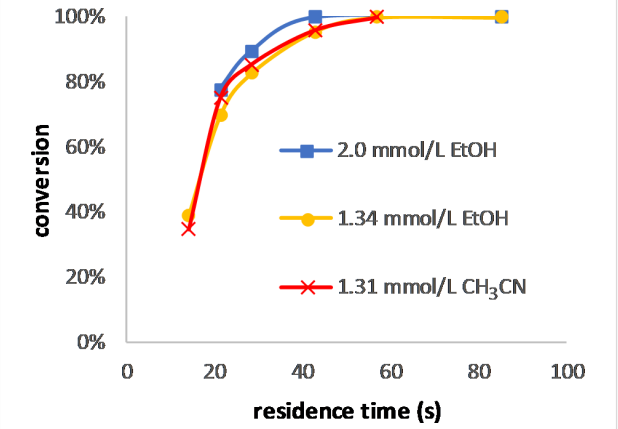

Figure 10: Conversion of citronellol at different concentrations of rose bengal (**D**).

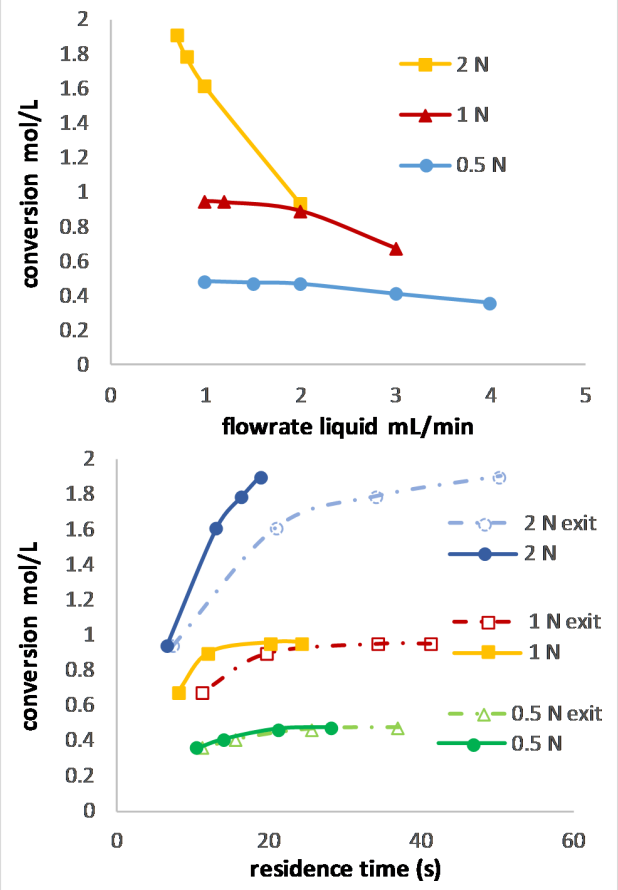

Figure 12: Absolute conversion of various concentrations of alpha-terpinene at 407 nm using 0.32 mmol/L of TPP (**H**) as a function of the liquid flow rate (top) and the residence time (bottom).

tion of the light power arose. The answer to this can be found in Figure 11: rather large changes in the conversion of citronellol were observed as a function of the light power, and a greater effect was unsurprisingly observed for the slower flow rate.

The effect of varying the concentration of the reactant concentration of alpha-terpinene while keeping the TPP (**H**) concentration constant (0.32 mmol/L) is shown in Figure 12.

Here, the ratio of alpha-terpinene to the catalyst decreased from 0.064 mol % to 0.016 mol %, and the conversion increased in a similar manner to that caused by the concentration changes. An exact comparison was not possible as it would be extremely difficult to calculate or even estimate the exact residence time. The residence times in Figure 12 were calculated based on the flow rate of the entrance and exit measurements (the conversion of the oxygen gas was considered). The reduction of the gas caused by the solubility of oxygen at the given pressure in the reaction mixture was also not considered, but for pure toluene, it would be 14% (0.5 N) or 4% (2 N) less gas volume [40]. Furthermore, the gas-to-liquid ratio change with the modification of the alpha-terpinene concentration impacts the flow

pattern (droplet/bubble size), which could, in turn, have an impact on the conversion [41]. But the main limitation was the light itself, as can be seen in Figure 11. About the same absolute conversion was obtained for similar liquid flow rates independent from the residence time.

Conclusion

We developed a reliable, quick, and simple approach to find the appropriate starting concentration of a photocatalyst for a photooxidation reaction in a flow reactor. This was achieved by linking the catalyst concentration to the channel height of the flow reactor and to the emission spectrum of the light source, using the Bouguer–Lambert–Beer law. Since the conditions applied were outside of, but close to the range of this law, the determined concentrations will be close to, but not exactly the optimum. The approach was tested with different light sources, and it was shown that it is important to match the LED to the reaction absorption spectrum. This is important as a variation of only a few nm can have a big impact on the catalyst concentration needed. We believe that this methodology will help in choosing the right catalyst and the right wavelength to eliminate scale-up issues encountered during the industrialization of photooxidation reactions.

Supporting Information

Supporting Information File 1

Descriptions of material and methods, flow setup, and LED characterization.
[https://www.beilstein-journals.org/bjoc/content/supplementary/1860-5397-16-78-S1.pdf]

Acknowledgements

We would like to thank Dr. Jürgen Kolz from Magritek for his support with NMR analytics and Dr. Edward “Ed” J Fewkes for his help with the manuscript and scientific discussions.

ORCID® iDs

Clemens R. Horn - https://orcid.org/0000-0002-8105-6932
Sylvain Gremetz - https://orcid.org/0000-0001-9851-0604

References

1. Politano, F.; Oksdath-Mansilla, G. *Org. Process Res. Dev.* **2018,** *22,* 1045–1062. doi:10.1021/acs.oprd.8b00213
2. Cambié, D.; Bottecchia, C.; Straathof, N. J. W.; Hessel, V.; Noël, T. *Chem. Rev.* **2016,** *116,* 10276–10341. doi:10.1021/acs.chemrev.5b00707
3. Beeler, A. B. *Chem. Rev.* **2016,** *116,* 9629–9630. doi:10.1021/acs.chemrev.6b00378
4. Garlets, Z. J.; Nguyen, J. D.; Stephenson, C. R. J. *Isr. J. Chem.* **2014,** *54,* 351–360. doi:10.1002/ijch.201300136
5. Knowles, J. P.; Elliott, L. D.; Booker-Milburn, K. I. *Beilstein J. Org. Chem.* **2012,** *8,* 2025–2052. doi:10.3762/bjoc.8.229
6. Noël, T. *J. Flow Chem.* **2017,** *7,* 87–93. doi:10.1556/1846.2017.00022
7. Di Filippo, M.; Bracken, C.; Baumann, M. *Molecules* **2020,** *25,* 356. doi:10.3390/molecules25020356
8. Pfoertner, K.-H.; Oppenländer, T. Photochemistry. *Ullmann's Encyclopedia of Industrial Chemistry;* Wiley-VCH: Weinheim, Germany, 2012. doi:10.1002/14356007.a19_573.pub2
9. Berton, M.; de Souza, J. M.; Abdiaj, I.; McQuade, D. T.; Snead, D. R. *J. Flow Chem.* **2020,** *10,* 73–92. doi:10.1007/s41981-019-00060-x
10. Lavric, E. D.; Woehl, P. *Chim. Oggi* **2009,** *27* (3), 45–48.
11. Woitalka, A.; Kuhn, S.; Jensen, K. F. *Chem. Eng. Sci.* **2014,** *116,* 1–8. doi:10.1016/j.ces.2014.04.036
12. Hone, C. A.; Roberge, D. M.; Kappe, C. O. *ChemSusChem* **2017,** *10,* 32–41. doi:10.1002/cssc.201601321
13. Nieves-Remacha, M. J.; Kulkarni, A. A.; Jensen, K. F. *Ind. Eng. Chem. Res.* **2013,** *52,* 8996–9010. doi:10.1021/ie4011707
14. Gemoets, H. P. L.; Su, Y.; Shang, M.; Hessel, V.; Luque, R.; Noël, T. *Chem. Soc. Rev.* **2016,** *45,* 83–117. doi:10.1039/c5cs00447k
15. Schenck, G. O. Light sources and light filters in preparative organic photochemistry. In *Preparative Organic Photochemistry;* Schönberg, A., Ed.; Springer: Berlin, Germany, 1968; pp 472–494. doi:10.1007/978-3-642-87918-0_46
16. Sender, M.; Ziegenbalg, D. *Chem. Ing. Tech.* **2017,** *89,* 1159–1173. doi:10.1002/cite.201600191
17. Ghazali, S. K.; Azim, F. S. S.; Adrus, N.; Jamaluddin, J. *J. Photopolym. Sci. Technol.* **2019,** *32,* 705–710. doi:10.2494/photopolymer.32.705
18. Cho, J.; Park, J. H.; Kim, J. K.; Schubert, E. F. *Laser Photonics Rev.* **2017,** *11,* 1600147. doi:10.1002/lpor.201600147
19. Fewkes, E. J.; Horn, C. R.; Logunov, S. L. Flow reactor for photochemical reaction. U.S. Patent US10,258,957, March 26, 2015. We have already used successfully LED at 300 nm, but the power of the LEDs is low (40 mW) and long residence times are required to obtain conversion.
20. Bonfield, H. E.; Knauber, T.; Lévesque, F.; Moschetta, E. G.; Susanne, F.; Edwards, L. J. *Nat. Commun.* **2020,** *11,* 804. doi:10.1038/s41467-019-13988-4
21. Yueh, H.; Gao, Q.; Porco, J. A., Jr.; Beeler, A. B. *Bioorg. Med. Chem.* **2017,** *25,* 6197–6202. doi:10.1016/j.bmc.2017.06.010
22. Gauron, G.; Ao, J.; Gremetz, S.; Horn, C. R. *Chim. Oggi* **2018,** *36* (4), 12–16.
23. Lévesque, F.; Seeberger, P. H. *Org. Lett.* **2011,** *13,* 5008–5011. doi:10.1021/ol2017643
24. Hunter, R.; Josland, S.; Moore, J.; Guthrie, D.; Robertson, M. J.; Oelgemöller, M. *Curr. Org. Chem.* **2018,** *22,* 2501–2508. doi:10.2174/1385272822666181109103342
25. Radjagobalou, R.; Blanco, J.-F.; Dechy-Cabaret, O.; Oelgemöller, M.; Loubière, K. *Chem. Eng. Process.* **2018,** *130,* 214–228. doi:10.1016/j.cep.2018.05.015
26. Hamami, Z. E.; Vanoye, L.; Fongarland, P.; de Bellefon, C.; Favre-Réguillon, A. *ChemPhotoChem* **2019,** *3,* 122–128. doi:10.1002/cptc.201800201
27. Bunsen, R.; Roscoe, H. *Ann. Phys. (Berlin, Ger.)* **1857,** *176,* 43–88. doi:10.1002/andp.18571760104
28. Bunsen, R.; Roscoe, H. *Ann. Phys. (Berlin, Ger.)* **1857,** *176,* 481–516. doi:10.1002/andp.18571760402

29. Bunsen, R.; Roscoe, H. *Ann. Phys. (Berlin, Ger.)* **1857,** *177,* 235–263. doi:10.1002/andp.18571770605
30. Mäntele, W.; Deniz, E. *Spectrochim. Acta, Part A* **2017,** *173,* 965–968. doi:10.1016/j.saa.2016.09.037
31. Mayerhöfer, T. G.; Mutschke, H.; Popp, J. *ChemPhysChem* **2016,** *17,* 1948–1955. doi:10.1002/cphc.201600114
32. Sambiagio, C.; Noël, T. *Trends Chem.* **2020,** *2,* 92–106. doi:10.1016/j.trechm.2019.09.003
33. Tolbin, A. Y.; Pushkarev, V. E.; Tomilova, L. G.; Zefirov, N. S. *Phys. Chem. Chem. Phys.* **2017,** *19,* 12953–12958. doi:10.1039/c7cp01514c
34. Ito, M. *J. Mol. Spectrosc.* **1960,** *4,* 106–124. doi:10.1016/0022-2852(60)90072-2
35. Taniguchi, M.; Lindsey, J. S. *Photochem. Photobiol.* **2018,** *94,* 290–327. doi:10.1111/php.12860
36. Fukuzumi, S.; Yuasa, J.; Miyagawa, T.; Suenobu, T. *J. Phys. Chem. A* **2005,** *109,* 3174–3181. doi:10.1021/jp050347u
37. Salker, A. V.; Gokakakar, S. D. *Int. J. Phys. Sci.* **2009,** *4* (6), 377–384.
38. Sharghi, H.; HassaniNejad, A. *Tetrahedron* **2004,** *60,* 1863–1868. doi:10.1016/j.tet.2003.12.030
39. Ludvíková, L.; Friš, P.; Heger, D.; Šebej, P.; Wirz, J.; Klán, P. *Phys. Chem. Chem. Phys.* **2016,** *18,* 16266–16273. doi:10.1039/c6cp01710j
40. Wu, X.; Deng, Z.; Yan, J.; Zhang, Z.; Zhang, F.; Zhang, Z. *Ind. Eng. Chem. Res.* **2014,** *53,* 9932–9937. doi:10.1021/ie5014772
41. Nakano, M.; Morimoto, T.; Noguchi, J.; Tanimoto, H.; Mori, H.; Tokumoto, S.-i.; Koishi, H.; Nishiyama, Y.; Kakiuchi, K. *Bull. Chem. Soc. Jpn.* **2019,** *92,* 1467–1473. doi:10.1246/bcsj.20190117

License and Terms

This is an Open Access article under the terms of the Creative Commons Attribution License (http://creativecommons.org/licenses/by/4.0). Please note that the reuse, redistribution and reproduction in particular requires that the authors and source are credited.

The license is subject to the *Beilstein Journal of Organic Chemistry* terms and conditions: (https://www.beilstein-journals.org/bjoc)

The definitive version of this article is the electronic one which can be found at: doi:10.3762/bjoc.16.78

BEILSTEIN JOURNAL OF ORGANIC CHEMISTRY

Recent applications of porphyrins as photocatalysts in organic synthesis: batch and continuous flow approaches

Rodrigo Costa e Silva[1], Luely Oliveira da Silva[1,2], Aloisio de Andrade Bartolomeu[1], Timothy John Brocksom[1] and Kleber Thiago de Oliveira[*1]

Review

Open Access

Address:
[1]Departamento de Química, Universidade Federal de São Carlos, São Carlos, SP, 13565-905, Brazil and [2]Departamento de Ciências Naturais, Universidade do Estado do Pará, Marabá, PA, 68502-100, Brazil

Email:
Kleber Thiago de Oliveira[*] - kleber.oliveira@ufscar.br

* Corresponding author

Keywords:
energy transfer; photocatalysis; photooxygenation; photoredox; porphyrins

Beilstein J. Org. Chem. **2020,** *16,* 917–955.
doi:10.3762/bjoc.16.83

Received: 26 February 2020
Accepted: 22 April 2020
Published: 06 May 2020

This article is part of the thematic issue "Advances in photoredox catalysis".

Guest Editor: T. Noël

© 2020 Costa e Silva et al.; licensee Beilstein-Institut.
License and terms: see end of document.

Abstract

In this review we present relevant and recent applications of porphyrin derivatives as photocatalysts in organic synthesis, involving both single electron transfer (SET) and energy transfer (ET) mechanistic approaches. We demonstrate that these highly conjugated photosensitizers show increasing potential in photocatalysis since they combine both photo- and electrochemical properties which can substitute available metalloorganic photocatalysts. Batch and continuous-flow approaches are presented highlighting the relevance of enabling technologies for the renewal of porphyrin applications in photocatalysis. Finally, the reaction scale in which the methodologies were developed are highlighted since this is an important parameter in the authors' opinion.

Introduction

In the last decade, photochemistry has re-emerged as a powerful tool for the scientific community. Although photochemical processes have been discovered over almost two centuries [1], only recently the scientific commuity has improved reactor technologies for the application of these processes on a large scale. The scalability of these processes had been limited by the requirement for small-volume batch reactors equipped with mercury vapor discharge lamps [1]. In general, the use of batch reactors on a large-scale is hampered due to the attenuation effect of photon transport (Bouguer–Lambert–Beer law) [1-3]. This effect limits the penetration of photons to only a short distance into the reaction vessel, provoking increases of the reaction time, photocatalyst loading, byproducts, overheating and so on. Notably, the use of continuous-flow reactors for photochemical applications allows us to overcome these issues, and leads to a drastic reduction of reaction time, lower photocatalyst loadings, minimization of the formation of byproducts [2] and uses visible light, which is considered a clean reagent [4]. Overall, visible light combined with organic photocatalysts such as porphyrinoids, make continuous-flow photochemistry a sustainable alternative approach being applied already by the chemical and pharmaceutical industries.

Porphyrinoid is the term given for a class of organic compounds containing four pyrrole rings connected by four methylene bridges, and include porphyrin, chlorin, bacteriochlorin, and isobacteriochlorin. The cores of the porphyrin and chlorin scaffolds contain respectively 22 π and 20 π electrons, whereas bacteriochlorins and isobacteriochlorins contain 18 π electrons (Figure 1). The 18 π electron aromatic system (Figure 1, in bold) of the porphyrinoids confers stability, planarity and special electronic characteristics to these compounds. As it is well-known, tetrapyrrolic compounds are considered to be the "pigments of life" since they play a key role in essential biological processes, such as photosynthesis (chlorophylls and bacteriochlorophylls), redox reactions for detoxification of anthropogenic chemicals (cytochrome P450) and oxygen transport (hemoglobin) [5,6].

Taking into account this big group of molecules, porphyrins are notable due to both their physicochemical and electronic properties, which can be fine-tuned by functionalization of the core structures [8]. The adequate tuning of the porphyrin properties can enable them to absorb light in almost all of the UV–vis spectral range. Porphyrins also have elevated molar absorptivity (ca 10^5 $L \cdot mol^{-1} \cdot cm^{-1}$) and appropriate electronic levels for both energy transfer (ET) and single electron transfer (SET) in many photoprocesses [9-11]. Additionally, it is possible to realize tuning in terms of chemical properties by changing substituents, thus producing robust, soluble or heterogeneous, readily available and low-cost photocatalysts.

The mechanisms of the photocatalytic activities of porphyrins are similar to other photocatalysts. Under light irradiation, one electron from the ground state (S_0) is promoted to the excited singlet state (S_1) which has a short lifetime (10^{-9} s). Therefore, fast intersystem-crossing of one electron gives the excited triplet state (T_1) with a relatively longer lifetime (10^{-6} s). While the porphyrin is in the triplet excited state, two distinct processes can be observed: a) single electron transfer (SET); and b) energy transfer (Figure 2) [12-14]. The first involves the exchange of electrons between the porphyrin and the substrate by an oxidative or reductive process, and the second involves energy transfer to surrounding molecules, such as molecular oxygen, heterocycles and other relevant molecules [15-17].

The excited states of porphyrins are also both potent oxidants and reductants when compared to the ground state. This phenomenon can be measured by the comparison of the standard reduction potentials for the photocatalyst in both ground and excited states [14]. For example, the oxidation potentials for ground [$E_{1/2}(TPP^{+\bullet}/TPP)$] and excited states [$E_{1/2}(TPP^{+\bullet}/TPP^{*})$] of tetraphenylporphyrin (TPP), whose electrochemical data are available [10], are +1.03 V and −0.42 V, respectively (both vs saturated calomel electrode (SCE)). These data indicate that the excited state of TPP is a more efficient electron donor than its ground state. At the same time, the reduction potential value suggests that the excited state of TPP ($E_{1/2}(TPP^{*}/TPP^{-\bullet})$ = +0.42 V vs SCE) is a more efficient electron acceptor than its ground state ($E_{1/2}(TPP/TPP^{-\bullet})$ = −1.03 V vs SCE). Thus, depending on the reaction system in which this photocatalyst is being used, reductive or oxidative processes can be accomplished.

In this review, we intend to highlight applications of porphyrins and their analogs in both photoredox and energy transfer photocatalyzed reactions. The idea of this review is also to

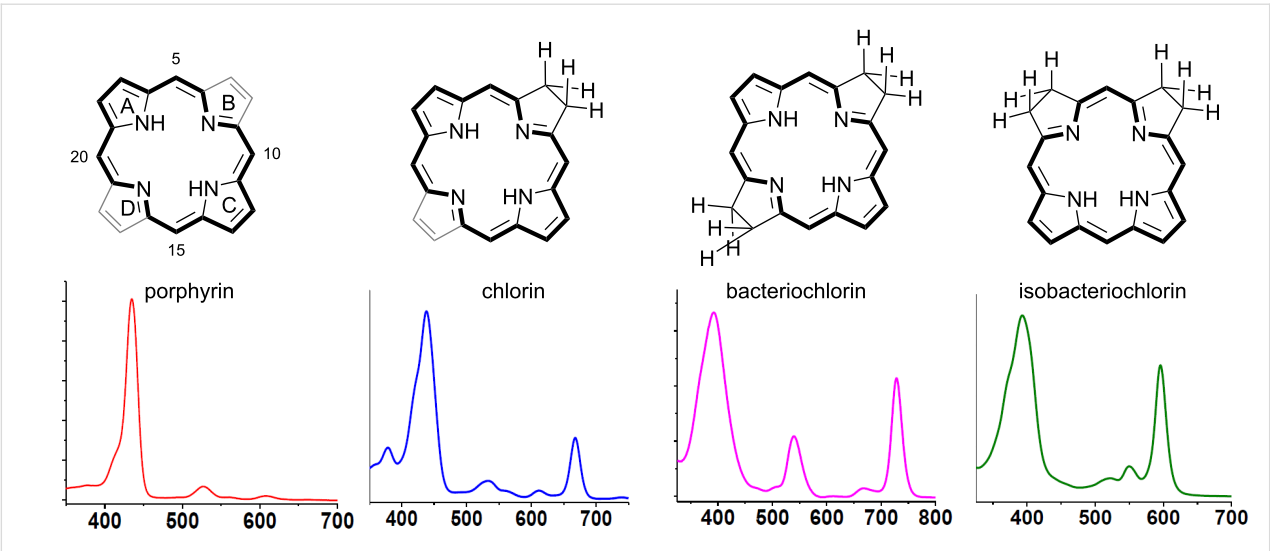

Figure 1: Chemical structures of the porphyrinoids and their absorption spectra: in bold are highlighted the 18 π aromatic system. Adapted from [7].

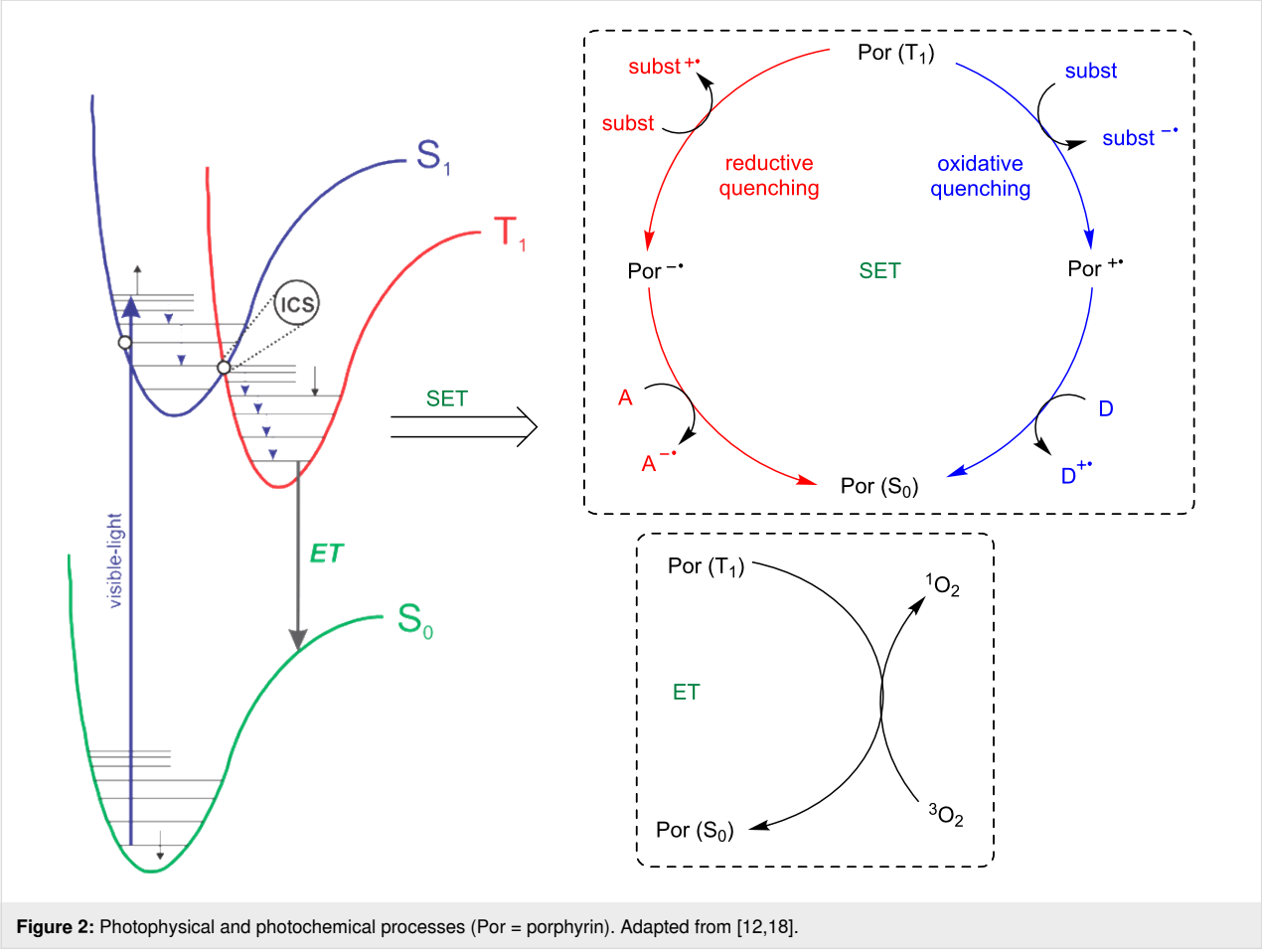

Figure 2: Photophysical and photochemical processes (Por = porphyrin). Adapted from [12,18].

cover representative chemical transformations and recent applications in both batch and continuous-flow conditions, and emphasizing as much as possible, the scale in which the reactions were described. It is important to clarify that other relevant reviews reporting applications of porphyrins in different perspectives can be found in the literature [19-21].

In addition, we emphasize that this review is organized into two topics. The first topic highlights the reactions that employ porphyrins as photoredox catalysts in both oxidative and reductive quenching. The use of porphyrins as a photosensitizer for singlet oxygen generation is presented in the second topic, which was subdivided into two sections: pericyclic reactions and heteroatom oxidations. The first section describes the use of singlet oxygen in pericyclic reactions with olefins and dienes, and the second deals with heteroatom oxidations carried out by singlet oxygen.

Review

Porphyrins as photoredox catalysts

Porphyrins and metalloporphyrins have been extensively studied as photosensitizers in singlet oxygen generation, but underexploited as photoredox catalysts up to now [10,22]. Remarkably the same system can be applied for both pathways, oxidative and reductive processes, beyond singlet oxygen generation [9,10,23]. Only a few photocatalysts can be applied in both photoredox processes (oxidative and reductive quenching), for example, $[Ru(bpy)_3)]^{2+}$, $[Ir(ppy)_3]$, eosin Y, and 4CzTPN [12] (Figure 3). However, some porphyrin and metalloporphyrin derivatives possess adequate potentials to be applied as photoredox catalysts in C–C and C-heteroatom bond formations [10,22]. Furthermore, supramolecular porphyrin-containing molecules, such as metal-organic (MOF) and covalent-organic frameworks (COF), have significantly expanded the use of these compounds in photoredox catalysis due to the singular electronic features of these materials and chemical robustness as catalysts.

The appearance of porphyrins as photoredox catalysts for C–C bond formation started in 2016 with the report from Gryko's group on the photoredox α-alkylation of aldehydes with diazo compounds using 1 mol % of TPP or ZnTPP as photocatalyst [10] (Scheme 1), thus obtaining functionalized aldehydes in 47–90% yields. These results are similar to those previously re-

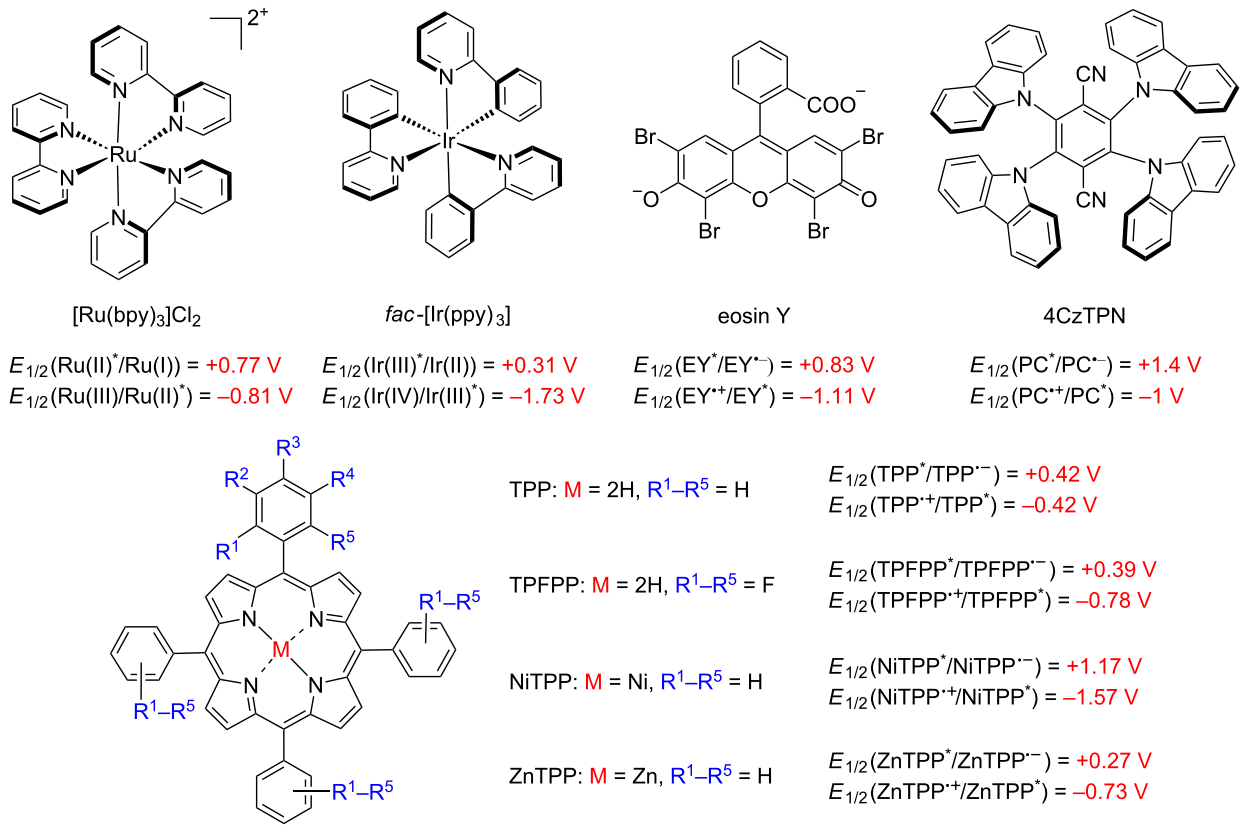

Figure 3: Main dual photocatalysts and their oxidative/reductive excited state potentials, including porphyrin derivatives. Adapted from [10,12,22].

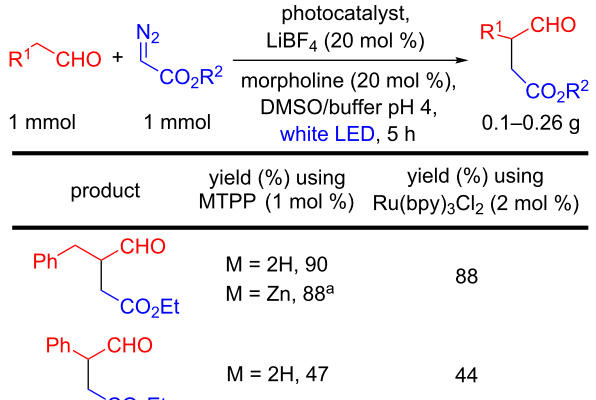

product	yield (%) using MTPP (1 mol %)	yield (%) using $Ru(bpy)_3Cl_2$ (2 mol %)
	M = 2H, 90 M = Zn, 88[a]	88
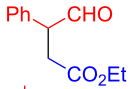	M = 2H, 47	44
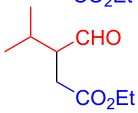	M = 2H, 66	63
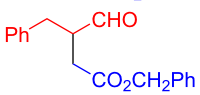	M = 2H, 83	78

Scheme 1: Photoredox alkylation of aldehydes with diazo acetates using porphyrins and a Ru complex. [a]Using a loading of 0.1 mol % for ZnTPP.

ported by the same authors using 2 mol % of a Ru complex as photocatalyst (44–88%) [24].

The mechanism proposed by the authors was supported by the detection of some reaction intermediates, and suggest that TPP works in both energy transfer and photoredox catalysis (Scheme 2).

Subsequently, Gryko's group reported a metal-free photoarylation of five-membered heteroarenes with aryldiazonium salts and *meso*-arylated porphyrin derivatives as photoredox catalyst [11]. Compounds such as furan, thiophene, and *N*-Boc-pyrrole derivatives were obtained by this methodology in 29–81% yields (Scheme 3). The key-step of this transformation involves the formation of an aryl radical by SET between the diazo compound and the porphyrin in its excited state (Scheme 3). The authors demonstrated that *meso*-arylated porphyrins can efficiently act by an oxidative quenching. However, issues about why an electron-poor porphyrin such as tetrakis(pentafluorophenyl)porphyrin (TPFPP) is more efficient in an oxidative quenching compared to an electron-rich (e.g., TPP) remained to be elucidated.

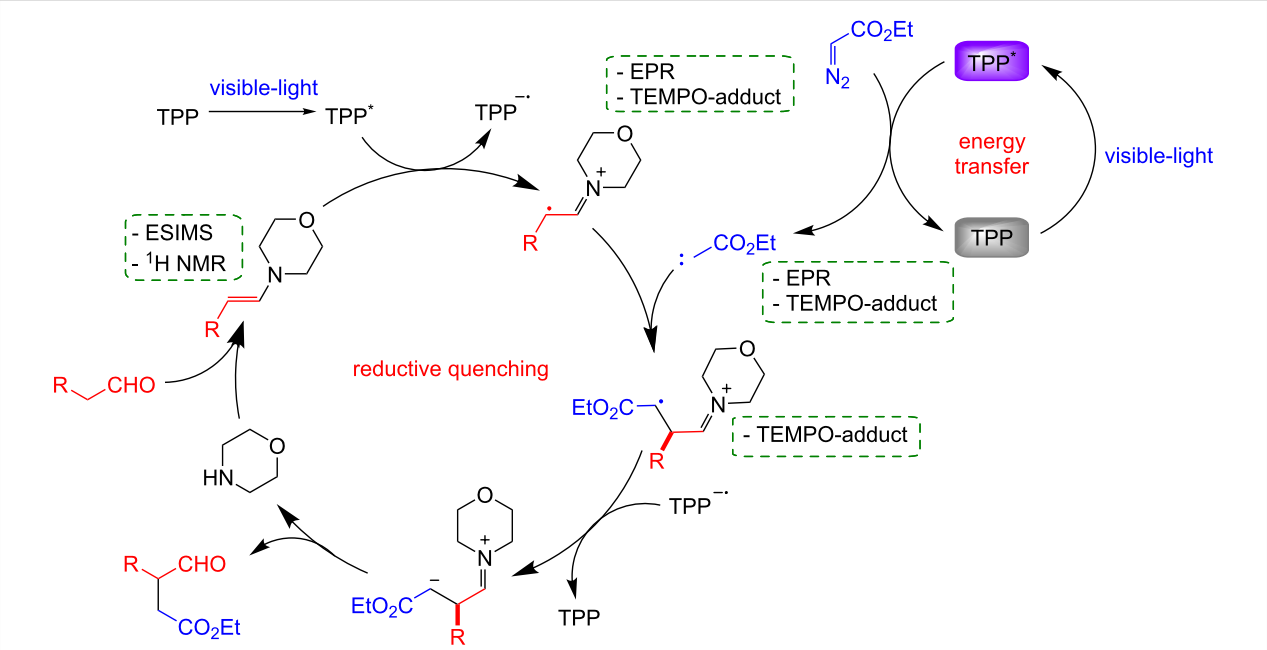

Scheme 2: Proposed mechanism for the alkylation of aldehydes with diazo acetates in the presence of TPP.

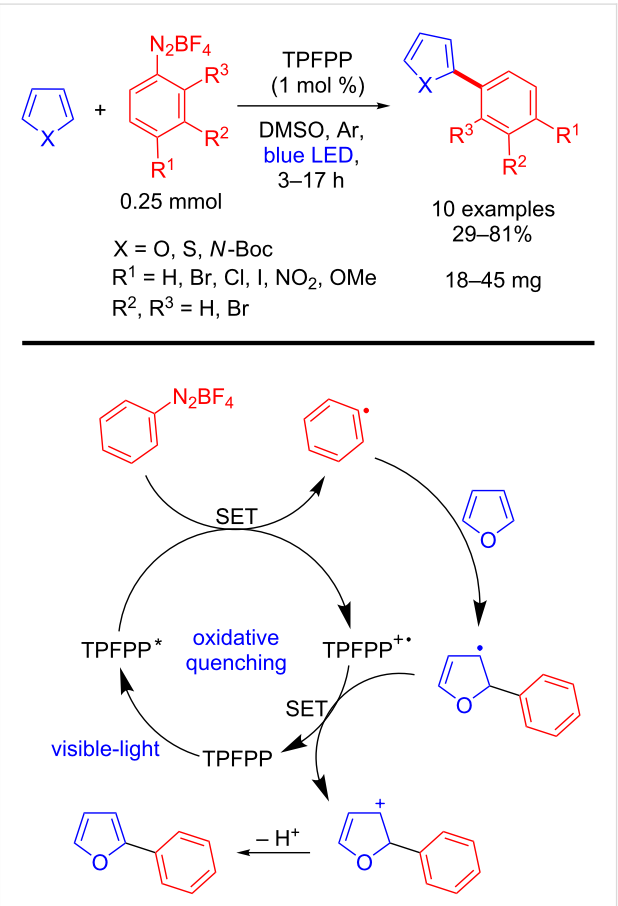

Scheme 3: Arylation of heteroarenes with aryldiazonium salts using TPFPP as photocatalyst, and corresponding mechanism.

In this regard, our research group has contributed in the last 10 years with new porphyrin/chlorin synthetic methodologies, and applications of these compounds in photomedicine [23,25-27]. Recently we reported a porphyrin-photocatalyzed protocol for the arylation of enol acetates and elucidated the mechanism explaining why the electron-deficient porphyrin TPFPP is more efficient than TPP in the whole process (Scheme 4A). Briefly, we have demonstrated that both porphyrins, in the excited state, are thermodynamically able to promote the first photooxidation step (Scheme 4B), however, the turnover of $TPFPP^+$ to TPFPP is much more favored which justifies the acceleration of the photocatalytic cycle. In this protocol, the scope of the diazonium salts, as well as the enol acetates are reported giving versatile α-aryl ketones/aldehydes in both batch and continuous-flow conditions (20 examples in 26–88% yields) [9].

A comparison between batch and flow conditions was performed showing that similar yields are obtained (batch 82% vs flow 85%), but under continuous-flow conditions the reaction time (residence time, t_R) is three times less (Scheme 5A). Our group also developed an end-to-end two-step protocol under continuous-flow conditions, in which the aryldiazonium salt was generated in situ and used directly in the photoarylation of isopropenyl acetate. The corresponding α-aryl ketone was obtained in 28–53% overall yield depending on the scale. An 8 h experiment was conducted in a continuous steady-state mode, producing the same α-aryl ketone in 48% yield on a 3 gram-scale (Scheme 5B).

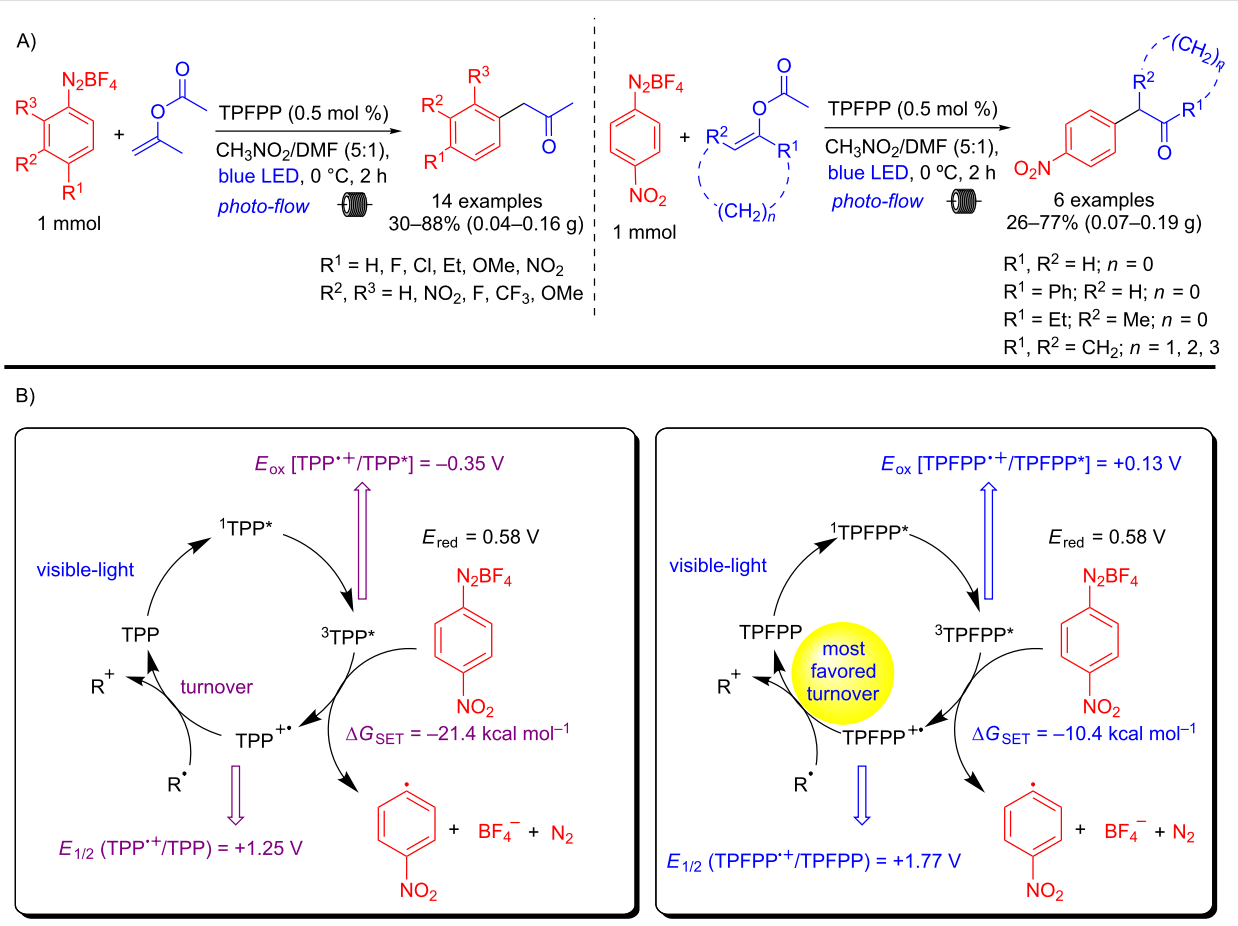

Scheme 4: A) Scope with different aryldiazonium salts and enol acetates. B) Photocatalytic cycles and comparison between TPP and TPFPP.

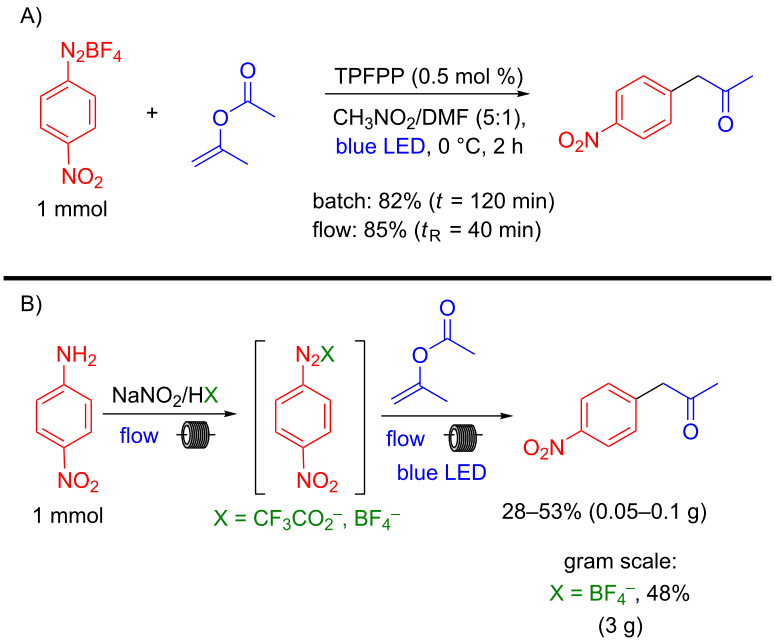

Scheme 5: Photoarylation of isopropenyl acetate A) Comparison between batch and continuous-flow approaches and B) end-to-end protocol.

Photoredox catalysis is not limited to regular N_4-porphyrins (with four pyrrole units), but also can occur with other porphyrinoid compounds. Porphyrins containing other heteroatoms present physicochemical and electronic properties that are quite different from regular N_4-porphyrins. These structures absorb and emit light at lower energies, as for example the thiaporphyrins that absorb beyond 650 nm [8,28]. Derksen and co-workers studied bond-cleavage reactions that can occur in biological microenvironments, using a light source with wavelengths frequently employed in photomedicine (650–850 nm) and thiophene-containing porphyrins [28]. The authors reported that *meso*-5,10,15,20-tetraphenyl-21-monothiaporphyrin (STPP), combined with Hantzsch ester (HEH) and *N*,*N*-diisopropylethylamine (DIPEA), promoted the dehalogenation of α-functionalized carbonyl-containing compounds under red light (λ > 645 nm) in a reductive quenching. DIPEA and HEH act respectively as electron and hydrogen donors. The protocol was efficient for dehalogenations with bromine- and iodine-containing acetophenone derivatives (75–98% yields). However, it was much less efficient with chloro ketones (12–40% yields) and not effective with α-bromo esters and α-bromo amides (Scheme 6).

Many metalloporphyrins are applied as catalysts in industrial processes, such as in the oxidation of cyclohexane to cyclohexanone catalyzed by Co(II) tetraphenylporphyrin on a ton-scale [21]. Recently, Sarkar and co-workers reported the use of nickel(II) tetraphenylporphyrin (NiTPP) as an efficient photocatalyst in both oxidative and reductive quenching [22]. The ability of NiTPP as both photooxidant and photoreductant was observed in maleimide annulation and chalcogenylation reactions, respectively (Scheme 7). For both processes, nickel(II) was determinant for the success of these protocols, as demonstrated by the nonmetallated TPP which did not work.

The tetrahydroquinoline products were obtained in up to 1.1 gram-scale, after 20 h under blue LED irradiation (18 W), for both *N*-alkyl/aryl maleimides (57–92% yields) and the *p*-substituted *N*,*N*-dimethylanilines (78–97% yields). Mixtures of regioisomers were obtained when a *m*-substituted *N*,*N*-dimethylaniline was used. The authors have proposed a reductive quenching pathway mechanism for this protocol (Scheme 8).

The use of NiTPP as photoreductant was also exploited in the selenylation and thiolation reactions of anilines (Scheme 7 and Scheme 9). The methodology involves the in situ formation of the aryldiazonium salt by diazotization with *tert*-butyl nitrite followed by the formation of a trivalent radical chalcogenide. Oxidation to the chalcogenide cation by SET with the cation-radical NiTPP (path a, Scheme 9) or SET with the aryldiazonium salt leads to the other aryl radical species (path b, Scheme 9). The thio- and selenoethers were obtained after solvolysis. Excellent yields (up to 94%) were reported for both selenylation and thiolation of anilines with electron-withdrawing and electron-donating groups in the *ortho*, *meta* and *para* positions. Moreover, the methodology also showed effectiveness for heteroarenes such as pyridines and benzothiazoles.

The authors also evaluated the use of NiTPP as a photoredox catalyst for other transformations involving both oxidative and reductive quenchings. The NiTPP-catalyzed reactions between *N*-phenyltetrahydroisoquinoline and dimethyl malonate, nitromethane, indoles, and dialkyl phosphonates furnished the α-substituted *N*-phenyltetrahydroisoquinolines in yields equal or better than with the originally used photocatalysts, such as eosin and Ir-complex [29-31] (Scheme 10). For an oxidative quenching, the photoarylation of heteroarenes and alkynes with

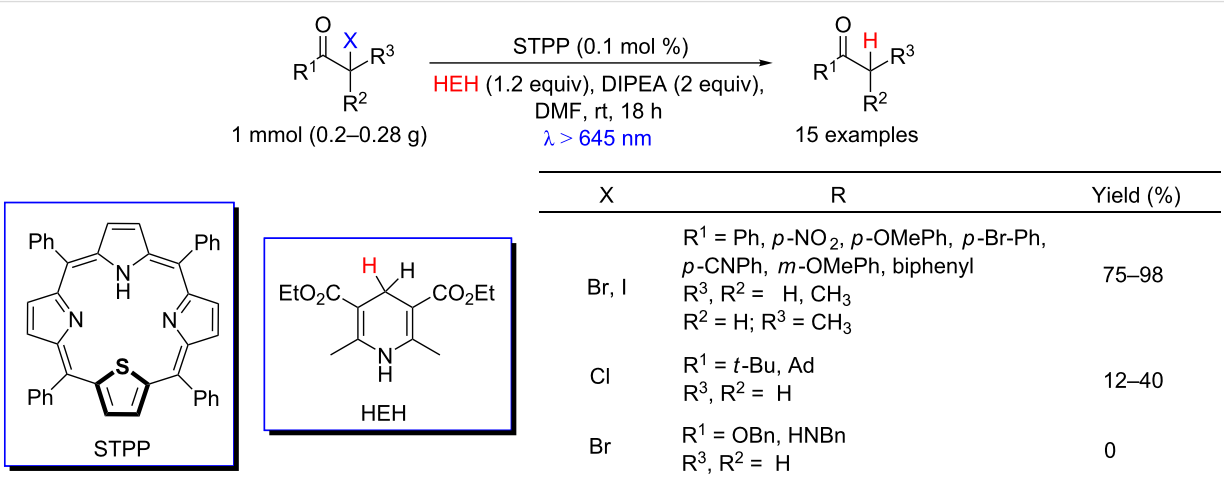

X	R	Yield (%)
Br, I	R^1 = Ph, *p*-NO_2, *p*-OMePh, *p*-Br-Ph, *p*-CNPh, *m*-OMePh, biphenyl R^3, R^2 = H, CH_3 R^2 = H; R^3 = CH_3	75–98
Cl	R^1 = *t*-Bu, Ad R^3, R^2 = H	12–40
Br	R^1 = OBn, HNBn R^3, R^2 = H	0

Scheme 6: Dehalogenation induced by red light using thiaporphyrin (STPP).

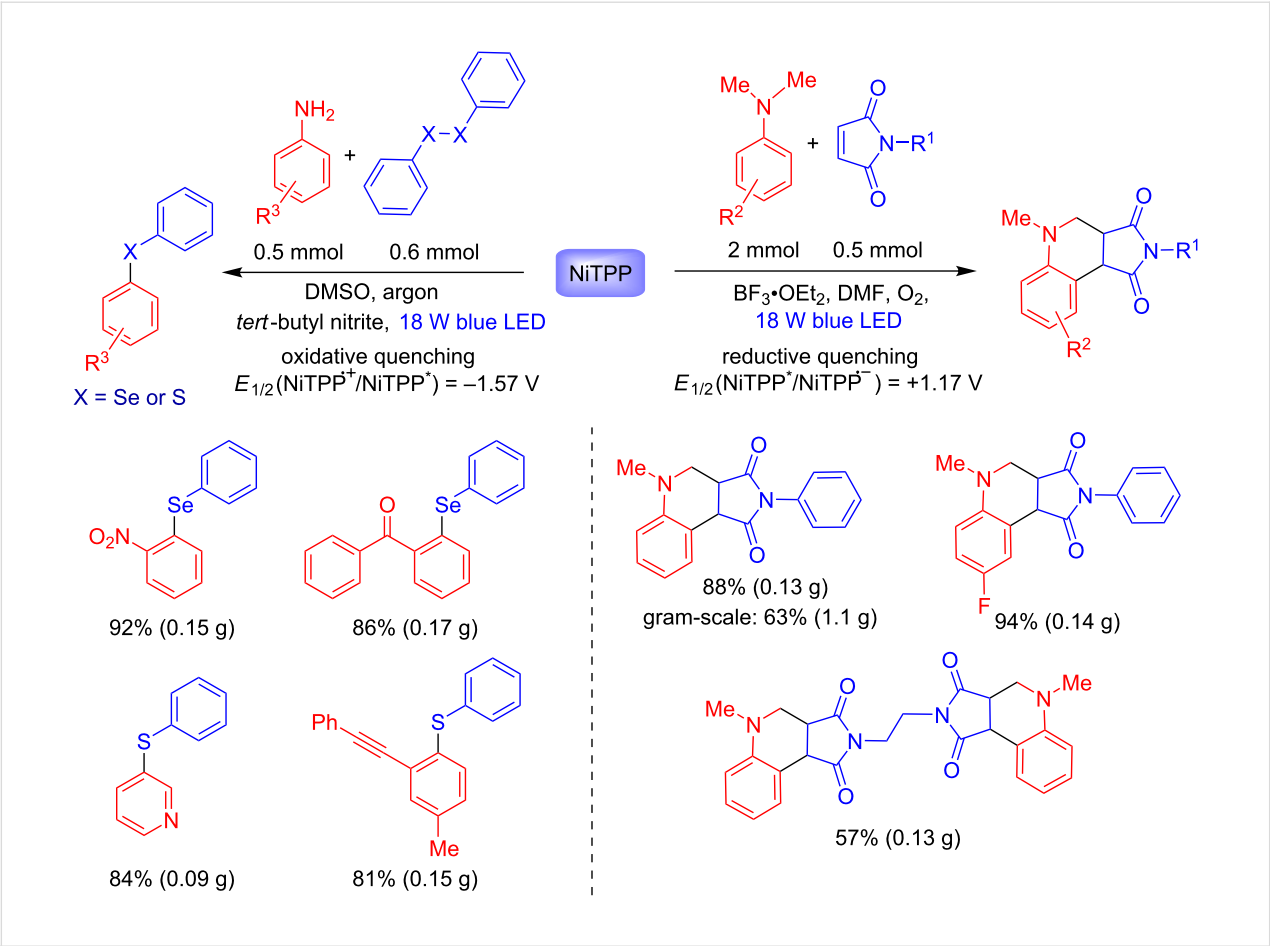

Scheme 7: Applications of NiTPP as both photoreductant and photooxidant.

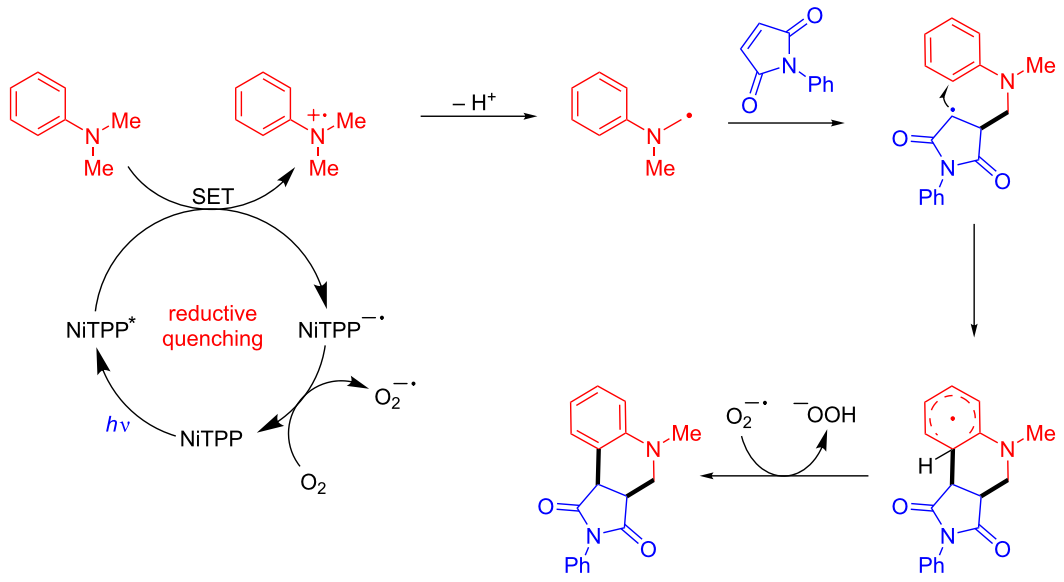

Scheme 8: Proposed mechanism for obtaining tetrahydroquinolines by reductive quenching.

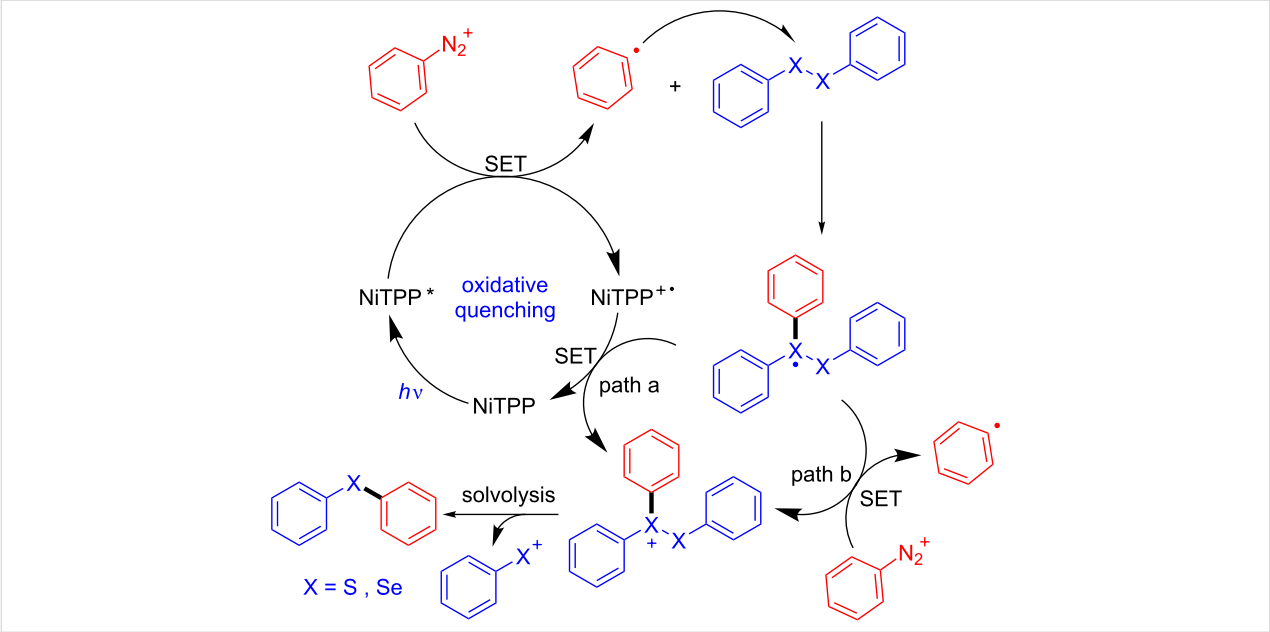

Scheme 9: Selenylation and thiolation of anilines.

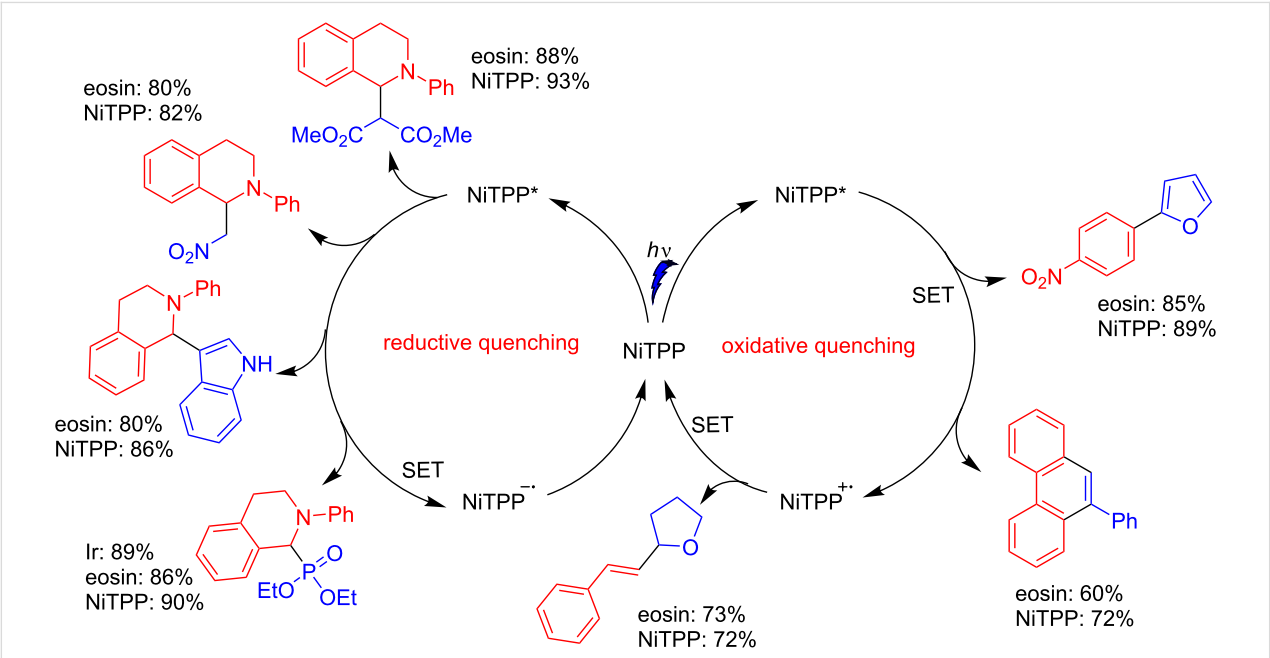

Scheme 10: NiTPP as photoredox catalyst in oxidative and reductive quenching, in comparison with other photocatalysts.

aryldiazonium salts, and the oxidative decarboxylative coupling between cinnamic acid and tetrahydrofuran also showed better results when NiTPP was used instead of eosin [32-34] (Scheme 10).

Regarding protocols involving Ni complexes as catalysts, MacMillan and co-workers showed that Ni metallocatalysis can be successfully combined with photocatalysis (with Ir complexes) in a dual catalysis platform, which enables sp^3–sp^3 and sp^2–sp^3 bond formations [35]. In this context, metalloporphyrins emerge as an interesting platform for dual catalysis due to their ability to promote both metallocatalysis and photocatalysis in a one-pot system [36-39].

Martin and co-workers carried out the C–O bond cleavage of alcohols using a cobalt porphyrin under visible light irradiation

and a carbon monoxide atmosphere (Scheme 11) [36]. The authors hypothesized that the C–O bond cleavage could be achieved via cobalt-mediated alcohol carbonylation followed by radical decarboxylation of the alkoxycarbonyl intermediate. In a proof-of-concept study, they proceeded with the carbonylation of 1-phenylethanol using Co(II) tetrakis(4-methoxyphenyl)porphyrin (CoTMPP) in the dark, furnishing the alkoxycarbonyl intermediate in 92% yield. The combination of this intermediate with a thiophenol derivative and Hantzsch ester (HEH) afforded ethylbenzene in 94% yield (86% overall yield) under both blue and green LED irradiation. The thiophenol and HEH were used as H donors for both the benzyl and thiyl radicals, respectively. The HEH was needed to avoid the dimerization of the thiophenol to the disulfide (Scheme 11).

Fu and co-workers have demonstrated the huge versatility of rhodium porphyrins for photocatalysis. In 2015, they showed that the hydration of terminal alkynes to ketones can be photocatalyzed by rhodium(III) tetrakis(*p*-sulfonylphenyl)porphyrin (Rh^{III}TSPP) [37]. The coupling between Rh^{III}(TSPP) and terminal alkynes produced the β-carbonylalkylrhodium porphyrin as a photoactive intermediate, whose irradiation produced the $PhCOCH_2$ radical and Rh^{II}(TSPP)(CH_3OH) (Scheme 12). Then the Rh^{II}(TSPP)(CH_3OH) reacted with methanol to furnish H-Rh^{III}(TSPP)(CH_3OH) and Rh^{III}(TSPP)$(CH_3OH)_2$. The ketones were produced in 64–91% yields after H transfer between H-Rh^{III}(TSPP)(CH_3OH) and the $PhCOCH_2$ radical.

The same strategy was applied for the highly regioselective photoinduced hydro-defluorination of perfluoroarenes with Rh^{III}(TSPP) [38]. The oxidative addition of the perfluoroarene to the metal complex furnished the active rhodium aryl complex intermediate, which led to the product after visible light irradiation. The hydro-defluorination products were obtained with good TON (up to 880) and high selectivity (91–99.5%), even though the aryl C–F bonds present a high bond dissociation energy (BDE) (Scheme 13).

Using a similar photocatalytic system, 2-methyl-2,3-dihydrobenzofuran was produced by an intramolecular hydro-functionalization of *ortho*-allylphenol with rhodium(III) tetrakis(*p*-methoxyphenyl)porphyrin (Rh^{III}TMPP) as photocatalyst (Scheme 14) [39]. The active intermediate (2,3-dihydrobenzofuran-2-yl)methyl rhodium porphyrin furnished the desired product in 82% yield.

Zhang and co-workers reported a protocol for an oxidative hydroxylation of arylboronic acids by a reductive quenching using a MOF Sn(IV) porphyrin-containing photocatalyst (UNLPF-12) under visible light irradiation. The authors ob-

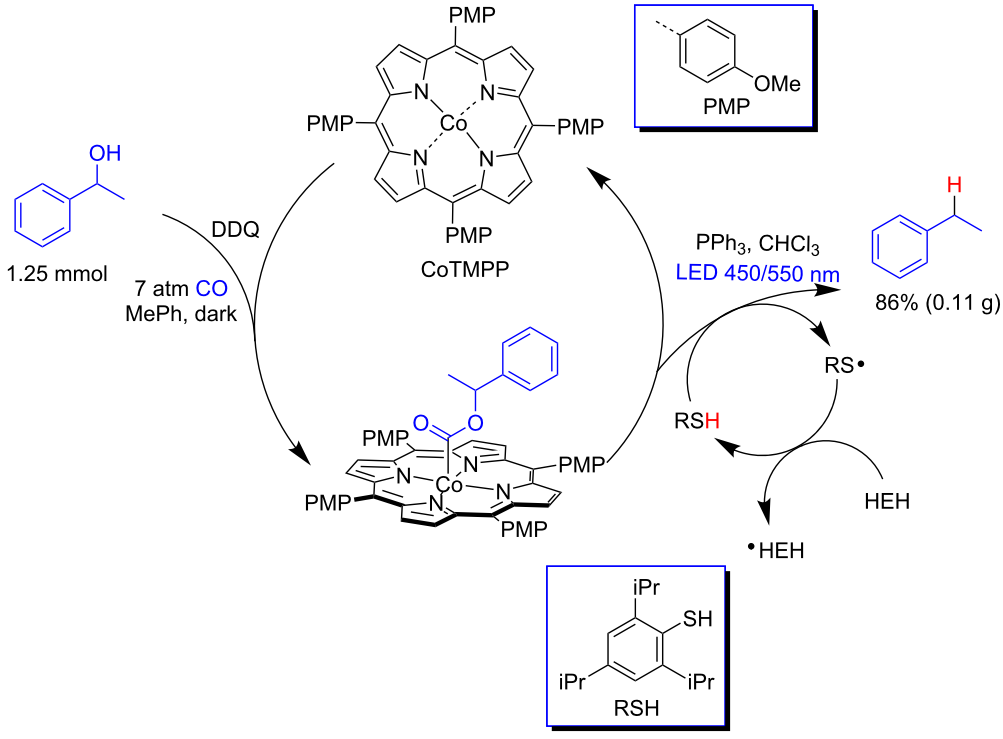

Scheme 11: C–O bond cleavage of 1-phenylethanol using a cobalt porphyrin (CoTMPP) under visible light.

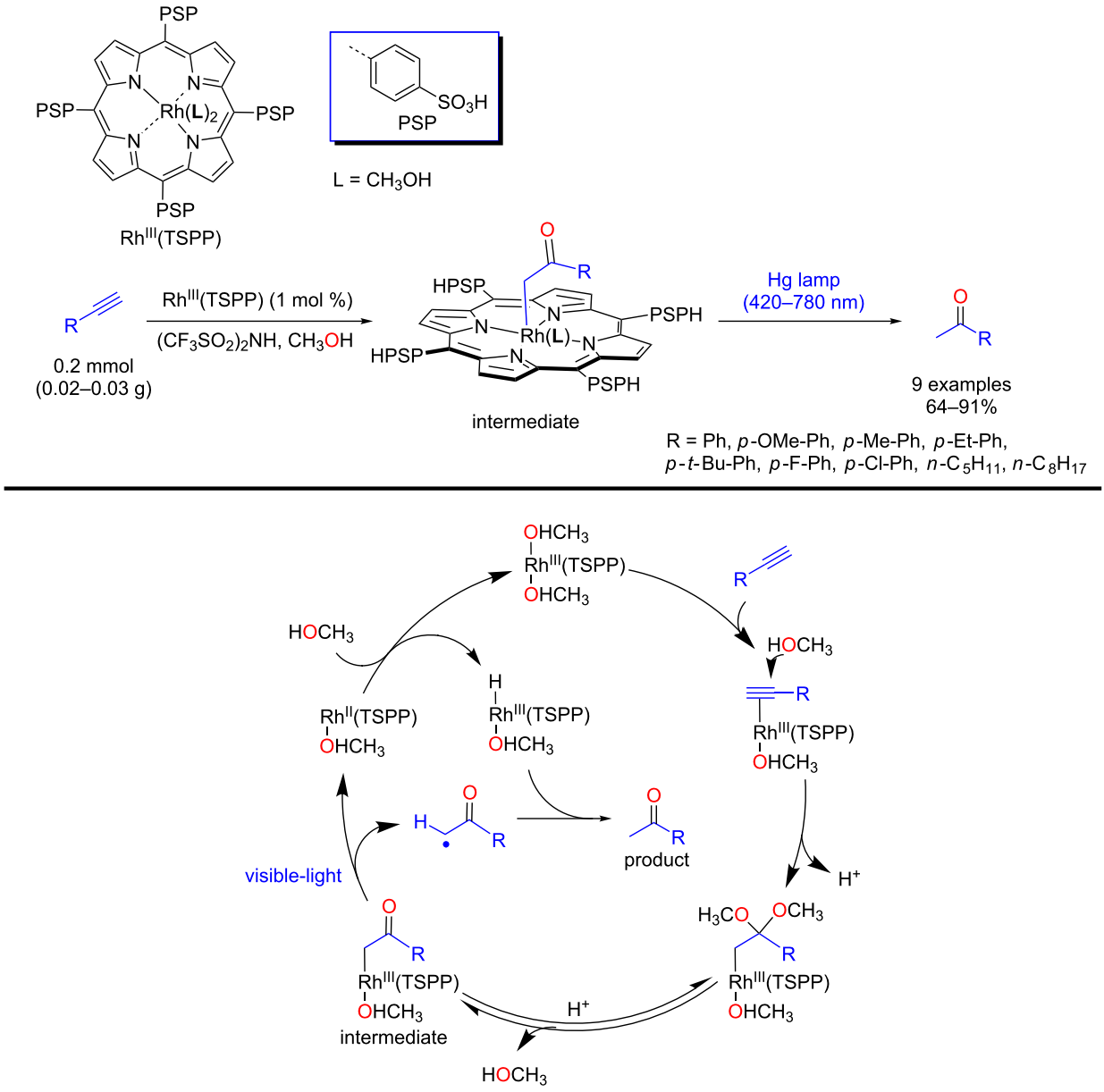

Scheme 12: Hydration of terminal alkynes by Rh^{III}(TSPP) under visible light irradiation.

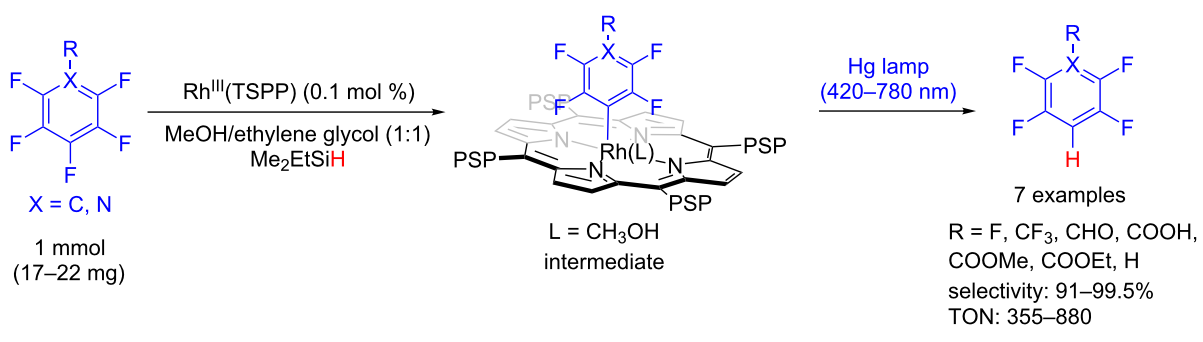

Scheme 13: Regioselective photocatalytic hydro-defluorination of perfluoroarenes by Rh^{III}(TSPP).

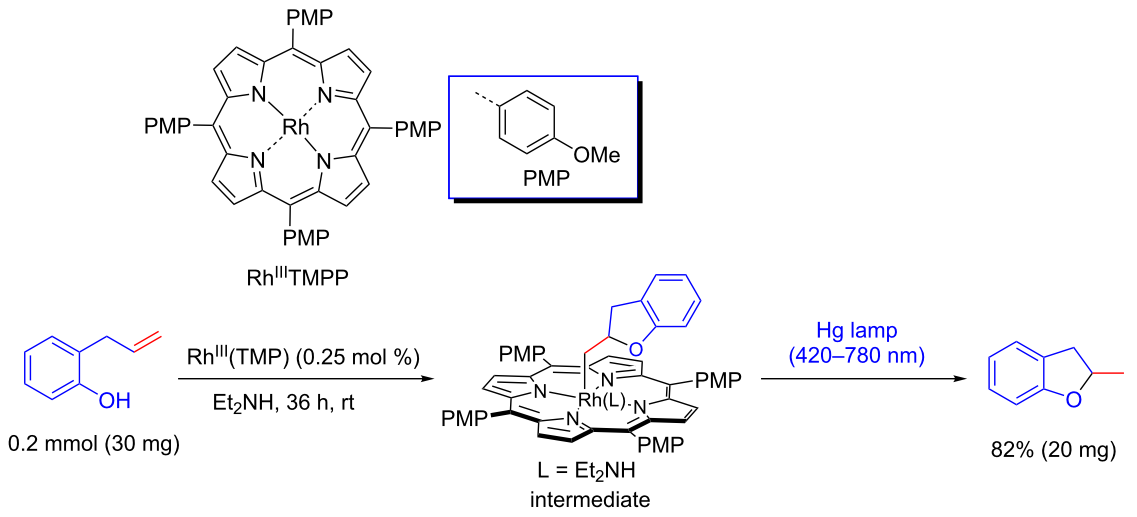

Scheme 14: Formation of 2-methyl-2,3-dihydrobenzofuran by intramolecular hydro-functionalization of allylphenol using Rh^{III}TMPP under visible light irradiation.

tained a variety of phenolic products in 83–96% yields (Scheme 15) [40].

The key steps of the mechanism are both the generation of superoxide radical anion by a reductive quenching and the rearrangement of the hydroperoxide intermediate [41]. The heterogeneous protocol using MOF porphyrins was significantly faster than the corresponding homogeneous photocatalysis, which was attributed to higher photostability of the porphyrins as MOF material. The UNLPF-12 presented practically the same photocatalytic efficiency even after the fourth recycle (from 99% to 95%), while the yield of the homogeneous photocatalysis dropped drastically in its second recycle (from 99% to 12%).

In this regard, Horiuchi, Matsuoka and co-workers reported the synthesis of a Zr-based MOF with *meso*-tetrakis(4-carboxyphenyl)porphyrin (TCPP) (MOF-525, $Zr_6(OH)_4O_4(C_{48}N_4O_8H_{26})_3$) [42] and showed its photocatalytic efficiency for oxidative hydroxylation of arylboronic acids [43]. The phenol products were obtained in quantitative yields for all evaluated arylboronic acids, but accompanied by long reaction times (Scheme 16).

In 2014, Yang, Huang, Wang and co-workers reported a photocatalytic sulfonation of alkenes to β-ketosulfones (widely used in the synthesis of compounds with biological activities [44]), using porphyrins supported in CN materials (Scheme 17) [45]. The thermal decomposition of urea at 550 °C for 2 h afforded the CN polymer, which possesses abundant $–NH_2$ functional groups. The heterogeneous photocatalyst carbon nitride-hemin (CNH) was prepared after an amidation reaction between a carboxyl group of Fe(III) protoporphyrin IX and an amino group of the CN mediated by 1-(3-dimethylaminopropyl)-3-ethylcarbodiimide hydrochloride (EDC) and *N*-hydroxysuccinimide (NHS).

The CNH was then applied as photocatalyst in the photoinduced sulfonation of styrene with *p*-methylbenzenesulfinic acid. The corresponding β-ketosulfone was obtained in 94% yield. However, the yield presented a slight decrease after 5 reuse cycles (from 94% to 85% yield). The methodology was applied to a variety of alkenes and the sulfinic acid, and the protocol was compatible with terminal, disubstituted and heteroarene alkenes (Scheme 18).

Relevant yields (up to 90%) were obtained for both electron-rich and electron-deficient groups in the arylsulfinic acid and alkyl sulfinates, such as sodium ethylsulfinate and sodium methylsulfinate (Scheme 19). The authors also showed that the methodology can be applied to the sulfonation of steroid drug arimistane in 45% yield (Scheme 20). The mechanistic studies on this reaction are ongoing with initial suggestions of the coupling between the sulfonyl radical and the radical alkene as a key step for this transformation.

In 2019, Ghaffari-Moghaddam, Oveisi and co-workers reported the synthesis of a new multifunctional MOF, namely Fe@PCN-222(Fe), and its application in the synthesis of quinazolin-4-(3*H*)-ones by the one-pot reaction between alcohols and 2-aminobenzamide under an oxidative quenching, visible light irradiation using air or oxygen as oxidant (60–81% yields). The

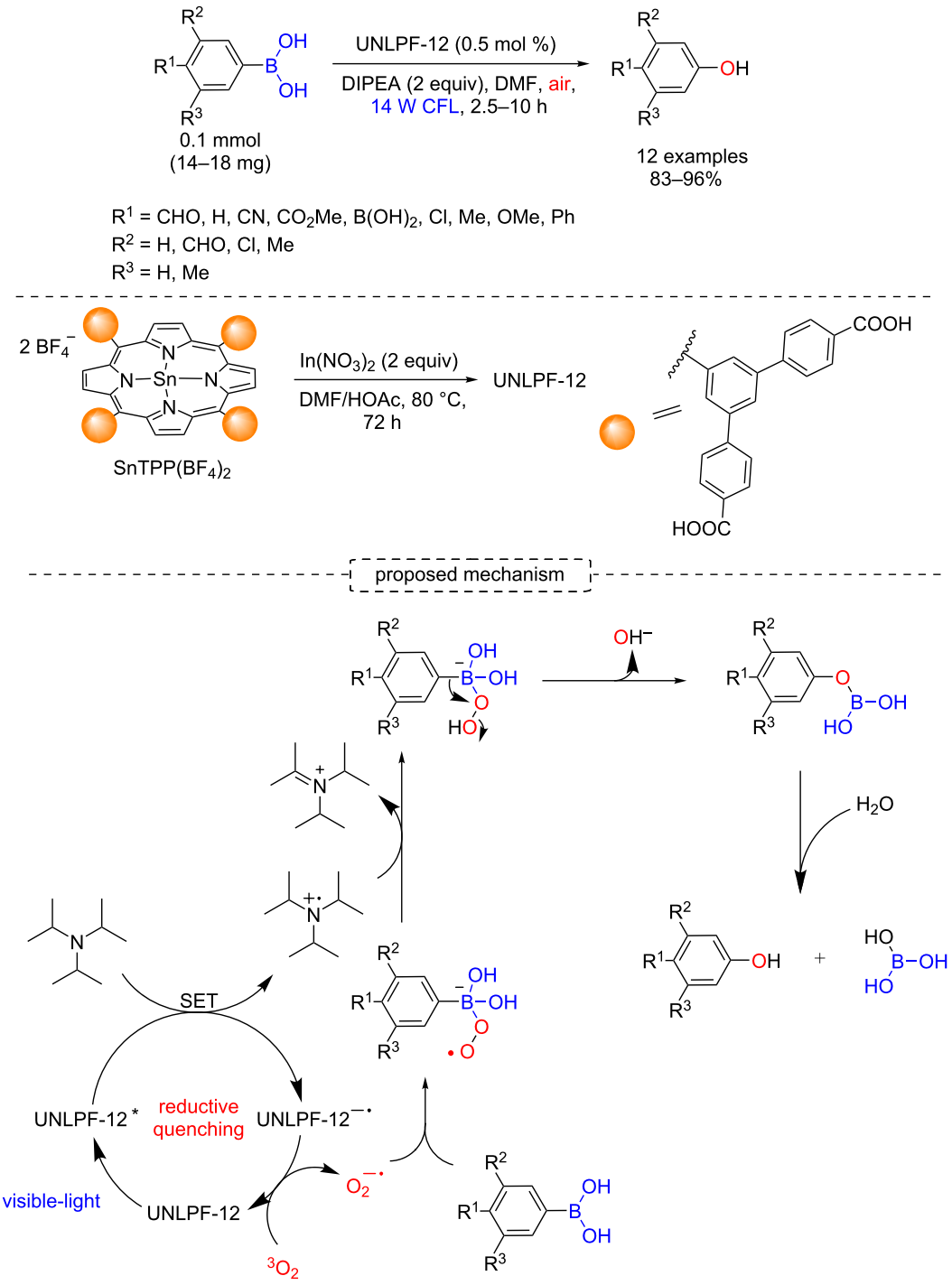

Scheme 15: Photocatalytic oxidative hydroxylation of arylboronic acids using UNLPF-12 as heterogeneous photocatalyst.

authors propose the generation of the superoxide radical anion with the MOF. The superoxide radical anion oxidizes the alcohol to aldehyde, which is then converted to an imine after coupling with the amine. The products are obtained after cyclization and oxidation of the cyclic intermediates (Scheme 21) [46].

Similarly, Jiang and co-workers reported the selective photooxidation of alcohols to aldehydes without over-oxidation to the carboxylic acids using Pt/PCN-224(Zn), a Zn porphyrin MOF incorporated with Pt nanocrystals (NC), as photocatalyst [47]. According to the authors, the synergism between NC and the porphyrin is important for this transformation and a wide

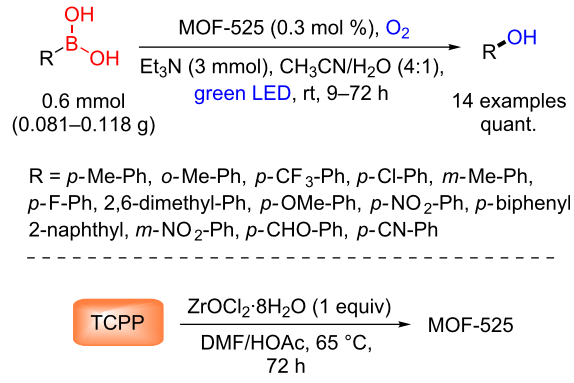

Scheme 16: Photocatalytic oxidative hydroxylation of arylboronic acids using MOF-525 as heterogeneous photocatalyst.

variety of aldehydes were obtained with excellent conversions (>99%) using this heterogeneous photocatalyst (Scheme 22).

Metal complexes such as Pd and Pt porphyrins possess long-living triplet excited states and higher excited state potentials for oxidations [48]. In this regard, various benzoic acids were also obtained by photooxidation of benzaldehydes using Pt porphyrin (Pt-TMP) [49] and Pd porphyrin (2Pd) [50] (Scheme 23). Overall, the fine-tuning of the electrochemical potential of metals and porphyrins enables the oxidation of alcohols to aldehydes or aldehydes to carboxylic acids in a very controlled and chemoselective manner.

Regarding porphyrin-mediated reduction reactions, we have selected one representative example reported by

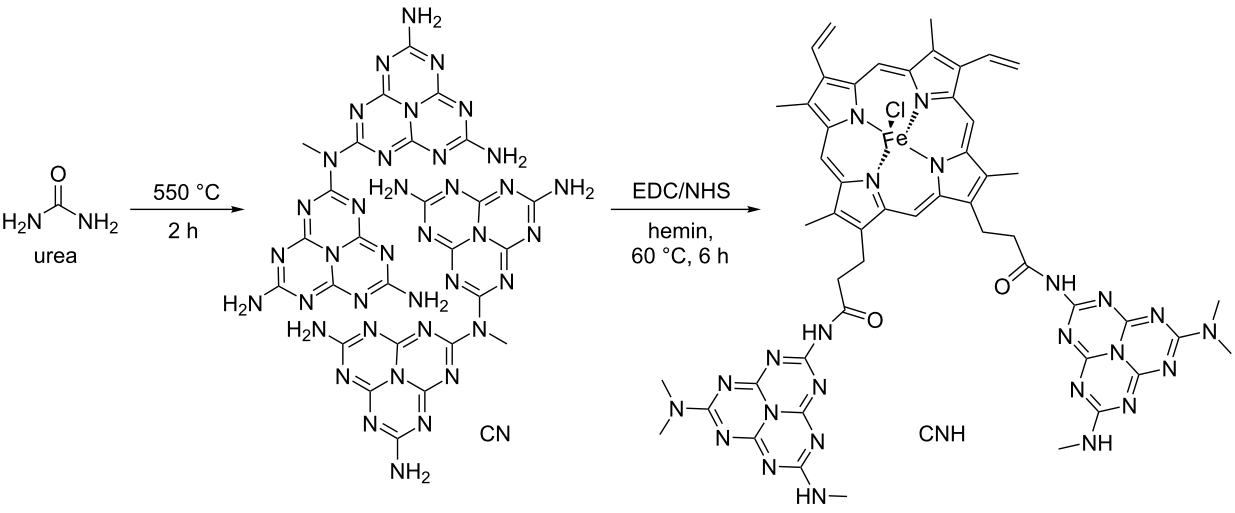

Scheme 17: Preparation of the heterogeneous photocatalyst CNH.

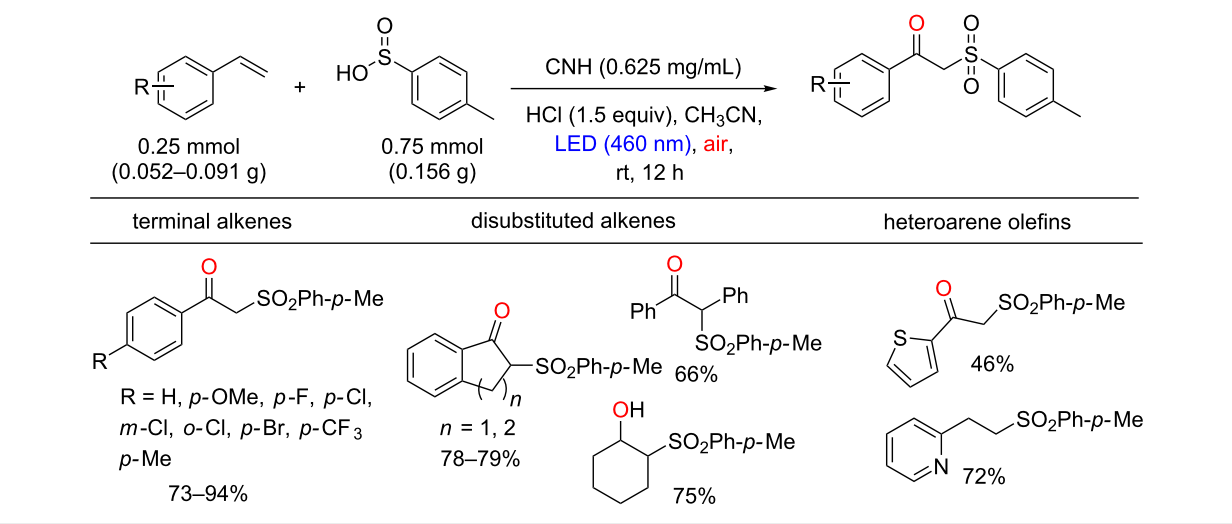

Scheme 18: Photoinduced sulfonation of alkenes with sulfinic acid using CNH as photocatalyst.

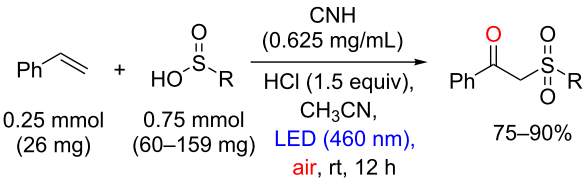

Scheme 19: Sulfonic acid scope of the sulfonation reactions.

Nagaraja and co-workers. They have shown a heterogeneous photocatalytic reduction of nitroaromatic compounds to the corresponding anilines using a Ni(II)-MOF, $[Ni_3(Ni\text{-}TCPP)_2(\mu_2\text{-}H_2O)_2(H_2O)_4(DMF)_2]\cdot 2DMF$ (where NiTCPP = Ni(II) *meso*-tetrakis(4-carboxyphenyl)porphyrin [51]) with excellent conversion (>99%) (Scheme 24). Surprisingly, they did not observe the target product when NiTCPP was used as photocatalyst.

Finally, it has been found that heterogeneous porphyrin-based photocatalysis also can be applied to the reduction of carbon dioxide (CO_2). Many photocatalytic materials containing porphyrins have been developed for CO_2 reactions in organic synthesis, including photoinduced transformations [52-55]. Nagaraja and co-workers reported the first porphyrin-based MOF for photoinduced cycloaddition of carbon dioxide with epoxides [56]. The synthesis of a 3D supramolecular framework, $[\{Mn(TCPP)_{0.5}(H_2O)\}\cdot 2H_2O]_n$, where Mn(TCPP) is

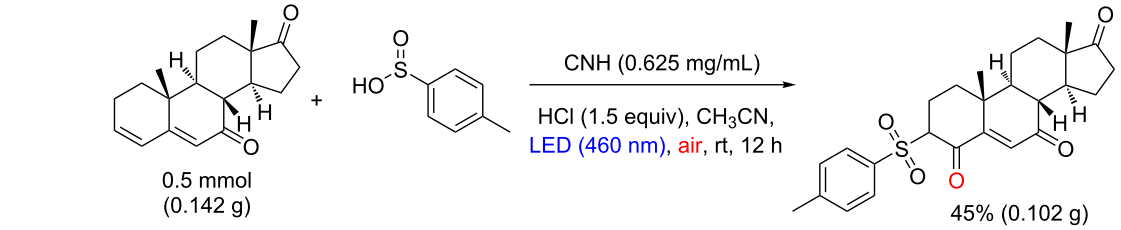

Scheme 20: Regioselective sulfonation reaction of arimistane.

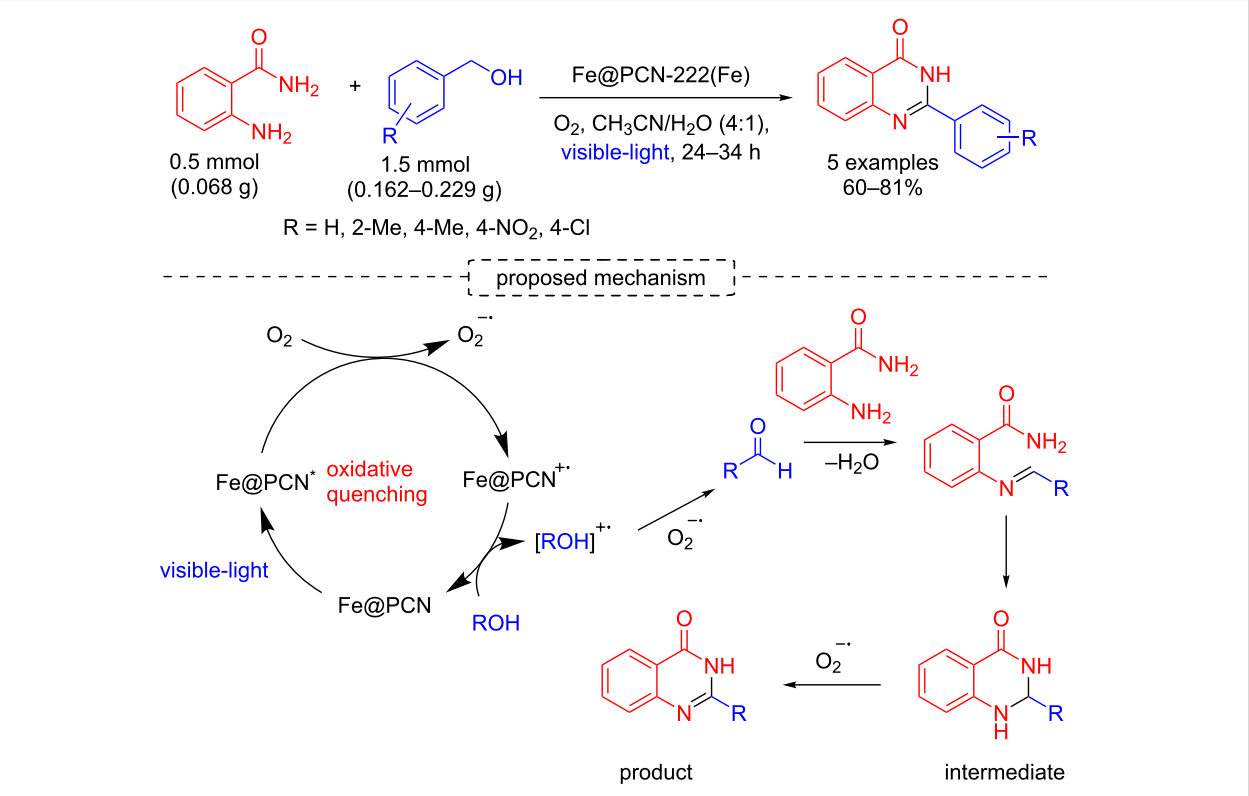

Scheme 21: Synthesis of quinazolin-4-(3*H*)-ones.

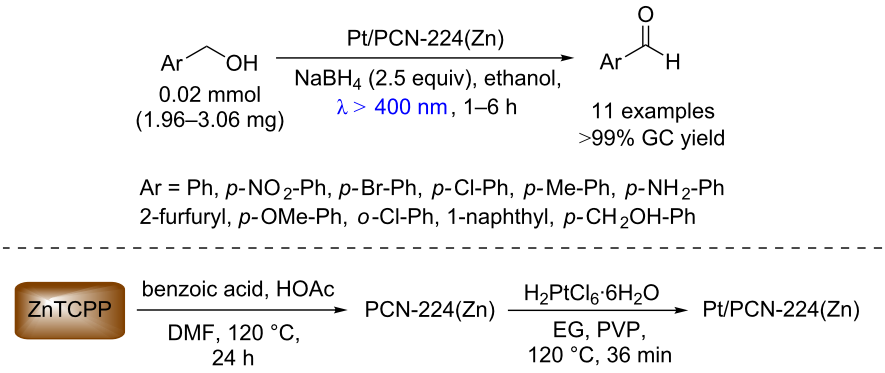

Scheme 22: Selective photooxidation of aromatic benzyl alcohols to benzaldehydes using Pt/PCN-224(Zn).

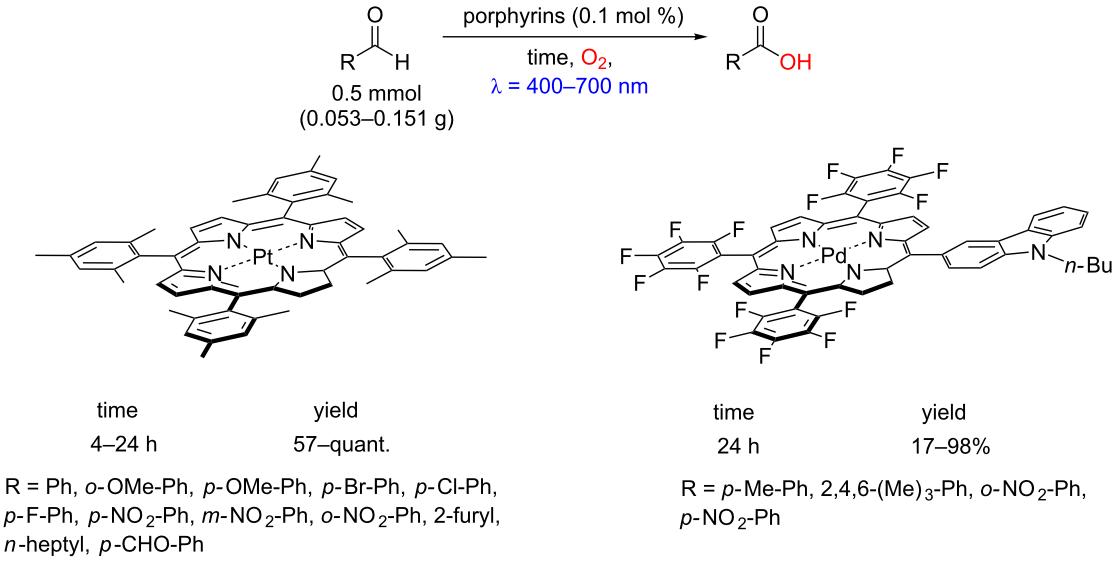

Scheme 23: Photooxidation of benzaldehydes to benzoic acids using Pt or Pd porphyrins.

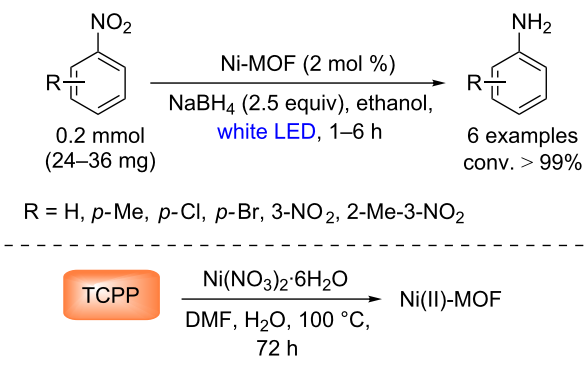

Scheme 24: Photocatalytic reduction of various nitroaromatics using a Ni-MOF.

Mn(II) *meso*-tetrakis(4-carboxyphenyl)porphyrin, was derived from $MnCl_2·6H_2O$ and TCPP. The cycloaddition product, a cyclic carbonate, was obtained from different epoxides, whose conversion was proportional to the substrate size, using MOF1 and tetra-*n*-butylammonium bromide (TBAB) as photocatalyst and co-catalyst, respectively (Scheme 25). A successful gram-scale protocol was developed opening up perspectives for using these materials in CO_2 reuse.

Porphyrins as energy transfer photocatalysts

General aspects

As previously mentioned, porphyrins in their excited state can also return to the ground state by energy transfer. In this section, we highlight the process of energy transfer from the

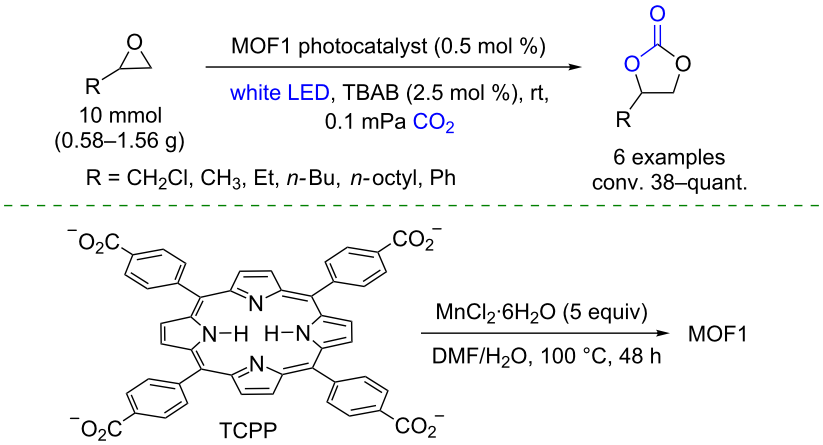

Scheme 25: Photoinduced cycloadditions of CO_2 with epoxides by MOF1.

triplet excited state of porphyrins to the steady state of molecular oxygen (triplet state). In this process, well-known singlet oxygen ($^1O_2$) is generated.

Singlet oxygen can be considered a very versatile reagent in organic synthesis since it promotes many mild oxidation processes instead of combustion [23,57-60]. This excited state form of molecular oxygen can be produced by chemical and photochemical methods, with this second the easier and most cost-competitive manner [61,62].

Singlet oxygen exists in a very unique electronic configuration relative to other molecules, and presents two singlet states, $^1O_2(^1\Delta_g)$ and $^1O_2(^1\Sigma_g^+)$ (Figure 4) [63]. The species $^1O_2(^1\Delta_g)$ has both electrons paired in a single orbital, while the electrons of the species $^1O_2(^1\Sigma_g^+)$ are paired in different orbitals. Both singlet states can be formed competitively, however, the conversion from $^1O_2(^1\Sigma_g^+)$ to $^1O_2(^1\Delta_g)$ is extremely fast in liquid-phase ($k = 10^{-11}$ s), making the $^1O_2(^1\Delta_g)$ the main photoactive species in solution [63-65].

Singlet oxygen is a highly reactive electrophile toward electron-rich organic molecules/atoms such as alkenes, dienes, and heteroatoms (N, P, S, Se, etc.) making this molecule very effective in pericyclic reactions and heteroatom oxidations (Scheme 26) [61,67,68]. In this section, both reactions are presented and discussed.

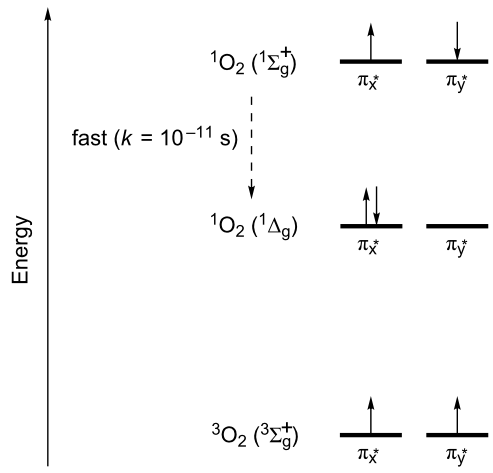

Figure 4: Electronic configurations of the species of oxygen. Adapted from [66].

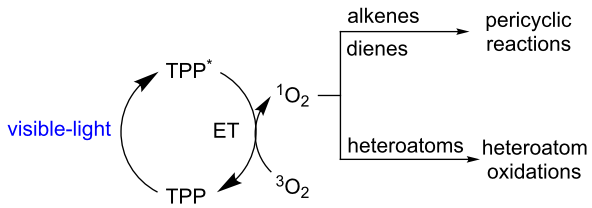

Scheme 26: TPP-photocatalyzed generation of $^1O_2$ and its application in organic synthesis. Adapted from [67-69].

Singlet oxygen in pericyclic reactions

Many important organic transformations can be performed by singlet oxygen including ene, [2 + 2] and [4 + 2] cycloaddition reactions for the formation of hydroperoxides, dioxetanes, and endoperoxides, respectively (Scheme 27). The mechanistic foundations that allow the predictability and the rational use of these reactions in organic synthesis are well-established. However, studies about the pathways in which these pericyclic reactions with singlet oxygen occur (stepwise or concerted) are still ongoing. The generally accepted mechanisms for these reactions are shown in Scheme 27, and propose a stepwise mecha-

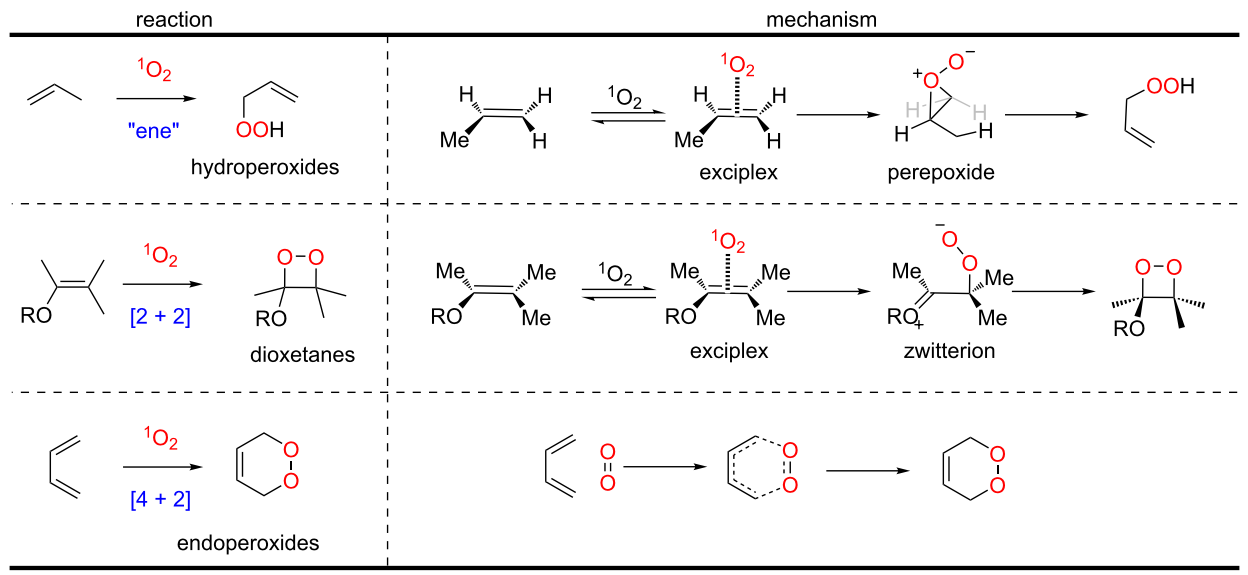

Scheme 27: Pericyclic reactions involving singlet oxygen and their mechanisms. Adapted from [67].

nism for ene and [2 + 2] cycloaddition, and a concerted mechanism for [4 + 2] cycloaddition [67].

In this part of the review, we decided to highlight the historically relevant protocols and recent reactions involving $^1O_2$, mostly developed with porphyrin photocatalysis. No examples of the use of chlorins, bacteriochlorins and isobacteriochlorins will be included, except two seminal examples of chlorophyll a use (formally, chlorophyll a is a chlorin derivative). However, for a broad coverage of different aspects and relevant examples on photooxygenation in organic synthesis, we recommend relevant reviews published by Greer [70] and Crutchley [71].

Undoubtedly, the large-scale preparation of ascaridole, published in 1944 by Schenck and Ziegler [72,73], is a remarkable example of the use of chlorophyll a in photooxygenation reactions (Scheme 28). In this seminal scaled-up preparation the authors were able to produce 10 g of ascaridole per batch, showing an additional example of batch numbering up of photoreactors with dozens of glass batch systems scattered in an open garden under sunlight irradiation; notably, ascaridole is an effective anthelmintic natural drug obtained in this protocol from another readily available natural product α-terpinene.

Several other approaches have been described in both synthesis and derivatizations of ascaridole. However, the Meunier group publication [74] on new antimalarial drugs can be highlighted (Scheme 29). The authors report a 3.4 gram-scale preparation of ascaridole, in this case a synthetic intermediate, using TPP as photocatalyst.

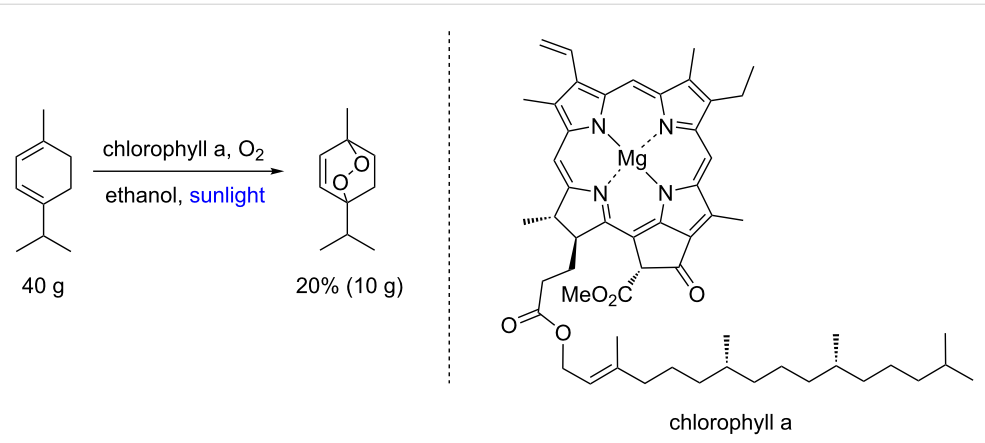

Scheme 28: First scaled up ascaridole preparation from α-terpinene.

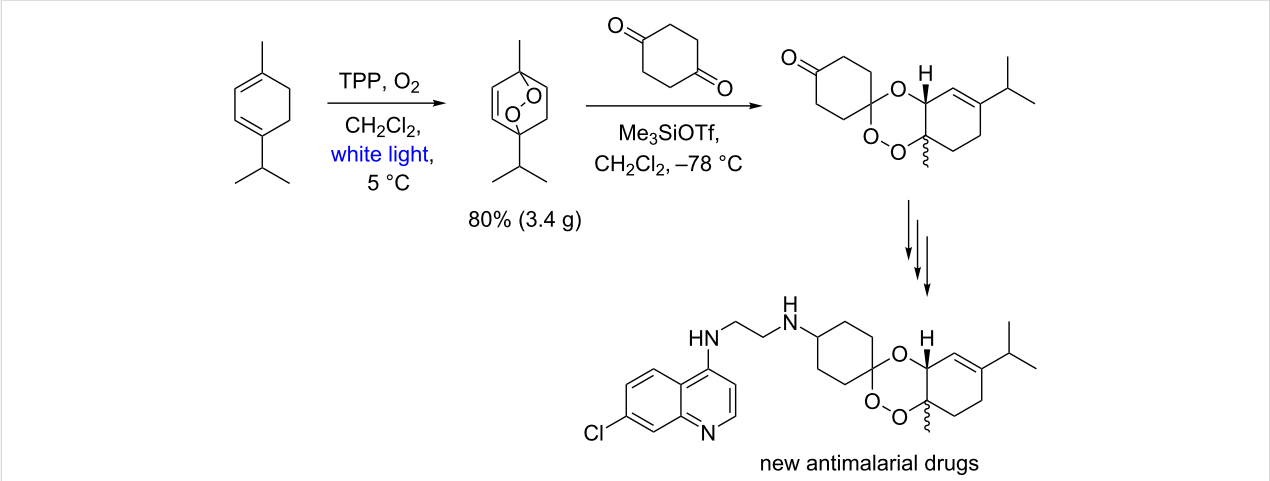

Scheme 29: Antimalarial drug synthesis using an endoperoxidation approach.

Another example of a scaled-up endoperoxide approach involves the stereoselective singlet oxygen addition to (−)-colchicine photocatalyzed by hematoporphyrin, giving relevant bioactive colchicine derivatives (Scheme 30) [75,76].

A valuable protocol for the (−)-pinocarvone synthesis was described by Eickhoff [77] and recently adapted to continuous-flow conditions by Lapkin and co-workers [78]. In the original protocol the authors were able to produce up to 21.4 g per batch (1.5 h, 97% yield) using TPP as photocatalyst (Scheme 31). In the recent continuous protocol described by Lapkin et al. 1.9 g per day is obtained using the same reaction conditions and a PFA-tube photoreactor (segmented-flow with O_2).

One very relevant example of a photooxygenation protocol is the Seeberger group's semi-synthesis of the antimalarial API artemisinin (Scheme 32) [79]. They have established a gram-scale continuous protocol with a photooxygenation promoted by

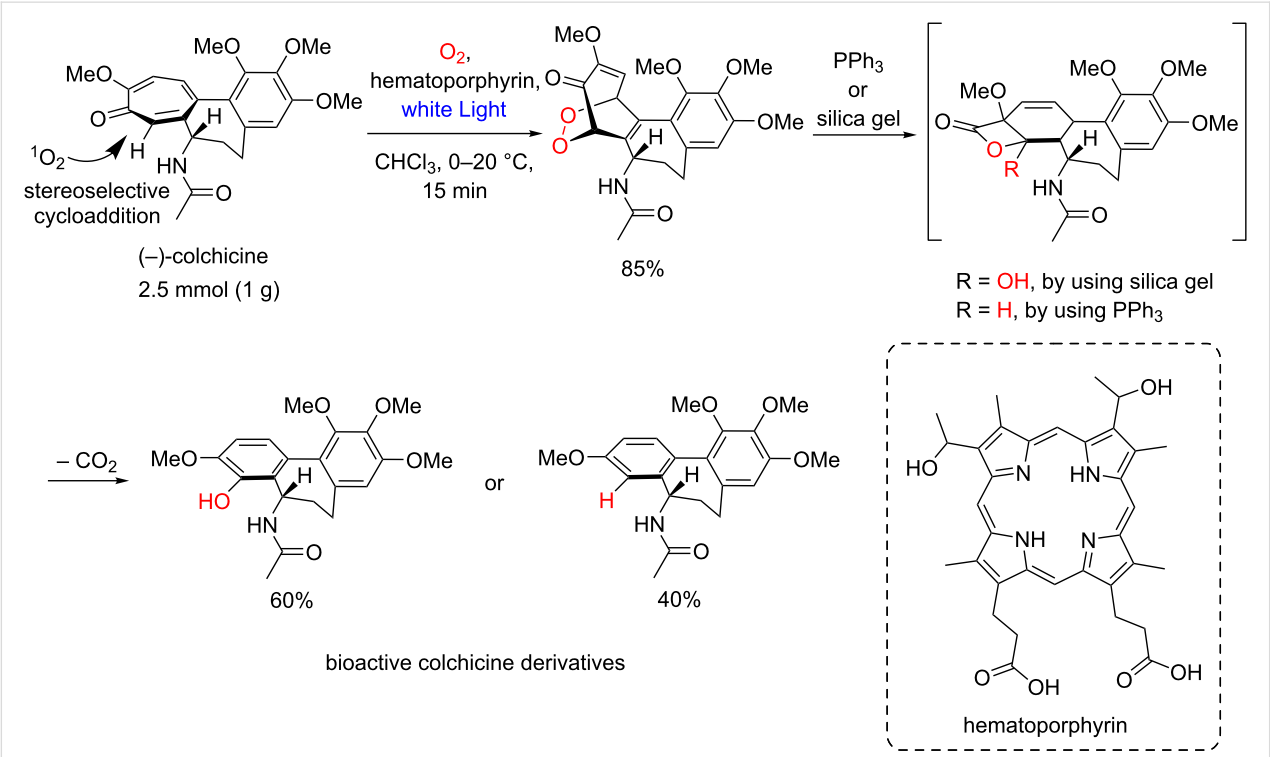

Scheme 30: Photooxygenation of colchicine.

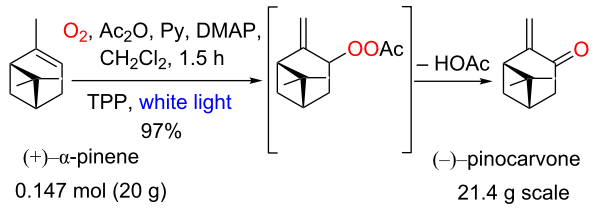

Scheme 31: Synthesis of (–)-pinocarvone from abundant (+)-α-pinene.

TPP starting from dihydroartemisinic acid**.** This work is crucial for the success of the subsequent industrial process introduced by the pharmaceutical company Sanofi [80].

After this seminal publication, a consortium between Sanofi and UK/China universities also reported a green protocol for artemisinin synthesis using supercritical CO_2 as a novelty (Scheme 33) [81]. They have also used TPP (immobilized acidic form) as photosensitizer and were able to produce up to 2.4 g of artemisinin per batch. The importance of artemisinin

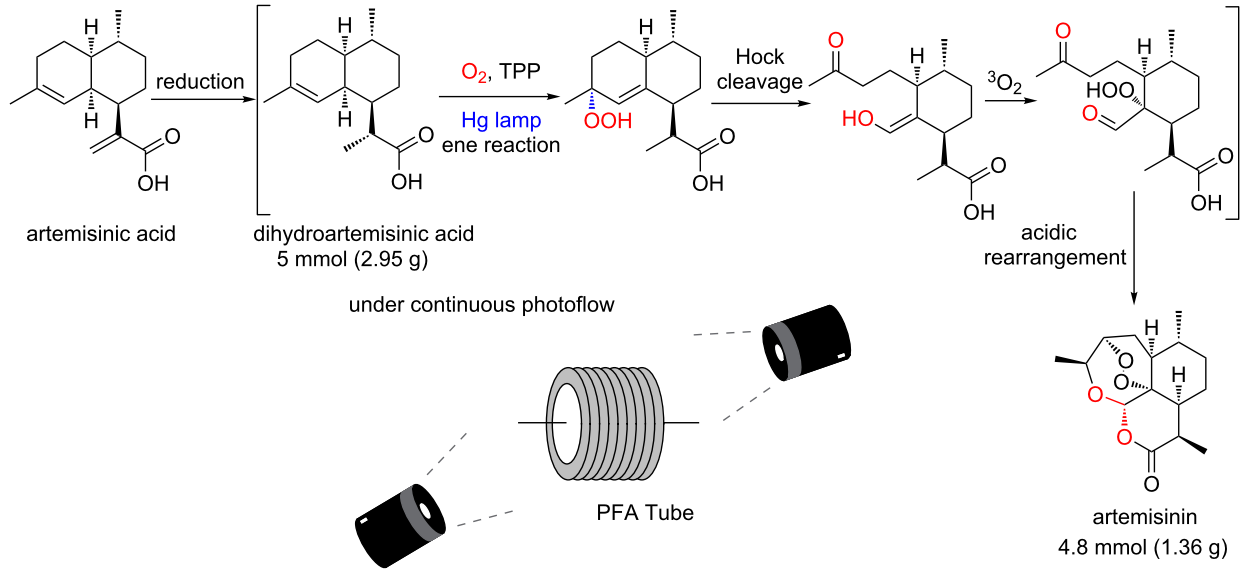

Scheme 32: Seeberger's semi-synthesis of artemisinin.

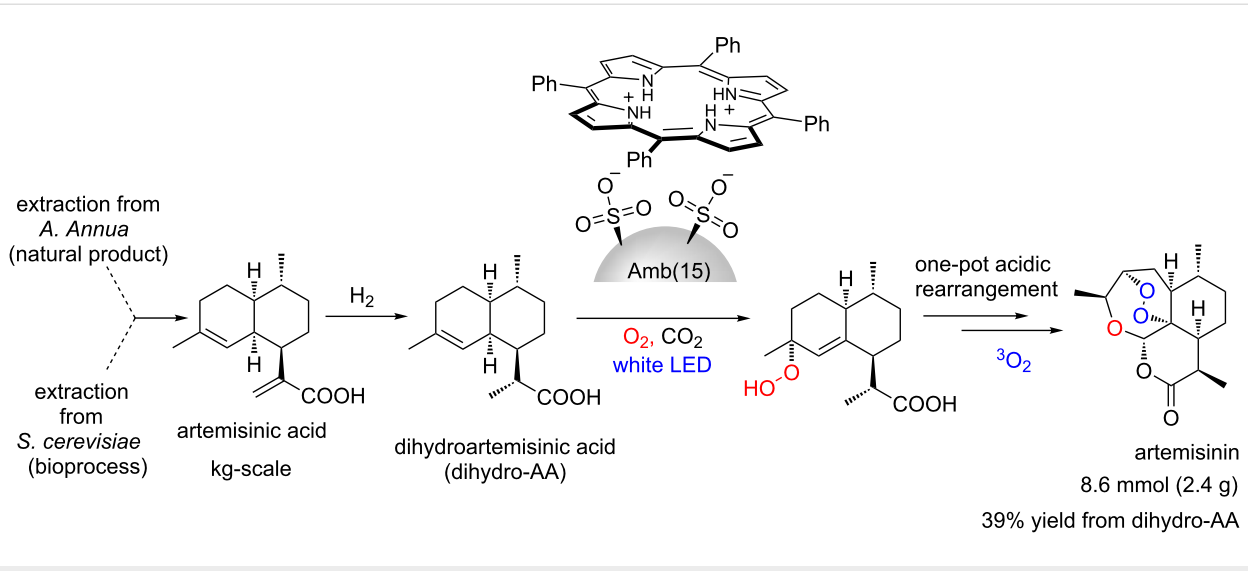

Scheme 33: Synthesis of artemisinin using TPP and supercritical CO_2.

for Big Pharma has been confirmed during the last 20–30 years with many relevant publications.

As mentioned before, our focus in this part of the review is the use of porphyrins as photocatalysts, but we decided to select another relevant example using chlorophyll a (a chlorin-type derivative) for artemisinin preparation. Gilmore and co-workers have shown that the extract in toluene from *Artemisia annua* plants contains both the substrate (dihydroartemisinic acid) and the photocatalyst (chlorophyll a). The combination of the extract with trifluoroacetic acid promptly furnishes artemisinin, under continuous-flow conditions (3 min) using red light (87% yield) or under blue light irradiation (5 min, 88% yield) (Scheme 34) [82].

The most recent approach for artemisinin synthesis was described by Wang, Zhou and co-workers [83,84] using porphyrin-based MOFs to produce singlet oxygen, and then repeating the same synthetic strategy for artemisinin production (starting from artemisinic acid).

Photooxygenation reactions were also described in the syntheses of carbasugars which are unnatural molecular motifs with broad interest in medicine [85]. A relevant example was described by Balci and co-workers for the preparation of quercitol derivatives (Scheme 35) [86]. In this case, gram to multigram-scale double photooxygenation reactions were described using TPP as photocatalyst.

We have described a study on endoperoxydations followed by rearrangement to yield naphthoquinones starting from α-naphthols and using porphyrins as photocatalysts (Scheme 36) [23]. Eleven examples were described from mg to g-scale reactions, and including protocols with 24 h experiments under continuous-flow conditions using a very simple home-made photoreactor (segmented flow – PFA tube reactor). We have compared

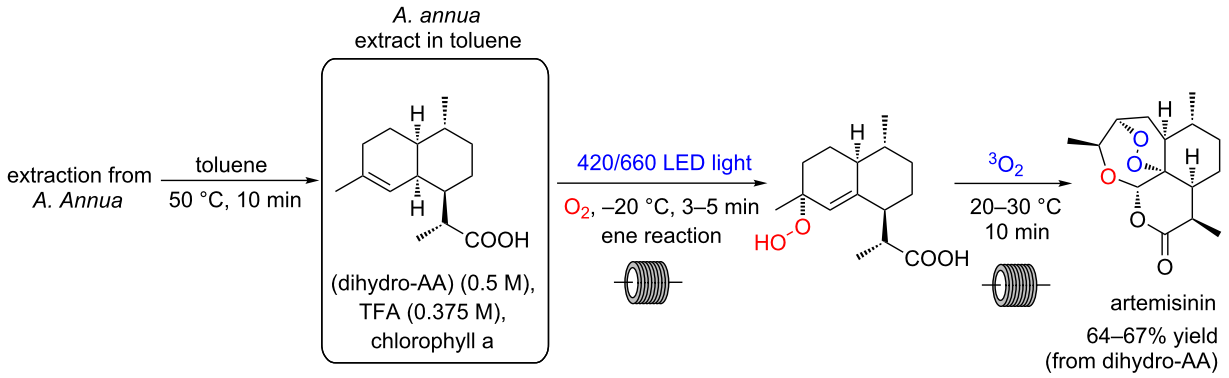

Scheme 34: Synthesis of artemisinin using chlorophyll a.

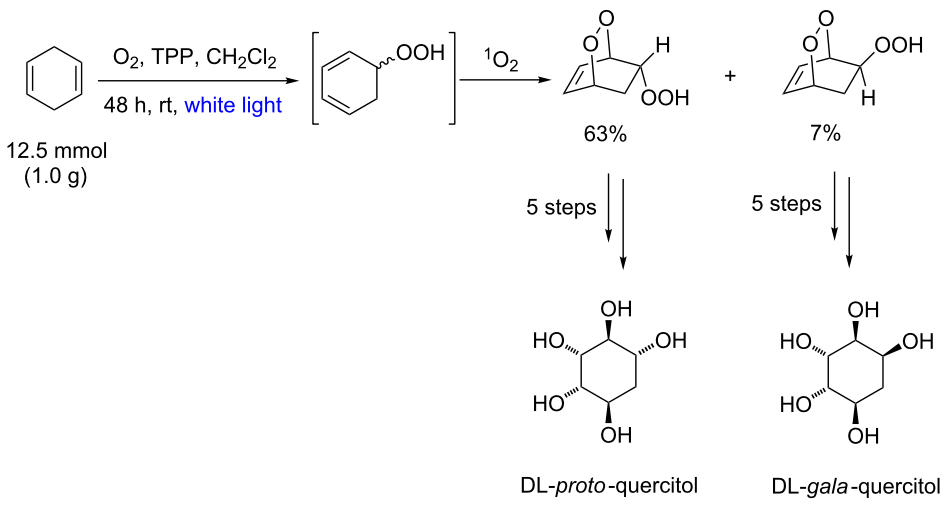

Scheme 35: Quercitol stereoisomer preparation.

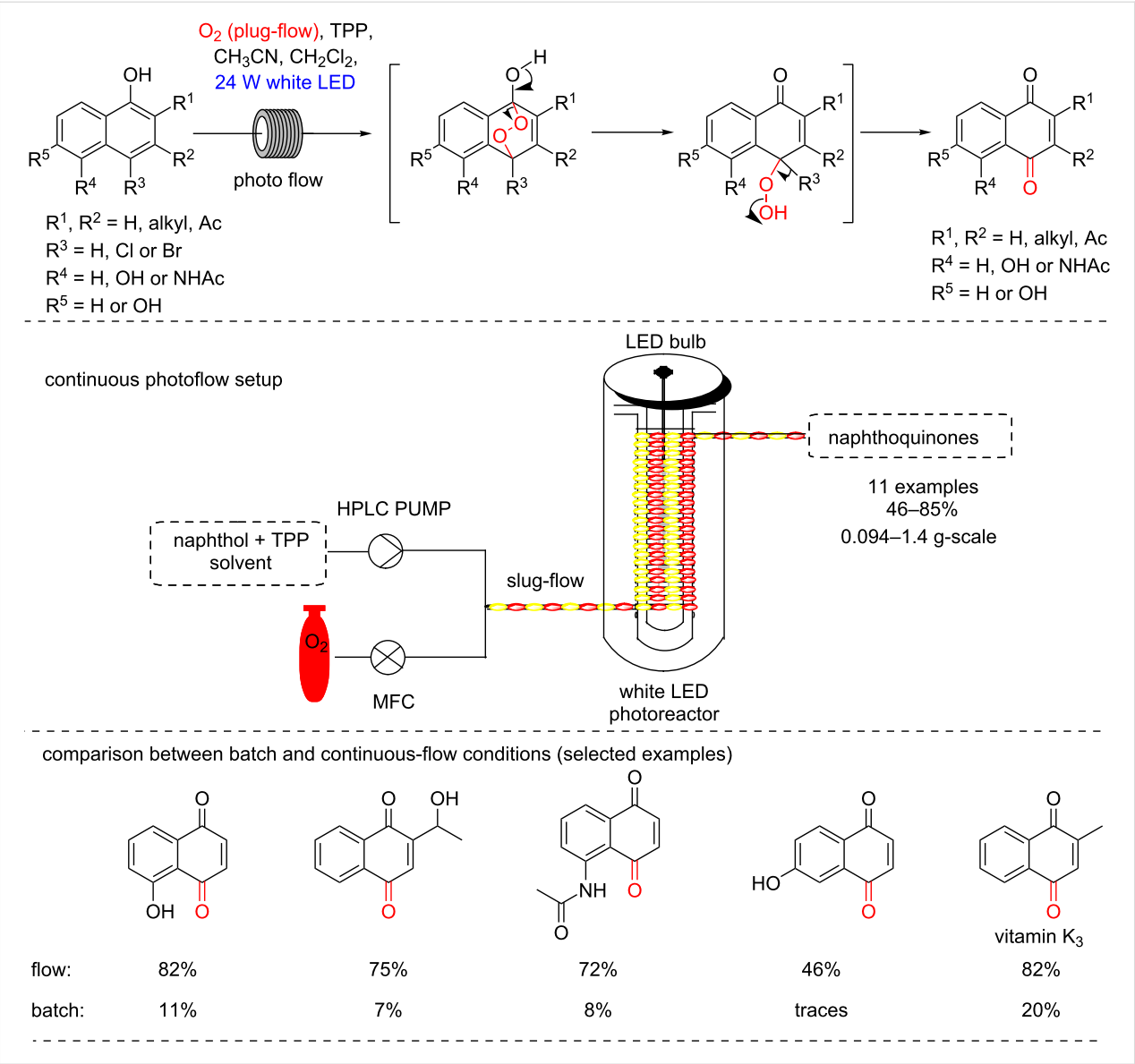

Scheme 36: Photocatalyzed preparation of naphthoquinones.

the same reaction conditions in both batch (7–20% yield) and continuous-flow conditions (up to 82% yield) and thus showed a very improved protocol when using continuous conditions.

Subsequently, we reported a comprehensive methodology involving photooxygenations of conjugated dienes and rearrangements, thus leading to relevant oxidized products (Scheme 37) [87]. In this methodology, we developed in both batch and continuous-flow conditions, a porphyrin-based protocol for endoperoxidation of the diene, followed by the Kornblum–DeLaMare rearrangement and further telescoped transformations. This protocol yields different classes of products such as furans, tropone, diketones and hydroxyenones, all of them starting from the corresponding functionalized dienes. A scope with 23 substrates is presented and the products were obtained in 10–96% yield with scalability (up to 1 g-scale in a telescoped protocol).

In 2019, Opatz and co-workers reported one of the most efficient and elegant total syntheses of (–)-oxycodone, using as key steps an electrochemical cyclization and an endoperoxidation photocatalyzed by TPP in an almost gram-scale (Scheme 38) [88].

In 2020, Burchill and George reported a 0.5 g-scale ene-reaction with singlet oxygen and a cromene derivative, thus giving a conjugated enone after a Kornblum–DeLaMare rearrangement (Scheme 39) [89]. Further photochemical [2 + 2] cycloaddition

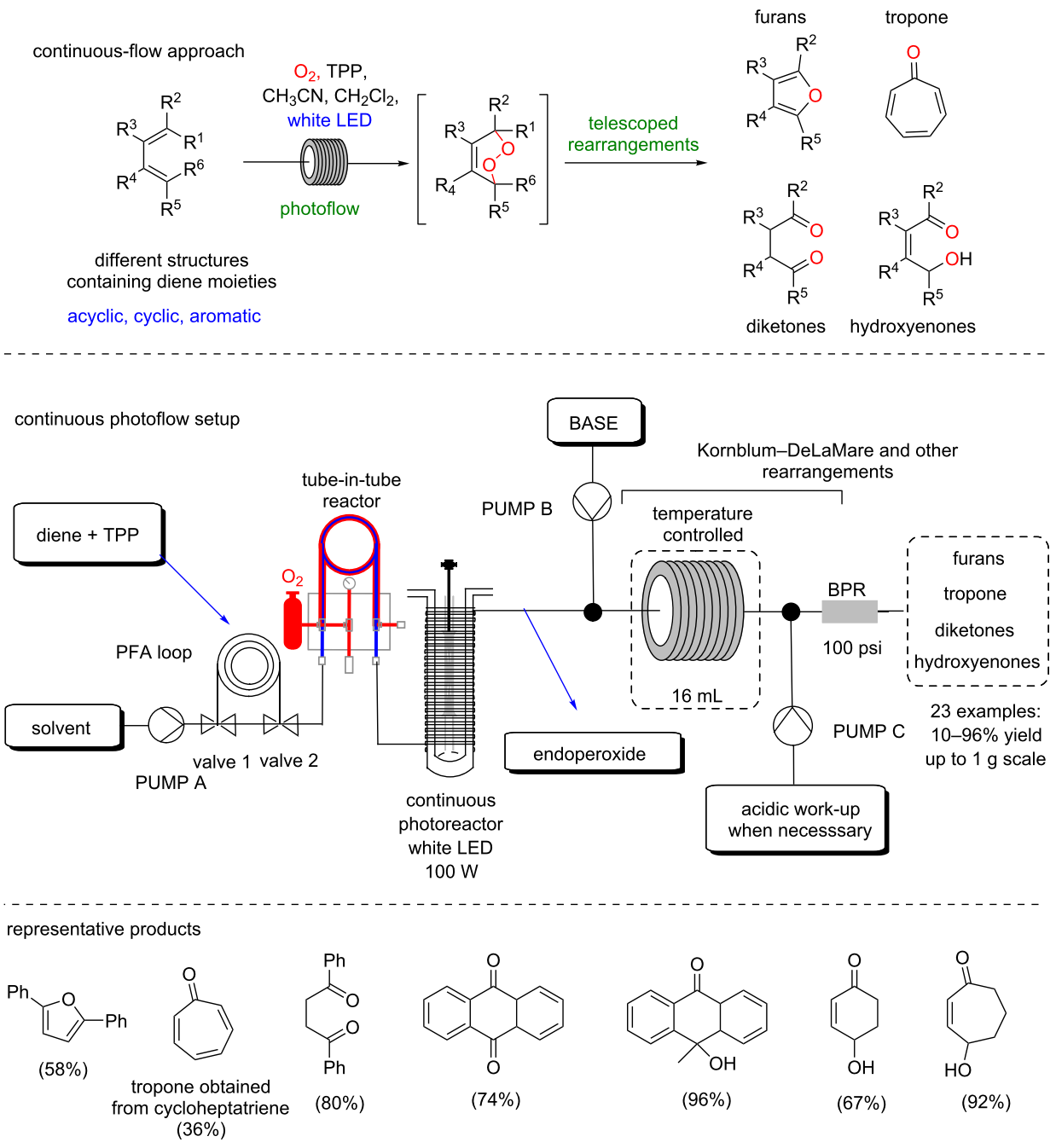

Scheme 37: Continuous endoperoxidation of conjugated dienes and subsequent rearrangements leading to oxidized products.

and hydrolysis allowed them to obtain rhodonoid A in 30% overall yield. Other similar natural products (rhodonoid B, E and F) were also prepared by the same synthetic strategy.

Singlet oxygen has also been efficiently used for enantioselective and chemoselective oxidations of many organic compounds. Notably, the Gryko's group recently described an enantio- and diastereoselective approach involving a porphyrin-based photooxygenation of aldehydes with sequential reduction to yield chiral diols in yields up to 91% and significant er (up to 96:4), but low dr (up to 66:33) (Scheme 40) [90].

Another relevant example has been described by Meng and co-workers with the synthesis of α-hydroxy-β-keto esters using

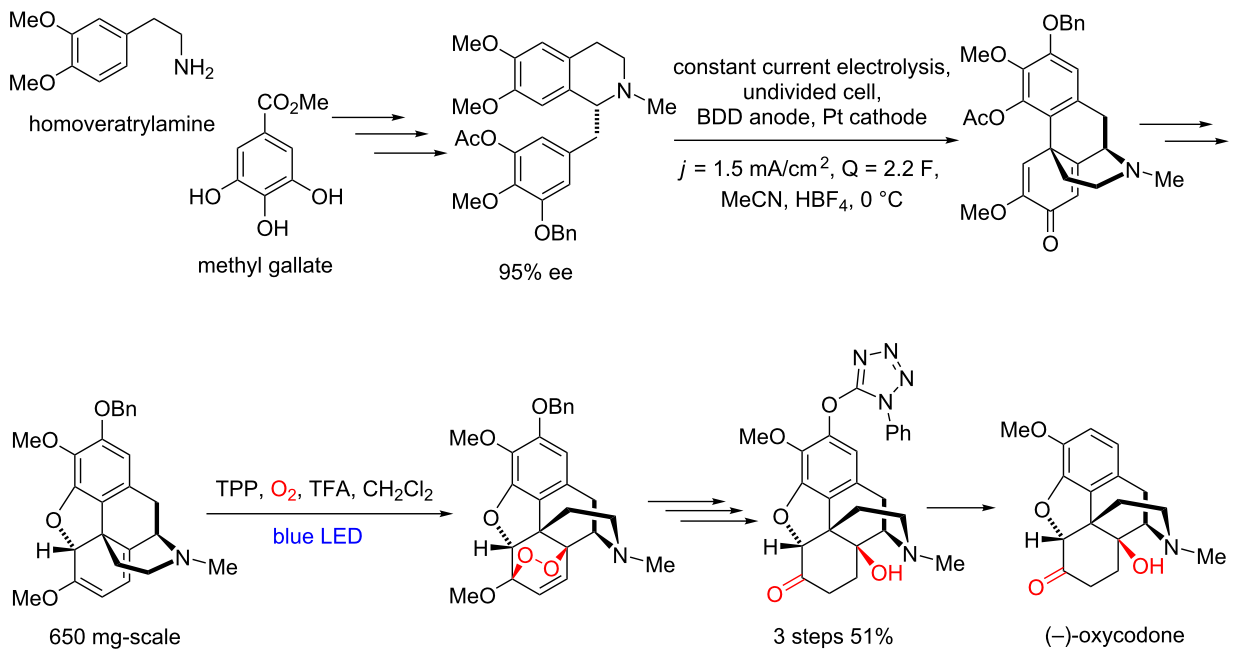

Scheme 38: The Opatz group total synthesis of (–)-oxycodone.

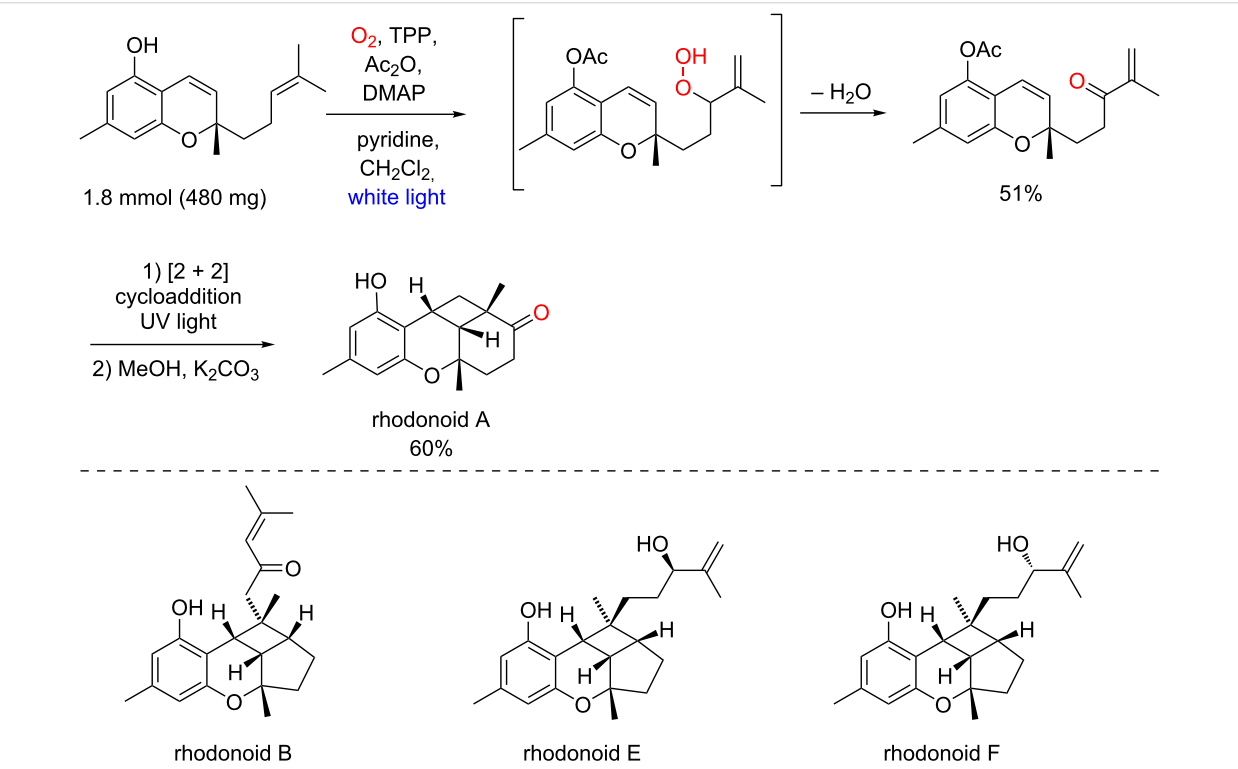

Scheme 39: Biomimetic syntheses of rhodonoids A, B, E, and F.

TPP, a visible-light source, and a phase-transfer catalyst (PTC) as enantio-catalyst [91]. They reported the preparation of indanone-α-hydroxy-β-keto esters in 81–93% yields and 39–75% ee (Scheme 41). The mechanism of this reaction involves the attack of the enolate paired with the chiral counter ion PTC to the singlet oxygen electrophile to give the hydroper-

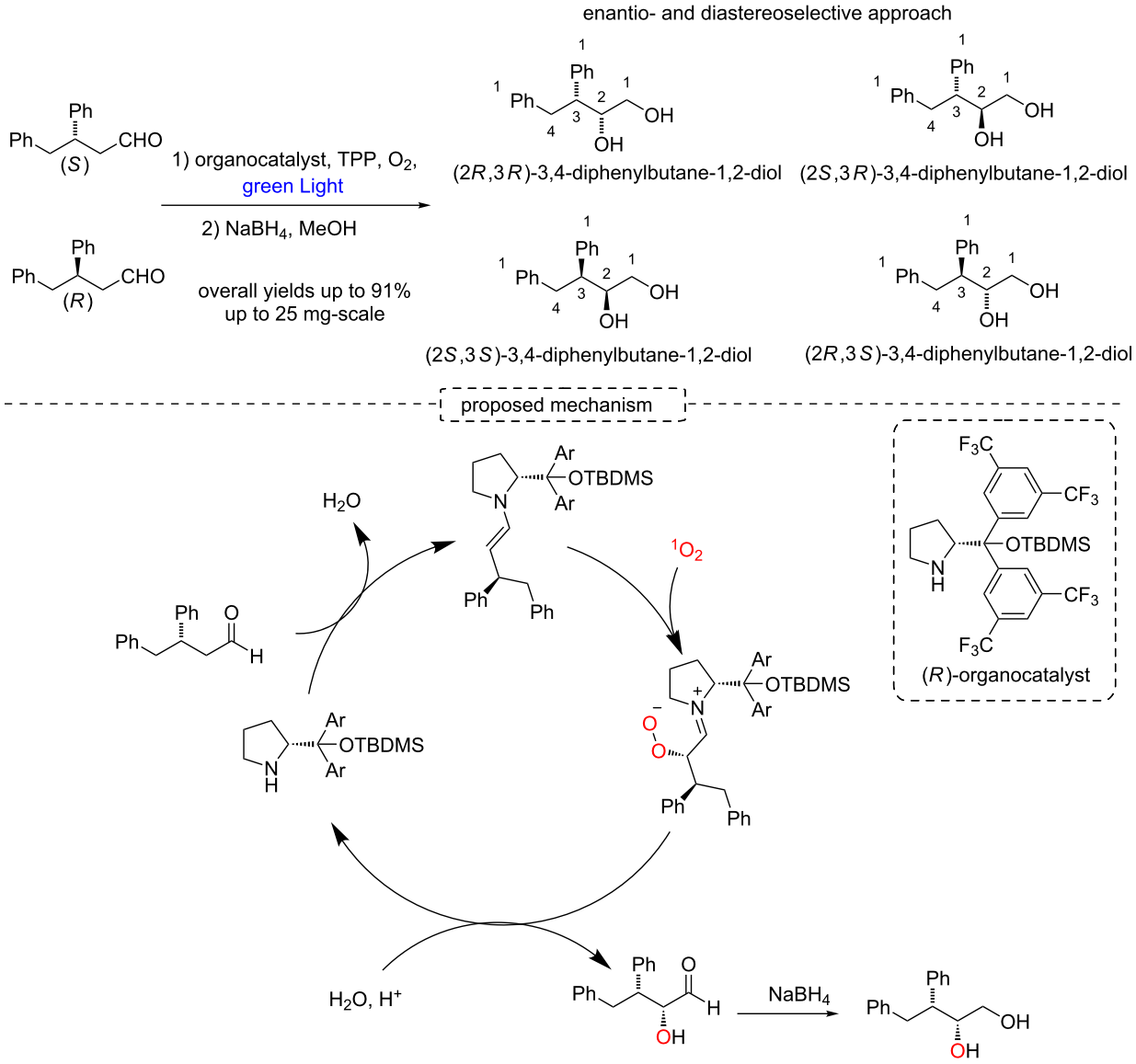

Scheme 40: α-Photooxygenation of chiral aldehydes.

oxide intermediate, which is converted to α-hydroxy-β-keto esters (Scheme 41) [91].

Later, these results were improved by the development of a new chiral PTC and re-optimization of the experimental conditions [92]. The new protocol furnished the indanone derivatives in 70–99% yields and 62–90% ee. Furthermore, the methodology was also applied to oxidations of β-keto amides (71–99% yields) and with 5–66% ee (Scheme 42).

In 2018, Meng and co-workers developed a bifunctional photo-organocatalyst combining both the photosensitizer and the chirality inducer. Relevant enantiomeric excesses were observed (up to 86% ee) in the oxidation of both β-keto esters and β-keto amides (Scheme 43) [93].

Singlet oxygen in heteroatom oxidations

Singlet oxygen reacts readily with electron pairs of heteroatoms, such as sulfur, selenium, phosphorus, and nitrogen, due to their electrophilicity. The interaction between singlet oxygen and the heteroatom occurs in both physical and chemical quenching leading to the formation of covalent products [67].

Sulfur oxidation: One of the first examples reported for heteroatom oxidation by singlet oxygen was the oxidation of sulfides

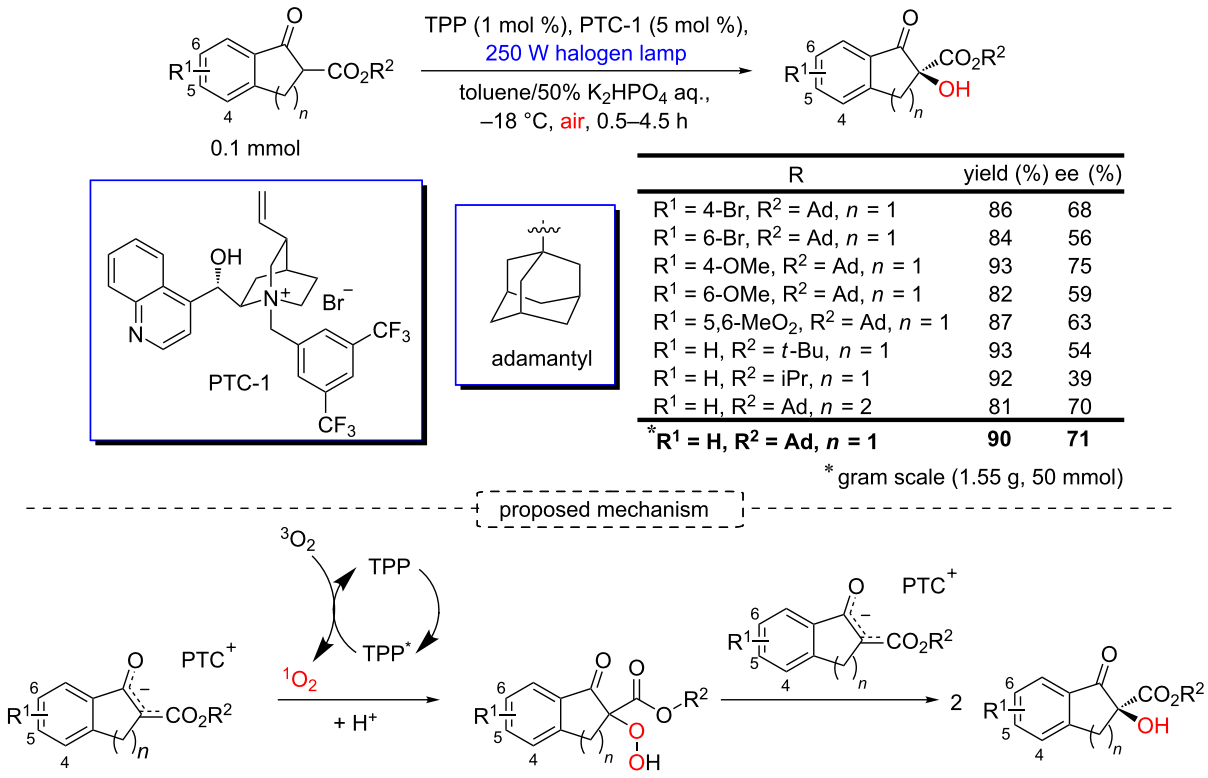

R	yield (%)	ee (%)
R^1 = 4-Br, R^2 = Ad, n = 1	86	68
R^1 = 6-Br, R^2 = Ad, n = 1	84	56
R^1 = 4-OMe, R^2 = Ad, n = 1	93	75
R^1 = 6-OMe, R^2 = Ad, n = 1	82	59
R^1 = 5,6-MeO_2, R^2 = Ad, n = 1	87	63
R^1 = H, R^2 = t-Bu, n = 1	93	54
R^1 = H, R^2 = iPr, n = 1	92	39
R^1 = H, R^2 = Ad, n = 2	81	70
***R^1 = H, R^2 = Ad, n = 1**	**90**	**71**

* gram scale (1.55 g, 50 mmol)

Scheme 41: Asymmetric photooxidation of indanone β-keto esters by singlet oxygen using PTC as a chiral inducer, and the related mechanism.

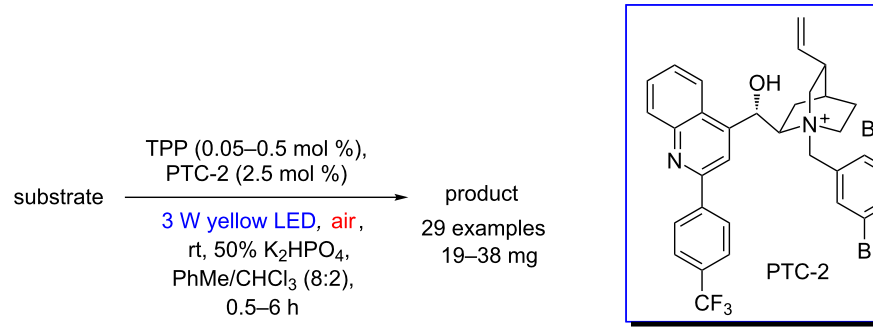

substrate	scope	product	yield (%)	ee (%)
n = 1, 2	R^1 = Ad, t-Amyl, 3-Ethyl amyl, t-Bu, iPr, Me R^2 = H, 5-Cl, 5-Br, 4-Br, 6-Br, 6-F, 6-Me, 4-OMe, 6-OMe, 7-Br, 5,6-di-OMe, 5,7-di-Br, 7-OMe		70–99	62–90
n = 1, 2	NR^1 = NH-Ph,NH-iPr, NCH_3-Ph, 4-Me-piperidine R^2 = H, 5-Br		71–99	5–66

Scheme 42: Asymmetric photooxidation of both β-keto esters and β-keto amides by singlet oxygen using PTC-2 as a chiral organocatalyst.

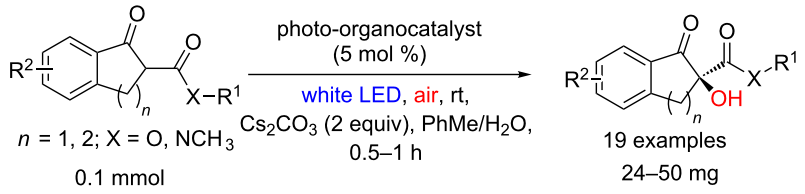

representative examples

Product	TPP + TPC-2		photo-organocatalyst	
	yield (%)	ee (%)	yield (%)	ee (%)
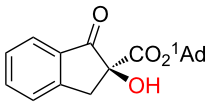	98	90	95	86
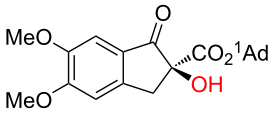	97	88	88	82
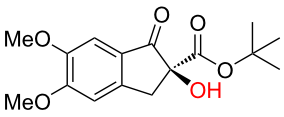	92	72	89	60
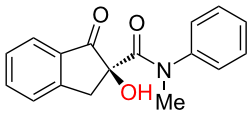	73	66	44	52

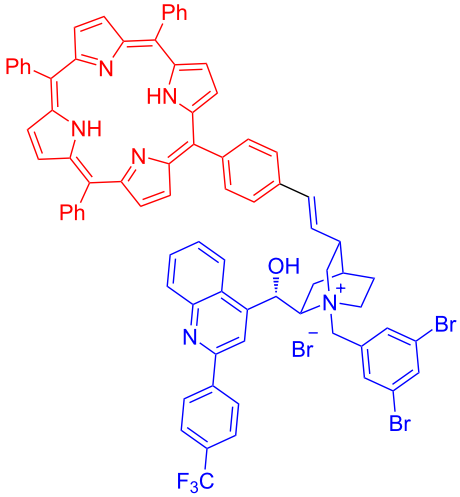

Scheme 43: Bifunctional photo-organocatalyst used for the asymmetric oxidation of β-keto esters and β-keto amides by singlet oxygen.

to sulfoxides [67]. Sulfoxides are important intermediates in organic synthesis, and with applications in medicine and pharmacology [94], justifying many studies on this topic.

The accepted mechanism for sulfide oxidation to sulfoxide involves the chemical quenching of singlet oxygen by sulfur compounds which leads to the persulfoxide intermediate. From this intermediate, a variety of reaction pathways are suggested to give the oxidized product, including the quenching with a second molecule of sulfide (Scheme 44) [67,95,96].

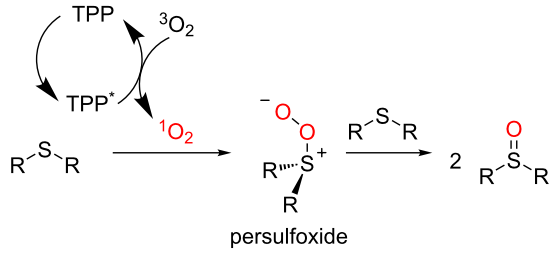

Scheme 44: Mechanism of singlet oxygen oxidation of sulfides to sulfoxides.

Recent advances have also been achieved using photostable porphyrins and/or heterogeneous catalysts. Mojarrad and Zakavi reported that the oxidation of sulfides using diprotonated porphyrins as photocatalysts under sunlight irradiation furnished the corresponding sulfoxides with high chemoselectivity (up to 100%), scalability (up to 2.6 mmol) and high yields (up to 100%) [94]. According to the authors, the protonation of the porphyrins causes a red-shift of the photosensitizer with an increase of singlet oxygen generation and photocatalytic activity under the sunlight irradiation. Furthermore, the steric hindrance around the porphyrin core, caused by the diacids, enhanced the catalyst photostability, allowing a lowers porphyrin load. The authors evaluated various protonated-TPPs, using CF_3COOH, $Cl_2CHCOOH$, $HClO_4$ and H_2SO_4 acids, and they concluded that $H_4TPP(ClO_4)_2$ and $H_4TPP(Cl_2CHCOO)_2$ were

the most stable and efficient photocatalysts of the series (Scheme 45).

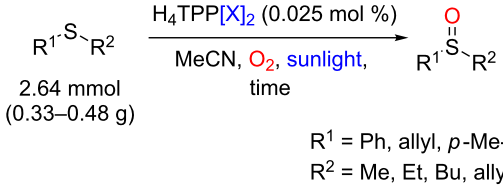

X	time (h)	conversion (%)	selectivity (%)
CF_3COO^-	2–18	90–99 (54–93)[a]	66–98
Cl_2CHCOO^-	1–6	96–99 (85–95)[a]	91–100
ClO_4^-	1–5	90–quant.	46–100
HSO_4^-	2–16	96–quant.	52–94

Scheme 45: Controlled oxidation of sulfides to sulfoxides using protonated porphyrins as photocatalysts. [a]Isolated yield.

Che and co-workers showed that Pd(II) *meso*-tetrakis(pentafluorophenyl)porphyrin (PdTPFPP) can be used for the conversion of sulfides to sulfoxides via oxidation by singlet oxygen [97]. A series of sulfides was oxidized to the corresponding sulfoxides in 87–94% yields using only 0.05 mol % of the photocatalyst (TON: 1880) (Scheme 46).

The controlled oxidation of sulfides to sulfoxides by singlet oxygen was also reported using heterogeneous photocatalysts. A Sn porphyrin-based porous aromatic framework (SnPor@PAF) with a broad and strong optical absorption in the visible light region was used for this transformation [98]. Luo, Ji and co-workers synthesized this material by a Yamamoto homo coupling reaction using a well-designed brominated tin porphyrin (SnTBPP) as monomer (Scheme 47). The irradiation of this material in the presence of both sulfides and molecular

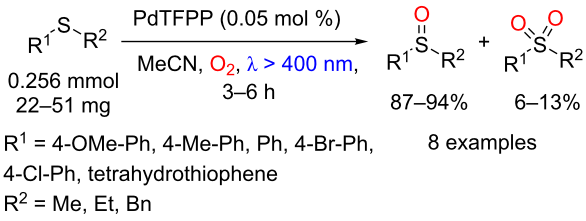

Scheme 46: Photochemical oxidation of sulfides to sulfoxides using PdTPFPP as photocatalyst.

oxygen furnished a variety of sulfoxides in 70–97% yields. The SnPor@PAF presented the same photocatalytic activity of its monomer (SnTBPP) with the advantage of its easy recovery and reuse. The authors did not observe any decrease in the photocatalytic activity of the material even after four reuses.

Another very promising catalytic platform for this transformation is the covalent organic framework (COF), a class of porous crystalline polymers built from molecular building blocks linked via covalent bonds. Recently, Sun, Wang and co-workers built both 2D- and 3D-porphyrin COFs (2D-PdPor-COF and 3D-PdPor-COF, respectively) from the same porphyrin, Pd(II) *meso*-tetrakis(4-formylphenyl)porphyrin (*p*-PdPor-CHO) (Scheme 48) [99]. In the 2D-COF, the functional moieties in the adjacent layers have strong π–π interactions that could be beneficial for the charge mobility. On the other hand, the three-dimensionally organized (3D-COF) allows open sites. Therefore, for the first time, the photocatalytic activity of the same porphyrin was evaluated in distinct dimensional frameworks.

The authors showed that the photocatalytic performance of COF-porphyrin (2D-COF = 48% and 3D-COF = 98%) was significantly higher than in the case of homogeneous photocatalysis (*p*-PdPor-CHO = 23%) (Scheme 49A). Among COF-porphyrins, the 3D-COF presented the highest activity for all smaller substrates, such as the *p*-Me-Ph substituent (99%), but

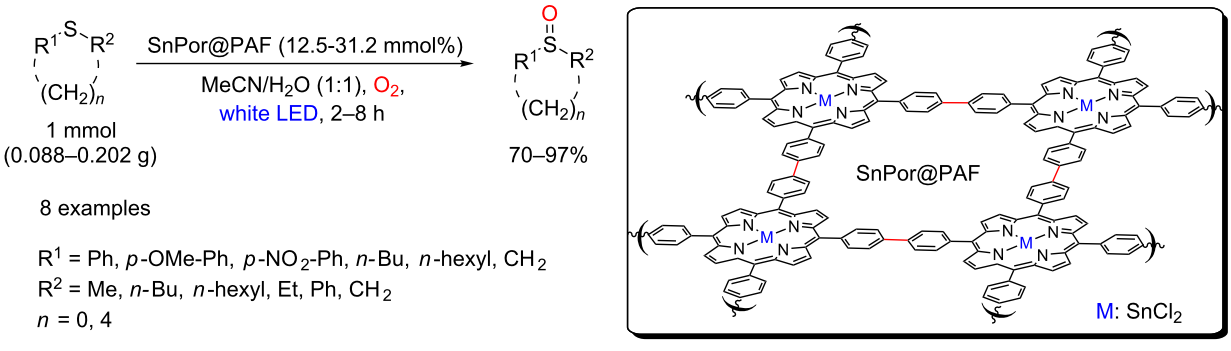

Scheme 47: Controlled oxidation of sulfides to sulfoxides using SnPor@PAF as a photosensitizer.

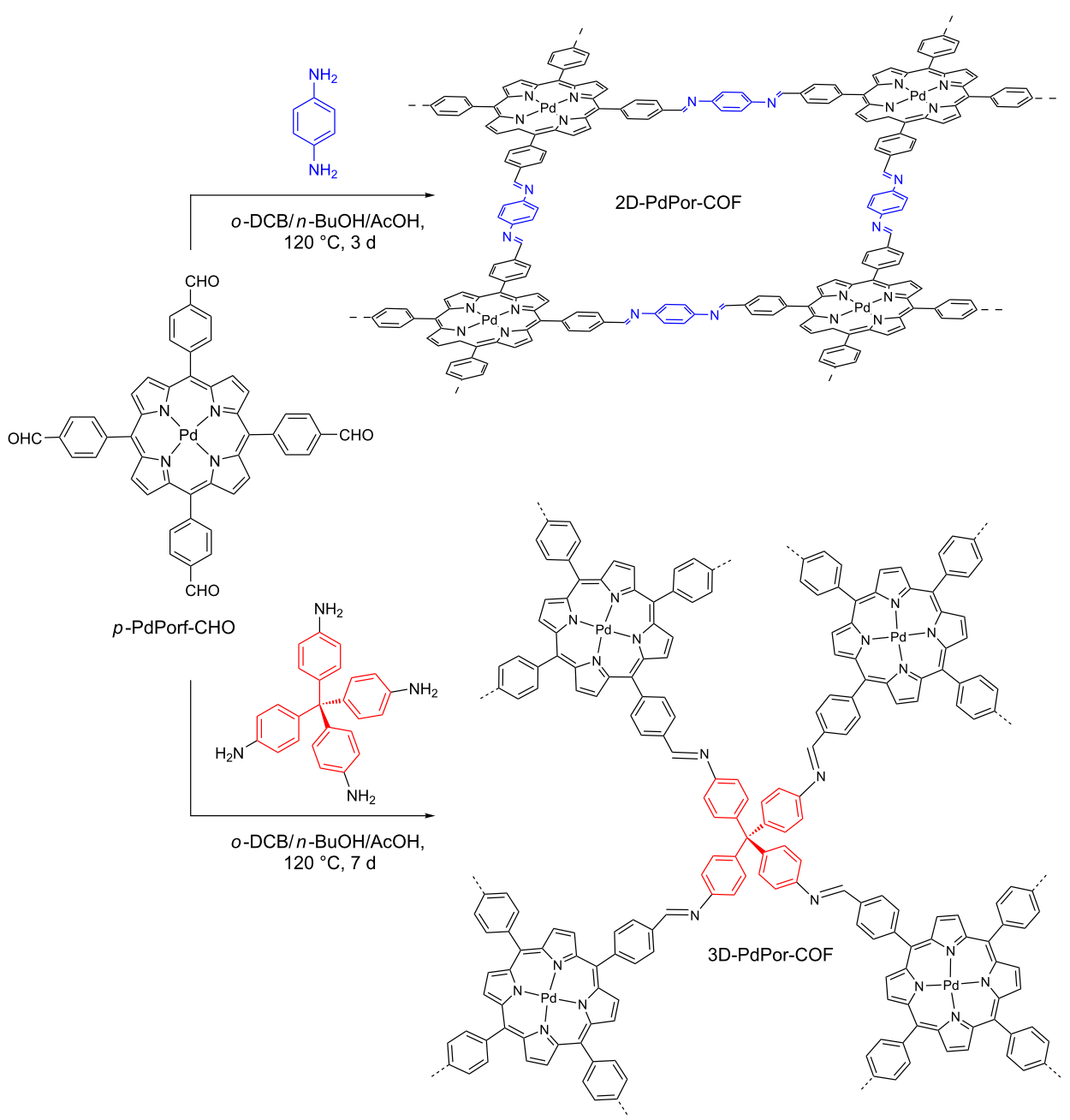

Scheme 48: Syntheses of 2D-PdPor-COF and 3D-Pd-COF.

lower activity for the bigger naphthyl substrate (38%). The achieved yields for 2D-COF were moderate for all the evaluated substrates (39–60%) (Scheme 49B). Thus, the authors suggested that the 3D-COF, whose porous size (0.63 nm) is smaller than the 2D-COF (1.87 nm), acts as a size-selective photocatalyst. Furthermore, the photocatalytic activity of 2D-COF is lower due to the π–π interaction between framework layers.

Nitrogen oxidation: Amines are well-known as very efficient physical and chemical quenchers for singlet oxygen [67,100,101]. A myriad of chemical transformations come from this process, whose crucial step involves the formation of a charge-transfer complex between singlet oxygen and the amine. Subsequently, hydrogen-atom abstraction leads to the radical intermediate, which can undergo SET with a hydroperoxyl radical to afforded an iminium ion, then giving an imine after deprotonation (Scheme 50).

Adopting this strategy, Che and co-workers obtained several imines in 90–99% yield from secondary amines [102]

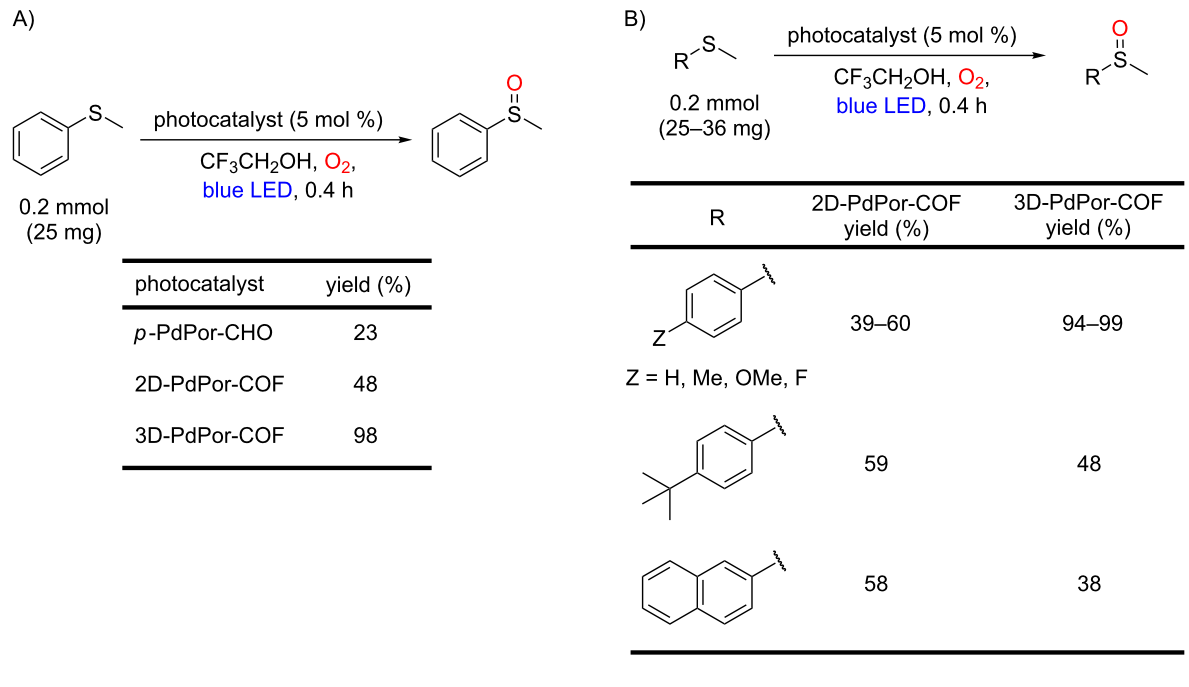

photocatalyst	yield (%)
p-PdPor-CHO	23
2D-PdPor-COF	48
3D-PdPor-COF	98

R	2D-PdPor-COF yield (%)	3D-PdPor-COF yield (%)
Z	39–60	94–99
	59	48
	58	38

Scheme 49: Photocatalytic oxidation of A) thioanisole to methyl phenyl sulfoxide and B) various aryl sulfides, using 2D-PdPor-COF, 3D-PdPor-COF, and *p*-PdPor-CHO.

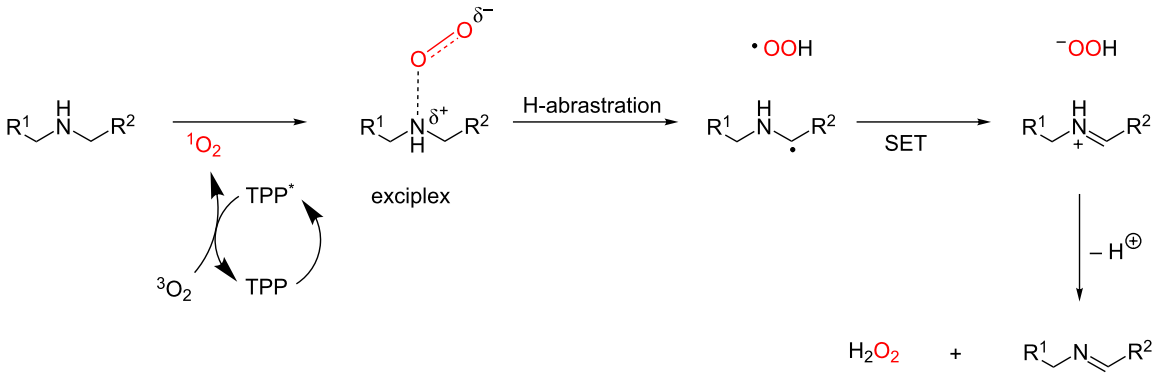

Scheme 50: General mechanism for oxidation of amines to imines.

(Scheme 51). The authors observed that the oxidation is regioselective, occurring at the less substituted position of nonsymmetric dibenzylamines, and they have demonstrated scalability of the protocol (products in up to 3.8 g scale).

Similarly, using Pd-TPFPP the oxidation of amines to imines was achieved in 88–99% yields with low loading (0.005 mol %, 13000 TON h^{-1}) after 1.5 h of irradiation with visible light (Scheme 52) [97].

The oxidation of amines to imines was also described using heterogeneous catalysis.

Zhang and co-workers demonstrated that the MOF (Sn^{IV})porphyrin-containing photocatalyst (UNLPF-12) can be used for the oxidation of primary amines to imines in 88–99% yields under visible light irradiation (Scheme 53) [40]. In this case, the authors observed the oxidative coupling between the primary amines and their respective imines to produce the secondary imines.

Wang and co-workers reported the synthesis, characterization, and application of interesting metal-free heterogeneous photocatalysts, 2D porphyrin-COFs (Por-COF), which were obtained by condensation between *meso*-tetrakis(4-formylphenyl)por-

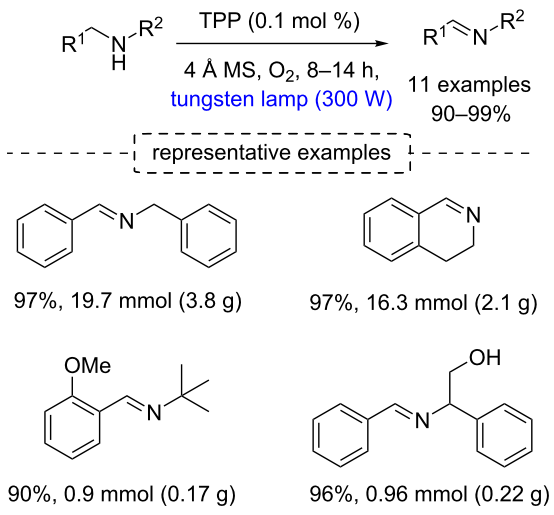

Scheme 51: Oxidation of secondary amines to imines.

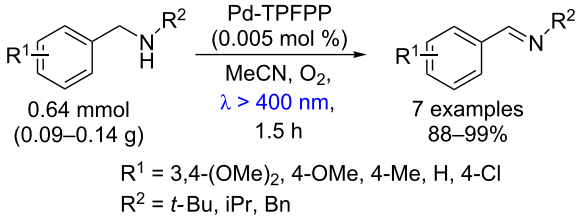

Scheme 52: Oxidation of secondary amines using Pd-TPFPP as photocatalyst.

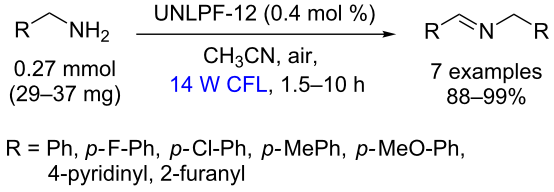

Scheme 53: Oxidative amine coupling using UNLPF-12 as heterogeneous photocatalyst.

phyrin (*p*-Por-CHO) and benzene-1,4-diamine, and 1,4-phenylenediacetonitrile, for Por-COF-1 and Por-COF-2, respectively (Scheme 54) [103]. The sp^2 carbon-linked COF conferred high chemical stability to the material (Por-COF-2) due to the low reversibility of the double bond formation.

Initially, the photocatalytic oxidative amine coupling was selected as a reaction model [103]. The authors observed that the imine-based Por-COF-1, decomposed completely, and no target product was detected. Nevertheless, the Por-COF-2 presented high photocatalytic activity for this transformation. The *N*-benzylidenebenzylamines were obtained in excellent yields (86–99%) for primary and secondary amine derivatives bearing electron-donating and electron-withdrawing groups (Scheme 55).

Imines are useful building blocks for the synthesis of biologically active compounds [104]. These compounds can be trapped with nucleophiles to produce the α-amino-substituted compounds, and be employed as substrates for a variety of chemical transformations such as Ugi- and Mannich-type reactions.

In this regard, Seeberger and co-workers reported the primary/secondary amine oxidation under continuous-flow conditions using TPP as photocatalyst for singlet oxygen generation, and subsequently, the product imines were trapped with trimethylsilyl cyanide (TMSCN) for producing the α-aminonitriles (Scheme 56) [105]. A library of α-aminonitriles was produced by this methodology (conditions A). However, when primary amines were used, the authors observed an oxidative coupling between the amines and their respective *N*-substituted imines, which were trapped with TMSCN to afford the corresponding nitriles. The authors solved this problem by cooling the reaction to −50 °C and using 4 mol % of tetra-*n*-butylammonium fluoride (TBAF) as an activator of TMSCN (conditions B). Following this second protocol, the primary α-aminonitriles were rapidly prepared in relevant yields (up to 87%) and converted to the corresponding α-amino acids by hydrolysis of the nitrile (Scheme 57).

Ferroud's group showed that the α-photocyanation of amines can be efficiently applied in complex molecules. The authors reported a highly regio- and diastereoselective photocyanation of both catharanthine and 16-*O*-acetylvindoline alkaloids with TMSCN and using TPP as photocatalyst (Scheme 58) [106,107].

Che and co-workers showed that a variety of nucleophiles can be used for the α-functionalization of *N*-aryltetrahydroisoquinolines using a low Pd-TPFPP loading. This photocatalyst provided the α-aminonitriles in 71–85%, β-nitroamines in 72–83%, β-diester amines in 68–74%, and α-amino phosphonates in 63–84% yields (Scheme 59) [97].

The Ugi-type multicomponent reactions between imines, carboxylic acids, and isocyanides, and Mannich-type reactions between iminium and carbonyl groups have found many applications in organic synthesis [108]. Che's group employed the methodology of oxidation of an amine with singlet oxygen to produce an imine, which was used as a substrate in the Ugi-type reaction. Thus, the oxidations of both 1,2,3,4-tetrahydroisoquinoline and dibenzylamine using TPP were carried out with

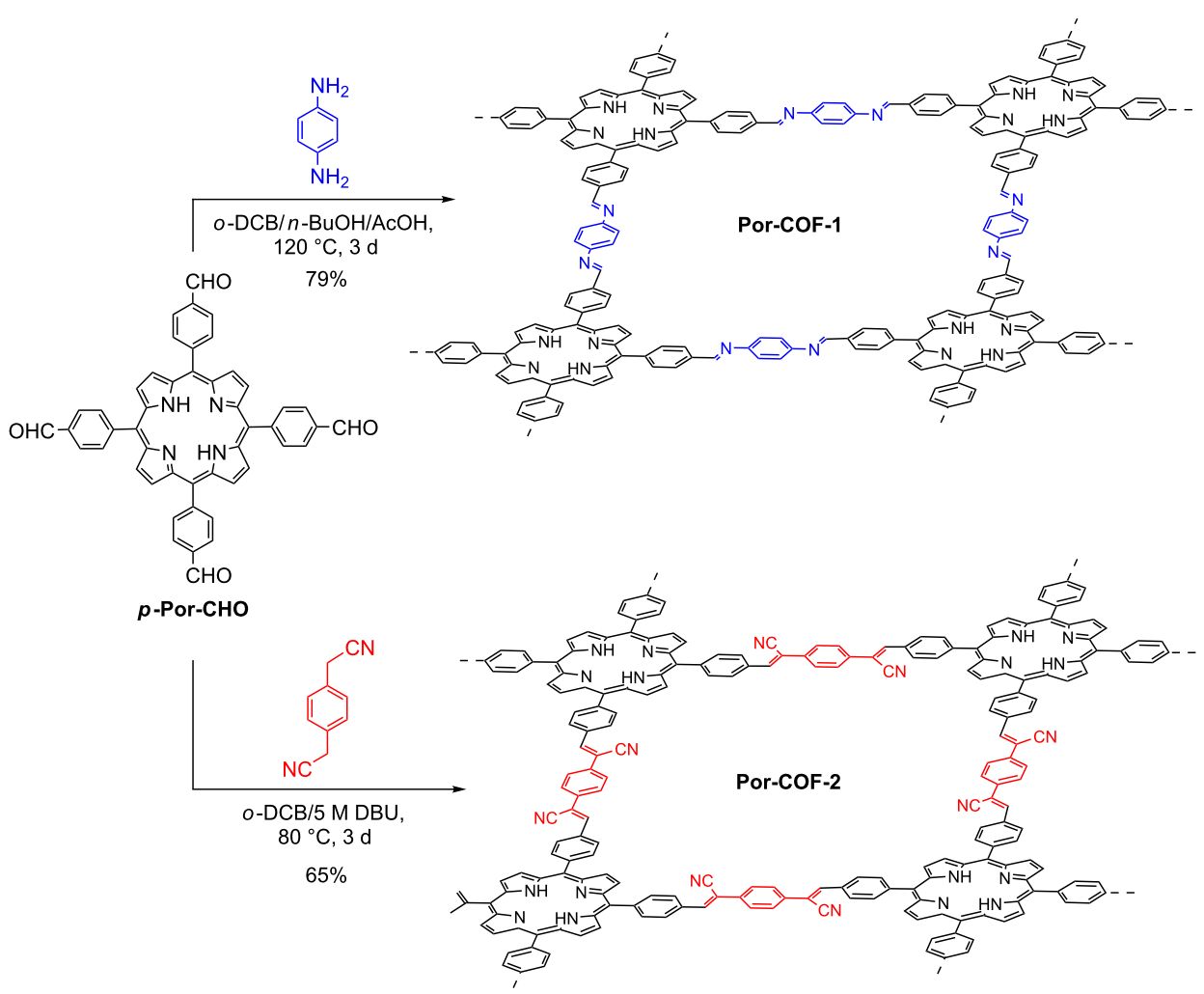

Scheme 54: Synthesis of Por-COF-1 and Por-COF-2.

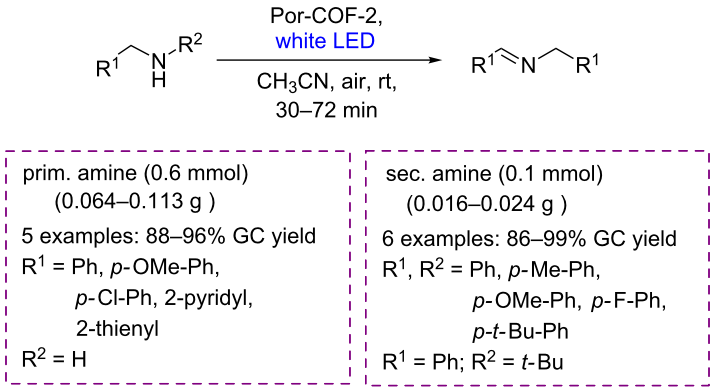

Scheme 55: Photocatalytic oxidation of amines to imines by Por-COF-2.

high yield and selectivity, and the Ugi products were obtained after removal of the solvent and direct addition of isocyanide and carboxylic acid. The Ugi products were obtained in 41–89% and 72–96% yields from 1,2,3,4-tetrahydroisoquinoline (Scheme 60) and dibenzylamine (Scheme 61), respectively [102].

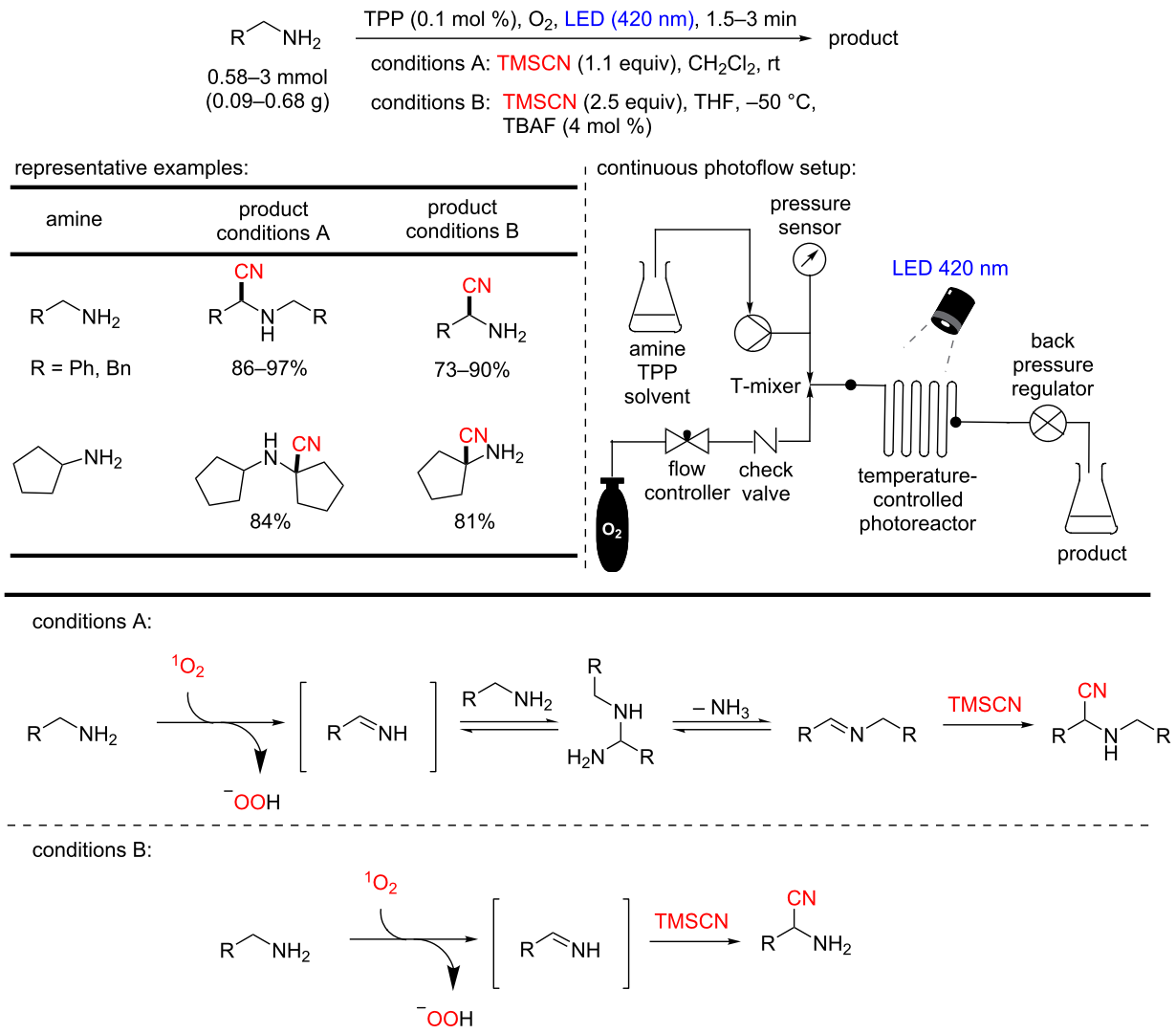

Scheme 56: Photocyanation of primary amines.

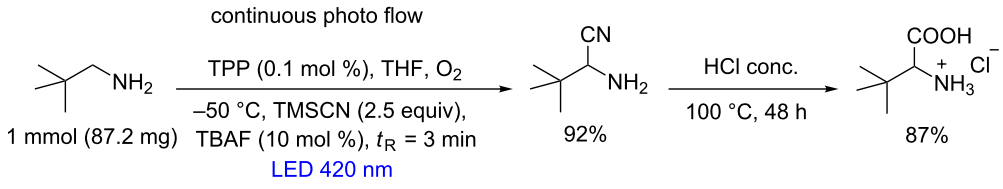

Scheme 57: Synthesis of D,L-*tert*-leucine hydrochloride.

Furthermore, Che and co-workers obtained a wide range of Mannich-type products by coupling *N*-aryltetrahydroisoquinoline, ketones, and L-proline using a low PdTPFPP loading (Scheme 62) [97].

Zhang and co-workers demonstrated that the MOF-catalyst (UNLPF-12) can also be used for the Mannich reactions. The authors reported that the coupling between *N*-aryltetrahydroisoquinolines and acetone using visible light and UNLPF-12 afforded the Mannich products in 87–98% yields (Scheme 63) [40].

As previously shown (Scheme 50), the oxidation of amines to imines by singlet oxygen furnishes hydrogen peroxide as a by-

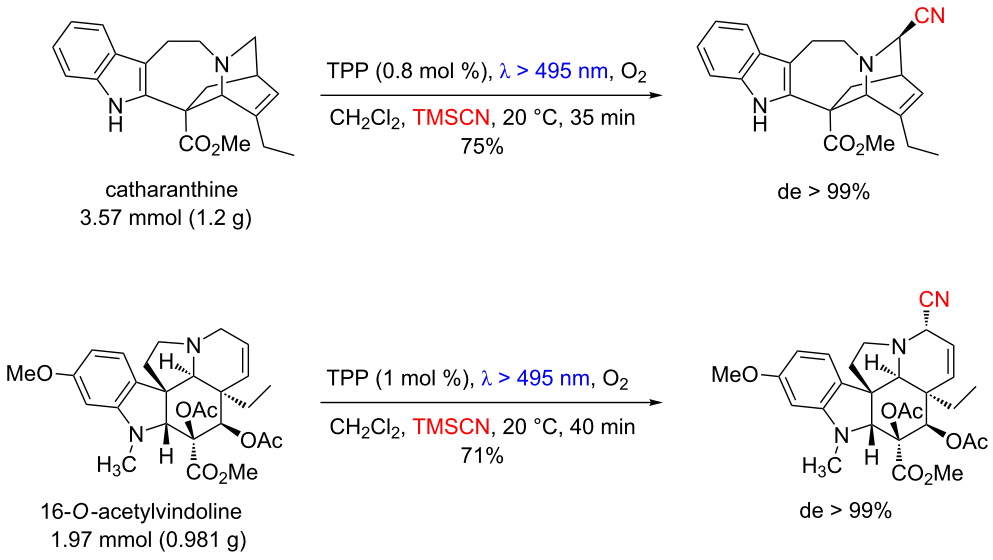

Scheme 58: Photocyanation of catharanthine and 16-*O*-acetylvindoline using TPP.

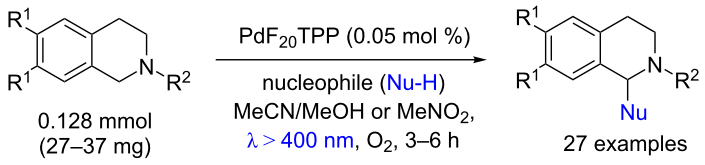

R^1 = H, OMe
R^2 = 4-OMe-Ph, 4-Me-Ph, Ph, 4-Br-Ph, 4-Cl-Ph

Nu	yield (%)
CN	71–85
CH_2NO_2	72–83
$CH(CO_2Me)_2$	68–74
$PO(OR^3)_2$ R^3 = Me, Et	63–84

Scheme 59: Photochemical α-functionalization of *N*-aryltetrahydroisoquinolines using Pd-TPFPP as photocatalyst.

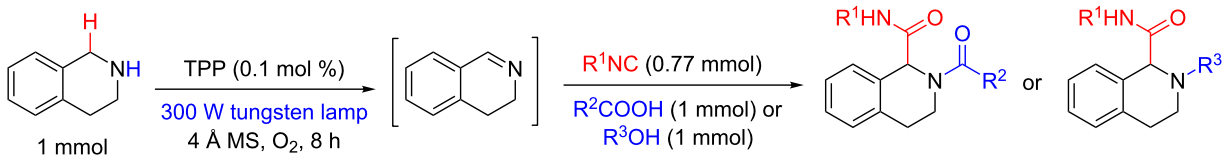

R^1 = *t*-Bu, Bn
R^2 = Ph, cinnamyl
R^3 = *o*-NO_2-Ph

Scheme 60: Ugi-type reaction with 1,2,3,4-tetrahydroisoquinoline using molecular oxygen and TPP.

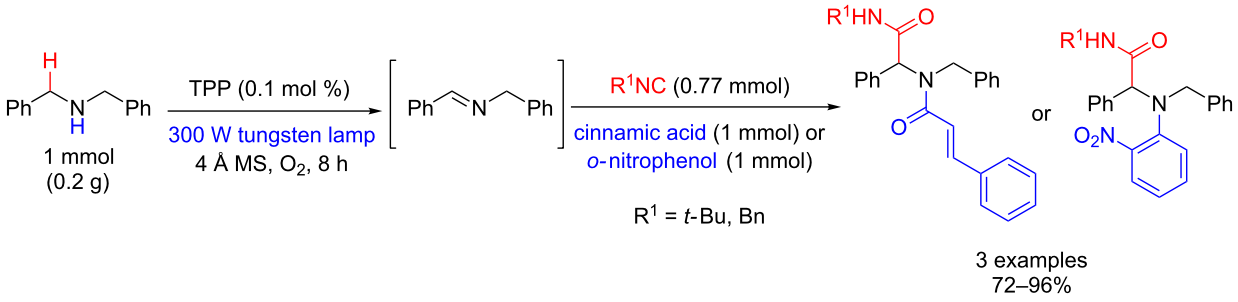

Scheme 61: Ugi-type reaction with dibenzylamines using molecular oxygen and TPP.

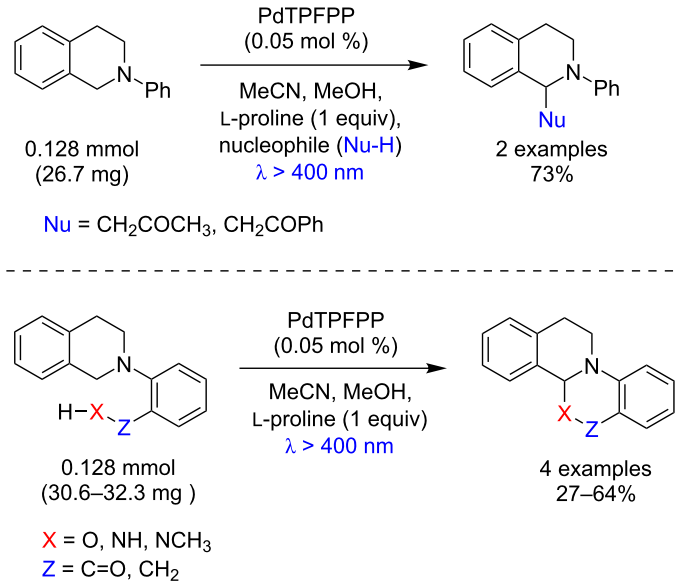

Scheme 62: Mannich-type reaction of tertiary amines using PdTPFPP as photocatalyst.

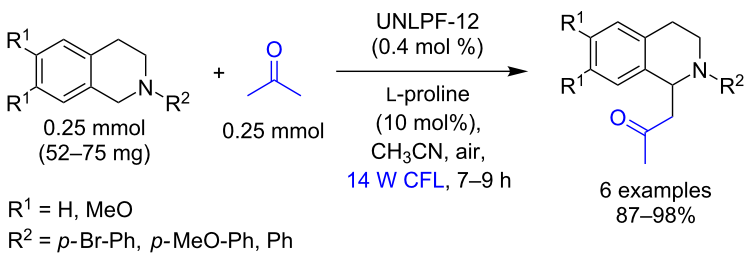

Scheme 63: Oxidative Mannich reaction using UNLPF-12 as heterogeneous photocatalyst.

product. In 2014, Seeberger and co-workers used this byproduct, in a continuous-flow approach, as an epoxidation agent of an electron-deficient olefin intermediate, which was formed by deaminative Mannich coupling between the imine and nucleophiles such as malononitrile and methyl cyanoacetate (Scheme 64) [109].

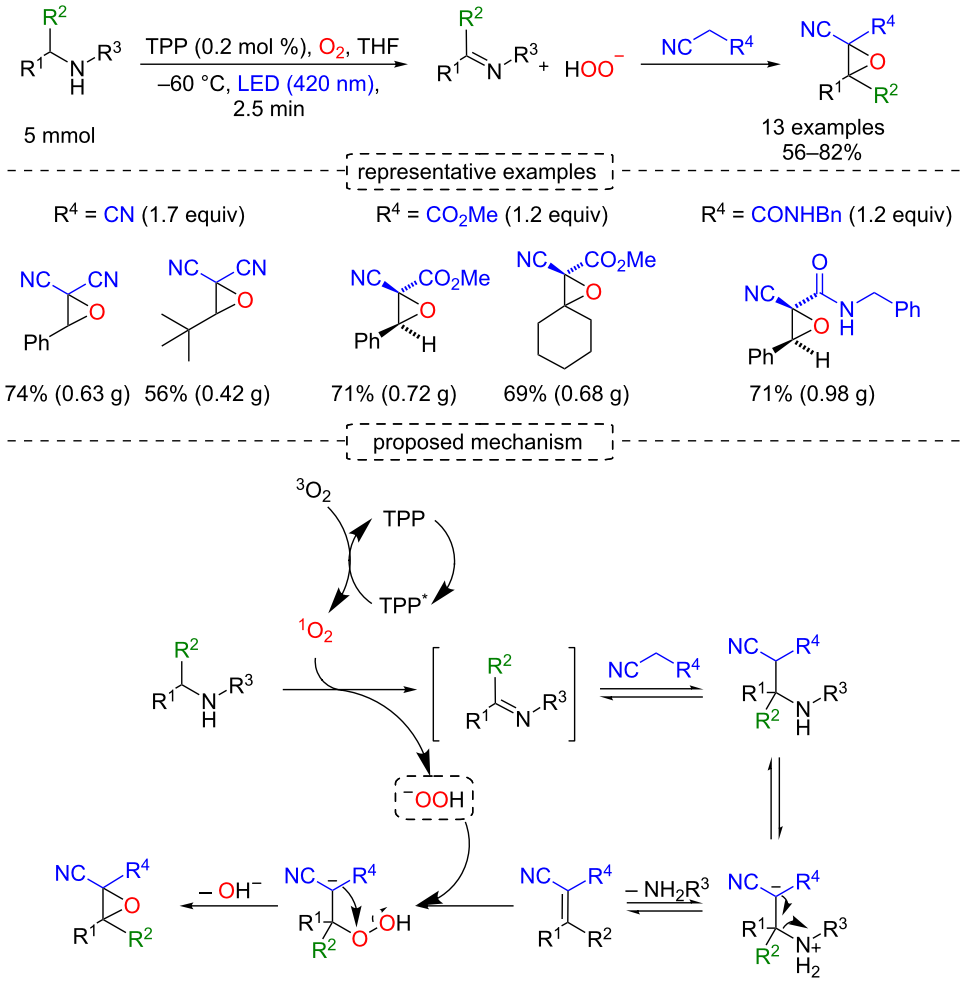

Scheme 64: Transformation of amines to α-cyanoepoxides and the proposed mechanism.

Overall, a variety of additional examples of porphyrin-photocatalyzed heteroatom oxidations are continuously under development, and we have highlighted herein the most relevant in the authors' opinion.

Conclusion

As demonstrated in this review, porphyrin derivatives have gained attention in preparative organic synthesis in the last 10 years with growing applications in photocatalysis. Relevant chemical transformations have been reported with scalability, which makes porphyrin chemistry more valuable and with potential for further preparative and industrial applications. Many challenges must still be solved in terms of the availability of these photocatalysts to make them cost-competitive; however, the very low loading of these compounds (less than 0.5–1 mol %), high TON and easy recovery can be considered important advantages. For the authors of this review, porphyrin photochemically mediated transformations in organic synthesis are definitively a very important field for further exploration in both single electron and energy transfer.

Funding

The authors would like to thank the São Paulo Research Foundation FAPESP (grant number: 2018/00106-7 and 2013/07276-1; fellowships: 2018/00879-6, 2014/24506-3) as well as the Conselho Nacional de Pesquisa - CNPq (Grant 407990/2018-6 and K.T.O. research fellowship 303890/2019-3) and the Coordenação de Aperfeiçoamento de Pessoal de Nível Superior – Brasil (CAPES) – Financial Code 001, for the financial support.

ORCID® iDs

Rodrigo Costa e Silva - https://orcid.org/0000-0002-8180-7492
Luely Oliveira da Silva - https://orcid.org/0000-0002-5544-7438
Aloisio de Andrade Bartolomeu - https://orcid.org/0000-0002-8191-778X
Kleber Thiago de Oliveira - https://orcid.org/0000-0002-9131-4800

References

1. Garlets, Z. J.; Nguyen, J. D.; Stephenson, C. R. J. *Isr. J. Chem.* **2014,** *54,* 351–360. doi:10.1002/ijch.201300136
2. Cambié, D.; Bottecchia, C.; Straathof, N. J. W.; Hessel, V.; Noël, T. *Chem. Rev.* **2016,** *116,* 10276–10341. doi:10.1021/acs.chemrev.5b00707
3. Noël, T. *J. Flow Chem.* **2017,** *7,* 87–93. doi:10.1556/1846.2017.00022
4. Oelgemoeller, M. *Chem. Eng. Technol.* **2012,** *35,* 1144–1152. doi:10.1002/ceat.201200009
5. Lesage, S.; Xu, H.; Durham, L. *Hydrol. Sci. J.* **1993,** *38,* 343–354. doi:10.1080/02626669309492679
6. Biesaga, M.; Pyrzyńska, K.; Trojanowicz, M. *Talanta* **2000,** *51,* 209–224. doi:10.1016/s0039-9140(99)00291-x
7. de Oliveira, K. T.; Momo, P. B.; de Assis, F. F.; Ferreira, M. A. B.; Brocksom, T. J. *Curr. Org. Synth.* **2014,** *11,* 42–58. doi:10.2174/15701794113106660085
8. Chatterjee, T.; Shetti, V. S.; Sharma, R.; Ravikanth, M. *Chem. Rev.* **2017,** *117,* 3254–3328. doi:10.1021/acs.chemrev.6b00496
9. de Souza, A. A. N.; Silva, N. S.; Müller, A. V.; Polo, A. S.; Brocksom, T. J.; de Oliveira, K. T. *J. Org. Chem.* **2018,** *83,* 15077–15086. doi:10.1021/acs.joc.8b02355
10. Rybicka-Jasińska, K.; Shan, W.; Zawada, K.; Kadish, K. M.; Gryko, D. *J. Am. Chem. Soc.* **2016,** *138,* 15451–15458. doi:10.1021/jacs.6b09036
11. Rybicka-Jasińska, K.; König, B.; Gryko, D. *Eur. J. Org. Chem.* **2017,** 2104–2107. doi:10.1002/ejoc.201601518
12. Marzo, L.; Pagire, S. K.; Reiser, O.; König, B. *Angew. Chem., Int. Ed.* **2018,** *57,* 10034–10072. doi:10.1002/anie.201709766
13. Wang, C.-S.; Dixneuf, P. H.; Soulé, J.-F. *Chem. Rev.* **2018,** *118,* 7532–7585. doi:10.1021/acs.chemrev.8b00077
14. Prier, C. K.; Rankic, D. A.; MacMillan, D. W. C. *Chem. Rev.* **2013,** *113,* 5322–5363. doi:10.1021/cr300503r
15. Cho, H. S.; Jeong, D. H.; Yoon, M.-C.; Kim, Y. H.; Kim, Y.-R.; Kim, D.; Jeoung, S. C.; Kim, S. K.; Aratani, N.; Shinmori, H.; Osuka, A. *J. Phys. Chem. A* **2001,** *105,* 4200–4210. doi:10.1021/jp010385n
16. Dekkiche, H.; Buisson, A.; Langlois, A.; Karsenti, P.-L.; Ruhlmann, L.; Harvey, P. D.; Ruppert, R. *Inorg. Chem.* **2016,** *55,* 10329–10336. doi:10.1021/acs.inorgchem.6b01594
17. Jacobs, R.; Stranius, K.; Maligaspe, E.; Lemmetyinen, H.; Tkachenko, N. V.; Zandler, M. E.; D'Souza, F. *Inorg. Chem.* **2012,** *51,* 3656–3665. doi:10.1021/ic202574q
18. Ngo, K. T.; Rochford, J. Principles of Photochemical Activation Toward Artificial Photosynthesis and Organic Transformations. *Green Chemistry;* Elsevier: Amsterdam, Netherlands, 2018; pp 729–752. doi:10.1016/b978-0-12-809270-5.00026-1
19. Nakagaki, S.; Castro, K. A. D. F.; Neves, M. d. G. P. M. S.; Faustino, M. d. A.; Iamamoto, Y. *J. Braz. Chem. Soc.* **2019,** *30,* 2501–2535. doi:10.21577/0103-5053.20190153
20. Pereira, M. M.; Dias, L. D.; Calvete, M. J. F. *ACS Catal.* **2018,** *8,* 10784–10808. doi:10.1021/acscatal.8b01871
21. Barona-Castaño, J.; Carmona-Vargas, C.; Brocksom, T.; de Oliveira, K. *Molecules* **2016,** *21,* 310. doi:10.3390/molecules21030310
22. Mandal, T.; Das, S.; De Sarkar, S. *Adv. Synth. Catal.* **2019,** *361,* 3200–3209. doi:10.1002/adsc.201801737
23. de Oliveira, K. T.; Miller, L. Z.; McQuade, D. T. *RSC Adv.* **2016,** *6,* 12717–12725. doi:10.1039/c6ra00285d
24. Rybicka-Jasińska, K.; Ciszewski, Ł. W.; Gryko, D. *Adv. Synth. Catal.* **2016,** *358,* 1671–1678. doi:10.1002/adsc.201600084
25. Momo, P. B.; Bellete, B. S.; Brocksom, T. J.; de Souza, R. O. M. A.; de Oliveira, K. T. *RSC Adv.* **2015,** *5,* 84350–84355. doi:10.1039/c5ra16962c
26. Moritz, M. N. O.; Gonçalves, J. L. S.; Linares, I. A. P.; Perussi, J. R.; de Oliveira, K. T. *Photodiagn. Photodyn. Ther.* **2017,** *17,* 39–47. doi:10.1016/j.pdpdt.2016.10.005
27. Diogo, P.; Fernandes, C.; Caramelo, F.; Mota, M.; Miranda, I. M.; Faustino, M. A. F.; Neves, M. G. P. M. S.; Uliana, M. P.; de Oliveira, K. T.; Santos, J. M.; Gonçalves, T. *Front. Microbiol.* **2017,** *8,* 498. doi:10.3389/fmicb.2017.00498
28. Lee, J.; Papatzimas, J. W.; Bromby, A. D.; Gorobets, E.; Derksen, D. J. *RSC Adv.* **2016,** *6,* 59269–59272. doi:10.1039/c6ra11374e
29. Hari, D. P.; König, B. *Org. Lett.* **2011,** *13,* 3852–3855. doi:10.1021/ol201376v
30. Meng, Q.-Y.; Zhong, J.-J.; Liu, Q.; Gao, X.-W.; Zhang, H.-H.; Lei, T.; Li, Z.-J.; Feng, K.; Chen, B.; Tung, C.-H.; Wu, L.-Z. *J. Am. Chem. Soc.* **2013,** *135,* 19052–19055. doi:10.1021/ja408486v
31. Rueping, M.; Zhu, S.; Koenigs, R. M. *Chem. Commun.* **2011,** *47,* 8679–8681. doi:10.1039/c1cc12907d
32. Hari, D. P.; Schroll, P.; König, B. *J. Am. Chem. Soc.* **2012,** *134,* 2958–2961. doi:10.1021/ja212099r
33. Xiao, T.; Dong, X.; Tang, Y.; Zhou, L. *Adv. Synth. Catal.* **2012,** *354,* 3195–3199. doi:10.1002/adsc.201200569
34. Liu, Z.; Wang, L.; Liu, D.; Wang, Z. *Synlett* **2015,** *26,* 2849–2852. doi:10.1055/s-0035-1560661
35. Zuo, Z.; Ahneman, D. T.; Chu, L.; Terrett, J. A.; Doyle, A. G.; MacMillan, D. W. C. *Science* **2014,** *345,* 437–440. doi:10.1126/science.1255525
36. Chambers, D. R.; Juneau, A.; Ludwig, C. T.; Frenette, M.; Martin, D. B. C. *Organometallics* **2019,** *38,* 4570–4577. doi:10.1021/acs.organomet.9b00552
37. Liu, X.; Liu, L.; Wang, Z.; Fu, X. *Chem. Commun.* **2015,** *51,* 11896–11898. doi:10.1039/c5cc04015a
38. Liu, X.; Wang, Z.; Zhao, X.; Fu, X. *Inorg. Chem. Front.* **2016,** *3,* 861–865. doi:10.1039/c5qi00269a
39. Liu, X.; Wang, Z.; Fu, X. *Dalton Trans.* **2016,** *45,* 13308–13310. doi:10.1039/c6dt01653g
40. Johnson, J. A.; Luo, J.; Zhang, X.; Chen, Y.-S.; Morton, M. D.; Echeverría, E.; Torres, F. E.; Zhang, J. *ACS Catal.* **2015,** *5,* 5283–5291. doi:10.1021/acscatal.5b00941
41. Zou, Y.-Q.; Chen, J.-R.; Liu, X.-P.; Lu, L.-Q.; Davis, R. L.; Jørgensen, K. A.; Xiao, W.-J. *Angew. Chem., Int. Ed.* **2012,** *51,* 784–788. doi:10.1002/anie.201107028
42. Morris, W.; Volosskiy, B.; Demir, S.; Gándara, F.; McGrier, P. L.; Furukawa, H.; Cascio, D.; Stoddart, J. F.; Yaghi, O. M. *Inorg. Chem.* **2012,** *51,* 6443–6445. doi:10.1021/ic300825s
43. Toyao, T.; Ueno, N.; Miyahara, K.; Matsui, Y.; Kim, T.-H.; Horiuchi, Y.; Ikeda, H.; Matsuoka, M. *Chem. Commun.* **2015,** *51,* 16103–16106. doi:10.1039/c5cc06163f
44. Markitanov, Y. M.; Timoshenko, V. M.; Shermolovich, Y. G. *J. Sulfur Chem.* **2014,** *35,* 188–236. doi:10.1080/17415993.2013.815749
45. Wen, J.; Yang, X.; Sun, Z.; Yang, J.; Han, P.; Liu, Q.; Dong, H.; Gu, M.; Huang, L.; Wang, H. *Green Chem.* **2020,** *22,* 230–237. doi:10.1039/c9gc03580j
46. Ghaleno, M. R.; Ghaffari-Moghaddam, M.; Khajeh, M.; Reza Oveisi, A.; Bohlooli, M. *J. Colloid Interface Sci.* **2019,** *535,* 214–226. doi:10.1016/j.jcis.2018.09.099

47. Chen, Y.-Z.; Wang, Z. U.; Wang, H.; Lu, J.; Yu, S.-H.; Jiang, H.-L. *J. Am. Chem. Soc.* **2017,** *139,* 2035–2044. doi:10.1021/jacs.6b12074
48. Drouet, S.; Paul-Roth, C. O.; Fattori, V.; Cocchi, M.; Williams, J. A. G. *New J. Chem.* **2011,** *35,* 438–444. doi:10.1039/c0nj00561d
49. Hajimohammadi, M.; Mofakham, H.; Safari, N.; Manesh, A. M. *J. Porphyrins Phthalocyanines* **2012,** *16,* 93–100. doi:10.1142/s1088424612004483
50. Pandey, V.; Jain, D.; Pareek, N.; Gupta, I. *Inorg. Chim. Acta* **2020,** *502,* 119339. doi:10.1016/j.ica.2019.119339
51. Deenadayalan, M. S.; Sharma, N.; Verma, P. K.; Nagaraja, C. M. *Inorg. Chem.* **2016,** *55,* 5320–5327. doi:10.1021/acs.inorgchem.6b00296
52. Nogueira, A. E.; Oliveira, J. A.; da Silva, G. T. S. T.; Ribeiro, C. *Sci. Rep.* **2019,** *9,* 1316. doi:10.1038/s41598-018-36683-8
53. Liu, W.; Li, X.; Wang, C.; Pan, H.; Liu, W.; Wang, K.; Zeng, Q.; Wang, R.; Jiang, J. *J. Am. Chem. Soc.* **2019,** *141,* 17431–17440. doi:10.1021/jacs.9b09502
54. Wang, D.; Huang, R.; Liu, W.; Sun, D.; Li, Z. *ACS Catal.* **2014,** *4,* 4254–4260. doi:10.1021/cs501169t
55. Li, L.; Zhang, S.; Xu, L.; Wang, J.; Shi, L.-X.; Chen, Z.-N.; Hong, M.; Luo, J. *Chem. Sci.* **2014,** *5,* 3808–3813. doi:10.1039/c4sc00940a
56. Sharma, N.; Dhankhar, S. S.; Nagaraja, C. M. *Microporous Mesoporous Mater.* **2019,** *280,* 372–378. doi:10.1016/j.micromeso.2019.02.026
57. Hugelshofer, C. L.; Magauer, T. *J. Am. Chem. Soc.* **2015,** *137,* 3807–3810. doi:10.1021/jacs.5b02021
58. Terent'ev, A. O.; Borisov, D. A.; Vil', V. A.; Dembitsky, V. M. *Beilstein J. Org. Chem.* **2014,** *10,* 34–114. doi:10.3762/bjoc.10.6
59. Lopes, N. S.; Yoshitake, A. M.; Silva, A. F.; Oliveira, V. X., Jr.; Silva, L. S.; Pinheiro, A. A. S.; Ciscato, L. F. M. L. *Chem. Biol. Drug Des.* **2015,** *86,* 1373–1377. doi:10.1111/cbdd.12599
60. Zheng, D.-Y.; Chen, E.-X.; Ye, C.-R.; Huang, X.-C. *J. Mater. Chem. A* **2019,** *7,* 22084–22091. doi:10.1039/c9ta07965c
61. Di Mascio, P.; Martinez, G. R.; Miyamoto, S.; Ronsein, G. E.; Medeiros, M. H. G.; Cadet, J. *Chem. Rev.* **2019,** *119,* 2043–2086. doi:10.1021/acs.chemrev.8b00554
62. Wahlen, J.; De Vos, D. E.; Jacobs, P. A.; Alsters, P. L. *Adv. Synth. Catal.* **2004,** *346,* 152–164. doi:10.1002/adsc.200303224
63. Schweitzer, C.; Schmidt, R. *Chem. Rev.* **2003,** *103,* 1685–1758. doi:10.1021/cr010371d
64. Davies, M. J. *Biochem. Biophys. Res. Commun.* **2003,** *305,* 761–770. doi:10.1016/s0006-291x(03)00817-9
65. Kearns, D. R. *Chem. Rev.* **1971,** *71,* 395–427. doi:10.1021/cr60272a004
66. Fridovich, I. *Med. Princ. Pract.* **2013,** *22,* 131–137. doi:10.1159/000339212
67. Clennan, E. L.; Pace, A. *Tetrahedron* **2005,** *61,* 6665–6691. doi:10.1016/j.tet.2005.04.017
68. Saito, I.; Matsuura, T.; Inoue, K. *J. Am. Chem. Soc.* **1983,** *105,* 3200–3206. doi:10.1021/ja00348a040
69. Saito, I.; Matsuura, T.; Inoue, K. *J. Am. Chem. Soc.* **1981,** *103,* 188–190. doi:10.1021/ja00391a035
70. Ghogare, A. A.; Greer, A. *Chem. Rev.* **2016,** *116,* 9994–10034. doi:10.1021/acs.chemrev.5b00726
71. DeRosa, M. C.; Crutchley, R. J. *Coord. Chem. Rev.* **2002,** *233–234,* 351–371. doi:10.1016/s0010-8545(02)00034-6
72. Günther; Schenck, O.; Ziegler, K. *Naturwissenschaften* **1944,** *32,* 157. doi:10.1007/bf01467891
73. Schenck, G. O. *Angew. Chem.* **1952,** *64,* 12–23. doi:10.1002/ange.19520640105
74. Dechy-Cabaret, O.; Benoit-Vical, F.; Loup, C.; Robert, A.; Gornitzka, H.; Bonhoure, A.; Vial, H.; Magnaval, J.-F.; Séguéla, J.-P.; Meunier, B. *Chem. – Eur. J.* **2004,** *10,* 1625–1636. doi:10.1002/chem.200305576
75. Brecht, R.; Haenel, F.; Seitz, G.; Frenzen, G.; Pilz, A.; Massa, W.; Wocadlo, S. *Liebigs Ann./Recl.* **1997,** 851–857. doi:10.1002/jlac.199719970510
76. Brecht, R.; Büttner, F.; Böhm, M.; Seitz, G.; Frenzen, G.; Pilz, A.; Massa, W. *J. Org. Chem.* **2001,** *66,* 2911–2917. doi:10.1021/jo991171t
77. Mihelich, E. D.; Eickhoff, D. J. *J. Org. Chem.* **1983,** *48,* 4135–4137. doi:10.1021/jo00170a060
78. Loponov, K. N.; Lopes, J.; Barlog, M.; Astrova, E. V.; Malkov, A. V.; Lapkin, A. A. *Org. Process Res. Dev.* **2014,** *18,* 1443–1454. doi:10.1021/op500181z
79. Lévesque, F.; Seeberger, P. H. *Angew. Chem., Int. Ed.* **2012,** *51,* 1706–1709. doi:10.1002/anie.201107446
80. Turconi, J.; Griolet, F.; Guevel, R.; Oddon, G.; Villa, R.; Geatti, A.; Hvala, M.; Rossen, K.; Göller, R.; Burgard, A. *Org. Process Res. Dev.* **2014,** *18,* 417–422. doi:10.1021/op4003196
81. Amara, Z.; Bellamy, J. F. B.; Horvath, R.; Miller, S. J.; Beeby, A.; Burgard, A.; Rossen, K.; Poliakoff, M.; George, M. W. *Nat. Chem.* **2015,** *7,* 489–495. doi:10.1038/nchem.2261
82. Triemer, S.; Gilmore, K.; Vu, G. T.; Seeberger, P. H.; Seidel-Morgenstern, A. *Angew. Chem., Int. Ed.* **2018,** *57,* 5525–5528. doi:10.1002/anie.201801424
83. Wang, Y.; Feng, L.; Pang, J.; Li, J.; Huang, N.; Day, G. S.; Cheng, L.; Drake, H. F.; Wang, Y.; Lollar, C.; Qin, J.; Gu, Z.; Lu, T.; Yuan, S.; Zhou, H.-C. *Adv. Sci.* **2019,** *6,* 1802059. doi:10.1002/advs.201802059
84. Feng, L.; Wang, Y.; Yuan, S.; Wang, K.-Y.; Li, J.-L.; Day, G. S.; Qiu, D.; Cheng, L.; Chen, W.-M.; Madrahimov, S. T.; Zhou, H.-C. *ACS Catal.* **2019,** *9,* 5111–5118. doi:10.1021/acscatal.8b04960
85. Roscales, S.; Plumet, J. *Int. J. Carbohydr. Chem.* **2016,** 1–42. doi:10.1155/2016/4760548
86. Salamci, E.; Seçen, H.; Sütbeyaz, Y.; Balci, M. *J. Org. Chem.* **1997,** *62,* 2453–2457. doi:10.1021/jo962092+
87. de Souza, J. M.; Brocksom, T. J.; McQuade, D. T.; de Oliveira, K. T. *J. Org. Chem.* **2018,** *83,* 7574–7585. doi:10.1021/acs.joc.8b01307
88. Lipp, A.; Selt, M.; Ferenc, D.; Schollmeyer, D.; Waldvogel, S. R.; Opatz, T. *Org. Lett.* **2019,** *21,* 1828–1831. doi:10.1021/acs.orglett.9b00419
89. Burchill, L.; George, J. H. *J. Org. Chem.* **2020,** *85,* 2260–2265. doi:10.1021/acs.joc.9b02968
90. Walaszek, D. J.; Jawiczuk, M.; Durka, J.; Drapała, O.; Gryko, D. *Beilstein J. Org. Chem.* **2019,** *15,* 2076–2084. doi:10.3762/bjoc.15.205
91. Lian, M.; Li, Z.; Cai, Y.; Meng, Q.; Gao, Z. *Chem. – Asian J.* **2012,** *7,* 2019–2023. doi:10.1002/asia.201200358
92. Wang, Y.; Zheng, Z.; Lian, M.; Yin, H.; Zhao, J.; Meng, Q.; Gao, Z. *Green Chem.* **2016,** *18,* 5493–5499. doi:10.1039/c6gc01245k
93. Tang, X.-f.; Feng, S.-h.; Wang, Y.-k.; Yang, F.; Zheng, Z.-h.; Zhao, J.-n.; Wu, Y.-f.; Yin, H.; Liu, G.-z.; Meng, Q.-w. *Tetrahedron* **2018,** *74,* 3624–3633. doi:10.1016/j.tet.2018.05.023
94. Mojarrad, A. G.; Zakavi, S. *Catal. Sci. Technol.* **2018,** *8,* 768–781. doi:10.1039/c7cy02308a
95. Jensen, F.; Greer, A.; Clennan, E. L. *J. Am. Chem. Soc.* **1998,** *120,* 4439–4449. doi:10.1021/ja973782d
96. Bonesi, S. M.; Fagnoni, M.; Monti, S.; Albini, A. *Photochem. Photobiol. Sci.* **2004,** *3,* 489. doi:10.1039/b316891c

97. To, W.-P.; Liu, Y.; Lau, T.-C.; Che, C.-M. *Chem. – Eur. J.* **2013,** *19,* 5654–5664. doi:10.1002/chem.201203774
98. Jiang, J.; Luo, R.; Zhou, X.; Chen, Y.; Ji, H. *Adv. Synth. Catal.* **2018,** *360,* 4402–4411. doi:10.1002/adsc.201800730
99. Meng, Y.; Luo, Y.; Shi, J.-L.; Ding, H.; Lang, X.; Chen, W.; Zheng, A.; Sun, J.; Wang, C. *Angew. Chem., Int. Ed.* **2020,** *59,* 3624–3629. doi:10.1002/anie.201913091
100. Young, R. H.; Martin, R. L. *J. Am. Chem. Soc.* **1972,** *94,* 5183–5185. doi:10.1021/ja00770a006
101. Ogryzlo, E. A.; Tang, C. W. *J. Am. Chem. Soc.* **1970,** *92,* 5034–5036. doi:10.1021/ja00720a005
102. Jiang, G.; Chen, J.; Huang, J.-S.; Che, C.-M. *Org. Lett.* **2009,** *11,* 4568–4571. doi:10.1021/ol9018166
103. Chen, R.; Shi, J.-L.; Ma, Y.; Lin, G.; Lang, X.; Wang, C. *Angew. Chem., Int. Ed.* **2019,** *58,* 6430–6434. doi:10.1002/anie.201902543
104. Naito, T. *Chem. Pharm. Bull.* **2008,** *56,* 1367–1383. doi:10.1248/cpb.56.1367
105. Ushakov, D. B.; Gilmore, K.; Kopetzki, D.; McQuade, D. T.; Seeberger, P. H. *Angew. Chem., Int. Ed.* **2014,** *53,* 557–561. doi:10.1002/anie.201307778
106. Cocquet, G.; Rool, P.; Ferroud, C. *J. Chem. Soc., Perkin Trans. 1* **2000,** 2277–2281. doi:10.1039/b001114m
107. Ferroud, C.; Cocquet, G.; Guy, A. *Tetrahedron Lett.* **1999,** *40,* 5005–5008. doi:10.1016/s0040-4039(99)00922-3
108. Rocha, R. O.; Rodrigues, M. O.; Neto, B. A. D. *ACS Omega* **2020,** *5,* 972–979. doi:10.1021/acsomega.9b03684
109. Ushakov, D. B.; Gilmore, K.; Seeberger, P. H. *Chem. Commun.* **2014,** *50,* 12649–12651. doi:10.1039/c4cc04932b

License and Terms

This is an Open Access article under the terms of the Creative Commons Attribution License (http://creativecommons.org/licenses/by/4.0). Please note that the reuse, redistribution and reproduction in particular requires that the authors and source are credited.

The license is subject to the *Beilstein Journal of Organic Chemistry* terms and conditions: (https://www.beilstein-journals.org/bjoc)

The definitive version of this article is the electronic one which can be found at: doi:10.3762/bjoc.16.83

BEILSTEIN JOURNAL OF ORGANIC CHEMISTRY

Accelerating fragment-based library generation by coupling high-performance photoreactors with benchtop analysis

Quentin Lefebvre*, Christophe Salomé and Thomas C. Fessard

Full Research Paper

Open Access

Address:
SpiroChem AG, Rosental area, WRO-1047-3, Mattenstrasse 24, 4058 Basel, Switzerland

Email:
Quentin Lefebvre* - quentin.lefebvre@spirochem.com

* Corresponding author

Keywords:
benchtop analytics; fragment-based library; heterocyclic sp^2–sp^3 fragments; *N*-arylation; photoredox-nickel dual catalysis

Beilstein J. Org. Chem. **2020,** *16,* 982–988.
doi:10.3762/bjoc.16.87

Received: 27 February 2020
Accepted: 27 April 2020
Published: 12 May 2020

This article is part of the thematic issue "Advances in photoredox catalysis".

Guest Editor: T. Noël

© 2020 Lefebvre et al.; licensee Beilstein-Institut.
License and terms: see end of document.

Abstract

Herein we report a workflow coupling photoredox-nickel dual-catalyzed *N*-arylation reactions to benchtop analysis for the efficient generation of fragment-based libraries. Technological advances in photoreactor design facilitated reliable and reproducible experimentation. Knowledge on the reactivity under previously reported reaction conditions of spirocyclic and strained heterocyclic building blocks, viewed as chemistry informers, could thus be rapidly accessed, identifying privileged or challenging scaffolds and paving the way for further exploration.

Introduction

Heterocyclic sp^2–sp^3 fragments are sought-after in fragment-based libraries, as they offer improved pharmacokinetic properties over more classical, "flat" scaffolds [1]. Specifically, bicyclo- and spiroalkanes are sp^3-rich (more 3D-like), conformationally-restricted and strained building blocks that are underrepresented in screening collections. These are of high value to medicinal chemists to provide defined exit vectors and facilitate rational lead evolution [2-7]. Thus, we were interested in developing reliable synthetic methods and technologies to apply metal-catalyzed cross-coupling reactions to such scaffolds, which often exhibit different reactivity from unstrained substrates [8]. *N*-Arylation of spirocyclic amines would be a very efficient strategy for the modular synthesis of heterocyclic sp^2–sp^3 fragments, but their lack of stability to strongly basic conditions and heating might be an issue in palladium-catalyzed cross-coupling reactions [9]. Recently, milder cross-coupling methods using more abundant and affordable metals such as nickel, in combination with photochemistry or electrochemistry, significantly improved accessibility to *N*-arylated complex amines [10-12].

Results and Discussion

As we initiated a high-throughput program of fragment-based library generation and after shortcomings using more classical

cross-coupling conditions, we turned our attention to the photoredox-nickel dual-catalysis strategy recently reported by MacMillan and Buchwald [10]. The reported conditions use lower temperatures and a mild base. Inspired by work at Merck on chemical informers, we decided to exploit our library of spirocyclic amines and strained scaffolds to generate a focused list of potential products [13]. We wanted to perform parallel reactions on small scale to gain further knowledge on the reactivity of these building blocks for future applications. Reaction times had to be short, and analysis, work-up and purification had to be streamlined. To comply with these project specifications, and because of the relative high cost of starting amines, the reported conditions of dual-catalyzed *N*-arylation were slightly altered: a smaller excess of amine was used, and dimethyl sulfoxide (DMSO) was chosen as solvent instead of dimethylformamide (DMF) or dimethylacetamide (DMA) to improve work-up and purification. The workflow was devised to ensure maximal productivity, using parallel experimentation coupled to benchtop analysis tools, namely thin-layer chromatography–mass spectrometry (TLC–MS, purchased from https://www.advion.com/rsc-product-note/direct-mass-analysis-of-tlc-plates/) and low-field nuclear magnetic resonance (NMR, purchased from https://www.nanalysis.com/) analysis (Scheme 1).

To ensure reproducibility of the reactions, we used a custom-made, high intensity photoreactor which enables accurate control of irradiation and heat [14,15]. Indeed, homogeneous irradiation and temperature in screening decreases the risk of false negatives triggered by high variability of reaction conditions compared to a single vial reactor. Active water cooling protects the LEDs from overheating, while additional air cooling with bespoke fans prevents the vessels to heat over 50 °C. Each vessel is placed at equal distance of a 35 W high power blue LED (Figure 1).

Reaction monitoring by TLC–MS enabled rapid and precise assessment of the success of each parallel reaction. As seen in Figure 2, a single TLC plate reporting five different reactions could be analyzed in five minutes, and the identity of the major product confirmed by mass.

Finally, after work-up and automated purification, a preliminary quality control (QC) could be performed using a benchtop 60 MHz NMR machine (Figure 3). Structural information was obtained to corroborate mass spectrometry data, an important information when dealing with strained bicycles or spirocycles, which could be prone to skeletal rearrangement. If diagnostic peaks of solvent impurities coming from the column eluents were observed, the purified material was dried further. Thus, costly and time-consuming measurements using a high-field NMR machine could be avoided: Only the final QC was performed on a 400 MHz NMR machine.

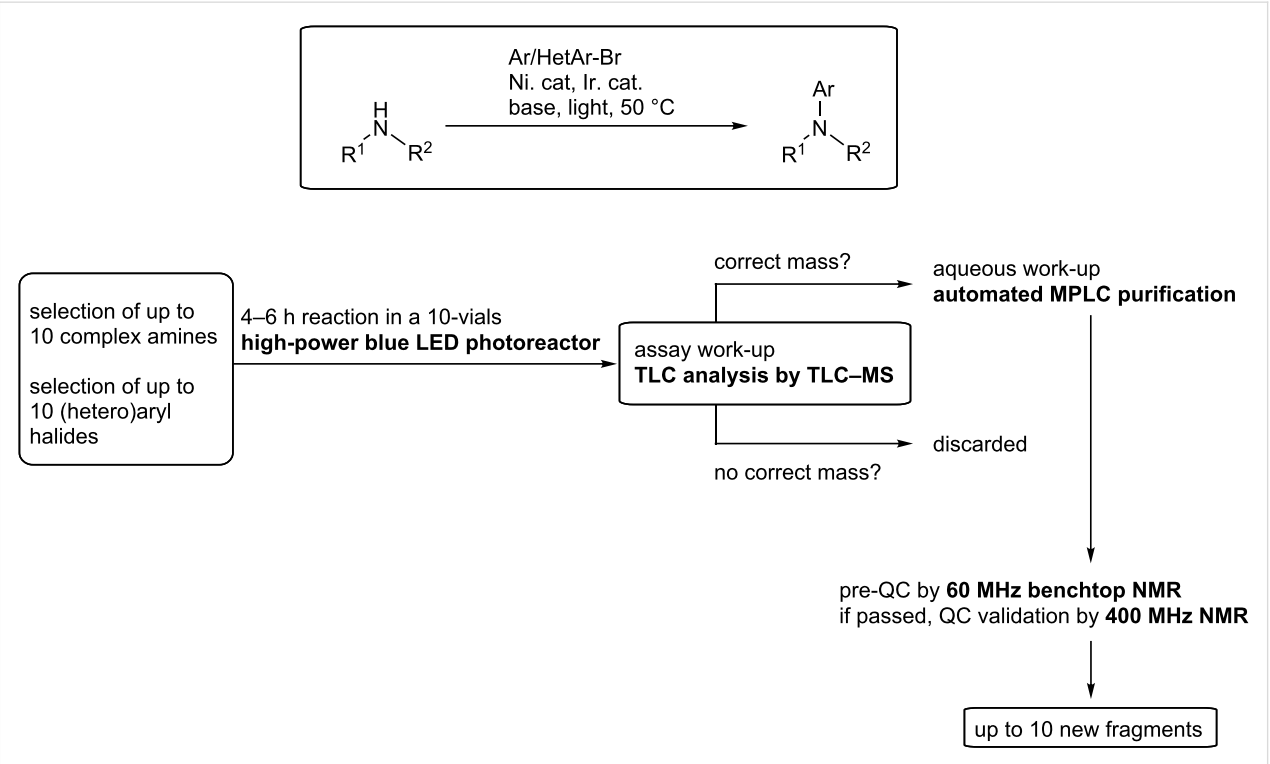

Scheme 1: One-day workflow for fragment-based library generation. QC: Quality control. MPLC: Medium-pressure liquid chromatography.

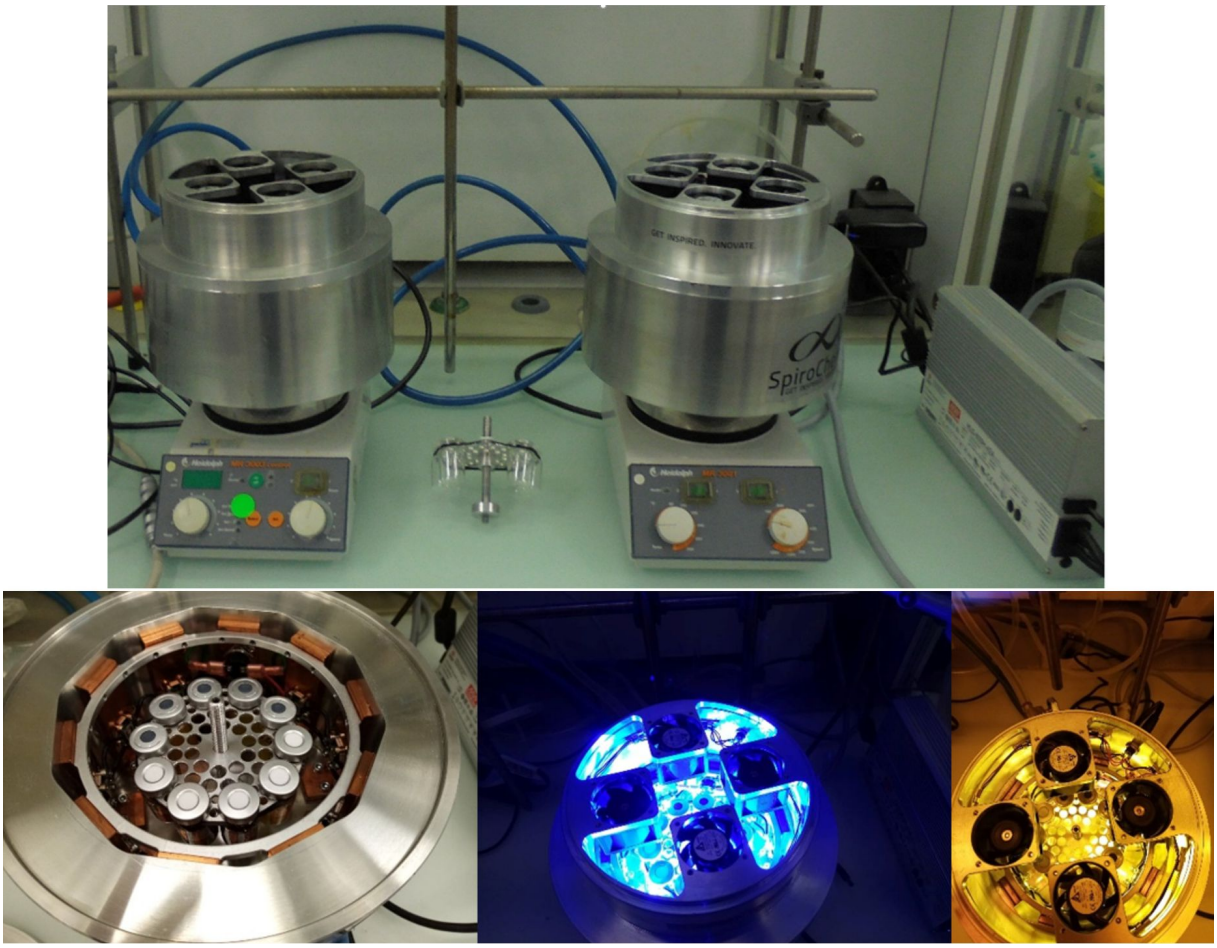

Figure 1: Top: high-power blue LED photoreactors. Bottom, from left to right: photoreactor OFF, ON, and ON through protective yellow filter.

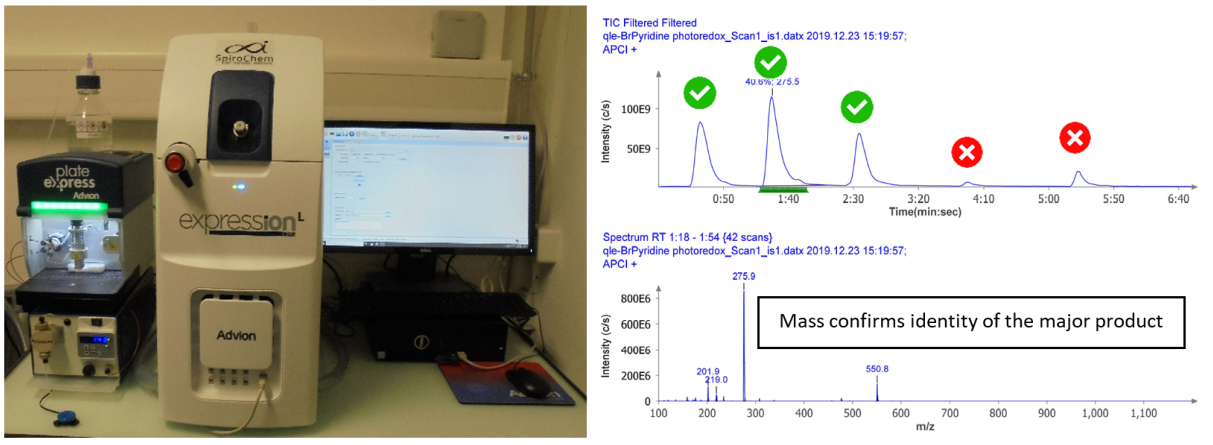

Figure 2: TLC–MS equipment: analysis of 5 reactions in 5 minutes.

In 4 days of experimentation, 29 combinations of bicycloalkylamines or spirocyclic amines with (hetero)aryl bromides were probed using this workflow, and the results are depicted in Scheme 2 and Scheme 3. To provide attractive heterocyclic sp^2–sp^3 fragments, we mainly focused on coupling 3-bromopyridine to five different classes of complex amines: bicy-

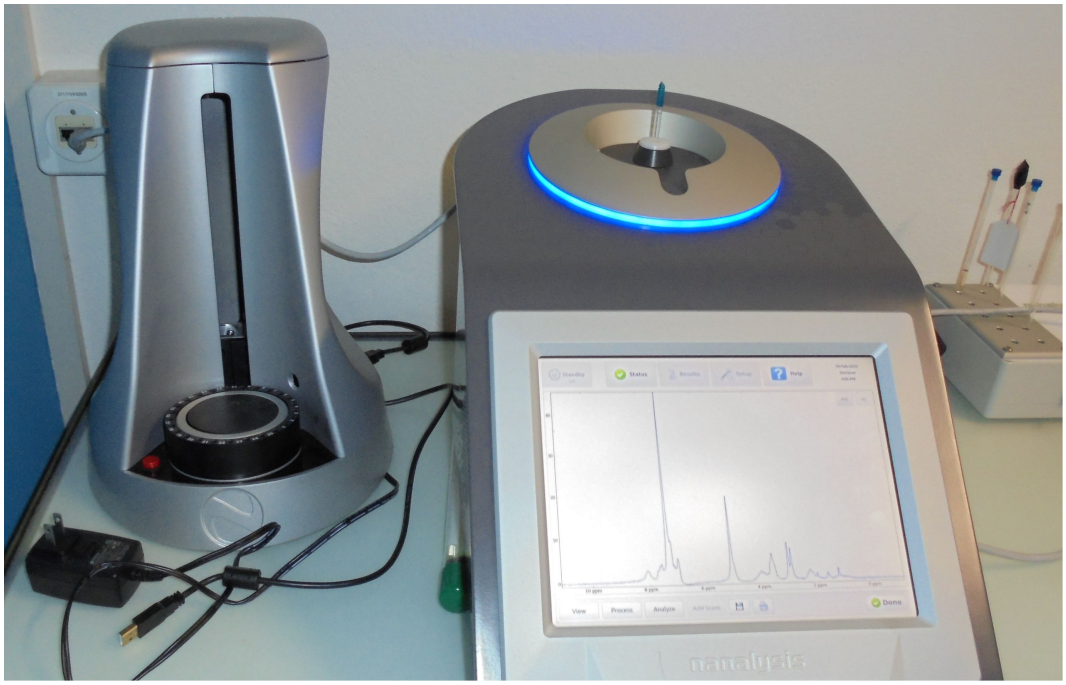

Figure 3: Pre-QC validation by 60 MHz benchtop NMR.

clopentanamines, azetidines, spiroazetidines, spiropyrrolidines and spiropiperidines. Functional group tolerance was probed by using functionalized building blocks bearing esters, carbamates, alcohols, tertiary amines, ethers, sulfones and fluorine atoms (Scheme 2 and Scheme 3).

Out of the 15 reactions showing product formation by TLC–MS, 7 gave the product in sufficient purity after one round of purification, while 8 were contaminated with solvent impurities, or obtained in too low yields for appropriate NMR analysis. Fourteen did not give the expected product, often showing low consumption of the aryl bromide. This corresponds to a success rate of 24% for product purification and isolation, and 52% for product formation. Although our focused library is not as functional-group-dense as the chemistry informer library used by Merck, these results are in line with previous findings on C–N cross-coupling conditions. In these works, nickel-photoredox-catalyzed cross-couplings were the most successful with success rates up to 50% [10]. This was an improvement from non-photocatalyzed conditions, where success rates of 11–33% were observed for palladium-catalyzed cross-coupling reactions, and ranged from 6% to 50% for copper-catalyzed cross-coupling reactions [13].

Much information could be obtained from this screening. Electron-deficient aryl bromides led to better yields than neutral and electron-rich partners, as observed in previous reports on photochemically- or electrochemically-mediated nickel-catalyzed cross-couplings. Electron-deficient aniline products are less prone to oxidative decomposition. BCP-amines were viable coupling partners but gave the corresponding products **1a–e** in poor purities. Simple azetidines partook the reaction to give **2a–c** while azaspiro[3,3]heptane analogues were unreactive. The higher reactivity of azaspiro[3,4]octane example **3d** highlights the distinct reactivity of azaspiro[3,3]heptanes. On one hand, a rationalization of this observation could be traced back to the first step of the catalytic cycle. Reduction of the nickel(II) pre-catalyst to nickel(0) is believed to occur by β-hydride elimination on a sacrificial amount of amine [10]. The strained character of azaspiro[3,3]heptane might prevent this event. On the other hand, pyramidalization at nitrogen is much more important in azetidines [16-18]. This might lower the oxidation potential of the arylated product and promote oxidative decomposition. Several spirocyclic compounds with larger ring sizes could be coupled to 3-bromopyridine to give products **4c**, **4d, 5a** and **5b**, provided that steric hindrance was not too high (see **5c**). Surprisingly, oxetanes appear to be incompatible with the reaction conditions (see **4a**, **4f**, **5d** and **5f**), despite a successful report on their decarboxylative arylation under nickel-photoredox-catalyzed conditions [19]. As this report and MacMillan's report use more basic, but less nucleophilic bases than DABCO, namely Barton's base and MTBE, the issue might come from ring opening [20,21].

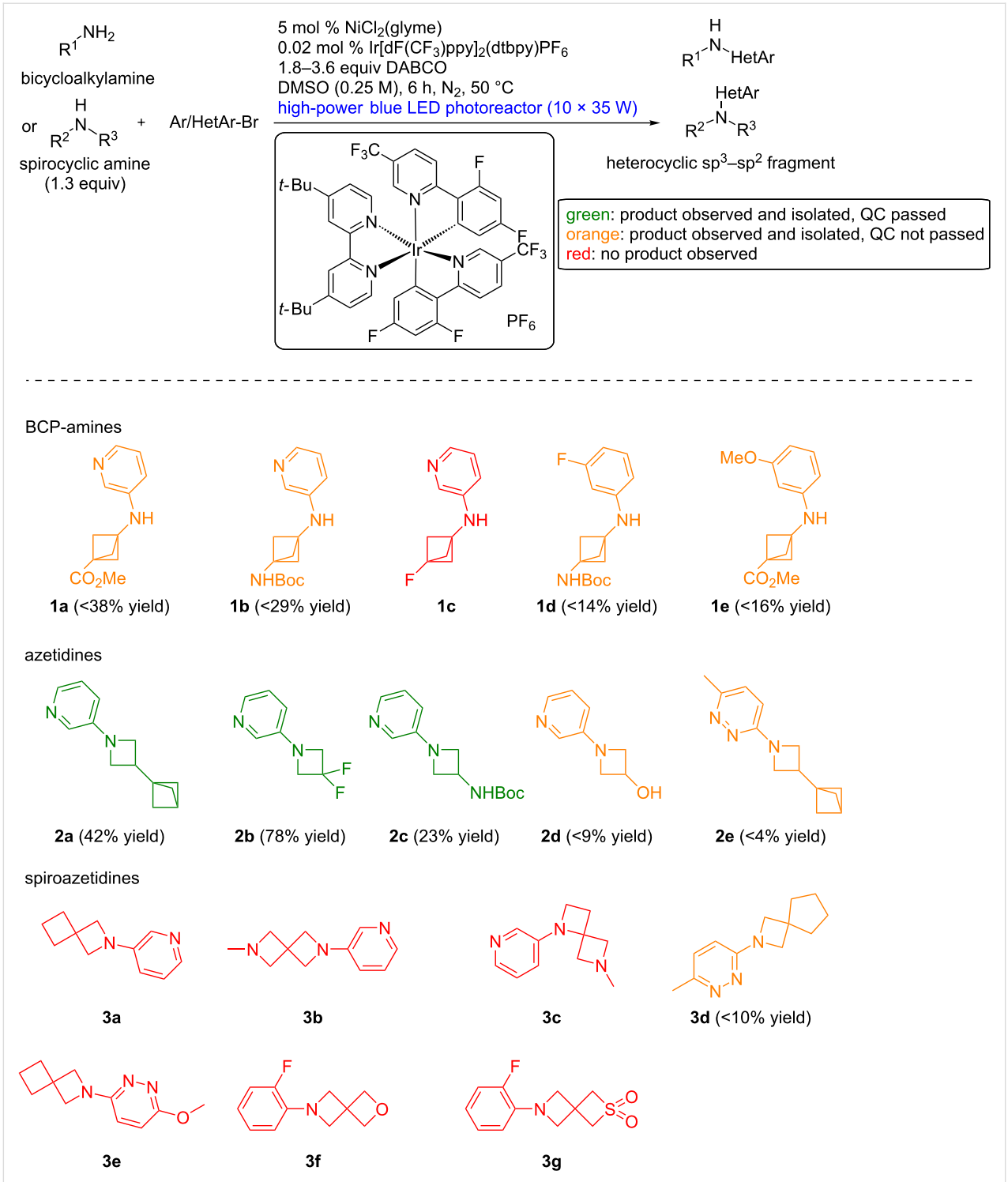

Scheme 2: Scope of the fragment-based library generation: BCP-amines and azetidines. See Supporting Information File 1 for experimental details.

Conclusion

In summary, we have developed a new workflow allowing to efficiently perform photoredox-nickel dual-catalyzed reactions in parallel for fragment-based library generation. We have screened 29 combinations of complex spirocyclic amines and (hetero)aryl halides to get an insight into the specific reactivity of these building blocks. The workflow combined a powerful photoreactor with precise and reproducible conditions control with benchtop analytical tools such as TLC–MS and low-field NMR. This enabled the identifica-

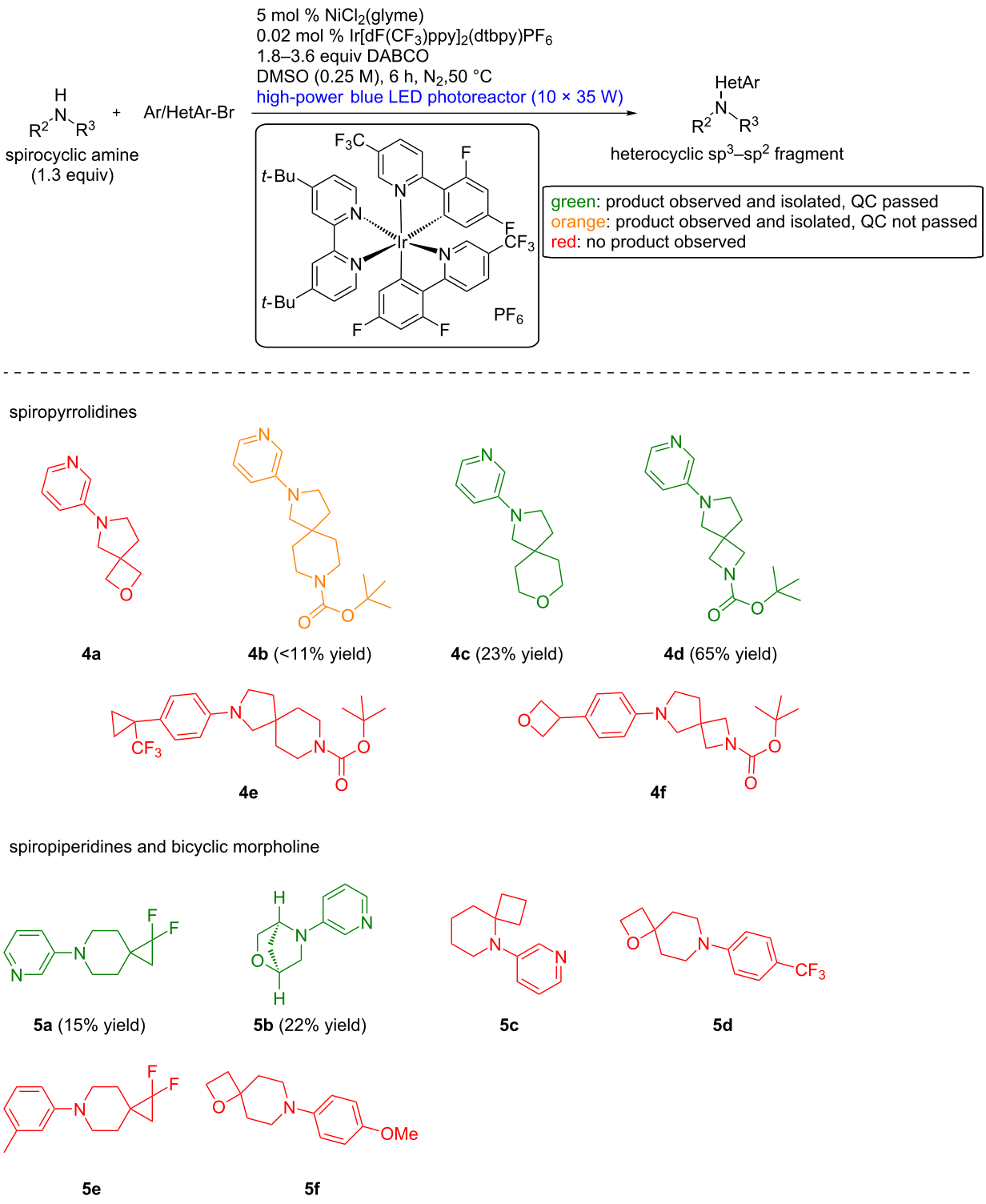

Scheme 3: Scope of the fragment-based library generation: pyrrolidines, piperidines and morpholines. See Supporting Information File 1 for experimental details.

tion of privileged spirocyclic scaffolds compatible with this chemistry, and challenging substrates requiring additional investigations. The knowledge obtained within this four-day experimentation period could be built-upon in-house and allowed the efficient synthesis of original heterocyclic sp^2–sp^3 fragments.

Supporting Information

Supporting Information File 1

Experimental part.
[https://www.beilstein-journals.org/bjoc/content/supplementary/1860-5397-16-87-S1.pdf]

Acknowledgements

Aurélien Kauffer is acknowledged for his help with scope investigation, and Benson Jelier is acknowledged for this photoreactor design.

Confilct of Interest

The authors declare a conflict of interest as they are employees and CEO of SpiroChem AG, a Swiss fine chemicals company commercializing the building blocks and fragments described in this work.

ORCID® iDs

Quentin Lefebvre - https://orcid.org/0000-0003-0307-1966
Christophe Salomé - https://orcid.org/0000-0001-9668-8134

References

1. Lovering, F.; Bikker, J.; Humblet, C. *J. Med. Chem.* **2009,** *52,* 6752–6756. doi:10.1021/jm901241e
2. Carreira, E. M.; Fessard, T. C. *Chem. Rev.* **2014,** *114,* 8257–8322. doi:10.1021/cr500127b
3. Guérot, C.; Tchitchanov, B. H.; Knust, H.; Carreira, E. M. *Org. Lett.* **2011,** *13,* 780–783. doi:10.1021/ol103050c
4. Burkhard, J. A.; Guérot, C.; Knust, H.; Rogers-Evans, M.; Carreira, E. M. *Org. Lett.* **2010,** *12,* 1944–1947. doi:10.1021/ol1003302
5. Burkhard, J. A.; Wagner, B.; Fischer, H.; Schuler, F.; Müller, K.; Carreira, E. M. *Angew. Chem., Int. Ed.* **2010,** *49,* 3524–3527. doi:10.1002/anie.200907108
6. Li, D. B.; Rogers-Evans, M.; Carreira, E. M. *Org. Lett.* **2011,** *13,* 6134–6136. doi:10.1021/ol2025313
7. Li, D. B.; Rogers-Evans, M.; Carreira, E. M. *Org. Lett.* **2013,** *15,* 4766–4769. doi:10.1021/ol402127b
8. Bollenbach, M.; Lecroq, W.; Wagner, P.; Fessard, T.; Schmitt, M.; Salomé, C. *Chem. Commun.* **2019,** *55,* 1623–1626. doi:10.1039/c8cc09110b
9. Burkhard, J.; Carreira, E. M. *Org. Lett.* **2008,** *10,* 3525–3526. doi:10.1021/ol801293f
10. Corcoran, E. B.; Pirnot, M. T.; Lin, S.; Dreher, S. D.; DiRocco, D. A.; Davies, I. W.; Buchwald, S. L.; MacMillan, D. W. C. *Science* **2016,** *353,* 279–283. doi:10.1126/science.aag0209
11. Li, C.; Kawamata, Y.; Nakamura, H.; Vantourout, J. C.; Liu, Z.; Hou, Q.; Bao, D.; Starr, J. T.; Chen, J.; Yan, M.; Baran, P. S. *Angew. Chem., Int. Ed.* **2017,** *56,* 13088–13093. doi:10.1002/anie.201707906
12. Lim, C.-H.; Kudisch, M.; Liu, B.; Miyake, G. M. *J. Am. Chem. Soc.* **2018,** *140,* 7667–7673. doi:10.1021/jacs.8b03744
13. Kutchukian, P. S.; Dropinski, J. F.; Dykstra, K. D.; Li, B.; DiRocco, D. A.; Streckfuss, E. C.; Campeau, L.-C.; Cernak, T.; Vachal, P.; Davies, I. W.; Krska, S. W.; Dreher, S. D. *Chem. Sci.* **2016,** *7,* 2604–2613. doi:10.1039/c5sc04751j
14. Jelier, B. J.; Tripet, P. F.; Pietrasiak, E.; Franzoni, I.; Jeschke, G.; Togni, A. *Angew. Chem., Int. Ed.* **2018,** *57,* 13784–13789. doi:10.1002/anie.201806296
15. Rössler, S. L.; Jelier, B. J.; Tripet, P. F.; Shemet, A.; Jeschke, G.; Togni, A.; Carreira, E. M. *Angew. Chem., Int. Ed.* **2019,** *58,* 526–531. doi:10.1002/anie.201810261
16. Revilla-López, G.; Warren, J. G.; Torras, J.; Jiménez, A. I.; Cativiela, C.; Alemán, C. *Biopolymers* **2012,** *98,* 98–110. doi:10.1002/bip.21716
17. Schnitzer, T.; Möhler, J. S.; Wennemers, H. *Chem. Sci.* **2020,** *11,* 1943–1947. doi:10.1039/c9sc05410c
18. Grimm, J. B.; English, B. P.; Chen, J.; Slaughter, J. P.; Zhang, Z.; Revyakin, A.; Patel, R.; Macklin, J. J.; Normanno, D.; Singer, R. H.; Lionnet, T.; Lavis, L. D. *Nat. Methods* **2015,** *12,* 244–250. doi:10.1038/nmeth.3256
19. Kolahdouzan, K.; Khalaf, R.; Grandner, J. M.; Chen, Y.; Terrett, J. A.; Huestis, M. P. *ACS Catal.* **2020,** *10,* 405–411. doi:10.1021/acscatal.9b03596
20. Baidya, M.; Mayr, H. *Chem. Commun.* **2008,** 1792–1794. doi:10.1039/b801811a
21. Maji, B.; Stephenson, D. S.; Mayr, H. *ChemCatChem* **2012,** *4,* 993–999. doi:10.1002/cctc.201200143

License and Terms

This is an Open Access article under the terms of the Creative Commons Attribution License (http://creativecommons.org/licenses/by/4.0). Please note that the reuse, redistribution and reproduction in particular requires that the authors and source are credited.

The license is subject to the *Beilstein Journal of Organic Chemistry* terms and conditions: (https://www.beilstein-journals.org/bjoc)

The definitive version of this article is the electronic one which can be found at:
doi:10.3762/bjoc.16.87

BEILSTEIN JOURNAL OF ORGANIC CHEMISTRY

Photocatalysis with organic dyes: facile access to reactive intermediates for synthesis

Stephanie G. E. Amos‡, Marion Garreau‡, Luca Buzzetti‡ and Jerome Waser*

Review

Open Access

Address:
Laboratory of Catalysis and Organic Synthesis, Ecole Polytechnique Fédérale de Lausanne, EPFL, SB ISIC LCSO, BCH 4306 1015 Lausanne, Switzerland

Email:
Jerome Waser* - jerome.waser@epfl.ch

* Corresponding author ‡ Equal contributors

Keywords:
organic dyes; photocatalysis; photoredox catalysis; radicals; reactive intermediates

Beilstein J. Org. Chem. **2020,** *16,* 1163–1187.
doi:10.3762/bjoc.16.103

Received: 21 March 2020
Accepted: 11 May 2020
Published: 29 May 2020

This article is part of the thematic issue "Advances in photoredox catalysis".

Guest Editor: T. Noël

© 2020 Amos et al.; licensee Beilstein-Institut.
License and terms: see end of document.

Abstract

Organic dyes have emerged as a reliable class of photoredox catalysts. Their great structural variety combined with the easy fine-tuning of their electronic properties has unlocked new possibilities for the generation of reactive intermediates. In this review, we provide an overview of the available approaches to access reactive intermediates that employ organophotocatalysis. Our contribution is not a comprehensive description of the work in the area but rather focuses on key concepts, accompanied by a few selected illustrative examples. The review is organized along the type of reactive intermediates formed in the reaction, including C(sp^3) and C(sp^2) carbon-, nitrogen-, oxygen-, and sulfur-centered radicals, open-shell charged species, and sensitized organic compounds.

Review

Introduction

In the last decade, synthetic organic chemistry has experienced the renaissance of photocatalysis. Since the early seminal reports [1-4], inspired by pioneering works in photochemistry [5-7], this field has attracted increasing attention, and organic chemists have developed a wide variety of photocatalytic reactions [8-11]. One of the reasons for this rapid growth resides in the availability of visible light-absorbing transition metal complexes. These catalysts can harvest the energy of visible-light photons and transfer it to organic molecules, giving access to key reactive intermediates. For instance, ruthenium and iridium polypyridyl complexes played a central role in the rapid expansion of photocatalytic methods [12]. These catalysts typically absorb light in the blue region and promote different activation modes, including photoinduced electron transfer (PET) and energy transfer (EnT), which respectively lead to the formation of open-shell and electronically excited species. These reactive intermediates are then used to forge new chemical bonds or to induce structural modifications within the organic substrates. The versatility of these metal complexes is due to their wide operational redox windows, which allows them to interact via their excited states with different classes of molecules. However, the relatively high cost of these photocatalysts, their toxicity,

and the limited abundance of the coordinating transition metals can hamper their applicability [13]. For these reasons, the quest for cheaper, more sustainable, and environmentally benign photocatalysts is of high importance, and organic dyes represent a powerful platform for pursuing this goal.

The ability of organic dyes to absorb light and promote transformations is known since the early stage of photochemistry, and they represent attractive alternatives to the established transition metal-based photocatalysts [14-18]. In addition to their ready availability and low cost, these molecules are often biocompatible, and they can be easily functionalized in order to modulate their spectroscopical and redox features.

In the last years, several classes of organic dyes, such as acridiniums (**OD1**–**4**), cyanoarenes (**OD5**–**8**), diaryl ketones (**OD9**/**10**), flavins (**OD11**/**12**), xanthenes (**OD13**–**15**), thiazines (**OD16**/**17**) and various other dyes, such as **OD18**–**21**, have been exploited (Figure 1), and the field of organic photocatalysis has been extensively covered by various reviews [16,19-25]. Most of these reports are organized according to the structural features of the dye and/or their applications in synthetic chemistry. In contrast, this review will focus on the different possible conceptual approaches based on organic photocatalysts for the generation of reactive intermediates. After a short introduction on activation modes in photocatalysis, selected case studies where organic dyes have been exploited for generating carbon-centered radicals, charged open-shell species, and heteroatom-centered radicals will be covered. The last short section will be devoted to activated organic substrates generated by energy transfer. C(sp) radicals will not be discussed. To the best of our knowledge, no report on an organophotocatalyzed generation of a C(sp) species has been disclosed yet. Each presented approach will be accompanied by one selected example, which we found particularly illustrative. This report is therefore in no means comprehensive, and readers searching to gain deeper insight into photocatalytic processes and/or for an exhaustive coverage of applications should refer to more complete specialized reviews and books [26-30]. We hope this report can motivate general synthetic chemists to consider photocatalytic approaches mediated by organic dyes as valuable tools for accessing important reactive intermediates and guide them in the first choice of a catalyst and a method.

Activation modes in photocatalysis

Electronically excited photocatalysts interact with organic molecules via three main pathways: electron transfer (ET), EnT, and atom transfer (AT).

In the first case (Scheme 1, box 1), the excited photocatalyst (**PC***) undergoes a single-electron transfer (SET) with a suitable electron acceptor **A** or electron donor **D**. In an oxidative quenching cycle, **PC*** acts as a reductant donating an electron to **A**. This generates the oxidized form of the photocatalyst, $\mathbf{PC}^{\bullet+}$, and a reduced acceptor, $\mathbf{A}^{\bullet-}$. Alternatively, in a reductive quenching cycle, **PC*** acts as an oxidant promoting an SET oxidation of the electron donor **D**. This leads to the reduced photocatalyst $\mathbf{PC}^{\bullet-}$ and the oxidized donor $\mathbf{D}^{\bullet+}$. Following this initial SET, a second electron transfer must occur to ensure the catalyst turnover and restore the ground state photocatalyst: $\mathbf{PC}^{\bullet+}$ needs to be reduced by an electron donor **D**, whereas $\mathbf{PC}^{\bullet-}$ needs to undergo an oxidation by an electron acceptor **A**. In each of these steps, the role of **A** or **D** is assumed by a redox-active agent, either the substrate, a sacrificial electron donor/acceptor, or a reactive intermediate. This approach, usually named photoredox catalysis, has known a remarkable growth in the last decade and has given access to both neutral and charged radical species. The thermodynamic feasibility of these SETs is related to the redox potentials of the species involved. The values of the redox potentials discussed in this review are generally taken from the original publications described in the corresponding paragraphs.

In the second case (Scheme 1, box 2), the excited photocatalyst can engage in an EnT mechanism. Upon the excitation and intersystem crossing, the triplet state photocatalyst ^{3}**PC*** can interact directly with a ground state species **Sub** and transfer the triplet energy to generate an excited state **Sub*** and the ground state **PC**. In most cases, **Sub*** is in the triplet state if it is an organic molecule. A common exception to this is molecular oxygen, which upon excitation attains a more reactive singlet state.

In the third mode of activation, atom transfer (AT, Scheme 1, box 3), the excited state photocatalyst **PC*** can abstract an atom, typically hydrogen, from a suitable substrate **Sub-X**, leading to the direct formation of an open-shell species, $\mathbf{Sub}^{\bullet}$. In this case, the catalytic cycle is closed by a subsequent atom transfer that restores the ground state photocatalyst **PC**.

C(sp^3) radicals

Carbon-centered sp^3 carbon (C(sp^3)) radicals are important reactive intermediates for the construction of C–C and C–heteroatom bonds [31]. Their addition onto unsaturated systems, such as olefins and arenes, is particularly efficient. Additionally, alkyl radicals can undergo translocations, abstracting atoms from different sites. Recently, the ability of transition metal complexes to intercept alkyl radicals has been exploited for expanding the possibility of C–C bond formation reactions to cross-couplings. In all of these transformations, the substituents on the alkyl radical determine if it reacts as a nucleophile or an electrophile [32].

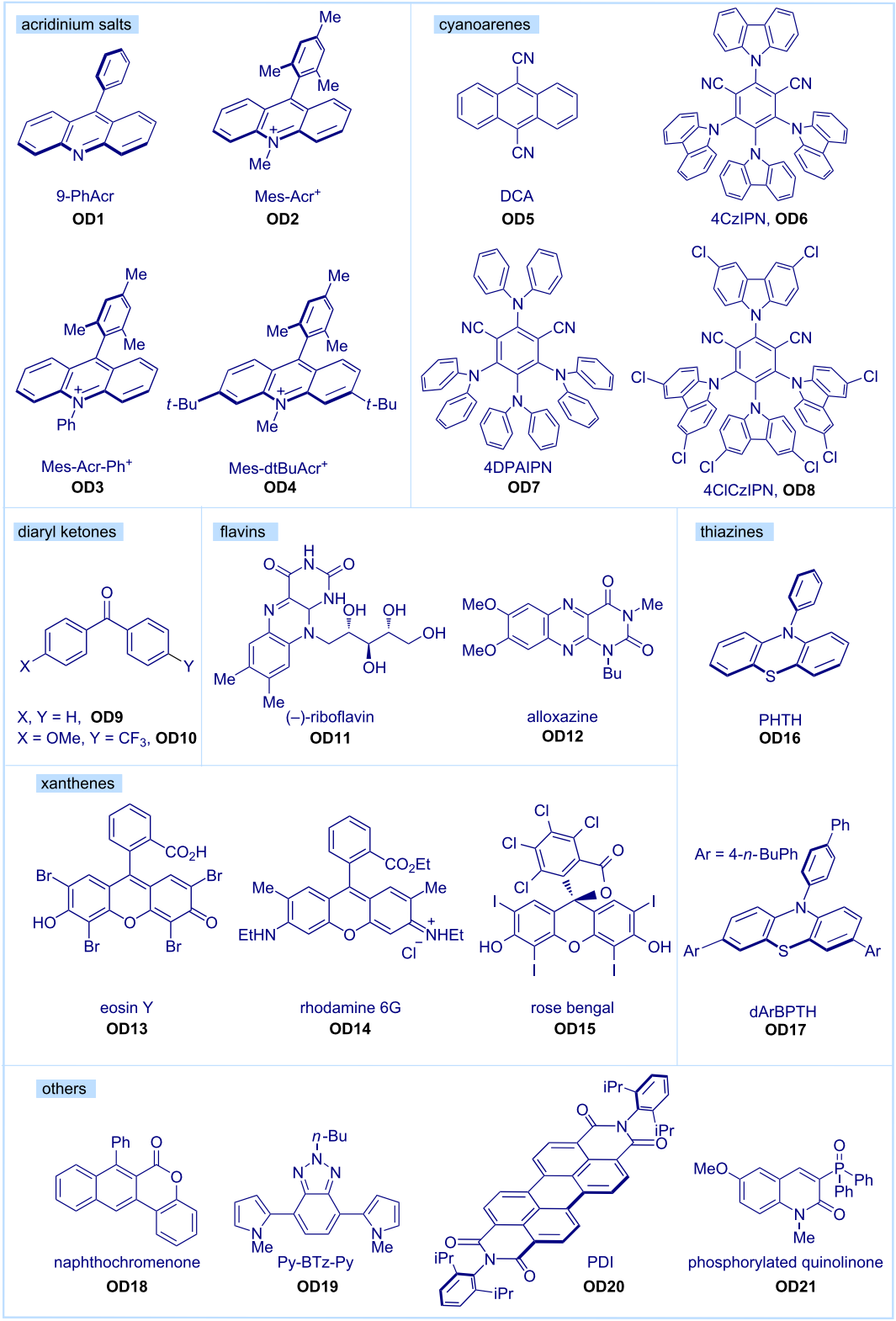

Figure 1: Selected examples of organic dyes. Mes-Acr$^+$: 9-mesityl-10-methylacridinium, DCA: 9,10-dicyanoanthracene, 4CzIPN: 1,2,3,5-tetrakis(carbazol-9-yl)-4,6-dicyanobenzene, 4DPAIPN: 1,3-dicyano-2,4,5,6-tetrakis(*N*,*N*-diphenylamino)benzene, PHTH: 10-phenylphenothiazine, dArBPTH: 10-([1,1'-biphenyl]-4-yl)-3,7-bis(4-butylphenyl)-10*H*-phenothiazine, Py-BTz-Py: butyl-4,7-bis(1-methyl-1*H*-pyrrol-2-yl)-2*H*-benzo[*d*][1,2,3]triazole, PDI: *N*,*N*-bis(2,6-diisopropylphenyl)perylene-3,4,9,10-bis(dicarboximide).

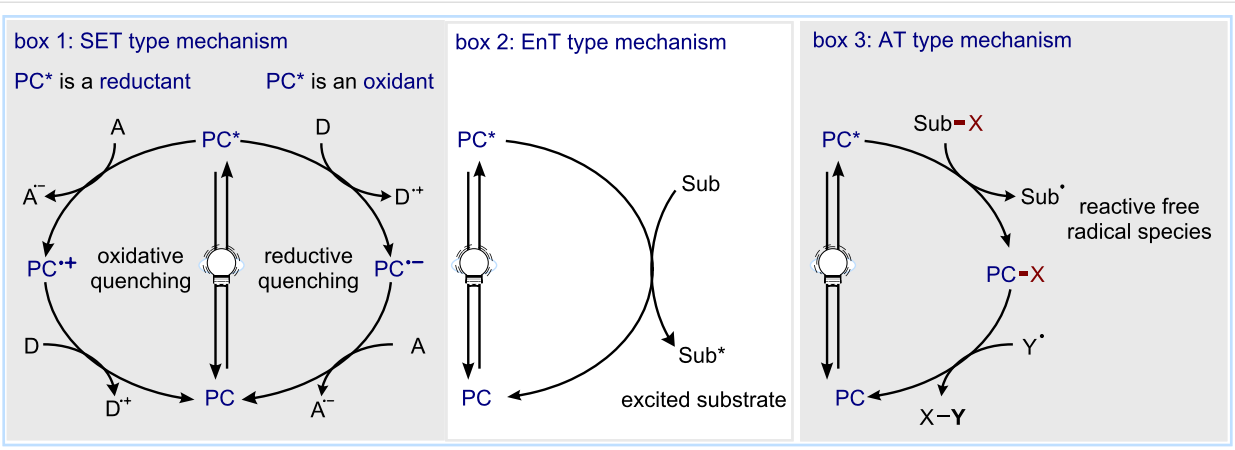

Scheme 1: Activation modes in photocatalysis.

Recently, photoredox catalysis has emerged as a powerful tool to access C(sp^3) radicals, and organic dyes (ODs) have been demonstrated to act as competent photocatalysts for these light-mediated reactions. The main strategies used include decarboxylations from carboxylic acid derivatives (CO_2X), such as carboxylates or RAEs (Redox Active Esters), oxidative fragmentations, and reductive fragmentations of various redox-active groups (X) as well as hydrogen atom abstractions (Scheme 2).

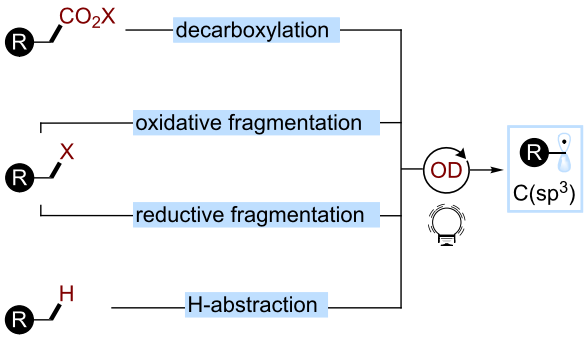

Scheme 2: Main strategies for the formation of C(sp^3) radicals used in organophotocatalysis.

Decarboxylation

Carboxylic acids are naturally abundant functionalities that provide an easy access to C(sp^3) radicals. Since the dawn of organic chemistry, several radical decarboxylations have been developed, including the Kolbe electrolysis [33,34], the Hunsdiecker reaction [35], and the Barton decarboxylation [36-38]. More recently, photoredox catalysis has appeared as a mild alternative to these venerable transformations [39,40], allowing the smooth generation of alkyl radicals from carboxylic acid derivatives. One of the main strategies for accessing C(sp^3) radicals from carboxylic acids relies on the oxidation of the CO_2H group. However, the high oxidation potential of these species makes them difficult to be directly activated by the excited state photocatalyst. For these reasons, the photocatalyzed decarboxylation often proceeds on the corresponding carboxylates, which are easier to be oxidized. This photoinduced SET, followed by the loss of CO_2 as the sole byproduct, gives access to the desired C(sp^3) radicals. Organic dyes are competent photocatalysts for these transformations, with many reports having appeared in the last five years.

For example, Nicewicz developed a photocatalytic hydrodecarboxylation of primary, secondary, and tertiary carboxylic acids in 2015 (Scheme 3) [41]. The use of the strong oxidant Mes-Acr-Ph$^+$ (**OD3**, $E(PC^{+}*/PC) \approx 2$ V) as organic photocatalyst leads to the oxidation/decarboxylation of the in situ-generated carboxylates ($E_{ox} \approx 1.3$ V). An organic disulfide cocatalyst, $(PhS)_2$, activated by the reduced photocatalyst, was found to act as a co-base (PhS^-) and a hydrogen atom source (PhSH). The reaction allows the direct conversion of carboxylic acids, e.g.,

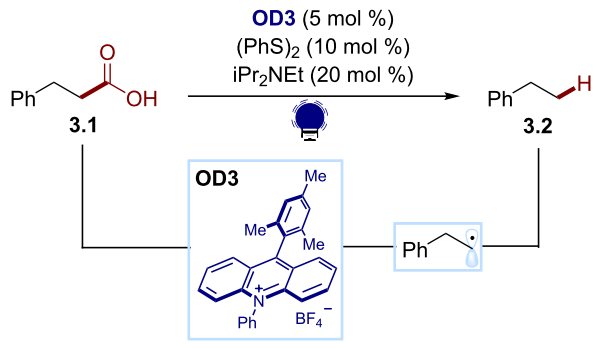

Scheme 3: Illustrative example for the photocatalytic oxidative generation of radicals from carboxylic acids: the hydrodecarboxylation reported by Nicewicz and co-workers [41].

3.1 to the corresponding alkanes, e.g., **3.2**. The scope includes carboxylic acids that were previously recalcitrant to other oxidative photocatalytic decarboxylations due to their high oxidation potential.

Other organic dyes, including several acridinium salts, have been successfully applied in organophotocatalytic decarboxylation protocols. For example, rhodamine 6G (**OD14**, $E(PC^{+}*/PC) \approx 1.2$ V) [42] was used for the photocatalytic decarboxylative azidation of cyclic amino acids and rose bengal (**OD15**) [43] for a decarboxylative amination of indoline-2-carboxylic acids with azodicarboxylate esters.

Another photocatalytic strategy for accessing C(sp^3) radicals from carboxylic acids proceeds through a reductive decarboxylation pathway. This approach relies on the conversion of the acid into an easy reducible moiety, such as a redox-active ester (RAE). These species can accept one electron from the photocatalyst, and the ensuing reduced species releases the corresponding C(sp^3) radical after a fragmentation and CO_2 loss. This approach represents an alternative to oxidative decarboxylations, allowing the design of a photocatalytic cycle based on the SET reduction of the substrate. Furthermore, the relatively low reduction potential of these species ($E_{red} \approx -1.1$ V for *N*-acetoxyphthalimide) [44] brings them into the operational range of various organic dyes, allowing mild reaction conditions.

König reported a visible light-promoted photochemical reductive decarboxylation/alkylation of carboxylic acid analogs (Scheme 4) [45]. In this protocol, the carboxylic acids are converted into the corresponding RAE **4.1** by a condensation with *N*-hydroxyphthalimide. The organic dye eosin Y (**OD13**, $E(PC/PC^{-}) \approx -1.1$ V), in the presence of the sacrificial electron donor DIPEA, can reduce these species under green light irradiation. The ensuing decarboxylation provides a C(sp^3) radical,

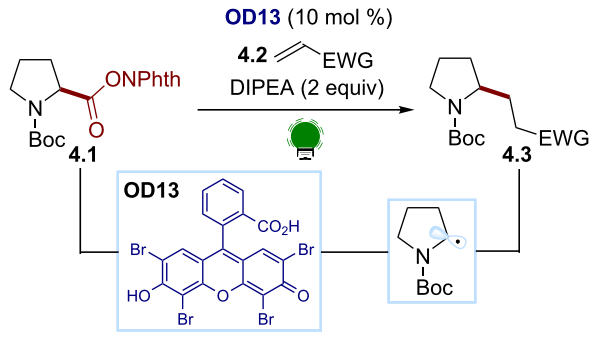

Scheme 4: Illustrative example for the photocatalytic reductive generation of C(sp^3) radicals from redoxactive esters: the decarboxylative Giese reaction reported by König and co-workers [45].

which undergoes a radical conjugate addition with a suitable Michael acceptor **4.2**, providing the desired alkylation products **4.3**.

A similar strategy for radical generations was applied by Glorius and co-workers. They exploited a combination of organophotoredox and copper catalysis to achieve the conversion of carboxylic acids into alkenes using *N*,*N*-diaryldihydrophenazine as an organic photocatalyst [46]. Rose bengal (**OD15**) was also exploited as an organic photocatalyst to trigger the reductive fragmentation of phthalimide-based redox-active esters [47].

Other oxidative fragmentations

In addition to the decarboxylation reactions, organic photoredox catalysis can be exploited to access C(sp^3) radicals via the oxidative fragmentation of different redox-active functional groups (Figure 2) [48]. Among them, dihydropyridines (DHPs), silicates, and tetrafluoroborate salts were recently exploited in organophotocatalytic reactions. These functionalities can act as donors in reductive quenching manifolds and release the desired C(sp^3) radicals after the fragmentation of the oxidized form. Due to their attitude towards SET oxidations, these substrates are valuable alkyl radical precursors; however, they are generally less available than carboxylic acids, and the fragmentations release stoichiometric amounts of byproducts.

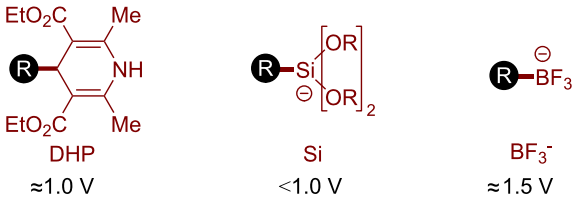

Figure 2: Common substrates for the photocatalytic oxidative generation of C(sp^3) radicals.

The organic dye 4CzIPN (**OD6**), due to its oxidative abilities in the excited state ($E(PC*/PC^{-}) \approx 1.35$ V), has proved to be a versatile organic photocatalyst for accessing C(sp^3) radicals through oxidative fragmentations. In particular, it has been used for generating an alkyl radical from the 4-alkyl-1,4-dihydropyridine (DHP) **5.1** in a metallaphotoredox protocol for the synthesis of alkylated (hetero)arenes (Scheme 5a) [49]. These substrates, easily synthesized from the corresponding aldehydes, can undergo a facile SET oxidation with the excited state of 4CzIPN. The ensuing fragmentation of the pyridyl group releases the C(sp^3) radical, which is intercepted by an organometallic intermediate, obtained by the oxidative addition of a nickel catalyst to the (hetero)aryl bromide **5.2**. The desired

(hetero)arene product **5.3** is obtained after the reductive elimination of the nickel complex. In this method, the reduced organic photocatalyst (E(PC/PC$^-$) ≈ −1.2 V) is responsible for turning over the nickel catalytic cycle by reducing the Ni(I) intermediate.

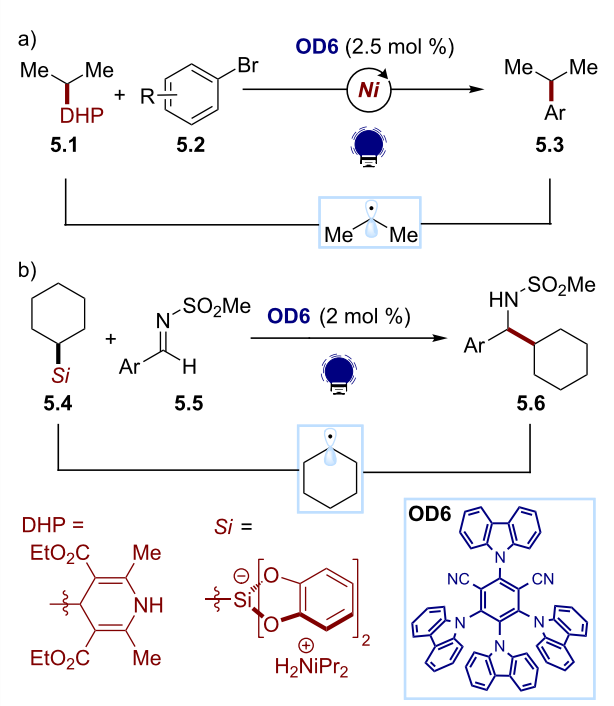

Scheme 5: Illustrative example for the photocatalytic oxidative generation of radicals from dihydropyridines and silicates: the nickel-catalyzed cross-coupling with aryl bromides and addition to imines reported by Molander and co-workers [49,50].

Organosilicates can also be exploited as alkyl radical sources in organic photocatalytic reactions. For example, Molander and co-workers developed a photochemical protocol for the radical alkylation of imines using ammonium alkylbis(catecholato)silicates **5.4** as the C(sp^3) radical precursors (Scheme 5b) [50]. 4CzIPN (**OD6**) was found again to be the best organic photocatalyst, triggering the oxidative fragmentation of the bis(catecholato)silicate. The so-formed alkyl radical adds to the imine substrate **5.5**, yielding the desired amine product **5.6**.

Finally, the same group developed a photochemical radical alkylation of heteroarenes with alkyl trifluoroborate salts (Scheme 6) [51]. In this reaction, the photoinduced oxidative fragmentation of the alkyl trifluoroborate salt **6.1** was promoted by the acridinium photocatalyst **OD2**. The resulting alkyl radical can be intercepted by a protonated heteroarene **6.2**. The addition of potassium persulfate leads to the regeneration of the photocatalyst and the rearomatization of the intermediate, delivering the desired alkylated heteroarene **6.3**.

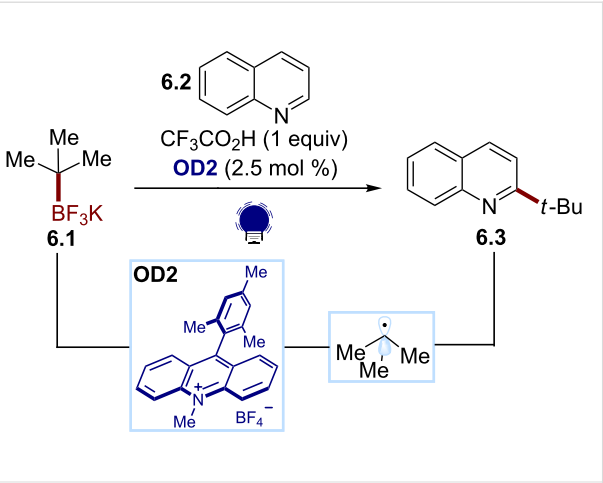

Scheme 6: Illustrative example for the photocatalytic oxidative generation of C(sp^3) radicals from trifluoroborates: the addition to quinolines reported by Molander and co-workers [51].

Other reductive fragmentations

Another organophotocatalytic strategy for accessing C(sp^3) radicals relies on the reductive homolytic cleavage of easily reducible functional groups. In this case, the substrates can act as acceptors in SET reductions, and the alkyl radical is obtained after the fragmentation of the reduced intermediates. Due to their availability and their attitude to undergo reductive fragmentations, alkyl halides have been extensively used as C(sp^3) radicals sources.

Recently, Dell'Amico and co-workers reported a new class of naphthochromenone-based organic dyes, which, due to the wide redox window (E = 3.22 eV, +1.65 V/−1.77 V), can be exploited as photocatalysts for various transformations, including the reductive dehalogenation of benzylic halides (Scheme 7) [52]. In this protocol, the excited state photocatalyst **OD18** can generate C(sp^3) radicals through the reductive cleavage of various benzyl halides **7.1** (I, Br, Cl). The radical is then intercepted by an H atom donor (Hantzsch ester), which delivers the corresponding toluene derivative **7.2**.

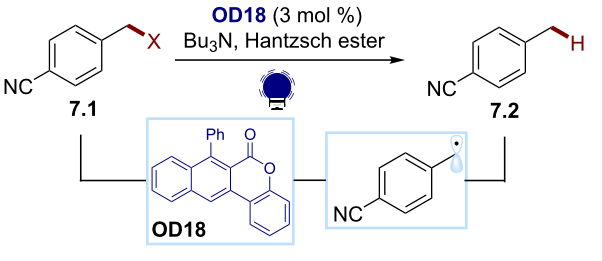

Scheme 7: Illustrative example for the photocatalytic reductive generation of C(sp^3) radicals from benzylic halides: the reduction with a Hantzsch ester reported by Dell'Amico and co-workers [52].

Other organic dyes can promote the reductive fragmentation of alkyl halides. For instance, König and Zeitler demonstrated that a combination of eosin Y (**OD13**) with a sacrificial electron donor can trigger the reductive debromination of several α-carbonyl halides [53]. Riboflavin (**OD11**) [54] and thiaporphyrin [55] have been applied as well as organic photocatalysts for similar reductive dehalogenations.

Hydrogen atom transfer

Photocatalytic hydrogen atom transfer (HAT) represents a valuable strategy for accessing C(sp^3) radicals. This method allows the direct cleavage of a C–H bond and the consequent generation of alkyl radicals without relying on the presence of redox-active functional groups. This results in a superior atom economy compared to other methods for radical generation [56]. Within this field, organic dyes can act as competent photocatalysts for direct HAT processes. Specifically, upon light excitation, photoactive carbonyl compounds, such as benzophenone and its derivatives, reach an electronically excited triplet state: a biradical capable of abstracting an H atom from C–H bonds. Recently, Martin exploited this feature in a nickel-catalyzed process for the alkylation of arenes (Scheme 8) [57].

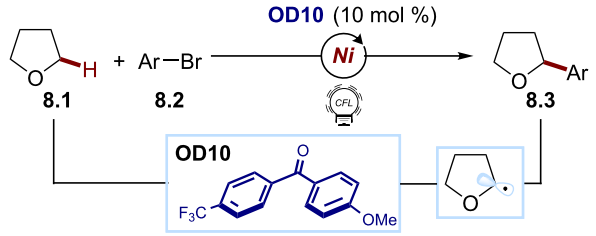

Scheme 8: Illustrative example for the photocatalytic generation of C(sp^3) radicals via direct HAT: the cross-coupling with aryl bromides reported by Martin and co-workers [57].

In this report, the excited state of a push–pull benzophenone **OD10** can abstract an H atom from the substrate tetrahydrofuran (**8.1**), giving access to the key C(sp^3) radical. The nickel catalyst, after an oxidative addition with the aryl bromide **8.2** and intercepting the alkyl radical species, gave the radical cross-coupling product **8.3** upon a reductive elimination.

Other diaryl ketone dyes, such as 9-fluorenone, have been successfully employed for the generation of C(sp^3) radicals via HAT [58]. Interestingly, Wu and co-workers demonstrated that eosin Y (**OD13**) can also act as a direct HAT catalyst under visible-light irradiation [59]. Organic photoredox catalysis can also drive indirect HAT processes. In these reactions, the excited state of the photocatalyst engages in SET or energy transfer events with suitable cocatalysts for hydrogen shuttling, such as thiols. This results in the formation of active species that promote the H abstraction from the substrates. MacMillan exploited this strategy for the deuteration and tritiation of biologically relevant compounds using D_2O and T_2O as hydrogen isotope sources (Scheme 9) [60]. The SET oxidation of the thiol cocatalyst **9.2**, triggered by the excited photocatalyst 4CzIPN (**OD6**), generates a sulfur-centered radical capable of driving the HAT process with the substrate **9.1**. The trapping of the ensuing C(sp^3) radical with the deuterated or tritiated thiol results in the incorporation of deuterium or tritium in multiple positions within the product **9.3**.

C(sp^2) radicals

Aryl radicals

Considering the importance of arylation reactions in organic synthesis [61], aryl radicals are important intermediates to develop new synthetic methods [62]. Their reactivity was first explored in the Meerwein arylation as well as the Gomberg–Bachman and the Sandmeyer reaction [63-65]. Simi-

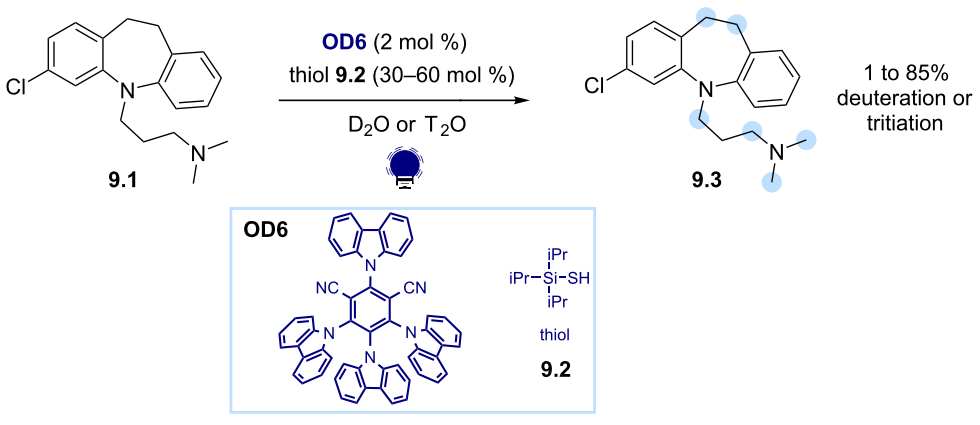

Scheme 9: Illustrative example for the photocatalytic generation of C(sp^3) radicals via indirect HAT: the deuteration and tritation of C–H bonds reported by MacMillan and co-workers [60].

lar to C(sp^3) radicals, aryl radicals add to unsaturated systems, such as (hetero)arenes, alkenes, or alkynes. They can also perform atom abstractions, in particular HATs and halogen abstractions [66]. The generation of such species generally occurs through the homolytic cleavage of a peripheral σ bond [67,68]. In the majority of the cases, a leaving group is reduced and fragments to the aryl radical. The precursors of choice encompass aryl diazonium salts, haloarenes, and sulfur(IV) or sulfur(VI) compounds (Scheme 10).

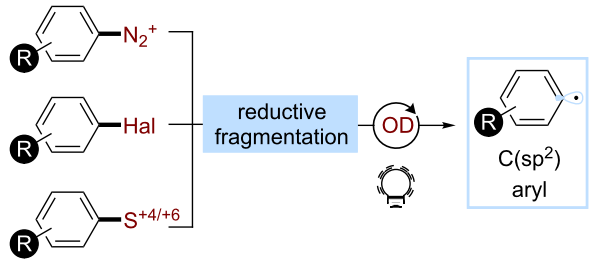

Scheme 10: Selected precursors for the generation of aryl radicals using organophotocatalysis.

Aryl radicals from aryl diazonium salts. Aryl diazonium salts are attractive substrates for accessing aryl radicals. Despite their intrinsic thermal instability and exothermic decomposition [69,70], these species are straightforward to synthesize and can be easily reduced (E_{red} ≈ −0.1 V to −0.3 V) [71,72]. This makes them valuable electron acceptors for photocatalytic strategies. The SET reduction results in the generation of an aryl radical upon the irreversible loss of N_2 as the sole byproduct. As first reported by König and co-workers, organic dyes can be successfully employed as photocatalysts for accessing aryl radicals from these substrates [73]. In this work (Scheme 11), eosin Y (**OD13**) was used for the organophotocatalytic reduction of the aryl diazonium salts **11.1** under visible-light irradiation. The

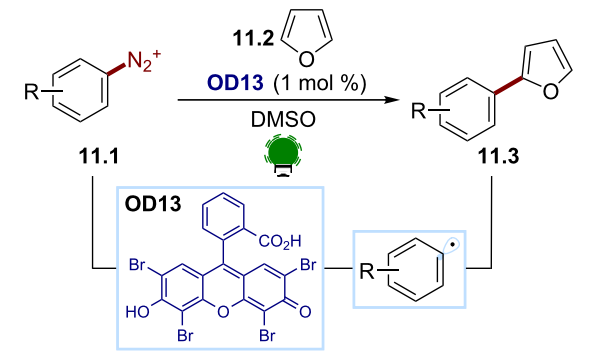

Scheme 11: Illustrative example for the photocatalytic reductive generation of aryl radicals from aryl diazonium salts: the photocatalytic Meerwein arylation reported by König and co-workers [73].

key aryl radical was trapped with heteroarenes, such as **11.2**, to give the arylation products **11.3**. Recently, similar methodologies for aryl radical generations have been developed exploiting flow techniques [74] and different organophotocatalysts, such as a metal-free porphyrin [75] and rhodamine 6G (**OD14**) [76].

Aryl radicals from aryl halides. Aryl halides are generally more difficult to reduce than aryl diazonium salts (E_{red} < −1.2 V) [77,78]. However, they are more available and bench-stable. Their reduction potential is dependent on the substitution pattern and on the nature of the halide: as a trend, aryl iodides are easier to reduce than aryl bromides and aryl chlorides [67,77]. Under organophotocatalytic conditions, the reduction can be achieved following two main strategies for accessing stronger reduction potentials: (a) tuning the electronics of the organic dye or b) tuning the stability of the reduced photocatalyst, allowing a second photoexcitation.

For an example of the first strategy, Zhang and co-workers designed a new photocatalyst: Py-BTz-Py (**OD19**, Scheme 12), which was reducing enough ($E(PC^{\bullet+}/PC^*)$ ≈ −2.0 V) to activate the aryl iodides **12.1** for the synthesis of the arylated heteroarenes **12.3** via an intermolecular process [79]. Alemán and co-workers used PHTH (**OD16**) for the synthesis of various heteroatom-containing bicycles **12.4** through a tethered electrophile approach [80].

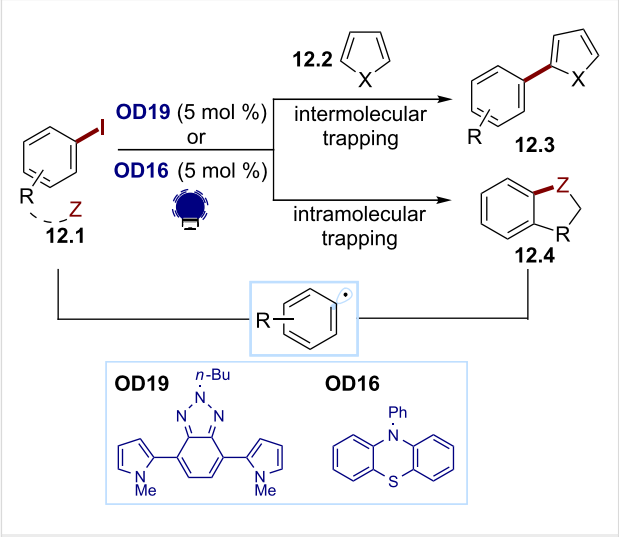

Scheme 12: Illustrative examples for the photocatalytic reductive generation of aryl radicals from haloarenes: the photocatalytic heteroarylation of arenes reported by Zhang and co-workers (top) [79] and the intramolecular heterobicycle synthesis reported by Alemán and co-workers (bottom) [80].

For the second strategy, König and co-workers developed an organic dye-based consecutive photoinduced electron transfer (conPET) strategy for the reduction of various aryl halides in

2014 [81]. As depicted in Scheme 13 (box 1), the conPET mechanism involves a first PET (PET_1), where the excited photocatalyst (**PC***) is reduced by a sacrificial electron donor **D**, such as a trialkylamine. The ensuing radical anion ($\mathbf{PC}^{\bullet-}$), associated to an extended π-system, is persistent enough to absorb a second photon. The resulting excited state of the radical anion ($\mathbf{PC}^{\bullet-}$*) is a strong reductant ($E(PC/PC^{\bullet-}*) < -1.5$ V), which can reduce the electron acceptor (**A**), resulting in a second PET (PET_2). With this strategy, the authors could reduce a broad variety of aryl halides **13.1** using *N*,*N*-bis(2,6-diisopropylphenyl)perylene-3,4,9,10-bis(dicarboximide), (PDI, **OD20**) as a conPET photocatalyst for the generation of an aryl radical (box 2). The latter could be hydrogenated or heteroarylated to give the desired dehalogenated products **13.3** or arylheteroarenes **13.4**. Other organic dyes, such as dicyanoanthracene (**OD5**) and rhodamine 6G (**OD14**), have been successfully used in similar conPET strategies for the aryl radical-mediated derivatization of aryl bromides [82,83]. A similar double SET approach, where the first reduction of dicyanoanthracene (**OD5**) is achieved electrochemically, was recently disclosed by Lambert and Lin. In this report, the photoexcited radical anion of the dye was exploited for accessing aryl radicals as intermediates of a reductive borylation of aryl halides [84].

Other sources of aryl radicals. In addition to aryl diazonium salts and aryl halides, arylsulfonyl chlorides can be reduced with common organic dyes due to their relatively low reduction potential [78]. As an example, Gu and co-workers reported the use of eosin Y (**OD13**) for the SET reduction/desulfonylation of the arylsulfonyl chlorides **14.1** (Scheme 14) [85,86]. The ensuing aryl radical is trapped by an aryl isonitrile **14.2**, affording the bisarylation product **14.3**.

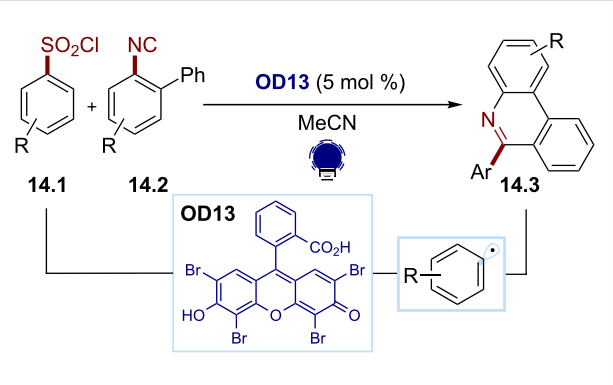

Scheme 14: Illustrative example for the photocatalytic reductive generation of aryl radicals from arylsulfonyl chlorides: the phenanthridine synthesis via aryl radical addition to isonitriles reported by Gu and co-workers [85].

The direct organophotocatalytic activation of the C–H bond of an arene represents an atom-economical and attractive strategy for the generation of aryl radicals. Although inaccessible to date, a two-step strategy was recently developed by the Procter group. They reported a one-pot organophotocatalytic strategy for the heteroarylation of nonprefunctionalized arenes (Scheme 15) [87]. First, a triaryl sulfonium salt **15.3** is generated from the substrate **15.1** using dibenzothiophene *S*-oxide (DBTSO, **15.2**). Then, under visible-light irradiation, **15.3** could be reduced with PHTH (**OD16**) to generate an aryl radical that could further be trapped by a heteroarene **15.4**, such as pyrrole or thiophene, furnishing the arylation product **15.5**.

Acyl, oxylacyl, and carbamoyl radicals and their analogues

The photocatalyzed generation of acyl radicals is of great interest as they are precursors for the synthesis of diverse car-

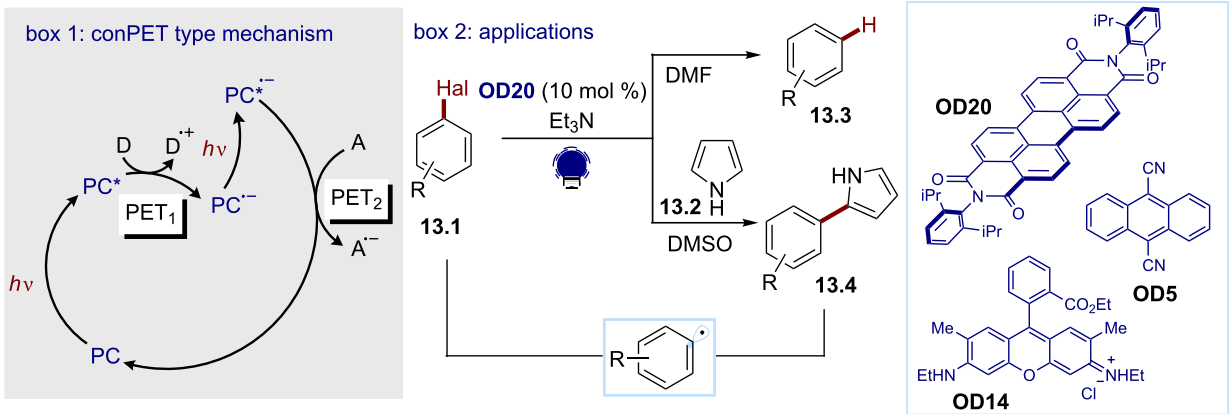

Scheme 13: Illustrative example for the photocatalytic reductive generation of aryl radicals from aryl halides using a conPET strategy. Box 1: conPET mechanism and box 2: the dehalogenation and heteroarylation of aryl radicals reported by König and co-workers [81].

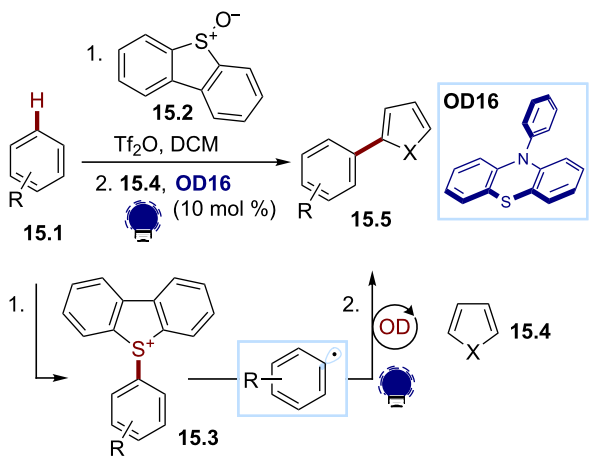

Scheme 15: Illustrative example for the reductive photocatalytic generation of aryl radicals from triaryl sulfonium salts: the one-pot C–H heteroarylation of arenes reported by Procter and co-workers [87].

bonyl compounds [88]. The acyl radical is generally considered as a nucleophilic radical and reacts rapidly with electron-poor π-systems: heteroarenes and electron-poor alkenes in particular. Using the tools of organophotocatalysis, this reactive intermediate can be directly obtained from carbonyl derivatives, such as aldehydes, α-keto acids, oxalates, or carbamates through oxidative or reductive decarboxylations, oxidative fragmentation, or H-abstraction (Scheme 16).

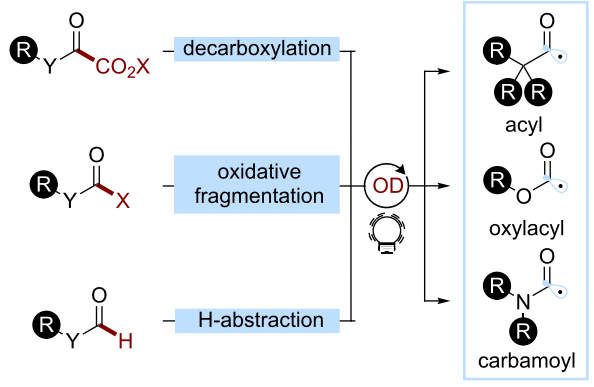

Scheme 16: Main strategies towards acyl radicals used in organophotocatalysis.

A common way to access such radicals is through the decarboxylation of α-keto acids. Both reductive and oxidative strategies were implemented. In 2016, Wang and co-workers developed an organophotocatalyzed acylation of indoles (Scheme 17) [89]. They successfully converted the aryl and alkyl α-keto acids **17.1** to the 3-acylindoles **17.3** using rose bengal (**OD15**) as a photocatalyst under aerobic conditions. Mechanistic studies suggest that rose bengal (**OD15**) acts as an energy transfer sensitizer generating singlet oxygen. The authors proposed that the latter would be responsible for the H atom abstraction from the α-keto acid. The α-keto carboxyl radical undergoes a decarboxylation, leading to the desired acyl radical.

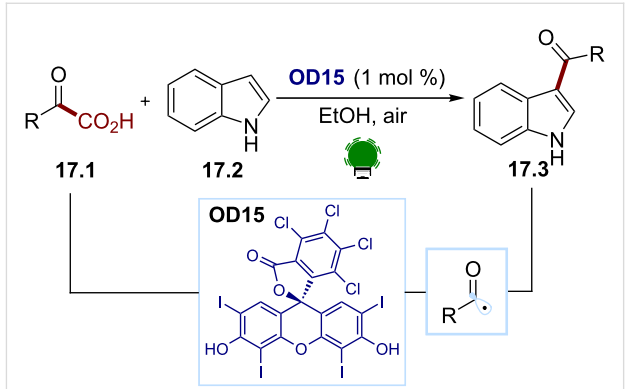

Scheme 17: Illustrative example for the decarboxylative photocatalytic generation of acyl radicals from α-keto acids: the photocatalytic acylation of indole (**17.2**) reported by Wang and co-workers [89].

Acyl radicals can also be accessed through the oxidative cleavage of a redox-active group, such as acylsilanes or 1,4-dihydropyridine derivatives. In 2018, Fagnoni and co-workers developed an organophotocatalytic method to access nonsymmetrical ketones through the oxidation of the alkyl acylsilanes **18.1** (E_{ox} ≈ +1.3 V) by an acridinium photocatalyst **OD2** ($E(PC^{+}*/PC)$ ≈ 2.1 V, Scheme 18) [90]. After the fragmentation, the acyl radical can add to various Michael acceptors **18.2** to afford the desired ketone **18.3**.

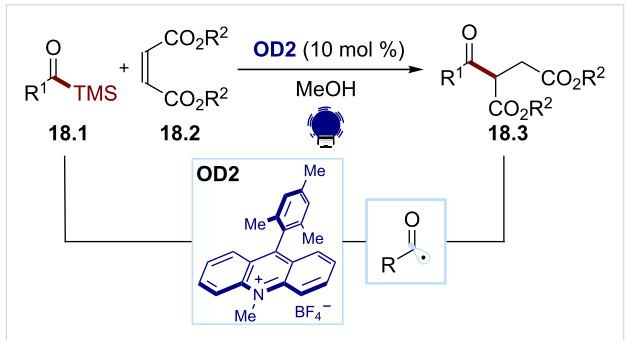

Scheme 18: Illustrative example for the oxidative photocatalytic generation of acyl radicals from acyl silanes: the acylation of electron-poor olefins reported by Fagnoni and co-workers [90].

Recently, the Melchiorre group reported a carbamoyl radical-mediated metallaphotoredox synthesis of arylamides (Scheme 19) [91]. In this protocol, excited-state 4CzIPN (**OD6**) oxidizes a 4-carbamoyl-1,4-dihydropyridine **19.1**, which then fragments, releasing the corresponding pyridinium and the

desired carbamoyl radical. The latter can be intercepted by an organonickel species resulting from the oxidative addition of the nickel catalyst to the aryl bromides **19.2**. The arylamides **19.3** are obtained following a reductive elimination, and the resulting Ni(I) species is reduced by the photocatalyst, and thus closing the catalytic cycle.

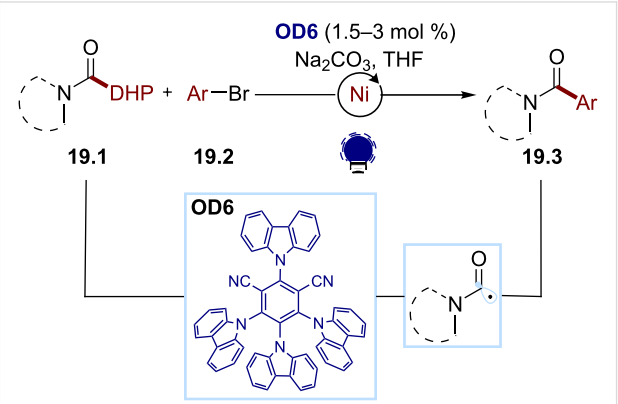

Scheme 19: Illustrative example for the oxidative photocatalytic generation of carbamoyl radicals from 4-carbamoyl-1,4-dihydropyridines: the metallaphotoredox synthesis of aryl amides reported by Melchiorre and co-workers [91].

Finally, Yadav and co-workers developed a method for a chalcone synthesis using an H abstraction approach to access an acyl radical (Scheme 20) [92]. The authors proposed that the excited triplet state of the photocatalyst *N*-hydroxyphthalimide (NHPI, **OD22**, similar to the benzophenone photocatalysts **OD9** and **OD10**) can abstract an H atom from the aldehyde substrate **20.1**. The resulting acyl radical adds to the (*E*)-β-nitrostyrene **20.2**, and the following denitrosylation affords the chalcones **20.3**.

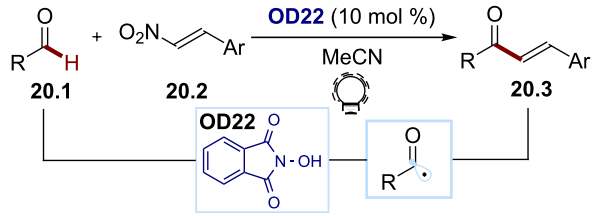

Scheme 20: Illustrative example of the photocatalytic HAT approach for the generation of acyl radicals from aldehydes: the vinylation of aldehydes reported by Yadav and co-workers [92].

Alkenyl and aryl radical ions (radical cations and radical anions)

Recently, the exploitation of alkenyl and aryl radical ions has emerged as a platform for the functionalization of small molecules. They appear as attractive intermediates for a direct alkene difunctionalization or arene C–H functionalization. In particular, radical cations are strong electrophiles and undergo nucleophilic additions with two-electron donors (Scheme 21a) [93,94]. In contrast, radical anions can act as very strong single-electron nucleophiles and are often subject to fragmentation to give a

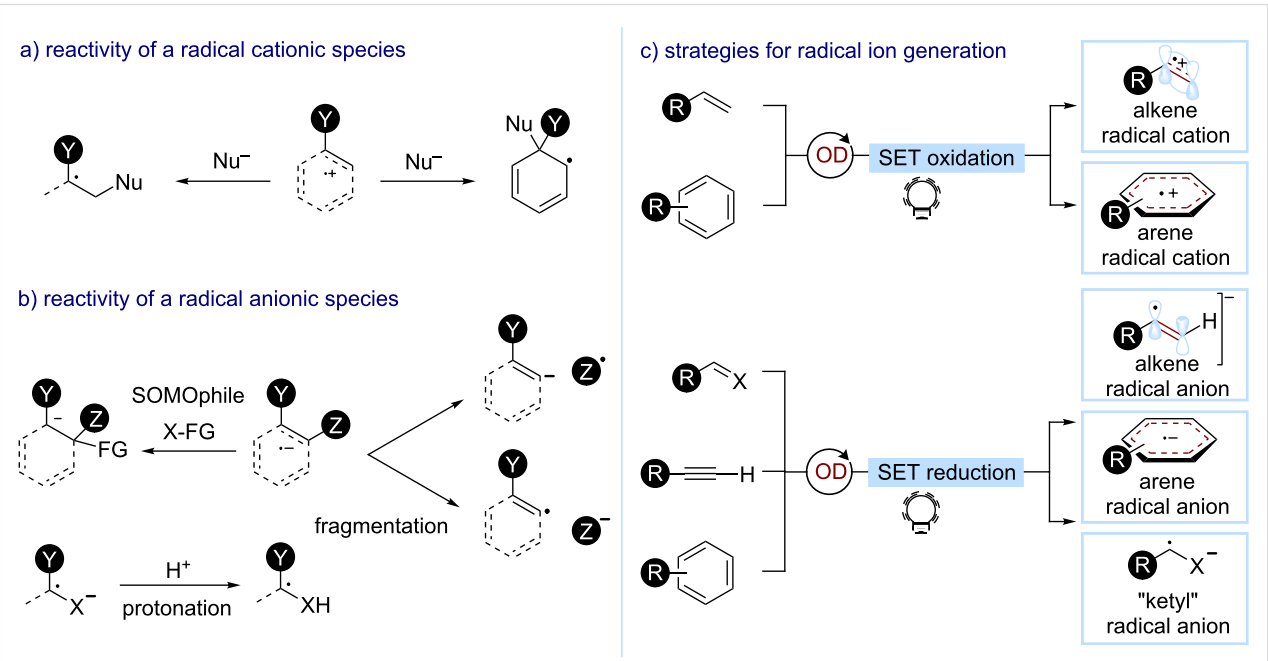

Scheme 21: General reactivity of a) radical cations; b) radical anions; c) the main strategies towards aryl and alkenyl radical ions used in organophotocatalysis.

neutral free radical and a charged species (Scheme 21b) [77,95]. When a fragmentation is not favored, these charged radicals can be intercepted and lead to different selectivities when compared to a traditional two-electron chemistry (e.g., anti-Markovnikov vs Markovnikov or *ipso*-S_NAr reactions). Heteroatom-containing radical anions, such as ketyl radicals, constitute a special class of substrates that usually undergo a protonation to form C(sp^3) radicals.

Alkenyl or aryl radical ions are generally accessed through SET. The presence of electron-donating groups facilitates the oxidation of the precursor to the radical cations, while electron-poor alkynes and arenes can undergo SET reductions to generate the corresponding radical anions (Scheme 21c). Organophotocatalysis has been successfully exploited to promote these SETs and access charged alkenyl and aryl radicals. The reduction of carbon–heteroatom double bonds is especially easy and leads to the formation of ketyl radical anions or their equivalents with other heteroatoms. However, organophotocatalysts have been only rarely used for this type of reduction.

C_2-charged radical species

Since 2013, the Nicewicz group has developed a multitude of methodologies for the anti-Markovnikov hydrofunctionalization of alkenes, exploiting the reactivity of alkene radical cations generated using organic dyes [96,97]. Their seminal work reported the oxidation of the alkenols **22.1** by the Fukuzumi dye (**OD2**, Scheme 22) [98]. The so-formed radical cation undergoes an intramolecular nucleophilic 5/6/7-*exo*-*trig*-cyclization to give the cyclic ethers **22.3**. Mes-Acr-Me^+ (**OD2**) is a strong enough oxidant ($E(PC^{+}*/PC) \approx 2.1$ V), allowing the oxidation of unactivated alkenes ($1.2 \leq E_{ox} \leq 1.9$ V). In this transformation, the cocatalyst **22.2** acts as an H atom shuttle. This alkene radical cation-based strategy has been extended to various hydrofunctionalizations of styrenes with mineral acids (hydrochloric acid, hydrofluoric acid, phosphoric acids, and sulfonic acids) [99]. During these studies, they optimized the structure of the Mes-Acr^+ dye to improve the catalyst turnover. When changing the group on the nitrogen atom of the acridinium scaffold from an alkyl group (Me in **OD2**) to an aryl group (Ph in **OD3**), they could limit the photocatalyst bleaching due to the demethylation of the organic dye.

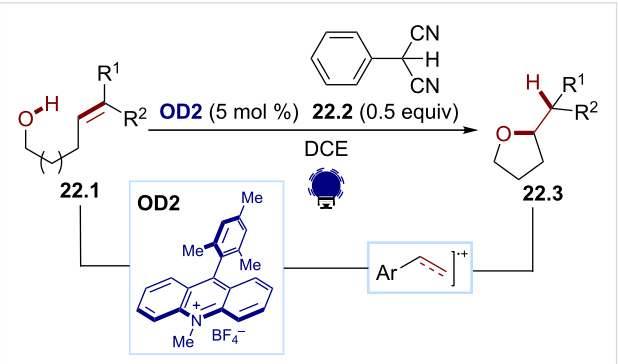

Scheme 22: Illustrative example for the oxidative photocatalytic generation of alkene radical cations from alkenes: the hydroetherification of alkenes reported by Nicewicz and co-workers [98].

Alkene radical anions have been less exploited than their cationic equivalents. In 2017, the Lei group developed a Markovnikov-selective hydrosulfonylation reaction (Scheme 23) [100]. The alkynes **23.1** could be successfully converted to the vinyl sulfones **23.3** in the presence of the aryl sulfones **23.2** using eosin Y (**OD13**) as a photocatalyst. A tentative mechanism was proposed by the authors: under visible-light irradiation, the arylsulfinic acid could be oxidized to the corresponding sulfonyl radical by the excited state of eosin Y (**OD13**). The resulting reduced eosin $Y^{\bullet-}$ could then perform a reduction of the alkyne to generate a radical anionic species. The latter would be subsequently protonated before recombining with the sulfonyl radical to afford the desired vinyl sulfones.

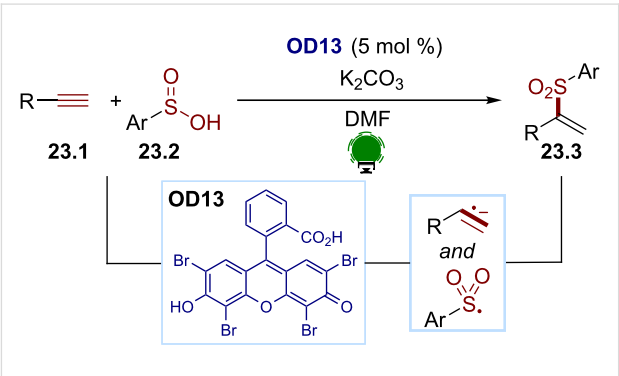

Scheme 23: Illustrative example for the reductive photocatalytic generation of an alkene radical anion from alkynes: the Markovnikov-selective sulfonylation of alkynes reported by Lei and co-workers [100].

C–X radical anions and derived neutral radicals

Amidst charged radical species, ketyl radicals play a central role in organic synthesis (Figure 3). As intermediates, they are more stable because the charge is mainly localized on the oxygen atom. They are postulated to be the intermediate of important reactions, such as the pinacol [101] or the McMurry coupling [102]. Recently, photocatalysis has been used to access ketyl radicals through the reduction of ketones with a suitable transition metal-based photocatalyst [103] or organic dye [104]. The protonation of this type of radicals occurs on the heteroatom and leads to versatile neutral C(sp^3) radicals. Such processes can also occur via concerted proton-coupled electron transfer mechanisms [105]. Similarly, the photocatalyzed reduction of imines followed by protonation, as well as the reduction of

iminium compounds, gives access to α-amino radicals [106]. Most approaches are based on inorganic photocatalysts. As a rare example of the use of an organic dye, Dixon and co-workers used eosin Y (**OD13**) to reduce imines and generate the α-amino C(sp^3) radical upon protonation (Scheme 24) [107]. This radical is then trapped with a suitable Michael acceptor **24.2** to obtain the corresponding allylation product **24.3** after a desulfonylation.

Figure 3: Structure of C–X radical anions and their neutral derivatives.

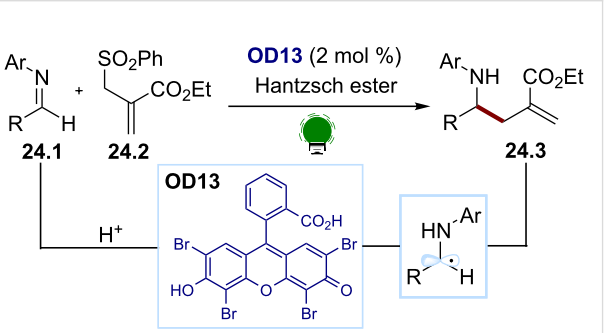

Scheme 24: Illustrative example for the photocatalytic reduction of imines and the generation of an α-amino C(sp^3) radical: the umpolung of imines for allylations reported by Dixon and co-workers [107].

Enones can also be subject to SET reductions through photoredox catalysis, and this can lead to [2 + 2] cycloadditions [2,108]. Similar intermediates can also be generated through the direct activation of the ß-C–H bond [109]. However, organic dyes have not yet been broadly applied for such transformations.

Charged aryl radical species

Arene radical cations are valuable intermediates that enable the direct C–H functionalization of the aromatic species. They can be accessed through the oxidation of arenes under relatively strong oxidative conditions (E_{ox} > +1.0 V).

Following up their work on alkene oxidations, Nicewicz and co-workers have developed several strategies for arene functionalizations through arene radical cation intermediates. Their work relies on the careful tuning of the Mes-Acr^+ scaffold. In 2015, they developed a site-selective C–H amination of arenes (Scheme 25) [110]. The arenes **25.1** could be aminated by various N-heterocycles **25.2** for the synthesis of the C–H functionalization products **25.3** with fine-tuned Mes-di(*t*-Bu)Acr^+ (**OD4**) as a photocatalyst. In this transformation, the arene is first oxidized by the excited state of the photocatalyst, generating the arene radical cation **I**. The latter then undergoes a nucleophilic attack of the N-heterocycle, affording the radical adduct **II**. TEMPO and O_2 act as oxidants for the formation of the final aromatic compound via the peroxo radical **III** when using O_2. Nicewicz and co-workers noticed that the presence of nucleophilic peroxide radicals generated from O_2 led to the degradation of the classical Mes-Acr^+ photocatalyst. The presence of bulky *tert*-butyl groups in the 3- and 6-positions provided a greater catalyst stability in presence of such nucleophilic radicals. This arene radical cation strategy has been further extended to cyanations, aminations, and fluorinations [111-116].

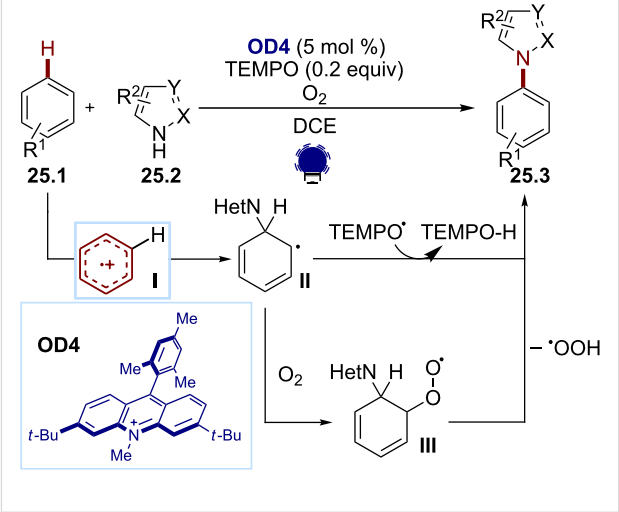

Scheme 25: Illustrative example for the oxidative photocatalytic generation of aryl radical cations from arenes: the C–H amination of arenes reported by Nicewicz and co-workers [110].

Arene radical anions, resulting from the reduction of aromatic compounds, are transient species that can enable aryl radical generations, in particular with haloarenes (see the section on aryl radicals from aryl halides). Notably, cyanobenzenes have been reported to undergo reductions and lead to *ipso*-substitution in place of the cyano group [117]. However, these methodologies rely on either a transition metal photocatalyst [118,119] or the formation of EDA complexes (electron donor–acceptor complexes) [120-123], and no method involving organophotocatalysts has been reported yet to the best of our knowledge.

Nitrogen-centered radicals (NCRs)

Biologically relevant compounds often contain C–N bonds, rendering the development of efficient methodologies for their formation of paramount importance. Building on the seminal

work of Zard [124], NCRs have emerged as key reactive intermediates. The reductive cleavage of weak N–X (X = halogen, S, O) bonds using a stoichiometric initiator or high temperatures set the path for key developments for the generations of NCRs, for instance, in the Hofmann–Löffler–Freytag reaction. With the rise of photoredox catalysis, they could be accessed under milder conditions in the last years [125-132].

NCRs can be organized into four main classes depending on the nitrogen atom hybridization and the substitution of the N atom, including iminyl, amidyl, aminyl, and aminium units (Scheme 26). The reactivity depends on the philicity of each species. In a general manner, NCRs are prone to the addition to unsaturated systems, either inter- or intramolecularly as well as HAT and Norrish type I fragmentations. Each of these steps generates a C-centered radical, later subject to termination. The variety of possible transformations has already been reviewed [125-132].

Iminyl radicals have an ambiphilic character. Amidyl radicals are electrophilic, with the substitution playing an important role [133-135]. As they are prone to efficient HAT, C(sp^3)–H couplings at remote positions have been intensively studied [128,130,132,136]. Aminyl and aminium radicals display the opposite philicity: aminyls are nucleophilic, whereas upon protonation, the generated aminium is strongly electrophilic. N-Centred radical cations have been employed as key intermediates in amine syntheses [137,138]. These species can further react, according to the structure of the substrate, to form either iminium ions or C-centered radicals, such as α-amino radicals.

Several approaches for their efficient generation with organic dyes have been proposed, using SET oxidations and oxidative or reductive fragmentations. The hydroxylamine scaffold plays a prevalent role in the generation of various NCRs, both through oxidative or reductive fragmentation. *N*-aminopyridinium salts are also emerging starting materials.

Iminyl radical generation

Hydroxylamines have emerged as key precursors for iminyl radical generation [128]. Their redox properties can be easily tuned through the substitution pattern of the electrophore. They can be subjected to either oxidative or reductive SET with an excited photoredox catalyst. The most used scaffolds consist of electron-poor *O*-acyl and *O*-aryl hydroxylamines, which are prone to reduction, and α-*N*-oxy acids, which undergo oxidations followed by β-scission [128,136,139].

Leonori first described how *O*-aryl oximes **27.1** can be used to efficiently generate an iminyl radical in the presence of eosin Y (**OD13**, Scheme 27) [140]. This methodology was employed in hydroimination and iminohydroxylation cyclization reactions to give the pyrrolines **27.2**. The transformation proceeds via a SET reduction of the electron-poor aromatic moiety on the oxime to give a radical anion, which then fragments. Electrochemical studies highlighted that *O*-aryl hydroxylamines bearing nitro groups were within the reduction range of excited eosin Y (E_{red} between −0.55 and −0.93 V vs SCE, **OD13**, $E(PC^{\bullet+}/PC^*) \approx -1.1$ V).

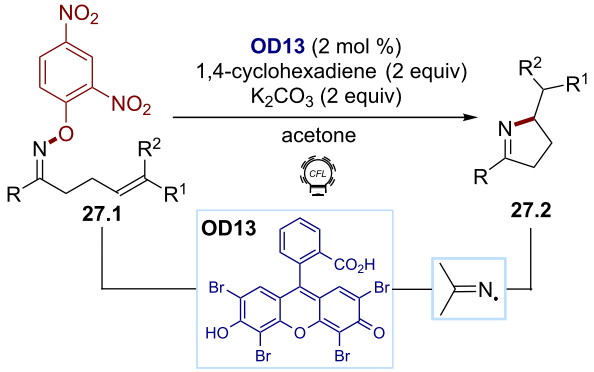

Scheme 27: Illustrative example for the photocatalytic reductive generation of iminyl radicals from *O*-aryl oximes: the hydroimination/cyclization reported by Leonori and co-workers [140].

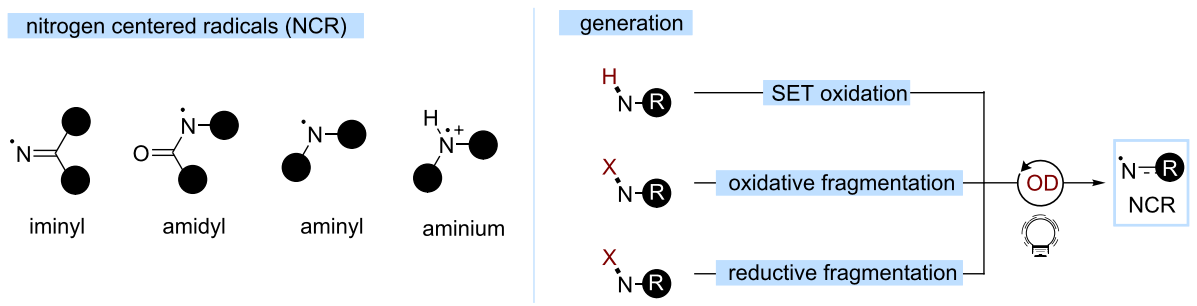

Scheme 26: NCR classifications and generation.

Oxidative strategies have also been described using the hydroxylamine scaffold, affording an efficient and general access to iminyl radicals. The first reports were released simultaneously by Leonori and Studer (Scheme 28) [141,142]. α-*N*-Oxy acid **28.1** carboxylates (E_{ox} = +1.6 V vs SCE for the caesium carboxylate) can be oxidized by the strongly oxidizing dye Mes-Acr-Me$^+$ (**OD2**, $E(PC^{+}*/PC)$ ≈ 2.1 V). After the decarboxylation and β-scission, the corresponding iminyl radicals were submitted to various radical traps, Y-FG, to provide diverse imino-functionalized products **28.2**. A large variety of functionalizations was possible, such as halogenations, azidations, olefinations, or alkynylations. This activation mode was employed by the same group in a cascade strategy, which allowed a remote functionalization [143]. To extend the scope of such transformations, our group reported novel organic dyes in 2018, such as 4ClCzIPN (**OD8**), obtained through fine-tuning of 4CzIPN (**OD6**), which are both strong oxidants and reductants [144].

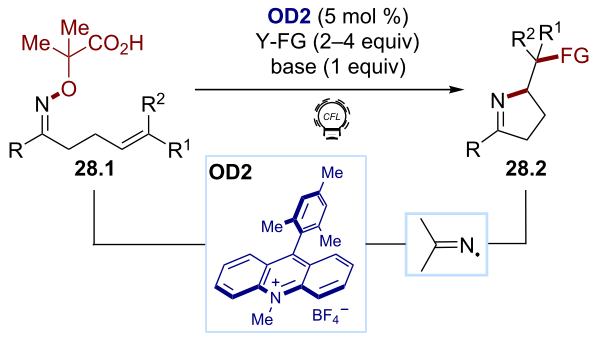

Scheme 28: Illustrative example for the photocatalytic oxidative generation of iminyl radicals from α-*N*-oxy acids: the imino functionalization reported by Leonori and co-workers [141].

In the search for a more atom-economical approach, the group of Li developed an iminyl radical formation by the N–H bond cleavage from the diarylimines **29.1** (Scheme 29) [145]. The direct oxidation of **29.1** was achieved using Mes-Acr-Me$^+$ (**OD2**) and a cobalt cocatalyst, ensuring an efficient dehydrogenation. Various N-heterocycles **29.3** were accessed via a radical cyclization cascade with the alkyne derivatives **29.2**.

Amidyl radical generation

The oxidation of amides is more difficult compared to amines, with reduction potentials from 1.2 to 2.0 V vs SCE [138]. This has rendered the development of a general strategy for direct amidyl radical formations challenging. A successful approach has been the incorporation of a photolabile moiety on the nitrogen atom. Similar to the iminyl radical generation, the use of hydroxylamine derivatives has turned out to be very efficient [128,139].

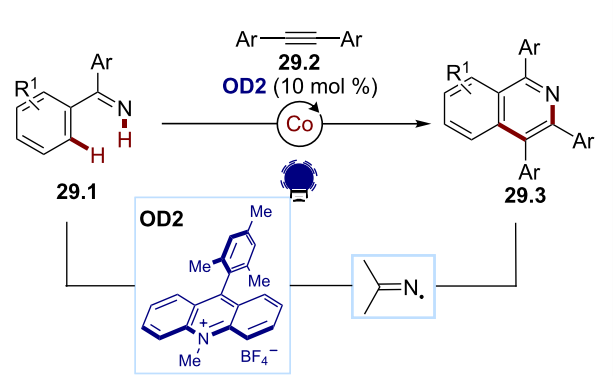

Scheme 29: Illustrative example for the photocatalytic oxidative generation of iminyl radicals via an N–H bond oxidation: the radical cyclization reported by Li and co-workers [145].

The generation of amidyl radicals using organophotoredox catalysis was first reported by Pandey and Laha in 2015 (Scheme 30) [146]. They developed an intermolecular cross-dehydrogenative benzylic C(sp^3) amination between the aryl substrates **30.1** and the amides **30.2** for the synthesis of the Weinreb amides **30.3** using DCA (**OD5**) as an organic dye. Under visible-light irradiation, the SET oxidation of **30.2** by the excited state of DCA, followed by a deprotonation, afforded the amidyl radical. This radical behaved as a powerful HAT reagent, allowing the formation of the benzylic radical from **30.1**. The absence of any activating group on the nitrogen renders this process atom-economical.

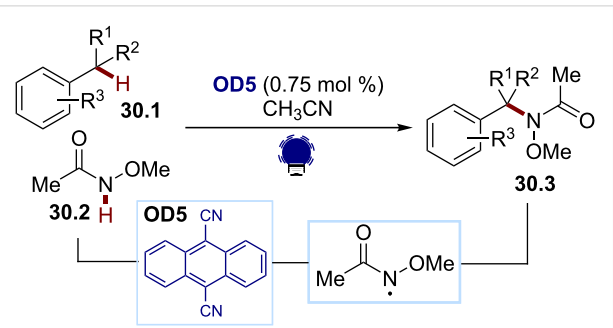

Scheme 30: Illustrative example for the photocatalytic oxidative generation of amidyl radicals from Weinreb amides: the cross-dehydrogenative benzylic C(sp^3)–H amination reported by Pandey and Laha [146].

In 2016, the Leonori group paved the way for the generation of amidyl radicals by SET reductions of hydroxylamines (Scheme 31) [134]. The previously described approach for iminyl radical formations was employed [140]. The same tunable aryloximes **31.1** were used as electrophores to generate the desired amidyl radicals. This methodology allowed the development of a hydroamination/cyclization cascade to give the heterocycles **31.2** and intermolecular *N*-arylations. A modified

electrophore, *p*-CF_3-substituted hydroxamide, was later proposed by the Yu group with a different dye, (2,4,6-tri(9*H*-carbazol-9-yl)-5-chloroisophthalonitrile (3CzClIPN) [147].

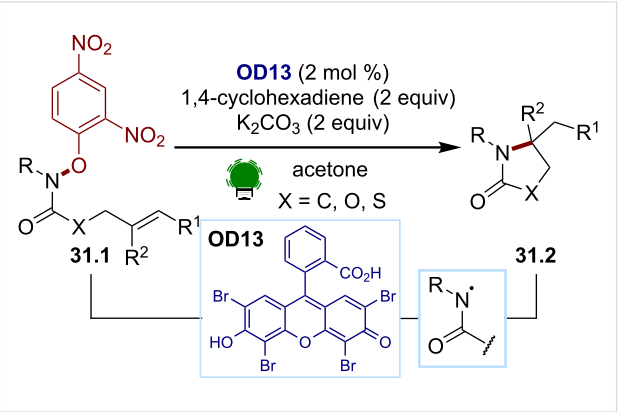

Scheme 31: Illustrative example for the photocatalytic reductive generation of amidyl radicals from hydroxylamines: the hydroamination/cyclization reported by Leonori and co-workers [134].

The *N*-aminopyridinium salts **32.2** are another scaffold for the generation of amidyl radicals via SET. After the reduction, a fragmentation affords the desired amidyl radicals together with the corresponding pyridines. The reduction potential of such species was around −0.75 V vs Ag/Ag^+, depending on the substitution pattern. This scaffold was employed recently by the Hong group to achieve an intermolecular alkene 1,2-aminopyridylation to give the difunctionalized products **32.3** (Scheme 32) [148]. Eosin Y (**OD13**) was an efficient dye for the SET reduction of the *N*-aminopyridinium salts, which act as bifunctional reagents as the released pyridine later added to the olefin **32.1**.

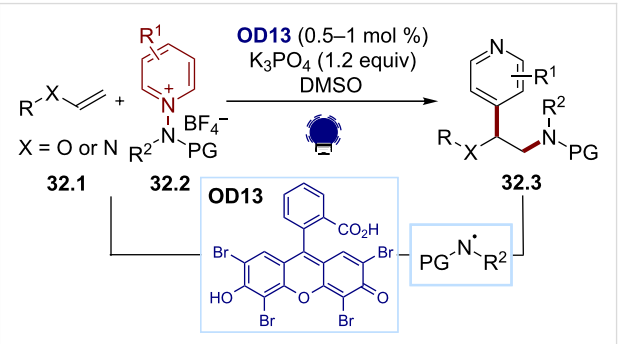

Scheme 32: Illustrative example for the photocatalytic reductive generation of amidyl radicals from *N*-aminopyridinium salts: the intermolecular alkene 1,2-aminopyridylation reported by Hong and co-workers [148].

The generation of amidyl radicals by the SET oxidation of hydroxylamines has also been explored. As for iminyl radicals, this enables the trapping of the subsequently formed carbon-centered radicals with various reagents. Studer and co-workers disclosed an amidofluorination of unactivated alkenes and the styrenes **33.1** to give the fluorinated amides **33.3**, employing the α-amido-oxy acids **33.2** and Mes-Acr-Me^+ (**OD2**, Scheme 33) [149]. The same electrophore allowed a remote functionalization of amides to take place, as disclosed by the Leonori group [135]. 4CzIPN (**OD6**) was reported to be a suitable dye for the SET oxidation of such carboxylates.

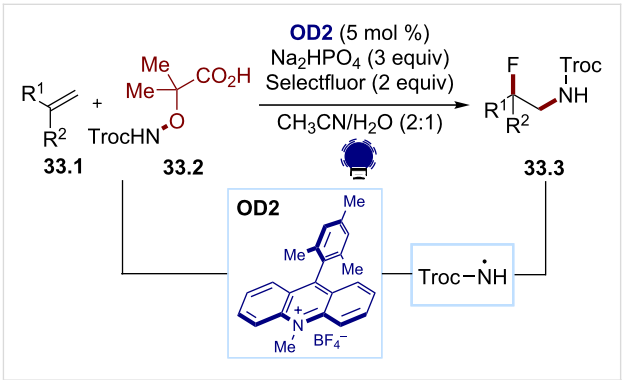

Scheme 33: Illustrative example for the photocatalytic oxidative generation of amidyl radicals from α-amido-oxy acids: the amidofluorination of unactivated alkenes reported by Studer and co-workers [149].

Aminyl and aminium radical generation

The prevalent strategy for accessing aminium radicals is SET oxidations. The efficiency of this approach is closely related to the stabilization of the generated radical on the substrate (delocalization, electronic effects) or through a strain release ring-opening driving force.

N-Aryltetrahydroquinolines **34.1** have been intensively studied as a privileged scaffold for N-centred radical cation formations [138]. After iminium formation, formed by subsequent HAT on the amine radical cation, various nucleophiles can add, resulting in diverse functionalizations. In 2011, König and co-workers [150] demonstrated that eosin Y (**OD13**) was an efficient dye for an aza-Henry reaction [151], affording the tetrahydroquinolines **34.2** (Scheme 34). Simultaneously, the Tan group described the use of rose bengal (**OD15**) in the same transformation [152].

Regarding the strain release approach, the Xiao group reported a synthesis of the pyrroles **35.3** in 2014 [153]. They can be accessed via a photocatalytic formal [3 + 2] cycloaddition of the 2*H*-azirines **35.1** and the alkynes **35.2** (Scheme 35). The use of Mes-Acr-Me^+ (**OD2**) was successful due to its high reduction potential in the excited state, together with an intense absorption in the visible-light region. The transformation proceeds via the single-electron oxidation of 2*H*-azirines, forming a nitrogen-centered radical cation, which is prone to ring opening.

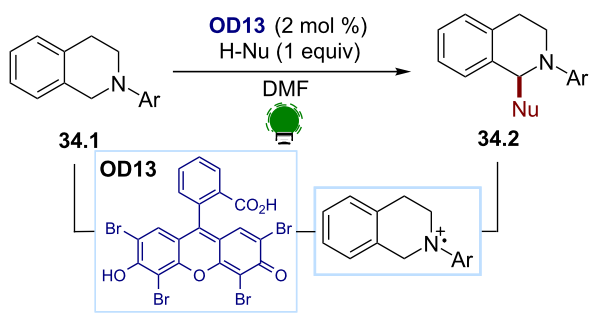

Scheme 34: Illustrative example for the photocatalytic oxidative generation of aminium radicals: the *N*-aryltetrahydroisoquinoline functionalization reported by König and co-workers [150].

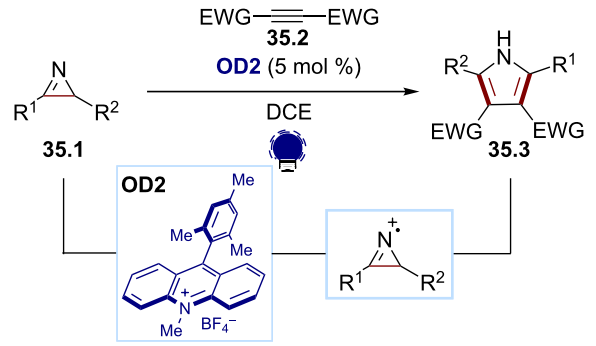

Scheme 35: Illustrative example for the photocatalytic oxidative generation of nitrogen-centered radical cations from 2*H*-azirines: the pyrrole synthesis reported by Xiao and co-workers [153].

The driving force of the ring strain release and irreversible ring opening of nitrogen-containing small rings was also exploited by our group in 2019 (Scheme 36) [154]. Starting from the aminocyclopropanes **36.1** and the cyclopropenes **36.2**, a [3 + 2] annulation led to the bicyclo[3.1.0]hexanes **36.3**. Under visible-light irradiation, the excited-state photocatalyst **OD7** performs an SET oxidation of an cyclopropylaniline **36.1**, leading to an N-centred radical cation after ring opening. The latter undergoes a [3 + 2] annulation with cyclopropenes **36.2**, affording a bicyclic product **36.3**. The key to the broad substrate tolerance relied on using 4DPAIPN (**OD7**), which is a mild oxidant but a strong reductant (E(PC*/PC$^{\bullet-}$) = +0.90 and E(PC/PC$^{\bullet-}$) = −1.65 V vs SCE) [155].

As another class of nitrogen radicals, hydrazonyl radicals can be formed from the direct N–H bond oxidation of the hydrazones **37.1**, as reported by the Xiao group (Scheme 37) [156]. This strategy was based on a cooperative TEMPO and photoredox catalysis. The SET oxidation of the anion of the β,γ-unsaturated hydrazones **37.1** is mediated by TEMPO$^+$, itself formed by an SET oxidation with the excited state of Mes-Acr-Me$^+$ (**OD2**).

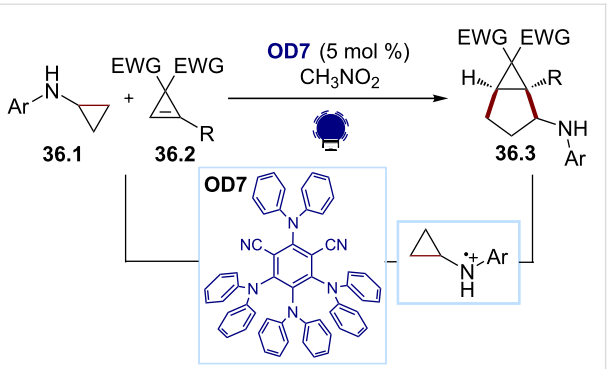

Scheme 36: Illustrative example for the photocatalytic oxidative generation of nitrogen-centered radical cations from cyclopropylanilines: the [3 + 2] annulation of cyclopropylanilines and cyclopropenes reported by our group [154].

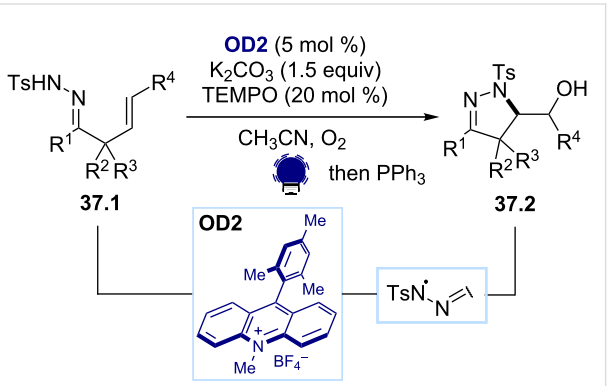

Scheme 37: Illustrative example for the photocatalytic oxidative generation of hydrazonyl radical from hydrazones: the pyrazoline synthesis reported by Xiao and co-workers [156].

The pyrazolines **37.2** are formed through an intramolecular addition to the alkene, followed by a reaction with oxygen.

Finally, a remote functionalization of protected amines was also disclosed by Leonori and co-workers in their report on amidyl radical formations by SET oxidations of α-oxyamido acids using 4CzIPN (**OD6**, Scheme 28) [135].

Oxygen-centered radicals

Oxygen-centered radicals (O-radicals) represent an important class of heteroatom-centered radicals. In particular, their ability to promote radical translocations, especially HATs, and to undergo β-fragmentations makes them valuable reactive intermediates in organic synthesis [157-161]. Organic photoredox catalysis can be exploited to access O-radicals from different classes of substrates. In particular, *N*-alkoxypyridinium and alkyl hydroperoxides have been exploited as competent O-radical sources (Scheme 38). These substrates can be activated through SET reduction and energy transfer, respectively.

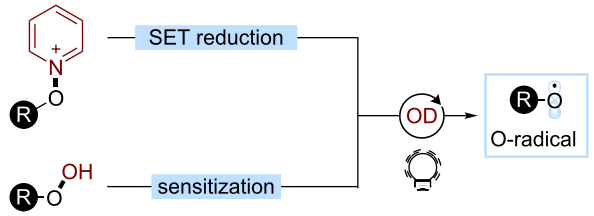

Scheme 38: Generation of O-radicals.

The cleavage of the N–O or O–O bond releases the desired O-radical.

The ability of *N*-alkoxypyridinium salts to generate O-radicals under organophotocatalytic conditions was exploited by Hong, Baik, and co-workers (Scheme 39a) [160]. They reported the use of the phosphorylated quinolinone derivative **OD21** as a photocatalyst, which triggers the photoinduced SET reduction of the *N*-alkoxypyridinium salt **39.1**, leading to the formation of the key O-radical. This species rapidly undergoes a 1,5-HAT. The formed nucleophilic C-centered radical then adds selectively onto the C4 position of another pyridinium substrate **39.1**. The formed *N*-alkoxylated intermediate is converted into the desired product **39.2** after oxidation and releases another alkoxy radical at the same time. The measured quantum yield ($\Phi = 4.4$) indicates that a chain mechanism is operative. Recently, the same group applied a similar organophotocatalytic system to perform a ring closure/pyridylation radical cascade for the synthesis of tetrahydrofuran derivatives (Scheme 39b) [161].

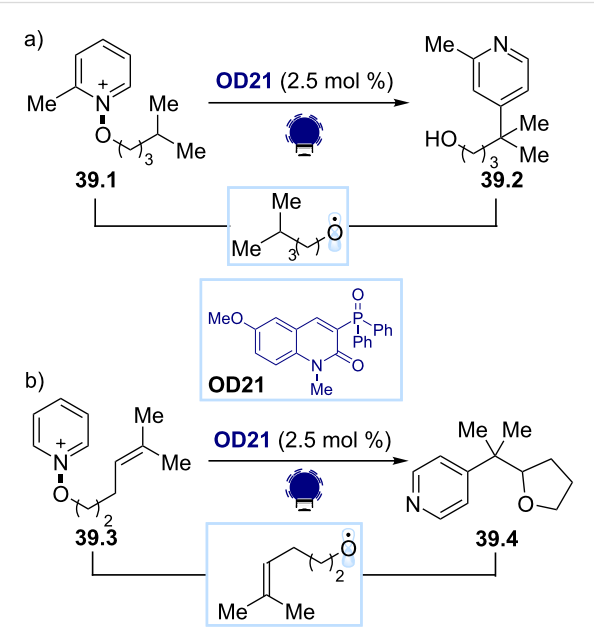

Scheme 39: Illustrative examples for the photocatalytic generation of O-radicals from *N*-alkoxypyridinium salts reported by Hong, Baik and co-workers [160,161].

Eosin Y (**OD13**) has been demonstrated to be another competent photocatalyst for the generation of O-centered radicals from *N*-alkoxypyridynium salts. These radicals have been used as initators for the synthesis of highly functionalized benzo[*b*]phosphole oxides from arylphosphine oxide and alkynes [162].

Alkyl hydroperoxides can act as oxidants in photocatalytic cycles, furnishing the desired alkoxy radicals. Several organic dyes have been exploited in these processes, including eosin Y (**OD13**) [163] and acridine red [164]. Wang and co-workers relied on this approach for the development of an organophotocatalytic vinylation of tetrahydrofuran derivatives with alkynes (Scheme 40) [165]. In this method, the photoexcited **OD13** induces the cleavage of the weak O–O bond of *tert*-butyl peroxide (**40.1**), generating a hydroxy radical and a *tert*-butoxy radical. The latter promotes an H abstraction from the substrate tetrahydrofuran (**8.1**), giving access to an α-oxy C(sp^3) radical, which is trapped by an alkyne **40.2**, providing the desired vinylation product **40.3**.

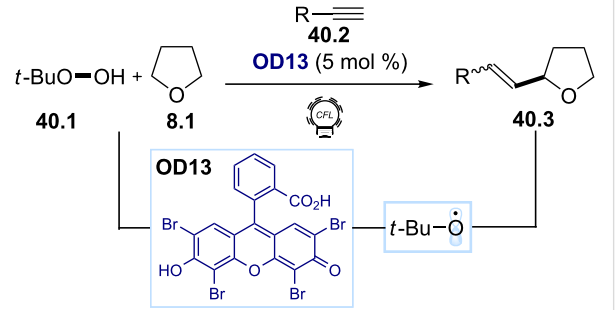

Scheme 40: Illustrative examples for the photocatalytic generation of O-radicals from alkyl hydroperoxides: the vinylation of tetrahydrofurans reported by Wang and co-workers [165].

Sulfur-centered radicals

Thiyl (sulfenyl) radicals

Thiyl radicals are common, versatile, strong nucleophilic radicals. They are efficient at performing atom abstractions, in particular with H-atoms, adding to π-systems and electrophiles, such as carbonyl compounds [166]. They can be generated from the UV irradiation of disulfides, sulfides or even thiols [167]. However, their use in organophotocatalysis is scarce. In substoichiometric quantities, they are efficient H atom shuttles and play a primordial role in hydrogen transfer mechanisms. For this reason, one of their major applications is the HAT to the cocatalyst (Scheme 3 and Scheme 9) [41,60]. In stoichiometric amounts, they generally add efficiently to π-systems and can be

applied in thiol-ene reactions. Recently, Dilman and co-workers published a hydrosulfenylation of the β-difluorostyrenes **41.2** for the synthesis of the thioethers **41.3** using 9-PhAcr (**OD1**) as a photocatalyst (Scheme 41) [168]. The formed thioethers **41.3** could then be used as a *gem*-difluoroalkyl radical source for further transformations. Interestingly, 9-PhAcr (**OD1**) can only act as a photocatalyst in its protonated form. The thiol **41.1** acts as a proton source for **OD1**, allowing it to undergo a photoexcitation, leading to the excited state that can then oxidize the thiolate and generate the key S-centered radical. The latter then adds to the styrene. Other reports describe the use of phenyl glyoxylic acid [169] or eosin Y (**OD13**) for thiol-ene [170] and thiol-yne reactions [171].

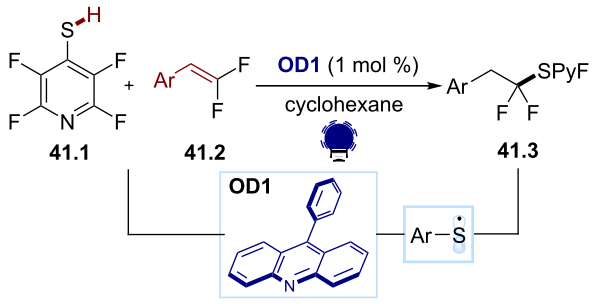

Scheme 41: Illustrative example for the oxidative photocatalytic generation of thiyl radicals from thiols: the thiol-ene reaction with β-difluorostyrenes reported by Dilman and co-workers [168].

Sulfonyl radicals

Sulfonyl radicals show a good reactivity with π-systems, allowing the synthesis of nonsymmetrical sulfones [172]. However, they are also prone to fragmentations, resulting in the desulfonylation of the substrate and the generation of the corresponding C-centered radical. Sulfonyl radicals can be obtained from the fragmentation of sulfonic acid analogues, such as sulfonyl chlorides or sulfonyl hydrazides under reductive or oxidative conditions. Sulfinic acids can also be readily oxidized in the presence of a base, affording the desired sulfonyl radical (Scheme 42).

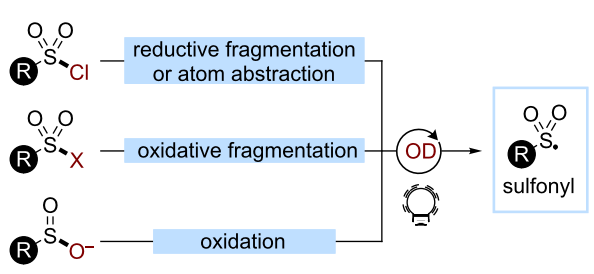

Scheme 42: Main strategies and reagents for the generation of sulfonyl radicals used in organophotocatalysis.

The fragmentation of sulfonyl chloride derivatives requires relatively strong reductive conditions. Most reductions occur at −1.30 V or lower values (with the exception of CF_3SO_2Cl: E_{red} = –0.18 V). Organophotocatalysis has been exploited to promote this reduction. For example, Chen and co-workers designed the new organic dye **OD17** in 2018 (Scheme 43, $E(PC^{\bullet+}/PC^*) \approx -1.9$ V), able of reducing the arylsulfonyl chlorides **43.1** (E_{red} = −0.94 V) to initiate the synthesis of the polyacrylates and polyacrylamides **43.3** [173].

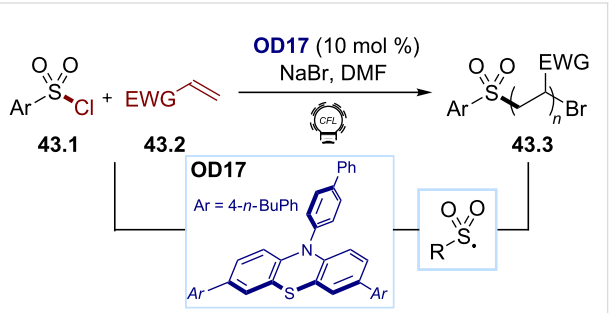

Scheme 43: Illustrative example for the reductive photocatalytic generation of sulfonyl radicals from arylsulfonyl chlorides: the acrylate and acrylamide polymerization reported by Chen and co-workers [173].

To bypass the strong reductive conditions communally used for the activation of sulfamoyl chlorides to form the corresponding sulfamoyl radicals, Gouverneur and co-workers developed an efficient method based on chloride abstractions. They could successfully convert the sulfamoyl chlorides **44.1** to the alkyl sulfonamides **44.4** using eosin Y (**OD13**) as a photocatalyst and the supersilane **44.3** for a halogen abstraction (Scheme 44) [174]. Under visible-light irradiation, the excited state **OD13*** can oxidize the silane, generating, after deprotonation, a silyl radical, which can efficiently abstract the chlorine atom, resulting in the nucleophilic sulfamoyl radical. The latter can then

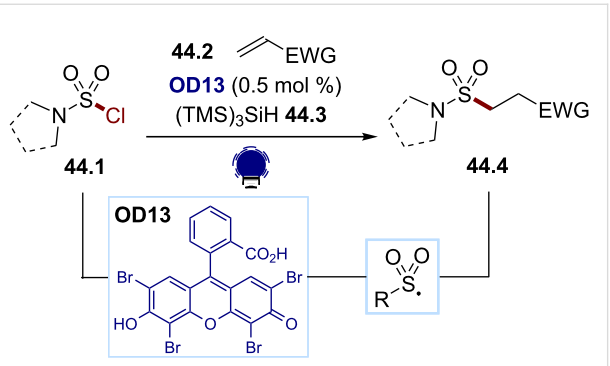

Scheme 44: Illustrative example of a Cl atom abstraction strategy for the photocatalytic generation of sulfamoyl radicals from sulfamoyl chlorides: the radical chlorine abstraction for a Giese reaction reported by Gouverneur and co-workers [174].

undergo a Giese addition to an electron-deficient alkene **44.2**, affording the desired alkyl sulfonamides **44.4**.

The SET oxidation of sulfinic acids and sulfinates for the generation of sulfonyl radicals has been thoroughly explored over the past decades [172]. These oxidations occur under mildly oxidative conditions, and eosin Y (**OD13**) stands out as an efficient photocatalyst for these steps [175-177]. This strategy is also compatible with transition metal catalysis, as shown by Lei and co-workers with an organophotocatalyzed radical cross-coupling method using the aryl sulfinic acids **45.1** and the styrenes **45.2** to generate the allyl sulfones **45.3** (Scheme 45) [178]. Under visible-light irradiation, the aryl sulfinic acid **45.1** is oxidized by the excited-state photocatalyst, a bis(tetrabutylammonium) salt of eosin Y, **OD23**, generating the desired sulfonyl radical. The latter adds to the styrene **45.2**, and the formed benzylic radical is intercepted by the cobalt catalyst, which can promote a dehydrogenation to form the allyl sulfone **45.3**. The colbalt cocatalyst secures the turnover of the photocatalyst by reducing it back to its ground state.

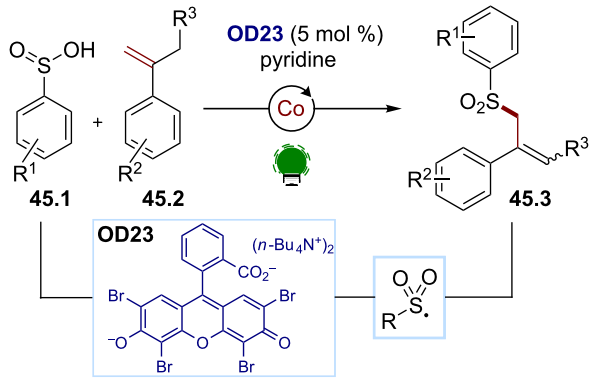

Scheme 45: Illustrative example for the oxidative photocatalytic generation of sulfonyl radicals from sulfinic acids: the metallaphotoredox allyl sulfone synthesis reported by Lei and co-workers [178].

Excited reactive intermediates (energy transfer)

In addition to electron transfer and atom transfer, EnT is one of the key modes of activation employed in photocatalysis. In order to act as a good energy transfer catalyst, an organic molecule, upon light irradiation, should undergo a productive intersystem crossing (ISC) and reach an electronically excited triplet state. The latter can transfer its energy to a ground-state substrate in a process named "sensitization". The so-formed excited substrate is a valuable reactive intermediate for achieving various transformations and structural modifications. This approach has been widely exploited to generate singlet O_2, a versatile oxidant often applied in organic synthesis [179].

Additionally, energy sensitization has emerged has a powerful strategy for promoting the contrathermodynamic *E*-to-*Z* isomerization of olefins. Inspired by the mechanism of vision in mammals, which implies a triplet state-mediated *E*-to-*Z* isomerization of retinal, Gilmour and co-workers reported an organophotocatalytic method for the isomerization of the α,β-unsaturated esters **46.1** (Scheme 46) [180]. In this protocol, (−)-riboflavin (**OD11**) is exploited as an organic photocatalyst, capable of absorbing light, transferring its triplet energy to the *E*-substrate and triggering the isomerization of the double bond with a high level of selectivity.

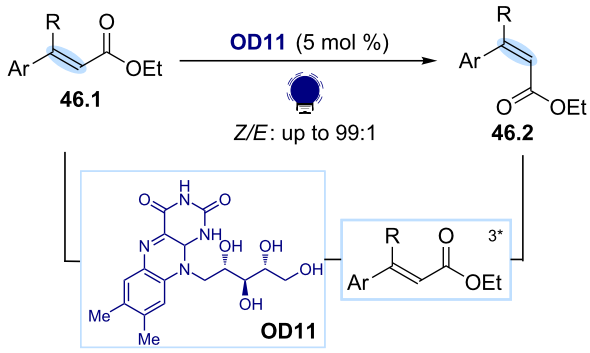

Scheme 46: Illustrative example for the photocatalytic generation of electronically excited triplet states: the *E*-to-*Z* isomerization of olefins reported by Gilmour and co-workers [180].

Recently, the same group extended this strategy to the geometrical isomerization of several classes of substrates, including β-ionyl derivatives [181], alkenylsilanes [182], and vinyl phosphonates [183]. In addition to riboflavin, other organic dyes, such as benzophenone, anthracene, 2-iodo-9-fluorenone [184], and carbazole- and cyanobenzene-based organophotocatalysts [185] have been successfully employed as photosensitizers for these isomerizations.

Another application of photosensitization is related to the development of thermally forbidden [2 + 2] cycloadditions. These reactions can be promoted by the direct excitation of the substrate, generally using UV light. However, the key triplet state intermediate can also be accessed by the energy transfer from a suitable photosensitizer. Seminal reports by Bach [186] and Sivaguru [187] demonstrated that thioxanthone-based organic dyes can promote these transformations. It has been shown that flavin-based dyes can also act as photosensitizers for this reaction (Scheme 47) [188]. In particular, alloxazine (**OD12**), which is structurally similar to flavin, has been used for promoting an intramolecular [2 + 2] cycloaddition of the dienes **47.1** to form the cyclobutane **47.2**.

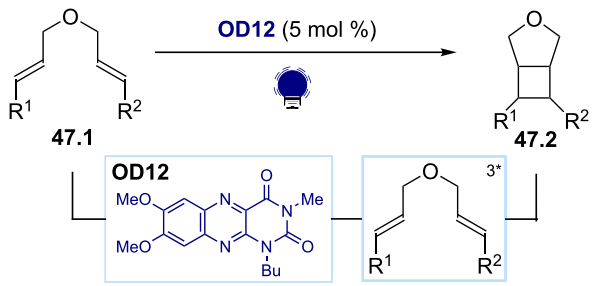

Scheme 47: Illustrative example for the photocatalytic generation of electronically excited triplet states: the [2 + 2] cycloaddition of dienes reported by Chibulka and co-workers [188].

Conclusion

Organic dyes have emerged as efficient, cheap, and sustainable catalysts for photochemical transformations. In the last years, new scaffolds offering valuable alternatives to the established transition metal-based photocatalysts have appeared.

The structures of these light-absorbing molecules can be tuned, improving their photophysical properties and broadening their field of application. This has allowed the development of various organophotocatalytic methods, involving photoredox, energy, or atom transfer steps for accessing key reactive intermediates, including both open-shell species and excited-state molecules. In this review, we provided an overview on these reactive intermediates, and how they can be formed by using organic dyes as the photocatalysts. Each approach was illustrated by a few selected examples, with no effort to be exhaustive. Organic dyes have demonstrated a compatibility with other catalytic processes, such as metal catalysis and organocatalysis, further extending the possibilities for bond formations [29,189]. Furthermore, these scaffolds are invariably less toxic than their inorganic counterparts, rendering them available for an application in biological systems [155,190], and promising developments are also expected in emerging fields, such as photoelectrochemistry [84,191,192].

We believe that organophotocatalysis has consolidated its foundation and will play an increasingly important role in the development of novel photochemical transformations. This conceptual review summarizing the state-of-the art for the generation of reactive intermediates using organic dyes, shows the impressive progress that has already been realized in the last decade, and will give a first insight in the field for general synthetic chemists.

ORCID® iDs

Luca Buzzetti - https://orcid.org/0000-0002-1096-8272
Jerome Waser - https://orcid.org/0000-0002-4570-914X

References

1. Nicewicz, D. A.; MacMillan, D. W. C. *Science* **2008,** *322,* 77–80. doi:10.1126/science.1161976
2. Ischay, M. A.; Anzovino, M. E.; Du, J.; Yoon, T. P. *J. Am. Chem. Soc.* **2008,** *130,* 12886–12887. doi:10.1021/ja805387f
3. Narayanam, J. M. R.; Tucker, J. W.; Stephenson, C. R. J. *J. Am. Chem. Soc.* **2009,** *131,* 8756–8757. doi:10.1021/ja9033582
4. Ravelli, D.; Dondi, D.; Fagnoni, M.; Albini, A. *Chem. Soc. Rev.* **2009,** *38,* 1999. doi:10.1039/b714786b
5. Ciamician, G.; Silber, P. *Ber. Dtsch. Chem. Ges.* **1908,** *41,* 1928–1935. doi:10.1002/cber.19080410272
6. Ciamician, G. *Science* **1912,** *36,* 385–394. doi:10.1126/science.36.926.385
7. Juris, A.; Balzani, V.; Barigelletti, F.; Campagna, S.; Belser, P.; von Zelewsky, A. *Coord. Chem. Rev.* **1988,** *84,* 85–277. doi:10.1016/0010-8545(88)80032-8
8. Yoon, T. P.; Ischay, M. A.; Du, J. *Nat. Chem.* **2010,** *2,* 527–532. doi:10.1038/nchem.687
9. Narayanam, J. M. R.; Stephenson, C. R. J. *Chem. Soc. Rev.* **2011,** *40,* 102–113. doi:10.1039/b913880n
10. Shaw, M. H.; Twilton, J.; MacMillan, D. W. C. *J. Org. Chem.* **2016,** *81,* 6898–6926. doi:10.1021/acs.joc.6b01449
11. Ravelli, D.; Protti, S.; Fagnoni, M. *Chem. Rev.* **2016,** *116,* 9850–9913. doi:10.1021/acs.chemrev.5b00662
12. Arias-Rotondo, D. M.; McCusker, J. K. *Chem. Soc. Rev.* **2016,** *45,* 5803–5820. doi:10.1039/c6cs00526h
13. Zhang, X.; Li, Y.; Hao, X.; Jin, K.; Zhang, R.; Duan, C. *Tetrahedron* **2018,** *74,* 1742–1748. doi:10.1016/j.tet.2018.01.040
14. Selsted, M. E.; Becker, H. W., III. *Anal. Biochem.* **1986,** *155,* 270–274. doi:10.1016/0003-2697(86)90436-7
15. Neckers, D. C. *J. Photochem. Photobiol., A* **1989,** *47,* 1–29. doi:10.1016/1010-6030(89)85002-6
16. Romero, N. A.; Nicewicz, D. A. *Chem. Rev.* **2016,** *116,* 10075–10166. doi:10.1021/acs.chemrev.6b00057
17. Pitre, S. P.; McTiernan, C. D.; Scaiano, J. C. *ACS Omega* **2016,** *1,* 66–76. doi:10.1021/acsomega.6b00058
18. Fagnoni, M.; Protti, S.; Ravelli, D. *Photoorganocatalysis in organic synthesis;* World Scientific: London, 2019. doi:10.1142/q0180
19. Ravelli, D.; Fagnoni, M.; Albini, A. *Chem. Soc. Rev.* **2013,** *42,* 97–113. doi:10.1039/c2cs35250h
20. Hari, D. P.; König, B. *Chem. Commun.* **2014,** *50,* 6688–6699. doi:10.1039/c4cc00751d
21. Joshi-Pangu, A.; Lévesque, F.; Roth, H. G.; Oliver, S. F.; Campeau, L.-C.; Nicewicz, D.; DiRocco, D. A. *J. Org. Chem.* **2016,** *81,* 7244–7249. doi:10.1021/acs.joc.6b01240
22. Sideri, I. K.; Voutyritsa, E.; Kokotos, C. G. *Org. Biomol. Chem.* **2018,** *16,* 4596–4614. doi:10.1039/c8ob00725j
23. Shang, T.-Y.; Lu, L.-H.; Cao, Z.; Liu, Y.; He, W.-M.; Yu, B. *Chem. Commun.* **2019,** *55,* 5408–5419. doi:10.1039/c9cc01047e
24. White, A.; Wang, L.; Nicewicz, D. *Synlett* **2019,** *30,* 827–832. doi:10.1055/s-0037-1611744
25. Zilate, B.; Fischer, C.; Sparr, C. *Chem. Commun.* **2020,** *56,* 1767–1775. doi:10.1039/c9cc08524f
26. Wardle, B. *Principles and applications of photochemistry;* John Wiley & Sons: Hoboken, NJ, USA, 2009.
27. Klán, P.; Wirz, J. *Photochemistry of Organic Compounds;* John Wiley and Sons: Chichester, UK, 2011.

28. Balzani, V.; Ceroni, P.; Juris, A. *Photochemistry and photophysics: concepts, research, applications;* Wiley-VCH: Weinheim, Germany, 2014.
29. Twilton, J.; Le, C.; Zhang, P.; Shaw, M. H.; Evans, R. W.; MacMillan, D. W. C. *Nat. Rev. Chem.* **2017,** *1,* 0052. doi:10.1038/s41570-017-0052
30. Wang, C.-S.; Dixneuf, P. H.; Soulé, J.-F. *Chem. Rev.* **2018,** *118,* 7532–7585. doi:10.1021/acs.chemrev.8b00077
31. Romero, K. J.; Galliher, M. S.; Pratt, D. A.; Stephenson, C. R. J. *Chem. Soc. Rev.* **2018,** *47,* 7851–7866. doi:10.1039/c8cs00379c
32. Yi, H.; Zhang, G.; Wang, H.; Huang, Z.; Wang, J.; Singh, A. K.; Lei, A. *Chem. Rev.* **2017,** *117,* 9016–9085. doi:10.1021/acs.chemrev.6b00620
33. Kolbe, H. *Ann. Chem. Pharm.* **1849,** *69,* 257–294. doi:10.1002/jlac.18490690302
34. Vijh, A. K.; Conway, B. E. *Chem. Rev.* **1967,** *67,* 623–664. doi:10.1021/cr60250a003
35. Hunsdiecker, H.; Hunsdiecker, C. *Ber. Dtsch. Chem. Ges. B* **1942,** *75,* 291–297. doi:10.1002/cber.19420750309
36. Barton, D. H. R.; Dowlatshahi, H. A.; Motherwell, W. B.; Villemin, D. *J. Chem. Soc., Chem. Commun.* **1980,** 732. doi:10.1039/c39800000732
37. Barton, D. H. R.; Crich, D.; Motherwell, W. B. *Tetrahedron Lett.* **1983,** *24,* 4979–4982. doi:10.1016/s0040-4039(01)99826-0
38. Barton, D. H. R.; Crich, D.; Motherwell, W. B. *J. Chem. Soc., Chem. Commun.* **1983,** 939. doi:10.1039/c39830000939
39. Xuan, J.; Zhang, Z.-G.; Xiao, W.-J. *Angew. Chem., Int. Ed.* **2015,** *54,* 15632–15641. doi:10.1002/anie.201505731
40. Huang, H.; Jia, K.; Chen, Y. *ACS Catal.* **2016,** *6,* 4983–4988. doi:10.1021/acscatal.6b01379
41. Griffin, J. D.; Zeller, M. A.; Nicewicz, D. A. *J. Am. Chem. Soc.* **2015,** *137,* 11340–11348. doi:10.1021/jacs.5b07770
42. Marcote, D. C.; Street-Jeakings, R.; Dauncey, E.; Douglas, J. J.; Ruffoni, A.; Leonori, D. *Org. Biomol. Chem.* **2019,** *17,* 1839–1842. doi:10.1039/c8ob02702a
43. Zhang, M.-J.; Schroeder, G. M.; He, Y.-H.; Guan, Z. *RSC Adv.* **2016,** *6,* 96693–96699. doi:10.1039/c6ra17524d
44. Horner, L.; Jordan, M. *Justus Liebigs Ann. Chem.* **1978,** 1518–1525. doi:10.1002/jlac.197819780916
45. Schwarz, J.; König, B. *Green Chem.* **2016,** *18,* 4743–4749. doi:10.1039/c6gc01101b
46. Tlahuext-Aca, A.; Candish, L.; Garza-Sanchez, R. A.; Glorius, F. *ACS Catal.* **2018,** *8,* 1715–1719. doi:10.1021/acscatal.7b04281
47. Jia, J.; Lefebvre, Q.; Rueping, M. *Org. Chem. Front.* **2020,** *7,* 602–608. doi:10.1039/c9qo01428d
48. Yoshida, J.-i.; Kataoka, K.; Horcajada, R.; Nagaki, A. *Chem. Rev.* **2008,** *108,* 2265–2299. doi:10.1021/cr0680843
49. Gutiérrez-Bonet, Á.; Tellis, J. C.; Matsui, J. K.; Vara, B. A.; Molander, G. A. *ACS Catal.* **2016,** *6,* 8004–8008. doi:10.1021/acscatal.6b02786
50. Patel, N. R.; Kelly, C. B.; Siegenfeld, A. P.; Molander, G. A. *ACS Catal.* **2017,** *7,* 1766–1770. doi:10.1021/acscatal.6b03665
51. Matsui, J. K.; Primer, D. N.; Molander, G. A. *Chem. Sci.* **2017,** *8,* 3512–3522. doi:10.1039/c7sc00283a
52. Mateos, J.; Rigodanza, F.; Vega-Peñaloza, A.; Sartorel, A.; Natali, M.; Bortolato, T.; Pelosi, G.; Companyó, X.; Bonchio, M.; Dell'Amico, L. *Angew. Chem., Int. Ed.* **2020,** *59,* 1302–1312. doi:10.1002/anie.201912455
53. Neumann, M.; Füldner, S.; König, B.; Zeitler, K. *Angew. Chem., Int. Ed.* **2011,** *50,* 951–954. doi:10.1002/anie.201002992
54. Martinez-Haya, R.; Miranda, M. A.; Marin, M. L. *Eur. J. Org. Chem.* **2017,** 2164–2169. doi:10.1002/ejoc.201601494
55. Lee, J.; Papatzimas, J. W.; Bromby, A. D.; Gorobets, E.; Derksen, D. J. *RSC Adv.* **2016,** *6,* 59269–59272. doi:10.1039/c6ra11374e
56. Capaldo, L.; Ravelli, D. *Eur. J. Org. Chem.* **2017,** 2056–2071. doi:10.1002/ejoc.201601485
57. Shen, Y.; Gu, Y.; Martin, R. *J. Am. Chem. Soc.* **2018,** *140,* 12200–12209. doi:10.1021/jacs.8b07405
58. Xia, J.-B.; Zhu, C.; Chen, C. *J. Am. Chem. Soc.* **2013,** *135,* 17494–17500. doi:10.1021/ja410815u
59. Fan, X.-Z.; Rong, J.-W.; Wu, H.-L.; Zhou, Q.; Deng, H.-P.; Tan, J. D.; Xue, C.-W.; Wu, L.-Z.; Tao, H.-R.; Wu, J. *Angew. Chem., Int. Ed.* **2018,** *57,* 8514–8518. doi:10.1002/anie.201803220
60. Loh, Y. Y.; Nagao, K.; Hoover, A. J.; Hesk, D.; Rivera, N. R.; Colletti, S. L.; Davies, I. W.; MacMillan, D. W. C. *Science* **2017,** *358,* 1182–1187. doi:10.1126/science.aap9674
61. McGlacken, G. P.; Bateman, L. M. *Chem. Soc. Rev.* **2009,** *38,* 2447–2464. doi:10.1039/b805701j
62. Bonin, H.; Sauthier, M.; Felpin, F.-X. *Adv. Synth. Catal.* **2014,** *356,* 645–671. doi:10.1002/adsc.201300865
63. Sandmeyer, T. *Ber. Dtsch. Chem. Ges.* **1884,** *17,* 1633–1635. doi:10.1002/cber.18840170219
64. Gomberg, M.; Bachmann, W. E. *J. Am. Chem. Soc.* **1924,** *46,* 2339–2343. doi:10.1021/ja01675a026
65. Meerwein, H.; Büchner, E.; van Emster, K. *J. Prakt. Chem.* **1939,** *152,* 237–266. doi:10.1002/prac.19391520705
66. Galli, C. *Chem. Rev.* **1988,** *88,* 765–792. doi:10.1021/cr00087a004
67. Fry, A. J.; Krieger, R. L. *J. Org. Chem.* **1976,** *41,* 54–57. doi:10.1021/jo00863a012
68. Ghosh, I.; Marzo, L.; Das, A.; Shaikh, R.; König, B. *Acc. Chem. Res.* **2016,** *49,* 1566–1577. doi:10.1021/acs.accounts.6b00229
69. Sheng, M.; Frurip, D.; Gorman, D. *J. Loss Prev. Process Ind.* **2015,** *38,* 114–118. doi:10.1016/j.jlp.2015.09.004
70. Filimonov, V. D.; Krasnokutskaya, E. A.; Kassanova, A. Z.; Fedorova, V. A.; Stankevich, K. S.; Naumov, N. G.; Bondarev, A. A.; Kataeva, V. A. *Eur. J. Org. Chem.* **2019,** 665–674. doi:10.1002/ejoc.201800887
71. Andrieux, C. P.; Pinson, J. *J. Am. Chem. Soc.* **2003,** *125,* 14801–14806. doi:10.1021/ja0374574
72. Raicopol, M.; Necula, L.; Ionita, M.; Pilan, L. *Surf. Interface Anal.* **2012,** *44,* 1081–1085. doi:10.1002/sia.4830
73. Hari, D. P.; Schroll, P.; König, B. *J. Am. Chem. Soc.* **2012,** *134,* 2958–2961. doi:10.1021/ja212099r
74. Vidyacharan, S.; Ramanjaneyulu, B. T.; Jang, S.; Kim, D.-P. *ChemSusChem* **2019,** *12,* 2581–2586. doi:10.1002/cssc.201900736
75. de Souza, A. A. N.; Silva, N. S.; Müller, A. V.; Polo, A. S.; Brocksom, T. J.; de Oliveira, K. T. *J. Org. Chem.* **2018,** *83,* 15077–15086. doi:10.1021/acs.joc.8b02355
76. Gong, X.; Li, X.; Xie, W.; Wu, J.; Ye, S. *Org. Chem. Front.* **2019,** *6,* 1863–1867. doi:10.1039/c9qo00410f
77. Pause, L.; Robert, M.; Savéant, J.-M. *J. Am. Chem. Soc.* **1999,** *121,* 7158–7159. doi:10.1021/ja991365q
78. Roth, H.; Romero, N.; Nicewicz, D. *Synlett* **2016,** *27,* 714–723. doi:10.1055/s-0035-1561297

79. Wang, L.; Byun, J.; Li, R.; Huang, W.; Zhang, K. A. I. *Adv. Synth. Catal.* **2018,** *360,* 4312–4318. doi:10.1002/adsc.201800950
80. Garrido-Castro, A. F.; Salaverri, N.; Maestro, M. C.; Alemán, J. *Org. Lett.* **2019,** *21,* 5295–5300. doi:10.1021/acs.orglett.9b01911
81. Ghosh, I.; Ghosh, T.; Bardagi, J. I.; König, B. *Science* **2014,** *346,* 725–728. doi:10.1126/science.1258232
82. Shaikh, R. S.; Düsel, S. J. S.; König, B. *ACS Catal.* **2016,** *6,* 8410–8414. doi:10.1021/acscatal.6b02591
83. Neumeier, M.; Sampedro, D.; Májek, M.; de la Peña O'Shea, V. A.; Jacobi von Wangelin, A.; Pérez-Ruiz, R. *Chem. – Eur. J.* **2018,** *24,* 105–108. doi:10.1002/chem.201705326
84. Kim, H.; Kim, H.; Lambert, T. H.; Lin, S. *J. Am. Chem. Soc.* **2020,** *142,* 2087–2092. doi:10.1021/jacs.9b10678
85. Gu, L.; Jin, C.; Liu, J.; Ding, H.; Fan, B. *Chem. Commun.* **2014,** *50,* 4643–4645. doi:10.1039/c4cc01487a
86. Gu, L.; Jin, C.; Wang, W.; He, Y.; Yang, G.; Li, G. *Chem. Commun.* **2017,** *53,* 4203–4206. doi:10.1039/c6cc10305g
87. Aukland, M. H.; Šiaučiulis, M.; West, A.; Perry, G. J. P.; Procter, D. J. *Nat. Catal.* **2020,** *3,* 163–169. doi:10.1038/s41929-019-0415-3
88. Raviola, C.; Protti, S.; Ravelli, D.; Fagnoni, M. *Green Chem.* **2019,** *21,* 748–764. doi:10.1039/c8gc03810d
89. Shi, Q.; Li, P.; Zhu, X.; Wang, L. *Green Chem.* **2016,** *18,* 4916–4923. doi:10.1039/c6gc00516k
90. Capaldo, L.; Riccardi, R.; Ravelli, D.; Fagnoni, M. *ACS Catal.* **2018,** *8,* 304–309. doi:10.1021/acscatal.7b03719
91. Alandini, N.; Buzzetti, L.; Favi, G.; Schulte, T.; Candish, L.; Collins, K. D.; Melchiorre, P. *Angew. Chem., Int. Ed.* **2020,** *59,* 5248–5253. doi:10.1002/anie.202000224
92. Tripathi, S.; Kapoor, R.; Yadav, L. D. S. *Adv. Synth. Catal.* **2018,** *360,* 1407–1413. doi:10.1002/adsc.201701559
93. Arnold, D. R.; Lamont, L. J. *Can. J. Chem.* **1989,** *67,* 2119–2127. doi:10.1139/v89-330
94. Arnold, D. R.; Du, X.; Chen, J. *Can. J. Chem.* **1995,** *73,* 307–318. doi:10.1139/v95-042
95. Holy, N. L.; Marcum, J. D. *Angew. Chem., Int. Ed. Engl.* **1971,** *10,* 115–124. doi:10.1002/anie.197101151
96. Romero, N. A.; Nicewicz, D. A. *J. Am. Chem. Soc.* **2014,** *136,* 17024–17035. doi:10.1021/ja506228u
97. Margrey, K. A.; Nicewicz, D. A. *Acc. Chem. Res.* **2016,** *49,* 1997–2006. doi:10.1021/acs.accounts.6b00304
98. Hamilton, D. S.; Nicewicz, D. A. *J. Am. Chem. Soc.* **2012,** *134,* 18577–18580. doi:10.1021/ja309635w
99. Wilger, D. J.; Grandjean, J.-M. M.; Lammert, T. R.; Nicewicz, D. A. *Nat. Chem.* **2014,** *6,* 720–726. doi:10.1038/nchem.2000
100. Wang, H.; Lu, Q.; Chiang, C.-W.; Luo, Y.; Zhou, J.; Wang, G.; Lei, A. *Angew. Chem., Int. Ed.* **2017,** *56,* 595–599. doi:10.1002/anie.201610000
101. Mukaiyama, T.; Sato, T.; Hanna, J. *Chem. Lett.* **1973,** *2,* 1041–1044. doi:10.1246/cl.1973.1041
102. McMurry, J. E.; Fleming, M. P. *J. Am. Chem. Soc.* **1974,** *96,* 4708–4709. doi:10.1021/ja00821a076
103. Nakajima, M.; Fava, E.; Loescher, S.; Jiang, Z.; Rueping, M. *Angew. Chem., Int. Ed.* **2015,** *54,* 8828–8832. doi:10.1002/anie.201501556
104. Gualandi, A.; Rodeghiero, G.; Della Rocca, E.; Bertoni, F.; Marchini, M.; Perciaccante, R.; Jansen, T. P.; Ceroni, P.; Cozzi, P. G. *Chem. Commun.* **2018,** *54,* 10044–10047. doi:10.1039/c8cc04048f
105. Tarantino, K. T.; Liu, P.; Knowles, R. R. *J. Am. Chem. Soc.* **2013,** *135,* 10022–10025. doi:10.1021/ja404342j
106. Trowbridge, A.; Reich, D.; Gaunt, M. J. *Nature* **2018,** *561,* 522–527. doi:10.1038/s41586-018-0537-9
107. Fuentes de Arriba, A. L.; Urbitsch, F.; Dixon, D. J. *Chem. Commun.* **2016,** *52,* 14434–14437. doi:10.1039/c6cc09172e
108. Du, J.; Skubi, K. L.; Schultz, D. M.; Yoon, T. P. *Science* **2014,** *344,* 392–396. doi:10.1126/science.1251511
109. Ma, J.; Rosales, A. R.; Huang, X.; Harms, K.; Riedel, R.; Wiest, O.; Meggers, E. *J. Am. Chem. Soc.* **2017,** *139,* 17245–17248. doi:10.1021/jacs.7b09152
110. Romero, N. A.; Margrey, K. A.; Tay, N. E.; Nicewicz, D. A. *Science* **2015,** *349,* 1326–1330. doi:10.1126/science.aac9895
111. Margrey, K. A.; McManus, J. B.; Bonazzi, S.; Zecri, F.; Nicewicz, D. A. *J. Am. Chem. Soc.* **2017,** *139,* 11288–11299. doi:10.1021/jacs.7b06715
112. Margrey, K. A.; Levens, A.; Nicewicz, D. A. *Angew. Chem., Int. Ed.* **2017,** *56,* 15644–15648. doi:10.1002/anie.201709523
113. McManus, J. B.; Nicewicz, D. A. *J. Am. Chem. Soc.* **2017,** *139,* 2880–2883. doi:10.1021/jacs.6b12708
114. Tay, N. E. S.; Nicewicz, D. A. *J. Am. Chem. Soc.* **2017,** *139,* 16100–16104. doi:10.1021/jacs.7b10076
115. Chen, W.; Huang, Z.; Tay, N. E. S.; Giglio, B.; Wang, M.; Wang, H.; Wu, Z.; Nicewicz, D. A.; Li, Z. *Science* **2019,** *364,* 1170–1174. doi:10.1126/science.aav7019
116. Holmberg-Douglas, N.; Nicewicz, D. A. *Org. Lett.* **2019,** *21,* 7114–7118. doi:10.1021/acs.orglett.9b02678
117. Bonesi, S. M.; Fagnoni, M. *Chem. – Eur. J.* **2010,** *16,* 13572–13589. doi:10.1002/chem.201001478
118. Chen, M.; Zhao, X.; Yang, C.; Xia, W. *Org. Lett.* **2017,** *19,* 3807–3810. doi:10.1021/acs.orglett.7b01677
119. Chatterjee, A.; König, B. *Angew. Chem., Int. Ed.* **2019,** *58,* 14289–14294. doi:10.1002/anie.201905485
120. Mizuno, K.; Ikeda, M.; Otsuji, Y. *Tetrahedron Lett.* **1985,** *26,* 461–464. doi:10.1016/s0040-4039(00)61911-1
121. Tsujimoto, K.; Nakao, N.; Ohashi, M. *J. Chem. Soc., Chem. Commun.* **1992,** 366–367. doi:10.1039/c39920000366
122. Arceo, E.; Jurberg, I. D.; Álvarez-Fernández, A.; Melchiorre, P. *Nat. Chem.* **2013,** *5,* 750–756. doi:10.1038/nchem.1727
123. Crisenza, G. E. M.; Mazzarella, D.; Melchiorre, P. *J. Am. Chem. Soc.* **2020,** *142,* 5461–5476. doi:10.1021/jacs.0c01416
124. Zard, S. Z. *Chem. Soc. Rev.* **2008,** *37,* 1603. doi:10.1039/b613443m
125. Xiong, T.; Zhang, Q. *Chem. Soc. Rev.* **2016,** *45,* 3069–3087. doi:10.1039/c5cs00852b
126. Chen, J.-R.; Hu, X.-Q.; Lu, L.-Q.; Xiao, W.-J. *Chem. Soc. Rev.* **2016,** *45,* 2044–2056. doi:10.1039/c5cs00655d
127. Kärkäs, M. D. *ACS Catal.* **2017,** *7,* 4999–5022. doi:10.1021/acscatal.7b01385
128. Davies, J.; Morcillo, S. P.; Douglas, J. J.; Leonori, D. *Chem. – Eur. J.* **2018,** *24,* 12154–12163. doi:10.1002/chem.201801655
129. Zhao, Y.; Xia, W. *Chem. Soc. Rev.* **2018,** *47,* 2591–2608. doi:10.1039/c7cs00572e
130. Stateman, L.; Nakafuku, K.; Nagib, D. *Synthesis* **2018,** *50,* 1569–1586. doi:10.1055/s-0036-1591930
131. Jiang, H.; Studer, A. *Chem. Soc. Rev.* **2020,** *49,* 1790–1811. doi:10.1039/c9cs00692c
132. Kumar, G.; Pradhan, S.; Chatterjee, I. *Chem. – Asian J.* **2020,** *15,* 651–672. doi:10.1002/asia.201901744
133. Horner, J. H.; Musa, O. M.; Bouvier, A.; Newcomb, M. *J. Am. Chem. Soc.* **1998,** *120,* 7738–7748. doi:10.1021/ja981244a

134. Davies, J.; Svejstrup, T. D.; Fernandez Reina, D.; Sheikh, N. S.; Leonori, D. *J. Am. Chem. Soc.* **2016,** *138,* 8092–8095. doi:10.1021/jacs.6b04920
135. Morcillo, S. P.; Dauncey, E. M.; Kim, J. H.; Douglas, J. J.; Sheikh, N. S.; Leonori, D. *Angew. Chem., Int. Ed.* **2018,** *57,* 12945–12949. doi:10.1002/anie.201807941
136. Walton, J. *Molecules* **2016,** *21,* 63. doi:10.3390/molecules21010063
137. Shi, L.; Xia, W. *Chem. Soc. Rev.* **2012,** *41,* 7687. doi:10.1039/c2cs35203f
138. Hu, J.; Wang, J.; Nguyen, T. H.; Zheng, N. *Beilstein J. Org. Chem.* **2013,** *9,* 1977–2001. doi:10.3762/bjoc.9.234
139. Jiang, H.; Studer, A. *CCS Chem.* **2019,** 38–49. doi:10.31635/ccschem.019.20180026
140. Davies, J.; Booth, S. G.; Essafi, S.; Dryfe, R. A. W.; Leonori, D. *Angew. Chem., Int. Ed.* **2015,** *54,* 14017–14021. doi:10.1002/anie.201507641
141. Davies, J.; Sheikh, N. S.; Leonori, D. *Angew. Chem., Int. Ed.* **2017,** *56,* 13361–13365. doi:10.1002/anie.201708497
142. Jiang, H.; Studer, A. *Angew. Chem., Int. Ed.* **2017,** *56,* 12273–12276. doi:10.1002/anie.201706270
143. Dauncey, E. M.; Morcillo, S. P.; Douglas, J. J.; Sheikh, N. S.; Leonori, D. *Angew. Chem., Int. Ed.* **2018,** *57,* 744–748. doi:10.1002/anie.201710790
144. Le Vaillant, F.; Garreau, M.; Nicolai, S.; Gryn'ova, G.; Corminboeuf, C.; Waser, J. *Chem. Sci.* **2018,** *9,* 5883–5889. doi:10.1039/c8sc01818a
145. Tian, W.-F.; Wang, D.-P.; Wang, S.-F.; He, K.-H.; Cao, X.-P.; Li, Y. *Org. Lett.* **2018,** *20,* 1421–1425. doi:10.1021/acs.orglett.8b00193
146. Pandey, G.; Laha, R. *Angew. Chem., Int. Ed.* **2015,** *54,* 14875–14879. doi:10.1002/anie.201506990
147. Chen, H.; Guo, L.; Yu, S. *Org. Lett.* **2018,** *20,* 6255–6259. doi:10.1021/acs.orglett.8b02737
148. Moon, Y.; Park, B.; Kim, I.; Kang, G.; Shin, S.; Kang, D.; Baik, M.-H.; Hong, S. *Nat. Commun.* **2019,** *10,* 4117. doi:10.1038/s41467-019-12216-3
149. Jiang, H.; Studer, A. *Angew. Chem., Int. Ed.* **2018,** *57,* 10707–10711. doi:10.1002/anie.201804966
150. Hari, D. P.; König, B. *Org. Lett.* **2011,** *13,* 3852–3855. doi:10.1021/ol201376v
151. Condie, A. G.; González-Gómez, J. C.; Stephenson, C. R. J. *J. Am. Chem. Soc.* **2010,** *132,* 1464–1465. doi:10.1021/ja909145y
152. Pan, Y.; Kee, C. W.; Chen, L.; Tan, C.-H. *Green Chem.* **2011,** *13,* 2682. doi:10.1039/c1gc15489c
153. Xuan, J.; Xia, X.-D.; Zeng, T.-T.; Feng, Z.-J.; Chen, J.-R.; Lu, L.-Q.; Xiao, W.-J. *Angew. Chem., Int. Ed.* **2014,** *53,* 5653–5656. doi:10.1002/anie.201400602
154. Muriel, B.; Gagnebin, A.; Waser, J. *Chem. Sci.* **2019,** *10,* 10716–10722. doi:10.1039/c9sc03790j
155. Garreau, M.; Le Vaillant, F.; Waser, J. *Angew. Chem., Int. Ed.* **2019,** *58,* 8182–8186. doi:10.1002/anie.201901922
156. Hu, X.-Q.; Chen, J.; Chen, J.-R.; Yan, D.-M.; Xiao, W.-J. *Chem. – Eur. J.* **2016,** *22,* 14141–14146. doi:10.1002/chem.201602597
157. Guo, J.-J.; Hu, A.; Zuo, Z. *Tetrahedron Lett.* **2018,** *59,* 2103–2111. doi:10.1016/j.tetlet.2018.04.060
158. Capaldo, L.; Ravelli, D. *Chem. Commun.* **2019,** *55,* 3029–3032. doi:10.1039/c9cc00035f
159. Wu, X.; Zhu, C. *Chem. Commun.* **2019,** *55,* 9747–9756. doi:10.1039/c9cc04785a
160. Kim, I.; Park, B.; Kang, G.; Kim, J.; Jung, H.; Lee, H.; Baik, M.-H.; Hong, S. *Angew. Chem., Int. Ed.* **2018,** *57,* 15517–15522. doi:10.1002/anie.201809879
161. Kim, Y.; Lee, K.; Mathi, G. R.; Kim, I.; Hong, S. *Green Chem.* **2019,** *21,* 2082–2087. doi:10.1039/c9gc00414a
162. Quint, V.; Morlet-Savary, F.; Lohier, J.-F.; Lalevée, J.; Gaumont, A.-C.; Lakhdar, S. *J. Am. Chem. Soc.* **2016,** *138,* 7436–7441. doi:10.1021/jacs.6b04069
163. Devari, S.; Rizvi, M. A.; Shah, B. A. *Tetrahedron Lett.* **2016,** *57,* 3294–3297. doi:10.1016/j.tetlet.2016.06.046
164. Zhu, X.; Xie, X.; Li, P.; Guo, J.; Wang, L. *Org. Lett.* **2016,** *18,* 1546–1549. doi:10.1021/acs.orglett.6b00304
165. Li, J.; Zhang, J.; Tan, H.; Wang, D. Z. *Org. Lett.* **2015,** *17,* 2522–2525. doi:10.1021/acs.orglett.5b01053
166. Dénès, F.; Pichowicz, M.; Povie, G.; Renaud, P. *Chem. Rev.* **2014,** *114,* 2587–2693. doi:10.1021/cr400441m
167. Glass, R. S. *Top. Curr. Chem.* **2018,** *376,* 22. doi:10.1007/s41061-018-0197-0
168. Zubkov, M. O.; Kosobokov, M. D.; Levin, V. V.; Kokorekin, V. A.; Korlyukov, A. A.; Hu, J.; Dilman, A. D. *Chem. Sci.* **2020,** *11,* 737–741. doi:10.1039/c9sc04643g
169. Limnios, D.; Kokotos, C. G. *Adv. Synth. Catal.* **2017,** *359,* 323–328. doi:10.1002/adsc.201600977
170. Guerrero-Corella, A.; Martinez-Gualda, A. M.; Ahmadi, F.; Ming, E.; Fraile, A.; Alemán, J. *Chem. Commun.* **2017,** *53,* 10463–10466. doi:10.1039/c7cc05672a
171. Zalesskiy, S. S.; Shlapakov, N. S.; Ananikov, V. P. *Chem. Sci.* **2016,** *7,* 6740–6745. doi:10.1039/c6sc02132h
172. Chaudhary, R.; Natarajan, P. *ChemistrySelect* **2017,** *2,* 6458–6479. doi:10.1002/slct.201701156
173. Zhao, Y.; Gong, H.; Jiang, K.; Yan, S.; Lin, J.; Chen, M. *Macromolecules* **2018,** *51,* 938–946. doi:10.1021/acs.macromol.8b00134
174. Hell, S. M.; Meyer, C. F.; Laudadio, G.; Misale, A.; Willis, M. C.; Noël, T.; Trabanco, A. A.; Gouverneur, V. *J. Am. Chem. Soc.* **2020,** *142,* 720–725. doi:10.1021/jacs.9b13071
175. Yang, W.; Yang, S.; Li, P.; Wang, L. *Chem. Commun.* **2015,** *51,* 7520–7523. doi:10.1039/c5cc00878f
176. Huang, M.-H.; Zhu, Y.-L.; Hao, W.-J.; Wang, A.-F.; Wang, D.-C.; Liu, F.; Wei, P.; Tu, S.-J.; Jiang, B. *Adv. Synth. Catal.* **2017,** *359,* 2229–2234. doi:10.1002/adsc.201700124
177. Storozhenko, O. A.; Festa, A. A.; Detistova, G. I.; Rybakov, V. B.; Varlamov, A. V.; Van der Eycken, E. V.; Voskressensky, L. G. *J. Org. Chem.* **2020,** *85,* 2250–2259. doi:10.1021/acs.joc.9b02960
178. Zhang, G.; Zhang, L.; Yi, H.; Luo, Y.; Qi, X.; Tung, C.-H.; Wu, L.-Z.; Lei, A. *Chem. Commun.* **2016,** *52,* 10407–10410. doi:10.1039/c6cc04109d
179. Ghogare, A. A.; Greer, A. *Chem. Rev.* **2016,** *116,* 9994–10034. doi:10.1021/acs.chemrev.5b00726
180. Metternich, J. B.; Gilmour, R. *J. Am. Chem. Soc.* **2015,** *137,* 11254–11257. doi:10.1021/jacs.5b07136
181. Livingstone, K.; Tenberge, M.; Pape, F.; Daniliuc, C. G.; Jamieson, C.; Gilmour, R. *Org. Lett.* **2019,** *21,* 9677–9680. doi:10.1021/acs.orglett.9b03842
182. Faßbender, S. I.; Molloy, J. J.; Mück-Lichtenfeld, C.; Gilmour, R. *Angew. Chem., Int. Ed.* **2019,** *58,* 18619–18626. doi:10.1002/anie.201910169
183. Onneken, C.; Bussmann, K.; Gilmour, R. *Angew. Chem., Int. Ed.* **2020,** *59,* 330–334. doi:10.1002/anie.201911651

184. Cai, W.; Fan, H.; Ding, D.; Zhang, Y.; Wang, W. *Chem. Commun.* **2017,** *53,* 12918–12921. doi:10.1039/c7cc07984b
185. Lu, J.; Pattengale, B.; Liu, Q.; Yang, S.; Shi, W.; Li, S.; Huang, J.; Zhang, J. *J. Am. Chem. Soc.* **2018,** *140,* 13719–13725. doi:10.1021/jacs.8b07271
186. Alonso, R.; Bach, T. *Angew. Chem., Int. Ed.* **2014,** *53,* 4368–4371. doi:10.1002/anie.201310997
187. Kumarasamy, E.; Raghunathan, R.; Jockusch, S.; Ugrinov, A.; Sivaguru, J. *J. Am. Chem. Soc.* **2014,** *136,* 8729–8737. doi:10.1021/ja5034638
188. Mojr, V.; Svobodová, E.; Straková, K.; Neveselý, T.; Chudoba, J.; Dvořáková, H.; Cibulka, R. *Chem. Commun.* **2015,** *51,* 12036–12039. doi:10.1039/c5cc01344e
189. Silvi, M.; Melchiorre, P. *Nature* **2018,** *554,* 41–49. doi:10.1038/nature25175
190. Bottecchia, C.; Noël, T. *Chem. – Eur. J.* **2019,** *25,* 26–42. doi:10.1002/chem.201803074
191. Capaldo, L.; Quadri, L. L.; Ravelli, D. *Angew. Chem., Int. Ed.* **2019,** *58,* 17508–17510. doi:10.1002/anie.201910348
192. Yu, Y.; Guo, P.; Zhong, J.-S.; Yuan, Y.; Ye, K.-Y. *Org. Chem. Front.* **2020,** *7,* 131–135. doi:10.1039/c9qo01193e

License and Terms

This is an Open Access article under the terms of the Creative Commons Attribution License (http://creativecommons.org/licenses/by/4.0). Please note that the reuse, redistribution and reproduction in particular requires that the authors and source are credited.

The license is subject to the *Beilstein Journal of Organic Chemistry* terms and conditions: (https://www.beilstein-journals.org/bjoc)

The definitive version of this article is the electronic one which can be found at: doi:10.3762/bjoc.16.103

BEILSTEIN JOURNAL OF ORGANIC CHEMISTRY

Photocatalytic trifluoromethoxylation of arenes and heteroarenes in continuous-flow

Alexander V. Nyuchev[1], Ting Wan[1], Borja Cendón[1,2], Carlo Sambiagio[1], Job J. C. Struijs[1], Michelle Ho[1], Moisés Gulías[2], Ying Wang[3] and Timothy Noël[*1]

Full Research Paper

Open Access

Address:
[1]Micro Flow Chemistry and Synthetic Methodology, Department of Chemical Engineering and Chemistry, Eindhoven University of Technology, Het Kranenveld, Bldg 14 – Helix, 5600 MB Eindhoven, The Netherlands, [2]Centro Singular de Investigación en Química Biolóxica e Materiais Moleculares (CIQUS) and Departamento de Química Orgánica, Universidade de Santiago de Compostela, 15782 Santiago de Compostela, Spain and [3]Discovery Chemistry and Technologies, AbbVie Inc., 1 North Waukegan, Road, North Chicago, Illinois 60064, United States of America

Email:
Timothy Noël* - t.noel@tue.nl

* Corresponding author

Keywords:
C–H functionalization; continuous-flow; organic synthesis; photoredox catalysis; trifluoromethoxylation

Beilstein J. Org. Chem. **2020,** *16,* 1305–1312.
doi:10.3762/bjoc.16.111

Received: 12 April 2020
Accepted: 24 May 2020
Published: 15 June 2020

This article is part of the thematic issue "Advances in photoredox catalysis".

Associate Editor: B. Nay

© 2020 Nyuchev et al.; licensee Beilstein-Institut.
License and terms: see end of document.

Abstract

The first example of photocatalytic trifluoromethoxylation of arenes and heteroarenes under continuous-flow conditions is described. Application of continuous-flow microreactor technology allowed to reduce the residence time up to 16 times in comparison to the batch procedure, while achieving similar or higher yields. In addition, the use of inorganic bases was demonstrated to increase the reaction yield under batch conditions.

Introduction

The number of fluorine-containing compounds and their influence in medicine and agrochemistry are increasing every year [1,2]. The introduction in a drug (or a bioactive compound in general) of single fluorine atoms, or multiple fluorine-containing substituents, such as -CF_3, -SCF_3, -CF_2H/-CF_2-, has a range of effects on the pharmacokinetics and pharmacodynamics of the molecule [3]. Among other fluorine-based substituents, the trifluoromethoxy group (-OCF_3) has until recently remained less explored and understood [4]. Nonetheless, it possesses unique properties, for example, a high electronegativity (χ = 3.7), and a high lipophilicity (Hansch-Leo parameter π = 1.04, intermediate between the -CF_3 and the -SCF_3 values, respectively, 0.88 and 1.44) [4]. From a pharmaceutical perspective, the former property provides stability of the drug under physiological conditions, and the latter ensures better solubility and transport across the physiological lipophilic environment (e.g., dissolution in lymph and cell membrane penetration) [5]. In trifluoromethoxylated aryls, the -OCF_3 group

assumes a peculiar orthogonal conformation relative to the aromatic ring, partially due to the hyperconjugation of an oxygen lone pair with an antibonding C–F orbital, and partially to the steric hindrance of the -CF_3 group [6,7]. These interactions result in a relative conformational flexibility, where the -OCF_3 group can rotate between the two sides of the aromatic ring (Scheme 1A). This property might be responsible for stronger binding affinities of trifluoromethoxylated compounds

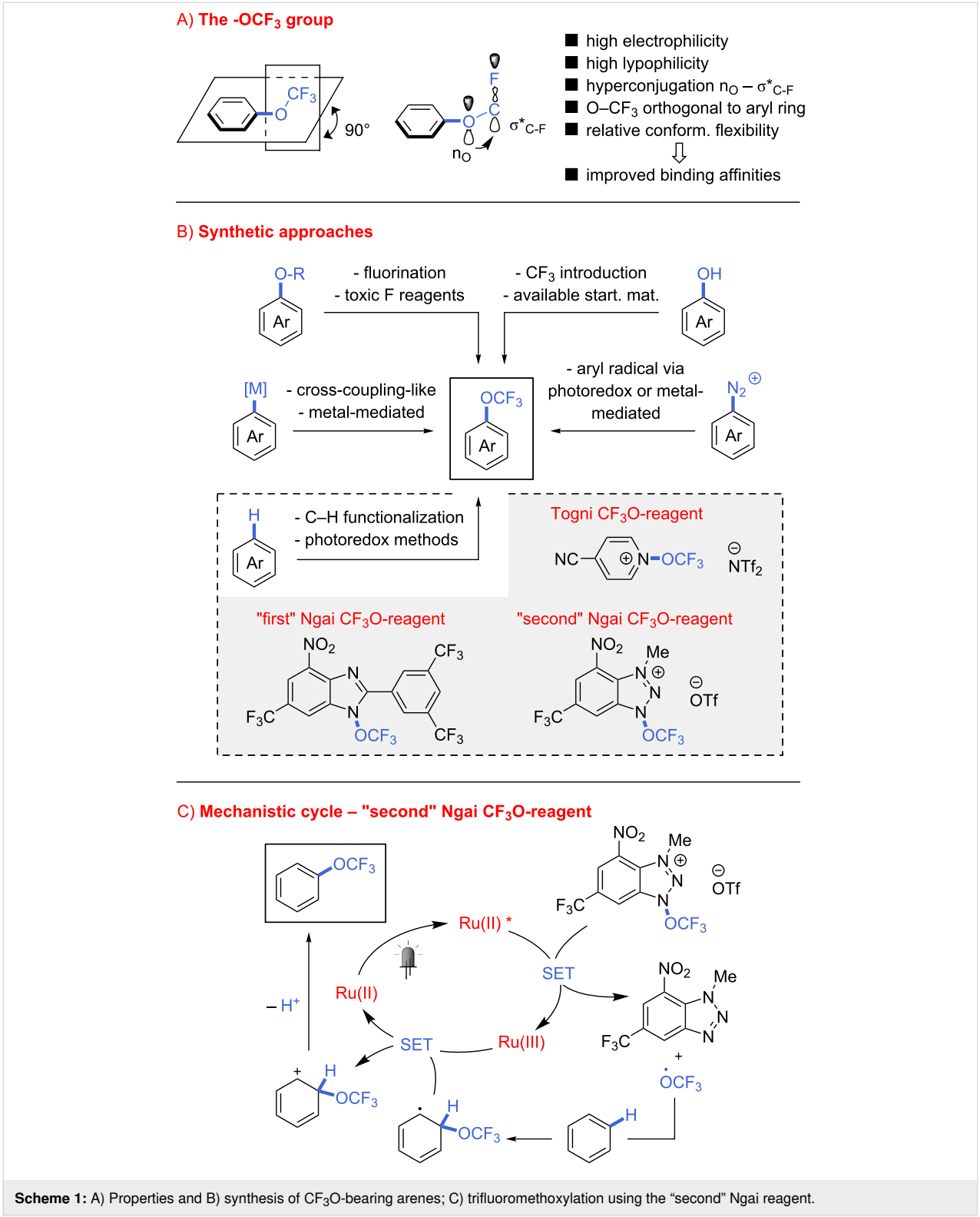

Scheme 1: A) Properties and B) synthesis of CF_3O-bearing arenes; C) trifluoromethoxylation using the “second” Ngai reagent.

with the active sites in enzymes, proteins, or other biomolecules [8,9].

Several procedures for the synthesis of trifluoromethyl aryl ethers were reported from the mid-1900s, mostly based on the transformation of pre-functionalized aryls, such as trichloromethyl ethers, fluoroformates, or carbonochloridothionate derivatives. These procedures typically required harsh conditions and the use of aggressive and toxic chemicals like BF_3, HF, MoF_6, SF_4, and SbF_3 [10]. Alternative approaches were recently reported [8,9,11], for example the trifluoromethylation of hydroxyaryls [12-14], and the direct introduction of the -OCF_3 moiety into an organometallic species [15], a diazo compound [16,17], or an unfunctionalized C–H bond (Scheme 1B). The latter method is particularly interesting, partially due to the general interest of the community into C–H functionalization methodologies [18,19], and partially thanks to the synthetic possibilities enabled by photoredox catalysis, a field widely explored in recent years [20-22]. In 2018, Ngai [23,24] and Togni [25] reported simple photoredox protocols for the radical trifluoromethoxylation of unfunctionalized (hetero)arenes by using specifically designed CF_3O radical-releasing agents (Scheme 1B).

Table 1: Reaction optimization under flow conditions.

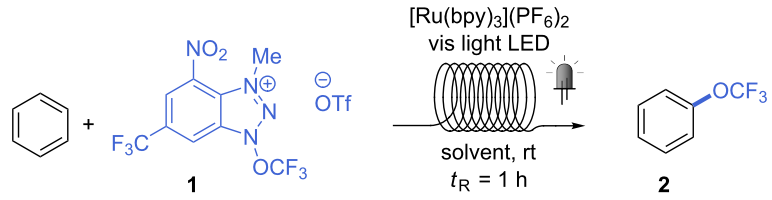

Entry	Equiv of substrate	Solvent, conc. of **1** (M)	Light source	Cat. (%)	Yield (%)[a]
1	25	CH_3CN/CH_2Cl, 0.04	465 nm, 18 W	1	40
2	25	CH_3CN/CH_2Cl, 0.04	400 nm, 10 W	1	52
3	25	CH_3CN, 0.04	400 nm, 10 W	1	53
4	25	CH_3CN, 0.04	400 nm, 10 W	2	68
5	25	CH_3CN, 0.08	400 nm, 10 W	1	65
6	25	CH_3CN, 0.08	400 nm, 10 W	2	64
7	10	CH_3CN, 0.08	400 nm, 10 W	1	57
8	10	CH_3CN, 0.08	400 nm, 10 W	1	63[b]
9	10	CH_3CN, 0.2	400 nm, 10 W	1	61
10	**10**	**CH_3CN, 0.08**	**400 nm, 10 W**	**1**	**73[c]**
		control experiments			
11	25	CH_3CN, 0.04	465 nm, 18 W	1	10[d]
12	25	CH_3CN, 0.04	400 nm, 10 W	0	17
13	25	CH_3CN, 0.04	465 nm, 18 W	0	0

[a] ^{19}F NMR yields are reported; [b] Degassed solvent; [c] Freshly prepared; [d] $[Ir(dtbbpy)(ppy)_2]PF_6$ as catalyst.

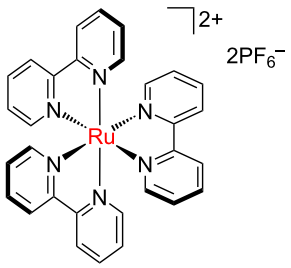

$[Ru(bpy)_3](PF_6)_2$

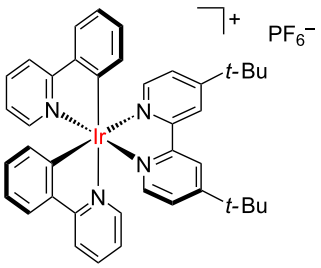

$[Ir(dtbbpy)(ppy)_2]PF_6$

Following our long-standing interest in the development of continuous-flow approaches for C–H functionalization [18,26] and photochemical methodologies [27-31], herein we report the first application of flow methods for the direct trifluoromethoxylation of arenes and heteroarenes.

Results and Discussion

Among the three reagents shown in Scheme 1B, we decided to use the "second" Ngai reagent (**1**, Scheme 1C) for our investigation, as less side-products (derived from alternative radical formation from the other two reagents [23,25]) and tolerance towards water and air gives this reagent a certain advantage over the others [24]. To transfer the batch procedure into continuous-flow conditions, the concentration of **1** was initially decreased from the original 0.2 M to 0.04 M, and the amount of substrate increased from 10 to 25 equivalents, while the same catalyst ($[Ru(bpy)_3](PF_6)_2$) and reaction medium (CH_3CN/CH_2Cl_2 1:1) were used. Upon irradiation with blue light (465 nm, 18 W LED), the desired trifluoromethoxybenzene (**2**) was obtained in 40% yield after a residence time of 1 h (Table 1, entry 1). A 400 nm LED light led to a higher yield (52%, Table 1, entry 2), thus this light source was used for further investigations. As CH_2Cl_2 is not a recommended solvent, especially for industrial and pharmaceutical applications [32], we tested the reaction in pure acetonitrile. As the same yield was obtained (Table 1, entry 3), this solvent was chosen as reaction medium for the following experiments. Either doubling the amount of catalyst or reducing the concentration resulted in considerably higher reaction yields (68 and 65%, Table 1, entries 4 and 5). Increased catalyst loading at 0.08 M produced no improvement (Table 1, entry 6). We next tested the reaction using a lower excess of substrate (10 equiv), obtaining product **2** in 57% yield (Table 1, entry 7). Little improvement was seen upon degassing the reaction mixture prior to the reaction (three freeze-pump-thaw cycles, 63%, Table 1, entry 8). Performing the reaction at 0.2 M concentration gave 61% yield (Table 1, entry 9). Last, we were particularly pleased to see that a sensible increase in yield could be obtained by using a freshly prepared reagent **1** in the reaction (the activity of reagent **1** persists at a primary level during near two weeks when stored in the dark at −20 °C). A yield of 73% could be achieved at 0.08 M, without the tedious degassing procedure (Table 1, entry 10).

Finally, a few control experiments were performed (Table 1, entries 11–13). A more expensive Ir photocatalyst was tested under blue light irradiation, but a poor 10% yield was obtained. Experiments in the absence of photocatalyst under violet or blue light gave respectively 17% and 0% yield. The little product obtained with 400 nm light can be explained by the photodecomposition of **1**, which generates small amounts of CF_3O radical (this has been shown for the "first" Ngai reagent [23]).

Under the conditions shown in Table 1, entry 10, we then set to figure out the optimal residence time (t_R) for the reaction (Scheme 2). Yields of around 70% were observed for the trifluoromethoxylation of benzene even at 20 minutes residence time, which demonstrates the effectiveness of the flow process (a yield of 63% was obtained in batch over 16 h [24]). However, unreacted **1** was observed at this residence time, and full conversion could be obtained only after 1 h. Moreover, a resi-

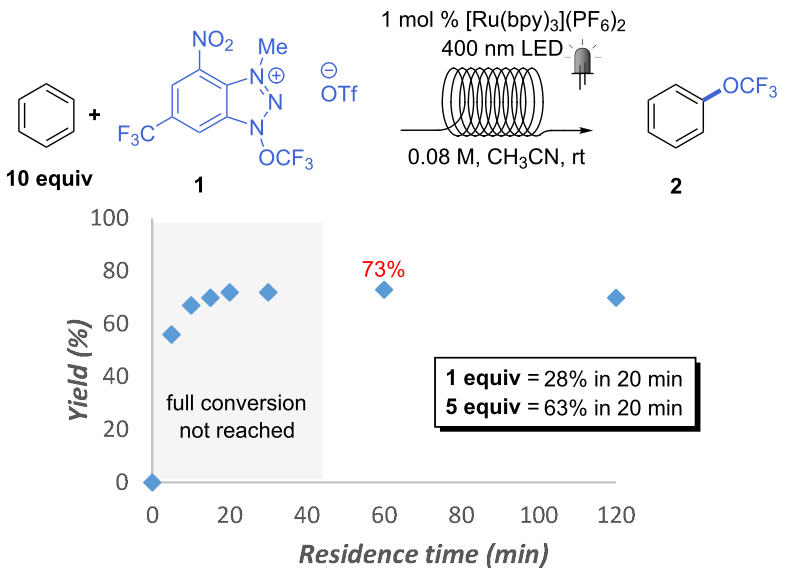

Scheme 2: Optimization of residence time. ^{19}F NMR yields are reported.

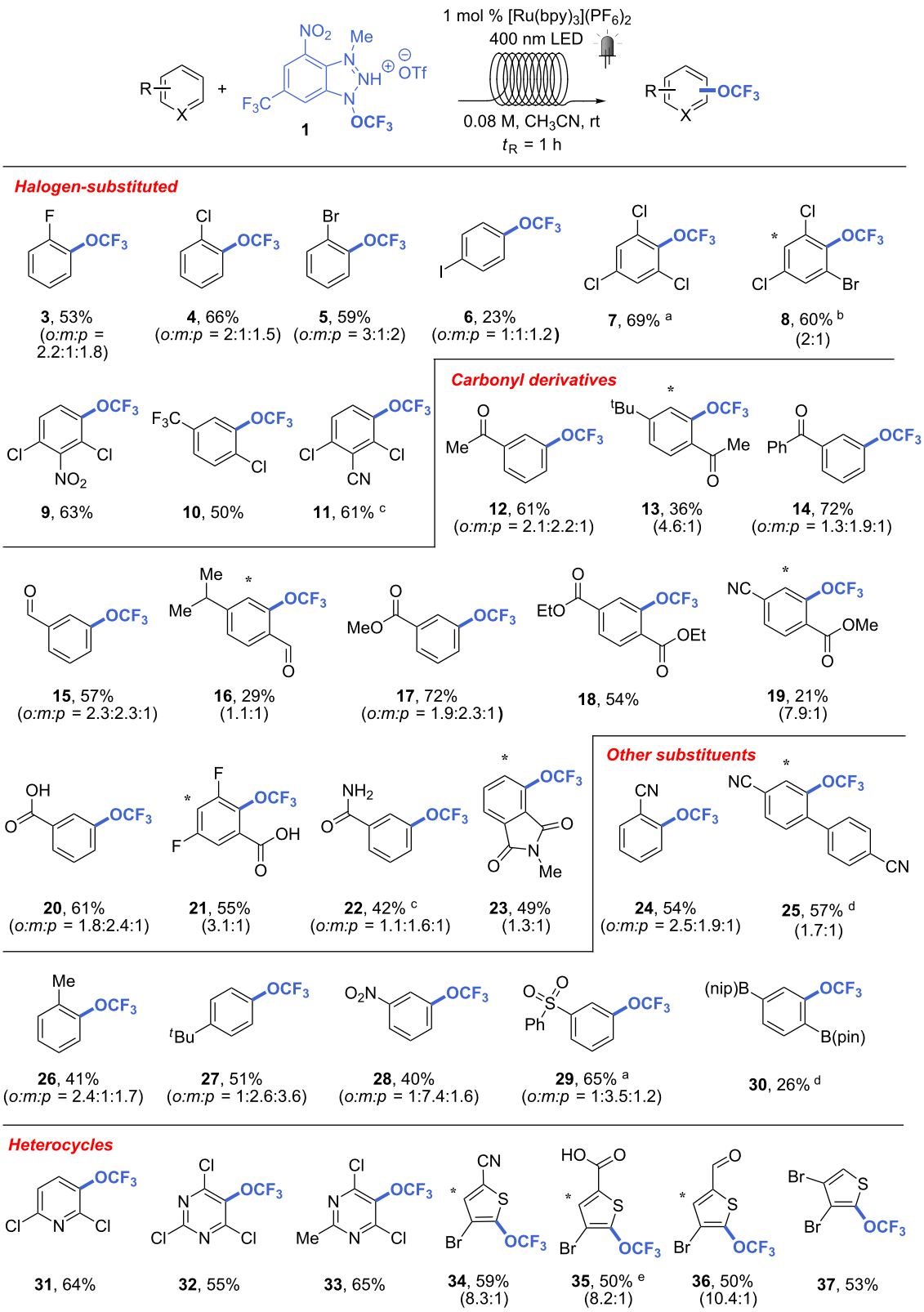

Scheme 3: Scope of photoredox trifluoromethoxylation in continuous-flow. In case of different products, the major isomer is shown. The position of the CF_3O group in the minor isomer is marked with a star. ^{19}F NMR yields are reported. [a] CH_3CN/CH_2Cl_2 3:2, 0.08 M; [b] CH_3CN/CH_2Cl_2 1:1, 0.05 M; [c] CH_3CN/CH_2Cl_2 5:3, 0.05 M; [d] CH_3CN/CH_2Cl_2 3:2, 0.02 M; [e] CH_3CN/CH_2Cl_2 5:4, 0.057 M.

dence time of 20 minutes proved not sufficient for several other substrates, thus 1 h was chosen as the standard for the following scope. It is worth mentioning that a lower excess of substrate at 20 minutes residence time gave much lower yields of **2** (63 and 28% for 5 and 1 equiv, respectively).

With the optimized conditions in hands, we proceeded to investigate the trifluoromethoxylation of different arenes and heteroarenes in acetonitrile. Solvent mixtures and lower concentrations had to be used in some cases due to solubility issues. As can be seen in Scheme 3, trifluoromethoxylation occurs preferentially at the most electron-rich site of the arenes, although sensitivity to steric hindrance was observed. The reactions with halogenated aryls occurred smoothly, leading to products **3**–**11** in good yields. An exception is represented by iodobenzene, which could be methoxylated in only 23% yield (product **6**). Similar results were obtained with carbonyl-containing compounds. Different aromatic ketones, aldehydes, esters, and carboxylic acids were transformed to the corresponding trifluoromethoxylated compounds (**12**–**23**) with generally good to high yields, except for **13**, **16**, **19** and **22** which were obtained in moderate or poor yields. Other synthetically useful substituents, including cyano, nitro, phenylsulphonyl, (pinacolato)boron, and alkyl groups could be tolerated in the reaction (**24**–**30**), leading to a yield range between 26 and 65%. The trifluoromethoxylation of pyridine, pyrimidine, and thiophene derivatives also took place smoothly, giving products **31**–**37** in good yields (50–65%).

Overall, the yields obtained for different products were similar to those reported by Ngai [24] and Togni [25] using batch protocols. In addition, in comparison with Ngai's protocol, this flow method allows for a much reduced reaction (residence) time, therefore, demonstrating the potentials of this technology

Table 2: Influence of bases on the photoredox trifluoromethoxylation in batch and flow.

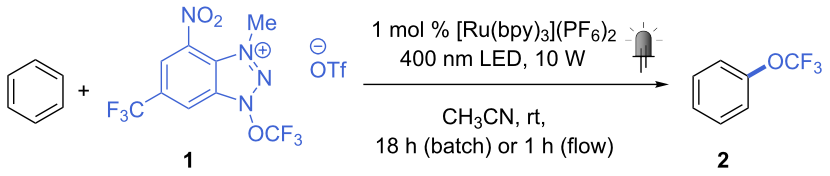

Entry	Equiv of substrate	Conc. of **1** (M)	Base	Yield (%)[a]
			organic/soluble bases	
1	10	0.08	$(Bu_4N)H_2PO_4$, 1 equiv	20
2	10	0.08	$(Bu_4N)H_2PO_4$, 1 equiv	6 (flow)
3	25	0.04	DIPEA, 1 equiv	18
4	25	0.04	DBU, 1 equiv	14 (flow)
5	25	0.04	$(Bu_4N)OAc$, 1 equiv	0 (flow)
			inorganic bases	
6	25	0.04	K_2CO_3, 1 equiv	54
7	25	0.04	K_2HPO_4, 1 equiv	86
8	25	0.04	K_2HPO_4, 1 equiv	7[b] (flow)
9	10	0.04	K_2HPO_4, 1 equiv	68
10	10	0.08	K_2HPO_4, 1 equiv	78
11	10	0.08	K_2HPO_4, 0.5 equiv	78
12	10	0.08	K_2HPO_4, 0.25 equiv	77
13	10	0.08	K_2HPO_4, 2 equiv	70
14	**10**	**0.08**	**KH_2PO_4, 1 equiv**	**89**
15	**10**	**0.08**	**KH_2PO_4, 1 equiv**	**75[c] (flow)**
16	10	0.08	KH_2PO_4, 0.5 equiv	64
17	10	0.08	KH_2PO_4, 0.25 equiv	63
18	10	0.08	KH_2PO_4, 2 equiv	78
19	10	0.08	K_3PO_4, 1 equiv	54

[a] ^{19}F NMR yields are reported; [b] 100 equiv of H_2O added; [c] 5 minutes of irradiation in batch before flow reaction.

for the synthesis of trifluoromethoxylated compounds. The use of acetonitrile as solvent, rather than the CH_3CN/CH_2Cl_2 mixture previously used [24], further increase the value of this protocol [32] for the synthesis of medicinally relevant molecules.

Based on the reaction mechanism proposed by Ngai and co-authors (Scheme 1C) [24], we hypothesized that the addition of base could potentially improve the reaction outcome. To prove this idea, we performed a series of experiments under batch and flow conditions (Table 2). Organic or soluble bases such as amines and tetrabutylammonium salts (Table 2, entries 1–5) proved unfortunately not successful, neither in batch nor flow, so we extended the investigation to inorganic bases. Among the bases tested, potassium hydrogenphosphates K_2HPO_4 and KH_2PO_4 led to increased yields, reaching up to 86% or 89% in batch (Table 2, entries 7 and 14). Because of the high yields obtained, the use of these bases in flow was investigated. The addition of water [33] allows these bases to be solubilized, preventing clogging; however, this strategy led to a mere 7% yield (Table 2, entry 8). During batch experiments we noted that after several minutes of irradiation, a homogeneous solution was obtained. Thus, we thought of using this trick for the flow process: irradiation of the reaction mixture in batch for 5 minutes, followed by injection into the microcapillary, provided **2** in 75% yield (Table 2, entry 15).

These conditions were also applied to a few other substrates, for the sake of comparison (Figure 1).

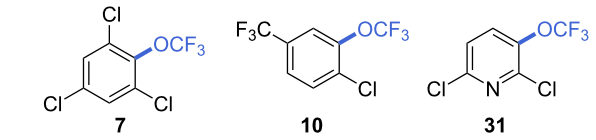

Figure 1: Effect of KH_2PO_4 – other substrates. [a] Conditions as for entry 15 (Table 2), 1 h residence time; [b] conditions as for entry 14 (Table 2), 18 h reaction time; [c] 0.5 equiv KH_2PO_4, CH_3CN/CH_2Cl_2 1:1; [d] 2 equiv KH_2PO_4. ^{19}F NMR yields are reported.

Under flow conditions, products **7**, **10**, and **31** were obtained in yields comparable to the base-free method. However, the addition of KH_2PO_4 in batch results in considerably improved yields for the same compounds (64–92%). These experiments demonstrated that the addition of bases indeed represent an interesting modification of the previous protocol, despite being substrate-dependent.

Conclusion

In summary, we have developed the first continuous-flow trifluoromethoxylation of arenes and heteroarenes. The use of flow photochemistry allows the reaction to occur 16 times faster than in batch, while at the same time achieving similar yields. Thanks to the intrinsic properties of microflow systems, especially for the scale-up of photochemical processes, we anticipate this procedure could be useful in medicinal chemistry applications. In addition, although no beneficial effect could be achieved in flow by the addition of bases, we proved this has a significant effect on the reaction in batch, leading to higher yields. This discovery will be useful for the development of future trifluoromethoxylation methodologies.

Supporting Information

Supporting Information File 1

Procedure for continuous-flow and batch trifluoromethoxylation reactions and ^{19}F NMR spectra of compounds **2**–**37**.
[https://www.beilstein-journals.org/bjoc/content/supplementary/1860-5397-16-111-S1.pdf]

Funding

We acknowledge financial support from AbbVie. T.W. acknowledges support from the China Scholarship Council (CSC). B.C. thanks MINECO for the FPI fellowship BES-2017-079784. C.S. acknowledges the European Union for a Marie Curie European post-doctoral fellowship (FlowAct, Grant No. 794072).

ORCID® iDs

Alexander V. Nyuchev - https://orcid.org/0000-0002-0460-0543
Ting Wan - https://orcid.org/0000-0002-3520-9723
Borja Cendón - https://orcid.org/0000-0003-1783-0839
Carlo Sambiagio - https://orcid.org/0000-0001-8536-103X
Job J. C. Struijs - https://orcid.org/0000-0002-6051-2927
Michelle Ho - https://orcid.org/0000-0002-8041-112X
Moisés Gulías - https://orcid.org/0000-0001-8093-2454
Ying Wang - https://orcid.org/0000-0001-9516-3483
Timothy Noël - https://orcid.org/0000-0002-3107-6927

References

1. Szpera, R.; Moseley, D. F. J.; Smith, L. B.; Sterling, A. J.; Gouverneur, V. *Angew. Chem., Int. Ed.* **2019,** *58,* 14824–14848. doi:10.1002/anie.201814457
2. Mei, H.; Han, J.; Fustero, S.; Medio-Simon, M.; Sedgwick, D. M.; Santi, C.; Ruzziconi, R.; Soloshonok, V. A. *Chem. – Eur. J.* **2019,** *25,* 11797–11819. doi:10.1002/chem.201901840
3. Purser, S.; Moore, P. R.; Swallow, S.; Gouverneur, V. *Chem. Soc. Rev.* **2008,** *37,* 320–330. doi:10.1039/b610213c

4. Jeschke, P.; Baston, E.; Leroux, F. R. *Mini-Rev. Med. Chem.* **2007,** *7,* 1027–1034. doi:10.2174/138955707782110150
5. Landry, M. L.; Crawford, J. J. *ACS Med. Chem. Lett.* **2020,** *11,* 72–76. doi:10.1021/acsmedchemlett.9b00489
6. Lee, K. N.; Lei, Z.; Morales-Rivera, C. A.; Liu, P.; Ngai, M.-Y. *Org. Biomol. Chem.* **2016,** *14,* 5599–5605. doi:10.1039/c6ob00132g
7. Federsel, D.; Herrmann, A.; Christen, D.; Sander, S.; Willner, H.; Oberhammer, H. *J. Mol. Struct.* **2001,** *567-568,* 127–136. doi:10.1016/s0022-2860(01)00541-5
8. Lee, K. N.; Lee, J. W.; Ngai, M. Y. *Synlett* **2016,** *27,* 313–319. doi:10.1055/s-0035-1560516
9. Lee, J. W.; Lee, K. N.; Ngai, M.-Y. *Angew. Chem., Int. Ed.* **2019,** *58,* 11171–11181. doi:10.1002/anie.201902243
10. Tlili, A.; Toulgoat, F.; Billard, T. *Angew. Chem., Int. Ed.* **2016,** *55,* 11726–11735. doi:10.1002/anie.201603697
11. Ghiazza, C.; Billard, T.; Tlili, A. *Chem. – Eur. J.* **2019,** *25,* 6482–6495. doi:10.1002/chem.201806234
12. Umemoto, T.; Adachi, K.; Ishihara, S. *J. Org. Chem.* **2007,** *72,* 6905–6917. doi:10.1021/jo070896r
13. Stanek, K.; Koller, R.; Togni, A. *J. Org. Chem.* **2008,** *73,* 7678–7685. doi:10.1021/jo8014825
14. Liu, J.-B.; Chen, C.; Chu, L.; Chen, Z.-H.; Xu, X.-H.; Qing, F.-L. *Angew. Chem., Int. Ed.* **2015,** *54,* 11839–11842. doi:10.1002/anie.201506329
15. Huang, C.; Liang, T.; Harada, S.; Lee, E.; Ritter, T. *J. Am. Chem. Soc.* **2011,** *133,* 13308–13310. doi:10.1021/ja204861a
16. Yang, S.; Chen, M.; Tang, P. *Angew. Chem., Int. Ed.* **2019,** *58,* 7840–7844. doi:10.1002/anie.201901447
17. Yang, Y.-M.; Yao, J.-F.; Yan, W.; Luo, Z.; Tang, Z.-Y. *Org. Lett.* **2019,** *21,* 8003–8007. doi:10.1021/acs.orglett.9b03000
18. Govaerts, S.; Nyuchev, A.; Noel, T. *J. Flow Chem.* **2020,** *10,* 13–71. doi:10.1007/s41981-020-00077-7
19. Sambiagio, C.; Schönbauer, D.; Blieck, R.; Dao-Huy, T.; Pototschnig, G.; Schaaf, P.; Wiesinger, T.; Zia, M. F.; Wencel-Delord, J.; Besset, T.; Maes, B. U. W.; Schnürch, M. *Chem. Soc. Rev.* **2018,** *47,* 6603–6743. doi:10.1039/c8cs00201k
20. Romero, N. A.; Nicewicz, D. A. *Chem. Rev.* **2016,** *116,* 10075–10166. doi:10.1021/acs.chemrev.6b00057
21. Prier, C. K.; Rankic, D. A.; MacMillan, D. W. C. *Chem. Rev.* **2013,** *113,* 5322–5363. doi:10.1021/cr300503r
22. Narayanam, J. M. R.; Stephenson, C. R. J. *Chem. Soc. Rev.* **2011,** *40,* 102–113. doi:10.1039/b913880n
23. Zheng, W.; Morales-Rivera, C. A.; Lee, J. W.; Liu, P.; Ngai, M.-Y. *Angew. Chem., Int. Ed.* **2018,** *57,* 9645–9649. doi:10.1002/anie.201800598
24. Zheng, W.; Lee, J. W.; Morales-Rivera, C. A.; Liu, P.; Ngai, M.-Y. *Angew. Chem., Int. Ed.* **2018,** *57,* 13795–13799. doi:10.1002/anie.201808495
25. Jelier, B. J.; Tripet, P. F.; Pietrasiak, E.; Franzoni, I.; Jeschke, G.; Togni, A. *Angew. Chem., Int. Ed.* **2018,** *57,* 13784–13789. doi:10.1002/anie.201806296
26. Santoro, S.; Ferlin, F.; Ackermann, L.; Vaccaro, L. *Chem. Soc. Rev.* **2019,** *48,* 2767–2782. doi:10.1039/c8cs00211h
27. Sambiagio, C.; Noël, T. *Trends Chem.* **2020,** *2,* 92–106. doi:10.1016/j.trechm.2019.09.003
28. Cambié, D.; Bottecchia, C.; Straathof, N. J. W.; Hessel, V.; Noël, T. *Chem. Rev.* **2016,** *116,* 10276–10341. doi:10.1021/acs.chemrev.5b00707
29. Bottecchia, C.; Rubens, M.; Gunnoo, S. B.; Hessel, V.; Madder, A.; Noël, T. *Angew. Chem., Int. Ed.* **2017,** *56,* 12702–12707. doi:10.1002/anie.201706700
30. Straathof, N. J. W.; Cramer, S. E.; Hessel, V.; Noël, T. *Angew. Chem., Int. Ed.* **2016,** *55,* 15549–15553. doi:10.1002/anie.201608297
31. Wei, X.-J.; Abdiaj, I.; Sambiagio, C.; Li, C.; Zysman-Colman, E.; Alcázar, J.; Noël, T. *Angew. Chem., Int. Ed.* **2019,** *58,* 13030–13034. doi:10.1002/anie.201906462
32. Henderson, R. K.; Jiménez-González, C.; Constable, D. J. C.; Alston, S. R.; Inglis, G. G. A.; Fisher, G.; Sherwood, J.; Binks, S. P.; Curzons, A. D. *Green Chem.* **2011,** *13,* 854–862. doi:10.1039/c0gc00918k
33. The use of water was reported not to interfere with the reaction [24].

License and Terms

This is an Open Access article under the terms of the Creative Commons Attribution License (http://creativecommons.org/licenses/by/4.0). Please note that the reuse, redistribution and reproduction in particular requires that the authors and source are credited.

The license is subject to the *Beilstein Journal of Organic Chemistry* terms and conditions: (https://www.beilstein-journals.org/bjoc)

The definitive version of this article is the electronic one which can be found at: doi:10.3762/bjoc.16.111

BEILSTEIN JOURNAL OF ORGANIC CHEMISTRY

Distinctive reactivity of *N*-benzylidene-[1,1'-biphenyl]-2-amines under photoredox conditions

Shrikant D. Tambe, Kwan Hong Min, Naeem Iqbal and Eun Jin Cho*

Full Research Paper

Open Access

Address:
Department of Chemistry, Chung-Ang University, 84 Heukseok-ro, Dongjak-gu, Seoul 06974, Republic of Korea

Email:
Eun Jin Cho* - ejcho@cau.ac.kr

* Corresponding author

Keywords:
1,2-diamine; diversity; imine; photocatalysis; visible light

Beilstein J. Org. Chem. **2020,** *16,* 1335–1342.
doi:10.3762/bjoc.16.114

Received: 30 March 2020
Accepted: 02 June 2020
Published: 18 June 2020

This article is part of the thematic issue "Advances in photoredox catalysis".

Guest Editor: T. Noël

© 2020 Tambe et al.; licensee Beilstein-Institut.
License and terms: see end of document.

Abstract

A simple photocatalytic method was developed for the synthesis of unsymmetrical 1,2-diamines by the unprecedented reductive coupling of *N*-benzylidene-[1,1'-biphenyl]-2-amines with an aliphatic amine. The presence of a phenyl substituent in the aniline moiety of the substrate was critical for the reactivity. The reaction proceeded via radical–radical cross-coupling of α-amino radicals generated by proton-coupled single-electron transfer in the presence of an Ir photocatalyst. On the other hand, symmetrical 1,2-diamines were selectively produced from the same starting materials by the judicious choice of the reaction conditions, showcasing the distinct reactivity of *N*-benzylidene-[1,1'-biphenyl]-2-amines. The developed method can be employed for the synthesis of various bulky vicinal diamines, which are potential ligands in stereoselective synthesis.

Introduction

The selective formation of distinct valuable compounds from the same starting material is a highly attractive divergent approach, though it represents significant synthetic challenges. Recent advances in visible-light photocatalysis, mediated by visible-light-absorbing photosensitizers, have allowed ready access to complex molecules in a controlled manner, where subtle differences in the reaction conditions opened up distinct reaction pathways [1-5].

Imines are versatile substrates that can be converted into various azo compounds, depending upon the reaction conditions [6-9]. In particular, the reactivities of *N*-benzylidenes have been extensively explored under visible-light photocatalysis [10-16]. *N*-Benzylidenes can undergo facile single-electron reduction to generate α-amino radical intermediates, which can participate in diverse processes, depending upon the nature of the substrates and the reaction conditions (Scheme 1a). Various amine systems are generated from such intermediates via a wide range of processes, including hydrogen atom abstraction [17,18], the addition to unsaturated compounds [19-21], radical–radical coupling [22-30], and cyclization reactions [31-33]. Among these diverse applications, the Rueping group has

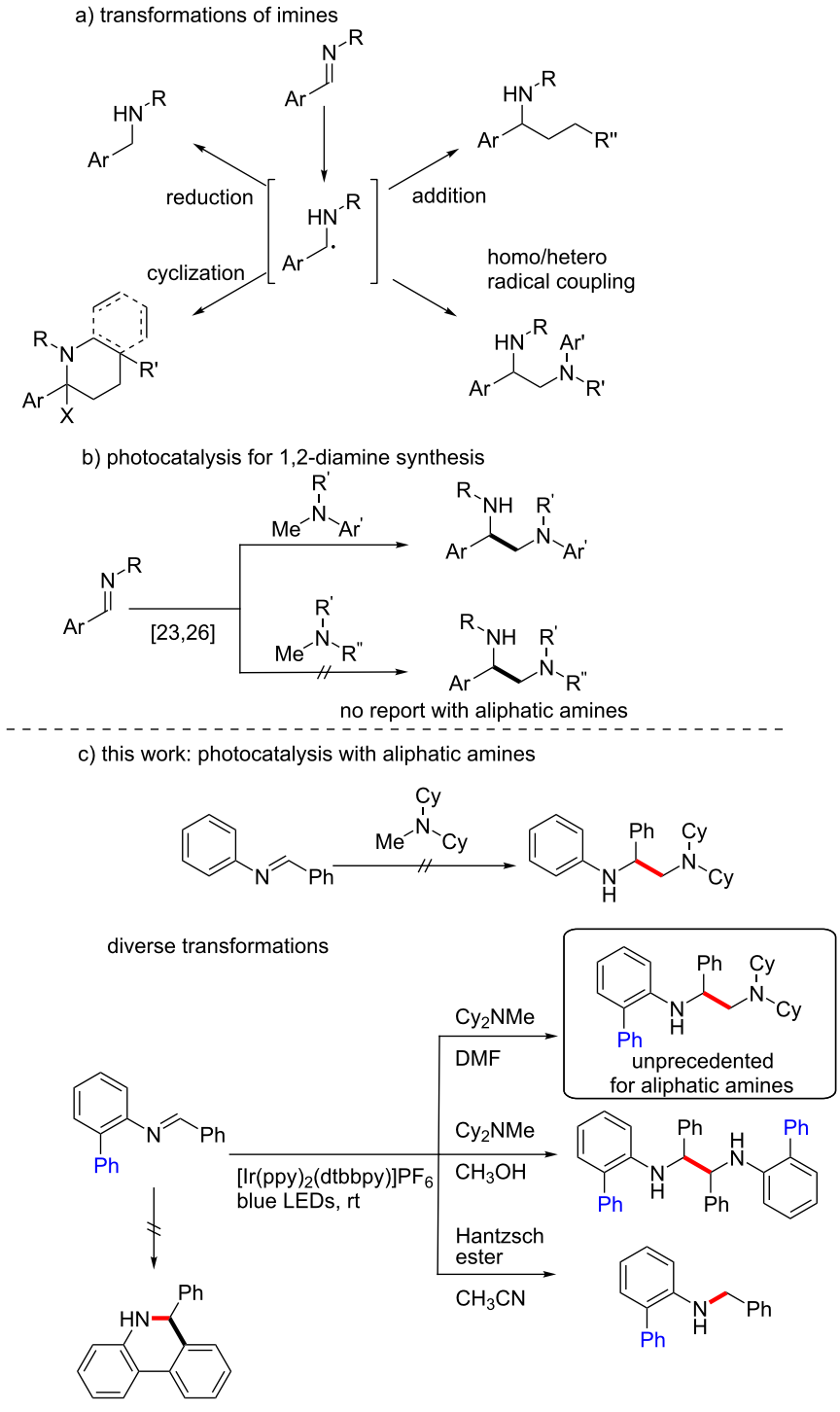

Scheme 1: Photocatalytic transformations of imines.

reported excellent examples of the reductive umpolung homocoupling of imines and heterocoupling with α-amino radicals for the synthesis of symmetrical and unsymmetrical vicinal diamines (Scheme 1b) [23,26]. Notably, 1,2-diamines have widespread applications as core structures in a variety of natural products, pharmaceuticals, and agrochemicals [34-38] and are valuable ligands [39,40] in stereoselective organic synthesis. Despite the availability of a plethora of synthetic methods for 1,2-diamines [41-45], the reported photocatalytic synthetic methods are mainly limited to aniline-based substrates and do not encompass aliphatic amines.

We planned the synthesis of 1,2-diamine compounds having an aliphatic amine moiety by the intermolecular coupling of *N*-benzylidines with aliphatic amines that not only act as coupling partner but also as electron donors in the photoredox cycle, and the results are reported herein. We began with the reaction of simple *N*-benzylideneaniline. However, this substrate did not furnish the desired products under several different photocatalysis conditions, including those reported by Rueping. We hypothesized that the structural modification of the substrate might affect its reactivity, and to our delight, the introduction of an *ortho*-phenyl moiety on the *N*-benzylideneaniline species provided the desired 1,2-diamine product, wherein the *N*,*N*-dicyclohexylmethylamine (Cy_2NMe) acted as both the coupling partner and an electron donor in the photoredox cycle (Scheme 1c). It is likely that the presence of the additional phenyl group in the substrate stabilizes the α-amino radical intermediate and modulates its reactivity [46,47]. In addition to the cross-coupled 1,2-diamines, we envisioned the generation of other valuable structural motifs via the careful control of the reaction conditions for the reaction of the biphenyl imine derivative *N*-benzylidene-[1,1'-biphenyl]-2-amine.

Results and Discussion

With the initial results in hand, we attempted the optimization of the reaction conditions to improve the yield of the 1,2-diamine product (Table 1). Among the series of photocatalysts tested, ranging from the Ru/Ir polypyridyl complexes to organic

Table 1: Reaction optimization.[a]

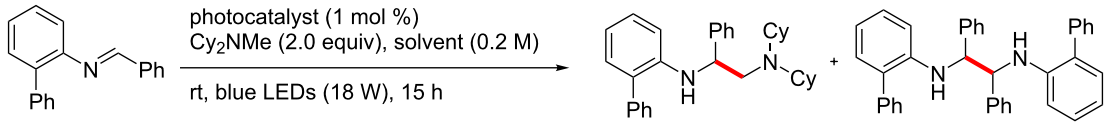

entry	photocatalyst	variation	solvent	yield (%)[b]	
				2a	**3a**
1	$[Ru(bpy)_3]Cl_2·6H_2O$	–	CH_3CN	12	0
2	$[Ru(bpz)_3](PF_6)_2$	–	CH_3CN	0	0
3	$Ir(dFppy)_3$	–	CH_3CN	0	0
4	$Ir(ppy)_3$	–	CH_3CN	3	25
5	$[Ir(dF(CF_3)ppy)_2(dtbpy)]PF_6$	–	CH_3CN	38	5
6	$[Ir(dtbbpy)(ppy)_2]PF_6$	–	CH_3CN	60	11
7	TTPP	–	CH_3CN	0	0
8	crystal violet	–	CH_3CN	0	0
9	eosin-Y	–	CH_3CN	38	0
10	$[Ir(dtbbpy)(ppy)_2]PF_6$	Cy_2NMe (1 equiv)	CH_3CN	14	55
11	$[Ir(dtbbpy)(ppy)_2]PF_6$	no Cy_2NMe	CH_3CN	0	trace
12	no catalyst	–	CH_3CN	0	0
13	$[Ir(dtbbpy)(ppy)_2]PF_6$	no light	CH_3CN	0	0
14	$[Ir(dtbbpy)(ppy)_2]PF_6$	–	DCM	0	16
15	$[Ir(dtbbpy)(ppy)_2]PF_6$	–	DMF	72 (71)	7
16	$[Ir(dtbbpy)(ppy)_2]PF_6$	–	DCE	22	11
17	$[Ir(dtbbpy)(ppy)_2]PF_6$	–	DMSO	37	6
18	$[Ir(dtbbpy)(ppy)_2]PF_6$	–	dioxane	50	13
19	$[Ir(dtbbpy)(ppy)_2]PF_6$	–	TFE	0	20
20	$[Ir(dtbbpy)(ppy)_2]PF_6$	–	acetone	22	trace
21	$[Ir(dtbbpy)(ppy)_2]PF_6$	–	EtOAc	36	8
22	$[Ir(dtbbpy)(ppy)_2]PF_6$	–	CH_3OH	4	75 (75)
23	$[Ir(dtbbpy)(ppy)_2]PF_6$	–	DMF/CH_3OH (1:1)	35	29
24	$[Ir(dtbbpy)(ppy)_2]PF_6$	–	DMF/H_2O (1:1)	25	10
25	$[Ir(dtbbpy)(ppy)_2]PF_6$	–	CH_3CN/H_2O (1:1)	15	14

[a]Reaction conditions: **1a** (0.1 mmol), under argon atmosphere. [b]The yields were determined by ^1H NMR spectroscopy using 1,3,5-trimethoxybenzene as the internal standard, and the isolated yields are mentioned in parentheses.

dyes, $[Ir(dtbbpy)(ppy)_2]PF_6$ was found to be the best and afforded **2a** in 60% yield, along with 11% of the homocoupled product **3a** (Table 1, entries 1–9). The amount of Cy_2NMe was critical for achieving selectivity, and less than two equivalents of Cy_2NMe gave greater amounts of the homocoupled product **3a** (Table 1, entry 10). Control experiments showed that the photocatalyst, amine base, and light source are integral aspects of the reaction (Table 1, entries 11–13). DMF was found to be the best solvent and yielded **2a** selectively (Table 1, entries 15–22). On the other hand, the homocoupled **3a** was selectively obtained in protic solvents (Table 1, entries 19 and 22), and in particular, CH_3OH showed a good reactivity and formed **3a** in 75% yield. Unexpectedly, the cyclized product with the tethered phenyl ring proposed in Scheme 1c was not generated under any of the photocatalytic conditions evaluated.

With the optimized conditions in hand, the generality of the transformations was investigated using a wide variety of phenyl-substituted *N*-benzylideneaniline derivatives (Scheme 2). First, the C–C cross-coupling process with Cy_2NMe was

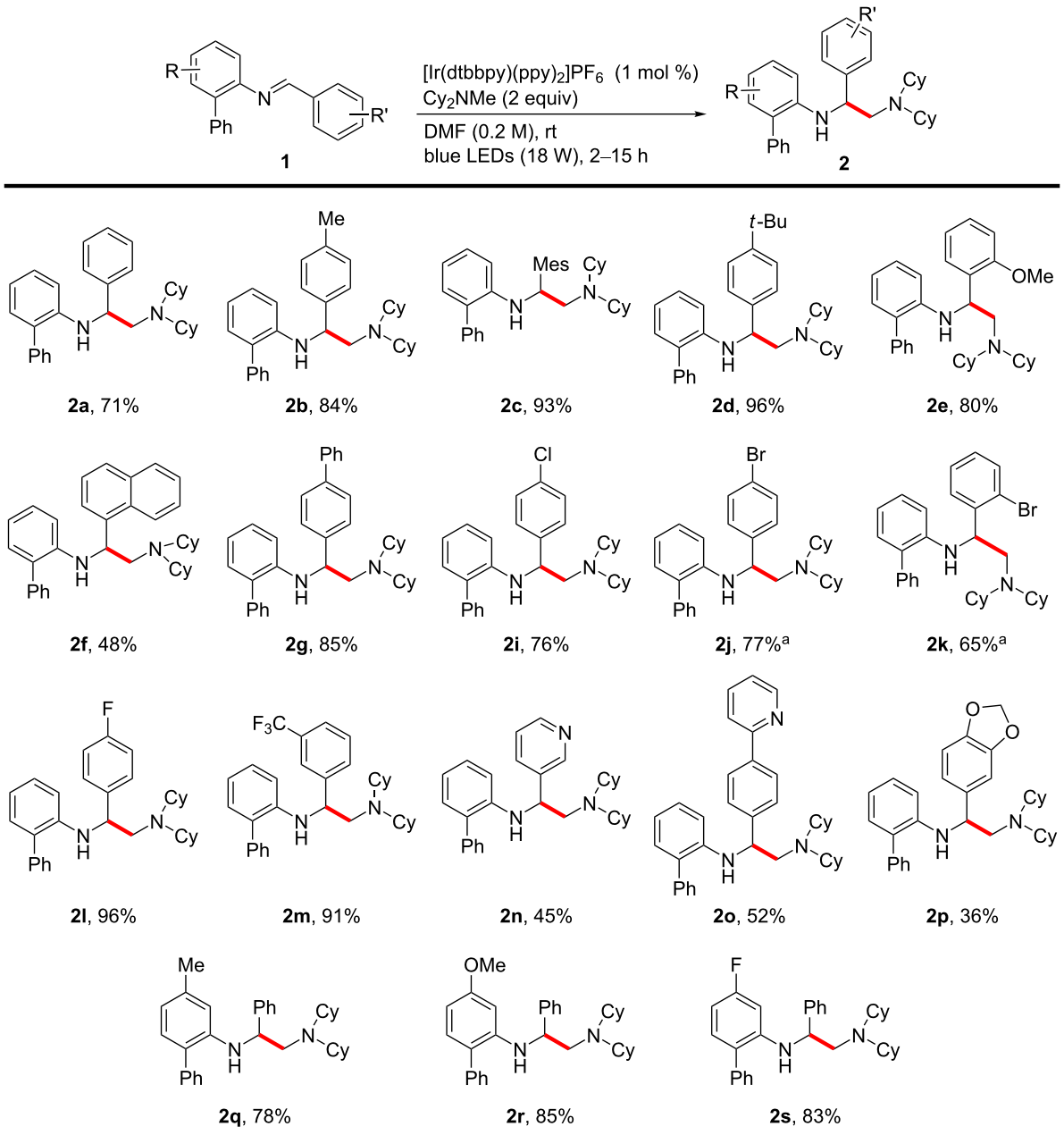

Scheme 2: Substrate scope for the radical cross-couplings. Reaction conditions: **1** (0.3 mmol), under argon atmosphere, isolated yields. [a]The debrominated product was also detected, and the yield represents the mixture of the brominated and debrominated product.

explored, with variations of the benzylidene moiety. The reactions with both electron-donating (**2b**–**2e**) and electron-withdrawing substituents (**2i**–**2m**) proceeded well. Several functional groups, such as benzylic ones (**2b** and **2c**), ethers (**2e**), halogens (**2i** and **2l**) [48-50], the medicinally important CF_3 group (**2m**), and acetals (**2p**) were tolerated under these mild reaction conditions. The substitution pattern of the aryl groups, such as *ortho* (**2c**, **2e**, and **2k**), *meta* (**2m** and **2p**), and *para* substitution (**2b**–**2d**, **2g**, **2i**, **2l**, **2o**, and **2p**), did not have any significant impact on the reaction outcome. The heteroaryl ring-bearing substrates (**2n** and **2o**) also underwent the transformation, and furnished the valuable vicinal diamine products. The modifications on the aniline moiety were also suitable, and substrates with both electron-donating (**2q** and **2r**) and electron-withdrawing (**2s**) substituents underwent the cross-coupling with excellent reactivities. We also tried the transformation with aliphatic amines other than Cy_2NMe, such as TMEDA, TEA, and DIPEA. However, these reactions proceeded with a poor chemoselectivity and resulted in the formation of mixtures of several types of amine compounds.

A photochemical quantum yield, determined by using the standard ferrioxalate actinometry, was 83% for the radical cross-coupling between **1a** and Cy_2NMe (see Supporting Information File 1 for details).

Next, the homocoupling reactions of substituted (*E*)-*N*-benzylidene-[1,1'-biphenyl]-2-amines were studied in CH_3OH (Scheme 3) [51-56]. It is noteworthy that the resulting symmetrical 1,2-diamine compounds are potential ligands for a variety of organic transformations. The dimerization reactions proceeded well, regardless of the electron density or position of the substituent on the benzylidene moiety. Interestingly, the homocoupling process was highly stereoselective, resulting in the formation of only one diastereomer, probably due to the bulky substitution pattern of the substrates. The structure of the homocoupled 1,2-diamine product **3a** was unambiguously confirmed using X-ray crystallography [57].

To further extend the diversity of the reactivity of the imines in this process, we also attempted the use of a reducing agent in

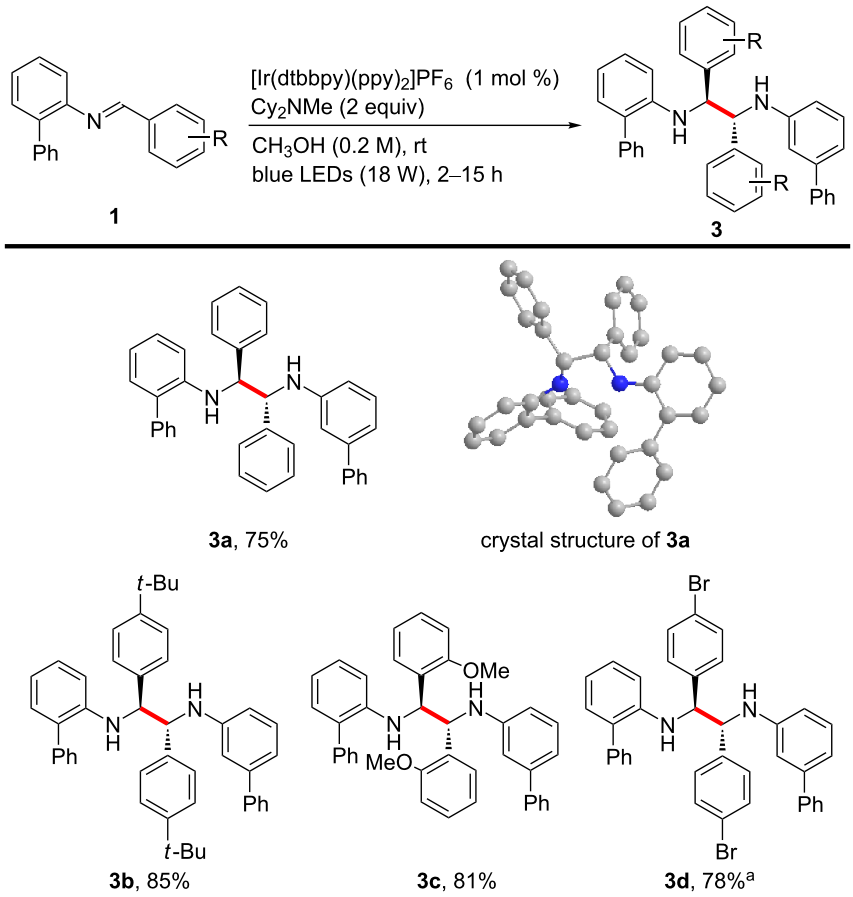

Scheme 3: Substrate scope for the homocoupling. Reaction conditions: **1** (0.3 mmol), under argon atmosphere, isolated yield. [a]The debrominated product was also detected, and the yield represents the mixture of the brominated and debrominated product.

the reaction of **1a**. Pleasingly, the reaction of **1a** with 2 equivalents of the Hantzsch ester in CH_3CN produced the reduced amine product **4a** in 67% yield (Scheme 4) [17,18,58-61].

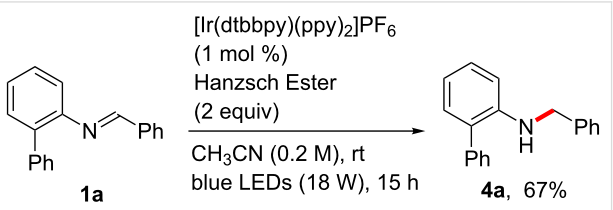

Scheme 4: Reduction of the imine **1a** to the amine **4a**.

Based on these observations, a plausible reaction mechanism was proposed for the developed transformation (Scheme 5). Upon visible-light irradiation, the excited photocatalyst $[Ir^{III}]^*$ is formed and is reductively quenched by single-electron transfer from Cy_2NMe, resulting in the generation of the highly reducing $[Ir^{II}]$ species and the radical cation **A**. To validate the reductive quenching pathway, we carried out Stern–Volmer quenching experiments (Figure S1, Supporting Information File 1). The emission intensity of the excited Ir complex significantly decreased in proportion to the concentration of Cy_2NMe, while it was much less affected by the concentration of **1a**, confirming the proposed working mode. The formation of **2a** might be attributed to the proton-coupled electron transfer [62-66] from $[Ir^{II}]$ to the imine **1a**, where the radical cation **A** donates a proton to **1a** to form the α-amino radical intermediates **B** and **C**, which undergo cross-coupling to give the desired unsymmetrical vicinal diamine **2a**. On the other hand, in CH_3OH, **1a** preferentially abstracts a proton from CH_3OH rather than from **A**, which, in turn, prevents the generation of the α-amino radical **C** from Cy_2NMe, resulting in the homocoupling of **B** to selectively form the symmetrical diamine product **3a**.

Conclusion

We developed a divergent synthetic approach for the valuable 1,2-diamine motif from *N*-benzylidene-[1,1'-biphenyl]-2-amines by slight alterations to the reaction conditions. The in situ-generated α-amino radical intermediates successfully underwent cross- and homocoupling to yield the unsymmetrical and symmetrical 1,2-diamines, respectively. The presence of the phenyl substituent at the aniline moiety was critical in the heterocoupling with aliphatic amines. Furthermore, the reduced amine product was also obtained by employing the Hantzsch ester. The developed method can be employed for the synthesis of bulky vicinal diamines with potential applications as ligands for stereoselective synthesis.

Experimental

An oven-dried resealable tube, equipped with a magnetic stir bar, was charged with the *N*-benzylidene-[1,1'-biphenyl]-2-amine derivative (0.3 mmol), $[Ir(dtbbpy)(ppy)_2]PF_6$ (0.003 mmol), and Cy_2NMe (0.6 mmol). The reaction mixture was purged with argon for 20 min. Then, degassed DMF or CH_3OH was added to the reaction mixture under inert conditions. The reaction mixture was stirred at ambient temperature for 2–15 h under visible-light irradiation with blue LEDs (18 W). The progress of the reaction was monitored by using TLC. Upon the completion of the reaction, the crude product was diluted with ethyl acetate and washed with brine. The organic layer was dried over anhydrous $MgSO_4$ and concentrated in vacuo. The desired vicinal diamine product was purified by silica-gel column chromatography using hexane/EtOAc as the eluent.

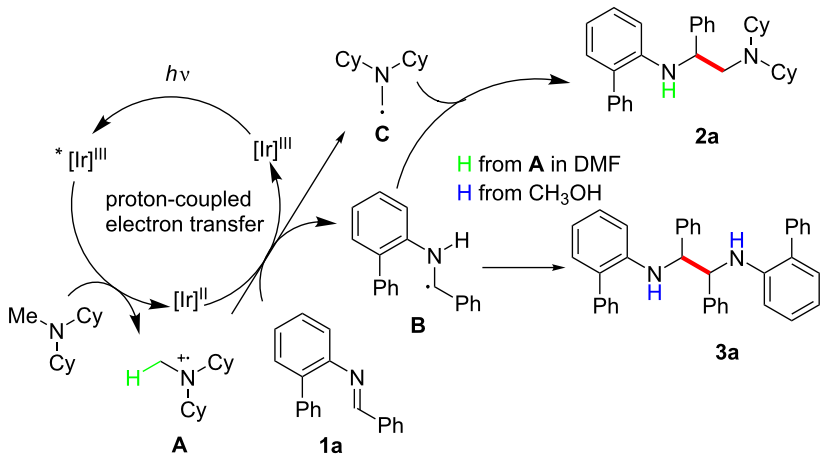

Scheme 5: Proposed mechanism.

Supporting Information

Supporting Information File 1

Additional experimental details and analytical data.
[https://www.beilstein-journals.org/bjoc/content/supplementary/1860-5397-16-114-S1.pdf]

Supporting Information File 2

Crystal data for **3a**.
[https://www.beilstein-journals.org/bjoc/content/supplementary/1860-5397-16-114-S2.cif]

Funding

This research was supported by Chung-Ang University Research Scholarship Grants in 2019 and by the National Research Foundation of Korea (NRF-2020R1A2C2009636).

ORCID® iDs

Eun Jin Cho - https://orcid.org/0000-0002-6607-1851

Preprint

A non-peer-reviewed version of this article has been previously published as a preprint doi:10.3762/bxiv.2020.35.v1

References

1. Cheng, Q.-Q.; Yedoyan, J.; Arman, H.; Doyle, M. P. *J. Am. Chem. Soc.* **2016,** *138,* 44–47. doi:10.1021/jacs.5b10860
2. Iqbal, N.; Jung, J.; Park, S.; Cho, E. J. *Angew. Chem., Int. Ed.* **2014,** *53,* 539–542. doi:10.1002/anie.201308735
3. Liu, Z.; Xu, H.; Yao, T.; Zhang, J.; Liu, L. *Org. Lett.* **2019,** *21,* 7539–7543. doi:10.1021/acs.orglett.9b02810
4. Mose, R.; Preegel, G.; Larsen, J.; Jakobsen, S.; Iversen, E. H.; Jørgensen, K. A. *Nat. Chem.* **2017,** *9,* 487–492. doi:10.1038/nchem.2682
5. Park, D. D.; Min, K. H.; Kang, J.; Hwang, H. S.; Soni, V. K.; Cho, C.-G.; Cho, E. J. *Org. Lett.* **2020,** *22,* 1130–1134. doi:10.1021/acs.orglett.9b04646
6. Miyabe, H.; Yoshioka, E.; Kohtani, S. *Curr. Org. Chem.* **2010,** *14,* 1254–1264. doi:10.2174/138527210791330477
7. Belowich, M. E.; Stoddart, J. F. *Chem. Soc. Rev.* **2012,** *41,* 2003–2024. doi:10.1039/c2cs15305j
8. Lei, J.; Huang, J.; Zhu, Q. *Org. Biomol. Chem.* **2016,** *14,* 2593–2602. doi:10.1039/c6ob00087h
9. Otero, A.; Chapela, M.-J.; Atanassova, M.; Vieites, J. M.; Cabado, A. G. *Chem. Res. Toxicol.* **2011,** *24,* 1817–1829. doi:10.1021/tx200182m
10. Cambié, D.; Bottecchia, C.; Straathof, N. J. W.; Hessel, V.; Noël, T. *Chem. Rev.* **2016,** *116,* 10276–10341. doi:10.1021/acs.chemrev.5b00707
11. Chatterjee, T.; Iqbal, N.; You, Y.; Cho, E. J. *Acc. Chem. Res.* **2016,** *49,* 2284–2294. doi:10.1021/acs.accounts.6b00248
12. Chen, J.-R.; Hu, X.-Q.; Lu, L.-Q.; Xiao, W.-J. *Chem. Soc. Rev.* **2016,** *45,* 2044–2056. doi:10.1039/c5cs00655d
13. Marzo, L.; Pagire, S. K.; Reiser, O.; König, B. *Angew. Chem., Int. Ed.* **2018,** *57,* 10034–10072. doi:10.1002/anie.201709766
14. Prier, C. K.; Rankic, D. A.; MacMillan, D. W. C. *Chem. Rev.* **2013,** *113,* 5322–5363. doi:10.1021/cr300503r
15. Romero, N. A.; Nicewicz, D. A. *Chem. Rev.* **2016,** *116,* 10075–10166. doi:10.1021/acs.chemrev.6b00057
16. Schultz, D. M.; Yoon, T. P. *Science* **2014,** *343,* 1239176. doi:10.1126/science.1239176
17. Guo, X.; Okamoto, Y.; Schreier, M. R.; Ward, T. R.; Wenger, O. S. *Eur. J. Org. Chem.* **2020,** 1288–1293. doi:10.1002/ejoc.201900777
18. Xi, Z.-W.; Yang, L.; Wang, D.-Y.; Pu, C.-D.; Shen, Y.-M.; Wu, C.-D.; Peng, X.-G. *J. Org. Chem.* **2018,** *83,* 11886–11895. doi:10.1021/acs.joc.8b01651
19. Lee, K. N.; Lei, Z.; Ngai, M.-Y. *J. Am. Chem. Soc.* **2017,** *139,* 5003–5006. doi:10.1021/jacs.7b01373
20. Qi, L.; Chen, Y. *Angew. Chem., Int. Ed.* **2016,** *55,* 13312–13315. doi:10.1002/anie.201607813
21. Wu, G.; Wang, J.; Liu, C.; Sun, M.; Zhang, L.; Ma, Y.; Cheng, R.; Ye, J. *Org. Chem. Front.* **2019,** *6,* 2245–2249. doi:10.1039/c9qo00407f
22. Chen, M.; Zhao, X.; Yang, C.; Xia, W. *Org. Lett.* **2017,** *19,* 3807–3810. doi:10.1021/acs.orglett.7b01677
23. Fava, E.; Millet, A.; Nakajima, M.; Loescher, S.; Rueping, M. *Angew. Chem., Int. Ed.* **2016,** *55,* 6776–6779. doi:10.1002/anie.201511235
24. Hager, D.; MacMillan, D. W. C. *J. Am. Chem. Soc.* **2014,** *136,* 16986–16989. doi:10.1021/ja5102695
25. Jeffrey, J. L.; Petronijević, F. R.; MacMillan, D. W. C. *J. Am. Chem. Soc.* **2015,** *137,* 8404–8407. doi:10.1021/jacs.5b05376
26. Nakajima, M.; Fava, E.; Loescher, S.; Jiang, Z.; Rueping, M. *Angew. Chem., Int. Ed.* **2015,** *54,* 8828–8832. doi:10.1002/anie.201501556
27. Okamoto, S.; Ariki, R.; Tsujioka, H.; Sudo, A. *J. Org. Chem.* **2017,** *82,* 9731–9736. doi:10.1021/acs.joc.7b01838
28. Okamoto, S.; Kojiyama, K.; Tsujioka, H.; Sudo, A. *Chem. Commun.* **2016,** *52,* 11339–11342. doi:10.1039/c6cc05867a
29. Patel, N. R.; Kelly, C. B.; Siegenfeld, A. P.; Molander, G. A. *ACS Catal.* **2017,** *7,* 1766–1770. doi:10.1021/acscatal.6b03665
30. Uraguchi, D.; Kinoshita, N.; Kizu, T.; Ooi, T. *J. Am. Chem. Soc.* **2015,** *137,* 13768–13771. doi:10.1021/jacs.5b09329
31. Fava, E.; Nakajima, M.; Nguyen, A. L. P.; Rueping, M. *J. Org. Chem.* **2016,** *81,* 6959–6964. doi:10.1021/acs.joc.6b01006
32. Leitch, J. A.; Fuentes de Arriba, A. L.; Tan, J.; Hoff, O.; Martínez, C. M.; Dixon, D. J. *Chem. Sci.* **2018,** *9,* 6653–6658. doi:10.1039/c8sc01704b
33. Rono, L. J.; Yayla, H. G.; Wang, D. Y.; Armstrong, M. F.; Knowles, R. R. *J. Am. Chem. Soc.* **2013,** *135,* 17735–17738. doi:10.1021/ja4100595
34. Viso, A.; Fernández de la Pradilla, R.; García, A.; Flores, A. *Chem. Rev.* **2005,** *105,* 3167–3196. doi:10.1021/cr0406561
35. Lucet, D.; Le Gall, T.; Mioskowski, C. *Angew. Chem., Int. Ed.* **1998,** *37,* 2580–2627. doi:10.1002/(sici)1521-3773(19981016)37:19<2580::aid-anie2580>3.0.co;2-l
36. Bogatcheva, E.; Hanrahan, C.; Nikonenko, B.; Samala, R.; Chen, P.; Gearhart, J.; Barbosa, F.; Einck, L.; Nacy, C. A.; Protopopova, M. *J. Med. Chem.* **2006,** *49,* 3045–3048. doi:10.1021/jm050948+
37. Kano, T.; Sakamoto, R.; Akakura, M.; Maruoka, K. *J. Am. Chem. Soc.* **2012,** *134,* 7516–7520. doi:10.1021/ja301120z
38. Saibabu Kotti, S. R. S.; Timmons, C.; Li, G. *Chem. Biol. Drug Des.* **2006,** *67,* 101–114. doi:10.1111/j.1747-0285.2006.00347.x
39. Kizirian, J.-C. *Chem. Rev.* **2008,** *108,* 140–205. doi:10.1021/cr040107v

40. Bennani, Y. L.; Hanessian, S. *Chem. Rev.* **1997,** *97,* 3161–3196. doi:10.1021/cr9407577
41. Cai, C.-Y.; Shu, X.-M.; Xu, H.-C. *Nat. Commun.* **2019,** *10,* 4953. doi:10.1038/s41467-019-13024-5
42. Ichikawa, S.; Dai, X.-J.; Buchwald, S. L. *Org. Lett.* **2019,** *21,* 4370–4373. doi:10.1021/acs.orglett.9b01592
43. Mwenda, E. T.; Nguyen, H. M. *Org. Lett.* **2017,** *19,* 4814–4817. doi:10.1021/acs.orglett.7b02256
44. Xiao, L.; Zhao, Y.; Qiao, S.; Sun, Z.; Santoro, O.; Redshaw, C. *Dalton Trans.* **2020,** *49,* 1456–1472. doi:10.1039/c9dt04332b
45. Yu, L.; Somfai, P. *Angew. Chem., Int. Ed.* **2019,** *58,* 8551–8555. doi:10.1002/anie.201902642
46. Aurrecoechea, J. M.; Suero, R. *ARKIVOC* **2004,** No. 14, 10–35. doi:10.3998/ark.5550190.0005.e02
47. McNally, A.; Prier, C. K.; MacMillan, D. W. C. *Science* **2011,** *334,* 1114–1117. doi:10.1126/science.1213920
48. Kim, H.; Lee, C. *Org. Lett.* **2011,** *13,* 2050–2053. doi:10.1021/ol200455n
49. Narayanam, J. M. R.; Tucker, J. W.; Stephenson, C. R. J. *J. Am. Chem. Soc.* **2009,** *131,* 8756–8757. doi:10.1021/ja9033582
50. Kim, H.; Lee, C. *Angew. Chem., Int. Ed.* **2012,** *51,* 12303–12306. doi:10.1002/anie.201203599
51. Machrouhi, F.; Namy, J.-L. *Tetrahedron Lett.* **1999,** *40,* 1315–1318. doi:10.1016/s0040-4039(98)02673-2
52. VellemÄe, E.; Tsubrik, O.; Mäeorg, S.; Mäeorg, U. *J. Chem. Res.* **2006,** 149–150. doi:10.3184/030823406776330792
53. Jiang, H.-F.; Huang, X.-Z. *J. Supercrit. Fluids* **2007,** *43,* 291–294. doi:10.1016/j.supflu.2007.07.005
54. Kumar, A.; Samuelson, A. G. *Chem. – Asian J.* **2010,** *5,* 1830–1837. doi:10.1002/asia.200900711
55. Rao, C. N.; Hoz, S. *J. Am. Chem. Soc.* **2011,** *133,* 14795–14803. doi:10.1021/ja205885q
56. Zhu, Y.; Buchwald, S. L. *J. Am. Chem. Soc.* **2014,** *136,* 4500–4503. doi:10.1021/ja501560x
57. CCDC 1991125 contain the supplementary crystallographic data for this article, which can be obtained free of charge from The Cambridge Crystallographic Data Centre.
58. Cheng, X.; Huang, W. *Synlett* **2016,** *28,* 148–158. doi:10.1055/s-0036-1588129
59. Jung, J.; Kim, J.; Park, G.; You, Y.; Cho, E. J. *Adv. Synth. Catal.* **2016,** *358,* 74–80. doi:10.1002/adsc.201500734
60. Park, G.; Yi, S. Y.; Jung, J.; Cho, E. J.; You, Y. *Chem. – Eur. J.* **2016,** *22,* 17790–17799. doi:10.1002/chem.201603517
61. Wang, P.-Z.; Chen, J.-R.; Xiao, W.-J. *Org. Biomol. Chem.* **2019,** *17,* 6936–6951. doi:10.1039/c9ob01289c
62. Gentry, E. C.; Knowles, R. R. *Acc. Chem. Res.* **2016,** *49,* 1546–1556. doi:10.1021/acs.accounts.6b00272
63. Hoffmann, N. *Eur. J. Org. Chem.* **2017,** 1982–1992. doi:10.1002/ejoc.201601445
64. Jiang, H.; Studer, A. *CCS Chem.* **2019,** 38–49. doi:10.31635/ccschem.019.20180026
65. Pannwitz, A.; Wenger, O. S. *Chem. Commun.* **2019,** *55,* 4004–4014. doi:10.1039/c9cc00821g
66. Weinberg, D. R.; Gagliardi, C. J.; Hull, J. F.; Murphy, C. F.; Kent, C. A.; Westlake, B. C.; Paul, A.; Ess, D. H.; McCafferty, D. G.; Meyer, T. J. *Chem. Rev.* **2012,** *112,* 4016–4093. doi:10.1021/cr200177j

License and Terms

This is an Open Access article under the terms of the Creative Commons Attribution License (http://creativecommons.org/licenses/by/4.0). Please note that the reuse, redistribution and reproduction in particular requires that the authors and source are credited.

The license is subject to the *Beilstein Journal of Organic Chemistry* terms and conditions: (https://www.beilstein-journals.org/bjoc)

The definitive version of this article is the electronic one which can be found at: doi:10.3762/bjoc.16.114

BEILSTEIN JOURNAL OF ORGANIC CHEMISTRY

An overview on disulfide-catalyzed and -cocatalyzed photoreactions

Yeersen Patehebieke

Review

Open Access

Address:
School of Chemistry and Chemical Engineering, Nanjing University, Nanjing, 210023, China

Email:
Yeersen Patehebieke - yeersen@nju.edu.cn

Keywords:
cycloaddition; disulfide catalyst; isomerization; oxidation; photocatalysis; thiyl radical

Beilstein J. Org. Chem. **2020,** *16,* 1418–1435.
doi:10.3762/bjoc.16.118

Received: 15 April 2020
Accepted: 12 June 2020
Published: 23 June 2020

This article is part of the thematic issue "Advances in photoredox catalysis".

Guest Editor: T. Noël

© 2020 Patehebieke; licensee Beilstein-Institut.
License and terms: see end of document.

Abstract

Disulfides are versatile catalysts. They can be photocatalysts, hydrogen atom transfer (HAT) catalysts, cocatalysts, or initiators in photocatalytic reactions. Under photoirradiation, organic disulfides can be easily cleaved into free thiyl radicals (RS$^{\bullet}$) and can reversibly add to unsaturated multiple bonds to catalyze a variety of functionalization reactions under mild conditions. In photoredox catalysis reactions, an excellent electron transfer ability and excellent radical properties also made these thiyl radicals powerful HAT catalysts. They have increasingly been proven useful in various types of organic photoreactions, such as cyclizations, anti-Markovnikov additions, aromatic olefin carbonylations, isomerizations, etc. They are a class of green, economic, mild, and chemoselective radical catalysts that deserve more attention. The present review highlights the recent progress in the field of disulfide-catalyzed and -cocatalyzed photocatalytic reactions for different reaction types.

Introduction

Organic disulfides are often used as the skeleton for drugs, pesticides, rubber auxiliaries, polymers, and electronic materials [1]. Over the past decade, organic disulfide-involving photoreactions have attracted increasing attention. Disulfides have versatile catalytic abilities: they can be a photocatalyst, HAT catalyst, initiator, or cocatalyst in organic synthesis. The thiyl radicals (RS$^{\bullet}$) formed under illumination conditions have the unique ability of promote radical bond-forming reactions. Their ability to reversibly add to unsaturated bonds, promoting a variety of reactions, renders them a class of green, economic, mild, and chemoselective radical catalyst. Apart from this, they are also excellent HAT catalysts in photoredox catalysis systems [2,3]. In various types of organic photochemistry reactions, such as cyclizations, anti-Markovnikov additions, oxidations, or isomerizations, disulfides have increasingly proven their power. Herein, we briefly describe the progress in the field

of disulfide-involving photocatalysis in recent years for different reaction types.

Review

Cycloaddition reactions

As early as 1988, Feldman and co-workers reported an example of a [3 + 2] cycloaddition reactions under UV irradiation with azobis(isobutyronitrile) (AIBN) as the free radical initiator and phenyl disulfide as the catalyst, in which the three-membered rings containing double bonds and substituted olefins were transformed into five-membered-ring structures with high regioselectivity [4]. Based on this reaction, Maruoka reported in 2016 that *N*-tosylvinylaziridines and alkenes could undergo cyclization reactions to generate pyrrolidines, catalyzed by substituted aryl disulfides under ultraviolet-light irradiation (Scheme 1) [5].

In 1997, Jung and co-workers used similar disulfide-catalyzed [3 + 2] cycloaddition reactions for the synthesis of polycyclic frameworks. The irradiation of vinylcyclopropanes with alkenes or alkynes in the presence of dibutyl disulfide afford the desired bi- or tricyclic products with 54–88% yield (Scheme 2) [6].

In 2014, Maruoka and co-workers reported an excellent thiyl radical-catalyzed enantioselective cyclization reaction of vinyl-

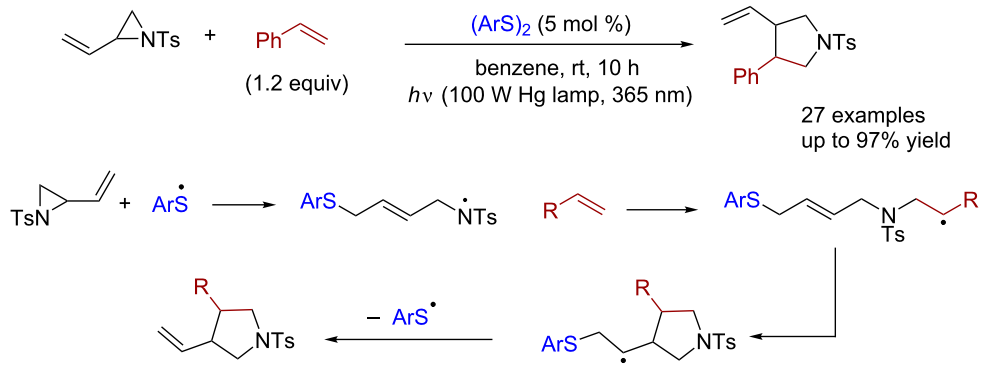

Scheme 1: [3 + 2] cyclization catalyzed by diaryl disulfide.

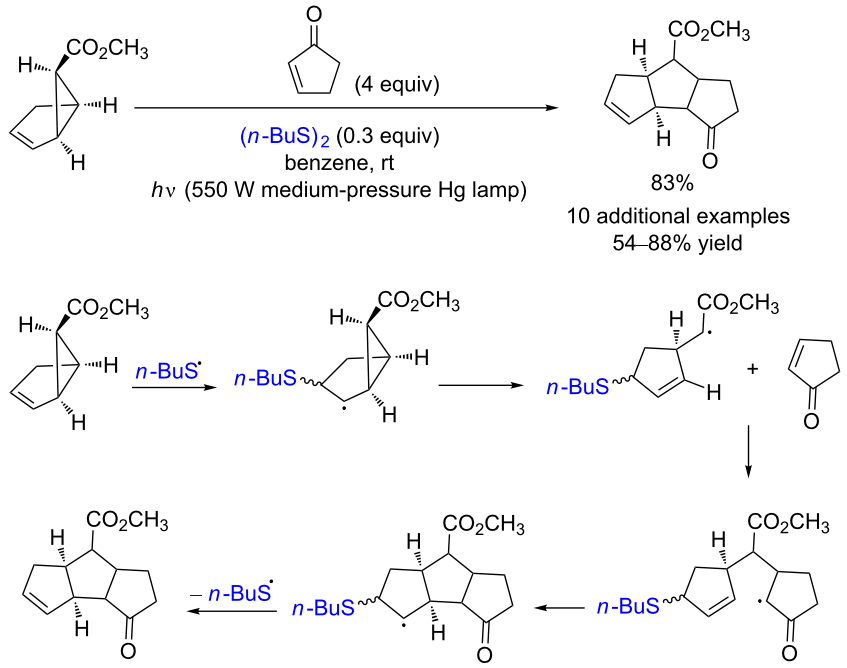

Scheme 2: [3 + 2] cycloaddition catalyzed by disulfide.

cyclopropanes with alkenes [7]. For the extension of this concept, in 2018, Miller and co-workers reported a UV-light-promoted disulfide-bridged peptide-catalyzed enantioselective cycloaddition of vinylcyclopropanes with olefins [8]. The reaction mechanism of this cycloaddition process was similar to other thiyl radical-catalyzed cycloaddition cascade reactions. The alkylthiyl radical generated by the homolysis of a disulfide-bridged peptide precatalyst under UV-light irradiation triggers the reaction by adding to vinylcyclopropane to form the radical intermediate **1**. Then, the addition of olefins to this intermediate **1** gives the intermediate **2**, and the succeeding cyclization step yields the final product **3** and regenerates the active thiyl radical catalyst (Scheme 3). Vinylcyclopropanes engage with the peptide backbone via an H-bonding interaction, and in order to achieve a high enantioselectivity, the amide functionalization of the peptide at the 4-proline position is essential. Amide-substituted vinylcyclopropanes have a relatively good H-bond-donating ability, so they are more successful substrates for this transformation. Although multiple olefins can be successful olefinic coupling partners for this reaction, electron-rich olefins bearing an α-heteroatom would be preferable for achieving a better enantioselectivity.

In 1990, Singleton and co-workers reported disulfide-catalyzed [3 + 2] methylenecyclopentane annulations of olefins with methylenecyclopropanes. This regioselective, mild, and protecting group-free annulation requires only an equimolar amount of the reacting alkene and does not require an excess of

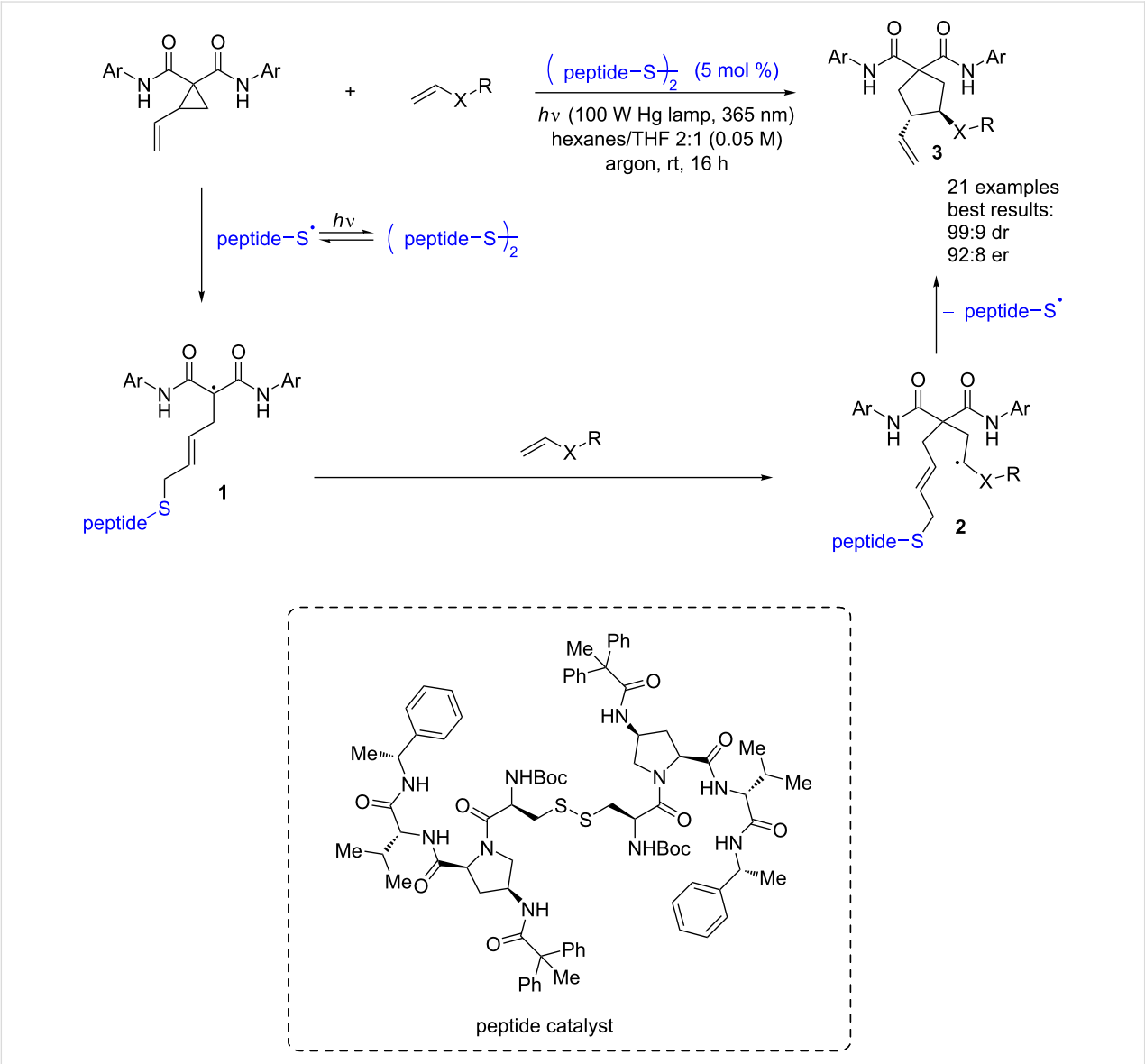

Scheme 3: Disulfide-bridged peptide-catalyzed enantioselective cycloaddition.

the reacting alkene, unlike other methods [9]. Furthermore, the stereochemistry of the product can be modulated by changing the stereochemical structure of the disulfide catalyst [10]. The simple reaction mechanism is shown in Scheme 4a. Thiyl radicals, which are generated under irradiation, trigger the reaction by adding to the methylenecyclopropane **4**, which affords the cyclopropylcarbinyl radical **5**. Then, the radical **5** opens to form the homoallylic radical **6**, followed by the addition of olefins to this radical form the 5-hexenyl radical **7**. The ring closure of the radical **7** and the elimination of a thiyl radical furnishes the final product **9**. When it came to annulations of complex olefins, this method could not give satisfactory results. In order to overcome this weakness, the authors also developed disulfide-catalyzed [3 + 2] methylenecyclopentane annulations of unactivated alkenes with methylenecyclopropanecarboxylates and -dicarboxylates **11** (Scheme 4b) [11]. This annulation method is also applicable for the synthesis of a wide variety of cyclopentane derivatives [12].

In 2017, Huang and co-workers reported a [4 + 2] cycloaddition reaction promoted by blue LED light, using aromatic olefins as the precursor, an acridinium photoredox catalyst (Mes–Acr–Ph$^+$BF$_4^-$), and disulfide as the HAT cocatalyst, to generate the tetralin skeleton, which is widely seen in drugs and pesticide synthesis (Scheme 5) [13]. Diphenyl disulfide played an important role in the [4 + 2] cycloaddition process. Without diphenyl disulfide, only the product of the [2 + 2] cycloaddition was observed.

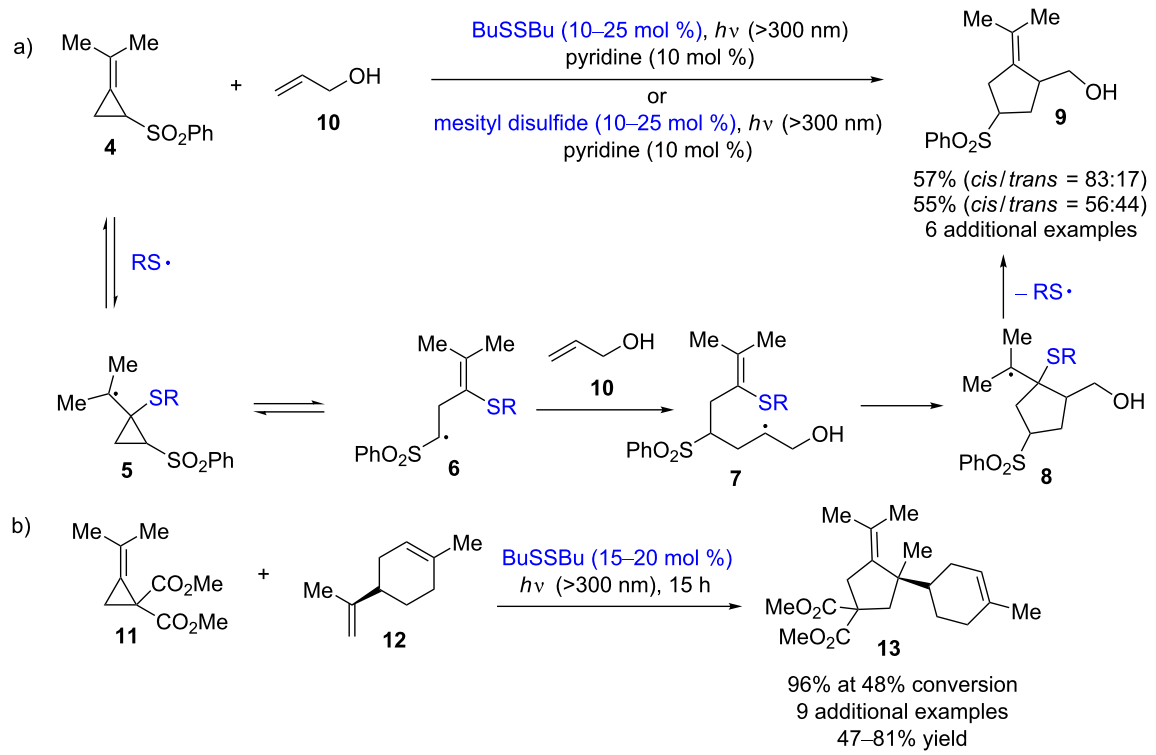

Scheme 4: Disulfide-catalyzed [3 + 2] methylenecyclopentane annulations.

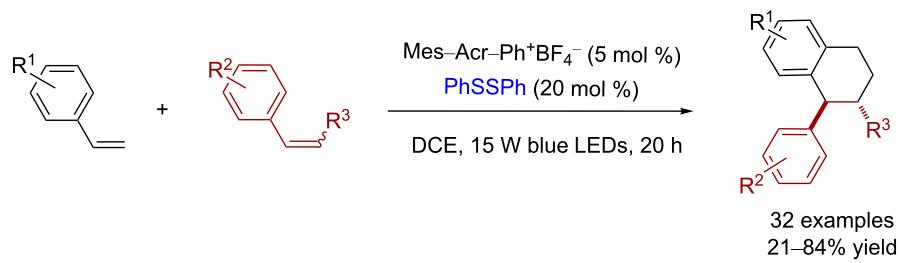

Scheme 5: Disulfide as a HAT cocatalyst in the [4 + 2] cycloaddition reaction.

Huang and co-workers proposed a polar radical crossover cycloaddition mechanism for this Diels–Alder cycloaddition (Scheme 6). The electron transfer from the electron-rich styrene **14** to the activated acridinium photocatalyst **15** oxidizes the styrene **14** to form the styrene radical **16** and the acridine radical **17** (Mes–Acr–Ph•). The subsequent reaction of the formed styrene radical **16** with another styrene **18** gives the radical species **19** and the reoxidation of the acridine radical **17** by a thiyl radical, which is generated by the homolysis of diphenyl disulfide, regenerating the photocatalyst. In a non-polar solvent, PhSSPh accelerates the [4 + 2] cycloaddition of the radical cation **19**, but the electron-relay catalyst promotes the [2 + 2] cycloaddition. The radical cation **19** can undergo two different types of cyclizations, subject to the relative reactivity of its radical and cation center. The α-substituted cation **19** favors the radical cyclization path because the stabilization by an α-substituent makes its cation center more stable and less reactive. In contrast, the non-α-substituted cation **19** prefers the cationic cyclization. However, the two cyclization processes form the intermediates **20** and **21**, respectively, which have the same 5-electron 6-carbon cation radical character. Finally, the subsequent deprotonation and HAT by PhS^- and PhSH yields the desired [4 + 2] cycloaddition products **22** and **23**, respectively.

In 1991, Kim and co-workers reported a disulfide-catalyzed ring expansion of cyclobutanone, cyclopentanone, and three carbon ring-expanded 1,3-diones from vinyl spiro epoxides [14]. The reaction is initiated by the addition of a thiyl radical to the vinyl epoxide **24**, followed by the epoxide fragmentation to the alkoxy radical **25**. Then, the β-cleavage to form the carbon-centered radical **26**, the final cyclization, and an elimination give the desired product **27** (Scheme 7). The use of PhSSPh obviated the undesired reactions, which occurred when using Ph_3SnH and Bu_3SnH, respectively, as the catalyst for this reaction.

Oxidation reactions

Not only can disulfide catalysts induce cycloadditions of olefins but also catalyze the formation of four-membered ring interme-

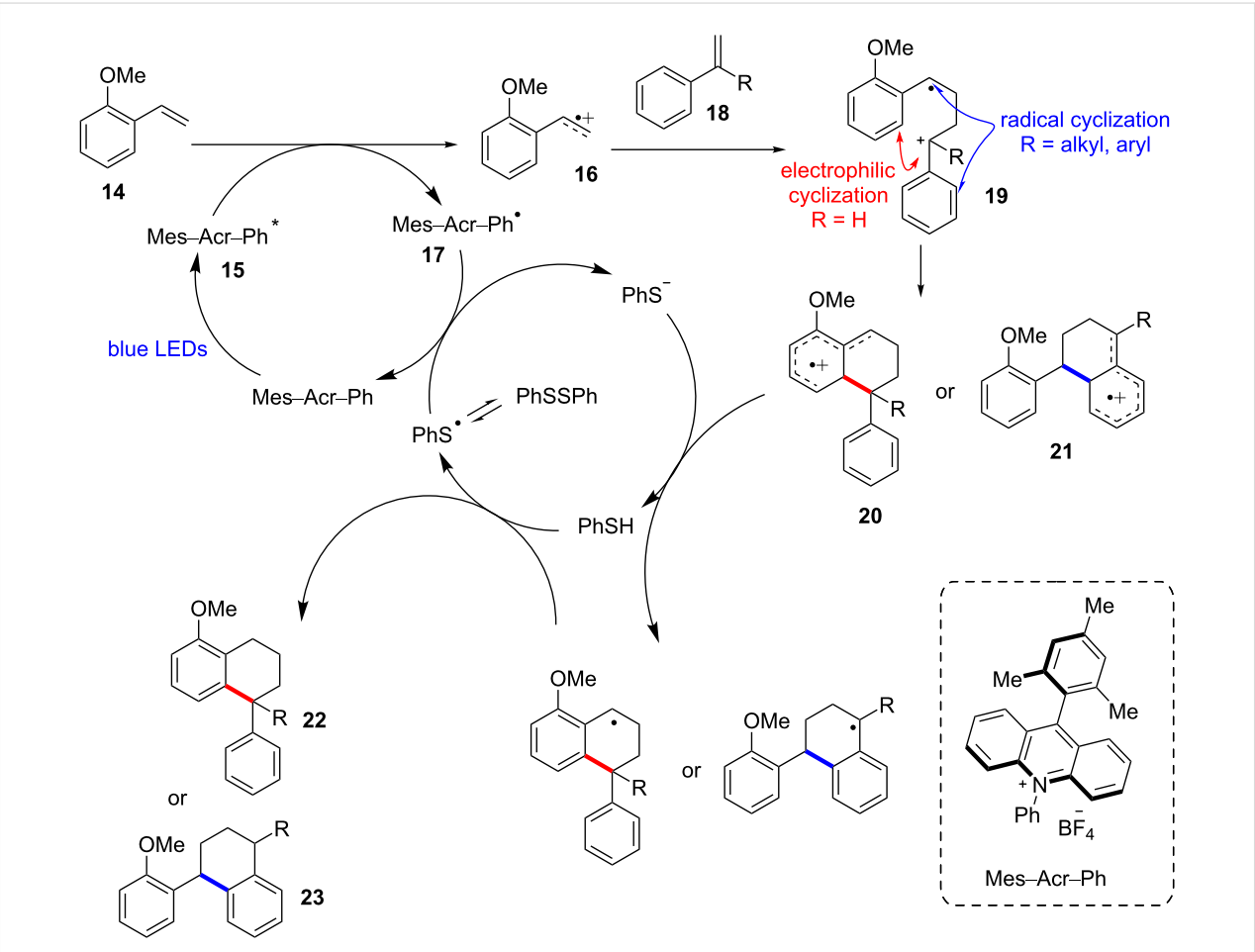

Scheme 6: Proposed mechanism of the [4 + 2] cycloaddition reaction using disulfide as a HAT cocatalyst.

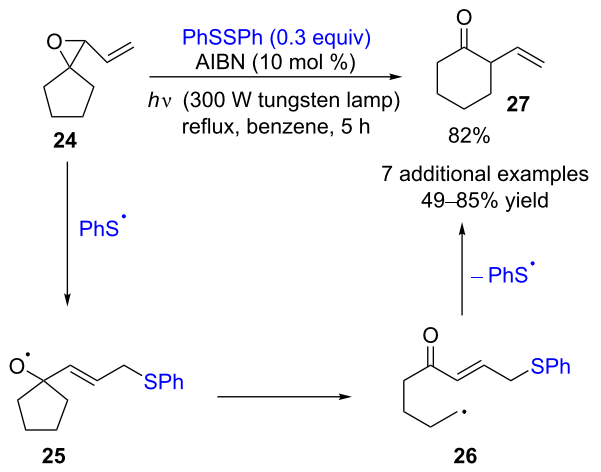

Scheme 7: Disulfide-catalyzed ring expansion of vinyl spiro epoxides.

diates between double or triple bonds and oxygen, and thus converting unsaturated hydrocarbons to carbonyl compounds. Regarding the oxidation of alkynes, Wang reported a method for preparing diaryl-1,2-diketones from diarylalkynes in the presence of visible light, oxygen, and disulfide [15]. The diaryl-1,2-diketone products can serve as an important structural component of many natural products and bioactive molecules. This method works for a broad range of substrates with high yields (77–97%). A plausible mechanism for this reaction is that by the excitation with visible light, the homolytic cleavage of disulfide generates an arylthiyl radical (ArS•), which adds to diphenylacetylene to form a free-radical intermediate **28**. Subsequently, this intermediate traps a molecule of singlet oxygen ($^1O_2$), and the thiyl radical is regenerated to give the four-membered ring intermediate **29**. Finally, the rearrangement of the four-membered intermediate provides the diketone **30** as the product (Scheme 8).

In 2017, Wang and co-workers reported an oxidative cleavage of aromatic alkenes at ambient temperature with visible-light irradiation, using electron-rich aryl disulfides as the photocatalyst and oxygen as the oxidant [16]. At room temperature, bis(4-methoxyphenyl) disulfide was employed as the metal-free photocatalyst under visible-light and 1 bar of O_2 to realize the aerobic oxidative cleavage of the C=C bonds. Under these mild conditions, monosubstituted and 1,1-disubstituted arylolefins could be effectively cleaved into the corresponding aldehydes or ketones. The proposed mechanism is that disulfide is split by visible light to form thiyl radicals, which catalyzes the combination of the olefin with O_2 to form the intermediate dioxetane that decomposes into ketone or aldehyde products (Scheme 9). However, in the absence of light or oxygen, disulfide could not catalyze the oxidative cleavage of olefins. It was proposed that disulfide and the olefin might be able to form a charge-transfer complex, which may rationalize the unconventional homolysis of the aromatic S–S bond by visible light.

In 2019, Meng and co-workers reported a visible light-mediated disulfide-catalyzed metal-free and base-free α-functionali-

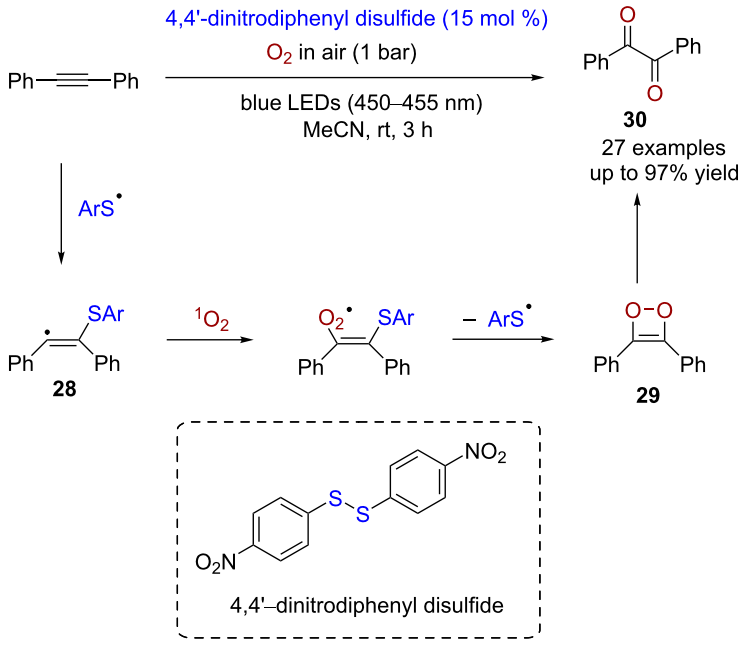

Scheme 8: Disulfide-catalyzed aerobic oxidation of diarylacetylene.

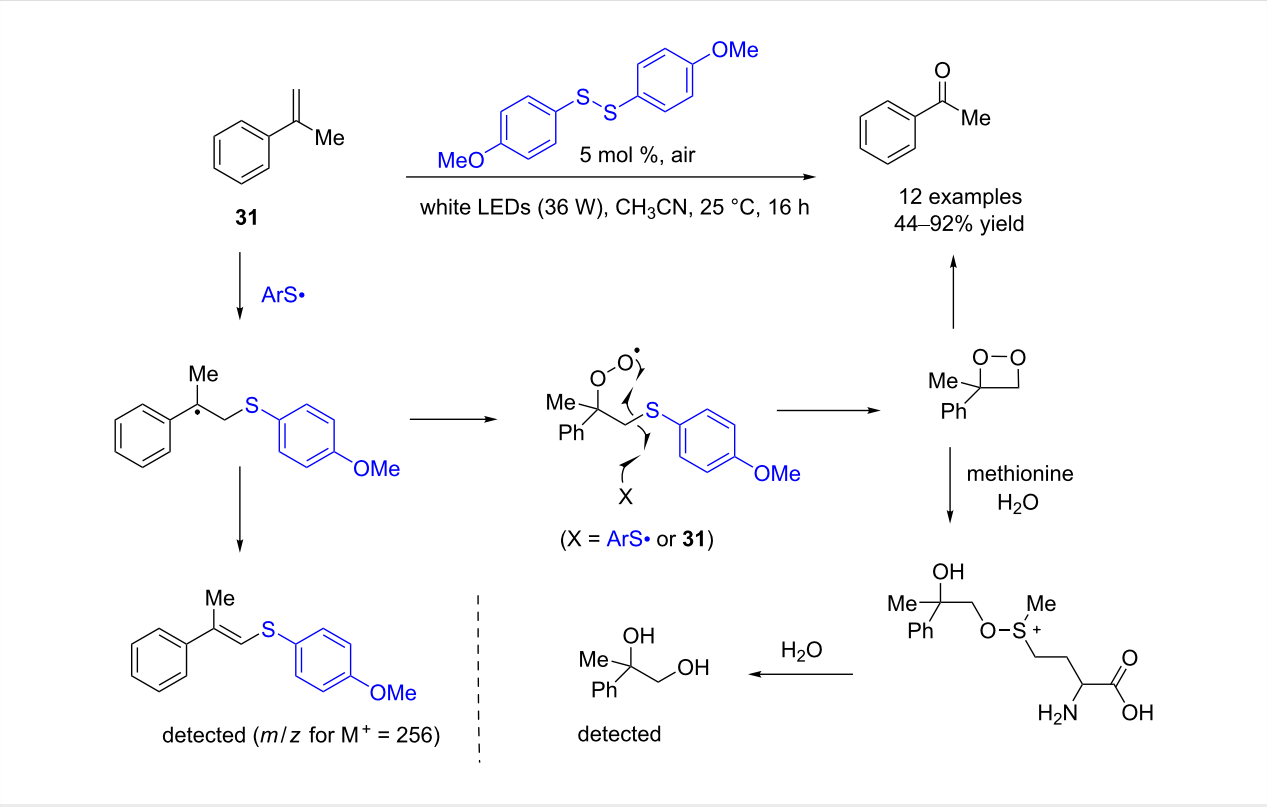

Scheme 9: Disulfide-catalyzed aerobic photooxidative cleavage of olefins.

zation of 1,3-dicarbonyl compounds [17]. Under visible-light irradiation, the α-hydroxylation or α-hydroxymethylation of 1,3-dicarbonyl compounds, was efficiently implemented via this disulfide, which induced an aerobic oxidation. The hydroxylation and hydroxymethylation of a broad range of β-keto esters and β-keto amides that had electron-donating or -withdrawing groups on the phenyl ring gave good to excellent yields (42–98%, Scheme 10). One exceptional decrease in the yield of the hydroxylation product (13–33%) occurred when β-keto esters with methoxy groups on the phenyl ring were used, but the hydroxymethylation yield was just undulated slightly. Other carbonyl compounds, 1,3-diones, and functionalized five-, six-, and seven-membered keto ester derivatives did not show any desired reaction. In combination with a continuous-flow strategy, this disulfide-catalyzed aerobic oxidation process can be scaled up to a gram-scale.

A plausible mechanism of the reaction is shown in Scheme 11. The hydroxylation starts with the formation of the photoexcited disulfide–enol complex **35** from the disulfide–enol complex **34** under irradiation. Then, the photoexcited complex **35** reacts with triplet oxygen ($^3O_2$) to yield the reactive $^1O_2$. The subsequent reaction of singlet oxygen with the disulfide–enol complex **34** furnishes the desired hydroxylation product **36** and frees the disulfide for the next cycle. The generation of the disulfide–olefin complex **37** from styrene and disulfide initiates the hydroxymethylation. The following $^3O_2$ trapping by the intermediate **38**, which is generated by the addition of a thiyl

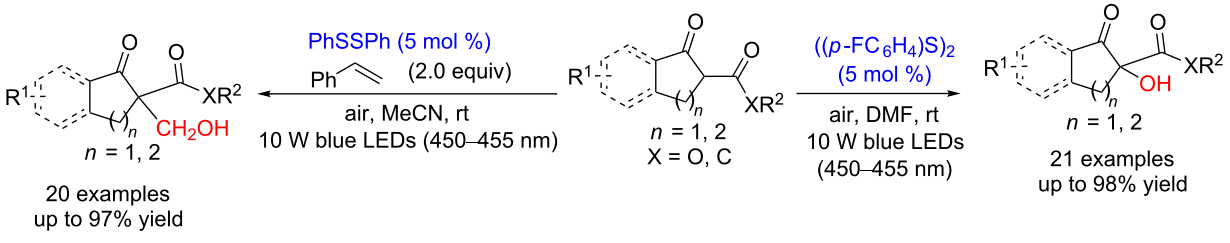

Scheme 10: Disulfide-catalyzed aerobic oxidation of 1,3-dicarbonyl compounds.

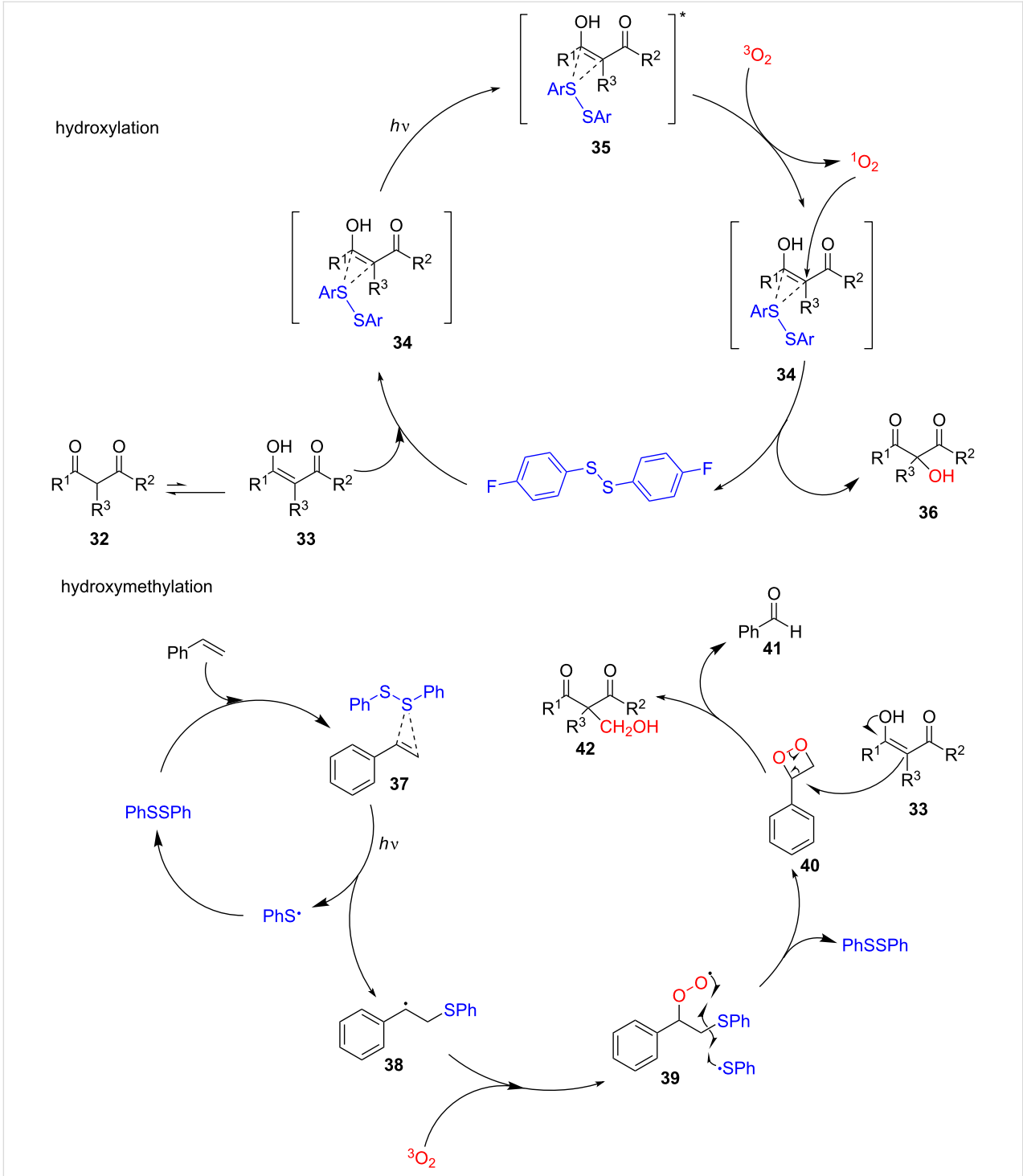

Scheme 11: Proposed mechanism of the disulfide-catalyzed aerobic oxidation of 1,3-dicarbonyl compounds.

radical to the styrene under irradiation, gives the intermediate species **39**. The abstraction of a thiyl radical from the intermediate **39** yields the key intermediate dioxetane **40** and regenerates the disulfide. Finally, the reaction between the enol **33** and the dioxetane **40** affords benzaldehyde (**41**) and the product **42**.

In 2008, Tsuboi and co-workers reported a photoinduced oxidation of allyl alcohols to acrylaldehydes at room temperature, catalyzed by diphenyl disulfide derivatives [18]. In the proposed mechanism, disulfide is split by the photoirradiation to form thiyl radicals. Then, the abstraction of the α-hydrogen atom from allyl alcohol by the thiyl radical produces thio-

phenol and an allylic radical. Next, the single-electron transfer (SET) from the allylic radical to another thiyl radical generates the allylic cation. Subsequently, the proton abstraction from the hydroxy group by the SET-generated thiolate gives the final oxidation product (Scheme 12). Interestingly, compared to the diphenyl disulfide-catalyzed oxidation, which gives only 23–44% yield, the use of dendrimer disulfides gives the products in much better yields (38–63%).

Similar to oxidations, disulfide can also be used as the catalyst to construct functional groups that contain heteroatoms. Ogawa and co-workers reported a class of efficient diboration reactions. Under light irradiation, disulfide was used as the photocatalyst to facilitate the addition of bis(pinacolato)diboron (B_2pin_2) to terminal alkynes [19], and the corresponding diboryl alkenes were generated with a yield of 43–75% (Scheme 13).

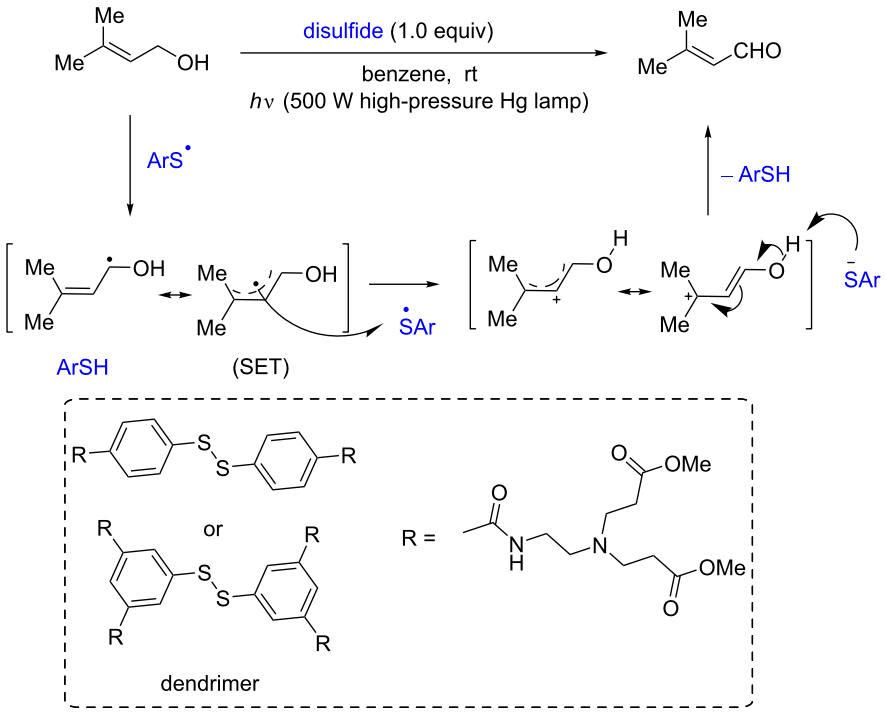

Scheme 12: Disulfide-catalyzed oxidation of allyl alcohols.

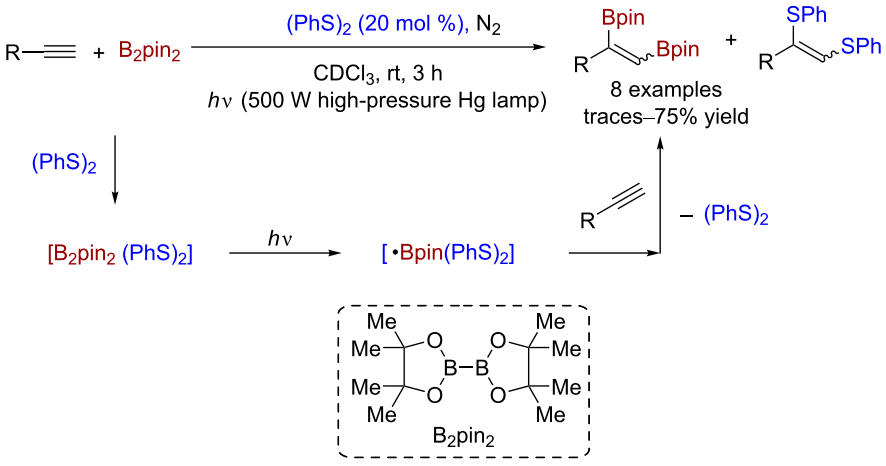

Scheme 13: Disulfide-catalyzed diboration of alkynes.

Reductive dehalogenation reactions

In 2013, Curran and co-workers reported a light-induced dehalogenative reduction with polarity reversion catalyzed by diphenyl disulfide or boryl bissulfide (diMe–Imd–BH(SPh)$_2$) as the catalyst and 1,3-dimethylimidazol-2-ylidene·borane (diMe–Imd–BH$_3$) as the initiator [20]. Thiyl radicals formed by diphenyl disulfide under light can further generate the active HAT catalyst thiophenol in situ. The yield of the reductive dehalogenation or dehalogenative radical cyclization could reach up to 40–98% (Scheme 14).

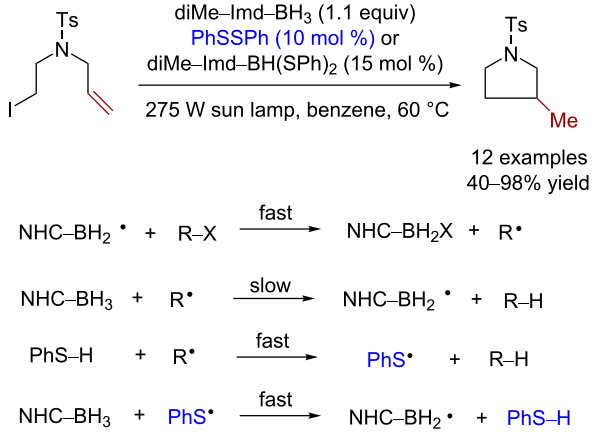

Scheme 14: Dehalogenative radical cyclization catalyzed by disulfide.

The introduction of fluorine-containing groups can effectively change the physical and chemical properties and biological activities of organic molecules [21,22]. The addition reaction using disulfide as the visible-light catalyst is an effective and atom-economic method for introducing fluorine-containing groups. In 2016, Cheng and co-workers reported a hydrodifluoroacetamidation of alkenes in which disulfide served as the photocatalyst with the Hantzsch ester as the reducing agent (Scheme 15) [23]. These reactions do not require costly transition-metal complexes, and they do not involve the oxidative regeneration of a photoredox catalyst or a carbocation species, which suppresses the formation of side products that are observed when using other methods.

The suggested mechanism by Cheng and co-workers is shown in Scheme 16. The reaction could go through two possible pathways. The generation of the phenyl thiyl radical **43** by homolysis of diphenyl disulfide under visible light triggers the HAT-initialized pathway 1. The hydrogen abstraction from the Hantzsch ester **44** by the thiyl radical **43** gives the ester radical **45**. Then, the subsequent SET from the Hantzsch ester radical **45** to the acetamide **46** forms the amide radical **48**, the protonated pyridine **47**, and bromide. The following addition of alkenes to the generated difluoroamide radical **48** gives the intermediate **49**. Finally, the desired difluoroalkylation product **50** is produced by a subsequent HAT from thiophenol to the intermediate **49**, and the thiyl radical **43** regenerates for the next catalytic cycle. The other plausible reaction pathway 2 starts with a SET from the excited Hantzsch ester **44** to the acetamide **46** to form the intermediate difluoroamide radical **48** and the cationic radical **51**. The subsequent addition of alkenes to the formed radical **48** and HAT from the intermediate **51** to the phenyl thiyl radical **43** yields the intermediate **49**, thiophenol, the protonated pyridine **47**, and bromide. Finally, HAT from the thiophenol to the intermediate **49** gives the difluoroalkylation product **50**.

Alkene functionalization reactions

The olefin hydration is an important method to synthesize alcohols, and realizing the anti-Markovnikov regioselectivity is extremely challenging. In 2017, Lei and co-workers reported a class of disulfide-cocatalyzed anti-Markovnikov olefin hydration reactions [24]. In this reaction, 9-mesityl-10-methylacridinium (Acr$^+$–Mes–ClO$_4^-$) and diphenyl disulfide are used as the photoredox catalyst to prepare the corresponding primary and secondary alcohols from terminal and internal olefins. The substrate scope is broad, with excellent regioselectivities and yields up to 96% (Scheme 17).

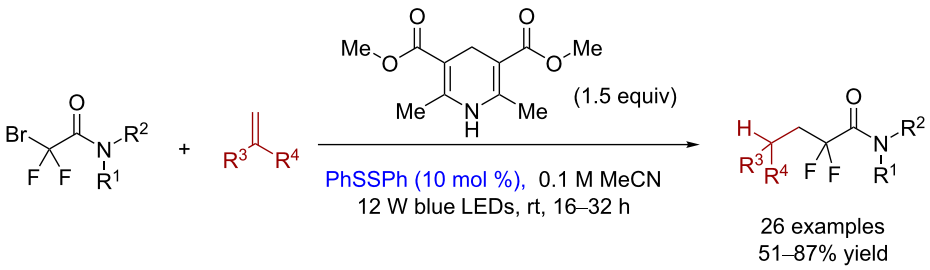

Scheme 15: Hydrodifluoroacetamidation of alkenes catalyzed by disulfide.

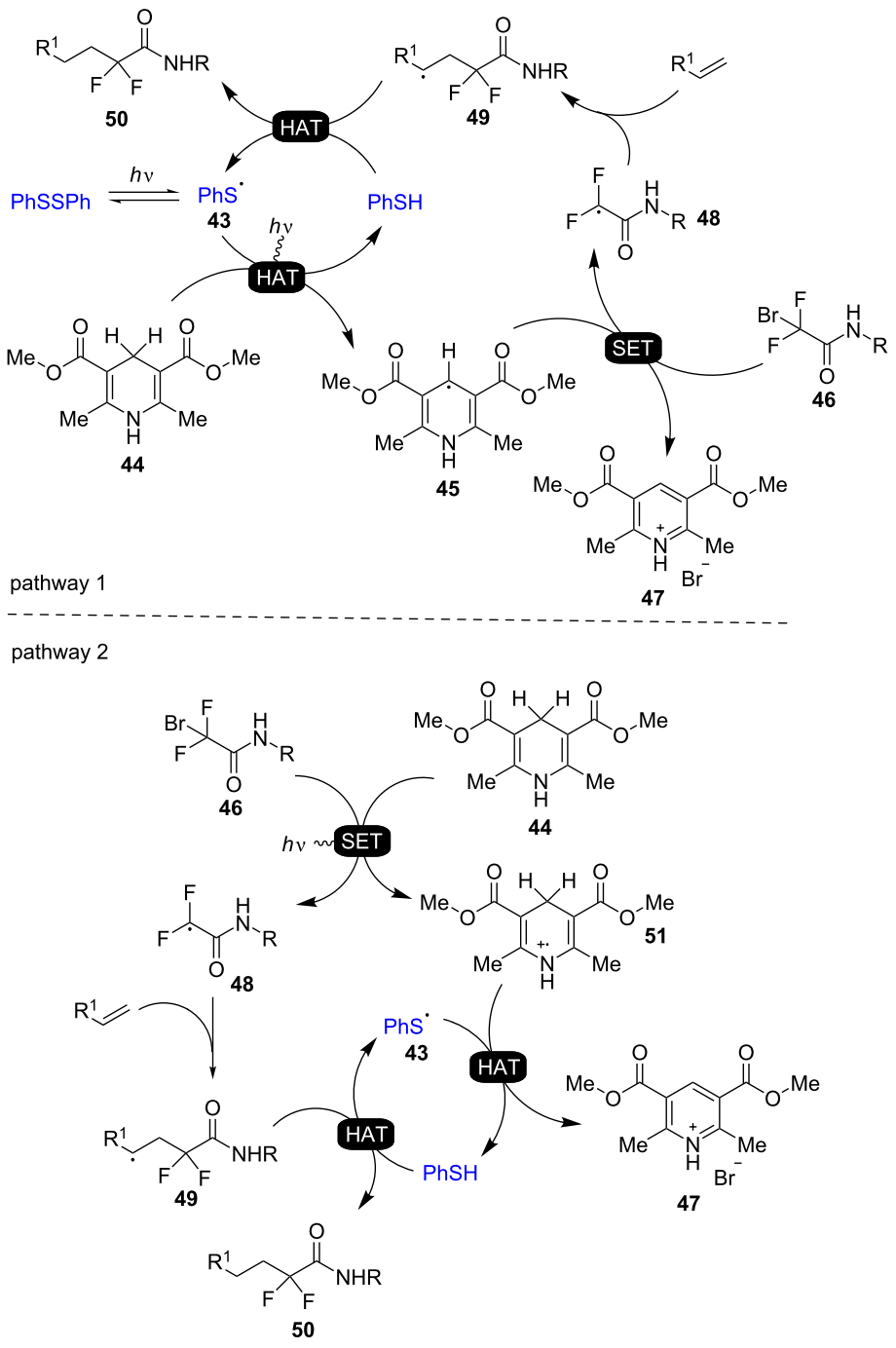

Scheme 16: Plausible mechanism of the hydrodifluoroacetamidation of alkenes catalyzed by disulfide.

Decarboxylation reactions

Carboxylic acid often serves as an inexpensive and abundant source of biomass-derived molecules. Decarboxylative transformations of carboxylic acids into value-added chemical products (such as biofuels) are a key objective in organic synthesis [25]. In 2014, Wallentin and co-workers reported a type of decarboxylation reaction of α-amino acids, α-hydroxy acids, and phenylacetic acids using an acridinium photoredox catalyst (Mes–Acr–Me) and bis(4-chlorophenyl) disulfide as catalysts (Scheme 18) [26].

The proposed mechanism for this reaction is shown in Scheme 19. The reaction begins with the photoexcitation of the catalyst Mes–Acr–Me, which generates the active species

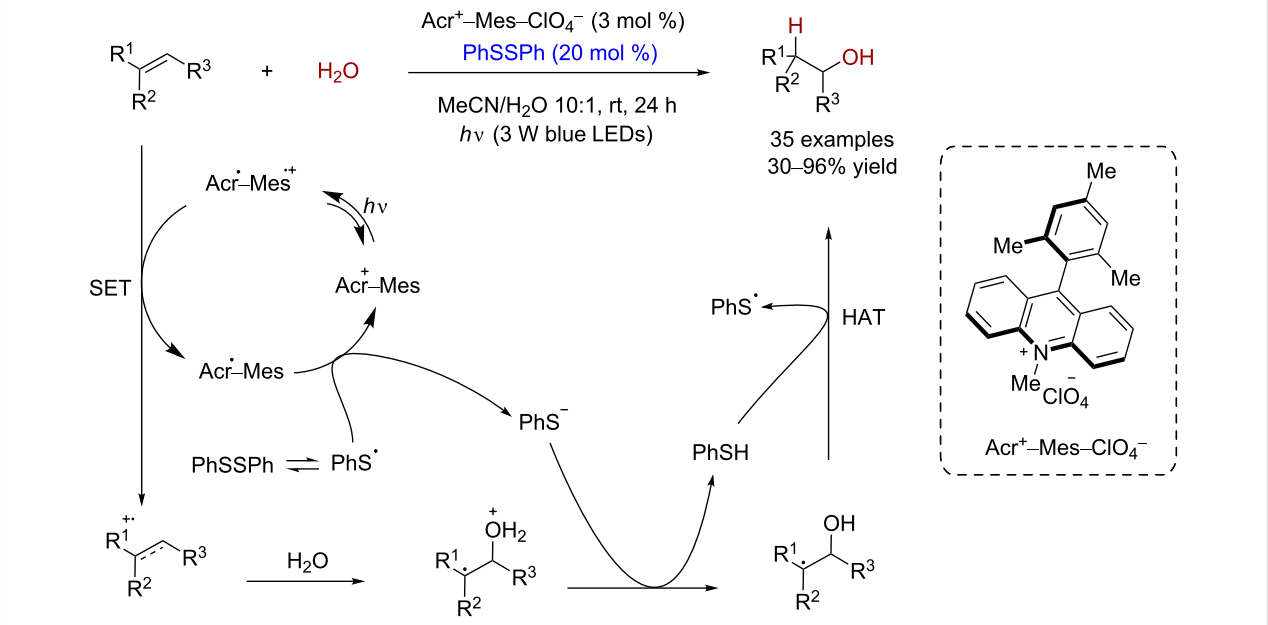

Scheme 17: Disulfide-cocatalyzed anti-Markovnikov olefin hydration reactions.

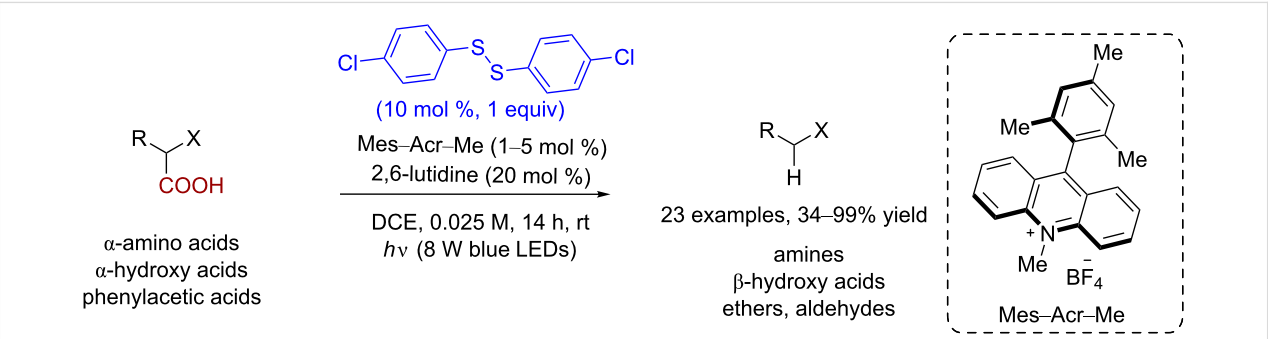

Scheme 18: Disulfide-catalyzed decarboxylation of carboxylic acids.

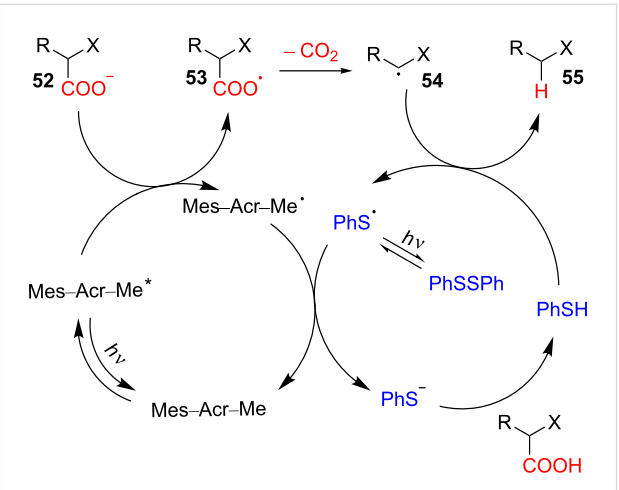

Scheme 19: Proposed mechanism of the disulfide-catalyzed decarboxylation of carboxylic acids.

Mes–Acr–Me*. Then, the single-electron oxidation of the deprotonated carboxylic acid **52** with Mes–Acr–Me* results in the formation of an acyloxyl radical **53**. The subsequent rearrangement of the radical **53** gives a carbon-centered radical **54** and carbon dioxide. The phenyl thiyl radical formed via the illumination of disulfide reoxidizes the reduced catalyst to regenerate the ground state of the photocatalyst Mes–Acr–Me. Then, the thiolate anion is protonated to give thiophenol, which then acts as a hydrogen-atom donor towards the carbon-centered radical **54** to furnish the final hydrodecarboxylation product **55**.

Nicewicz and co-workers also reported the decarboxylation of carboxylic acids and malonic acid derivatives catalyzed by an acridinium photoredox catalyst (Mes–Acr–Ph) and PhSSPh in 2015 (Scheme 20) [27]. This direct method of the organocatalytic decarboxylation of carboxylic acids to alkanes provided an efficient protocol for the synthesis of alkanes from carboxylic

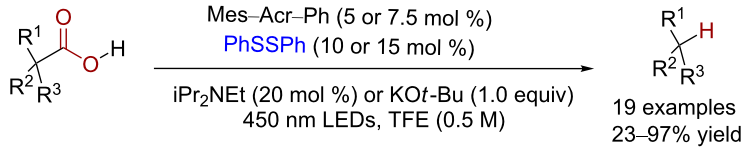

Scheme 20: Disulfide-catalyzed decarboxylation of carboxylic acids.

acid substrates previously inaccessible through other methods. The mechanism of this reaction is similar to the previously proposed mechanism in Scheme 19.

Isomerization reactions

Thiyl radical-mediated isomerizations of C=C bonds are an effective method in organic synthesis. In 1999, Harrowven and co-workers reported a photoinduced diphenyl disulfide-catalyzed conversion of maleate esters to fumarates and 5*H*-furanones [28]. Five equivalents of diphenyl disulfide and a maleate derivative, such as **56**, were refluxed in hexane for 4–72 hours under irradiation from a 125 W medium-pressure mercury lamp, and 5*H*-furanones were obtained in moderate to good yield (44–77%, Scheme 21). Under the same reaction conditions, unsubstituted maleate esters were also nearly quantitatively converted to the corresponding fumarate esters.

In 1996, Burton and co-workers reported the stereoselective synthesis of *cis*-1,2-difluorotriethylsilyethylene and its conversion to a variety of *cis*-1,2-difluoroethylene synthons, which are important building blocks in the preparation of fluorine-containing pharmaceuticals, polymers, and bioactive compounds. In the synthesis of these synthons, the key transformation, the isomerization of the *trans*-1,2-difluorotriethylsilylethylene **57** to the *cis* isomer **58**, is realized with phenyl disulfide under ultraviolet-light irradiation (Scheme 22) [29].

In 2009, Tsuboi and co-workers also reported a dendrimer disulfide-catalyzed isomerization of allyl alcohols to carbonyl compounds under high-pressure mercury lamp irradiation (λ > 300 nm) at room temperature. The yield of the reaction reached up to 91% (Scheme 23) [30]. Using the water-soluble dendrimer disulfide, the photoinduced isomerization in water

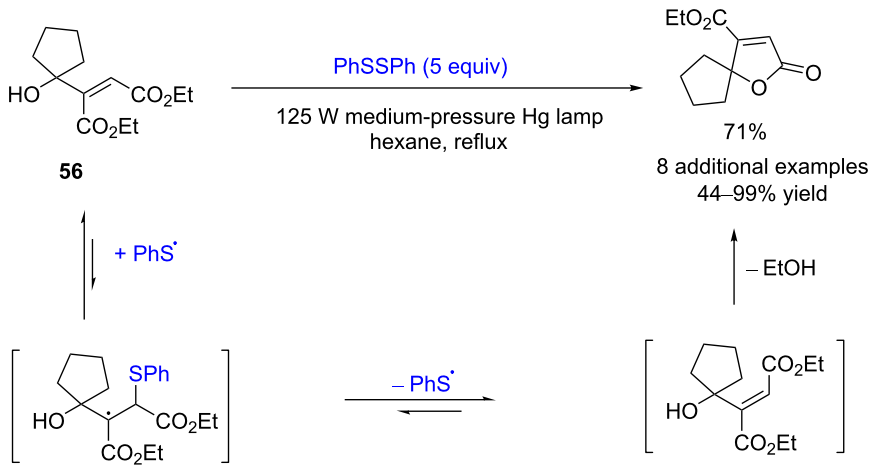

Scheme 21: Disulfide-catalyzed conversion of maleate esters to fumarates and 5*H*-furanones.

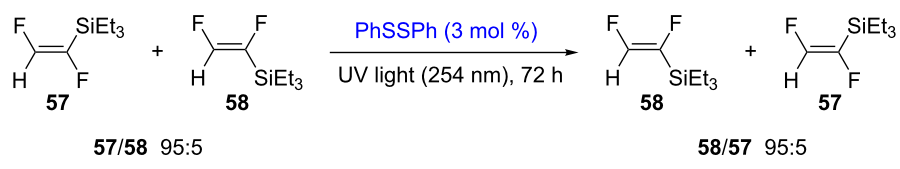

Scheme 22: Disulfide-catalyzed isomerization of difluorotriethylsilylethylene.

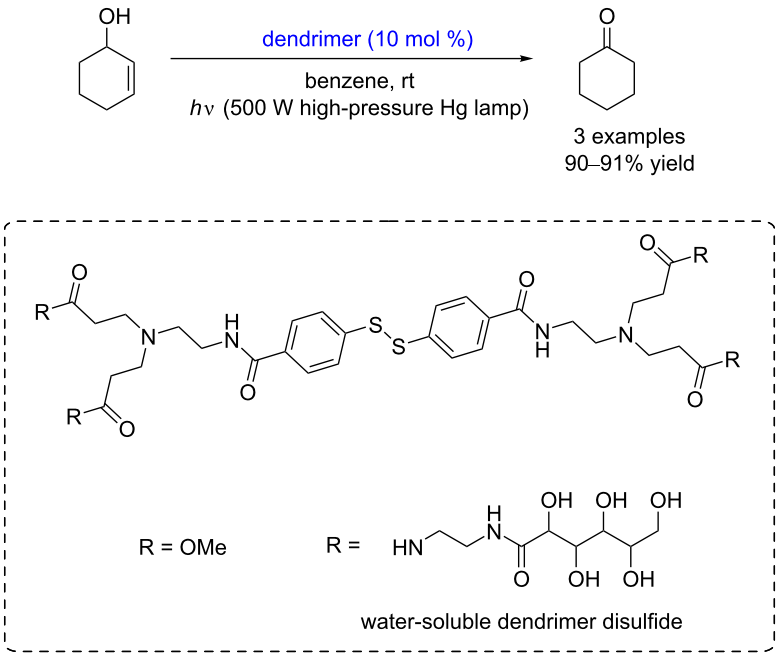

Scheme 23: Disulfide-catalyzed isomerization of allyl alcohols to carbonyl compounds.

was also successful. For the photoinduced oxidation reaction of allyl alcohols, the dendrimer disulfide is a better mediator than diphenyl disulfide, because dendritic substituents are quite effective in inhibiting side reactions initiated by the addition of sulfanyl radicals to the unsaturated bonds.

A plausible mechanism of the catalytic isomerization is shown in Scheme 24. The oxidation step of isomerization is initiated by thiyl radicals, which are generated under illumination. Then, the formed thiyl radical abstracts an α-hydrogen atom from allyl alcohols to give thiophenol and the allylic radical **59**. The subsequent SET from the radical **60** to the thiyl radical yields the allylic cation **61** and a thiolate anion. The following proton abstraction by this thiolate anion from the intermediate **62** gives the enone **63** and thiophenol to complete the oxidation. In the hydrogenation step, the addition of a thiyl radical to the enone **63** and posterior hydrogen transfer from thiol to the intermediate **64** forms the ketone intermediate **65** (pathway 1). This ketone intermediate **65** is also accessible by an ionic addition in the dark (pathway 2). The tautomerization of the ketone **65** yields the enol form **66**, which reacts with a thiyl radical (pathway 3) or a thiolate anion (pathway 4) to regenerate the disulfide. Finally, the formed intermediates **67** and **68** furnish the final product **69** by hydrogen (pathway 3) or proton transfer processes (pathway 4), respectively.

Disulfide-catalyzed isomerization processes also found applications in total synthesis, medium- and large-ring syntheses, and conjugate diene isomerization processes. In 2006, Crimmins successfully used this isomerization method in the syntheses of ophirin B and astrogorgin (Scheme 25) [31]. In the reaction, the intermediate **70** reacts with benzyloxymethylenetriphenylphosphane to give the dienes **71** and **72** as a 3:1 mixture. At room temperature, the resulting (*E*,*E*)-isomer **71** is quantitatively converted into the desired oxatricyclic system **74** via a diastereoselective Diels–Alder cycloaddition process. However, the (*Z*,*E*)-isomer **72** remains unreactive under these reaction conditions. In order to convert the unreactive isomer **72** to the reactive isomer **71**, different isomerization methods were tested. When iodine was used as the isomerization agent, the hydrolysis of the enol moiety took place, and the irradiation with Me_6Sn_2 and Bu_6Sn_2 did not initiate any isomerization of the (*Z*,*E*)-isomer **72**. Under irradiation with a catalytic amount of diphenyl disulfide, the isomerization of the (*Z*,*E*)-isomer **72** to the (*E*,*E*)-isomer **71** was successfully achieved. In the reaction, the irradiation of the (*Z*,*E*)-isomer **72** with diphenyl disulfide also produced the (*E*,*Z*)-isomer **73**. But in the presence of PhSSPh, the new isomer **73** could also be converted to the desired (*E*,*E*)-isomer **71**.

In the total synthesis of the macrocyclic antibiotic antitumor agent (+)-hitachimycin, Smith used a disulfide-catalyzed isomerization [32] to synthesize the intermediate **75** with an *E*-configuration, which was unsuccessful to be prepared by the Schlosser modification of the Wittig olefination (Scheme 26) [33].

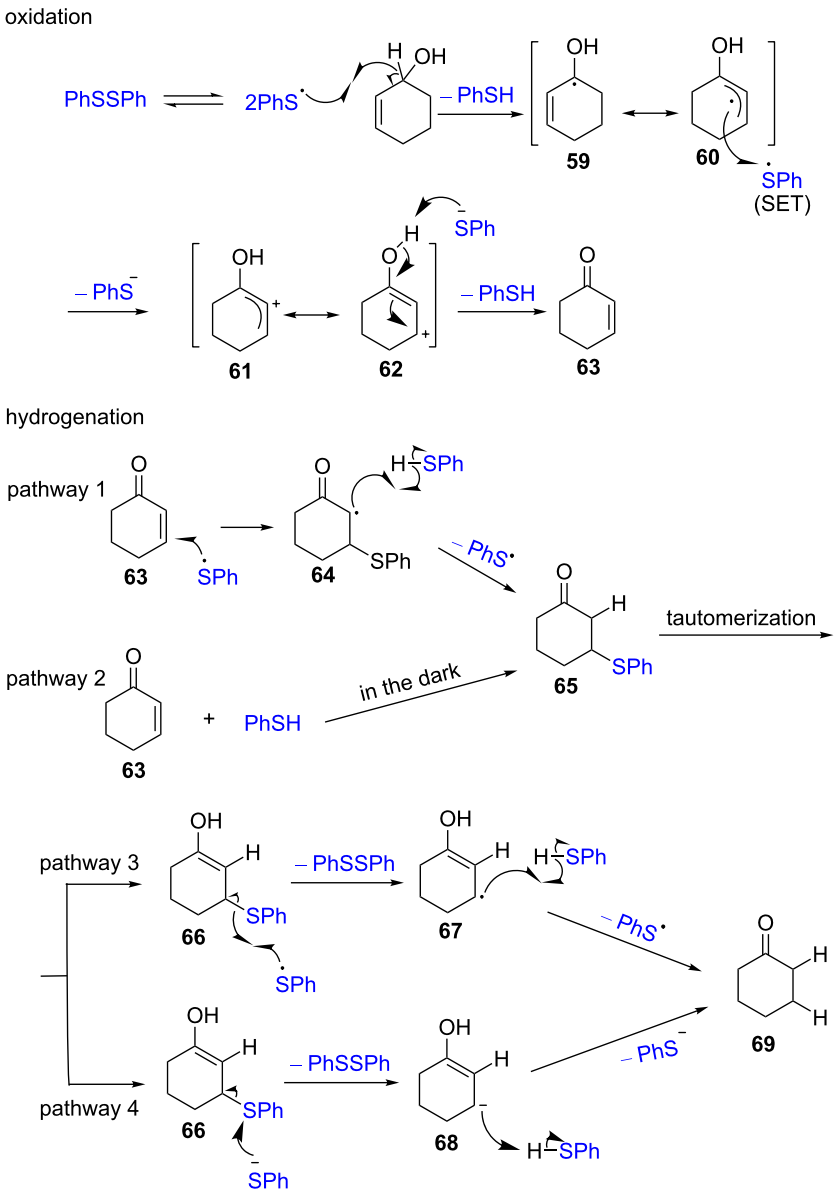

Scheme 24: Proposed mechanism for the disulfide-catalyzed isomerization of allyl alcohols to carbonyl compounds.

A similar isomerization method was also used by Holmes in the synthesis of (−)-gloeosporone. Under irradiation conditions, diphenyl disulfide helped to convert the *Z*-alkene **76** to the *E*-alkene **77** (Scheme 27) [34].

Conclusion

In conclusion, under photoirradiation, organic disulfides can be easily cleaved into free radicals and can reversibly add to unsaturated multiple bonds to catalyze a variety of functionalization reactions under mild conditions. Disulfide-catalyzed oxidations of alkenes and alkynes are highly attractive because the reagents involved in the reaction process are simple and inexpensive, plus they only require molecular oxygen or air. In addition, disulfide-catalyzed cyclization reactions are also very effective for the generation of five- and six-membered rings. The unique high selectivity and mildness of disulfide-catalyzed isomerizations enables the broad applications of this method, especially in cases where this cannot be achieved by other isomerization methods. Overall, it should become an effective tool in the organic chemist's toolbox. Although disulfide-catalyzed photoreactions have gained some interest from researchers, their full potential has not been discovered and released yet. They are environmentally friendly and efficient catalyst that deserve more attention.

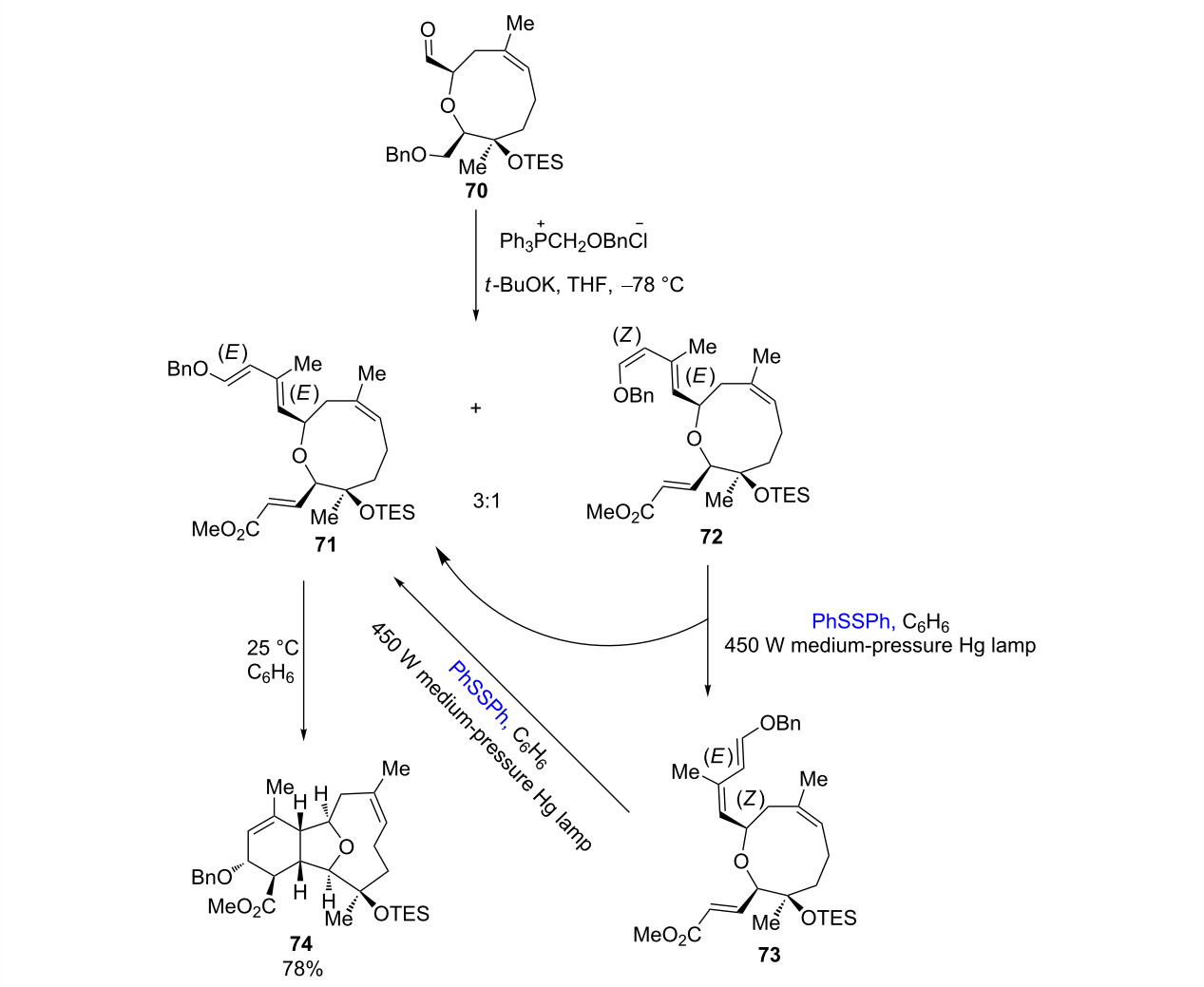

Scheme 25: Diphenyl disulfide-catalyzed enantioselective synthesis of ophirin B.

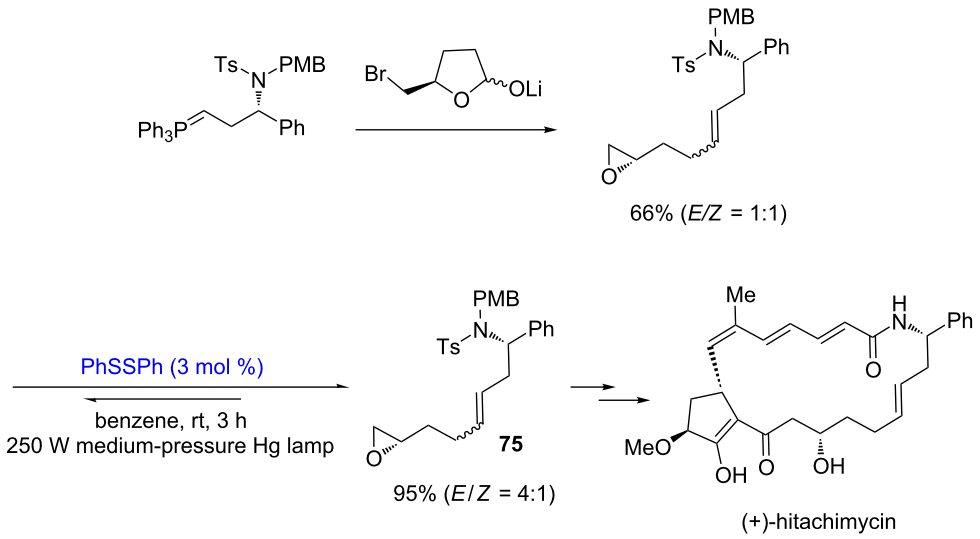

Scheme 26: Disulfide-catalyzed isomerization in the total synthesis of (+)-hitachimycin.

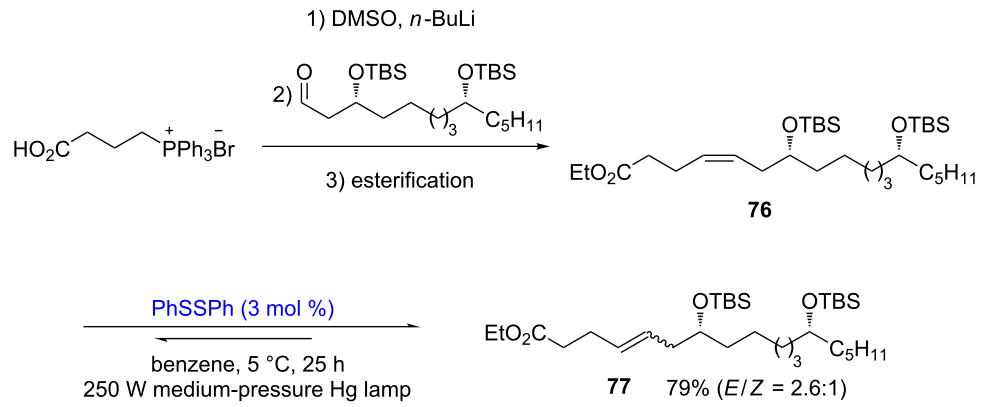

Scheme 27: Disulfide-catalyzed isomerization in the synthesis of (–)-gloeosporone.

Acknowledgements

I thank Prof. Xiao Wang (Nanjing University) for helpful discussions.

Funding

I thank the National Natural Science Foundation of China (NSFC, Grant # 21872068) for financial support.

References

1. Cremlyn, R. J. *An Introduction to Organosulfur Chemistry;* John Wiley & Sons, Inc.: Hoboken, NJ, 1996.
2. Dénès, F.; Pichowicz, M.; Povie, G.; Renaud, P. *Chem. Rev.* **2014,** *114,* 2587–2693. doi:10.1021/cr400441m
3. Breder, A.; Depken, C. *Angew. Chem., Int. Ed.* **2019,** *58,* 17130–17147. doi:10.1002/anie.201812486
4. Feldman, K. S.; Romanelli, A. L.; Ruckle, R. E.; Miller, R. F. *J. Am. Chem. Soc.* **1988,** *110,* 3300–3302. doi:10.1021/ja00218a050
5. Hashimoto, T.; Takino, K.; Hato, K.; Maruoka, K. *Angew. Chem., Int. Ed.* **2016,** *55,* 8081–8085. doi:10.1002/anie.201602723
6. Jung, M. E.; Rayle, H. L. *J. Org. Chem.* **1997,** *62,* 4601–4609. doi:10.1021/jo9706133
7. Hashimoto, T.; Kawamata, Y.; Maruoka, K. *Nat. Chem.* **2014,** *6,* 702–705. doi:10.1038/nchem.1998
8. Ryss, J. M.; Turek, A. K.; Miller, S. J. *Org. Lett.* **2018,** *20,* 1621–1625. doi:10.1021/acs.orglett.8b00364
9. Singleton, D. A.; Church, K. M. *J. Org. Chem.* **1990,** *55,* 4780–4782. doi:10.1021/jo00303a002
10. Singleton, D. A.; Church, K. M.; Lucero, M. J. *Tetrahedron Lett.* **1990,** *31,* 5551–5554. doi:10.1016/s0040-4039(00)97894-8
11. Singleton, D. A.; Huval, C. C.; Church, K. M.; Priestley, E. S. *Tetrahedron Lett.* **1991,** *32,* 5765–5768. doi:10.1016/s0040-4039(00)93550-0
12. Huval, C. C.; Singleton, D. A. *J. Org. Chem.* **1994,** *59,* 2020–2024. doi:10.1021/jo00087a015
13. Wang, L.; Wu, F.; Chen, J.; Nicewicz, D. A.; Huang, Y. *Angew. Chem., Int. Ed.* **2017,** *56,* 6896–6900. doi:10.1002/anie.201702940
14. Kim, S.; Lee, S. *Tetrahedron Lett.* **1991,** *32,* 6575–6578. doi:10.1016/0040-4039(91)80225-u
15. Zhu, X.; Li, P.; Shi, Q.; Wang, L. *Green Chem.* **2016,** *18,* 6373–6379. doi:10.1039/c6gc01487a
16. Deng, Y.; Wei, X.-J.; Wang, H.; Sun, Y.; Noël, T.; Wang, X. *Angew. Chem., Int. Ed.* **2017,** *56,* 832–836. doi:10.1002/anie.201607948
17. Zhao, J.; Yang, F.; Yu, Z.; Tang, X.; Wu, Y.; Ma, C.; Meng, Q. *Chem. Commun.* **2019,** *55,* 13008–13011. doi:10.1039/c9cc06544j
18. Tsuboi, T.; Takaguchi, Y.; Tsuboi, S. *Bull. Chem. Soc. Jpn.* **2008,** *81,* 361–368. doi:10.1246/bcsj.81.361
19. Yoshimura, A.; Takamachi, Y.; Han, L.-B.; Ogawa, A. *Chem. – Eur. J.* **2015,** *21,* 13930–13933. doi:10.1002/chem.201502425
20. Pan, X.; Lalevée, J.; Lacôte, E.; Curran, D. P. *Adv. Synth. Catal.* **2013,** *355,* 3522–3526. doi:10.1002/adsc.201300752
21. Fujiwara, T.; O'Hagan, D. *J. Fluorine Chem.* **2014,** *167,* 16–29. doi:10.1016/j.jfluchem.2014.06.014
22. Zhou, Y.; Wang, J.; Gu, Z.; Wang, S.; Zhu, W.; Aceña, J. L.; Soloshonok, V. A.; Izawa, K.; Liu, H. *Chem. Rev.* **2016,** *116,* 422–518. doi:10.1021/acs.chemrev.5b00392
23. Huang, W.; Chen, W.; Wang, G.; Li, J.; Cheng, X.; Li, G. *ACS Catal.* **2016,** *6,* 7471–7474. doi:10.1021/acscatal.6b02420
24. Hu, X.; Zhang, G.; Bu, F.; Lei, A. *ACS Catal.* **2017,** *7,* 1432–1437. doi:10.1021/acscatal.6b03388
25. Straathof, A. J. J. *Chem. Rev.* **2014,** *114,* 1871–1908. doi:10.1021/cr400309c
26. Cassani, C.; Bergonzini, G.; Wallentin, C.-J. *Org. Lett.* **2014,** *16,* 4228–4231. doi:10.1021/ol5019294
27. Griffin, J. D.; Zeller, M. A.; Nicewicz, D. A. *J. Am. Chem. Soc.* **2015,** *137,* 11340–11348. doi:10.1021/jacs.5b07770
28. Harrowven, D. C.; Hannam, J. C. *Tetrahedron* **1999,** *55,* 9341–9346. doi:10.1016/s0040-4020(99)00496-2
29. Fontana, S. A.; Davis, C. R.; He, Y.-B.; Burton, D. J. *Tetrahedron* **1996,** *52,* 37–44. doi:10.1016/0040-4020(95)00861-2
30. Tsuboi, T.; Takaguchi, Y.; Tsuboi, S. *Heteroat. Chem.* **2009,** *20,* 1–11. doi:10.1002/hc.20504
31. Crimmins, M. T.; Brown, B. H.; Plake, H. R. *J. Am. Chem. Soc.* **2006,** *128,* 1371–1378. doi:10.1021/ja056334b
32. Thalmann, A.; Oertle, K.; Gerlach, H. *Org. Synth.* **1985,** *63,* 192. doi:10.15227/orgsyn.063.0192

33. Smith, A. B.; Rano, T. A.; Chida, N.; Sulikowski, G. A. *J. Org. Chem.* **1990,** *55,* 1136–1138. doi:10.1021/jo00291a005
34. Curtis, N. R.; Holmes, A. B.; Looney, M. G.; Pearson, N. D.; Slim, G. C. *Tetrahedron Lett.* **1991,** *32,* 537–540. doi:10.1016/s0040-4039(00)79490-1

License and Terms

This is an Open Access article under the terms of the Creative Commons Attribution License (http://creativecommons.org/licenses/by/4.0). Please note that the reuse, redistribution and reproduction in particular requires that the authors and source are credited.

The license is subject to the *Beilstein Journal of Organic Chemistry* terms and conditions: (https://www.beilstein-journals.org/bjoc)

The definitive version of this article is the electronic one which can be found at: doi:10.3762/bjoc.16.118

BEILSTEIN JOURNAL OF ORGANIC CHEMISTRY

Photocatalyzed syntheses of phenanthrenes and their aza-analogues. A review

Alessandra Del Tito[1], Havall Othman Abdulla[1,2], Davide Ravelli[1], Stefano Protti[1] and Maurizio Fagnoni[*1]

Review

Open Access

Address:
[1]Photogreen Lab, Department of Chemistry, University of Pavia, Viale Taramelli 12, 27100 Pavia, Italy and [2]Chemistry Department, College of Science, Salahaddin University, Erbil, Iraq

Email:
Maurizio Fagnoni[*] - fagnoni@unipv.it

* Corresponding author

Keywords:
phenanthrenes; phenanthridines; photocatalysis; radicals; visible light

Beilstein J. Org. Chem. **2020,** *16,* 1476–1488.
doi:10.3762/bjoc.16.123

Received: 22 April 2020
Accepted: 02 June 2020
Published: 25 June 2020

This article is part of the thematic issue "Advances in photoredox catalysis".

Guest Editor: T. Noël

© 2020 Del Tito et al.; licensee Beilstein-Institut.
License and terms: see end of document.

Abstract

Phenanthrenes and their aza-analogues have important applications in materials science and in medicine. Aim of this review is to collect recent reports describing their synthesis, which make use of radical cyclizations promoted by a visible light-triggered photocatalytic process.

Introduction

Phenanthrenes are widely investigated compounds, due to the impressive number of diverse applications involving this scaffold, ranging from medicinal chemistry [1] to materials sciences, including their use in optoelectronics [2,3] and in the design of dye-sensitized solar cells (DSSC) [4]. Typical methods for the construction of a phenanthrene core involve transition-metal-catalyzed cycloisomerizations starting from arynes [5,6], *o*-alkynyl-biaryls [7,8], or substituted *N*-tosylhydrazones [9].

However, since the introduction in 1964 of the Mallory photocyclization of stilbenes [10] leading to phenanthrenes, the interest in protocols for the construction of poly(hetero)aromatic cores under photochemical conditions has increased steadily, especially when solar light may be used [11].

Moreover, aza-analogues of phenanthrenes, in particular phenanthridines, are substructures present in a wide range of both natural and synthetic products, including trisphaeridine [12] (that exhibits an anti-HIV-I protease activity) and the antifungal sanguinarine [13]. Some phenantridinium derivatives are known as well, notably fagaronine (a DNA topoisomerase 1 inhibitor [14] and DNA intercalator), bicolorine (5-methyl-[1,3]dioxolo[4,5-*j*]phenanthridin-5-ium ion, a trypanocidal)

[15], and the antimalarian nitidine, as well as ethidium bromide (EB), that has been employed as a DNA- and RNA-fluorescent marker for a long time (some examples are collected in Figure 1). For these reasons, apart from the well-known dehydrative ring-closure of acyl-*o*-xenylamines in the presence of phosphorus oxychloride proposed by Morgan and Walls [16], several synthetic protocols for constructing the phenanthridine structure have been reported [17,18]. These include, among the others, the anionic ring-closure of 2-cyanobiaryls by using organometallic reagents [19,20], and an impressive number of transition-metal-catalyzed $C(sp^2)$–$C(sp^2)$ cross-coupling processes [21-23].

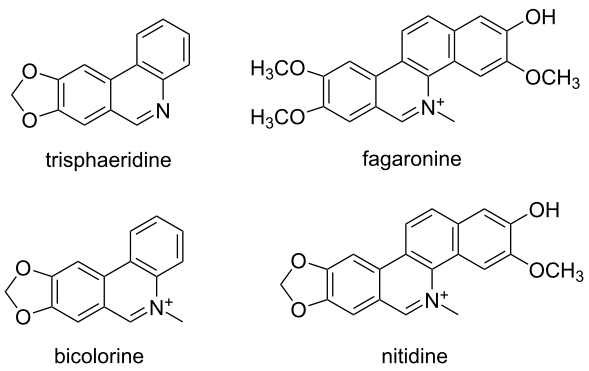

Figure 1: Bioactive phenanthridine and phenanthridinium derivatives.

In the last decade, however, photochemical reactions, especially those promoted by a photocatalyst, have revolutionized the way chemists can arrive to important chemical scaffolds [24-26]. Indeed, the photocatalytic approach combines unparalleled mild conditions, due to the use of photons as traceless reagents that leave no residue behind [27,28], with the exploitation of rather inexpensive visible light (or sunlight, when possible) irradiation [29]. In general terms, photocatalysis smoothly gives access to reactive radical intermediates [30], mainly carbon-centered [31-33], or nitrogen-centered radicals [34,35]. In turn, these species have been extensively employed in radical cyclizations for the synthesis of polycondensed aromatics, with a focus on those containing heteroatoms [36-39]. The aim of the present review is to summarize the recent efforts in the design and optimization of photocatalyzed procedures for the synthesis of phenanthrenes and their nitrogen-containing heteroarene analogues via the intermediacy of a radical. However, some interesting approaches carried out under photomediated or photocatalyst-free conditions have been likewise included for the sake of completeness.

Review

1 Synthesis of phenanthrenes

The photocatalyzed synthesis of the phenanthrene skeleton is a quite unexplored field, a notable exception being the seminal work published in 1984 by Cano-Yelo and Deronzier, where the authors reported one of the first applications of the $Ru(bpy)_3^{2+}$ complex in photoredox catalysis (Scheme 1). This contribution described a photo-Pschorr cyclization occurring on a stilbene diazonium salt (e.g., **1.1**$^+$) with the intermediacy of an aryl radical [40].

Alternative strategies for the synthesis of phenanthrenes have been later reported, including the adoption of [4 + 2] benzannulations between biaryl derivatives and alkynes [41,42]. Scheme 2 illustrates one of such cases where an aryl radical, formed via the photocatalyzed reduction of diazonium salt **2.1**$^+$, added to methyl propiolate. Ensuing cyclization of the resulting vinyl radical **2.2**$^\cdot$ finally yielded the desired phenanthrene **2.3** [41].

A different approach involves the intramolecular cyclization of α-bromochalcones (Scheme 3). Thus, compounds **3.1a–d** underwent a one-electron reduction by the excited photocatalyst *fac*-$Ir(ppy)_3$. Upon bromide anion loss, the α-keto vinyl radicals **3.2**$^\cdot$**a–d** were then formed, which smoothly added onto the vicinal aromatic ring in an intramolecular fashion, affording phenanthrene derivatives **3.3a–d** upon rearomatization. Notably, the process offers a wide substrate scope and the products are obtained with complete regioselectivity [43].

2 Synthesis of phenanthridines or related azaarenes

Under photocatalyzed conditions, phenanthridines are mostly obtained via an intramolecular radical cyclization occurring in a biphenyl moiety or a related system containing two aromatic

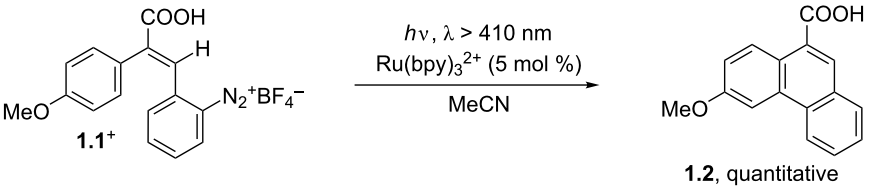

Scheme 1: Synthesis of phenanthrenes by a photo-Pschorr reaction.

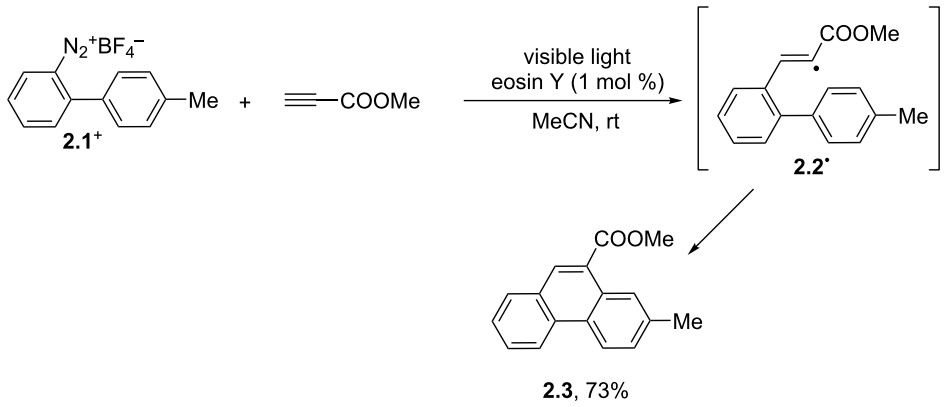

Scheme 2: Synthesis of phenanthrenes by a benzannulation reaction.

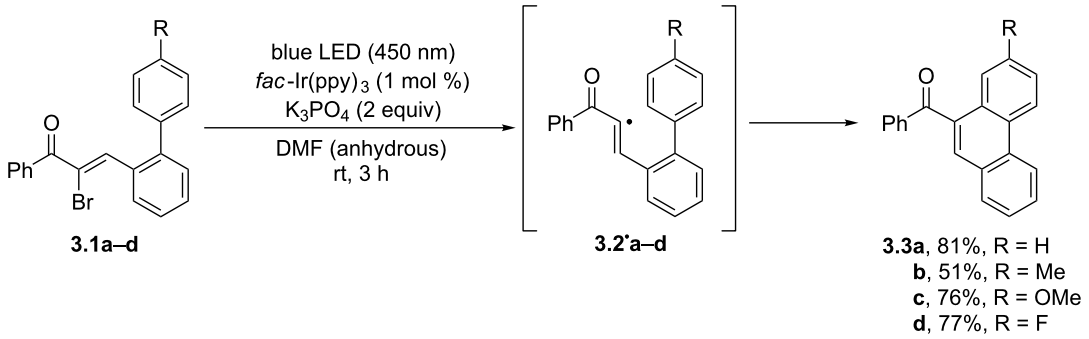

Scheme 3: Photocatalytic cyclization of α-bromochalcones for the synthesis of phenanthrenes.

rings. Either carbon-centered radicals (e.g., imidoyl, α-aminoalkyl, or phenyl) or nitrogen-centered radicals (e.g., iminyl or amidyl) can be used for this purpose as shown in Figure 2. Accordingly, the azaarene may be formed by an intramolecular C–C or C–N bond-formation event, as detailed in the following.

2.1 Synthesis of phenanthridines via photocatalyzed intramolecular C–C bond formation

A typical approach makes use of imidoyl radicals [30,44] as the key intermediates. Among the different methods proposed to construct the phenanthridine core, somophilic (radical) isocyanide addition [45-47] is probably the most adopted one, in view of the versatility and low cost of the starting substrates. Accordingly, several protocols for the synthesis under photocatalytic conditions of phenanthridines starting from 2-isocyano-1,1'-biaryls **4.1** have been reported, as summarized in Scheme 4. Along with substrate **4.1**, a radical source R–X and a photocatalyst (PC), which is activated upon visible-light irradiation, are usually required. Oxidative quenching of the photoexcited PC* by R–X (path a) affords, upon loss of the nucleofugal group X^-,

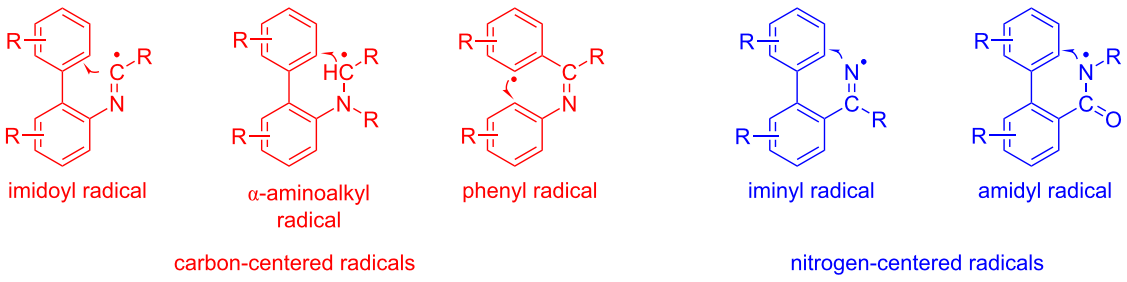

Figure 2: Carbon-centered and nitrogen-centered radicals used for the synthesis of phenanthridines.

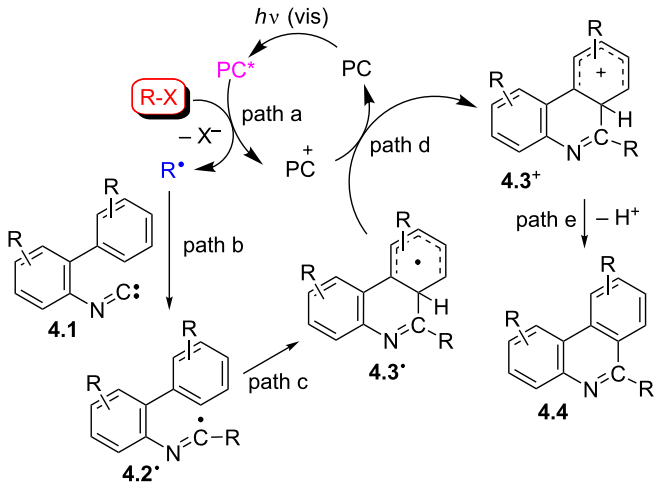

Scheme 4: General scheme describing the synthesis of phenanthridines from isocyanides via imidoyl radicals.

the intermediate R•, that is in turn trapped by **4.1** (path b). The resulting imidoyl radical **4.2**• undergoes cyclization to **4.3**• (path c) that is oxidized by PC•+, thus restoring the starting photocatalyst PC and forming the Wheland intermediate **4.3**$^+$ (path d). Deprotonation of **4.3**$^+$ (path e) finally yields the desired phenanthridine **4.4**.

Different radical sources R–X have been adopted to generate carbon or heteroatom-based radicals according to the general photocatalytic strategy gathered in Scheme 4, for their use in the construction of phenanthridine scaffolds. As an example, unsubstituted alkyl radicals were easily accessed by the photocatalyzed reduction of the corresponding bromides, in turn promoting an efficient radical addition onto isonitriles. In one instance, the dimeric gold complex $[Au_2(dppm)_2]Cl_2$ (dppm = bis(diphenylphosphino)methane) acted as the photocatalyst and activated the bromoalkanes through an oxidative quenching mechanism [48]. Phenanthridines may be also formed by the initial addition of an electrophilic radical onto isonitriles. Thus, a library of 6-alkylated phenanthridines (**5.2a–d** in Scheme 5) and other nitrogen-based heterocycles have been prepared from biaryls **5.1a–d** in up to excellent yields at room temperature by using α-bromoesters as radical precursors and [*fac*-Ir(ppy)$_3$] as the photoredox catalyst [49].

A similar photocatalyzed tandem insertion/cyclization approach based on isocyanides and amino acid/peptide-derived Katritzky salts as precursors of α-carbonyl radicals was likewise reported [50]. On the contrary, the Mn(acac)$_3$ photocatalyzed ring opening of cyclopropanol **6.2** gave an easy access to a β-carbonyl radical **6.5**•, which in turn added onto 2-biphenyl isocyanide **6.1** to give the corresponding 6-β-ketoalkyl phenanthridine **6.3** in a good yield (Scheme 6) [51].

The synthesis of perfluoroalkylated phenanthridines has been the subject of several studies in recent years. Accordingly, the use of perfluoroalkyl iodides and bromides for the synthesis of 6-trifluoroethyl [52], 6-difluoromethylphosphonated [53,54], and 6-mono- and difluoroalkyl- [55,56] phenanthridines was investigated. On the other hand, Umemoto's reagent **7.2** was

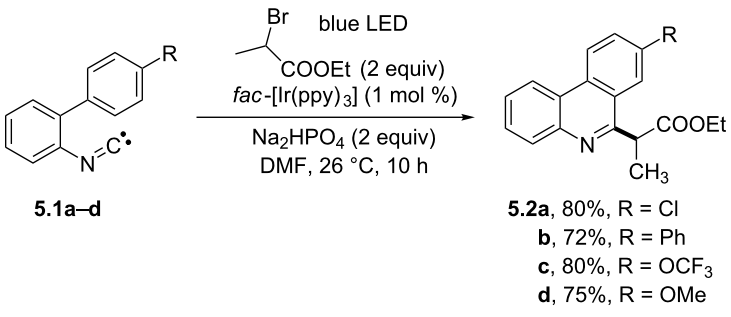

Scheme 5: Synthesis of substituted phenanthridines involving the intermediacy of electrophilic radicals.

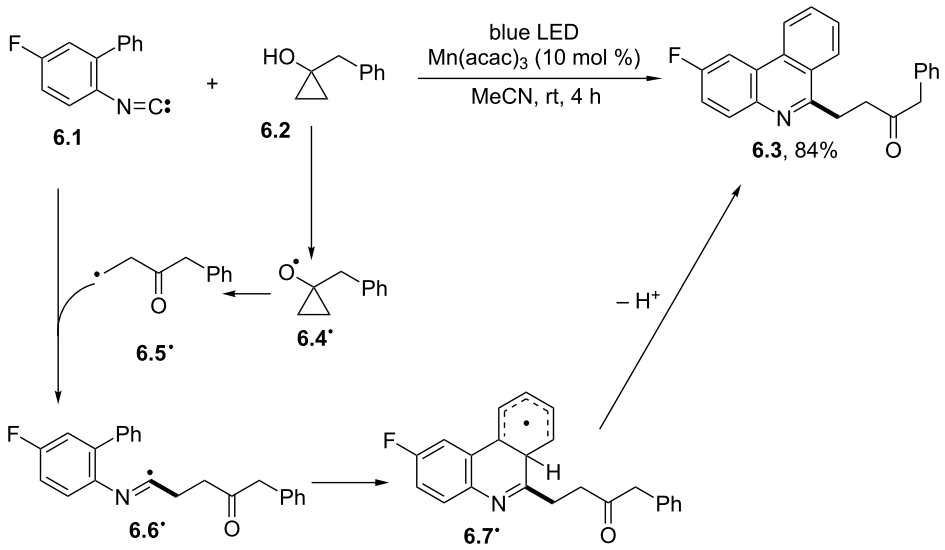

Scheme 6: Photocatalyzed synthesis of 6-β-ketoalkyl phenanthridines.

widely employed to introduce a trifluoromethyl group. In one instance, the visible-light irradiation of isocyanides **7.1** in the presence of excess **7.2** (4 equiv) and the $Ru(bpy)_3^{2+}$ photoredox catalyst afforded the desired trifluoromethylated products **7.3a–d** in satisfactory yields (Scheme 7, path a) [57]. Tri-, di-, and monofluoroalkylated derivatives were also obtained by using fluoroalkyl heteroaryl sulfones [58] or sodium sulfinates (in the presence of persulfate) [59] as the alkylating agents. In an alternative approach, sodium triflinate was adopted as the trifluoromethyl radical source along with diacetyl, that played the dual role of photomediator and reaction medium [60]. The same trifluoromethylated derivatives were obtained from **7.1** in the presence of CF_3SO_2Cl upon direct UV light irradiation by a Xe arc lamp (280–780 nm), in a photocatalyst-free fashion [61]. Easily scalable and thermally stable arylthiodifluoromethyl 2-pyridyl sulfones were likewise exploited in the visible-light photocatalyzed arylthiodifluoromethylation of differently substituted isocyanides [62].

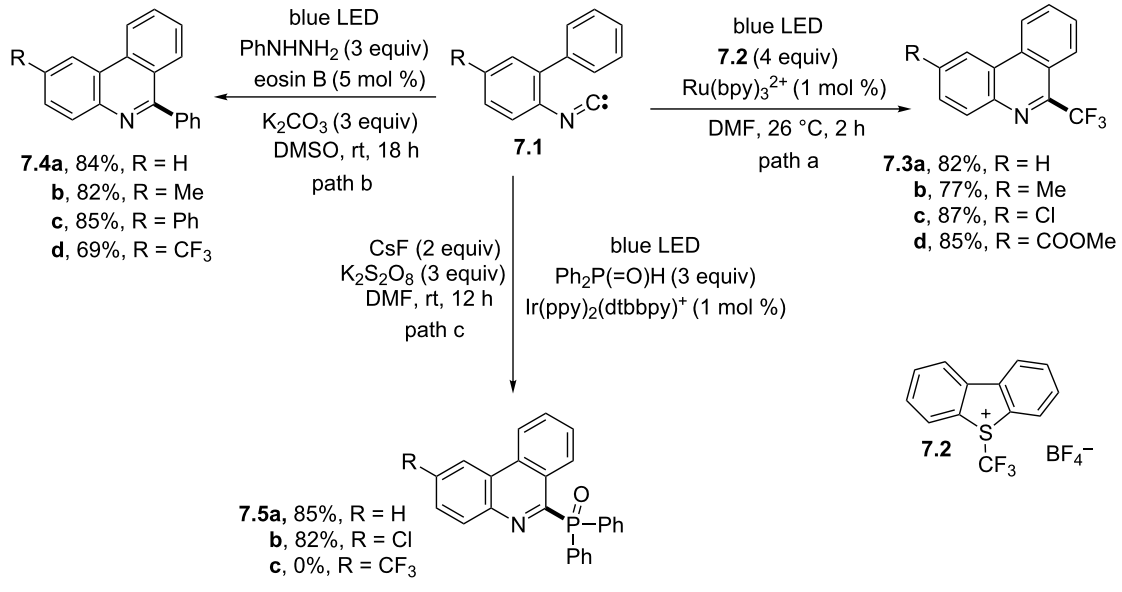

Scheme 7: Synthesis of 6-substituted phenanthridines through the addition of trifluoromethyl (path a), phenyl (path b), and phosphonyl (path c) radicals to isonitriles.

6-Arylphenanthridines were obtained under photoredox-catalyzed conditions by using diaryldiodonium salts [57], arylsulfonyl chlorides [63], or aryl bromides [64] as the source of aryl radicals. A peculiar case is described in Scheme 7, path b, where arylhydrazines functioned as arylating agents to afford derivatives **7.4a–d** by having recourse to the photoorganocatalyst eosin B dye [65]. The generation of phenyl radicals from arylhydrazines was assured even when using the covalent organic framework 2D-COF-1 in place of eosin B [66]. Notably, the use of 2D-COF-1 allowed to extend the protocol to the synthesis of 6-alkylphenanthridines starting from alkylhydrazines [66].

However, a heteroatom-based radical may be used for the addition onto isonitriles as well. One such example dealt with the photoredox tandem phosphonylation/cyclization of diphenylphosphine oxides with 2-arylphenylisonitriles. Here, the sequential formation of C–P and C–C bonds gave P(=O)Ph_2-containing phenanthridines **7.5a–c** (Scheme 7, path c), which occurred in the presence of a base (CsF or Cs_2CO_3) and an external oxidant ($K_2S_2O_8$). Notably, the presence of electron-withdrawing groups on the biphenyl unit inhibited the process in some instances [67]. Starting from the same kind of substrates, 6-thiocyanatophenanthridines were isolated in discrete to excellent yields, in the presence of ammonium thiocyanate (NH_4SCN) as the thiolating agent [68].

A very peculiar case is that described in Scheme 8 for the synthesis of 6-(trifluoromethyl)-7,8-dihydrobenzo[*k*]phenanthridine **8.6** by the trifluoromethylation of methylenecyclopropane **8.2**. The reaction started with the generation of the trifluoromethyl radical via the Ir^{III} photocatalyzed reduction of Togni's reagent **8.1**. The fluorinated radical added onto the isonitrile group present in **8.2** to give radical **8.3**$^{\bullet}$, which in turn gave intermediate **8.4**$^{\bullet}$ upon cyclization onto the methylenecyclopropane double bond. Ring opening of the strained cyclopropyl ring liberated an alkyl radical (in intermediate **8.5**$^{\bullet}$) that readily cyclized onto the adjacent aromatic ring to give **8.6** in a good yield. The oxidation of **8.6** under radical conditions finally afforded the desired phenanthridine **8.7** in 90% yield [69].

Carbon-based radicals could be likewise generated via a C–H hydrogen-atom transfer path. As an example, ethers were used as hydrogen donors and underwent a C–H cleavage step promoted by a photogenerated *tert*-butoxyl radical. The so-obtained α-oxyalkyl radical intermediates were then trapped by biphenyl (or vinyl) isocyanides to afford functionalized phenanthridines, such as **9.3a** (or quinolines) (Scheme 9, path a) [70]. A photogenerated nitrogen-based radical was likewise used to cleave the C–H bond α-to-nitrogen in amides to form the corresponding α-amidoalkyl radicals for the synthesis of a set of 6-amidophenanthridines (e.g., **9.3b**) with significant antitumor and antimicrobial activities (Scheme 9, path b) [71].

Despite their extensive use, 2-isocyanobiphenyls or related isonitriles were not the only available substrates for the preparation of phenanthridines with the intermediacy of imidoyl radicals. As an example, the process depicted in Scheme 10 involved a visible-light homolytic radical aromatic substitution (HAS) starting from trifluoroacetimidoyl chlorides **10.1a–e**. Thus, the photocatalyzed cleavage of the C(sp^2)–Cl bond in **10.1a–e** generated the corresponding imidoyl radicals **10.2**$^{\bullet}$**a–e** that, upon intramolecular radical cyclization, afforded 6-(trifluoromethyl)phenanthridines **10.3a–e** in very good yields [72].

A complementary approach in the synthesis of 6-arylphenanthridines started from *N*-(2-aminoaryl)benzoimine **11.1** and involved the formation of a C(sp^2)–C(sp^2) bond via an aryl

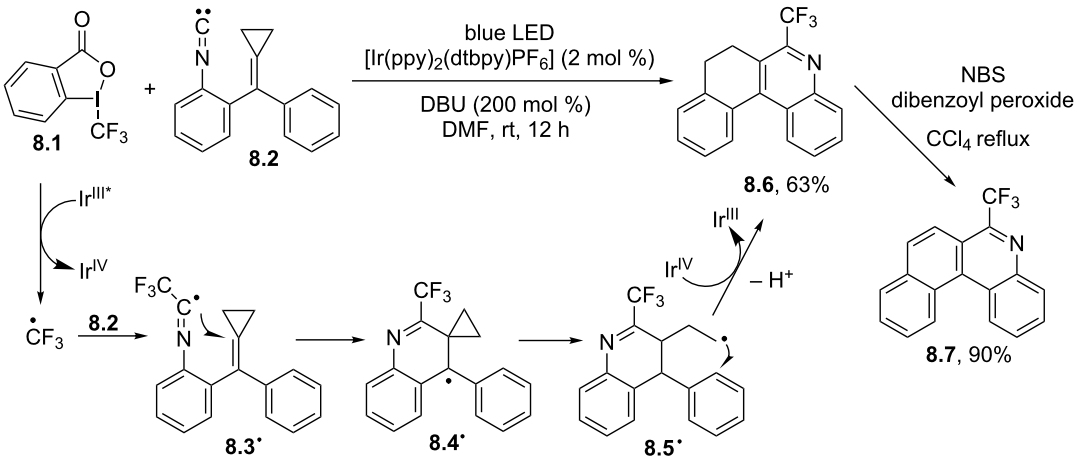

Scheme 8: Synthesis of 6-(trifluoromethyl)-7,8-dihydrobenzo[*k*]phenanthridine.

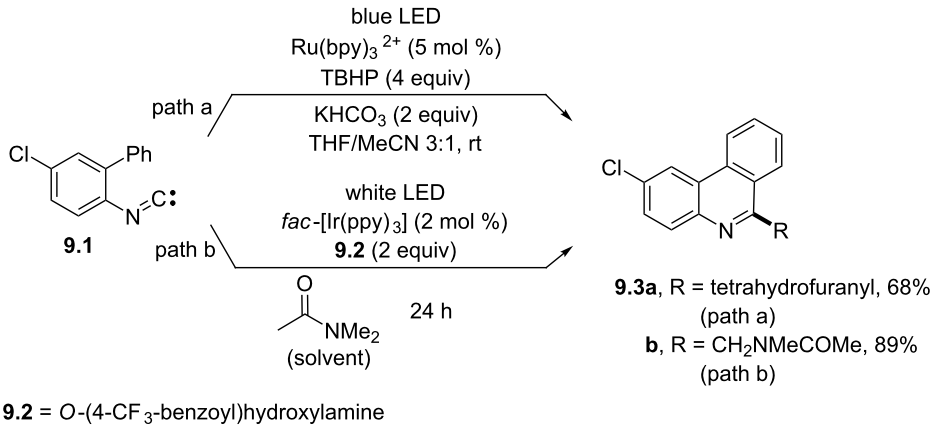

Scheme 9: Phenanthridine syntheses by using photogenerated radicals formed through a C–H bond homolytic cleavage in THF (path a) and *N*,*N*-dimethylacetamide (path b).

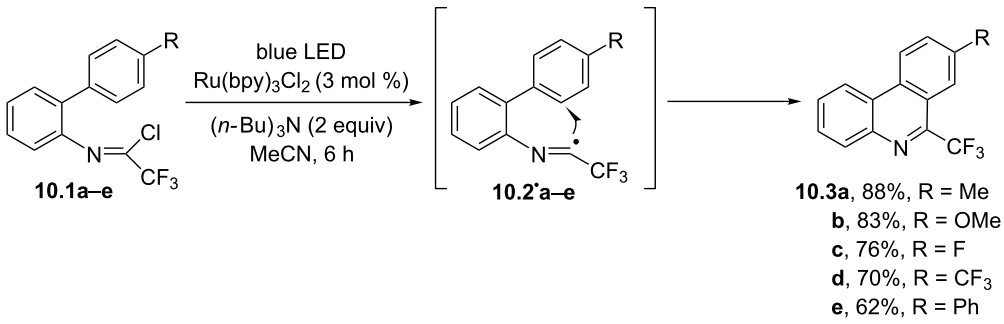

Scheme 10: Trifluoroacetimidoyl chlorides as starting substrates for the synthesis of 6-(trifluoromethyl)phenanthridines **10.3a–e**.

radical intermediate (Scheme 11). Thus, compound **11.1** was in situ converted to the corresponding diazonium salt **11.2**$^+$, which, upon reduction and nitrogen extrusion, formed the reactive aryl radical **11.3**$^•$. In turn, the latter radical smoothly cyclized to form the desired phenanthridine **11.4** in excellent yield. Notably, the reaction could be readily applied to benzoimines having different substituents on the aromatic ring bearing the amino group [73].

Glycine derivatives having a biaryl group attached to the *N*-terminus were successfully exploited for the construction of phenanthridine 6-carboxylates (Scheme 12). Notably, the process occurred in water under metal-free conditions in the presence of rose bengal (5 mol %) and made use of molecular oxygen as the terminal oxidant. Thus, *N*-biarylglycine esters **12.1a–d** promoted the reductive quenching of the excited photocatalyst, in turn triggering the formation of radicals **12.2**$^•$**a–d**. These smoothly underwent radical cyclization to give the corresponding methyl 5,6-dihydrophenanthridine-6-carboxylates and then the desired phenanthridine 6-carboxylates **12.3a–d** in good yields. Noteworthy, the reaction could be scaled up to a 10 mmol amount, allowing to obtain grams of the

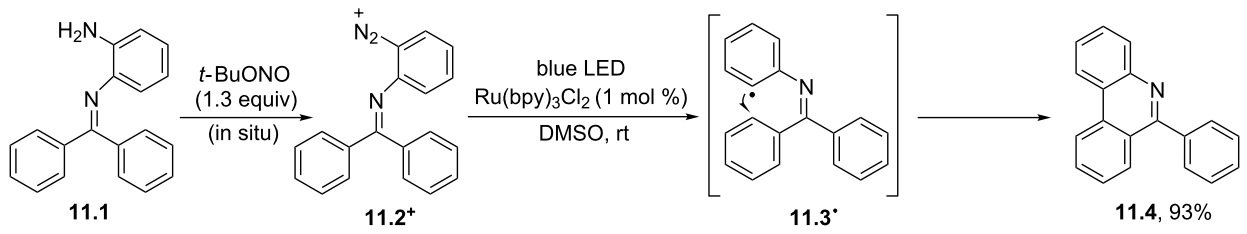

Scheme 11: Synthesis of phenanthridines via aryl–aryl-bond formation.

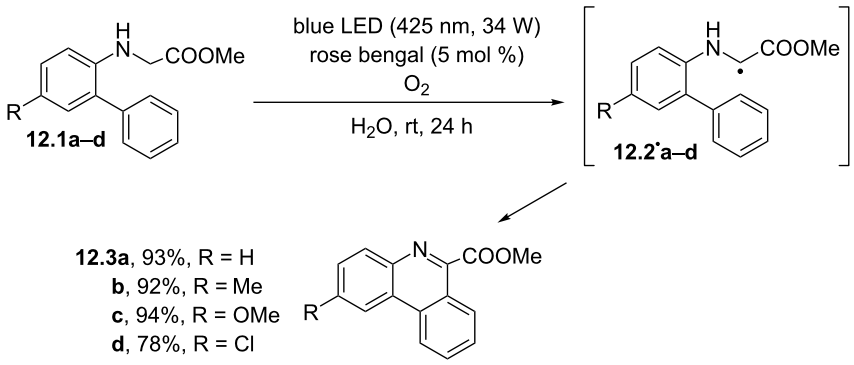

Scheme 12: Oxidative conversion of *N*-biarylglycine esters to phenanthridine-6-carboxylates.

desired phenanthridines, which could be isolated in a pure form by a simple filtration [74].

Azaarenes different from phenanthridines (e.g., benzo[*f*]quinolines) could be likewise prepared by photocatalytic means. Thus, a highly regioselective strategy for the synthesis of a library of polyheteroaromatic compounds under photocatalytic conditions was reported (Scheme 13). The process made use of *fac*-Ir(ppy)$_3$ (0.3 mol %) as the photoredox catalyst and occurred at room temperature under extremely mild conditions. The approach was based on the one-electron reduction of diazonium salts (see the case of **13.3**$^+$ in Scheme 13), formed in situ by the reaction of the chosen 2-heteroaryl aniline (e.g., **13.1**) with *tert*-butyl nitrite (1.5 equiv). Formation of the aryl radical **13.4**$^•$ and following addition onto an alkyne moiety (e.g., the 2-thienyl derivative **13.2**) afforded vinyl radical **13.5**$^•$. The final intramolecular cyclization of **13.5**$^•$ and re-aromatization smoothly yielded the desired polyheteroaromatic derivative (see the case of **13.6**; 84% yield). Interestingly, all the obtained scaffolds bear two heteroatoms in close proximity to each other, prone to be engaged in a bidentate-type metal-coordination complex [75].

2.2 Synthesis of phenanthridines via photocatalyzed C–N bond formation

As mentioned in the introduction, the examples gathered here involve the intermediacy of *N*-centered radicals. As a representative case, the photocatalyzed reduction of acyloximes **14.1a**,**b** offered a smooth entry to iminyl radicals (Scheme 14) [76]. The process took place at room temperature and involved the cleavage of a C–O bond, followed by a cyclization to give access to the benzo[*c*]phenanthridine alkaloids noravicine (**14.2a**) and nornitidine (**14.2b**) in almost quantitative yields [77].

Acyloximes could be likewise formed in situ by the reaction of aldehydes with *O*-(4-cyanobenzoyl)hydroxylamine (**15.2**). The resulting adducts then underwent the same visible-light photo-

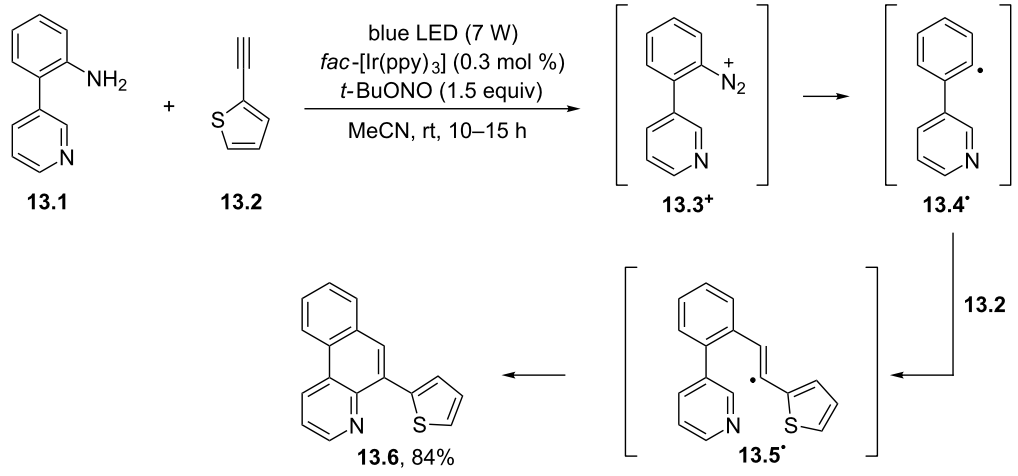

Scheme 13: Photocatalytic synthesis of benzo[*f*]quinolines from 2-heteroaryl-substituted anilines and heteroarylalkynes.

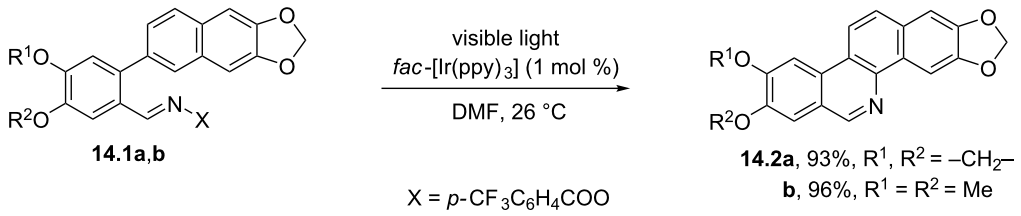

Scheme 14: Synthesis of noravicine (**14.2a**) and nornitidine (**14.2b**) alkaloids.

catalyzed cyclization with the intermediacy of iminyl radicals. Notably, the method was applied to the two-step synthesis of the alkaloid trisphaeridine (**15.3**) on a gram-scale quantity (Scheme 15) [78].

O-2,4-Dinitrophenyloximes were competent substrates for the photocatalyzed generation of iminyl radicals. In this case, the reaction was photoorganocatalyzed by eosin Y and took place in the presence of an excess (3 equiv) of a sacrificial donor, such as iPr_2NEt [79]. Later, it was discovered that phenanthridines could be formed starting again from *O*-2,4-dinitrophenyloximes under photocatalyst-free conditions, by exploiting the capability of these oximes to form visible light absorbing EDA (electron donor–acceptor) complexes with Et_3N. Thus, a good variety of highly functionalized phenanthridines was prepared in excellent yields [80].

Another approach for the visible-light-promoted generation of iminyl radicals (e.g., **16.2˙a**,**b**) involved the addition of electrophilic radicals onto a vinyl azide (see the case of **16.1** in Scheme 16). Different radicals were used for this purpose. As an example, an α-carboxyethyl alkyl radical was formed from the corresponding α-bromoester under white LED irradiation in the presence of an Ir^{III}-based photocatalyst. The addition of this intermediate onto the C–C double bond of **16.1** gave radical **16.2˙a** upon nitrogen loss, which underwent an intramolecular cyclization and finally afforded the substituted phenanthridine **16.3a** in a satisfactory yield (Scheme 16, path a) [81]. The same azide **16.1** underwent trifluoromethyl radical addition to give the corresponding substituted phenanthridine. The $F_3C^{\bullet}$ radical was formed by the Fukuzumi catalyst Mes-Acr^+ photocatalyzed oxidation of the Langlois reagent [82].

Sulfur-centered radicals may be generated via the reduction of sulfonyl chlorides and in turn exploited to construct 6-(sulfonylmethyl)phenanthridines via C–S bond formation. A typical case is shown in Scheme 16, path b. The process was initiated by the reduction of tosyl chloride (Ts–Cl) by a Ru^{II}-based photocatalyst. The resulting sulfonyl radical afforded phenanthridine **16.3b** in a very good yield [83]. A related sulfonylation process was developed, starting from sulfonyl hydrazines in place of sulfonyl chlorides. In this case, the Ru^{II}-based photocatalyst was able to reduce *tert*-butyl peroxybenzoate, triggering the release of a *tert*-butoxyl radical. This was in turn able to oxidize the hydrazine, allowing the liberation of the desired sulfonyl radical, prone to start a tandem sulfonylation/annulation of vinyl azides [84].

Recently, the phenanthridine core was assembled through a radical cascade triggered by the trifluoromethylthiolation of *N*-(*o*-cyanobiaryl)acrylamides. The process occurred under visible-light irradiation (6 W blue LED) in the presence of the *fac*-$Ir(ppy)_3$ photocatalyst (2 mol %). Among the tested sources of the $CF_3S^{\bullet}$ radical, *N*-(trifluoromethyl)thiosaccharin (**17.2**) offered the best performance (Scheme 17). Thus, the oxidative quenching of the excited Ir^{III}-based photocatalyst allowed the generation of the desired (trifluoromethyl)thiyl radical, which added onto the double bond of **17.1a–d**, and finally delivered the desired products **17.5a–d** in good yields, through the intermediacy of radicals **17.3˙a–d** and iminyl radicals **17.4˙a–d** [85].

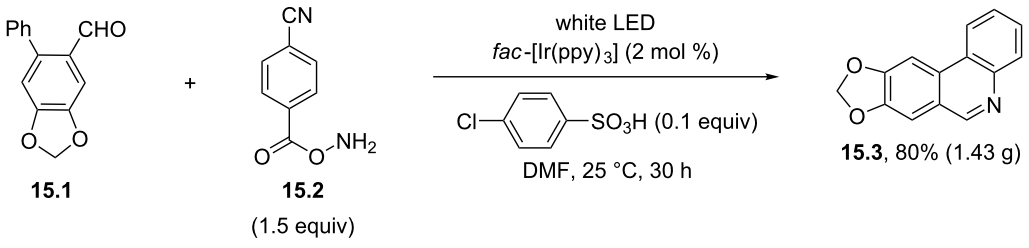

Scheme 15: Gram-scale synthesis of the alkaloid trisphaeridine (**15.3**).

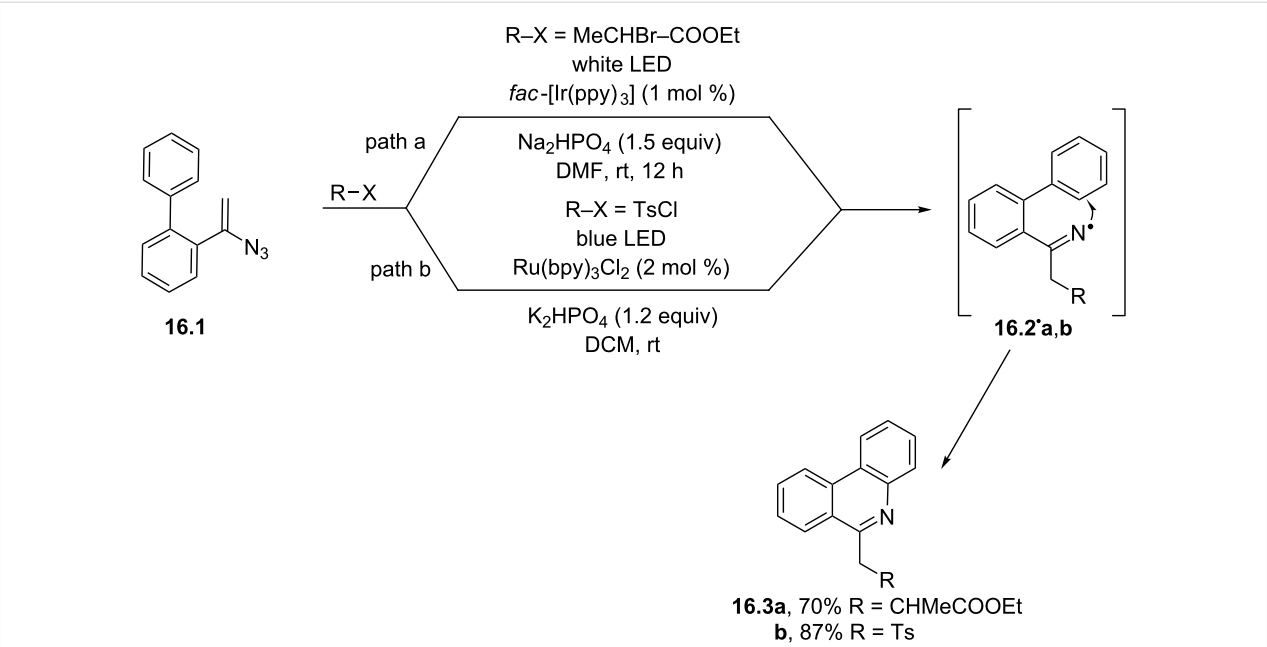

Scheme 16: Synthesis of phenanthridines starting from vinyl azides.

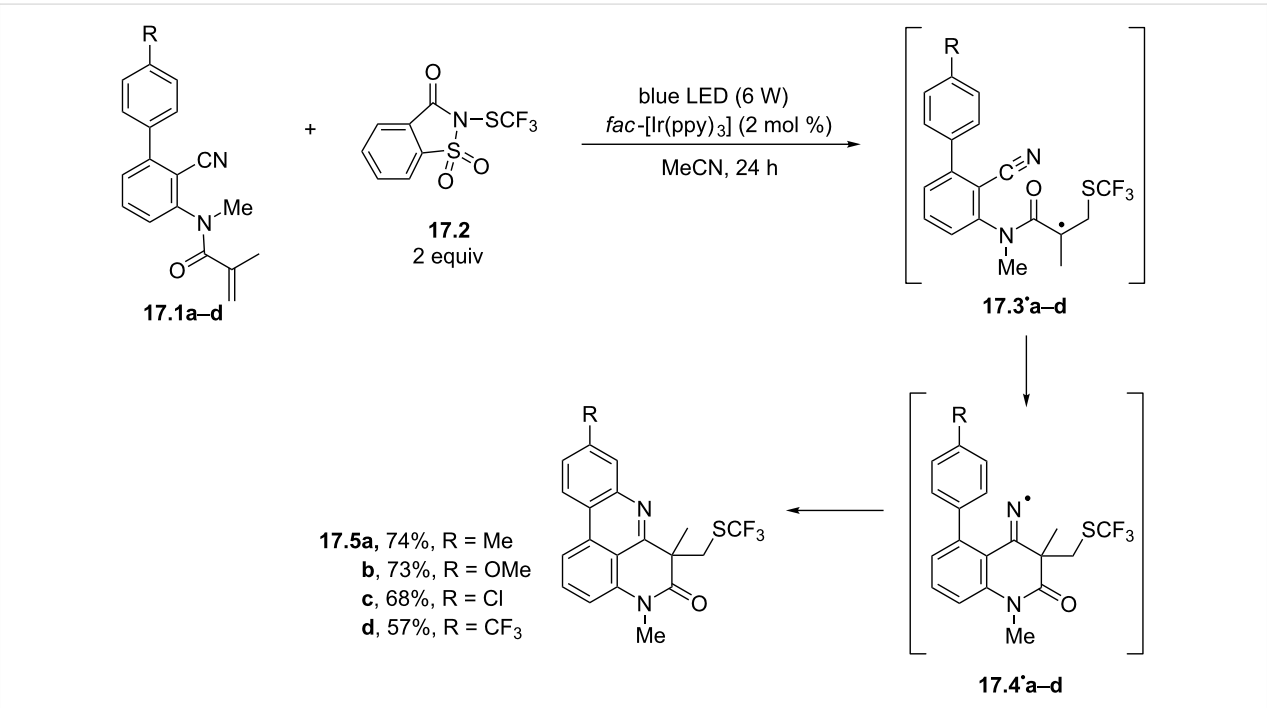

Scheme 17: Synthesis of pyrido[4,3,2-*gh*]phenanthridines **17.5a–d** through the radical trifluoromethylthiolation of *N*-(*o*-cyanobiaryl)acrylamides **17.1a–d**.

The double bond of acrylamides embedded into a 1,7-enyne framework likewise allowed the construction of the phenanthridone core by reaction with diethyl bromomalonate in the presence of *fac*-Ir(ppy)$_3$. Notably, this process was characterized by mild conditions, operational simplicity, excellent functional group tolerance and offered high yields [86]. By following analogous approaches, the addition of perfluoroalkyl [87], acyloxy [88], or alkyl [89,90] radicals to the carbon–carbon double bond of the *N*-(*o*-cyanobiaryl)acrylamide skeleton led to the construction of differently substituted pyrido[4,3,2-*gh*]phenanthridines.

Photocatalytically generated amidyl radicals were adopted for a direct oxidative C–H amidation, offering a straightforward access to phenanthridones (Scheme 18). The process took place upon blue LED irradiation (20–24 h at 60 °C were required) of the chosen substrates (e.g., **18.1a–d**) in the presence of the Ir-based photoredox catalyst $Ir[dF(CF_3)ppy]_2(bpy)PF_6$ (2.5 mol %) and a phosphate base (50 mol %). Thus, the latter played a key role in the PCET event which triggered the activation of the N–H bond in **18.1a–d** and led to the *N*-centered radicals **18.2˙a–d**. Ensuing cyclization onto the pendant aromatic group, followed by rearomatization enabled by molecular oxygen, gave the desired products **18.3a–d** in good yields [91]. Notably, a metal-free version of this strategy, based on the use of the 1-chloroanthraquinone photoorganocatalyst, was likewise reported [92]. A dual-catalytic system, comprising of eosin Y sodium salt (1 mol %) as photoredox catalyst and the thermal catalyst $Pd(OAc)_2$ (5 mol %), was involved in the design of an efficient annulation between benzamides and in situ-generated arynes. The process occurred under oxygen saturated atmosphere at room temperature, likewise offering a straightforward access to the phenanthridone backbone [93].

Conclusion

Photocatalysis is an important tool for the generation and exploitation of reactive intermediates in synthesis. The versatility of this approach allows to form in a straightforward manner several carbon and nitrogen-based radicals useful to forge C–C or C–N bonds (frequently, in an intramolecular fashion) for the construction of the tricyclic scaffold of phenanthrenes and their nitrogen-containing analogues, mainly phenanthridines. The adoption (in most cases) of visible light to promote the processes makes the photocatalytic approach one of the mildest methods available for the construction of these (hetero)aromatic rings. Most of the protocols illustrated herein, however, involved the use of rather expensive transition-metal-based (e.g., on Ru or Ir) photocatalysts, that still represents an issue in terms of sustainability. In this context, the use of photoorgano-catalysts [24] is a promising opportunity on the route towards metal-free protocols for the synthesis of the phenanthrene and phenanthridine cores, a topic of current interest also in related thermal methods [94,95].

Funding

Havall Othman Abdulla is grateful to the Chemistry Department, College of Science, Salahaddin University-Erbil (Iraq) for financial support.

ORCID® iDs

Alessandra Del Tito - https://orcid.org/0000-0003-1785-4080
Davide Ravelli - https://orcid.org/0000-0003-2201-4828
Stefano Protti - https://orcid.org/0000-0002-5313-5692
Maurizio Fagnoni - https://orcid.org/0000-0003-0247-7585

References

1. Kovács, A.; Vasas, A.; Hohmann, J. *Phytochemistry* **2008,** *69,* 1084–1110. doi:10.1016/j.phytochem.2007.12.005
2. Kim, H.; Schulte, N.; Zhou, G.; Müllen, K.; Laquai, F. *Adv. Mater.* **2011,** *23,* 894–897. doi:10.1002/adma.201003797
3. Raouafi, S.; Aloui, F.; Raouafi, A.; Hassine, B. B. *C. R. Chim.* **2017,** *20,* 697–703. doi:10.1016/j.crci.2017.03.004
4. Jiang, H.; Ren, Y.; Zhang, W.; Wu, Y.; Socie, E. C.; Carlsen, B. I.; Moser, J.-E.; Tian, H.; Zakeeruddin, S. M.; Zhu, W.-H.; Grätzel, M. *Angew. Chem., Int. Ed.* **2020,** *59,* 9324–9329. doi:10.1002/anie.202000892
5. Peña, D.; Pérez, D.; Guitián, E.; Castedo, L. *Org. Lett.* **1999,** *1,* 1555–1557. doi:10.1021/ol990864t
6. Hu, J.-T.; Zheng, B.; Chen, Y.-C.; Xiao, Q. *Org. Chem. Front.* **2018,** *5,* 2045–2050. doi:10.1039/c8qo00368h
7. Fürstner, A.; Mamane, V. *J. Org. Chem.* **2002,** *67,* 6264–6267. doi:10.1021/jo025962y
8. Matsuda, T.; Kato, K.; Goya, T.; Shimada, S.; Murakami, M. *Chem. – Eur. J.* **2016,** *22,* 1941–1943. doi:10.1002/chem.201504937
9. Ye, F.; Shi, Y.; Zhou, L.; Xiao, Q.; Zhang, Y.; Wang, J. *Org. Lett.* **2011,** *13,* 5020–5023. doi:10.1021/ol201788v
10. Jørgensen, K. B. *Molecules* **2010,** *15,* 4334–4358. doi:10.3390/molecules15064334

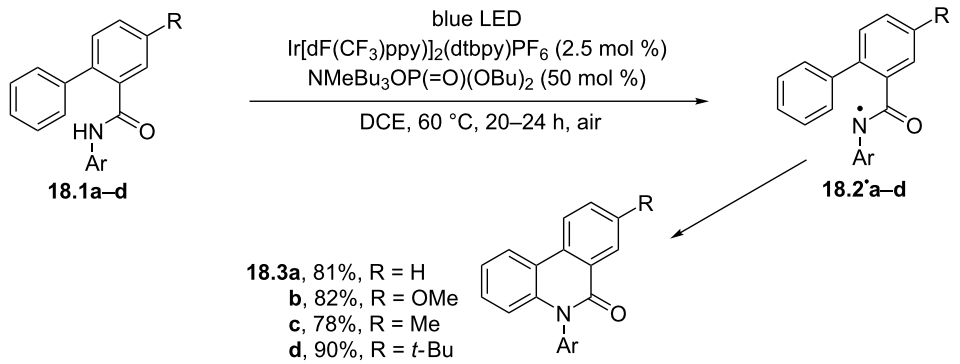

Scheme 18: The direct oxidative C–H amidation involving amidyl radicals for the synthesis of phenanthridones.

11. Protti, S.; Artioli, G. A.; Capitani, F.; Marini, C.; Dore, P.; Postorino, P.; Malavasi, L.; Fagnoni, M. *RSC Adv.* **2015,** *5,* 27470–27475. doi:10.1039/c5ra02855h
12. Harayama, T.; Akamatsu, H.; Okamura, K.; Miyagoe, T.; Akiyama, T.; Abe, H.; Takeuchi, Y. *J. Chem. Soc., Perkin Trans. 1* **2001,** 523–528. doi:10.1039/b008683p
13. Yang, X.-J.; Miao, F.; Yao, Y.; Cao, F.-J.; Yang, R.; Ma, Y.-N.; Qin, B.-F.; Zhou, L. *Molecules* **2012,** *17,* 13026–13035. doi:10.3390/molecules171113026
14. Larsen, A. K.; Grondard, L.; Couprie, J.; Desoize, B.; Comoe, L.; Jardillier, J.-C.; Riou, J.-F. *Biochem. Pharmacol.* **1993,** *46,* 1403–1412. doi:10.1016/0006-2952(93)90105-6
15. Bouquet, J.; Rivaud, M.; Chevalley, S.; Deharo, E.; Jullian, V.; Valentin, A. *Malar. J.* **2012,** *11,* 67. doi:10.1186/1475-2875-11-67
16. Morgan, G. T.; Walls, L. P. *J. Chem. Soc.* **1931,** 2447–2456. doi:10.1039/jr9310002447
17. Tumir, L.-M.; Radić Stojković, M.; Piantanida, I. *Beilstein J. Org. Chem.* **2014,** *10,* 2930–2954. doi:10.3762/bjoc.10.312
18. Keller, P. A. In *Science of Synthesis;* Black, D., Ed.; Georg Thieme Verlag KG: Stuttgart, Germany, 2004; Vol. 15, pp 1065–1095.
19. Lysén, M.; Kristensen, J. L.; Vedsø, P.; Begtrup, M. *Org. Lett.* **2002,** *4,* 257–259. doi:10.1021/ol0170051
20. Zhang, L.; Ang, G. Y.; Chiba, S. *Org. Lett.* **2010,** *12,* 3682–3685. doi:10.1021/ol101490n
21. Fan, J.; Li, L.; Zhang, J.; Xie, M. *Chem. Commun.* **2020,** *56,* 2775–2778. doi:10.1039/d0cc00300j
22. Candito, D. A.; Lautens, M. *Angew. Chem., Int. Ed.* **2009,** *48,* 6713–6716. doi:10.1002/anie.200902400
23. Jaiswal, Y.; Kumar, Y.; Pal, J.; Subramanian, R.; Kumar, A. *Chem. Commun.* **2018,** *54,* 7207–7210. doi:10.1039/c8cc03556c
24. Fagnoni, M.; Protti, S.; Ravelli, D., Eds. *Photoorganocatalysis in organic synthesis;* World Scientific Publishing Europe Ltd.: Singapore, 2019. doi:10.1142/q0180
25. Stephenson, C. R. J.; Yoon, T. P.; MacMillan, D. W. C. *Visible Light Photocatalysis in Organic Chemistry;* Wiley-VCH: Weinheim, Germany, 2018. doi:10.1002/9783527674145
26. Koenig, B., Ed. *Chemical Photocatalysis;* De Gruyter: Berlin, Germany, 2013.
27. Albini, A.; Fagnoni, M. *Green Chem.* **2004,** *6,* 1–6. doi:10.1039/b309592d
28. Protti, S.; Manzini, S.; Fagnoni, M.; Albini, A. The contribution of photochemistry to green chemistry. In *Eco-friendly synthesis of fine chemicals;* Ballini, R., Ed.; Royal Society of Chemistry: Cambridge. U.K., 2009; pp 80–111. doi:10.1039/9781847559760-00080
29. Ravelli, D.; Protti, S.; Fagnoni, M. Application of visible and solar light in organic synthesis. In *Applied Photochemistry: When Light Meets Molecules;* Bergamini, G.; Silvi, S., Eds.; Springer International Publishing: Switzerland, 2016; pp 281–342.
30. Chatgilialoglu, C.; Studer, A., Eds. *Encyclopedia of Radicals in Chemistry, Biology and Materials;* John Wiley & Sons, Ltd: Chichester, United Kingdom, 2012. doi:10.1002/9781119953678
31. Ravelli, D.; Protti, S.; Fagnoni, M. *Chem. Rev.* **2016,** *116,* 9850–9913. doi:10.1021/acs.chemrev.5b00662
32. Goddard, J.-P.; Ollivier, C.; Fensterbank, L. *Acc. Chem. Res.* **2016,** *49,* 1924–1936. doi:10.1021/acs.accounts.6b00288
33. Pitre, S. P.; Weires, N. A.; Overman, L. E. *J. Am. Chem. Soc.* **2019,** *141,* 2800–2813. doi:10.1021/jacs.8b11790
34. Xiong, T.; Zhang, Q. *Chem. Soc. Rev.* **2016,** *45,* 3069–3087. doi:10.1039/c5cs00852b
35. Kärkäs, M. D. *ACS Catal.* **2017,** *7,* 4999–5022. doi:10.1021/acscatal.7b01385
36. Zlot-skii, S. S.; Kochinashvili, M. V.; Rakhmankulov, D. L. *Chem. Heterocycl. Compd.* **1993,** *29,* 857–877. doi:10.1007/bf00534261
37. Russell Bowman, W.; Fletcher, A. J.; Potts, G. B. S. *J. Chem. Soc., Perkin Trans. 1* **2002,** 2747–2762. doi:10.1039/b108582b
38. Naito, T. *Pure Appl. Chem.* **2008,** *80,* 717–726. doi:10.1351/pac200880040717
39. Crespi, S.; Fagnoni, M. Photocatalyzed Formation of Heterocycles. In *Free-Radical Synthesis and Functionalization of Heterocycles;* Landais, Y., Ed.; *Topics in Heterocyclic Chemistry*, Vol. 54; Springer: Cham, Switzerland, 2018; pp 1–69. doi:10.1007/7081_2017_13
40. Cano-Yelo, H.; Deronzier, A. *J. Chem. Soc., Perkin Trans. 2* **1984,** 1093–1098. doi:10.1039/p29840001093
41. Xiao, T.; Dong, X.; Tang, Y.; Zhou, L. *Adv. Synth. Catal.* **2012,** *354,* 3195–3199. doi:10.1002/adsc.201200569
42. Chatterjee, T.; Lee, D. S.; Cho, E. J. *J. Org. Chem.* **2017,** *82,* 4369–4378. doi:10.1021/acs.joc.7b00413
43. Nagode, S. B.; Kant, R.; Rastogi, N. *Eur. J. Org. Chem.* **2018,** 1533–1537. doi:10.1002/ejoc.201800011
44. Lei, J.; Huang, J.; Zhu, Q. *Org. Biomol. Chem.* **2016,** *14,* 2593–2602. doi:10.1039/c6ob00087h
45. Ryu, I.; Sonoda, N.; Curran, D. P. *Chem. Rev.* **1996,** *96,* 177–194. doi:10.1021/cr9400626
46. Yang, X.-L.; Chen, F.; Zhou, N.-N.; Yu, W.; Han, B. *Org. Lett.* **2014,** *16,* 6476–6479. doi:10.1021/ol503335k
47. Fang, H.; Zhao, J.; Ni, S.; Mei, H.; Han, J.; Pan, Y. *J. Org. Chem.* **2015,** *80,* 3151–3158. doi:10.1021/acs.joc.5b00058
48. Rohe, S.; McCallum, T.; Morris, A. O.; Barriault, L. *J. Org. Chem.* **2018,** *83,* 10015–10024. doi:10.1021/acs.joc.8b01380
49. Jiang, H.; Cheng, Y.; Wang, R.; Zheng, M.; Zhang, Y.; Yu, S. *Angew. Chem., Int. Ed.* **2013,** *52,* 13289–13292. doi:10.1002/anie.201308376
50. Zhu, Z.-F.; Zhang, M.-M.; Liu, F. *Org. Biomol. Chem.* **2019,** *17,* 1531–1534. doi:10.1039/c8ob02786b
51. Wang, L.; Ding, Q.; Li, X.; Peng, Y. *Asian J. Org. Chem.* **2019,** *8,* 385–390. doi:10.1002/ajoc.201800733
52. Fu, W.; Zhu, M.; Xu, C.; Zou, G.; Wang, Z.; Ji, B. *J. Fluorine Chem.* **2014,** *168,* 50–54. doi:10.1016/j.jfluchem.2014.08.022
53. Wang, S.; Jia, W.-L.; Wang, L.; Liu, Q. *Eur. J. Org. Chem.* **2015,** 6817–6821. doi:10.1002/ejoc.201500988
54. Zhu, M.; Fu, W.; Zou, G.; Xu, C.; Wang, Z. *J. Fluorine Chem.* **2015,** *180,* 1–6. doi:10.1016/j.jfluchem.2015.07.028
55. Zhang, Z.; Tang, X.; Dolbier, W. R., Jr. *Org. Lett.* **2015,** *17,* 4401–4403. doi:10.1021/acs.orglett.5b02061
56. Sun, X.; Yu, S. *Org. Lett.* **2014,** *16,* 2938–2941. doi:10.1021/ol501081h
57. Wang, R.; Jiang, H.; Cheng, Y.; Kadi, A. A.; Fun, H.-K.; Zhang, Y.; Yu, S. *Synthesis* **2014,** *46,* 2711–2726. doi:10.1055/s-0034-1379217
58. Rong, J.; Deng, L.; Tan, P.; Ni, C.; Gu, Y.; Hu, J. *Angew. Chem., Int. Ed.* **2016,** *55,* 2743–2747. doi:10.1002/anie.201510533
59. Fang, J.; Shen, W.-G.; Ao, G.-Z.; Liu, F. *Org. Chem. Front.* **2017,** *4,* 2049–2053. doi:10.1039/c7qo00473g
60. Li, J.; Caiuby, C. A. D.; Paixão, M. W.; Li, C.-J. *Eur. J. Org. Chem.* **2018,** 2498–2503. doi:10.1002/ejoc.201701487
61. Tang, X.; Song, S.; Liu, C.; Zhu, R.; Zhang, B. *RSC Adv.* **2015,** *5,* 76363–76367. doi:10.1039/c5ra16645d

62. Wei, J.; Gu, D.; Wang, S.; Hu, J.; Dong, X.; Sheng, R. *Org. Chem. Front.* **2018,** *5,* 2568–2572. doi:10.1039/c8qo00644j
63. Gu, L.; Jin, C.; Liu, J.; Ding, H.; Fan, B. *Chem. Commun.* **2014,** *50,* 4643–4645. doi:10.1039/c4cc01487a
64. Li, X.; Liang, D.; Huang, W.; Sun, H.; Wang, L.; Ren, M.; Wang, B.; Ma, Y. *Tetrahedron* **2017,** *73,* 7094–7099. doi:10.1016/j.tet.2017.10.074
65. Xiao, T.; Li, L.; Lin, G.; Wang, Q.; Zhang, P.; Mao, Z.-w.; Zhou, L. *Green Chem.* **2014,** *16,* 2418–2421. doi:10.1039/c3gc42517g
66. Liu, S.; Pan, W.; Wu, S.; Bu, X.; Xin, S.; Yu, J.; Xu, H.; Yang, X. *Green Chem.* **2019,** *21,* 2905–2910. doi:10.1039/c9gc00022d
67. Li, C.-X.; Tu, D.-S.; Yao, R.; Yan, H.; Lu, C.-S. *Org. Lett.* **2016,** *18,* 4928–4931. doi:10.1021/acs.orglett.6b02413
68. Singh, M.; Yadav, A. K.; Yadav, L. D. S.; Singh, R. K. P. *Synlett* **2018,** *29,* 176–180. doi:10.1055/s-0036-1590921
69. Yuan, Y.-C.; Liu, H.-L.; Hu, X.-B.; Wei, Y.; Shi, M. *Chem. – Eur. J.* **2016,** *22,* 13059–13063. doi:10.1002/chem.201602920
70. Feng, S.; Li, T.; Du, C.; Chen, P.; Song, D.; Li, J.; Xie, X.; She, X. *Chem. Commun.* **2017,** *53,* 4585–4588. doi:10.1039/c7cc01813d
71. Zhou, H.; Deng, X. Z.; Zhang, A. H.; Tan, R. X. *Org. Biomol. Chem.* **2016,** *14,* 10407–10414. doi:10.1039/c6ob02113a
72. Fu, W.; Zhu, M.; Xu, F.; Fu, Y.; Xu, C.; Zou, D. *RSC Adv.* **2014,** *4,* 17226–17229. doi:10.1039/c4ra02384f
73. Natarajan, P.; Kumar, N.; Sharma, M. *Org. Chem. Front.* **2016,** *3,* 1265–1270. doi:10.1039/c6qo00275g
74. Natarajan, P.; Chuskit, D.; Priya. *Green Chem.* **2019,** *21,* 4406–4411. doi:10.1039/c9gc01557d
75. Chatterjee, T.; Choi, M. G.; Kim, J.; Chang, S.-K.; Cho, E. J. *Chem. Commun.* **2016,** *52,* 4203–4206. doi:10.1039/c6cc00562d
76. Yin, W.; Wang, X. *New J. Chem.* **2019,** *43,* 3254–3264. doi:10.1039/c8nj06165c
77. Jiang, H.; An, X.; Tong, K.; Zheng, T.; Zhang, Y.; Yu, S. *Angew. Chem., Int. Ed.* **2015,** *54,* 4055–4059. doi:10.1002/anie.201411342
78. An, X.-D.; Yu, S. *Org. Lett.* **2015,** *17,* 2692–2695. doi:10.1021/acs.orglett.5b01096
79. Liu, X.; Qing, Z.; Cheng, P.; Zheng, X.; Zeng, J.; Xie, H. *Molecules* **2016,** *21,* 1690. doi:10.3390/molecules21121690
80. Sun, J.; He, Y.; An, X.-D.; Zhang, X.; Yu, L.; Yu, S. *Org. Chem. Front.* **2018,** *5,* 977–981. doi:10.1039/c7qo00992e
81. Sun, X.; Yu, S. *Chem. Commun.* **2016,** *52,* 10898–10901. doi:10.1039/c6cc05756j
82. Qin, H.-T.; Wu, S.-W.; Liu, J.-L.; Liu, F. *Chem. Commun.* **2017,** *53,* 1696–1699. doi:10.1039/c6cc10035j
83. Mao, L.-L.; Zheng, D.-G.; Zhu, X.-H.; Zhou, A.-X.; Yang, S.-D. *Org. Chem. Front.* **2018,** *5,* 232–236. doi:10.1039/c7qo00790f
84. Mao, L.-L.; Quan, L.-X.; Zhu, X.-H.; Ji, C.-B.; Zhou, A.-X.; Chen, F.; Zheng, D.-G. *Synlett* **2019,** *30,* 955–960. doi:10.1055/s-0037-1611758
85. Zhu, M.; Fu, W.; Guo, W.; Tian, Y.; Wang, Z.; Ji, B. *Org. Biomol. Chem.* **2019,** *17,* 3374–3380. doi:10.1039/c9ob00342h
86. Gao, F.; Yang, C.; Ma, N.; Gao, G.-L.; Li, D.; Xia, W. *Org. Lett.* **2016,** *18,* 600–603. doi:10.1021/acs.orglett.5b03662
87. Liu, X.; Wu, Z.; Zhang, Z.; Liu, P.; Sun, P. *Org. Biomol. Chem.* **2018,** *16,* 414–423. doi:10.1039/c7ob02804k
88. Li, X.; Fang, X.; Zhuang, S.; Liu, P.; Sun, P. *Org. Lett.* **2017,** *19,* 3580–3583. doi:10.1021/acs.orglett.7b01553
89. Yu, Y.; Cai, Z.; Yuan, W.; Liu, P.; Sun, P. *J. Org. Chem.* **2017,** *82,* 8148–8156. doi:10.1021/acs.joc.7b01447
90. Yu, Y.; Yuan, W.; Huang, H.; Cai, Z.; Liu, P.; Sun, P. *J. Org. Chem.* **2018,** *83,* 1654–1660. doi:10.1021/acs.joc.7b03080
91. Moon, Y.; Jang, E.; Choi, S.; Hong, S. *Org. Lett.* **2018,** *20,* 240–243. doi:10.1021/acs.orglett.7b03600
92. Usami, K.; Yamaguchi, E.; Tada, N.; Itoh, A. *Eur. J. Org. Chem.* **2020,** 1496–1504. doi:10.1002/ejoc.201900536
93. Zhao, J.; Li, H.; Li, P.; Wang, L. *J. Org. Chem.* **2019,** *84,* 9007–9016. doi:10.1021/acs.joc.9b00893
94. Maiti, D.; Halder, A.; De Sarkar, S. *Adv. Synth. Catal.* **2019,** *361,* 4941–4948. doi:10.1002/adsc.201900995
95. Lu, Y.; Chen, L.; Chen, X.; Yao, M.; Luo, Z.; Zhang, Y. *Synthesis* **2020,** *52,* 290–296. doi:10.1055/s-0039-1690218

License and Terms

This is an Open Access article under the terms of the Creative Commons Attribution License (http://creativecommons.org/licenses/by/4.0). Please note that the reuse, redistribution and reproduction in particular requires that the authors and source are credited.

The license is subject to the *Beilstein Journal of Organic Chemistry* terms and conditions: (https://www.beilstein-journals.org/bjoc)

The definitive version of this article is the electronic one which can be found at: doi:10.3762/bjoc.16.123

BEILSTEIN JOURNAL OF ORGANIC CHEMISTRY

Heterogeneous photocatalysis in flow chemical reactors

Christopher G. Thomson, Ai-Lan Lee* and Filipe Vilela*

Review

Open Access

Address:
Institute of Chemical Sciences, School of Engineering and Physical Sciences, Heriot-Watt University, Edinburgh, EH14 4AS Scotland, United Kingdom

Email:
Ai-Lan Lee* - A.Lee@hw.ac.uk; Filipe Vilela* - F.Vilela@hw.ac.uk

* Corresponding author

Keywords:
air purification; flow chemistry; heterogeneous photoredox catalysis; organic synthesis; reactor design; water purification

Beilstein J. Org. Chem. **2020,** *16,* 1495–1549.
doi:10.3762/bjoc.16.125

Received: 28 February 2020
Accepted: 07 May 2020
Published: 26 June 2020

This article is part of the thematic issue "Advances in photoredox catalysis".

Guest Editor: T. Noël

© 2020 Thomson et al.; licensee Beilstein-Institut.
License and terms: see end of document.

Abstract

The synergy between photocatalysis and continuous flow chemical reactors has shifted the paradigms of photochemistry, opening new avenues of research with safer and scalable processes that can be readily implemented in academia and industry. Current state-of-the-art photocatalysts are homogeneous transition metal complexes that have favourable photophysical properties, wide electrochemical redox potentials, and photostability. However, these photocatalysts present serious drawbacks, such as toxicity, limited availability, and the overall cost of rare transition metal elements. This reduces their long-term viability, especially at an industrial scale. Heterogeneous photocatalysts (HPCats) are an attractive alternative, as the requirement for the separation and purification is largely removed, but typically at the cost of efficiency. Flow chemical reactors can, to a large extent, mitigate the loss in efficiency through reactor designs that enhance mass transport and irradiation. Herein, we review some important developments of heterogeneous photocatalytic materials and their application in flow reactors for sustainable organic synthesis. Further, the application of continuous flow heterogeneous photocatalysis in environmental remediation is briefly discussed to present some interesting reactor designs that could be implemented to enhance organic synthesis.

Review

1 Introduction

1.1 Scope of the review

This review aims to be of interest to synthetic organic chemists who are considering applying heterogeneous photocatalysis (HPC) and flow chemistry in their research, and especially those who are already involved in one of the two areas. Many independent reviews have focused on individual types of HPCat materials [1-7], and their applications in organic synthesis [8-11], solar fuel production [12-17], and environmental remediation [18-23]. Herein, we review the recent applications of HPCats in flow reactors for organic synthesis, as to the best of our knowledge, there is no review dedicated to this important and developing research area. Within the introduction, we cover the importance of the field and some important historical devel-

opments of photocatalysis (Section 1.2). We also discuss the synergy between flow chemistry and HPCats that allows chemists and engineers to achieve more efficient irradiance and mass transport, leading to a higher productivity (Section 1.3). Section 2 covers the fundamental aspects and recent developments of the major categories of HPCat materials. Section 3 details the types of flow reactors that HPCats can be applied in, with a discussion of the advantages and disadvantages to guide the reader in selecting the reactor best suited to their system. Following this, in Section 4, we review the recent applications of HPCats in flow reactors for synthetic organic chemistry through photoredox catalysis (PRC, Section 4.1) and energy transfer catalysis (EnT, Section 4.2). The final two subsections review the importance of HPCats in flow reactors for the photocatalytic remediation of wastewater (Section 4.3) and air pollution (Section 4.4), an increasingly significant area of research to prevent damage to the environment and human health. We conclude in Section 5 with a summary and our perspective on the future of HPCats in flow as a methodology for sustainable and scalable photosynthesis.

1.2 Importance of the review and brief historical perspective

With growing socioeconomic and political pressure to act on anthropogenic emissions and subsequent environmental damage, much of the scientific community has shifted its focus to the development of sustainable methodologies, particularly in synthetic chemistry. The prospect of utilising light as a renewable source of energy to drive chemical reactions is an appealing solution to this problem, which has led photocatalysis to become one of the most active areas of chemical research in recent years. A crude search of the Web of Science database for the term "Photocatalysis" shows the exponential growth of interest in this area since the 1990s, with almost 8000 publications on the topic in 2019 alone (Figure 1A). The credit for the development of this field is often given to MacMillan [24], Yoon [25], and Stephenson [26], whose seminal papers in 2008 and 2009 elegantly demonstrated the photocatalytic ability of ruthenium–bipyridyl complexes to drive chemical reactions with visible light through single-electron transfer processes, now referred to as visible light photoredox catalysis (PRC). A similar query on the Web of Science for the term "Photoredox" clearly shows the surge in PRC research following those reports, from 2010 onwards (Figure 1A). However, what is interesting is that PRC is still only a fraction of all photocatalysis research, which was already a vibrant field prior to 2010. This 20-year period of photocatalysis development can be largely attributed to the developing field of HPC and the work of Fujishima and Honda, who first reported the photocatalytic decomposition of water on illuminated titanium dioxide (TiO_2) electrodes in 1972 [27]. This critical report began the field of semiconductor HPC, and in combination with the development of organic electronics, established fundamental principles that still underpin much of the cutting-edge photocatalysis research performed today.

Equally as impressive to the volume of photocatalysis publications are the broad interdisciplinary contributions to its develop-

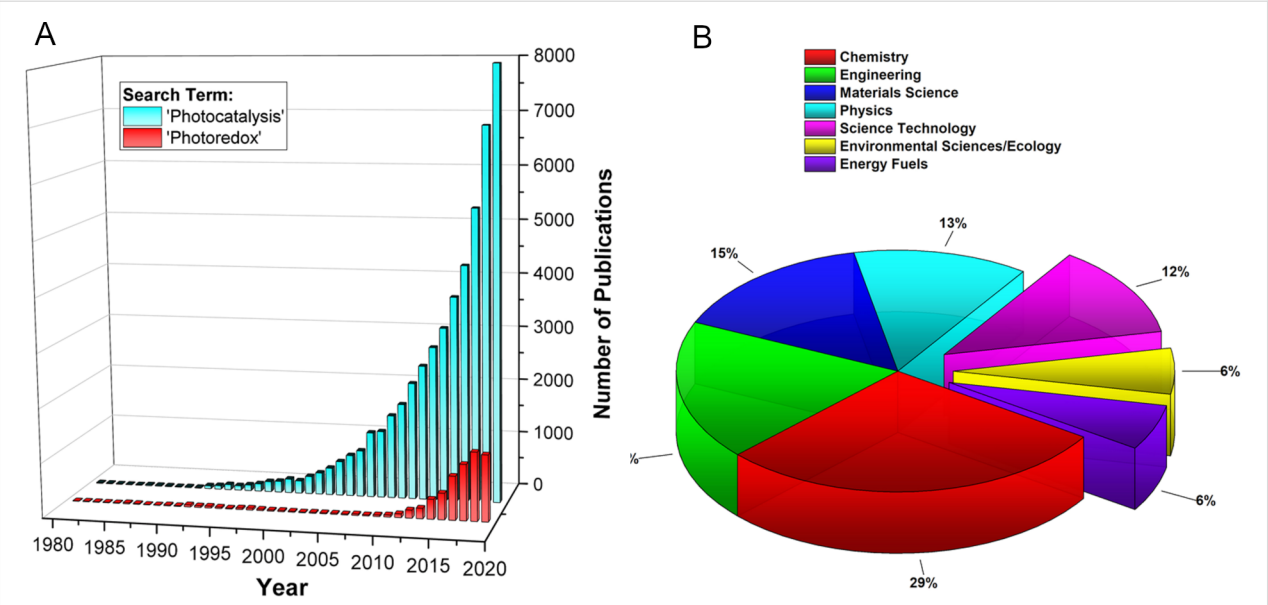

Figure 1: A) Bar chart of the publications per year for the topics "Photocatalysis" (49,662 instances) and "Photoredox" (6166 instances) between 1980 and 2019, queried from the Web of Science database. B) Pie chart of "Photocatalysis" publications by research areas for the top seven categories (contains 74% of the total data set) using the same data as in A.

ment. Analysing the same data set of photocatalysis publications by discipline reveals that significant contributions came from engineering, materials science, and physics, in addition to chemistry (Figure 1B). This reflects the multiplex nature of photocatalysis as it requires an advanced chemical and photophysical theory to rationalise its complex mechanisms, as well as skilled engineering and reactor design to overcome the limitations of photon and mass transport.

Photocatalysis provides a unique route to carry out complex chemical transformations under mild conditions that are often impossible with "standard" organic synthetic procedures. The earliest report of synthetic photochemistry can be traced back to Trommsdorf in 1834, who observed that crystals of santonine would shatter when exposed to sunlight [28]. Credit for the pioneering of photochemistry is usually given to Ciamician, the "grandfather of photochemistry", who reported many interesting transformations of chemical solutions when irradiated by sunlight [29,30]. His visionary work was unfortunately limited to primitive glassware and solar irradiation, with low-yielding reactions extending for several months (Figure 2A) [29,31]. Modern day photocatalysis coupled with flow chemistry has dramatically enhanced the efficiencies and led to photochemical flow reactors being developed by organisations such as Vapourtec Ltd. (Figure 2B) and Corning Inc. (Figure 2C and D), capable of producing photochemical products on a kg/day scale [32-38].

Whilst heterogeneous catalysts are generally preferred in many industrial-scale processes [39], photocatalysis for organic synthesis is dominated by homogeneous organic dyes and phosphorescent transition metal complexes [40-42]. This is largely due

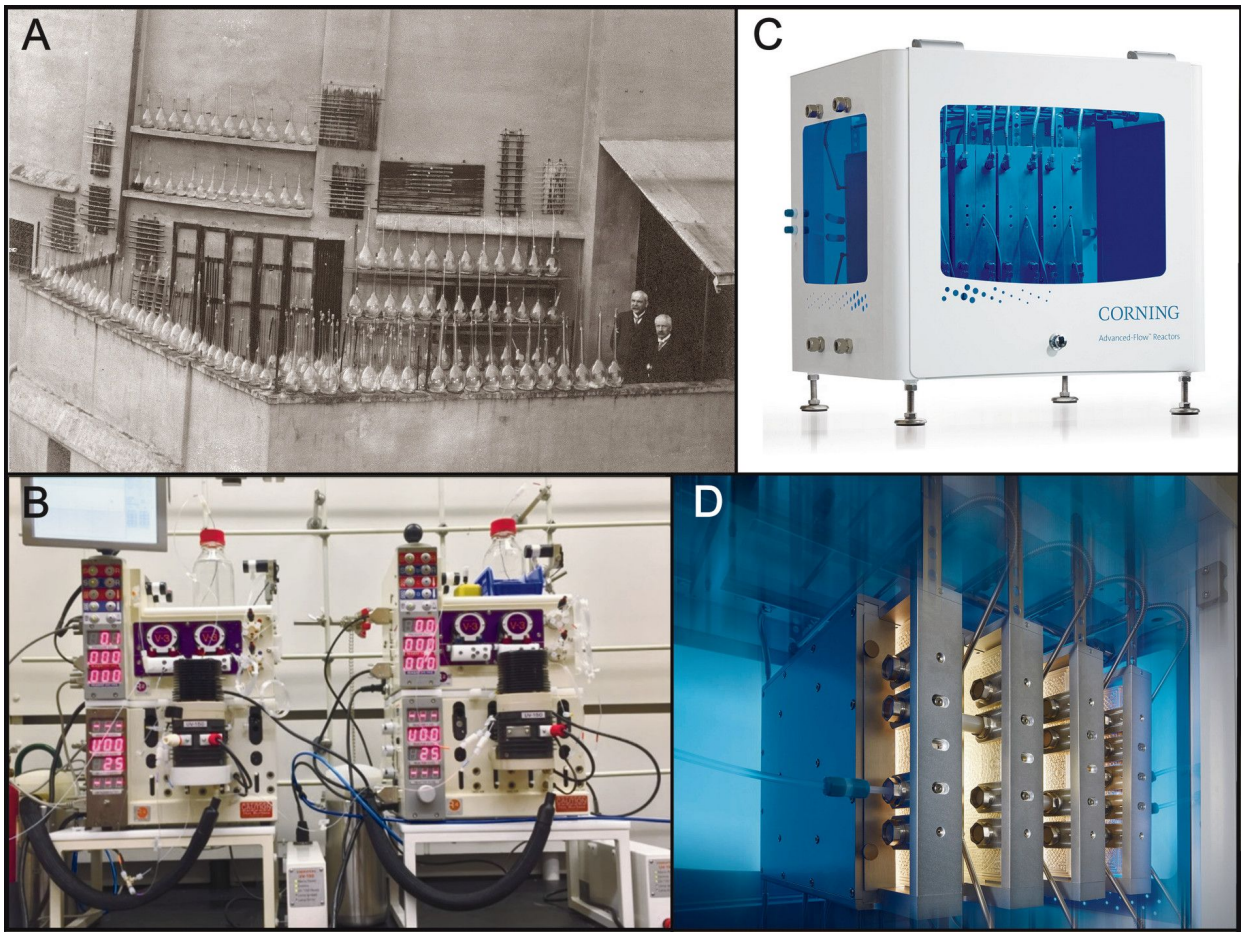

Figure 2: A) Professor Giacomo Ciamician and Dr. Paolo Silber on their roof laboratory at the University of Bologna, Italy, ca. 1912. Reprinted with permission, courtesy of Alma Mater Studiorum University of Bologna- University Museum System - "Giacomo Ciamician" Chemistry Collection. B) Image of two connected Vapourtec Ltd. R-Series photoreactors running in series, used by Merck for a g/h-scale photochemical synthesis. Reprinted with permission from [36], Copyright 2018 Wiley-VCH Verlag GmbH & Co. KGaA. C) Image of a Corning Inc. G3 photoreactor, capable of a 1000 tons/year production. Reprinted with permission, Copyright 2018 Corning Incorporated. D) Image of an illuminated G3 photoreactor interior featuring vertical flow panels with patented HEART design static mixing channels. Reprinted with permission, Copyright 2018 Corning Incorporated.

to the higher efficiency of molecular photocatalysts, which disperse in solution and can be irradiated uniformly, especially in narrow flow channels [43]. The photophysical properties and surface structure of HPCats are more challenging to characterise and requires specialised techniques that are not readily available and often require multidisciplinary collaborations [44]. Additionally, the penetration of light through the bulk of the HPCat is difficult and can render large quantities of the material redundant. Overcoming these issues and producing efficient HPCats and reactors that can compete with transition metal complex photocatalysts has been described as one of the greatest challenges and opportunities in the field of photocatalysis [43,45,46]. This has led to great progress within the last decade, with new HPCat materials and reactor designs beginning to shift the photocatalysis paradigms towards HPCats because of their advantages of reduced purification and facile recycling.

1.3 Benefits of heterogeneous photocatalysts in flow

In addition to separation and recycling, HPCats show advantages such as an enhanced photostability and selectivity [47,48]. A heterogeneous catalyst with a high surface area is often associated with a greater number of surface-active sites for catalysis to occur and makes morphological control critical to the catalyst efficiency. This generally holds true for HPCats, but the anisotropic surface environment of a HPCat is prone to having more trapping states for charge carriers (see Section 2), leading to more surface charge recombination events that are non-productive [49].

Often, it is only the surface and outermost layers of the HPCat that can be penetrated and activated by the incident irradiation, rendering the HPCat bulk redundant. As the mean free path of photons is proportional to their wavelength, irradiating a system with longer wavelength irradiation that still exceeds the band gap energy can enhance the depth of the photon penetration and provide more charge separation events. Upconversion photocatalysis is an emerging field of research that utilises near-infrared (NIR) radiation to penetrate deep into a reaction medium or material [50]. Multiple NIR photons are then combined through energy transfer processes by an upconversion system to produce higher-frequency, ultraviolet (UV), or visible light photons that are reemitted in close proximity to, or directly from within the HPCat solid matrix [51]. This is discussed in more detail in Section 2.5.

The "Achilles' heel" of all heterogeneous catalysts is mass transport limitations, the circumstance in which a process becomes diffusion-limited and independent of the catalyst efficiency [43]. This is often thought of as an "engineering problem" by chemists, which will be solved through the reactor design [52], but smart design of the HPCat structure and the interfaces by the chemist can contribute, as is shown later in this review.

Fortunately, many of the complexities listed above are largely overcome through flow chemistry. The significant enhancement of the homogeneous photochemistry efficiency in flow is mostly attributed to the small reactor channel dimensions, reducing the path length of the light required to totally irradiate the reaction solution in accordance with the Beer–Lambert law (Equation 1) where the light attenuation (A) is the ratio of the incident light intensity (I_0) to the transmitted light intensity (I) and is proportional to the molar attenuation coefficient of the photocatalyst (ε), its concentration (c), and the optical path length (l).

$$A = \log_{10}\left(\frac{I_0}{I}\right) = \varepsilon \cdot c \cdot l \tag{1}$$

This also applies to immobilising an HPCat in a flow reactor, which generally confines and concentrates the material within a transparent vessel with high surface-to-volume ratio, permitting a more efficient and targeted irradiation. In contrast to batch photochemistry, only the reaction medium in contact with the HPCat is irradiated, preventing overirradiation of the reaction mixture, which can lead to photodecomposition of the reactants and products [32,43]. Pumping the reaction mixture through the reactor forces the solution to flow around, or through the HPCats solid matrix, which greatly enhances mass transfer at the catalyst surface. The narrow, usually microscale, channels of flow reactors offer an unparalleled control over reaction conditions as the high surface-to-volume ratio results in an extremely efficient heat exchange. This maintains a narrow free energy profile in flow reactors and can enhance selectivity [43,53,54]. This also prevents potential hot spots forming due to a photothermal effect, which could potentially alter selectivity and lead to the loss of material [55-57]. Flow chemistry also enables chemists to safely use hazardous gaseous reagents that are otherwise avoided, whilst simultaneously increasing the gas/liquid–gas/solid interfacial surface area which enhances reactivity [58-61]. This was highlighted by Noël and co-workers, who demonstrated the safe use of gaseous CF_3I as a reagent for the continuous flow PRC trifluoromethylation of 5-membered heterocycles, such as *N*-methylpyrrole (**1**, Scheme 1), with a high conversion and selectivity for the monofunctionalised product **2** [62]. The system achieved full conversion for a variety of aromatic heterocycle substrates within 8–20 min, transformations that would require days in batch protocols (Scheme 1) [62].

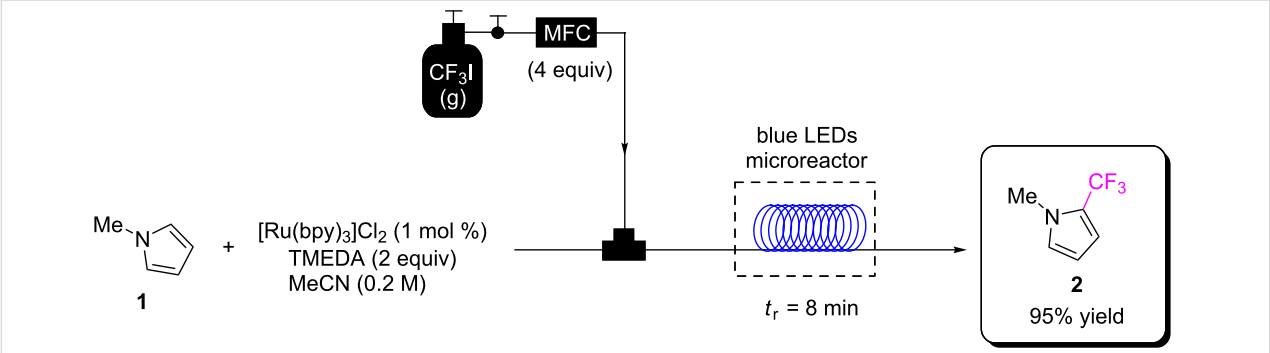

Scheme 1: PRC trifluoromethylation of *N*-methylpyrrole (**1**) using hazardous gaseous CF_3I safely in a flow reactor [62]. MFC = mass flow controller, t_r = reactor residence time, TMEDA = tetramethylethylenediamine.

Flow systems can be pressurised easily with back pressure regulators, enhancing the solubility of gaseous reagents in the reaction solvents [36,63]. Flow processes are also commonly monitored with in-line and on-line spectroscopies, such as UV–vis, FTIR, mass spectrometry, and NMR [63-68]. These systems can be automated to ensure consistency and to remove the need for laborious manual sampling. In-line and on-line monitoring is well aligned with automated synthesis and high-throughput reaction screening, both of which are progressive areas of chemical research [69-73].

2 Heterogeneous photocatalysts

Probably the first report of HPC was published by Renz in 1921, who observed the partial reduction of titania (TiO_2) in the presence of glycerol when irradiated with sunlight [74]. The use of titania as a pigment had been practiced for centuries, and the observation that TiO_2-based surface coatings exposed to sunlight irradiation would "chalk" (the formation of a loose white powder on the paint surface) had been recognised as the decomposition of organic components in the coating, leaving the TiO_2 powder exposed [75]. In 1938, Goodeve and Kitchener used this knowledge to perform the first study on the photodegradation of organic dyes with TiO_2 powder [76]. A series of subsequent reports that were historically relevant to developing TiO_2- and semiconductor-based photocatalysis followed, which can be explored in a review by Fujishima [75]. It was not until the landmark paper by Honda and Fujishima in 1972 that the field of HPC and photoelectochemistry flourished [27]. This paper reported what is now known as the Honda–Fujishima effect in which TiO_2 was found to split water to oxygen and hydrogen gas under strong UV irradiation. This gained significant attention in the wider scientific community for the potential generation of solar fuels [27,75] and formed the foundation of modern heterogeneous photocatalysis.

With this brief historical perspective in mind, it is perhaps not surprising that TiO_2 as a material for photocatalysis is incredibly well studied and characterised. TiO_2 has excellent physicochemical properties, good biocompatibility, is abundant in nature, and subsequently inexpensive. For these reasons, the application of TiO_2 in photocatalysis is still substantial and has featured in approximately 50% of all photocatalysis publications from 2015–2019, by analysis of the same data set presented in Figure 2A. In this section, we will cover the fundamentals and recent advances in material design of the main categories of HPCats, beginning with TiO_2 as a model system for metal oxide and inorganic semiconductor HPCats.

2.1 Inorganic semiconductor photocatalysis

Semiconductors are defined as materials that have a conductivity between that of an insulator and a conductor [77]. The origin of conductivity is based on the quantum states of electrons in a solid, known as the band theory. Bands are groups of electronic quantum states that arise from the atomic or molecular orbitals of a solid material, leading to continuums of indiscrete energy states [77]. TiO_2 is a crystalline material with three common lattice arrangements named anatase, brookite, and rutile (Figure 3A). The different lattice structures influence the atomic orbital environments and energy, which alters the photophysical and charge transport properties of the material, which has been studied in great detail [78-82]. The titanium and oxygen atomic orbitals generate a filled band, the valence band (VB), of mainly oxygen 2p electron density and an empty band of unoccupied Ti 3d states, the conduction band (CB), separated by a gap of energy potentials with no quantum states, the band gap (E_g), corresponding to 3.18 eV for anatase TiO_2 (Figure 3B) [78,79].

The semiconductor E_g defines the minimum frequency of photons required to excite an electron from the valence band to the conduction band, the critical primary event required for photocatalysis to occur. The band structure can be engineered by controlling the polymorphism, morphology, and size (e.g., TiO_2 nanoparticles) or by introducing impurities into the crystal

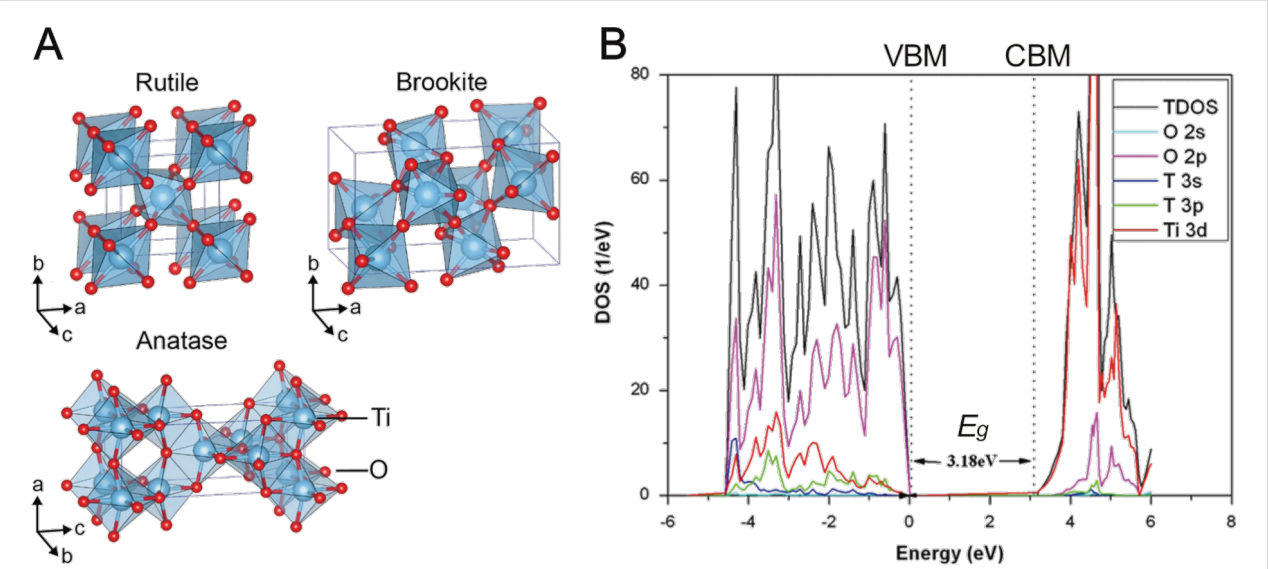

Figure 3: A) Unit cells of the three most common crystal structures of TiO_2: rutile, brookite, and anatase. Reprinted from [83] (copyright held by the authors), published by Springer Nature under a Creative Commons Attribution 4.0 International License http://creativecommons.org/licenses/by/4.0/. B) Theoretical density of the states diagram for anatase TiO_2, with dashed lines indicating the conduction band minimum (CBM) and the valence band maximum (VBM), which yields the band gap energy (E_g) of 3.18 eV. Adapted from [78].

lattice, otherwise known as doping [44,84-86]. Semiconductor doping adds additional filled or vacant quantum states to the band structure that lie within the band gap, reducing the E_g and typically resulting in a bathochromic shift in absorption. Synthetic TiO_2 commonly has oxygen atom vacancy defects, especially at its surface, resulting in Ti^{3+} ions that produce quantum states close to the conduction band minimum. These states lower the E_g, enabling visible light absorption and producing reactive centres on the catalyst surface, which has been synthetically controlled to improve the photocatalytic CO_2 reduction performance by Zhang and co-workers using plasma treatment [87].

The general process of photocatalysis in metal oxide semiconductors is illustrated in Figure 4 and is as follows: the photoexcitation of an electron across the band gap generates an energetic electron in the CB (e^-_{CB}) and leaves behind a positively charged electron vacancy in the VB, referred to as a hole (h^+_{VB}). These electron/hole pairs are the charge carriers that allow the oxidation and reduction of substrates in photocatalysis. Initially, the electron/hole pair is in a bound state, held together by electrostatic attraction and treated as a single neutral quasiparticle called an exciton. A quasiparticle is a mathematical solution applied to microscopically complicated systems which account for experimentally observed phenomena, such as the reduced velocity of particles within a solid. By treating them as pseudo-particles that have the same charge but increased mass, this better reflects experimental observations and permits better system modelling [82].

In materials with high dielectric constants, the charges are shielded from each other, and the exciton readily dissociates into free charge carriers. Following the charge separation, the charge carries migrate to a reactive site on the surface of the material to oxidise or reduce a substrate, respective of their charge. A reactive site is generally a point where a substrate has adsorbed to the HPCat surface and is within the proximity required for an electron transfer or energy transfer process to occur. Substrate reduction and oxidation by an excited electron and hole, respectively, returns the semiconductor to its initial state and activates the substrate to further reactivity at the surface or in the bulk solution, completing the photocatalyst cycle.

Charge carriers must overcome competing processes that result in the immobilisation and recombination of charge carriers. The photogenerated electron/hole pair will spontaneously undergo bulk or surface recombination if they cannot efficiently separate, which is influenced by the dielectric properties of the material and delocalisation of the quantum states. Highly localised quantum states in the band gap, such as those introduced by dopants and defects in the bulk lattice, are known as trap states and can immobilise charge carriers, increasing the probability of charge recombinations [89].

Serpone et al. found that 85% of the photogeneration events resulted in a recombination after 10 ns of illuminating TiO_2 particles [90]. This implies that higher irradiation intensity may hinder photocatalysis by increasing the charge carrier density and subsequently the rate of recombination [91].

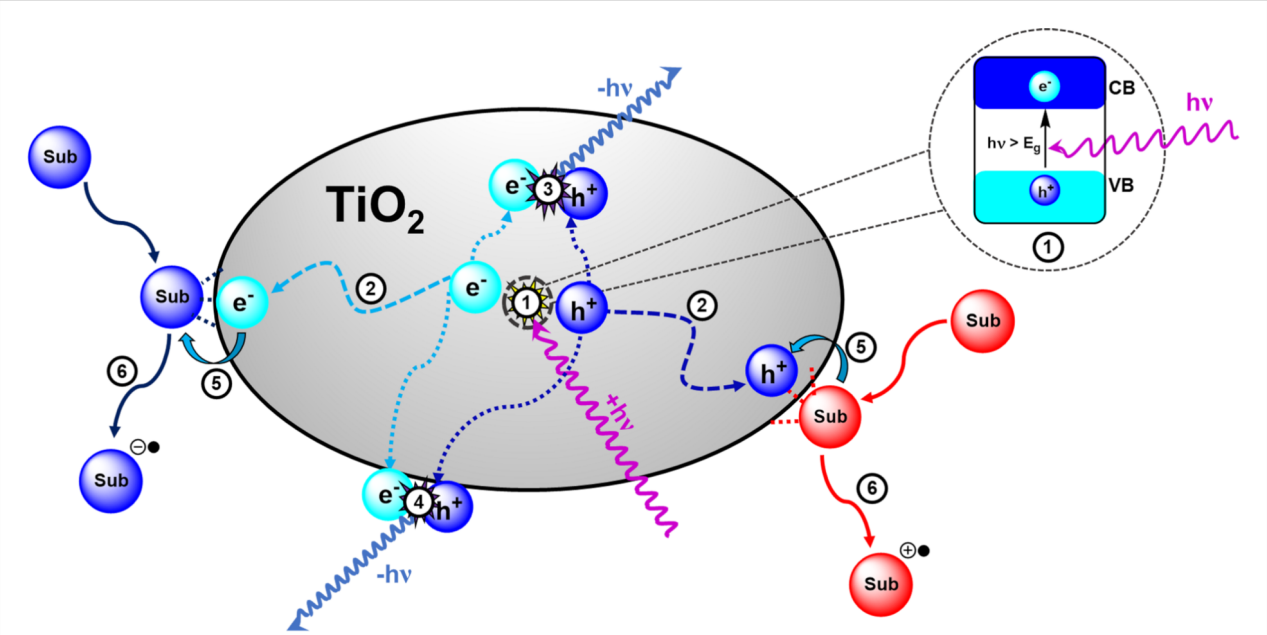

Figure 4: Illustration of the key semiconductor photocatalysis events: 1) A photon with a frequency exceeding the band gap energy (E_g) excites an electron from the VB to the CB, producing an exciton (fs). 2) The exciton dissociates into free charge carriers (e^-_{CB} and h^+_{VB}) and migrate to the semiconductor surface. 3) and 4) e^-_{CB} and h^+_{VB} are immobilised by trapping states within the bulk (3) or at the surface (4, 100 ps–250 ns) and recombine radiatively (–*hν*, 1 ps–10 μs) or non-radiatively (10–100 ns). 5) The substrate (Sub) species transfer and adsorb to the surface where they are oxidised or reduced by the e^-_{CB} and h^+_{VB}, respectively (1 ns–ms). 6) The oxidised/reduced substrates desorb from the surface and transfer into the bulk solution to undergo further chemical processes (>ms). Approximate timescales were reported by Bahnemann and co-workers (fs = 10^{-15}, ps = 10^{-12}, ns = 10^{-9}, μs = 10^{-6}, ms = 10^{-3} s) [88].

The abrupt termination of an ordered lattice continuity at a surface leads to chemical and structural differences from the bulk material. TiO_2, for example, has surface hydroxides, oxygen anions, and Ti^{3+} cations, which produce high energy states from incomplete bonding. This energy is alleviated though surface relaxation, a process in which the surface changes its structure to reduce its energy, or by the adsorption of substrates to fill and stabilise vacancies. Water molecules adsorb to oxygen vacancies on the TiO_2 surface and undergo a 2-electron reduction and proton transfer to an adjacent oxide atom, forming two bridging-hydroxyls. Subsequently, an adsorbed O_2 molecule is reduced by the bridging hydroxyls to form two terminal hydroxides and fill the initial oxygen surface vacancy (Figure 5) [92].

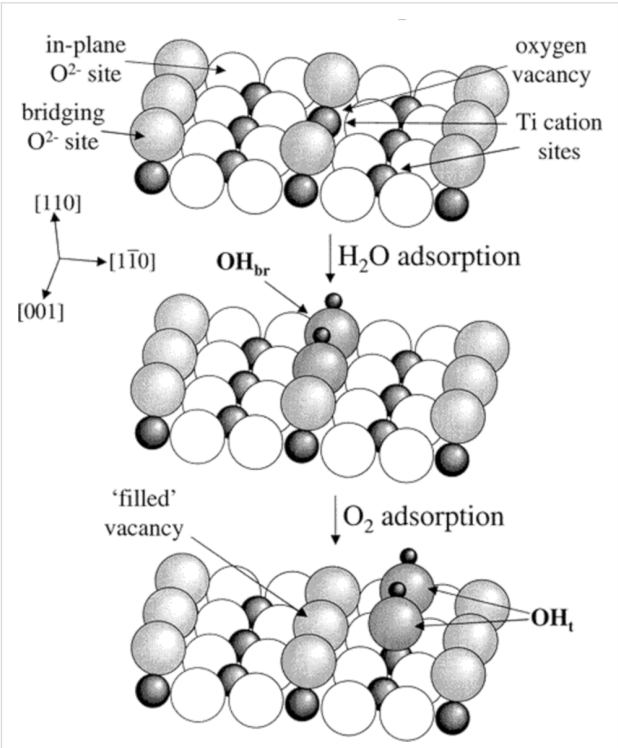

Figure 5: Photocatalytic splitting of water by oxygen vacancies on a TiO_2(110) surface. Reprinted with permission from [92]. Copyright 2003 American Chemical Society.

Organic molecules generally weakly associate with the surface via physisorption. However, functionalised molecules and ions can strongly bind through chemisorption by covalent bonds, hydrogen bonding, or electrostatic attraction and have been shown to influence the photophysical properties of TiO_2, generally causing a bathochromic shift of the absorption spectrum through direct VB/adsorbate electron transfer transitions [93,94]. HPCats modified with coordinating transition metal complexes also usually display significant changes to their absorption spectrum through the introduction of metal-to-ligand, ligand-to-metal, ligand-to-ligand, and metal-to-metal

charge–transfer transitions [95]. These transitions are commonly observed in metal–organic framework (MOF) HPCats, discussed more in Section 2.5. Dye-sensitised semiconductor photocatalysts have organic photosensitiser molecules immobilised to their surface. This strategy is typically used to activate a wide-band gap semiconductor towards visible light excitation [95]. The photosensitiser can inject electrons to the semiconductor conduction band via direct HOMO–CB transition (type II excitation) or indirectly by exciting the photosensitiser HOMO–LUMO transition, followed by a LUMO–CB charge transfer (type I excitation). The direct VB-to-LUMO or VB-to-ligand transition is also enabled and produces a hypsochromic shift in the HPCat absorption spectrum. An excellent review of coordination chemistry controlled design of heterogeneous photocatalysis has been published by Xiong and co-workers, and we recommend exploring the article for further details [95].

Molecules with functional groups such as carboxylic acid present complex surface topologies from bridging and bidentate binding modes [91]. Yoshida and co-workers studied the adsorption of benzene derivatives on TiO_2 surfaces by solid-state NMR and revealed the chemical shifts varied for different atoms, indicating the multiple orientations of related adsorbates to the surface (Figure 6) [96].

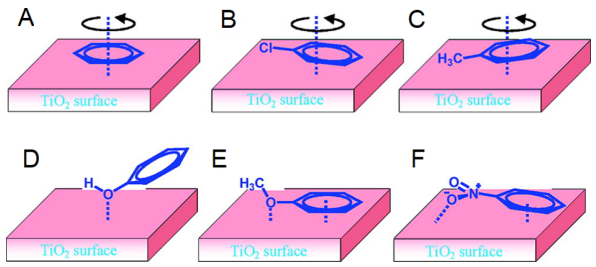

Figure 6: Proposed adsorption modes of A) benzene, B) chlorobenzene, C) toluene, D) phenol, E) anisole, and F) nitrobenzene on a TiO_2 surface. Reprinted with permission from [96]. Copyright 2011 American Chemical Society.

Due to the amphoteric nature of metal oxide surfaces, the pH value of the system has a significant influence on photocatalysis by altering the Coulombic forces between the surface and substrate. The pH value at which the concentration of surface charge centers is equal is termed the point of zero charge (PZC), which is 5.80 for TiO_2, approximately 8.5 for most metal oxides, and approximately 2.0 for metal sulphides [97]. Guillard and co-workers studied the photocatalytic degradation of basic organic dyes containing sulfonate groups, remazol black 5 (**3**, Figure 7) and procion red MX-5B (**4**, Figure 7), and showed a significant enhancement of **4** adsorption when the pH value was reduced to 3 (Figure 7) [98]. The authors stated that this reflected a higher positive charge density on the TiO_2 surface at a lower pH value, which favours the adsorption of the dye via its negatively charged sulfonate groups. However, at a natural pH value, the increasing dye concentration gradually raises the pH value of the system and negatively charges the TiO_2 surface, leading to an electrostatic repulsion that prevents the dye adsorption.

2.2 Organic semiconductor photocatalysis

Polyaniline was the first conductive polymer reported by Henry Letheby in 1862 [99,100], but the potential of organic electronics was not realised until the 1960s, and the seminal work of Heeger, MacDiarmid, and Shirakawa, leading to their shared award of the 2000 Chemistry Nobel Prize for "the discovery and development of conductive polymers" [101]. For the following 60 years, and still to this day, organic electronics is a vibrant field of research within materials chemistry and physics as a potential source of sustainable photovoltaics [102], flexible electronics [103], improved organic light emitting diodes (OLEDs) [104], organic field effect transistors (OFETs) [105,106], and more recently, photocatalysts [3,5,10,15]. These materials have semiconducting properties due to extended conjugation producing a continuum of bonding and antibonding molecular orbital states which form band structures, analogous with inorganic semiconductors. Hence, the mechanisms of organic semiconductor photocatalysis and the photogeneration of charge carriers is identical to those discussed in the previous section and illustrated in Figure 4. The differences between inorganic and organic semiconductors are primarily the transport of charge within the material, which arise from the drastically different properties and various degrees of crystallinity of organic semiconductors, which we will now briefly discuss.

In amorphous polymer chains, charge transport is limited to intraplanar transport along the conjugated network. In crystalline and graphitic organic materials, the close packing of two-dimensional sheets permits interplanar charge transport in the third dimension, allowing the delocalisation of charge over several molecular layers [107]. The complex models used to describe charge transport in organic materials with differing degrees of disorder is well described by Liu, Noh, and co-workers [108]. The relative permittivity or dielectric constant ($\varepsilon_r(\omega)$), which influences the screening of the charge carriers within the material is drastically different for inorganic and organic semiconductors. High $\varepsilon_r(\omega)$ materials, such as silicon ($\varepsilon_r(\omega) = 12$) or GaAs ($\varepsilon_r(\omega) = 13$), effectively screen the Coulombic attraction between excitons to 10s of meV, allowing the charge carriers to easily dissociate at room temperature [109,110]. Organic polymer materials, such poly(*p*-phenylene vinylene, $\varepsilon_r(\omega) = 2$), typically have low $\varepsilon_r(\omega)$ values, which

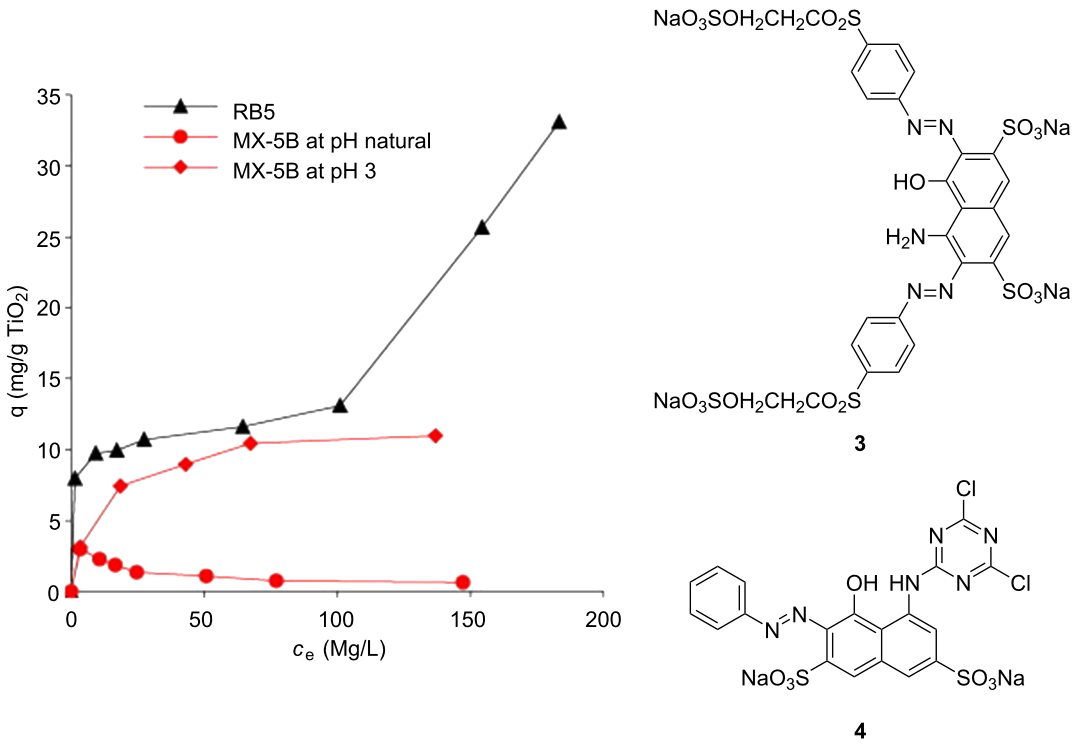

Figure 7: Structures of the sulfonate-containing organic dyes RB5 (**3**) and MX-5B (**4**) and the adsorption isotherms of the dyes on a TiO_2 surface at varied pH. The additional adsorption of **3** is due to the formation of a bilayer. Reprinted from [98].

prevents the screening of excitons and leads to much stronger binding energies of 0.1–1 eV, which greatly exceeds the available thermal energy at room temperature [111-113]. This is problematic for photovoltaics and photocatalysts but a useful property for OLEDs where the radiative decay of the charge recombination is desired [112,114].

Charge carriers are normally localised to only a few atoms and cause large distortions in the local electronic structure. This small spatial confinement of the photogenerated excitons is normally only a few nm^3 and accounts for the large binding energy, as opposed to in a Si crystal, which has an exciton diameter in the order of 10s of nm^3 [115]. Organic molecules will typically have large geometric relaxations to cope with the localised loss of conjugation and polarisation of the surrounding medium, which is enhanced by low $\varepsilon_r(\omega)$ values [115-118]. The charge is transported in organic materials by "hopping" between the quantum states. The amorphous nature of most polymers produces a low symmetry and anisotropy for the charge transport. Hence, the charge mobility in organic semiconductors is typically much lower than in crystalline inorganic materials [115]. Conjugated polymers that are rigid will generally have faster intrachain charge transport rather than interlayer hopping transport (Figure 8) [107,115]. The process is highly dependent on the temperature and electronic disorder as each hop requires the reorganisation of the molecules in the chain [115].

A particularly popular organic semiconductor photocatalyst in the recent literature is graphitic carbon nitride (g-C_3N_4) [23]. g-C_3N_4 was one of the first synthetic polymers, first reported in 1834 by Liebig, which he named "melon" [119]. The material consists of two-dimensional sheets of hexatopic, hexagonal sp^2-hybridised carbon and nitrogen atoms, linked by bridging tertiary amines (Figure 9) [120]. The material is crystalline as sheets are held together by strong π-stacking and Van der Waals interactions, rendering the material insoluble in most solvents [120,121]. g-C_3N_4 materials are typical organic semiconductors with band gaps of approximately 2–5 eV, usually showing a maximum absorbance at 420 nm, which yields its characteristic yellow colour [120].

Significant interest in g-C_3N_4 photocatalysts was generated in 2009 by Wang, Domen, and co-workers, who reported the metal-free photolysis of water was possible with the all-organic semiconductor material, a sacrificial electron donor, and visible light irradiation [120]. Prior to this report, poly(*p*-phenylene) had been utilised for hydrogen production but using high intensity, short-wave UV radiation, and only a modest efficiency was obtained [122]. As a result, research into g-C_3N_4 grew exponen-

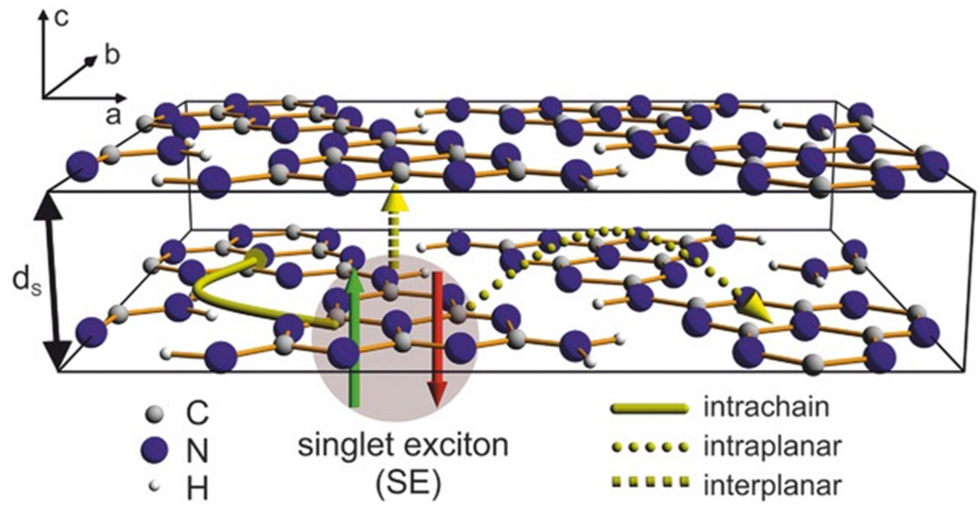

Figure 8: Idealised triclinic unit cell of a g-C_3N_4 type polymer, displaying possible hopping transport scenarios of an exciton via intrachain (solid), intraplanar (dotted) or interplanar (dashed). Reprinted with permission from [107], Copyright 2015 Wiley-VCH.

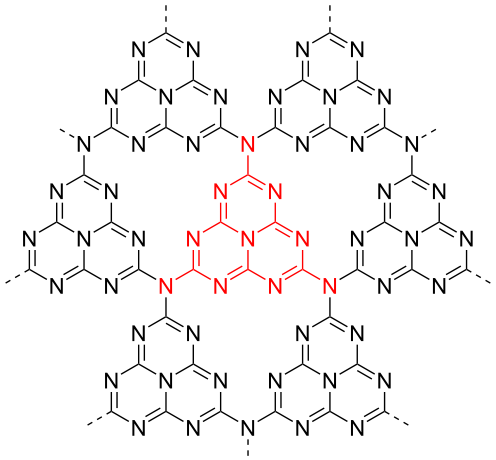

Figure 9: Idealised structure of a perfect g-C_3N_4 sheet. The central unit highlighted in red represents one tri-s-triazine (melem) unit [120].

tially and paved the way for the development of many other organic materials for photocatalysis applications [120,123-127]. Despite its structural similarities to graphite, the charge carrier mobility in g-C_3N_4 is significantly different. Transient absorption and transient photoluminescence (TRPL) spectroscopy analysis of a set of g-C_3N_4 materials found that the charge transport was predominantly interplanar, perpendicular to the sheets [107]. The work of Merschjann and co-workers critically analysed the non-exponential TRPL spectral decay of g-C_3N_4 and found that the initial photon excitation and subsequent exciton dissociation into free polarons (quasiparticle equivalent to e^-_{CB} and h^+_{VB} charge carriers) occurs over 200 femtoseconds. The resulting polarons migrate by "hopping" between the sheets until they eventually recombine over a period of approximately 10^{-13}–10^{-6} s (Figure 10) [107].

Mesoporous graphitic carbon nitride (mpg-C_3N_4) has recently been reported by Antonietti, König, and co-workers to be an effective, stable, and recyclable HPCat for a large scope of arene and heteroarene functionalisation reactions, traditionally performed with transition metal complexes (Scheme 2) [128]. The group were able to bifunctionalise *N*-phenylpyrrole with a variety of functional groups at room temperature to yield alkyl, halo, and trifluoromethyl products, such as the examples **5** and **6** (Scheme 2).

Chen, Wang and co-workers recently studied methods to reduce the exciton binding energy in linear conjugated polymers to enhance the charge separation and subsequent photocatalytic hydrogen evolution (Figure 11) [129]. Four conjugated polymers containing dibenzothiophene sulfone (FSO) monomers, linked by either biphenyl (FSO-BP), fluorene (FSO-F), 2,8-dibenzothiophene (FSO-FS_z), or 3,7-dibenzothiophene (FSO-FS) monomers were synthesised and applied in the photocatalytic hydrogen evolution reaction (HER). The FSO-FS polymer displayed the highest rates of hydrogen evolution (170 μmol·h^{-1}), significantly higher than its structural isomer FSO-FS_z. The authors studied the charge transfer dynamics of the different polymers through temperature-dependent photoluminescence, photoelectrochemical measurements, TRPL spectroscopy, and density functional theory (DFT) calculations. They found that the HER efficiency correlated to the excited state lifetime and exciton binding energy. The FSO-BP and FSO-FS_z hindered the charge transfer and mobility due to the phenyl–phenyl dihedral angle or sharp bends in the polymer

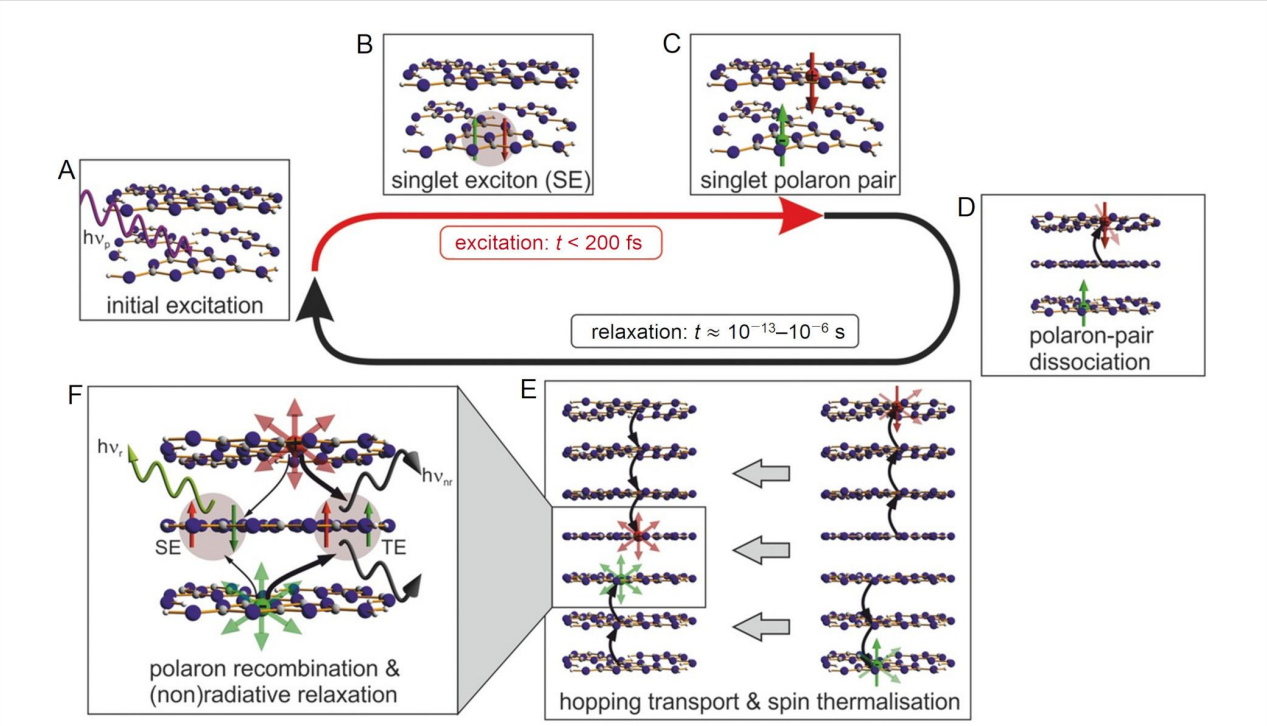

Figure 10: Timeline of the key processes of charge transport following the photoexcitation of g-C_3N_4, leading to the radiative recombination of a singlet exciton or the non-radiative recombination of a triplet exciton. A) and B) Photoexcitation and generation of singlet excitons (SE). C) Dissociation of the SE into singlet polaron pairs on adjacent sheets, and D) further dissociation into free polarons. E) Diffusive Brownian motion of the free polarons, essentially confined within channels along the stacking direction. The spin thermalization is depicted, leading to a loss of the spin coherence. F) Recombination of the free polarons. Depending on the spin states of the polarons, singlet (SE) or triplet (TE) excitons are recovered, which relax radiatively (SE) or non-radiatively (TE). Reprinted with permission from [107], Copyright 2015 Wiley-VCH.

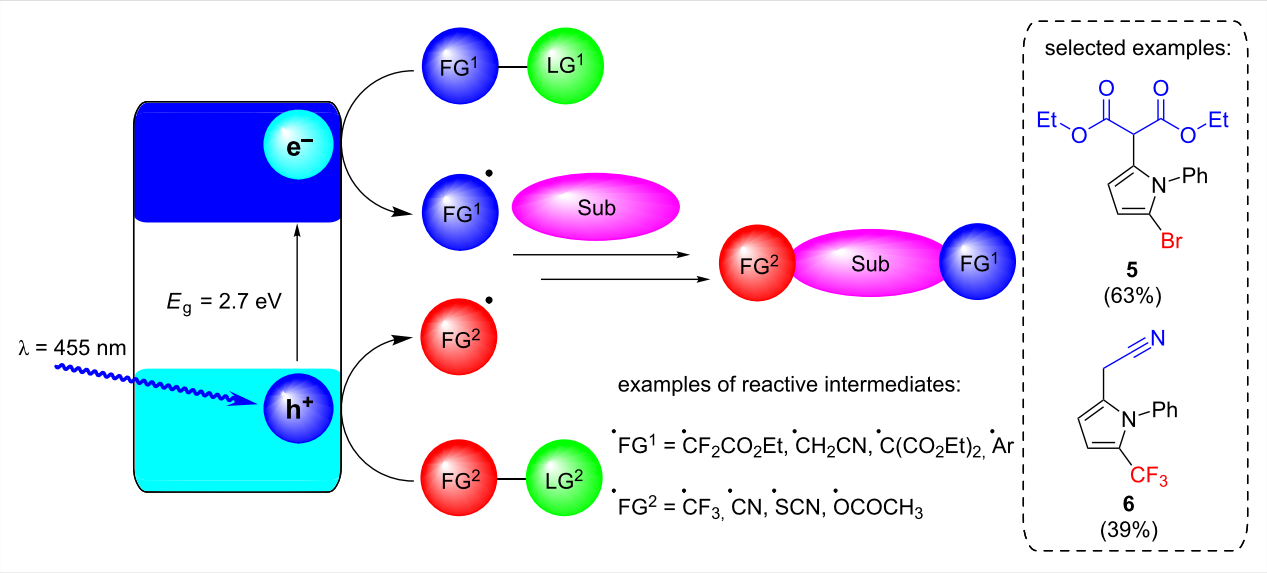

Scheme 2: Photocatalytic bifunctionalisation of heteroarenes using mpg-C_3N_4, with the selected examples **5** and **6** [128]. Sub = heteroarene substrate (e.g., *N*-phenylpyrrole), FG = functional group, LG = leaving group (e.g., Br, SO_2Na).

chain, whereas the FSO-F and FSO-FS polymers had ridged planar chains that facilitated the charge transfer [129]. The FSO-FS dibenzothiophene unit had an extended conjugation onto the sulphur atom in the excited state, which improved the charge delocalisation [129]. This demonstrated that novel material design can overcome typical limitations of organic semicon-

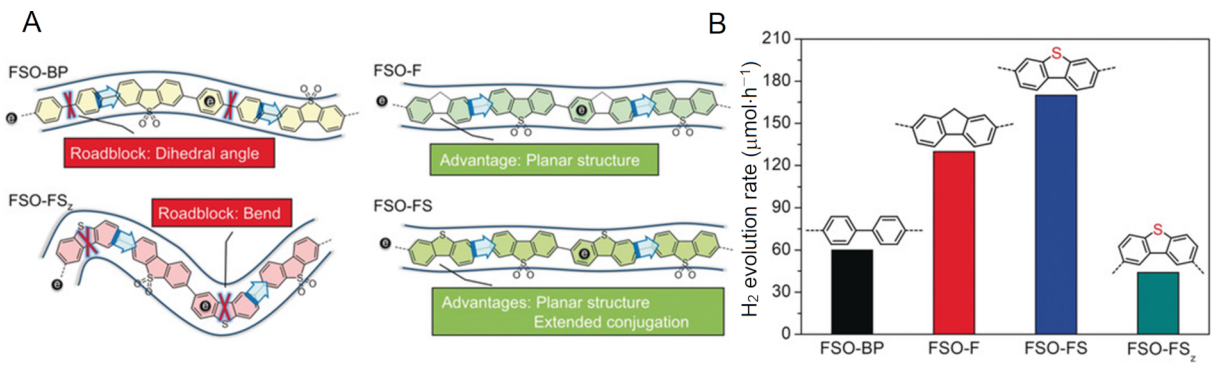

Figure 11: A) Structure of four linear conjugated polymer photocatalysts for hydrogen evolution, displaying the advantages and disadvantages obtained from each monomer and FSO combination with respect to exciton binding energy. B) H_2 evolution rate of each polymer, reflecting the relative charge separation energy, rate of charge transport and excited state lifetimes being optimal in the FSO-FS polymer. Adapted with permission from [129], Copyright 2019 Wiley-VCH.

ductors to produce more efficient photocatalysts with an enhanced charge transport. The authors did not discuss the formation of triplet excitons through intersystem crossing, which is facilitated by sulphur spin–orbit coupling, as shown by Ji, Zhao, Jacquemin, and co-workers [130], and may have contributed to extending the excited state lifetime and reducing the binding energy of excitons in FSO-FS relative to FSO-F.

2.3 Immobilised molecular photocatalysts

A strategy that combines many of the benefits of homogenous and heterogeneous photocatalysis is immobilising a molecular photocatalyst to a solid support. Most materials have inherent surface functionalities or can be modified to act as supports through covalent or electrostatic interactions, presenting a plethora of strategies to immobilise any photocatalyst with a complimentary functional group. As the immobilised photocatalyst is generally non-conjugated to the support, its photophysical properties are generally unaltered from the homogeneous equivalent, and the complex semiconductor charge dynamics are avoided. Alternatively, semiconductor supports can be used that can be irradiated at different wavelengths and inject electrons to the photocatalyst or vice versa. The same methodology is commonly applied in dye-sensitised solar cells [102]. Additionally, as only the surface of the support is functionalised with photoactive units, they are more likely to be accessible to the reaction media and the excitation photons, preventing the photocatalyst from being wasted in the bulk material. The immobilisation will generally reduce the reaction kinetics of the homogeneous photocatalyst as it is no longer dispersed in solution, but this can be mitigated through flow chemistry as previously discussed. This combines the ease of separation and recyclability of a heterogeneous catalyst, with the detailed characterisation, accessibility and synthetic versatility of a homogeneous photocatalyst.

Some desirable properties of a solid support are hence; (i) a strong, irreversible affinity for the catalyst to the support surface, (ii) stability towards the reaction conditions and reactive photogenerated intermediates, (iii) transparency to the wavelengths of radiation used to excite the catalyst, and preferably elastic scattering of the incident light, (iv) a high surface area and porosity, and (v) a strong affinity for the association of reactants to the surface and rapid dissociation of photochemical products.

A few of these strategies are represented in Figure 12 and discussed in more detail within this section. Specific examples and applications are also given later in the review (see Section 4).

Some example methods of immobilising catalysts include covalently bonding the catalyst to a polymer support either by incorporating a monomer with a photocatalytic moiety or post synthetically coupling a photocatalyst to a polymer via direct synthesis. Examples of this from our own group include the synthesis of a polystyrene gel with a photocatalytic cross-linking monomer, 4,7-bis(4-vinylphenyl)benzo[*c*][1,2,5]thiadiazole (St-BTZ) [47]. Additionally, we showed the direct synthesis of a BODIPY photocatalyst as a postsynthetic modification to an aldehyde-functionalised conjugated polymer and applied the material for singlet oxygen photosensitisation [131]. Both of these were applied as HPCats in a commercial flow reactor for photocatalysis. Whilst flow chemistry is generally used to enhance the efficiency of HPC processes, we recently demonstrated that it can also enhance the efficiency of synthesising and purifying immobilised photosensitisers [63]. A BODIPY photosensitiser was immobilised to an aldehyde-functionalised Merrifield resin (poly(styrene-*co*-divinylbenzene-*co*-4-formylstyrene)) in continuous flow and concurrently in an analogous batch procedure. The coupling efficiency was initially found to

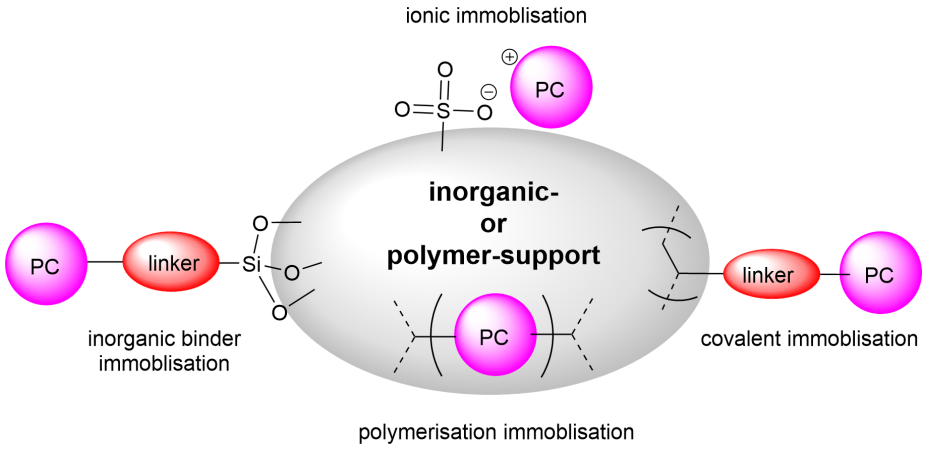

Figure 12: Graphical representation of the common methods used to immobilise molecular photocatalysts (PC) onto solid supports.

be almost double in flow versus batch [63]. The materials were also purified in flow and Soxhlet extractions, respectively, with the same solvent mixtures and time periods. The Soxhlet-extracted batch HPCats were found to have significant quantities of the homogeneous BODIPY still trapped in the resins after the extraction, which led to a dramatic loss in photosensitisation efficiency over multiple recycles as it was progressively washed out. The flow-purified resins displayed no loss of efficiency over the recycles, indicating the flow purification had effectively removed the homogeneous photocatalyst. The flow synthesis also prevented the formation of a chlorinated byproduct identified on the batch resins as an intermediate, and purification could be applied to wash out reactants from the first step of the one-pot synthesis, a potentially useful synthetic advantage of postsynthetic modifications in flow [63].

Poliakoff, George, and co-workers reported a porphyrin photosensitiser ionically immobilised to sulphonate-cross-linked ion exchange polystyrene resins (amberlyst-15) for the synthesis of artemisinin (**49**). This resulted in a bifunctional material, which acts as a HPCat and heterogeneous Brønsted acid catalyst, which are both required for independent steps in the synthesis [132]. They suggested that the porphyrin was protonated by the amberlyst-15 sulphonate groups and immobilised to the solid surface by electrostatic forces, rationalising the observed change in porphyrin colour from a purple powder to green when immobilised. The immobilisation of porphyrins onto polystyrene supports has been reported prior to this through covalent and electrostatic attractions but often suffered from poor coupling yields and low loadings [133-136]. Similarly, ionic immobilisation is common with transition metal complexes as they are often inherently cationic species. Amara and co-workers recently showed that $[Ru(bpy)_3]^{2+}$ could be immobilised on silica particles with a dramatic increase in the efficiency of the photooxidation of terpenes [137]. Polymer networks containing bipyridyl units have been designed to immobilise transition metal complexes through coordinate bonding for the oxidative coupling of amines [138]. $[Ru(bpy)_3]^{2+}$ units were synthesised with ethynyl groups *para*-substituted to the nitrogen heteroatom on four of the six pyridine rings. The ethynyl groups were subsequently cross-linked by oxidative homocoupling to form a highly cross-linked polymer [138].

Zhang and co-workers recently demonstrated that the dispersibility of polymer nanoparticle-supported benzothiadiazole photocatalysts could be improved in a range of different solvents by copolymerising classical solubilising monomers with the same St-BTZ photocatalyst monomer previously reported by Vilela and co-workers [47,139]. They showed that the supported photocatalyst material was an effective HPCat for pharmaceutically relevant transformations in the optimal solvent for the reaction, despite the native solubility of the photocatalyst being poor in those solvents [139].

2.4 Solid-supported semiconductors and metal nanoparticles

For the same reasons outlined in the previous section, the immobilisation of thin films of semiconductors and the deposition of metal nanoparticle photocatalysts can improve the irradiation, increase surface area, and reduce the redundancy of the bulk material.

One particularly interesting approach to a supported TiO_2 catalyst system was reported by Bloh and co-workers in which a thin layer of TiO_2 was immobilised onto a spherical SiO_2

coated polymer support, which encased a wireless LED light source (TiO_2@WLE, Figure 13) [140]. This allowed the efficient irradiation of the TiO_2 HPCat from within the reaction mixture and has the benefit of not requiring external LED sources or transparent reactor vessels. The LEDs were powered wirelessly using resonant inductive coupling, and were used for the photocatalytic generation of H_2O_2, the degradation of methylene blue dye, and the reduction of nitrobenzene to aniline. Although it was an interesting and novel approach to efficiently irradiating HPCats, the report did not address the potential concerns with the heat dissipation from the LEDs, which could be problematic when scaling up. Additionally, the attrition of the free floating TiO_2@WLE spheres, leading to potential damage or leaching of the TiO_2 layer, was not investigated.

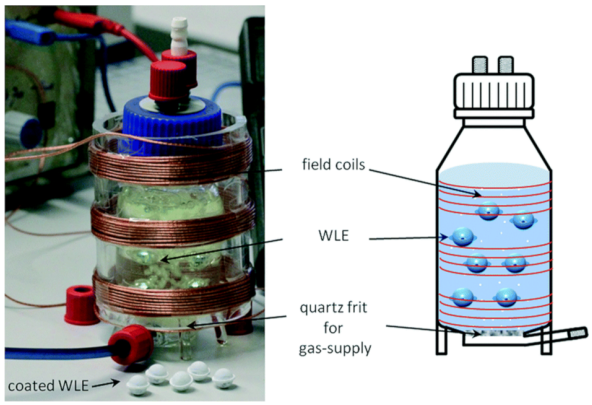

Figure 13: Wireless light emitter-supported TiO_2 (TiO_2@WLE) HPCat spheres powered by resonant inductive coupling via field coils wrapped around the reactor. Reprinted with permission from [140], Copyright 2017 The Royal Society of Chemistry.

The excellent chemical and thermal stability of metal alloys makes them ideal supports for applications in high-pressure and -temperature systems, such as stainless steel (FeCrAl) substrates used in car exhaust catalytic converters [141,142]. TiO_2 has been deposited on stainless steel previously by thermal atomic layer deposition [143], dip-coating [144], chemical vapour deposition [145], and plasma treatment [146]. Dip-coating has also been commonly applied to coat other inorganic substrates, such as glass spheres, carbon nanotubes, and diatomite with TiO_2 thin films for photocatalysis applications [147-150]. Scaiano and co-workers deposited platinum nanoparticles on TiO_2(P25) powder as a stable HPCat for reductive dehalogenations and cyclisations, and reported its enhanced photocatalytic activity relative to unmodified TiO_2 [151].

Electrochemical deposition techniques, such as electrospray and electrospinning, can also be applied to form photocatalytic composite materials. This has been shown for MnO_2 deposited on titanium sheets and nanotubes for photocatalysis [152]. Ray and Lalman deposited nanofiber TiO_2 to a metal support via electrospinning a solution of titanium tetraisopropoxide and polyvinyl acetate (PVAc) to form a TiO_2-PVAc composite material. TiO_2-PVAc was subsequently calcinated at 400–500 °C to remove the organic material and form pure TiO_2 nanofibers, which were applied for the photocatalytic degradation of phenol [153].

Photodeposition is commonly used to deposit metal atoms or nanoparticles on semiconductor surfaces, which can greatly influence the photophysical properties of the semiconductor substrate through their localised surface plasmon resonances (see Section 2.5). Alternatively, they can receive charge carriers from the HPCat support to drive a cocatalyst cycle and simultaneously facilitate the charge separation across a heterojunction, hindering recombination [154,155]. Suárez and co-workers used the photodeposition of platinum onto tungsten oxide (WO_3) powder, before immobilising within a zeolite framework to produce visible light-active HPCats for the degradation of pollutants in air [156]. Scaiano and co-workers have also utilised photodeposition to fuse samarium oxide nanoparticles to TiO_2 and ceria (CeO_2) as a bifunctional heterogeneous photoredox Lewis acid catalyst for reductive cyclisation reactions, previously reported with ruthenium transition metal complex photocatalysts [157].

Both electrochemical and photochemical deposition techniques have recently been shown to have interesting enhancements when coupled with ultrasonic irradiation [158]. Ultrasonic irradiation, from 20 kHz to 1 GHz, does not directly interact with molecular energy levels. However, the extreme conditions generated from an ultrasound wave expanding within a liquid medium are capable of breaking chemical bonds, including the sonolysis of water to hydrogen and hydroxyl radicals [159]. These conditions arise from a process known as acoustic cavitation in which the expanding phase of the acoustic wave creates microscopic voids within the solution, which collapse by implosion, producing conditions equivalent to approximately 5000 °C and 1800 atm at the implosion centre [160].

The resulting sonoelectrodeposition and sonophotodeposition methodologies have been shown to enhance mass transfer during synthesis and provide more control over the morphology and size distribution of the deposited nanoparticles [158]. Colmenares and co-workers have reported these methodologies for the synthesis of TiO_2 HPCats doped with various transition metals, such as Fe, Pd, Pt, and Au [159-161]. For more information, we recommend a recent review published by Magdziarz and Colmenares [158].

2.5 Other heterogeneous photocatalyst materials

The section above broadly categorised HPCats as either inorganic semiconductors, organic semiconductors, immobilised molecular photocatalysts, or solid-supported semiconductor HPCats. There are of course a vast number of different examples for each of these categories, with subtle differences between them; inorganic semiconductors other than TiO_2, such as ceria (CeO_2) [157], CdS [162], polyoxometalates [163,164], quantum dots [165-168], and many other examples [18,169,170]. Organic semiconductors could include conjugated porous polymers (CPPs) [3,10,171], covalent organic frameworks (COFs) [172-175], and hybrid materials, such as metal–organic frameworks (MOFs) [1,176,177]. MOFs, for example, have three distinct origins of photocatalysis; (i) semiconducting metal cluster nodes, (ii) photocatalytic organic ligands (struts) that connect the nodes, and (iii) as a solid support for other HPCat materials immobilised in the void spaces of the porous material [1,176-180]. Each material has its own subtle differences but generally adheres to the fundamental principles discussed in Sections 2.1 and 2.2, and can be explored in detail in independent reviews [1,6,176,181,182].

Some examples are more unique, such as metal nanoparticle (NPs) photocatalysis. Despite having a conductor band structure,and therefore no band gap, the nanoscale of these materials produces visible light absorptions. This is due to the oscillating electron density within metallic NPs, which can couple with the electric field of photons with wavelengths similar to the dimensions of the NPs [181]. This is called the localised surface plasmon resonance (LSPR), and is responsible for the brilliant colours observed in colloidal solutions of noble metal NPs [6,181-187]. The photon absorption polarises the electron density of the nanoparticle and produces energetically excited electrons above, and holes below the Fermi level that can undergo photoredox processes with substrates [185,188-190].

Supramolecular photocatalysts are an interesting class of materials which utilise non-bonding interactions to control photochemical processes, a biomimetic strategy that imitates enzyme catalysis [191]. Supramolecular self-assemblies and coordination polymers based on perylene diimide (PDI) aggregates have become a popular choice of heterogeneous photocatalyst. As PDI is a large, planar, polyaromatic hydrocarbon molecule, it spontaneously forms ordered 1D supramolecular assemblies through efficient π–π stacking and side chain interactions [192]. Despite the PDI units having only non-bonding interactions, the narrow π–π stacking provides a sufficient π orbital overlap to produce semiconductor-type electronic band structures and an efficient interplanar charge transport similar to g-C_3N_4 [192]. Duan and co-workers reported the synthesis of a zinc PDI assembly as a heterogeneous photocatalyst for the reduction of aryl halides [193]. The material could undergo consecutive photoinduced electron transfers (ConPET) in which the material enters an excited state and is reduced by a sacrificial electron donor (NEt_3). The resulting Zn-PDI radical anion then undergoes a second photon absorption to achieve a superreducing electronic excited state capable of reducing stable aryl halides (Figure 14) [193]. More recently, PDI self-assemblies have been reported as efficient HPCats for the hydrogen evolution reaction [194] and degradation of phenol [192].

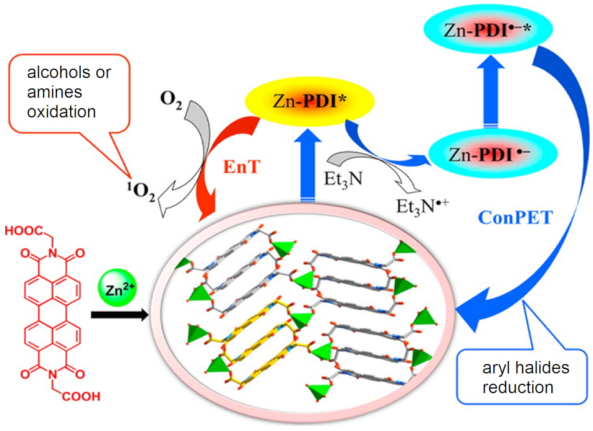

Figure 14: Graphical representation of zinc–perylene diimide (Zn-PDI) supramolecular assembly photocatalysis via consecutive photoinduced electron transfer (ConPET). EnT = energy transfer, $^1O_2$ = singlet oxygen (see Section 4.2). Reprinted with permission from [193], Copyright 2016 American Chemical Society.

Another important material design applied in heterogeneous photocatalysis that we have so far not mentioned are Z-schemes and heterojunction photocatalysts [7,195,196]. Z-scheme systems comprise two or more independent semiconductors with similar E_g values but differing valence band and conduction band potentials. By fusing the two materials to form a heterojunction and concurrently photoexciting both semiconductors, the least reducing e^-_{CB} and oxidising h^+_{VB} of the two semiconductors will recombine at the heterojunction. This leaves the more reducing e^-_{CB} and oxidising h^+_{VB} of each semiconductor with no opposing charge carrier, preventing recombination and expanding the redox potentials of the fused material [7]. The history and recent developments of these materials was reviewed by Anusuyadevi, Marre, Yu, and co-workers [7,196].

As briefly mentioned in Section 1.3, upconversion photocatalysis is a developing field of research that permits using long-wavelength irradiation to deeply penetrate through a reaction medium and material surface and activate the bulk of the material. Congreve, Rovis, Campos, and co-workers utilised triplet fusion upconversion to drive a series of homogeneous

photoredox transformations with >700 nm photons [50]. They reported a photocatalytic atom transfer radical polymerisation for the synthesis of cross-linked PMMA using the upconversion photocatalyst system and either a blue laser or a NIR (730 nm) laser. The blue laser would excite the photocatalyst component directly, whilst the NIR laser activated the sensitiser component, which sequentially transfers the energy to the photocatalyst to achieve the same excited state indirectly. The polymerisations were performed with a variety of light-blocking media placed between the laser source and the reaction medium. This included bacon strips to imitate light transmission through flesh, as this is relevant for photocatalyst applications in photodynamic therapy [197-199]. They reported that the NIR photons penetrated 293 times deeper into the polymerisation medium and enabled the reaction to be applicable on a multigram scale through silicon moulds, which could not be achieved with the blue laser [50].

Heterogeneous upconversion systems are generally crystalline nanomaterials comprising a host matrix of typically $NaYF_4$, doped with a mixture of lanthanide ions, which act as light-absorbing sensitisers (e.g., Yb^{3+}) and energy-combining activators (e.g., Er^{3+}, Tm^{3+}) [51,200,201]. Li and co-workers reported the synthesis of $NaYF_4$:Yb^{3+}(20%), Tm^{3+}(0.5%) upconversion nanocrystals coated with a thin layer of CeO_2 and sequentially with a layer of ZnO [200]. This formed a core–shell nanocomposite of the upconversion nanocrystals, coated in a type II heterojunction photocatalyst system (Scheme 3) [7,200]. The material was applied in the photocatalytic degradation of an organic dye, methyl orange, and was shown to have direct photocatalytic activity when irradiated with visible or NIR radiation. Additionally, the activity of the coated upconversion nanocrystals under simulated solar irradiation was greatly enhanced relative to pure CeO_2, as the composite material could utilise shorter wavelength irradiation directly, as well as longer wavelengths via the upconversion system [200].

Hao, Jin, Du, and co-workers reported a similar strategy of coating octahedral YF_3:Yb,Tm microparticles with a thin layer of epitaxially grown BiOCl HPCat [201]. The epitaxial interface was found to be important for the efficient non-radiative energy transfer and upconversion emission reabsorption. The group reported similar observations of a direct NIR irradiation-driven photocatalytic ability for the degradation of methyl orange and for water photolysis. Consistent with the report of Li and co-workers, the BiOCl-coated YF_3:Yb,Tm also showed an improved activity over pure BiOCl under simultaneous visible light (>420 nm) and NIR irradiation, as the composite material could utilise more wavelengths [201]. A few other examples of lanthanide-doped upconversion materials for photocatalysis exist in the literature and were reviewed by Ma and co-workers, who also provided more details on the complex mechanisms upconversion by lanthanide ions [51].

Now that we have established the fundamental processes and recent developments of heterogeneous photocatalysts, we will discuss the development of flow reactor systems designed to apply HPCats before reviewing their application in organic synthesis as well as water and air purification.

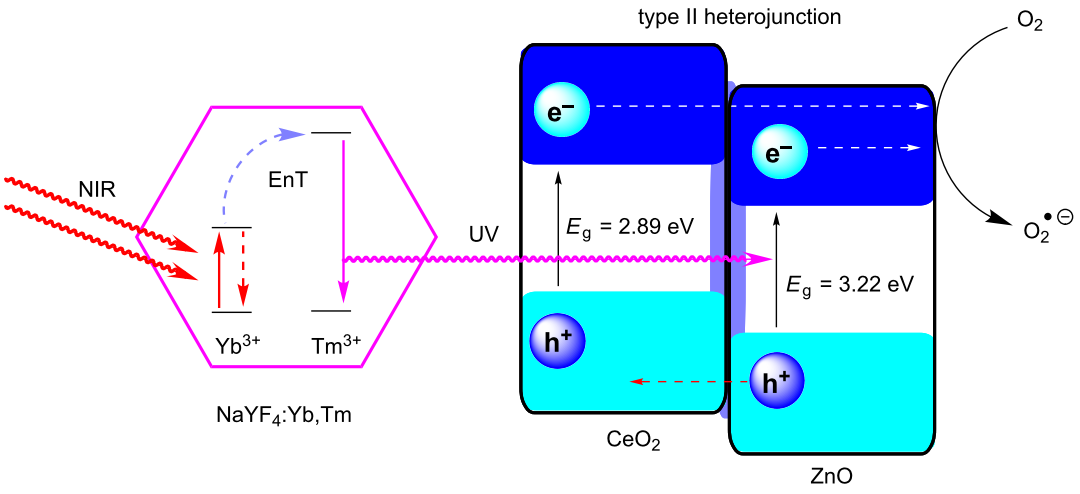

Scheme 3: Upconversion of NIR photons to the UV frequency by $NaYF_4$:Yb,Tm nanocrystals sequentially coated with CeO_2 and ZnO HPCat layers. Two or more NIR photons are sequentially absorbed by Yb^{3+} ions (sensitisers), and the energy is transferred to Tm^{3+} ions (activators), which emit a single higher-energy photon. The upconverted photons drive the charge separation in the HPCat layers for the photocatalysis. NIR = near infrared irradiation, UV = ultraviolet photons, EnT = energy transfer. The CeO_2/ZnO type II heterojunction enhances the charge carrier separation and supresses the recombination [200].

3 Flow reactors for heterogeneous photocatalysts

The consideration of different reactors that can be employed for irradiating heterogeneous photocatalysts is important for maximising the efficiency of the intended system. Homogeneous photocatalysis is normally a simple choice between a three-dimensional transparent coil or a two-dimensional microfluidic device, with the common objective of generating a short path length for the efficient and uniform irradiation of a solution flowing through a narrow channel. HPCats have three main reactor categories for implementation in flow; (i) immobilised within a fixed bed, (ii) immobilised through coating to a reactor's surface, or (iii) a free-flowing suspension (Figure 15). Within these categories are further subdivisions or evolutions that each carry unique advantages and disadvantages, which we will now discuss in more detail.

Fixed bed reactors are typically transparent columns made from inert materials, such as borosilicate glass, sealed at each end by porous frits that allow liquids to flow through the reactor, but not solids. External light sources irradiate from the sides, as liquid reagents flow through the bed and into contact with the immobilised HPCat. Annular fixed beds may also have a light source placed within the central cavity for enhanced irradiance. As the HPCat is confined to the reactor, no filtration of the outflow is required to recover the HPCat, and the reactor can be reused continuously.

As depicted in Figure 15A, depending on the free volume, the direction of the flow, and the relative densities of the solvent and HPCat, the fixed bed can be utilised in three different modes of operation: (i) a packed bed in which the HPCat fills the volume of the reactor, forcing the solution to flow through the material's pores or voids between the compact material surfaces, (ii) a fluidised bed in which the bed has the free volume for the HPCat to disperse and move freely in the flowing solution whilst remaining confined to the reactor, and (iii) a mixed bed, a hybrid between the two aforementioned regimes in which the reactor has a free volume, but portions of the HPCat are compacted and the rest is mobile. The three regimes have different advantages and disadvantages, which we have outlined in Table 1. Mixed/hybrid bed reactors have a combination of advantages and disadvantages of both the packed and the fluidised bed reactors and therefore have been omitted from the table. The more intricate details of the fluid dynamics and reactor engineering are beyond the scope of this review but can be explored in engineering text books and review articles [43,202-206].

Fixed beds are therefore a versatile choice of reactor for heterogeneous photocatalysis in flow. However, fixed bed reactors suffer from a relatively low surface-to-volume ratio compared with the dimensions of a microchannel, shielding the HPCat packed within the centre of the reactor from irradiation [207]. This is often overcome by copacking an inert, transparent material, such as glass beads, with the HPCat to disperse the photoactive material [208,209]. Fixed beds are generally quite expensive and limited to column or annular designs, which makes controlling the mixing and the sequential addition of the reagents generally not possible.

Coated reactors immobilise the HPCat as a thin film on the surface of channels within a microfluidic device [210,211]. Coated reactors overcome the disadvantages of fixed beds by permitting much greater freedom of design with respect to the channel dimensions and the flow paths. This enabled custom flow

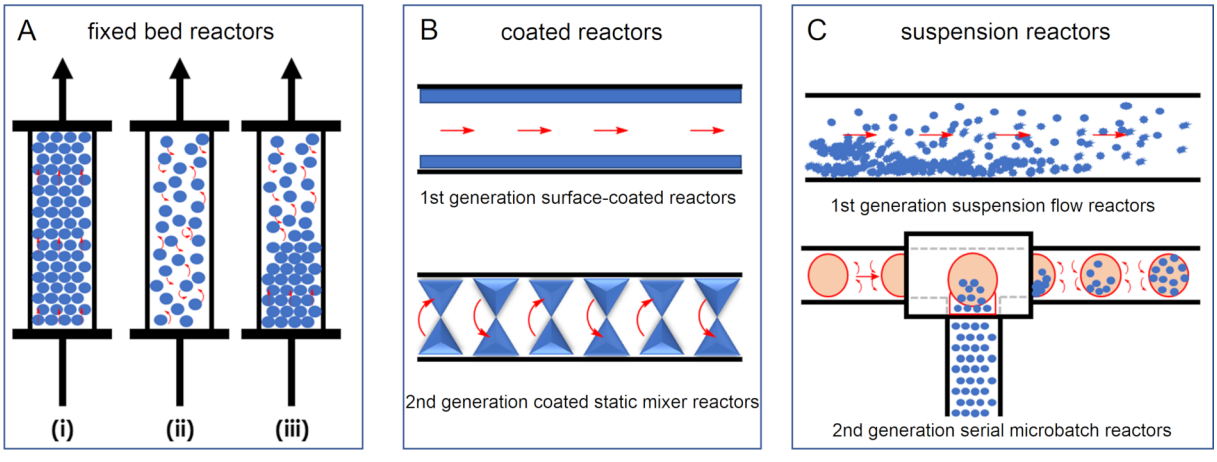

Figure 15: Types of reactors employed in heterogeneous photocatalysis in flow. A) Fixed bed reactors and the subcategories of (i) packed bed, (ii) fluidised bed, and (iii) hybrid/mixed bed. B) Coated reactors in which the HPCat is immobilised onto a surface. C) Suspension reactors that have the HPCat freely flowing through reactor channels.

Table 1: Advantages and disadvantages of fixed bed reactor modes of operation.

packed bed		fluidised bed	
advantages	disadvantages	advantages	disadvantages
* The solution is forced into contact with the immobilised catalyst. * The catalyst is stationary, reducing material damage through attrition. * The confinement of the HPCat to the reactor creates a high relative concentration of the catalyst compared to the flowing reagents.	* The flow of immiscible liquid/liquid or liquid/gas mixtures through the bed is difficult. * Poorer mixing can reduce the selectivity and produce hotspots within the reactor.	* Improved mixing removes hotspots, which can enhance the selectivity in thermal processes [202,203].	* The free volume allows some reagents to pass through the reactor without necessarily contacting the HPC.

channel designs that can precisely control the addition of reagents, residence time, and mixing, optimised for the specific reaction [32,58,212]. As the active HPCat is only present as a thin layer on the channel surface, it can be efficiently irradiated.

In first generation coated reactors, the HPCat is confined to the surface of linear flow channels. This presents mass transport limitations as reagents must diffuse to the channel surface to react, making the channel surface-to-volume ratio a limiting factor for the productivity [213]. Second-generation coated reactors combat this issue by employing static mixers as the HPCat substrate to generate a turbulent flow and to enhance the mass transport within the channels [214-217]. There are limitations as the HPCat and reactor device must have compatible functional groups to be deposited or immobilised and must be compatible with the intended reaction system's solvents and reagents. The freedom of design advantage also carries the disadvantage that these reactors have a limited commercial availability and often require manufacture by the intended user.

The final type of the reactor provides solutions to the limitations of immobilising HPCats by not immobilising the HPCat. Suspension or slurry reactors operate by dispersing the HPCat as small particles within the reaction solution and pumping them together through a flow reactor system. Most homogeneous photocatalysis reactor setups will be suitable for an HPC suspension flow so that there is no need to invest in a reactor exclusively for a HPCat. In order to pump suspensions, either a syringe pump or a peristaltic pump will be required as HPLC piston pumps are not compatible with solids [43]. Care must be taken to prevent the suspended HPCat from sedimenting in the syringe and creating a non-uniform suspension [218]. The HPCat employed must have small dimensions to remain in suspension throughout the flow system, typically a powder with particles <100 μm for channels with 1 mm internal diameter. This may require grinding the HPCat with a mortar and pestle or a ball mill, which may be undesirable for materials with intricate and sensitive nanostructures.

Whilst the HPCat is well dispersed throughout the flowing medium, the local environment around the flowing particles can be relatively static, hence the mass transport of reagents to the suspended catalyst remains suboptimal [207]. Second generation suspension reactors function by dosing HPCats suspended in a viscous ionic liquid into reaction media droplets, which are separated by segments of a carrier gas. The segmented slug flow generates Taylor flow cycles, which efficiently mix the individual suspensions to prevent the sedimentation and enhance the mass transport within the local environment [207]. An issue remains for industrial applications as both generations require filtration for the HPCat recovery and purification, although this is less cumbersome than recovering a homogeneous photocatalyst.

In summary, we have generalised the advantages and disadvantages of each reactor system in Table 2 to guide the reader in choosing the best option for their intended HPCat and reaction system. In the following sections of the review, we will denote the type of reactor used in the reaction schemes by the graphics displayed in the first column of Table 2, for ease of reference.

4 Applications of heterogeneous photocatalysts in continuous flow reactors

With the fundamental photocatalysis processes and recent design developments of HPCats and their compatible reactor types now in perspective, we will proceed to review the recent reports of heterogeneous photocatalysis in flow. This section is divided into four parts: HPC in flow for organic synthesis through photoredox (Section 4.1) and energy transfer photocatalysis (Section 4.2) and two final sections on water (Section 4.3) and air purification (Section 4.4).

Table 2: Advantages and disadvantages of different HPCat flow reactor systems.

system	advantages	disadvantages
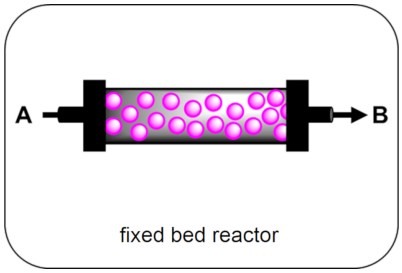 fixed bed reactor	• Multiple modes of operation • Compatible with any HPCat & solvents • Deactivated catalyst is easily removed and replaced • Immobilised catalyst is easily recycled & purified • Commercially available	• Borosilicate columns are expensive and fragile • Reactor dimensions are limited • Low surface-to-volume ratio prevents efficient irradiation • Pressure drop across the bed can be problematic
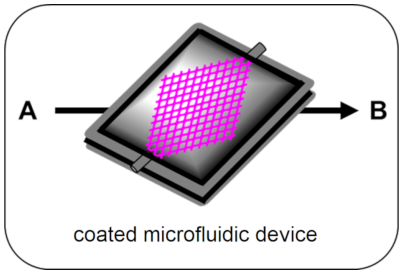 coated microfluidic device	• Freedom of reactor design • Thin film HPCat efficiently irradiated • High HPCat surface area • Static mixers can be coated to enhance mass-transport	• Lack of commercial availability • Limited by immobilisation compatibility of reactor material and HPCat • Reactor material and solvent system compatibility needs consideration • Commercial static mixers are expensive • Difficult or impossible to regenerate or replace deactivated catalyst
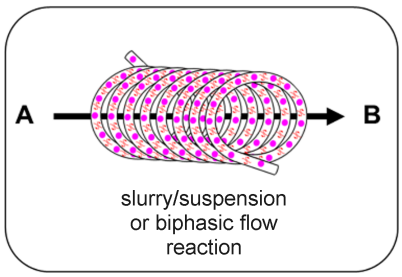 slurry/suspension or biphasic flow reaction	• Easily assembled from cheap materials • Efficient mixing and irradiation	• Prone to blockages • Requires very small HPCat particles • Some HPCats and solvents may be incompatible • Filtration will be required to reclaim and recycle HPCat

4.1 Heterogeneous photoredox catalysis in flow

Photoredox catalysis was first reported in the 1970s by Kellogg and co-workers [219,220], followed shortly by other reports from early pioneers [219-229], but the field failed to gain momentum due to a lack of cheap and powerful LED technology. Today's LED technology is becoming increasingly powerful and less expensive, as predicted by Haitz's law (the LED equivalent of Moore's law) [230,231]. As discussed previously, this changed in 2008 after three seminal papers from the groups of MacMillan, Yoon, and Stephenson, who used ruthenium complexes and visible light to catalyse single-electron transfer reactions [24-26]. These reports demonstrated that photochemical synthesis could be achieved with visible light, initiating the realisation of Ciamician's vision of harnessing the power of solar-irradiation to power artificial photosynthesis, stated in "The photochemistry of the future" as [29]:

"[…] inside of these will take place the photochemical processes that hitherto have been the guarded secret of the plants […]".

Following a photoinduced charge separation event in a semiconductor HPCat or immobilised molecular photocatalyst, the materials' reduction and oxidation potentials are simultaneously increased by the formation of an excited electron and electron vacancy. The electrochemical potentials of the reaction substrates should be compatible with the HPCats' excited state potentials, as this largely dictates whether a photoredox process will be successful. This has made electrochemical analysis, such as cyclic voltammetry, a core tool of modern photocatalyst characterisation [232,233]. The electrochemical potentials of some common semiconductor and molecular photocatalysts are displayed in Figure 16 [128].

The photoredox cycle then proceeds as illustrated in Scheme 4 for an immobilised molecular photocatalyst, and as previously illustrated in Figure 4 for a semiconductor HPCat. The overall photoredox process can be defined as net oxidative or net reductive, depending on the quenching cycle. The intermediate reduced or oxidised HPCat is returned to its initial state by a sacrificial electron donor or acceptor, respectively. If the initial

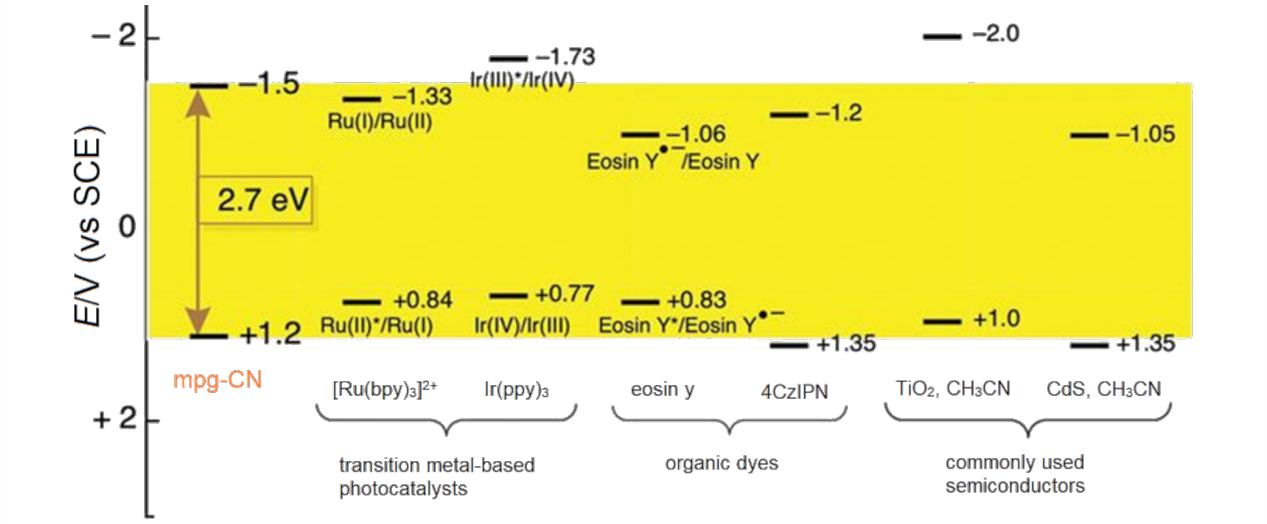

Figure 16: Electrochemical potential of common semiconductor, transition metal, and organic dye-based photocatalysts [128]. Reprinted with permission from AAAS.

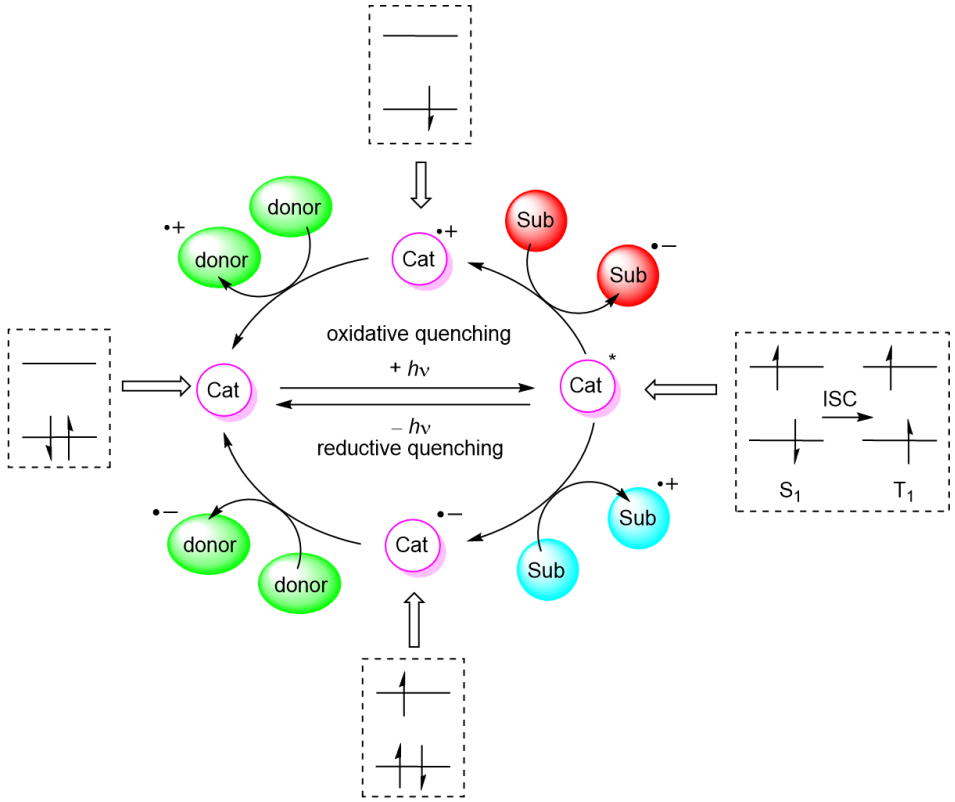

Scheme 4: Possible mechanisms of an immobilised molecular photoredox catalyst by oxidative or reductive quenching. ISC = intersystem crossing, Sub = substrate, Cat = photocatalyst, Cat* = electronic excited state photocatalyst, +/- *hν* = absorption/emission of photon, S_1 = first singlet electronic excited state, T_1 = first triplet electronic excited state.

substrate reacts and forms an intermediate, which subsequently reduces or oxidises the intermediate HPCat to complete the photocatalytic cycle, the process is termed net-neutral photoredox catalysis.

A recent report from Seeberger, Gilmore, and co-workers looked to overcome the inherent disadvantage of light penetration when performing heterogeneous photocatalysis in a fixed bed reactor, as discussed in the previous section [207]. To over-

come this, the group optimised a multiphasic system of serial microbatch reactors (SMBRs) in which a modified g-C_3N_4 previously reported by Antonietti and co-workers [126] was suspended in an ionic liquid and periodically dosed into a segmented flow of a aryloxyacetic acid (**7**) and SelectFluor (**8**) solution separated by nitrogen pockets (Scheme 5). The liquid/gas slug flow regime generates Taylor flow cycles that efficiently mix the individual liquid slugs and keep the HPCat suspended.

The CMB-C_3N_4 is formed of cyanuric acid (C), melamine (M), and 5 mol % barbituric acid (B), which is calcined to yield the modified g-C_3N_4 with heterojunctions formed in situ. CMB-C_3N_4 has been shown to be superior to g-C_3N_4 and meso-

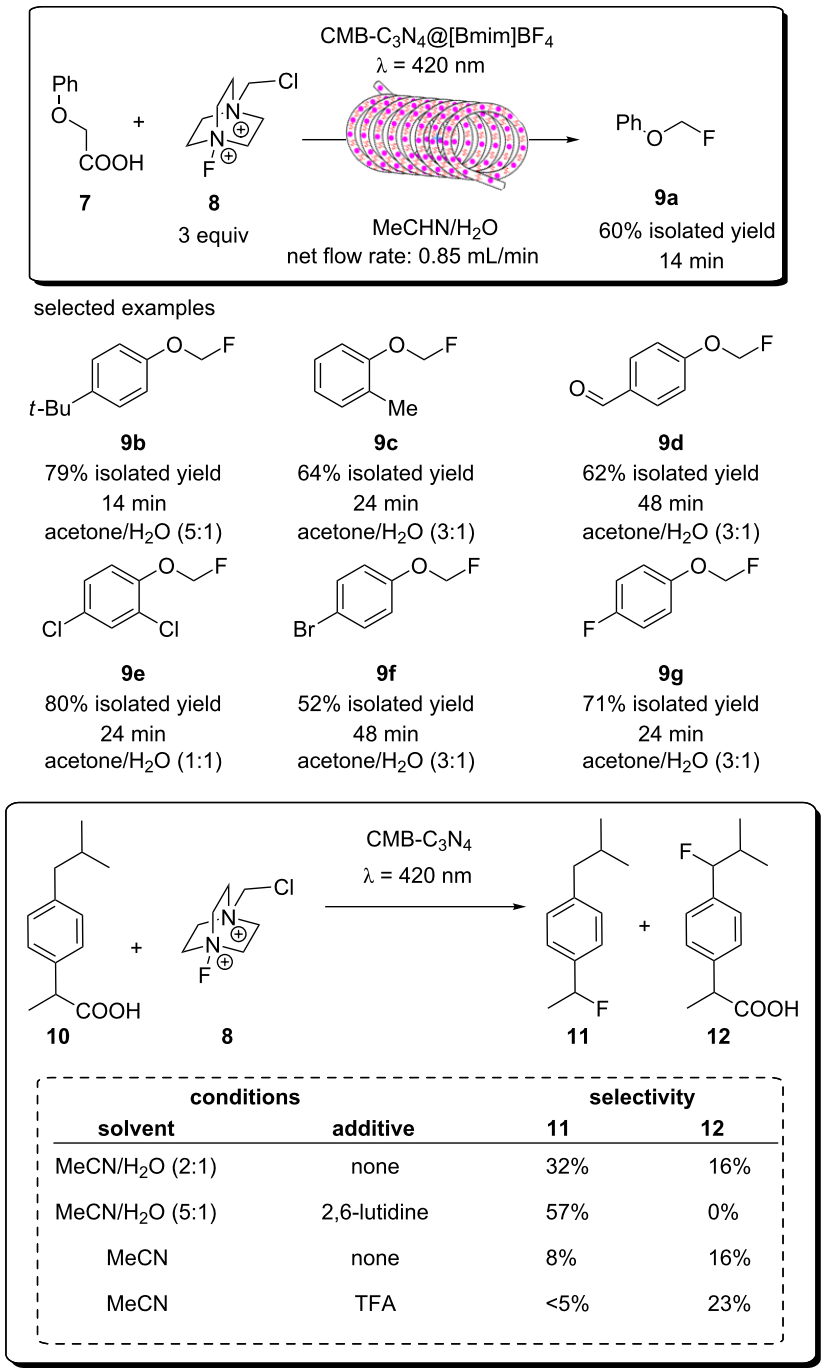

Scheme 5: Scheme of the CMB-C_3N_4 photocatalytic decarboxylative fluorination of aryloxyacetic acids, with the selected examples **9a–g** and the selectivity control in the fluorination of ibuprofen (**10**) being shown [207].

porous g-C_3N_4 (mpg-C_3N_4) in the photocatalytic hydrogen evolution reaction due to a better charge separation across the heterojunction of the material [126]. The suspensions were optimised by manipulating the flow rates of the three component phases until uniform suspensions were produced and maintained by the internal vortices created by the Taylor flow cycles. They reported a broad scope of aryloxyacetic acids with various substitutions on the benzene ring, **9a**–**g** (Scheme 5), with >60% isolated yield under optimised conditions. Interestingly, this transformation has been performed with strongly oxidising homogeneous iridium photocatalysts and a sacrificial base, but no additives were necessary with the modified CMB-C_3N_4 HPCat [234]. It is important to note that while the system provided efficient irradiation, the reaction required a three-step extraction process to recover the catalyst, product, and ionic liquid. Fortunately, the HPCat, ionic liquid, and product could all be recovered and purified through sequential filtrations and extractions, without the need for a laborious column chromatography purification. The substrate scope included ibuprofen (**10**), which could be selectively fluorinated to give **11** or **12** by the addition of lutidine or trifluoroacetic acid additives, respectively [207]. The reaction has been well studied with transition metal photoredox photocatalysts and TiO_2 in batch, and was proposed to occur via the same mechanism [126,207,235,236].

A recent report from Rueping and co-workers utilised g-C_3N_4 as a heterogeneous photocatalyst to develop desilylative and decarboxylative couplings to generate secondary and tertiary amine derivatives (Scheme 6) [208]. Following the photoinduced charge separation and migration to the g-C_3N_4 surface, α-amino acids and α-silylamines are oxidised by the h^+_{VB}, leading to the subsequent decarboxylation or desylilation, respectively, to yield the common α-amino alkyl radical **I** (Scheme 6), which undergoes addition, allylation, and heteroarylation reactions. The resulting radical intermediate **II** is reduced by the e^-_{CB} and subsequently protonated to yield the product. The reactions proceeded with good yields of generally >70% across a broad range of substrates in a batch photochemi-

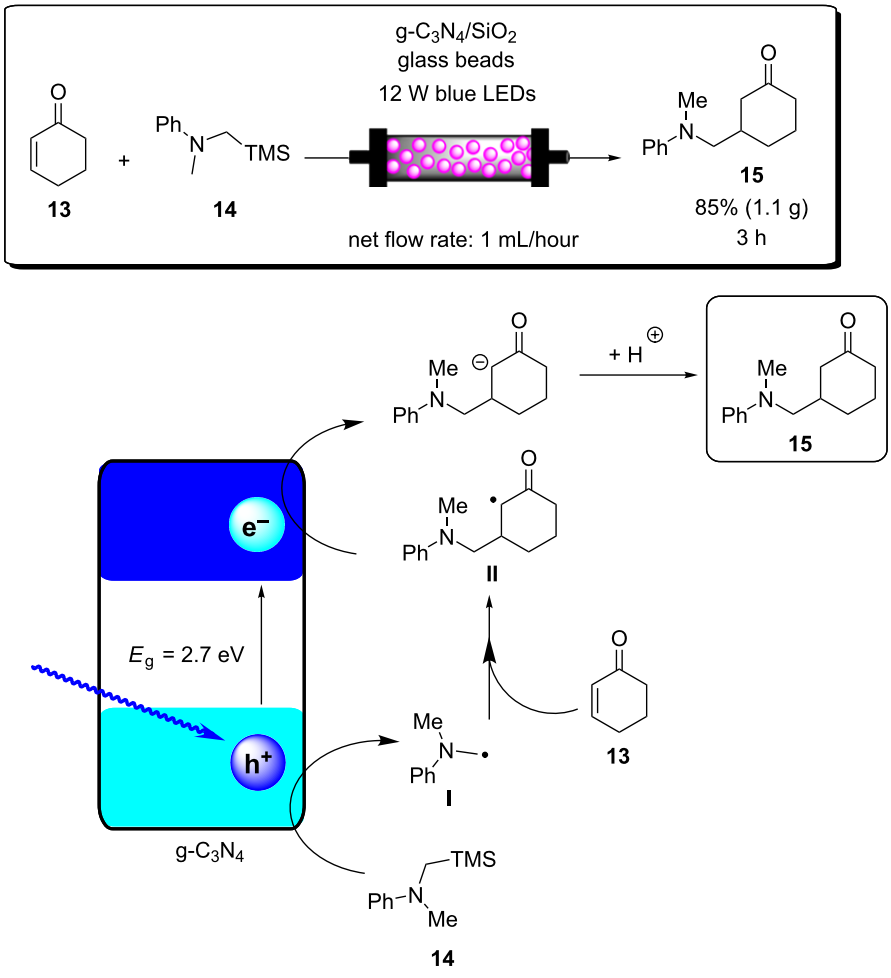

Scheme 6: Scheme of the g-C_3N_4 photocatalytic desilylative coupling reaction in flow and proposed mechanism [208].

cal reactor. The g-C_3N_4 HPCat was recycled 8 times in the desilylative coupling of an α-silylamine and acrylonitrile derivative, maintaining >90% conversion after a total of 16 hours of irradiation. The group resourcefully utilised a glass chromatography column as a fixed bed reactor to perform the continuous flow synthesis of 3-((methyl(phenyl)amino)methyl)cyclohexanone (**15**, Scheme 6). The column was packed with glass beads to reduce the internal reactor volume before a mixture of silica gel and g-C_3N_4 was added and filled the voids between the glass beads. The column was wrapped in a blue LED array ribbon to complete the reactor. 2-Cyclohexenone (**13**) and 1.3 equivalents of the α-silylamine **14** were passed through the column at a flow rate of 1 mL·h^{-1}, controlled by a plunger, resulting in a total residence time of 3 hours before the solution containing product **15** eluted to a collection flask. The setup was very effective and allowed for a gram-scale synthesis of the desired product with 85% yield, only a slight reduction of the batch-optimised yield of 95%. However, the 85% flow yield was achieved in only 3 hours, a significant reduction from 17 hours in batch. This report elegantly demonstrates the significant enhancement of heterogeneous photocatalysis that can be achieved when continuous flow is employed, and this demonstrates a simple and resourceful method to implement heterogeneous flow chemistry that is accessible without investing in expensive flow reactors and pumps.

Blechert and co-workers reported a similar reactor setup for the radical cyclisation of the linear unsaturated alkyl 2-bromo-1,3-dicarbonyl compound **16** (Scheme 7) [237]. mpg-C_3N_4 was combined with silica gel and glass beads and immobilised in a length of transparent FEP tubing, which was arranged in a spiral, and fixed between two microscope slides to form a fixed bed-type reactor with a high surface-to-volume ratio. The substrate **16** in THF was supplied to the reactor by a syringe pump at 124 µL/min for an optimised residence time of 5 minutes. The reaction was previously reported using a $[Ru(bpy)_3]Cl_2$

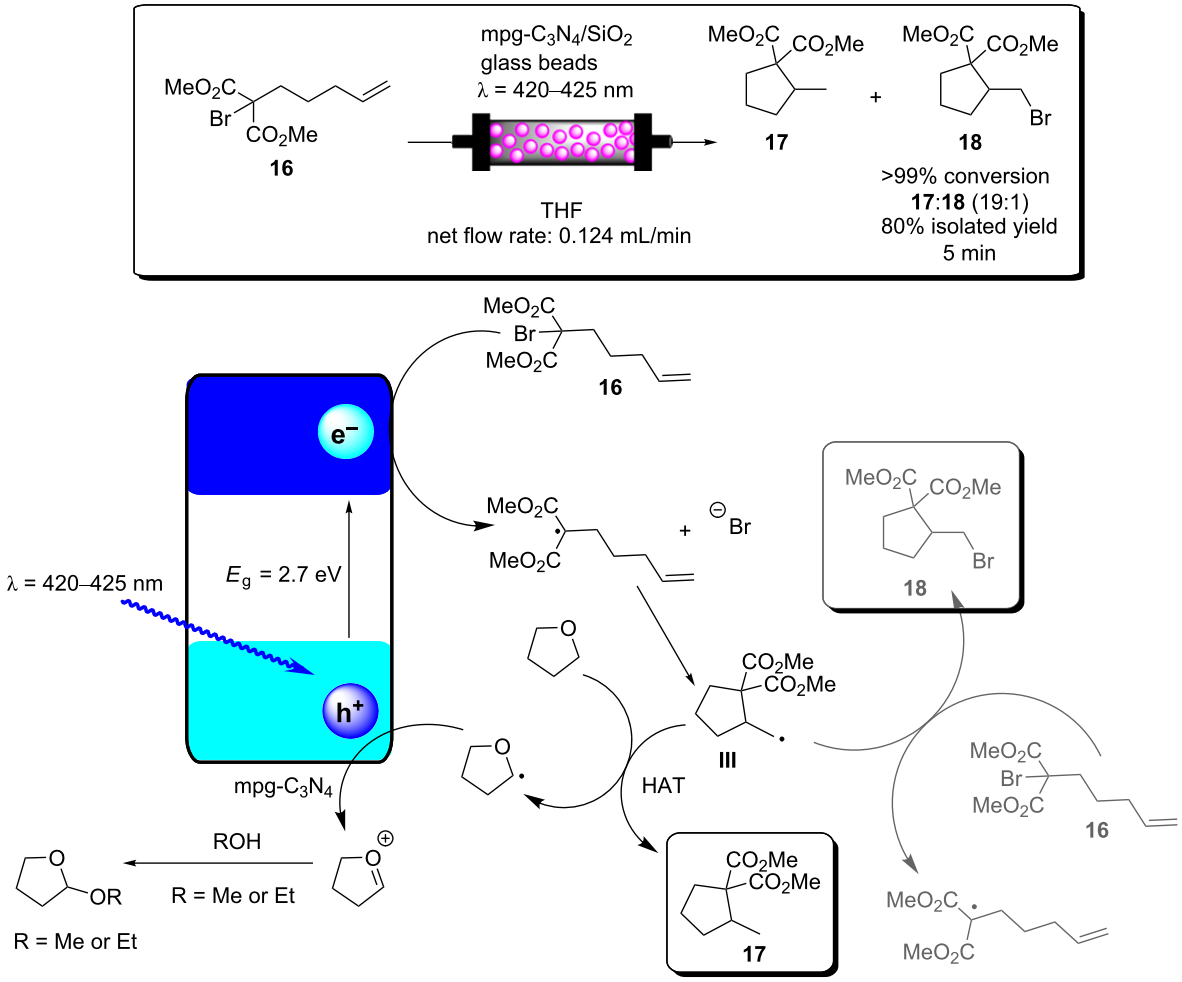

Scheme 7: Proposed mechanism of the radical cyclisation of unsaturated alkyl 2-bromo-1,3-dicarbonyl compounds using mpg-C_3N_4 as a heterogeneous photocatalyst [237].

photocatalyst in DMF with TEA as a sacrificial electron donor, which required 12 hours of irradiation for a high conversion on average [238]. During the optimisation, Blechert and co-workers found that by using THF as a solvent, they could achieve a high conversion at a reduced reaction time of 4 hours, and with no need for the TEA additive. They found that THF was able to undergo hydrogen atom transfer with the radical product precursor **III**, yielding the cyclic product **17**. The THF radical then reduces the h^+_{VB} to complete the cycle, in place of TEA (Scheme 7) [237]. The brominated minor product, **18**, was suggested to result from the intermediate **III** abstracting a bromine atom from a second equivalent of **16**, or alternatively by **III** being oxidised by the h^+_{VB} to form a cationic species that reacts with the liberated bromides from the initial reduction of **16**.

The alkylation of benzylamine with various alcohols using a photocatalytic microfluidic device was reported by Matsushita and co-workers in 2007 and demonstrated the importance of the reactor design for the photocatalysis efficiency (Scheme 8) [213]. The microreactor comprised a quartz substrate with microchannels 40 mm long, 500 µm wide, and either 300, 500, or 1000 µm in depth. The bottom and side walls of the channels were coated in TiO_2 via sol–gel spin coating, before being calcined at 770 °C for 2 hours in air. Platinum particles were deposited on the TiO_2 layer via photodeposition from chloroplatinic acid using a mercury lamp irradiation source. The device was then covered with a transparent quartz window and sealed under pressure to yield a HPCat-coated microfluidic device. The photocatalysis experiments were performed using a syringe pump to flow a 1.0 mM solution of the amine substrate **19** (Scheme 8) in methanol, ethanol, or isopropanol under an inert nitrogen atmosphere. The flowing reaction solution was irradiated at 365 nm by UV LEDs in the microfluidic device for 30–150 seconds. The reaction was found to proceed rapidly and achieved 85% yield of *N*-ethylbenzylamine (**20**, Scheme 8) after 150 seconds in the 500 µm channel coated with Pt@TiO_2. The reaction was found to proceed more efficiently with platinum-free TiO_2-coated channels, achieving the same conversion after only 90 seconds. However, the authors did not suggest why the platinum particles were reducing the efficiency. The yield was intimately linked with the channel depth as after 90 seconds of irradiation, the platinum-free TiO_2 300 µm channel provided a 14% increase in yield over the 500 µm channel, and a 28% increase over the 1000 µm channel. This was attributed to the higher surface-to-volume ratio of the 300 µm channels. An analogous catalytic system, reported by Ohtani and co-workers, was performed in batch and required significantly longer reaction times of 5–10 hours to achieve a comparable conversion [239]. Interestingly, the batch system, over extended periods of irradiation, led to the production of the *N*,*N*-dialkylated benzylamine **21** (Scheme 8) with Pt@TiO_2 particles suspended in an alcohol solution. No formation of the dialkylated product was observed with the microfluidic flow reactor, which the authors proposed was due to the much shorter irradiation times, providing an enhanced control over the product selectivity. The reaction was proposed to occur by the photoreduction of the alcohol solvent adsorbed at the TiO_2 surface to generate H_2 gas and a corresponding carbonyl compound via an alkoxy intermediate. The carbonyl compound subsequently condensed with the amine substrate to generate an imine, which was reduced to the secondary amine by the H_2 produced in situ.

L-Pipecolinic acid (**22**) was synthesised using a similar TiO_2-modified microfluidic device (TMFD) by Kitamori, Kim, and co-workers (Scheme 9) [240]. The TMFD was fabricated from two pyrex glass substrates, with 700 µm wide and 3.5 µm deep channels. A 300 nm film of anatase TiO_2 nanoparticles was immobilised to the channels using a sol–gel method and characterised by cross-sectional scanning electron microscopy. Photocatalytic activity of the device was initially assessed by the successful photodegradation of methylene blue dye. The photodeposition was used to deposit platinum nanoparticles as a reductive centre for the photoredox deaminative cyclisation of L-lysine (**23**) to **22**. The TMFD could achieve near-full conversion of **23** (87%) after 52 seconds residence time, but with only 22% selectivity for both **22** and D-pipecolinic acid. This reduced the enantiopurity of the starting material to 50% ee, resulting in

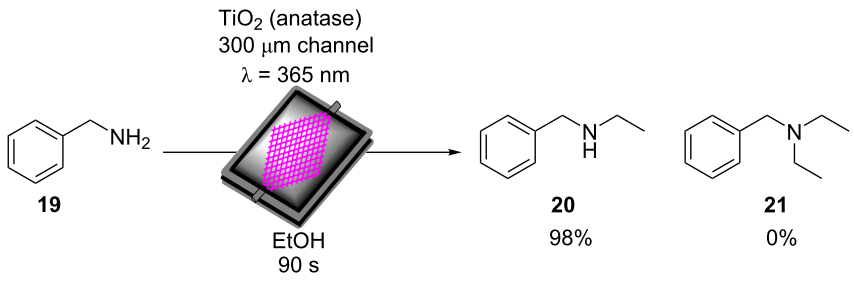

Scheme 8: N-alkylation of benzylamine and schematic of the TiO_2-coated microfluidic device [213].

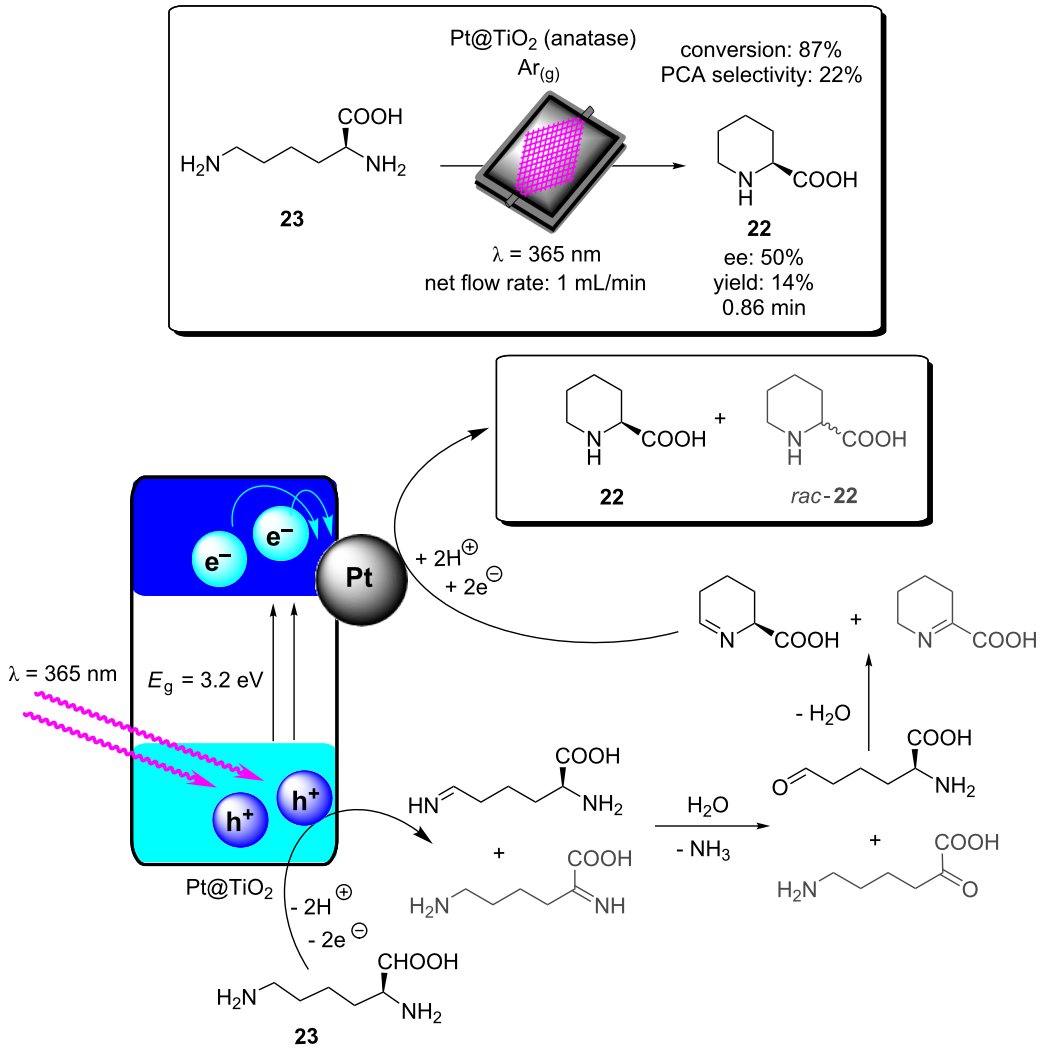

Scheme 9: Proposed mechanism of the Pt@TiO_2 photocatalytic deaminitive cyclisation of L-lysine (**23**) to L-pipecolinic acid (**22**) [240,241].

only 14% yield of **22**. Near-identical results were obtained by the group using commercial Pt@TiO_2(P25) particles in a batch photoreactor after 1 hour, showing that the TMFD flow conversion rate was ≈70 times higher.

Vilela and co-workers reported an efficient continuous flow process for the oxidation of the aryl boronic acid **24** and pinacol esters to the corresponding phenol **25** using different polymer architectures with a common 2,1,3-benzothiadiazole (BTZ) photocatalyst core immobilised as a cross-linker in the polymer backbones. Polystyrene beads (PS-BTZ beads), gels, and a high-internal-phase emulsion-templated polymer monolith (PS-BTZ polyHIPE), all containing the same BTZ core, were synthesised to assess the effects of the morphology on the photocatalytic efficiency (Scheme 10) [47]. Phenylboronic acid (**24**), two equivalents of Hünig's base (DIPEA, **26**) and 5 mol % of the HPCat (with respect to the immobilised BTZ unit) were irradiated at 420 nm under aerobic conditions in continuous flow. The mechanism was proposed to be the same as that previously reported by Xiao and co-workers, who used a homogeneous $[Ru(bpy)_3]Cl_2$ photocatalyst [242]. A single-electron transfer between the HPCat and **26** forms the radical cation **IV** (Scheme 10). The reduced HPCat is oxidatively quenched by O_2, which generates superoxide radicals and returns the HPCat to the ground state. The superoxide radical proceeds to oxidise **24** to the corresponding radical intermediate **V**, followed by a hydrogen atom transfer with **IV** to form the peroxide adduct **VI**. This undergoes a rearrangement to eliminate a hydroxy group and yields the boric acid **27**, which is hydrolysed to yield the final product **25**.

The 5% poly(styrene-*co*-(4,7-distyrene-2,1,3-benzothiadiazole)) copolymer gel achieved a full conversion in a batch reactor within 18–72 hours for a variety of phenylboronic acid deriva-

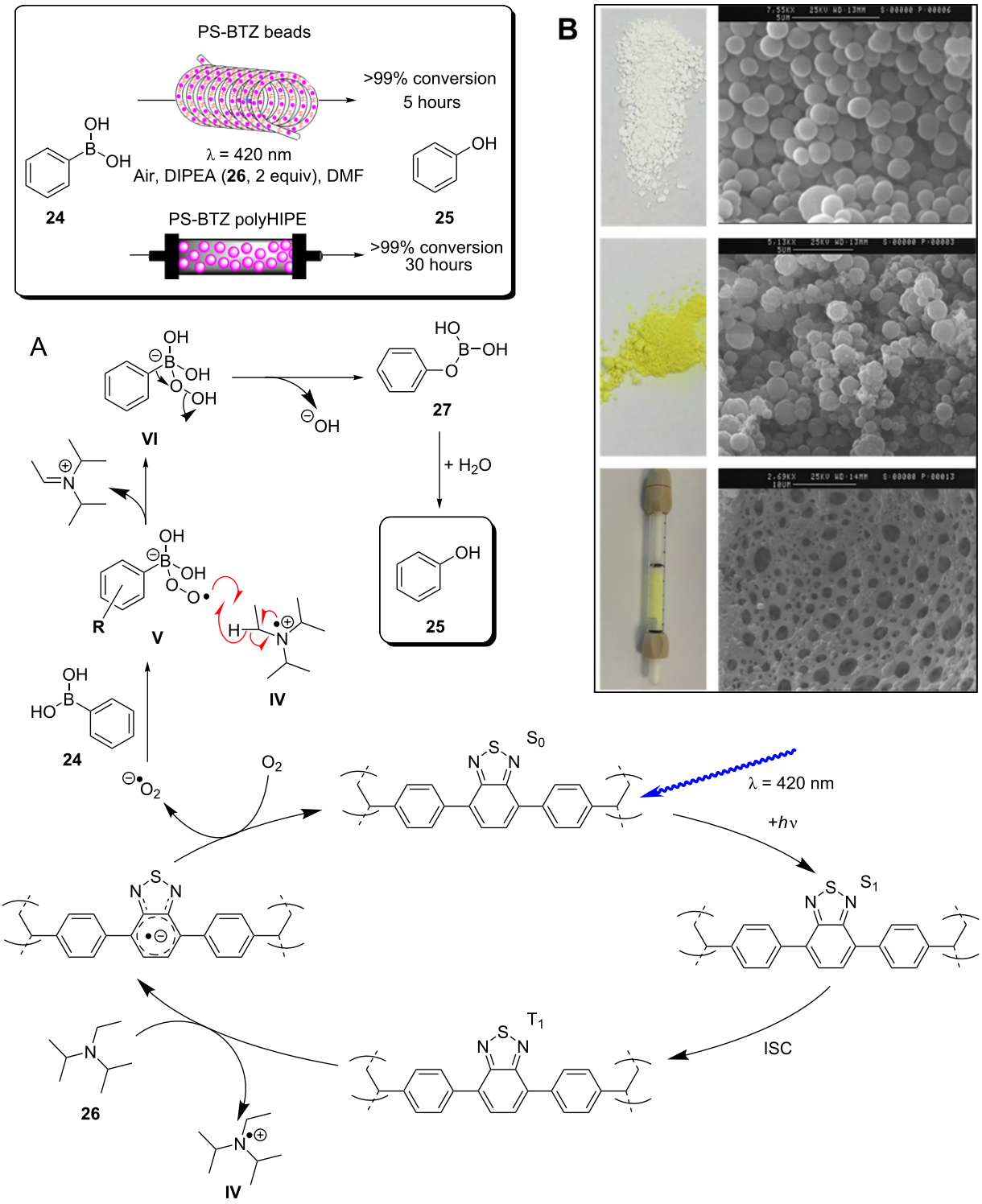

Scheme 10: A) Proposed mechanism for the photocatalytic oxidation of phenylboronic acid (**24**). B) Photos and SEM images of (top) white polystyrene beads with no St-BTZ, (middle) yellow PS-BTZ beads, and (bottom) PS-BTZ polyHIPE monolith (photographed within a fixed bed reactor) [47,242]. Figure 10B was adapted from [47], Copyright 2017 American Chemical Society.

tives, substituted with electron-withdrawing or -donating groups. The PS-BTZ beads were also applied in the batch oxidation of **25** and showed a remarkable rate enhancement, reducing the reaction time to 10 hours. The PS-BTZ beads were then applied in a continuous flow slurry reactor, pumped through a Vapourtec E-series photochemical reactor coil, equipped with a 60 W 420 nm LED module. This further reduced the reaction time by 50%, achieving full conversion to **25** in just 5 hours. The PS-BTZ polyHIPE was applied as a HPCat for the oxidation of **24** under continuous flow conditions using a fixed bed reactor, but required 30 hours of irradiation to achieve a full conversion, less efficient than the 5% gel HPCat batch protocol. The authors found this poor efficiency disappointing, but noted that the material had been exposed to over 80 hours of intense irradiation prior to that reaction, which likely reduced the material's performance.

As well as the significant enhancements of performing heterogeneous photocatalysis in a continuous flow, this work illustrates the importance of the morphological control in the design of photocatalytic materials and its effect on the photocatalysis efficiency. This is a significant advantage of organic polymer materials over metal oxide-based photocatalysts, which are far more restricted with respect to controlling the nanostructure and porosity.

Liu and co-workers recently reported the synthesis of a series of carbazole-derived conjugated microporous polymers (CMPs) as HPCats for the aza-Henry reaction in continuous flow [243]. Biscarbazole monomers linked by either a benzene (DA-CMP1), 4,7-diphenylbenzo[1,2,5]thiadiazole (DA-CMP2), or anthracene-9,10-dione (DA-CMP3), were synthesised and then polymerised by an $FeCl_3$-catalysed oxidative coupling to generate three donor–acceptor-type CMPs (Scheme 11). The CMPs were proposed to oxidise *N*-phenyltetrahydroisoquinoline (**28**) to an amine radical cation intermediate **VII**. Then, superoxide radicals generated by the e^-_{CB} abstract a proton from **VII** to form the radical **VIII**. **VIII** is then further oxidised by molecular oxygen or an h^+_{VB} to generate the iminium cation **IX**. **IX** can then react with a range of nucleophiles, such as nitromethane, to yield the C–H functionalised products in good yields (>70%). DA-CMP3 was found to be the most efficient HPCat for the aza-Henry reactions studied. DA-CMP3 was recycled 10 times without a loss of efficiency or selectivity in the conversion of **28** to **29**. The group applied DA-CMP3 in continuous flow using a fixed bed reactor and syringe pumps to concurrently pump the reaction mixture and oxygen through the catalyst bed, which was externally irradiated by a 460 nm LED module. Full conversion of **28** to the product **29** was obtained, and the reaction time was reduced by 25% through application of the flow reactor.

Kappe and co-workers reported a continuous flow synthesis and application of spherical and rod morphology TiO_2 nanocrystals (TiO_2-NCs) as HPCats. The TiO_2-NCs were applied as HPCats for the reductive cyclisation of *N*,*N*-dimethylaniline (**30**) and methylmaleimide (**31**) to form the fused tricyclic tetrahydroquinoline **32** (Scheme 12) [244]. The morphology of the prepared TiO_2-NCs could be controlled by varying the temperature of the stainless steel reactor coil placed in a GC oven, yielding rod-NCs at 250 °C and spherical-NCs at 300 °C. This was attributed to a transition between a kinetic and thermodynamic growth regime at the lower and higher tempratures, respectivley, facilitated by the extremely efficient heating of the coil flow reactor due to its high surface area. The large-scale production of monodispersed spherical TiO_2-NCs HPCats was investigated and estimated at 57.6 g/day, with only a ca. 5-minute residence time required in the flow reactor. The authors suggested that the smaller spherical TiO_2-NCs (5 ± 1 nm) with their high surface area would be efficient photocatalysts, and demonstrated this by flowing a suspension of the TiO_2-NCs through a transparent PFA coil, irradiated by a UVA torch (≈365 nm) at 0.5 mL/min for 5 hours. As proposed, the spherical TiO_2-NCs achieved a 91% isolated yield of **32**, whilst the rod TiO_2-NCs only produced ≈54% under identical conditions [244]. The authors proposed the mechanism occurred as reported by Bian and co-workers, who used a $[Ru(bpy)_3]^{2+}$ photocatalyst for the same transformation [245]. The mechanism is shown in Scheme 12 and is overall very similar to the aza-Henry reaction mechanism discussed previously (Scheme 11).

Noël and co-workers reported a procedure for the batch and flow heterogeneous photocatalysis synthesis of disulfides, a key functionality that controls the protein folding in nature and is used industrially in vulcanizing reagents [209]. The group utilised a fixed bed reactor packed with glass beads and TiO_2 nanoparticles with 200 μL void space for the combined gas/liquid reactant phases (Scheme 13). The group had previously reported similar transformations using eosin Y as a homogeneous photocatalyst, and the TiO_2 mechanism was proposed to be similar [246]. In the presence of a diamine base (TMEDA), TiO_2 was activated towards visible light absorption and facilitated a proton-coupled electron transfer between the HPCat and the thiol substrates [246]. The resulting thiol radical couples with a thiolate to yield a radical anion, which is subsequently oxidised to form the desired disulfide products **33a**–**e**. The group demonstrated that the system could efficiently perform homothiol as well as the more elusive heterothiol couplings with a remarkable rate enhancement, reducing the reaction time required for high conversion from multiple hours in batch to 5 minutes or less in flow (Scheme 13) [209].

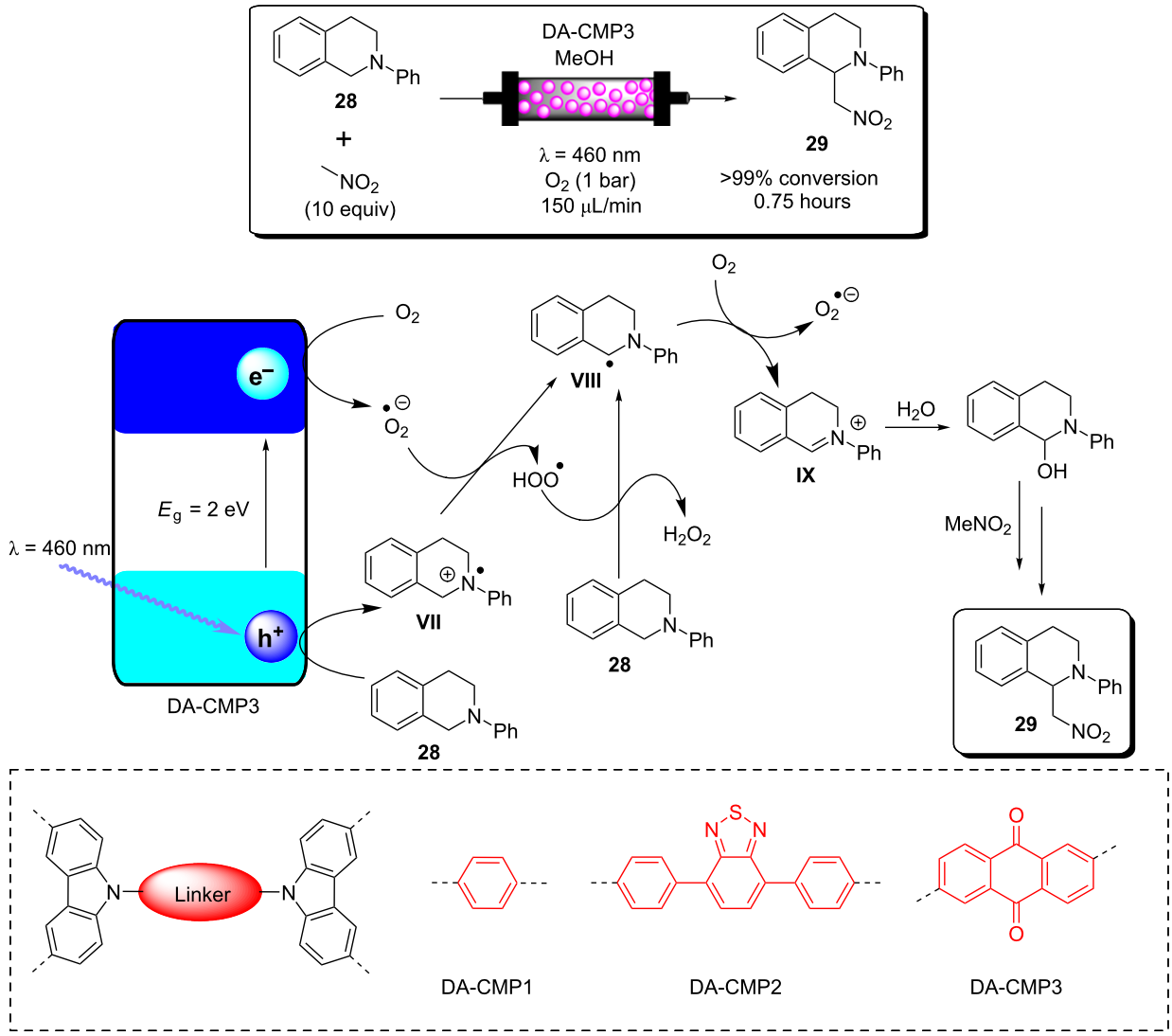

Scheme 11: Proposed mechanism for the DA-CMP3 photocatalytic aza-Henry reaction performed in a continuous flow. The repeating unit structures of the three DA-CMPs are shown in the dashed box [243].

Ciambelli and co-workers showed that a MoO_x/TiO_2 heterogeneous photocatalyst could oxidise cyclohexane (**34**) to benzene with high selectivity under UVA irradiation (Scheme 14) [247]. The gas phase photocatalytic oxidation was performed within an annular fixed bed photoreactor, surrounded by six 40 W UVA lamps, with an additional lamp in the central void space. The reactor was prepacked with quartz flakes, and the MoO_x/TiO_2 was deposited in situ by evaporating an aqueous slurry of the HPCat inside the reactor. The nitrogen gas flow was controlled by an MFC and bubbled through a solution of **34** to achieve a vapour concentration of 1000 ppm. This mixed with a flow of oxygen in N_2 (1500 ppm) and H_2O in N_2 (1600 ppm) before entering the irradiated packed bed reactor. 15% conversion of **34** and 65% selectivity for benzene were achieved with an 8 wt % MoO_x/TiO_2 catalyst (8MoDT) after 5 minutes of irradiation. However, this rapidly declined to a steady state conversion of 2.3% after 15 minutes. Interestingly, when TiO_2 or molybdenum supported on γ-alumina (Al_2O_3) were used as the HPCat independently, the activity was significantly lower, and the selectivity for CO_2 was 100%, showing that the MoO_x/TiO_2 pairing was critical for the formation of the oxidative dehydrogenation products [247].

Rueping and co-workers reported a continuous flow system for the C–H functionalisation of heteroarenes with aryl diazonium salts, utilising a TiO_2-coated microfluidic falling-film microreactor (FFMR, Scheme 15) [248]. The group had previously studied the same reaction in batch and identified an interesting mechanism as the diazonium salt forms an adsorbed azoether species **X** on the TiO_2 surface (Scheme 15), which sensitises the

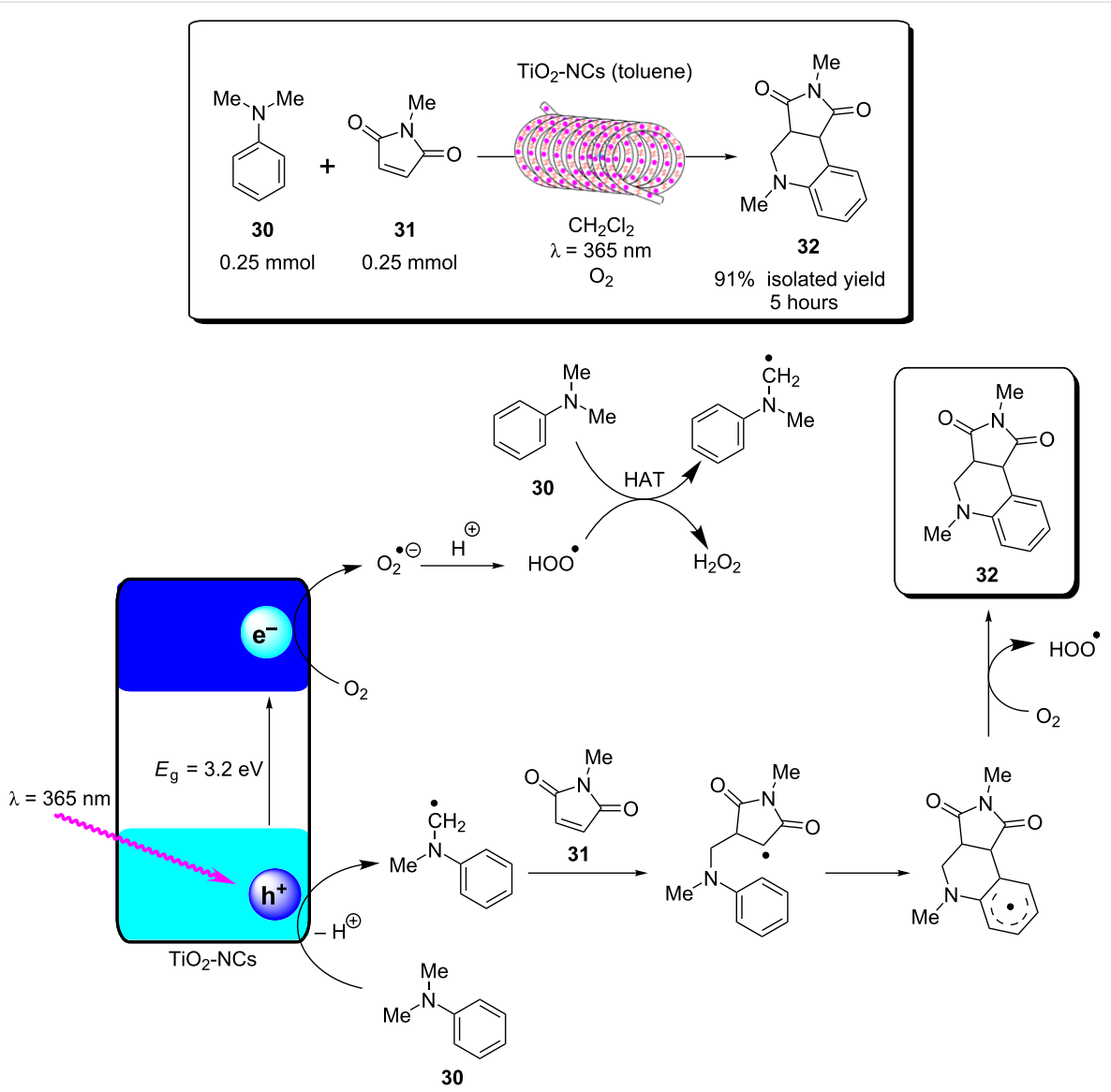

Scheme 12: Proposed mechanism for the formation of the cyclic product **32** by TiO_2-NC HPCats in a slurry flow reactor [244].

TiO_2 to visible light absorption (λ_{max} = 480 nm) [94]. The aryl diazonium tetrafluoroborate salt **35** is in equilibrium with the azoether species **XI**, formed with the ethanol solvent. **XI** is then displaced by TiO2 surface oxides to form the adsorbed species **X**. The chemisorbed **X** lowers the band gap to approximately 2.6 eV, and excitation by 455 nm LEDs leads to a direct single-electron transfer from the valence band to **X**, resulting in an aryl radical **XII** and the loss of N_2. The **XII** radical undergoes an addition with a heteroarene **36** (furan, thiophene, or pyridine) to give the radical **XIII**, which is oxidised by the TiO_2 h^+_{VB} to give the functionalised heteroarene product **37** [94]. The group produced the first example of a falling-film microstructured reactor (FFMR) with TiO_2 coated to the stainless steel microchannels. The reactants were pumped via an HPLC pump to the FFMR at 0.5 mL·min^{-1} where the solution flow meets a countercurrent flow of N_2 gas to facilitate mixing and self-draining [248]. The FFMR showed an impressive 6000-times enhancement in the specific reactor performance over the group's previous batch procedure (batch: 5.4 × 10^{-5} mol·L^{-1}·min^{-1}, flow: 0.32 mol·L^{-1}·min^{-1}) [94,248]. The percentage yield for many of the compounds was also enhanced in the FFMR (see the selected examples **37a–c**, Scheme 15). The FFMR was used in a large-scale continuous operation experiment in which the reactor was irradiated for 180 minutes, and the conversion to the product **37d** was assessed by ^{19}F NMR. The results showed a constant conversion of 77% across the 180-minute run, consistent with the scope evaluation and demonstrating the photostability of the reactor.

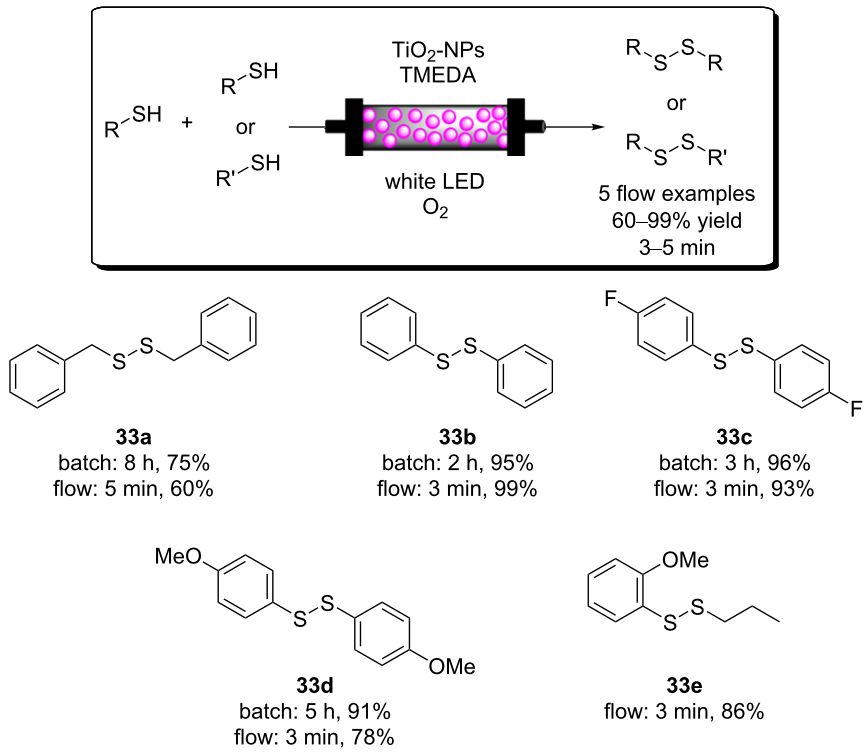

Scheme 13: Reaction scheme for the photocatalytic synthesis of homo and hetero disulfides in flow and scope of the flow disulfide products **33a–e**, with yields and reactions times in batch and flow reactors given [209].

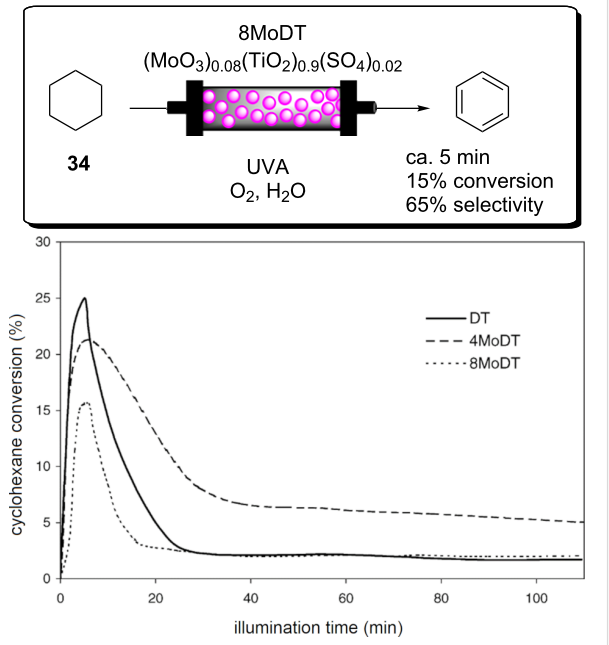

Scheme 14: Reaction scheme for the MoO_x/TiO_2 HPCat oxidation of cyclohexane (**34**) to benzene. The graph shows the cyclohexane conversion over time using DT (anatase TiO_2 with 2 wt % of sulphate), 4MoDT and 8MoDT (4.7 and 8.0 wt % MoO_3 impregnated DT TiO_2, respectively). Reprinted from [247].

Xu, Vilela, and co-workers reported a trifunctional, nanoporous graphene-analogue material for heterogeneous visible light photoredox catalysis, Lewis base organocatalysis, and the removal of lead pollution from water [249]. The material was formed through an efficient metal-free synthesis using hexahydroxytriphenylene (HOTT) and hexachlorohexaazatrinaphthylene (HATN-Cl_6) monomers that form a tritopic conjugated network via six base-catalysed S_NAr substitutions, yielding the desired HOTT-HATN polymer with 89% recovery. The material was found to be extremely efficient at removing lead from aqueous waste, reducing a 10 ppm/50 mL solution of $Pb(NO_3)_2$ to <15–20 ppb in 5 minutes, a level deemed acceptable by many global health organisations [249]. The material also functioned as an efficient organocatalyst for the Knoevenagel condensation of a range of benzaldehyde derivatives with malononitrile, achieving a full conversion in 3 hours on average and no loss in efficiency over 4 cycles. Finally, the group demonstrated the material's efficiency as a HPCat in the aerobic oxidative coupling of the benzylamines **38** in flow (Scheme 16). The material was applied in a suspension reactor, pumped through a transparent coil, concurrently with a flow of O_2 gas, and irradiated by a white or blue LED. The flow system achieved full conversion in approximately 6 hours with various benzaldehyde derivatives to the corresponding benzyl benzaldimines **39a–f**

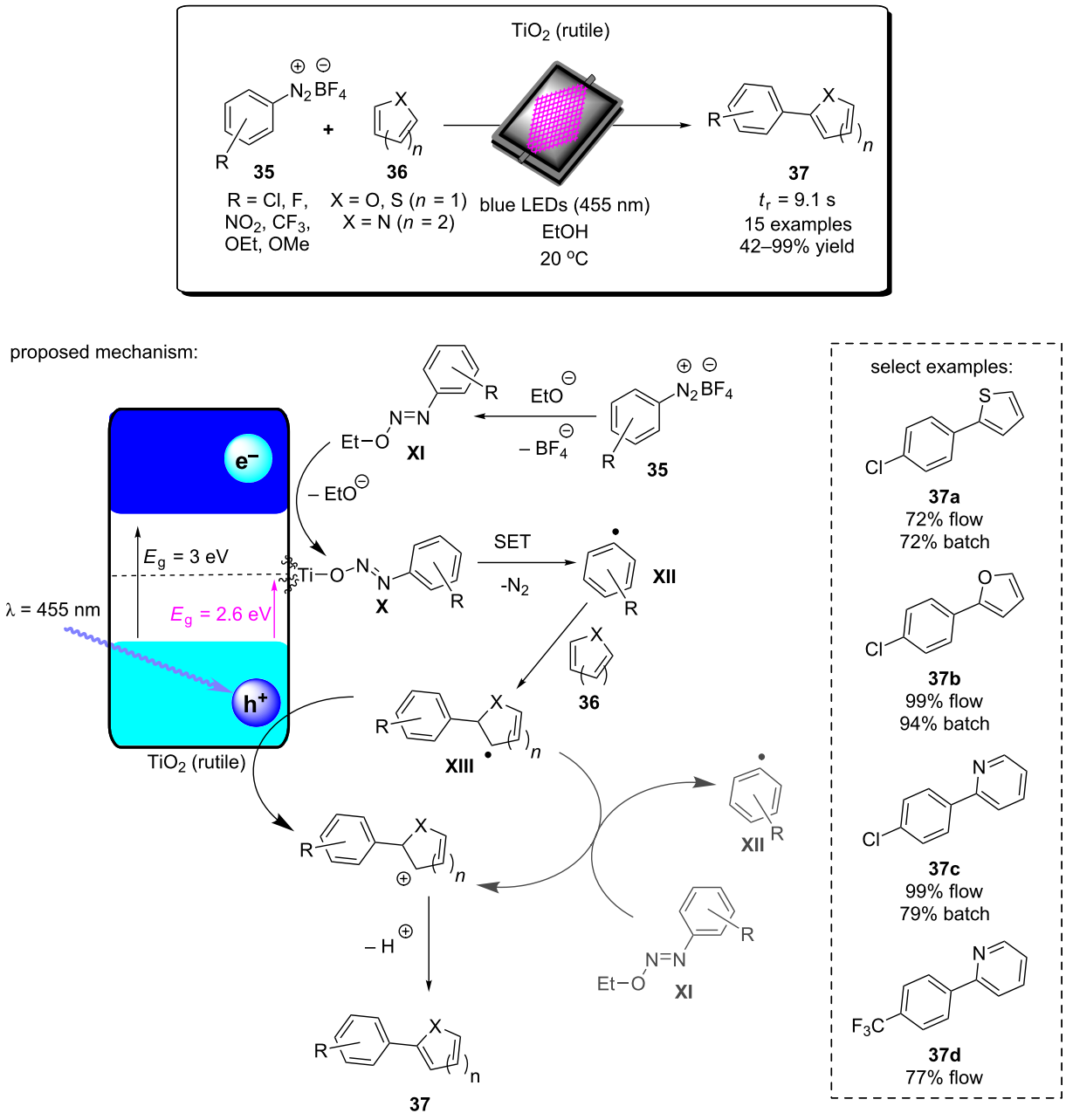

Scheme 15: Proposed mechanism of the TiO_2 HPC heteroarene C–H functionalisation via aryl radicals generated from aryl diazonium salts [94,248]. The select examples **37a**–**c**, prepared by using 4-chlorobenzenediazonium tetrafluoroborate with various heteroarenes, are shown with isolated yields for the flow and the batch reactor. The product **37d** was obtained from the long-term (180 min) continuous operation experiment, with a constant yield of 77%, assessed by ^{19}F NMR spectroscopy using an internal standard.

(Scheme 16). Electron-donating *para*-functional groups generally reduced the reaction time from 6 to 5 hours, and electron-withdrawing substituents conversely increased the reaction time to 7 hours. The reaction can plausibly occur via a photoredox or photosensitised singlet oxygen mediated mechanism. The authors tested the HPCat for the singlet oxygen production using α-terpinene (**44**) as a singlet oxygen trap (discussed in the next section), which proved successful. However, we would argue that this is not conclusive evidence that the mechanism occurs via singlet oxygen and not photoredox, as other reports tend to favour the photoredox mechanism for TiO_2 and transition metal-based photocatalysts [250-253]. Additionally, photoredox and photosensitisation ability are not mutually exclusive, so the positive result for singlet oxygen production does

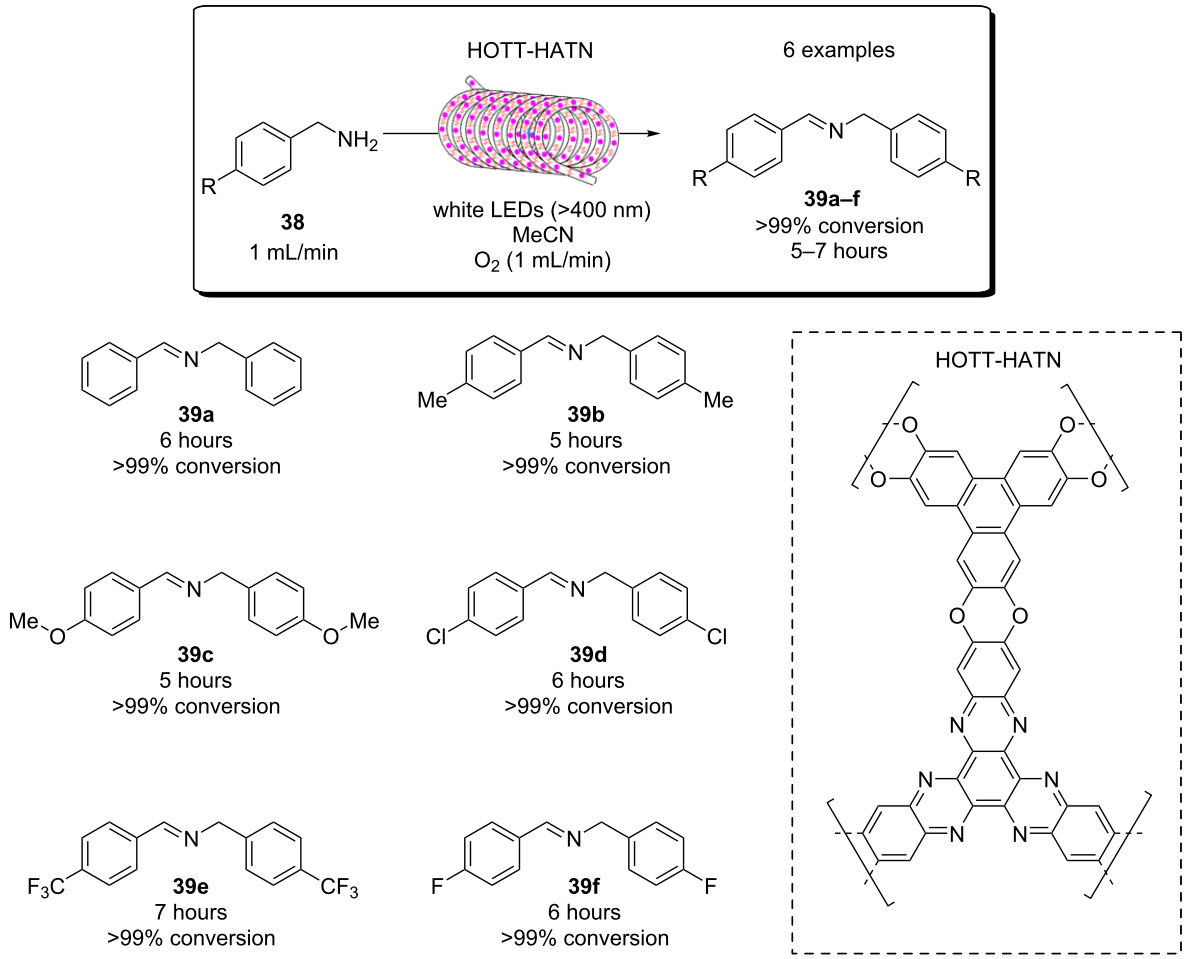

Scheme 16: Scheme of the oxidative coupling of benzylamines with the HOTT-HATN HPCat and selected examples of the benzyl benzaldimine products **39a–f**. The structure of HOTT-HATN is displayed in the dashed box [249].

not eliminate the possibility of a photoredox mechanism in this reaction, or the two pathways could occur in tandem. We suggest more conclusive evidence is required to elucidate the true mechanism.

Colmenares, Nair, and co-workers recently reported the design of a microflow reactor coated with commercial ZnO nanoparticles (ZnO-NPs) as HPCats for the selective oxidation of benzyl alcohol (**40**) to benzaldehyde (**41**, Scheme 17) [254]. The microflow reactor was composed of a transparent fluorinated ethylene propylene (FEP) tubing coil (0.8 mm internal diameter), which had ZnO-NPs deposited in a flow channel surface through an ultrasound deposition treatment method [254]. The ZnO-NP-coated reactor coil was housed in a cylindrical metal casing with an array of UV-LEDs irradiating at 375 nm with a power density of 16.6 $W \cdot m^{-2}$. Solutions of **40** (1 mM) in either acetonitrile or water were pumped through the reactor at 0.053 $mL \cdot min^{-1}$ for a total of 6 hours. The acetonitrile solution in the flow reactor system achieved a peak selectivity of 98% for **41** after 15 minutes of initiating the experiment, and a specific conversion rate of 1.8 $mol \cdot m^{-2} \cdot h^{-1}$. The specific conversion rate of **40** was more than 2 orders of magnitude higher using water as solvent, peaking at 288 $mol \cdot m^{-2} \cdot h^{-1}$. However, the selectivity for **41** was reduced significantly to <15%. For both solvents, the microflow reactor had significantly higher specific conversion rates than the analogous batch photochemical reactions, which only achieved 0.07 $mol \cdot m^{-2} \cdot h^{-1}$ and 0.6 $mol \cdot m^{-2} \cdot h^{-1}$ in acetonitrile and water, respectively. The coated microflow reactor system was recycled over 5 runs to test the stability of the ZnO-NPs deposited in the FEP tubing. They reported a negligible decrease in the specific conversion rate for both solvent systems over 30 hours of testing, although selectivity for **41** decreased over the 5 cycles by approximately 10%. The group suggested that this was due to byproducts and unreacted starting material from previous runs adsorbing to the ZnO-NP surface. The photocatalysis reaction samples were

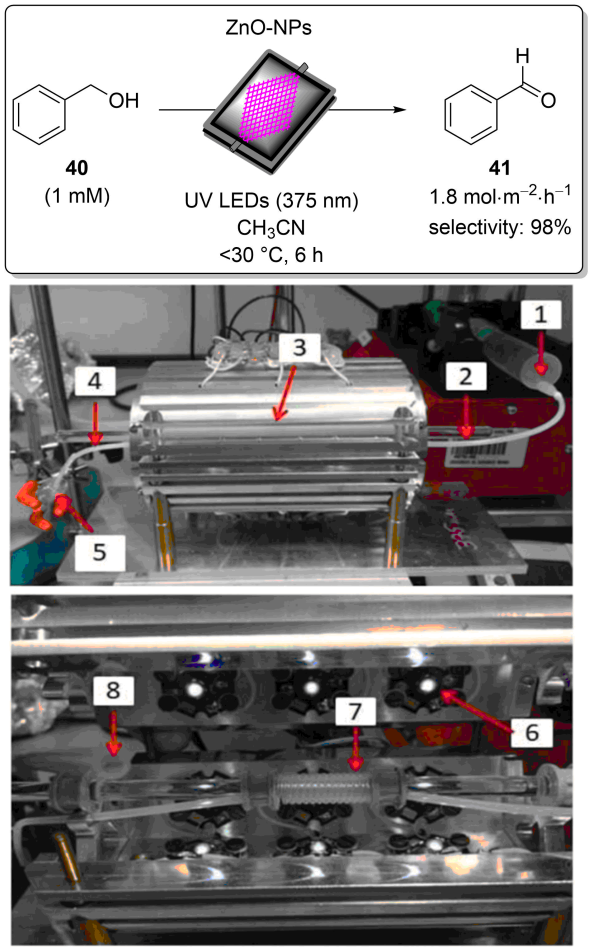

Scheme 17: Photocatalysis oxidation of benzyl alcohol (**40**) to benzaldehyde (**41**) in a microflow reactor coated with ZnO nanoparticles through ultrasonic-assisted deposition. Images of the microflow photoreactor set-up: (1) syringe infusion pump, (2) teflon tube, (3) metal covering containing the LED and the photocatalytic microreactor, (4) teflon tube, (5) sample collector, (6) UV LED, (7) ZnO-US-FEP microtube, and (8) air cooling tube. Reprinted with permission from [254], Copyright 2019 The Royal Society of Chemistry.

analysed by energy-dispersive X-ray fluorescence (EDXRF) spectroscopy, which found no traces of Zn^{2+} ions in the solutions. This, in combination with the recycling experiments led the group to conclude that the ultrasonic deposition was an effective and stable method for the deposition of HPCat nanoparticles [254].

Earlier this year, Colmenares, Pradhan, and co-workers subsequently published a similar report utilising commercial TiO_2(P25) and their own sol–gel-synthesised TiO_2 nanoparticles (TiO_2-SG) as HPCats for the oxidation of **40** to **41** [255]. The TiO_2 materials were immobilised by the ultrasonic deposition on the surface of perfluoroalkoxy alkane (PFA) tubing using the same method developed for the ZnO-NPs under theoretically optimised conditions obtained from Design Experiment software [255]. Coated microflow reactors were produced both with and without an ultrasound treatment for comparison, and they reported that the ultrasound-assisted deposition reactors had approximately 50% higher quantities of immobilised TiO_2. The TiO_2(P25) and TiO_2-SG nanoparticles were first tested and compared for the oxidation of **40** in a batch photoreactor for 60 minutes. TiO_2(P25) displayed much higher conversion rate relative to TiO_2-SG, which became inactive within the first 20 minutes. However, the selectivity of TiO_2-SG for **41** was >80% for the duration of the experiment, significantly higher than TiO_2(P25), which displayed a steady state selectivity of approximately 28%. Interestingly, when immobilised in microflow reactors, the HPCat efficiencies were reversed with TiO_2-SG achieving approximately double the conversion of TiO_2(P25). The selectivity of TiO_2-SG remained consistent with the batch reactor, however, the selectivity of immobilised TiO_2(P25) was dramatically enhanced to >75%. However, both microflow reactors displayed a fixed conversion across the 60 minutes of the reaction, which was achieved within the first 10 minutes. Overall, the TiO_2-SG microtube flow reactor achieved the highest yields of **41** with a 6 μmol·m^{-2}·min^{-1} specific conversion rate and 87% selectivity. This was an inferior result to their previously published ZnO-NPs system. However, the study showed the versatility of the ultrasonic-assisted deposition methodology and provides an interesting example of selectivity enhancement through flow chemistry [255].

4.2 Heterogeneous energy transfer catalysis in flow

Photosensitisation, or energy transfer catalysis, is a process by which the photon energy absorbed by a HPCat is transferred to a substrate through electronic transitions and without changing the redox states of either species. This can occur via two main mechanisms; Dexter and Förster energy transfer (Figure 17). Dexter energy transfer is a simultaneous transfer of two electrons between an excited photocatalyst and a ground state acceptor. The photocatalyst-excited electron transfers to the LUMO of the ground state acceptor, whilst an acceptor HOMO

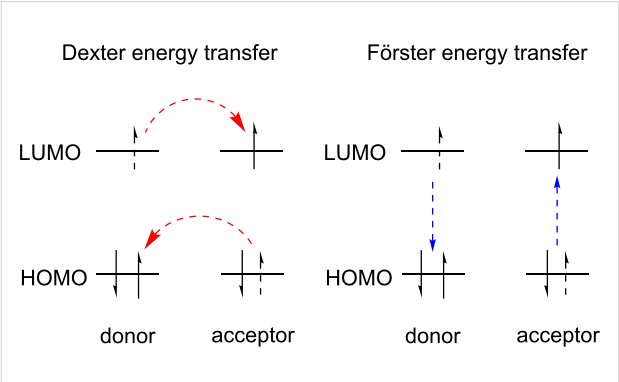

Figure 17: Mechanisms of Dexter and Forster energy transfer.

electron simultaneously transfers to the photocatalyst HOMO vacancy. This produces no net change in the redox states but causes the substrate to enter an electronic excites state and returns the HPCat to its ground state, effectively transferring energy between the two species. The Dexter mechanism is restricted to short distances as the donor and acceptor must have an orbital overlap for this to occur [256].

Förster resonance energy transfer (FRET) involves no intermolecular electron exchange and occurs over very large separations of 30 to 100 nm [256,257]. In this process, an excited state energy donor and a ground state acceptor transfer energy through resonance of their electronic emission and absorption frequencies and is largely dictated by Frank–Condon parameters (Figure 17) [256]. FRET is therefore limited by the requirement that the energy donor's emission spectrum has an overlap with the energy acceptor's absorption spectrum.

Once an acceptor has been photosensitised to an electronic excited state, changes in the molecular polarisation, bond strengths, or spin multiplicity enables unique chemical reactivity and has been utilised for pericyclic reactions, isomerisations, and atom abstraction reactions [258]. Photosensitisation was the basis of most photochemical organic syntheses prior to the advent of photoredox catalysis [259]. A very detailed tutorial review on energy transfer photocatalysis by Glorius and co-workers is recommended for further reading [258].

An interesting example of heterogeneous energy transfer photocatalysis was reported by Rueping and co-workers in which an iridium complex photocatalyst was immobilised in an ionic liquid phase that was immiscible with the organic substrate phase. The system was applied in flow for the isomerisation of various *trans*-aromatic alkenes to the corresponding *cis*-alkene (Scheme 18) [260]. The novelty of this study was that the molecular photocatalyst was immobilised in an ionic liquid acting as a liquid-phase HPCat due to its immiscibility with the reaction-substrate organic phase. As the biphasic flow system has a large interfacial surface area relative to a batch reaction, the heterogeneous energy transfer across the interface was efficient, and the isomerisation occurred in almost quantitative yield and >99:1 *Z*:*E* ratio for most of the *trans*-alkenes studied. *E*-stilbene (**42**) is triplet-sensitised by the $[Ir(ppy)_2(bpy)]PF_6$ photocatalyst, as shown in Scheme 18. The triplet state of the stilbene **XIV** is a diradical and has a lower bond order, permitting the free rotation of the alkene bond before relaxing back to the singlet state in either the *E*- or *Z*-isomeric form. The group proposed that the high efficiency of the reaction was due to the differing triplet state energies (E_{T*}) of *E*- and *Z*-stilbene (**42** and **43**), which permits the triplet sensitisation of *E*-stilbene (**42**, E_{T*} = 2.2 eV) by the $[Ir(ppy)_2(bpy)](PF_6)$ photocatalyst (E_{T*} = 2.1 eV) as the triplet state energies are similar. However, the *Z*-stilbene (**43**, E_{T*} = 2.5 eV) triplet state energy is too high for an energy transfer to occur and makes the isomerisation irreversible, leading to high yields and selectivity of the desired *Z*-isomer. The differing density of the two phases provided an automatic separation of the catalyst and product in the collection vessel, permitting a continuous recycling loop of the photocatalyst ionic liquid phase [260].

Singlet oxygen is a reactive oxygen species formed by a photosensitised electronic transition in which the unpaired π-electrons of triplet ground state molecular oxygen ($^3\Sigma_g^-$) are paired with the inversion of one electron's angular momentum to yield a singlet excited state ($^1\Delta_g$). There is a low energy barrier of 94 kJ/mol to achieve the transition, but the direct transition is forbidden by quantum mechanical spin selection rules, and hence requires triplet photosensitisation to occur [261]. Singlet oxygen is a unique reactant for the oxidation of organic compounds and has been frequently applied in the total synthesis of natural products and pharmaceutical agents [262,263], including the Nobel Prize-winning antimalarial drug artemisinin (**49**) [132,264]. A photosensitised singlet oxygen Alder-ene [4 + 2] cycloaddition was a key step in the total synthesis of canataxpropellane (Scheme 19), reported recently by Gaich and co-workers, described as one of the most complex natural products ever isolated [265,266].

Vilela and co-workers reported a continuous flow process to generate photosensitised singlet oxygen for the oxidation of α-terpinene (**44**) to ascaridole (**45**) using a conjugated microporous polymer (CMP) templated with silica nanoparticles (SiO_2NPs) as a porogen (Scheme 20) [267]. The CMP was synthesised via a Sonogashira palladium-catalysed cross-coupling of 4,7-dibromobenzo[*c*]-2,1,5-thiadiazole and 1,4-diethynylbenzene using various concentrations of SiO_2NPs (6.25, 12.5, 25, 55 and 60 mg·mL^{-1}) as a templating agent to control the porosity and surface area of the resulting CMP_X (X = SiO_2NPs mg·mL^{-1}). The SiO_2NPs could be chemically removed from the polymer matrix through treatment with aqueous NH_4HF_2, without damaging the polymer material. The surface area and total pore volume of the native, non-templated CMP_0 could be more than doubled using a SiO_2NPs concentration of 60 mg·mL^{-1}. The polymers were suspended in a 0.1 M solution of **44** in $CDCl_3$ and irradiated with 420 nm photons in a slurry flow reactor, comprised of a syringe pump and FEP tubing within an enclosed reactor lined with tin foil. The templating strategy had a significant influence on the photosensitisation efficiency, increasing the conversion of **44** from 26% with CMP_0 to 96% with CMP_60 in a single pass of the reactor. Interestingly the increase in SiO_2NP concentration from

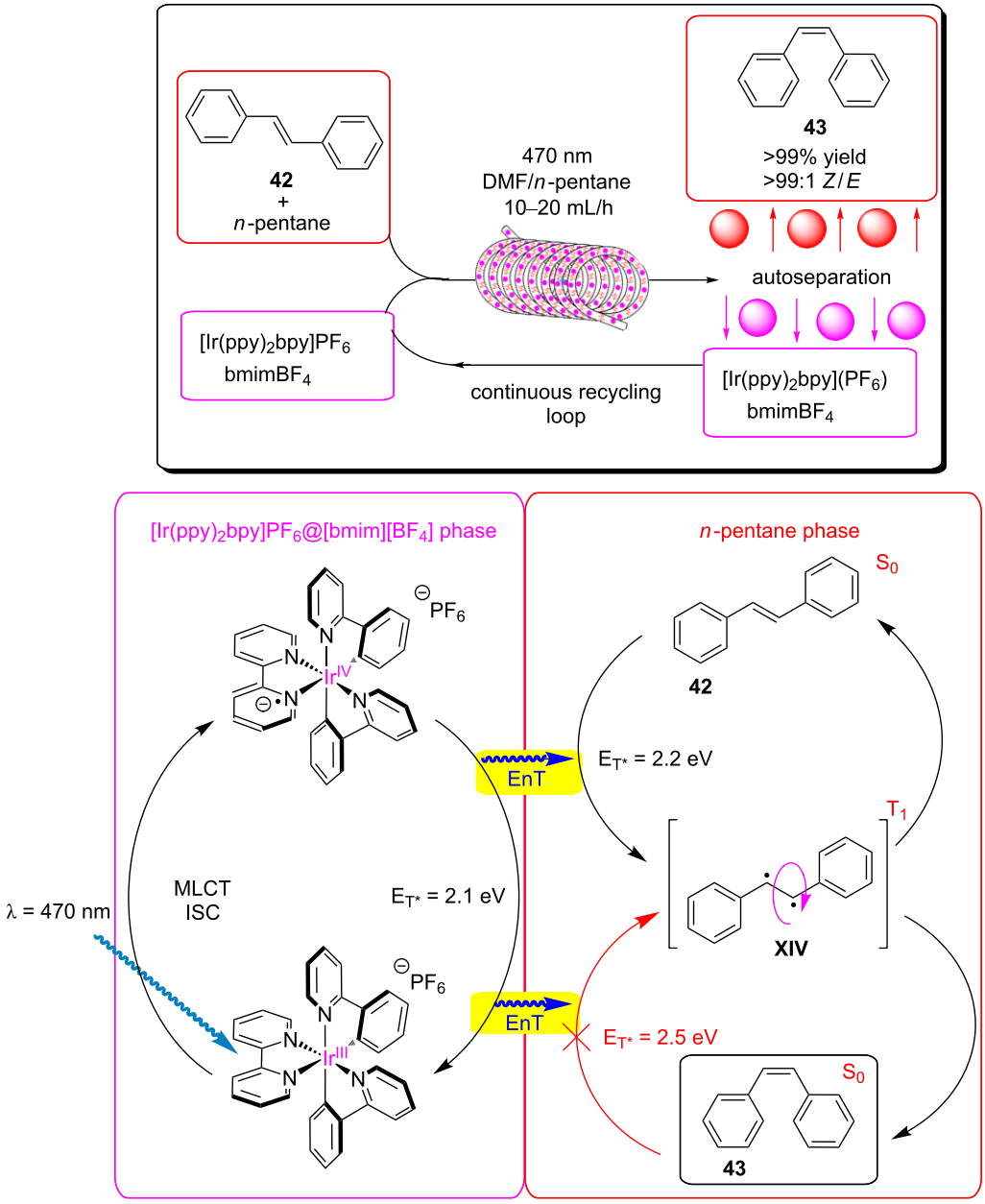

Scheme 18: Continuous flow process for the isomerisation of alkenes with an ionic liquid-immobilised photocatalyst [260].

0–60 mg·mL^{-1} led to an exponential increase in the surface area and a linear increase in the pore volume. However, the photosensitisation enhancement was non-linear. CMP_6.25 raised the conversion from 26% to 81%, but concentrations of 12.5, 25, and 55 mg·mL^{-1} had little effect and provided conversions slightly lower than what CMP_6.25 achieved. The authors postulated the possible influence of the dispersibility and effective surface area on the efficiency. The CMPs generate singlet oxygen through triplet–triplet annihilation energy transfer, involving a CMP triplet exciton and triplet ground state molecular oxygen transfer energy, returning the CMP to its ground state and producing singlet oxygen. Singlet oxygen then undergoes a concerted but asynchronous Alder-ene [4 + 2] cycloaddition with **44** to yield the endoperoxide product **45** [268].

Following this, Vilela and co-workers have reported a number of different CMP materials for the photosensitisation of singlet oxygen in continuous flow, including BODIPY CMPs (BDP_CMP, PHTT_BDP) [131] and a water-dispersible polyamide-based BTZ CMP (PA_ABT, Scheme 21) [269]. All of these were applied for the photosensitisation of singlet oxygen and the subsequent oxidation of **44** to **45** using a slurry

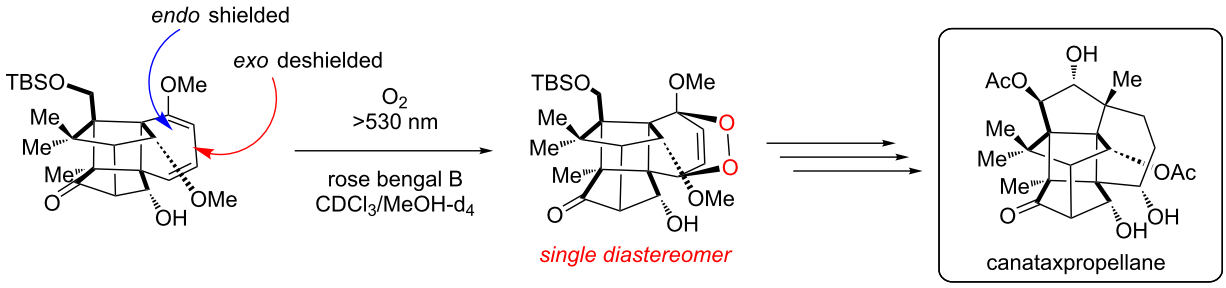

Scheme 19: Singlet oxygen synthetic step in the total synthesis of canataxpropellane [265].

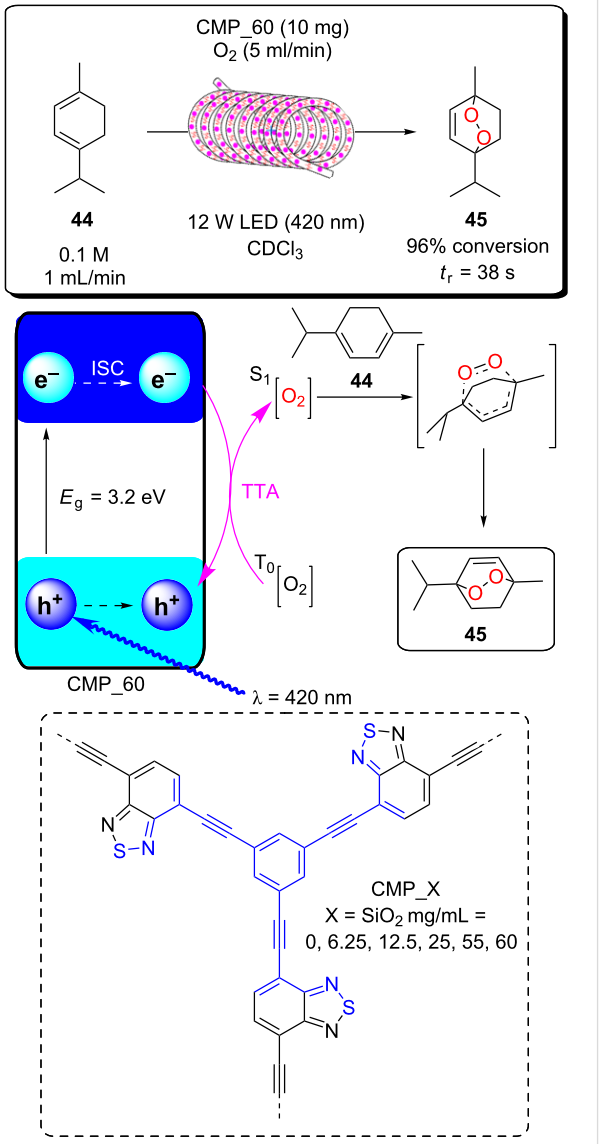

Scheme 20: Scheme and proposed mechanism of the singlet oxygen photosensitisation by CMP_X HPCats, with the structure of CMP_X CPP displayed in the inset. The section of the polymer structure in blue represents one repeating unit. ISC = intersystem crossing [267].

reactor system and a commercial flow reactor (Vapourtec Ltd. E-Series Photochem) equipped with a reactor coil, irradiated by a 60 W LED module of various monochromatic wavelengths.

Poliakoff, George, and co-workers have pioneered the use of supercritical CO_2 ($scCO_2$) as a reaction medium for photosensitised singlet oxygen production in flow, including using immobilised molecular photosensitisers (Scheme 22) [132,270-272]. Oxygen is completely miscible with $scCO_2$, which eliminates the mass transport limitations of oxygen to the photosensitiser but does require specialised equipment and operation at high pressure (10–18 MPa) [272]. They first reported a series of porphyrin, xanthene, and $[Ru(bpy)_3]^{2+}$ photosensitisers immobilised to polymer resins, polyvinyl chloride films, and SiO_2 aerogels as support materials [271]. Many of the materials produced were efficient singlet oxygen photosensitisers in the $scCO_2$ flow system, driving the oxidation of **44** and citronellol (**46**, Scheme 22) but suffered from rapid photobleaching or leaching of the immobilised photosensitiser. They identified a 5-(4-carboxyphenyl)-10,15,20-tris(2,6-dichlorophenyl)porphyrin (TDCPP-COOH) photosensitiser covalently immobilised to aminopoly(vinyl chloride) resins via an amide bond as the optimal HPCat for the system, maintaining high space–time yields (≈80–100 $mmol \cdot L^{-1} \cdot min^{-1}$) for both reactions over 320 minutes of continuous operation. The HPCat was immobilised in a transparent, fixed bed sapphire tube reactor for high-pressure operation (18 MPa) and irradiated by two arrays containing four 1000 lumen white LEDs mounted on aluminium heat sinks. The conversion of **44** was monitored by on-line GLC analysis, but the conversion of **46** to the hydroperoxides **47** and **48** was monitored manually by ^1H NMR spectroscopy due to the thermal instability of the products. The oxidation of **46** occurs by a Schenk-ene group transfer pericyclic reaction (Scheme 22). The mechanism is proposed to occur stepwise, first forming the exciplex **XV**, which leads to the perepoxide intermediate **XVI**. The **XVI** species then undergoes the ene pericyclic rearrangement by abstracting a proton to yield the hydroperoxide products **47** and **48**. The true depth of study re-

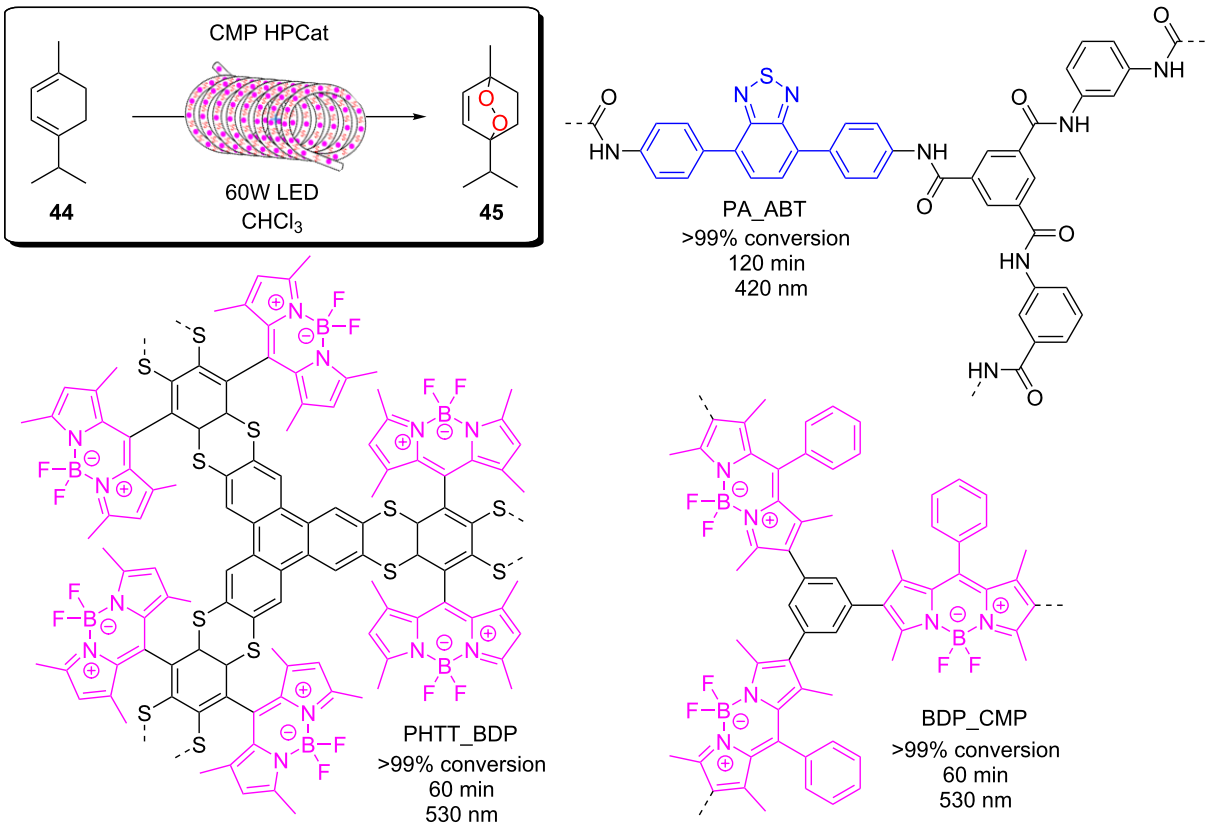

Scheme 21: Structures of CMP HPCat materials applied by Vilela and co-workers for the singlet oxygen photosensitisation in continuous flow [131,269].

quired for the early elucidation of this mechanism is surprising, and was reviewed in detail by Clennan [273].

The same group later reported a bifunctional heterogeneous photosensitiser and Brønsted acid catalyst for the continuous flow synthesis of artemisinin (**49**, Scheme 23) [132]. They had intended to use an amberlyst-15 ion exchange resin (sulfonated cross-linked-polystyrene resins) as a heterogeneous Brønsted acid catalyst within the same sapphire tube reactor described above, and a homogeneous tetraphenylporphyrin (TPP) photosensitiser within the $scCO_2$ phase to perform the final steps of the artemisinin (**49**) semisynthesis, simultaneously within the same reactor [274]. The authors were surprised to find that the TPP had become immobilised to the resins, indicated by a colour change from the grey resins to dark green. They reported that the TPP photosensitiser had been protonation by the amberlyst-15 resins, resulting in a strong electrostatic immobilisation and formation of the bifunctional TPP-Amb heterogeneous catalyst. TPP-Amb could efficiently generate singlet oxygen for the Schenk-ene oxidation of dihydroartemisinic acid (**50**) to the hydroperoxides **51** and **52**. The TPP-Amb then utilises its Brønsted acid catalyst ability to drive the Hock cleavage of **51** to form the intermediate **53**. This undergoes an autooxidation by molecular oxygen and a subsequent cyclisation cascade to form **49**, which is obtained directly from the flow reactor outlet in 50% yield (Scheme 23) [132].

In a similar strategy to that reported by Rueping and co-workers discussed at the beginning of this section [260], Bourne, George, and co-workers had previously reported singlet oxygen photosensitisation in a $scCO_2$ flow reactor system, using what we will describe as a "pseudo-HPCat" [272]. The group produced a highly fluorophilic porphyrin photosensitiser derived from 5,10,15,20-tetrakis(pentafluorophenyl)porphyrin (TPFPP) with perfluoroalkyl chains (F8) to enhance the solubility in $scCO_2$ and a HFE-7500 fluorous solvent (Scheme 24). The organic substrate was pumped neat to a three-way mixer where it met a flow of $scCO_2/O_2$ (6%) and a flow of the F8/HFE fluorous phase (Scheme 24). In the presence of $scCO_2$ at 18 MPa, the three phases became a miscible single phase, which passed through the irradiated sapphire tube reactor before being depressurised and collecting the liquid outflow. As the mixture is depressurised, excess CO_2 and oxygen returns to a gaseous phase and is vented into the atmosphere. The remaining prod-

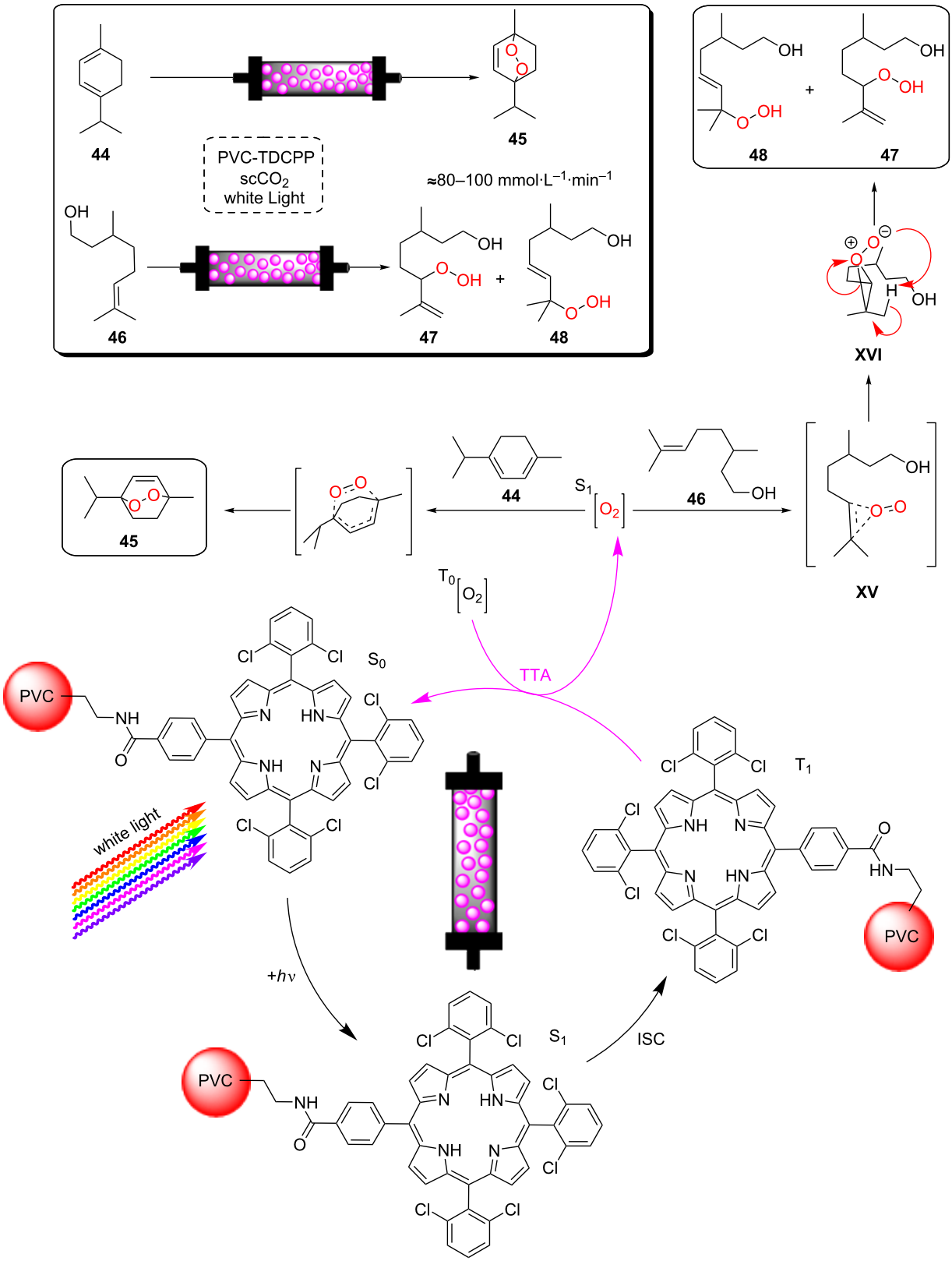

Scheme 22: Polyvinylchloride resin-supported TDCPP photosensitisers applied for singlet oxygen photosensitisation in $scCO_2$. The mechanism of the photosensitisation of singlet oxygen and the subsequent oxidation of citronellol (**46**) and α-terpinene (**44**) [271].

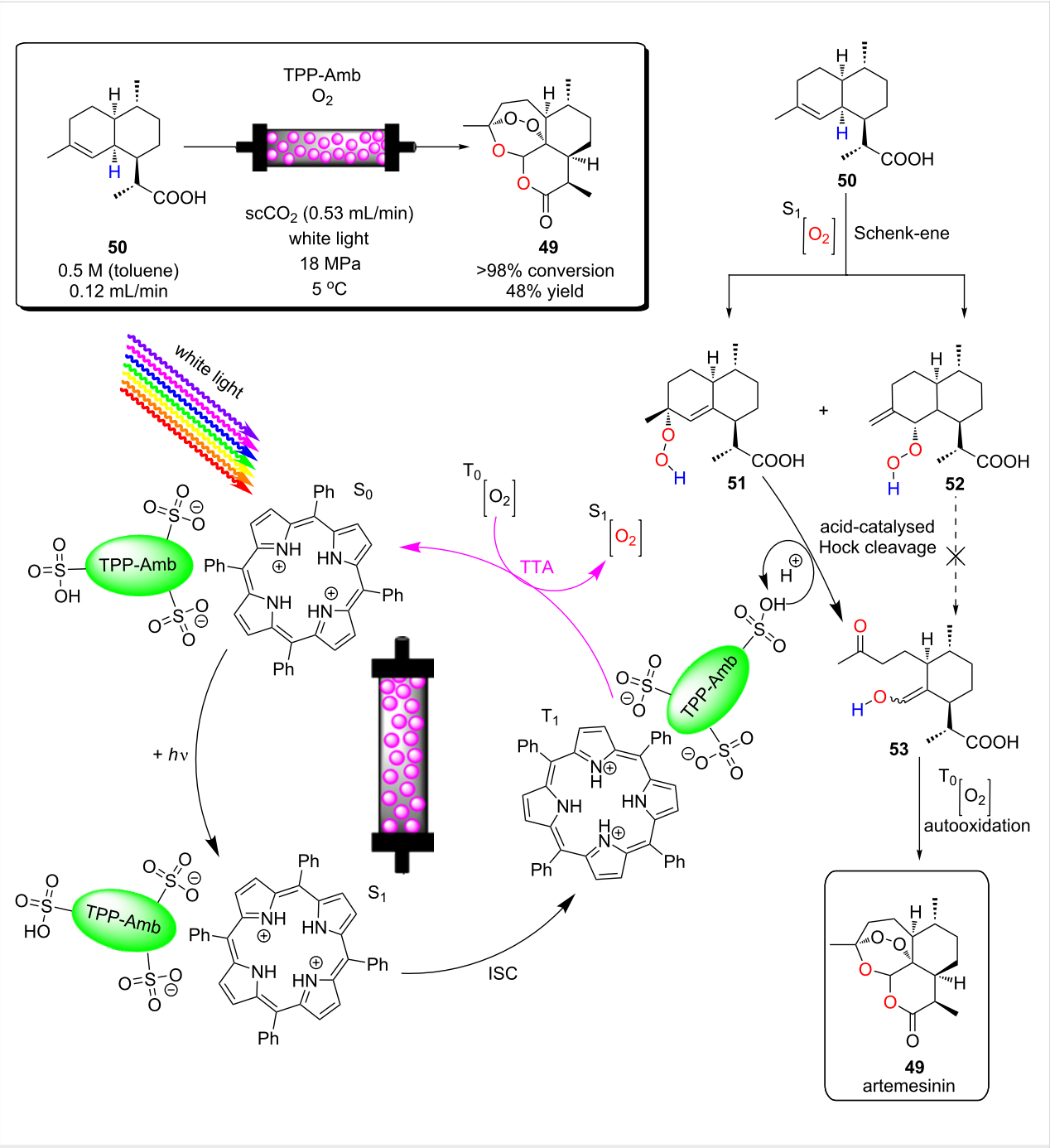

Scheme 23: Structure of the ionically immobilised TPP photosensitiser on amberlyst-15 ion exchange resins (TPP-Amb) and proposed mechanim of the tandem singlet oxygen photosensitisation and Brønsted acid catalysis in the flow synthesis of artemesinin (**49**). Note that the acid-catalysed Hock cleavage step is independent from the TPP electronic state, as this could be misinterpreted from the mechanism shown [132].

uct and fluorous phases become immiscible and separate, aided by an ultrasonic bath and some MeOH additive to reduce the viscosity of the organic products. This allowed the F8@HFE to be continuously recycled by pumping the fluorous phase directly from the base of the collection vessel, achieving a homogeneous reaction system free of mass transport limitations whilst retaining the separation benefits associated with a HPCat [272]. They found the turnover number of this system in a single pass was 27 times greater than their previous report using a TPFPP photocatalyst with dimethyl carbonate as a solubilising additive [270]. 12 mL of the F8@HFE fluorous phase could be recycled ten times to produce 240 mL of the product before photocatalyst leaching to the organic phase became problematic and reduced efficiency. The volatility of HFE-7500 led

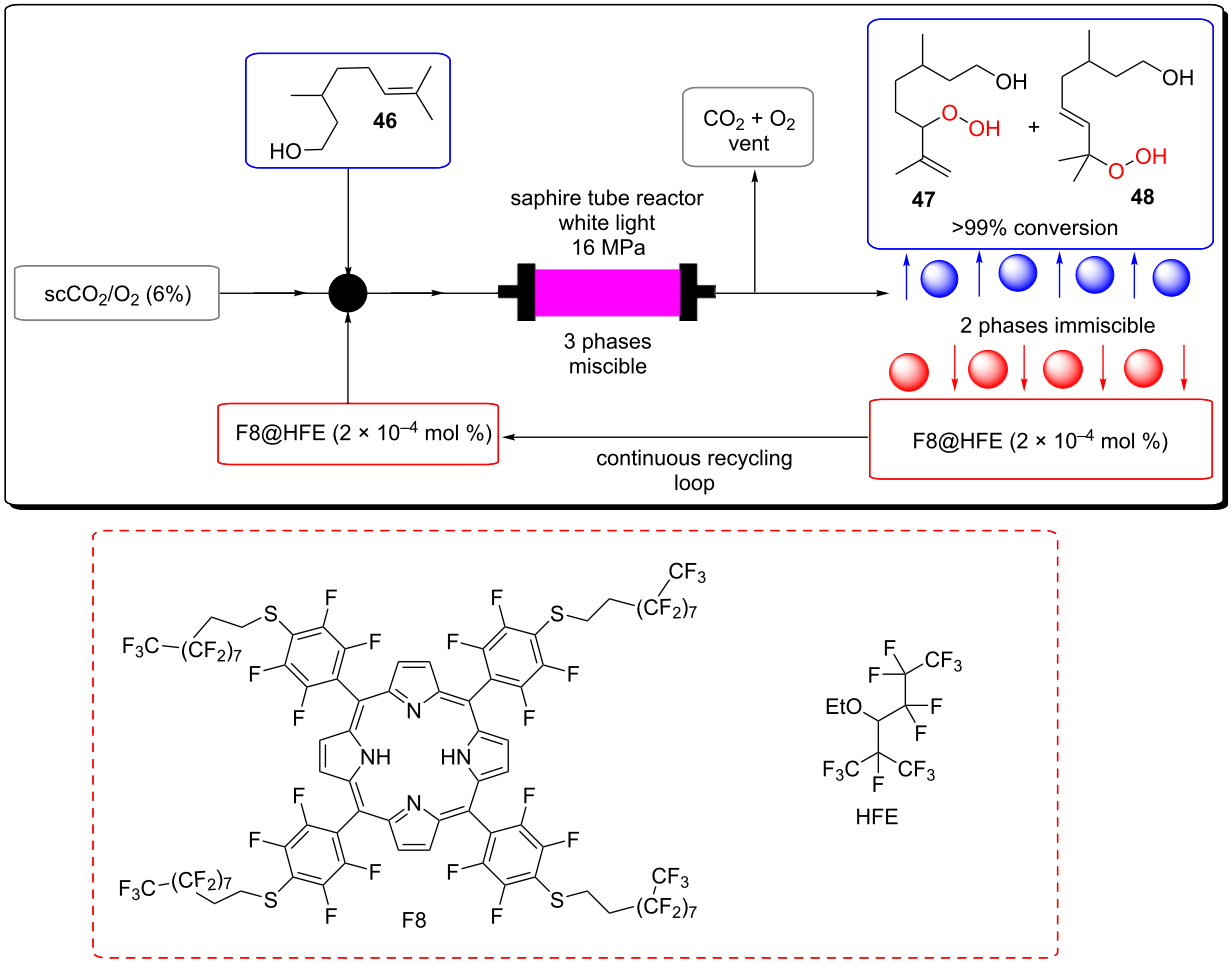

Scheme 24: Photosensitised singlet oxygen oxidation of citronellol (**46**) in $scCO_2$, with automatic phase separation of the fluorous solvent and photosensitiser for a continuous operation [272].

to only 55% recovery per cycle, and HFE had to be continuously replenished during the recycling process to account for this. However, the authors suggested that a more sophisticated depressurising set-up could have prevented this issue.

As mentioned in Section 2.3, our group recently reported a polymer-supported BODIPY photosensitiser, synthesised and applied in continuous flow for the generation of photosensitised singlet oxygen [63]. The BODIPY was immobilised through a non-conjugated position of the molecule so that the photophysical properties would be comparable to the homogeneous analogues of the immobilised species. Interestingly, we found that despite being non-conjugated to the chromophore, the linker strategy enhanced the photosensitisation ability of the molecule by reducing a photoinduced electron transfer (PET) between the BODIPY core and the meso-substituted linker. Chlorinated BODIPY derivatives were serendipitously isolated from an unexpected side reaction and provided an even greater reduction in PET and a suspected enhancement in the triplet state quantum yield due to the chlorines providing a mild heavy atom effect. The oxidation of α-terpinene (**44**) was used as a model reaction to assess the photosensitisation efficiency of the material. An in-line ^{1}H NMR benchtop spectrometer was employed to optimise the pressure and flow rate through the irradiated fixed bed reactor containing the HPCat (Scheme 25). It was found that an optimal pressure of 5.5 bar made the biphasic flow of air and the liquid reagents in $CHCl_3$ miscible, which greatly enhanced the reactivity by increasing the concentration of dissolved O_2 and improving mass transport. The polystyrene-supported, ester-linked BODIPY (PS-Est-BDP) material was irradiated for 24 hours while continuously cycling the reaction mixture through the fixed bed. The same material was recycled four times without loss of photosensitisation ability, albeit with low yields. The material was postsynthetically modified in flow

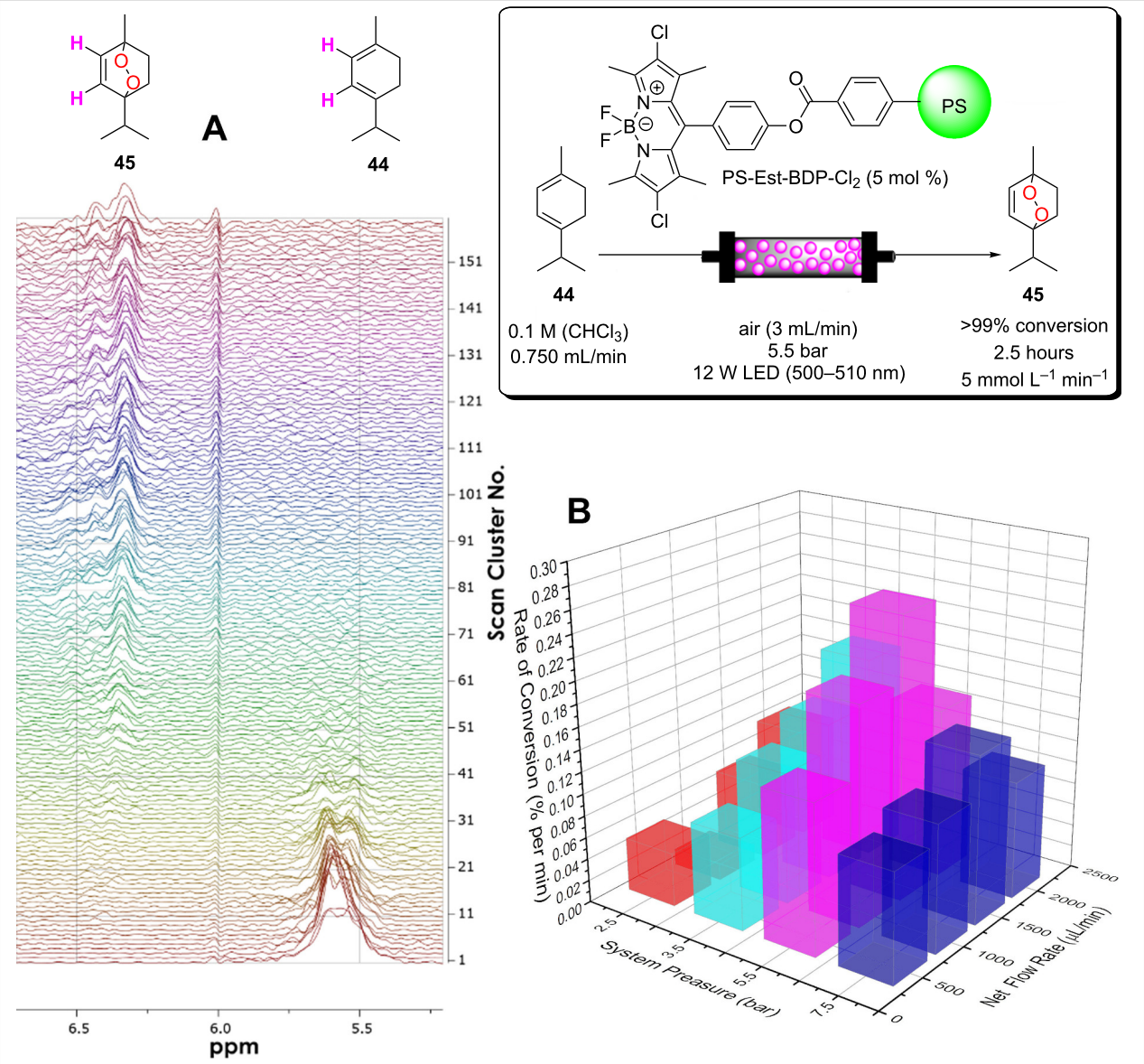

Scheme 25: Schematic of PS-Est-BDP-Cl_2 being applied for singlet oxygen photosensitisation in flow. A) Pseudo-2D ^{1}H NMR trace from the in-line monitoring of the **44** and **45** alkene proton signals during the reaction. B) Graph of the conversion per minute at varied pressure and flow rate during the process optimisation. Adapted from [63], published by Springer Nature under a Creative Commons Attribution 4.0 International License http://creativecommons.org/licenses/by/4.0/.

for a second time in an attempt to increase the photosensitisation efficiency. *N*-chlorosuccinimide in hexafluoroisopropanol solvent was pumped through the immobilised PS-Est-BDP material to chlorinate the chromophore and form PS-Est-BDP-Cl_2 (Scheme 25), the immobilised equivalent of the optimal homogeneous photosensitser. This, in combination with the optimised conditions established by the in-line ^{1}H NMR, resulted in a 24-fold enhancement in efficiency compared to the initial material and conditions and produced a HPCat flow reactor system that was more efficient than the equivalent homogeneous batch reaction (>99% conversion, 2.5 hours in flow, 3 hours in batch). The chlorinated PS-Est-BDP-Cl_2 resin's efficiency rapidly declined to ≈65% after 5 cycles (12.5 hours), implicating a higher singlet oxygen photosensitisation efficiency with a faster deactivation or cleavage of the photocatalyst from the resin.

3D-printed reaction vessels that incorporate an active catalyst within the surface of the vessel have been pioneered by the group of Cronin to produce the bespoke reaction vessels for organic synthesis [275-277]. This provides an interesting approach for the fabrication of flow reactors with a complete freedom of design and the potential to print intricate static mixing architectures and flow channels in all three dimensions. 3D printing flow reactors embedded with a photocatalyst

is a source of challenge and opportunity, as printing a photocatalytic monomer via stereolithographic 3D printing (light-initiated polymerisation) has some intuitive compatibility concerns.

Xuan, Vilela, and co-workers recently published the first example of this through the additive manufacturing of a HPCat microfluidic device. The previously published St-BTZ monomer was incorporated into a commercial PMMA resin (Clear FLGPCL02, Formlabs Inc.) to obtain a St-BTZ (0.5 wt %)/PMMA resin mixture [47,278]. The additive manufactured resin mixture was applied in a commercial stereolithograph apparatus (SLA) 3D printer (Form 1+, Formlabs Inc.), and the printing process was optimised to account for the photocatalyst's absorption of the SLA 3D printer's 405 nm laser, which initiates the free-radical polymerisation of the resin. The microfluidic device was designed using computer-aided design software and fabricated with a 1 mm channel diameter, 500 micron wall thickness, and a total reactor volume of 0.1 mL. The device was applied for the photosensitisation of singlet oxygen, using the oxidation of 2-furoic acid (**54**) to 5-hydroxy-5*H*-furan-2-one (**55**) in water as a model reaction (Scheme 26). The oxidation mechanism is similar to **44** and begins with an Alder-ene [4 + 2] cycloaddition. However, the intermediate endoperoxide **XVII** then decarboxylates to liberate CO_2. The subsequent protonation yields the product **55**.

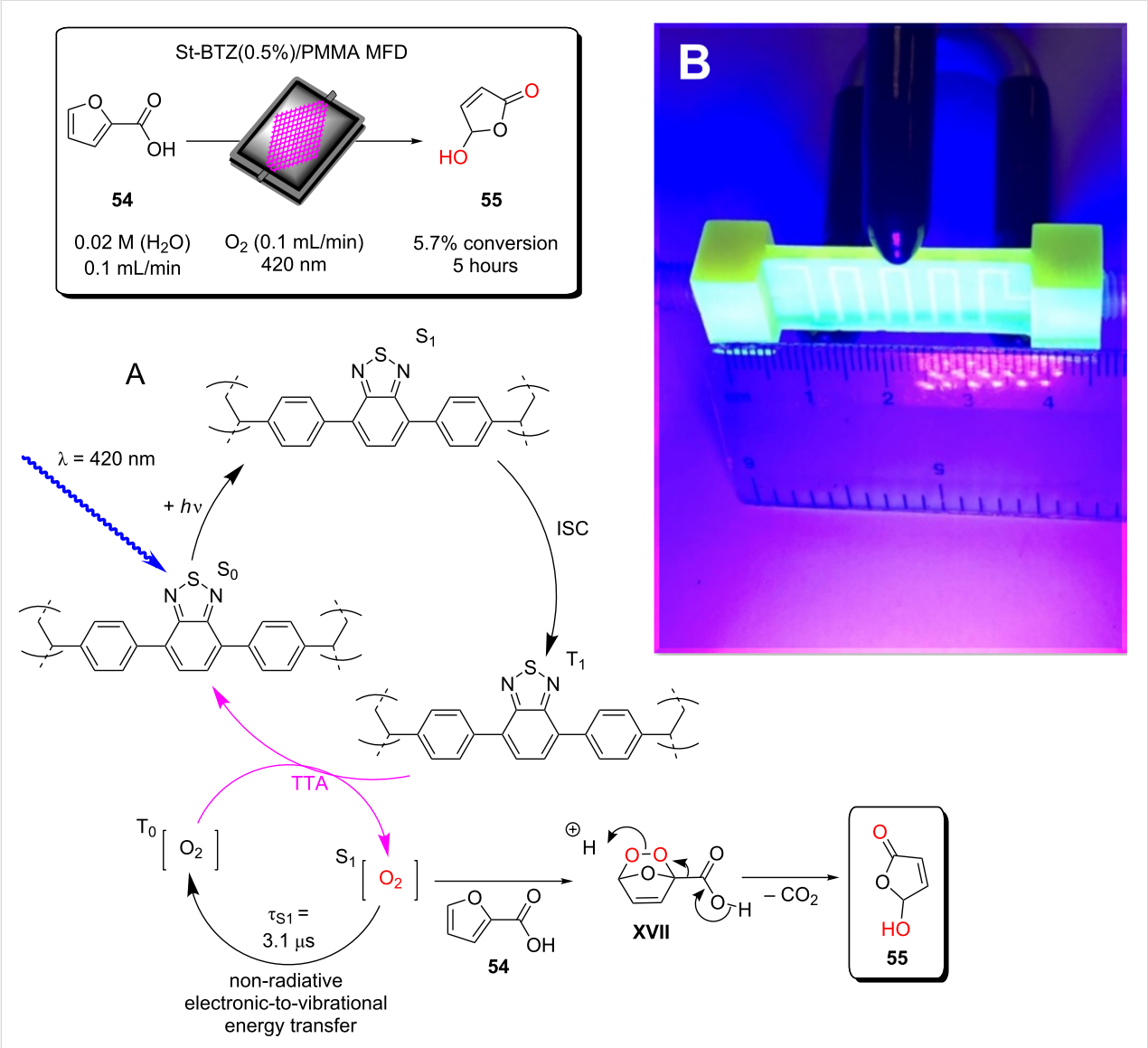

Scheme 26: Reaction scheme of the singlet oxygen oxidation of furoic acid (**54**) using a 3D-printed microfluidic device containing a photocatalyst monomer additive [278]. A) Proposed oxidation mechanism [280]. B) Image of the MFD in operation, reprinted from http://www.VilelaLAB.co.uk with permission.

The device was tested for 5 hours with continuous cycling of the reaction mixture and showed full selectivity of the lactone product but only obtained ≈6% conversion. The low conversion can be attributed to a few factors: (i) Water was used as a solvent for a compatibility with the printed polymer, which provides a very short lifetime of singlet oxygen (ca. 3.1 μs) before non-radiatively decaying to the ground state [279]. (ii) The dispersion of the photocatalyst throughout the polymer material may have resulted in significant unproductive excitation in the bulk and external surfaces of the microfluidic device, reducing the productive excitation of photocatalyst in the flow channel surfaces. The authors stated that work is ongoing to develop solvent-resistant resins and intricate reactor designs that will help to overcome these issues [278].

4.3 Photocatalytic water purification in flow

Approximately 4 billion people globally experience severe water scarcity for at least one month of the year [281]. Global water consumption has been increasing by 1% per year since the 1980s, which is projected to continue as the agriculture industry expands to meet global food demands [281]. On average, 780,000 people die each year from diseases associated with unsanitary water, an order of magnitude higher than conflict-related deaths. The removal of hazardous chemical species and biological pathogens from water is therefore a critical global issue to sustain development and provide humanity with the basic human right to clean drinking water. Powerful oxidising heterogeneous photoredox catalysts can degrade pollutants and kill bacteria without introducing chemical agents and require only sunlight for their operation, which is conveniently an abundant resource for many countries that are affected by poor water sanitation. The implementation of flow reactors facilitates purification process and provides easy manipulation of conditions to emulate the environment or to demonstrate scalability for industrial wastewater treatment.

Goetz and co-workers studied the use of TiO_2 bound by SiO_2 to non-woven cellulosic fibres as a HPCat for the removal of *E. coli* from water under UV irradiation in continuous flow [282]. The use of continuous flow was critical for providing realistic comparisons to industrial wastewater treatment plant scales. The flow reactor system employed used a centrifugal pump to drive a closed reactor loop and ensure homogeneous mixing of the solution throughout the entire system. The input and output of the *E. coli* solution, before and after treatment, was driven by a multichannel peristaltic pump. The 2-dimensional immobilised TiO_2 HPCat was placed in a flat-plate reactor, covered with a transparent PMMA sheet, and placed in front of an array of UVA LEDs. The effects of varying the photon flux and flow rate was studied, and both parameters were found to influence the number of the deactivated bacterial cells. At 35 $W \cdot m^{-2}$ of UVA light irradiation, an intensity consistent with solar irradiation, the HPCat system was calculated to have a treatment capacity of $15–30 \times 10^5$ $MPN \cdot h^{-1} \cdot L^{-1}$ (MPN = most probable number of bacteria, calculated by the optical density at 600 nm). Due to the complex biomolecular structure of living cells, photocatalytic disinfection has many mechanisms and has been well studied and modelled elsewhere [283]. In general, the HPCat produces reactive oxygen species (ROS), such as singlet oxygen, hydroxyl radicals, and superoxide radicals. ROS react with unsaturated phospholipids within the cell membrane to generate peroxides and radical cascades that ultimately rupture the membrane structure and kill the cell (Figure 18). Vulnerable surface proteins and polysaccharides can also be deactivated by ROS, preventing cell function and leading to apoptosis or necrosis (programmed or involuntary cell death). The complimentary surface charges of the TiO_2 HPCat and bacterial cells can favour surface adsorption, permitting direct oxidation and reduction processes with the membrane that may also be important processes during disinfection [283].

The treatment of aqueous dyes from textile waste streams is problematic due to their large-scale production, solubility, and inefficient bioremediation [18]. The HPCat generation of ROS and direct photoredox processes can efficiently degrade many dyes to species that are easily removed or completely mineralised to CO_2, water, and harmless anionic species. Lu and co-workers reported a continuous flow slurry reactor using commercial TiO_2 (Degussa P25) for the remediation of a variety of aqueous pollutants, such as phenol, Cr(VI), and an organic dye (acid orange 7, AO7) as well as for the photoredox-catalysed reduction of *p*-nitrophenol to *p*-aminophenol [214]. The aim of the study was to see the effects of positioning a static mixer unit within the illuminated photoreactor or the dark silicon pipes, which connected the photoreactor chambers. This was to assess the contributions of the surface and bulk solution processes to the photocatalysis efficiency, inspired by the light and dark reactions of natural photosynthesis. Interestingly, the group found that in the cases where photocatalysis occurred by direct electron transfer between the HPCat and a strongly adsorbed substrate (e.g., Cr(VI) and AO7), the static mixer had no effect on the reaction. For reactions that occur primarily through the generation of ROS, which desorb and react primarily in the bulk solution, the static mixer gave significant rate enhancements of 20–90%. Of the systems that were enhanced, the position of the mixer had no effect on the rate, showing that the homogeneous dark reaction occurring in the bulk solution is limiting the efficiency of the reactor more so than the radical generation at the HPCat surface. They suggested that as the placement in the light or dark had no influence, the static mixers and photochemical reactors could be sep-

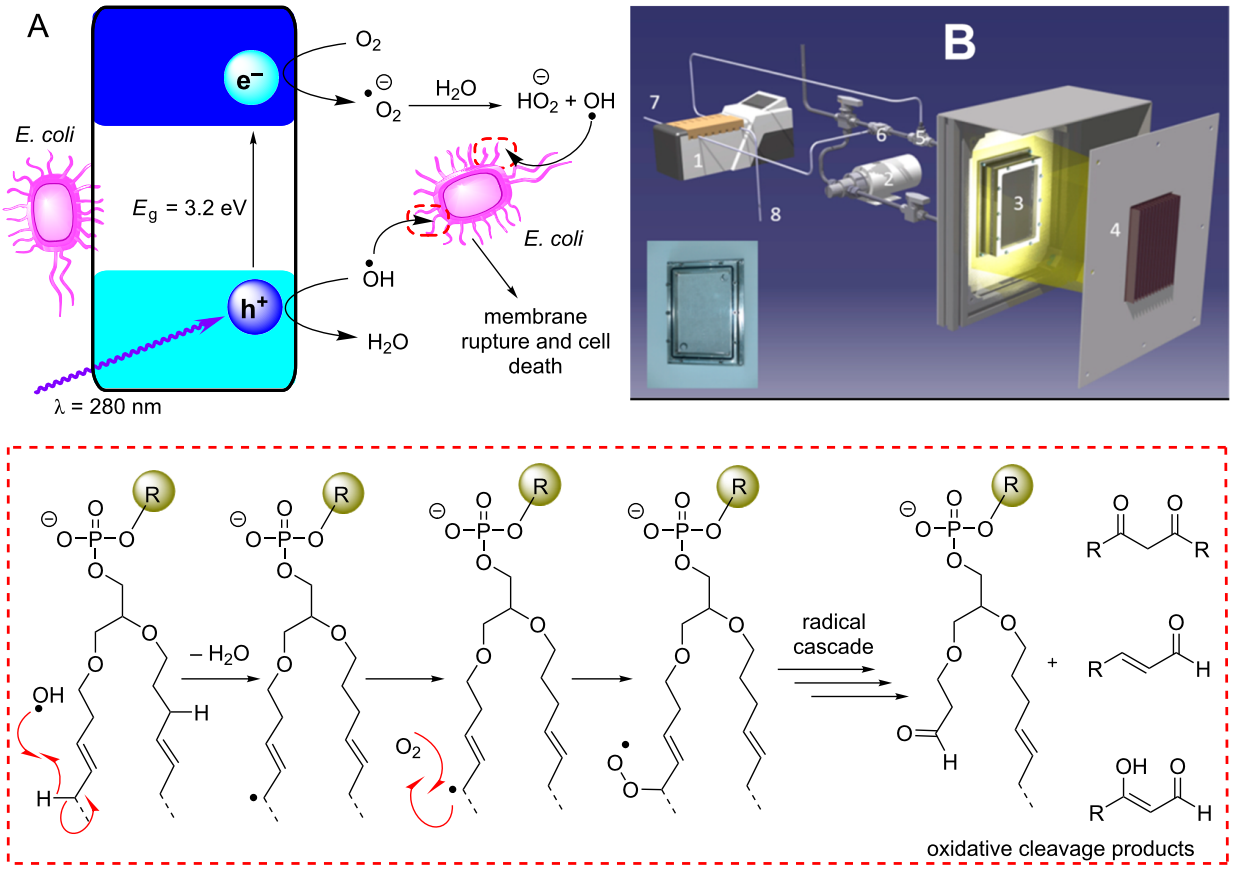

Figure 18: A) Photocatalytic bactericidal mechanism by ROS oxidative cleavage of membrane lipids (R = H, amino acid, membrane proteins) [282,283]. B) Graphical flow scheme of the cellulose fibre-supported TiO_2 HPCat for the bactericidal photocatalytic removal of *E. coli* from water. (1) Peristaltic pump, (2) centrifugal pump, (3) photoreactor, (4) UV panel, (5) withdrawal valve, (6) feed valve, (7) effluent to be treated, and (8) treated effluent. Adapted with permission from [282]. Copyright 2017 American Chemical Society.

arated into individual components of a flow system, providing process intensification without complicated reactor designs, trying to incorporate large irradiation surface areas and static mixing in a single unit. The mechanism for select examples of photocatalytic pollutant degradation in water have been studied in detail and are represented in Figure 19, along with a schematic of the flow system used in the study [284-287].

Later in the same year, the group reported the same setup for the degradation of model water pollutants, but featuring five larger Kenics static mixer units in each of the irradiated quartz tubes for process intensification [216]. Terephthalic acid was used as a fluorescence probe sensor for hydroxyl radicals, revealing that the concentration of hydroxyl radicals in the bulk solution was enhanced by the static mixer units. They again observed that the photocatalytic degradation localised at the HPCat surface was not enhanced by the static mixing units, but the bulk solution phase degradation by the ROS was significantly enhanced, especially at lower flow rates [216].

Following this report, Vilar and co-workers recently reported the use of Kenics static mixers as a support material for TiO_2 and Fe_2O_3 HPCats, applied by dip-coating and spray coating [215]. The group placed the coated static mixer units in a borosilicate column surrounded by a compound parabolic collector (CPC) solar concentrator and applied the reactor for the degradation of aqueous oxytetracycline (**56**, Figure 20). Antibiotics pollution in waste water is a serious issue due to concerns of bacteria developing resistance, but many waste streams and water treatment facilities are not effective in their removal through conventional bioremediation [288]. The group's system was able to completely degrade **56** to dissolved organic carbons in under an hour with the Fe_2O_3 spray-coated static mixer, and in just over two hours with the TiO_2-coated mixer in the presence of H_2O_2. The byproducts were further degraded to low-molecular-weight carboxylic acids and gaseous byproducts, removing approximately 60% of the initially dissolved organic carbon after 6 hours with both supported catalysts. The superior activity of the Fe_2O_3-coated static mixer was

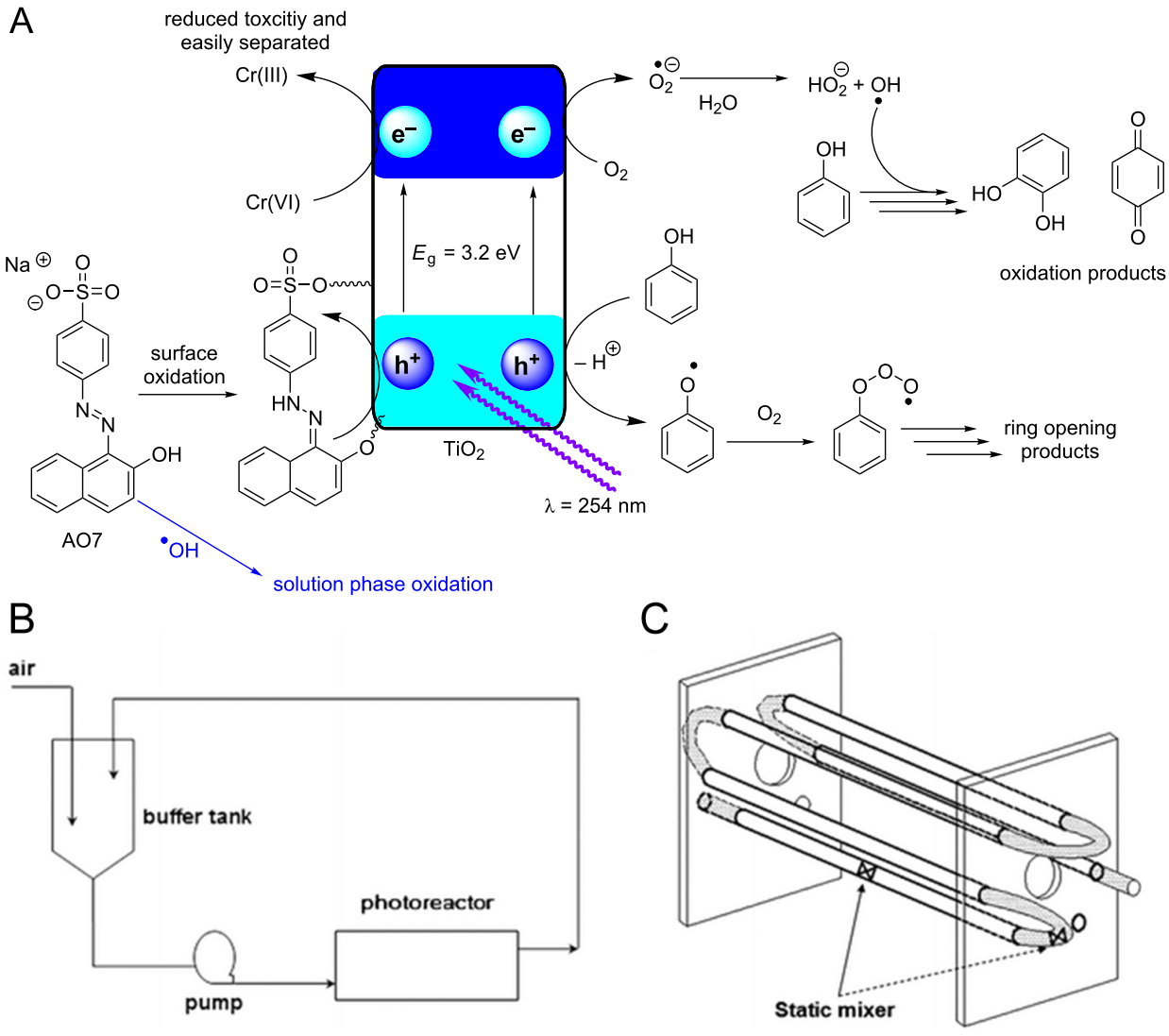

Figure 19: A) Suggested mechanisms for the aqueous pollutant degradation by TiO_2 in a slurry flow reactor [284-287]. B) Flow schematic of the slurry reactor and C) more detailed schematic of the irradiated reactor with a static mixer in the dark silicone tubing (dashed arrow) or an irradiated quartz tube (solid arrow). Reprinted with permission from [214], Copyright 2011 The Royal Society of Chemistry.

found to be partially due to a significant leaching of Fe ions into the solution, resulting in a significant contribution from homogeneous Fenton and photo-Fenton processes. The Fenton reaction is the production of hydroxyl radicals from H_2O_2 by Fe ions and can be catalytic under light irradiation or an applied voltage (vide infra) [289]. The amount of iron leached from the coating decreased over three cycles, and the group suggested that a fraction of the spray-coated HPCat was unstable and easily detached. Once removed by sequential reaction cycles, the Fe leaching dropped to undetectable amounts. They identified no leaching of TiO_2 from the spray-coated static mixer. The static mixer support provided an efficient mixing of a laminar flow input, and its geometry enhanced the illumination of the immobilised HPCat by providing front and side irradiation from the CPC. The mixing was sufficient with only two coated static mixer units, and increasing to six did not significantly improve the rate of **56** degradation. The flow scheme and structure of **56** are displayed in Figure 20 [215].

Ruiz-Ruiz and co-workers studied the complete mineralisation of aqueous salicylic acid (**57**) by combing solar photoelectro-Fenton and solar heterogeneous photocatalysis in a single continuous flow process (Scheme 27) [290]. Salicylic acid (**57**) is commonly employed in cosmetic, pharmaceutical, and food formulations and has been detected in the wastewater of urban areas in many countries at concentrations of up to 50 $\mu g \cdot L^{-1}$

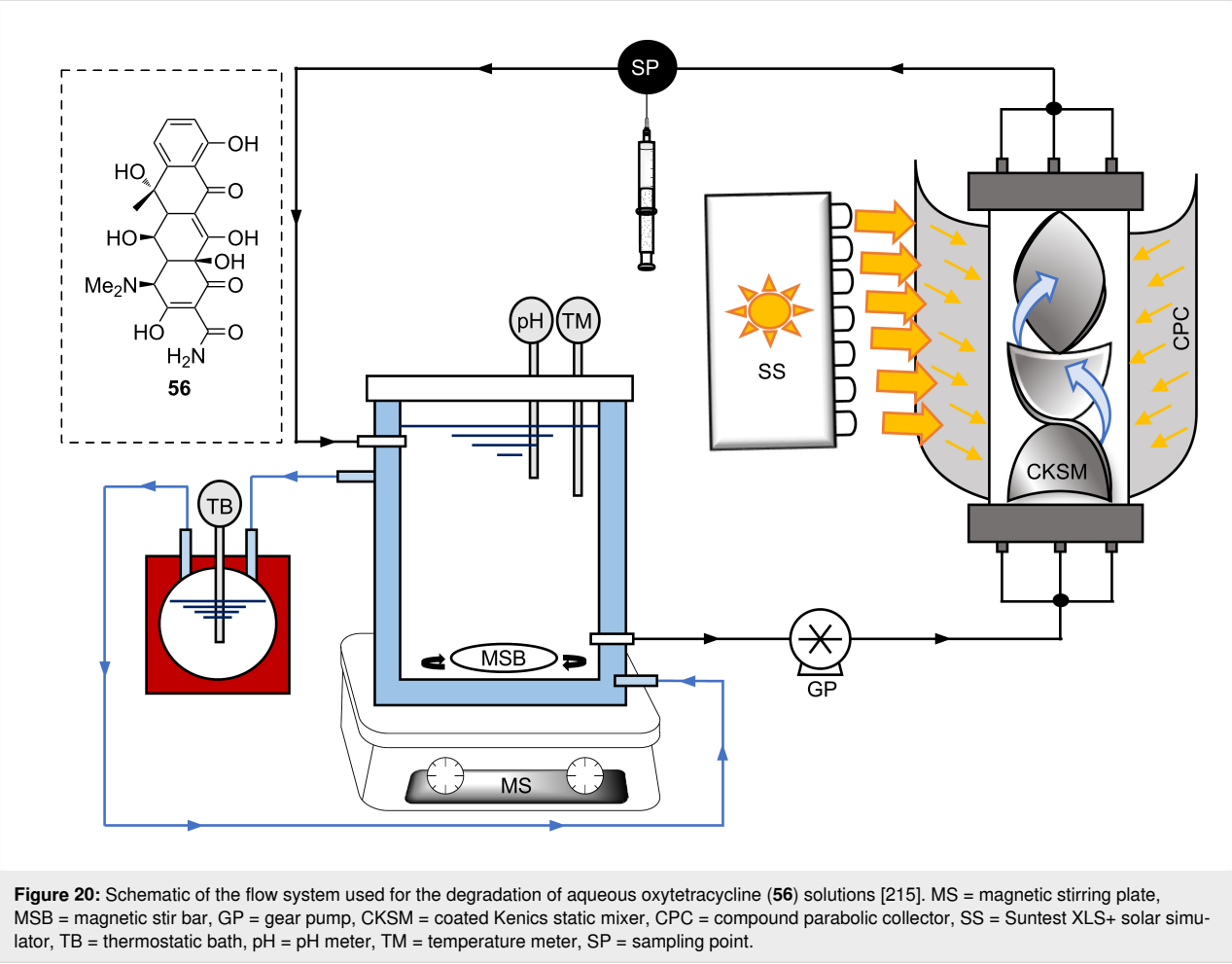

Figure 20: Schematic of the flow system used for the degradation of aqueous oxytetracycline (**56**) solutions [215]. MS = magnetic stirring plate, MSB = magnetic stir bar, GP = gear pump, CKSM = coated Kenics static mixer, CPC = compound parabolic collector, SS = Suntest XLS+ solar simulator, TB = thermostatic bath, pH = pH meter, TM = temperature meter, SP = sampling point.

[291-293]. The flow system had a 3-litre capacity and featured a Pt/air diffusion (anode/cathode) electrochemical cell, a solar photoreactor, and a HPCat reactor filled with TiO_2 immobilised on glass spheres. The individual reactors generated hydroxyl radicals through water electrolysis at the Pt anode, photocatalysis at the TiO_2 surface, and via Fenton's reaction between the added Fe^{2+} catalyst and H_2O_2, which was generated in situ by the cathode. The efficiency of the solar and electrochemical reactors individually and in combination, without the addition of Fe^{2+}, led to the poor removal and mineralisation of **57**, which the authors proposed to be due to the lower oxidation power of the surface-generated hydroxyl radicals.

The electro-Fenton reaction in the absence of the solar reactors did efficiently degrade salicylic acid (**57**) to low-molecular-weight carboxylic acid byproducts. However, the carboxylic acid byproducts formed were resistant to further degradation. The optimal system was a combination of all three processes, as the carboxylic acid byproducts were susceptible to photolysis and further oxidation on the TiO_2 HPCat surface. The system was able to achieve 87% mineralisation of a 165 $mg{\cdot}L^{-1}$ solution of salicylic acid (**57**) after 360 minutes of simultaneous water electrolysis, photolysis, and Fenton's reactions.

4.4 Photocatalytic air purification in flow

Air pollution contributed to approximately 5 million deaths globally in 2017 [294]. The anthropogenic emission of volatile organic compounds (VOCs), nitrous oxides (NO_x), and other hazardous chemical species is the leading cause of acid rain, airborne particulate concentration, smog, and ozone formation in the troposphere [294]. These issues are particularly prevalent in developing countries with rapidly expanding industries and those still dependent on burning coal as an energy source. However, the sociodemographic pattern of ozone pollution shows that the highest ppb levels occur in more developed countries as the nitrous oxides and VOC pollutant precursors are correlated with industrialisation and economic development [294]. HPCats can efficiently remediate toxic gaseous pollutants, especially porous materials with high surface areas, which are much better suited to binding and reacting with gaseous substrates than a gas/liquid system. A heterogeneous solid/gas phase reaction also naturally lends itself to flow chemistry as the expected ap-

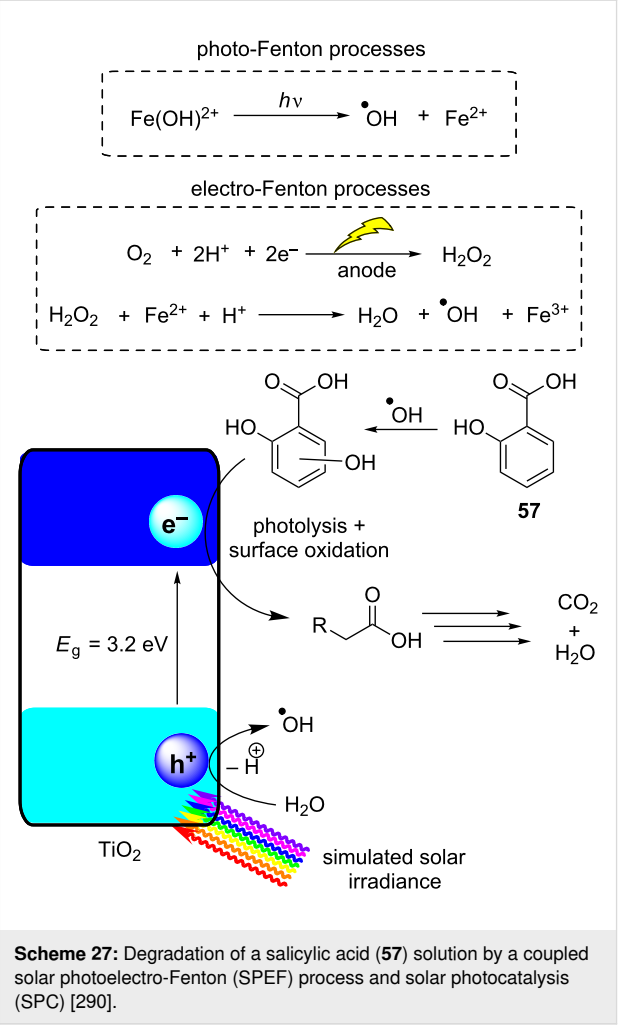

Scheme 27: Degradation of a salicylic acid (**57**) solution by a coupled solar photoelectro-Fenton (SPEF) process and solar photocatalysis (SPC) [290].

plication of the HPCat would be at the end of a gas exhaust stream.

Herrmann and co-workers recently demonstrated the photocatalytic ability of TiO_2 in the remediation of nitrous oxide pollutants in the air using a fixed bed flow reactor and UV irradiation [295]. The flow system featured 5 mass flow controller units and 3 mixing chambers, which allowed control over the flow rates and concentrations of nitrous oxides, water vapour, and compressed air. The group manipulated the conditions to simulate the atmosphere and found that the humidity and mixing ratios were the most important factors to consider, consistent with the involvement of the adsorbed water molecules on the TiO_2 photocatalyst forming hydroxyl and superoxide species that then oxidise adsorbed NO and NO_x species. The study highlighted the careful choice of the system conditions to accurately simulate the concentrations of pollutants in the atmosphere. This was in order to make the collected data independent of the reactor dimensions so it could be accurately extrapolated to any simulated atmospheric conditions. Contrary to the heterogeneous solid/solution photocatalysis discussed earlier in this review, gas phase heterogeneous photocatalysis processes are almost exclusively surface-based phenomena that occur in elementary steps between adsorbed species.

The efficient oxidative degradation of gaseous *n*-decane was achieved in another report by Vilar and co-workers in which a cellulose acetate sheet was coated with a thin film of TiO_2 as the HPCat (Figure 21A) [296]. The HPCat sheet was placed between a borosilicate window slab and a micro-meso-structured photoreactor. This comprised a slab of acrylic that had flow channels mechanically engraved into the material, forming a two-dimensional coated reactor with microchannels connecting to millimetre-scale "meso-chambers" in a diagonal "crisscross" pattern (Figure 21B). The design was inspired by the NETmix technology, developed by Dias and co-workers [297], and acts as an efficient static mixer unit for solution and gas flow streams.

The reactor was able to efficiently oxidise gaseous *n*-decane in the presence of water vapour to aldehyde and ketone byproducts, with a consistent performance over 72 hours of continuous irradiation. The authors proposed that a longer retention time within the reactor would sequentially oxidise and degrade the byproducts to smaller-carbon-chain intermediates and eventually lead to a total mineralisation. It was reported that 75 mg of TiO_2 was the optimal loading, as higher loadings were observed to reduce the efficiency. This was due to the layer thickness of TiO_2, increasing and reducing the surface area as the surface-immobilised layers became inaccessible to the gas flow. Additionally, the authors proposed the higher TiO_2 layer depth contributed to the "back-irradiation" phenomenon in which the photogenerated charge carriers are further from the HPCat/gas interface, and charge recombination becomes significant. An increasing flow rate facilitated mixing in the NETmix-type static mixer channel design and enhanced the photodegradation efficiency up to a point where the residence time of the gaseous reagents in the reactor became the limiting factor.

Conclusion

Heterogeneous photocatalysis and flow chemistry form a synergistic pairing that has the potential to become the "power couple" of photochemistry. The typical disadvantages of HPCats are largely mitigated through continuous flow reactors' improved mass transport and irradiation. In this review, we have covered the different types of HPCats and how they function as photocatalysts. Enhancing charge transport and separation in semiconductor HPCats is a key factor to improve photocatalytic activity, which can be achieved through materials design and band gap engineering. The physical nature of metal

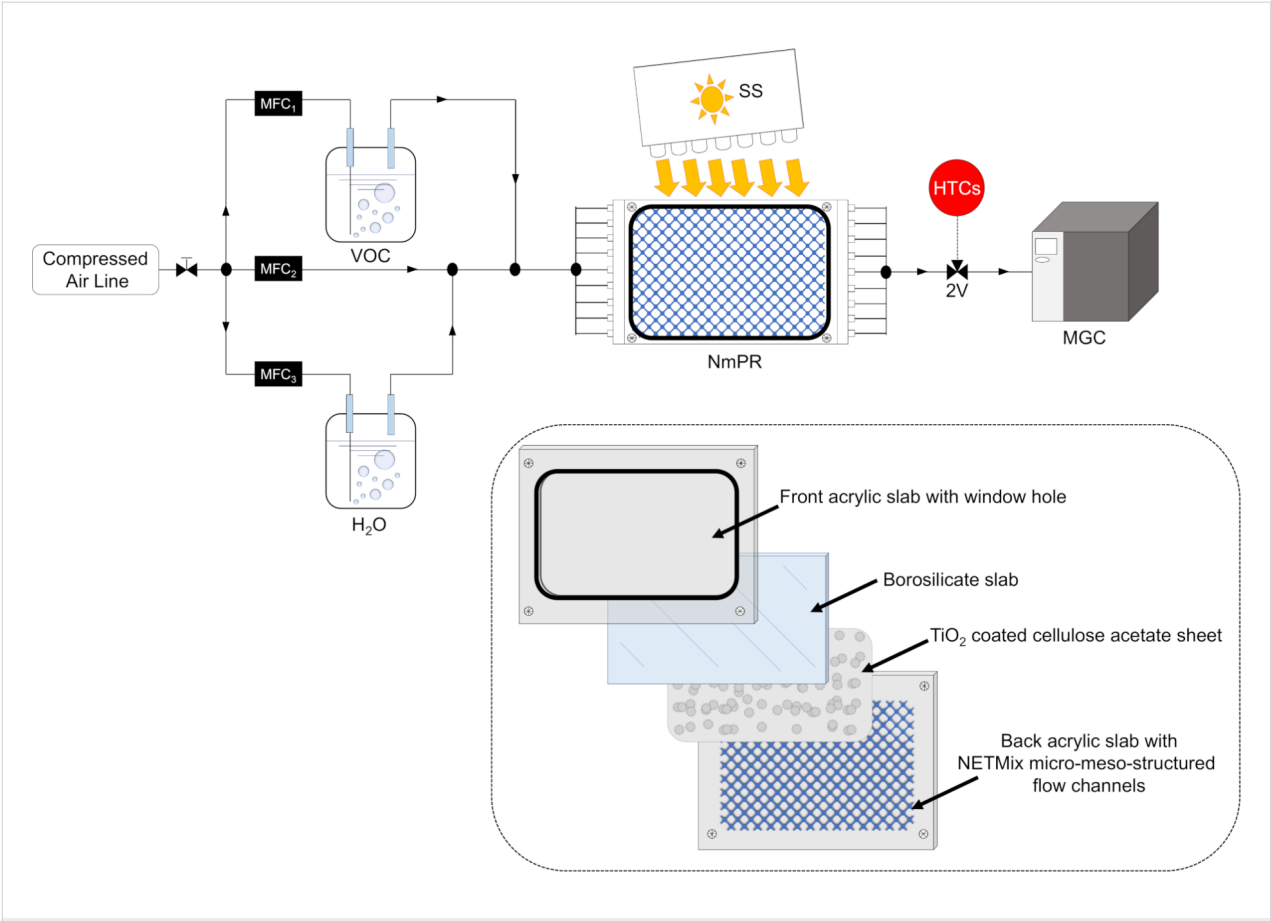

Figure 21: A) Schematic flow diagram using the TiO_2-coated NETmix microfluidic device for an efficient mass transport during the degradation of gaseous volatile organic compounds [296]. MFC = mass flow controller, VOC = volatile organic compound reservoir Woulff bottle, H_2O = water reservoir Woulff bottle, MGC = master gas chromatograph, 2V = two-way valve, NmPR = NETmix photoreactor, SS = Suntest solar simulator, HTCs = humidity, temperature, and CO_2 sensor. B) Graphical representation of the component layers that form the NETmix microfluidic device fabricated by Vilar and co-workers [296].

oxide surfaces and the substrate's adsorption have also been described, which could influence the performance of a HPCat regardless of its charge transport efficiency. The different types of flow reactors and systems that HPCats can be applied in, as well as their advantages and disadvantages, were discussed with the objective of guiding the reader toward the best reactor to suit their intended system.

Finally, we reviewed the different photoredox catalysis and energy transfer catalysis synthetic transformations that have been achieved with HPCats in flow reactors. The photocatalytic removal of pollutants from waste water and air were discussed with an emphasis on the flow systems and photoreactor designs that utilise static mixing technology, which could be effective if applied in organic synthesis. A recurring trend throughout the examples of heterogeneous photocatalysis discussed was that flow chemistry can significantly reduce the reaction times and increase the process productivity, often by orders of magnitude compared to analogous batch reactor protocols.

We suggest that the development of HPCats in continuous flow will lead to a new paradigm for sustainable photochemical syntheses. However, this is highly dependent upon advancements in several areas of scientific research, as represented in Figure 1B. We believe that interdisciplinary collaborations will provide rational design principles for more efficient HPCat materials and flow reactors, which will collectively exceed the capabilities of rare transition metal complex photocatalysts and provide more sustainable, large-scale photosynthetic methodologies.

Acknowledgements

The authors would like to thank Rob Leightley and Vapourtec Ltd. for recommending some relevant papers. We also wish to thank Guillaume Gauron and Corning Incorporated for kindly providing permission to use the images in Figure 2C and 2D, as well as providing some useful references. We wish to thank the CRITCAT CDT for providing training to C. G. T. We wish to thank Cristina Nisi and the Alma Mater Studiorum Università di

Bologna - Sistema Museale di Ateneo - Collezione di Chimica "Giacomo Ciamician" for providing permission to reprint the image in Figure 2A. C. G. T. would like to thank Emmanouil Broumidis, Samuel Patterson, and Cathryn Shepherd (VilelaLAB, Heriot-Watt University) for support. C. G. T. also wishes to thank Andrew Francis Tiberia (Lawrence Group, University of Edinburgh) for useful discussions and Silvia Genovese (University of Edinburgh) for her excellent translation skills and help with the acquisition of the figure permissions.

Funding

We would like to thank the Engineering and Physical Sciences Research Council, Heriot-Watt University and the CRITICAT Centre for Doctoral Training for financial support (Ph.D. studentship to C. G. T; Grant code: EP/L014419/1).

ORCID® iDs

Christopher G. Thomson - https://orcid.org/0000-0003-2272-4029
Ai-Lan Lee - https://orcid.org/0000-0001-9067-8664
Filipe Vilela - https://orcid.org/0000-0003-2701-9759

References

1. Wang, J.-L.; Wang, C.; Lin, W. *ACS Catal.* **2012,** *2,* 2630–2640. doi:10.1021/cs3005874
2. Wen, J.; Xie, J.; Chen, X.; Li, X. *Appl. Surf. Sci.* **2017,** *391,* 72–123. doi:10.1016/j.apsusc.2016.07.030
3. Wong, Y.-L.; Tobin, J. M.; Xu, Z.; Vilela, F. *J. Mater. Chem. A* **2016,** *4,* 18677–18686. doi:10.1039/c6ta07697a
4. Xu, Y.; Jin, S.; Xu, H.; Nagai, A.; Jiang, D. *Chem. Soc. Rev.* **2013,** *42,* 8012. doi:10.1039/c3cs60160a
5. Li, R.; Byun, J.; Huang, W.; Ayed, C.; Wang, L.; Zhang, K. A. I. *ACS Catal.* **2018,** *8,* 4735–4750. doi:10.1021/acscatal.8b00407
6. Kale, M. J.; Avanesian, T.; Christopher, P. *ACS Catal.* **2014,** *4,* 116–128. doi:10.1021/cs400993w
7. Xu, Q.; Zhang, L.; Yu, J.; Wageh, S.; Al-Ghamdi, A. A.; Jaroniec, M. *Mater. Today* **2018,** *21,* 1042–1063. doi:10.1016/j.mattod.2018.04.008
8. Cherevatskaya, M.; König, B. *Russ. Chem. Rev.* **2014,** *83,* 183–195. doi:10.1070/rc2014v083n03abeh004427
9. Herrmann, J.-M. *Top. Catal.* **2005,** *34,* 49–65. doi:10.1007/s11244-005-3788-2
10. Savateev, A.; Antonietti, M. *ACS Catal.* **2018,** *8,* 9790–9808. doi:10.1021/acscatal.8b02595
11. Riente, P.; Noël, T. *Catal. Sci. Technol.* **2019,** *9,* 5186–5232. doi:10.1039/c9cy01170f
12. Vyas, V. S.; Lau, V. W.-h.; Lotsch, B. V. *Chem. Mater.* **2016,** *28,* 5191–5204. doi:10.1021/acs.chemmater.6b01894
13. Maeda, K.; Domen, K. *J. Phys. Chem. Lett.* **2010,** *1,* 2655–2661. doi:10.1021/jz1007966
14. Tentu, R. D.; Basu, S. *Curr. Opin. Electrochem.* **2017,** *5,* 56–62. doi:10.1016/j.coelec.2017.10.019
15. Zhang, G.; Lan, Z.-A.; Wang, X. *Angew. Chem., Int. Ed.* **2016,** *55,* 15712–15727. doi:10.1002/anie.201607375
16. Ni, M.; Leung, M. K. H.; Leung, D. Y. C.; Sumathy, K. *Renewable Sustainable Energy Rev.* **2007,** *11,* 401–425. doi:10.1016/j.rser.2005.01.009
17. Ahmad, H.; Kamarudin, S. K.; Minggu, L. J.; Kassim, M. *Renewable Sustainable Energy Rev.* **2015,** *43,* 599–610. doi:10.1016/j.rser.2014.10.101
18. Pelaez, M.; Nolan, N. T.; Pillai, S. C.; Seery, M. K.; Falaras, P.; Kontos, A. G.; Dunlop, P. S. M.; Hamilton, J. W. J.; Byrne, J. A.; O'Shea, K.; Entezari, M. H.; Dionysiou, D. D. *Appl. Catal., B* **2012,** *125,* 331–349. doi:10.1016/j.apcatb.2012.05.036
19. Saadati, F.; Keramati, N.; Ghazi, M. M. *Crit. Rev. Environ. Sci. Technol.* **2016,** *46,* 757–782. doi:10.1080/10643389.2016.1159093
20. Ahmed, S. N.; Haider, W. *Nanotechnology* **2018,** *29,* 342001. doi:10.1088/1361-6528/aac6ea
21. Mondal, K.; Moitra, P. *Metal-semiconductor core–shell nanostructured photocatalysts for environmental applications and their recycling process;* Elsevier: Amsterdam, Netherlands, 2017; pp 133–157. doi:10.1016/b978-0-323-44922-9.00006-5
22. Demeestere, K.; Dewulf, J.; Van Langenhove, H. *Crit. Rev. Environ. Sci. Technol.* **2007,** *37,* 489–538. doi:10.1080/10643380600966467
23. Wang, Y.; Wang, X.; Antonietti, M. *Angew. Chem., Int. Ed.* **2012,** *51,* 68–89. doi:10.1002/anie.201101182
24. Nicewicz, D. A.; MacMillan, D. W. C. *Science* **2008,** *322,* 77–80. doi:10.1126/science.1161976
25. Ischay, M. A.; Anzovino, M. E.; Du, J.; Yoon, T. P. *J. Am. Chem. Soc.* **2008,** *130,* 12886–12887. doi:10.1021/ja805387f
26. Narayanam, J. M. R.; Tucker, J. W.; Stephenson, C. R. J. *J. Am. Chem. Soc.* **2009,** *131,* 8756–8757. doi:10.1021/ja9033582
27. Fujishima, A.; Honda, K. *Nature* **1972,** *238,* 37–38. doi:10.1038/238037a0
28. Trommsdorff, H. *Ann. Pharm. (Lemgo, Ger.)* **1834,** *11,* 190–207. doi:10.1002/jlac.18340110207
29. Ciamician, G. *Science* **1912,** *36,* 385–394. doi:10.1126/science.36.926.385
30. Thorpe, T. E. *Nature* **1922,** *109,* 245–246. doi:10.1038/109245a0
31. Ciamician, G.; Silber, P. *Ber. Dtsch. Chem. Ges.* **1908,** *41,* 1928–1935. doi:10.1002/cber.19080410272
32. Oelgemoeller, M. *Chem. Eng. Technol.* **2012,** *35,* 1144–1152. doi:10.1002/ceat.201200009
33. Reiser, O. *Chem* **2016,** *1,* 344–345. doi:10.1016/j.chempr.2016.08.005
34. Beatty, J. W.; Douglas, J. J.; Miller, R.; McAtee, R. C.; Cole, K. P.; Stephenson, C. R. J. *Chem* **2016,** *1,* 456–472. doi:10.1016/j.chempr.2016.08.002
35. Oelgemöller, M. *Chem. Rev.* **2016,** *116,* 9664–9682. doi:10.1021/acs.chemrev.5b00720
36. Corcoran, E. B.; Lévesque, F.; McMullen, J. P.; Naber, J. R. *ChemPhotoChem* **2018,** *2,* 931–937. doi:10.1002/cptc.201800098
37. Williams, J. D.; Nakano, M.; Gérardy, R.; Rincón, J. A.; de Frutos, Ó.; Mateos, C.; Monbaliu, J.-C. M.; Kappe, C. O. *Org. Process Res. Dev.* **2019,** *23,* 78–87. doi:10.1021/acs.oprd.8b00375
38. Steiner, A.; Williams, J. D.; de Frutos, O.; Rincón, J. A.; Mateos, C.; Kappe, C. O. *Green Chem.* **2020,** *22,* 448–454. doi:10.1039/c9gc03662h
39. Ma, Z.; Zaera, F. *Heterogeneous Catalysis by Metals;* Encyclopedia of Inorganic Chemistry; John Wiley & Sons, Ltd: Chichester, United Kingdom, 2006. doi:10.1002/0470862106.ia084

40. Romero, N. A.; Nicewicz, D. A. *Chem. Rev.* **2016,** *116,* 10075–10166. doi:10.1021/acs.chemrev.6b00057
41. Twilton, J.; Le, C.; Zhang, P.; Shaw, M. H.; Evans, R. W.; MacMillan, D. W. C. *Nat. Rev. Chem.* **2017,** *1,* 0052. doi:10.1038/s41570-017-0052
42. Prier, C. K.; Rankic, D. A.; MacMillan, D. W. C. *Chem. Rev.* **2013,** *113,* 5322–5363. doi:10.1021/cr300503r
43. Plutschack, M. B.; Pieber, B.; Gilmore, K.; Seeberger, P. H. *Chem. Rev.* **2017,** *117,* 11796–11893. doi:10.1021/acs.chemrev.7b00183
44. Tan, H. L.; Abdi, F. F.; Ng, Y. H. *Chem. Soc. Rev.* **2019,** *48,* 1255–1271. doi:10.1039/c8cs00882e
45. Friedmann, D.; Hakki, A.; Kim, H.; Choi, W.; Bahnemann, D. *Green Chem.* **2016,** *18,* 5391–5411. doi:10.1039/c6gc01582d
46. Lang, X.; Chen, X.; Zhao, J. *Chem. Soc. Rev.* **2014,** *43,* 473–486. doi:10.1039/c3cs60188a
47. Tobin, J. M.; McCabe, T. J. D.; Prentice, A. W.; Holzer, S.; Lloyd, G. O.; Paterson, M. J.; Arrighi, V.; Cormack, P. A. G.; Vilela, F. *ACS Catal.* **2017,** *7,* 4602–4612. doi:10.1021/acscatal.7b00888
48. Kou, J.; Lu, C.; Wang, J.; Chen, Y.; Xu, Z.; Varma, R. S. *Chem. Rev.* **2017,** *117,* 1445–1514. doi:10.1021/acs.chemrev.6b00396
49. Ozawa, K.; Emori, M.; Yamamoto, S.; Yukawa, R.; Yamamoto, S.; Hobara, R.; Fujikawa, K.; Sakama, H.; Matsuda, I. *J. Phys. Chem. Lett.* **2014,** *5,* 1953–1957. doi:10.1021/jz500770c
50. Ravetz, B. D.; Pun, A. B.; Churchill, E. M.; Congreve, D. N.; Rovis, T.; Campos, L. M. *Nature* **2019,** *565,* 343–346. doi:10.1038/s41586-018-0835-2
51. Zhang, Q.; Yang, F.; Xu, Z.; Chaker, M.; Ma, D. *Nanoscale Horiz.* **2019,** *4,* 579–591. doi:10.1039/c8nh00373d
52. Loubière, K.; Oelgemöller, M.; Aillet, T.; Dechy-Cabaret, O.; Prat, L. *Chem. Eng. Process.* **2016,** *104,* 120–132. doi:10.1016/j.cep.2016.02.008
53. Yoshida, J.-i.; Takahashi, Y.; Nagaki, A. *Chem. Commun.* **2013,** *49,* 9896–9904. doi:10.1039/c3cc44709j
54. Wong, J. Y. F.; Tobin, J. M.; Vilela, F.; Barker, G. *Chem. – Eur. J.* **2019,** *25,* 12439–12445. doi:10.1002/chem.201902917
55. Chen, Y.; Li, L.; Chen, W.; Chen, H.; Yin, J. *Chin. Chem. Lett.* **2019,** *30,* 1353–1360. doi:10.1016/j.cclet.2019.02.003
56. Qiu, J.; Wei, W. D. *J. Phys. Chem. C* **2014,** *118,* 20735–20749. doi:10.1021/jp5042553
57. Zhang, C.; Liang, H. Q.; Xu, Z. K.; Wang, Z. *Adv. Sci.* **2019,** *6,* 1900883. doi:10.1002/advs.201900883
58. Gemoets, H. P. L.; Su, Y.; Shang, M.; Hessel, V.; Luque, R.; Noël, T. *Chem. Soc. Rev.* **2016,** *45,* 83–117. doi:10.1039/c5cs00447k
59. Hone, C. A.; Kappe, C. O. *Top. Curr. Chem.* **2019,** *377,* No. 2. doi:10.1007/s41061-018-0226-z
60. Hone, C. A.; Roberge, D. M.; Kappe, C. O. *ChemSusChem* **2017,** *10,* 32–41. doi:10.1002/cssc.201601321
61. Straathof, N. J. W.; Su, Y.; Hessel, V.; Noël, T. *Nat. Protoc.* **2016,** *11,* 10–21. doi:10.1038/nprot.2015.113
62. Straathof, N. J. W.; Gemoets, H. P. L.; Wang, X.; Schouten, J. C.; Hessel, V.; Noël, T. *ChemSusChem* **2014,** *7,* 1612–1617. doi:10.1002/cssc.201301282
63. Thomson, C. G.; Jones, C. M. S.; Rosair, G.; Ellis, D.; Marques-Hueso, J.; Lee, A.-L.; Vilela, F. *J. Flow Chem.* **2020,** *10,* 327–345. doi:10.1007/s41981-019-00067-4
64. Bristow, T. W. T.; Ray, A. D.; O'Kearney-McMullan, A.; Lim, L.; McCullough, B.; Zammataro, A. *J. Am. Soc. Mass Spectrom.* **2014,** *25,* 1794–1802. doi:10.1007/s13361-014-0957-1
65. Giraudeau, P.; Felpin, F.-X. *React. Chem. Eng.* **2018,** *3,* 399–413. doi:10.1039/c8re00083b
66. Carter, C. F.; Lange, H.; Ley, S. V.; Baxendale, I. R.; Wittkamp, B.; Goode, J. G.; Gaunt, N. L. *Org. Process Res. Dev.* **2010,** *14,* 393–404. doi:10.1021/op900305v
67. Yue, J.; Falke, F. H.; Schouten, J. C.; Nijhuis, T. A. *Lab Chip* **2013,** *13,* 4855–4863. doi:10.1039/c3lc50876e
68. Schlindwein, W.; Bezerra, M.; Almeida, J.; Berghaus, A.; Owen, M.; Muirhead, G. *Pharmaceutics* **2018,** *10,* 166. doi:10.3390/pharmaceutics10040166
69. Steiner, S.; Wolf, J.; Glatzel, S.; Andreou, A.; Granda, J. M.; Keenan, G.; Hinkley, T.; Aragon-Camarasa, G.; Kitson, P. J.; Angelone, D.; Cronin, L. *Science* **2019,** *363,* eaav2211. doi:10.1126/science.aav2211
70. Sanderson, K. *Nature* **2019,** *568,* 577–579. doi:10.1038/d41586-019-01246-y
71. Poechlauer, P.; Colberg, J.; Fisher, E.; Jansen, M.; Johnson, M. D.; Koenig, S. G.; Lawler, M.; Laporte, T.; Manley, J.; Martin, B.; O'Kearney-McMullan, A. *Org. Process Res. Dev.* **2013,** *17,* 1472–1478. doi:10.1021/op400245s
72. Poechlauer, P.; Manley, J.; Broxterman, R.; Gregertsen, B.; Ridemark, M. *Org. Process Res. Dev.* **2012,** *16,* 1586–1590. doi:10.1021/op300159y
73. Baxendale, I. R.; Braatz, R. D.; Hodnett, B. K.; Jensen, K. F.; Johnson, M. D.; Sharratt, P.; Sherlock, J.-P.; Florence, A. J. *J. Pharm. Sci.* **2015,** *104,* 781–791. doi:10.1002/jps.24252
74. Renz, C. *Helv. Chim. Acta* **1921,** *4,* 961–968. doi:10.1002/hlca.192100401101
75. Fujishima, A.; Zhang, X.; Tryk, D. A. *Surf. Sci. Rep.* **2008,** *63,* 515–582. doi:10.1016/j.surfrep.2008.10.001
76. Goodeve, C. F.; Kitchener, J. A. *Trans. Faraday Soc.* **1938,** *34,* 570–579. doi:10.1039/tf9383400570
77. Bird, J. P. *Semiconductors: An Introduction;* Elsevier: Amsterdam, Netherlands, 2002; pp 1–16. doi:10.1016/b0-08-043152-6/01854-4
78. Yan, H.; Wang, X.; Yao, M.; Yao, X. *Prog. Nat. Sci.: Mater. Int.* **2013,** *23,* 402–407. doi:10.1016/j.pnsc.2013.06.002
79. Peng, H.; Li, J.; Li, S.-S.; Xia, J.-B. *J. Phys.: Condens. Matter* **2008,** *20,* 125207. doi:10.1088/0953-8984/20/12/125207
80. Etacheri, V.; Di Valentin, C.; Schneider, J.; Bahnemann, D.; Pillai, S. C. *J. Photochem. Photobiol., C* **2015,** *25,* 1–29. doi:10.1016/j.jphotochemrev.2015.08.003
81. Lan, Y.; Lu, Y.; Ren, Z. *Nano Energy* **2013,** *2,* 1031–1045. doi:10.1016/j.nanoen.2013.04.002
82. Landmann, M.; Rauls, E.; Schmidt, W. G. *J. Phys.: Condens. Matter* **2012,** *24,* 195503. doi:10.1088/0953-8984/24/19/195503
83. Haggerty, J. E. S.; Schelhas, L. T.; Kitchaev, D. A.; Mangum, J. S.; Garten, L. M.; Sun, W.; Stone, K. H.; Perkins, J. D.; Toney, M. F.; Ceder, G.; Ginley, D. S.; Gorman, B. P.; Tate, J. *Sci. Rep.* **2017,** *7,* 15232. doi:10.1038/s41598-017-15364-y
84. Smith, A. M.; Nie, S. *Acc. Chem. Res.* **2010,** *43,* 190–200. doi:10.1021/ar9001069
85. Kowalska, E.; Wei, Z.; Janczarek, M. *Band-gap Engineering of Photocatalysts: Surface Modification versus Doping;* Wiley-VCH: Weinheim, Germany, 2018; pp 447–484. doi:10.1002/9783527808175.ch16
86. Hao, H.; Zhang, L.; Wang, W.; Zeng, S. *Catal. Sci. Technol.* **2018,** *8,* 1229–1250. doi:10.1039/c7cy01853c
87. Zhang, Y.; Wang, X.; Dong, P.; Huang, Z.; Nie, X.; Zhang, X. *Green Chem.* **2018,** *20,* 2084–2090. doi:10.1039/c7gc02963b

88. Friedmann, D.; Mendive, C.; Bahnemann, D. *Appl. Catal., B* **2010,** *99,* 398–406. doi:10.1016/j.apcatb.2010.05.014
89. Kisch, H. *Angew. Chem., Int. Ed.* **2013,** *52,* 812–847. doi:10.1002/anie.201201200
90. Serpone, N.; Lawless, D.; Khairutdinov, R.; Pelizzetti, E. *J. Phys. Chem.* **1995,** *99,* 16655–16661. doi:10.1021/j100045a027
91. Henderson, M. A. *Surf. Sci. Rep.* **2011,** *66,* 185–297. doi:10.1016/j.surfrep.2011.01.001
92. Henderson, M. A.; Epling, W. S.; Peden, C. H. F.; Perkins, C. L. *J. Phys. Chem. B* **2003,** *107,* 534–545. doi:10.1021/jp0262113
93. Nagao, M.; Suda, Y. *Langmuir* **1989,** *5,* 42–47. doi:10.1021/la00085a009
94. Zoller, J.; Fabry, D. C.; Rueping, M. *ACS Catal.* **2015,** *5,* 3900–3904. doi:10.1021/acscatal.5b00668
95. Gao, C.; Wang, J.; Xu, H.; Xiong, Y. *Chem. Soc. Rev.* **2017,** *46,* 2799–2823. doi:10.1039/c6cs00727a
96. Yuzawa, H.; Aoki, M.; Itoh, H.; Yoshida, H. *J. Phys. Chem. Lett.* **2011,** *2,* 1868–1873. doi:10.1021/jz200621w
97. Kosmulski, M. *Adv. Colloid Interface Sci.* **2009,** *152,* 14–25. doi:10.1016/j.cis.2009.08.003
98. Sahel, K.; Perol, N.; Chermette, H.; Bordes, C.; Derriche, Z.; Guillard, C. *Appl. Catal., B* **2007,** *77,* 100–109. doi:10.1016/j.apcatb.2007.06.016
99. Letheby, H. *J. Chem. Soc.* **1862,** *15,* 161–163. doi:10.1039/js8621500161
100. Rasmussen, S. C. *Substantia* **2017,** *1,* 99–109. doi:10.13128/substantia-30
101. Shirakawa, H.; Louis, E. J.; MacDiarmid, A. G.; Chiang, C. K.; Heeger, A. J. *J. Chem. Soc., Chem. Commun.* **1977,** 578–580. doi:10.1039/c39770000578
102. Inganäs, O. *Adv. Mater. (Weinheim, Ger.)* **2018,** *30,* 1800388. doi:10.1002/adma.201800388
103. Zou, M.; Ma, Y.; Yuan, X.; Hu, Y.; Liu, J.; Jin, Z. *J. Semicond.* **2018,** *39,* 011010. doi:10.1088/1674-4926/39/1/011010
104. Ostroverkhova, O. *Chem. Rev.* **2016,** *116,* 13279–13412. doi:10.1021/acs.chemrev.6b00127
105. Torsi, L.; Magliulo, M.; Manoli, K.; Palazzo, G. *Chem. Soc. Rev.* **2013,** *42,* 8612–8628. doi:10.1039/c3cs60127g
106. Yang, J.; Zhao, Z.; Wang, S.; Guo, Y.; Liu, Y. *Chem* **2018,** *4,* 2748–2785. doi:10.1016/j.chempr.2018.08.005
107. Merschjann, C.; Tschierlei, S.; Tyborski, T.; Kailasam, K.; Orthmann, S.; Hollmann, D.; Schedel-Niedrig, T.; Thomas, A.; Lochbrunner, S. *Adv. Mater. (Weinheim, Ger.)* **2015,** *27,* 7993–7999. doi:10.1002/adma.201503448
108. Liu, C.; Huang, K.; Park, W.-T.; Li, M.; Yang, T.; Liu, X.; Liang, L.; Minari, T.; Noh, Y.-Y. *Mater. Horiz.* **2017,** *4,* 608–618. doi:10.1039/c7mh00091j
109. Gregg, B. A.; Hanna, M. C. *J. Appl. Phys.* **2003,** *93,* 3605–3614. doi:10.1063/1.1544413
110. Armin, A.; Stoltzfus, D. M.; Donaghey, J. E.; Clulow, A. J.; Nagiri, R. C. R.; Burn, P. L.; Gentle, I. R.; Meredith, P. *J. Mater. Chem. C* **2017,** *5,* 3736–3747. doi:10.1039/c7tc00893g
111. Nguyen, T. P.; Tran, V. H. *Mater. Sci. Eng., B* **1995,** *31,* 255–260. doi:10.1016/0921-5107(94)01162-1
112. Zhao, X.-Y.; Liu, H.-J. *Polym. Int.* **2010,** *59,* 597–606. doi:10.1002/pi.2809
113. Volksen, W.; Miller, R. D.; Dubois, G. *Chem. Rev.* **2010,** *110,* 56–110. doi:10.1021/cr9002819
114. Brebels, J.; Manca, J. V.; Lutsen, L.; Vanderzande, D.; Maes, W. *J. Mater. Chem. A* **2017,** *5,* 24037–24050. doi:10.1039/c7ta06808e
115. Mikhnenko, O. V.; Blom, P. W. M.; Nguyen, T.-Q. *Energy Environ. Sci.* **2015,** *8,* 1867–1888. doi:10.1039/c5ee00925a
116. Nelson, J. *Mater. Today* **2011,** *14,* 462–470. doi:10.1016/s1369-7021(11)70210-3
117. Dennler, G.; Scharber, M. C.; Brabec, C. J. *Adv. Mater. (Weinheim, Ger.)* **2009,** *21,* 1323–1338. doi:10.1002/adma.200801283
118. Shoaee, S.; Deledalle, F.; Shakya Tuladhar, P.; Shivanna, R.; Rajaram, S.; Narayan, K. S.; Durrant, J. R. *J. Phys. Chem. Lett.* **2015,** *6,* 201–205. doi:10.1021/jz502385n
119. Liebig, J. *Ann. Pharm. (Lemgo, Ger.)* **1834,** *10,* 1–47. doi:10.1002/jlac.18340100102
120. Wang, X.; Maeda, K.; Thomas, A.; Takanabe, K.; Xin, G.; Carlsson, J. M.; Domen, K.; Antonietti, M. *Nat. Mater.* **2009,** *8,* 76–80. doi:10.1038/nmat2317
121. Zhang, Y.; Thomas, A.; Antonietti, M.; Wang, X. *J. Am. Chem. Soc.* **2009,** *131,* 50–51. doi:10.1021/ja808329f
122. Yanagida, S.; Kabumoto, A.; Mizumoto, K.; Pac, C.; Yoshino, K. *J. Chem. Soc., Chem. Commun.* **1985,** 474–475. doi:10.1039/c39850000474
123. Kailasam, K.; Epping, J. D.; Thomas, A.; Losse, S.; Junge, H. *Energy Environ. Sci.* **2011,** *4,* 4668–4674. doi:10.1039/c1ee02165f
124. Liu, J.; Liu, Y.; Liu, N.; Han, Y.; Zhang, X.; Huang, H.; Lifshitz, Y.; Lee, S.-T.; Zhong, J.; Kang, Z. *Science* **2015,** *347,* 970–974. doi:10.1126/science.aaa3145
125. Shalom, M.; Inal, S.; Neher, D.; Antonietti, M. *Catal. Today* **2014,** *225,* 185–190. doi:10.1016/j.cattod.2013.12.013
126. Shalom, M.; Guttentag, M.; Fettkenhauer, C.; Inal, S.; Neher, D.; Llobet, A.; Antonietti, M. *Chem. Mater.* **2014,** *26,* 5812–5818. doi:10.1021/cm503258z
127. Lublow, M.; Fischer, A.; Merschjann, C.; Yang, F.; Schedel-Niedrig, T.; Veyan, J.-F.; Chabal, Y. J. *J. Mater. Chem. A* **2014,** *2,* 12697–12702. doi:10.1039/c4ta01711k
128. Ghosh, I.; Khamrai, J.; Savateev, A.; Shlapakov, N.; Antonietti, M.; König, B. *Science* **2019,** *365,* 360–366. doi:10.1126/science.aaw3254
129. Lan, Z.-A.; Zhang, G.; Chen, X.; Zhang, Y.; Zhang, K. A. I.; Wang, X. *Angew. Chem., Int. Ed.* **2019,** *58,* 10236–10240. doi:10.1002/anie.201904904
130. Ji, S.; Ge, J.; Escudero, D.; Wang, Z.; Zhao, J.; Jacquemin, D. *J. Org. Chem.* **2015,** *80,* 5958–5963. doi:10.1021/acs.joc.5b00691
131. Tobin, J. M.; Liu, J.; Hayes, H.; Demleitner, M.; Ellis, D.; Arrighi, V.; Xu, Z.; Vilela, F. *Polym. Chem.* **2016,** *7,* 6662–6670. doi:10.1039/c6py01393g
132. Amara, Z.; Bellamy, J. F. B.; Horvath, R.; Miller, S. J.; Beeby, A.; Burgard, A.; Rossen, K.; Poliakoff, M.; George, M. W. *Nat. Chem.* **2015,** *7,* 489–495. doi:10.1038/nchem.2261
133. Ribeiro, S.; Serra, A. C.; Rocha Gonsalves, A. M. d. A. *ChemCatChem* **2013,** *5,* 134–137. doi:10.1002/cctc.201200532
134. Johnson Inbaraj, J.; Vinodu, M. V.; Gandhidasan, R.; Murugesan, R.; Padmanabhan, M. *J. Appl. Polym. Sci.* **2003,** *89,* 3925–3930. doi:10.1002/app.12610
135. Griesbeck, A. G.; El-Idreesy, T. T.; Bartoschek, A. *Adv. Synth. Catal.* **2004,** *346,* 245–251. doi:10.1002/adsc.200303181
136. Ribeiro, S. M.; Serra, A. C.; Rocha Gonsalves, A. M. d. A. *J. Catal.* **2008,** *256,* 331–337. doi:10.1016/j.jcat.2008.04.001
137. Tambosco, B.; Segura, K.; Seyrig, C.; Cabrera, D.; Port, M.; Ferroud, C.; Amara, Z. *ACS Catal.* **2018,** *8,* 4383–4389. doi:10.1021/acscatal.8b00890
138. Wang, J.-L.; Wang, C.; deKrafft, K. E.; Lin, W. *ACS Catal.* **2012,** *2,* 417–424. doi:10.1021/cs300027n

139. Ferguson, C. T. J.; Huber, N.; Kuckhoff, T.; Zhang, K. A. I.; Landfester, K. *J. Mater. Chem. A* **2020,** *8,* 1072–1076. doi:10.1039/c9ta11242a
140. Burek, B. O.; Sutor, A.; Bahnemann, D. W.; Bloh, J. Z. *Catal. Sci. Technol.* **2017,** *7,* 4977–4983. doi:10.1039/c7cy01537b
141. Konstantas, G.; Stamatelos, A. M. *Proc. Inst. Mech. Eng., Part D* **2007,** *221,* 355–373. doi:10.1243/09544070jauto329
142. Putrasari, Y.; Untoro, P.; Hasan, S.; Huda, N.; Sebayang, D. *J. Mechatronics, Electr. Power, Veh. Technol.* **2012,** *1,* 53–60.
143. Kang, H.; Lee, C.-S.; Kim, D.-Y.; Kim, J.; Choi, W.; Kim, H. *Appl. Catal., B* **2011,** *104,* 6–11. doi:10.1016/j.apcatb.2011.03.010
144. Fernández, A.; Lassaletta, G.; Jiménez, V. M.; Justo, A.; González-Elipe, A. R.; Herrmann, J.-M.; Tahiri, H.; Ait-Ichou, Y. *Appl. Catal., B* **1995,** *7,* 49–63. doi:10.1016/0926-3373(95)00026-7
145. Maury, F.; Mungkalasiri, J. *Key Eng. Mater.* **2009,** *415,* 1–4. doi:10.4028/www.scientific.net/kem.415.1
146. de Sousa, R. R. M.; de Araújo, F. O.; da Costa, J. A. P.; Nishimoto, A.; Viana, B. C.; Alves, C., Jr. *Mater. Res. (Sao Carlos, Braz.)* **2016,** *19,* 1207–1212. doi:10.1590/1980-5373-mr-2015-0358
147. Wang, B.; de Godoi, F. C.; Sun, Z.; Zeng, Q.; Zheng, S.; Frost, R. L. *J. Colloid Interface Sci.* **2015,** *438,* 204–211. doi:10.1016/j.jcis.2014.09.064
148. Dong, Y.; Tang, D.; Li, C. *Appl. Surf. Sci.* **2014,** *296,* 1–7. doi:10.1016/j.apsusc.2013.12.128
149. Hench, L. L.; West, J. K. *Chem. Rev.* **1990,** *90,* 33–72. doi:10.1021/cr00099a003
150. Miranda-García, N.; Suárez, S.; Maldonado, M. I.; Malato, S.; Sánchez, B. *Catal. Today* **2014,** *230,* 27–34. doi:10.1016/j.cattod.2013.12.048
151. McTiernan, C. D.; Pitre, S. P.; Ismaili, H.; Scaiano, J. C. *Adv. Synth. Catal.* **2014,** *356,* 2819–2824. doi:10.1002/adsc.201400547
152. Xu, X.; Zhou, X.; Li, X.; Yang, F.; Jin, B.; Xu, T.; Li, G.; Li, M. *Mater. Res. Bull.* **2014,** *59,* 32–36. doi:10.1016/j.materresbull.2014.06.025
153. Ray, S.; Lalman, J. A. *Mater. Today: Proc.* **2016,** *3,* 1582–1591. doi:10.1016/j.matpr.2016.04.046
154. Wenderich, K.; Mul, G. *Chem. Rev.* **2016,** *116,* 14587–14619. doi:10.1021/acs.chemrev.6b00327
155. Srikanth, B.; Goutham, R.; Badri Narayan, R.; Ramprasath, A.; Gopinath, K. P.; Sankaranarayanan, A. R. *J. Environ. Manage.* **2017,** *200,* 60–78. doi:10.1016/j.jenvman.2017.05.063
156. Jansson, I.; Yoshiiri, K.; Hori, H.; García-García, F. J.; Rojas, S.; Sánchez, B.; Ohtani, B.; Suárez, S. *Appl. Catal., A* **2016,** *521,* 208–219. doi:10.1016/j.apcata.2015.12.015
157. Hodgson, G. K.; Scaiano, J. C. *ACS Catal.* **2018,** *8,* 2914–2922. doi:10.1021/acscatal.7b04032
158. Magdziarz, A.; Colmenares, J. *Molecules* **2017,** *22,* 216. doi:10.3390/molecules22020216
159. Magdziarz, A.; Colmenares, J. C.; Chernyayeva, O.; Łomot, D.; Sobczak, K. *J. Mol. Catal. A: Chem.* **2016,** *425,* 1–9. doi:10.1016/j.molcata.2016.09.021
160. Colmenares, J. C.; Lisowski, P.; Łomot, D.; Chernyayeva, O.; Lisovytskiy, D. *ChemSusChem* **2015,** *8,* 1676–1685. doi:10.1002/cssc.201403125
161. Magdziarz, A.; Colmenares, J. C.; Chernyayeva, O.; Kurzydłowski, K.; Grzonka, J. *ChemCatChem* **2016,** *8,* 536–539. doi:10.1002/cctc.201501250
162. Meng, S.; Ning, X.; Chang, S.; Fu, X.; Ye, X.; Chen, S. *J. Catal.* **2018,** *357,* 247–256. doi:10.1016/j.jcat.2017.11.015
163. Long, D.-L.; Tsunashima, R.; Cronin, L. *Angew. Chem., Int. Ed.* **2010,** *49,* 1736–1758. doi:10.1002/anie.200902483
164. Pope, M. T.; Müller, A. *Angew. Chem., Int. Ed. Engl.* **1991,** *30,* 34–48. doi:10.1002/anie.199100341
165. Li, J.; Gao, X.; Liu, B.; Feng, Q.; Li, X.-B.; Huang, M.-Y.; Liu, Z.; Zhang, J.; Tung, C.-H.; Wu, L.-Z. *J. Am. Chem. Soc.* **2016,** *138,* 3954–3957. doi:10.1021/jacs.5b12758
166. Han, Y.; Huang, H.; Zhang, H.; Liu, Y.; Han, X.; Liu, R.; Li, H.; Kang, Z. *ACS Catal.* **2014,** *4,* 781–787. doi:10.1021/cs401118x
167. Ipe, B. I.; Niemeyer, C. M. *Angew. Chem., Int. Ed.* **2006,** *45,* 504–507. doi:10.1002/anie.200503084
168. Fabregat, V.; Burguete, M. I.; Luis, S. V.; Galindo, F. *RSC Adv.* **2017,** *7,* 35154–35158. doi:10.1039/c7ra06036j
169. Hoffmann, M. R.; Martin, S. T.; Choi, W.; Bahnemann, D. W. *Chem. Rev.* **1995,** *95,* 69–96. doi:10.1021/cr00033a004
170. Abdullah, H.; Khan, M. M. R.; Ong, H. R.; Yaakob, Z. *J. CO2 Util.* **2017,** *22,* 15–32. doi:10.1016/j.jcou.2017.08.004
171. Dai, C.; Liu, B. *Energy Environ. Sci.* **2020,** *13,* 24–52. doi:10.1039/c9ee01935a
172. Fu, Y.; Zhu, X.; Huang, L.; Zhang, X.; Zhang, F.; Zhu, W. *Appl. Catal., B* **2018,** *239,* 46–51. doi:10.1016/j.apcatb.2018.08.004
173. Lin, S.; Hou, Y.; Deng, X.; Wang, H.; Sun, S.; Zhang, X. *RSC Adv.* **2015,** *5,* 41017–41024. doi:10.1039/c5ra04433b
174. Meier, C. B.; Sprick, R. S.; Monti, A.; Guiglion, P.; Lee, J.-S. M.; Zwijnenburg, M. A.; Cooper, A. I. *Polymer* **2017,** *126,* 283–290. doi:10.1016/j.polymer.2017.04.017
175. Liu, T.; Hu, X.; Wang, Y.; Meng, L.; Zhou, Y.; Zhang, J.; Chen, M.; Zhang, X. *J. Photochem. Photobiol., B* **2017,** *175,* 156–162. doi:10.1016/j.jphotobiol.2017.07.013
176. Huang, Y.-B.; Liang, J.; Wang, X.-S.; Cao, R. *Chem. Soc. Rev.* **2017,** *46,* 126–157. doi:10.1039/c6cs00250a
177. Liu, Y.; Howarth, A. J.; Hupp, J. T.; Farha, O. K. *Angew. Chem., Int. Ed.* **2015,** *54,* 9001–9005. doi:10.1002/anie.201503741
178. Zeng, L.; Guo, X.; He, C.; Duan, C. *ACS Catal.* **2016,** *6,* 7935–7947. doi:10.1021/acscatal.6b02228
179. Xia, Z.; He, C.; Wang, X.; Duan, C. *Nat. Commun.* **2017,** *8,* 361. doi:10.1038/s41467-017-00416-8
180. Fateeva, A.; Chater, P. A.; Ireland, C. P.; Tahir, A. A.; Khimyak, Y. Z.; Wiper, P. V.; Darwent, J. R.; Rosseinsky, M. J. *Angew. Chem., Int. Ed.* **2012,** *51,* 7440–7444. doi:10.1002/anie.201202471
181. Agrawal, A.; Cho, S. H.; Zandi, O.; Ghosh, S.; Johns, R. W.; Milliron, D. J. *Chem. Rev.* **2018,** *118,* 3121–3207. doi:10.1021/acs.chemrev.7b00613
182. Wu, N. *Nanoscale* **2018,** *10,* 2679–2696. doi:10.1039/c7nr08487k
183. Faucheaux, J. A.; Stanton, A. L. D.; Jain, P. K. *J. Phys. Chem. Lett.* **2014,** *5,* 976–985. doi:10.1021/jz500037k
184. Tsukamoto, D.; Shiraishi, Y.; Sugano, Y.; Ichikawa, S.; Tanaka, S.; Hirai, T. *J. Am. Chem. Soc.* **2012,** *134,* 6309–6315. doi:10.1021/ja2120647
185. Lu, X.; Rycenga, M.; Skrabalak, S. E.; Wiley, B.; Xia, Y. *Annu. Rev. Phys. Chem.* **2009,** *60,* 167–192. doi:10.1146/annurev.physchem.040808.090434
186. Ma, X.; Dai, Y.; Yu, L.; Huang, B. *Sci. Rep.* **2015,** *4,* 3986. doi:10.1038/srep03986
187. Linic, S.; Christopher, P.; Ingram, D. B. *Nat. Mater.* **2011,** *10,* 911–921. doi:10.1038/nmat3151

188. Peiris, S.; McMurtrie, J.; Zhu, H.-Y. *Catal. Sci. Technol.* **2016,** *6,* 320–338. doi:10.1039/c5cy02048d
189. Gogoi, N.; Borah, G.; Gogoi, P. K.; Chetia, T. R. *Chem. Phys. Lett.* **2018,** *692,* 224–231. doi:10.1016/j.cplett.2017.12.015
190. Beydoun, D.; Amal, R.; Low, G.; McEvoy, S. *J. Nanopart. Res.* **1999,** *1,* 439–458. doi:10.1023/a:1010044830871
191. Vallavoju, N.; Sivaguru, J. *Chem. Soc. Rev.* **2014,** *43,* 4084. doi:10.1039/c3cs60471c
192. Wei, W.; Zhu, Y. *Small* **2019,** *15,* 1903933. doi:10.1002/smll.201903933
193. Zeng, L.; Liu, T.; He, C.; Shi, D.; Zhang, F.; Duan, C. *J. Am. Chem. Soc.* **2016,** *138,* 3958–3961. doi:10.1021/jacs.5b12931
194. Kong, K.; Zhang, S.; Chu, Y.; Hu, Y.; Yu, F.; Ye, H.; Ding, H.; Hua, J. *Chem. Commun.* **2019,** *55,* 8090–8093. doi:10.1039/c9cc03465j
195. Tada, H.; Mitsui, T.; Kiyonaga, T.; Akita, T.; Tanaka, K. *Nat. Mater.* **2006,** *5,* 782–786. doi:10.1038/nmat1734
196. Xu, C.; Ravi Anusuyadevi, P.; Aymonier, C.; Luque, R.; Marre, S. *Chem. Soc. Rev.* **2019,** *48,* 3868–3902. doi:10.1039/c9cs00102f
197. Sharman, W. M.; Allen, C. M.; van Lier, J. E. *Drug Discovery Today* **1999,** *4,* 507–517. doi:10.1016/s1359-6446(99)01412-9
198. Castano, A. P.; Mroz, P.; Hamblin, M. R. *Nat. Rev. Cancer* **2006,** *6,* 535–545. doi:10.1038/nrc1894
199. Kamkaew, A.; Lim, S. H.; Lee, H. B.; Kiew, L. V.; Chung, L. Y.; Burgess, K. *Chem. Soc. Rev.* **2013,** *42,* 77–88. doi:10.1039/c2cs35216h
200. Cui, C.; Tou, M.; Li, M.; Luo, Z.; Xiao, L.; Bai, S.; Li, Z. *Inorg. Chem.* **2017,** *56,* 2328–2336. doi:10.1021/acs.inorgchem.6b03079
201. Wang, L.; Cui, D.; Ren, L.; Zhou, J.; Wang, F.; Casillas, G.; Xu, X.; Peleckis, G.; Hao, W.; Ye, J.; Dou, S. X.; Jin, D.; Du, Y. *J. Mater. Chem. A* **2019,** *7,* 13629–13634. doi:10.1039/c9ta02780g
202. Jašo, S.; Arellano-Garcia, H.; Wozny, G. *Comput.-Aided Chem. Eng.* **2011,** *29,* 377–381. doi:10.1016/b978-0-444-53711-9.50076-6
203. Stünkel, S.; Bittig, K.; Godini, H.-R.; Jaso, S.; Martini, W.; Arellano-Garcia, H.; Wozny, G. *Comput.-Aided Chem. Eng.* **2012,** *31,* 1692–1696. doi:10.1016/b978-0-444-59506-5.50169-3
204. Jakobsen, H. A. Packed Bed Reactors. *Chemical Reactor Modeling;* Springer: Berlin, Heidelberg, Germany, 2009; pp 953–984. doi:10.1007/978-3-540-68622-4_11
205. Fixed bed and other types of reactors. In *Process Systems Engineering;* Ranade, V. V., Ed.; Academic Press: Cambridge, MA, USA, 2002; Vol. 5, pp 403–423. doi:10.1016/s1874-5970(02)80014-5
206. Su, Y.; Straathof, N. J. W.; Hessel, V.; Noël, T. *Chem. – Eur. J.* **2014,** *20,* 10562–10589. doi:10.1002/chem.201400283
207. Pieber, B.; Shalom, M.; Antonietti, M.; Seeberger, P. H.; Gilmore, K. *Angew. Chem., Int. Ed.* **2018,** *57,* 9976–9979. doi:10.1002/anie.201712568
208. Cai, Y.; Tang, Y.; Fan, L.; Lefebvre, Q.; Hou, H.; Rueping, M. *ACS Catal.* **2018,** *8,* 9471–9476. doi:10.1021/acscatal.8b02937
209. Bottecchia, C.; Erdmann, N.; Tijssen, P. M. A.; Milroy, L.-G.; Brunsveld, L.; Hessel, V.; Noël, T. *ChemSusChem* **2016,** *9,* 1781–1785. doi:10.1002/cssc.201600602
210. Colmenares, J. C.; Varma, R. S.; Nair, V. *Chem. Soc. Rev.* **2017,** *46,* 6675–6686. doi:10.1039/c7cs00257b
211. Rashmi Pradhan, S.; Colmenares-Quintero, R. F.; Colmenares Quintero, J. C. *Molecules* **2019,** *24,* 3315. doi:10.3390/molecules24183315
212. Coyle, E. E.; Oelgemöller, M. *Photochem. Photobiol. Sci.* **2008,** *7,* 1313–1322. doi:10.1039/b808778d
213. Matsushita, Y.; Ohba, N.; Kumada, S.; Suzuki, T.; Ichimura, T. *Catal. Commun.* **2007,** *8,* 2194–2197. doi:10.1016/j.catcom.2007.04.033
214. Li, D.; Xiong, K.; Shi, K.; Yang, Z.; Liu, C.; Feng, X.; Lu, X. *Green Chem.* **2011,** *13,* 1784–1790. doi:10.1039/c1gc15082k
215. Díez, A. M.; Moreira, F. C.; Marinho, B. A.; Espíndola, J. C. A.; Paulista, L. O.; Sanromán, M. A.; Pazos, M.; Boaventura, R. A. R.; Vilar, V. J. P. *Chem. Eng. J.* **2018,** *343,* 597–606. doi:10.1016/j.cej.2018.03.041
216. Li, D.; Xiong, K.; Yang, Z.; Liu, C.; Feng, X.; Lu, X. *Catal. Today* **2011,** *175,* 322–327. doi:10.1016/j.cattod.2011.04.007
217. Boyle, C.; Skillen, N.; Stella, L.; Robertson, P. K. J. *Ind. Eng. Chem. Res.* **2019,** *58,* 2727–2740. doi:10.1021/acs.iecr.8b05709
218. Hartman, R. L. *Org. Process Res. Dev.* **2012,** *16,* 870–887. doi:10.1021/op200348t
219. Hedstrand, D. M.; Kruizinga, W. H.; Kellogg, R. M. *Tetrahedron Lett.* **1978,** *19,* 1255–1258. doi:10.1016/s0040-4039(01)94515-0
220. van Bergen, T. J.; Hedstrand, D. M.; Kruizinga, W. H.; Kellogg, R. M. *J. Org. Chem.* **1979,** *44,* 4953–4962. doi:10.1021/jo00394a044
221. Cano-Yelo, H.; Deronzier, A. *Tetrahedron Lett.* **1984,** *25,* 5517–5520. doi:10.1016/s0040-4039(01)81614-2
222. Sammes, P. G. *Q. Rev., Chem. Soc.* **1970,** *24,* 37–68. doi:10.1039/qr9702400037
223. Ishitani, O.; Yanagida, S.; Takamuku, S.; Pac, C. *J. Org. Chem.* **1987,** *52,* 2790–2796. doi:10.1021/jo00389a027
224. Pac, C.; Miyauchi, Y.; Ishitani, O.; Ihama, M.; Yasuda, M.; Sakurai, H. *J. Org. Chem.* **1984,** *49,* 26–34. doi:10.1021/jo00175a006
225. Ishitani, O.; Pac, C.; Sakurai, H. *J. Org. Chem.* **1983,** *48,* 2941–2942. doi:10.1021/jo00165a037
226. Pac, C.; Ihama, M.; Yasuda, M.; Miyauchi, Y.; Sakurai, H. *J. Am. Chem. Soc.* **1981,** *103,* 6495–6497. doi:10.1021/ja00411a040
227. Okada, K.; Okamoto, K.; Morita, N.; Okubo, K.; Oda, M. *J. Am. Chem. Soc.* **1991,** *113,* 9401–9402. doi:10.1021/ja00024a074
228. Fukuzumi, S.; Mochizuki, S.; Tanaka, T. *J. Phys. Chem.* **1990,** *94,* 722–726. doi:10.1021/j100365a039
229. Fukuzumi, S.; Koumitsu, S.; Hironaka, K.; Tanaka, T. *J. Am. Chem. Soc.* **1987,** *109,* 305–316. doi:10.1021/ja00236a003
230. The lighter way to enjoy synthesis. https://www.chemistryworld.com/features/photoredox-charge-of-the-led-brigade/3007944.article (accessed Feb 27, 2020).
231. *Nat. Photonics* **2007,** *1,* 23. doi:10.1038/nphoton.2006.78
232. Arias-Rotondo, D. M.; McCusker, J. K. *Chem. Soc. Rev.* **2016,** *45,* 5803–5820. doi:10.1039/c6cs00526h
233. Roth, H.; Romero, N.; Nicewicz, D. *Synlett* **2015,** *27,* 714–723. doi:10.1055/s-0035-1561297
234. Ventre, S.; Petronijevic, F. R.; MacMillan, D. W. C. *J. Am. Chem. Soc.* **2015,** *137,* 5654–5657. doi:10.1021/jacs.5b02244
235. Tarantino, G.; Hammond, C. *ACS Catal.* **2018,** *8,* 10321–10330. doi:10.1021/acscatal.8b02844
236. Rueda-Becerril, M.; Mahé, O.; Drouin, M.; Majewski, M. B.; West, J. G.; Wolf, M. O.; Sammis, G. M.; Paquin, J.-F. *J. Am. Chem. Soc.* **2014,** *136,* 2637–2641. doi:10.1021/ja412083f
237. Woźnica, M.; Chaoui, N.; Taabache, S.; Blechert, S. *Chem. – Eur. J.* **2014,** *20,* 14624–14628. doi:10.1002/chem.201404440
238. Tucker, J. W.; Nguyen, J. D.; Narayanam, J. M. R.; Krabbe, S. W.; Stephenson, C. R. J. *Chem. Commun.* **2010,** *46,* 4985–4987. doi:10.1039/c0cc00981d
239. Ohtani, B.; Osaki, H.; Nishimoto, S.; Kagiya, T. *J. Am. Chem. Soc.* **1986,** *108,* 308–310. doi:10.1021/ja00262a028

240. Takei, G.; Kitamori, T.; Kim, H. B. *Catal. Commun.* **2005,** *6,* 357–360. doi:10.1016/j.catcom.2005.02.010
241. Ohtani, B.; Pal, B.; Ikeda, S. *Catal. Surv. Asia* **2003,** *7,* 165–176. doi:10.1023/a:1025389725637
242. Zou, Y.-Q.; Chen, J.-R.; Liu, X.-P.; Lu, L.-Q.; Davis, R. L.; Jørgensen, K. A.; Xiao, W.-J. *Angew. Chem., Int. Ed.* **2012,** *51,* 784–788. doi:10.1002/anie.201107028
243. Zhi, Y.; Ma, S.; Xia, H.; Zhang, Y.; Shi, Z.; Mu, Y.; Liu, X. *Appl. Catal., B* **2019,** *244,* 36–44. doi:10.1016/j.apcatb.2018.11.032
244. Baghbanzadeh, M.; Glasnov, T. N.; Kappe, C. O. *J. Flow Chem.* **2013,** *3,* 109–113. doi:10.1556/jfc-d-13-00018
245. Ju, X.; Li, D.; Li, W.; Yu, W.; Bian, F. *Adv. Synth. Catal.* **2012,** *354,* 3561–3567. doi:10.1002/adsc.201200608
246. Talla, A.; Driessen, B.; Straathof, N. J. W.; Milroy, L.-G.; Brunsveld, L.; Hessel, V.; Noël, T. *Adv. Synth. Catal.* **2015,** *357,* 2180–2186. doi:10.1002/adsc.201401010
247. Ciambelli, P.; Sannino, D.; Palma, V.; Vaiano, V. *Catal. Today* **2005,** *99,* 143–149. doi:10.1016/j.cattod.2004.09.034
248. Fabry, D. C.; Ho, Y. A.; Zapf, R.; Tremel, W.; Panthöfer, M.; Rueping, M.; Rehm, T. H. *Green Chem.* **2017,** *19,* 1911–1918. doi:10.1039/c7gc00497d
249. Xiao, R.; Tobin, J. M.; Zha, M.; Hou, Y.-L.; He, J.; Vilela, F.; Xu, Z. *J. Mater. Chem. A* **2017,** *5,* 20180–20187. doi:10.1039/c7ta05534j
250. Iqbal, N.; Cho, E. J. *Adv. Synth. Catal.* **2015,** *357,* 2187–2192. doi:10.1002/adsc.201500257
251. Yu, C.; Lee, K.; You, Y.; Cho, E. J. *Adv. Synth. Catal.* **2013,** *355,* 1471–1476. doi:10.1002/adsc.201300376
252. Jeong, D.-C.; Lee, J.; Ro, Y. H.; Song, C. *Polym. Chem.* **2017,** *8,* 1923–1931. doi:10.1039/c7py00095b
253. Lang, X.; Ji, H.; Chen, C.; Ma, W.; Zhao, J. *Angew. Chem., Int. Ed.* **2011,** *50,* 3934–3937. doi:10.1002/anie.201007056
254. Nair, V.; Colmenares, J. C.; Lisovytskiy, D. *Green Chem.* **2019,** *21,* 1241–1246. doi:10.1039/c8gc03131b
255. Pradhan, S. R.; Nair, V.; Giannakoudakis, D. A.; Lisovytskiy, D.; Colmenares, J. C. *Mol. Catal.* **2020,** *486,* 110884. doi:10.1016/j.mcat.2020.110884
256. Scholes, G. D. *Annu. Rev. Phys. Chem.* **2003,** *54,* 57–87. doi:10.1146/annurev.physchem.54.011002.103746
257. Sahoo, H. *J. Photochem. Photobiol., C* **2011,** *12,* 20–30. doi:10.1016/j.jphotochemrev.2011.05.001
258. Strieth-Kalthoff, F.; James, M. J.; Teders, M.; Pitzer, L.; Glorius, F. *Chem. Soc. Rev.* **2018,** *47,* 7190–7202. doi:10.1039/c8cs00054a
259. Albini, A. *Synthesis* **1981,** 249–264. doi:10.1055/s-1981-29405
260. Fabry, D. C.; Ronge, M. A.; Rueping, M. *Chem. – Eur. J.* **2015,** *21,* 5350–5354. doi:10.1002/chem.201406653
261. DeRosa, M. C.; Crutchley, R. J. *Coord. Chem. Rev.* **2002,** *233–234,* 351–371. doi:10.1016/s0010-8545(02)00034-6
262. Margaros, I.; Montagnon, T.; Tofi, M.; Pavlakos, E.; Vassilikogiannakis, G. *Tetrahedron* **2006,** *62,* 5308–5317. doi:10.1016/j.tet.2006.01.110
263. Ghogare, A. A.; Greer, A. *Chem. Rev.* **2016,** *116,* 9994–10034. doi:10.1021/acs.chemrev.5b00726
264. Kopetzki, D.; Lévesque, F.; Seeberger, P. H. *Chem. – Eur. J.* **2013,** *19,* 5450–5456. doi:10.1002/chem.201204558
265. Schneider, F.; Samarin, K.; Zanella, S.; Gaich, T. *Science* **2020,** *367,* 676–681. doi:10.1126/science.aay9173
266. Chemists complete synthesis of molecule 'at the limits of complexity'. https://www.chemistryworld.com/news/chemists-complete-synthesis-of-molecule-at-the-limits-of-complexity/4011165.article (accessed Feb 14, 2020).
267. Zhang, K.; Kopetzki, D.; Seeberger, P. H.; Antonietti, M.; Vilela, F. *Angew. Chem., Int. Ed.* **2013,** *52,* 1432–1436. doi:10.1002/anie.201207163
268. Griesbeck, A. G.; de Kiff, A.; Neudörfl, J. M.; Sillner, S. *ARKIVOC* **2015,** No. iii, 101–110. doi:10.3998/ark.5550190.p008.994
269. Shen, J.; Steinbach, R.; Tobin, J. M.; Mouro Nakata, M.; Bower, M.; McCoustra, M. R. S.; Bridle, H.; Arrighi, V.; Vilela, F. *Appl. Catal., B* **2016,** *193,* 226–233. doi:10.1016/j.apcatb.2016.04.015
270. Bourne, R. A.; Han, X.; Poliakoff, M.; George, M. W. *Angew. Chem., Int. Ed.* **2009,** *48,* 5322–5325. doi:10.1002/anie.200901731
271. Han, X.; Bourne, R. A.; Poliakoff, M.; George, M. W. *Chem. Sci.* **2011,** *2,* 1059–1067. doi:10.1039/c0sc00641f
272. Hall, J. F. B.; Han, X.; Poliakoff, M.; Bourne, R. A.; George, M. W. *Chem. Commun.* **2012,** *48,* 3073–3075. doi:10.1039/c2cc17429d
273. Clennan, E. L. *Tetrahedron* **2000,** *56,* 9151–9179. doi:10.1016/s0040-4020(00)00794-8
274. Poliakoff, M. Towards Greener Photochemistry, presented at a Royal Society of Chemistry Lecture, March 2018, Edinburgh, U.K.
275. Symes, M. D.; Kitson, P. J.; Yan, J.; Richmond, C. J.; Cooper, G. J. T.; Bowman, R. W.; Vilbrandt, T.; Cronin, L. *Nat. Chem.* **2012,** *4,* 349–354. doi:10.1038/nchem.1313
276. Kitson, P. J.; Symes, M. D.; Dragone, V.; Cronin, L. *Chem. Sci.* **2013,** *4,* 3099–3103. doi:10.1039/c3sc51253c
277. Kitson, P. J.; Marie, G.; Francoia, J.-P.; Zalesskiy, S. S.; Sigerson, R. C.; Mathieson, J. S.; Cronin, L. *Science* **2018,** *359,* 314–319. doi:10.1126/science.aao3466
278. Zhakeyev, A.; Tobin, J.; Wang, H.; Vilela, F.; Xuan, J. *Energy Procedia* **2019,** *158,* 5608–5614. doi:10.1016/j.egypro.2019.01.579
279. Schweitzer, C.; Schmidt, R. *Chem. Rev.* **2003,** *103,* 1685–1758. doi:10.1021/cr010371d
280. Navio, J. A.; Fuentes Mota, J.; Pradera Adrian, M. A.; Garcia Gomez, M. *J. Photochem. Photobiol., A* **1990,** *52,* 91–95. doi:10.1016/1010-6030(90)87094-r
281. WWAP (UNESCO World Water Assessment Progxram), The United Nations World Water Development Report 2019: Leaving No One Behind, 2019, Paris, France.. https://unesdoc.unesco.org/ark:/48223/pf0000367306 (accessed March 16, 2020).
282. Kacem, M.; Plantard, G.; Brienza, M.; Goetz, V. *Ind. Eng. Chem. Res.* **2017,** *56,* 15001–15007. doi:10.1021/acs.iecr.7b03644
283. Dalrymple, O. K. Mechanistic Modeling of Photocatalytic Water Disinfection. Graduate Thesis, University of South Florida, FL, 2011.
284. Park, H.; Choi, W. *J. Phys. Chem. B* **2004,** *108,* 4086–4093. doi:10.1021/jp036735i
285. Ilisz, I.; László, Z.; Dombi, A. *Appl. Catal., A* **1999,** *180,* 25–33. doi:10.1016/s0926-860x(98)00355-x
286. Ma, C. M.; Shen, Y. S.; Lin, P. H. *Int. J. Photoenergy* **2012,** 1–7. doi:10.1155/2012/381971
287. Chen, Y.; Yang, S.; Wang, K.; Lou, L. *J. Photochem. Photobiol., A* **2005,** *172,* 47–54. doi:10.1016/j.jphotochem.2004.11.006
288. Homem, V.; Santos, L. *J. Environ. Manage.* **2011,** *92,* 2304–2347. doi:10.1016/j.jenvman.2011.05.023
289. Ameta, R.; Chohadia, A. K.; Jain, A.; Punjabi, P. B. Fenton and Photo-Fenton Processes. In *Advanced Oxidation Processes for Waste Water Treatment;* Ameta, S. C.; Ameta, R., Eds.; Elsevier: Amsterdam, Netherlands, 2018; pp 49–87.

290. Garza-Campos, B.; Brillas, E.; Hernández-Ramírez, A.; El-Ghenymy, A.; Guzmán-Mar, J. L.; Ruiz-Ruiz, E. J. *J. Hazard. Mater.* **2016,** *319,* 34–42. doi:10.1016/j.jhazmat.2016.02.050
291. Bu, Q.; Wang, B.; Huang, J.; Deng, S.; Yu, G. *J. Hazard. Mater.* **2013,** *262,* 189–211. doi:10.1016/j.jhazmat.2013.08.040
292. Tauxe-Wuersch, A.; De Alencastro, L. F.; Grandjean, D.; Tarradellas, J. *Water Res.* **2005,** *39,* 1761–1772. doi:10.1016/j.watres.2005.03.003
293. Miège, C.; Choubert, J. M.; Ribeiro, L.; Eusèbe, M.; Coquery, M. *Environ. Pollut.* **2009,** *157,* 1721–1726. doi:10.1016/j.envpol.2008.11.045
294. Health Effects Institute State of Global Air 2019, 2019, Boston, MA. http://www.stateofglobalair.org/sites/default/files/soga_2019_report.pdf (accessed April 16, 2020).
295. Mothes, F.; Ifang, S.; Gallus, M.; Golly, B.; Boréave, A.; Kurtenbach, R.; Kleffmann, J.; George, C.; Herrmann, H. *Appl. Catal., B* **2018,** *231,* 161–172. doi:10.1016/j.apcatb.2018.03.010
296. da Costa Filho, B. M.; Araujo, A. L. P.; Silva, G. V.; Boaventura, R. A. R.; Dias, M. M.; Lopes, J. C. B.; Vilar, V. J. P. *Chem. Eng. J.* **2017,** *310,* 331–341. doi:10.1016/j.cej.2016.09.080
297. Laranjeira, P. E.; Martins, A. A.; Lopes, J. C. B.; Dias, M. M. *AIChE J.* **2009,** *55,* 2226–2243. doi:10.1002/aic.11815

License and Terms

This is an Open Access article under the terms of the Creative Commons Attribution License (http://creativecommons.org/licenses/by/4.0). Please note that the reuse, redistribution and reproduction in particular requires that the authors and source are credited.

The license is subject to the *Beilstein Journal of Organic Chemistry* terms and conditions: (https://www.beilstein-journals.org/bjoc)

The definitive version of this article is the electronic one which can be found at: doi:10.3762/bjoc.16.125

BEILSTEIN JOURNAL OF ORGANIC CHEMISTRY

When metal-catalyzed C–H functionalization meets visible-light photocatalysis

Lucas Guillemard and Joanna Wencel-Delord*

Review

Open Access

Address:
Laboratoire d'Innovation Moléculaire et Applications (UMR CNRS 7042), Université de Strasbourg/Université de Haute-Alsace, ECPM, 25 rue Becquerel, 67087, Strasbourg, France

Email:
Joanna Wencel-Delord* - wenceldelord@unistra.fr

* Corresponding author

Keywords:
C–H activation; C–H functionalization; dual catalysis; photoredox catalysis; radical chemistry; sustainable synthesis; synergistic catalysis

Beilstein J. Org. Chem. **2020,** *16,* 1754–1804.
doi:10.3762/bjoc.16.147

Received: 02 April 2020
Accepted: 26 June 2020
Published: 21 July 2020

This article is part of the thematic issue "Advances in photoredox catalysis".

Guest Editor: T. Noël

© 2020 Guillemard and Wencel-Delord; licensee Beilstein-Institut.
License and terms: see end of document.

Abstract

While aiming at sustainable organic synthesis, over the last decade particular attention has been focused on two modern fields, C–H bond activation, and visible-light-induced photocatalysis. Couplings through C–H bond activation involve the use of non-prefunctionalized substrates that are directly converted into more complex molecules, without the need of a previous functionalization, thus considerably reduce waste generation and a number of synthetic steps. In parallel, transformations involving photoredox catalysis promote radical reactions in the absence of radical initiators. They are conducted under particularly mild conditions while using the visible light as a cheap and economic energy source. In this way, these strategies follow the requirements of environment-friendly chemistry. Regarding intrinsic advantages as well as the complementary mode of action of the two catalytic transformations previously introduced, their merging in a synergistic dual catalytic system is extremely appealing. In that perspective, the scope of this review aims to present innovative reactions combining C–H activation and visible-light induced photocatalysis.

Introduction

In recent years, the field of synthetic chemistry has witnessed a profound evolution. Indeed, due to the growing environmental awareness, organic chemists face nowadays an urgent need of developing much more sustainable and environmentally benign routes to afford molecular complexity from simple precursors, while concomitantly limiting the number of steps and waste generation. Following this general key objective, the landscape of organic synthesis has been clearly changed by the development of ecofriendly methodologies such as metal-catalyzed C–H activations, visible-light-induced photocatalysis, electrosynthesis, enzyme catalysis, and others. Each of these techniques aims at accessing complex molecules while limiting ecological footprint.

Over the last decade, the metal-catalyzed C–H activation established itself as one of the most rapidly expanding domain of

organic synthesis [1-14]. Indeed, this approach tends in rendering the classical metal-catalyzed cross-coupling more environmentally friendly, as simple, non-prefunctionalized substrates could be used in the presence of a metallic catalyst, able to insert selectively into one specific C–H bond. Accordingly, not only waste generation was significantly reduced, but also new retrosynthetic connections were envisioned, allowing the conception of more straightforward synthetic protocols [15-20]. Besides, the formation of previously inaccessible molecules could be expected. C–H activation reactions, generally do not change the oxidation state of the metal and are favored in the case of aromatic or vinylic substrates but are clearly more challenging when using aliphatic precursors [21-28].

In parallel, in the 21st century there is a real renaissance for photocatalysis, with great advances achieved mainly in visible-light-mediated reactions [29-43]. Various photosensitizers, initially based on noble metals (such as Ir and Ru polypyridine complexes) [38,39], and more recently, organic compounds (cyanoarenes, xanthenes, thiazines, pyryliums or acridiniums) [40], emerged. These molecules capable of harvesting visible light from simple household bulbs or easily accessible LEDs, opened the door towards the design of numerous electron or energy-transfer-type reactions under mild conditions and in the absence of toxic radical precursors [44-46].

Considering, on one hand, the fundamentally appealing properties of both, metal-catalyzed C–H functionalization reactions and visible-light-induced photocatalysis, and, on the other hand, their complementary reactivities, the combination of these two activation modes could provide new solutions for sustainable organic synthesis.

Indeed, new mutlicatalysis concepts have emerged recently and enabled the achievement of various yet unfeasible reactions [47]. Following this general goal, synergistic catalysis involving two catalysts and two catalytic cycles acting in a cooperative way to create a new bond, turned out to be a powerful strategy. According to a simplified representation, synergistic catalysis involves the concurrent activation of a nucleophile and an electrophile by means of two distinct catalysts. This simultaneous activation then produces two reactive species, one with a higher HOMO and another with a lower LUMO, in comparison to the respective ground-state energy of both substrates (Figure 1) [47]. By judiciously choosing the starting materials, the coupling of the activated intermediates promotes chemical transformations generally unattainable using traditional monocatalysis.

However, the potential of multicatalyzed mechanisms goes far beyond the category of synergistic catalysis and the interest in

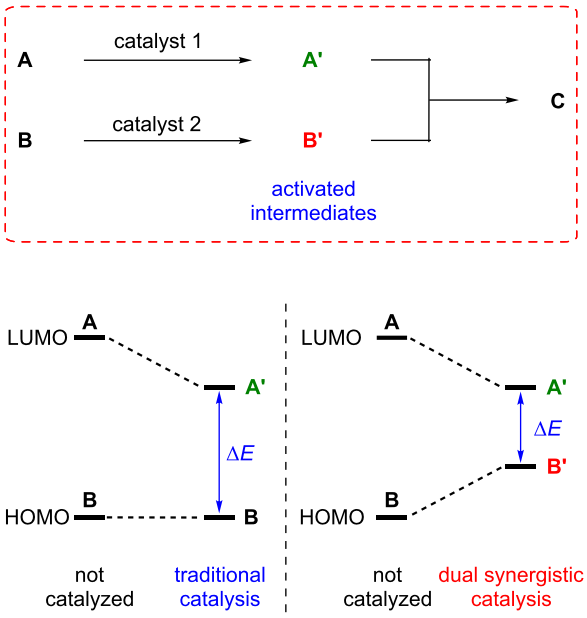

Figure 1: Concept of dual synergistic catalysis.

this field fructified in the development of different possible scenarios. First, if both the nucleophile and the electrophile are activated independently by distinct functional groups on the same catalyst, this is referred to as bifunctional catalysis (Figure 2, (1)) [48]. When the two catalysts work in a cooperative way to activate only one substrate, this is classified as double activation catalysis (Figure 2, (2)) [49,50]. Similarly, if both catalysts activate the same coupling partner but in a sequential fashion (the activated substrate leads to an intermediate further activated by the second catalyst), this falls in the category of cascade catalysis (Figure 2, (3)) [51,52]. Finally, the panel of these multicatalyzed reactions is complemented with the above-mentioned synergistic catalysis strategy, i.e., the simultaneous activation of an electrophile and a nucleophile by two distinct catalysts in order to achieve a single chemical transformation (Figure 2, (4)) [47].

Despite great advances achieved in the field of both, C–H activation and visible-light-induced photocatalysis, dual systems merging these two activation modes have remained underdeveloped until recently. In contrast, over the past decade, the design of new strategies combining photoredox catalysis with a second catalytic system has sparked significant interest from the scientific community. Accordingly, numerous unprecedented reactions involving photoredox catalysis in synergy with other activation modes including Brønsted/Lewis acid catalysis, organocatalysis, enzymatic biocatalysis, or electrocatalysis, have been achieved recently [53-58].

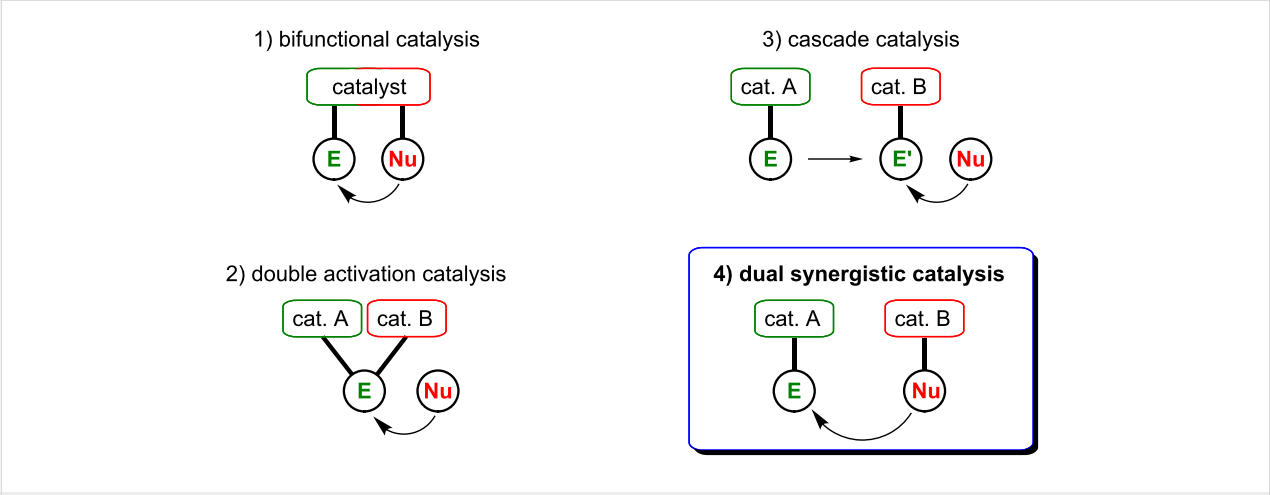

Figure 2: Classification of catalytic systems involving two catalysts.

In addition, various transformations merging photoredox catalysis with transition-metal catalysis have been disclosed [59-65]. Among these different strategies, visible-light photoredox catalysis combined with nickel catalysis is undoubtedly the most thoroughly investigated approach and consequently, the most widely described in the literature [66,67]. The interest of the scientific community towards this dual catalysis and further developments were pioneered by MacMillan [68] and Molander [69]. The general mechanism of such transformations involving the dual Ni/photoredox catalytic system is presented in Figure 3.

Following the idea of combining C–H activation and photoredox catalysis in multicatalyzed complex systems,

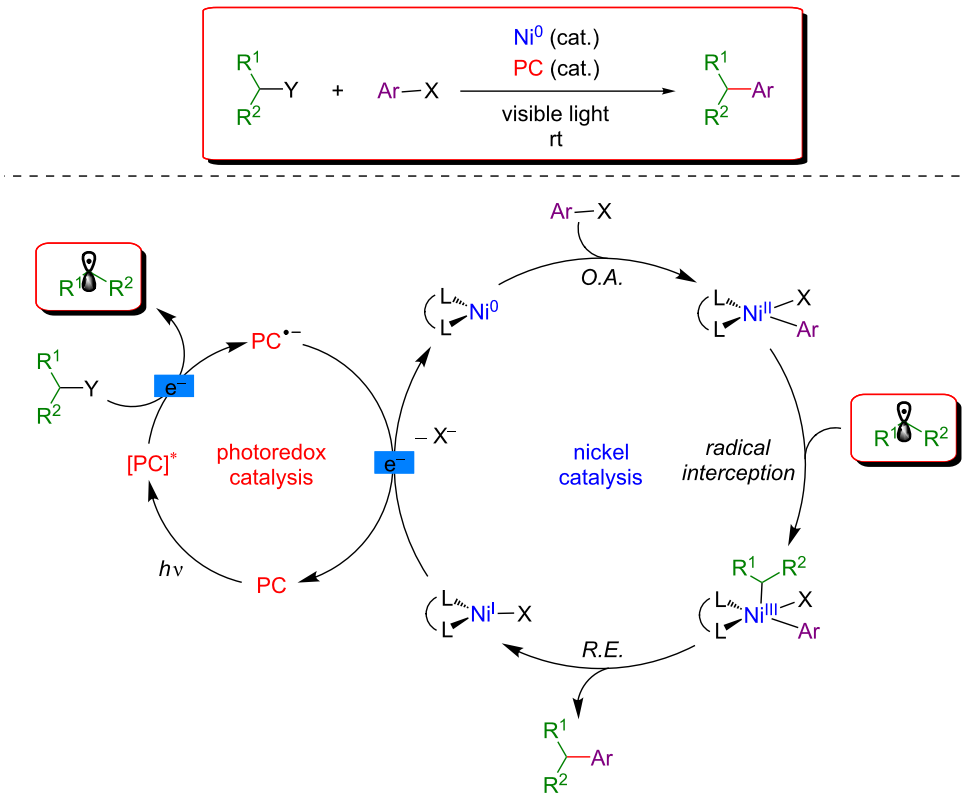

Figure 3: General mechanism for the dual nickel/photoredox catalytic system.

several different approaches were designed. The initial examples of merging these two domains concerned the development of "classical" C–H activation reactions, while a photoredox cycle was implemented to reoxidize the metal catalyst, thus obviating the need for a stoichiometric amount of metal-based oxidants, such as silver or copper salts.

In parallel, dual synergistic catalysis has emerged. In this case, C–H activation and photocatalysis were used separately to activate, via fundamentally very different activation modes, two coupling partners. The catalytic cycles were successfully interconnected and such strategies benefit from the cooperative activation of distinct substrates. Interception of the independently formed intermediate furnished the expected coupling products under generally mild reaction conditions. Furthermore, a merge of metal-catalyzed C–H functionalization and photocatalysis was also astutely employed to design modern versions of Sonogashira-type reactions as well as mild heteroaromatic functionalizations. Last but not least, a HAT-type process inducing the generation of alkyl radicals via selective C–H abstraction from the aliphatic precursors may be combined with a Ni-catalyzed process, thus delivering cross-coupled products.

The aim of this review is to present the variety of possibilities in combining transition metal C–H activation and visible-light photoactivation to reach sustainable synthesis. The particular focus is put on the mechanisms of such complex catalytic systems, highlighting the unique reactivity that arises from the original combination of these two activation modes. The advantages of the dual catalytic systems over traditional monocatalyzed approaches is also discussed, thus illustrating their sustainable character.

Review

Visible-light-mediated photocatalysis as a sustainable reoxidation strategy

In the context of traditional C–H bond activation, a catalytic amount of a transition metal (generally Pd, Rh and Ru) is frequently used in combination with a stoichiometric amount of an external oxidant (typically Cu or Ag salts). Such additional oxidants are required if transiently produced low-valent metal complexes need to be reoxidized by electron transfer to complete the catalytic cycle and regenerate the active catalytic species. The classical Fujiwara–Moritani reaction promoting the addition of arenes to olefins illustrates a general mechanism for such traditional C–H functionalization (Figure 4, left) [70-72]. The insertion of a metal catalyst X_2M into an aromatic C–H bond of a substrate (generally facilitated by the presence of a directing group (DG)), delivers a metal–aryl complex. Coordination and subsequent insertion of an alkene into the M–aryl bond then provides the desired coupling product after β-hydride elimination, together with a metal hydride or a low-valent metal complex. Hence, in order to reoxidize the metal catalyst, excess of an external oxidant, such as Cu(II) or Ag(I) salts, was frequently used.

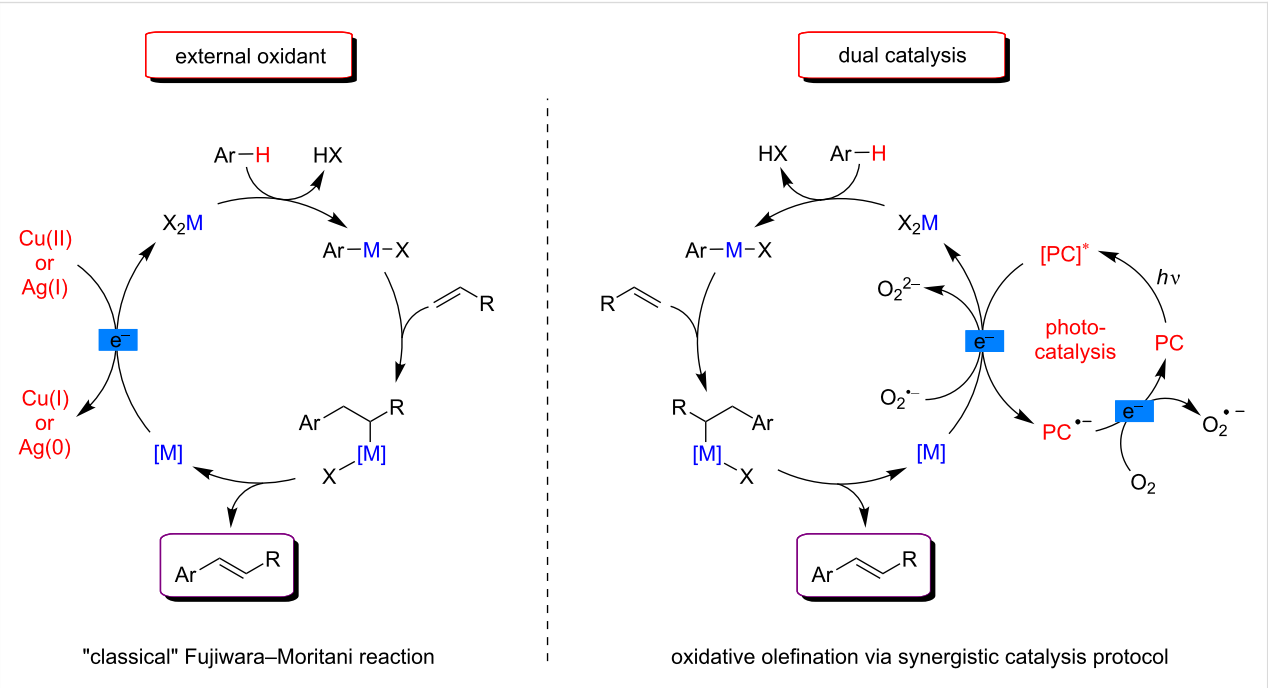

Figure 4: General mechanisms for C–H activation catalysis involving different reoxidation strategies.

On the other hand, photoredox catalysis has been mainly employed for electron-transfer reactions and, remarkably, few examples have been reported in which the photoredox process modifies the oxidation state of a catalyst [55,56]. Subsequently, C–H activation protocols benefiting from mild photocatalytic reoxidation have spread rapidly [60-62]. In such a case, a photocatalyst (PC) is introduced in the reaction media in order to transfer electrons from the low-valent metal complex formed in situ after reductive elimination of the product (Figure 4, right). In this way, the metalacyclic intermediate is reoxidized while the photosensitizer is reduced, thus completing the C–H activation catalytic cycle. By selecting judiciously a PC with adequate redox potentials, the ground state of the latter could be regenerated by means of a mild and abundant oxidant such as molecular oxygen. The overall process thus allowed the replacement of stoichiometric amounts of external oxidants with a suitable PC.

Following this general strategy, in 2014, Rueping and co-workers reported the pioneering contribution concerning the synthesis of indoles via an intramolecular C–H/C–H oxidative coupling of *N*-arylenamines under air atmosphere. This procedure was based on dual catalysis involving a double C–H activation system and photoredox catalysis (Figure 5) [73]. The coupling products were generally isolated in good yields, although this procedure required high temperature (120 °C).

Remarkably, molecular oxygen was used as the terminal oxidizing agent of the overall C–H functionalization reaction. The mechanistic studies revealed that both, the excited Ir photocatalyst and the superoxide anion generated during the transformation, were able to oxidize the low-valent Pd(0) species resulting from the reductive elimination (Figure 6). Under such dual catalysis protocol, various oxidant-sensitive functional groups were tolerated, thus rendering this methodology well suitable for the synthesis of a variety of indole derivatives.

Subsequently, the panel of oxidative Heck coupling reactions via a photoredox catalytic system combined with C–H activation using Rh [74] or Ru [75] was extended by Rueping's group.

In 2014, Rueping described the combination of rhodium and photoredox catalysis for the direct C–H *ortho*-olefination of arylamides (Figure 7) [74]. The procedure was performed under air at 80 °C and turned out to be efficient using a low loading of a Ru-based photosensitizer. A broad range of DGs could be installed on the aromatic coupling partner, including frequently used Weinreb amides or functionalized secondary and primary amides. Regarding the scope of olefin substrates, the reaction tolerated numerous functional groups including acrylates, vinyl silanes or sulfones which was interesting from the post-functionalization viewpoint, thus furnishing a large panel of compounds in excellent to good yields.

This C–H olefination of arenes was performed under aerobic conditions in order to reoxidize the photocatalyst (Figure 8). Interestingly, the desired products were also delivered while using a stoichiometric amount of the photocatalyst in the absence of oxygen, suggesting that a direct electron transfer from the photosensitizer allowed the reoxidation of the active catalyst. However, the participation of molecular oxygen cannot be excluded.

Rueping further demonstrated the capacity of the dual catalytic systems merging C–H activation with photoredox catalysis to

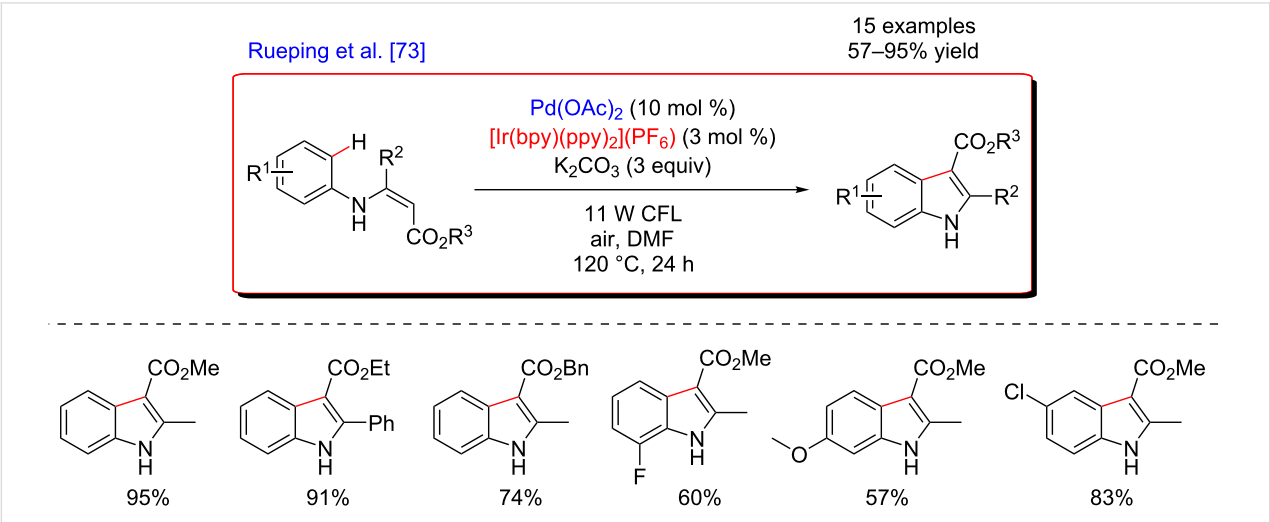

Figure 5: Indole synthesis via dual C–H activation/photoredox catalysis.

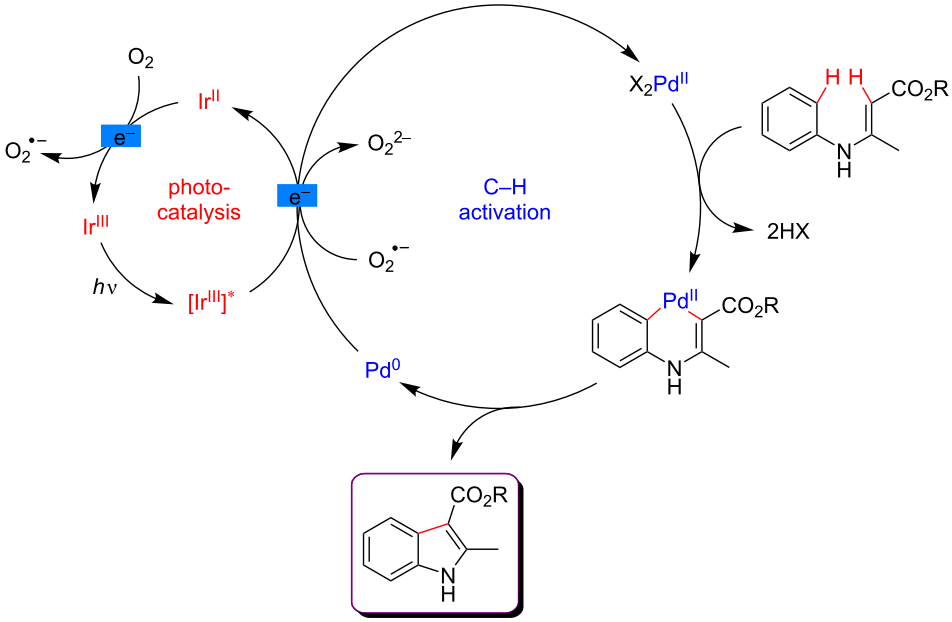

Figure 6: Proposed mechanism for the indole synthesis via dual catalysis.

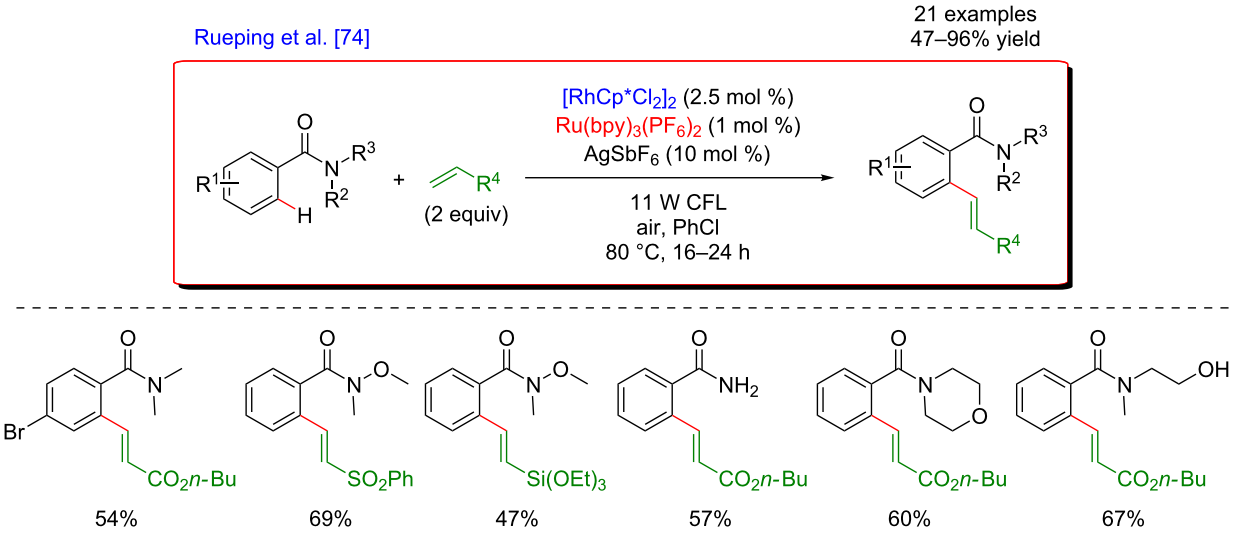

Figure 7: Oxidative Heck reaction on arenes via the dual catalysis.

allow in situ reoxidation of the metal catalyst. In 2015, a procedure combining ruthenium C–H activation of phenols derivatives bearing a pyridine moiety as DG and photoredox catalysis was disclosed (Figure 9) [75]. This *ortho*-olefination was performed under air atmosphere and required harsh reaction conditions with temperatures of up to 120 °C. The substituents on both substrates had a minor impact on the reaction outcome and the coupling products were isolated in comparable yields. The applicability of the reaction was underlined by its tolerance towards various functional groups such as aldehydes, ketones, and esters. Of note is that in some cases, partial hydrogenation of the double bond was observed, resulting probably from the generation of a ruthenium–hydride complex. However, this consecutive reactivity and the ratio between the olefin and alkane products could be controlled by adjusting the acidity of the reaction media.

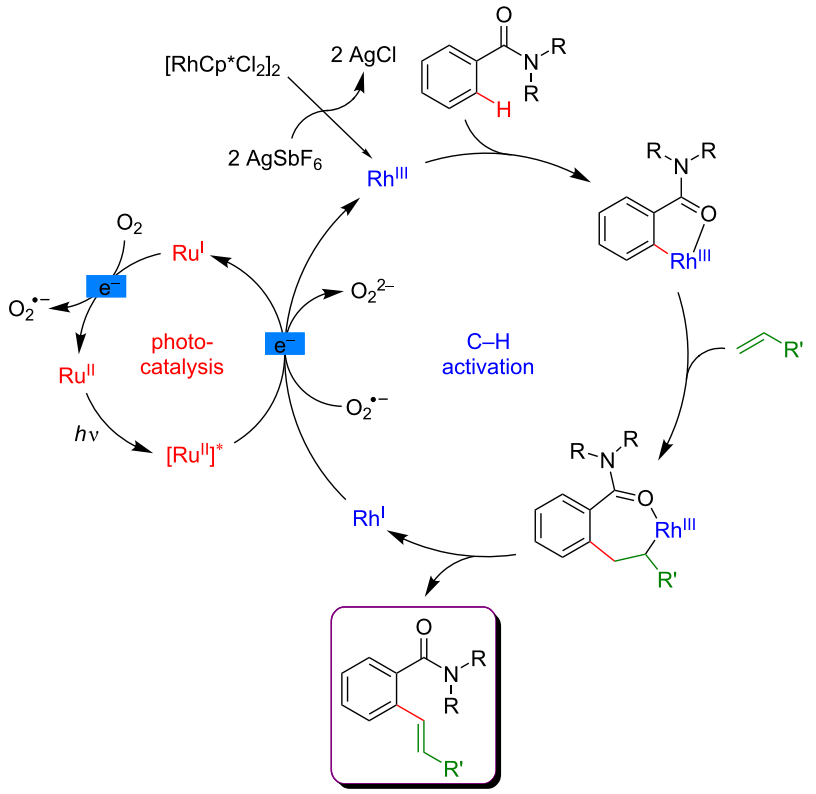

Figure 8: Proposed mechanism for the Heck reaction on arenes via dual catalysis.

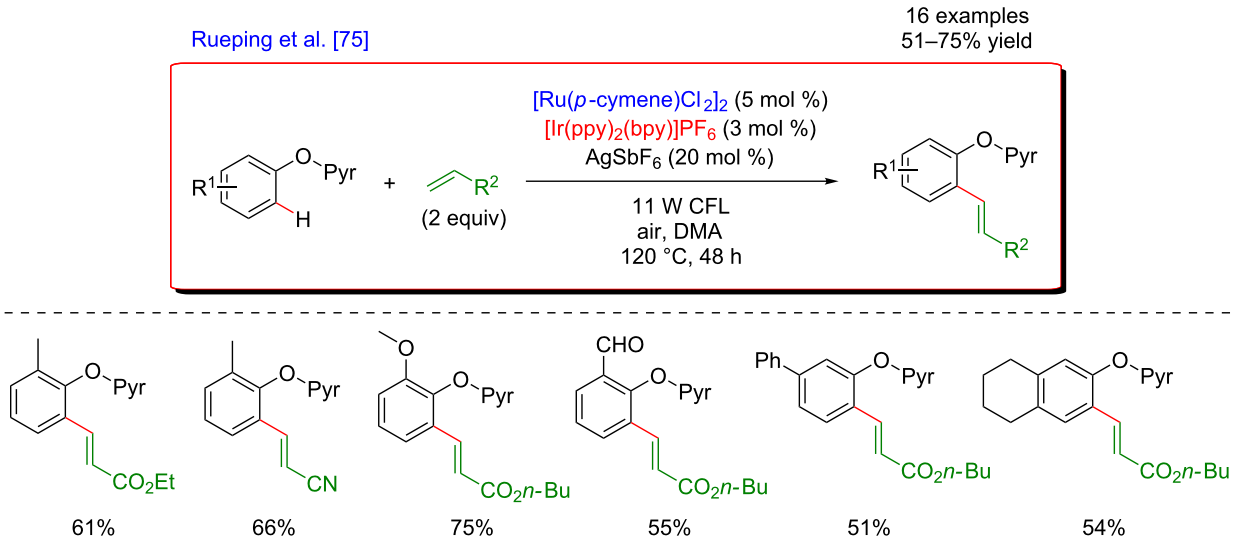

Figure 9: Oxidative Heck reaction on phenols via the dual catalysis.

As in the previously described examples, molecular oxygen plays a key role in the mechanism of the C–H functionalization (Figure 10). Indeed, both the photoexcited Ir-based catalyst and the superoxide radicals formed in situ from molecular oxygen allowed the reoxidation of the Ru(II) active species for C–H activation.

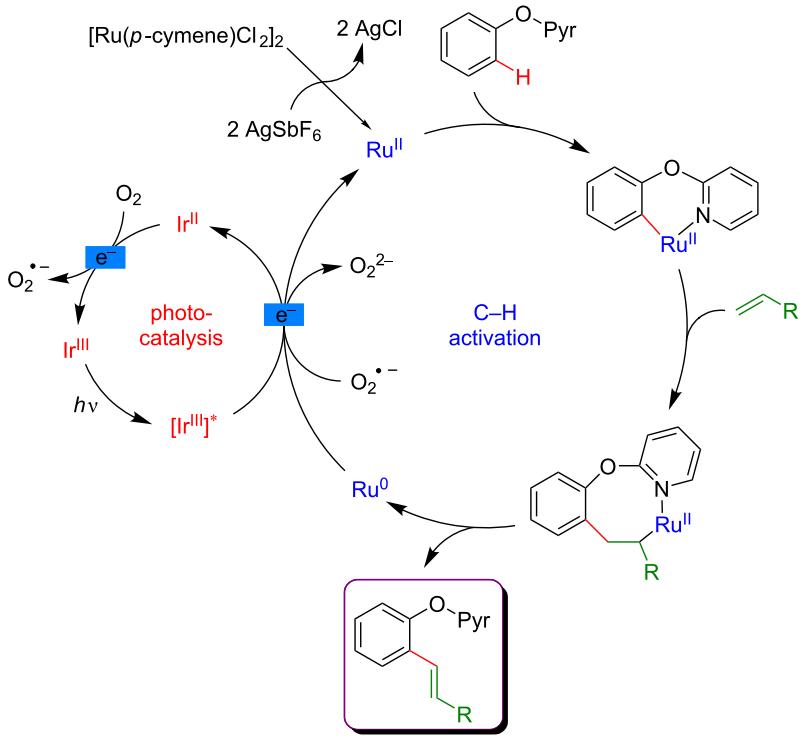

Figure 10: Proposed mechanism for the Heck reaction on phenols via dual catalysis.

In 2015, Cho's group became interested in implementing such mild and sustainable reoxidation protocol in a Pd-catalyzed C–H activation reaction, focusing mainly on an intramolecular direct C–N coupling. Thus, an efficient method for the synthesis of carbazoles via an intramolecular C–H amination was developed, using *N*-substituted 2-aminobiaryl derivatives as the substrates (Figure 11) [76]. This procedure was carried out at 80 °C and led to the formation of various interesting coupling products with excellent yields. Remarkably, a high functional group tolerance was observed, including heterocyclic substrates. In contrast, the *N*-substitution pattern clearly impacted the efficiency of the reaction. Indeed, exchanging the *N*-sulfonyl or

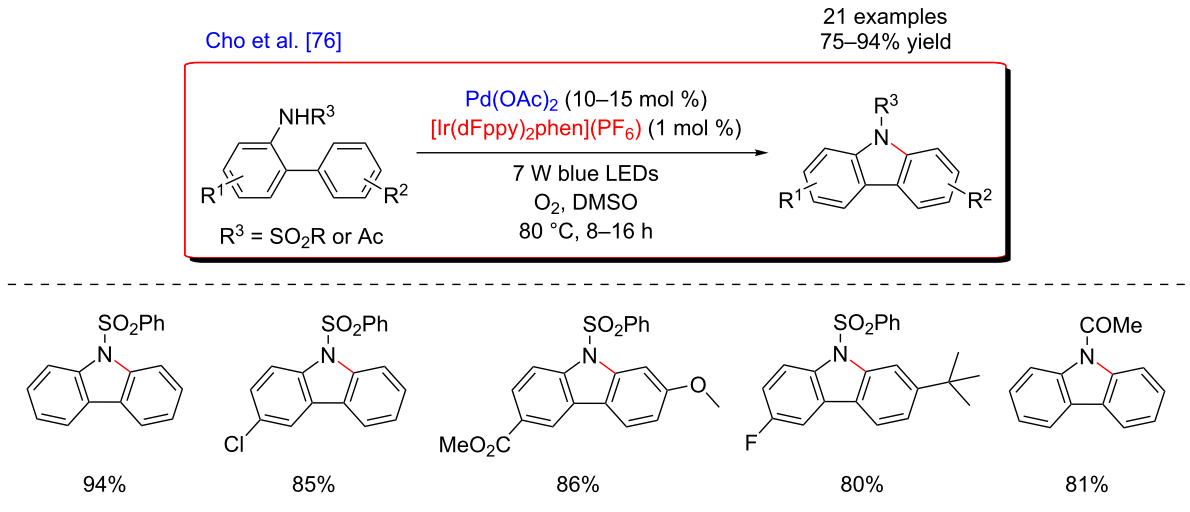

Figure 11: Carbazole synthesis via dual C–H activation/photoredox catalysis.

N-acetyl protecting group with other functionalities, such as hydrogen, benzyl, or alkyl, resulted in the shut of reactivity and no formation of the corresponding *N*-substituted carbazoles was observed.

Concerning the mechanism, the carbazole-forming reaction also required aerobic conditions in order to reoxidize the Ir-photocatalyst with molecular oxygen (Figure 12). A similar catalytic cycle than the one reported by Rueping was hence proposed for the C–H activation step. Nevertheless, the authors surmised that an alternative pathway via a Pd(III)/Pd(I) catalytic system could also be envisioned. In this scenario, the reductive elimination from a Pd(III) intermediate occurs prior to the one-electron oxidation by the photoexcited catalyst.

This contribution inspired also other research groups to investigate synergistic catalyses using Pd-based C–H catalysts. In 2016, Lei's group reported the aerobic intramolecular oxidative carbonylation of enamides for the synthesis of 1,3-oxazin-6-ones by merging palladium and photoredox catalysis (Figure 13) [77]. The transformation was performed at 80 °C under air atmosphere. This efficient approach for the construction of heterocycles exhibited a good functional group tolerance thus providing a broad range of products, isolated in moderate to good yields. A possible gram scale-up synthesis was also accomplished.

Within the mechanistic cycle, after initial vinylic C–H bond activation and insertion of CO into the C–Pd bond, the acylpalladium intermediate is converted into its conjugated analog under DABCO assistance (Figure 14). The Pd(0) species, liberated during the reductive elimination, is reoxidized via electron transfer with O_2 playing the role of the terminal oxidant.

In 2018, Sundararaju et al. reported the first example of dual catalysis employing cobalt, a non-noble metal, in combination with a photocatalyst. The strategy was utilized for the C–H bond annulation of benzamides with alkynes, furnishing isoquinolones, an important moiety in various natural products (Figure 15) [78]. The C–H activation step was assisted by an 8-quinolyl DG and occurred under an oxygen atmosphere at room temperature. A variety of benzamides bearing different substituents at the *ortho*- and *para*-positions gave the products in good to excellent yields, while the *meta*-substituted substrates were converted into a mixture of two isomeric products. Moreover, amides containing heterocycles such as thienyl, pyrazolyl, pyridyl, pyrimidyl, and 7-azaindolyl were found to be compatible with this transformation. While symmetrical alkynes led to the desired products in moderate to good yields, the unsymmetrical ones afforded a mixture of products with very high regioselectivity, with the favored formation of cyclized compounds bearing an aromatic unit in α-position to the nitrogen atom. Sensitive functional groups such as hydroxy, silyl, and ethynyl were tolerated by this protocol. Furthermore, this methodology was also extended towards the C–H annulation with dienes.

The proposed mechanism of this reaction requiring only oxygen as sole oxidant and implementing two photoredox cycles is presented in Figure 16. After a ligand exchange, Co(II) under-

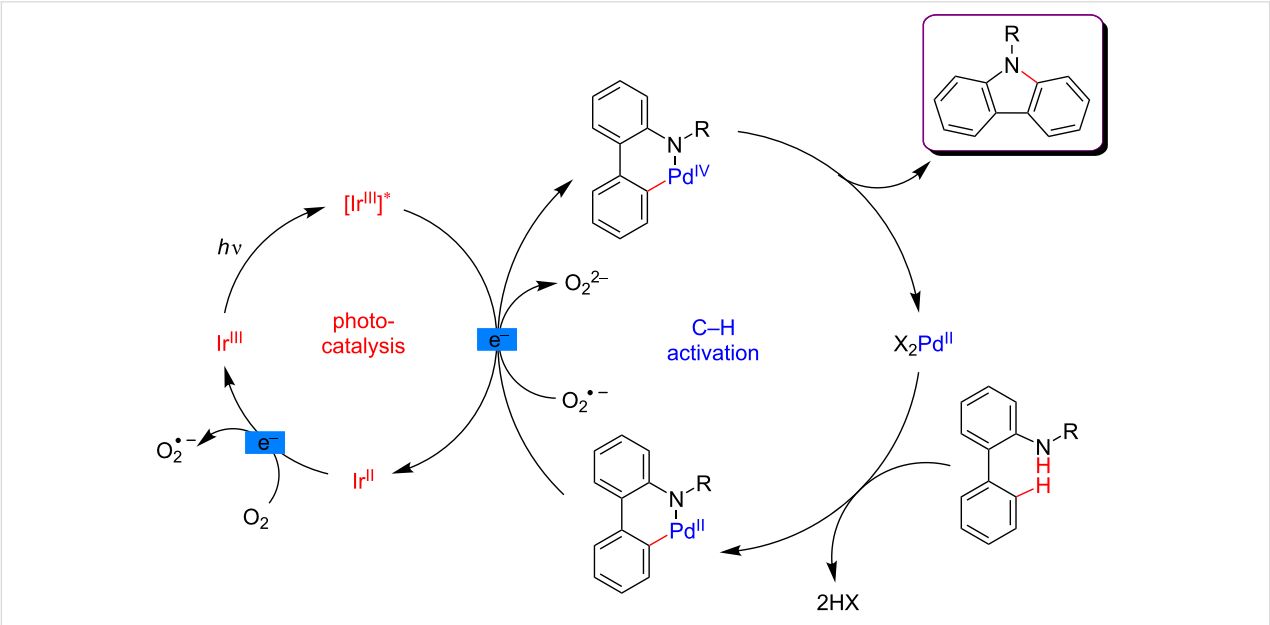

Figure 12: Proposed mechanism for the carbazole synthesis via dual catalysis.

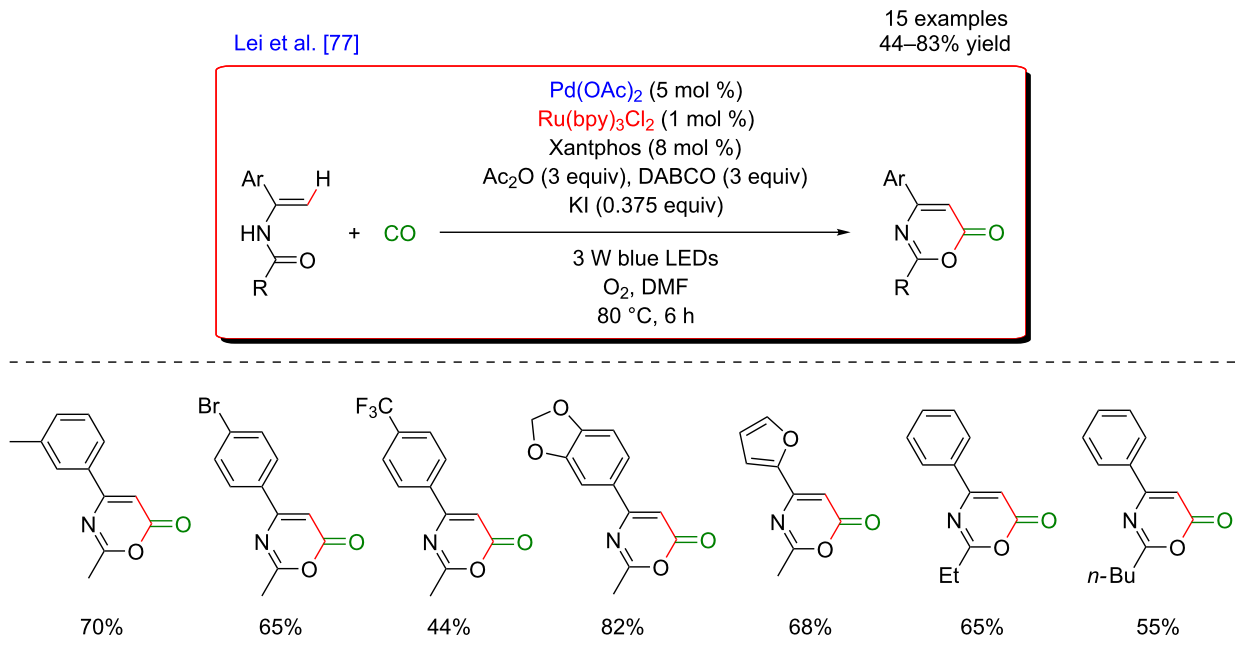

Figure 13: Carbonylation of enamides via the dual C–H activation/photoredox catalysis.

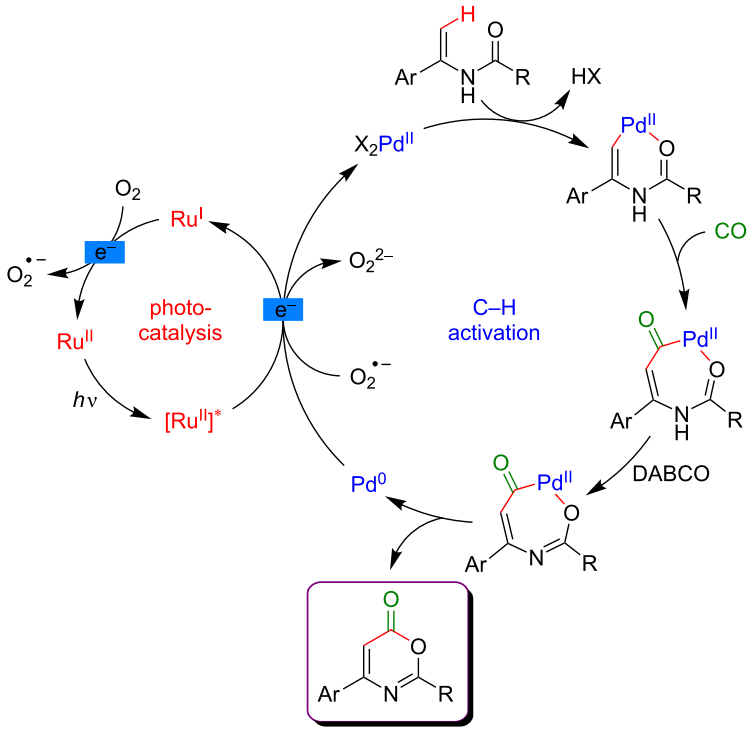

Figure 14: Proposed mechanism for carbonylation of enamides via dual catalysis.

goes a single-electron transfer (SET) oxidation to Co(III) with a concomitant formation of the reduced organic photocatalyst. The thus generated highly reactive Co(III) complex undergoes cyclometalation via a concerted metalation–deprotonation (CMD) process furnishing a cyclometalated intermediate. Thereafter, coordination and subsequent insertion of the alkyne

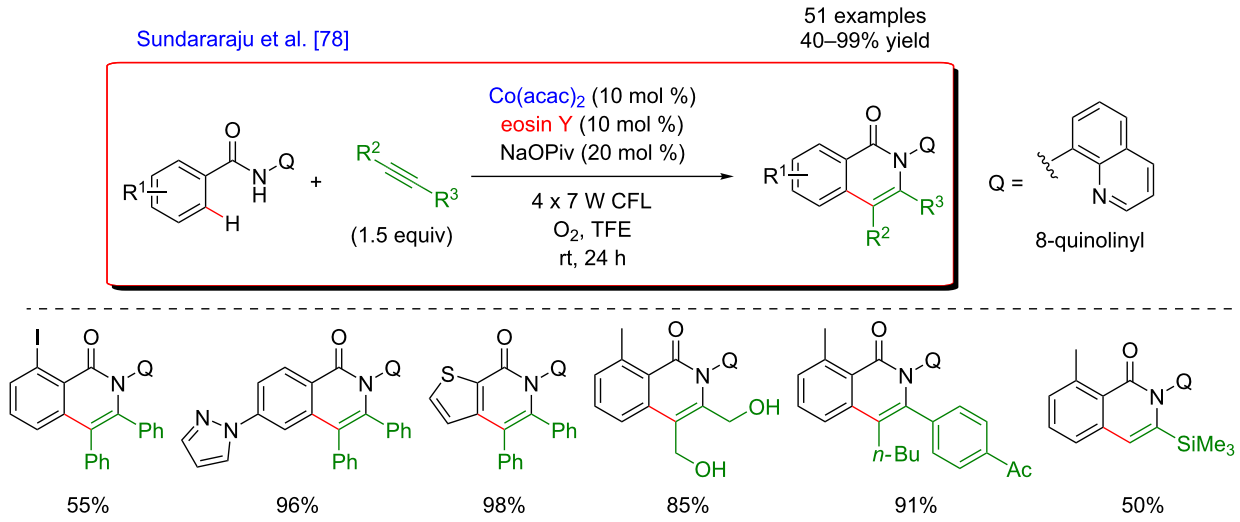

Figure 15: Annulation of benzamides via the dual C–H activation/photoredox catalysis.

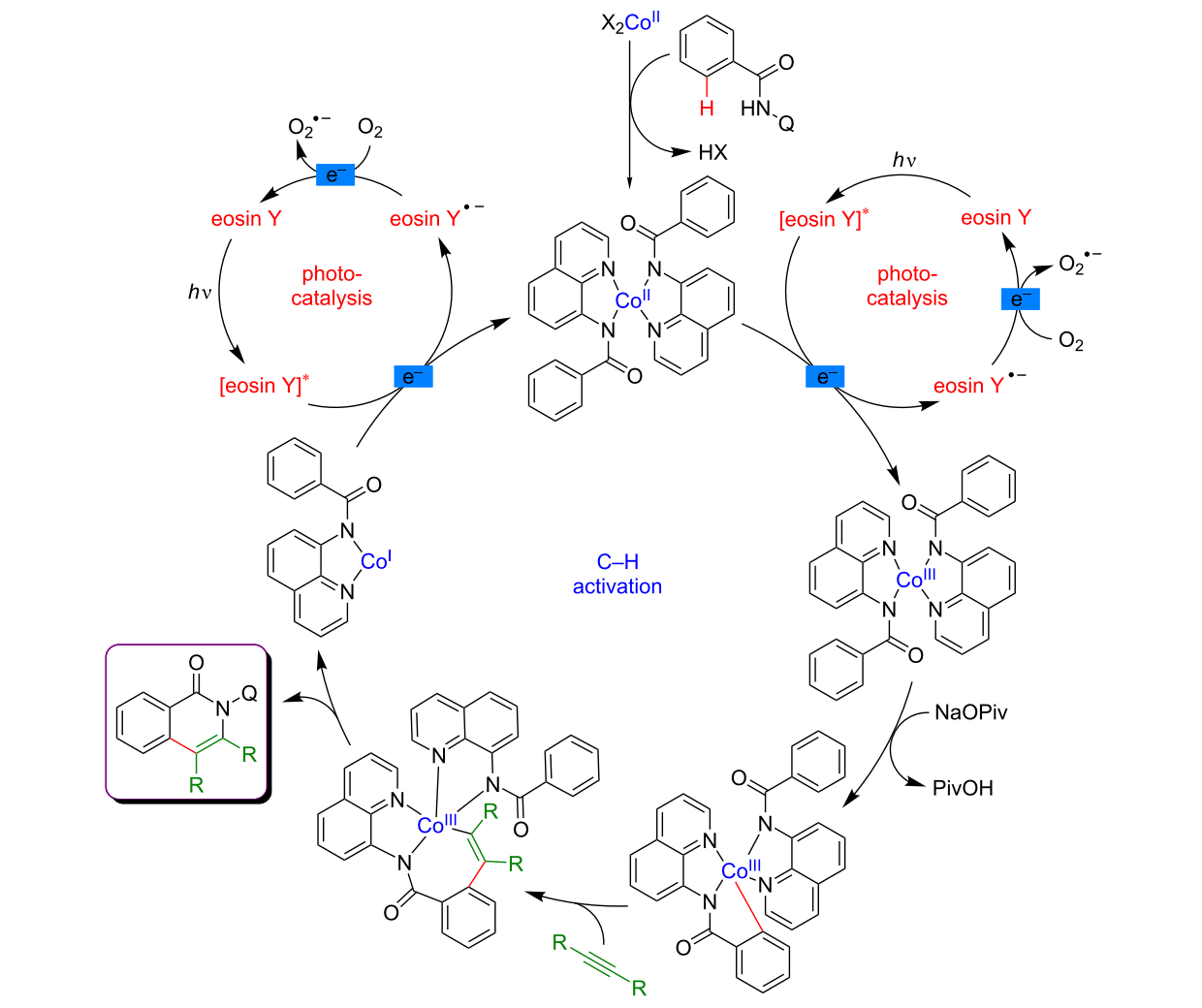

Figure 16: Proposed mechanism for the annulation of benzamides via dual catalysis.

into the Co–C bond delivers a seven-membered cobaltacycle. The desired coupling product is then liberated by reductive elimination, producing a Co(I) species. Finally, the photoexcited eosin Y reoxidizes Co(I) to Co(II), while the photosensitizer is reoxidized by molecular oxygen, thus completing the overall catalytic process.

In addition, a complementary strategy towards photocatalytic C–H annulation was disclosed by Rueping et al., allowing the synthesis of *N*-heterocycles such as indoles and pyrroles. The targeted heterocyclic products were obtained by cyclization of acetanilides with alkyne derivatives via a direct *ortho*-metalation pathway (Figure 17) [79]. Acetyl substituents acted as DG in this transformation performed under air at high temperatures. The coupling exhibited a broad substrate scope and the procedure tolerated a variety of even sensitive functional groups, including trifluoromethyl, ketone, or ester motifs. Unsymmetrical alkynes were also compatible, although the cyclization provided the desired heterocyclic compounds in decreased yields.

Once again, the use of Ru-based photocatalyst in combination with molecular oxygen as a terminal oxidant was crucial in this cyclization/C–H functionalization pathway (Figure 18). The classical C–H activation cycle involves an initial amide-directed *ortho*-metalation, followed by the insertion of an alkyne into the C–M bond. The key step of the dual catalysis is the reductive quenching of the photoexcited catalyst by Rh(I), a low-valent metal obtained after C–N reductive elimination. Hence, the Rh(III) active catalyst is regenerated and the resulting reduced photocatalyst is reoxidized to its ground state by molecular oxygen, thus closing both catalytic cycles. Remarkably, this transformation could also be efficiently performed with heterogeneous inorganic photocatalysts, as was illustrated by a reaction performed in the presence of WO_3.

The above-presented transformations are appealing as the use of stoichiometric amounts of a metal-based oxidant could be obviated with these dual catalysis strategies. Furthermore, in terms of the reactivity, the previously mentioned examples can be rather considered as improved, more sustainable versions of the known C–H methodologies.

Synergistic catalysis (activation of each coupling partner by one type of catalysis)

Synergistic catalysis refers to a dual catalytic system merging C–H bonds activation and visible-light photocatalysis. Following the definition of the synergistic catalysis presented in the introduction, both catalytic cycles enable the distinct activation of each coupling partner in a cooperative fashion (Figure 19). Such transformations will thus typically consist in the insertion of a transition metal into a C–H bond to produce a metalacyclic intermediate **1** which can intercept a radical **2** generated by photoredox catalysis. This interception leads to a new metallic key intermediate **3** by single-electron transfer (SET). The desired coupling product **4** is then obtained after a reductive elimination (Figure 19). Applying such an approach paved the way towards unprecedented couplings benefiting from a SET activation of one substrate, and a two-electron activation by a transition-metal catalyst of the other.

The main advantage of such a system is to promote highly regioselective reactions. Indeed, while radical transformations generally suffer from selectivity issues, interception of radicals by metal catalysts and further cross-coupling-type reactivity

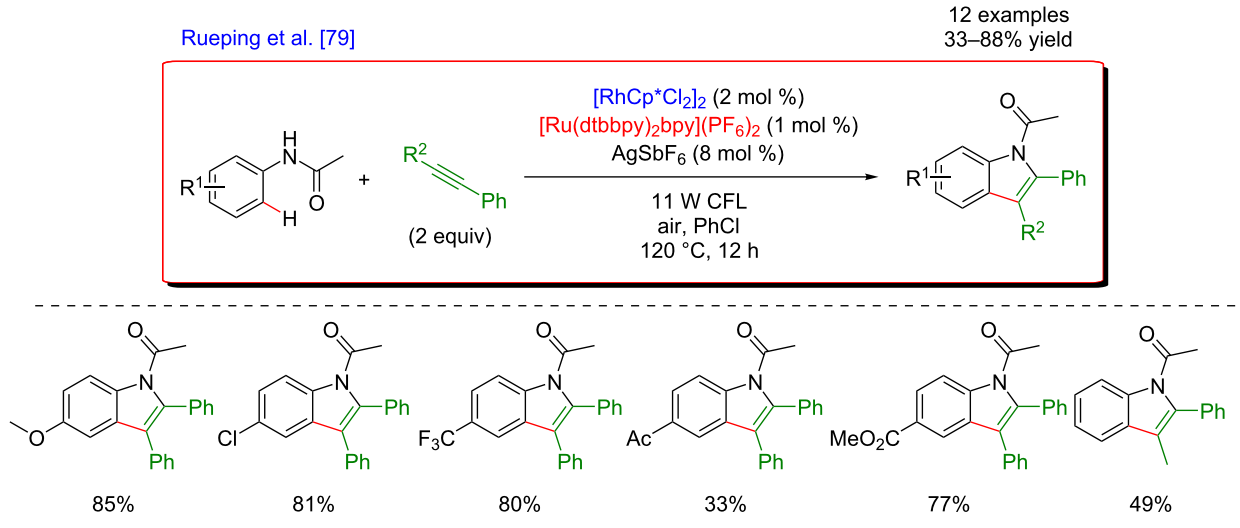

Figure 17: Synthesis of indoles via the dual C–H activation/photoredox catalysis.

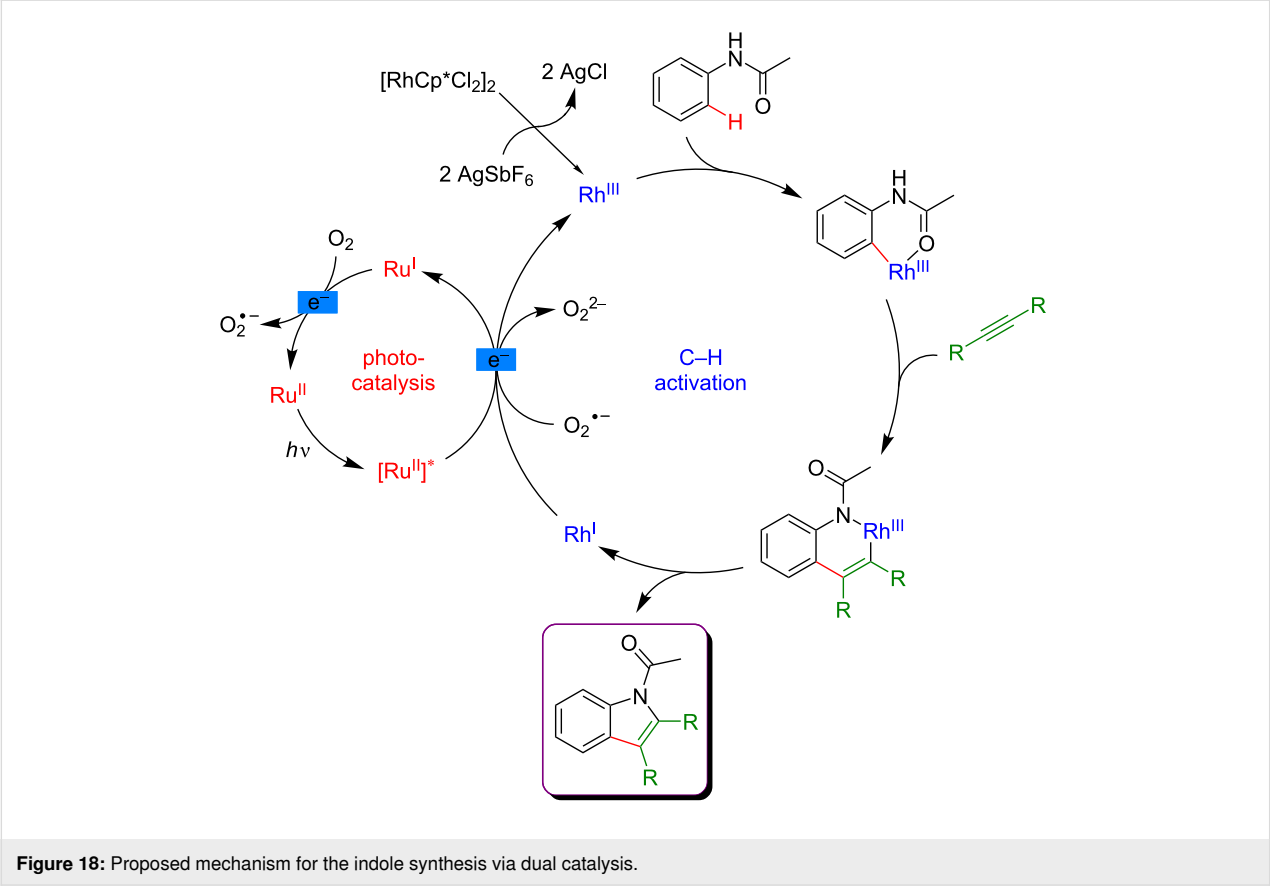

Figure 18: Proposed mechanism for the indole synthesis via dual catalysis.

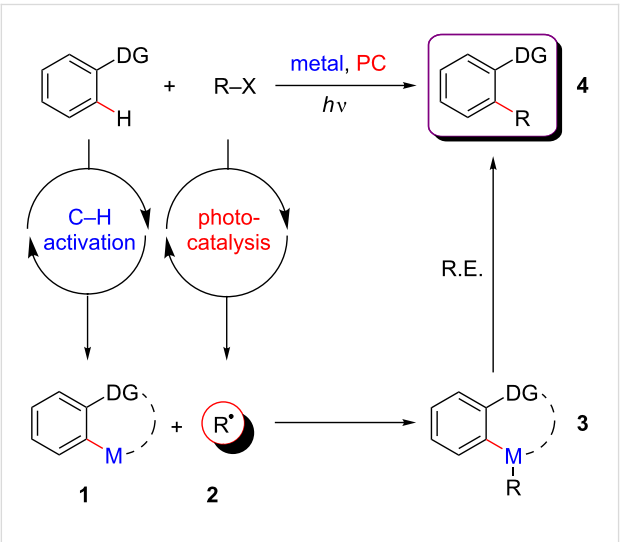

Figure 19: General concept of dual catalysis merging C–H activation and photoredox catalysis.

provides a unique tool to solve this critical issue. Besides, dual catalytic systems enable also umpolung-type reactivity, thus promoting unique bond-forming reactions, inaccessible via standard approaches due to the polarity mismatch. Finally, the combination of photocatalysis and metal-catalyzed C–H activations upholds the desired couplings under, usually, mild conditions and at room temperature, while utilization of non-prefunctionalized coupling partners reduces the waste formation. Last but not least, the use of visible light, one of the most economic and abundant source of energy to promote these transformations is in agreement with sustainable and eco-friendly chemistry.

Directed C–H activation

Pd-catalyzed arylation

The first example of dual catalysis merging C–H activation and photoredox catalysis was published in 2011 by Sanford [80]. The transformation concerned the direct arylation of various aromatic compounds bearing different DGs with aryldiazonium salts (Figure 20). In her initial study in 2005, Sanford reported a similar arylation and diazonium salts were already identified as appropriate coupling partners. However, harsh reaction conditions with high temperatures of 100 °C in acetic acid were necessary to promote the reaction [81]. The major enhancement was discovered while surmising that an identical product might be obtained, if the Ar• was generated in situ and used as a highly reactive coupling partner. Such methodology using a dual catalytic system thus provided a significant improvement compared to the initial protocols. Indeed, the reaction was

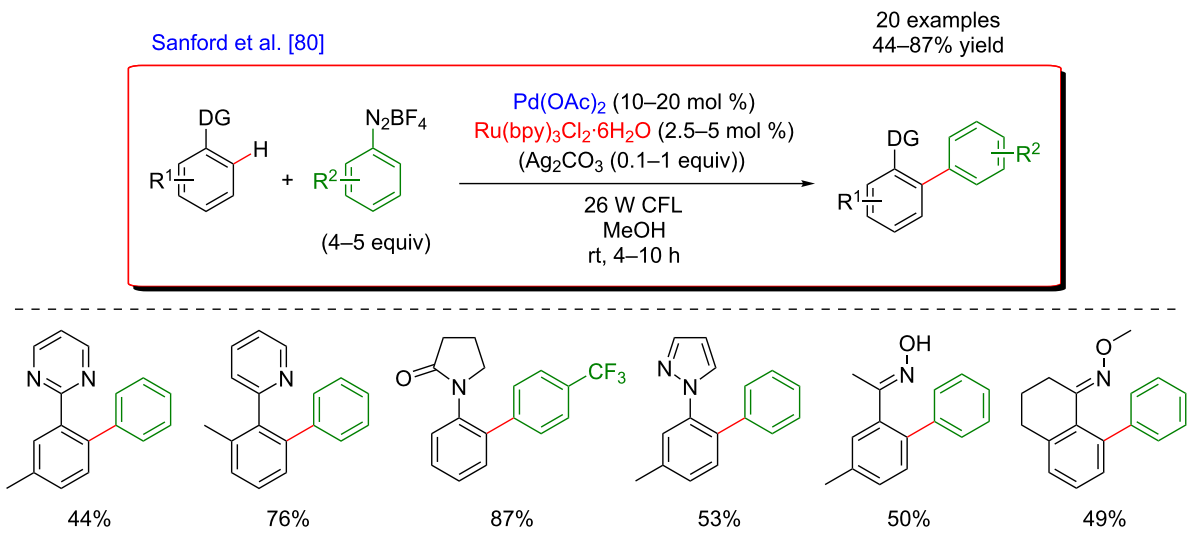

Figure 20: The first example of dual catalysis merging C–H activation and photoredox catalysis.

carried out at room temperature, demonstrating the capacity of photoredox catalysis to generate reactive species under exceptionally mild conditions. The combination between the photocatalyst $Ru(bpy)_3Cl_2·6H_2O$ and $Pd(OAc)_2$ promoted the formation of the coupling products in high yields when the reaction was irradiated with visible light. This new procedure exhibited a good functional group tolerance and turned out to be compatible with a wide range of DGs, including amides, pyrazoles, pyrimidines, and oximes (Figure 20). The mild arylation proceeded in good to excellent yields over 20 examples and worked with electron-deficient, electron-rich as well as relatively sterically hindered arylating reagents.

The mechanism proposed by the authors is presented in Figure 21. First, the DG-assisted C–H activation of the aromatic compounds by Pd(II) leads to the formation of the corresponding palladacycle. In parallel, the photocatalyst excited by visible light, Ru(II)* reduces the aryldiazonium salt, generating the corresponding aryl radical and the oxidized Ru(III). Then, the highly reactive radical species formed is intercepted by the palladacycle to produce a Pd(III) metallacycle intermediate bearing both coupling partners. This oxidative addition is the key step of the mechanism, thus making this transformation possible. A SET between this metallacycle and the Ru(III), rendering the reaction feasible at room temperature, regenerates the ground-state Ru(II) photocatalyst concomitantly with the formation of a Pd(IV) species. At this point, a reductive elimination provides the desired coupling product together with the Pd(II) catalyst, thus completing this synergistic catalytic system (Figure 21). However, a subsequent mechanistic study indicated that the order of the two last steps might be inversed, thus leading to the reductive elimination on the Pd(III) intermediate followed by the single-electron oxidation of the Pd(I) resulting species [82].

Thereafter, Sanford's group showed in 2012 the possibility to extend this C–H activation/photoredox dual catalytic system by using diaryliodonium salts as radical precursors [83]. Considering the higher reduction potentials of these compounds in comparison with the corresponding diazoniums, a stronger reductive iridium-based photocatalyst was necessary to generate the aryl radicals (Figure 22). Similar results were obtained with this new procedure. This modified protocol was also compatible with a diversity of DGs and diazonium salts, thus furnishing a panel of 20 biaryls in good yields.

Inspired by this work, several research groups independently published alternative procedures based on the same dual catalytic system merging C–H activation and photoredox catalysis.

In 2017, Xu's group reported a variation of the *ortho*-arylation of acetanilides and benzamides with aryldiazonium salts [84], now compatible with a cheaper photosensitizer, i.e., the organic Acr–H_2 molecule (Figure 23). In this study, 35 examples of the targeted coupling products were afforded in good to excellent yields. Various synthetically relevant functional groups, including halides, esters, amides, ethers, ketones, and aldehydes were compatible with the protocol. This outcome is interesting from the sophisticated molecule late-stage functionalization viewpoint. Furthermore, the quantum yield of the reaction was measured and turned out to be 6.5. This result indicated that the mechanism of this reaction involved a short radical chain process [85].

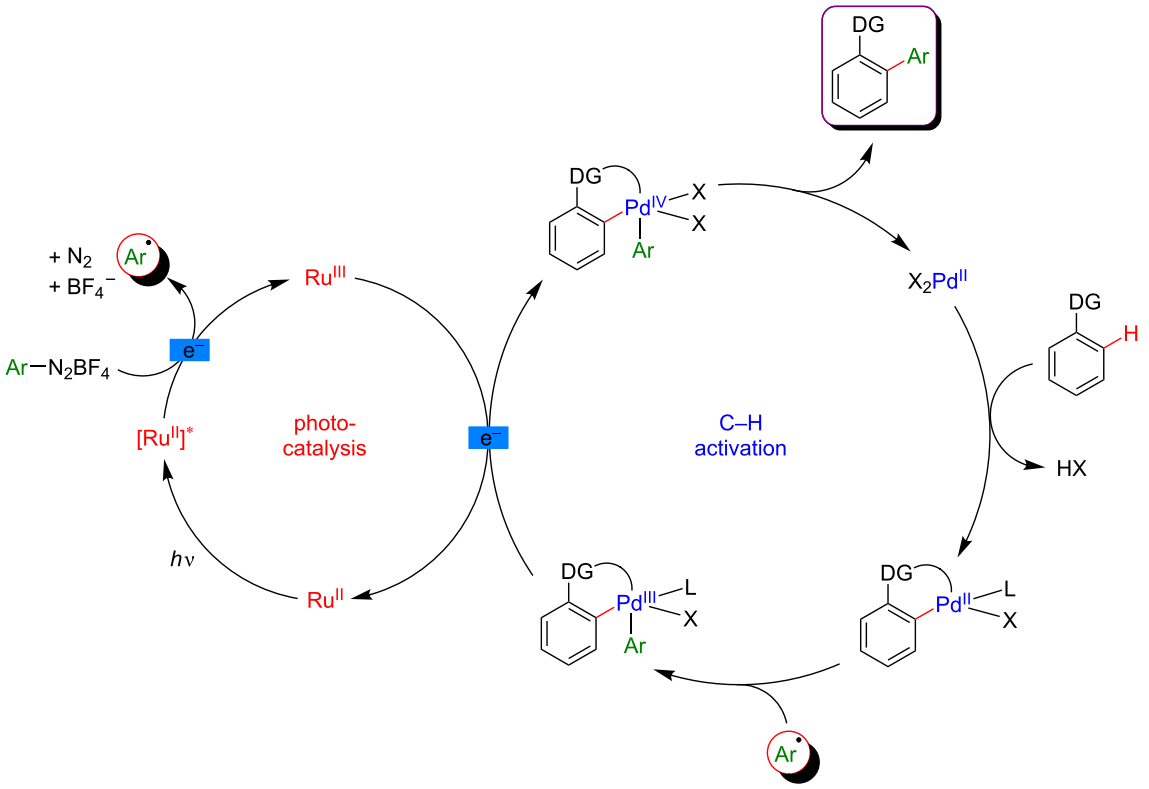

Figure 21: Proposed mechanism for the C–H arylation with diazonium salts via dual catalysis.

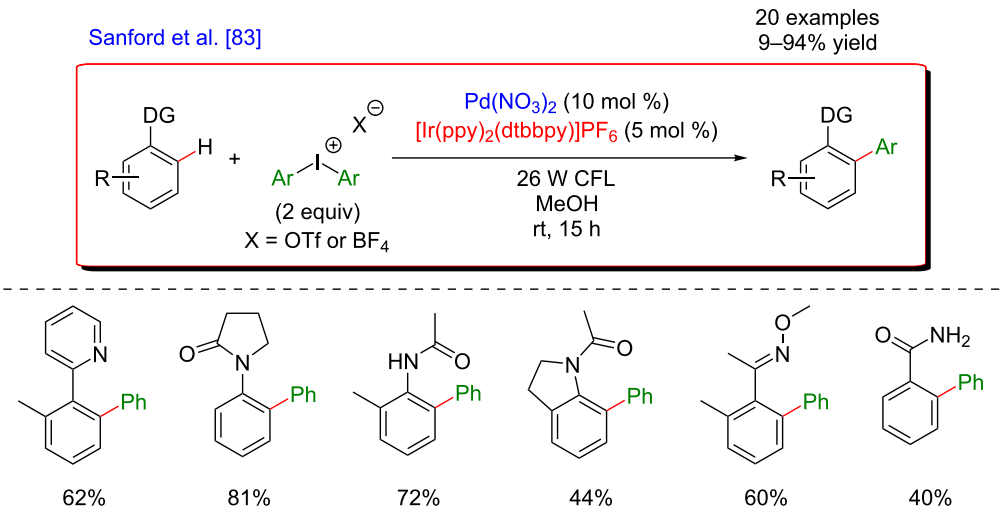

Figure 22: Dual catalysis merging C–H activation/photoredox using diaryliodonium salts.

The same year, a similar arylation was disclosed by Balaraman et al. using eosin Y as a photoredox catalyst (Figure 24) [86]. This methodology operated under mild conditions, was efficient using a low loading of both catalysts and could be scaled-up to a gram-scale. The procedure featured a good functional tolerance and was compatible with a wide range of both substrates, thus delivering 35 examples of coupling products in good to excellent yields. Furthermore, the authors easily accomplished the removal of the DG and performed the diversification of *ortho*-arylaniline derivatives products into synthetically

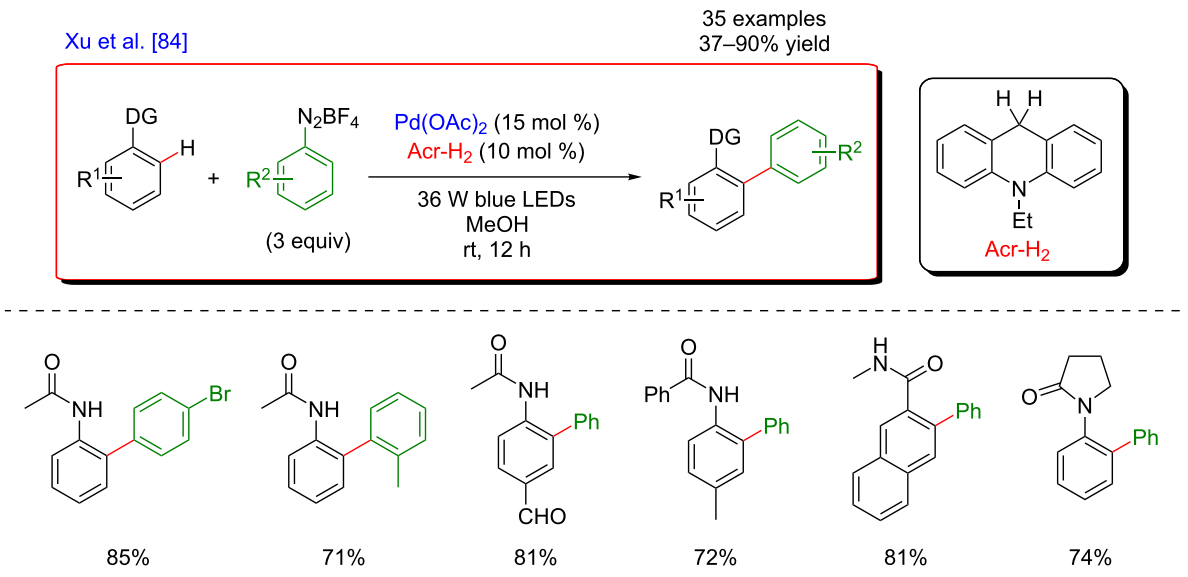

Figure 23: Direct arylation via the dual catalytic system reported by Xu.

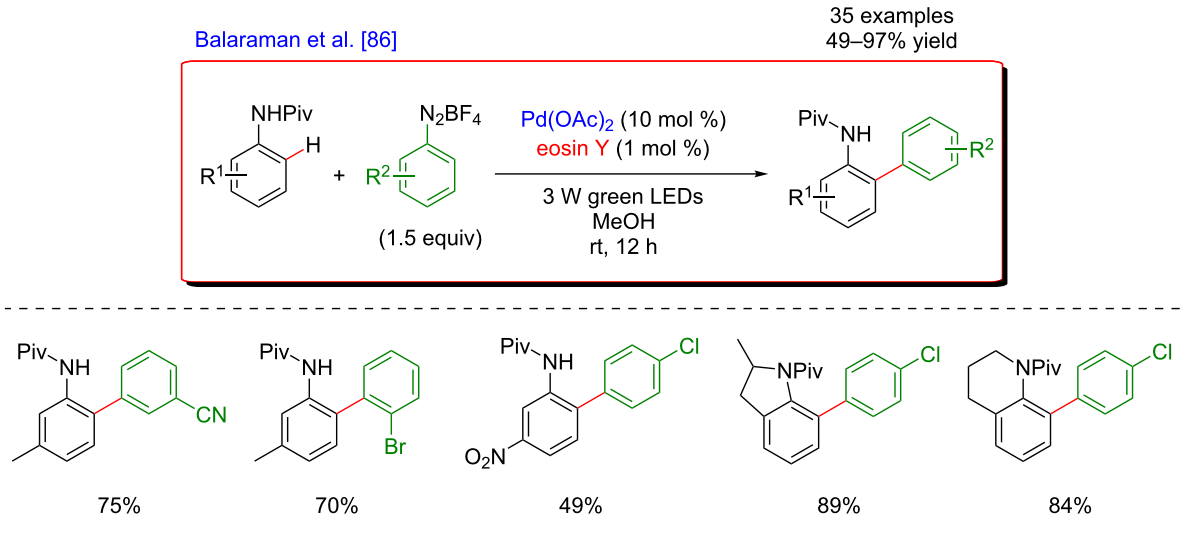

Figure 24: Direct arylation via dual catalytic system reported by Balaraman.

relevant *N*-heterocyclic compounds such as phenanthridine, carbazole, and dibenzo[*b*,*d*]azepine.

Simultaneously, Guo's group published the arylation of nucleosides bearing a purine moiety. The transformation was regioselective and tolerated various substituents at the N9 position of the purine, including sugar units (Figure 25) [87]. Interestingly, in this approach, the purine heterocycle acted as an inherent DG for the C–H activation step. The protocol provided a broad scope of products featuring good functional group tolerance, could be performed on a gram scale and occurred under mild conditions, essential features when working with biological systems. Thus, a variety of functionalized purines nucleosides that are potentially of great importance in medicinal chemistry were obtained in good yields.

In contrast to C(sp^2)–H bonds, C(sp^3)–H bond activation is much more challenging. Inspired by the potential of bicoordinating DGs to facilitate C(sp^3)–H metalation, Polyzos's group reported the direct arylation of aliphatic bonds with aryldiazonium salts via a palladium/photoredox dual catalysis (Figure 26) [88]. The method utilized an 8-aminoquinoline-derived biden-

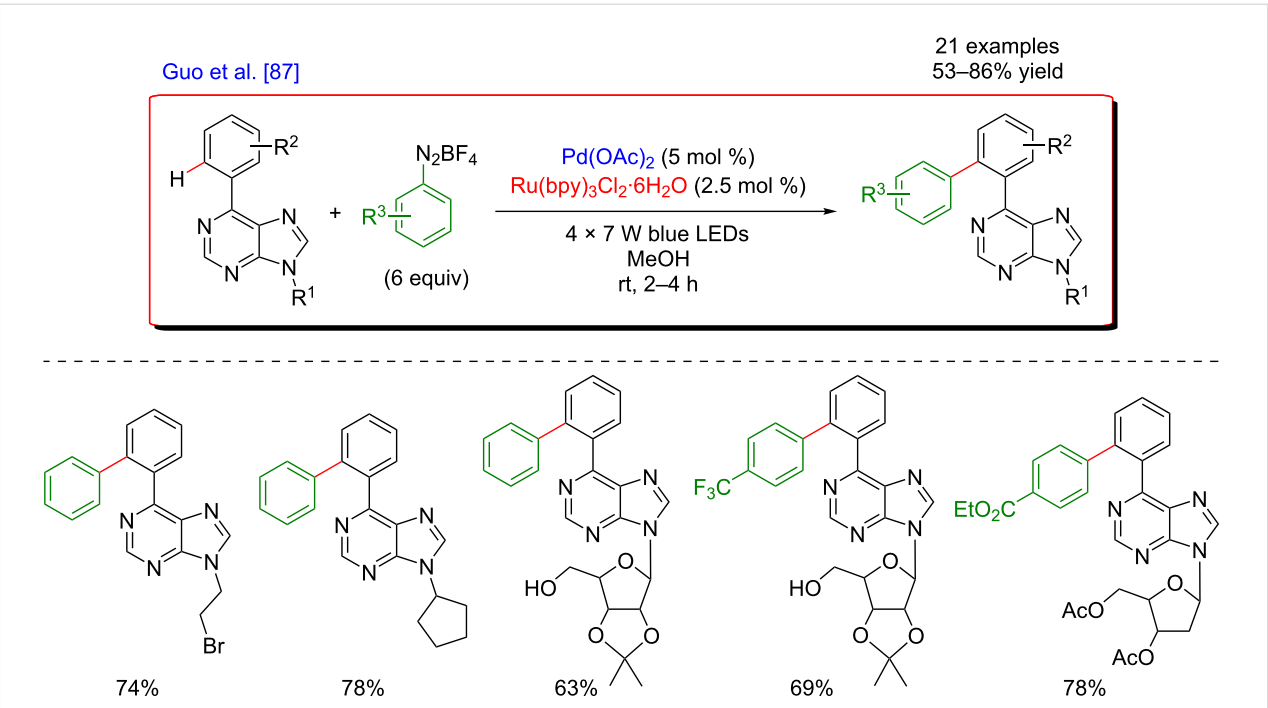

Figure 25: Direct arylation via dual catalytic system reported by Guo.

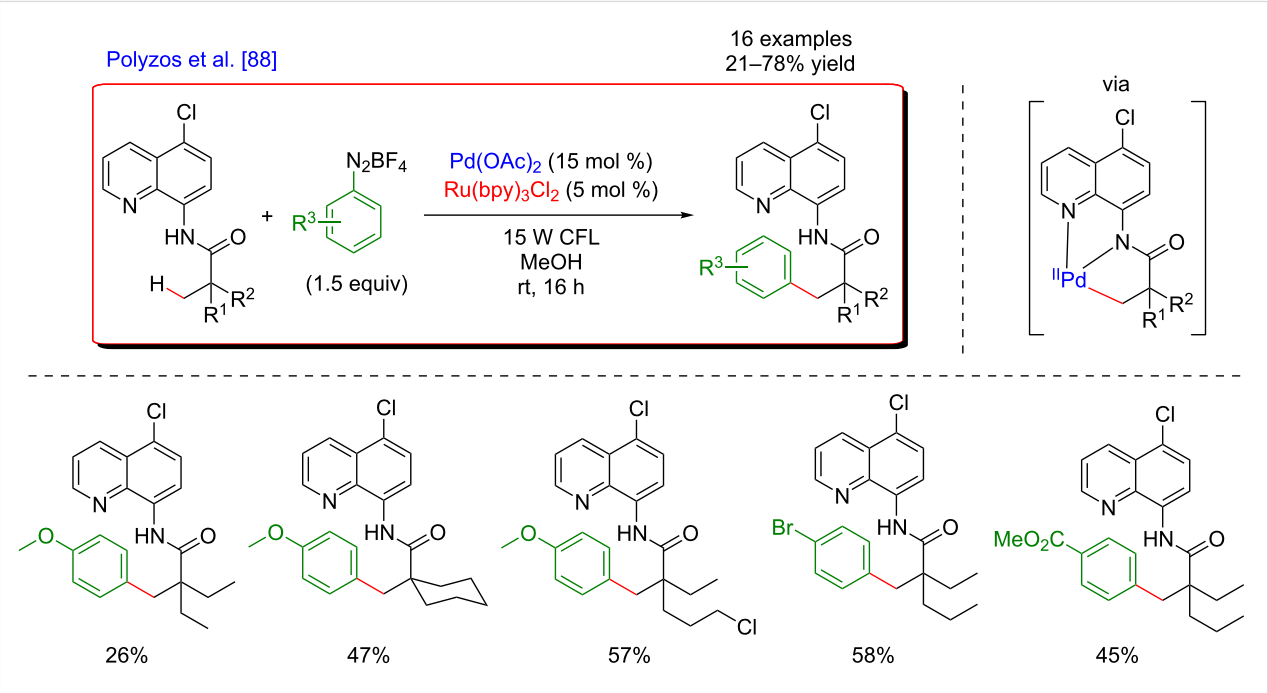

Figure 26: C(sp^3)–H bond arylation via the dual Pd/photoredox catalytic system.

tate auxiliary, and, in contrast with a vast majority of C(sp^3)–H bond activation reactions, was effective at room temperature. The coupling displayed high selectivity for β-methyl C(sp^3)–H bonds. Of note is that a substitution at the C5-position of the 8-aminoquinoline ring was beneficial for the C–H activation step as the functionalization of 5-chloro-8-aminoquinoline delivered the arylated products in increased yields. Carbocyclic rings, long alkyl chains, methoxy, chloride, and phenyl groups

were tolerated on the C–H substrates and electron-poor as well as electron-rich diazonium salts could be coupled smoothly.

Pd-catalyzed acylation

The dual catalytic system merging C–H activation and photoredox catalysis was also applied to C(sp^2)–H acylation reactions via the generation of acyl radicals. In 2015, Li, Wang and co-workers reported the *ortho*-acylation of acetanilide derivatives using α-ketoacids as coupling partners and employing synergistic catalysis combining palladium-catalyzed C–H activation and photoredox catalysis (Figure 27) [89]. Interestingly, the transformation occurred smoothly in the presence of eosin Y, an inexpensive (in comparison with Ir- or Ru-based photoredox catalysts), and easily accessible organic photocatalyst. The reaction, carried out at room temperature, promoted the introduction of various aromatic as well as aliphatic acyl motifs and was applicable to a broad range of substrates hence furnishing more than 30 acylated acetanilides in good to excellent yields.

The proposed mechanism involves an initial amide-directed C–H activation step to produce a palladacyclic intermediate. In parallel, the oxidative decarboxylation of the α-ketoacid induced by the photocatalyst in its excited state generates the corresponding acyl radical. The latter is intercepted by the palladacycle, leading to a Pd(III) species. Remarkably, the molecular oxygen enables to close the catalytic cycle by sequentially oxidizing the photoredox catalyst and the Pd(III) species via the formation of superoxide anion. In this way, the photocatalyst is regenerated in its ground state and the Pd(IV) intermediate undergoes fast reductive elimination, liberating the expected product (Figure 28).

In 2016, Wang et al. further demonstrated the possibility of extending this approach to the C(sp^2)–H acylation of azo- and azoxybenzene derivatives (Figure 29) [90]. Similarly, acyl radicals generated by photodecarboxylation of α-ketoacids were engaged in a dual catalytic system. The strategy used the Fukuzumi acridinium salt organic photocatalyst and $Pd(TFA)_2$ to promote the C–H activation step. In this case, the transformation was only compatible with aromatic α-ketoacids. Nevertheless, the reaction was performed at room temperature and tolerated a wide spectrum of both substrates bearing various functional groups, thus furnishing more than 30 acylated products in moderate to good yields. As the molecular oxygen was the terminal oxidant, the typical high loading of an external oxidant could be avoided.

Flow chemistry is an important technology for photochemical reactions due to the inherent lack of scalability issues as a consequence of the Beer–Lambert law of absorption. Consequently, continuous-flow chemistry represents one of the few ways in which pharmaceutically relevant quantities of compounds can be synthesized through photoinduced transformations [91]. In this context, great advances were also recently achieved in the field of direct C–H functionalization reactions under flow conditions. Persistent improvements enabled the development of innovative flow techniques, encompassing large-scale photochemical procedures, which were successfully applied to various C–H functionalization reactions [92,93].

In 2017, Noël, Van der Eycken and co-workers hence astutely combined the dual catalysis strategy with flow microreactor technology to achieve C2-acylation of indole derivatives with aldehydes (Figure 30) [94]. Both electron-rich and electron-

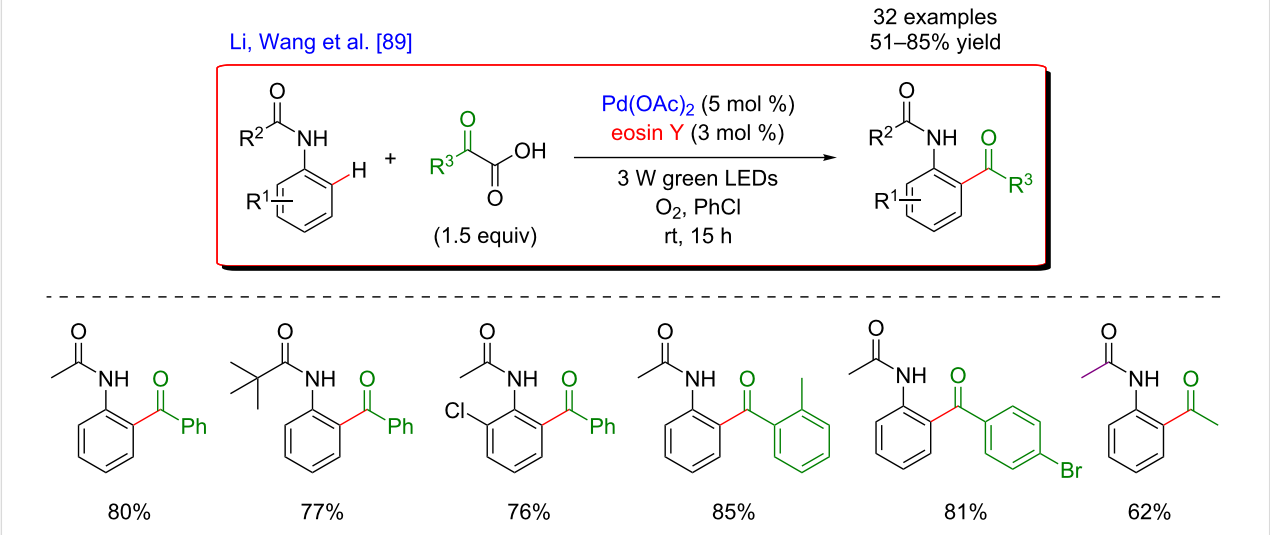

Figure 27: Acetanilide derivatives acylation via the dual C–H activation/photoredox catalysis.

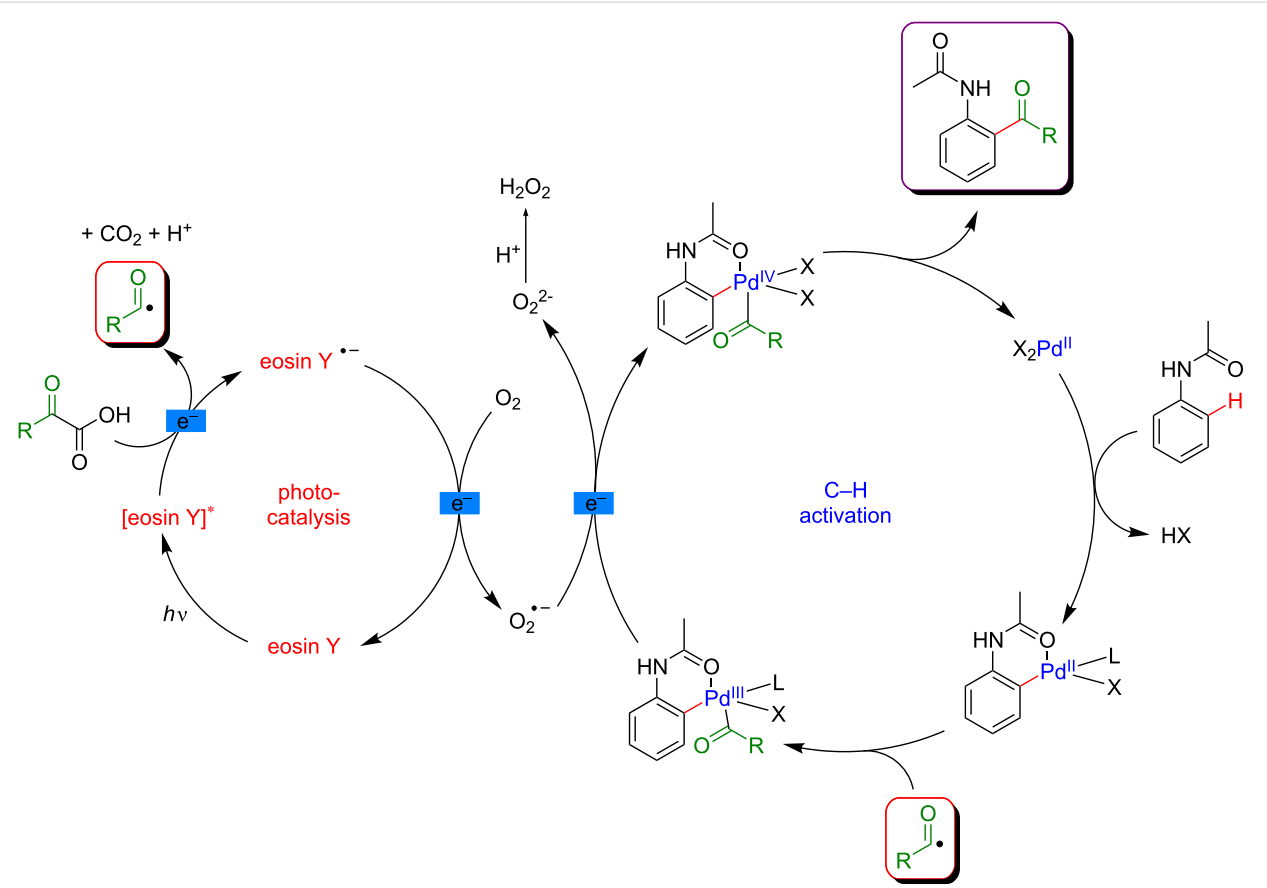

Figure 28: Proposed mechanism for the C–H acylation with α-ketoacids via dual catalysis.

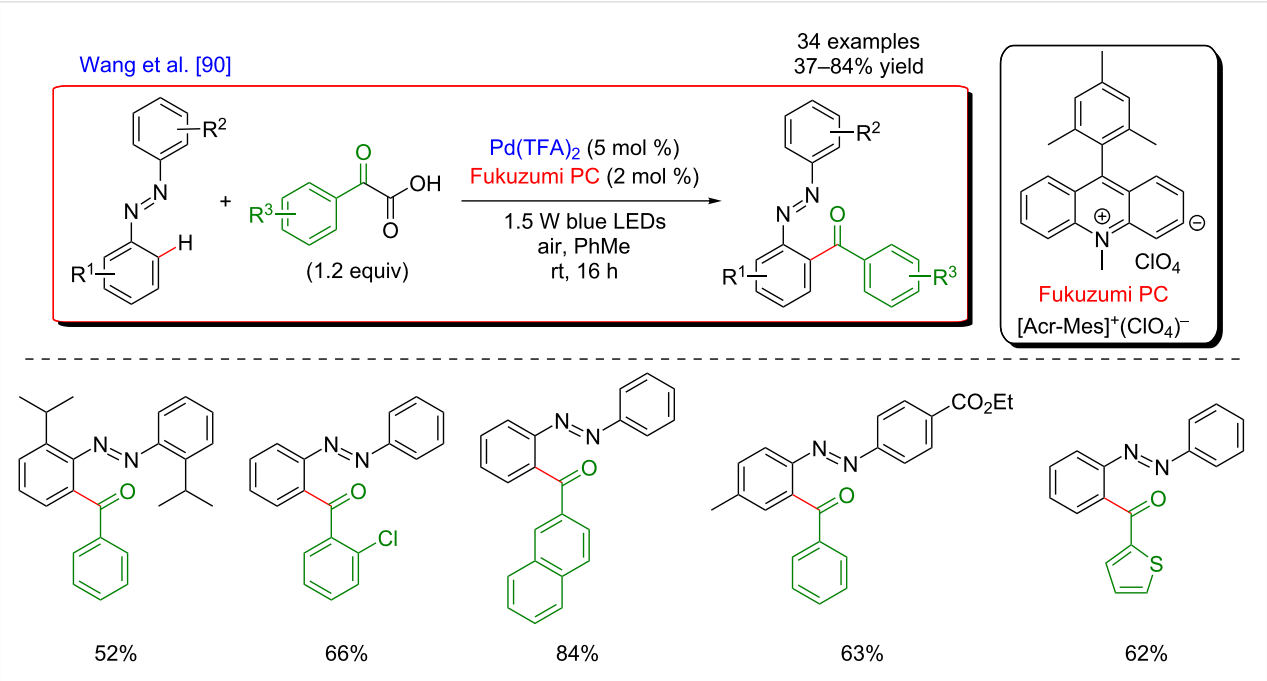

Figure 29: Acylation of azobenzenes via the dual catalysis C–H activation/photoredox.

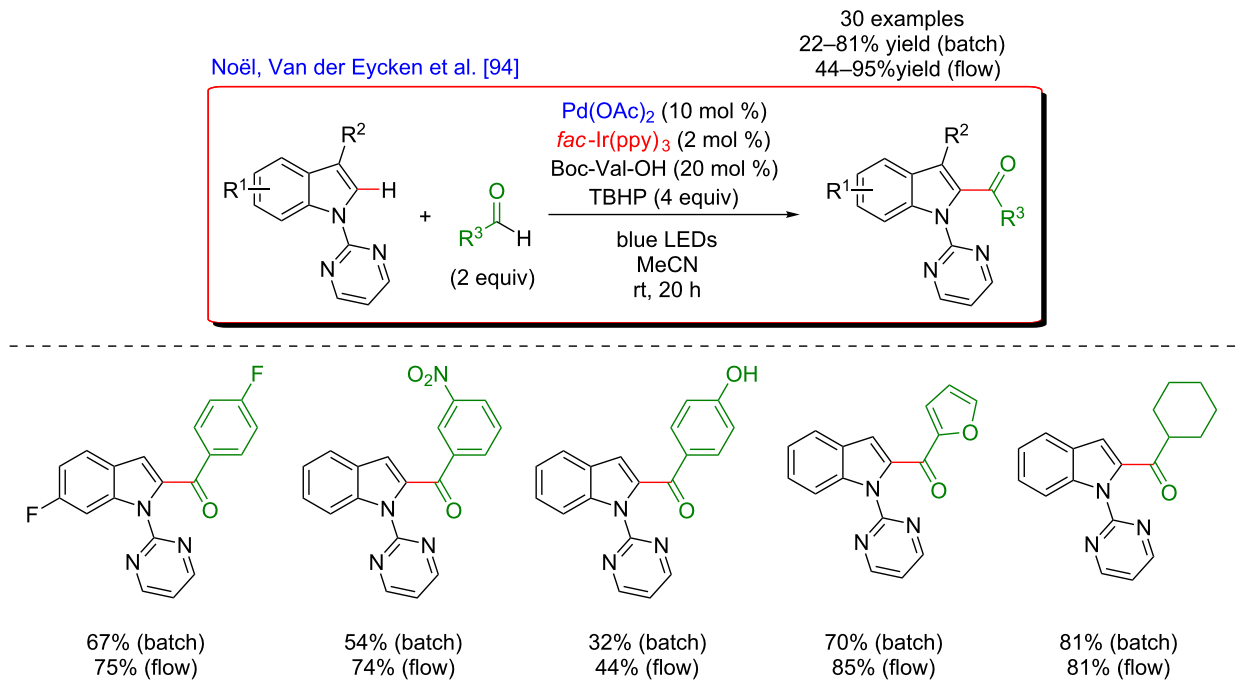

Figure 30: C2-acylation of indoles via the dual C–H activation/photoredox catalysis.

poor aromatic or aliphatic aldehydes were potent coupling partners for this procedure. The transformation also allowed the introduction of heterocyclic moieties at the C2-position of indoles, hence exhibiting a wide substrate scope of this coupling.

The proposed mechanism of this acylation is shown in Figure 31. As previously, distinct catalytic cycles involving photoredox catalysis and C–H activation act in a cooperative way to promote the formation of a new bond. The strategy is based on the presence of a pyrimidine DG at the N1-position of the indole in order to facilitate the C–H activation step. Furthermore, a peroxide (TBHP) is needed to oxidize the Ir-based photoredox catalyst and to generate the acyl radical via hydrogen atom transfer. From the mechanistic perspective this synergistic dual catalytic system merging C–H activation and photocatalysis is similar to the one described by Sanford for the arylation with diazonium salts.

The same year, Jana's group independently reported an analogous approach allowing the C2-acylation of indole derivatives with aldehydes (Figure 32). The only difference in comparison with Noël and Van der Eycken's procedure concerned the nature of the photocatalyst used for the transformation, which was a Ru-based photosensitizer in that case [95]. This time, the acylation reaction was exclusively performed in batch and the protocol was compatible with various substrates bearing synthetically useful functional groups. Numerous coupling products were hence obtained in good yields and the authors applied the methodology for the late-stage acylation of natural L-tryptophan as well as carbazole derivatives.

Cu-catalyzed transformations

Sporadic examples using copper as transition metal for C–H functionalization reactions in combination with photocatalysis were also reported in the literature. The key advantages of the use of Cu as catalyst are related to its great abundance, as well as its cheap and non-toxic character [14,96,97].

In 2016, Tan, Wang and co-workers developed a methodology allowing the *ortho*-perfluoroalkylation of benzamides. This reaction photoinduced by visible light was promoted by copper and used the bidentate 8-aminoquinoline moiety as the DG (Figure 33) [98]. Remarkably, eosin Y, a cheap organic photocatalyst, enhanced the generation of perfluoroalkyl radicals from the corresponding alkyl iodides but a stoichiometric amount of a simple copper salt, acting as both, the catalyst for C–H activation and the oxidizing agent, was also required. The reaction occurred at higher temperatures (60 °C) compared to other dual catalytic systems. A wide variety of benzamide substrates bearing different functional groups such as alkyl, phenyl, halogen, ethoxy, trifluoromethyl, nitro, and ester underwent efficiently the desired perfluoroalkylation. This coupling was sensitive to steric hindrance as *ortho*-substituted substrates were

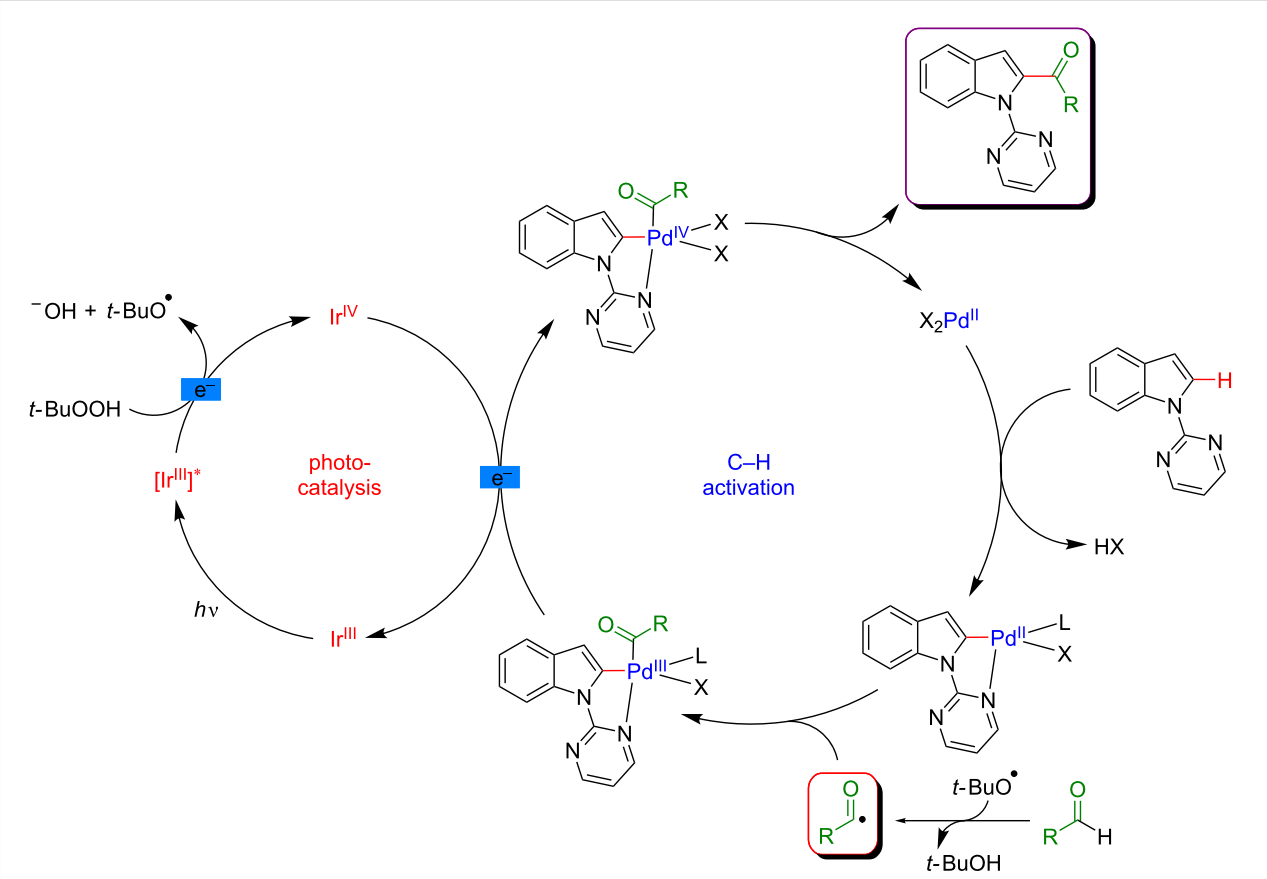

Figure 31: Proposed mechanism for the C2-acylation of indoles with aldehydes via dual catalysis.

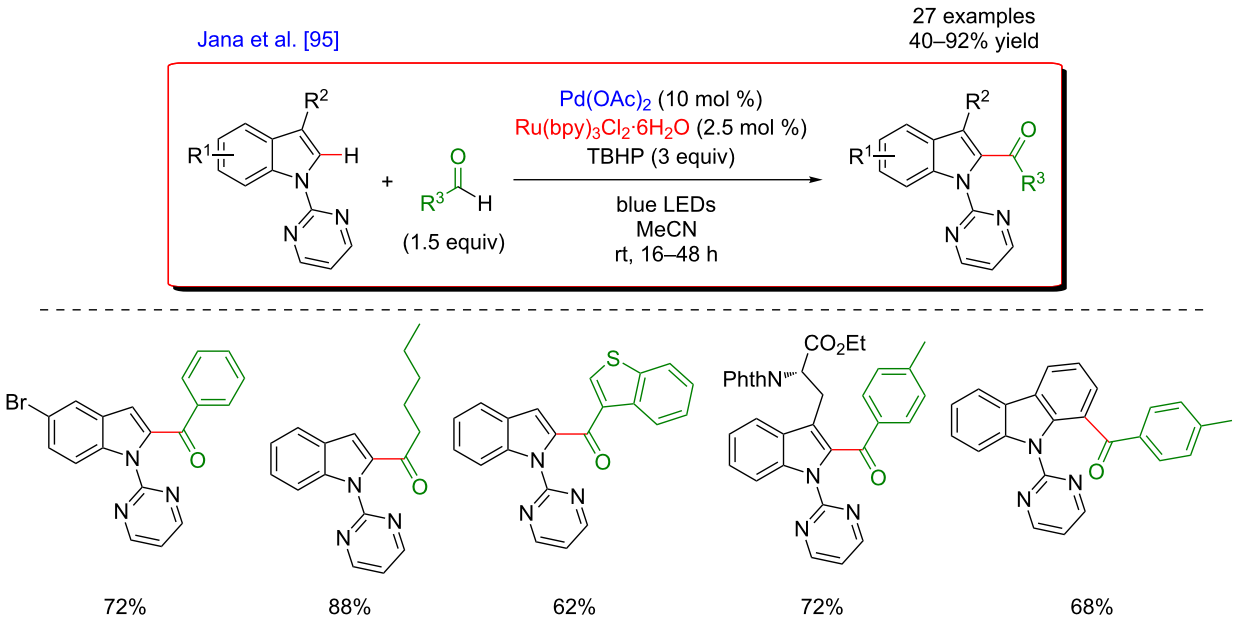

Figure 32: C2-acylation of indoles via the dual C–H activation/photoredox catalysis.

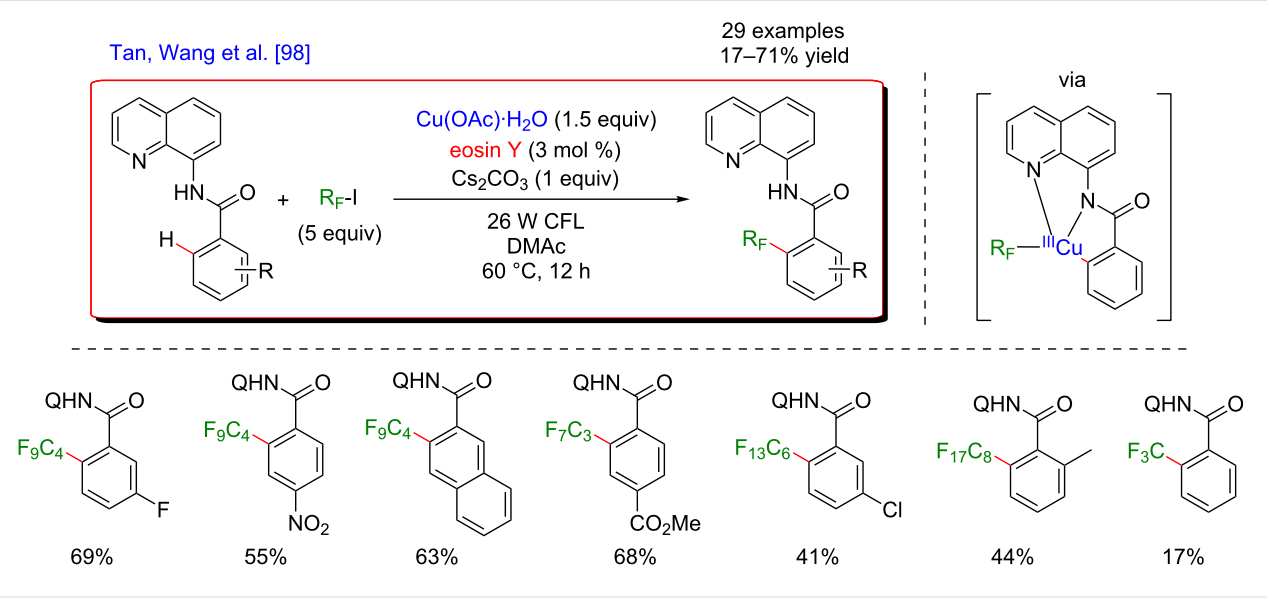

Figure 33: Perfluoroalkylation of arenes via the dual C–H activation/photoredox catalysis.

less efficiently converted into the desired products. Furthermore, various perfluoroalkyl iodides with different chain lengths were potent substrates, affording the corresponding perfluoralkylated products in moderate to good yields, except for trifluoromethyl iodide, presumably due to the low boiling point of CF_3I. Finally, the removal of the DG allowed the post-modification of the products into the corresponding perfluoroalkyl benzoic acid derivatives.

A plausible mechanism for the perfluoroalkylation of *N*-(quinolin-8-yl)benzamides is proposed in Figure 34. First, C–H activation of the benzamide substrate with copper produces a cyclometalated complex. Meanwhile, perfluoroalkyl radicals are generated by electron transfer between the perfluoroalkyl iodides and the excited photoredox catalyst. Interception of the perfluoroalkyl radical by the Cu(II) complex delivers a new Cu(III) metalacyclic intermediate which releases the desired *ortho*-functionalized product via reductive elimination.

In 2017, Yang, Wu, Wu et al. reported a mild and efficient protocol for the remote C4–H sulfonylation of 1-naphthylamine derivatives with sodium sulfinates in the presence of $K_2S_2O_8$ as the oxidant (Figure 35) [99]. This strategy was based on the use of a bidentate picolinamide DG promoting the direct C–H functionalization of the naphthalene ring. The transformation proceeded under either Cu/Ag co-catalysis or using the dual Ru/Cu photoredox system. In the latter case, the methodology was operative at room temperature within a short reaction time, affording the desired products in good to excellent yields. The described sulfonylation procedure was general and both electron-withdrawing or -donating substituents were well tolerated at different positions of the 1-naphthylamine derivatives. Aromatic, aliphatic as well as heterocyclic sodium sulfinates were also suitable coupling partners for this C–H functionalization. In addition, the reaction occurred smoothly on a gram scale and the DG could be subsequently removed by hydrolysis, further demonstrating the synthetic potential of this protocol.

The authors proposed a plausible mechanism involving a radical pathway and suggested that this C4–H sulfonylation reaction might proceed via a single electron-transfer process (Figure 36). In the first place, a bidentate chelated species is formed by the coordination of 1-naphthylamine derivatives with copper salt. The subsequent oxidation of this intermediate with potassium persulfate produces a Cu(III) species, furnishing a radical cation on the naphthyl ring after an intramolecular electron transfer. In the meantime, the sulfonyl radical is generated by oxidation of the sulfinate substrate via the photocatalytic cycle with the $Ru(bpy)_3$ catalyst and $K_2S_2O_8$ (the direct oxidation of sulfinate by persulfate could also be envisioned). Thereafter, a cationic intermediate is afforded by the radical combination between the sulfonyl radical and the 1-naphthyl derivative at the C4 position. Lastly, a proton-transfer process and dissociation result in the formation of the expected coupling product, accompanied by the regeneration of the Cu salt to close the catalytic cycle.

Direct metalation and visible-light absorption by a single catalyst: Ru and Rh-catalyzed photoinduced transformations

The dual catalytic systems, combining visible-light photocatalysis and C–H activation generally require the use of two distinct

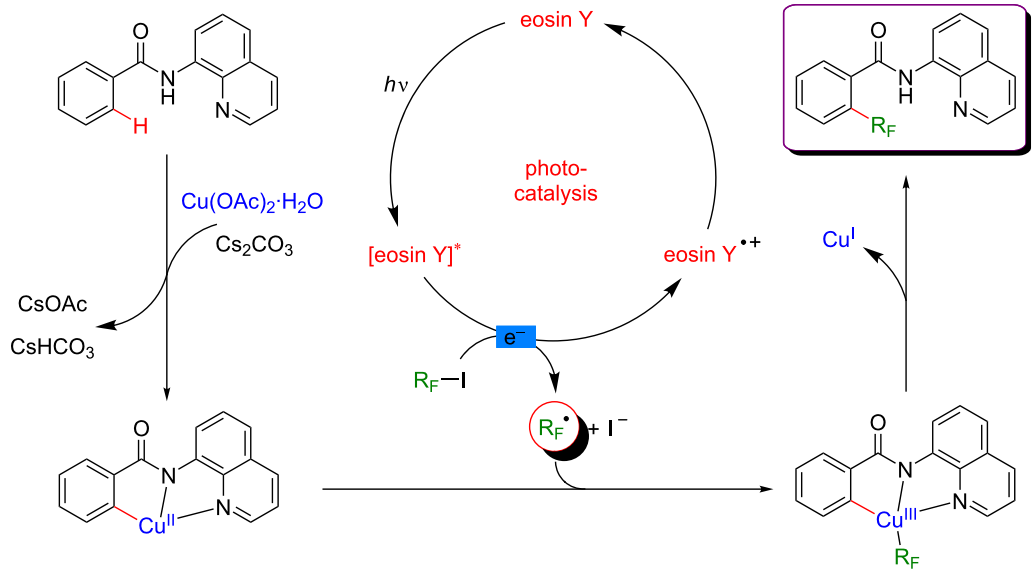

Figure 34: Proposed mechanism for perfluoroalkylation of arenes via dual catalysis.

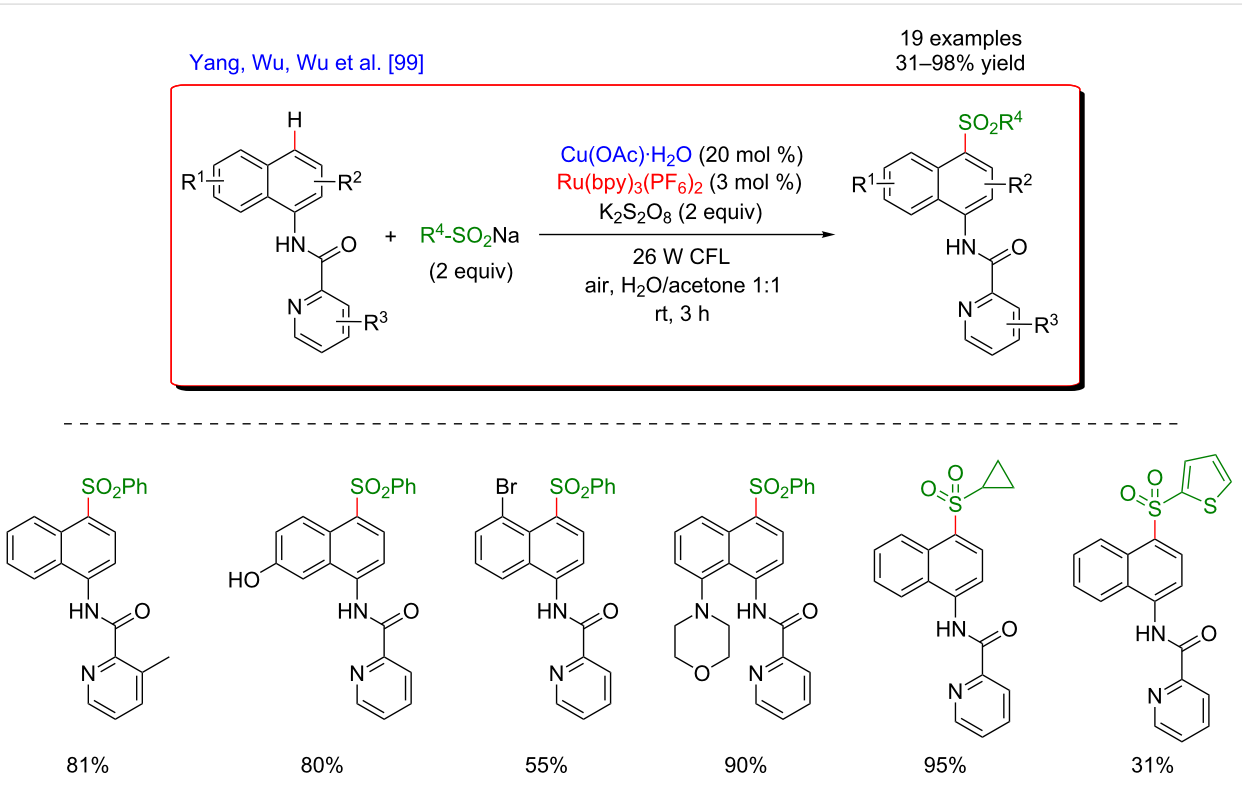

Figure 35: Sulfonylation of 1-naphthylamides via the dual C–H activation/photoredox catalysis.

metal catalysts, one able to activate a poorly reactive C–H bond and the second one harvesting the light in a photoredox process. Therefore, the design of alternative approaches, in which a single catalyst can play a double role, i.e., absorbing light and promoting bond-breaking/bond-forming events, seems extremely appealing as such metallaphotocatalysis could

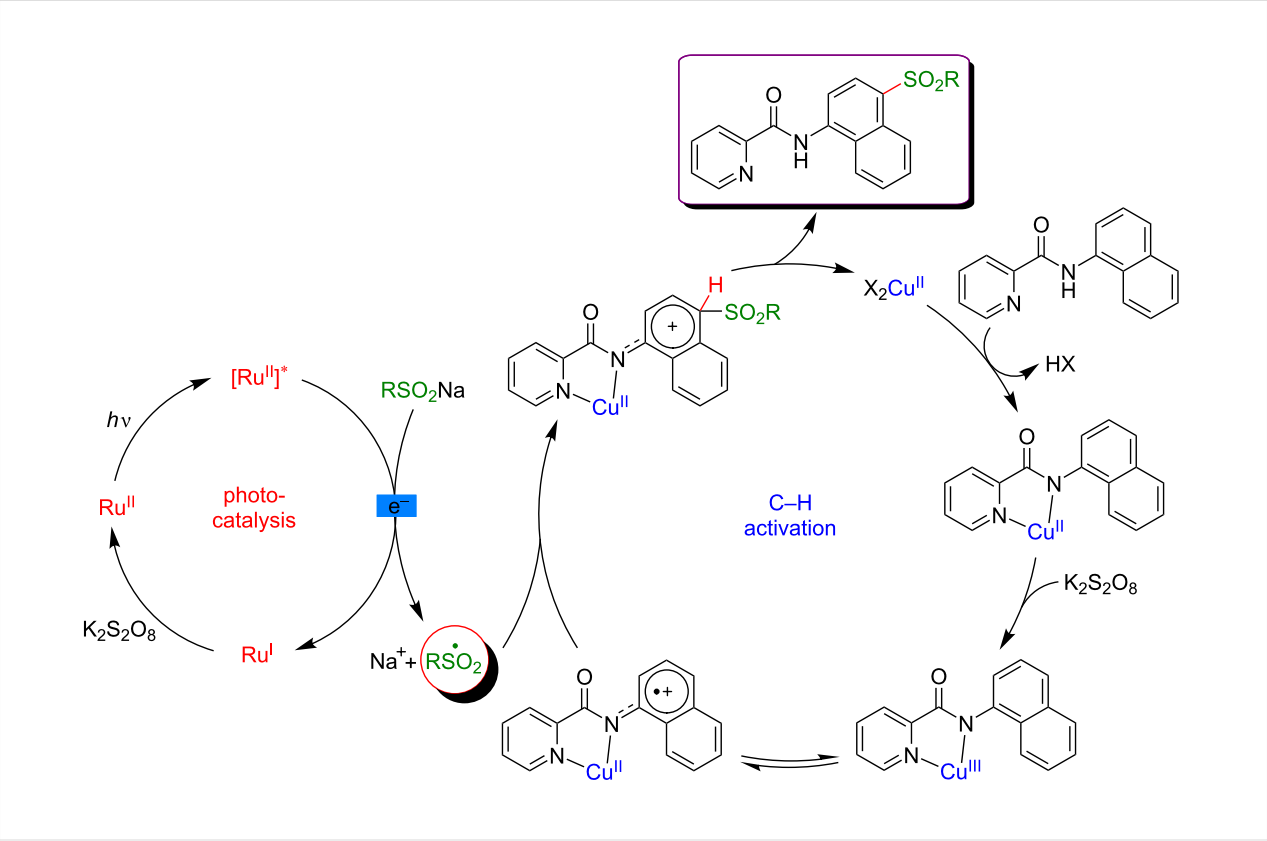

Figure 36: Proposed mechanism for sulfonylation of 1-naphthylamides via dual catalysis.

thus be envisioned under exogenous photosensitizer-free conditions.

The pioneering work in this extremely challenging research field was reported concomitantly by the groups of Ackermann [100] and Greaney [101], and concerned unique Ru-catalyzed *meta*-selective C–H alkylation of arenes. The ruthenium-catalyzed *meta*-selective C–H functionalization through arene σ-activation was already well established yet limited by harsh reaction conditions and elevated reaction temperatures. Both research groups hence hypothesized that the Ru-metallacyclic intermediate, generated via directed *ortho*-metalation should exhibit visible-light absorption property and thus, under visible-light irradiation, the overall catalytic cycle could benefit from the photocatalytic activation.

Following the initial hypothesis, the direct functionalization of phenylpyridine substrates turned out to be very efficient at room temperature while applying blue LED irradiation. Two slightly modified catalytic systems composed of a $[Ru(p\text{-cymene})Cl_2]_2$ catalyst and either K_2CO_3 or KOAc bases promoted the direct *meta*-selective C(sp^2)–H alkylation with secondary and tertiary alkyl halides, delivering the expected products in good to excellent yields (Figure 37 and Figure 38). The addition of diphenylphosphoric acid as a ligand guaranteed higher yields and a broader reaction scope [100], including C–H activation substrates bearing alternative and modifiable DGs such as pyrazoles or oxazolines, as well as synthetically meaningful σ-bromo esters. The mildness of the reaction conditions warranted tolerance of sensitive and/or biologically relevant sugar, menthol, and steroid motifs (Figure 37).

The mechanistic studies conducted by Ackermann et al. clearly showed that the metallacyclic intermediates resulting from the C–H cleavage step slightly, yet significantly absorbed light in the relevant blue region. This absorption was believed to trigger the overall catalytic cycle at room temperature as no product formation was observed in the dark. The mechanistic scenario thus foresees an initial pyridine-directed, *ortho*-C–H activation delivering the photoactive intermediate. Under visible-light irradiation, the SET process from the excited ruthenacycle to the haloalkane coupling partner leads to the formation of a stabilized alkyl radical (Figure 39). Next, radical attack at the *para*-position of the carbohydrate ring of the phenylpyridine substrate takes place. Final SET and subsequent rearomatization complete the catalytic cycle, delivering the expected *meta*-functionalized product and regenerating the catalytically competent ruthenium(II) species.

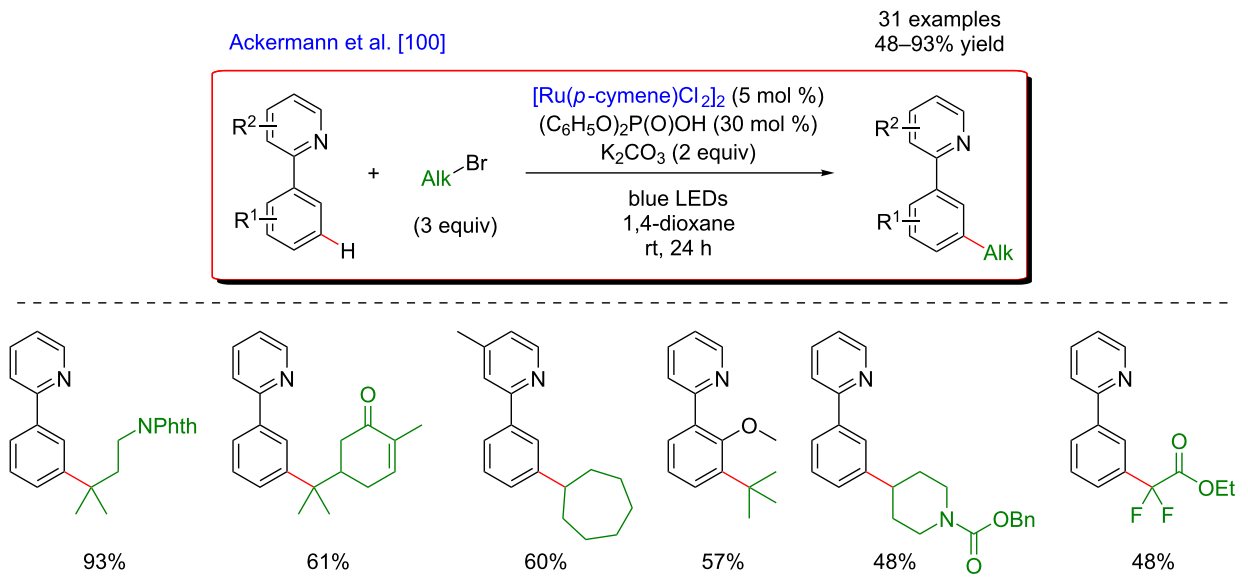

Figure 37: *meta*-C–H Alkylation of arenes via visible-light metallaphotocatalysis.

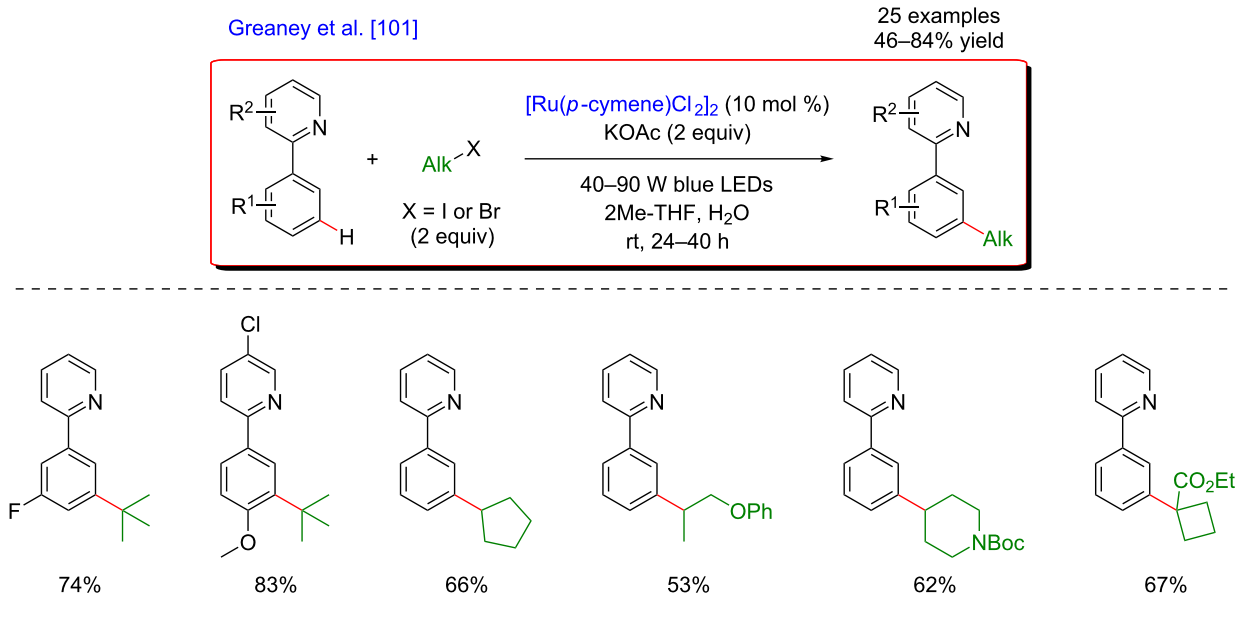

Figure 38: Alternative procedure for *meta*-C–H alkylation of arenes via metallaphotocatalysis.

A few months later, Baslé et al. exploited the same concept of merging C–H activation and photocatalysis while using a single metal catalyst. In this case, an original Rh–NHC complex was used for the *ortho*-directed C–H borylation of phenylpyridine substrates (Figure 40) [102]. As previously, the irradiation with visible light allowed performing this challenging borylation under mild reaction conditions, thus delivering, after oxidation of the crude reaction mixture with Oxone, a large panel of the corresponding hydroxylated pyridine products.

From the mechanistic point of view, this reaction is expected to differ from the previously described Ru-catalyzed *meta*-selective C–H alkylations by the nature of the metal-based photoactive species (Figure 41). Indeed, the NHC–Rh complex is

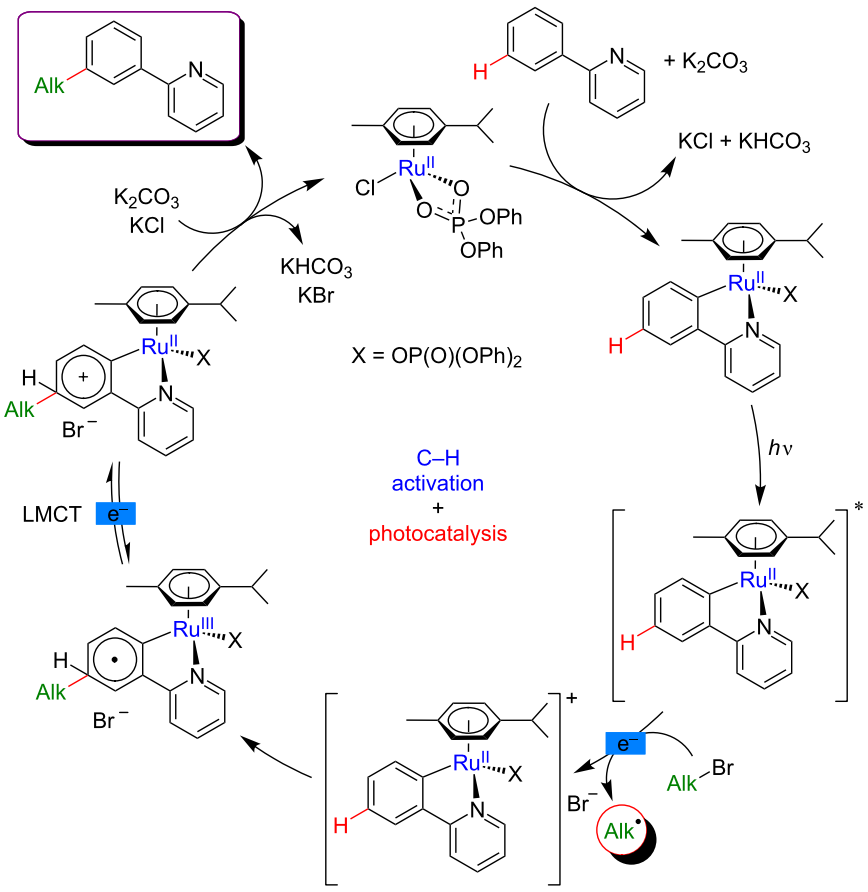

Figure 39: Proposed mechanism for *meta*-C–H alkylation of arenes via metallaphotocatalysis.

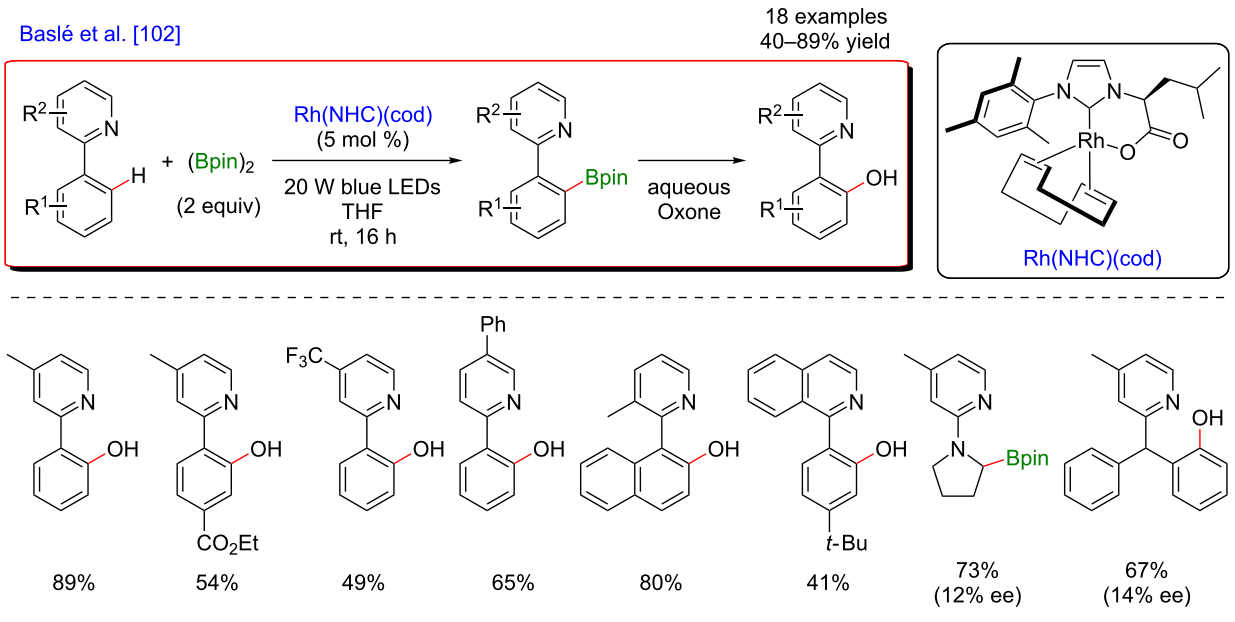

Figure 40: C–H borylation of arenes via visible-light metallaphotocatalysis.

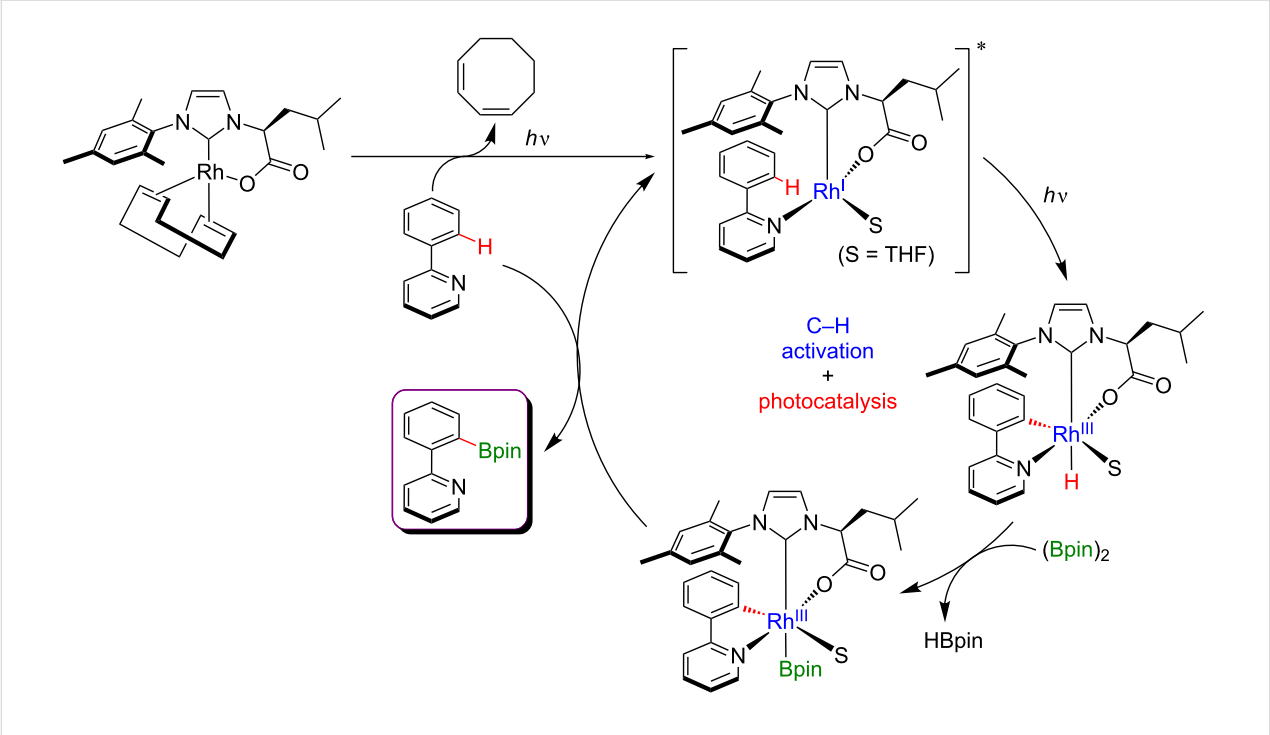

Figure 41: Proposed mechanism for C–H borylation of arenes via visible-light metallaphotocatalysis.

believed to be photoactive after coordination of the phenylpyridine substrate. The generated coordination complex becomes excited after the absorption of visible light and thus undergoes an oxidative *ortho*-C–H addition step via a metal-to-ligand charge transfer process, delivering the Rh(III) hydride species. Following borylation of the Rh(III) intermediate and subsequent reductive elimination liberate the expected coupling product with concomitant regeneration of the catalytically active NHC–Rh(I) complex.

The potential of the above-mentioned reactions is particularly interesting as indeed, a unique, double reactivity might be attributed to a single precatalyst with the in situ formation of photoactive intermediates. Remarkably, the generated metallaphotoredox catalyst is able to harvest visible light and triggers the expected transformation at room temperature.

Undirected C–H activation

In parallel to the development of the field of metal-catalyzed directed C–H activation, reactions involving the direct functionalization of simple aromatic compounds, depleted of a coordinating motif, have also attracted significant scientific interest [103]. Such couplings allowed constructing molecular complexity from very simple arenes such as benzene, toluene or mesitylene. However, such transformations frequently required rather harsh reaction conditions as well as the addition of strong oxidants and/or additives.

In order to provide a solution towards these limitations of the undirected C–H activation, the group of Lee initiated a project merging gold-catalyzed C–H activation with photoredox catalysis (Figure 42) [104]. Such a dual catalytic system should promote the desired C–C bond-forming reaction under oxidant-free conditions, while the use of the gold catalyst gives promise of accessing highly site-selective transformations. Indeed, electrophilic Au(III) species were able to site-selectively activate C–H bonds of activated electron-rich arenes thus generating Au(III)–Ar species.

Following this hypothesis, the desired undirected C–H arylation occurred smoothly between mesitylene (and several other electron-rich aromatic substrates) and aryldiazonium salts as coupling partner, using an Au(I) catalyst in combination with $Ru(bpy)_3(PF_6)_2$ as the photosensitizer under blue LED irradiation. Remarkably, the test reactions clearly indicated the low efficiency of this Ar–Ar cross-coupling in the absence of the photosensitizer and/or in the dark, while an unselective transformation took place when removing the Au catalyst. Under the optimized reaction conditions, this dual catalysis protocol was compatible with a panel of electron-poor aryldiazonium partners, affording the targeted biaryls in moderate to high yields.

Based on a literature survey, a plausible mechanism of this reaction is initiated by the addition of an aryl radical (generated from the corresponding diazonium precursor) to the Au(I) cata-

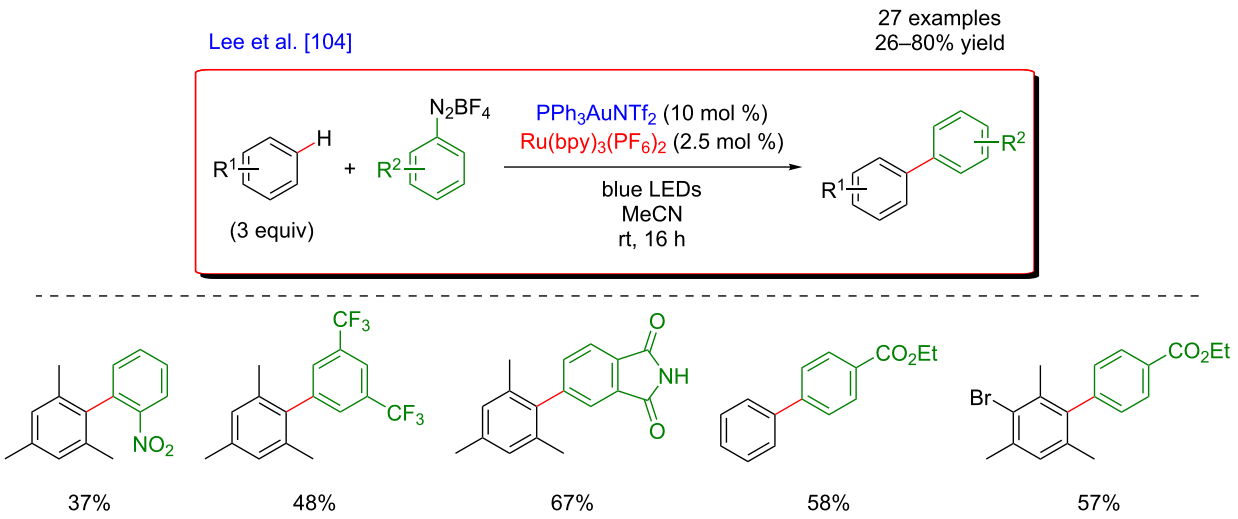

Figure 42: Undirected C–H aryl–aryl cross coupling via dual gold/photoredox catalysis.

lyst, followed by SET oxidation to provide an Ar–Au(III) intermediate (Figure 43). This Lewis-acidic Au species promotes the regioselective C–H auration of the electron-rich substrate, delivering a cationic intermediate that under deprotonation and subsequent reductive elimination furnishes the expected biaryl product. In parallel, the photocatalytic cycle warrants the mild generation of the Ar• radical as well as the key Au(II)/Au(III) oxidation.

More recently, an alternative strategy for the straight, non-directed arylation of (hetero)arenes was reported by Ackermann (Figure 44) [105]. Targeting more sustainable protocols, a manganese catalyst was selected to trigger the coupling between an aryldiazonium salt and simple (hetero)aryls. A unique reactivity was obtained under irradiation with blue LEDs and a continuous-flow process allowed achieving higher reactivity. Under the optimized reaction protocol, a range of biaryls was

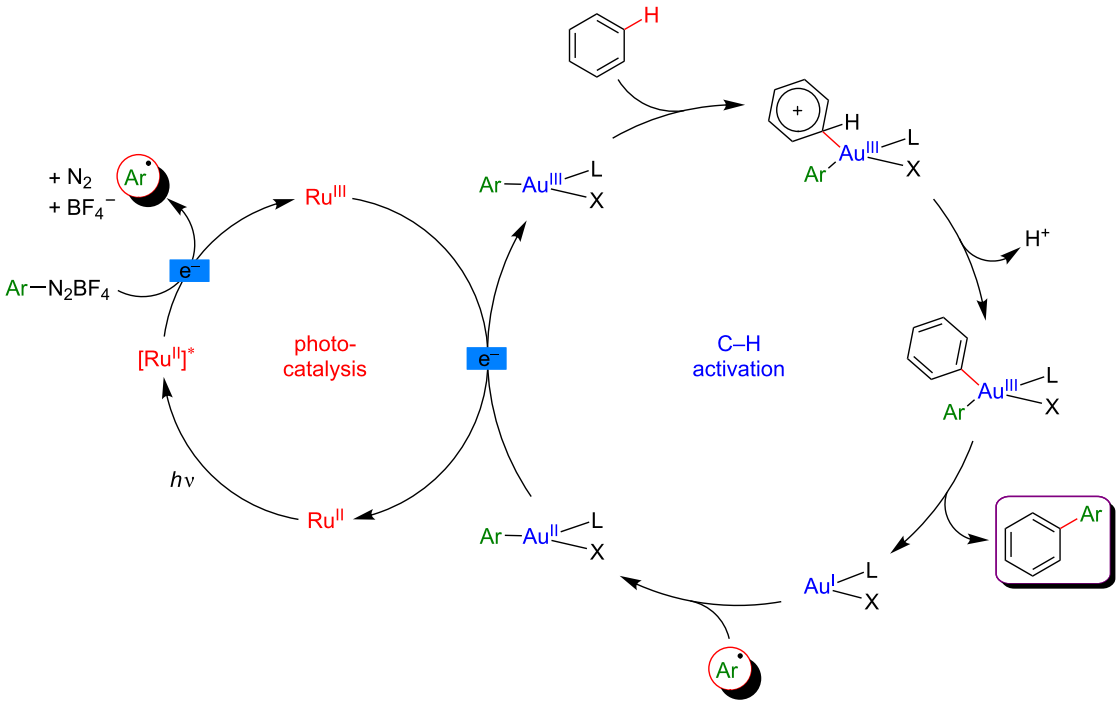

Figure 43: Proposed mechanism for the undirected C–H aryl–aryl cross-coupling via dual catalysis.

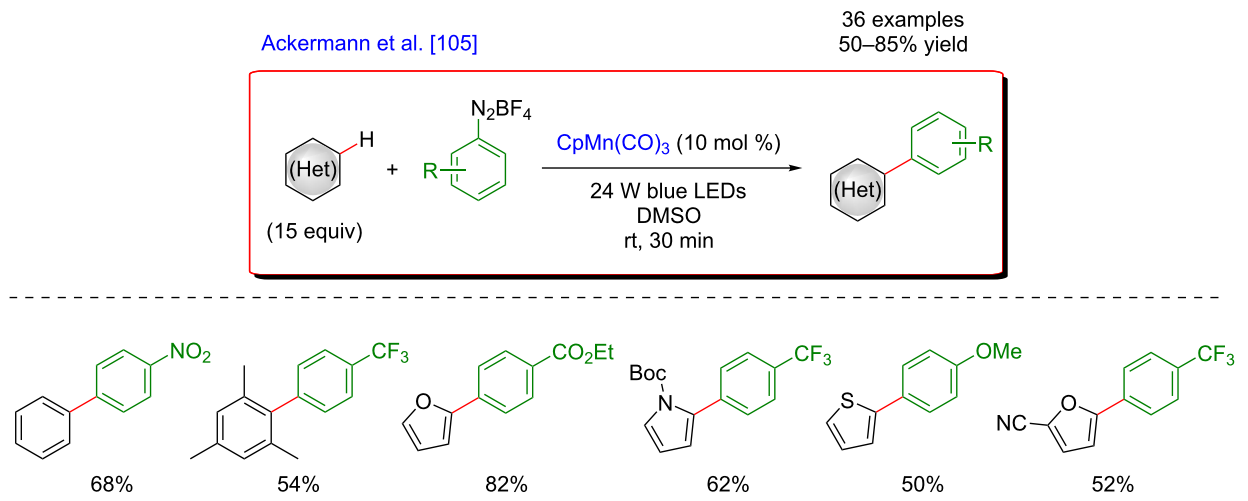

Figure 44: Undirected C–H arylation of (hetero)arenes via dual manganese/photoredox catalysis.

synthesized in moderate to good yields under very mild reaction conditions. Nevertheless, due to regioselectivity issues, this photo-flow direct arylation was mainly limited to symmetrical aryls. The site-selectivity issues could, however, be solved by using heteroarene coupling partners. Indeed, furans, thiophenes, and pyrroles underwent selectively the non-directed C–H functionalization, delivering a diversity of heteroaryl–aryl coupling products. Remarkably, the continuous-flow technique rendered this transformation perfectly suited for large-scale and rapid synthesis.

The mechanistic studies suggested a unique mode of action of this catalytic system (Figure 45). In the initial step both aromatic coupling partners coordinate to the Mn catalyst, thus generating a photoactive complex. Visible-light photoexcitation of the Ar–Mn species and subsequent electron transfer generate the aryl radical together with a cationic Mn species. The addition of the aryl radical to the (hetero)aromatic substrate affords a radical biaryl intermediate that provides the expected coupling product after oxidation and deprotonation.

C–H activation of heterocyclic substrates

The panel of C–H bond functionalization reactions encompasses also direct diversification of heteroaromatic compounds. Aromatic heterocycles are key molecular motifs in natural products and biologically active compounds and thus, the development of synthetic methods allowing their site-selective C–H functionalization have focused major attention of the scientific community [13,22]. However, these transformations frequently required noble metals, such as Pd, Rh and Ru, and rather harsh reaction conditions.

In 2016, Ackermann reported a clear advance towards more sustainable and milder C–H functionalization of azoles. His

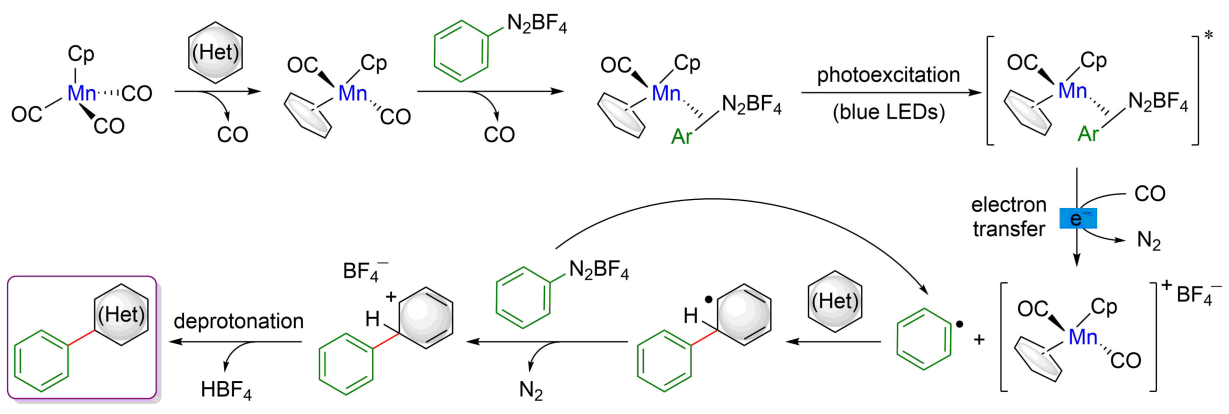

Figure 45: Proposed mechanism for the undirected arylation of (hetero)arenes via dual catalysis.

research group discovered that the abundant and inexpensive CuI catalyst allowed the direct arylation of benzoxazoles under UV-photoactivation (Figure 46) [106]. Remarkably, this totally site-selective photoinduced C–H arylation took place at room temperature and the use of amino acid ligands allowed a significant improvement of the reaction efficiency. The C–H coupling was compatible with a large panel of heteroaromatic substrates including benzoxazoles, oxazoles, thiazoles, and oxadiazoles, as well as non-aromatic oxazolines. Although the initial protocol necessitated the use of a photoreactor emitting UV light at 254 nm, the same reactivity was also reached under visible-light irradiation (blue LEDs), and in the presence of the photosensitizer, $Ir(ppy)_3$. This transformation hence illustrates clearly the potential of combining metal catalysis and photoinduction to design much milder and sustainable C–H transformations.

Subsequently, the concept of the photoinduced C–H functionalization of heteroaromatic compounds was extended towards the direct chalcogenation of azoles (Figure 47) [107]. The Ackermann group discovered that while using a Cu catalyst under photoirradiation, the heteroaryl substrates underwent site-selective thioarylation when employing elemental sulfur and aryl iodides as coupling partners. The reaction tolerated well various aryl iodides, including ones bearing generally sensitive functionalities such as cyano or ester groups, thus delivering a large panel of both electron-rich and electro-poor thioarylated

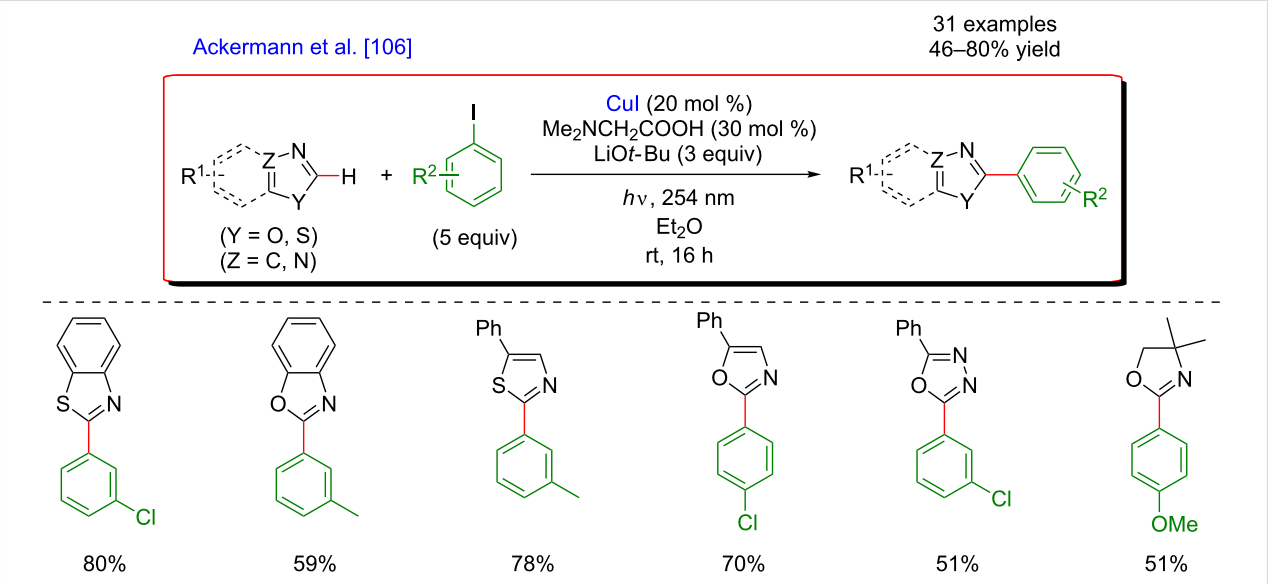

Figure 46: Photoinduced C–H arylation of azoles via copper catalysis.

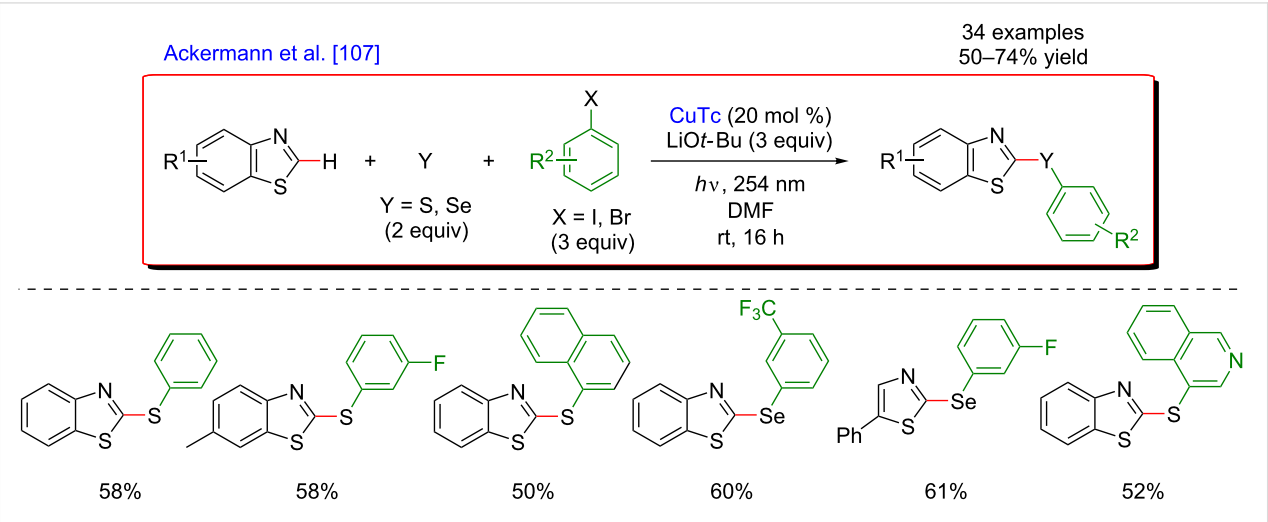

Figure 47: Photo-induced C–H chalcogenation of azoles via copper catalysis.

heteroaromatic products. Besides, this photo-assisted C–H functionalization was equally efficient when using elemental selenium, hence affording a variety of 2-arylselanylbenzothiazoles.

In 2019, Ackermann et al. demonstrated that a mild and direct C–H functionalization of azoles now was also achieved using an easily accessible cobaloxime catalyst in combination with visible-light irradiation (458 nm), harvested by an organic photosensitizer, an acridinium salt (Figure 48) [108]. Such a dual catalytic system enhanced the decarboxylative C–H adamantylation of heterocycles to occur at room temperature. Thanks to the compatibility of this protocol with various substituted azoles and more complex heterocycles such as benzimidazole, and caffeine derivatives, the strategy is now an appealing procedure to incorporate adamantyl scaffolds.

The proposed mechanism of this transformation combines two catalytic cycles (Figure 49). The photocatalytic transformation

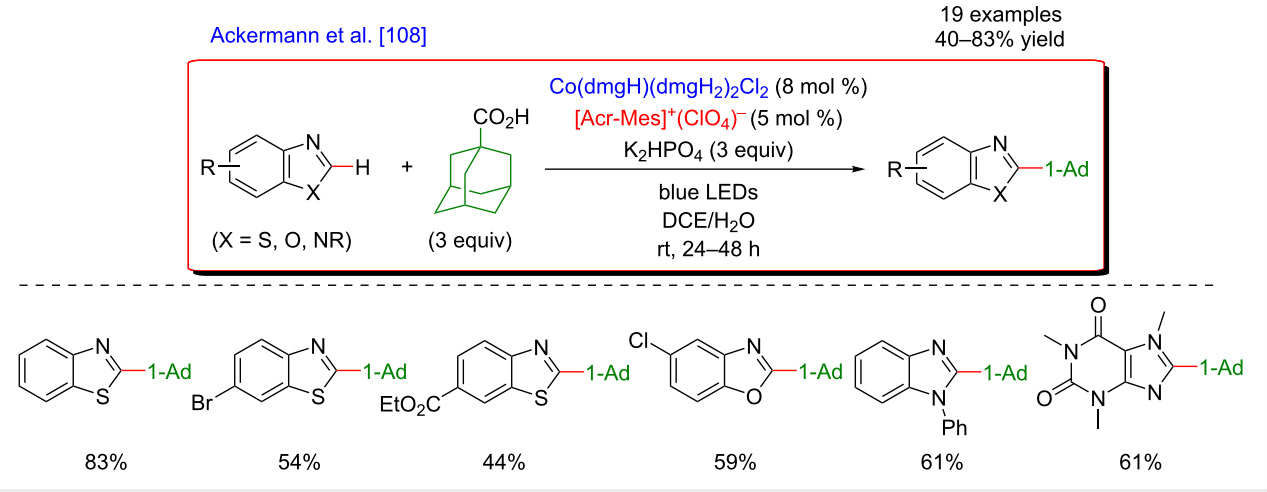

Figure 48: Decarboxylative C–H adamantylation of azoles via dual cobalt/photoredox catalysis.

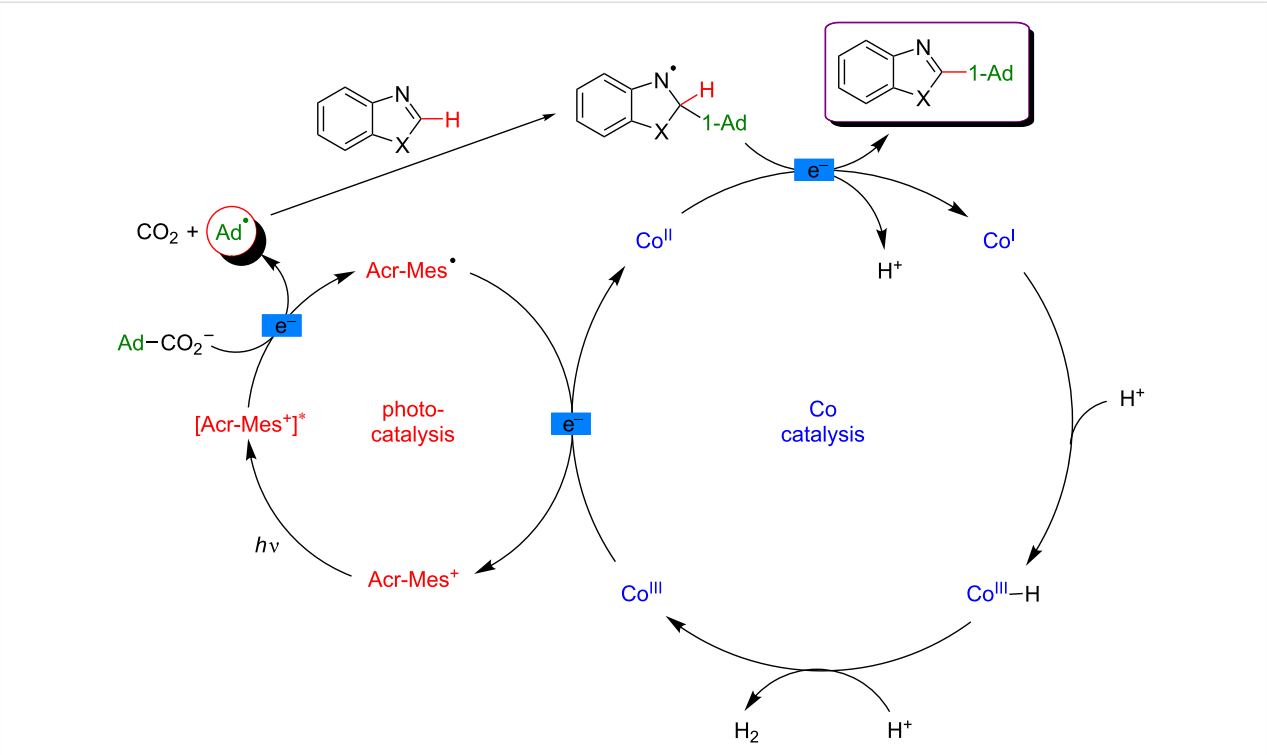

Figure 49: Proposed mechanism for the C–H adamantylation of azoles via dual catalysis.

implies the irradiation of the photosensitizer and oxidative decarboxylation of the adamantylcarboxylate substrate, delivering an adamantyl radical. The attack of the latter at the electrophilic C2 position of the benzothiazole generates a nitrogen-centered radical intermediate. Subsequent deprotonation of this intermediate and concomitant SET reduction of Co(II) into Co(I) delivers the functionalized product, while the Co(I) complex is believed to capture a proton. The resulting Co(III) species, after the release of H_2, is finally reduced to the active Co(II) catalyst via SET with concomitant oxidation of the Acr-Mes• radical to the Acr-Mes$^+$ ground-state photosensitizer.

Modern Sonogashira-type reactions

In traditional Sonogashira cross-coupling reactions, a catalytic amount of a transition metal (generally Pd) is used in combination with a copper salt co-catalyst. This way, the classical Sonogashira reaction promotes the C–C bond formation between terminal alkynes and aryl (or vinyl) halides via a dual Pd/Cu catalysis [109,110]. The general mechanism of this initially reported C–H functionalization protocol is illustrated in Figure 50 (left). The active Pd(0) catalyst undergoes oxidative addition with the aryl or vinyl halide coupling partner to furnish a Pd(II) species. In parallel, regarding the copper catalytic cycle, a π–alkyne complex is formed thanks to the presence of a base. This results in an increased acidity of the proton of the terminal alkyne substrate, and upon deprotonation, a copper acetylide is generated. The acetylide then reacts with the Pd(II) complex in a transmetalation step, producing an alkynyl Pd(II) intermediate and regenerating the copper catalyst. Finally, the reductive elimination yields the desired coupling product along with the regeneration of the active Pd catalytic species.

While the presence of copper salts was valuable for the efficiency of the transformation, their use in the "classical" Sonogashira cross couplings resulted in several drawbacks. Indeed, copper salts led to the generation of unwanted alkyne homocoupling side products and the requirement of rigorous inert atmosphere. Therefore, in order to exclude copper from the reaction mixture, significant attention was focused on the development of alternative Cu-free Sonogashira reactions [111,112]. In that respect, a possible variant relied on the use of a photoredox catalysis in combination with transition-metal catalysis (Figure 50, right). The mechanism of such a dual catalytic system is initiated by the generation of aryl radicals via SET from an excited photosensitizer to an appropriate radical precursor substrate. Such aryl radical reacts with a transition-metal catalyst (M), resulting in the generation of an oxidized M(+1) complex intermediate. An additional SET event with the photocatalyst thus allows the formation of a M(+2) oxidation state species. The subsequent formation of a σ-bonded alkynyl–M(+2) complex upon deprotonation allows final reductive elimination, delivering the expected coupling product along with the regenerated metal catalyst M. The overall process thus allowed the replacement of copper salts with a suitable photocatalyst.

The first example of such a dual catalytic system combining photoredox catalysis and palladium catalysis was reported in 2007 by Osawa's group [113]. The authors developed a Cu-free Sonogashira coupling between aryl halides and terminal alkynes (Figure 51). The efficiency of this transformation was clearly improved by visible-light irradiation of the reaction medium in the presence of a ruthenium-based photocatalyst, although the

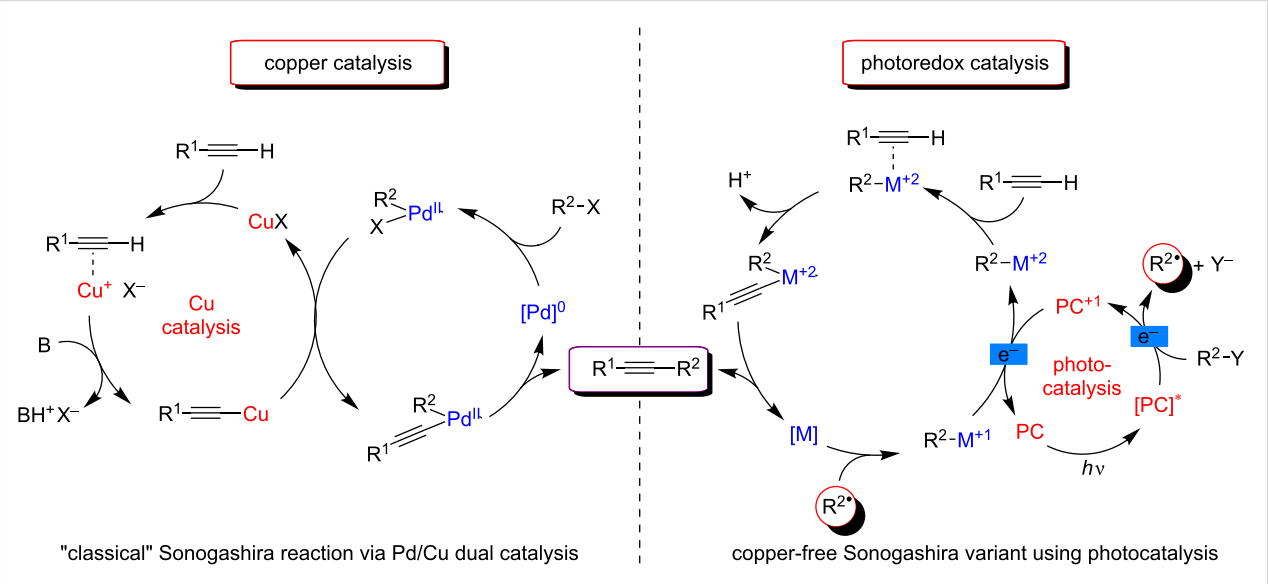

Figure 50: General mechanisms for the "classical" (left) and Cu-free variant (right) Sonogoshira reaction.

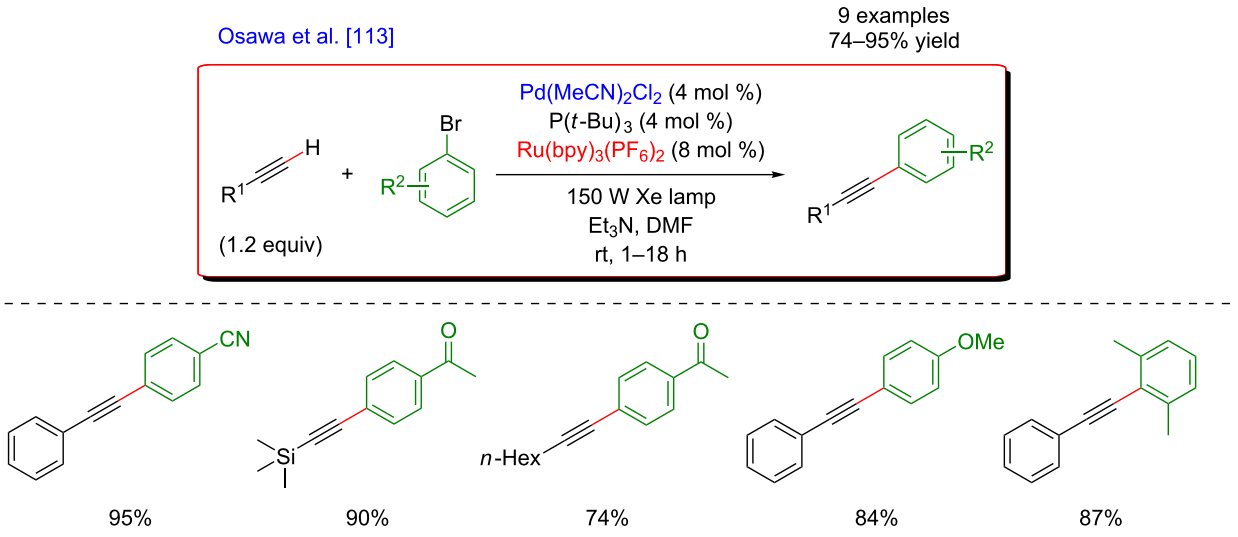

Figure 51: First example of a dual palladium/photoredox catalysis for Sonogashira-type couplings.

role of the latter was not fully elucidated (traces of the coupling product formed when performing the reaction in the dark).

More recently, an alternative protocol for a mild Sonogashira-type reaction implying dual catalysis was disclosed by Glorius et al. (Figure 52) [114]. The coupling between terminal alkynes and aryldiazonium salts was achieved at room temperature due to a synergistic system combining gold catalysis and photocatalysis. Under the optimized reaction conditions, merging a Au(I) catalyst and a Ru-based photosensitizer under irradiation with CFL, a large panel of terminal alkynes were coupled with aryldiazonium salts, furnishing the expected arylalkyne products in high yields. Remarkably, this protocol was efficient at room temperature and tolerated well a number of substituents including halogens, motifs frequently incompatible with Pd-based catalytic systems.

The mechanism of this transformation is initiated by the generation of aryl radicals via a SET process from the excited $[Ru(bpy)_3]^{2+}$ photocatalyst to the diazonium salt (Figure 53). The thus formed aryl radical then reacts with the Au(I) catalyst, resulting in the generation of an Ar–Au(II) intermediate. A

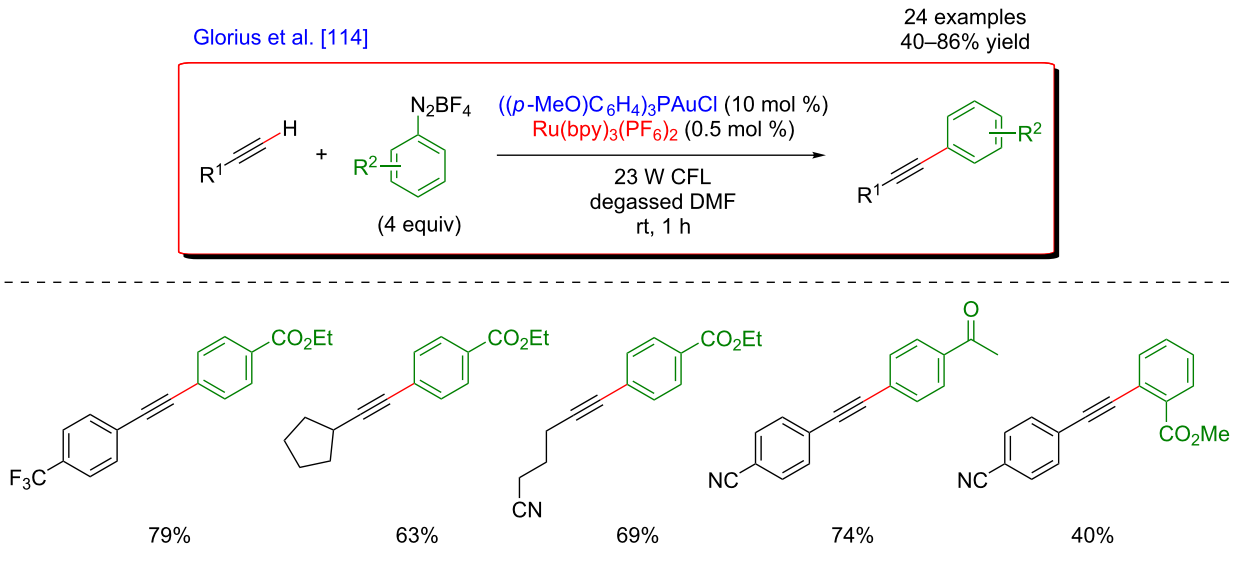

Figure 52: Arylation of terminal alkynes with diazonium salts via dual gold/photoredox catalysis.

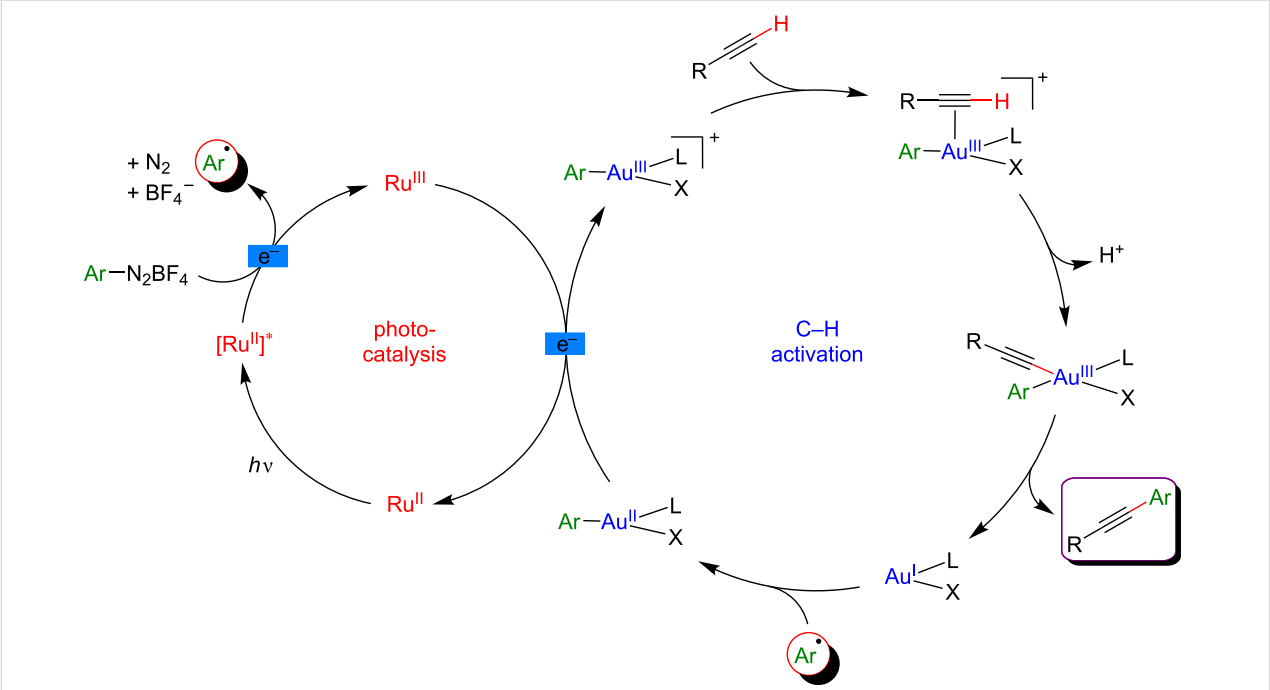

Figure 53: Proposed mechanism for the arylation of terminal alkynes via dual catalysis.

second SET event with the oxidized-photosensitizer (or alternatively with an additional equivalent of aryldiazonium salt) allows the formation of a Au(III) species, featuring high Lewis acidity. The subsequent generation of a σ-bonded alkynyl–Au(III) complex upon deprotonation allows final reductive elimination, delivering the expected coupling product along with the regeneration of the Au(I) catalyst.

C–H functionalization by merging visible-light-induced H-abstraction and metal-catalyzed cross-coupling

The field of synergistic metallaphotoredox catalysis for C–H functionalization is also complemented by a conceptually very different approach, based on a combination of hydrogen-atom-transfer (HAT) process and metal-catalyzed cross-couplings. In this transformation, a photoinduced event promotes the generation of species capable to abstract hydrogen from an aliphatic substrate generating an alkyl radical, that is subsequently trapped by a transition-metal catalyst, and thus enabling the cross-coupling-type bond-formation event to take place. This strategy is therefore very complementary to the previously presented ones, in which metal catalysis was generally employed to promote site-selective C–H activation. The formation of distinctive coupling products may thus be targeted.

α-Amino and α-ether C(sp^3)–H functionalization

The pioneering and groundbreaking discovery in metallaphotoredox C(sp^3)–H HAT-type functionalization was reported by MacMillan in 2015 [115]. The development of this transformation was initially inspired by the discovery that strong C–H bonds were homolytically cleaved in a highly selective manner by matching electronic polarity in a C–H bond and an HAT catalyst (Figure 54).

Indeed, when combining HAT and photoredox catalysis, strong C–H bonds in α position to the hydroxy group motif were selectively cleaved in the presence of weaker and activated C–H bonds. The thus generated α-oxy radicals, after addition to an electron-deficient acrylate, delivered alkyl radicals, that ultimately converted into the lactone-type products (Figure 55).

Based on this seminal work, the concept of polarity-match HAT selective C(sp^3)–H abstraction was subsequently used in combination with transition-metal catalysis. When combining a photoredox catalytic cycle (using an Ir(III)-based photosensitizer) with an organocatalytic cycle (allowing SET oxidation of quinuclidine, and subsequent HAT activation of amines), an α-amino C(sp^3)–H hydrogen abstraction smoothly occurred, delivering radical species, as competent coupling partners in Ni-catalyzed arylation reactions [116]. Remarkably, this complex catalytic system embracing three catalytic cycles was very general, allowing the α-arylation of not only diverse amines (including cyclic and acyclic ones), but also of ethers and amides. Besides, the reaction well tolerated various aryl bromides and aryl chlorides as coupling partners, including aromatics bearing challenging functional groups (sulfonyl and ester), and hetero-

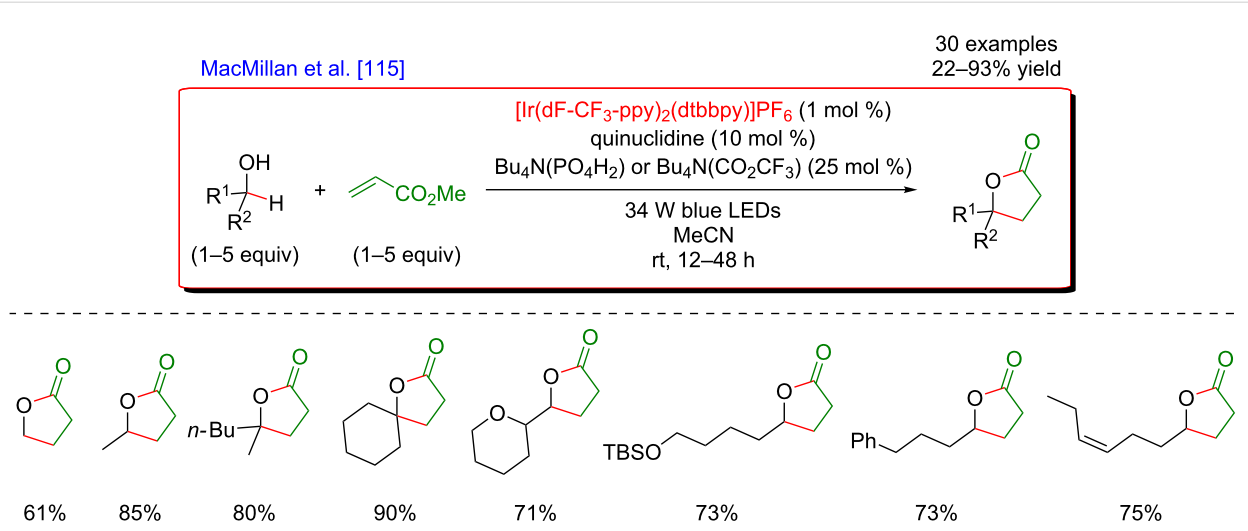

Figure 54: C–H Alkylation of alcohols promoted by H-atom transfer (HAT).

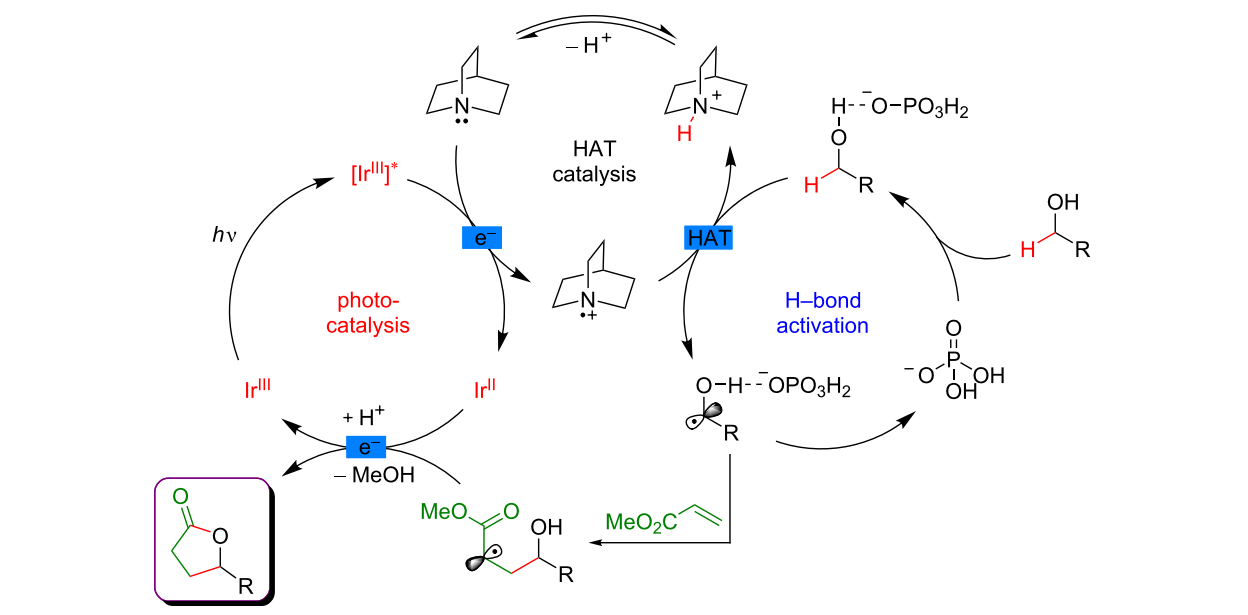

Figure 55: Proposed mechanism for the C–H alkylation of alcohols promoted by HAT.

cycles. The perfect orchestration of these three catalytic cycles warranted high efficiency of the coupling under mild reaction conditions (Figure 56).

The mechanism of this reaction starts by the excitation of the Ir(III) photocatalyst, furnishing a long-lived photoexcited state. SET between the *Ir(III) and 3-acetoxyquinuclidine (a tertiary amine HAT catalyst) generates an Ir(II) species together with key radical amine cation (Figure 57). This finely designed radical amine cation needs to be sufficiently electron-deficient to engender a kinetically selective HAT event at the most electron-rich site of the C–H substrate (polarity matching), thus affording the aliphatic α-amino radical. Of note is that this abstraction event is coherent with thermodynamic considerations, as the bond-dissociation energies (BDEs) of hydridic α-amino C–H bonds are lower than the N–H bond of quinuclidinium (C–H bond = 89 to 94 kcal/mol vs H–N^+ bond = 100 kcal/mol). In parallel, the Ni(II) precatalyst undergoes double SET reductions by the Ir PC to generate the catalytically active Ni(0) species. Oxidative addition of Ar–Br then furnishes the electrophilic Ni(II)–aryl intermediate, rapidly intercepting the α-amino radical. The Ni(III)–aryl–alkyl com-

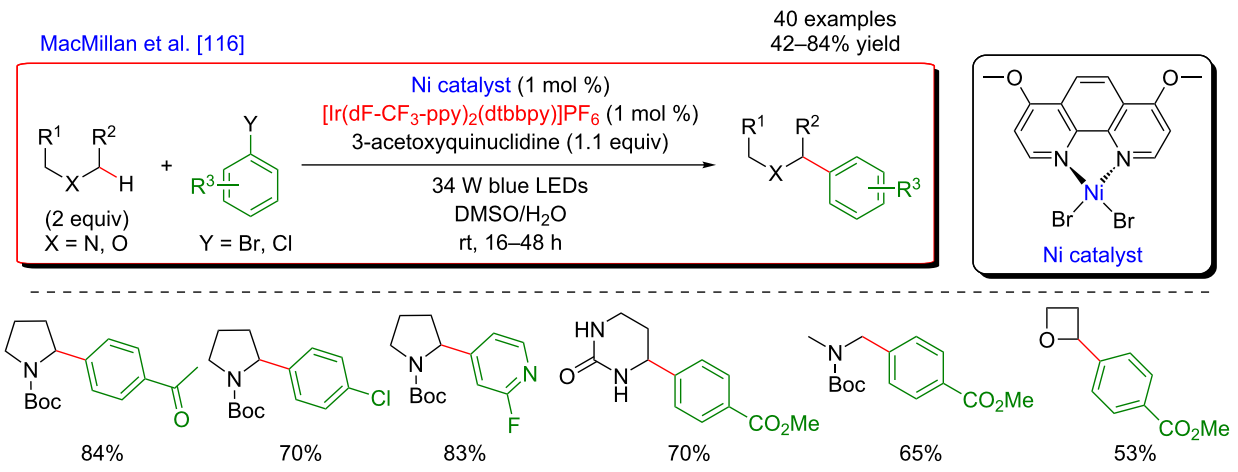

Figure 56: C(sp^3)–H arylation of latent nucleophiles promoted by H-atom transfer.

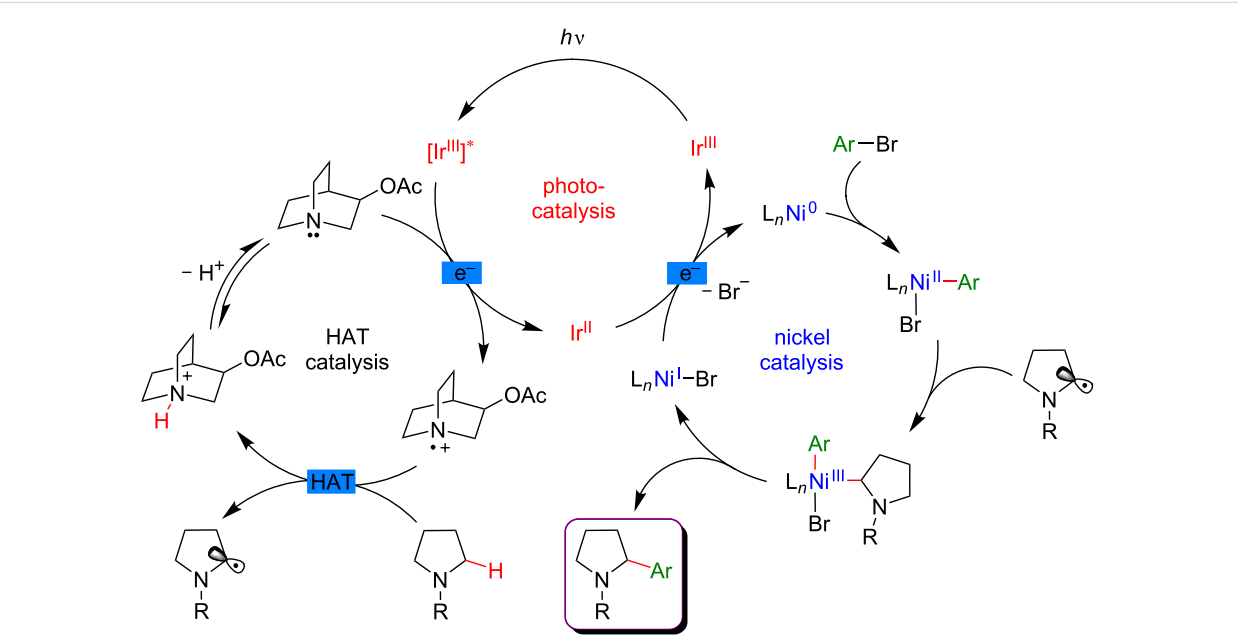

Figure 57: Proposed mechanism for the C(sp^3)–H arylation of latent nucleophiles promoted by HAT.

plex dispenses the coupling product via reductive elimination and a Ni(I) complex that is ready to undergo SET reduction thus re-engaging in a new catalytic cycle.

The concept of the selective generation of active aliphatic coupling partners by means of H-abstraction through polarity-induced effects and promotion of the C–C-bond formation via a combination of photo- and Ni catalysis also paved the way towards a new approach for the synthesis of benzylic alcohols, important scaffolds in medicinal chemistry [117]. MacMillan discovered that when submitting alcohols to the conditions promoting the HAT-type process, a chemoselective generation of α-C–OH carbon-centered radicals took place while suppressing the formation of the expected O-centered radicals. This perfectly designed catalytic system was very general and compatible with a diversity of aliphatic alcohols, including methanol, and various cyclic ones. Of note is also the particular chemoselectivity of this reaction, as the α-C–OH carbon-centered radicals were preferentially formed over α-C–OR and α-C–N radicals. In addition, diversely substituted aryl bromides and bromopyridine derivatives could be used as the coupling partners. The application of this methodology for the expedient

3-step Prozac's synthesis clearly highlights the potential of this methodology (Figure 58).

The addition of a Lewis acid (LA) is the key to success to trigger this uncommon reactivity as metal alkoxide species are formed, exhibiting greatly exchanged hydric character at the α-alkoxy C–H positions (Figure 59). The optimization study showed that $ZnCl_2$ was the optimal Lewis acid while quinuclidine played efficiently the role of the HAT catalyst. The thus generated aliphatic radical could now be engaged in the Ni catalytic cycle; after an oxidative addition of the Ni(0) species to the Ar–Br, the α-alkoxy radical is trapped, generating a Ni(III) species that facilitates the reductive elimination step, thus liberating the coupling product, i.e., the benzylic alcohol. The overall catalytic system is complemented with a photocatalytic cycle: the photoexcited Ir(III) photocatalyst promotes the oxidation of the HAT catalyst quinuclidine while the regeneration of the Ir(III) catalyst from Ir(II) warrants the efficient reduction of the Ni(I) intermediates into the catalytically active Ni(0) species.

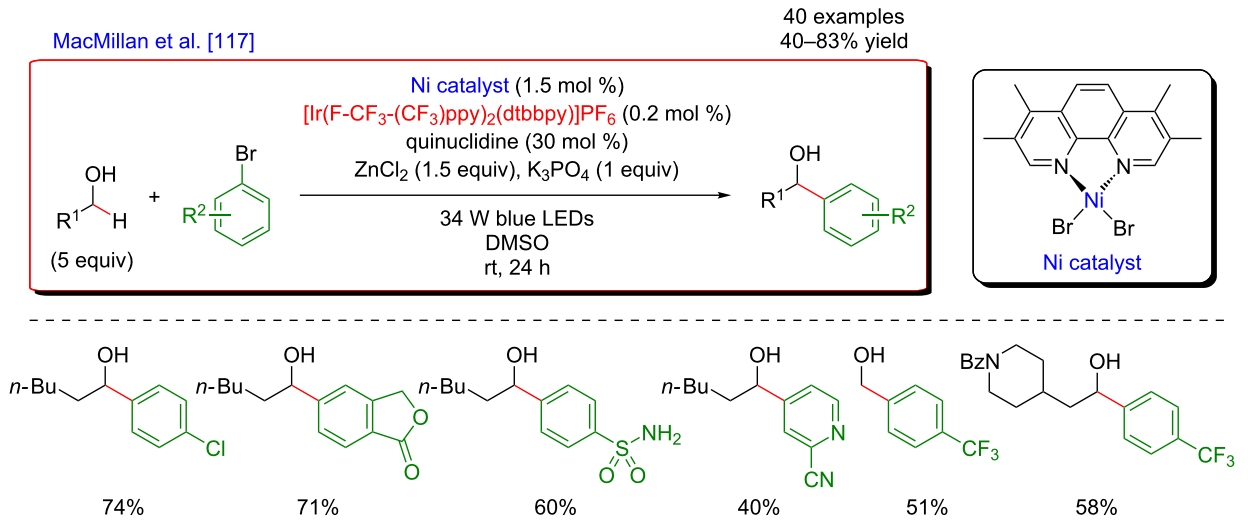

Figure 58: Direct α-arylation of alcohols promoted by H-atom transfer.

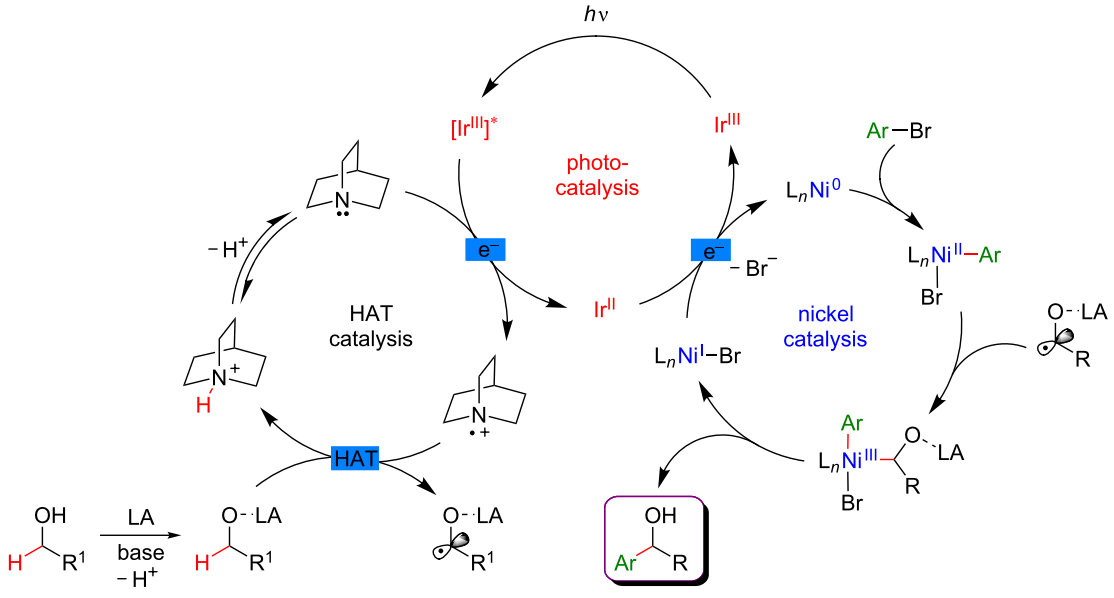

Figure 59: Proposed mechanism for the direct α-arylation of alcohols promoted by HAT.

Regarding the major advantage of this approach, i.e., a possibility to selectively cleave a strong C–H bond while avoiding functionalization of other, usually more reactive positions, it was not surprising that this strategy has been investigated further. Therefore, a complementary protocol for the α-arylation of arylamines was disclosed by Doyle (Figure 60) [118].

In this case, an α-amino radical is believed to be directly generated via a SET process with the photoexcited Ir(III) catalyst (Figure 61). In analogy to the system developed by MacMillan, the Ni catalytic cycle implies the oxidative addition of Ar–I to an in situ generated Ni(0) species delivering the Ni(II)–aryl intermediate, followed by trapping of the radical coupling partner. The expected C–C-bond formation occurring during the reductive elimination step furnishes the α-arylated amines. Of note is that this modified protocol, using a Ni complex coordinated with the BiOx ligand, KOH as a base, and DMF as solvent, was compatible with *N*-arylated amines, whereas *N*-Boc-protected substrates were generally used by MacMillan.

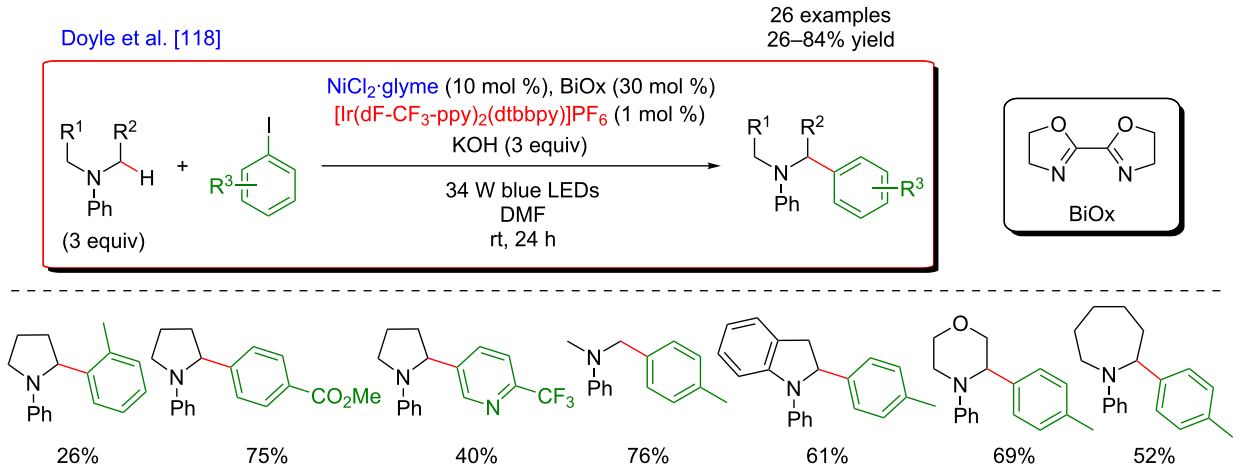

Figure 60: C–H arylation of amines via dual Ni/photoredox catalysis.

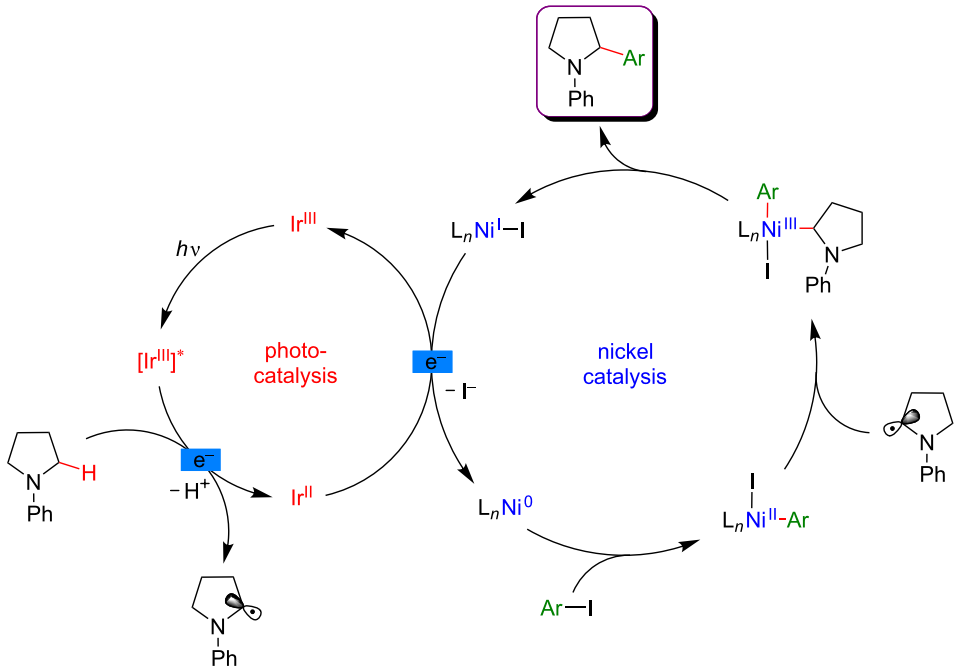

Figure 61: Proposed mechanism for the C–H arylation of amines via dual Ni/photoredox catalysis.

In 2018, a major advance in this field was disclosed by Martin [119]. The author hypothesized that a carefully selected triplet ketone sensitizer should be able, under light activation, to promote the HAT and SET steps, thus allowing both, hydrogen abstraction in the α-position to a heteroatom and reduction of the Ni(I) species. Accordingly, a direct functionalization of feedstock alkanes (such as THF) was achieved in the absence of a costly Ir-based photosensitizer. Following the initial hypothesis, the diarylketone was precisely selected with respect to its absorption in the visible-light range. The Ni catalyst was also supported with a bipyridine-type ligand, and under the optimized reaction conditions, the direct C(sp^3)–H arylation, and alkylation of THF were achieved smoothly (Figure 62). The protocol turned out to be highly tolerant with respect to various aromatic bromines, including *ortho*-substituted ones as well as aromatics bearing complex motifs, and bromoalkanes, even in the presence of a catalytic amount of the diarylketone photosensitizer. Besides, the reactivity was also efficiently extended towards the functionalization of ethers and benzylic C–H bonds.

The experimental mechanistic studies confirmed the initial working hypothesis, evoking the HAT process from the triplet excited state of the diarylketone delivering the key aliphatic radical, followed by SET to recover back the initial form of the diarylketone, with the concomitant generation of the catalytically active Ni(0) catalyst (Figure 63).

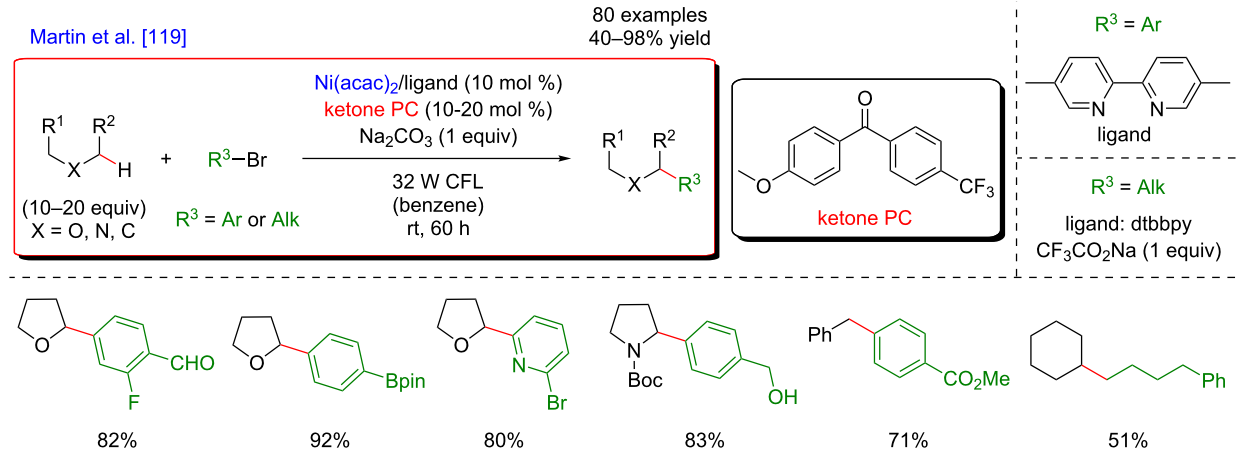

Figure 62: C–H functionalization of nucleophiles via excited ketone/nickel dual catalysis.

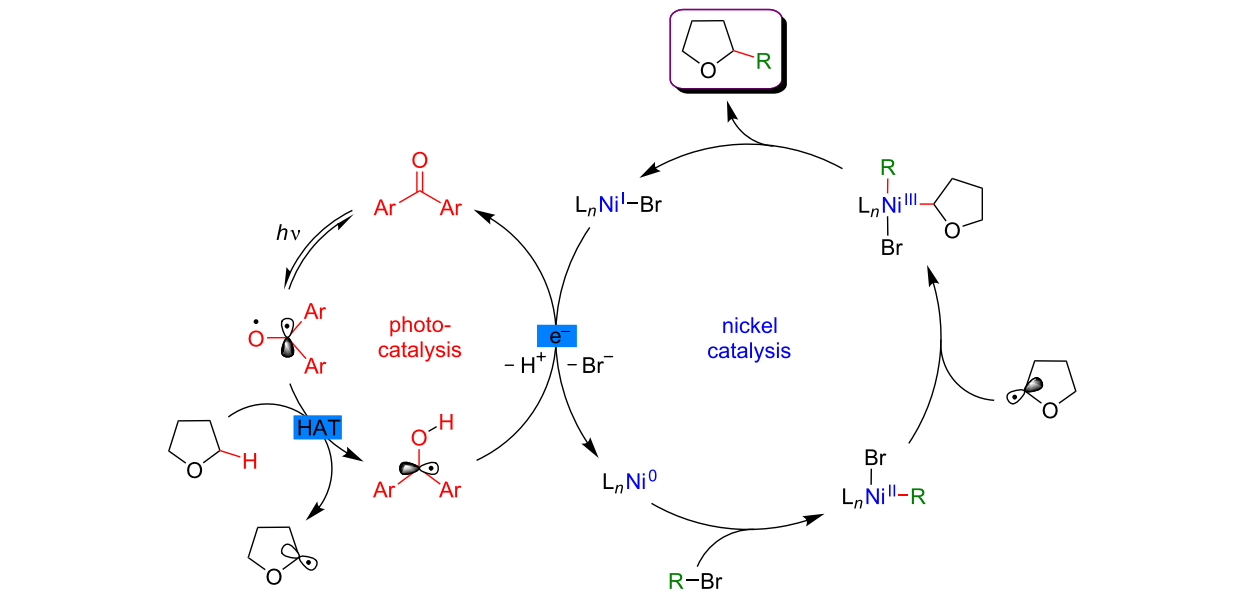

Figure 63: Proposed mechanism for the C–H functionalization enabled by excited ketones.

In 2017, the McMillan group applied the HAT approach to perform sp^3–sp^3 coupling. In this case, the polarity-match HAT process was combined with a Ni-catalyzed alkylation [120]. Following a comparable mechanistic scenario orchestrating three catalytic cycles (photoredox, organocatalytic, and Ni-based catalysis), aliphatic radicals in α-position to N, O, and S-atoms were generated and coupled with a large panel of alkyl bromides (both secondary and primary), thus delivering the aliphatic products in high yields and under very mild reaction conditions (Figure 64).

In contrast to the direct arylation reactions, in this sp^3–sp^3 coupling, the in situ generated catalytically active Ni(0) complex was believed to trap directly the alkyl radical, prior to the oxidative addition of the alkyl bromide (Figure 65).

The photocatalytic generation of α-amino radicals was also astutely combined with the Ni-catalyzed acylation reaction. In 2016, Doyle reported that a complex catalytic cycle combining an Ir(III) photosensitizer with a Ni(dtbbpy) catalyst and quinuclidine as base promoted, under blue LED irradiation, the direct

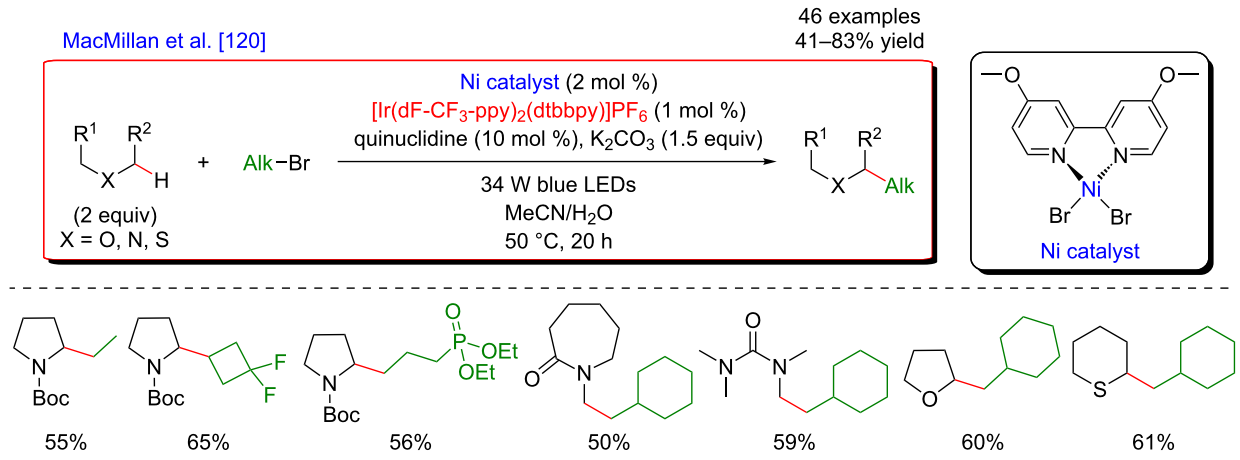

Figure 64: Selective sp^3–sp^3 cross-coupling promoted by H-atom transfer.

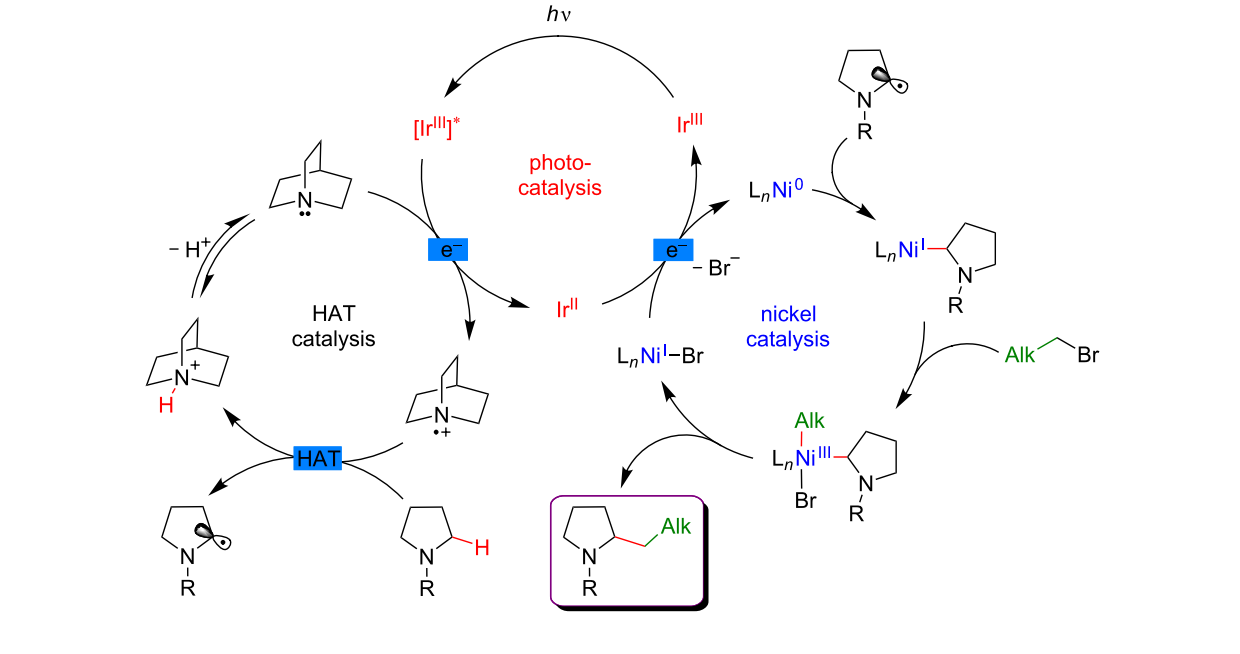

Figure 65: Proposed mechanism for the selective sp^3–sp^3 cross-coupling promoted by HAT.

coupling of arylamines and anhydrides, delivering a large panel of α-acetylated compounds in good yields (Figure 66) [121].

In this case, the Ni(0) active catalyst undergoes an oxidative addition into the acyl precursors and the thus generated Ni(II) complex intercepts an α-amino radical. The resulting Ni(III) species then promotes the rapid reductive elimination while forging the C–C bond formation. The authors suggested the formation of the α-amino radical from SET between the excited *Ir(III) photocatalyst and *N*-phenylpyrrolidine, followed by a deprotonation event. However, as quinuclidine was required in this transformation, a potential HAT-type reactivity could not be excluded (Figure 67).

Recently, the panel of metallaphotoredox C(sp^3)–H cross-coupling reactions was complemented with the direct alkenylation of ethers and amides. The reaction developed by Wu astutely applied a dual photocatalysis/Ni catalysis to achieve the hydro-

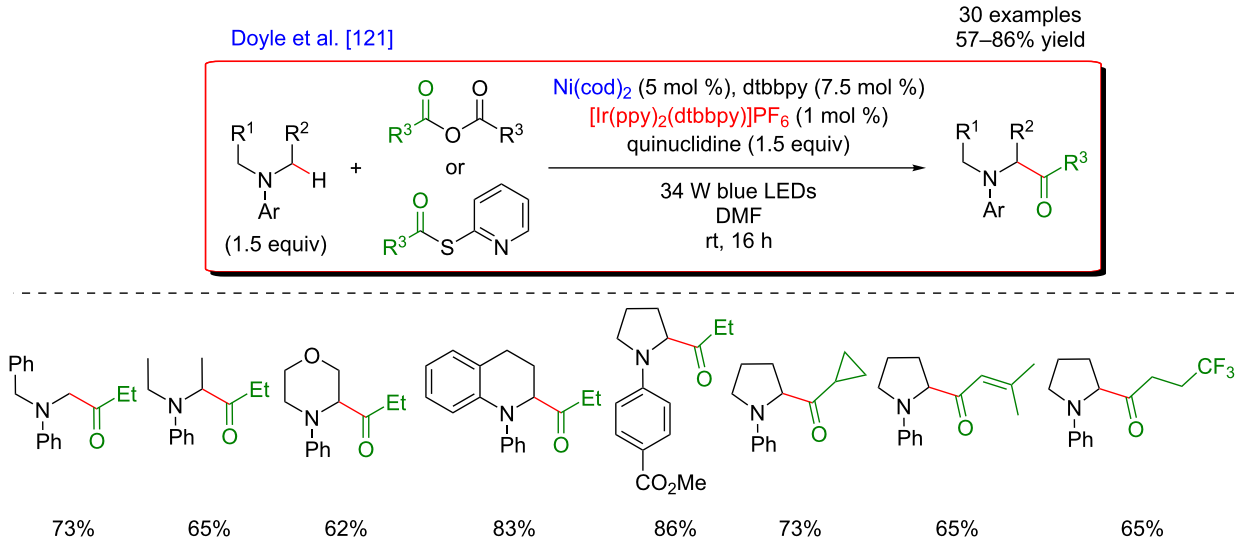

Figure 66: Direct C(sp^3)–H acylation of amines via dual Ni/photoredox catalysis.

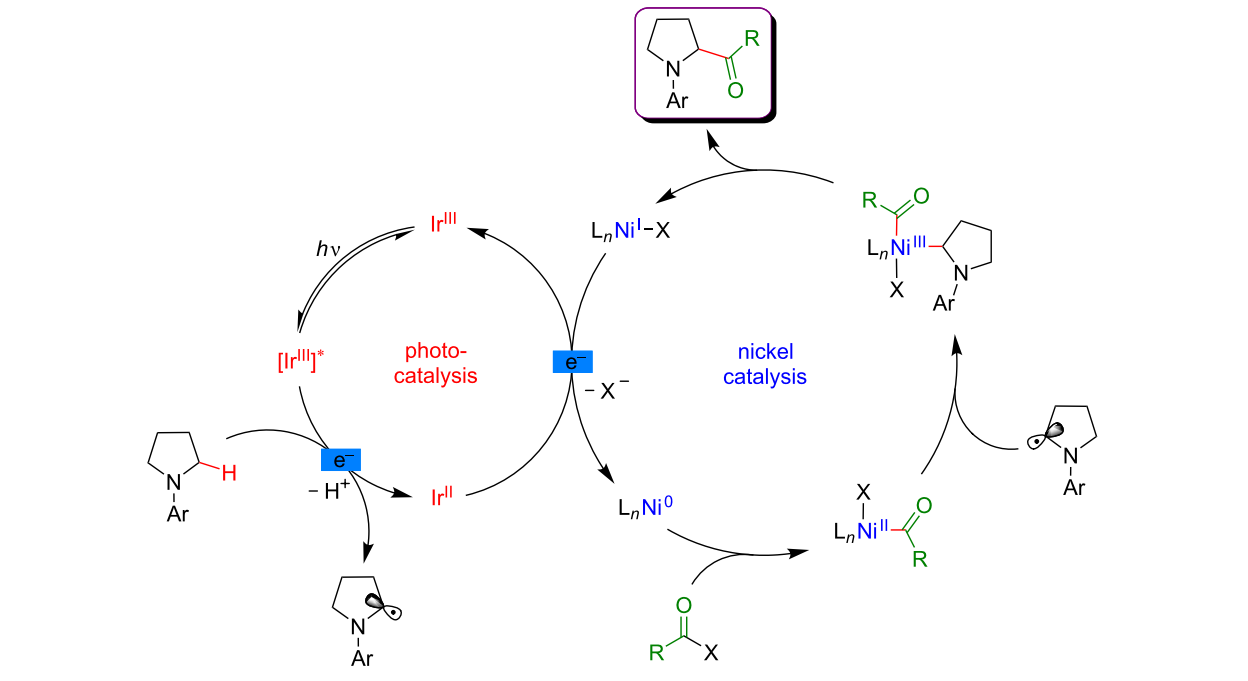

Figure 67: Proposed mechanism for the C–H acylation of amines via dual Ni/photoredox catalysis.

alkylation of internal alkenes using α-hetero C(sp^3)–H bond as the coupling partners (Figure 68) [122]. The expected olefinated ethers were obtained in high yields and generally high selectivity using a large panel of alkynes. Of note is that this coupling required an increased reaction temperature (60 °C).

From the mechanistic viewpoint, it was speculated that in contrast to other related dual catalytic systems, the photoexcited *Ir(III) complex oxidized the Ni(II)(dtbbpy)Cl_2 precatalyst to afford a Ni(III) species via SET (Figure 69). Photolysis of the latter Ni(III) species results in a Ni(II) intermediate and a chlorine radical. Hydrogen atom abstraction from an aliphatic substrate thus smoothly occurs in the presence of the chlorine radical, delivering an aliphatic radical that is rapidly trapped by the Ni(II) complex. As the thus generated Ni(III) complex could not undergo carbo-nickelation with alkynes, a reductive elimination is believed to take place delivering a Ni(I) species, together with α-chlorinated THF. The oxidative addition of HCl furnishes the key nickel hydride species. A SET reduction of this intermediate by the oxidation of the Ir(II) species delivers Ni(II) hydride, the active species prompt to undergo the regioselective hydronickelation of the alkyne. The final nucleophilic substitution with the in situ generated chlorinated THF produces the expected functionalized olefin.

Subsequently, the generality of this C(sp^3)–H alkenylation was extended towards a similar hydroalkylation of ynones, ynoates, and ynamides (Figure 70) [123].

Allylic C–H functionalization

The key step of the H-abstraction by a chlorine radical to achieve C(sp^3)–H functionalization was further explored by Rueping et al. [124]. When reacting tetramethylethylene with aryl bromides under a dual catalytic system including [AcrMes]ClO_4 as photosensitizer, combined with a Ni–dtbpy complex, lutidine as the base, under blue LED irradiation, the formation of vinyl bromides was achieved (Figure 71). Interestingly, this cross-coupling protocol was operative for both, aryl and vinyl bromides, and featured an important group tolerance with respect to the halogenated coupling partners, including heterocyclic motifs.

This cross-coupling involves the generation of an allylic radical via abstraction of the hydrogen atom by a bromine radical ($Br^•$, resulting from homolysis of the electronically excited Ni(III)–ArBr) which is trapped by the Ni(II)–Ar intermediate, with the reductive elimination step delivering the expected allylic compound (Figure 72).

Recently, the portfolio of allylic C(sp^3)–H functionalizations promoted via dual catalysis was extended by merging organophotoredox catalysis and chiral chromium hydride catalysts (Figure 73) [125].

In this case, the allylic radical was expected to be formed via an electron-transfer oxidation of the photoexcited acridinium catalyst. The allyl radicals, trapped by a carefully selected chiral Cr complex thus generate a nucleophilic species ready to engage in an asymmetric allylation of the aldehydes hence furnishing the chiral benzylic alcohols in moderate to good yields, and generally excellent regioselectivities (Figure 74).

Functionalization of aldehydes

The direct functionalization of formyl C–H bonds via metal-catalyzed cross-couplings attracts constant scientific attention as this approach allows building up of molecular complexity while

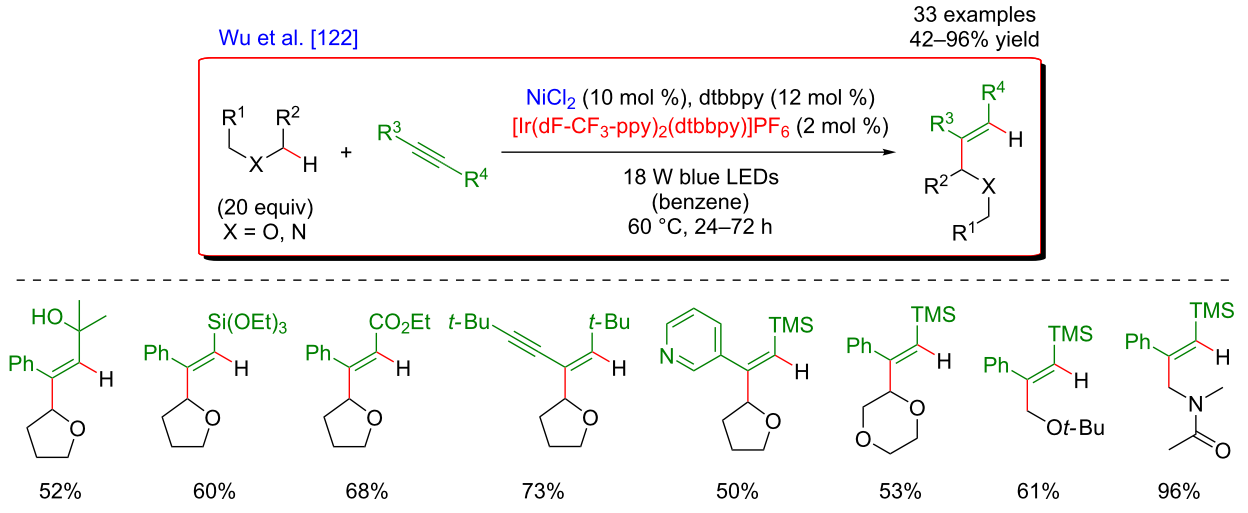

Figure 68: C–H hydroalkylation of internal alkynes via dual Ni/photoredox catalysis.

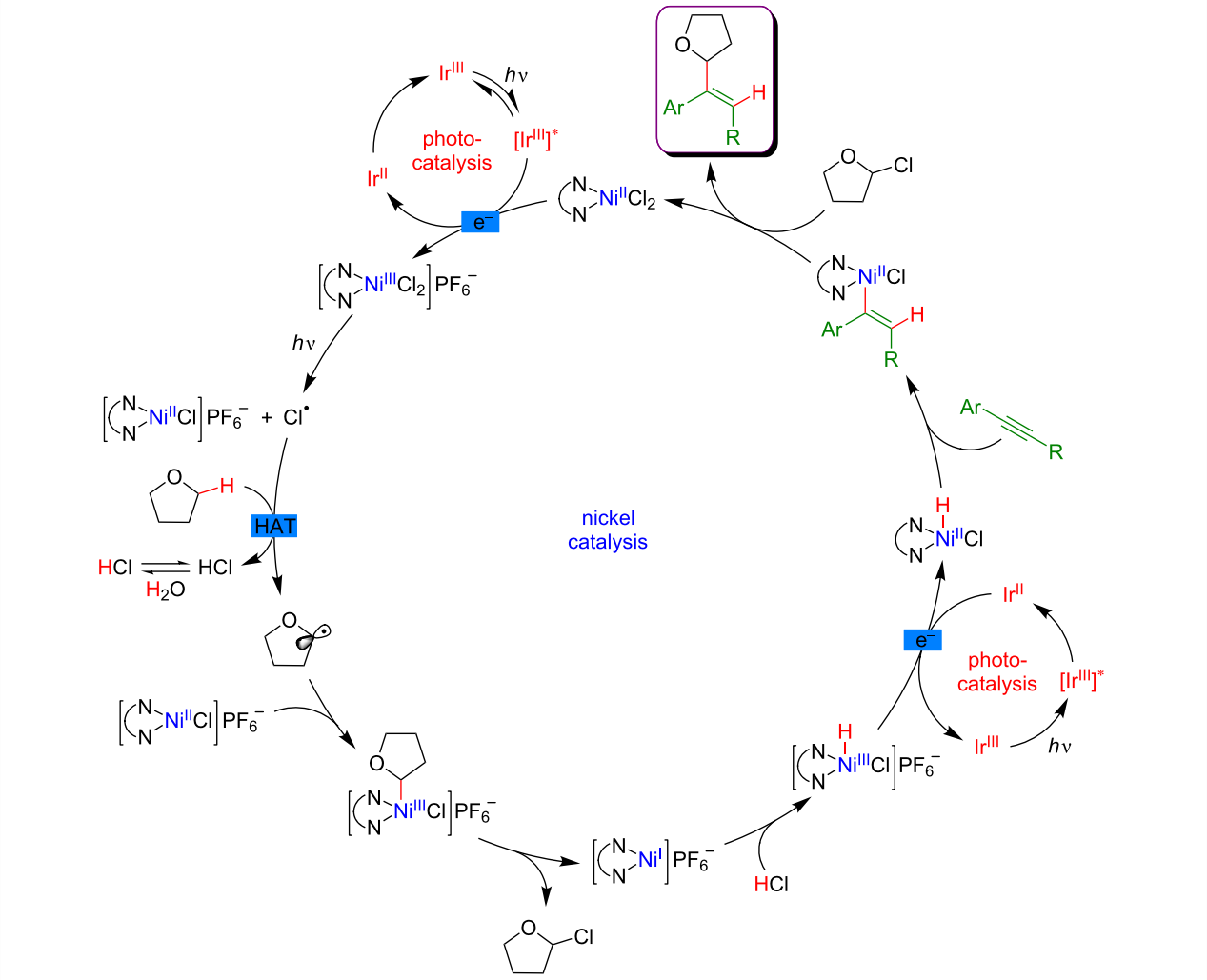

Figure 69: Proposed mechanism for the C–H hydroalkylation of internal alkynes.

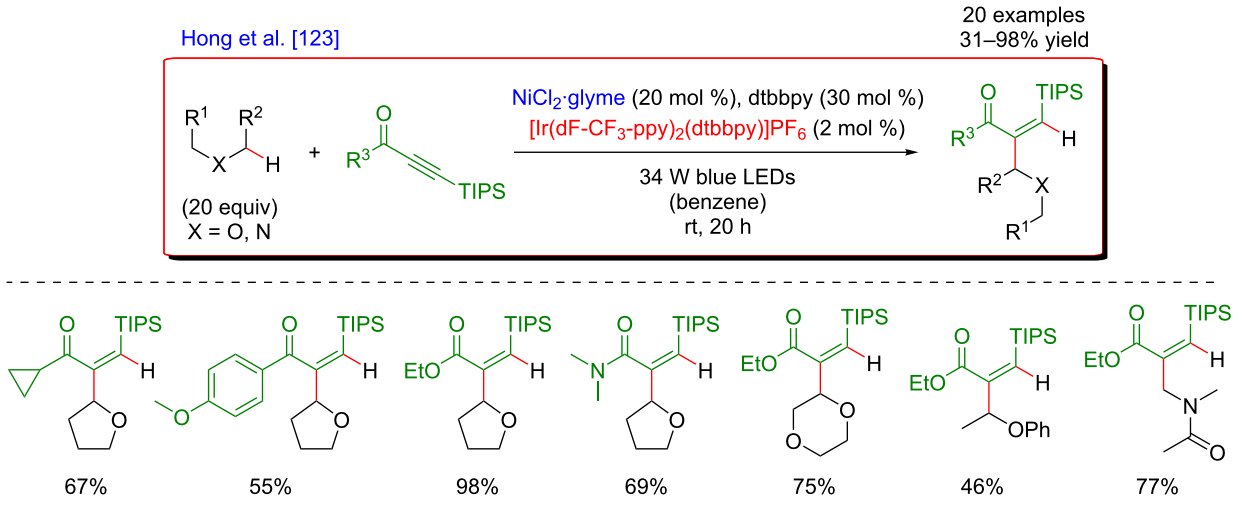

Figure 70: Alternative procedure for the C–H hydroalkylation of ynones, ynoates, and ynamides.

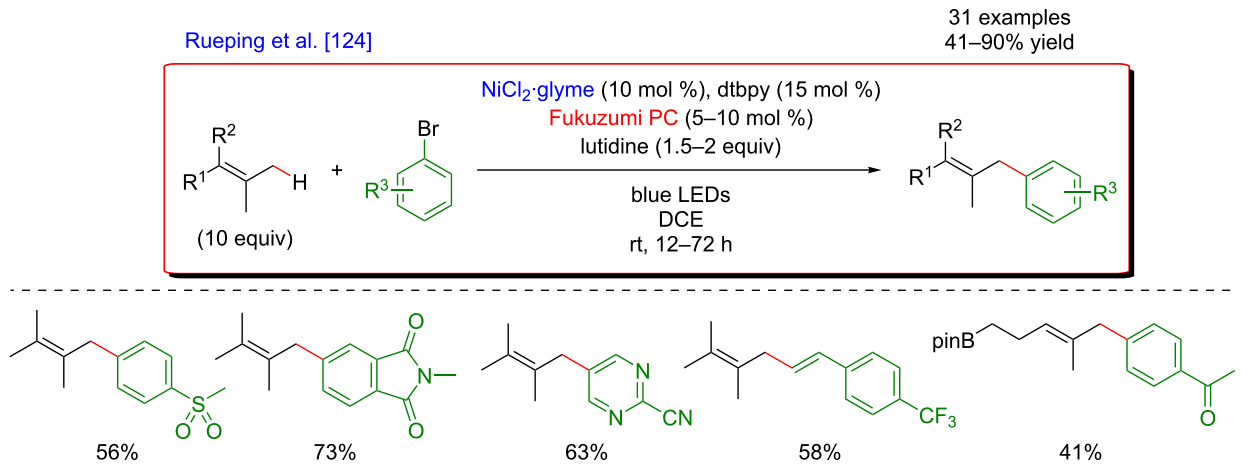

Figure 71: Allylic C(sp^3)–H activation via dual Ni/photoredox catalysis.

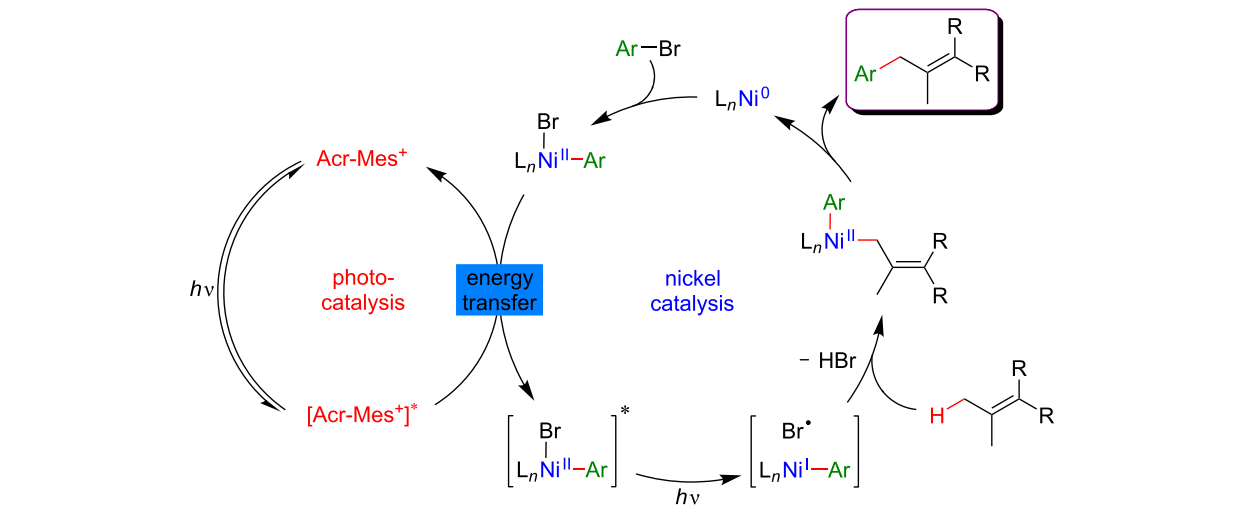

Figure 72: Proposed mechanism for the allylic C(sp^3)–H activation via dual Ni/photoredox catalysis.

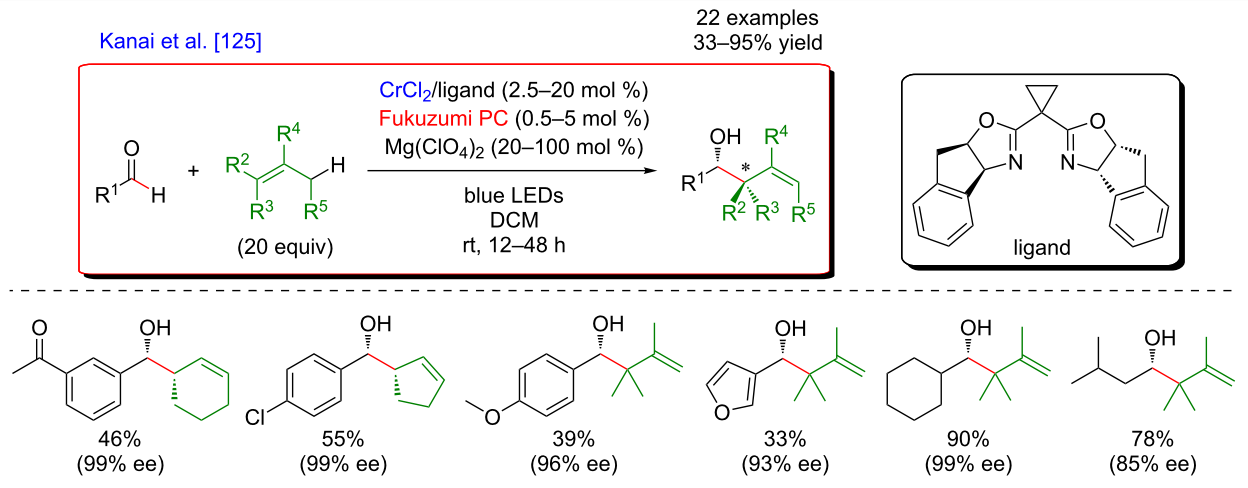

Figure 73: Asymmetric allylation of aldehydes via dual Cr/photoredox catalysis.

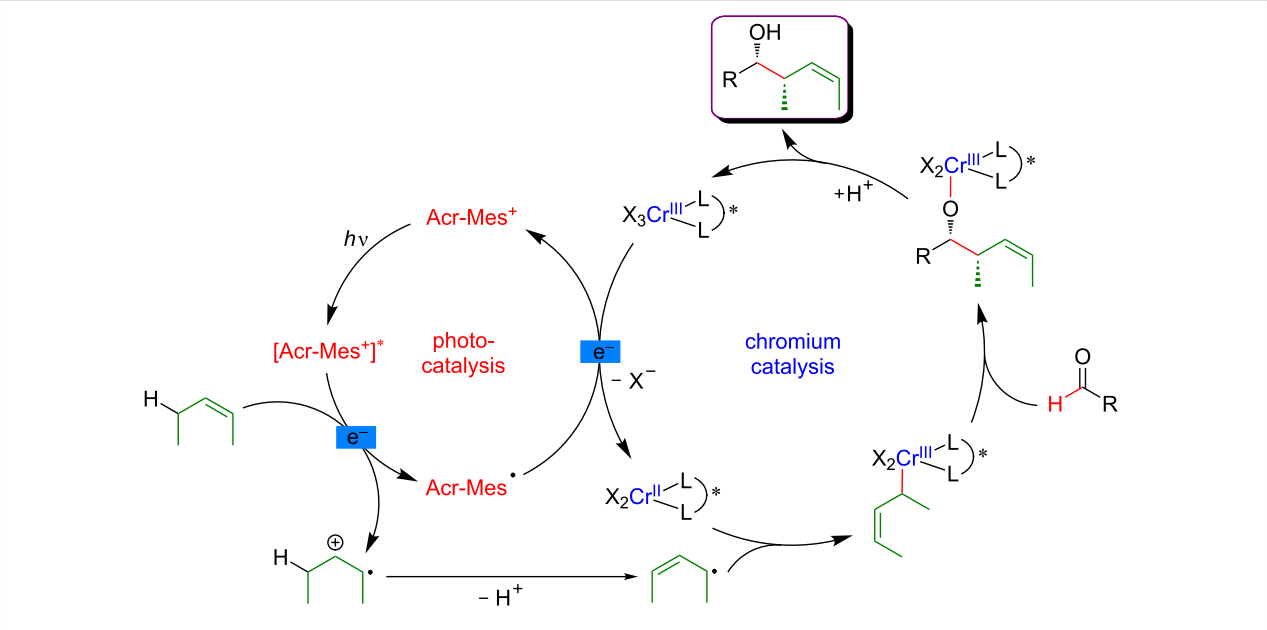

Figure 74: Proposed mechanism for the asymmetric allylation of aldehydes via dual catalysis.

respecting atom-economy. However, such reactions generally call for the use of stoichiometric amounts of oxidants or reductants, or the preinstallation of a directing group. Aiming for more sustainable C–H formylations, MacMillan hypothesized that formyl radical generation could be possible via an HAT-process while designing a complex system comprising three catalytic cycles, i.e., a photoredox, nickel, and HAT catalysis, might provide an appealing alternative protocol for the direct synthesis of ketones [126].

In accordance with this working hypothesis, the finely optimized catalytic system including an Ir-based photosensitizer, $NiBr_2$-dtbpy complex, quinuclidine, and K_2CO_3 base promoted effectively the cross-coupling between diverse aliphatic (cyclic and acyclic) aldehydes, and both, alkyl and aryl bromides (Figure 75). A remarkably large substrate scope could be revealed, delivering the expected ketones in moderate to good yields.

The proposed mechanistic scenario evokes initial irradiation of the Ir-based photosensitizer and a subsequent SET oxidation of quinuclidine to form a cationic radical (Figure 76). An HAT between the quinuclidine radical and the aldehyde furnishes the key acyl radical. Both, the hydric and relatively weak character

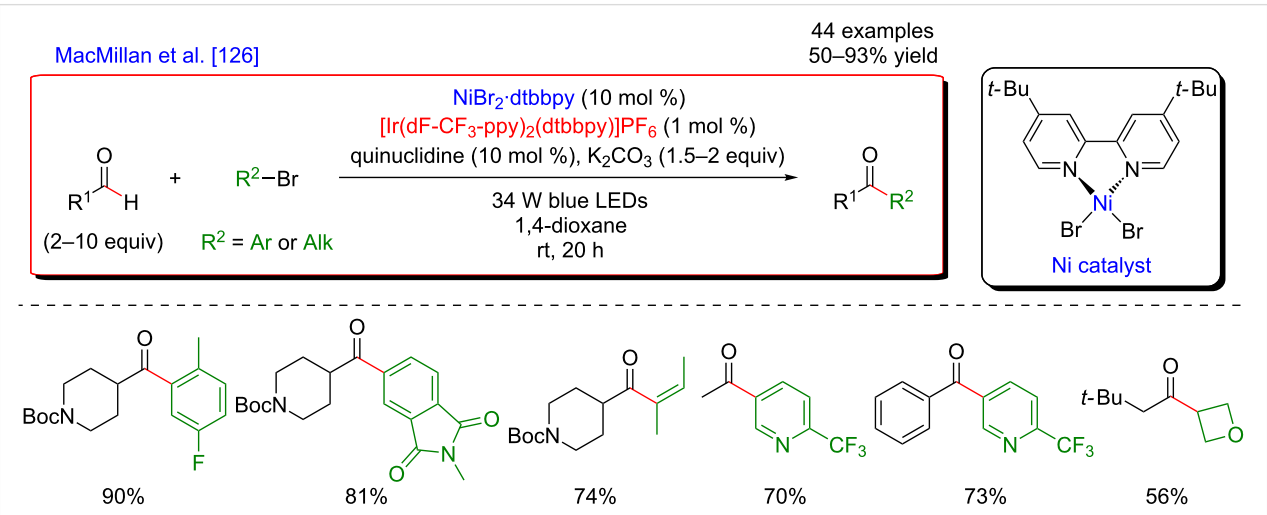

Figure 75: Aldehyde C–H functionalization promoted by H-atom transfer.

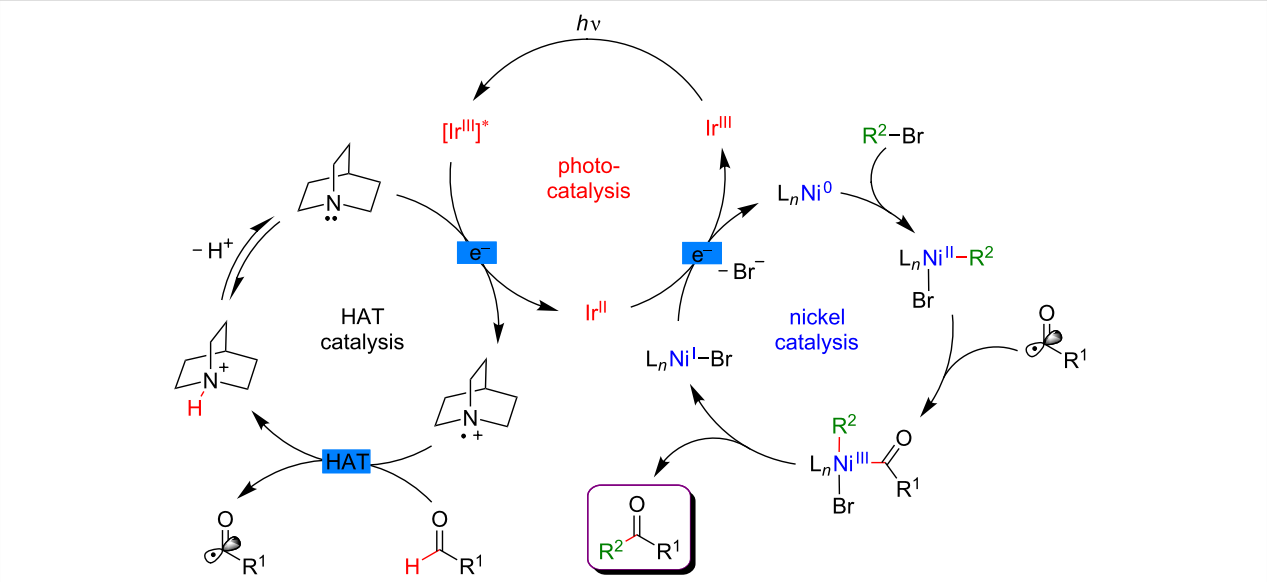

Figure 76: Proposed mechanism for the C–H functionalization of aldehydes promoted by HAT.

of this bond dictates the selectivity of this C–H bond cleavage event. In parallel, the Ni(I) complex engages with the reduced Ir(II) photosensitizer in an SET-type reaction delivering a Ni(0) species and regenerating the Ir(III) photocatalyst. The oxidative addition of Ni(0) to the Ar–Br bond then delivers the Ar–Ni(II)–Br species able to trap the acyl radical, thus forming a Ni(III)–Ac intermediate. Finally, the reductive elimination liberates the expected ketone while regenerating the Ni(I) complex.

Strong, neutral C–H bonds

In order to complete the panel of metallaphotoredox functionalization of C(sp^3)–H bonds, the group of MacMillan focused on the design of a catalytic system compatible with simple and non-activated aliphatic substrates. Based on their previous groundbreaking achievements in the HAT type C–H functionalization, they surmised that strong, C–H bond abstraction could be feasible by a catalyst possessing high-energy excited states, such as polyoxometalates (POMs), and in particular the decatungsten anion $[W_{10}O_{32}]^{4-}$ [127]. Such carbon-centered radicals could thus be rapidly intercepted in the Ni catalytic cycle, to undergo cross-coupling delivering the expected arylated alkanes. As foreseen, while using tetrabutylammonium decatungsten (TBADT) as the HAT catalyst, together with Ni(dtbbpy)Br_2 as the metallic precursor, the expected cross-coupling occurred smoothly using a Kessil lamp (390 nm). Remarkably, diverse of alkanes were applicable, and the regioselectivity of the reaction was dictated by TBADT, with the H-abstraction occurring preferentially at the less-hindered positions. Accordingly, a very large panel of functionalized products was isolated in good yields (Figure 77). This unique transformation was further extended towards the coupling with heteroaromatic halides and its synthetic potential was illustrated by the late-stage functionalization of a few natural products.

Following the overall mechanistic scenario, the photoexcitation of tetrabutylammonium decatungsten (TBADT) and subsequent intersystem crossing lead to the triplet excited state capable of abstract a $H^{\bullet}$ from the alkyl nucleophile (Figure 78). Deprotonation of the single reduced TBADT regenerates the HAT active $[W_{10}O_{32}]^{4-}$. The in situ reduction of the Ni(II) precatalyst delivers the catalytically active Ni(0) intermediate, rapidly intercepting the carbon-centered radical. Final oxidative addition of the thus generated alkyl-radical intermediate into the Ar–X bond furnishes a Ni(III) species, rapidly liberating the expected final product via a reductive elimination event.

More recently, the decatungstate-catalyzed HAT C(sp^3)–H abstraction was also combined with Cu to promote aliphatic trifluoromethylation [128]. As in the previous example, the site-selectivity of the H-abstraction step was directed into the most sterically accessible, electron-rich C(sp^3)–H bond. This unique and extremely broad methodology gave, therefore, access to original trifluoromethylated amines in general moderate to high yields and was perfectly suitable for a selective late-stage functionalization of even sophisticated molecular scaffolds, including drugs (Figure 79).

In parallel, the interception of a CF_3^+ species (generated via formal reduction of the Togni II reagent by the decatungstate reduced species) by a Cu(I) species followed by trapping of the

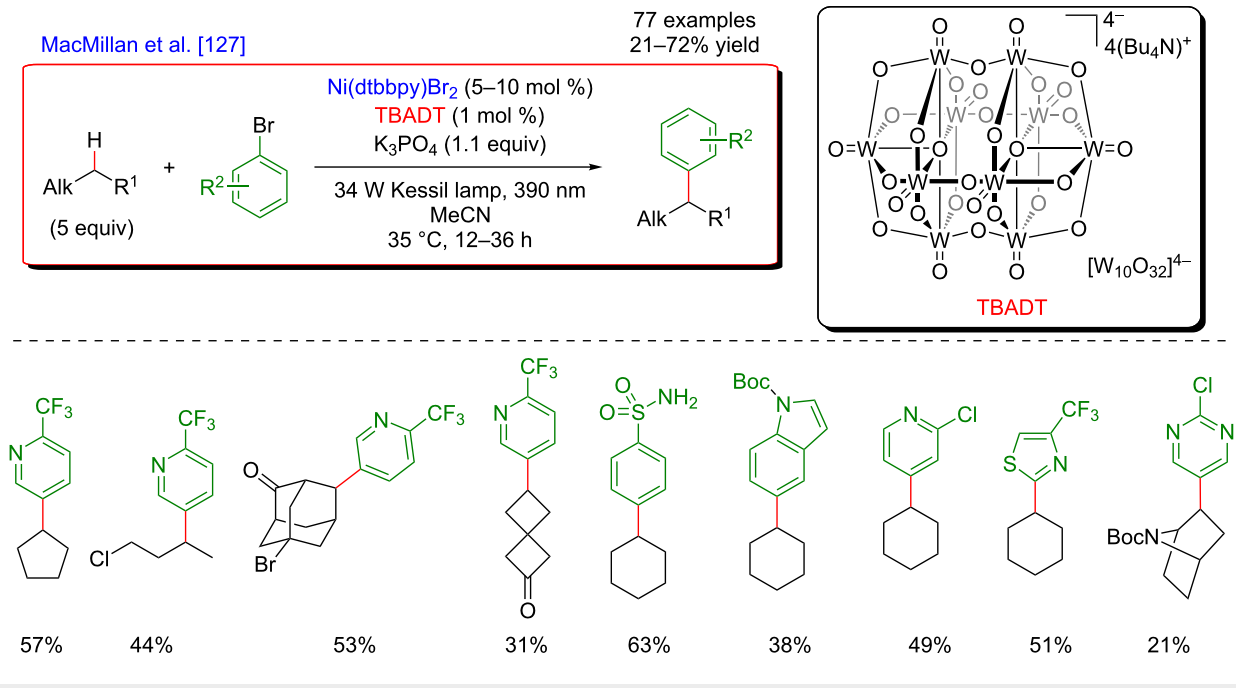

Figure 77: Direct C–H arylation of strong aliphatic bonds promoted by HAT.

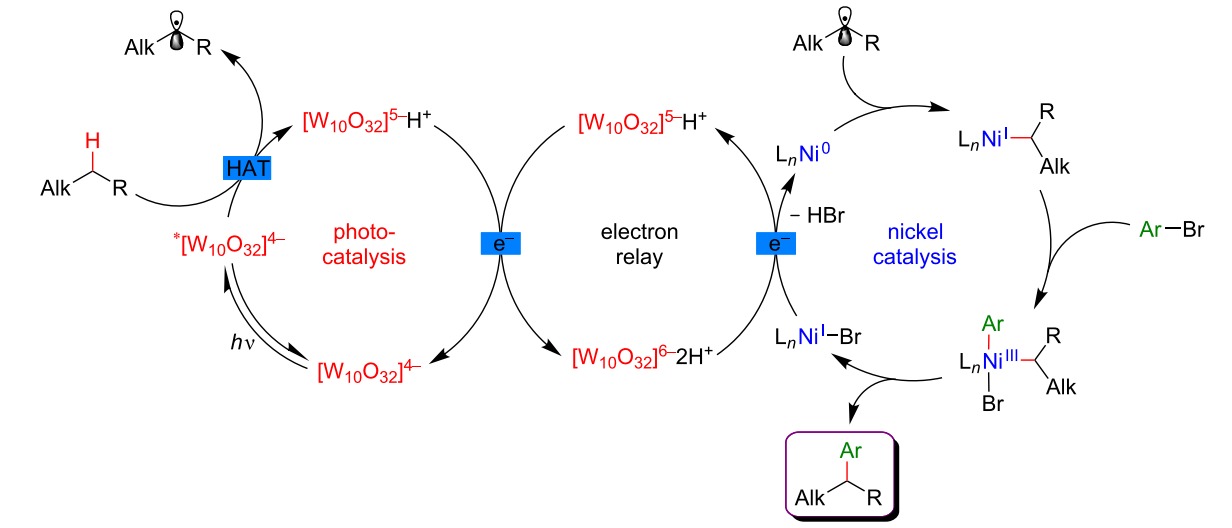

Figure 78: Proposed mechanism for the C–H arylation of strong aliphatic bonds promoted by HAT.

HAT-generated alkyl radial, allow the formation of the key Cu(III)–alkyl–CF_3 intermediate. Upon a reductive elimination step, the trifluoromethylated products were thus obtained (Figure 80).

Conclusion

Transition metal-catalyzed C–H bond activation and visible-light photocatalysis are amongst the most rapidly expanding fields in organic chemistry and these approaches display complementary characteristics and applications. Therefore, it is not surprising that over the last decade, the development of dual catalytic systems, combining these two different strategies in a single chemical transformation has attracted a growing attention of the scientific community. Initially, a visible-light photoredox cycle was used as a modern and astute solution to reoxidize the metal catalysts in various direct C–H functionalization reactions, thus obviating the need for a stoichiometric amount of an external oxidant. This approach permitted

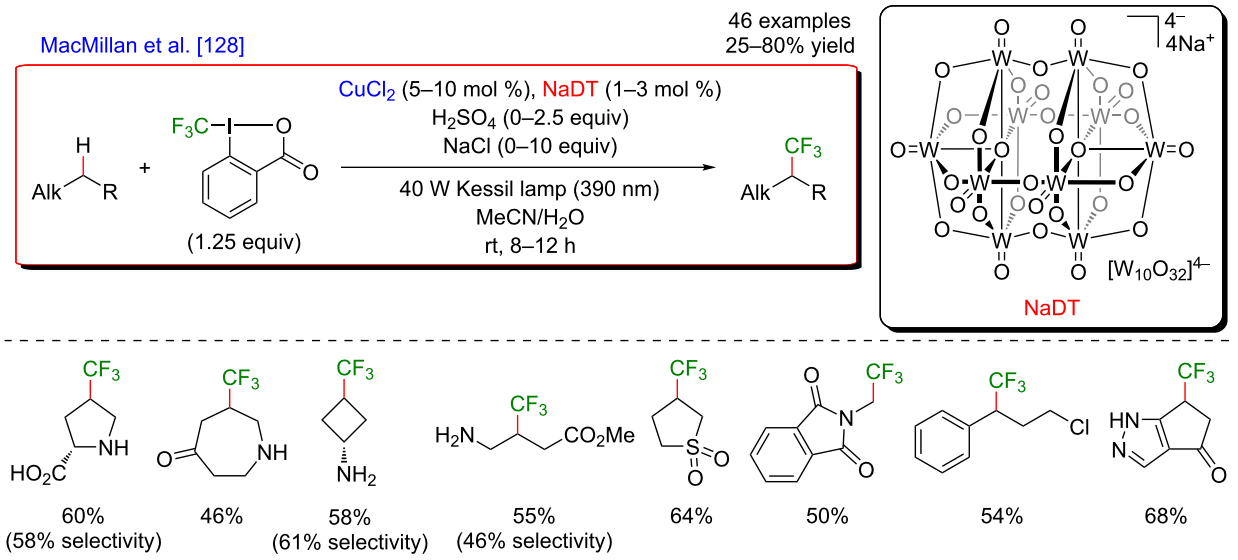

Figure 79: Direct C–H trifluoromethylation of strong aliphatic bonds promoted by HAT.

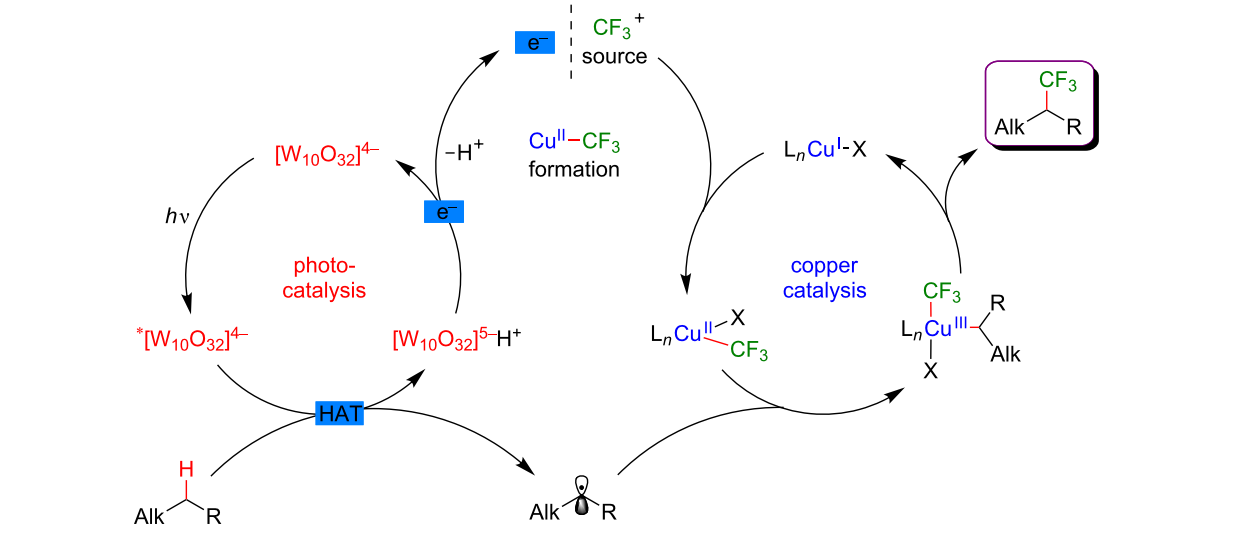

Figure 80: Proposed mechanism for the C–H trifluoromethylation of strong aliphatic bonds.

designing more ecofriendly and sustainable alternatives in comparison with "classical" C–H-activation reactions. Progressively, a second-generation of a "dual synergistic catalysis" system was disclosed. In such complex catalytic systems, both C–H activation and photocatalysis are used as independent but complementary activation modes, allowing the generation of two distinct reactive species, whose recombination furnishes coupling products under generally mild reaction conditions. Such synergistic dual catalysis gives thus a promise of devising previously inaccessible transformations and the synthesis of coupling products difficult to access via a traditional C–H activation strategy may be envisioned. Although this approach seems particularly tempting, the reported examples of such protocols still remain rare. The inherent complexity of this dual catalysis revolves around the fine orchestration of the two or even three distinct catalytic cycles acting in a cooperative way to successfully promote the formation of a new bond. Indeed, the design of catalytic conditions in adequation, perfectly compatible with both independent cycles and promoting the generation of reactive intermediates with comparable kinetics, is far from trivial.

Very recently, procedures in which a C–H activation catalytic cycle affords in situ generations of photoactive metallacyclic

intermediates, prompt to harvest the light and trigger subsequent catalytic steps, were disclosed. This metallaphotoredox catalysis, occurring under exogenous photosensitizer-free conditions, opens the way towards very original and environmentally benign transformations.

In parallel, a complementary strategy emerged, in which HAT-type processes were used to generate aliphatic radicals via selective C–H abstraction. Such aliphatic radicals turned out to be prominent coupling partners in Ni, and more recently, Cu cross-couplings, thus unlocking the door towards highly challenging $C(sp^3)$–$C(sp^2)$, $C(sp^3)$–$C(sp^3)$, and $C(sp^3)$–CF_3 couplings. Importantly, this approach allows the selective functionalization of strong C–H bonds, which is difficult to achieve via alternative routes.

Accordingly, such dual catalysis opens new perspectives in the field of organic synthesis. Certainly, despite the intrinsic difficulty in designing complex catalytic systems, many efforts will be concentrated on conceptualizing alternative modes of merging C–H bond activations and visible-light photocatalysis. In this way, the development of unique and unprecedented transformations can be expected, thus providing new solutions for sustainable and eco-responsible synthesis. Besides, mild reaction conditions, limited waste generation, and rapidly spreading implementation of photocatalysis render these coupling reactions of immense interest for industrial applications. In particular, the development of flow-type protocols for such dual catalysis may be foreseen, thus further increasing the synthetic potential of these reactions. Attention will therefore probably be focused on the general use of cheap, organic photocatalysts capable to harvest efficiently visible light.

Funding

We thank the CNRS (Centre National de la Recherche Scientifique), the “Ministère de l’Éducation Nationale et de la Recherche”, ANR (Agence Nationale de la Recherche) France for financial support. L. Guillemard acknowledges the ANR for a doctoral grant “2al-VisPhot-CH” N° ANR-15-CE29-0004-01.

ORCID® iDs

Lucas Guillemard - https://orcid.org/0000-0001-7938-2504
Joanna Wencel-Delord - https://orcid.org/0000-0002-7094-5443

References

1. Labinger, J. A.; Bercaw, J. E. *Nature* **2002,** *417,* 507–514. doi:10.1038/417507a
2. Lyons, T. W.; Sanford, M. S. *Chem. Rev.* **2010,** *110,* 1147–1169. doi:10.1021/cr900184e
3. Ackermann, L. *Chem. Rev.* **2011,** *111,* 1315–1345. doi:10.1021/cr100412j
4. Wencel-Delord, J.; Dröge, T.; Liu, F.; Glorius, F. *Chem. Soc. Rev.* **2011,** *40,* 4740–4761. doi:10.1039/c1cs15083a
5. Yeung, C. S.; Dong, V. M. *Chem. Rev.* **2011,** *111,* 1215–1292. doi:10.1021/cr100280d
6. Song, G.; Wang, F.; Li, X. *Chem. Soc. Rev.* **2012,** *41,* 3651–3678. doi:10.1039/c2cs15281a
7. Arockiam, P. B.; Bruneau, C.; Dixneuf, P. H. *Chem. Rev.* **2012,** *112,* 5879–5918. doi:10.1021/cr300153j
8. Rouquet, G.; Chatani, N. *Angew. Chem., Int. Ed.* **2013,** *52,* 11726–11743. doi:10.1002/anie.201301451
9. Chen, Z.; Wang, B.; Zhang, J.; Yu, W.; Liu, Z.; Zhang, Y. *Org. Chem. Front.* **2015,** *2,* 1107–1295. doi:10.1039/c5qo00004a
10. Gensch, T.; Hopkinson, M. N.; Glorius, F.; Wencel-Delord, J. *Chem. Soc. Rev.* **2016,** *45,* 2900–2936. doi:10.1039/c6cs00075d
11. Davies, H. M. L.; Morton, D. *J. Org. Chem.* **2016,** *81,* 343–350. doi:10.1021/acs.joc.5b02818
12. Wei, Y.; Hu, P.; Zhang, M.; Su, W. *Chem. Rev.* **2017,** *117,* 8864–8907. doi:10.1021/acs.chemrev.6b00516
13. Yang, Y.; Lan, J.; You, J. *Chem. Rev.* **2017,** *117,* 8787–8863. doi:10.1021/acs.chemrev.6b00567
14. Gandeepan, P.; Müller, T.; Zell, D.; Cera, G.; Warratz, S.; Ackermann, L. *Chem. Rev.* **2019,** *119,* 2192–2452. doi:10.1021/acs.chemrev.8b00507
15. McMurray, L.; O'Hara, F.; Gaunt, M. J. *Chem. Soc. Rev.* **2011,** *40,* 1885–1898. doi:10.1039/c1cs15013h
16. Gutekunst, W. R.; Baran, P. S. *Chem. Soc. Rev.* **2011,** *40,* 1976–1991. doi:10.1039/c0cs00182a
17. Newhouse, T.; Baran, P. S. *Angew. Chem., Int. Ed.* **2011,** *50,* 3362–3374. doi:10.1002/anie.201006368
18. Yamaguchi, J.; Yamaguchi, A. D.; Itami, K. *Angew. Chem., Int. Ed.* **2012,** *51,* 8960–9009. doi:10.1002/anie.201201666
19. Wencel-Delord, J.; Glorius, F. *Nat. Chem.* **2013,** *5,* 369–375. doi:10.1038/nchem.1607
20. Karimov, R. R.; Hartwig, J. F. *Angew. Chem., Int. Ed.* **2018,** *57,* 4234–4241. doi:10.1002/anie.201710330
21. Jazzar, R.; Hitce, J.; Renaudat, A.; Sofack-Kreutzer, J.; Baudoin, O. *Chem. – Eur. J.* **2010,** *16,* 2654–2672. doi:10.1002/chem.200902374
22. Ackermann, L. *Chem. Commun.* **2010,** *46,* 4866–4877. doi:10.1039/c0cc00778a
23. Wasa, M.; Engle, K. M.; Yu, J.-Q. *Isr. J. Chem.* **2010,** *50,* 605–616. doi:10.1002/ijch.201000038
24. Baudoin, O. *Chem. Soc. Rev.* **2011,** *40,* 4902–4911. doi:10.1039/c1cs15058h
25. Li, H.; Li, B.-J.; Shi, Z.-J. *Catal. Sci. Technol.* **2011,** *1,* 191–206. doi:10.1039/c0cy00076k
26. Qiu, G.; Wu, J. *Org. Chem. Front.* **2015,** *2,* 169–178. doi:10.1039/c4qo00207e
27. He, J.; Wasa, M.; Chan, K. S. L.; Shao, Q.; Yu, J.-Q. *Chem. Rev.* **2017,** *117,* 8754–8786. doi:10.1021/acs.chemrev.6b00622
28. Evano, G.; Theunissen, C. *Angew. Chem., Int. Ed.* **2019,** *58,* 7202–7236. doi:10.1002/anie.201806629
29. Fagnoni, M.; Dondi, D.; Ravelli, D.; Albini, A. *Chem. Rev.* **2007,** *107,* 2725–2756. doi:10.1021/cr068352x
30. Zeitler, K. *Angew. Chem., Int. Ed.* **2009,** *48,* 9785–9789. doi:10.1002/anie.200904056
31. Narayanam, J. M. R.; Stephenson, C. R. J. *Chem. Soc. Rev.* **2011,** *40,* 102–113. doi:10.1039/b913880n
32. Xuan, J.; Xiao, W.-J. *Angew. Chem., Int. Ed.* **2012,** *51,* 6828–6838. doi:10.1002/anie.201200223

33. Shi, L.; Xia, W. *Chem. Soc. Rev.* **2012,** *41,* 7687–7697. doi:10.1039/c2cs35203f
34. Tucker, J. W.; Stephenson, C. R. J. *J. Org. Chem.* **2012,** *77,* 1617–1622. doi:10.1021/jo202538x
35. Reckenthäler, M.; Griesbeck, A. G. *Adv. Synth. Catal.* **2013,** *355,* 2727–2744. doi:10.1002/adsc.201300751
36. Fukuzumi, S.; Ohkubo, K. *Chem. Sci.* **2013,** *4,* 561–574. doi:10.1039/c2sc21449k
37. Xi, Y.; Yi, H.; Lei, A. *Org. Biomol. Chem.* **2013,** *11,* 2387–2403. doi:10.1039/c3ob40137e
38. Prier, C. K.; Rankic, D. A.; MacMillan, D. W. C. *Chem. Rev.* **2013,** *113,* 5322–5363. doi:10.1021/cr300503r
39. Shaw, M. H.; Twilton, J.; MacMillan, D. W. C. *J. Org. Chem.* **2016,** *81,* 6898–6926. doi:10.1021/acs.joc.6b01449
40. Romero, N. A.; Nicewicz, D. A. *Chem. Rev.* **2016,** *116,* 10075–10166. doi:10.1021/acs.chemrev.6b00057
41. Xie, J.; Jin, H.; Hashmi, A. S. K. *Chem. Soc. Rev.* **2017,** *46,* 5193–5203. doi:10.1039/c7cs00339k
42. Wang, C.-S.; Dixneuf, P. H.; Soulé, J.-F. *Chem. Rev.* **2018,** *118,* 7532–7585. doi:10.1021/acs.chemrev.8b00077
43. Festa, A. A.; Voskressensky, L. G.; Van der Eycken, E. V. *Chem. Soc. Rev.* **2019,** *48,* 4401–4423. doi:10.1039/c8cs00790j
44. Yoon, T. P.; Ischay, M. A.; Du, J. *Nat. Chem.* **2010,** *2,* 527–532. doi:10.1038/nchem.687
45. Schultz, D. M.; Yoon, T. P. *Science* **2014,** *343,* 1239176. doi:10.1126/science.1239176
46. Strieth-Kalthoff, F.; James, M. J.; Teders, M.; Pitzer, L.; Glorius, F. *Chem. Soc. Rev.* **2018,** *47,* 7190–7202. doi:10.1039/c8cs00054a
47. Allen, A. E.; MacMillan, D. W. C. *Chem. Sci.* **2012,** *3,* 633–658. doi:10.1039/c2sc00907b
48. Shibasaki, M.; Kanai, M.; Matsunaga, S.; Kumagai, N. *Acc. Chem. Res.* **2009,** *42,* 1117–1127. doi:10.1021/ar9000108
49. Park, Y. J.; Park, J.-W.; Jun, C.-H. *Acc. Chem. Res.* **2008,** *41,* 222–234. doi:10.1021/ar700133y
50. Xu, H.; Zuend, S. J.; Woll, M. G.; Tao, Y.; Jacobsen, E. N. *Science* **2010,** *327,* 986–990. doi:10.1126/science.1182826
51. Han, Z.-Y.; Xiao, H.; Chen, X.-H.; Gong, L.-Z. *J. Am. Chem. Soc.* **2009,** *131,* 9182–9183. doi:10.1021/ja903547q
52. Lathrop, S. P.; Rovis, T. *J. Am. Chem. Soc.* **2009,** *131,* 13628–13630. doi:10.1021/ja905342e
53. Hopkinson, M. N.; Sahoo, B.; Li, J.-L.; Glorius, F. *Chem. – Eur. J.* **2014,** *20,* 3874–3886. doi:10.1002/chem.201304823
54. Xie, J.; Jin, H.; Xu, P.; Zhu, C. *Tetrahedron Lett.* **2014,** *55,* 36–48. doi:10.1016/j.tetlet.2013.10.090
55. Skubi, K. L.; Blum, T. R.; Yoon, T. P. *Chem. Rev.* **2016,** *116,* 10035–10074. doi:10.1021/acs.chemrev.6b00018
56. Lang, X.; Zhao, J.; Chen, X. *Chem. Soc. Rev.* **2016,** *45,* 3026–3038. doi:10.1039/c5cs00659g
57. Ravelli, D.; Protti, S.; Fagnoni, M. *Chem. Rev.* **2016,** *116,* 9850–9913. doi:10.1021/acs.chemrev.5b00662
58. Prier, C. K.; MacMillan, D. W. C. Dual Photoredox Catalysis: The Merger of Photoredox Catalysis with Other Catalytic Activation Modes. In *Visible Light Photocatalysis in Organic Chemistry;* Stephenson, C. R. J.; Yoon, T.; MacMillan, D. W. C., Eds.; Wiley-VCH: Weinheim, Germany, 2018; pp 299–333. doi:10.1002/9783527674145.ch10
59. Levin, M. D.; Kim, S.; Toste, F. D. *ACS Cent. Sci.* **2016,** *2,* 293–301. doi:10.1021/acscentsci.6b00090
60. Fabry, D. C.; Rueping, M. *Acc. Chem. Res.* **2016,** *49,* 1969–1979. doi:10.1021/acs.accounts.6b00275
61. Zhou, W.-J.; Zhang, Y.-H.; Gui, Y.-Y.; Sun, L.; Yu, D.-G. *Synthesis* **2018,** *50,* 3359–3378. doi:10.1055/s-0037-1610222
62. Twilton, J.; Le, C.; Zhang, P.; Shaw, M. H.; Evans, R. W.; MacMillan, D. W. C. *Nat. Rev. Chem.* **2017,** *1,* 0052. doi:10.1038/s41570-017-0052
63. McLean, E. B.; Lee, A.-L. *Tetrahedron* **2018,** *74,* 4881–4902. doi:10.1016/j.tet.2018.07.032
64. Dwivedi, V.; Kalsi, D.; Sundararaju, B. *ChemCatChem* **2019,** *11,* 5160–5187. doi:10.1002/cctc.201900680
65. De Abreu, M.; Belmont, P.; Brachet, E. *Eur. J. Org. Chem.* **2020,** 1327–1378. doi:10.1002/ejoc.201901146
66. Tellis, J. C.; Kelly, C. B.; Primer, D. N.; Jouffroy, M.; Patel, N. R.; Molander, G. A. *Acc. Chem. Res.* **2016,** *49,* 1429–1439. doi:10.1021/acs.accounts.6b00214
67. Gui, Y.-Y.; Sun, L.; Lu, Z.-P.; Yu, D.-G. *Org. Chem. Front.* **2016,** *3,* 522–526. doi:10.1039/c5qo00437c
68. Zuo, Z.; Ahneman, D. T.; Chu, L.; Terrett, J. A.; Doyle, A. G.; MacMillan, D. W. C. *Science* **2014,** *345,* 437–440. doi:10.1126/science.1255525
69. Tellis, J. C.; Primer, D. N.; Molander, G. A. *Science* **2014,** *345,* 433–436. doi:10.1126/science.1253647
70. Ferreira, E. M.; Zhang, H.; Stoltz, B. M. Oxidative Heck-Type Reactions (Fujiwara–Moritani Reactions). In *The Mizoroki–Heck Reaction;* Oestreich, M., Ed.; John Wiley & Sons, Ltd.: Chichester, UK, 2009; pp 345–382. doi:10.1002/9780470716076.ch9
71. Rauf, W.; Brown, J. M. *Chem. Commun.* **2013,** *49,* 8430–8440. doi:10.1039/c3cc44842h
72. Zhou, L.; Lu, W. *Chem. – Eur. J.* **2014,** *20,* 634–642. doi:10.1002/chem.201303670
73. Zoller, J.; Fabry, D. C.; Ronge, M. A.; Rueping, M. *Angew. Chem., Int. Ed.* **2014,** *53,* 13264–13268. doi:10.1002/anie.201405478
74. Fabry, D. C.; Zoller, J.; Raja, S.; Rueping, M. *Angew. Chem., Int. Ed.* **2014,** *53,* 10228–10231. doi:10.1002/anie.201400560
75. Fabry, D. C.; Ronge, M. A.; Zoller, J.; Rueping, M. *Angew. Chem., Int. Ed.* **2015,** *54,* 2801–2805. doi:10.1002/anie.201408891
76. Choi, S.; Chatterjee, T.; Choi, W. J.; You, Y.; Cho, E. J. *ACS Catal.* **2015,** *5,* 4796–4802. doi:10.1021/acscatal.5b00817
77. Liu, K.; Zou, M.; Lei, A. *J. Org. Chem.* **2016,** *81,* 7088–7092. doi:10.1021/acs.joc.6b00965
78. Kalsi, D.; Dutta, S.; Barsu, N.; Rueping, M.; Sundararaju, B. *ACS Catal.* **2018,** *8,* 8115–8120. doi:10.1021/acscatal.8b02118
79. Kim, H. J.; Fabry, D. C.; Mader, S.; Rueping, M. *Org. Chem. Front.* **2019,** *6,* 2319–2323. doi:10.1039/c9qo00206e
80. Kalyani, D.; McMurtrey, K. B.; Neufeldt, S. R.; Sanford, M. S. *J. Am. Chem. Soc.* **2011,** *133,* 18566–18569. doi:10.1021/ja208068w
81. Kalyani, D.; Deprez, N. R.; Desai, L. V.; Sanford, M. S. *J. Am. Chem. Soc.* **2005,** *127,* 7330–7331. doi:10.1021/ja051402f
82. Maestri, G.; Malacria, M.; Derat, E. *Chem. Commun.* **2013,** *49,* 10424–10426. doi:10.1039/c3cc46355a
83. Neufeldt, S. R.; Sanford, M. S. *Adv. Synth. Catal.* **2012,** *354,* 3517–3522. doi:10.1002/adsc.201200738
84. Jiang, J.; Zhang, W.-M.; Dai, J.-J.; Xu, J.; Xu, H.-J. *J. Org. Chem.* **2017,** *82,* 3622–3630. doi:10.1021/acs.joc.7b00140
85. Cismesia, M. A.; Yoon, T. P. *Chem. Sci.* **2015,** *6,* 5426–5434. doi:10.1039/c5sc02185e
86. Sahoo, M. K.; Midya, S. P.; Landge, V. G.; Balaraman, E. *Green Chem.* **2017,** *19,* 2111–2117. doi:10.1039/c6gc03438a

87. Liang, L.; Xie, M.-S.; Wang, H.-X.; Niu, H.-Y.; Qu, G.-R.; Guo, H.-M. *J. Org. Chem.* **2017,** *82,* 5966–5973. doi:10.1021/acs.joc.7b00659
88. Czyz, M. L.; Lupton, D. W.; Polyzos, A. *Chem. – Eur. J.* **2017,** *23,* 14450–14453. doi:10.1002/chem.201704045
89. Zhou, C.; Li, P.; Zhu, X.; Wang, L. *Org. Lett.* **2015,** *17,* 6198–6201. doi:10.1021/acs.orglett.5b03192
90. Xu, N.; Li, P.; Xie, Z.; Wang, L. *Chem. – Eur. J.* **2016,** *22,* 2236–2242. doi:10.1002/chem.201504530
91. Cambié, D.; Bottecchia, C.; Straathof, N. J. W.; Hessel, V.; Noël, T. *Chem. Rev.* **2016,** *116,* 10276–10341. doi:10.1021/acs.chemrev.5b00707
92. Santoro, S.; Ferlin, F.; Ackermann, L.; Vaccaro, L. *Chem. Soc. Rev.* **2019,** *48,* 2767–2782. doi:10.1039/c8cs00211h
93. Govaerts, S.; Nyuchev, A.; Noël, T. *J. Flow Chem.* **2020,** *10,* 13–71. doi:10.1007/s41981-020-00077-7
94. Sharma, U. K.; Gemoets, H. P. L.; Schröder, F.; Noël, T.; Van der Eycken, E. V. *ACS Catal.* **2017,** *7,* 3818–3823. doi:10.1021/acscatal.7b00840
95. Manna, M. K.; Bairy, G.; Jana, R. *Org. Biomol. Chem.* **2017,** *15,* 5899–5903. doi:10.1039/c7ob01418j
96. McCann, S. D.; Stahl, S. S. *Acc. Chem. Res.* **2015,** *48,* 1756–1766. doi:10.1021/acs.accounts.5b00060
97. Almasalma, A. A.; Mejía, E. *Synthesis* **2020,** in press. doi:10.1055/s-0040-1707815
98. Chen, X.; Tan, Z.; Gui, Q.; Hu, L.; Liu, J.; Wu, J.; Wang, G. *Chem. – Eur. J.* **2016,** *22,* 6218–6222. doi:10.1002/chem.201600229
99. Bai, P.; Sun, S.; Li, Z.; Qiao, H.; Su, X.; Yang, F.; Wu, Y.; Wu, Y. *J. Org. Chem.* **2017,** *82,* 12119–12127. doi:10.1021/acs.joc.7b01917
100. Gandeepan, P.; Koeller, J.; Korvorapun, K.; Mohr, J.; Ackermann, L. *Angew. Chem., Int. Ed.* **2019,** *58,* 9820–9825. doi:10.1002/anie.201902258
101. Sagadevan, A.; Greaney, M. F. *Angew. Chem., Int. Ed.* **2019,** *58,* 9826–9830. doi:10.1002/anie.201904288
102. Thongpaen, J.; Manguin, R.; Dorcet, V.; Vives, T.; Duhayon, C.; Mauduit, M.; Baslé, O. *Angew. Chem., Int. Ed.* **2019,** *58,* 15244–15248. doi:10.1002/anie.201905924
103. Kuhl, N.; Hopkinson, M. N.; Wencel-Delord, J.; Glorius, F. *Angew. Chem., Int. Ed.* **2012,** *51,* 10236–10254. doi:10.1002/anie.201203269
104. Gauchot, V.; Sutherland, D. R.; Lee, A.-L. *Chem. Sci.* **2017,** *8,* 2885–2889. doi:10.1039/c6sc05469b
105. Liang, Y.-F.; Steinbock, R.; Yang, L.; Ackermann, L. *Angew. Chem., Int. Ed.* **2018,** *57,* 10625–10629. doi:10.1002/anie.201805644
106. Yang, F.; Koeller, J.; Ackermann, L. *Angew. Chem., Int. Ed.* **2016,** *55,* 4759–4762. doi:10.1002/anie.201512027
107. Gandeepan, P.; Mo, J.; Ackermann, L. *Chem. Commun.* **2017,** *53,* 5906–5909. doi:10.1039/c7cc03107f
108. Koeller, J.; Gandeepan, P.; Ackermann, L. *Synthesis* **2019,** *51,* 1284–1292. doi:10.1055/s-0037-1611633
109. Chinchilla, R.; Nájera, C. *Chem. Rev.* **2007,** *107,* 874–922. doi:10.1021/cr050992x
110. Wu, Y.; Huo, X.; Zhang, W. *Chem. – Eur. J.* **2020,** *26,* 4895–4916. doi:10.1002/chem.201904495
111. Karak, M.; Barbosa, L. C. A.; Hargaden, G. C. *RSC Adv.* **2014,** *4,* 53442–53466. doi:10.1039/c4ra09105a
112. Chinchilla, R.; Nájera, C. *Chem. Soc. Rev.* **2011,** *40,* 5084–5121. doi:10.1039/c1cs15071e
113. Osawa, M.; Nagai, H.; Akita, M. *Dalton Trans.* **2007,** 827–829. doi:10.1039/b618007h
114. Tlahuext-Aca, A.; Hopkinson, M. N.; Sahoo, B.; Glorius, F. *Chem. Sci.* **2016,** *7,* 89–93. doi:10.1039/c5sc02583d
115. Jeffrey, J. L.; Terrett, J. A.; MacMillan, D. W. C. *Science* **2015,** *349,* 1532–1536. doi:10.1126/science.aac8555
116. Shaw, M. H.; Shurtleff, V. W.; Terrett, J. A.; Cuthbertson, J. D.; MacMillan, D. W. C. *Science* **2016,** *352,* 1304–1308. doi:10.1126/science.aaf6635
117. Twilton, J.; Christensen, M.; DiRocco, D. A.; Ruck, R. T.; Davies, I. W.; MacMillan, D. W. C. *Angew. Chem., Int. Ed.* **2018,** *57,* 5369–5373. doi:10.1002/anie.201800749
118. Ahneman, D. T.; Doyle, A. G. *Chem. Sci.* **2016,** *7,* 7002–7006. doi:10.1039/c6sc02815b
119. Shen, Y.; Gu, Y.; Martin, R. *J. Am. Chem. Soc.* **2018,** *140,* 12200–12209. doi:10.1021/jacs.8b07405
120. Le, C.; Liang, Y.; Evans, R. W.; Li, X.; MacMillan, D. W. C. *Nature* **2017,** *547,* 79–83. doi:10.1038/nature22813
121. Joe, C. L.; Doyle, A. G. *Angew. Chem., Int. Ed.* **2016,** *55,* 4040–4043. doi:10.1002/anie.201511438
122. Deng, H.-P.; Fan, X.-Z.; Chen, Z.-H.; Xu, Q.-H.; Wu, J. *J. Am. Chem. Soc.* **2017,** *139,* 13579–13584. doi:10.1021/jacs.7b08158
123. Go, S. Y.; Lee, G. S.; Hong, S. H. *Org. Lett.* **2018,** *20,* 4691–4694. doi:10.1021/acs.orglett.8b02017
124. Huang, L.; Rueping, M. *Angew. Chem., Int. Ed.* **2018,** *57,* 10333–10337. doi:10.1002/anie.201805118
125. Mitsunuma, H.; Tanabe, S.; Fuse, H.; Ohkubo, K.; Kanai, M. *Chem. Sci.* **2019,** *10,* 3459–3465. doi:10.1039/c8sc05677c
126. Zhang, X.; MacMillan, D. W. C. *J. Am. Chem. Soc.* **2017,** *139,* 11353–11356. doi:10.1021/jacs.7b07078
127. Perry, I. B.; Brewer, T. F.; Sarver, P. J.; Schultz, D. M.; DiRocco, D. A.; MacMillan, D. W. C. *Nature* **2018,** *560,* 70–75. doi:10.1038/s41586-018-0366-x
128. Sarver, P. J.; Bacauanu, V.; Schultz, D. M.; DiRocco, D. A.; Lam, Y.-h.; Sherer, E. C.; MacMillan, D. W. C. *Nat. Chem.* **2020,** *12,* 459–467. doi:10.1038/s41557-020-0436-1

License and Terms

This is an Open Access article under the terms of the Creative Commons Attribution License (http://creativecommons.org/licenses/by/4.0). Please note that the reuse, redistribution and reproduction in particular requires that the authors and source are credited.

The license is subject to the *Beilstein Journal of Organic Chemistry* terms and conditions: (https://www.beilstein-journals.org/bjoc)

The definitive version of this article is the electronic one which can be found at:
doi:10.3762/bjoc.16.147

BEILSTEIN JOURNAL OF ORGANIC CHEMISTRY

A complementary approach to conjugated *N*-acyliminium formation through photoredox-catalyzed intermolecular radical addition to allenamides and allencarbamates

Olusesan K. Koleoso[1,2], Matthew Turner[1], Felix Plasser[1] and Marc C. Kimber[*1]

Letter

Open Access

Address:
[1]School of Science, Department of Chemistry, Loughborough University, Loughborough, LE11 3TU, UK and [2]Department of Pharmaceutical Technology, Moshood Abiola Polytechnic, Abeokuta, Nigeria

Email:
Marc C. Kimber[*] - M.C.Kimber@lboro.ac.uk

* Corresponding author

Keywords:
allenamide; allene; intermolecular; *N*-acyliminium; photoredox

Beilstein J. Org. Chem. **2020,** *16,* 1983–1990.
doi:10.3762/bjoc.16.165

Received: 19 June 2020
Accepted: 05 August 2020
Published: 12 August 2020

This article is part of the thematic issue "Advances in photoredox catalysis".

Guest Editor: T. Noël

© 2020 Koleoso et al.; licensee Beilstein-Institut.
License and terms: see end of document.

Abstract

An intermolecular radical addition, using photoredox catalysis, to allenamides and allencarbamates is reported. This transformation synthesizes *N*-acyl-*N'*-aryl-*N*,*N'*-allylaminals, and proceeds by a conjugated *N*-acyliminium intermediate that previously has principally been generated by electrophilic activation methods. The radical adds to the central carbon of the allene giving a conjugated *N*-acyliminium that undergoes nucleophilic addition by arylamines and alcohols.

Introduction

Allenamides (Scheme 1, **1**) and their congeners have attracted considerable attention over the past 15 years due to their characteristic reactivity profiles [1-4]. The reactivity that an allenamide can display is distinct from a traditional allene due to the presence of an amide unit attached at the α-carbon. This substituent can donate electron density into the allene, principally onto the central β-carbon, that can be harnessed in subsequent chemical transformations leading to regiochemical confidence in the resulting products (Scheme 1).

Importantly, this unique reactivity has underpinned allenamide chemistry and led to the development of a number of innovative transformations, including cycloadditions [5-9], intramolecular cyclizations and intermolecular addition reactions [10-18], as well as the use of the allenamide building block in natural product synthesis [1].

Addition reactions of allenamides, which can also encompass intramolecular cyclizations, are typically promoted by the electrophilic activation of the β-carbon of the allenamide. This can be achieved using various electrophilic methods, including the use of Brönsted acids [15,19-22], halogenation sources [16,18,23-28], by means of oxidation [20,29-31] or through the use of a transition metal such as Au(I) [8,10-16,32-36]. The reaction of the allenamide with an electrophilic source promotes the formation of a conjugated *N*-acyliminium intermediate **2**

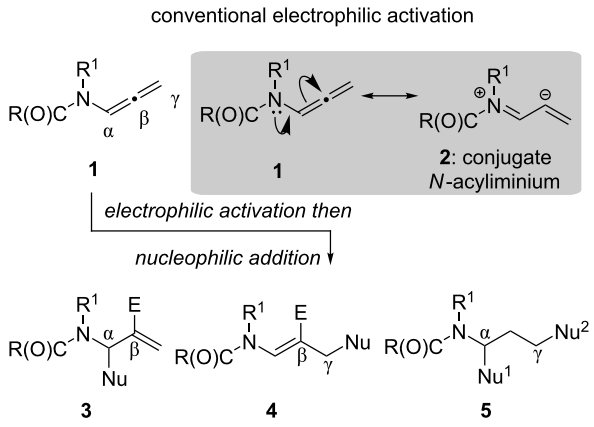

Scheme 1: Electrophilic activation of allenamides.

[37-40] that subsequently undergoes an addition reaction with a suitable nucleophile (Scheme 1).

Importantly, the electrophilic mediated formation of this key intermediate **2** have been the cornerstone for allenamide chemistry over the past 15 years. Therefore, given the importance of the allenamide building block we sought a new synthetic methodology that could generate this conjugated *N*-acyliminium intermediate **2**, that would not be dependent on conventional electrophilic activation modes (Scheme 2).

In principle, a new method for its generation could greatly enhance the value of the allenamide building block, as well as potentially unlocking new chemical reactivity yet unseen in the context of electrophilic activation. We envisaged that a route to the conjugated *N*-acyliminium intermediate could be achieved via an intermolecular addition of an electrophilic radical to an allenamide (**1**) followed by an oxidation process on the subsequently formed radical (Scheme 3) [41]. The thought process behind this approach is based on three observations; (i) Akita and co-workers disclosure on the photoredox-catalyzed oxytrifluoromethylation of allenes **6** to give 2-trifluoromethylated allyl acetates **7** [42-44]; (ii) that intramolecular radical cyclization of allenamides have been reported by Hsung and co-workers, where the radical adds principally to the central carbon of the allene (**10**) [45]; and (iii) the photoredox-catalyzed addition of radicals to enamides reported by Masson [46-49], and more recently by our own laboratory in the synthesis of

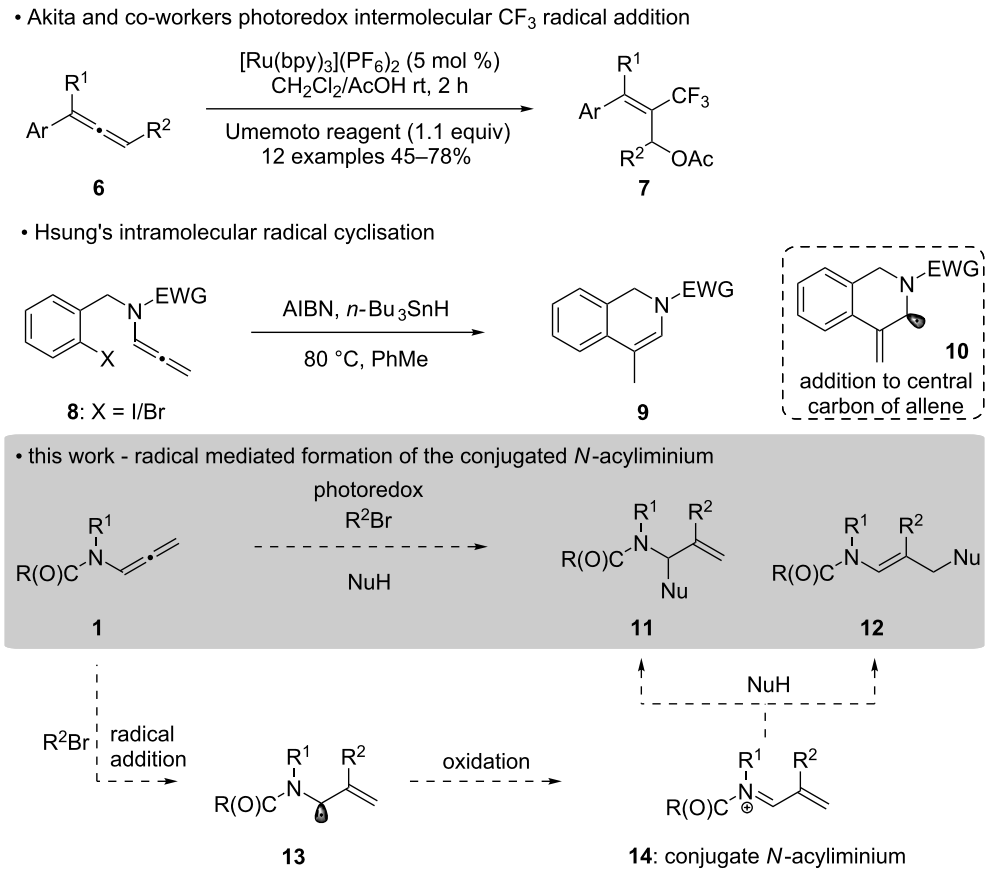

Scheme 2: The planned intramolecular radical addition to allenamides generating the conjugated *N*-acyliminium intermediate **14**.

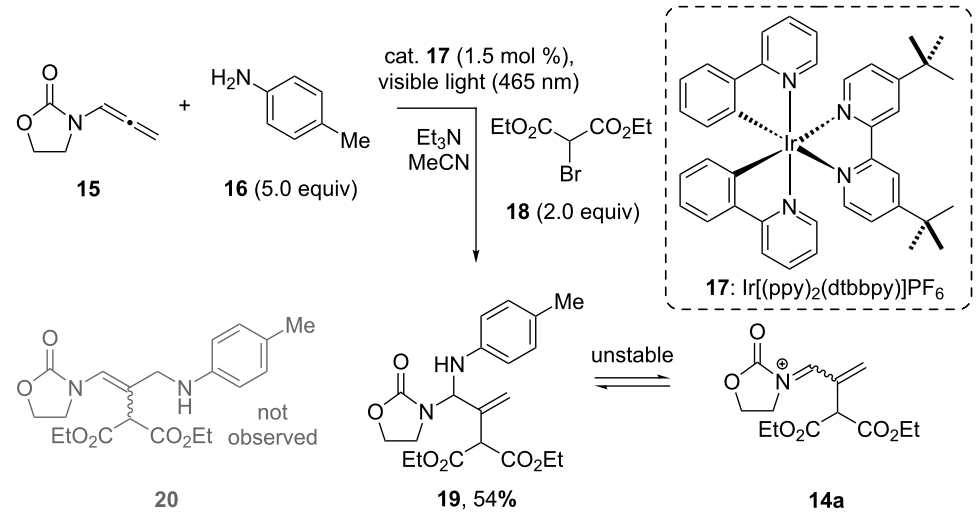

Scheme 3: Photoredox Ir-catalyzed intermolecular addition of bromide **18** and aniline **16** to allenamide **15**.

N,*N*'-aminals [50]. Therefore, photoredox-catalysis would be employed to generate an electrophilic radical that would add to the central carbon of the allenamide **1** to give a transient radical **13**, whose oxidation, facilitated by the photoredox catalyst [47,48], would provide the conjugated *N*-acyliminium **14**. The iminium **14** could then undergo traditional nucleophilic addition giving the addition product. Given that the iridium complex Ir[(ppy)$_2$(dtbbpy)]PF$_6$ had been effective [47,48,50] in this radical/cationic pathway with enamides we would now like to report our preliminary findings on the performance of allenamides. Specifically, the electron-withdrawing group on the allenamide and the nucleophile is examined. We provide evidence for the formation of the *N*-acyliminium intermediate through direct sample loop and flow injection analysis by HRESIMS, and DFT analysis of the *N*-acyliminium intermediate is provided to explain the addition product distribution.

Results and Discussion

We began our study by using the iridium catalyst Ir[(ppy)$_2$(dtbbpy)]PF$_6$ (**17**) and the reaction conditions used in the addition of amine nucleophiles to enamides [48,50]. By exploiting these reaction conditions, using diethyl bromomalonate (**18**), 4-anisidine (**16**) as the amine nucleophile, and allenamide **15** we were able to isolate *N*-acyl-*N*'-aryl-*N*,*N*'-allylaminal **19** as the sole identifiable product in 54% yield.

All of the starting allenamide **15** was consumed in the reaction, but the isolation of **19** proved very challenging and we can account for this instability by the identification of **14a** in the ^{1}H NMR spectrum of the crude reaction mixture. A comparable instability profile was observed in the formation of *N*-acyl-*N*'-aryl-*N*,*N*'-aminals derived from enamides [50]; however, to our knowledge, there are no reports of the isolation of analogous *N*-acyl-*N*'-aryl-*N*,*N*'-allylaminal substrates in the literature, consequently, these specific conditions were not optimized [51]. The evidence for the formation of **19** was the appearance of the methylene protons in ^{1}H NMR at δ 5.46 (d, *J* = 1.6 Hz, 1H) and δ 5.45 (d, *J* = 2.0 Hz, 1H) ppm, respectively. Crucially, it is apparent that using the photoredox conditions described in Scheme 3, the aniline nucleophile adds primarily at the α-position of the allenamide **15**; this is in contrast to the archetypal electrophilic activation modes where comparable nucleophiles add to the γ-position [37,39,40].

An examination of the allenamide unit under these conditions is shown in Scheme 4, and the six allenylamides/sulfonamides (**15**, **21**–**25**) were prepared using known conditions [52,53]. The allenamides derived from pyrrolidinone (**21**), piperidinone (**22**) and oxazolidinone (**15**) with 2,4-dimethylaniline all performed adequately in this reaction giving their *N*,*N*'-allylaminal products **26**, **27** and **28**, respectively. The isolated yields once again reflected the sensitivity of the *N*,*N*'-allylaminal functional group. The aminosulfonyl allenyl **23** failed to provide any discernable product, with only a complex mixture, as identified by ^{1}H NMR, being isolated. Significantly, in the ^{1}H NMR spectra of this complex mixture we observed complete fragmentation of the sulfonamide unit. Two chiral allenamides (**24** and **25**) were exposed to the photoredox conditions with 2,4-dimethylaniline, and it was observed that the predominant product in each case was *Z*-**30** and *Z*-**31**, respectively, which presumably result from γ-addition of the nucleophile. This was confirmed by ^{1}H NMR NOE analysis of *Z*-**30**, where an enhancement between the enamide proton and the methylene proton were observed, as shown in Scheme 4.

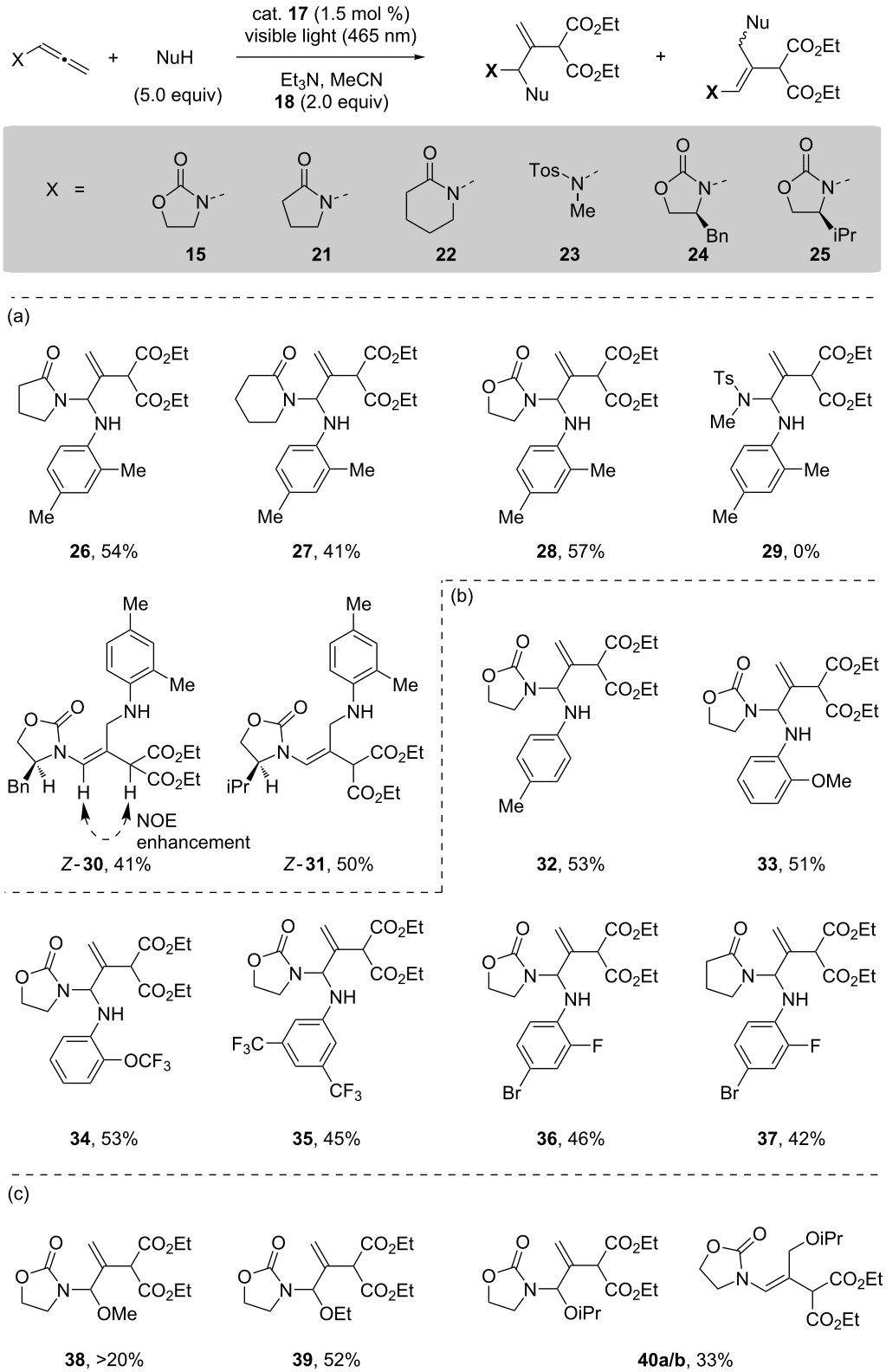

Scheme 4: Reaction scope (a) allenamide; (b) arylamine nucleophile; (c) alcohol nucleophile.

Given our interest in the *N*,*N*'-aminal functionality [50], we also explored variation of the arylamine nucleophile. 2,4-Dimethylaniline, *o*-anisole, 2-trifluoromethoxyaniline and 3,5-ditrifluoromethylaniline were all effective in this transformation, giving their labile *N*,*N*'-allylaminal products (**32** to **35**) in moderate to good isolated yields.

4-Bromo-2-fluoroaniline was also examined as a nucleophile, as we had previously shown this to be an effective aniline platform for developing linezolid analogues, and this delivered two *N*,*N*'-allylaminals **36** and **37**, respectively. Masson had previously explored oxygen nucleophiles in their photoredox-catalyzed addition to enamides [48]. Consequently, the use of excess methanol provided the addition product **38**, resulting from α-addition, in a modest isolated yield. The stability of product **38** was marginal, but an improved stability of the *N*,*O*'-allyl product was observed when ethanol was used as the nucleophile giving product **39** in 52% isolated yield. In contrast, isopropanol gave an inseparable mixture of the α- and γ-addition products, **40a/b** in 33% isolated yield. As with the case for the formation of **19**, all of the starting allenes were consumed in each reaction shown in Scheme 4.

A tentative mechanism for this transformation is described in Scheme 5a. Excitation of the Ir(III) complex **17** provides *Ir(III) that subsequently undergoes reductive quenching by Et_3N, delivering Ir(II) [48]. Single electron transfer from Ir(II) to **18** then generates an electrophilic radical R• together with stoichiometric bromide ion; R• subsequently adds to the β-carbon of the allenamide **15**, providing an α-aminoallyl radical **41**.

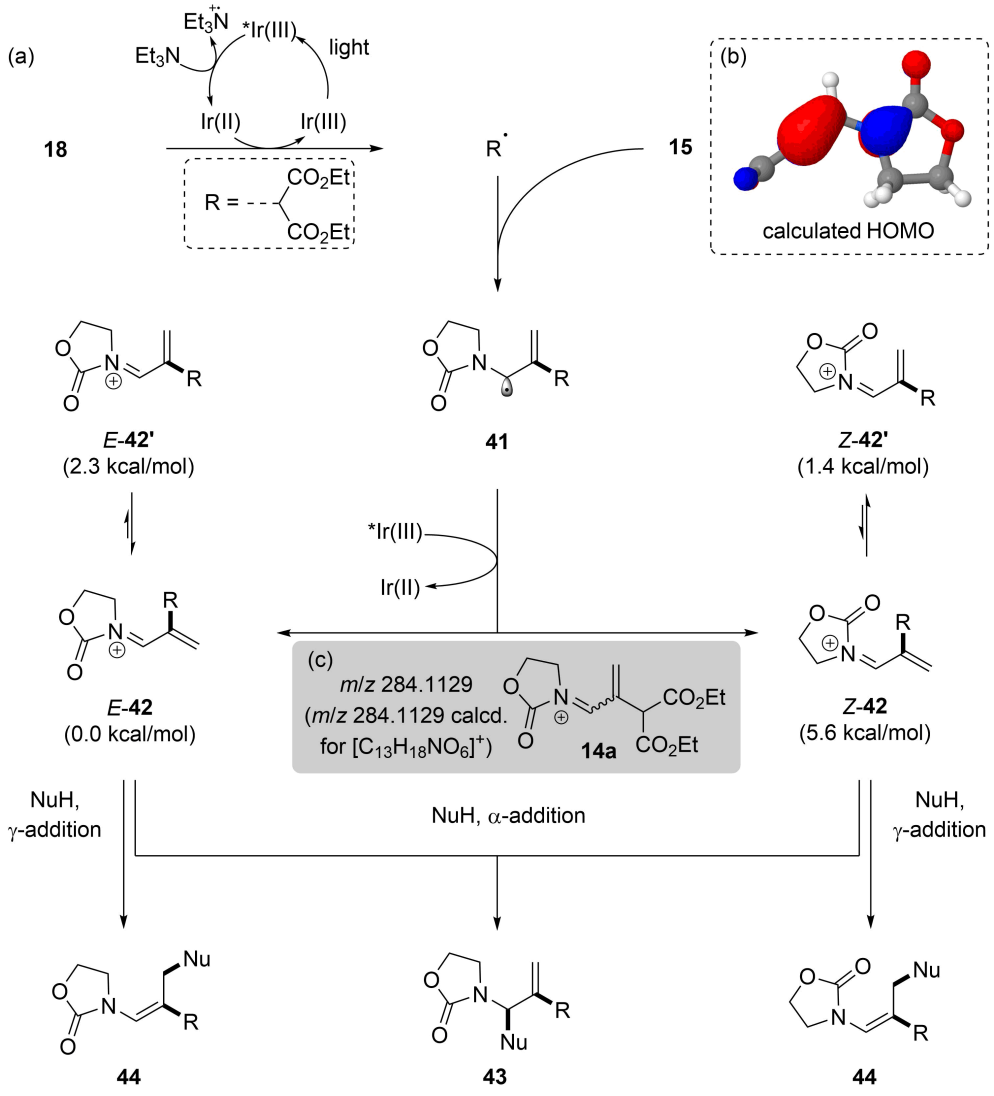

Scheme 5: (a) Tentative mechanism for the photoredox-catalyzed formation of the conjugated *N*-acyliminium intermediate; (b) the calculated HOMO [54] for allenamide **15**; (c) the identification of intermediate **14a** by direct sample loop and flow injection HRESIMS analysis.

To support this hypothesis the calculated HOMO of allenamide **15** is shown in Scheme 5b, signifying the increased nucleophilicity at the β-carbon [54]. Mechanistically, the formation of the key conjugated *N*-acyliminum **14a** from α-aminoallyl radical **41** is analogous to the photoredox initiated addition of radicals to enamides [46,48,49]. Consequently, the formation of **14a** can results from a SET event between the oxidized Ir(III) [55] and the α-aminoallyl radical **41**; a radical propagation pathway through the reduction of **18** was discounted, as the reaction required continuous irradiation.

To further support this mechanistic hypothesis, we used ESIMS to identify the formation of the conjugated *N*-acyliminium **14a**. The addition of **18** to allenamide **15** under the Ir-catalyzed photoredox conditions in the presence of 4-bromoaniline was monitored by direct sample loop and flow injection analysis by HRESIMS [56,57]. After 5 minutes we observed a peak at *m*/*z* 284.1129 that corresponded satisfactorily to the expected iminium complex **14a** (*m*/*z* 284.1129: calcd for $[C_{13}H_{18}NO_6]^+$); this peak persisted at 15, 30, 60 and 120 min time intervals, respectively.

Upon the oxidation of **41** two plausible iminium stereoisomers can be formed, *Z*-**42** and *E*-**42**, respectively, with each of these iminium stereoisomers existing in two further conformers designated *E*-**42'** and *Z*-**42'**. DFT calculations [54] were performed on all four of these proposed structures, where it was observed that *Z*-**42** was approx. 6 kcal/mol higher in energy, relative to the most stable isomer *E*-**42**, which was 1–2 kcal/mol lower in energy than *E*-**42'** and *Z*-**42'**, respectively. It is feasible that both *E*-**42** and *Z*-**42'** undergo nucleophilic addition at the α-position giving the observed *N*,*N'*-allylaminal product **43**. Conversely, addition of a nucleophile at the γ-position of *E*-**42** gives the observed *Z*-enamide **44**; and addition at the γ-position of *Z*-**42'** gives the same observed *Z*-enamide **44** after C–N bond rotation.

Conclusion

In conclusion, in this letter we have demonstrated the first intermolecular addition of an electrophilic radical, generated under photoredox conditions, to an allenamide building block. The addition of the radical occurs at the central carbon of the allene, giving a conjugated *N*-acyliminium intermediate after subsequent oxidation. We have established that the conjugated *N*-acyliminium intermediate can be formed from a broad range of allenamide precursors; additionally, the conjugated *N*-acyliminium intermediate can undergo nucleophilic addition with an arylamine or alcohol nucleophiles at the α- or γ-position, with the regioselectivity of the addition being controlled by steric factors. Significantly, the formation of the key conjugated *N*-acyliminium intermediate using these photoredox conditions can be seen as complementary to the well-developed electrophilic activation modes of allenamides. We are currently examining the full mechanism of this transformation, expanding the scope of substrates that can be used in the radical addition step, and alternative fates for the α-*N*-acyl radical **13** [58-60].

Supporting Information

Supporting Information File 1

Experimental details, analytical (^{1}H NMR, ^{13}C NMR) and ESIMS data.
[https://www.beilstein-journals.org/bjoc/content/supplementary/1860-5397-16-165-S1.pdf]

Funding

We gratefully acknowledge financial support from Loughborough University and the Tertiary Education Trust Fund (TETFund) Abuja, Nigeria (O.K.K.).

ORCID® iDs

Matthew Turner - https://orcid.org/0000-0001-6508-7010
Marc C. Kimber - https://orcid.org/0000-0003-2943-1974

Preprint

A non-peer-reviewed version of this article has been previously published as a preprint https://doi.org/10.26434/chemrxiv.9771986.v1

References

1. Lu, T.; Lu, Z.; Ma, Z.-X.; Zhang, Y.; Hsung, R. P. *Chem. Rev.* **2013,** *113,* 4862–4904. doi:10.1021/cr400015d
2. Mascareñas, J. L.; Varela, I.; López, F. *Acc. Chem. Res.* **2019,** *52,* 465–479. doi:10.1021/acs.accounts.8b00567
3. Praveen, C. *Coord. Chem. Rev.* **2019,** *392,* 1–34. doi:10.1016/j.ccr.2019.04.010
4. Standen, P. E.; Kimber, M. C. *Curr. Opin. Drug Discovery Dev.* **2010,** *13,* 645.
5. Yan, F.; Liang, H.; Ai, B.; Liang, W.; Jiao, L.; Yao, S.; Zhao, P.; Liu, Q.; Dong, Y.; Liu, H. *Org. Biomol. Chem.* **2019,** *17,* 2651–2656. doi:10.1039/c8ob03072c
6. Zhong, X.; Tang, Q.; Zhou, P.; Zhong, Z.; Dong, S.; Liu, X.; Feng, X. *Chem. Commun.* **2018,** *54,* 10511–10514. doi:10.1039/c8cc06416d
7. Ayres, J. N.; Williams, M. T. J.; Tizzard, G. J.; Coles, S. J.; Ling, K. B.; Morrill, L. C. *Org. Lett.* **2018,** *20,* 5282–5285. doi:10.1021/acs.orglett.8b02225
8. De, N.; Song, C. E.; Ryu, D. H.; Yoo, E. J. *Chem. Commun.* **2018,** *54,* 6911–6914. doi:10.1039/c8cc02570c
9. Zheng, W.-F.; Sun, G.-J.; Chen, L.; Kang, Q. *Adv. Synth. Catal.* **2018,** *360,* 1790–1794. doi:10.1002/adsc.201800021
10. Zhang, P.-C.; Han, J.; Zhang, J. *Angew. Chem., Int. Ed.* **2019,** *58,* 11444–11448. doi:10.1002/anie.201904805
11. Pirovano, V.; Brambilla, E.; Rizzato, S.; Abbiati, G.; Bozzi, M.; Rossi, E. *J. Org. Chem.* **2019,** *84,* 5150–5166. doi:10.1021/acs.joc.9b00143

12. Cui, J.; Meng, L.; Chi, X.; Liu, Q.; Zhao, P.; Zhang, D.-p.; Chen, L.; Li, X.; Dong, Y.; Liu, H. *Chem. Commun.* **2019,** *55,* 4355–4358. doi:10.1039/c9cc00797k
13. Banerjee, S.; Senthilkumar, B.; Patil, N. T. *Org. Lett.* **2019,** *21,* 180–184. doi:10.1021/acs.orglett.8b03651
14. An, J.; Lombardi, L.; Grilli, S.; Bandini, M. *Org. Lett.* **2018,** *20,* 7380–7383. doi:10.1021/acs.orglett.8b03018
15. Yang, K.; Bao, X.; Liu, S.; Xu, J.; Qu, J.; Wang, B. *Eur. J. Org. Chem.* **2018,** 6469–6473. doi:10.1002/ejoc.201801039
16. Li, Y.; Luo, G. L.; Li, X. X.; Zhao, Z. G. *New J. Chem.* **2018,** *42,* 16940–16947. doi:10.1039/c8nj03641a
17. Hédouin, J.; Schneider, C.; Gillaizeau, I.; Hoarau, C. *Org. Lett.* **2018,** *20,* 6027–6032. doi:10.1021/acs.orglett.8b02365
18. Yuan, X.; Re He Man, X. J. A. T.; Li, X.-X.; Zhao, Z.-G. *Tetrahedron* **2018,** *74,* 5674–5682. doi:10.1016/j.tet.2018.07.045
19. Yang, B.; Zhai, X.; Feng, S.; Hu, D.; Deng, Y.; Shao, Z. *Org. Lett.* **2019,** *21,* 330–334. doi:10.1021/acs.orglett.8b03934
20. Villar, L.; Uria, U.; Martínez, J. I.; Prieto, L.; Reyes, E.; Carrillo, L.; Vicario, J. L. *Angew. Chem., Int. Ed.* **2017,** *56,* 10535–10538. doi:10.1002/anie.201704804
21. Yang, X.; Toste, F. D. *Chem. Sci.* **2016,** *7,* 2653–2656. doi:10.1039/c5sc04202j
22. Manoni, E.; Gualandi, A.; Mengozzi, L.; Bandini, M.; Cozzi, P. G. *RSC Adv.* **2015,** *5,* 10546–10550. doi:10.1039/c4ra14942d
23. Li, H.-H.; Li, X.-X.; Zhao, Z.-G.; Lin, C.-B.; Ma, T.; Sun, C.-Y.; Yang, B.-W.; Fu, X.-L. *Tetrahedron Lett.* **2016,** *57,* 4640–4644. doi:10.1016/j.tetlet.2016.09.020
24. Li, H.; Li, X.; Zhao, Z.; Ma, T.; Sun, C.; Yang, B. *Chem. Commun.* **2016,** *52,* 10167–10170. doi:10.1039/c6cc05046h
25. Michihiko, N.; Hiroshi, O.; Masanori, W.; Kumi, O.; Osamu, N. *Tetrahedron* **1996,** *52,* 6581–6590. doi:10.1016/0040-4020(96)00314-6
26. Zhu, Y.; Yin, G.; Hong, D.; Lu, P.; Wang, Y. *Org. Lett.* **2011,** *13,* 1024–1027. doi:10.1021/ol103074d
27. Zhu, Y.; Yin, G.; Sun, L.; Lu, P.; Wang, Y. *Tetrahedron* **2012,** *68,* 10194–10200. doi:10.1016/j.tet.2012.09.092
28. Hyland, C. J. T.; Hegedus, L. S. *J. Org. Chem.* **2006,** *71,* 8658–8660. doi:10.1021/jo061340r
29. Rameshkumar, C.; Xiong, H.; Tracey, M. R.; Berry, C. R.; Yao, L. J.; Hsung, R. P. *J. Org. Chem.* **2002,** *67,* 1339–1345. doi:10.1021/jo011048d
30. Xiong, H.; Hsung, R. P.; Berry, C. R.; Rameshkumar, C. *J. Am. Chem. Soc.* **2001,** *123,* 7174–7175. doi:10.1021/ja0108638
31. Krenske, E. H.; Houk, K. N.; Lohse, A. G.; Antoline, J. E.; Hsung, R. P. *Chem. Sci.* **2010,** *1,* 387–392. doi:10.1039/c0sc00280a
32. Wang, Y.; Zhang, P.; Di, X.; Dai, Q.; Zhang, Z.-M.; Zhang, J. *Angew. Chem., Int. Ed.* **2017,** *56,* 15905–15909. doi:10.1002/anie.201709595
33. Fernández-Casado, J.; Nelson, R.; Mascareñas, J. L.; López, F. *Chem. Commun.* **2016,** *52,* 2909–2912. doi:10.1039/c5cc09533f
34. Wang, Y.; Zhang, P.; Liu, Y.; Xia, F.; Zhang, J. *Chem. Sci.* **2015,** *6,* 5564–5570. doi:10.1039/c5sc01827g
35. Rocchigiani, L.; Jia, M.; Bandini, M.; Macchioni, A. *ACS Catal.* **2015,** *5,* 3911–3915. doi:10.1021/acscatal.5b00502
36. Marcote, D. C.; Varela, I.; Fernández-Casado, J.; Mascareñas, J. L.; López, F. *J. Am. Chem. Soc.* **2018,** *140,* 16821–16833. doi:10.1021/jacs.8b10388
37. Slater, N. H.; Brown, N. J.; Elsegood, M. R. J.; Kimber, M. C. *Org. Lett.* **2014,** *16,* 4606–4609. doi:10.1021/ol502178v
38. Singh, S.; Elsegood, M. R. J.; Kimber, M. C. *Synlett* **2012,** *23,* 565–568. doi:10.1055/s-0031-1290335
39. Hill, A. W.; Elsegood, M. R. J.; Kimber, M. C. *J. Org. Chem.* **2010,** *75,* 5406–5409. doi:10.1021/jo101035n
40. Kimber, M. C. *Org. Lett.* **2010,** *12,* 1128–1131. doi:10.1021/ol1001494
41. Liu, L.; Ward, R. M.; Schomaker, J. M. *Chem. Rev.* **2019,** *119,* 12422–12490. doi:10.1021/acs.chemrev.9b00312
42. Tomita, R.; Koike, T.; Akita, M. *Chem. Commun.* **2017,** *53,* 4681–4684. doi:10.1039/c7cc01759f
43. Lu, N.; Zhang, Z.; Ma, N.; Wu, C.; Zhang, G.; Liu, Q.; Liu, T. *Org. Lett.* **2018,** *20,* 4318–4322. doi:10.1021/acs.orglett.8b01765
44. Dai, X.; Mao, R.; Guan, B.; Xu, X.; Li, X. *RSC Adv.* **2015,** *5,* 55290–55294. doi:10.1039/c5ra10491b
45. Shen, L.; Hsung, R. P. *Org. Lett.* **2005,** *7,* 775–778. doi:10.1021/ol047572z
46. Carboni, A.; Dagousset, G.; Magnier, E.; Masson, G. *Org. Lett.* **2014,** *16,* 1240–1243. doi:10.1021/ol500374e
47. Courant, T.; Masson, G. *J. Org. Chem.* **2016,** *81,* 6945–6952. doi:10.1021/acs.joc.6b01058
48. Courant, T.; Masson, G. *Chem. – Eur. J.* **2012,** *18,* 423–427. doi:10.1002/chem.201103062
49. Dagousset, G.; Carboni, A.; Magnier, E.; Masson, G. *Org. Lett.* **2014,** *16,* 4340–4343. doi:10.1021/ol5021477
50. Koleoso, O. K.; Elsegood, M. R. J.; Teat, S. J.; Kimber, M. C. *Org. Lett.* **2018,** *20,* 1003–1006. doi:10.1021/acs.orglett.7b03946
51. Given the instability of these reaction products, this and all subsequent reactions were performed on a 1.00 mmol scale.
52. Bousfield, T. W.; Kimber, M. C. *Tetrahedron Lett.* **2015,** *56,* 350–352. doi:10.1016/j.tetlet.2014.11.093
53. Wei, L.-L.; Xiong, H.; Douglas, C. J.; Hsung, R. P. *Tetrahedron Lett.* **1999,** *40,* 6903–6907. doi:10.1016/s0040-4039(99)01354-4
54. DFT geometry optimisations calculations were performed at the PBEh-3c level of theory; please see Supporting Information File 1.
55. Slinker, J. D.; Gorodetsky, A. A.; Lowry, M. S.; Wang, J.; Parker, S.; Rohl, R.; Bernhard, S.; Malliaras, G. G. *J. Am. Chem. Soc.* **2004,** *126,* 2763–2767. doi:10.1021/ja0345221
56. Al-Jawaheri, Y.; Turner, M.; Kimber, M. C. *Synthesis* **2018,** *50,* 2329–2336. doi:10.1055/s-0036-1591580
57. Qian, R.; Guo, H.; Liao, Y.; Guo, Y.; Ma, S. *Angew. Chem., Int. Ed.* **2005,** *44,* 4771–4774. doi:10.1002/anie.200463101
58. Trowbridge, A.; Reich, D.; Gaunt, M. J. *Nature* **2018,** *561,* 522–527. doi:10.1038/s41586-018-0537-9
59. Ryder, A. S. H.; Cunningham, W. B.; Ballantyne, G.; Mules, T.; Kinsella, A. G.; Turner-Dore, J.; Alder, C. M.; Edwards, L. J.; McKay, B. S. J.; Grayson, M. N.; Cresswell, A. J. *Angew. Chem., Int. Ed.* **2020,** in press. doi:10.1002/anie.202005294
60. Trowbridge, A.; Walton, S. M.; Gaunt, M. J. *Chem. Rev.* **2020,** *120,* 2613–2692. doi:10.1021/acs.chemrev.9b00462

License and Terms

This is an Open Access article under the terms of the Creative Commons Attribution License (http://creativecommons.org/licenses/by/4.0). Please note that the reuse, redistribution and reproduction in particular requires that the authors and source are credited.

The license is subject to the *Beilstein Journal of Organic Chemistry* terms and conditions: (https://www.beilstein-journals.org/bjoc)

The definitive version of this article is the electronic one which can be found at: doi:10.3762/bjoc.16.165

BEILSTEIN JOURNAL OF ORGANIC CHEMISTRY

Recent developments in enantioselective photocatalysis

Callum Prentice[1], James Morrisson[2], Andrew D. Smith[*1] and Eli Zysman-Colman[*1]

Review

Open Access

Address:
[1]Organic Semiconductor Centre, EaStCHEM, School of Chemistry, University of St Andrews, North Haugh, Fife, Scotland, KY16 9ST, United Kingdom and [2]Pharmaceutical Sciences, IMED Biotech Unit, AstraZeneca, Macclesfield SK102NA, United Kingdom

Email:
Andrew D. Smith[*] - ads10@st-andrews.ac.uk; Eli Zysman-Colman[*] - eli_journals@zysman-colman.com

* Corresponding author

Keywords:
enantioenrichment; enantionselective catalysis; enantioselective photocatalysis; photocatalysis; photochemistry

Beilstein J. Org. Chem. **2020,** *16,* 2363–2441.
https://doi.org/10.3762/bjoc.16.197

Received: 20 July 2020
Accepted: 09 September 2020
Published: 29 September 2020

This article is part of the thematic issue "Advances in photoredox catalysis".

Guest Editor: T. Noël

© 2020 Prentice et al.; licensee Beilstein-Institut.
License and terms: see end of document.

Abstract

Enantioselective photocatalysis has rapidly grown into a powerful tool for synthetic chemists. This review describes the various strategies for creating enantioenriched products through merging enantioselective catalysis and photocatalysis, with a focus on the most recent developments and a particular interest in the proposed mechanisms for each. With the aim of understanding the scope of each strategy, to help guide and inspire further innovation in this field.

Introduction

Enantioselective catalysis has become a central focus for organic synthetic chemistry, particularly since the Nobel prize was awarded to Sharpless, Knowles, and Noyori for their pioneering work in the field. In the last 15 years, photocatalysis has become a transformative synthetic strategy, including in enantioselective synthesis. From the pioneering work by MacMillan [1] and Bach [2], enantioselective photocatalysis has grown into a well-established field of its own. A large proportion of photocatalysis focuses on photoredox catalysis, which involves single electron transfer (SET) steps photoinitiated using visible light as the energy source, often leading to the generation of radicals and subsequent reaction of these radicals with the ground-state substrates [3]. Energy transfer catalysis is another significant branch of photocatalysis, in which photocatalysts (PCs) generate excited state substrates that can then undergo reactions that would be impossible in the ground state [4]. A challenge for enantioselective catalysis is stifling the racemic background reaction, which is generally achieved through a lower activation energy for the catalysed process relative to the non-catalysed. However, this is particularly difficult for enantioselective photocatalysis as the intermediates generated are highly reactive and activation energies are typically already low [5]. Even so, there are now a large number of reactions that have been developed that address these issues, with many different strategies and types of photocatalysts employed.

This review aims to cover the seminal work within enantioselective photocatalysis but with a focus on the most recent devel-

opments. There have been a number of reviews on or closely related to this topic, so this review will not contain an exhaustive list of all enantioselective photocatalytic reactions; however, this review does aim to cover the different strategies that have been developed [5-16]. There is a subset of reactions that achieve asymmetry via a stepwise photochemical process followed by a separate enantioselective catalysis step that will not be covered in this review [17-19]. Examples using cage complexes or other supramolecular reagents also lie outside the scope of this review. As all enantioselective photocatalysis requires a secondary mode of catalysis to induce enantioselectivity, the review will be organized according to these strategies. Mechanistic understanding is vital to furthering development of any field of organic chemistry, so the mechanisms proposed by the authors are included for many examples, although the level of mechanistic investigation that accompanies them is varied. The nature of the light source and its wavelength (λ_{exc}) can have significant effects on the outcome of the reaction; therefore, this information is indicated in the reaction schemes when it is disclosed by the authors. As with many reviews on enantioselective reactions, the percentage chemical yield and enantioselectivity (all values converted to nearest per cent enantiomeric ratio (er) for clarity) will be the common data for comparison; however, where possible the quantum yields of the photochemical reactions will also be provided as this latter metric provides the most accurate quantifier of the efficiency of a photochemical process. The quantum yield (Φ) of a reaction is often used as a mechanistic tool to probe whether a chain reaction is active ($\Phi > 1$) or not ($\Phi < 1$), although it should be noted that a reaction with $\Phi < 1$ could also still include a radical chain process with an inefficient initiation step (i.e., $\Phi_{initiation} << 1$) (Equation 1). A less common use of quantum yields by organic synthetic chemists is as a measure of how efficiently the reaction uses the light source. Considering photocatalysis is often purported as a green chemistry because it uses light, a more efficient use of light would result in a greener reaction.

$$\text{a)}\quad \Phi = \frac{\text{product formed}}{\text{photons absorbed}} \qquad (1)$$
$$\text{b)}\quad \Phi = \Phi_{initiation} \times \text{chain lenght}$$

where (a) is the definition of quantum yield and (b) is the quantum yield of a radical chain reaction.

Review

Enantioselective photocatalysis

Amine catalysis

Much of the history of amine catalysis used in photochemical reactions can be found in a review published by Zou and Bach [12], so the following are selected examples and recent developments of the field. Amine catalysis can be broadly split into enamine and iminium catalysis, both of which have been utilised in combination with photocatalysis. The first example of enamine catalysis in combination with photoredox catalysis was reported by Nicewicz and MacMillan [1] for the alpha alkylation of aldehydes **1** with various alkyl bromides bearing an electron-withdrawing substituent **2**, which while seemingly trivial, was not possible with enamine catalysis alone (Scheme 1). The proposed mechanism suggests a closed catalytic cycle is in operation; however, subsequent investigations by Yoon [20] found this reaction has a quantum yield >1 (Φ = 18), which signifies a chain propagation process is dominant. Therefore, according to Yoon's proposed mechanism, the reaction proceeds with the condensation of **1** with amine catalyst **3** to give enamine intermediate **4**. The initiation step is proposed to be a reductive quench of the photocatalyst using **4** as a sacrificial reductant to give $[Ru]^{\bullet-}$, which can then reduce **2** to give electrophilic radical **2**$^{\bullet}$. Addition of **2**$^{\bullet}$ to another molecule of **4** generates α-amino radical **5**$^{\bullet}$, which (depending on the EWG) can either reduce another molecule of **2** via a SET process or via an atom transfer (AT) process and propagate the chain reaction [21]. The SET route directly generates **2**$^{\bullet}$ and iminium ion intermediate **6**, but the AT goes through alkyl bromide **7**, before generating **6**. Hydrolysis of **6** furnishes the desired α-functionalised aldehydes **8** in excellent yields and enantioselectivities (12 examples, up to >99:1 er). Further work on this system expanded the scope to ketones [22] instead of aldehydes and varied the electron-withdrawing group to include fluorinated alkyl groups [23], electron-deficient arenes [24], and nitriles [25]. Additionally, Cozzi recently applied a novel aluminium-based photocatalyst **9** to this reaction, as an earth-abundant metal alternative albeit with slightly reduced enantioselectivities (8 examples, up to 96:4 er) [26]. Interestingly, as with some other photocatalysts used for this reaction, it is proposed the excited state of **9** is sufficiently reducing to initiate the chain mechanism through an oxidative quench.

Moving away from electronically activated halides, MacMillan et al. investigated a tricatalytic system, utilising enamine, photoredox, and HAT (hydrogen atom transfer) catalysis to allow the use of alkenes as the alkylating agent either in an intermolecular process using aldehydes **10** and alkenes **11** or intramolecularly using aldehydes **12** (Scheme 2) [27]. The proposed mechanism again proceeds via the formation of an enamine intermediate **13** that then reductively quenches the photocatalyst to form enaminyl radical **13**$^{\bullet+}$. However, in this reaction **13**$^{\bullet+}$ can then add to the alkene to give an alkyl radical **14**$^{\bullet+}$, followed by hydrogen atom abstraction from the thiol, acting as a HAT catalyst, to give iminium ion intermediate **15**. Hydrolysis of **15** generates the desired α-functionalised aldehydes **16** (14 examples up to 97:3 er) or cyclization products **17**

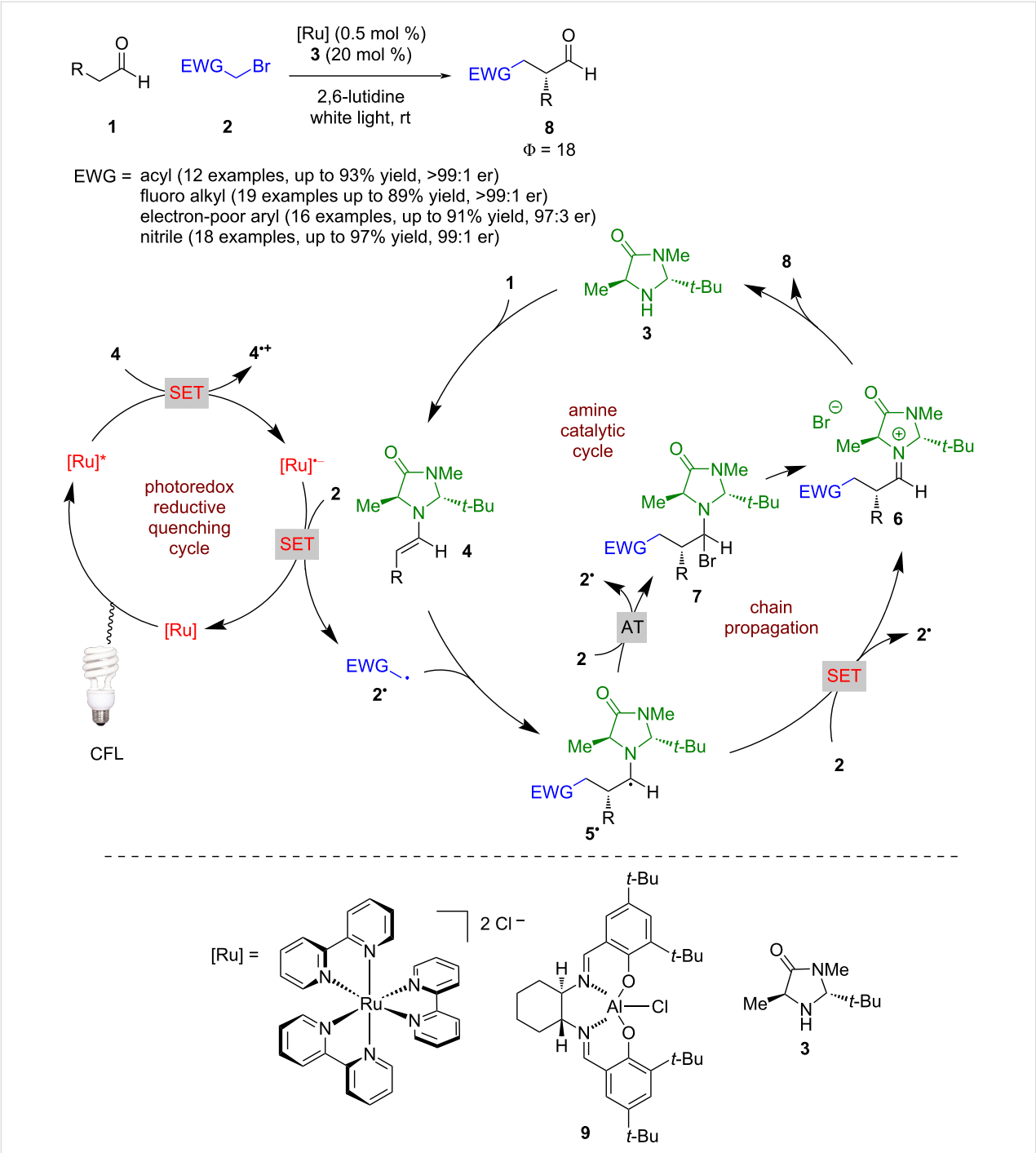

Scheme 1: Amine/photoredox-catalysed α-alkylation of aldehydes with alkyl bromides bearing electron-withdrawing groups.

(15 examples up to 98:2 er) in excellent yields and enantioselectivities. A SET process between thiyl radical **18**• and $[Ir]^{•-}$ is proposed to complete both catalytic cycles.

Another tricatalytic system developed by Tung et al. merged photoredox, cobalt, and amine catalysis towards the synthesis of α-functionalised ketones **21** from tetrahydroisoquinolines (THIQs) **22** and ketones **23** (Scheme 3) [28]. The proposed mechanism involves an oxidative quenching cycle using the $[Co^{III}]$ catalyst to generate $[Co^{II}]$ and $[Ru]^{•+}$, with the latter oxidising **22** to give radical cation **22**$^{•+}$ and turn over the photocatalytic cycle. The radical cation **22**$^{•+}$ is then proposed to participate in a two-step electron and proton exchange process with $[Co^{II}]$ to give $[H–Co^{III}]$ and iminium ion **24**, likely via a

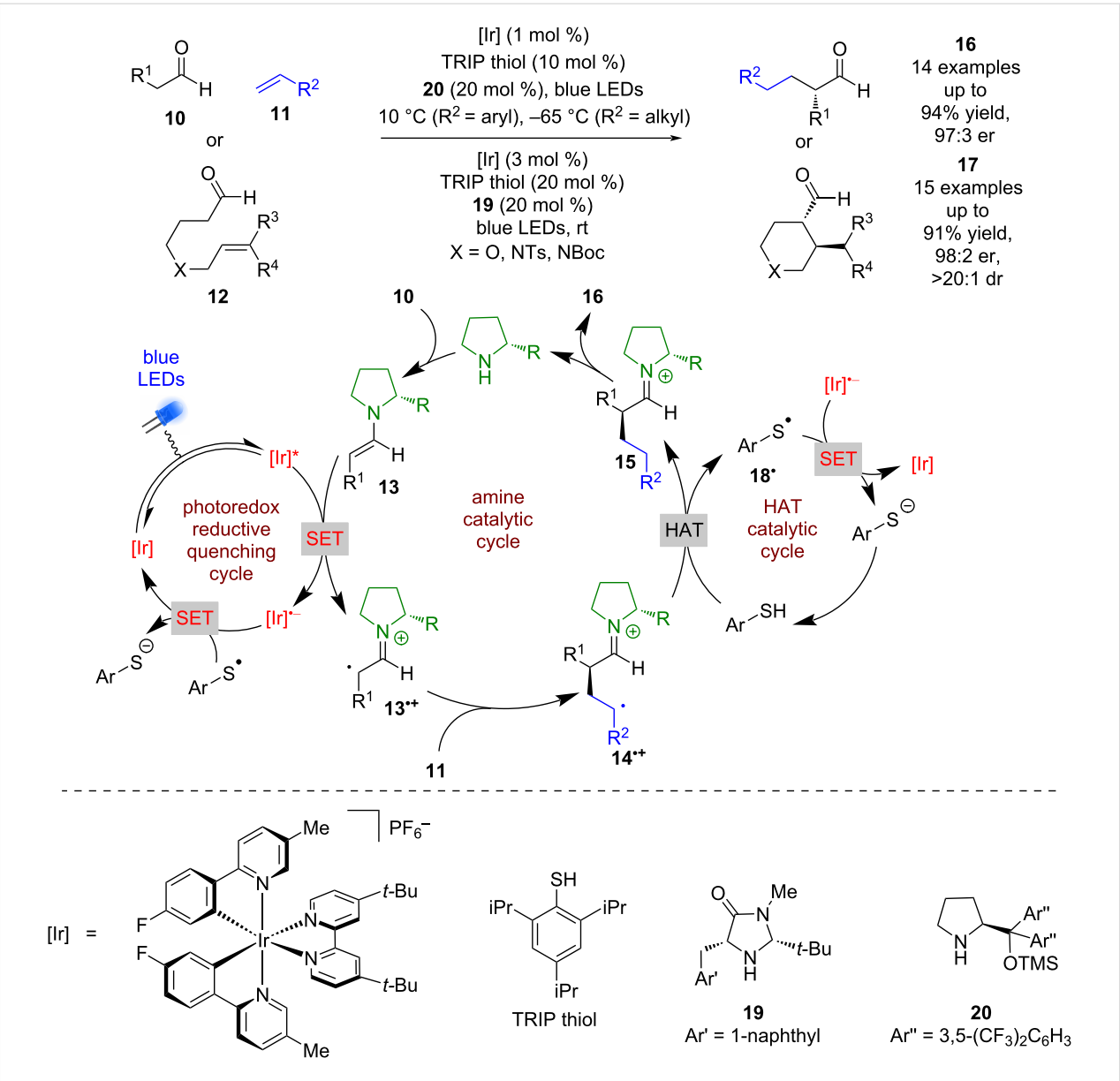

Scheme 2: Amine/HAT/photoredox-catalysed α-functionalisation of aldehydes using alkenes.

[Co^{I}] intermediate. [H–Co^{III}] can then reduce 3-nitrobenzoic acid to the corresponding aniline **25** to turn over the cobalt cycle. Simultaneously, **23** condenses with the chiral primary amine catalyst **26** to give enamine intermediate **27**, which can be intercepted by **24** to generate imine intermediate **28**, which is finally hydrolysed to turn over the amine catalytic cycle and releases the desired products **21** in excellent yields and enantioselectivities (35 examples, up to >99:1 er). Notably, if **23** is acyclic the product enantioselectivities are poorer (2 examples up to 87:13 er).

A similar reaction was later reported by Guan et al. using ketones **29** with 2-substituted indoles **30** as a precursor to imine **31**, for the synthesis of indolin-3-ones **32** in good yields and excellent enantioselectivities (21 examples, up to >99:1 er) (Scheme 4a) [29]. Zhang et al. recently added to the scope of this family of reactions with their use of aldehydes/ketones **33** with glycine derivatives **34** to synthesise the corresponding products **35** in good yields and excellent enantioselectivities (35 examples, up to 99:1 er) (Scheme 4b) [30].

The previous examples of enamine/photoredox catalysis have all required two or more separate catalysts. Currently, three different approaches have been developed that use a single catalyst. Alemán et al.'s approach combines the two catalytic motifs into a single bifunctional catalyst **38**, using thioxanthone as the

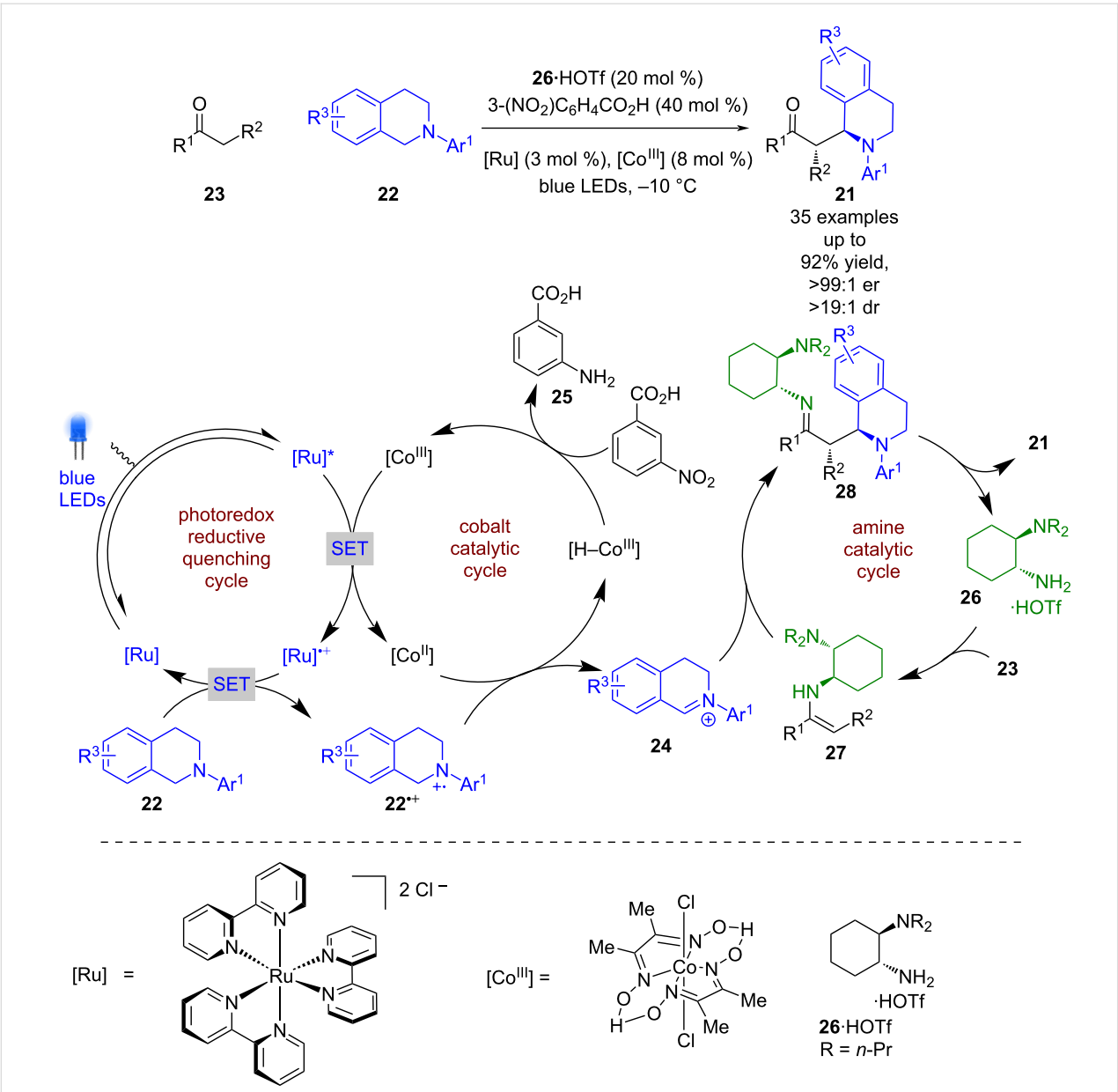

Scheme 3: Amine/cobalt/photoredox-catalysed α-functionalisation of ketones and THIQs.

chromophore (Scheme 5) [31]. The catalyst **38** was then applied to known reactions such as the α-functionalization of aldehydes and gave excellent yields and enantioselectivities (13 examples, up to >99:1 er).

Another approach that used a single catalyst was developed by Melchiorre et al., where they discovered that a conventional photocatalyst was not necessary to achieve similar transformations (Scheme 6) [32,33]. When an alkylating agent containing an aryl ring **40** (e.g., phenacyl/benzyl bromides) is used, the enamine intermediate **41** forms a coloured electron-donor acceptor (EDA) complex that can absorb visible light via an intermolecular charge-transfer state (EDA route) [14,34]. Mechanistic investigations [21] showed that after excitation of the EDA complex, the electrophilic radical **40**$^{\bullet}$ that is formed enters the same chain propagation cycle as in Scheme 1, whereas the radical cation **41**$^{\bullet+}$ is proposed to be unstable and decomposes. The third approach, also developed by Melchiorre et al., was based on their observation of similar reactivity when using bromomalonates **42** as substrates (direct excitation route) [35]. As no aryl ring is present, no EDA complex is formed, and thus direct excitation of the photoactive enamine intermediate affords an excited state enamine **41*** that can reduce **42** to initiate the chain reaction that produces the desired products **43** and **44** in

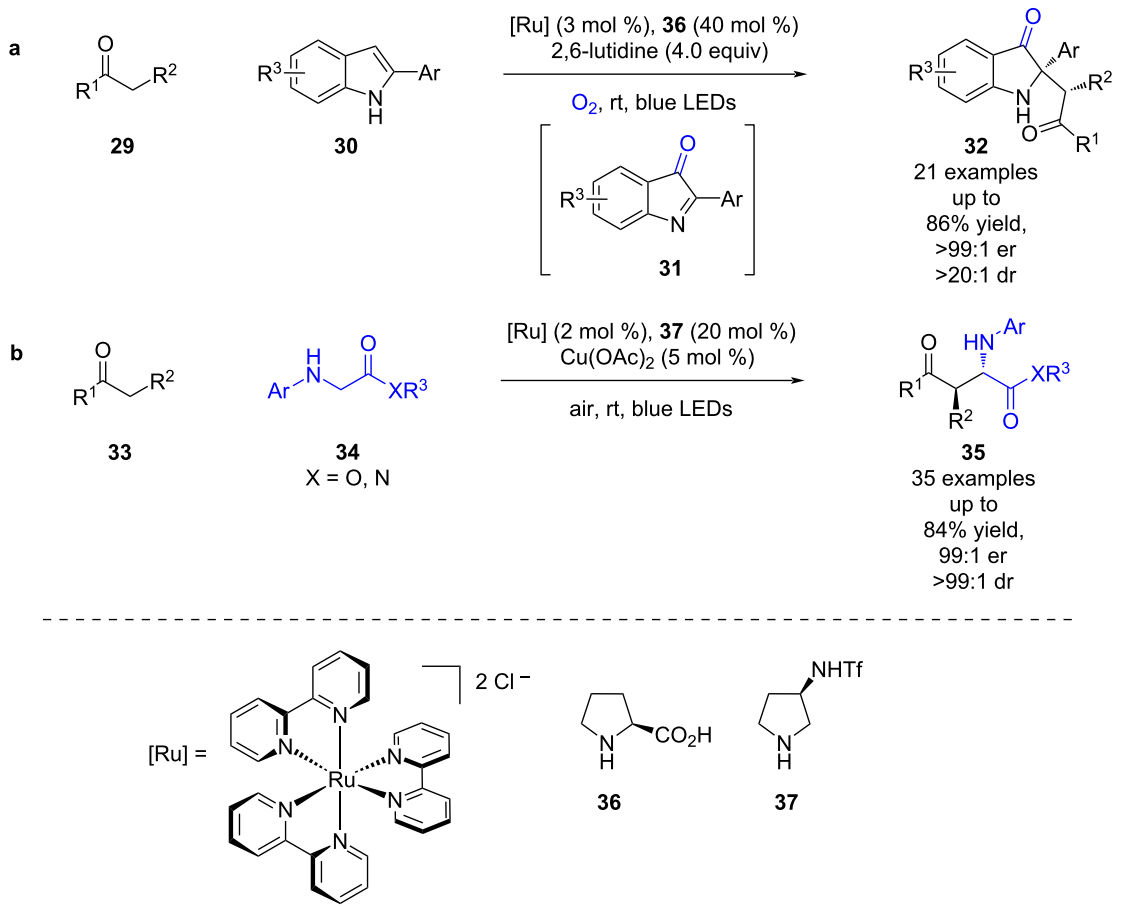

Scheme 4: Amine/photoredox-catalysed α-functionalisation of aldehydes or ketones with imines. (a) Using ketones with 2-substituted indoles. (b) Using ketones or aldehydes with glycine derivatives.

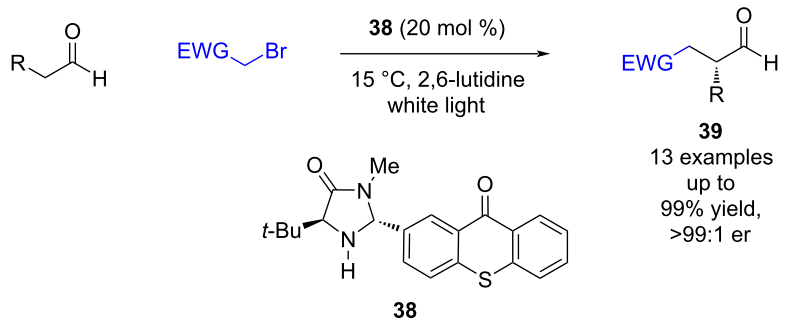

Scheme 5: Bifunctional amine/photoredox-catalysed enantioselective α-functionalisation of aldehydes.

excellent yields and enantioselectivities (15 examples, up to 97:3 er and 12 examples, up to 97:3 er, respectively). Subsequent progress using this methodology expanded the scope to the use of α-iodo sulfones **45**, which is proposed to proceed via the excited-state enamine [36].

While there is an abundance of known photoredox reactions that generate iminium ions catalytically either as a side product [37], or for further transformations [38], the use of iminium ions generated by chiral amines in combination with photoredox catalysts has been less explored. The first example was de-

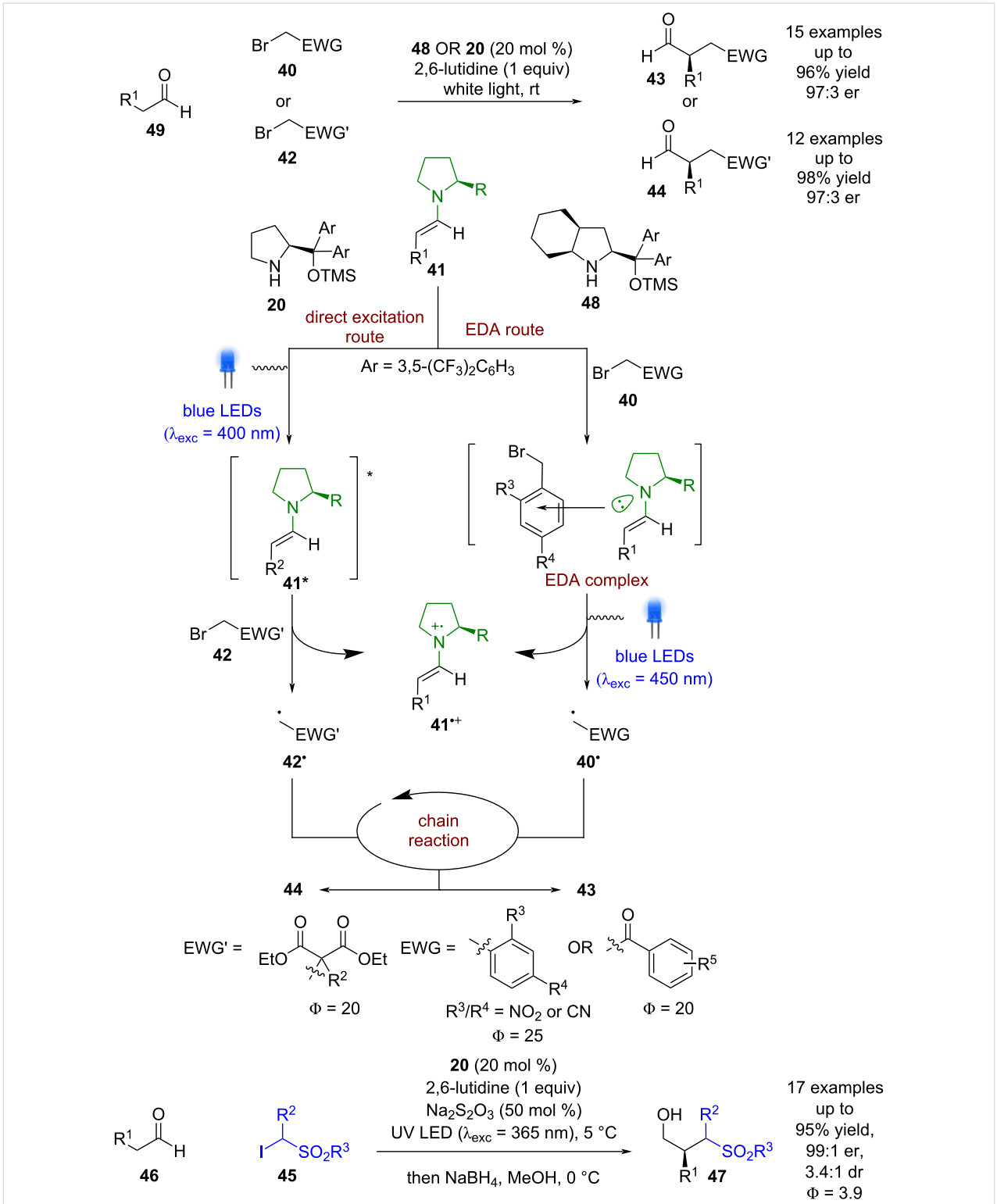

Scheme 6: Bifunctional amine/photoredox-catalysed α-functionalisation of aldehydes using amine catalysts via EDA complexes and direct excitation of intermediates.

veloped by Melchiorre et al. using a unique secondary amine catalyst containing a carbazole group **49** in combination with either tetrabutylammonium decatungstate (TBADT = [W]) or an iridium-based photocatalyst (Scheme 7a) [39]. The proposed mechanism begins with the condensation of **49** with enone **50** to form the iminium ion intermediate **51**. Concomitantly, the

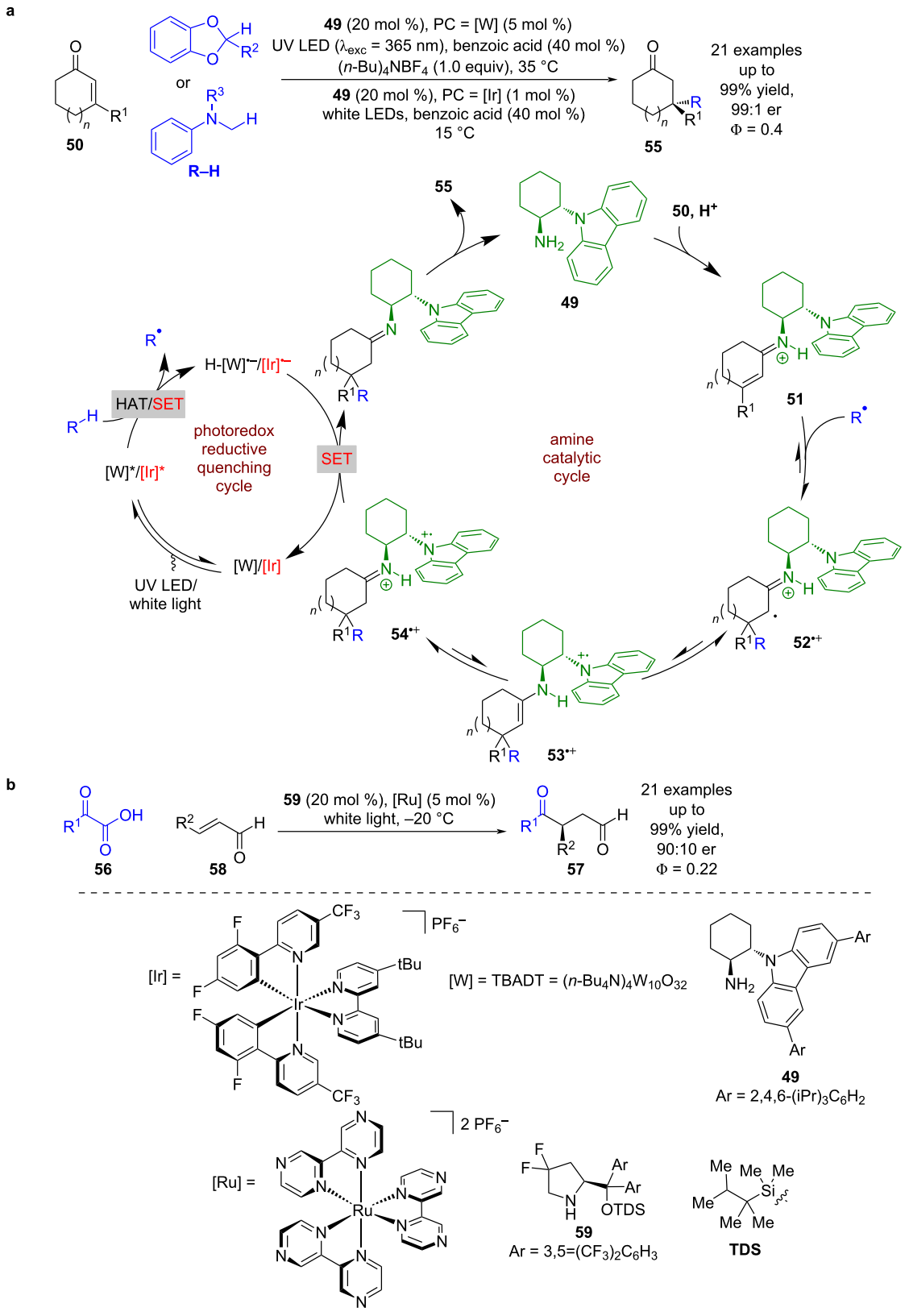

Scheme 7: Amine/photoredox-catalysed RCA of iminium ion intermediates. (a) Synthesis of quaternary stereocentres using benzodioxole derivatives or tertiary amines. (b) Synthesis of 1,4-dicarbonyls using carboxylic acids.

excited-state photocatalyst generates an alkyl radical R• from R–H, either through HAT ([W] with a benzodioxole derivative) or SET ([Ir] with a tertiary amine). This radical then adds to the β-position of the iminium ion generating an unstable iminyl radical **52**•+ that is quickly quenched by the nearby carbazole to form a more stable carbazole centred radical **53**•+. Rapid tautomerisation to imine **54**•+ precludes the undesired back electron transfer. Single electron reduction of **54**•+ by PC•− and hydrolysis provides the radical conjugate addition (RCA) products **55** with a quaternary stereocentre in excellent yields and enantioselectivities (21 examples, up to 99:1 er). The quantum yield was measured to be <1 (Φ = 0.4) for the iridium-catalysed reaction, suggesting that a radical chain process is not dominant. Subsequent investigations by Yu expanded the scope to acyl radicals generated from carboxylic acids **56**, affording enantioenriched 1,4-carbonyls **57** in excellent yields and good enantioselectivities (21 examples, up to 90:10 er) (Scheme 7b) [40]. The quantum yield was also measured to be <1 (Φ = 0.22), so a chain mechanism is likewise unlikely.

Interestingly, Melchiorre later found that with α-amino silanes **60**, no photocatalyst was required (Scheme 8) [41]. This was proposed to be due to the formation of an intramolecular EDA complex, which upon excitation can form cation **61**+ that can subsequently oxidise **60** to give a nucleophilic radical R• that enters a similar RCA cycle as for Scheme 7. However, in the absence of an external photocatalyst, radical cation intermediate **62**•+ is reduced by another molecule of **60**, thus propagating a radical chain mechanism that leads to the formation of ketones **63** in good yields and excellent enantioselectivities

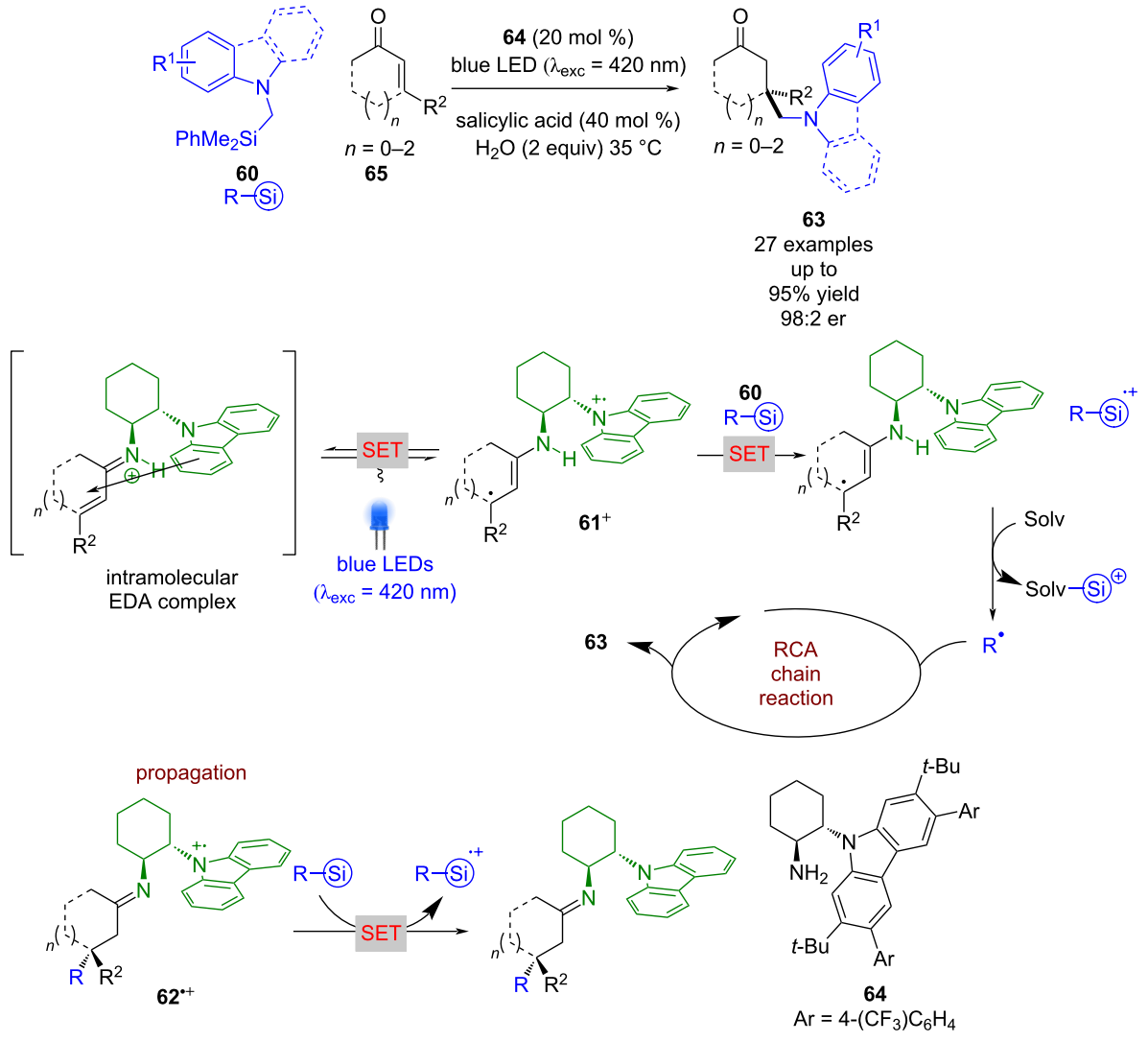

Scheme 8: Bifunctional amine/photoredox-catalysed RCA of enones in a radical chain reaction initiated by an intramolecular EDA complex.

(27 examples, up to 98:2 er). The authors were unable to measure the quantum yield in this case due to difficulties with the high-power LED that is typically required.

As with the enamine intermediates, Melchiorre et al. also demonstrated that iminium ions **66** can be excited directly without formation of an EDA complex (Scheme 9a) [42]. The

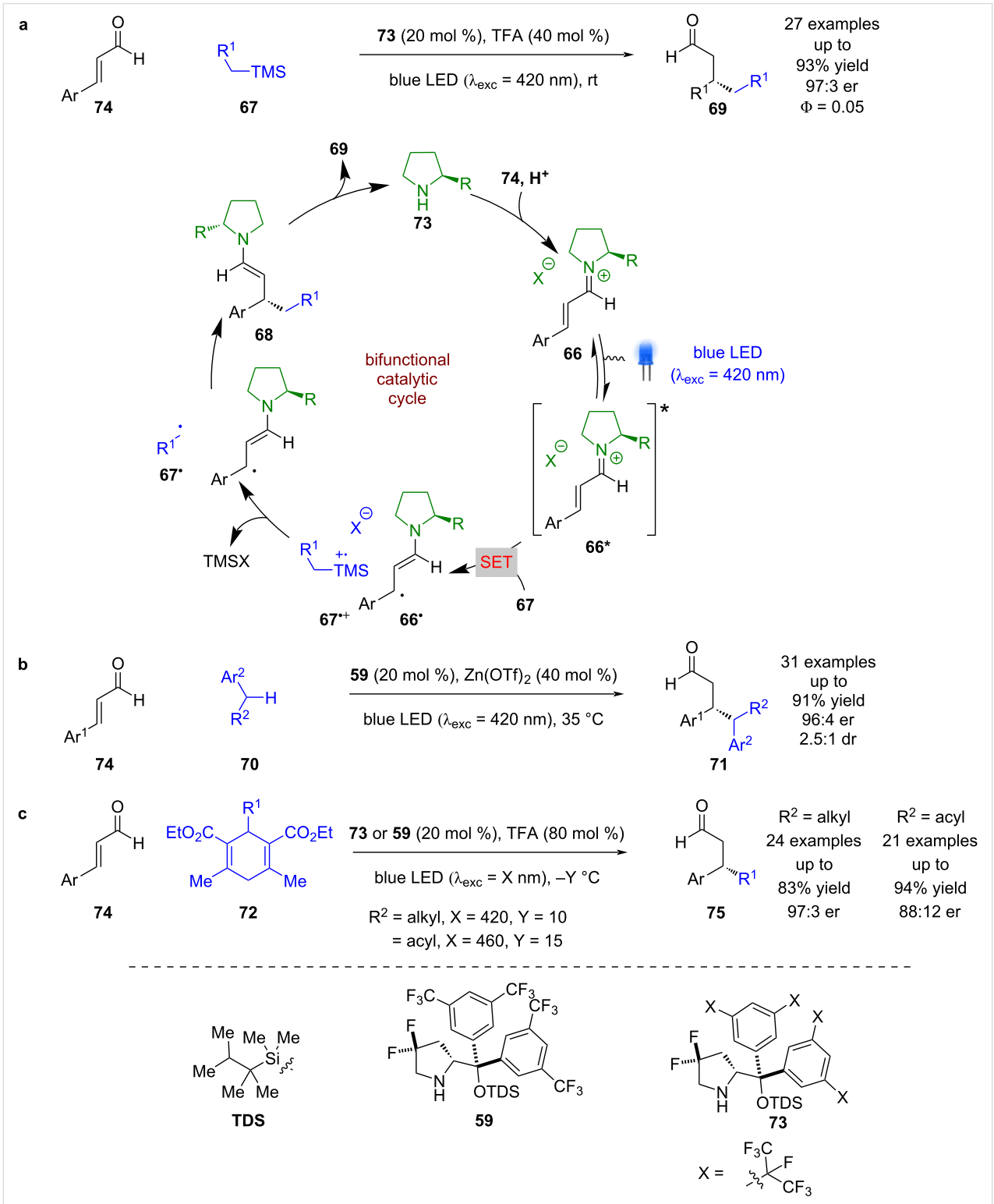

Scheme 9: Bifunctional amine/photoredox-catalysed RCA reactions of iminium ions with different radical precursors. (a) Silanes. (b) Toluene derivatives. (c) Alkyl and acyl DHP derivatives.

excited state iminium ion **66*** can oxidise silanes **67** via a SET process to give radical cation **67**$^{\bullet+}$ and alkyl radical **66**$^{\bullet}$. Loss of the TMS group generates alkyl radicals **67**$^{\bullet}$ that can couple with **66**$^{\bullet}$ enantioselectively to give enamine intermediate **68**, which after hydrolysis completes the catalytic cycle and releases the desired RCA products **69** in good yields and enantioselectivities (27 examples, up to 97:3 er). The quantum yield was determined to be <1 (Φ = 0.05) so a chain reaction is unlikely to be dominant. This reactivity was later extended to the use of toluene derivatives **70** to generate the corresponding RCA products **71** in good yields and enantioselectivities (31 examples, up to 96:4 er) (Scheme 9b) [43]. Melchiorre et al. also discovered that dihydropyridine (DHP) derivatives **72** could act as efficient radical precursors in this system, allowing for both alkyl [44] and acyl [45] RCA reactions. In the case of acyl DHPs, they propose that direct excitation of the DHP leads to radical generation rather than the iminium intermediate (Scheme 9c).

The same system was used for the radical cascade reaction between carboxylic acid/alcohol **76** and enal **77** (Scheme 10a) [46]. Analogously to the mechanism outlined in Scheme 9, it was proposed that formation of excited state iminium ion **66*** is used to oxidise **76** to give radical cation **76**$^{\bullet+}$ and alkyl radical **66**$^{\bullet}$. Nucleophilic addition from the carboxylic acid or alcohol gives neutral radical **76**$^{\bullet}$, which couples enantioselectively with **66**$^{\bullet}$ to give enamine intermediate **78**. Subsequent condensation releases the photocatalyst and the desired products **79** in good yields and excellent enantioselectivities (16 examples, up to 99:1 er). Recently, this process was extended to allenes **80** to give complex bicyclic products **81** in moderate yields and good enantioselectivities (20 examples, up to 92:8 er) (Scheme 9b) [47].

The Bach group recently developed an enantioselective synthesis of cyclobutane **82** from enal **83** and diene **84** (Scheme 11a) [48]. Most of the examples proceed via a stepwise approach with preformation of the corresponding iminium ion **85**. The only catalytic example achieves the same transformation by generating **85** in situ but has reduced yields and enantioselectivities (82:18 er vs 92:8 er for stepwise). Alemán et al. reported that a similar reaction could proceed catalytically and with a broad scope using amine catalyst **86** with enones **87** and alkenes **88** without the need for an external photocatalyst (Scheme 11b) [49]. The mechanism proposed by Alemán begins with the condensation of **86** with **87** to generate iminium ion **89**, which has a suitably low energy charge transfer state that can be photoexcited to generate singlet intermediate **89***. Subsequent enantioselective photocycloaddition with **88** via diradical **90** gives iminium ion intermediate **91**, which after hydrolysis affords the desired cyclobutane products **92** in excellent yields and good enantioselectivities (17 examples, up to 91:9 er). Bach proposes for their reaction that an external ruthenium photocatalyst generates the triplet excited state iminium ion through an energy transfer process, which is also observed by Alemán when using an external transition metal-based sensitiser.

Tertiary amine catalysts such as β-isocupreidine (β-ICD) have found limited use in combination with photoredox catalysis, likely due to their tendency to oxidise to form iminium ions. However, Jiang et al. have developed a process using acrolein (**94**) in the presence of tetrahydro-β-carbolines (THCs) **95** or THIQs **96** and a dicyanopyrazine-derived (DPZ) photocatalyst (Scheme 12) [50]. They propose that addition of β-ICD to acrolein is assisted by NaBArF to give a zwitterionic intermediate **97**, which is then intercepted by the photocatalytically generated iminium ion **98**, followed by loss of β-ICD to give enantioenriched products **99** or **100** in good yields and enantioselectivities (21 examples for THCs, up to 98:2 er and 10 examples for THIQs, up to 98:2 er).

N-Heterocyclic carbene catalysis

N-Heterocyclic carbene (NHC) catalysis was first used in combination with photoredox catalysis by Rovis in 2012. They showed that iminium ions **101** could be generated in an oxidative quenching cycle from THIQs **102** using a ruthenium-based photocatalyst and 1,3-dinitrobenzene (DNB) as a sacrificial oxidant (Scheme 13) [51]. These iminium ions could then be intercepted by a Breslow intermediate **103**, formed between aldehydes **104** and the NHC catalyst **105**, to generate intermediate **106**, which can then turn over the NHC and release the desired acylated products **107** in good yields and enantioselectivities (13 examples, up to 96:4 er).

There has been little development of enantioselective reactions using NHCs in photocatalysis since this work. Another example was reported by Rovis in 2013 using enal **108** in the presence of chiral NHC **109** to form extended Breslow intermediate **110** (Scheme 14) [52]. Photoisomerisation of **110** is then required for the following spirocyclisation reaction to intermediate **111** to proceed, which then releases the NHC catalyst and intermediate **112** for the synthesis of (–)-cephalimysin A in moderate yield and excellent enantioselectivity (98:2 er). Interestingly, there have been multiple reports of racemic reactions that combine photoredox and NHC catalysis [53-56], but few enantioselective examples, suggesting there is much progress yet to be made.

Brønsted acid catalysis

Using chiral amines and NHCs as catalysts to generate asymmetry relies upon the formation of covalently bonded intermediates such as enamines, iminium ions or Breslow intermediates within the catalytic cycle. The first example of merging non-

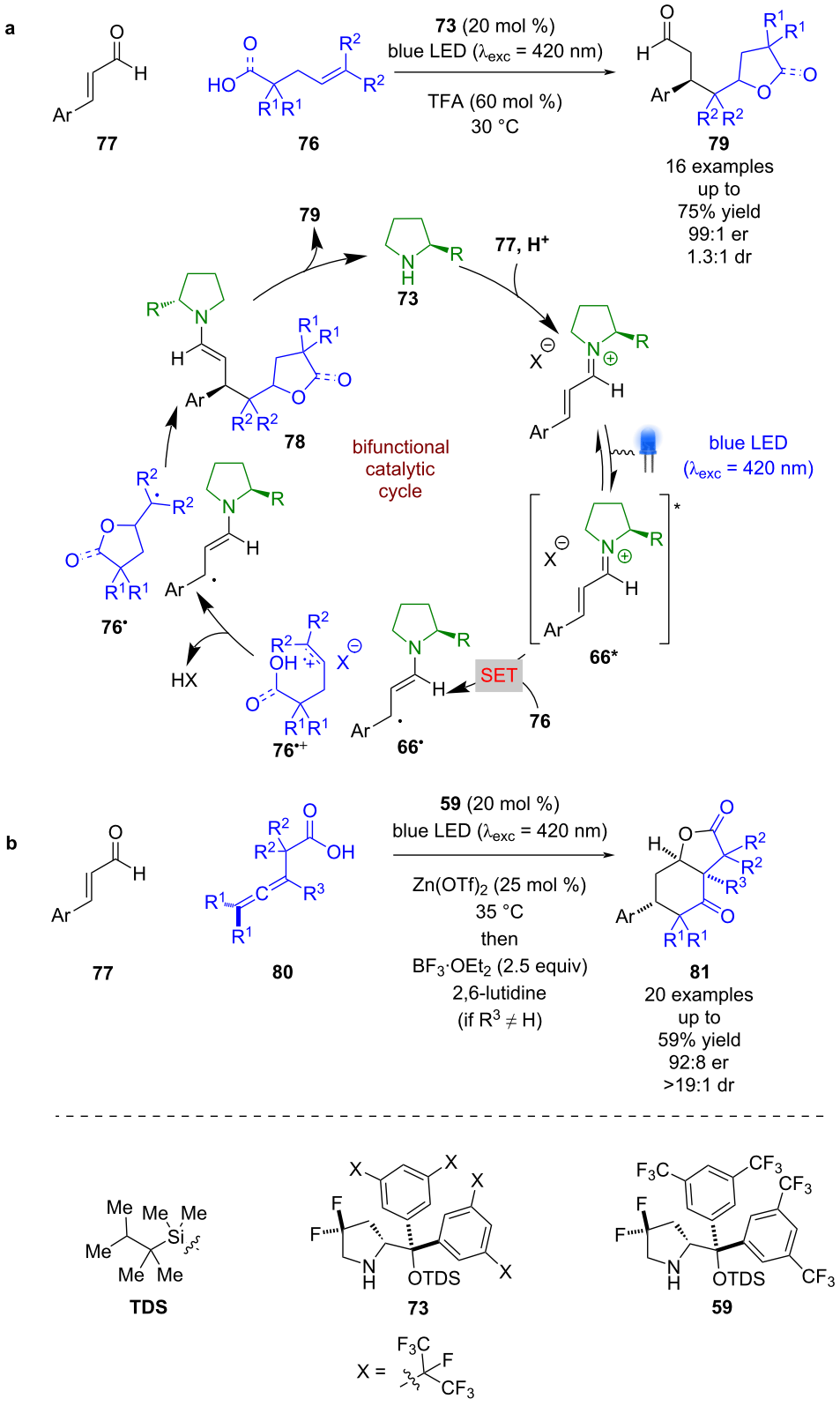

Scheme 10: Bifunctional amine/photoredox-catalysed radical cascade reactions between enones and alkenes with attached nucleophilic groups. (a) Alkenes with attached carboxylic acid or alcohol. (b) Allenes with attached carboxylic acid.

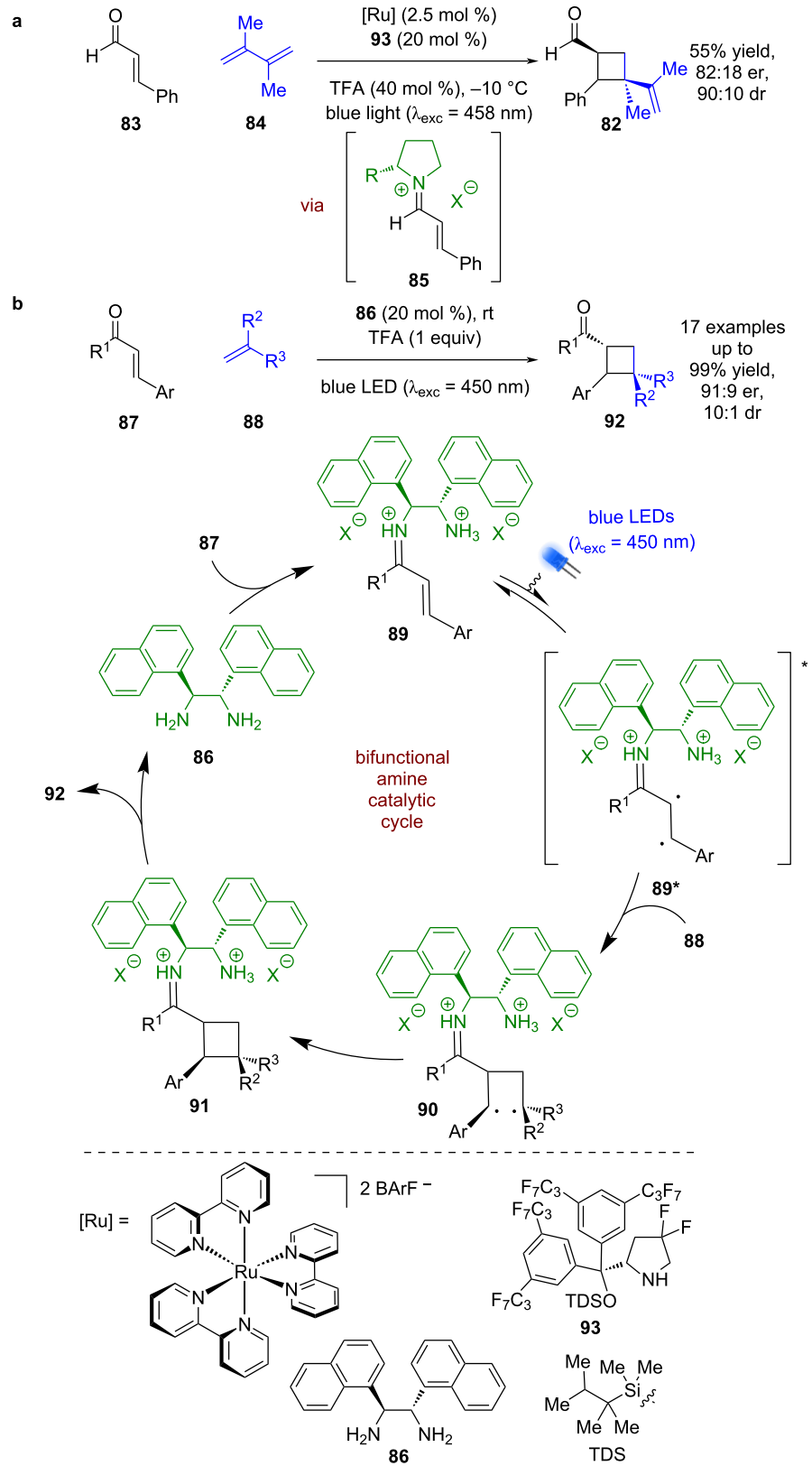

Scheme 11: Amine/photocatalysed photocycloadditions of iminium ion intermediates. (a) External photocatalyst used as triplet sensitiser with enals and dienes. (b) Bifunctional amine catalyst used with enones and alkenes.

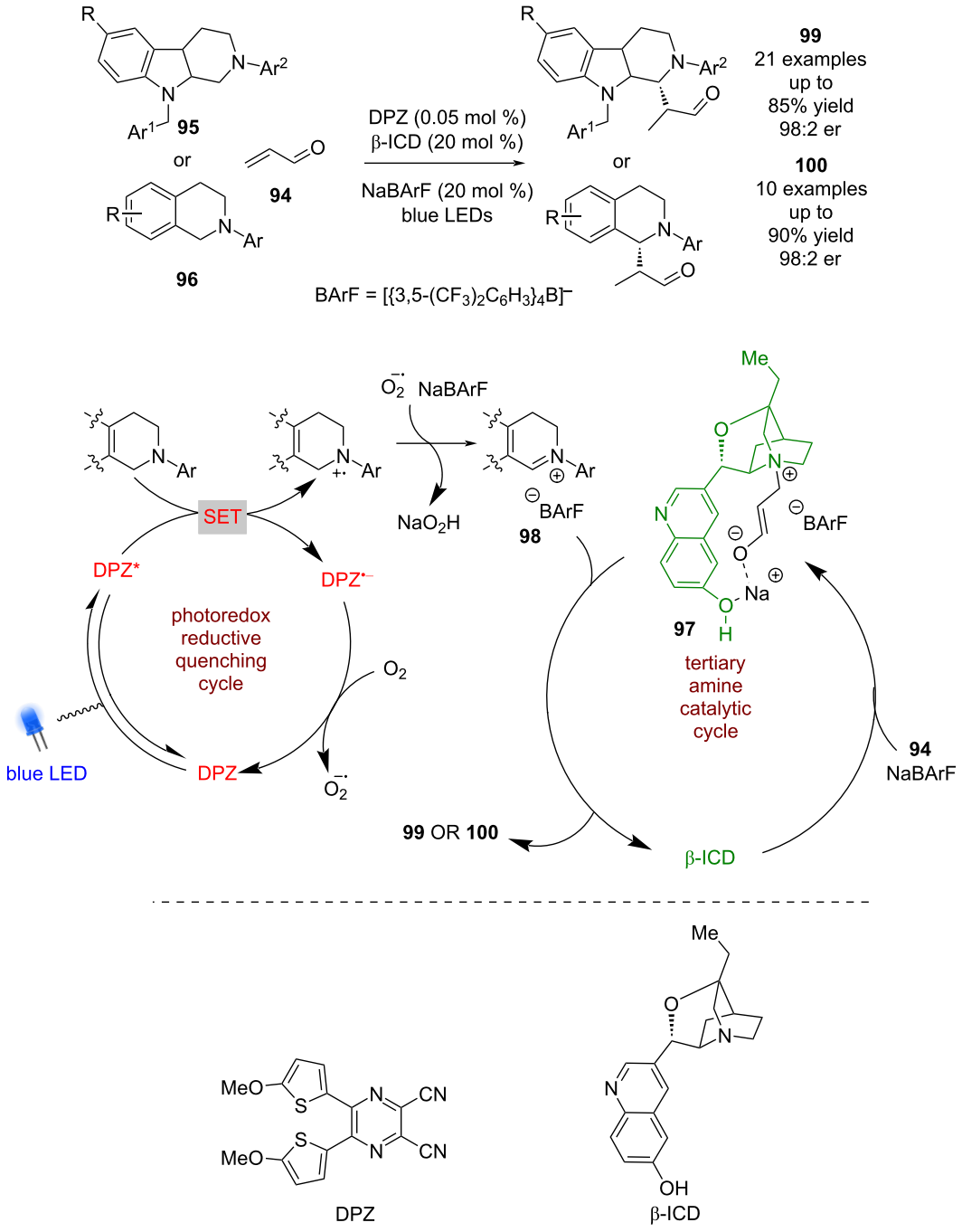

Scheme 12: Amine/photoredox-catalysed addition of acrolein (**94**) to iminium ions.

covalent catalysis with photoredox catalysis was reported by Rono and Knowles in 2013 (Scheme 15) [57]. They showed that using a chiral phosphoric acid (CPA), a photoredox catalyst and Hantzsch ester (HEH) as a HAT reagent, a concerted proton-coupled electron transfer (PCET) process is promoted to form ketyl radicals **113**•, which, in the presence of a hydrazone, cyclises to give *N*-centred radical **114**•. Subsequent HAT from HEH furnishes aza-pinacol product **115** in good yields and excellent enantioselectivities (14 examples, up to 98:2 er).

Since this initial report, a variety of processes have been developed using CPAs in combination with photoredox catalysis [58]. A significant contribution came from the Phipps group

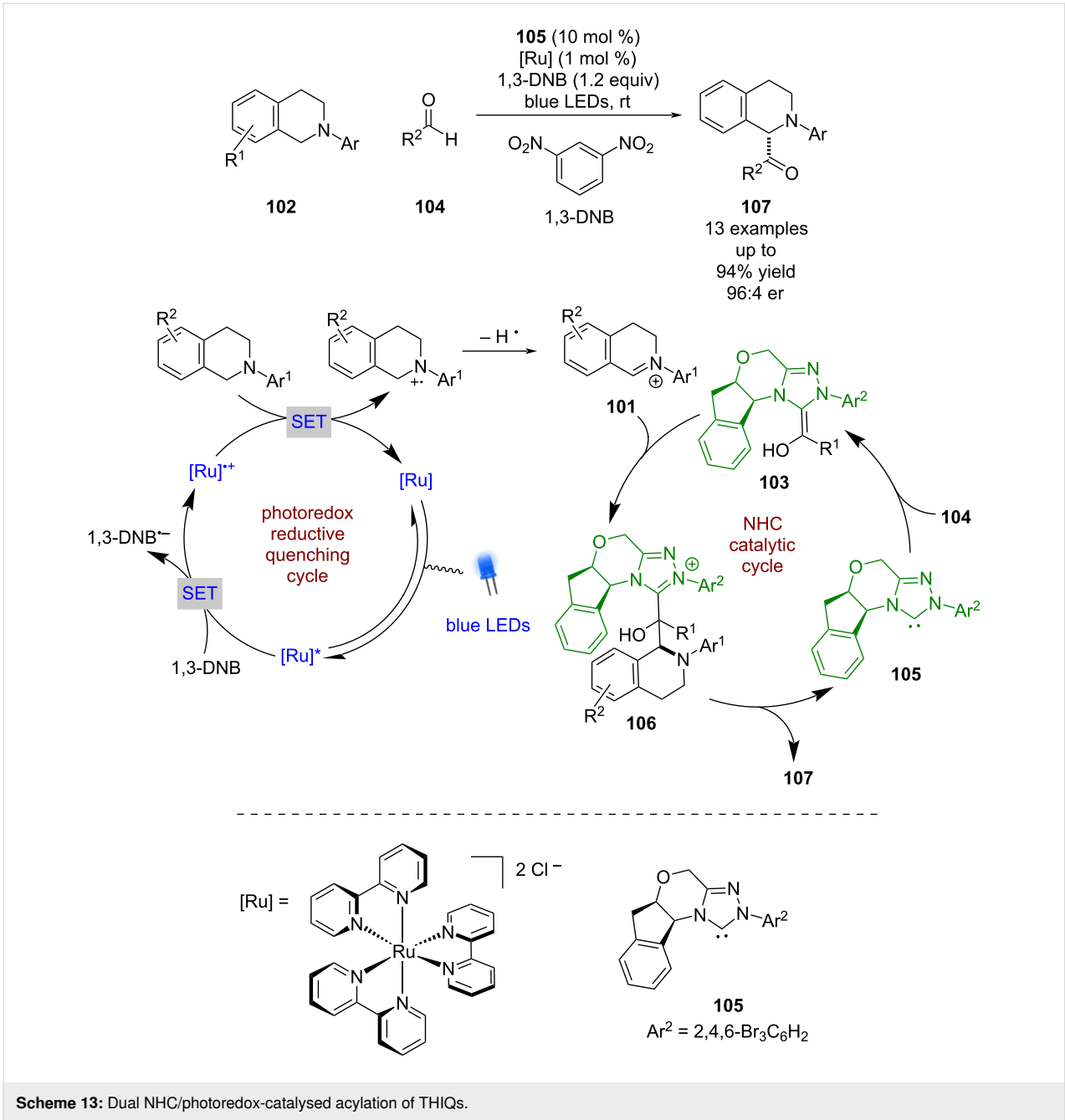

Scheme 13: Dual NHC/photoredox-catalysed acylation of THIQs.

with their work on enantioselective Minisci-type reactions (Scheme 16) [59]. Here, the CPA acts as a sacrificial reductant, with the photocatalyst proceeding through a reductive quenching cycle, generating $[Ir]^{\bullet-}$, which reduces the phthalimide ester **117** to give α-amino radicals **117**$^{\bullet}$ after decarboxylation. The CPA then activates the azaarene **118** through protonation and brings the two reactive species together in a hydrogen bonded complex **119**, which facilitates radical addition. After deprotonation and oxidation via SET, both catalysts are regenerated and Minisci-type products **120** are released in excellent yields and enantioselectivities (30 examples, up to 99:1 er). Pyridyl substrates are tolerated, but generally required the presence of electron-withdrawing groups for the reaction to proceed.

Jiang et al. developed a similar system for the enantioselective radical addition into 2-vinylazaarenes **122** using DPZ and either α-amino radicals [60] or ketyl radicals [61], with pyridines being well tolerated as substrates in this latter case (Scheme 17a). The same group also separately developed a Minisci-type reaction using phthalimide esters **123**; however, their system did not extend past isoquinoline substrates **124**

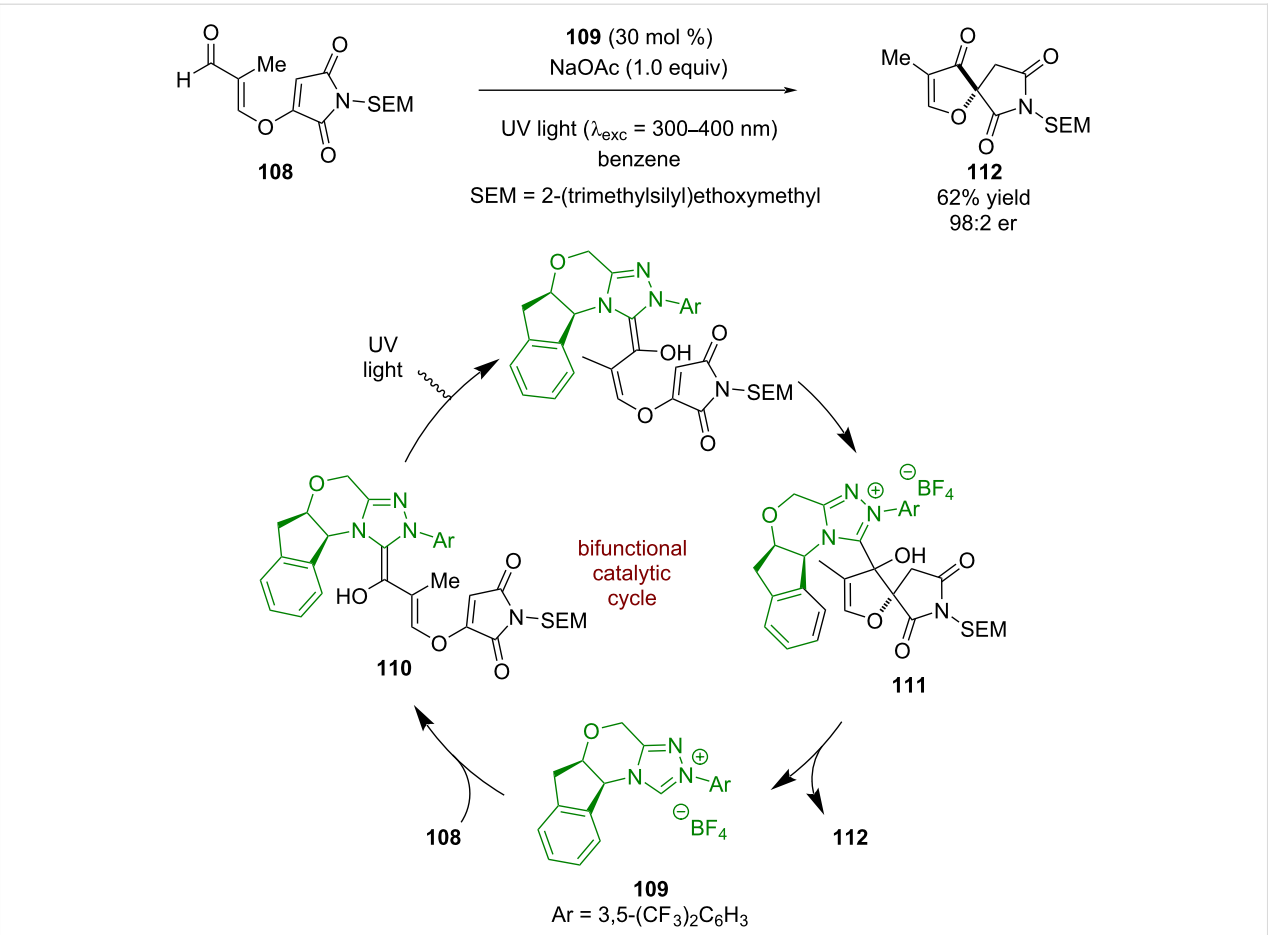

Scheme 14: NHC/photocatalysed spirocyclisation via photoisomerisation of an extended Breslow intermediate.

(Scheme 17b) [62]. Zheng and Studer expanded the scope of this type of reactivity to a three-component cascade reaction with alkyl bromides **125** and enamides **126** (Scheme 17c) [63]. Interestingly, they found some of their examples required the more strongly reducing photocatalyst $Ir(ppy)_3$ to achieve high yields, although the reason for this is unclear.

Jiang et al. continued to explore the reactivity landscape of CPAs and azaarenes, demonstrating that ketone **128** could be reduced enantioselectively (Scheme 18a) [64]. The proposed mechanism in this case also follows a reductive quenching cycle using DPZ, but this time includes a tertiary amine **129** as a sacrificial reductant to generate $DPZ^{\bullet-}$. As in the previous examples, the azaarene nitrogen is proposed to be protonated by the CPA to form chiral ion pair **130**, which is then reduced by $DPZ^{\bullet-}$ to give ketyl radical **130**$^{\bullet}$. The radical **130**$^{\bullet}$ is then reduced further to the carbanion **130**$^{-}$, which is protonated enantioselectively to give alcohols **131** in excellent yields and enantioselectivities (38 examples, up to 98:2 er). It is notable that pyridyl ketones do not perform well in this reaction (1 example, 70:30 er). A further extension of this methodology includes the deuteration of **128** and alkyl halides **132** using D_2O to afford **133** (18 examples, up to >99:1 er) and **134** (34 examples, up to 98:2 er), respectively (Scheme 18b) [65].

Jiang et al. also reported a series of radical coupling reactions using different CPAs **135a–g** and DPZ, with the first examples using α-bromoketones **136** and α-amino acids **137** as radical precursors (Scheme 19a) [66]. The proposed mechanism proceeds through a reductive quenching cycle to generate α-amino radical **137**$^{\bullet}$ and $DPZ^{\bullet-}$, which can reduce **136** to give α-carbonyl radical **136**$^{\bullet}$. The CPA is then proposed to form a ternary hydrogen-bonded complex **138** to mediate enantioselective radical coupling that furnishes the desired products **139** in good yields and excellent enantioselectivities (48 examples, up to 99:1 er). This methodology was later expanded to 2-oxindoles **140** [67] and 1,2-diketones **141** [68] to form the corresponding radical coupling products **142** (43 examples, up to 98:2 er) and **143** (30 examples, up to 99:1 er), respectively, in comparable yields and enantioselectivities to those of **139** (Scheme 19b).

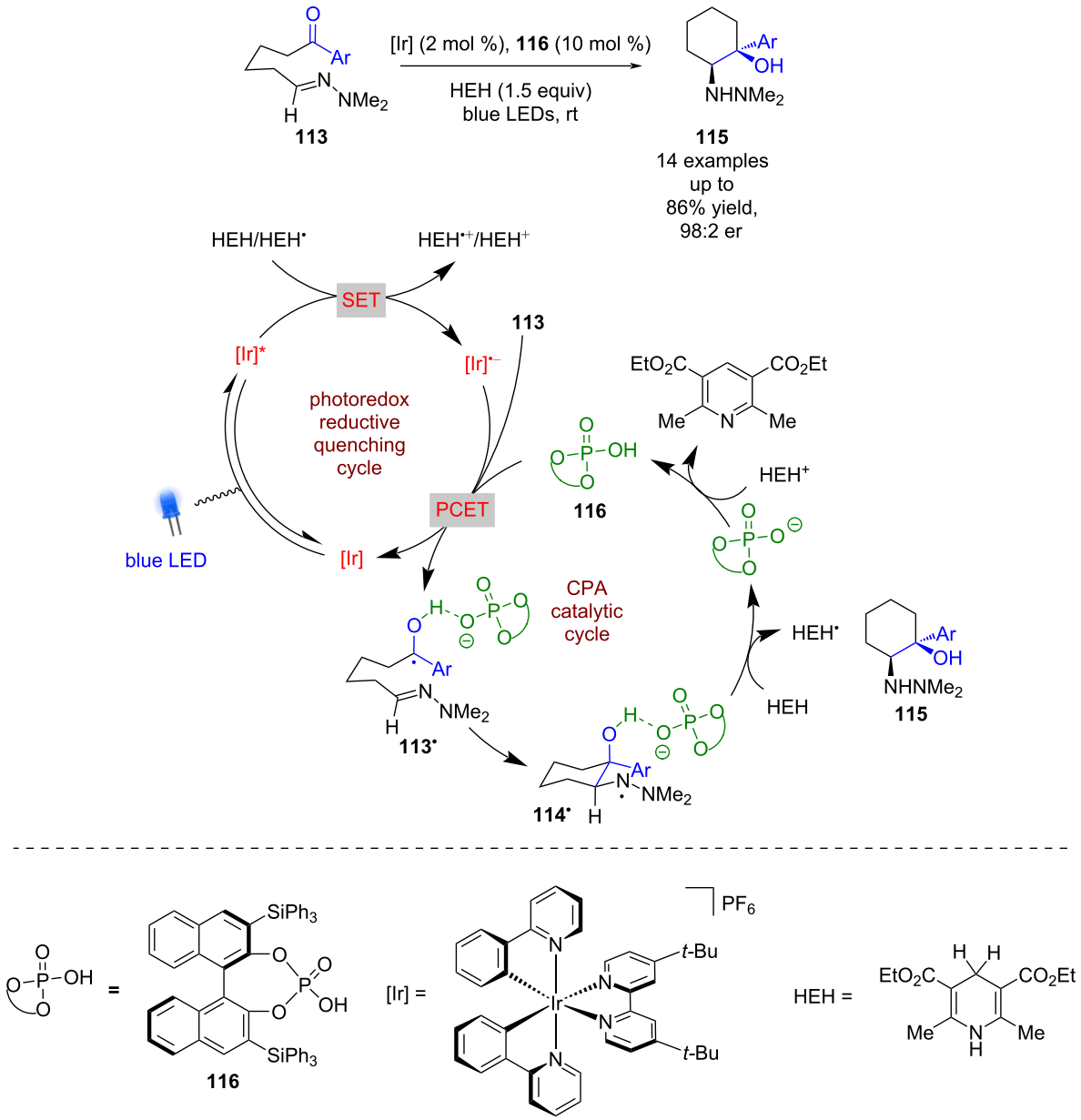

Scheme 15: CPA/photoredox-catalysed aza-pinacol cyclisation.

As previously mentioned, photoredox catalysis has been widely used for the generation of imines. The Jiang group applied this to the synthesis of substituted tetrahydroquinolines (THQs) **144** from α-amino acids **145** to give racemic products in good yields and found that the addition of a CPA provided good enantioselectivity (Scheme 20) [69]. The putative mechanism proceeds via a reductive quenching cycle to give α-amino radical **145**• after decarboxylation, which is then oxidised further to the imine **146** in the presence of oxygen. Imine **146** is in equilibrium with the enamine tautomer **147**, and the CPA-catalysed Povarov reaction between them gives the enantioenriched THQ **144** in good yields and enantioselectivities (4 examples, up to 97:3 er).

This reactivity has been extended to enamides **148**, with the imine generated from the α-amino acid **149** now reacting with **148** in a CPA-catalysed Povarov reaction rather than with its own tautomer (Scheme 21a) [70]. Zhang and You developed a catalytic dearomatisation reaction of indoles **150** using similar chemistry, where the generated imine **151** now reacts intramo-

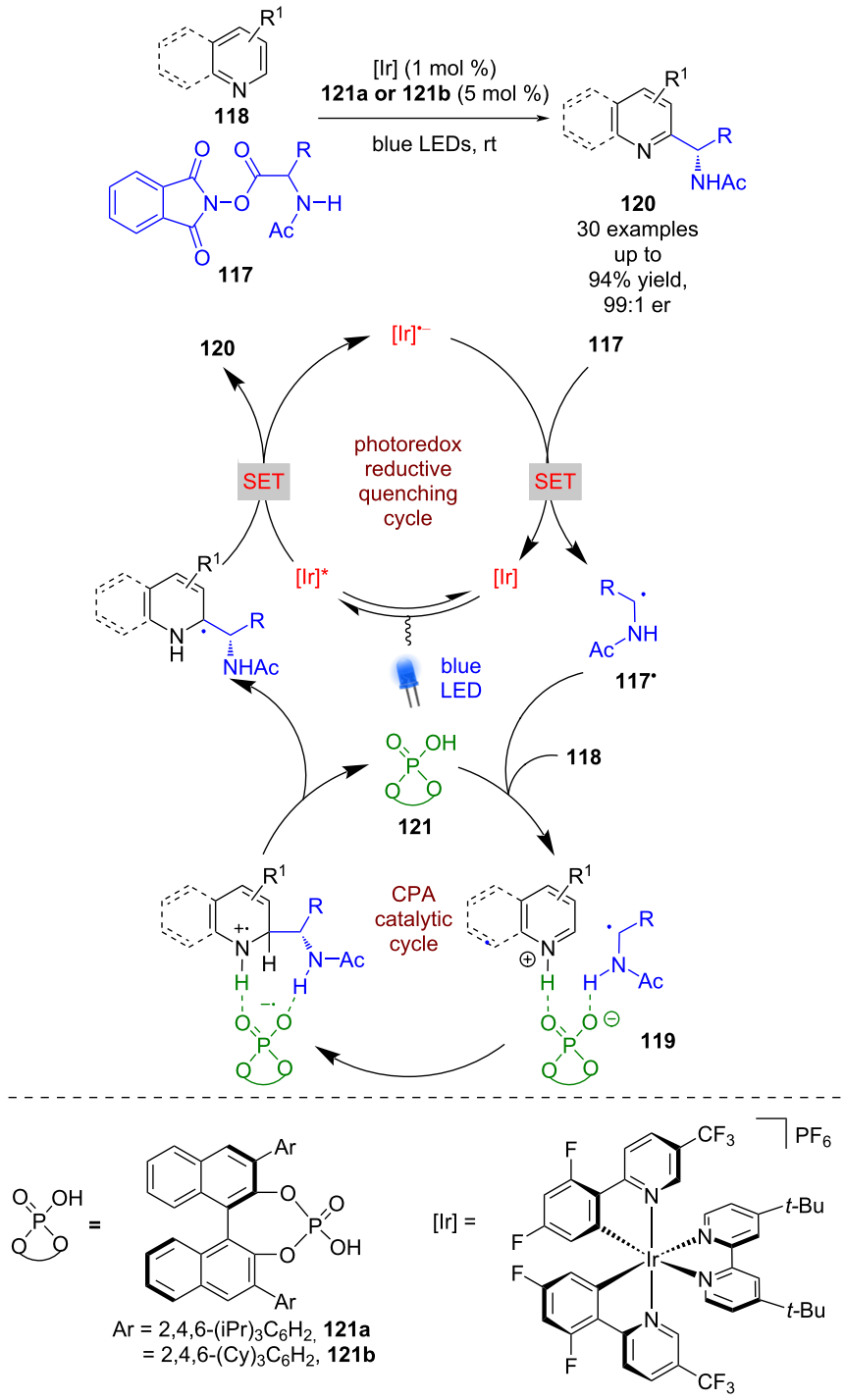

Scheme 16: CPA/photoredox-catalysed Minisci-type reaction between azaarenes and α-amino radicals.

lecularly with a pendant nucleophile and is further oxidised to a carbocation that is trapped intermolecularly by *N*-hydroxycarbamates **152** (Scheme 21b) [71].

Bach et al. has recently reported a bifunctional catalyst **154**, which contains both a photoactive thioxanthone unit and a CPA (Scheme 22) [72]. They have applied this photocatalyst to the [2 + 2] photocycloaddition of carboxylic acids **155** with alkenes **156**. A low yielding benzylation reaction was required for determination of enantioselectivities and a large excess of alkene was required for the reaction. The reaction is proposed to proceed via hydrogen-bonded complex **157**, that lowers the

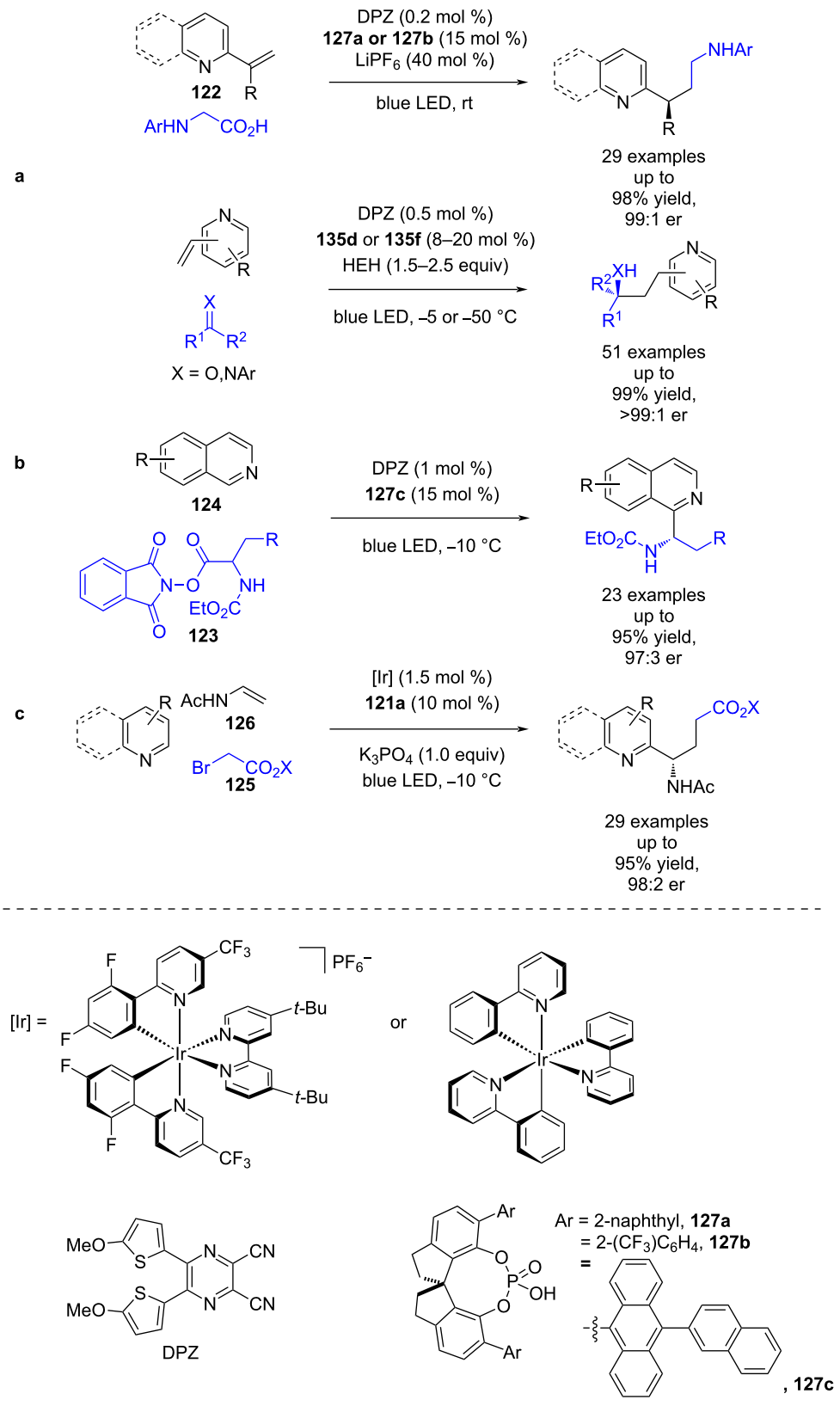

Scheme 17: CPA/photoredox-catalysed radical additions to azaarenes. (a) α-Amino radical or ketyl radical addition to 2-vinylazaarenes. (b) Minisci-type reaction using redox-active esters and isoquinolines. (c) Radical cascade reaction using α-carbonyl radicals with enamides.

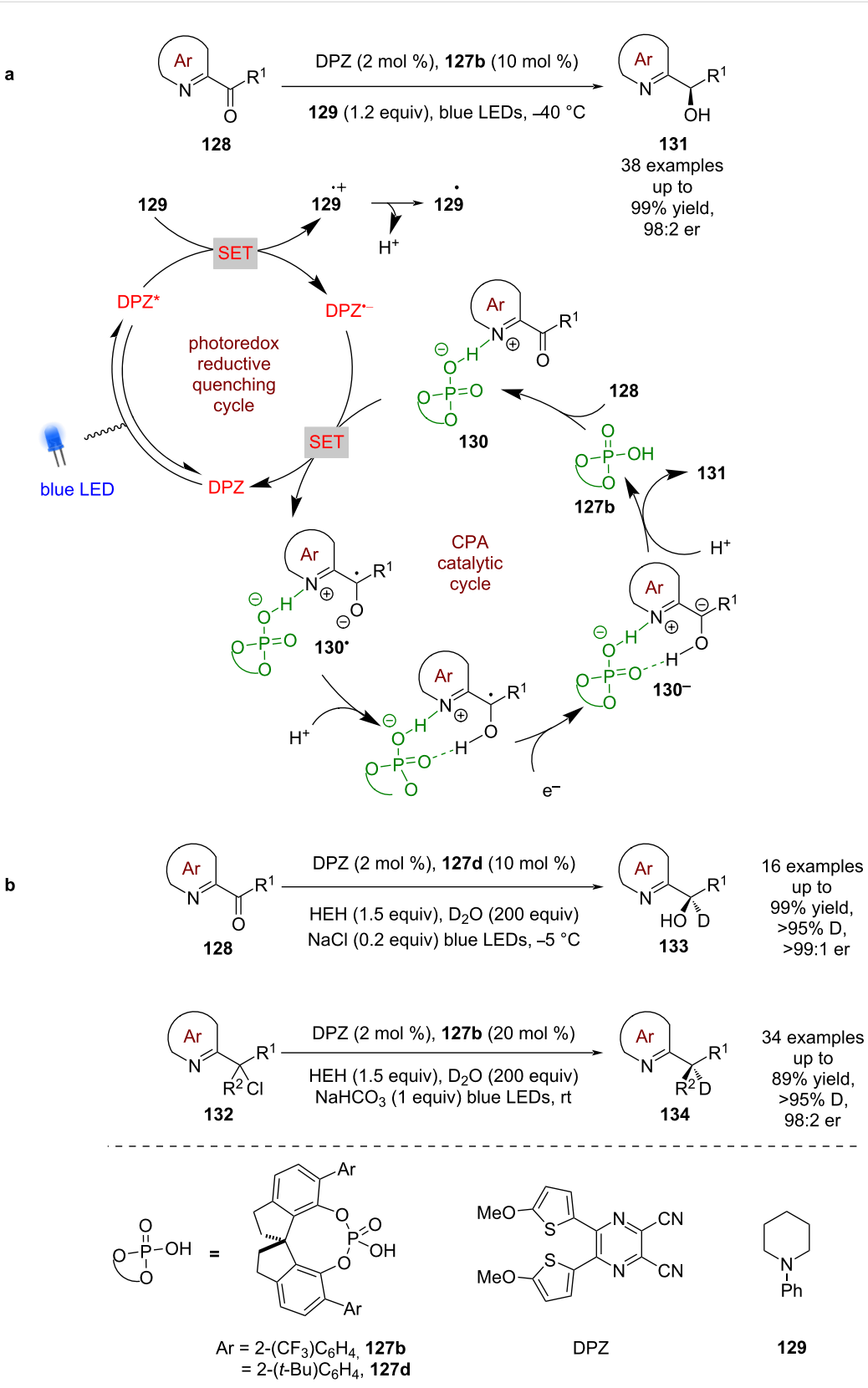

Scheme 18: CPA/photoredox-catalysed reduction of azaarene-derived substrates. (a) Reduction of ketones. (b) Extension to deuteration of ketones and alkyl halides.

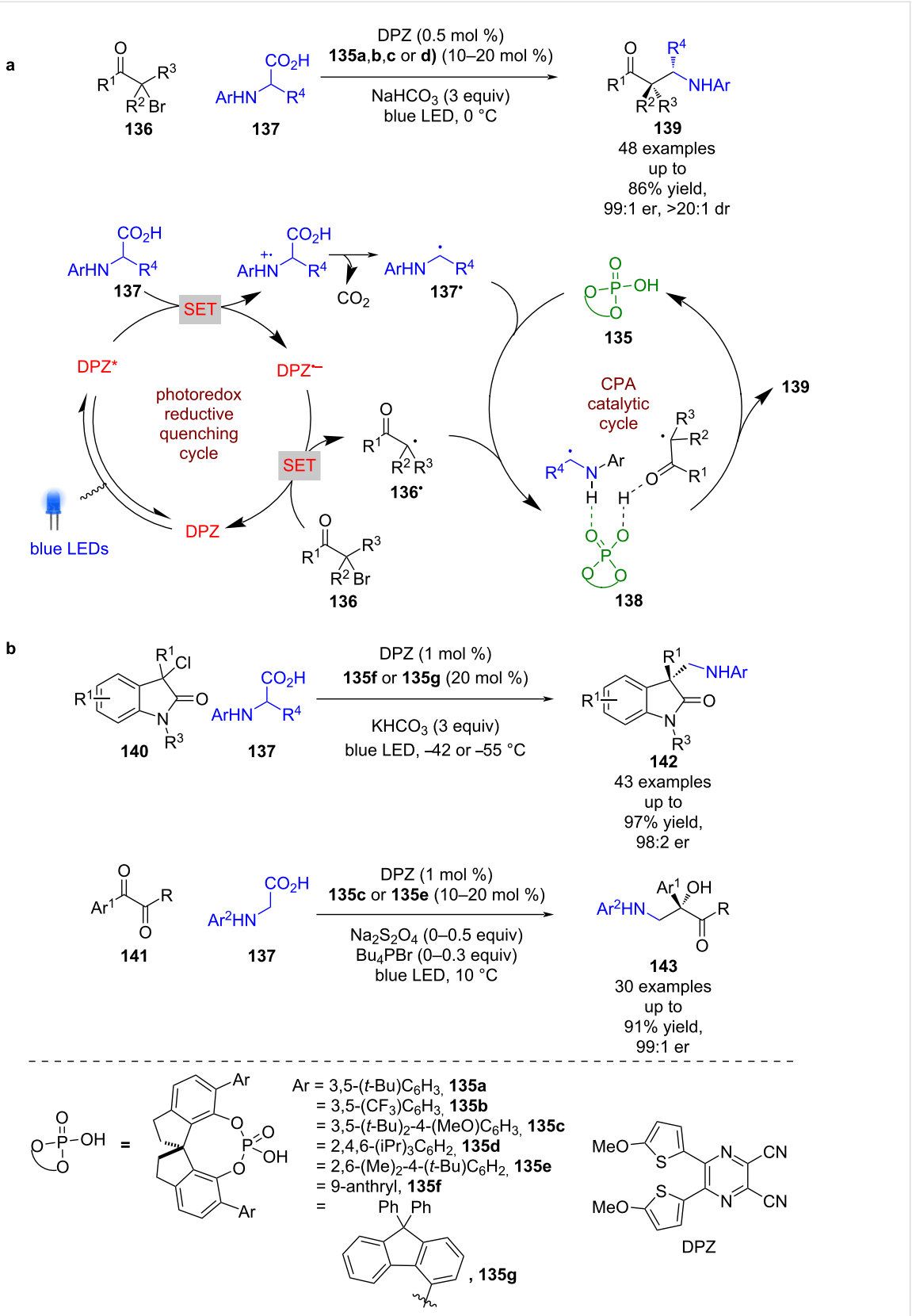

Scheme 19: CPA/photoredox-catalysed radical coupling reactions of α-amino radicals with α-carbonyl radicals. (a) Using α-bromoketones. (b) Using α-chloro-2-oxindoles or 1,2-diketones.

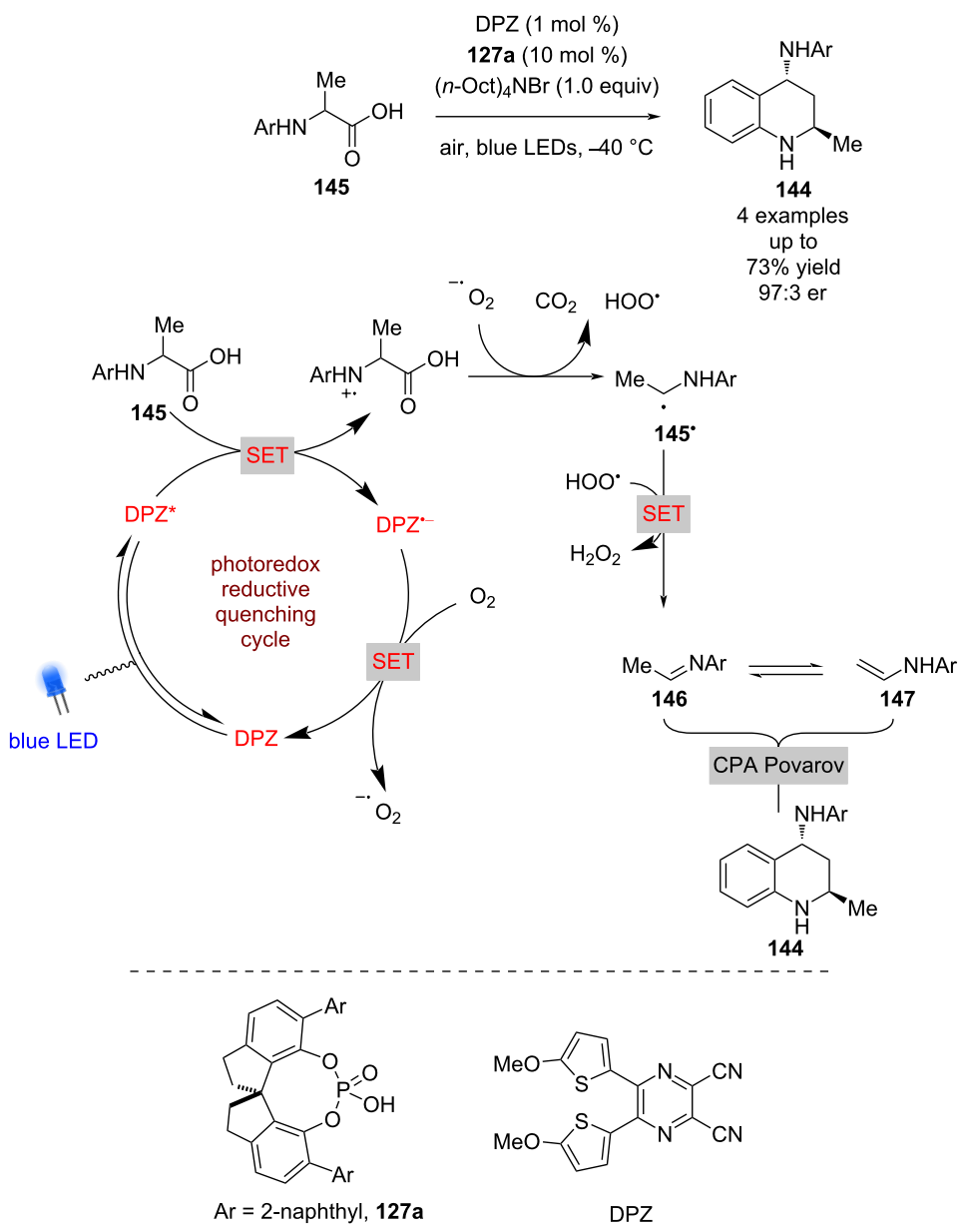

Scheme 20: CPA/photoredox-catalysed Povarov reaction.

triplet energy of the carboxylic acid so that a Dexter energy transfer process is possible from the photocatalyst to the substrate to promote **155** into its triplet state, which can then cyclise with **156** to give enantioenriched cycloaddition products **158**. The selectivity of this reaction is generally low (6 examples, up to 93:7 er, 67:33 rr) but this example does demonstrate an interesting proof of concept with potential for the development of processes using alternative bifunctional catalysts.

Phase-transfer catalysis

Phase-transfer catalysis (PTC) is another non-covalent mode of catalysis that has been combined with photocatalysis. The first example of PTC being used in combination with photocatalysis was developed by Gao towards the oxygenation of 1-indanone derived β-keto esters **159** (Scheme 23) [73]. Gao proposes tetraphenylporphyrin (TPP) acting as a sensitiser to form $^1O_2$ via photoinduced energy transfer, which is then trapped by enolate **160** in a chiral environment, provided by the PTC, to form a α-hydroperoxyl intermediate **161**. Subsequent deoxygenation by another molecule of **160** forms two molecules of the α-hydroxylated products **162** in excellent yields and moderate enantioselectivities (11 examples, up to 88:12 er). The selectivity has been improved further with the development of new PTCs [74-76], although the scope of the reaction remains limited.

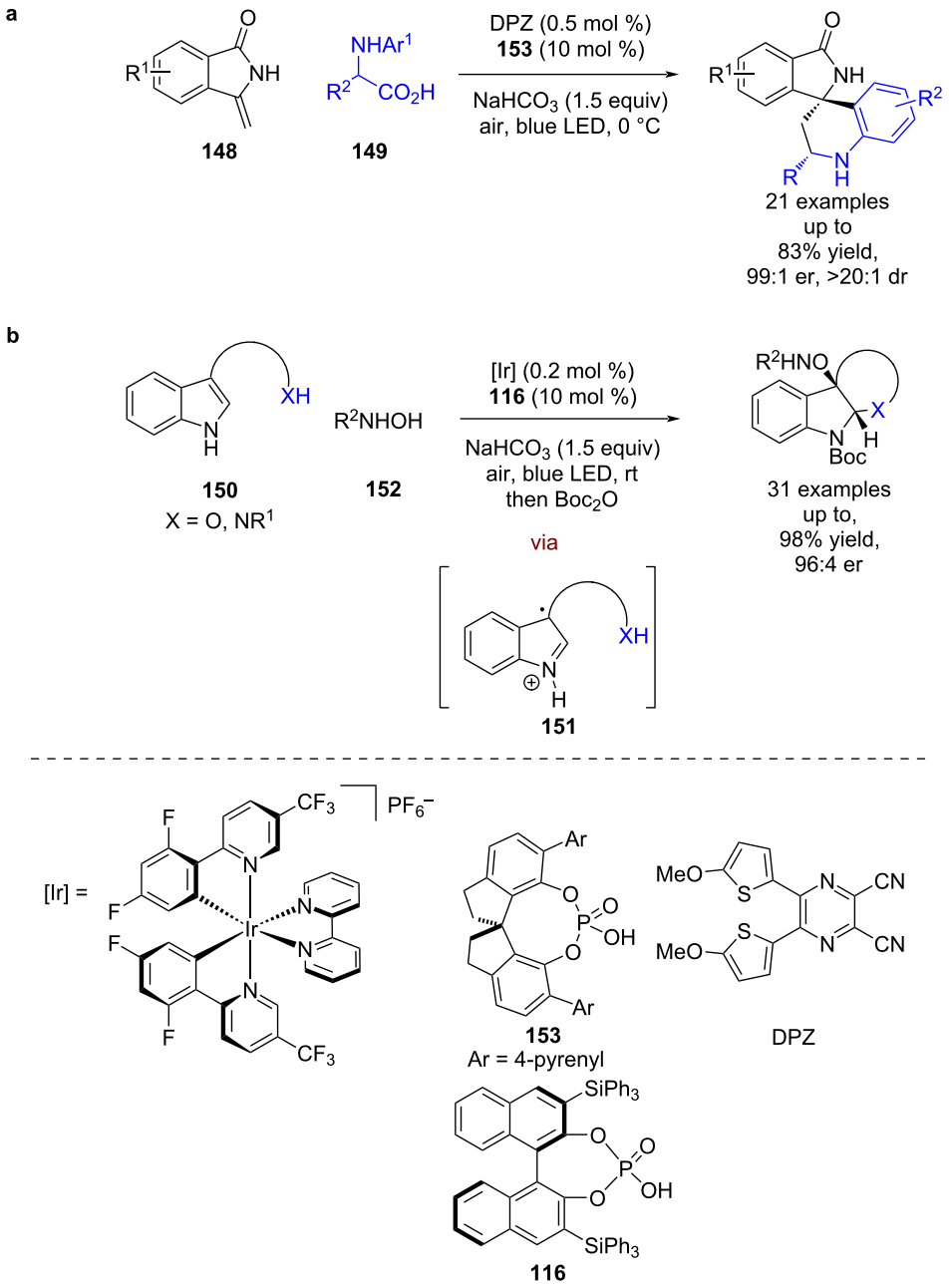

Scheme 21: CPA/photoredox-catalysed reactions with imines. (a) Decarboxylative imine generation followed by Povarov reaction with an enamide. (b) Imine trapped by intramolecular nucleophile and intermolecular nucleophile.

Building on these initial reports, Melchiorre et al. developed a perfluoroalkylation reaction of the same starting materials **159** using alkyl iodides **163** (Scheme 24) [77]. Interestingly, this takes place without the need for an external photocatalyst and is proposed to proceed via an intermediate EDA complex **164**, which, upon excitation, forms perfluoroalkyl radicals **163•** that add to the enolate substrate that is coordinated to a chiral counterion **165** to give ketyl radical anion **166•−**. The latter intermediate **166•−** can then abstract an iodine atom from another molecule of **163** to propagate the chain reaction and generate alkyl iodide **167**, which collapses to give the desired enantioenriched alkylation products **168** in moderate yields and excellent enantioselectivities (14 examples, up to 98:2 er). The quantum yield of the enantioselective reaction could not be ascertained due to the reaction being heterogenous, but the quantum yield for the racemic variant using an achiral base was >1 (Φ = 1.2), support-

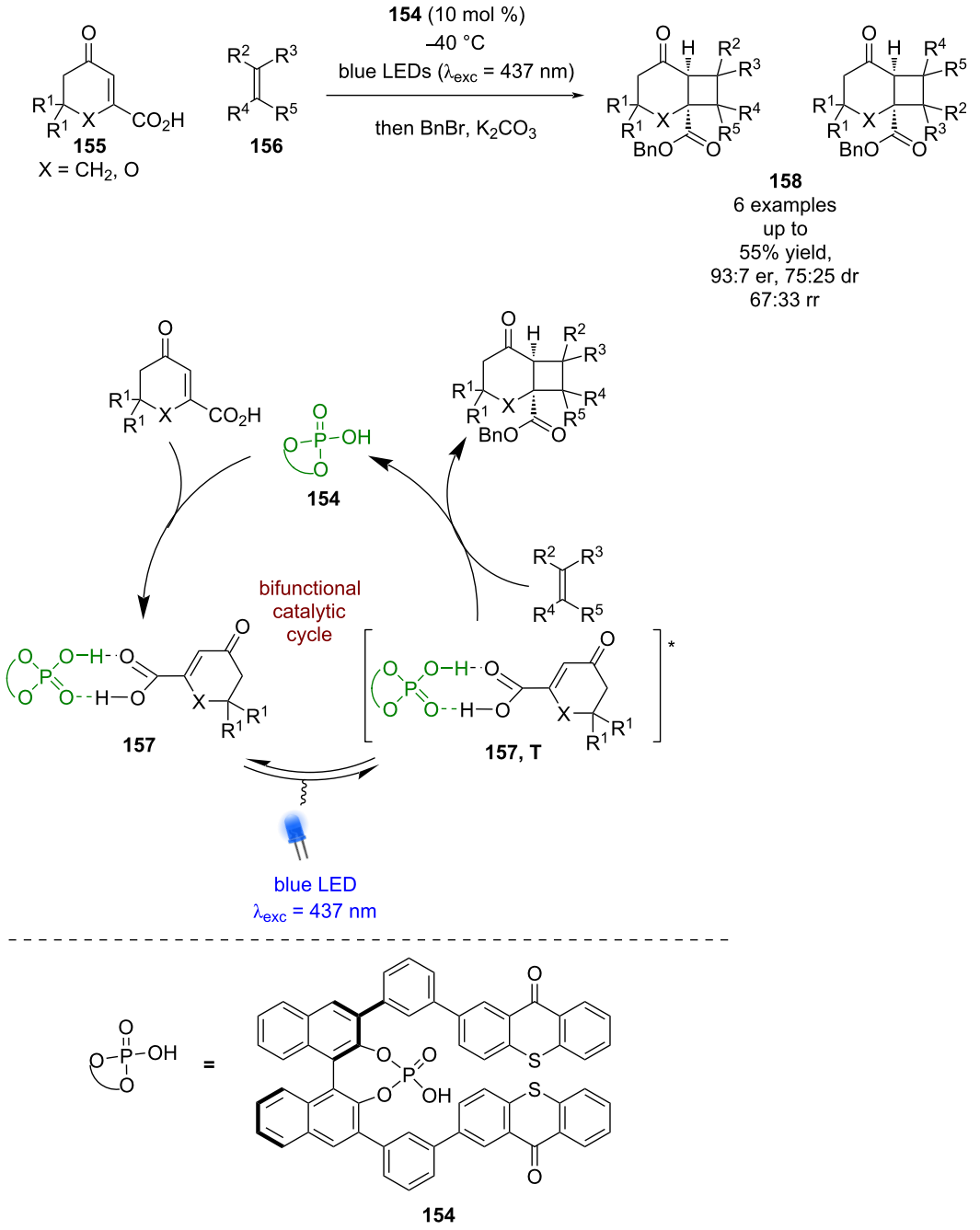

Scheme 22: Bifunctional CPA/photocatalysed [2 + 2] photocycloadditions.

ing the proposed radical chain process. While these results are promising for this mode of catalysis, more work is required to address the limited substrate scope.

Hydrogen bonding

Krische et al. were the first to develop a bifunctional hydrogen bonding photocatalyst **169** (Scheme 25) [78] that was used in an intramolecular enantioselective [2 + 2] photocycloaddition of quinolone **170**. The proposed mechanism proceeds via hydrogen-bonded complex **171**, which is sensitised by the pendant benzophenone to its triplet excited state **171***. The following cycloaddition completes the cycle and generates the desired cyclobutane product **173** in excellent conversion but poor enantioselectivity (60:40 er). While the enantioselectivity was low, this reaction represented an interesting proof of concept that would be later expanded by others.

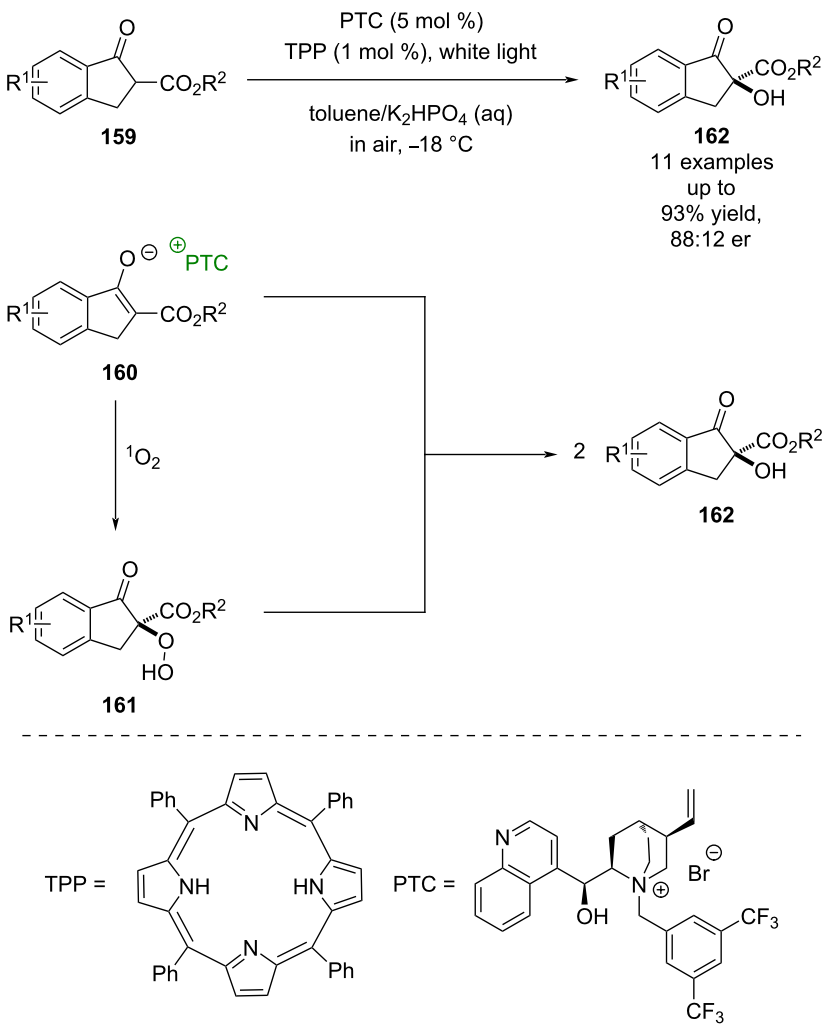

Scheme 23: PTC/photocatalysed oxygenation of 1-indanone-derived β-keto esters.

Later, Bach et al. developed a similar bifunctional hydrogen bonding photocatalyst **174**. Reactions using catalysts of this type are well covered in Bach's recent review on the subject [13]. Photocatalyst **174** was first used in a cyclisation reaction where the putative mechanism involves a hydrogen bonding complex **175** between the catalyst and quinolone substrate **176** (Scheme 26) [2]. Subsequent photoexcitation promotes a photoinduced electron transfer to generate diradical **177** that then adds to the alkene to form diradical **178**. A SET between the ketyl radical and the α-carbonyl radical generates enolate intermediate **179**, which after proton transfer regenerates the catalyst and releases the desired cyclisation product **180** in a moderate yield and enantioselectivity (85:15 er).

Photocatalyst **174** was next applied to the formal [2 + 2] photocycloaddition of quinolones **181**, which is analogous to the reaction developed by Krische et al. in Scheme 25. Similarly, the mechanism that is proposed proceeds through complex **182** that can be photosensitised into its triplet excited state **182*** (Scheme 27) [79,80]. However, the enantioselectivities for this reaction were poor (70:30 er), which prompted further catalyst design by changing the photosensitising group from benzophenone to xanthone **183** to improve enantioselectivity [79]. Xanthone has a higher triplet energy than benzophenone (3.2 eV vs 3.0 eV) and the authors attribute this difference to the increased efficiency; however, the efficiency of energy transfer is governed by spectral overlap between donor and acceptor. The much higher enantioselectivities observed (95:5 er) are attributed to a reduced amount of background reaction and the more rigid xanthone structure acting as a superior stereo-directing group.

Further variation to a thioxanthone unit **185**, which has a lower triplet energy (E_T = 2.7 eV), was used to investigate a similar

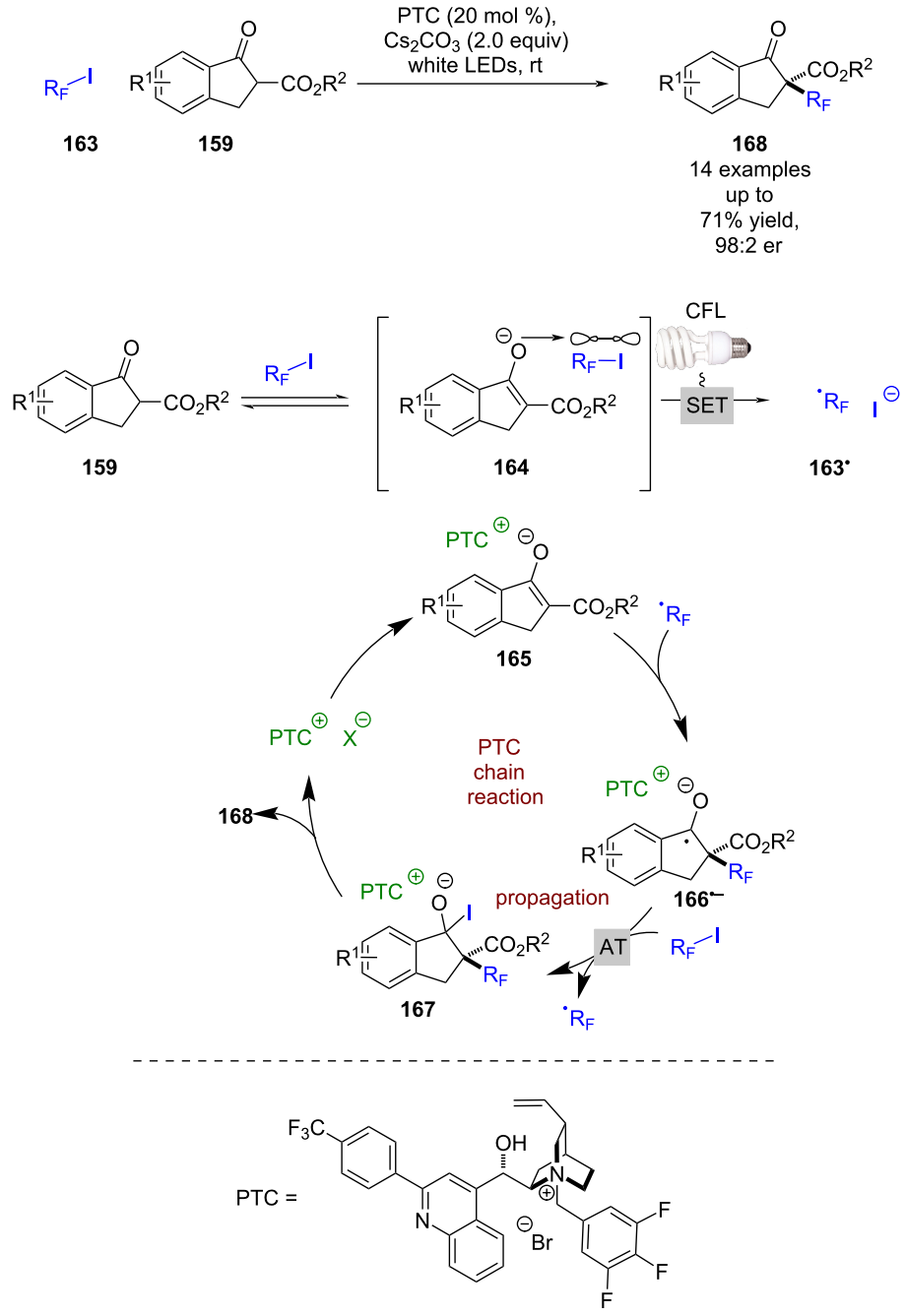

Scheme 24: PTC/photoredox-catalysed perfluoroalkylation of 1-indanone-derived β-keto esters via a radical chain reaction initiated by an EDA complex.

[2 + 2] photocycloaddition, giving comparable yields and enantioselectivities (7 examples, up to 97:3 er) (Scheme 28a) [81]. A lower energy wavelength irradiation was able to be used, which limited the amount of background reaction as the absorption spectra of photocatalyst and substrate were more clearly resolved. The first intermolecular process using these catalysts was the [2 + 2] photocycloaddition of 2-pyridones **186** and acetylenedicarboxylates **187** catalysed by *ent*-**183** to give cyclobutenes **188** (Scheme 28b) [82]. Another intermolecular reaction was later developed, this time using catalyst **185** for the [2 + 2] photocycloaddition of quinolones **189** and electron-deficient alkenes **190** to synthesise cyclobutanes **191** (Scheme 28c) [83]. Recently, Bach et al. also employed this methodology for the intramolecular [2 + 2] cycloaddition of quinolones **192** con-

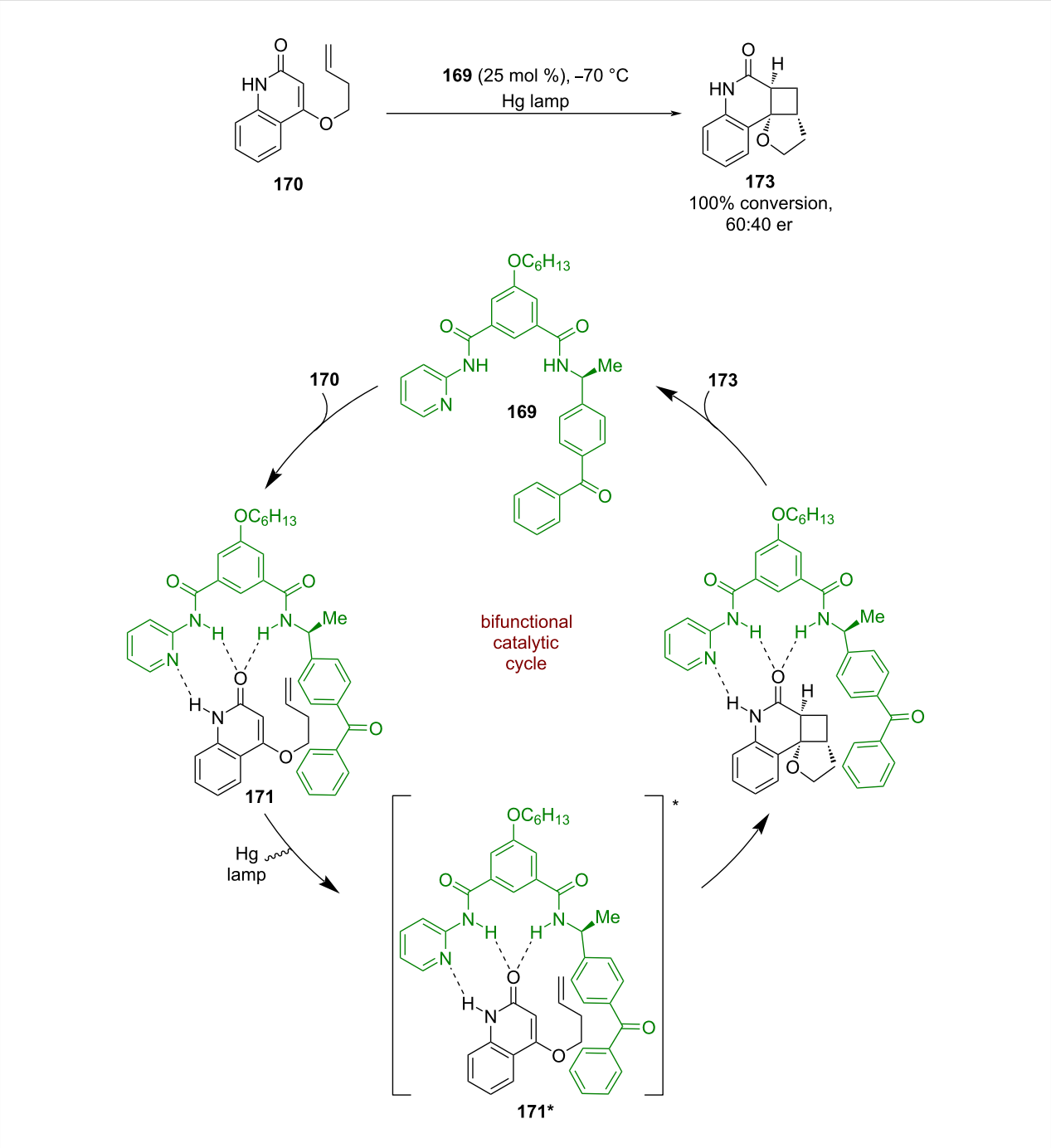

Scheme 25: Bifunctional hydrogen bonding/photocatalysed intramolecular [2 + 2] photocycloadditions of quinolones.

taining either a pendant alkene or allene to obtain cyclobutanes **193** (Scheme 28d) [84].

Recently, *ent*-**185** was applied by Bach to the deracemisation of allenes *rac*-**194** (Scheme 29) [85]. The proposed mechanism proceeds through configurationally isomeric hydrogen bonding complexes **195** and **195'**, with subsequent photoexcitation of the thioxanthone chromophore leading to racemisation of the allene through a triplet state intermediate **196**. In **195** there is additional steric repulsion between the large R group and the thioxanthone that is not present in **195'**, which results in a smaller association constant and a larger calculated separation between the allene and the chromophore in **195** (r = 510 pm) relative to **195'** (r = 363 pm). As the efficiency of Dexter energy transfer decreases exponentially with distance, the larger gap results in lower sensitisation rates for **190**. This, in combi-

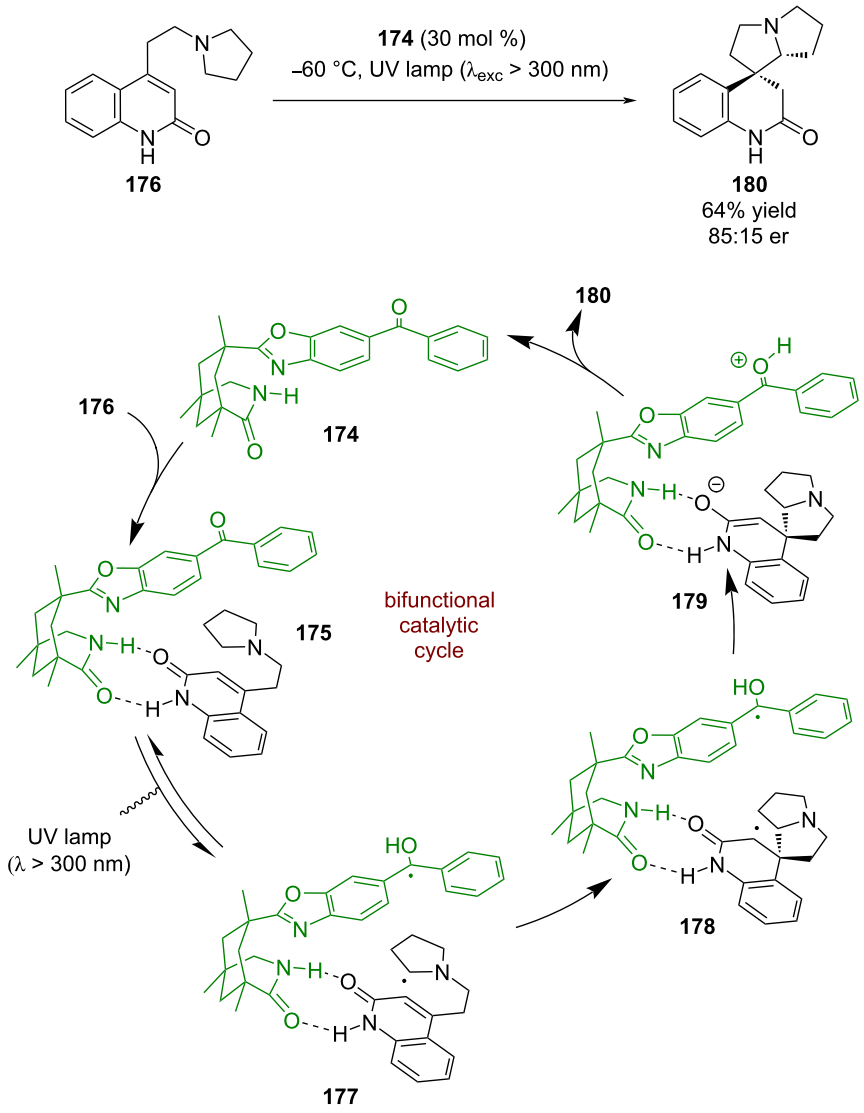

Scheme 26: Bifunctional hydrogen bonding/photocatalysed intramolecular RCA cyclisation of a quinolone.

nation with the difference in association constants, leads to greater racemisation of *ent*-**194** and, therefore, a deracemisation with excellent enantioselectivities and yields (17 examples, up to 99:1 er). Interestingly, the quantum yield for the reaction was measured to be 0.52, which the authors assert is quantitative based on the complete deracemisation in the reaction. Bach et al. recently extended this reactivity further to include 5-membered rings [86].

A similar mechanism is proposed for the deracemisation of sulfoxides *rac*-**197**; however, the enantioselectivities are lower (5 examples, up to 78:22 er), which the authors attribute to the catalyst differentiating between the sterics of an oxygen atom and a lone pair of electrons (Scheme 30a) [87]. Bach et al. also found that alkenes **198** can undergo a light-induced rearrangement to cyclopropane **199** in the presence of **185** (Scheme 30b) [88]. They discovered that **199** is configurationally unstable under the reaction conditions and propose that a similar deracemisation mechanism is responsible for the enantioselectivity via triplet state intermediate **200**, rather than proceeding via an enantioselective rearrangement.

Bifunctional hydrogen bonding photocatalysts have been developed by other groups as well. Sivaguru developed an atropisomeric thiourea-based catalyst **201** and used it for the intramolecular photocycloaddition of coumarins **202** (Scheme 31) [89]. The proposed mechanism for this reaction is similar to that proposed by Bach and Krische, proceeding via a key hydrogen

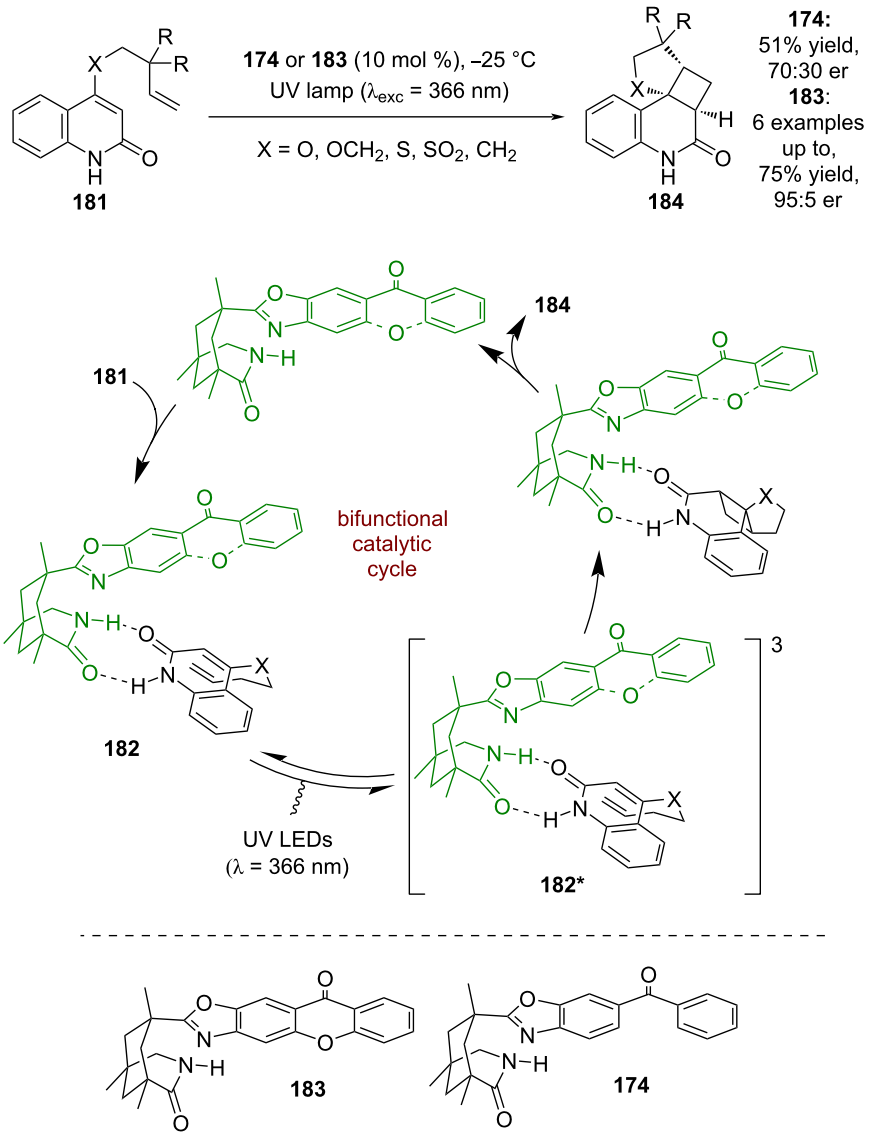

Scheme 27: Bifunctional hydrogen bonding/photocatalysed intramolecular [2 + 2] photocycloadditions of quinolones.

bonding complex **203**. Interestingly, this catalyst allowed for reactivity with lactones, whereas Bach's catalysts are limited to lactams.

Yoon et al. developed an iridium-based bifunctional hydrogen bonding photocatalyst **205**. To demonstrate the effectiveness of this photocatalyst system, they tested the intramolecular photocycloaddition of quinolones **206** (Scheme 32a) [90]. The proposed mechanism again proceeds via a triplet sensitisation of the substrate within a hydrogen bonding complex **207** that provides the desired products **208** in excellent yields and good enantioselectivities (13 examples, up to 96:4 er) and a quantum yield of 0.31 [91]. As with Bach's catalysts, the scope is limited to lactams. Yoon et al. then applied a similar catalyst to an intermolecular photocycloaddition between quinolone **209** and maleimide **210** (Scheme 32b) [92]. After extensive mechanistic investigations, the proposed mechanism for this reaction is markedly different to the intramolecular example in Scheme 32a. Firstly, the hydrogen-bonded complex **211** that forms is proposed to involve the alkoxy group rather than the N–H bond that is usually invoked. Then, upon photoexcitation, Dexter energy transfer to the maleimide is dominant to generate ^{3}maleimide rather than energy transfer to the quinolone. While some maleimide dimerisation is observed, which supports the presence of triplet maleimide, a rapid cycloaddition occurs with the now ground-state hydrogen-bonded quinolone–iridium com-

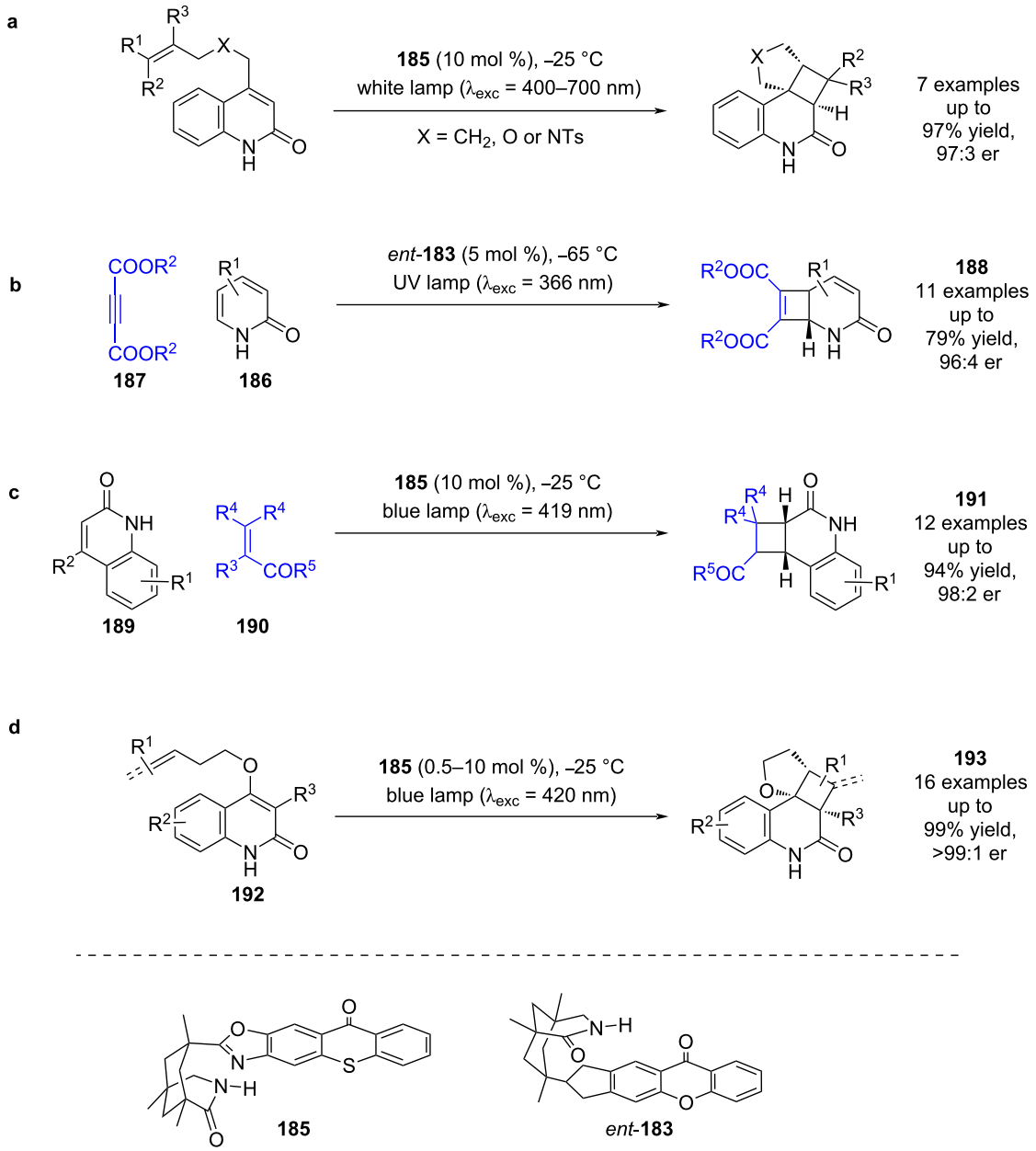

Scheme 28: Bifunctional hydrogen bonding/photocatalysed [2 + 2] photocycloaddition reactions. (a) First use of the thioxanthone-based bifunctional catalyst for an intramolecular cycloaddition. (b) Intermolecular cycloaddition of pyridines and acetylenedicarboxylates using a xanthone-based photocatalyst. (c) Intermolecular cycloaddition of quinolones with electron-deficient alkenes using a thioxanthone-based photocatalyst. (d) Intramolecular cycloaddition of quinolones with attached alkenes or allenes using a thioxanthone-based photocatalyst.

plex within the solvent cage pair **212** to give complex **213**. Subsequent displacement by another substrate molecule releases the desired products **214** in excellent yields and enantioselectivities (20 examples, up to >99:1 er), with a quantum yield of 0.013.

While there has been significant progress using bifunctional catalysts, dual catalytic systems can offer other modes of reactivity. For instance, Jiang et al. developed a urea-catalysed formal arylation of benzofuranones **215**, using naphthoquinones **216** to afford enantioenriched benzofuranones **217** (Scheme 33) [93]. They then expanded the scope of the naphthoquinone by coupling this reaction with a photocatalysed oxidation of naphthols **218** to generate **216** in situ. While no detailed mechanism has been proposed, based on prior work of Hawkins et al. [94] it is suggested that this reaction uses $^1O_2$

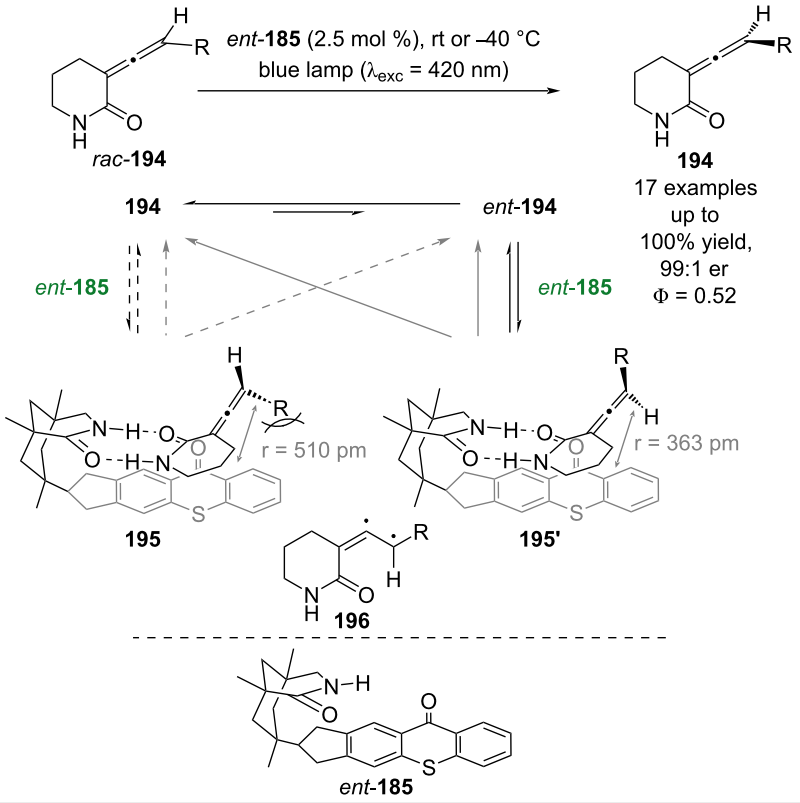

Scheme 29: Bifunctional hydrogen bonding/photocatalysed deracemisation of allenes.

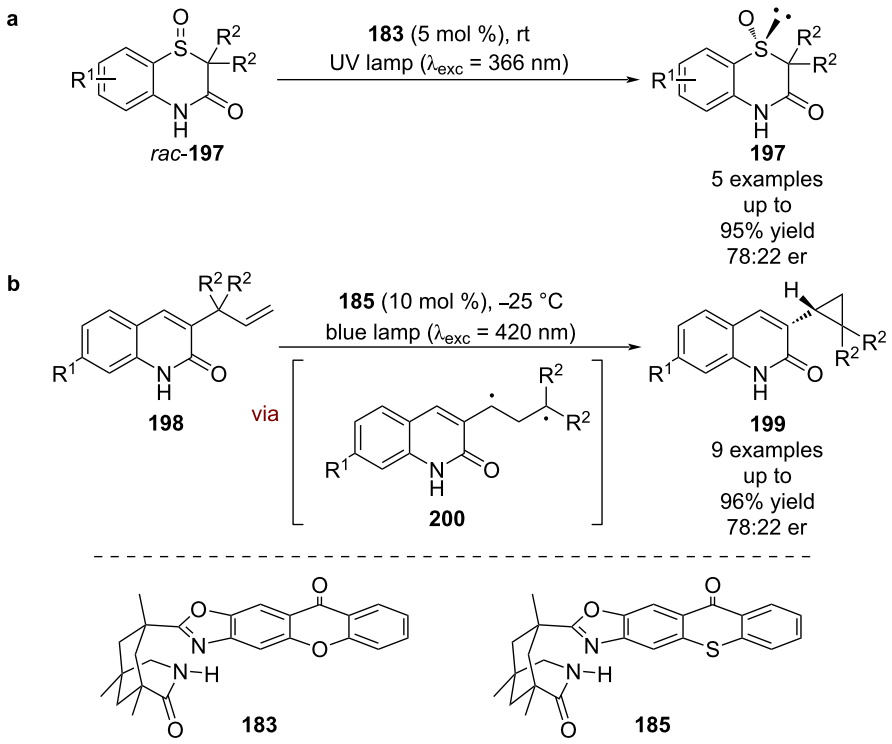

Scheme 30: Bifunctional hydrogen bonding/photocatalysed deracemisation reactions. (a) Deracemisation of sulfoxides. (b) Photochemical rearrangement followed by photocatalysed deracemisation of the resulting cyclopropane products.

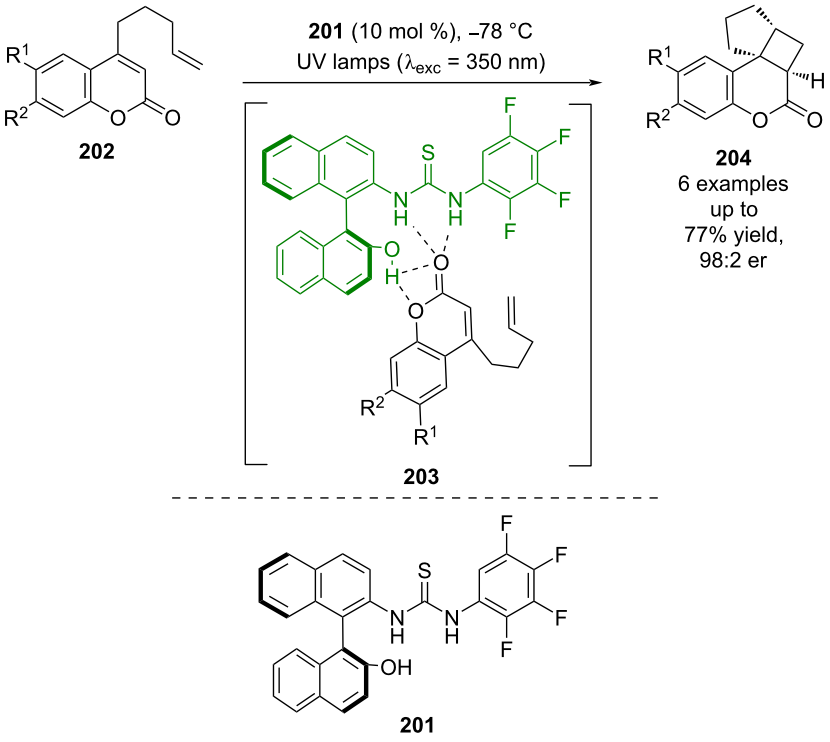

Scheme 31: Bifunctional hydrogen bonding/photocatalysed intramolecular [2 + 2] photocycloaddition of coumarins.

for the oxidation, and proceeds through transition state **219**‡ for the hydrogen-bonded catalysed nucleophilic addition step.

Jiang et al. recently applied a similar dual catalytic system to the dehalogenative protonation of α,α-chlorofluoro ketones **222** (Scheme 34) [95]. A reductive quenching cycle is proposed using tetrahydroquinoxaline **223** as a sacrificial reductant to generate $DPZ^{\bullet-}$, which then reduces the organocatalyst-bound substrate **224** to give α-carbonyl radical **224**•. Further reduction to the corresponding enolate and enantioselective protonation furnished the desired enantioenriched α-fluoroketones **225** in excellent yields and enantioselectivities (33 examples, up to >99:1 er).

Jiang et al. used a related system for the enantioselective reduction of 1,2-diketones **227** (Scheme 35a) [96]. In this case the catalyst **228** is proposed to form hydrogen-bonded complex **229**. THIQ **230** is used as a sacrificial reductant to generate $DPZ^{\bullet-}$, which reduces **229** to give radical anion intermediate **229**$^{\bullet-}$. Further reduction by **230** results in carbanion **229**$^{-}$, which is protonated enantioselectively to give the desired α-hydroxy ketones **231** in excellent yields and enantioselectivities (16 examples, up to 99:1 er). Within the same publication Jiang et al. expands this reactivity to activated imines **232**, using slightly modified conditions to obtain α-amino ketones **233** in excellent yields and good enantioselectivities (10 examples, up to 95:5 er) (Scheme 35b). It is also worth noting that this reaction works in the absence of DPZ (albeit with lower enantioselectivities for some examples), which is proposed to be due to the formation of an EDA complex between **230** and **229**.

CPAs were shown to be excellent partners for dual photoredox catalysis in the section "Brønsted acid catalysis", yet interestingly their conjugate bases can also be used as efficient hydrogen bonding catalysts. Knowles et al. showed that a tricatalytic system using chiral phosphate **235** can mediate the deracemisation of cyclic urea *rac*-**236** (Scheme 36) [97]. The proposed mechanism involves a reversible reductive quenching step to give two enantiomeric radical cations **236**$^{\bullet+}$ and *ent*-**236**$^{\bullet+}$. The acidified adjacent proton can then be abstracted by a base to give the racemic radical **236**•, which then undergoes HAT with a thiol HAT catalyst to complete the racemisation. If an appropriate chiral base is used, then *ent*-**236**$^{\bullet+}$ can be deprotonated, and therefore racemised faster than **236**$^{\bullet+}$, leading to a build-up of one enantiomer. This process initially achieved an er of 86:14, but with the inclusion of a complementary chiral HAT catalyst **237** and a radical scavenger (Ph_3CH), the er could be improved to 96:4.

Recently, Knowles et al. used a similar tricatalytic system for the enantioselective cyclisation of sulfonamides **238**

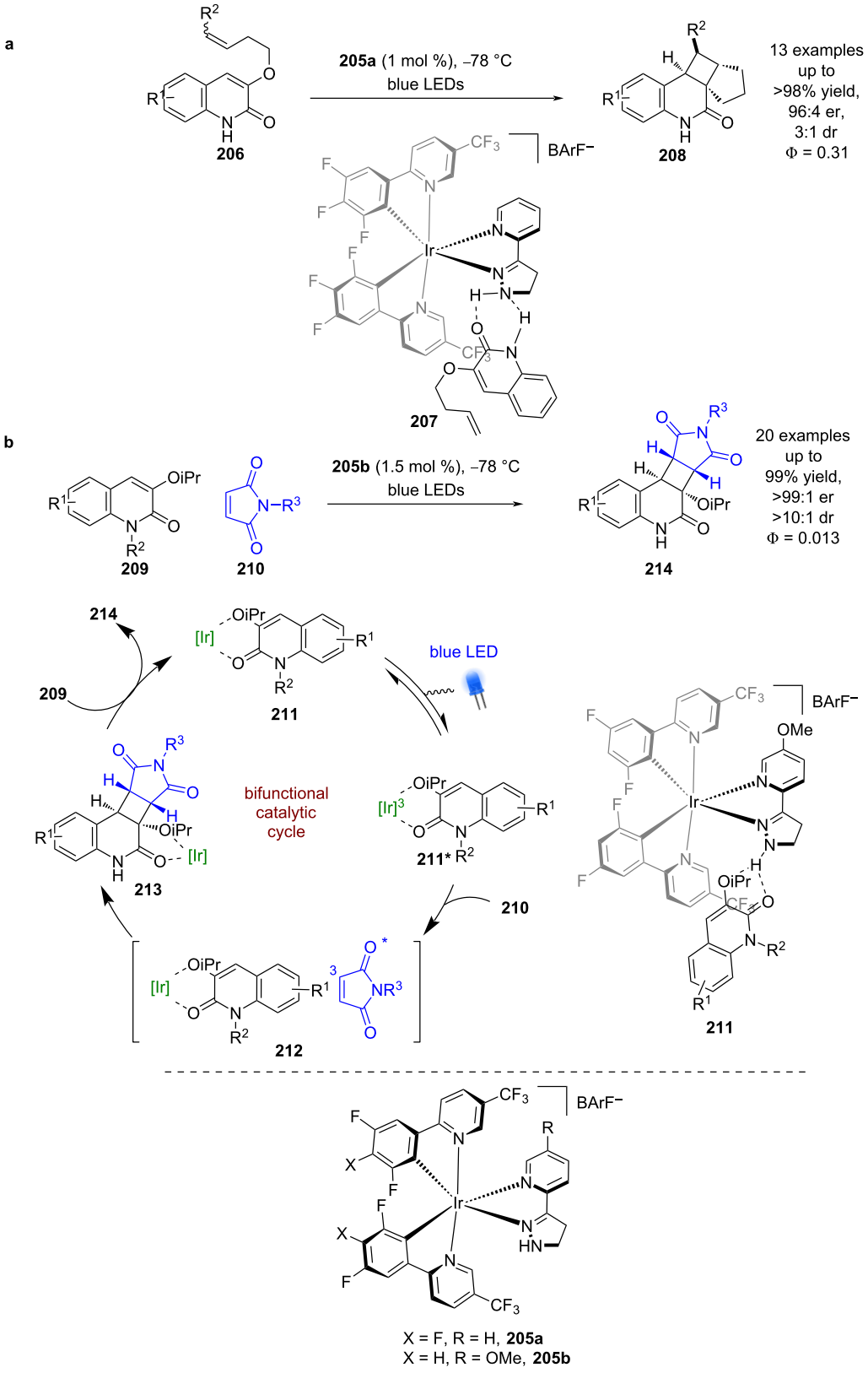

Scheme 32: Bifunctional hydrogen bonding/photocatalysed [2 + 2] photocycloadditions of quinolones. (a) Intramolecular cycloaddition of quinolones. (b) Intermolecular cycloaddition of quinolones and maleimides.

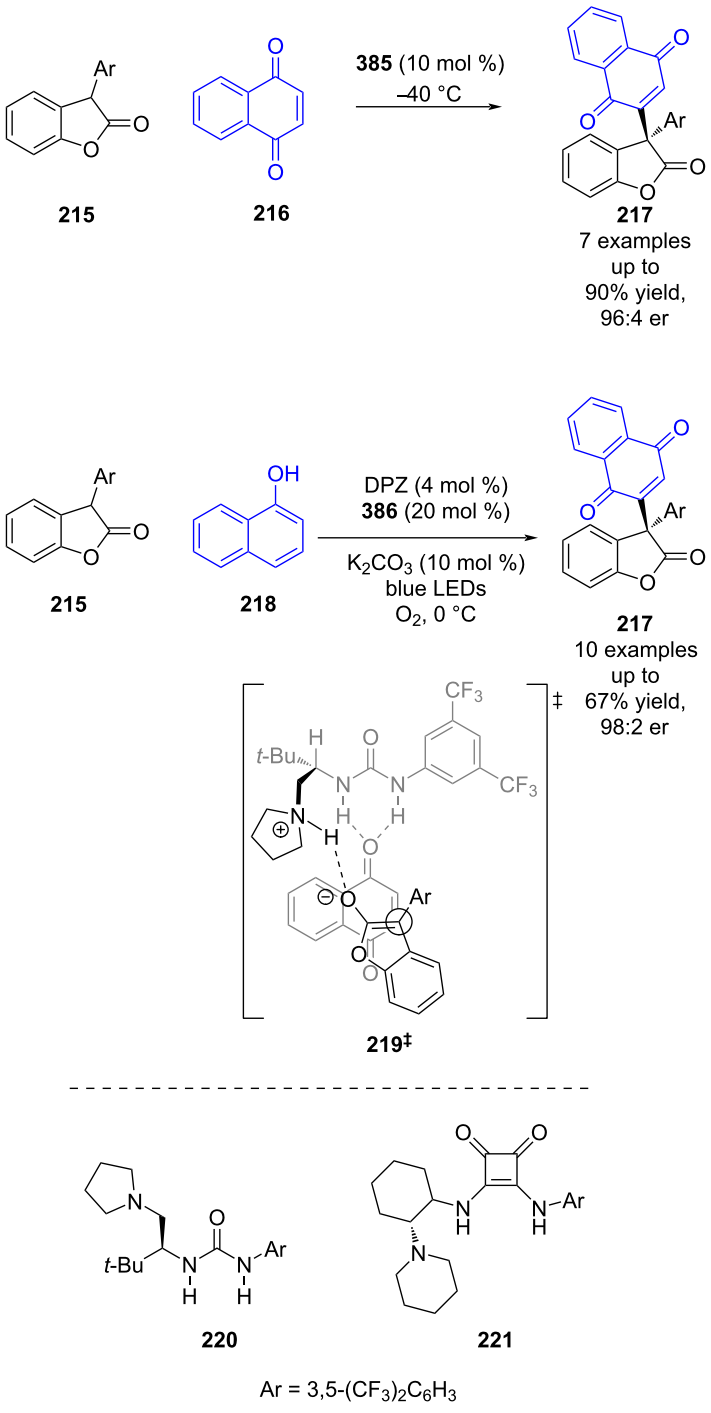

Scheme 33: Hydrogen bonding/photocatalysed formal arylation of benzofuranones.

(Scheme 37) [98]. In this case, the proposed mechanism involves a PCET step to give an *N*-centred radical that then cyclises enantioselectively to give the alkyl radical intermediate **239•**, which abstracts a hydrogen atom from TRIP-thiol to produce enantioenriched cyclic sulfonamides **239** in excellent yields and enantioselectivities (28 examples, up to 98:2 er).

Chiral phosphates have also been used to catalyse the enantioselective nucleophilic addition of indoles **241** to imines, which are

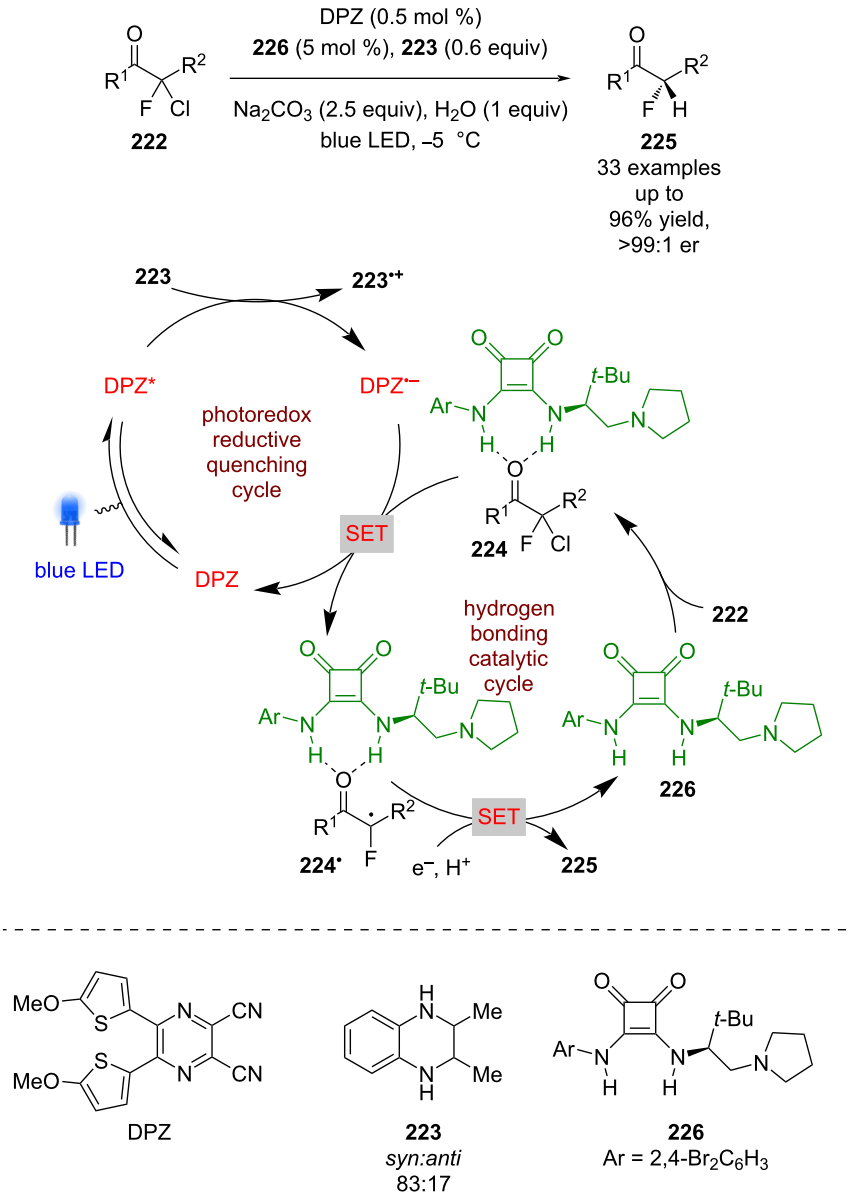

Scheme 34: Hydrogen bonding/photoredox-catalysed dehalogenative protonation of α,α-chlorofluoro ketones.

photocatalytically generated in situ from redox-active esters **242** (Scheme 38) [99]. The mechanism advanced by Wang et al. proposes that **241** acts as a sacrificial reductant to generate the reduced photocatalyst, which can then reduce **242** in a second SET step to give α-amino radical **242•** after decarboxylation. The excited photocatalyst is reductively quenched by **242•** to give the imine intermediate **243**. Indoles **241** and **243** are then brought together by the chiral phosphate catalyst **244** and the lithium counterion in a hydrogen-bonded complex **245** to give the desired enantioenriched products **246** in excellent yields and enantioselectivities (30 examples, up to 99:1 er).

Ion pair

Ion pair catalysis has interesting potential in combination with photoredox catalysis considering that the catalytic intermediates are often radical cations or anions. Despite this, there are relatively few examples of this dual catalytic mode. Ooi et al. reported an enantioselective synthesis of 1,2 diamines **247** from tertiary amines **248** and aldimines **249** (Scheme 39) [100]. The proposed mechanism involves a reductive quenching pathway with **248** to produce radical cations **248•+**, which following deprotonation and a [1,2]-radical shift generates α-amino radicals **248•**. Simultaneously, **249** is reduced by the reduced photocata-

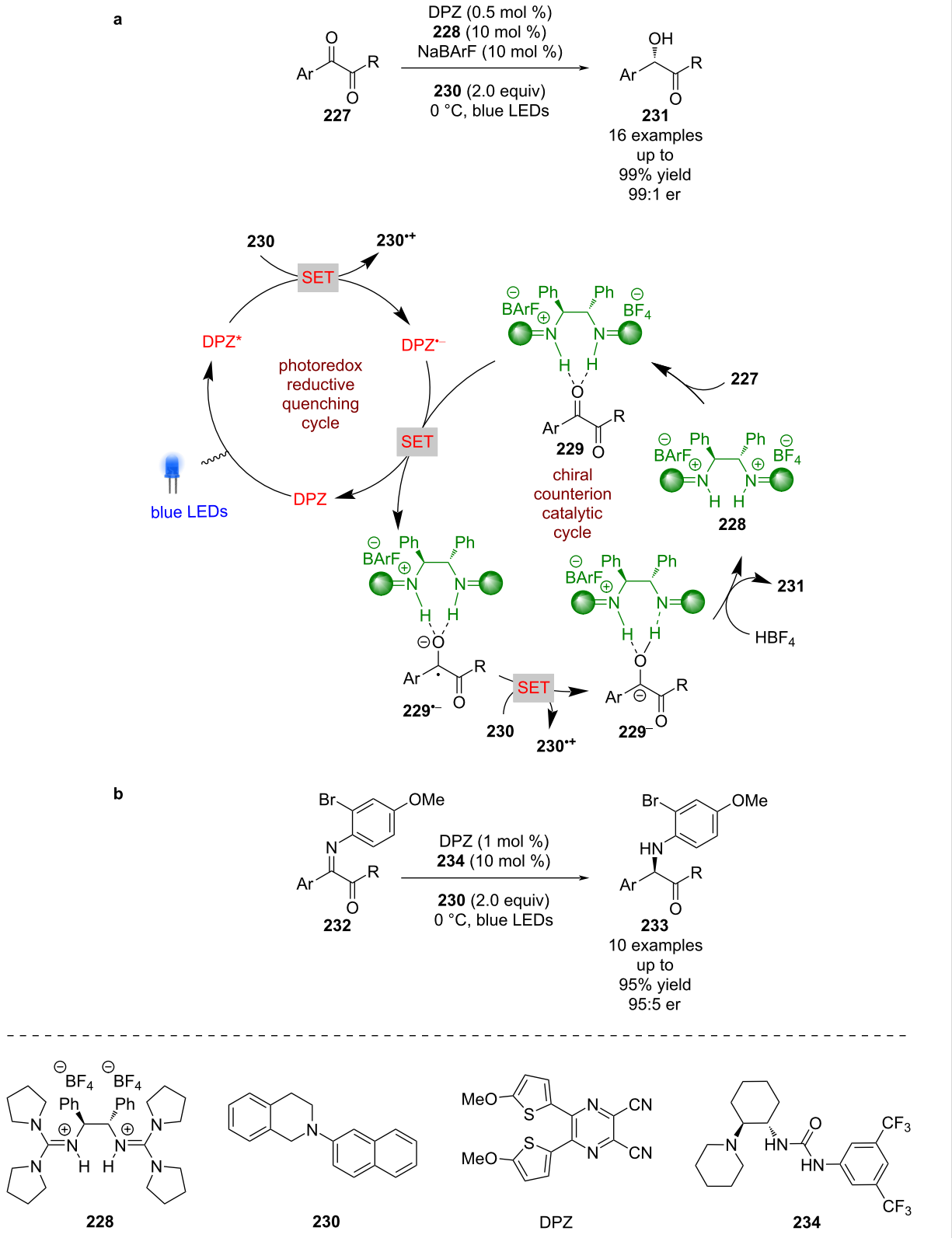

Scheme 35: Hydrogen bonding/photoredox-catalysed reductions. (a) Reduction of 1,2-diketones. (b) Reduction of imines.

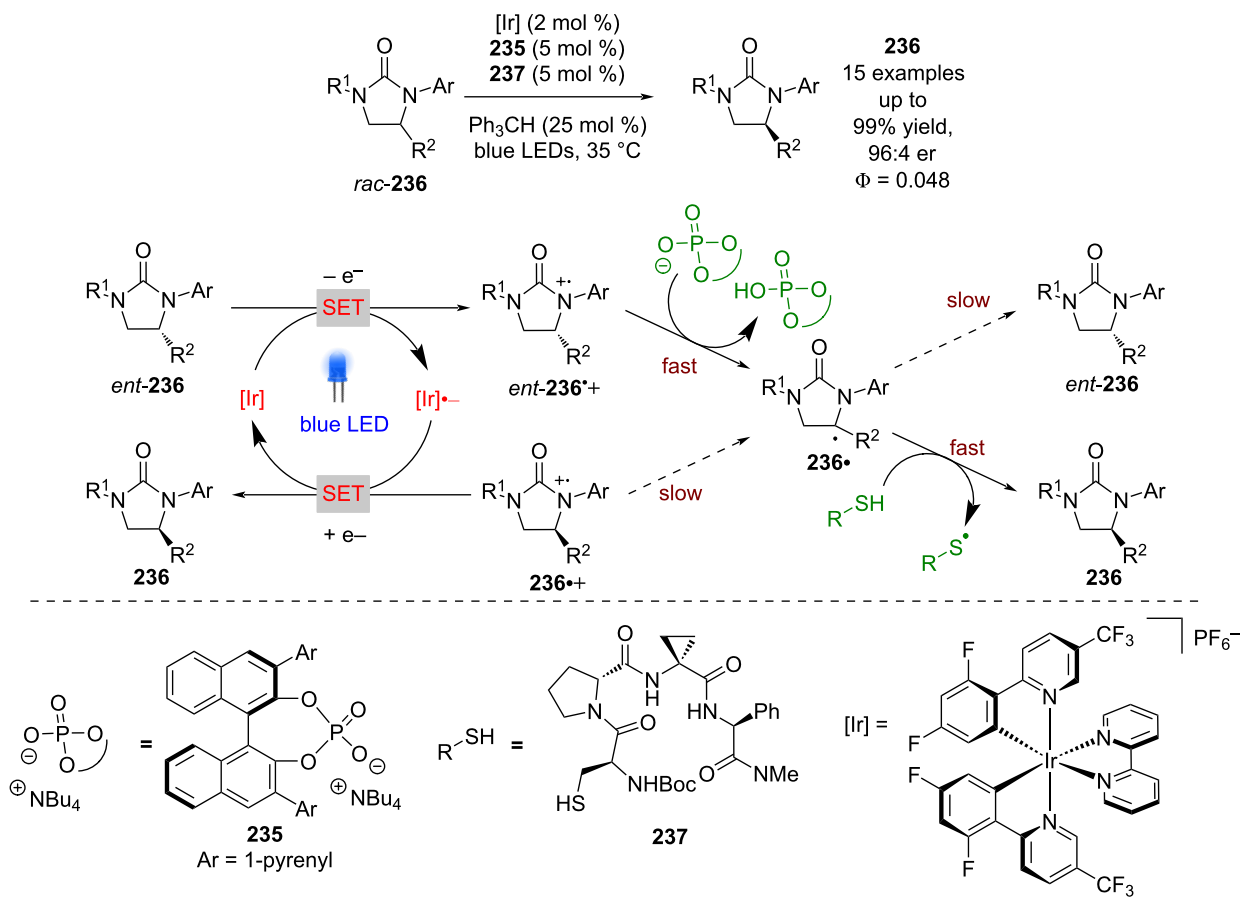

Scheme 36: Hydrogen bonding/HAT/photocatalysed deracemisation of cyclic ureas.

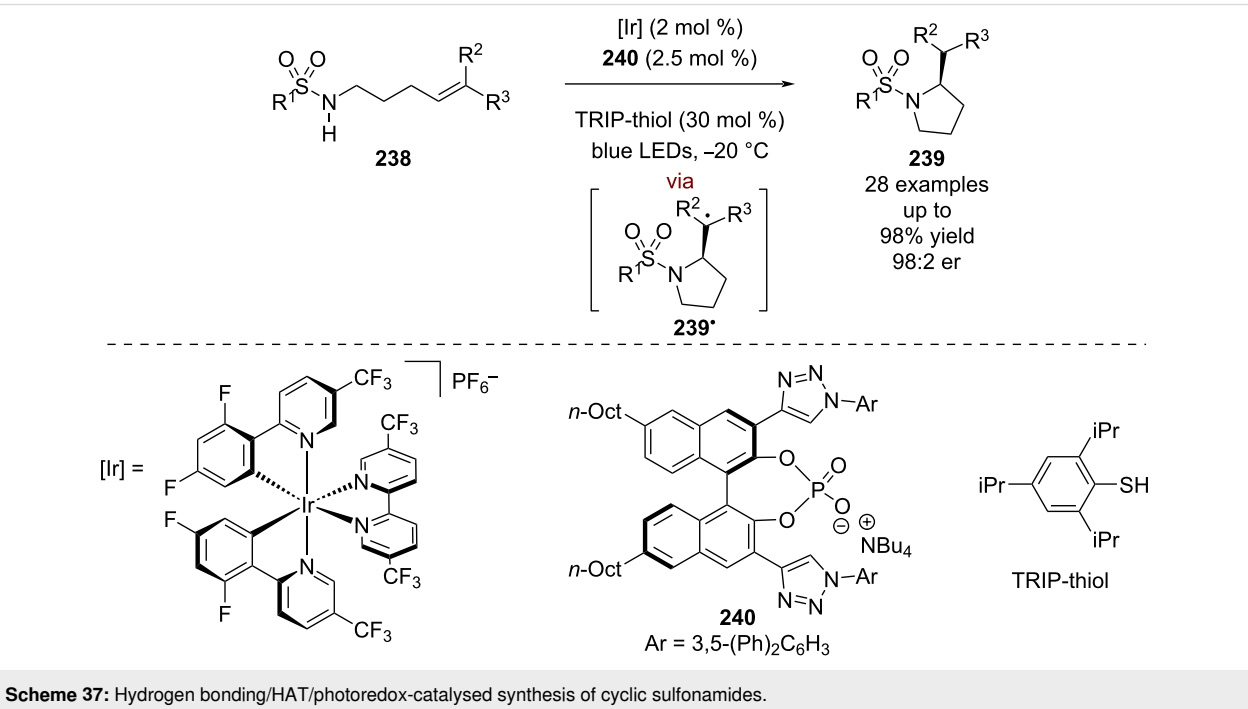

Scheme 37: Hydrogen bonding/HAT/photoredox-catalysed synthesis of cyclic sulfonamides.

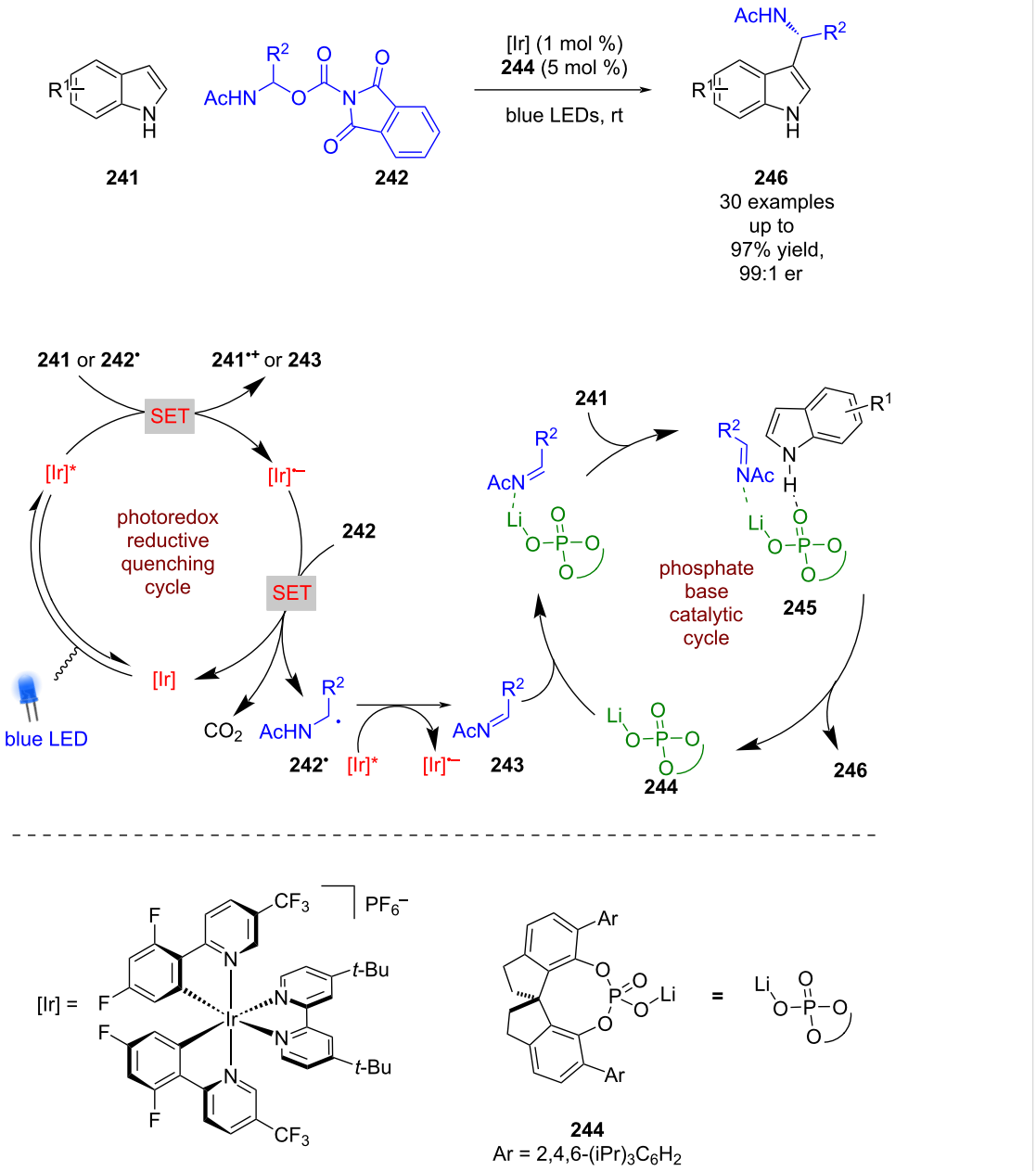

Scheme 38: Hydrogen bonding/photoredox-catalysed reaction between imines and indoles.

lyst to give radical anion **249**$^{\bullet-}$ that can then undergo a cation exchange with chiral cationic acid **250** and form a chiral ion pair **251**. The two radical species then couple enantioselectively within the chiral environment, producing **247** in excellent yields and enantioselectivities (17 examples, up to 99:1 er). The authors noted that they cannot rule out the alternative mechanism whereby a radical addition of **248**$^{\bullet}$ to an acid coordinated **249** is followed by a single electron reduction of the resulting *N*-centred radical.

The previous example used a chiral cation to induce enantioselectivity, while Luo et al. used a chiral phosphate base **251** as a counterion to Mes-Acr^{+} (Scheme 40) [101]. With this combination, they successfully developed an enantioselective variant of Nicewicz's hydroetherification reaction of alkenols **252** [102]. The proposed mechanism proceeds through a reductive quenching cycle that generates chiral ion pair **253**. Subsequent enantioselective cyclisation gives tertiary alkyl radical **254**$^{\bullet}$, which can abstract a hydrogen atom from 2-phenylmalonitrile

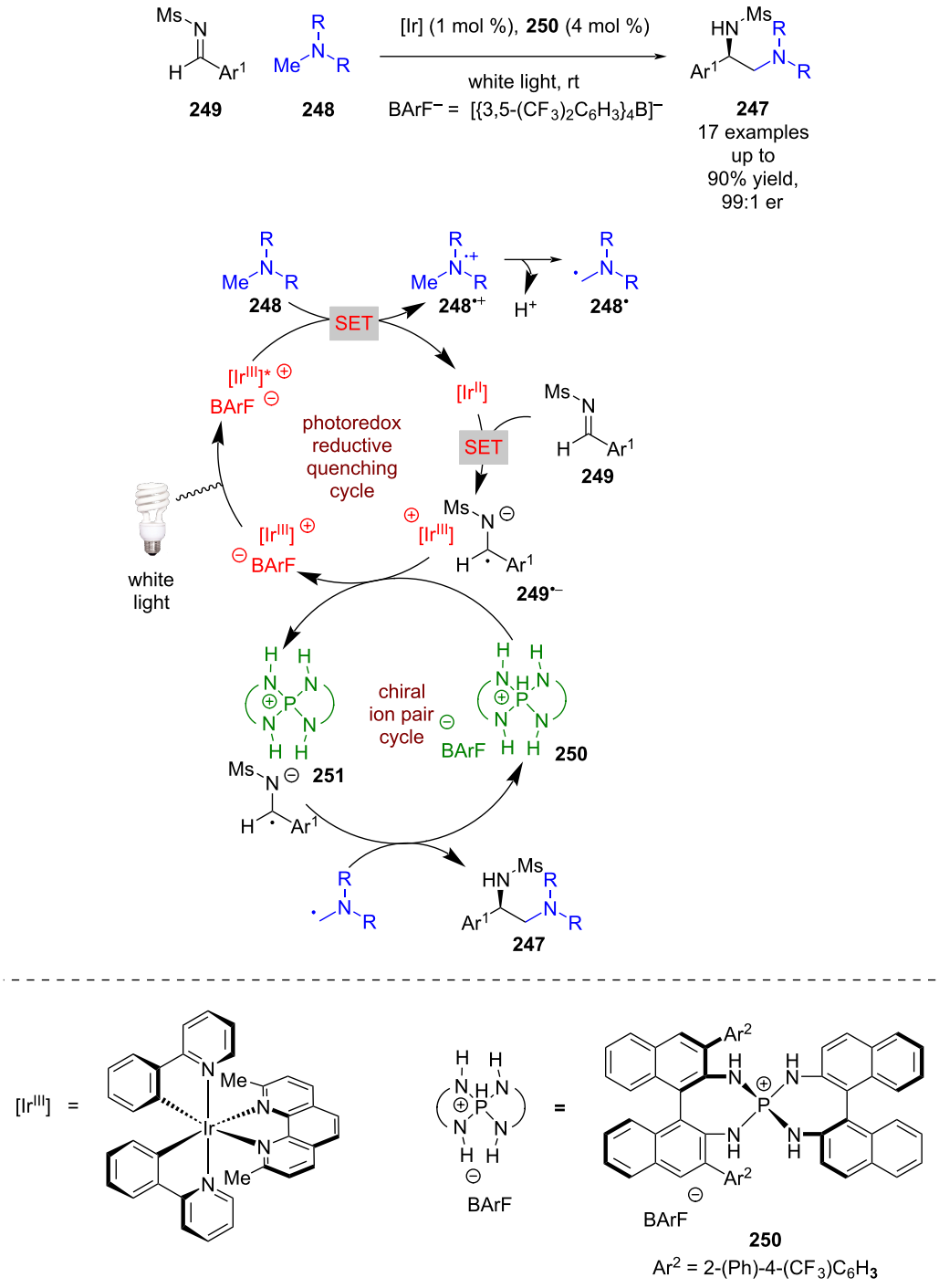

Scheme 39: Chiral cation/photoredox-catalysed radical coupling of two α-amino radicals.

(**255**) to afford the desired enantioenriched tetrahydrofuran **256** in excellent yields and moderate enantioselectivities (14 examples, up to 82:18 er).

Knowles et al. synthesised enantioenriched pyrroloindolines **257** from indoles **258** and TEMPO using an iridium-based photocatalyst and a similar chiral phosphate base **259** to that employed by Luo et al. (Scheme 41) [103]. The proposed mechanism implicates an oxidative quenching cycle using a sacrificial oxidant (TIPS-EBX), followed by a PCET step with hydrogen-bonded complex **260** to give chiral ion pair **260•**, which completes the photocatalytic cycle. Subsequent enantioselec-

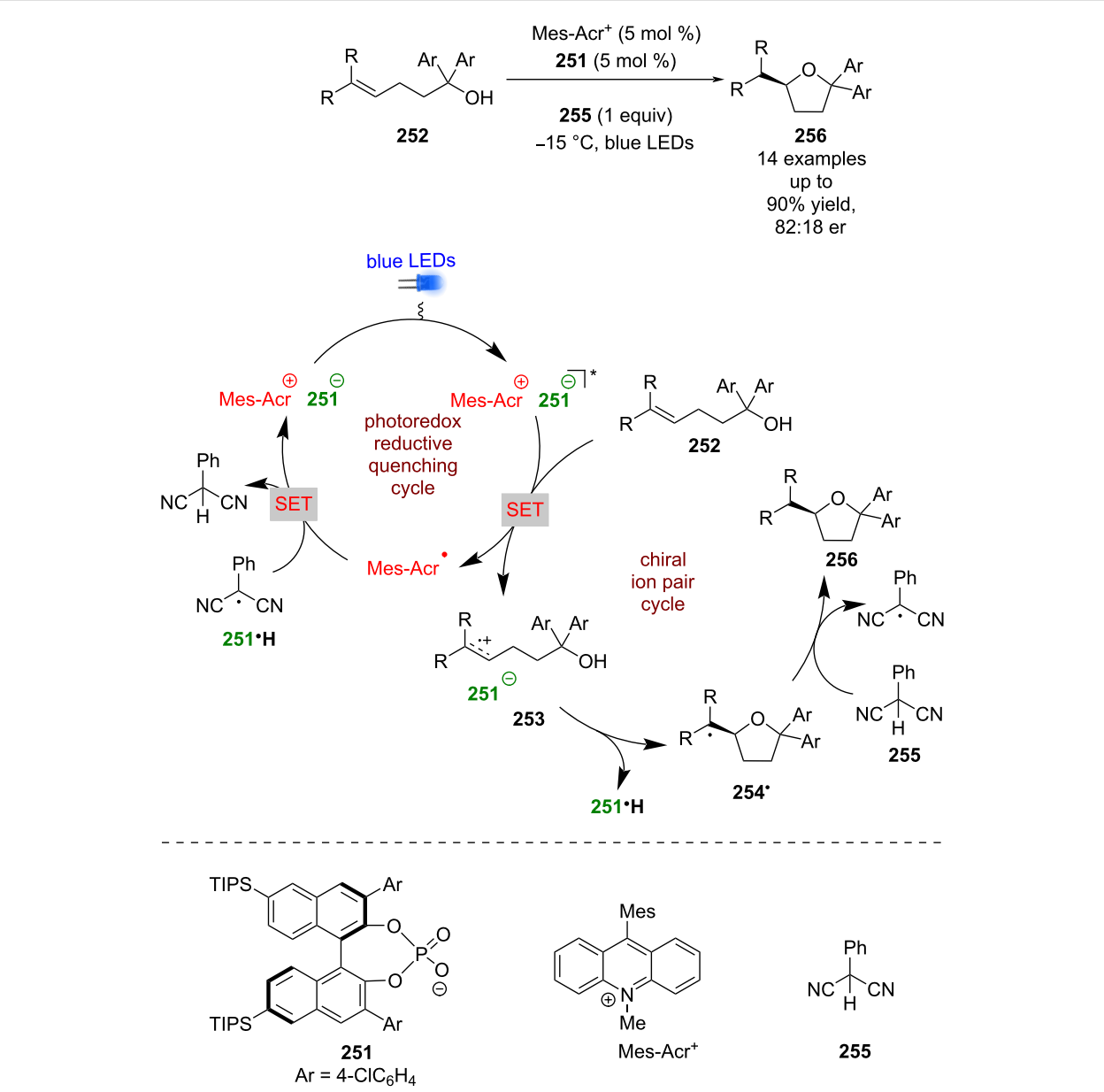

Scheme 40: Chiral phosphate/photoredox-catalysed hydroetherfication of alkenols.

tive radical coupling with TEMPO gives catalyst-bound iminium ion **261**, which then cyclises with the nearby amine to produce the desired product **257** in good yields and enantioselectivities (9 examples, up to 97:3 er).

Nicewicz et al. developed an enantioselective radical cation Diels–Alder reaction in both an intramolecular fashion, using alkenes **262**, and an intermolecular fashion, using alkene **263** and cyclopentadiene **264** (Scheme 42) [104]. Using a similar strategy to Luo et al., Nicewicz et al. uses a preformed chiral photocatalyst composed of a cationic triaryl pyrillium, TP, twinned with a chiral counterion **265**. With an electron-rich alkene, the reaction is proposed to proceed via a reductive quenching cycle to generate chiral ion pair $\mathbf{262}^{\bullet+}$ and $\mathrm{TP}^{\bullet}$. Subsequent enantioselective cycloaddition with a diene results in ion pair $\mathbf{266}^{\bullet+}$, which is then reduced by $\mathrm{TP}^{\bullet}$ to complete the catalytic cycle and affords the desired products **267** or **268** in moderate yields and enantioselectivities (3 examples, up to 75:25 er for **267** and 2 examples, up to 68:32 er for **268**).

Lewis acid catalysis

Lewis acids have been known for decades to activate carbonyl compounds through the formation of coordination complexes that increases carbonyl electrophilicity [105]. The use of chiral

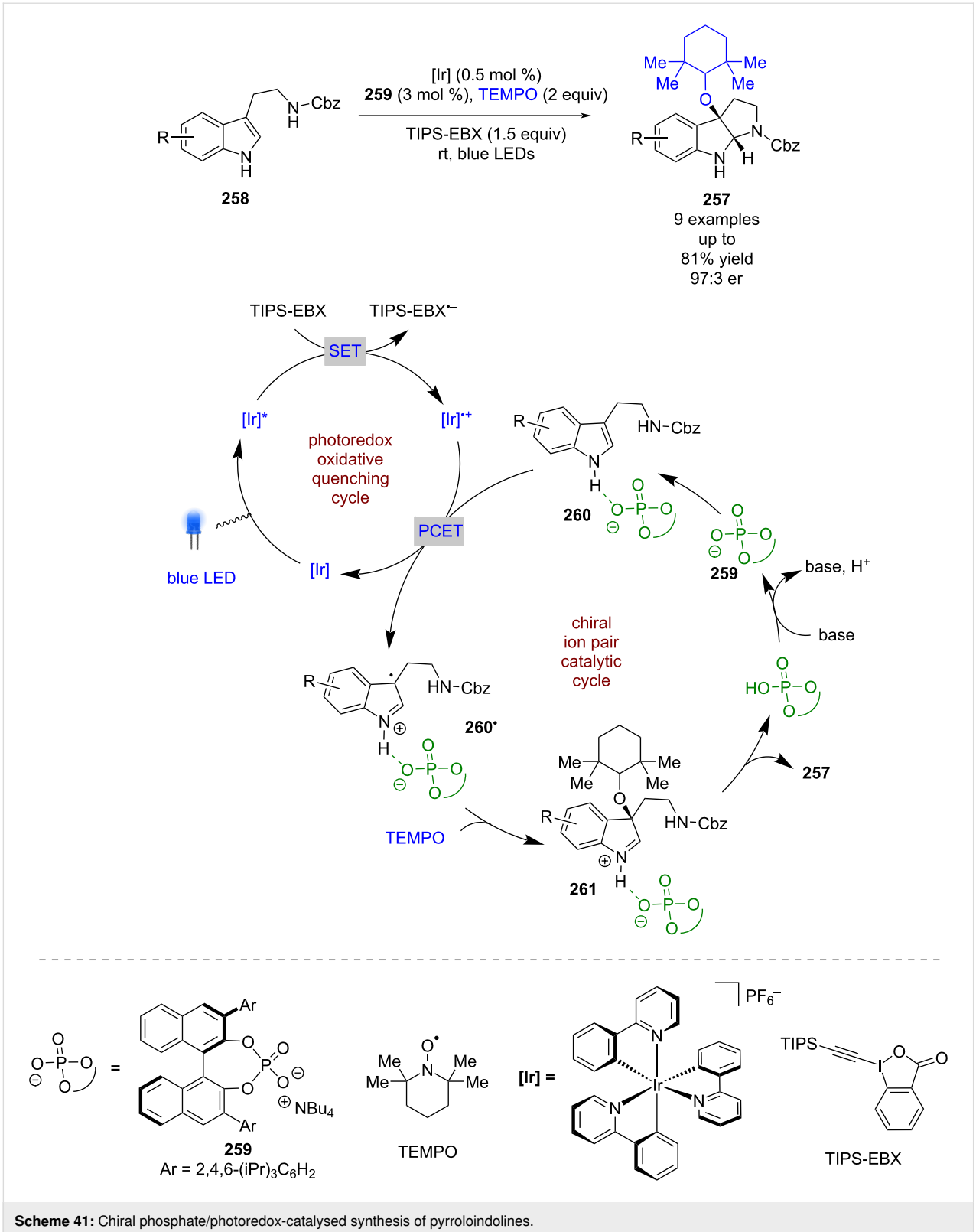

Scheme 41: Chiral phosphate/photoredox-catalysed synthesis of pyrroloindolines.

Lewis acids can induce asymmetry [106]. Yoon et al. applied this well-known form of catalysis to a photocatalytic system using enones **269** and **270** (Scheme 43a) [107]. Mechanistic studies of a closely related achiral reaction [20], showed this reaction likely operates via a radical chain mechanism. Initiation begins with the reductive quenching of the photocatalyst

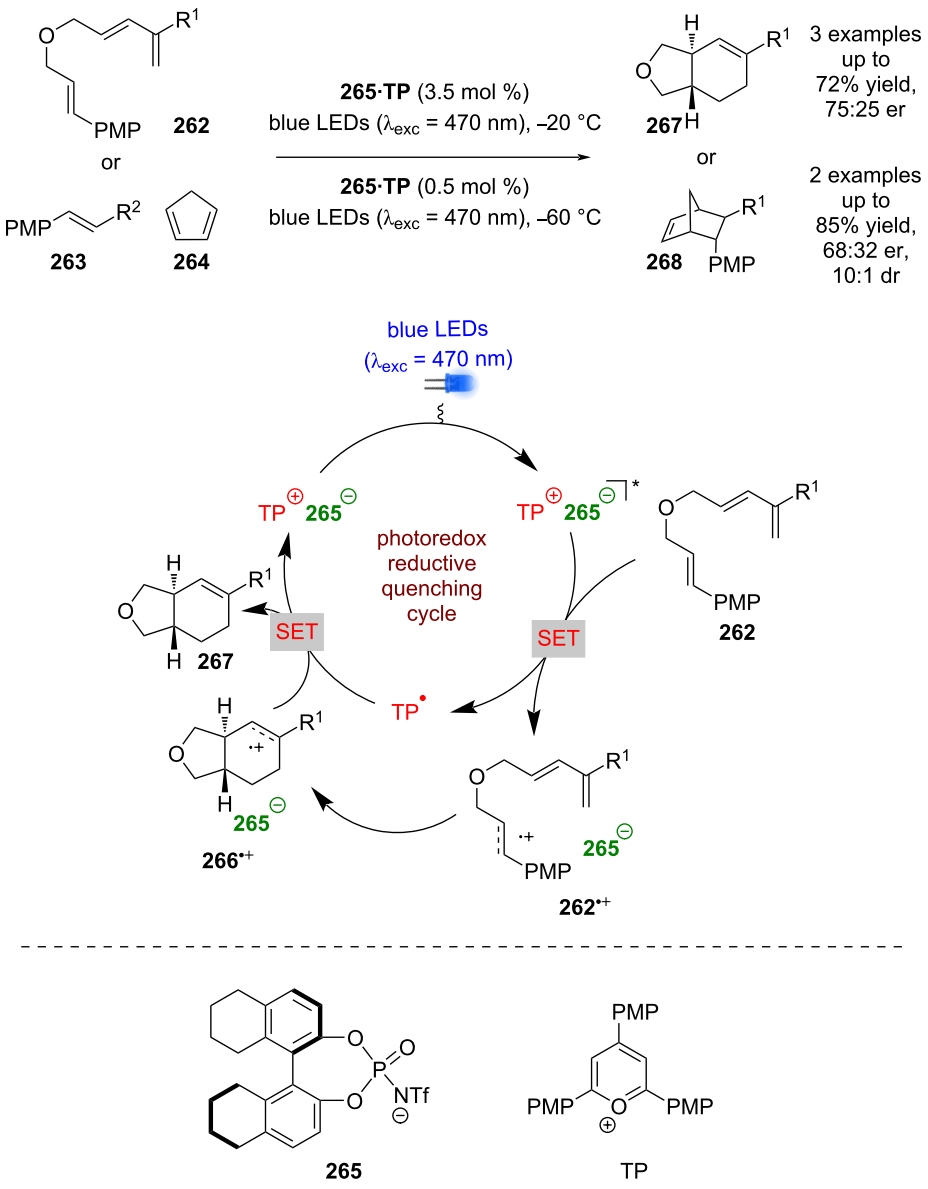

Scheme 42: Chiral anion/photoredox-catalysed radical cation Diels–Alder reaction.

using iPr_2NEt as a sacrificial reductant to give $[Ru]^{\bullet-}$, which then reduces the Lewis acid-coordinated enone **271** to give alkyl radical **271**•. In the presence of a second enone **270** and chiral ligands **L1**, an initial RCA occurs to generate α-carbonyl radical **272**•, followed by cyclisation with the enolate to give ketyl radical **273**•. Radical **273**• can then reduce another molecule of **271** to propagate the chain reaction and generate the desired formal photocycloaddition products **274** in good yields and enantioselectivities (12 examples, up to 97:3 er). Yoon et al. later expanded the scope of this reaction to cyclopropyl ketones **275** for the synthesis of formal [3 + 2] cycloaddition products **276** in excellent yields and enantioselectivities (21 examples, up to >99:1 er), this time using a gadolinium catalyst and chiral ligand **L2** (Scheme 43b) [108].

By altering the radical precursor to α-silyl amines **277** and using α,β-unsaturated amides **278**, Yoon et al. found that the reactions could be stopped at the RCA step to give enantioenriched 1,4-addition products **279** using a scandium catalyst and chiral ligand **L3** (Scheme 44a) [109]. The putative mechanism proceeds via a reductive quenching cycle to give nucleophilic α-amino radicals **277**•, which can add to the β-position of Lewis acid complex **280** to give the α-carbonyl radical **280**•. Instead of a cyclisation, this radical is then reduced by the reduced photo-

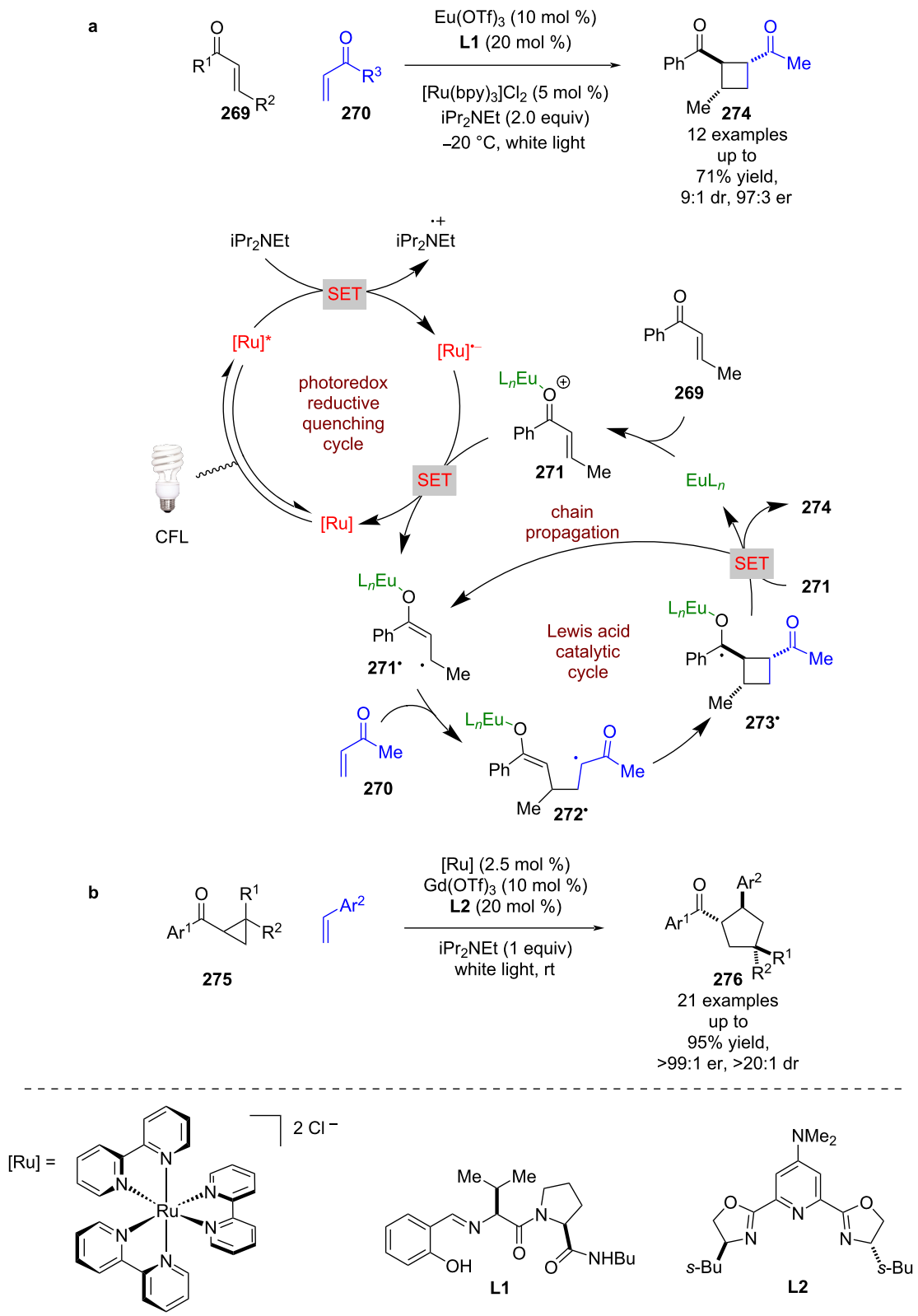

Scheme 43: Lewis acid/photoredox-catalysed cycloadditions of carbonyls. (a) Formal [2 + 2] cycloaddition of enones using europium Lewis acid. (b) Formal [3 + 2] cycloaddition of cyclopropyl ketones with styrenes using a gadolinium Lewis acid catalyst.

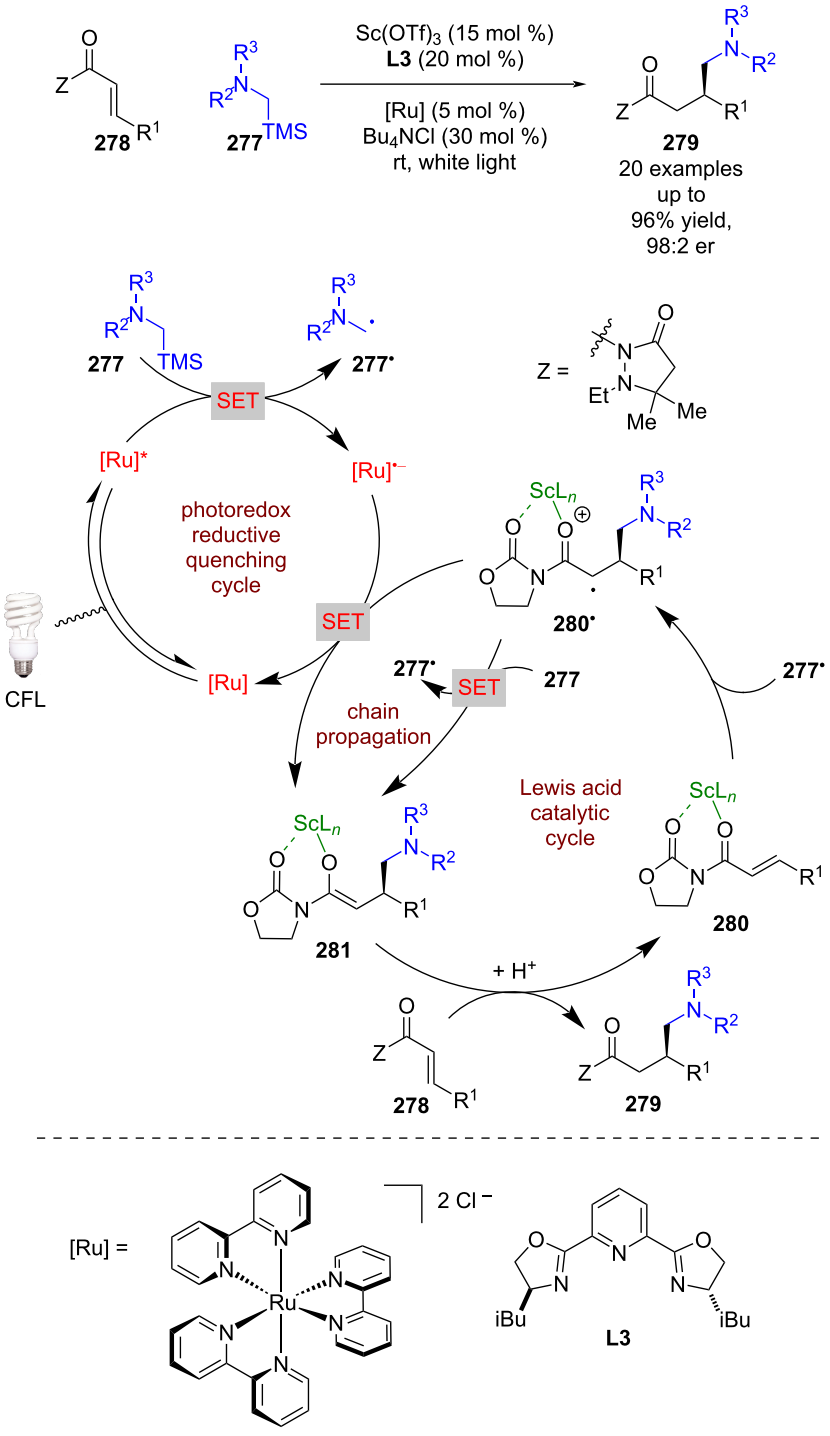

Scheme 44: Lewis acid/photoredox-catalysed RCA reaction using a scandium Lewis acid between α-amino radicals and α,β-unsaturated amides containing an oxazolidinone auxiliary.

catalyst to give the corresponding enolate **281**, which is then protonated to produce **279**. Alternatively, **280•** could be reduced by another molecule of **277**, propagating a radical chain process, as was determined to be the case in a previously developed achiral reaction variant [110]. To improve complexation to the Lewis acid in RCA reactions, an auxiliary (Z) is required; this auxiliary can be easily removed and recovered.

Shibasaki and Kumagai very recently developed a similar reaction using a copper Lewis acid catalyst and a different auxiliary containing amide **282** with α-silyl amines **277** to synthesise the corresponding RCA products **283** in excellent yields and enantioselectivities (22 examples, up to >99:1 er) (Scheme 45) [111].

Huang et al. applied a similar catalytic system to that reported by Yoon et al. to a different radical addition reaction between nitrones **284** and aldehydes **285** (Scheme 46) [112]. The proposed mechanism involves a reductive quenching cycle using TEEDA as a sacrificial reductant to generate $[Ru]^{\bullet-}$. Simultaneously the chiral Lewis acid catalyst forms complex **286** with both starting materials. $[Ru]^{\bullet-}$ then reduces the activated aldehyde to give ketyl radical anion **286**$^{\bullet-}$, which adds to the nitrone via a proposed 6-membered transition state to afford radical cation **286**$^{\bullet+}$. Subsequent hydrogen atom abstraction from TEEDA$^{\bullet+}$ generates complex **286**$^{-}$. Protonation and displacement by other substrate molecules releases the desired 1,2-amino alcohol products **287** in excellent yields and enantioselectivities (27 examples, up to >99:1 er).

Yoon et al. have also shown that these types of Lewis acid complexes can be used in an energy transfer process for the [2 + 2] cycloaddition of enones **288** with alkenes **289** (Scheme 47) [113,114]. The triplet energy of **288**, when complexed to the scandium Lewis acid (E_T = 1.43 eV), is significantly lower relative to the unbound substrate (E_T = 2.34 eV). They propose that Lewis acid coordination permits discrimination between bound and unbound substrate as it allows for selective triplet sensitisation of the bound substrate by the excited state ruthenium photocatalyst. The subsequent enantioselective [2 + 2] photocycloaddition gives cyclobutane products **290** in excellent yields and enantioselectivities (43 examples, up to >99:1 er).

Meggers et al. has contributed significantly to the field of enantioselective photocatalysis, introducing unique transition metal Lewis acids **291a–e** that can coordinate to ketone substrates and form chiral photoactive complexes **292**, which in many cases act as the in situ generated photocatalyst (Scheme 48) [115]. They have recently developed an example using an indazole-based ligand [116] to add to their well-established benzoxazole and benzothiazole ligands. Such complexes have then been used for α-functionalisations [117], RCAs [118], and cycloaddition reactions [119]. As much of Meggers work has been summarised previously [120], here we will include only recent examples from each reaction class.

If an enolisable ketone **293** is used, enolate complex **294** can be formed in the presence of base (Scheme 49a) [116]. The complex in this example is then proposed to proceed via an oxidative quenching cycle with bromo nitrile **295** to form α-cyano radicals **295**$^{\bullet}$ that then add to another molecule of **294** enantioselectively to give ketyl radical **296**$^{\bullet}$. These radicals are then oxidised by the oxidised photocatalyst to generate the metal-bound α-functionalised product **297**, which can be displaced by

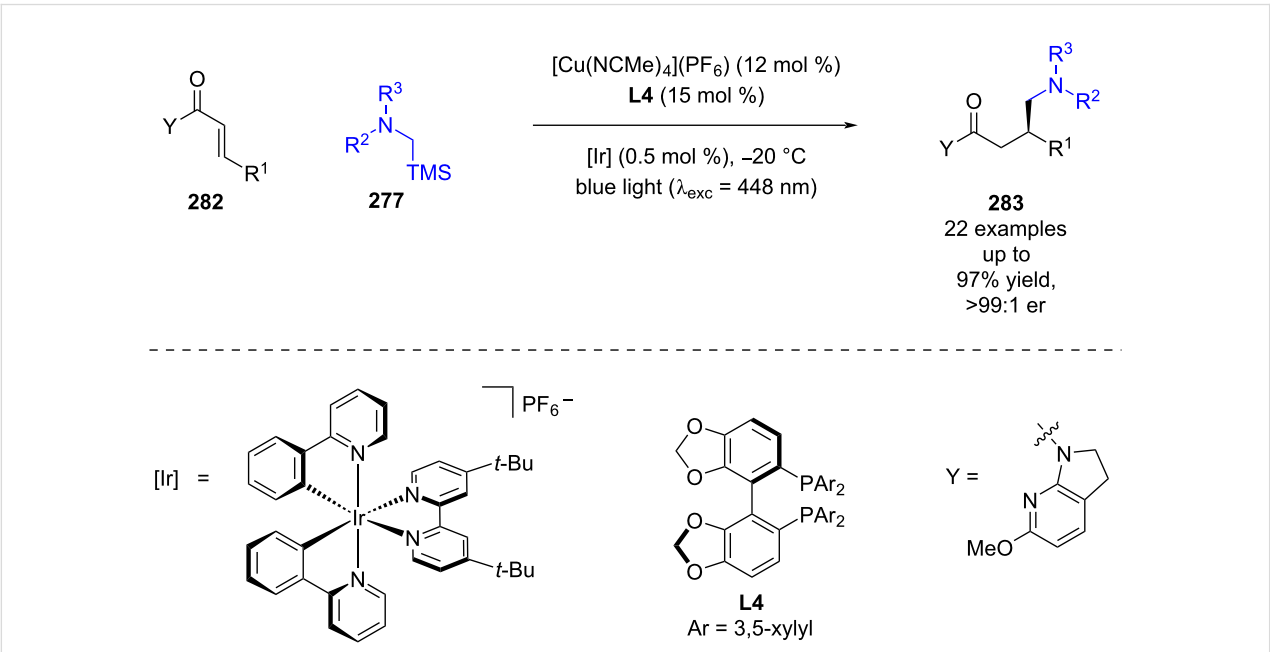

Scheme 45: Lewis acid/photoredox-catalysed RCA reaction using a copper Lewis acid between α-amino radicals and α,β-unsaturated amides containing an azaindoline auxiliary.

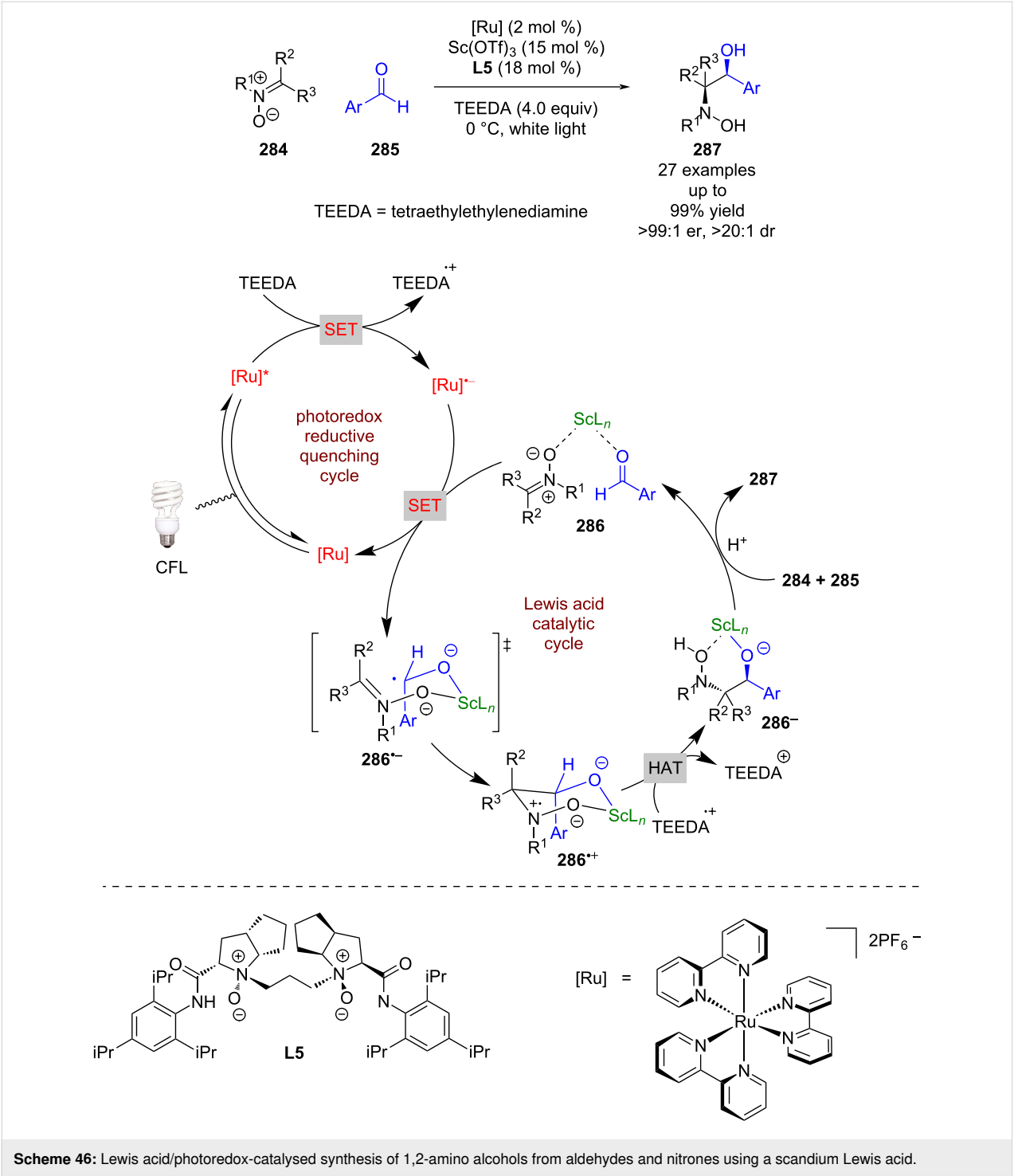

Scheme 46: Lewis acid/photoredox-catalysed synthesis of 1,2-amino alcohols from aldehydes and nitrones using a scandium Lewis acid.

another molecule of **293** to finish the catalytic cycle and furnish the desired product **298** in good yields and excellent enantioselectivities (11 examples, up to 98:2 er). While a chain propagation mechanism is possible, the quantum yield of the reaction is <1 (Φ = 0.046), so a closed cycle is likely the dominant mechanism in this case. Another recent example of this type of reactivity was developed by Xu et al. using amides **299** in a difluoroalkylation reaction; however, this reaction did require the use of an external photocatalyst (Scheme 49b) [121].

A limitation of this strategy is that only electrophilic radicals can be added to the nucleophilic enolate complex. Recently, Meggers showed that this type of reactivity can be reversed if an α-chloro ketone **301** is used with α-aminocarboxylic acids

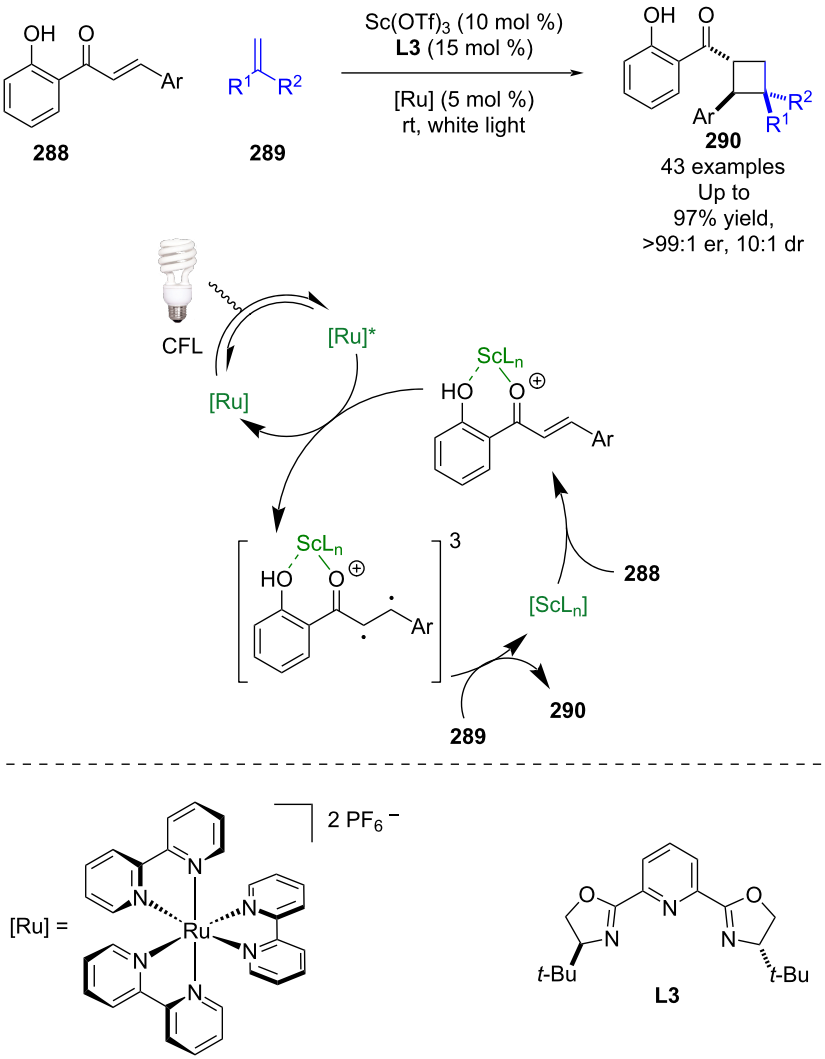

Scheme 47: Lewis acid/photocatalysed [2 + 2] photocycloadditions of enones and alkenes.

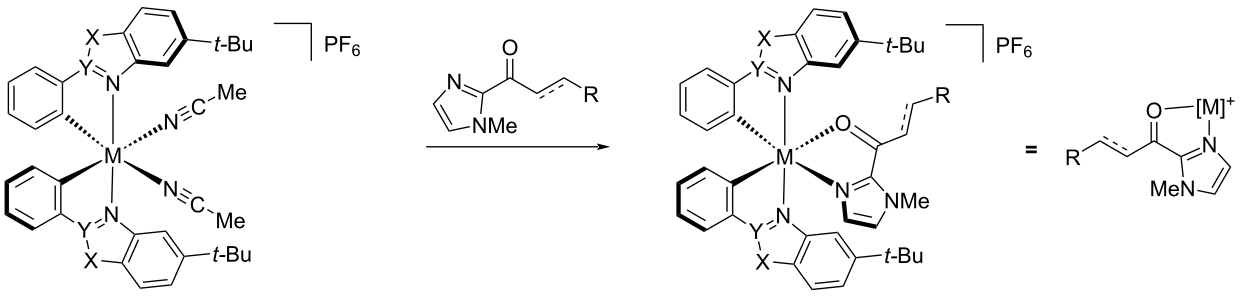

291a, M = Ir, X = O, Y = C
291b, M = Ir, X = S, Y = C
291c, M = Rh, X = O, Y = C
291d, M = Rh, X = S, Y = C
291e, M = Rh, X = C, Y = N

292

Scheme 48: Meggers's chiral-at-metal catalysts.

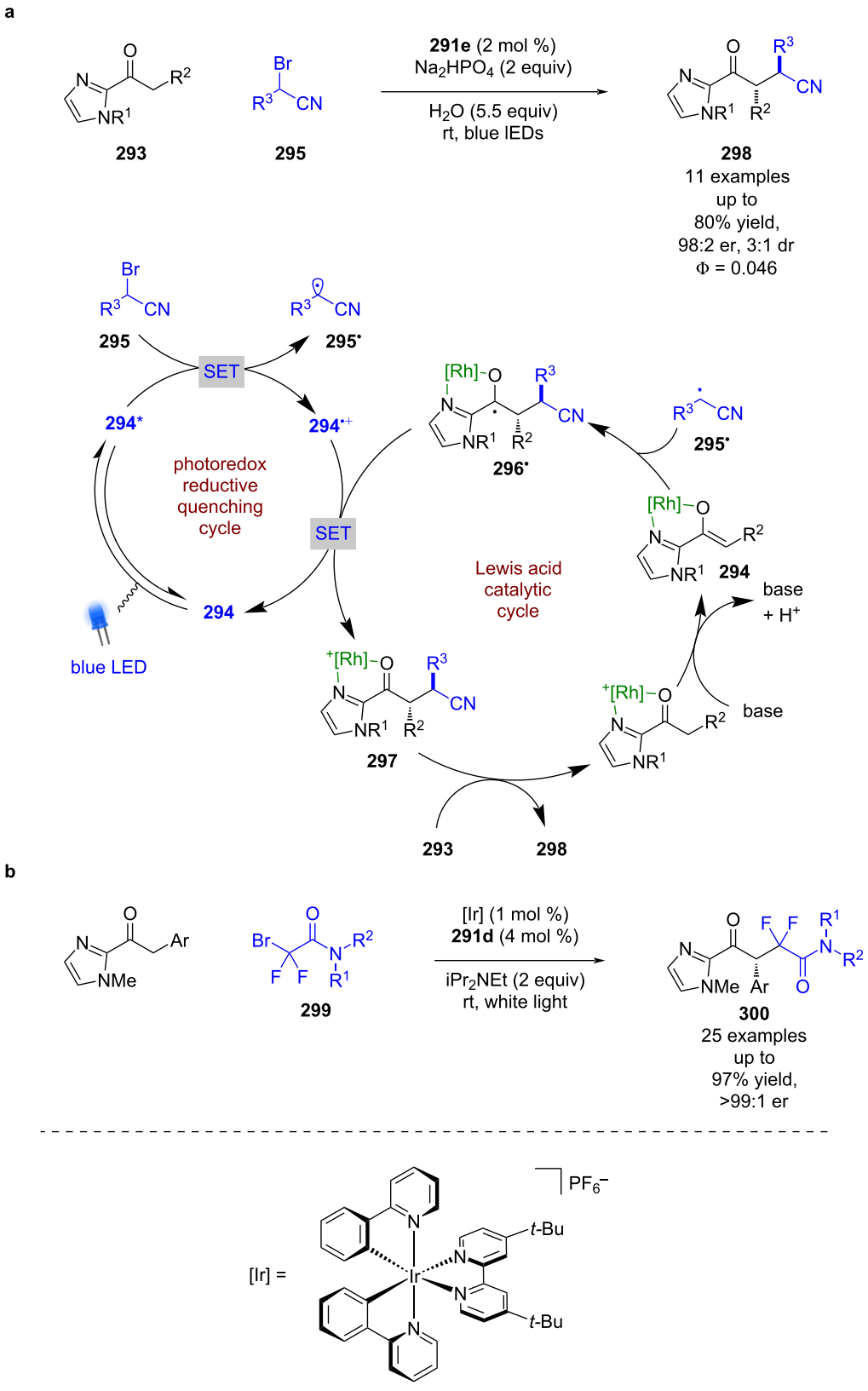

Scheme 49: Lewis acid/photoredox-catalysed α-functionalisation of ketones with alkyl bromides bearing electron-withdrawing groups. (a) Using bifunctional Lewis acid/photoredox catalyst. (b) Using a dual catalytic system.

302 (Scheme 50) [122]. In this reaction, **301** now forms coordination complex **303**, which upon excitation is proposed to initiate a SET with **302** to form an electrophilic α-carbonyl radical **303•** after loss of chloride, and a nucleophilic α-amino radical **302•** after decarboxylation. Enantioselective radical coupling gives the metal-bound product, which can be displaced by another molecule of **301** to complete the cycle and release ketone **304** in good yields and excellent enantioselectivities (16 examples, up to 99:1 er). In this case the quantum yield was measured to be <1 (Φ = 0.0027), which suggests that a chain mechanism is unlikely.

A recent example of these catalysts being used for RCAs exploited Eosin Y as an external HAT photocatalyst to generate acyl radicals **305•** from aldehydes **305**, which then add to the Lewis acid complex **306** enantioselectively to form α-carbonyl radicals **307•** (Scheme 51a) [118]. The reverse HAT step completes the photocatalytic cycle and produces the complexed RCA product **307**, which can be displaced by another substrate molecule **308** to finish the cycle and release the desired enantioenriched products **309** in moderate yields and excellent enantioselectivities (19 examples, up to >99:1 er). In the same work, Meggers et al. also used compounds **310a–g** as radical precursors, with a focus on 1,3-dioxolane **310c** as a formyl radical surrogate (Scheme 51b).

Meggers' complexes can also be used for photocycloadditions (Scheme 52) [123]. A recent example used enone **311** to form the corresponding metal complex **312**, which upon photoexcitation is proposed to behave like diradical **312***. HAT from the nearby aldehyde to the α-position produces acyl radical **313**, which undergoes intersystem crossing to the singlet state ketene **314** supported by DFT calculations. This intermediate then reacts through an enantioselective [4 + 2] cycloaddition via transition state **314**‡ to give the complexed cyclisation product **315**. This product is then displaced by another substrate molecule to finish the catalytic cycle and produce the cycloaddition products **316** as a single diastereomer with excellent yields and

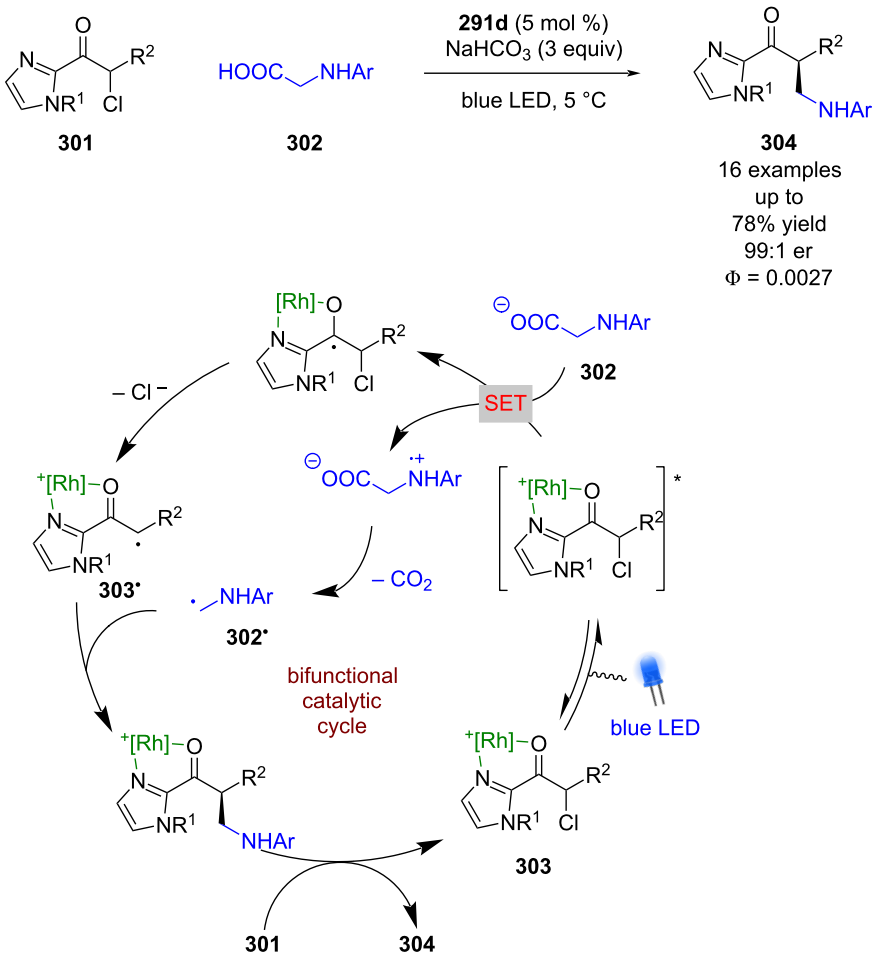

Scheme 50: Bifunctional Lewis acid/photoredox-catalysed radical coupling reaction using α-chloroketones and α-aminocarboxylic acids.

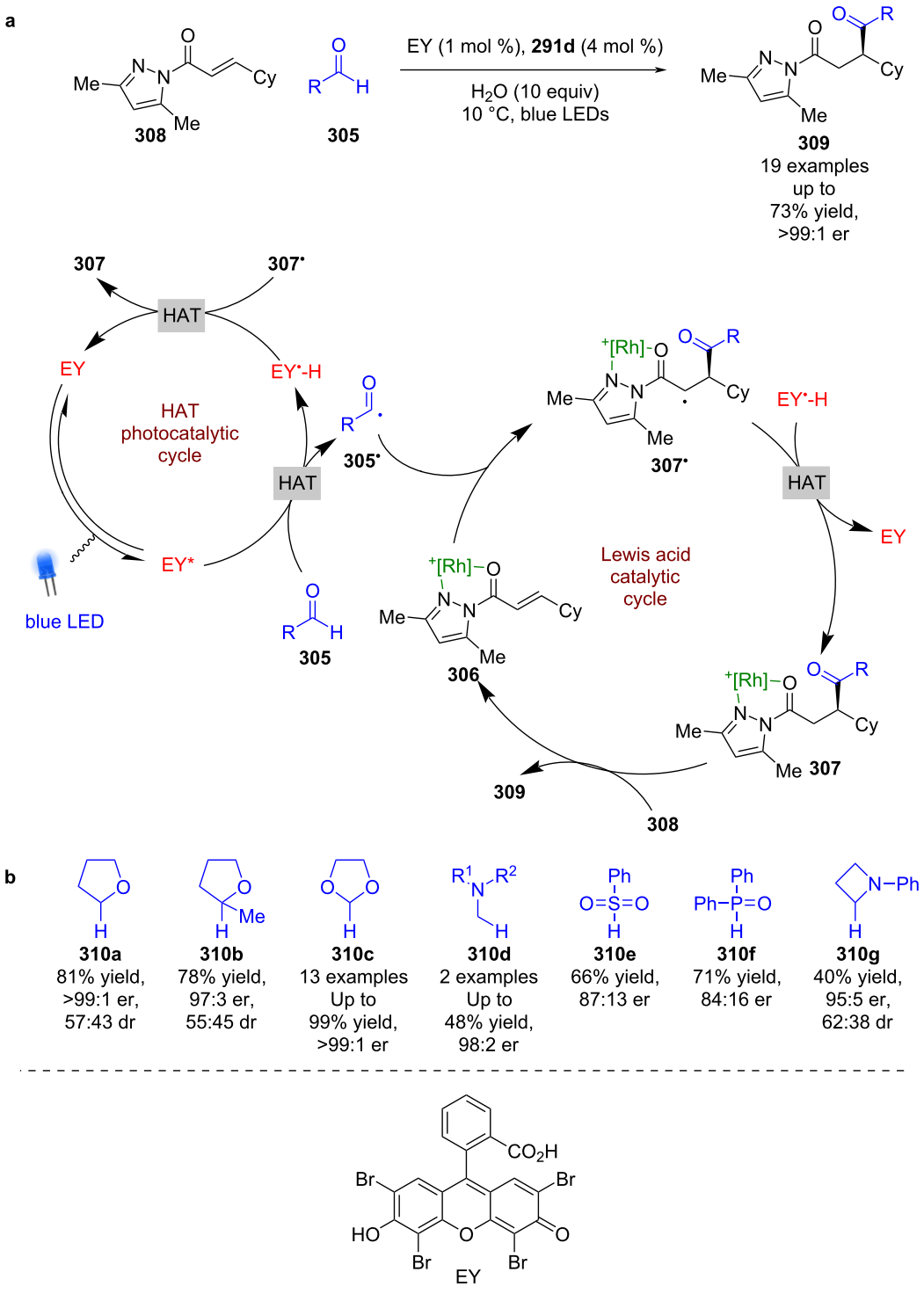

Scheme 51: Lewis acid/photocatalysed RCA of enones. (a) Using aldehydes as acyl radical precursors. (b) Other substrates used as radical precursors.

enantioselectivities (20 examples, up to >99:1 er). In this case, the auxiliary is not easily removed, which is a limitation of this mode of catalysis.

Recently, Xiao et al. developed a similar catalyst **317**, using a cobalt-based system where the chirality was conferred by the use of chiral ligands rather than metal-centred chirality, which

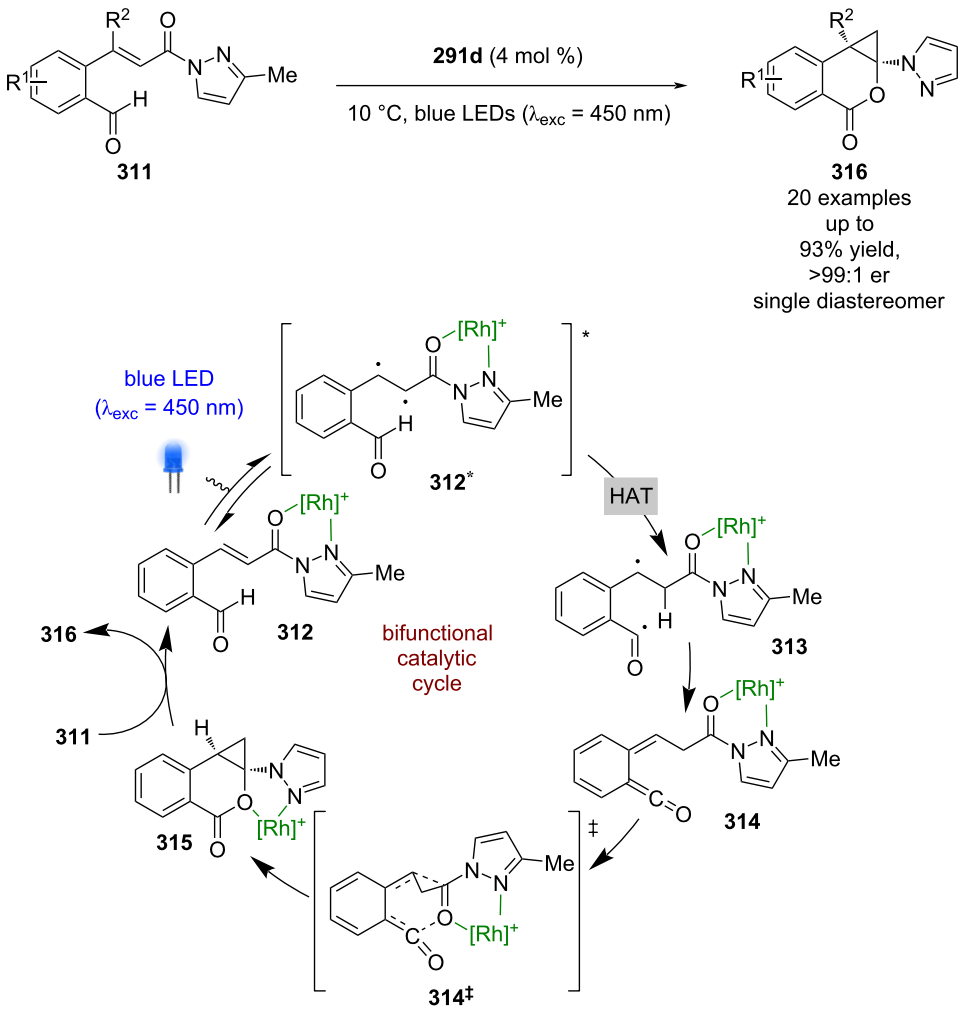

Scheme 52: Bifunctional Lewis acid/photocatalysis for a photocycloaddition of enones.

is the modus operandi of Meggers' technology (Scheme 53) [124]. They applied **317** to the enantioselective RCA reaction of enones **318** using DHPs **319** as radical precursors. If an alkyl DHP is used, then Fukuzumi's acridinium photocatalyst Mes-Acr$^+$ is required. The proposed mechanism proceeds via a reductive quenching cycle to generate alkyl radicals **319**$^\bullet$ and Mes-Acr$^\bullet$. The radical **319**$^\bullet$ then adds enantioselectively to the complex formed between **317** and **318** to give α-carbonyl radical **320**$^\bullet$, which is then reduced to the corresponding enolate **320** by Mes-Acr$^\bullet$ to turn over the photocatalytic cycle. Protonation of **320** and displacement by another molecule of **318** completes the Lewis acid cycle and affords the desired enantioenriched RCA products **321** in excellent yields and good enantioselectivities (26 examples, up to 96:4 er). If acyl DHPs are used, then no external photocatalyst is required, which is proposed to be due to direct excitation of the substrate as demonstrated previously by Melchiorre et al. [45]. The complexes generated do not seem able to act as photocatalysts, but the reactions do demonstrate high quantum yields for both alkyl (Φ = 0.57) and acyl (Φ = 0.86) substituents, suggesting efficient photocatalytic cycles.

Other bifunctional Lewis acid/photoredox catalysts have also been reported. Xiao et al. developed a chiral ligand with a thioxanthone photoactive moiety **L6**, which when used in combination with Ni(acac)$_2$ forms a bifunctional catalyst in situ (Scheme 54a) [125]. This system was then used for the oxygenation of β-ketoesters **322**, via Lewis acid complex **323** in a similar mechanism to that proposed by Gao et al. in their PTC reaction shown in Scheme 23 [73], to give α-hydroxy-β-ketoesters **324** in excellent yields and enantioselectivities (21 examples, up to 98:2 er). A similar system was then used for the alkylation of 1-indanone-derived substrates **325** although in this instance an external photocatalyst is required to

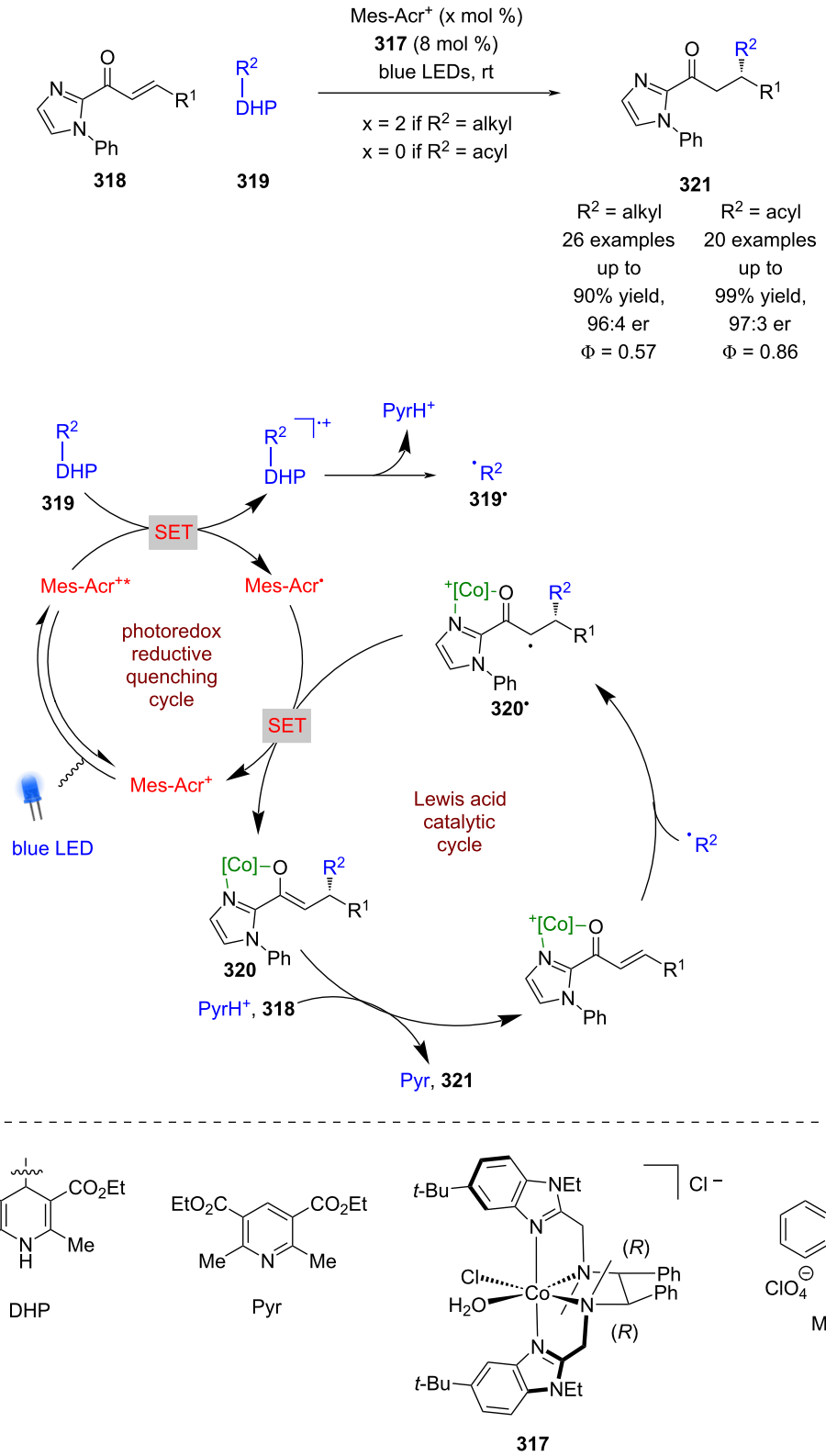

Scheme 53: Lewis acid/photoredox-catalysed RCA reactions of enones using DHPs as radical precursors.

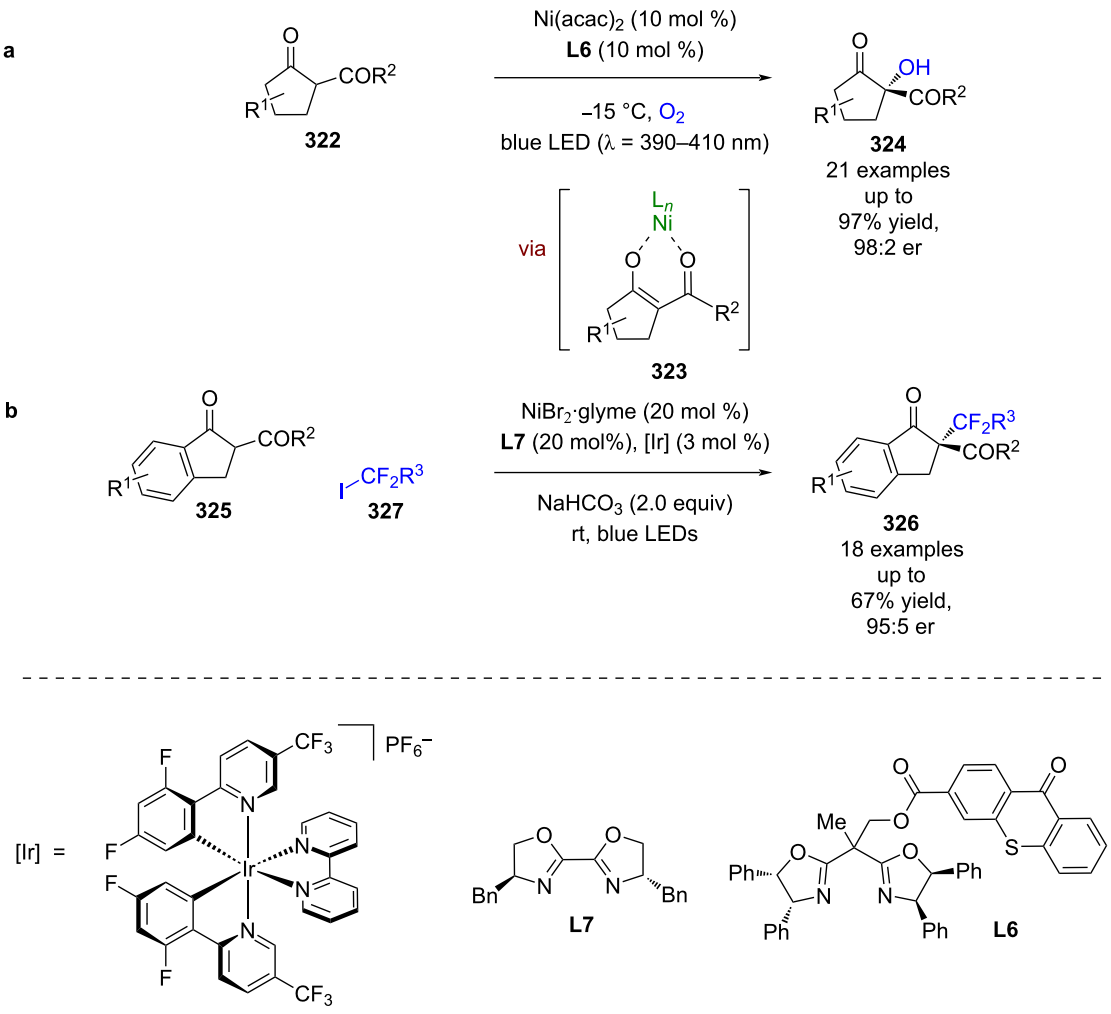

Scheme 54: Lewis acid/photoredox-catalysed functionalisation of β-ketoesters. (a) Hydroxylation reaction catalysed by a bifunctional nickel/thioxanthone catalyst. (b) Alkylation reaction catalysed by a nickel/iridium dual catalysis system.

obtain the desired products **326** in moderate yields and good enantioselectivities (18 examples, up to 95:5 er) (Scheme 54b) [126]. The putative mechanism is similar to that proposed by Melchiorre et al. for their PTC perfluoroalkylation process shown in Scheme 24 [77].

Gong et al. used a Cu(II) catalyst with chiral ligands **L8** or **L9** as a bifunctional catalyst for the enantioselective alkylation of two classes of cyclic imines **328** and **329** using trifluoroborate salts **330** (Scheme 55) [127]. Trifluoroborate salts are commonly used in photoredox catalysis as alkyl/aryl radical precursors, and generally undergo a single electron oxidation. However, Gong et al. proposes an alternative mechanism for this reaction involving a ligand exchange process to give alkyl copper(II) complex **331**, followed by a light-induced homolysis of the Cu–C bond to give alkyl radicals **330**$^{\bullet}$ and a reduced Cu(I) species. The alkyl radical **330**$^{\bullet}$ then adds to the copper-bound imine **332** enantioselectively to give *N*-centred radical **332**$^{\bullet}$, which is then reduced by Cu(I) to give the alkylation products bound to the copper catalyst **333**. Displacement by another molecule of substrate completes the cycle and releases **334** or **335** in excellent yields and enantioselectivities (27 examples, up to 97:3 er for **334** and 8 examples, up to 99:1 er for **335**). The quantum yield was measured to be <1 (Φ = 0.06), so a radical chain mechanism is unlikely to be dominant.

Gong et al. later expanded the scope of this system to α-silyl amines **336** as radical precursors and acyclic hydrazones **337** and found that in this case an oxazolidinone auxiliary was required to aid with complexation (Scheme 56a) [128]. 5,7,12,14-Pentacenetetrone (PT) can act as both a HAT catalyst and a photocatalyst so that the alkyl radicals can be generated via

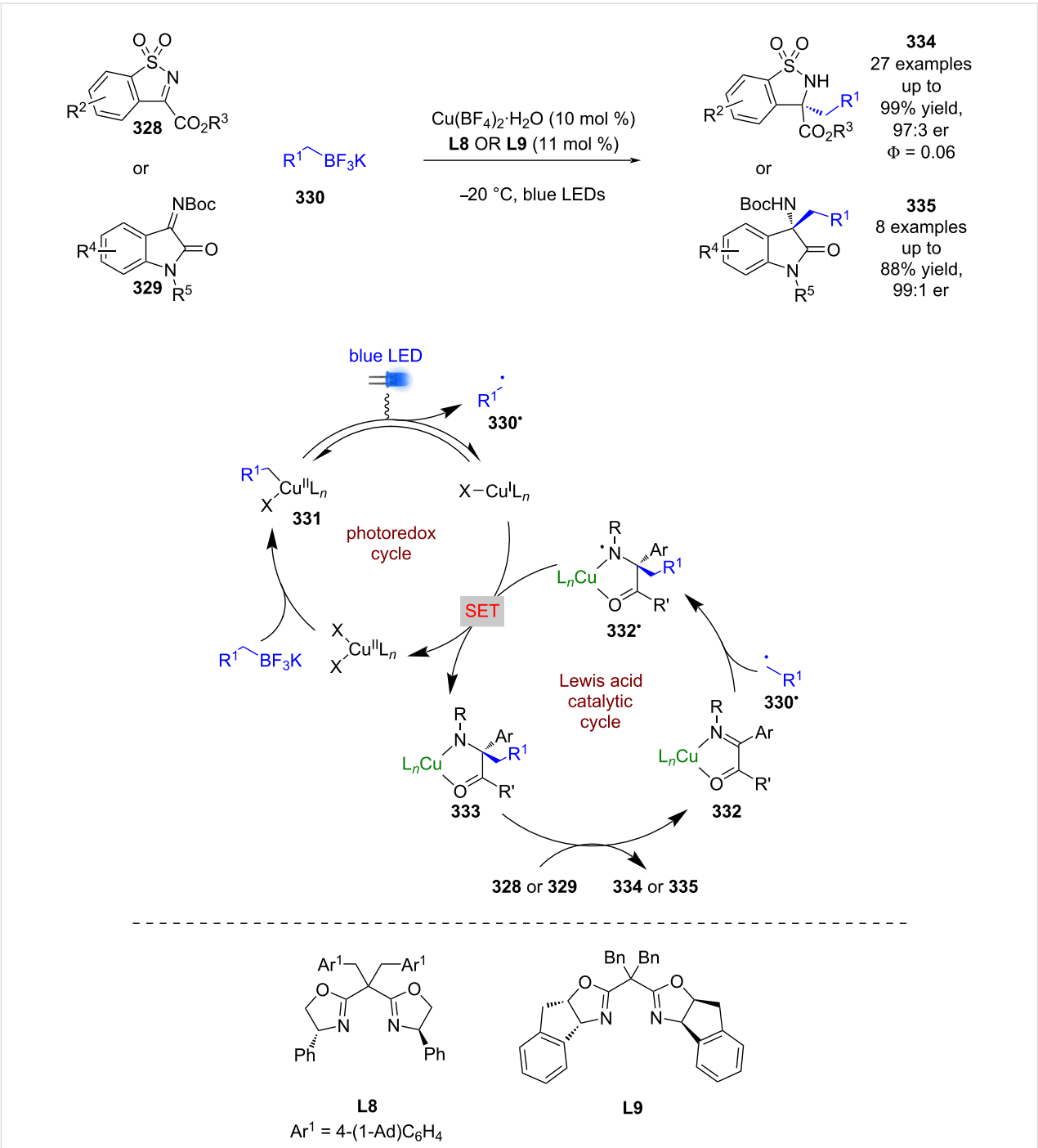

Scheme 55: Bifunctional copper-photocatalysed alkylation of imines.

C–H activation of simple alkanes **338** rather than using a redox-active group (Scheme 56b) [129]. Each reaction also had a quantum yield of <1 (Φ = 0.16 for **a** and Φ = 0.08 for **b**), so a radical chain mechanism is unlikely to be dominant.

Guo and Bach took a different approach to enantioselective Lewis acid/photocatalysis, building upon work by Lewis [130] and Barancyk [131] who showed that Lewis acids could catalyse photocycloadditions. A recognised significant challenge in making these reactions enantioselective, is outcompeting the racemic background pathway. Bach et al. found that $AlBr_3$-activated oxazaborolidine-based catalysts **341** could induce a bathochromic shift in the absorption spectrum of the coordination complex relative to the uncoordinated coumarin derivative

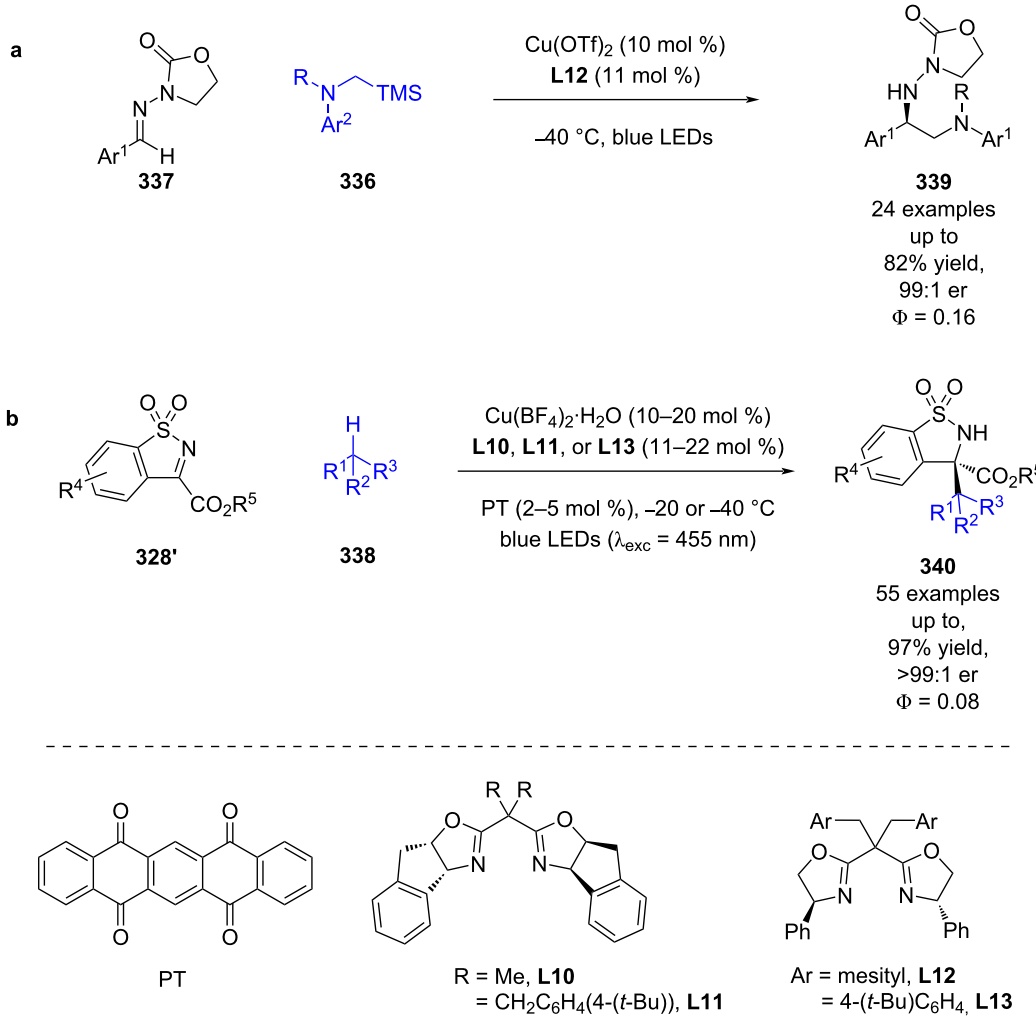

Scheme 56: Copper/photocatalysed alkylation of imines. (a) Bifunctional copper catalysis using α-silyl amines. (b) Dual copper/HAT-catalysed C–H activation of alkanes.

342, allowing for selective excitation of the former (Scheme 57) [132]. With a combination of low temperatures, high catalyst loading, and tuning the excitation wavelength, the cycloaddition product **343** could be obtained with high enantioselectivity (91:9 er) via the proposed transition state **344**‡. Interestingly, the quantum yield of the catalysed reaction was found to be much higher (Φ = 0.09) than the uncatalysed reaction ($\Phi \geq 0.002$), which is proposed to be due to both increased ISC rates and increased absorption at the excitation wavelength (λ_{exc} = 366 nm) [133].

Bach et al. later exploited this reactivity using quinolone **345** (Scheme 58a) [134]. Interestingly, this reaction had the opposite trend for quantum yields compared to **342**, with a higher quantum yield for the background reaction ($\Phi \geq 0.23$) than for the Lewis acid-catalysed reaction (Φ = 0.004), which is proposed to be due to a decrease in ISC rate when coordinated to the Lewis acid. The first intermolecular example using this catalyst system used cyclic ketones **346** with alkenes **347** to synthesise bicyclic compounds **348** (Scheme 58b) [135]. A similar reaction was also later developed for the cycloaddition of phenanthrene-derived aldehydes **349** with alkenes **350**, using 457 nm excitation, which was possible due to the increased conjugation of the substrate, and a lower catalyst loading (Scheme 58c) [136].

Recently, Bach et al. showed that these catalysts can also be used for photochemical rearrangements using 2,4-dienones **355** (Scheme 59) [137]. The proposed mechanism involves Lewis acid coordination to give complex **356**, which can be selectively excited in the presence of the unbound substrate. **356*** then rearranges enantioselectively to generate cationic interme-

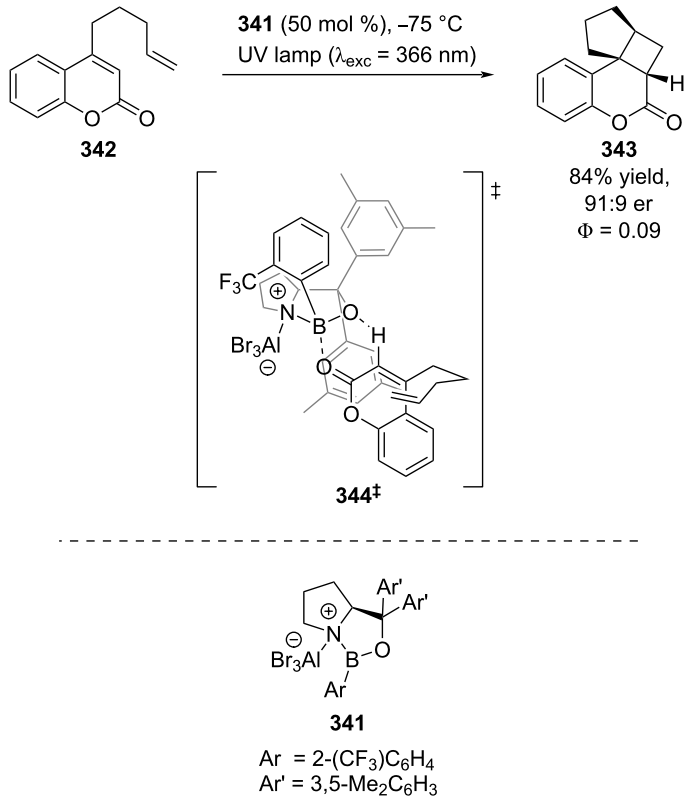

Scheme 57: Bifunctional Lewis acid/photocatalysed intramolecular [2 + 2] photocycloaddition.

diate $\mathbf{356}^{+}$, which then undergoes further rearrangement to furnish bicyclic products **357** in good yields and excellent enantioselectivities (15 examples, up to 99:1 er).

Previous work on photocycloadditions by Yoon et al. relied on adjacent phenols to form Lewis acid complexes, which is a significant synthetic limitation. To generalise the reaction and expand the substrate scope, Yoon et al. found that a combination of an oxazaborilidine Lewis acid **359** with an external photocatalyst allowed for the cycloaddition of simple cinnamate esters **360** with styrenes **361** (Scheme 60) [138]. Instead of exploiting the red-shift in absorption wavelength to confer photochemoselectivity, Yoon et al. proposed that complexation of the Lewis acid lowers the triplet energy of the coordination complex to such an extent that selective triplet sensitization via Dexter energy transfer from the photocatalyst and subsequent enantioselective [2 + 2] cycloaddition becomes operative as was proposed with the scandium catalysts in Scheme 47 [113,114].

This section has clearly demonstrated the immense diversity in types of Lewis acids that are compatible with photocatalysis, varying from heavy transition metal catalysts and lanthanoid catalysts to boron-centred ones. With this diversity in LA catalyst, comes a broad scope of reactivity that has been made possible by this class of dual mode catalysis.

Transition metal catalysis

The previous section included some examples of transition metals acting as Lewis acids, whereas this section focuses more on reactivity that is unique to transition metals, including inner sphere electron transfer events within the putative mechanisms. Transition metal complexes with achiral ligands have been widely used in combination with photocatalysts in racemic dual catalytic reactions [139,140], with nickel/photoredox catalysis becoming a commonly used combination [141,142]. Transition metal complexes with chiral ligands have also been used extensively in enantioselective catalysis. A recent review on enantioselective metallaphotoredox catalysis summarises the combination of these two bodies of work well [15]. This section is further categorised into subsections by the transition metal used.

Nickel catalysis: The first enantioselective example of this dual mode catalysis reported was a decarboxylative arylation of α-amino acids **363** with aryl bromides **364** bearing electron-withdrawing groups, developed by Fu and MacMillan using $NiCl_2$, chiral ligand **L14**, and a heteroleptic iridium-based

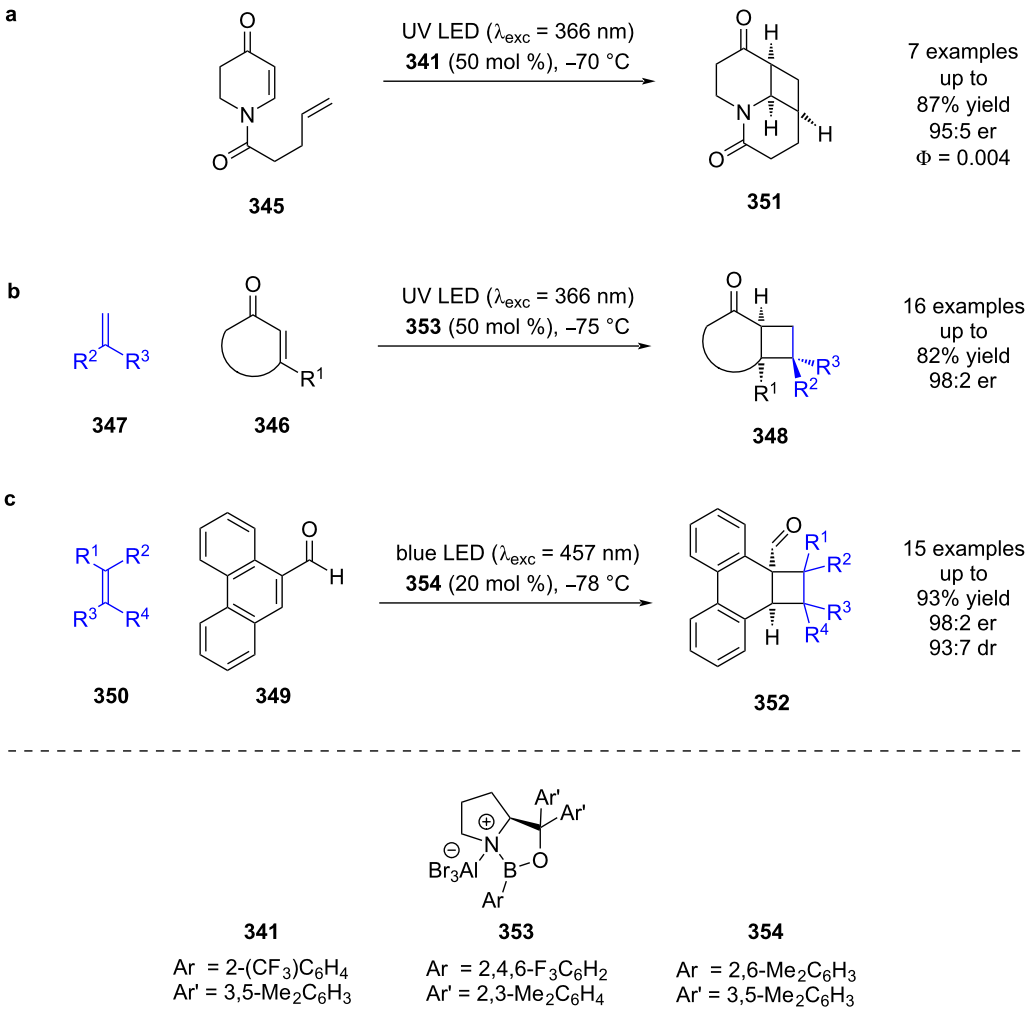

Scheme 58: Bifunctional Lewis acid/photocatalysed [2 + 2] photocycloadditions (a) Intramolecular cycloaddition of quinolones. (b) Intermolecular cycloaddition of cyclic enones with terminal alkenes. (c) Intermolecular cycloaddition of phenanthrene-derived aldehydes and tetrasubstituted alkenes.

photocatalyst (Scheme 61) [143]. The proposed mechanism involves a reductive quenching cycle resulting in α-amino radicals **363**•, and a nickel catalytic cycle that starts with oxidative addition of **364** onto a Ni^0 complex to give Ni^{II} intermediate **365**. **365** is then intercepted by **363**• to give a Ni^{III} intermediate **366**, which upon reductive elimination releases enantioenriched arylated products **367** in good yields and excellent enantioselectivities (26 examples, up to 98:2 er). Both catalytic cycles are completed by a SET step between Ni^I and $[Ir]^{\bullet-}$.

Following this report, a large array of reactions has been developed using chiral ligands with nickel/photoredox catalysis [144-146]. For example, Rovis and Doyle developed a desymmetrisation of cyclic *meso*-anhydrides **368** using benzyl trifluoroborate salts **369**, chiral ligand **L15**, $Ni(COD)_2$, and the photocatalyst 4CzIPN (Scheme 62a) [147]. More recently, Walsh and Mao used a similar dual catalyst system for the enantioselective cross-electrophile coupling of α-chloro esters **370** and aryl iodides **371** using Hantzsch ester as a sacrificial reductant (Scheme 62b) [148]. Montgomery and Martin achieved similar reactivity via a C–H arylation of benzamides **372** using aryl bromides **373**, although only a limited number of enantioselective examples were reported (Scheme 62c) [149].

Expansion to a system using TBADT by Wang, which is known to generate acyl radicals from aldehydes [150], allowed for the enantioselective acyl-carbamoylation of alkenes **377** with aldehydes **378** (Scheme 63) [151]. The putative mechanism in this case, based on prior work by MacMillan et al. [152], proceeds via HAT from **378** to the excited state photocatalyst to generate acyl radical **378**• and $[W]^{5-}H^+$. Subsequent addition of **378**• to Ni^0 affords Ni^I intermediate **379**, which oxidatively adds into

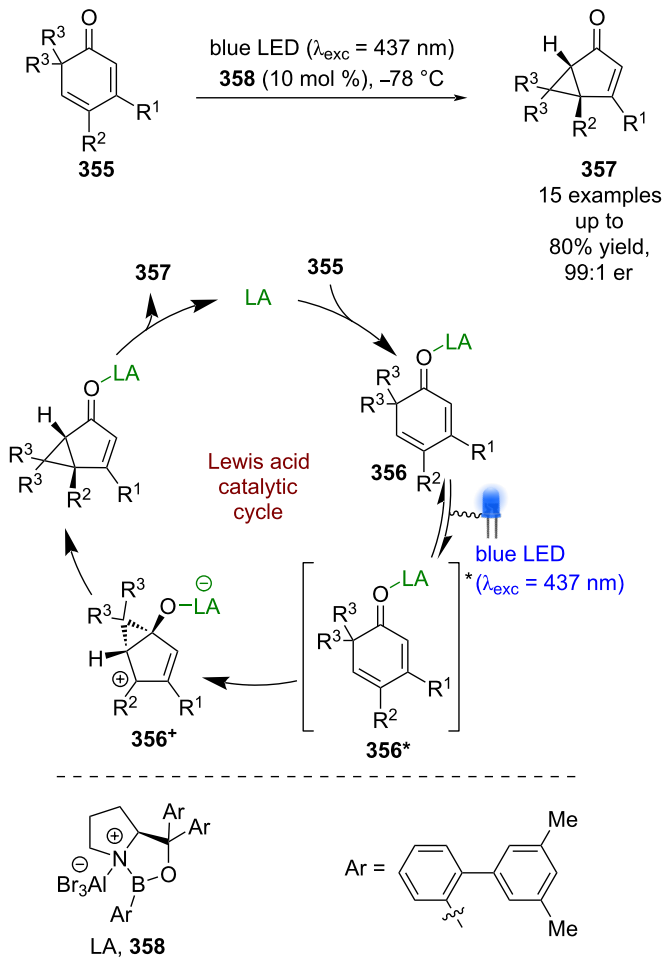

Scheme 59: Bifunctional Lewis acid/photocatalysed rearrangement of 2,4-dieneones.

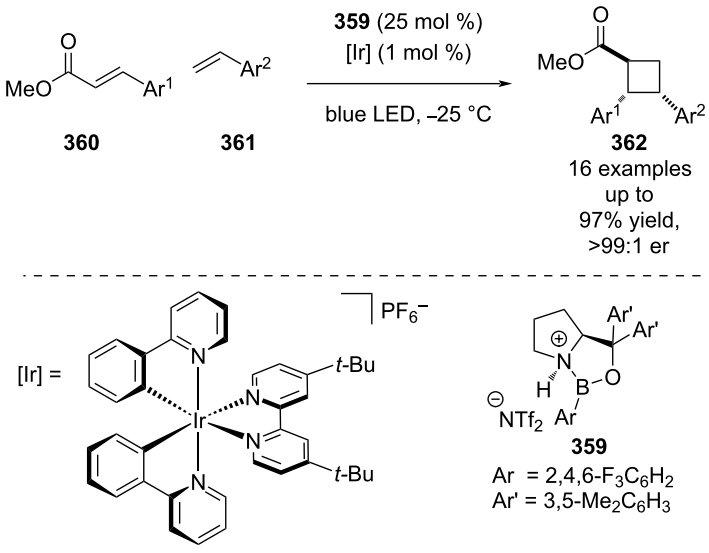

Scheme 60: Lewis acid/photocatalysed [2 + 2] cycloadditions of cinnamate esters and styrenes.

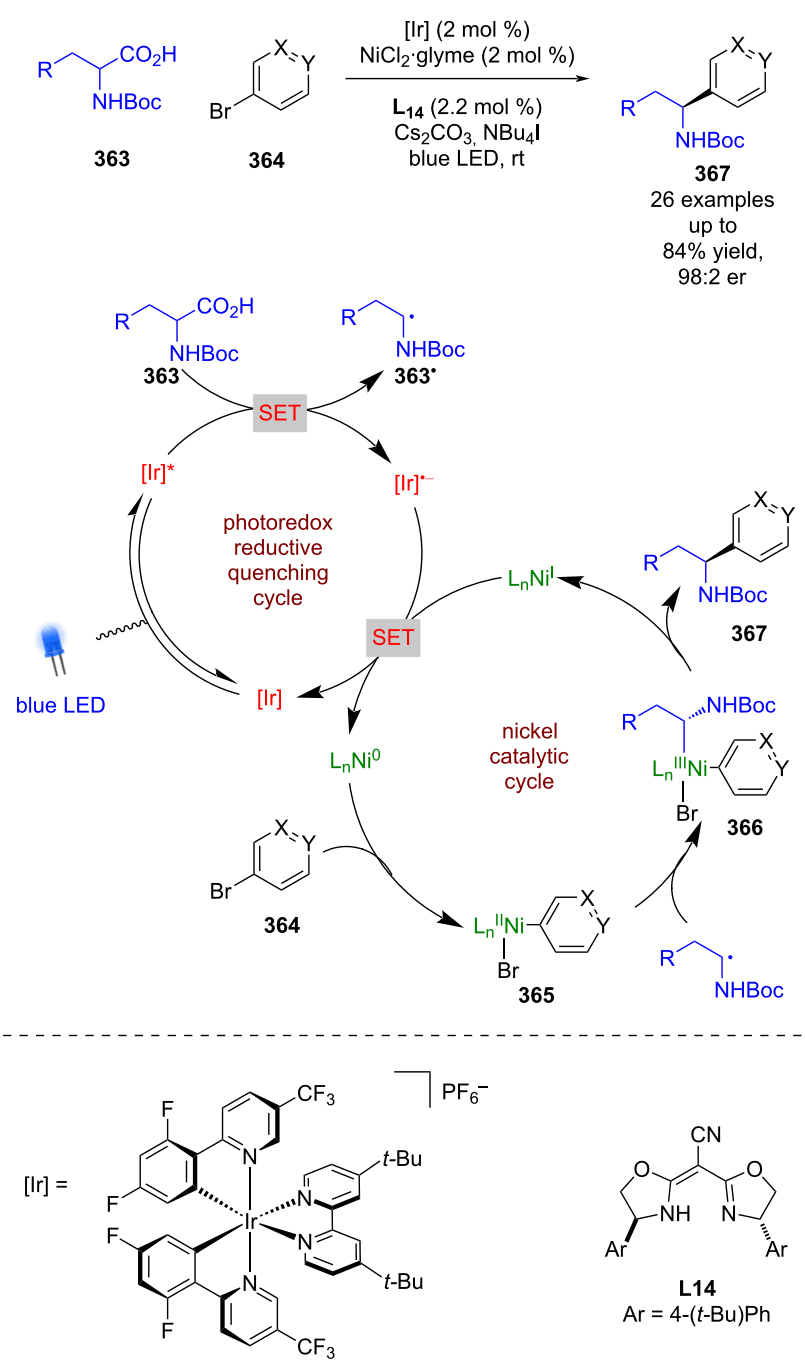

Scheme 61: Nickel/photoredox-catalysed arylation of α-amino acids using aryl bromides.

377 to give the Ni^{III} species **380**. **380** then undergoes an enantioselective migratory insertion to generate complex **381**, which can reductively eliminate to furnish the desired products **382** in excellent yields and enantioselectivities (36 examples, up to 98:2 er). Concomitantly $[W]^{5-}H^+$ undergoes a disproportionation reaction to generate $[W]^{4-}$ and $[W]^{6-}2H^+$, which reduces the Ni^I species and completes the cycle. This nickel catalytic cycle [Ni(0), Ni(I), Ni(III)] is different to that shown in Scheme 61 [Ni(0), Ni(I), Ni(II), Ni(III)], but both are plausible and it is difficult to determine which is in operation. Towards this, Molander and Gutierrez recently reported an interesting computational investigation that assessed the feasibility of different possible mechanisms for tertiary radicals in nickel/photoredox dual catalysis and concluded that multiple mechanisms are plausible, and which one is in operation is both substrate and ligand dependant [153].

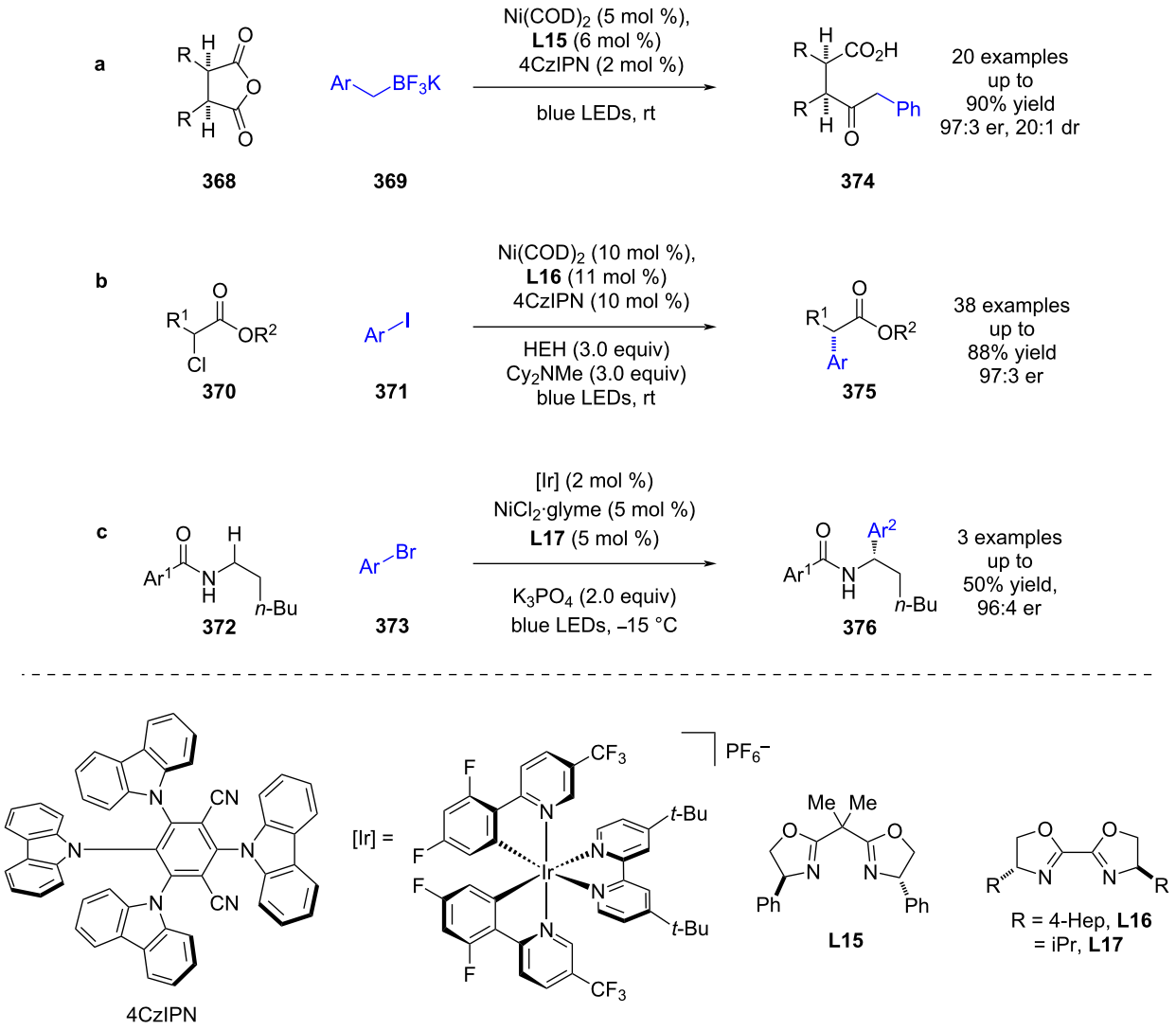

Scheme 62: Nickel/photoredox catalysis. (a) Desymmetrisation of cyclic *meso*-anhydrides using benzyl trifluoroborate salts. (b) Cross-electrophile coupling of α-chloro esters with aryl iodides, using Hantzsch ester as a sacrificial reductant. (c) C–H Arylation of benzamides with aryl bromides.

Copper catalysis: Other metal complexes have also been used in combination with photocatalysis. For example, Peters and Fu found that copper catalysts can mediate the C–N cross coupling of α-chloro amides **383** (Scheme 64) [154]. They propose that following ligand substitution with an indole or carbazole **384**, the resulting photoactive complex **385** is excited upon light absorption. The reaction then proceeds via an oxidative quenching pathway by **383** resulting in the Cu^{II} complex **386** and an alkyl radical **383•**, which then adds to copper to give a Cu^{III} intermediate **387** that reductively eliminates to complete the cycle and release enantioenriched C–N coupling product **388** in excellent yields and enantioselectivities (20 examples, up to >99:1 er).

Since this report, chiral copper complexes have been used in other enantioselective bifunctional photocatalysis reactions. Zhang et al., developed an enantioselective difunctionalisation of alkenes **389** using alkynes **390** and alkyl or aryl iodides **391** that proceeds via a radical cascade reaction (Scheme 65) [155]. They propose that the copper acetylide intermediate **392** is photoactive and photocatalyses the reaction, proceeding via an oxidative quenching pathway. The formed radicals then add to **389** to afford alkyl radical **393•**, which then adds to the Cu^{II} centre to give a Cu^{III} intermediate **394**, which upon enantioselective reductive elimination completes the cycle and generates the desired products **395** in good yields and excellent enantioselectivities (41 examples, up to 99:1 er). The quantum yield was

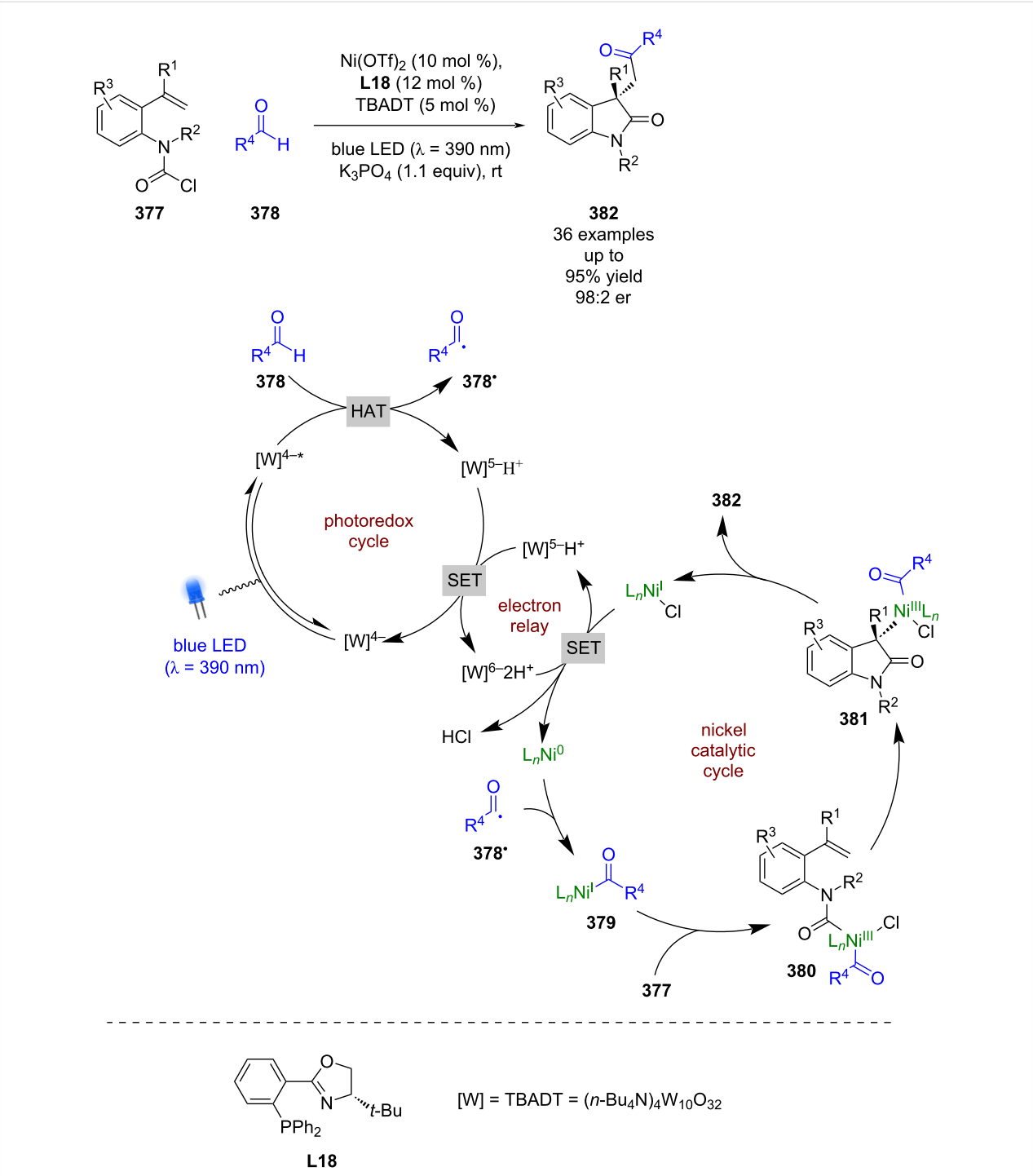

Scheme 63: Nickel/photoredox catalysis for the acyl-carbamoylation of alkenes with aldehydes using TBADT as a HAT catalyst.

measured to be <1 (Φ = 0.006), suggesting a radical chain mechanism is unlikely to be dominant.

Enantioselective copper catalysis has also been used in combination with an external photocatalyst. For instance, Liu et al. reported a decarboxylative cyanation of phthalimide esters **396** using a combination of CuBr, TMSCN, an iridium-based photocatalyst, and chiral ligand **L21** (Scheme 66) [156]. Based on previous cyanation reactions [157], they propose an oxidative quenching cycle where benzyl radicals **396•** are formed from **396** after a reductive decarboxylation, $[Ir]^{\bullet+}$ then oxidises the Cu^{I} catalyst to Cu^{II} which accepts a second cyanide ion to

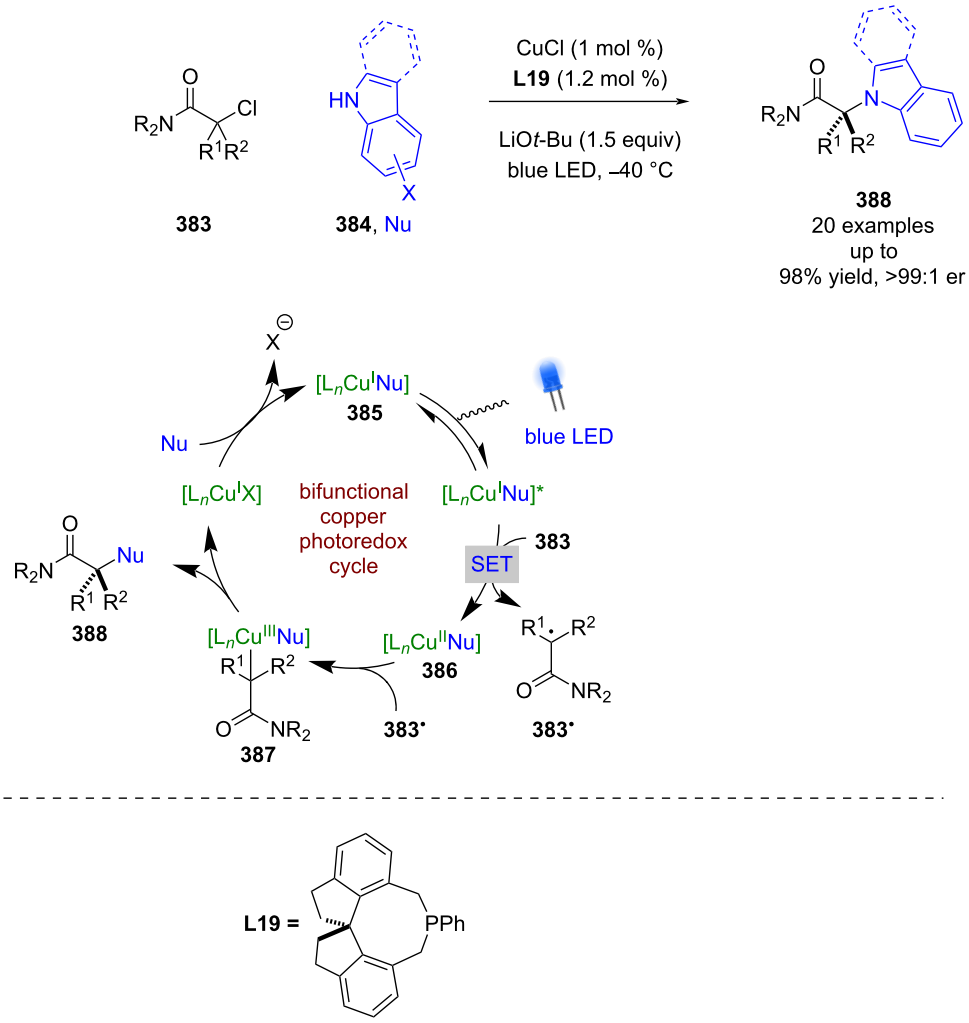

Scheme 64: Bifunctional copper/photoredox-catalysed C–N coupling between α-chloro amides and carbazoles or indoles.

generate the active dicyano species **397**. Radical addition of **396**• to **397** generates Cu^{III} intermediate **398**, which after reductive elimination regenerates the catalyst and produces enantioenriched nitriles **399** in excellent yields and enantioselectivities (31 examples, up to >99:1 er).

A series of cyanation reactions have subsequently been developed using similar reactivity. For example, propargyl radicals were successfully used in concert with the more strongly reducing Ph-PTZ photocatalyst, and with a different leaving group to achieve the first enantioselective propargylic radical cyanation (Scheme 67a) [158]. Employing oxime esters **400** as radical precursors afforded enantioenriched dicyano alkanes **401** (Scheme 67b) [159]. Han and Mei developed a radical cascade system using phthalimide esters **402**, styrenes **403**, and TMSCN to obtain enantioenriched difunctionalised products **404** (Scheme 67c) [160]. Wang and Xu reported a similar radical cascade process using a single catalyst system with perfluorinated alkyl iodides **405** and TMSCN to afford enantioenriched difunctionalised alkenes **406** via a similar mechanism to that proposed by Fu [154] in Scheme 64 (Scheme 67d) [161]. Notably, the quantum yields that were measured for these reactions were all <1, suggesting chain mechanisms may not be dominant but also showing reactions Scheme 67a (Φ = 0.65) and Scheme 67d (Φ = 0.51) are quite efficient processes.

Palladium catalysis: While there have now been many examples of dual palladium catalysis merged with photocatalysis [140], there are relatively few enantioselective variations. A highly enantioselective reaction using palladium and photoredox catalysis was reported by Yu et al. using chiral ligand **L23** in an allylic alkylation reaction (Scheme 68a) [162]. Using DHPs **407** as radical precursors, they propose an analogous set of catalytic cycles to those proposed for nickel cataly-

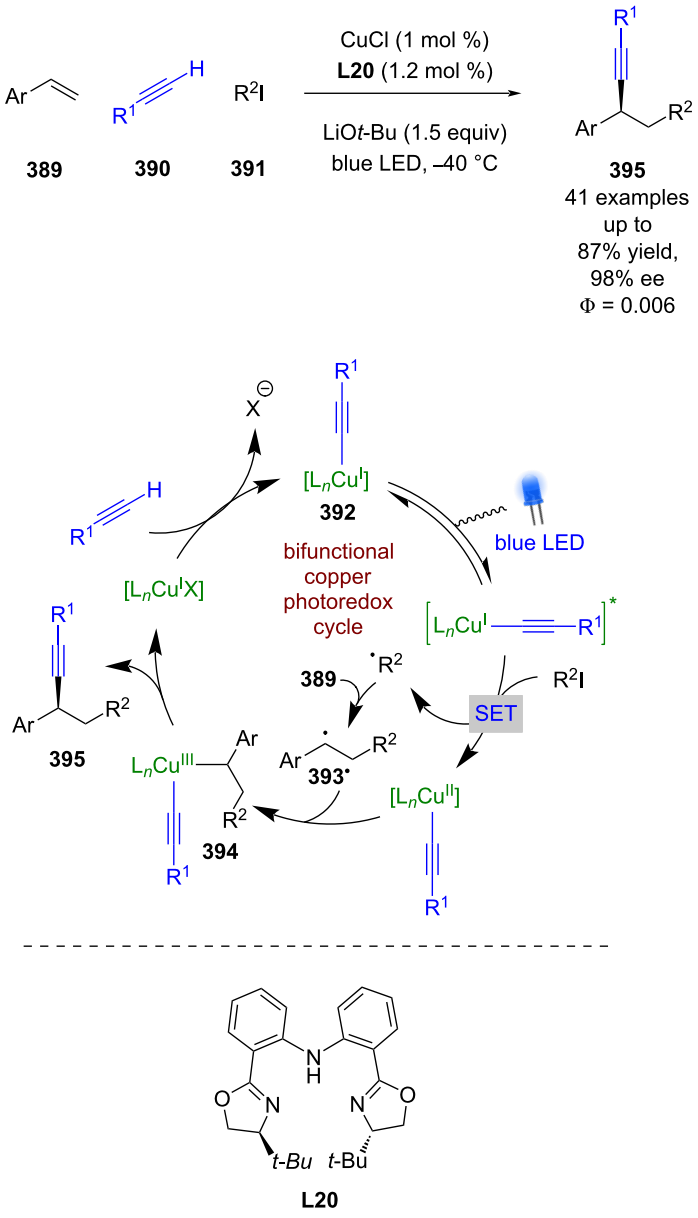

Scheme 65: Bifunctional copper/photoredox-catalysed difunctionalisation of alkenes with alkynes and alkyl or aryl iodides.

sis. The iridium-based photocatalyst proceeds via a reductive quenching cycle to form benzylic radicals **407**•; simultaneously Pd^0 reacts with alkene **408** to form a π-allyl palladium(II) complex **409**, which is then intercepted by **407**• to form a Pd^{III} intermediate **410**. Subsequent reductive elimination releases enantioenriched allylation products **411** in good yields and excellent enantioselectivities (43 examples, up to 99:1 er). A SET event between the resulting Pd^I and $[Ir]^{\bullet-}$ then completes both catalytic cycles. Yu et al. recently extended this reactivity to anilines **412** that can form α-amino radicals under similar reaction conditions to obtain the corresponding products **413** in comparable yields and enantioselectivities (31 examples, up to 98:2 er) (Scheme 68b) [163].

Manganese catalysis: Dual catalysis involving a manganese catalyst in combination with photoredox catalysis is far less explored. An example was reported by Nam et al. for the enantioselective epoxidation of terminal alkenes **414** using H_2O as the oxygen source (Scheme 69) [164]. The proposed mechanism uses a stoichiometric cobalt reagent as a sacrificial oxidant in an oxidative quenching cycle to generate $[Ru]^{\bullet+}$, which then oxidises Mn^{II} in the presence of water to $Mn^{III}OH$ and turn over

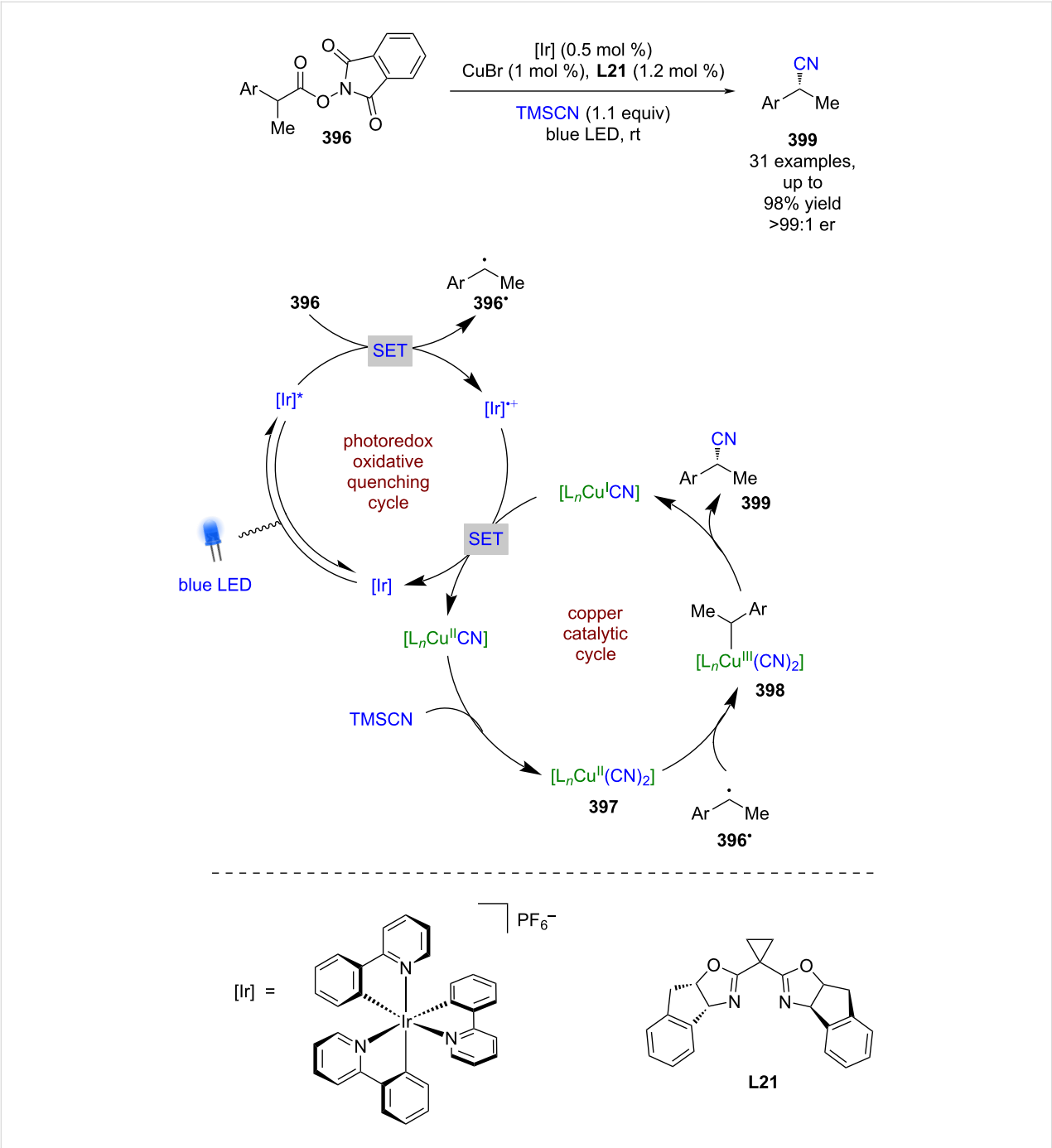

Scheme 66: Copper/photoredox-catalysed decarboxylative cyanation of benzyl phthalimide esters.

the photocatalytic cycle. Another similar SET event generates the active $Mn^{IV}O$ species, which catalyses the epoxidation of **414** to give epoxides **415** in moderate yields and enantioselectivities (6 examples, up to 80:20 er). The two SET events required imply a two-photon mechanism is in operation; however, this is not discussed further by the authors. Interestingly, acetic acid seems vital for both yield and enantioselectivity, although the reason for this remains unclear.

Chromium catalysis: Kanai et al. combined chromium catalysis with Mes-Acr^+ for the enantioselective allylation of aldehydes **417** in the presence of chiral ligand **L21** (Scheme 70) [165]. They proposed that the reaction proceeds via a reductive quenching cycle with unactivated alkenes **418** to form radical cations **418**$^{\bullet+}$ that can be deprotonated to give allylic radicals **418**$^{\bullet}$. Radicals **418**$^{\bullet}$ can then be intercepted by a Cr^{II} catalyst to form a Cr^{III} intermediate **419**, which can then nucleophilically

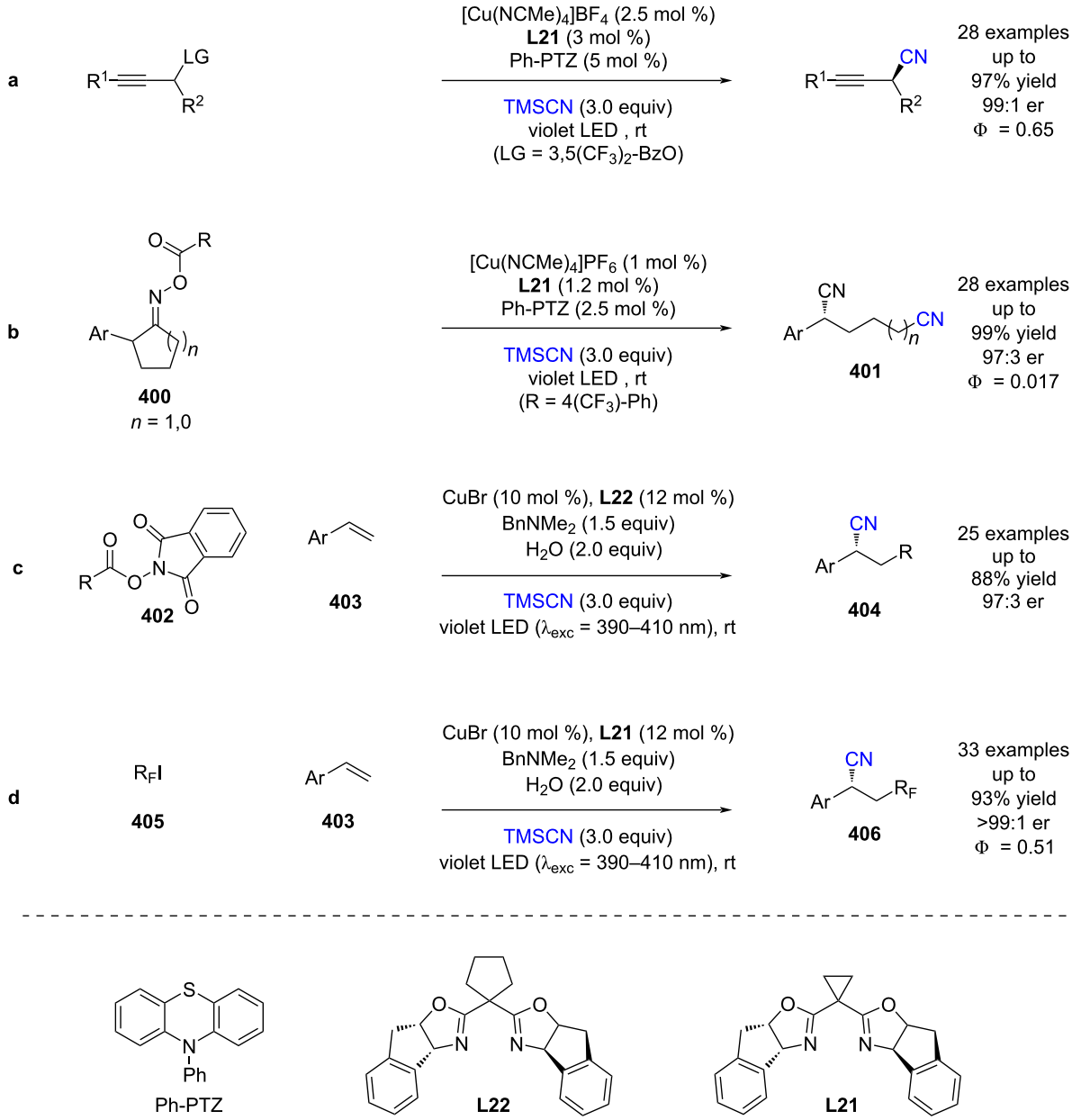

Scheme 67: Copper/photoredox-catalysed cyanation reactions using TMSCN. (a) Propargylic cyanation (b) Ring opening cyanation of oxime esters. (c) Radical relay reaction using phthalimide esters and styrenes. (d) Bifunctional catalyst for the difunctionalisation of alkenes using perfluoroalkyl iodides and styrenes.

add to the aldehyde to give enantioenriched alcohols **420** after protonation in excellent yields and enantioselectivities (22 examples, up to >99:1 er). The resulting Cr^{III} species can then undergo a SET event with $PC^{\bullet-}$ to complete both catalytic cycles.

Enzyme catalysis

Enzymes in nature use their bespoke binding environments to catalyse reactions with extreme selectivity; however, there are only a limited number of reactions that occur in nature where this is possible [166]. One method to extend their reactivity is to use them in combination with photocatalysis. There are now many examples that employ this strategy for both racemic and enantioselective transformations and these are well covered in Gulder's review [7]. One of the earliest enantioselective examples was reported by Hyster et al. for the dehalogenation of halolactones **421** in the presence of ketoreductases (KREDs) and NADPH (Scheme 71) [167]. The proposed mechanism im-

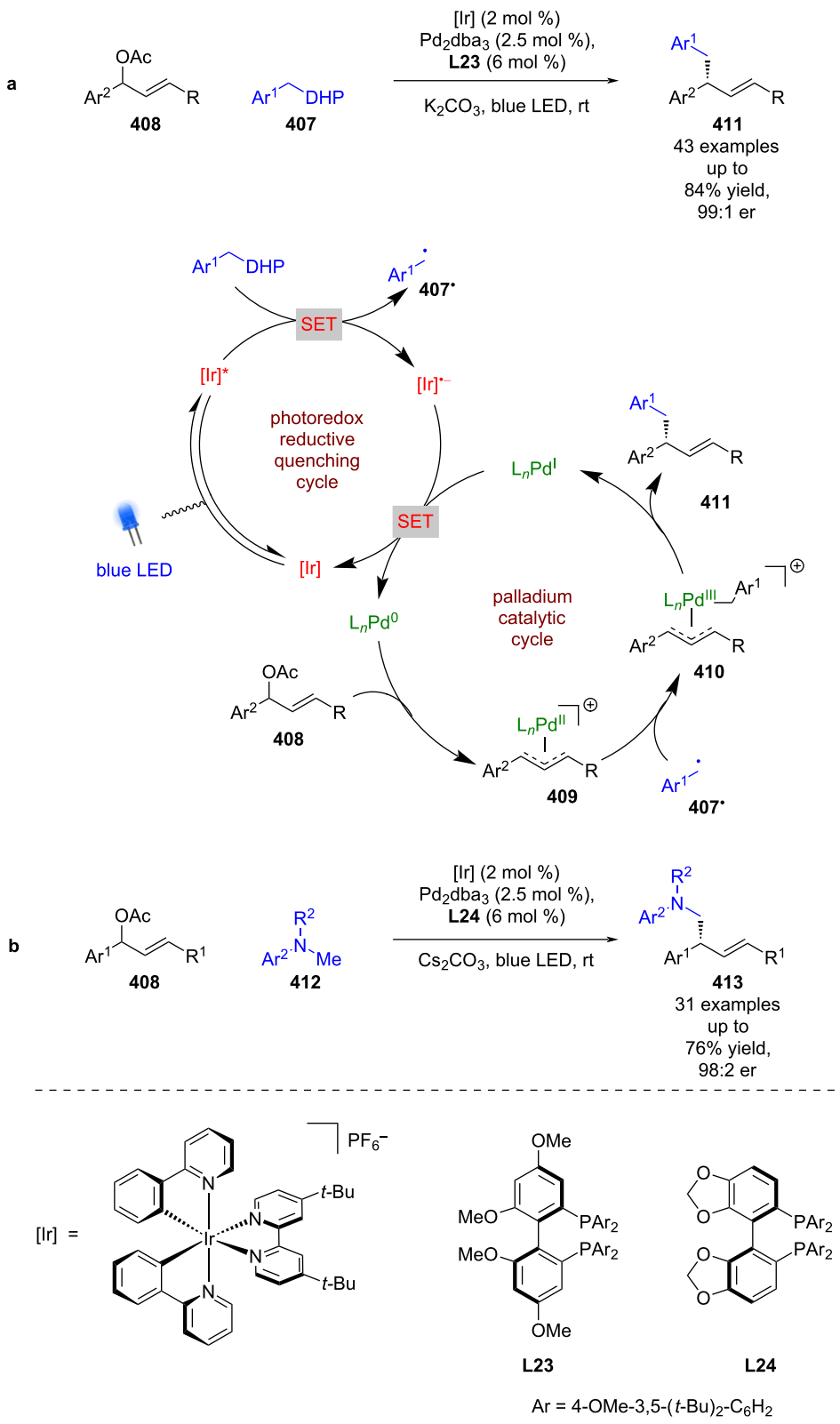

Scheme 68: Palladium/photoredox-catalysed allylic alkylation reactions. (a) Using alkyl DHPs as radical precursors. (b) Using tertiary amines as radical precursors.

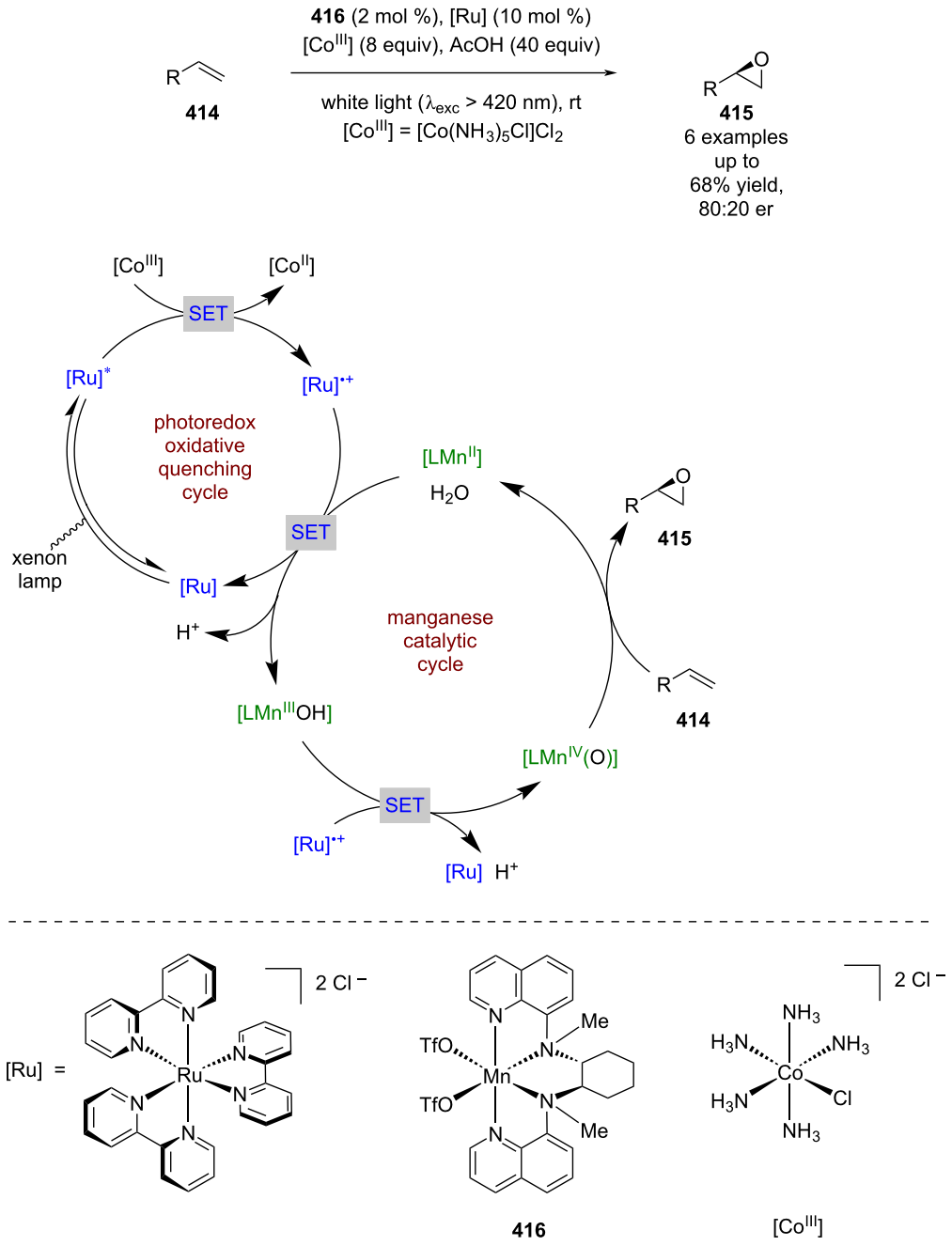

Scheme 69: Manganese/photoredox-catalysed epoxidation of terminal alkenes.

plicates an enzyme active site containing **421** and NADPH that forms an EDA complex, which upon photoexcitation gives intermediate **422**. Loss of bromide followed by enantioselective HAT from $NADPH^{\bullet+}$ gives enzyme-bound lactone **423** and $NADP^+$. Both compounds are then displaced by **421** and NADPH to complete the cycle, with $NADP^+$ being reduced either by isopropyl alcohol or glucose dehydrogenase (GDH). Different conditions can also be used to synthesise either enantiomer in excellent yields and enantioselectivities (9 examples, up to 98:2 and 97:3 er), which is important for enzymatic reactions as one cannot simply use the opposite enantiomer.

Hyster et al. expanded this methodology to the cyclisation reactions of α-chloro amides **424** (Scheme 72) [168]. In this instance, 'ene'-reductases (ERs) were found to be optimal and HAT occurs after radical addition to the pendant alkene to give

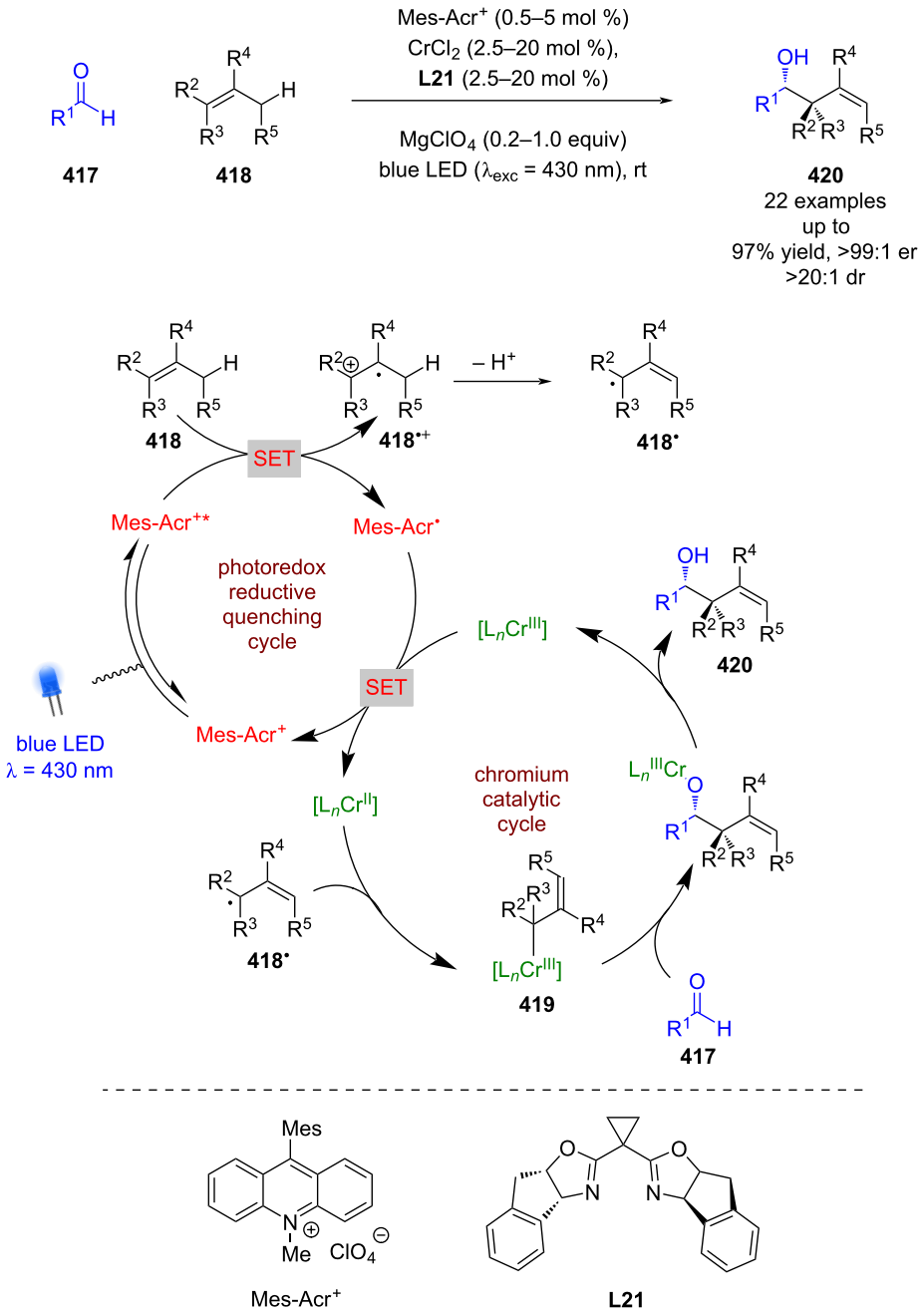

Scheme 70: Chromium/photoredox-catalysed allylation of aldehydes.

enantioenriched lactams **425** via tertiary radical **426** in excellent yields and enantioselectivities (16 examples, up to 99:1 er). The quantum yield of the reaction was determined to be <1 (Φ = 0.078), so a radical chain reaction is unlikely.

An example of enzymes being used in combination with an external photocatalyst was developed by Ward and Wenger using a water-soluble iridium photocatalyst for the enantioselective reduction of cyclic imines **427** (Scheme 73) [169]. The reaction is proposed to proceed via an oxidative quenching cycle to give alkyl radical **427•**, which is then trapped by ascorbic acid ($AscH_2$) in a HAT process to give a racemic mixture of cyclic amine **428**. When coupled with a highly selective enzyme-mediated oxidation using a monoamine oxidase (MAO-N-9), the (*S*)-enantiomer can be selectively removed and recycled to give the near enantiopure (*R*)-amine. The scope of this transformation was found to be limited to two substrates, allowing for little variation in structure or substituents.

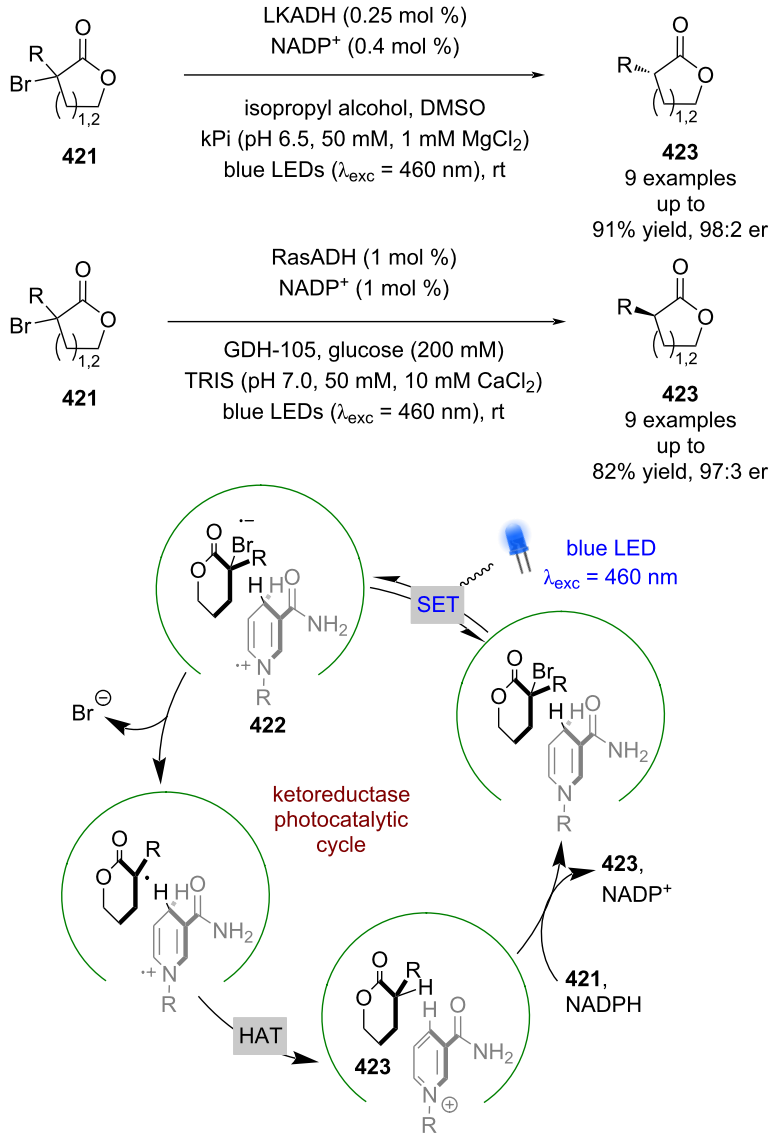

Scheme 71: Enzyme/photoredox-catalysed dehalogenation of halolactones.

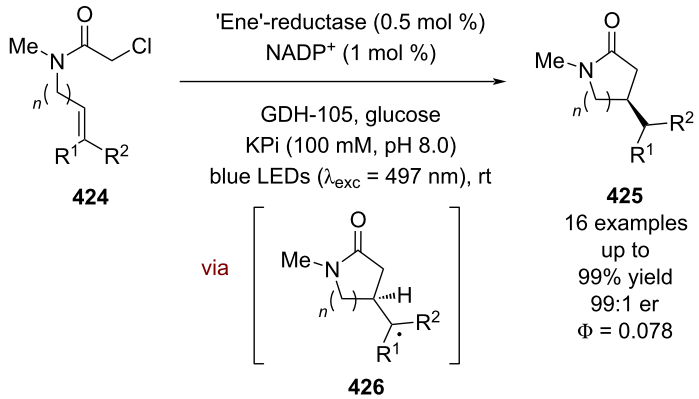

Scheme 72: Enzyme/photoredox-catalysed dehalogenative cyclisation.

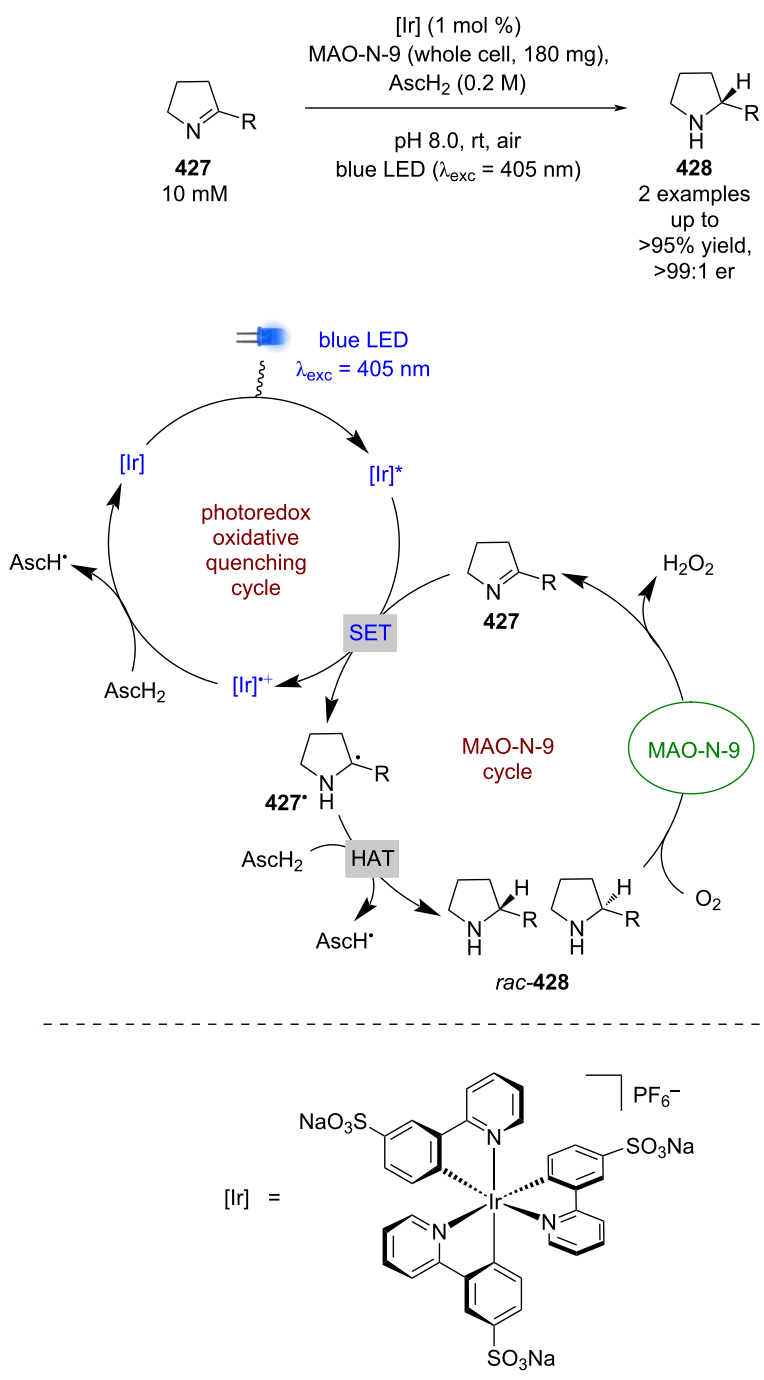

Scheme 73: Enzyme/photoredox-catalysed reduction of cyclic imines.

Zhao and Hartwig reported an enantioselective reduction of electron-deficient alkenes (Scheme 74) [170]. To do this, the authors assembled a collection of electron-deficient alkenes **429** that interacted with ERs for the selective reduction of either the (*E*) or (*Z*)-isomers. Separately, they optimised photoisomerisation conditions using either a flavin (FMN) or iridium-based photocatalyst, which proceeds through an energy transfer process. These reactions were combined for the enantioselective reduction of either the mismatched isomer of the alkene or mixtures of isomers where separation is not possible, in excellent yields and enantioselectivities (16 examples, up to >99:1 er).

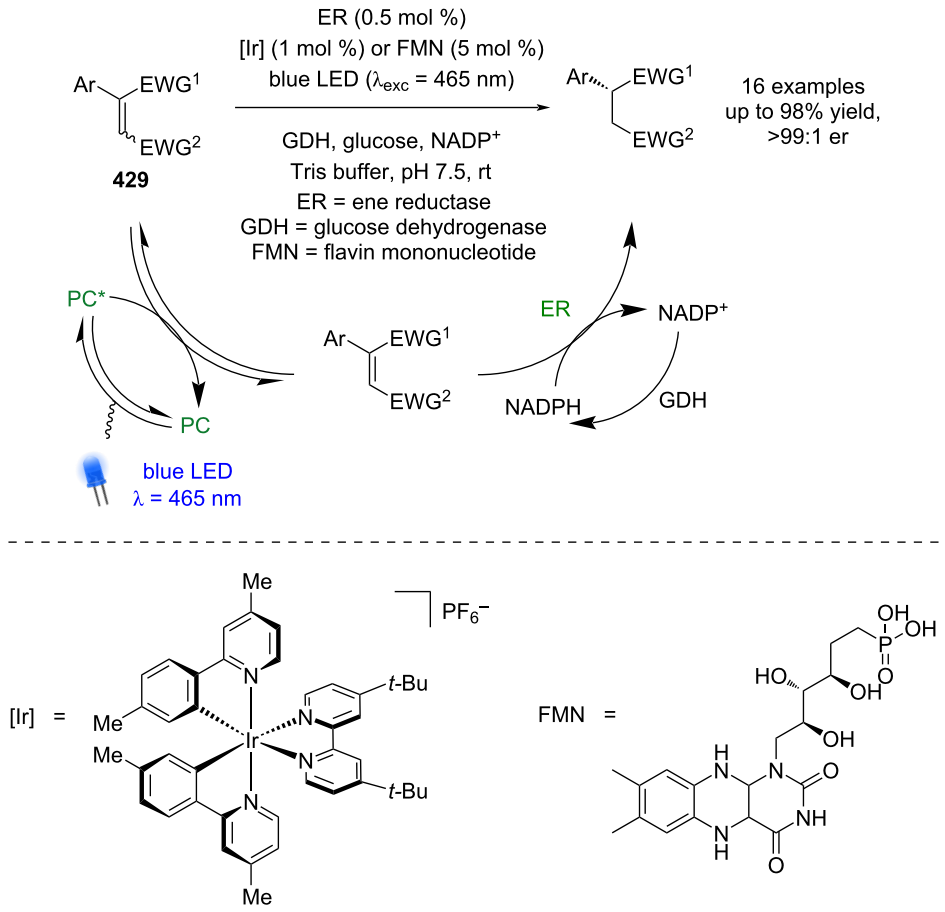

Scheme 74: Enzyme/photocatalysed enantioselective reduction of electron-deficient alkenes as mixtures of (*E*)/(*Z*)-isomers.

A significant challenge in many enantioselective photocatalysed reactions is minimising the amount of racemic background reaction. Hyster et al. proposed that the binding of a substrate by an enzyme could alter its redox properties so that the photoredox step only occurs within the enzyme binding site. They applied this hypothesis to a deacetoxylation reaction of tetralones **430** (Scheme 75a) [171]. The authors propose that Rose Bengal (RB) proceeds through a reductive quenching cycle in the presence of NADPH to give $RB^{\bullet-}$, which then reduces enzyme-bound **430** preferentially over free **430** to give radical anion $\mathbf{430}^{\bullet-}$. Deacetoxylation generates tertiary radical $\mathbf{431}^{\bullet}$ and subsequent enantioselective HAT with NADPH releases enantioenriched tetralone **431** after oxidation of $NADP^{\bullet}$ in good yields and enantioselectivities (12 examples, up to 97:3 er). This methodology was recently expanded to include heteroaromatic alkenes **432** using a similar single electron reduction to alkyl radical $\mathbf{432}^{\bullet}$ followed by ER-mediated enantioselective HAT to give reduced products **433** in excellent yields and enantioselectivities (22 examples, up to >99:1 er) (Scheme 75b) [172].

Guan and He developed a concurrent photooxidation and enzyme-mediated alkylation of indoles **434** with ketones **435** to obtain enantioenriched indole-3-ones **436** using wheat germ lipase (WGL) (Scheme 76) [173]. This reaction is proposed to proceed via a reductive quenching cycle, producing radical cation $\mathbf{434}^{\bullet+}$ and $[Ru]^{\bullet-}$, which is then oxidised by O_2 to complete the cycle and release $O_2^{\bullet-}$. Radical cation $\mathbf{434}^{\bullet+}$ can then trap $O_2^{\bullet-}$ to form hydroperoxyl intermediate **437**, that upon loss of water, is further oxidised to the indole-3-one **438**. Within the enzyme active site, **435** can nucleophilically add to **438** to give enantioenriched **436** in good yields and enantioselectivities (19 examples, up to 93:7 er).

Enzymes are commonly used for kinetic resolutions of primary amines [174]. However, by nature they are limited to a theoretical 50% yield; dynamic kinetic resolutions (DKRs) are a common adaptation that can increase the theoretical yield to 100% but require a mechanism for racemisation of the disfavoured enantiomer. Zhou et al. developed a dual catalytic system for the racemisation of amines **439** using HAT and

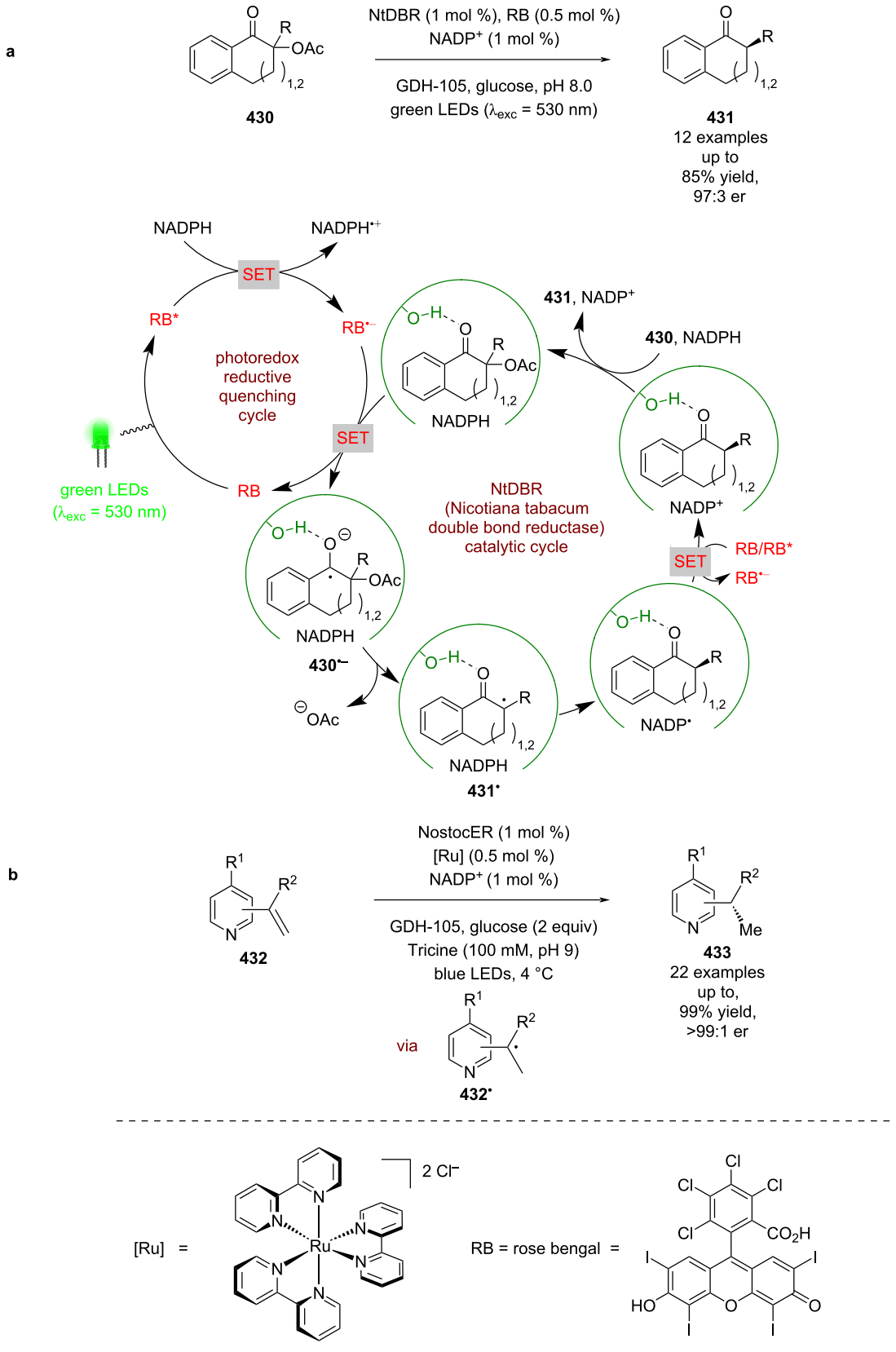

Scheme 75: Enzyme/photoredox catalysis. (a) Deacetoxylation of cyclic ketones. (b) Reduction of heteroaromatic alkenes.

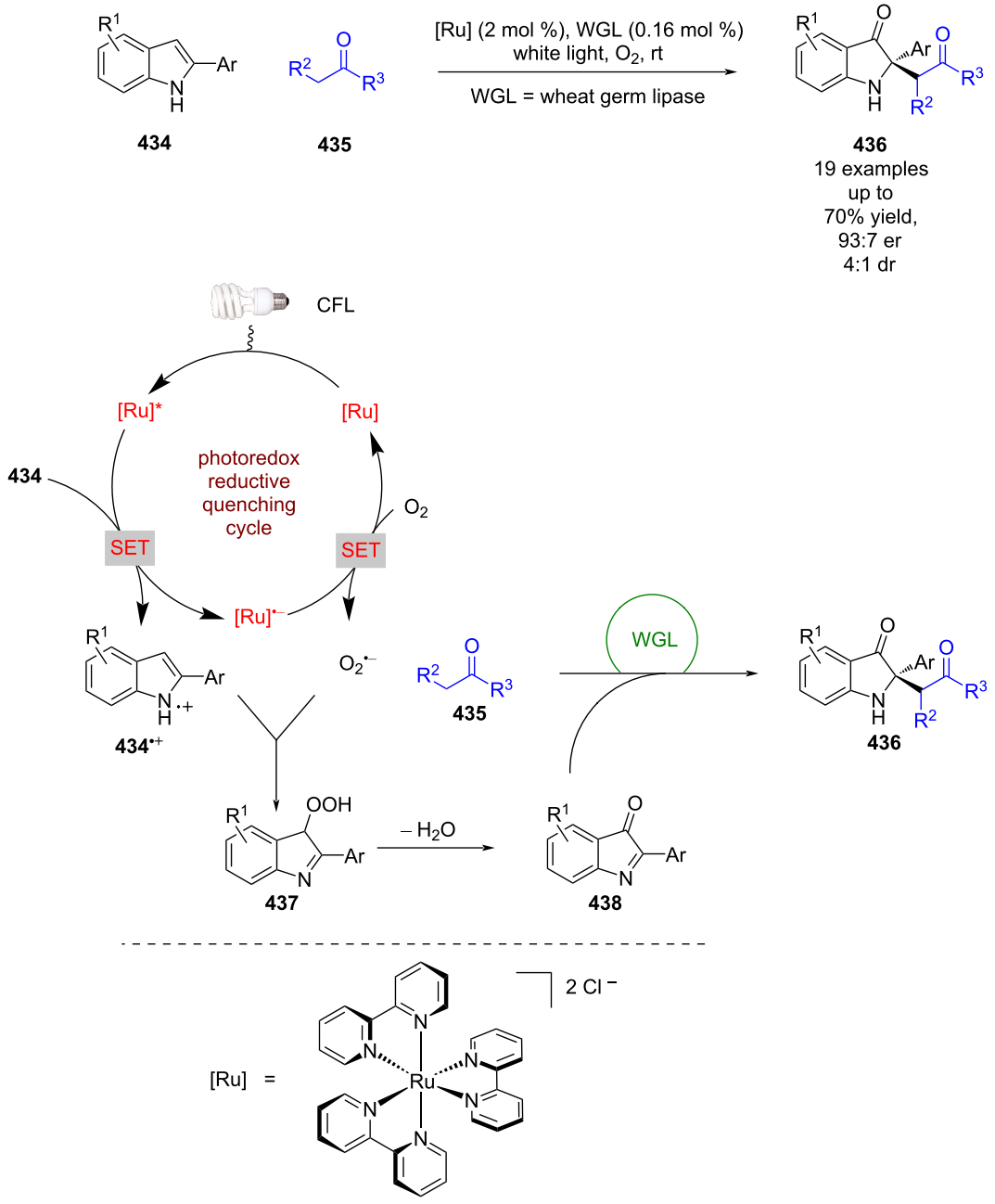

Scheme 76: Enzyme/photoredox-catalysed synthesis of indole-3-ones from 2-arylindoles.

photoredox catalysis [175]. They then combined this with an enzyme-mediated acylation to achieve a DKR of primary amines using Novozym 435 (Scheme 77). The proposed mechanism for this process involves a reductive quenching cycle with *n*-octylthiol to generate thiyl radicals **440•** and release of H^+. The thiyl radical **440•** is then implicated in either the turnover of the photocatalyst to regenerate the thiol or abstraction of a hydrogen atom from **439** to give α-amino radical **439•**, which in turn can abstract a hydrogen atom from the thiol to give either enantiomer of **439**, setting up a series of equilibria. When used in the presence of the appropriate enzyme and acylating reagent **441**, a single enantiomer is preferentially acylated to give enantioenriched amides **442** in excellent yields and enantioselectivities (20 examples, up to >99:1 er).

Cheruzel et al. has synthesised a series of hybrid metalloenzymes to include ruthenium photosensitising units [176,177] and have recently applied them as bifunctional photocatalysts

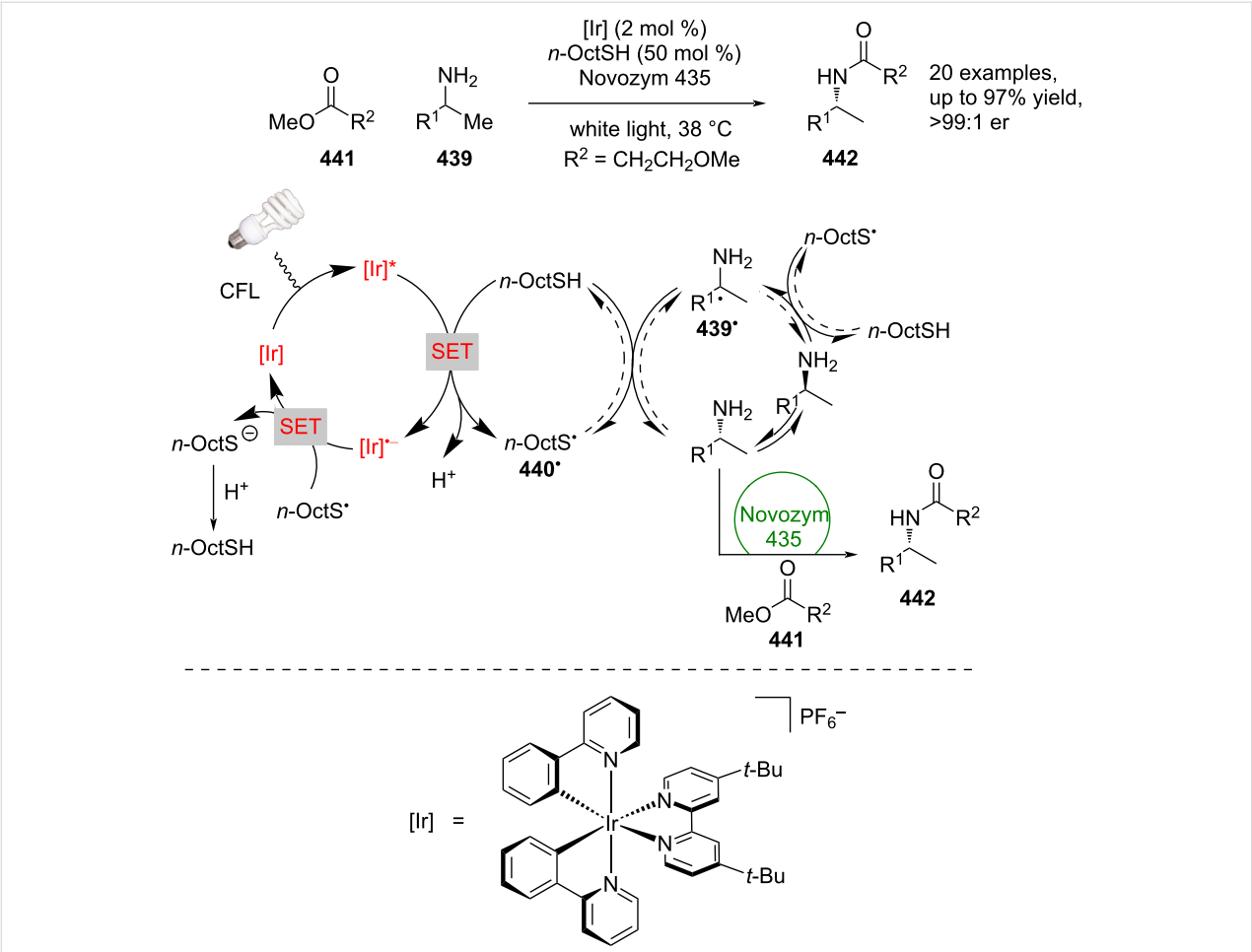

Scheme 77: Enzyme/HAT/photoredox catalysis for the DKR of primary amines.

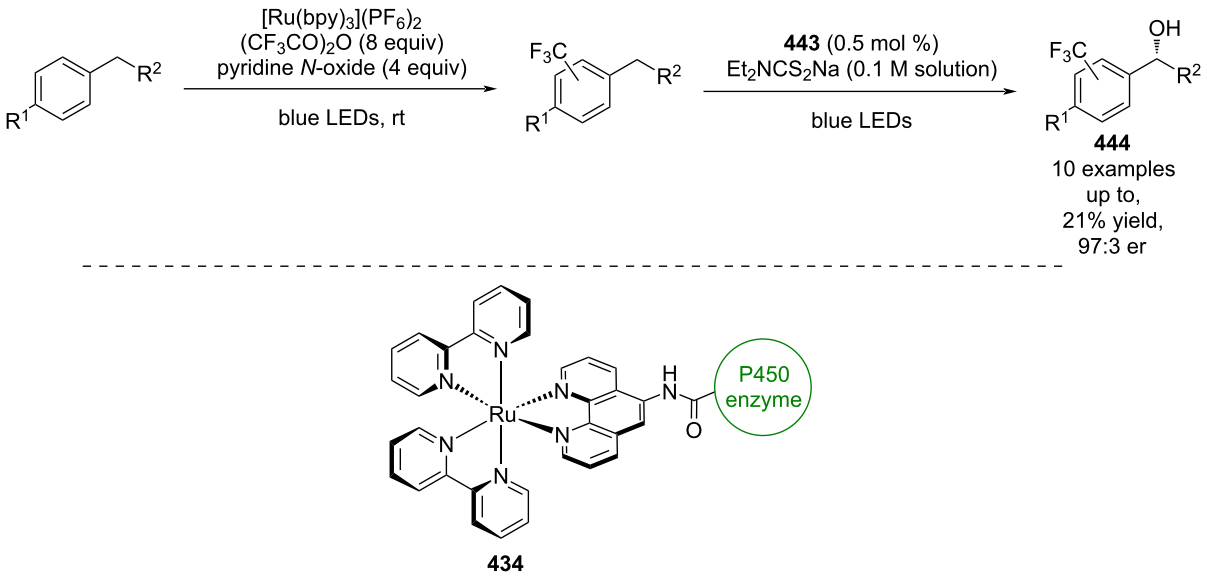

Scheme 78: Bifunctional enzyme/photoredox-catalysed benzylic C–H hydroxylation of trifluoromethylated arenes.

(Scheme 78) [178]. They combined a known trifluoromethylation reaction, with a hydroxylation catalysed by bifunctional photocatalyst **443** to synthesise alcohols **444**. Notably, the initial trifluoromethylation gives a mixture of isomers and the enzyme used can selectively oxidise different isomers, which explains the low yields.

Conclusion

Over the last 15 years enantioselective photocatalysis has seen tremendous growth. Well-established modes of enantioselective catalysis have been revolutionised by the introduction of photochemical processes, be that altering the behaviour of enzyme systems or utilising familiar catalytic intermediates, such as enamines or metal complexes, with photoredox-generated radicals.

There are certain photochemical processes that are still underutilised in the context of enantioselective photocatalysis. EnT reactions in particular are investigated far less than photoredox catalysis, leading to a field largely dominated by [2 + 2] cycloadditions with significantly less reaction diversity, even though the works of Bach and Meggers show the potential for greater reaction scope. Comparatively, enantioselective photoredox catalysis is well-established; however, a somewhat limited series of functional groups have been documented as radical precursors in this review, such as tertiary amines, carboxylic acids, and phthalimide esters. Recent developments in photoredox catalysis have allowed for the generation of radicals from much more challenging substrates by increasing the reducing power of the photocatalyst. It is expected that this will carry through to asymmetric catalysis and allow for a wider scope of enantioselective transformations.

Analogously, combinations of photocatalysts with new modes of enantioselective catalysis will also allow for new reactivity, for example, expanding transition metal dual catalysis systems to other metals or further developing existing systems such as NHC dual catalysis. Additionally, while there has been a considerable amount of research carried out using carbonyl-derived substrates, less functionalised starting materials generally have not been investigated to the same degree within enantioselective photocatalysis. Illustrative of this point, of the 114 reactions shown in this review, 92 of them exploit a carbonyl or carbonyl derivative for enantioselectivity.

Most photocatalytic transformations rely on external photocatalysts; however, as exemplified by the works of Melchiorre, Alemán, and others, recognising that substrates or intermediates can be themselves photoactive allows for the simplification of reaction procedures and also for new reactivity. It would be interesting to see further developments in this field by exploiting other potentially photoactive reaction intermediates in the same way.

As previously mentioned, a deeper underpinning understanding of the mechanisms and fundamental photophysics of enantioselective photocatalysis will significantly accelerate the development of new reactions. Therefore, both experimental and computational mechanistic investigations of existing reactions are crucial for the future of this field.

Acknowledgements

The Graphical abstract was illustrated by Yrral Galura, ykg.illani@gmail.com

Funding

We thank AstraZeneca for funding (C. P). A.D.S. thanks the Royal Society for a Wolfson Research Merit Award.

ORCID® iDs

Callum Prentice - https://orcid.org/0000-0002-2083-1499
Andrew D. Smith - https://orcid.org/0000-0002-2104-7313
Eli Zysman-Colman - https://orcid.org/0000-0001-7183-6022

References

1. Nicewicz, D. A.; MacMillan, D. W. C. *Science* **2008,** *322,* 77–80. doi:10.1126/science.1161976
2. Bauer, A.; Westkämper, F.; Grimme, S.; Bach, T. *Nature* **2005,** *436,* 1139–1140. doi:10.1038/nature03955
3. Fensterbank, L.; Goddard, J.-P.; Ollivier, C. Visible-Light-Mediated Free Radical Synthesis. *Visible Light Photocatalysis in Organic Chemistry;* John Wiley & Sons, 2018; pp 25–71. doi:10.1002/9783527674145.ch2
4. Strieth-Kalthoff, F.; James, M. J.; Teders, M.; Pitzer, L.; Glorius, F. *Chem. Soc. Rev.* **2018,** *47,* 7190–7202. doi:10.1039/c8cs00054a
5. Brimioulle, R.; Lenhart, D.; Maturi, M. M.; Bach, T. *Angew. Chem., Int. Ed.* **2015,** *54,* 3872–3890. doi:10.1002/anie.201411409
6. Jiang, C.; Chen, W.; Zheng, W.-H.; Lu, H. *Org. Biomol. Chem.* **2019,** *17,* 8673–8689. doi:10.1039/c9ob01609k
7. Seel, C. J.; Gulder, T. *ChemBioChem* **2019,** *20,* 1871–1897. doi:10.1002/cbic.201800806
8. Brenninger, C.; Jolliffe, J. D.; Bach, T. *Angew. Chem., Int. Ed.* **2018,** *57,* 14338–14349. doi:10.1002/anie.201804006
9. Huo, H.; Meggersa, E. *Chimia* **2016,** *70,* 186–191. doi:10.2533/chimia.2016.186
10. Coote, S. C.; Bach, T. Enantioselective Photocatalysis. *Visible Light Photocatalysis in Organic Chemistry;* John Wiley & Sons, 2018; pp 335–361. doi:10.1002/9783527674145.ch11
11. Silvi, M.; Melchiorre, P. *Nature* **2018,** *554,* 41–49. doi:10.1038/nature25175
12. Zou, Y.-Q.; Hörmann, F. M.; Bach, T. *Chem. Soc. Rev.* **2018,** *47,* 278–290. doi:10.1039/c7cs00509a
13. Burg, F.; Bach, T. *J. Org. Chem.* **2019,** *84,* 8815–8836. doi:10.1021/acs.joc.9b01299

14. Holden, C. M.; Melchiorre, P. Photochemistry and Excited-State Reactivity of Organocatalytic Intermediates. In *Photochemistry;* Albini, A.; Protti, S., Eds.; Royal Society of Chemistry: Cambridge. U.K., 2019; Vol. 47, pp 344–378. doi:10.1039/9781788016520-00344
15. Zhang, H.-H.; Chen, H.; Zhu, C.; Yu, S. *Sci. China: Chem.* **2020,** *63,* 637–647. doi:10.1007/s11426-019-9701-5
16. Saha, D. *Chem. – Asian J.* **2020,** *15,* 2129–2152. doi:10.1002/asia.202000525
17. Arokianathar, J. N.; Frost, A. B.; Slawin, A. M. Z.; Stead, D.; Smith, A. D. *ACS Catal.* **2018,** *8,* 1153–1160. doi:10.1021/acscatal.7b02697
18. Betori, R. C.; May, C. M.; Scheidt, K. A. *Angew. Chem., Int. Ed.* **2019,** *58,* 16490–16494. doi:10.1002/anie.201909426
19. Rostoll-Berenguer, J.; Blay, G.; Muñoz, M. C.; Pedro, J. R.; Vila, C. *Org. Lett.* **2019,** *21,* 6011–6015. doi:10.1021/acs.orglett.9b02157
20. Cismesia, M. A.; Yoon, T. P. *Chem. Sci.* **2015,** *6,* 5426–5434. doi:10.1039/c5sc02185e
21. Bahamonde, A.; Melchiorre, P. *J. Am. Chem. Soc.* **2016,** *138,* 8019–8030. doi:10.1021/jacs.6b04871
22. Zhu, Y.; Zhang, L.; Luo, S. *J. Am. Chem. Soc.* **2014,** *136,* 14642–14645. doi:10.1021/ja508605a
23. Nagib, D. A.; Scott, M. E.; MacMillan, D. W. C. *J. Am. Chem. Soc.* **2009,** *131,* 10875–10877. doi:10.1021/ja9053338
24. Shih, H.-W.; Vander Wal, M. N.; Grange, R. L.; MacMillan, D. W. C. *J. Am. Chem. Soc.* **2010,** *132,* 13600–13603. doi:10.1021/ja106593m
25. Welin, E. R.; Warkentin, A. A.; Conrad, J. C.; MacMillan, D. W. C. *Angew. Chem., Int. Ed.* **2015,** *54,* 9668–9672. doi:10.1002/anie.201503789
26. Gualandi, A.; Marchini, M.; Mengozzi, L.; Kidanu, H. T.; Franc, A.; Ceroni, P.; Cozzi, P. G. *Eur. J. Org. Chem.* **2020,** 1187. doi:10.1002/ejoc.201901801
27. Capacci, A. G.; Malinowski, J. T.; McAlpine, N. J.; Kuhne, J.; MacMillan, D. W. C. *Nat. Chem.* **2017,** *9,* 1073–1077. doi:10.1038/nchem.2797
28. Yang, Q.; Zhang, L.; Ye, C.; Luo, S.; Wu, L.-Z.; Tung, C.-H. *Angew. Chem., Int. Ed.* **2017,** *56,* 3694–3698. doi:10.1002/anie.201700572
29. Dong, C.-L.; Ding, X.; Huang, L.-Q.; He, Y.-H.; Guan, Z. *Org. Lett.* **2020,** *22,* 1076–1080. doi:10.1021/acs.orglett.9b04613
30. Yang, X.; Xie, Z.; Li, Y.; Zhang, Y. *Chem. Sci.* **2020,** *11,* 4741–4746. doi:10.1039/d0sc00683a
31. Rigotti, T.; Casado-Sánchez, A.; Cabrera, S.; Pérez-Ruiz, R.; Liras, M.; de la Peña O'Shea, V. A.; Alemán, J. *ACS Catal.* **2018,** *8,* 5928–5940. doi:10.1021/acscatal.8b01331
32. Arceo, E.; Jurberg, I. D.; Álvarez-Fernández, A.; Melchiorre, P. *Nat. Chem.* **2013,** *5,* 750–756. doi:10.1038/nchem.1727
33. Arceo, E.; Bahamonde, A.; Bergonzini, G.; Melchiorre, P. *Chem. Sci.* **2014,** *5,* 2438–2442. doi:10.1039/c4sc00315b
34. Crisenza, G. E. M.; Mazzarella, D.; Melchiorre, P. *J. Am. Chem. Soc.* **2020,** *142,* 5461–5476. doi:10.1021/jacs.0c01416
35. Silvi, M.; Arceo, E.; Jurberg, I. D.; Cassani, C.; Melchiorre, P. *J. Am. Chem. Soc.* **2015,** *137,* 6120–6123. doi:10.1021/jacs.5b01662
36. Filippini, G.; Silvi, M.; Melchiorre, P. *Angew. Chem., Int. Ed.* **2017,** *56,* 4447–4451. doi:10.1002/anie.201612045
37. Narayanam, J. M. R.; Tucker, J. W.; Stephenson, C. R. J. *J. Am. Chem. Soc.* **2009,** *131,* 8756–8757. doi:10.1021/ja9033582
38. Freeman, D. B.; Furst, L.; Condie, A. G.; Stephenson, C. R. J. *Org. Lett.* **2012,** *14,* 94–97. doi:10.1021/ol202883v
39. Murphy, J. J.; Bastida, D.; Paria, S.; Fagnoni, M.; Melchiorre, P. *Nature* **2016,** *532,* 218–222. doi:10.1038/nature17438
40. Zhao, J.-J.; Zhang, H.-H.; Shen, X.; Yu, S. *Org. Lett.* **2019,** *21,* 913–916. doi:10.1021/acs.orglett.8b03840
41. Cao, Z.-Y.; Ghosh, T.; Melchiorre, P. *Nat. Commun.* **2018,** *9,* 3274. doi:10.1038/s41467-018-05375-2
42. Silvi, M.; Verrier, C.; Rey, Y. P.; Buzzetti, L.; Melchiorre, P. *Nat. Chem.* **2017,** *9,* 868–873. doi:10.1038/nchem.2748
43. Mazzarella, D.; Crisenza, G. E. M.; Melchiorre, P. *J. Am. Chem. Soc.* **2018,** *140,* 8439–8443. doi:10.1021/jacs.8b05240
44. Verrier, C.; Alandini, N.; Pezzetta, C.; Moliterno, M.; Buzzetti, L.; Hepburn, H. B.; Vega-Peñaloza, A.; Silvi, M.; Melchiorre, P. *ACS Catal.* **2018,** *8,* 1062–1066. doi:10.1021/acscatal.7b03788
45. Goti, G.; Bieszczad, B.; Vega-Peñaloza, A.; Melchiorre, P. *Angew. Chem.* **2019,** *131,* 1226–1230. doi:10.1002/ange.201810798
46. Bonilla, P.; Rey, Y. P.; Holden, C. M.; Melchiorre, P. *Angew. Chem., Int. Ed.* **2018,** *57,* 12819–12823. doi:10.1002/anie.201808183
47. Perego, L. A.; Bonilla, P.; Melchiorre, P. *Adv. Synth. Catal.* **2020,** *362,* 302–307. doi:10.1002/adsc.201900973
48. Hörmann, F. M.; Kerzig, C.; Chung, T. S.; Bauer, A.; Wenger, O. S.; Bach, T. *Angew. Chem., Int. Ed.* **2020,** *59,* 9659–9668. doi:10.1002/anie.202001634
49. Rigotti, T.; Mas-Ballesté, R.; Alemán, J. *ACS Catal.* **2020,** *10,* 5335–5346. doi:10.1021/acscatal.0c01413
50. Wei, G.; Zhang, C.; Bureš, F.; Ye, X.; Tan, C.-H.; Jiang, Z. *ACS Catal.* **2016,** *6,* 3708–3712. doi:10.1021/acscatal.6b00846
51. DiRocco, D. A.; Rovis, T. *J. Am. Chem. Soc.* **2012,** *134,* 8094–8097. doi:10.1021/ja3030164
52. Lathrop, S. P.; Rovis, T. *Chem. Sci.* **2013,** *4,* 1668. doi:10.1039/c3sc22292f
53. Dai, L.; Ye, S. *Org. Lett.* **2020,** *22,* 986–990. doi:10.1021/acs.orglett.9b04533
54. Dai, L.; Xia, Z.-H.; Gao, Y.-Y.; Gao, Z.-H.; Ye, S. *Angew. Chem., Int. Ed.* **2019,** *58,* 18124–18130. doi:10.1002/anie.201909017
55. Yang, W.; Hu, W.; Dong, X.; Li, X.; Sun, J. *Angew. Chem., Int. Ed.* **2016,** *55,* 15783–15786. doi:10.1002/anie.201608371
56. Mavroskoufis, A.; Rajes, K.; Golz, P.; Agrawal, A.; Ruß, V.; Götze, J. P.; Hopkinson, M. N. *Angew. Chem., Int. Ed.* **2020,** *59,* 3190–3194. doi:10.1002/anie.201914456
57. Rono, L. J.; Yayla, H. G.; Wang, D. Y.; Armstrong, M. F.; Knowles, R. R. *J. Am. Chem. Soc.* **2013,** *135,* 17735–17738. doi:10.1021/ja4100595
58. Li, S.; Xiang, S.-H.; Tan, B. *Chin. J. Chem.* **2020,** *38,* 213–214. doi:10.1002/cjoc.201900472
59. Proctor, R. S. J.; Davis, H. J.; Phipps, R. J. *Science* **2018,** *360,* 419–422. doi:10.1126/science.aar6376
60. Yin, Y.; Dai, Y.; Jia, H.; Li, J.; Bu, L.; Qiao, B.; Zhao, X.; Jiang, Z. *J. Am. Chem. Soc.* **2018,** *140,* 6083–6087. doi:10.1021/jacs.8b01575
61. Cao, K.; Tan, S. M.; Lee, R.; Yang, S.; Jia, H.; Zhao, X.; Qiao, B.; Jiang, Z. *J. Am. Chem. Soc.* **2019,** *141,* 5437–5443. doi:10.1021/jacs.9b00286
62. Liu, X.; Liu, Y.; Chai, G.; Qiao, B.; Zhao, X.; Jiang, Z. *Org. Lett.* **2018,** *20,* 6298–6301. doi:10.1021/acs.orglett.8b02791
63. Zheng, D.; Studer, A. *Angew. Chem., Int. Ed.* **2019,** *58,* 15803–15807. doi:10.1002/anie.201908987
64. Qiao, B.; Li, C.; Zhao, X.; Yin, Y.; Jiang, Z. *Chem. Commun.* **2019,** *55,* 7534–7537. doi:10.1039/c9cc03661j
65. Shao, T.; Li, Y.; Ma, N.; Li, C.; Chai, G.; Zhao, X.; Qiao, B.; Jiang, Z. *iScience* **2019,** *16,* 410–419. doi:10.1016/j.isci.2019.06.007

66. Li, J.; Kong, M.; Qiao, B.; Lee, R.; Zhao, X.; Jiang, Z. *Nat. Commun.* **2018,** *9,* 2445. doi:10.1038/s41467-018-04885-3
67. Zeng, G.; Li, Y.; Qiao, B.; Zhao, X.; Jiang, Zhiyong. *Chem. Commun.* **2019,** *55,* 11362–11365. doi:10.1039/c9cc05304b
68. Liu, Y.; Liu, X.; Li, J.; Zhao, X.; Qiao, B.; Jiang, Z. *Chem. Sci.* **2018,** *9,* 8094–8098. doi:10.1039/c8sc02948b
69. Shao, T.; Yin, Y.; Lee, R.; Zhao, X.; Chai, G.; Jiang, Z. *Adv. Synth. Catal.* **2018,** *360,* 1754–1760. doi:10.1002/adsc.201800135
70. Li, J.; Gu, Z.; Zhao, X.; Qiao, B.; Jiang, Z. *Chem. Commun.* **2019,** *55,* 12916–12919. doi:10.1039/c9cc07380a
71. Cheng, Y.-Z.; Zhao, Q.-R.; Zhang, X.; You, S.-L. *Angew. Chem., Int. Ed.* **2019,** *58,* 18069–18074. doi:10.1002/anie.201911144
72. Pecho, F.; Zou, Y.-Q.; Gramüller, J.; Mori, T.; Huber, S. M.; Bauer, A.; Gschwind, R. M.; Bach, T. *Chem. – Eur. J.* **2020,** *26,* 5190–5194. doi:10.1002/chem.202000720
73. Lian, M.; Li, Z.; Cai, Y.; Meng, Q.; Gao, Z. *Chem. – Asian J.* **2012,** *7,* 2019–2023. doi:10.1002/asia.201200358
74. Wang, Y.; Zheng, Z.; Lian, M.; Yin, H.; Zhao, J.; Meng, Q.; Gao, Z. *Green Chem.* **2016,** *18,* 5493–5499. doi:10.1039/c6gc01245k
75. Wang, Y.; Yin, H.; Tang, X.; Wu, Y.; Meng, Q.; Gao, Z. *J. Org. Chem.* **2016,** *81,* 7042–7050. doi:10.1021/acs.joc.6b00856
76. Tang, X.-F.; Zhao, J.-N.; Wu, Y.-F.; Zheng, Z.-H.; Feng, S.-H.; Yu, Z.-Y.; Liu, G.-Z.; Meng, Q.-W. *Org. Biomol. Chem.* **2019,** *17,* 7938–7942. doi:10.1039/c9ob01379b
77. Woźniak, Ł.; Murphy, J. J.; Melchiorre, P. *J. Am. Chem. Soc.* **2015,** *137,* 5678–5681. doi:10.1021/jacs.5b03243
78. Cauble, D. F.; Lynch, V.; Krische, M. J. *J. Org. Chem.* **2003,** *68,* 15–21. doi:10.1021/jo020630e
79. Müller, C.; Bauer, A.; Bach, T. *Angew. Chem., Int. Ed.* **2009,** *48,* 6640–6642. doi:10.1002/anie.200901603
80. Müller, C.; Bauer, A.; Maturi, M. M.; Cuquerella, M. C.; Miranda, M. A.; Bach, T. *J. Am. Chem. Soc.* **2011,** *133,* 16689–16697. doi:10.1021/ja207480q
81. Alonso, R.; Bach, T. *Angew. Chem., Int. Ed.* **2014,** *53,* 4368–4371. doi:10.1002/anie.201310997
82. Maturi, M. M.; Bach, T. *Angew. Chem., Int. Ed.* **2014,** *53,* 7661–7664. doi:10.1002/anie.201403885
83. Tröster, A.; Alonso, R.; Bauer, A.; Bach, T. *J. Am. Chem. Soc.* **2016,** *138,* 7808–7811. doi:10.1021/jacs.6b03221
84. Li, X.; Jandl, C.; Bach, T. *Org. Lett.* **2020,** *22,* 3618–3622. doi:10.1021/acs.orglett.0c01065
85. Hölzl-Hobmeier, A.; Bauer, A.; Silva, A. V.; Huber, S. M.; Bannwarth, C.; Bach, T. *Nature* **2018,** *564,* 240–243. doi:10.1038/s41586-018-0755-1
86. Plaza, M.; Jandl, C.; Bach, T. *Angew. Chem., Int. Ed.* **2020,** *59,* 12785–12788. doi:10.1002/anie.202004797
87. Wimberger, L.; Kratz, T.; Bach, T. *Synthesis* **2019,** *51,* 4417–4424. doi:10.1055/s-0039-1690034
88. Tröster, A.; Bauer, A.; Jandl, C.; Bach, T. *Angew. Chem., Int. Ed.* **2019,** *58,* 3538–3541. doi:10.1002/anie.201814193
89. Vallavoju, N.; Selvakumar, S.; Jockusch, S.; Sibi, M. P.; Sivaguru, J. *Angew. Chem., Int. Ed.* **2014,** *53,* 5604–5608. doi:10.1002/anie.201310940
90. Skubi, K. L.; Kidd, J. B.; Jung, H.; Guzei, I. A.; Baik, M.-H.; Yoon, T. P. *J. Am. Chem. Soc.* **2017,** *139,* 17186–17192. doi:10.1021/jacs.7b10586
91. Skubi, K. L.; Swords, W. B.; Hofstetter, H.; Yoon, T. P. *ChemPhotoChem* **2020,** *4,* 685–690. doi:10.1002/cptc.202000094
92. Zheng, J.; Swords, W. B.; Jung, H.; Skubi, K. L.; Kidd, J. B.; Meyer, G. J.; Baik, M.-H.; Yoon, T. P. *J. Am. Chem. Soc.* **2019,** *141,* 13625–13634. doi:10.1021/jacs.9b06244
93. Liu, Y.; Li, J.; Ye, X.; Zhao, X.; Jiang, Z. *Chem. Commun.* **2016,** *52,* 13955–13958. doi:10.1039/c6cc07105h
94. Griffiths, J.; Chu, K.-Y.; Hawkins, C. *J. Chem. Soc., Chem. Commun.* **1976,** 676–677. doi:10.1039/c39760000676
95. Hou, M.; Lin, L.; Chai, X.; Zhao, X.; Qiao, B.; Jiang, Z. *Chem. Sci.* **2019,** *10,* 6629–6634. doi:10.1039/c9sc02000d
96. Lin, L.; Bai, X.; Ye, X.; Zhao, X.; Tan, C.-H.; Jiang, Z. *Angew. Chem., Int. Ed.* **2017,** *56,* 13842–13846. doi:10.1002/anie.201707899
97. Shin, N. Y.; Ryss, J. M.; Zhang, X.; Miller, S. J.; Knowles, R. R. *Science* **2019,** *366,* 364–369. doi:10.1126/science.aay2204
98. Roos, C. B.; Demaerel, J.; Graff, D. E.; Knowles, R. R. *J. Am. Chem. Soc.* **2020,** *142,* 5974–5979. doi:10.1021/jacs.0c01332
99. Shen, M.-L.; Shen, Y.; Wang, P.-S. *Org. Lett.* **2019,** *21,* 2993–2997. doi:10.1021/acs.orglett.9b00442
100. Uraguchi, D.; Kinoshita, N.; Kizu, T.; Ooi, T. *J. Am. Chem. Soc.* **2015,** *137,* 13768–13771. doi:10.1021/jacs.5b09329
101. Yang, Z.; Li, H.; Li, S.; Zhang, M.-T.; Luo, S. *Org. Chem. Front.* **2017,** *4,* 1037–1041. doi:10.1039/c6qo00806b
102. Hamilton, D. S.; Nicewicz, D. A. *J. Am. Chem. Soc.* **2012,** *134,* 18577–18580. doi:10.1021/ja309635w
103. Gentry, E. C.; Rono, L. J.; Hale, M. E.; Matsuura, R.; Knowles, R. R. *J. Am. Chem. Soc.* **2018,** *140,* 3394–3402. doi:10.1021/jacs.7b13616
104. Morse, P. D.; Nguyen, T. M.; Cruz, C. L.; Nicewicz, D. A. *Tetrahedron* **2018,** *74,* 3266–3272. doi:10.1016/j.tet.2018.03.052
105. Mukaiyama, T.; Narasaka, K.; Banno, K. *Chem. Lett.* **1973,** *2,* 1011–1014. doi:10.1246/cl.1973.1011
106. Wadamoto, M.; Ozasa, N.; Yanagisawa, A.; Yamamoto, H. *J. Org. Chem.* **2003,** *68,* 5593–5601. doi:10.1021/jo020691c
107. Du, J.; Skubi, K. L.; Schultz, D. M.; Yoon, T. P. *Science* **2014,** *344,* 392–396. doi:10.1126/science.1251511
108. Amador, A. G.; Sherbrook, E. M.; Yoon, T. P. *J. Am. Chem. Soc.* **2016,** *138,* 4722–4725. doi:10.1021/jacs.6b01728
109. Ruiz Espelt, L.; McPherson, I. S.; Wiensch, E. M.; Yoon, T. P. *J. Am. Chem. Soc.* **2015,** *137,* 2452–2455. doi:10.1021/ja512746q
110. Ruiz Espelt, L.; Wiensch, E. M.; Yoon, T. P. *J. Org. Chem.* **2013,** *78,* 4107–4114. doi:10.1021/jo400428m
111. Pagire, S. K.; Kumagai, N.; Shibasaki, M. *Chem. Sci.* **2020,** *11,* 5168–5174. doi:10.1039/d0sc01890b
112. Ye, C.-X.; Melcamu, Y. Y.; Li, H.-H.; Cheng, J.-T.; Zhang, T.-T.; Ruan, Y.-P.; Zheng, X.; Lu, X.; Huang, P.-Q. *Nat. Commun.* **2018,** *9,* 410. doi:10.1038/s41467-017-02698-4
113. Miller, Z. D.; Lee, B. J.; Yoon, T. P. *Angew. Chem., Int. Ed.* **2017,** *56,* 11891–11895. doi:10.1002/anie.201706975
114. Blum, T. R.; Miller, Z. D.; Bates, D. M.; Guzei, I. A.; Yoon, T. P. *Science* **2016,** *354,* 1391–1395. doi:10.1126/science.aai8228
115. Huo, H.; Harms, K.; Meggers, E. *J. Am. Chem. Soc.* **2016,** *138,* 6936–6939. doi:10.1021/jacs.6b03399
116. Steinlandt, P. S.; Zuo, W.; Harms, K.; Meggers, E. *Chem. – Eur. J.* **2019,** *25,* 15333–15340. doi:10.1002/chem.201903369
117. Huang, X.; Webster, R. D.; Harms, K.; Meggers, E. *J. Am. Chem. Soc.* **2016,** *138,* 12636–12642. doi:10.1021/jacs.6b07692
118. Kuang, Y.; Wang, K.; Shi, X.; Huang, X.; Meggers, E.; Wu, J. *Angew. Chem., Int. Ed.* **2019,** *58,* 16859–16863. doi:10.1002/anie.201910414

119. Huang, X.; Lin, J.; Shen, T.; Harms, K.; Marchini, M.; Ceroni, P.; Meggers, E. *Angew. Chem., Int. Ed.* **2018,** *57,* 5454–5458. doi:10.1002/anie.201802316
120. Huang, X.; Meggers, E. *Acc. Chem. Res.* **2019,** *52,* 833–847. doi:10.1021/acs.accounts.9b00028
121. Liang, H.; Xu, G.-Q.; Feng, Z.-T.; Wang, Z.-Y.; Xu, P.-F. *J. Org. Chem.* **2019,** *84,* 60–72. doi:10.1021/acs.joc.8b02316
122. Zhou, Z.; Nie, X.; Harms, K.; Riedel, R.; Zhang, L.; Meggers, E. *Sci. China: Chem.* **2019,** *62,* 1512–1518. doi:10.1007/s11426-019-9584-x
123. Zhang, C.; Chen, S.; Ye, C.-X.; Harms, K.; Zhang, L.; Houk, K. N.; Meggers, E. *Angew. Chem., Int. Ed.* **2019,** *58,* 14462–14466. doi:10.1002/anie.201905647
124. Zhang, K.; Lu, L.-Q.; Jia, Y.; Wang, Y.; Lu, F.-D.; Pan, F.; Xiao, W.-J. *Angew. Chem., Int. Ed.* **2019,** *58,* 13375–13379. doi:10.1002/anie.201907478
125. Ding, W.; Lu, L.-Q.; Zhou, Q.-Q.; Wei, Y.; Chen, J.-R.; Xiao, W.-J. *J. Am. Chem. Soc.* **2017,** *139,* 63–66. doi:10.1021/jacs.6b11418
126. Liu, J.; Ding, W.; Zhou, Q.-Q.; Liu, D.; Lu, L.-Q.; Xiao, W.-J. *Org. Lett.* **2018,** *20,* 461–464. doi:10.1021/acs.orglett.7b03826
127. Li, Y.; Zhou, K.; Wen, Z.; Cao, S.; Shen, X.; Lei, M.; Gong, L. *J. Am. Chem. Soc.* **2018,** *140,* 15850–15858. doi:10.1021/jacs.8b09251
128. Han, B.; Li, Y.; Yu, Y.; Gong, L. *Nat. Commun.* **2019,** *10,* 3804. doi:10.1038/s41467-019-11688-7
129. Li, Y.; Lei, M.; Gong, L. *Nat. Catal.* **2019,** *2,* 1016–1026. doi:10.1038/s41929-019-0357-9
130. Lewis, F. D.; Howard, D. K.; Oxman, J. D. *J. Am. Chem. Soc.* **1983,** *105,* 3344–3345. doi:10.1021/ja00348a069
131. Lewis, F. D.; Barancyk, S. V. *J. Am. Chem. Soc.* **1989,** *111,* 8653–8661. doi:10.1021/ja00205a015
132. Guo, H.; Herdtweck, E.; Bach, T. *Angew. Chem., Int. Ed.* **2010,** *49,* 7782–7785. doi:10.1002/anie.201003619
133. Brimioulle, R.; Bauer, A.; Bach, T. *J. Am. Chem. Soc.* **2015,** *137,* 5170–5176. doi:10.1021/jacs.5b01740
134. Brimioulle, R.; Bach, T. *Science* **2013,** *342,* 840–843. doi:10.1126/science.1244809
135. Poplata, S.; Bach, T. *J. Am. Chem. Soc.* **2018,** *140,* 3228–3231. doi:10.1021/jacs.8b01011
136. Stegbauer, S.; Jandl, C.; Bach, T. *Angew. Chem., Int. Ed.* **2018,** *57,* 14593–14596. doi:10.1002/anie.201808919
137. Leverenz, M.; Merten, C.; Dreuw, A.; Bach, T. *J. Am. Chem. Soc.* **2019,** *141,* 20053–20057. doi:10.1021/jacs.9b12068
138. Daub, M. E.; Jung, H.; Lee, B. J.; Won, J.; Baik, M.-H.; Yoon, T. P. *J. Am. Chem. Soc.* **2019,** *141,* 9543–9547. doi:10.1021/jacs.9b04643
139. De Abreu, M.; Belmont, P.; Brachet, E. *Eur. J. Org. Chem.* **2020,** 1327–1378. doi:10.1002/ejoc.201901146
140. Twilton, J.; Le, C.; Zhang, P.; Shaw, M. H.; Evans, R. W.; MacMillan, D. W. C. *Nat. Rev. Chem.* **2017,** *1,* 0052. doi:10.1038/s41570-017-0052
141. Gui, Y.-Y.; Sun, L.; Lu, Z.-P.; Yu, D.-G. *Org. Chem. Front.* **2016,** *3,* 522–526. doi:10.1039/c5qo00437c
142. Tellis, J. C.; Kelly, C. B.; Primer, D. N.; Jouffroy, M.; Patel, N. R.; Molander, G. A. *Acc. Chem. Res.* **2016,** *49,* 1429–1439. doi:10.1021/acs.accounts.6b00214
143. Zuo, Z.; Cong, H.; Li, W.; Choi, J.; Fu, G. C.; MacMillan, D. W. C. *J. Am. Chem. Soc.* **2016,** *138,* 1832–1835. doi:10.1021/jacs.5b13211
144. Cheng, X.; Lu, H.; Lu, Z. *Nat. Commun.* **2019,** *10,* 3549. doi:10.1038/s41467-019-11392-6
145. Pezzetta, C.; Bonifazi, D.; Davidson, R. W. M. *Org. Lett.* **2019,** *21,* 8957–8961. doi:10.1021/acs.orglett.9b03338
146. Shen, Y.; Gu, Y.; Martin, R. *J. Am. Chem. Soc.* **2018,** *140,* 12200–12209. doi:10.1021/jacs.8b07405
147. Stache, E. E.; Rovis, T.; Doyle, A. G. *Angew. Chem., Int. Ed.* **2017,** *56,* 3679–3683. doi:10.1002/anie.201700097
148. Guan, H.; Zhang, Q.; Walsh, P. J.; Mao, J. *Angew. Chem., Int. Ed.* **2020,** *59,* 5172–5177. doi:10.1002/anie.201914175
149. Rand, A. W.; Yin, H.; Xu, L.; Giacoboni, J.; Martin-Montero, R.; Romano, C.; Montgomery, J.; Martin, R. *ACS Catal.* **2020,** *10,* 4671–4676. doi:10.1021/acscatal.0c01318
150. Esposti, S.; Dondi, D.; Fagnoni, M.; Albini, A. *Angew. Chem., Int. Ed.* **2007,** *46,* 2531–2534. doi:10.1002/anie.200604820
151. Fan, P.; Lan, Y.; Zhang, C.; Wang, C. *J. Am. Chem. Soc.* **2020,** *142,* 2180–2186. doi:10.1021/jacs.9b12554
152. Perry, I. B.; Brewer, T. F.; Sarver, P. J.; Schultz, D. M.; DiRocco, D. A.; MacMillan, D. W. C. *Nature* **2018,** *560,* 70–75. doi:10.1038/s41586-018-0366-x
153. Yuan, M.; Song, Z.; Badir, S. O.; Molander, G. A.; Gutierrez, O. *J. Am. Chem. Soc.* **2020,** *142,* 7225–7234. doi:10.1021/jacs.0c02355
154. Kainz, Q. M.; Matier, C. D.; Bartoszewicz, A.; Zultanski, S. L.; Peters, J. C.; Fu, G. C. *Science* **2016,** *351,* 681–684. doi:10.1126/science.aad8313
155. Zhang, Y.; Sun, Y.; Chen, B.; Xu, M.; Li, C.; Zhang, D.; Zhang, G. *Org. Lett.* **2020,** *22,* 1490–1494. doi:10.1021/acs.orglett.0c00071
156. Wang, D.; Zhu, N.; Chen, P.; Lin, Z.; Liu, G. *J. Am. Chem. Soc.* **2017,** *139,* 15632–15635. doi:10.1021/jacs.7b09802
157. Zhang, W.; Wang, F.; McCann, S. D.; Wang, D.; Chen, P.; Stahl, S. S.; Liu, G. *Science* **2016,** *353,* 1014–1018. doi:10.1126/science.aaf7783
158. Lu, F.-D.; Liu, D.; Zhu, L.; Lu, L.-Q.; Yang, Q.; Zhou, Q.-Q.; Wei, Y.; Lan, Y.; Xiao, W.-J. *J. Am. Chem. Soc.* **2019,** *141,* 6167–6172. doi:10.1021/jacs.9b02338
159. Chen, J.; Wang, P.-Z.; Lu, B.; Liang, D.; Yu, X.-Y.; Xiao, W.-J.; Chen, J.-R. *Org. Lett.* **2019,** *21,* 9763–9768. doi:10.1021/acs.orglett.9b03970
160. Sha, W.; Deng, L.; Ni, S.; Mei, H.; Han, J.; Pan, Y. *ACS Catal.* **2018,** *8,* 7489–7494. doi:10.1021/acscatal.8b01863
161. Guo, Q.; Wang, M.; Peng, Q.; Huo, Y.; Liu, Q.; Wang, R.; Xu, Z. *ACS Catal.* **2019,** *9,* 4470–4476. doi:10.1021/acscatal.9b00209
162. Zhang, H.-H.; Zhao, J.-J.; Yu, S. *J. Am. Chem. Soc.* **2018,** *140,* 16914–16919. doi:10.1021/jacs.8b10766
163. Zhang, H.-H.; Zhao, J.-J.; Yu, S. *ACS Catal.* **2020,** *10,* 4710–4716. doi:10.1021/acscatal.0c00871
164. Shen, D.; Saracini, C.; Lee, Y.-M.; Sun, W.; Fukuzumi, S.; Nam, W. *J. Am. Chem. Soc.* **2016,** *138,* 15857–15860. doi:10.1021/jacs.6b10836
165. Mitsunuma, H.; Tanabe, S.; Fuse, H.; Ohkubo, K.; Kanai, M. *Chem. Sci.* **2019,** *10,* 3459–3465. doi:10.1039/c8sc05677c
166. Bornscheuer, U. T.; Kazlauskas, R. J. Enzymatic Catalytic Promiscuity and the Design of New Enzyme Catalyzed Reactions. *Enzyme Catalysis in Organic Synthesis;* John Wiley & Sons, 2012; pp 1693–1733. doi:10.1002/9783527639861.ch41
167. Emmanuel, M. A.; Greenberg, N. R.; Oblinsky, D. G.; Hyster, T. K. *Nature* **2016,** *540,* 414–417. doi:10.1038/nature20569
168. Biegasiewicz, K. F.; Cooper, S. J.; Gao, X.; Oblinsky, D. G.; Kim, J. H.; Garfinkle, S. E.; Joyce, L. A.; Sandoval, B. A.; Scholes, G. D.; Hyster, T. K. *Science* **2019,** *364,* 1166–1169. doi:10.1126/science.aaw1143

169. Guo, X.; Okamoto, Y.; Schreier, M. R.; Ward, T. R.; Wenger, O. S. *Chem. Sci.* **2018,** *9,* 5052–5056. doi:10.1039/c8sc01561a
170. Litman, Z. C.; Wang, Y.; Zhao, H.; Hartwig, J. F. *Nature* **2018,** *560,* 355–359. doi:10.1038/s41586-018-0413-7
171. Biegasiewicz, K. F.; Cooper, S. J.; Emmanuel, M. A.; Miller, D. C.; Hyster, T. K. *Nat. Chem.* **2018,** *10,* 770–775. doi:10.1038/s41557-018-0059-y
172. Nakano, Y.; Black, M. J.; Meichan, A. J.; Sandoval, B. A.; Chung, M. M.; Biegasiewicz, K. F.; Zhu, T.; Hyster, T. K. *Angew. Chem., Int. Ed.* **2020,** *59,* 10484–10488. doi:10.1002/anie.202003125
173. Ding, X.; Dong, C.-L.; Guan, Z.; He, Y.-H. *Angew. Chem., Int. Ed.* **2019,** *58,* 118–124. doi:10.1002/anie.201811085
174. van den Wittenboer, A.; Hilterhaus, L.; Liese, A. Industrial Applications of Enzymes in Emerging Areas. *Enzyme Catalysis in Organic Synthesis;* John Wiley & Sons, 2012; pp 1837–1846. doi:10.1002/9783527639861.ch45
175. Yang, Q.; Zhao, F.; Zhang, N.; Liu, M.; Hu, H.; Zhang, J.; Zhou, S. *Chem. Commun.* **2018,** *54,* 14065–14068. doi:10.1039/c8cc07990k
176. Ener, M. E.; Lee, Y.-T.; Winkler, J. R.; Gray, H. B.; Cheruzel, L. *Proc. Natl. Acad. Sci. U. S. A.* **2010,** *107,* 18783–18786. doi:10.1073/pnas.1012381107
177. Tran, N.-H.; Nguyen, D.; Dwaraknath, S.; Mahadevan, S.; Chavez, G.; Nguyen, A.; Dao, T.; Mullen, S.; Nguyen, T.-A.; Cheruzel, L. E. *J. Am. Chem. Soc.* **2013,** *135,* 14484–14487. doi:10.1021/ja409337v
178. Sosa, V.; Melkie, M.; Sulca, C.; Li, J.; Tang, L.; Li, J.; Faris, J.; Foley, B.; Banh, T.; Kato, M.; Cheruzel, L. E. *ACS Catal.* **2018,** *8,* 2225–2229. doi:10.1021/acscatal.7b04160

License and Terms

This is an Open Access article under the terms of the Creative Commons Attribution License (https://creativecommons.org/licenses/by/4.0). Please note that the reuse, redistribution and reproduction in particular requires that the authors and source are credited.

The license is subject to the *Beilstein Journal of Organic Chemistry* terms and conditions: (https://www.beilstein-journals.org/bjoc)

The definitive version of this article is the electronic one which can be found at: https://doi.org/10.3762/bjoc.16.197

BEILSTEIN JOURNAL OF ORGANIC CHEMISTRY

Dawn of a new era in industrial photochemistry: the scale-up of micro- and mesostructured photoreactors

Emine Kayahan[‡1], Mathias Jacobs[‡1], Leen Braeken[1,2], Leen C.J. Thomassen[1,2], Simon Kuhn[2], Tom van Gerven[2] and M. Enis Leblebici[*1,2]

Review

Open Access

Address:
[1]Center for Industrial Process Technology, Department of Chemical Engineering, KU Leuven, Diepenbeek, Belgium and [2]Process Engineering for Sustainable Systems, Department of Chemical Engineering, KU Leuven, Leuven, Belgium

Email:
M. Enis Leblebici[*] - muminenis.leblebici@kuleuven.be

* Corresponding author ‡ Equal contributors

Keywords:
microreactor; microreactor scale-up; monolith reactors; packed bed reactor; photoreactor scale-up

Beilstein J. Org. Chem. **2020,** *16,* 2484–2504.
https://doi.org/10.3762/bjoc.16.202

Received: 12 June 2020
Accepted: 15 September 2020
Published: 08 October 2020

This article is part of the thematic issue "Advances in photoredox catalysis".

Guest Editor: T. Noël

© 2020 Kayahan et al.; licensee Beilstein-Institut.
License and terms: see end of document.

Abstract

Photochemical activation routes are gaining the attention of the scientific community since they can offer an alternative to the traditional chemical industry that mainly utilizes thermochemical activation of molecules. Photoreactions are fast and selective, which would potentially reduce the downstream costs significantly if the process is optimized properly. With the transition towards green chemistry, the traditional batch photoreactor operation is becoming abundant in this field. Process intensification efforts led to micro- and mesostructured flow photoreactors. In this work, we are reviewing structured photoreactors by elaborating on the bottleneck of this field: the development of an efficient scale-up strategy. In line with this, micro- and mesostructured bench-scale photoreactors were evaluated based on a new benchmark called photochemical space time yield ($mol \cdot day^{-1} \cdot kW^{-1}$), which takes into account the energy efficiency of the photoreactors. It was manifested that along with the selection of the photoreactor dimensions and an appropriate light source, optimization of the process conditions, such as the residence time and the concentration of the photoactive molecule is also crucial for an efficient photoreactor operation. In this paper, we are aiming to give a comprehensive understanding for scale-up strategies by benchmarking selected photoreactors and by discussing transport phenomena in several other photoreactors.

Review

Introduction

In the traditional chemical industry, thermochemical activation routes are mostly preferred. Light can also activate some molecules, which leads to fast and selective reaction pathways. Photochemistry spans a number of reactions. For organic chemistry, 8000 photoreactions have been listed since 1975 [1]. Despite the huge portfolio, there is a lack of industrial applications of photochemistry. Van Gerven et al. listed five industrial applications of photochemistry in commercial wastewater treat-

ment installations [2]. In addition, artemisinin, which is a drug to treat malaria, was produced in an industrial-scale photoreactor in a Sanofi production facility in Italy [3]. Furthermore, the production of some fine chemicals, such as ε-caprolactam, rose oxide, and vitamin D on an industrial scale has already been proven to be successful [4]. These examples show that photochemistry is a viable alternative to conventional chemistry approaches. In addition to specialty chemicals and wastewater treatment, photochemical pathways can also be used for methanol production [5], N_2 fixation [6], and CO_2 sequestration [7]. Still, photochemistry has not been exploited much in industry since the distribution of light inside a photoreactor brings a lot of complexity to the reactor design. Unlike thermochemical reactions, it is not feasible to scale up photoreactions by increasing the dimensions of the reactor due to the exponential attenuation of light. Nonuniform light distribution often leads to a lower selectivity and longer reaction times, which in turn lowers the productivity [8,9]. Since photoreactions are intrinsically quite fast, mass transfer limitations should also be taken into account while designing multiphase photoreactors, and this complicates the design even further [10].

Photoreactions are typically performed in batch reactors. With the process intensification efforts towards green chemistry approaches, continuous flow technologies, micro- and mesostructured flow photoreactors having emerged as alternatives to batch operation. Due to the small characteristic length of microreactors, more uniform light distribution could be obtained. The elimination of overirradiation or dark zones results in less side product formation. Mass transfer limitations can be alleviated in these photoreactors with the help of various catalyst structures, beads, static mixers, and/or Taylor flow [4,11]. In addition, these reactors allow safer operation since it is easier to control overheating and the handling of hazardous chemicals in smaller volumes [4,11]. In addition to photomicroreactors, micro- and mesostructures in larger-scale photoreactors, such as packed beds and monoliths coated with catalysts can also enhance the mass transfer and operate at microreactor reaction rates. Together with photomicroreactors, these structured reactors are opening a new era in photochemistry by providing a platform for enhancing the photoreaction rates and easier scale-up.

One of the hurdles in scaling up of photoreactors is the lack of a consensus on a benchmark to compare different scales and geometries. The simplest benchmark is the apparent rate constant k_{app} [12-15] shown in Equation 1.

$$k_{app}\ [\mathrm{s}^{-1}] = \frac{c_0\ [\mathrm{mol}\cdot\mathrm{m}^{-3}] - c\ [\mathrm{mol}\cdot\mathrm{m}^{-3}]}{c\ [\mathrm{mol}\cdot\mathrm{m}^{-3}]\cdot\tau\ [\mathrm{s}]} \quad (1)$$

where c_0 is the initial concentration, c the concentration at the end of the reaction, and τ the residence time.

The comparison of the reaction rate constants for different reactor types, such as a photomicroreactor and a batch photoreactor are often used to point out how much the reactor design could change the performance of photoreactions. Takei et al. reported a reaction rate that is 70 times higher in a photomicroreactor compared to a batch cuvette, with the same yield for the synthesis of L-pipecolinic acid [16]. The rate of methylene blue reduction increased more than 150 times in a photomicroreactor compared to a batch system [17]. Still, it should be kept in mind that such comparisons are often strongly biased due to the difference in the photons absorbed in different reactor geometries and the possible difference in mass transfer limitations. Another benchmark is the quantum yield ϕ. This value is defined by the IUPAC as the number of defined events occurring per photon absorbed by the system. This is shown in Equation 2.

$$\phi\ [\frac{\mathrm{mol}}{\mathrm{einstein}}] = \frac{\text{number of reactant consumed or product formed [mol]}}{\text{amount of photons absorbed [einstein]}} \quad (2)$$

The photonic efficiency ξ (Equation 3) is defined by the IUPAC as the ratio of the reaction rate to the rate of incident photons within a defined wavelength interval [18]. This benchmark expresses the light efficiency. However, it does not provide information about the productivity.

$$\zeta = \frac{r\ [\mathrm{mol}\cdot\mathrm{s}^{-1}]}{\varphi\ [\mathrm{einstein}\cdot\mathrm{s}^{-1}]} \quad (3)$$

where r is the reaction rate and φ is the rate of incident photons.

The aforementioned benchmarks focus on the efficiency of the photochemical process and do not consider the photon transport to the reactor, energy utilization, and throughput, and thus they are not suitable for comparing the scaled-up photoreactors. The space time yield (STY), as shown in Equation 4, is the amount of product produced per unit of time and reactor volume and is often used to compare scaled-up (nonphoto)reactors [19]. However, this benchmark does not include the energy consumption of the lamp utilized to provide the necessary energy. In a study by Leblebici et al., a new benchmark, the photochemical space time yield (PSTY), was proposed and used to compare different photoreactors, as shown in Equation 5. This benchmark relates the productivity to the energy efficiency. Therefore, it is commonly applied in recent studies to assess the scalability of the process [15,20-22].

$$\mathrm{STY}\ [\frac{\mathrm{mol}}{\mathrm{m^3 \cdot s}}] = \frac{n\ [\mathrm{mol}]}{V_{\mathrm{reactor}}\ [\mathrm{m^3}] \cdot t\ [\mathrm{s}]} = \frac{c_0\ [\mathrm{mol \cdot m^{-3}}] \cdot \chi_{\mathrm{a}}}{\tau\ [\mathrm{s}]} \quad (4)$$

$$\mathrm{PSTY}\ [\frac{\mathrm{mol}}{\mathrm{kW \cdot day}}] = \frac{\mathrm{STY}\ [\mathrm{mol \cdot m^{-3} \cdot s^{-1}}]}{P\ [\mathrm{kW}] / V_{\mathrm{reactor}}\ [\mathrm{m^3}]} \quad (5)$$

where STY is the space time yield, n is the amount of product produced, t is the time, V_{reactor} is the reactor volume, c_0 is the starting concentration, χ_{a} is the conversion, τ is the residence time, PSTY is the photocatalytic space time yield, and P is the lamp power.

In this paper, together with photomicroreactors, larger-scale photoreactors that contain micro- and mesostructures will be discussed since the performance and the problems related to scaling up are comparable. Our aim is to give an overview on the scale-up of photochemical reactions by discussing transport phenomena and technical challenges. In addition, we are assessing several high-throughput structured photoreactors using the PSTY to reveal the successful scale-up strategies in literature.

Design considerations

The complexity of the photochemical processes leads to significant challenges in the photoreactor design. In addition to the general reactor design considerations, such as the selection of a suitable reactor material and geometry, the selection of a proper light source needs to be considered. The reactor material should be inert to the reaction medium and transparent to the wavelength range that drives the photochemical reaction. Ideally, the light source should emit light only in the wavelength range of interest and should have a high energy efficiency. In addition, the solvent should not absorb light strongly nor be a quencher of the photoreaction. In order to avoid excessive heating of the light source, cooling systems might be necessary. The distribution of light inside the reactor brings a lot of complexity into the design. Since most photoactive molecules are strong absorbers of light, light usually decays within a few millimeters inside a photoreactor, which limits the dimensions of the photoreactors. As a result, many photoreactor units are usually required to achieve the desired throughput. In order to obtain similar reaction conditions, the flow needs to be distributed to all photoreactor units uniformly. In heterogeneous reactions, the flow field also affects the mass transport significantly. Structures such as beads or monoliths are frequently used to enhance the mass transfer, which in turn affects the flow field. If the photoactive molecule is the reactant, it depletes as the reaction proceeds. This introduces more variation to the light field, depending on the degree of mixing and the reaction rate. Due to the interplay of different transport phenomena, a mathematical description is often needed for a proper reactor design. The flow field (momentum transport), mass transport, and light field (radiative transport) need to be coupled to compute the reaction kinetics (Figure 1) [11].

Microstructured chips used in photochemistry have various channel geometries, such as straight line, serpentine, square serpentine, and spiral, as shown in Figure 2. Serpentine and square serpentine are used to increase the residence time and for mixing. Microcapillaries (Figure 2f) wrapped around a light cylinder are also commonly used in photochemistry.

While designing microreactors, it is important to distinguish different applications. The lab-on-a-chip concept has enabled researchers to work on intrinsic kinetics. Intrinsic data acquisition is crucial while designing and operating large-scale reactors. Several microreactors, such as a spiral channel microreactor carved on a flat aluminum plate [23], a capillary tube [24], a

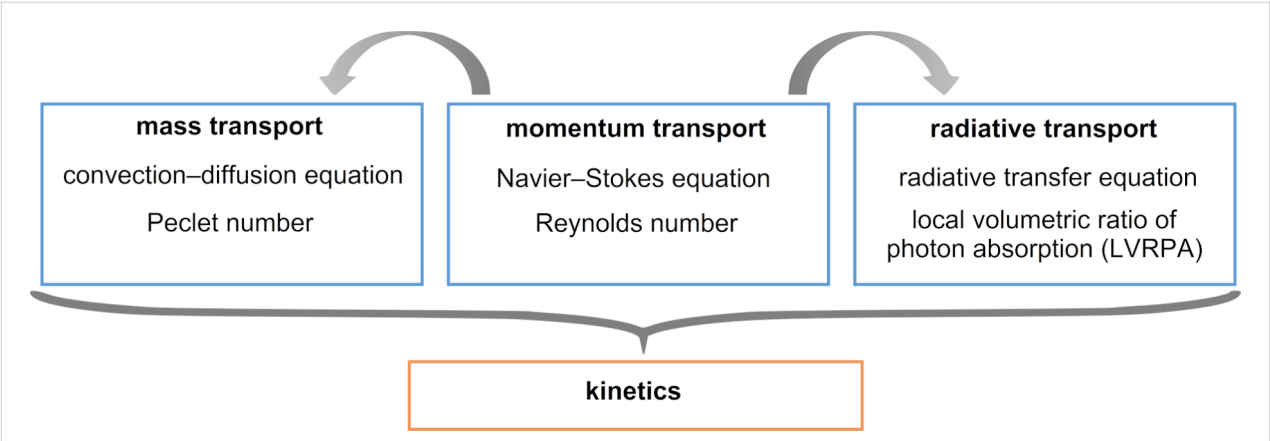

Figure 1: The momentum transport affects the mass transfer and the light field. All transport phenomena need to be coupled to compute the kinetics.

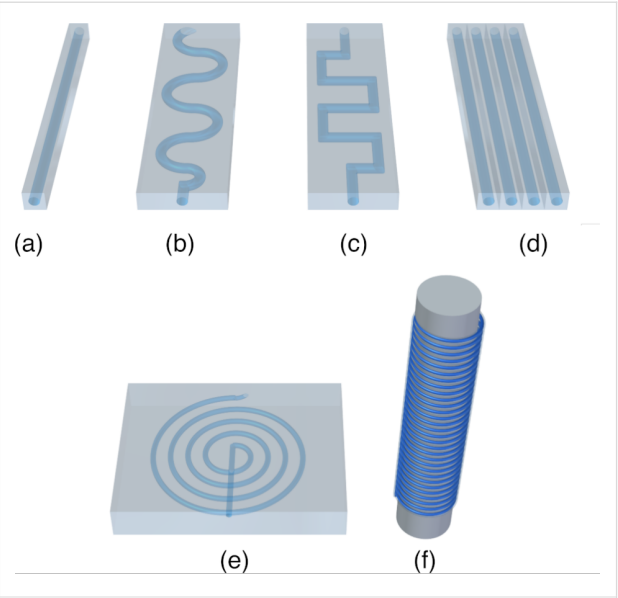

Figure 2: Common photomicroreactor designs: (a) Straight channel, (b) serpentine channel, (c) square serpentine channel, (d) planar microchannel array, (e) spiral-shaped microreactor, and (f) capillary photomicroreactor.

microchannel cast, and cured on polydimethylsiloxane (PDMS) slab [25] or a rectangular slab micromachined on teflon [26] were used to determine the intrinsic kinetics of different photochemical reactions. Such demonstrations suggest that if they are scaled up properly, microreactors could be operated with intrinsic kinetics. This would reduce the reactor size and downstream the processing costs while increasing the safety. The design considerations for microreactors that aim at large-scale chemical synthesis are significantly different from the lab-on-a-chip concept. While gathering intrinsic kinetic data, energy efficiency is not a concern. Optimal photon flux should be provided to make sure that the reactor is operated without light transfer limitations. In addition, the utilization of one microchannel or a capillary tube would be enough as long as there is adequate mixing to overcome mass transfer limitations in multiphase reaction systems. On the other hand, studies aiming at the scale-up of microreactors should consider the distribution of the flow and light to all units of the microreactors, as well as the energy efficiency. A systematic scale-up strategy would be to increase the concentration of the chemicals and the reactor dimensions by keeping the yield constant while assessing the energy efficiency of the photoreactor by using benchmarks, such as PSTY. Then, the best reactor dimensions and operational parameters could be chosen. The PSTY of several photoreactor designs will be discussed in the next section.

Scaling up and energy efficiency

Photoreactors cannot be scaled up by the conventional strategy of enlarging the dimensions due to the light attenuation effect. The heterogeneous flow dynamics and the light field complicate the design further. As a result, photochemical processes are hard to predict and to scale up. Several large-scale slurry reactor designs for multiphase reactions, such as the fountain reactor [27], the fluidized bed reactor [28], and spinning disc reactors [29,30] have been utilized in the field of photochemistry. Although such large-scale slurry reactors can improve the mass transfer, distributing light properly in a large-scale slurry reactor remains a challenge. The rapid attenuation of light inside photoreactors limits the dimensions of photoreactors. As a result, microstructured reactors are gaining more attention from researchers in this field. Leblebici et al. compared twelve commonly used photoreactor designs [22]. The microstructured reactor [25] resulted in the highest STY but the lowest PSTY due to the high power consumption of the light source [22]. In that work, a 120 W UV light source was used to illuminate a 1.5 µL reactor [25]. However, through the selection of a proper light source along with a systematic scale-up strategy by increasing the reactor dimensions and the concentration of the absorbing species gradually, microstructured photoreactors have the potential to achieve the highest PSTYs. It is also important to note that the PSTY does not account for the quantum yield. Therefore, the molecular and electronic features of the reactants, which could significantly affect the PSTY value, are not accounted for when comparing different reactions. As such, it is hard to make global conclusions just by looking at the PSTY value, especially when intermolecular and intramolecular reactions or homogenous and heterogeneous reactions are compared. Since the quantum yield of most photochemical reactions is not known, the PSTY still gives a good comparison between different reactor geometries. The PSTY especially gains importance when characterizing and deciding on the operational conditions of a photoreactor when a specific photoreaction is to be scaled up.

The flow and light need to be distributed properly to all units of the microstructured reactors while scaling up in order to ensure the same reaction conditions everywhere. For multiphase reactions, mass transfer issues need to be tackled with the design as well. Microreactors could be scaled up by numbering up the channels, which is also referred to as scaling out, or scaled up by enlarging the dimensions of the microchannels. Another way of scaling up reactors, which can work with intrinsic kinetics, is to create micro- or mesostructures in large vessels. Translucent packed bed reactors and aerosol photoreactors are examples of such designs. Below, we will discuss several scale-up strategies applied in photochemistry.

Most researchers that utilize photomicroreactors suggest that scaling up can be achieved by numbering up. One of the most used photomicroreactors are capillaries wrapped around a light

source. Such microcapillaries can be scaled up by connecting them either in parallel or in series (Figure 3a and Figure 3b). In a previous study, five polymer-based microcapillaries with a length of 11.5 m and an inner diameter of 0.8 mm were wrapped around two Pyrex® glass columns. UV lamps were placed inside the glass columns. A representative setup is given in Figure 3a. The addition of isopropanol to 2(5*H*)-furanone in the presence of the photosensitizer 4,4'-dimethoxy-benzophenone (DMBP) was studied. A single multisyringe pump was used to supply the reactants to the photomicroreactors. This kind of scaling up is called external numbering up since each reactor is fed directly by the pump. This numbering-up strategy allowed to run ten parallel microreactors at the same time. This microreactor setup used 30% less energy than the batch reactor, without the requirement of cooling [31]. The PSTY in this paper was calculated based on the same reaction being performed at the same time in ten parallel reactors (Table 1, entry 1). The reactions that are presented in Table 1 are shown in Figure 4. The PSTY was around 9.5 mol·day^{-1}·kW^{-1} when the yield was 72%. To achieve almost complete conversion (94%), the residence time was increased twice. That decreased the PSTY to 6.26 mol·day^{-1}·kW^{-1}. Still, this microcapillary reactor outperformed all other reactors that were compared in this paper. This was because the large reactor volume (10 × 5 mL) was illuminated effectively by two low-power lamps (2 × 18 W). In addition, several photosensitizer and reactant concentrations were screened before the reaction was scaled up. With the selected photosensitizer concentration (10 mM), the light transmission through the 0.8 mm diameter microcapillary was around 65%. A higher DMBP concentration caused precip-

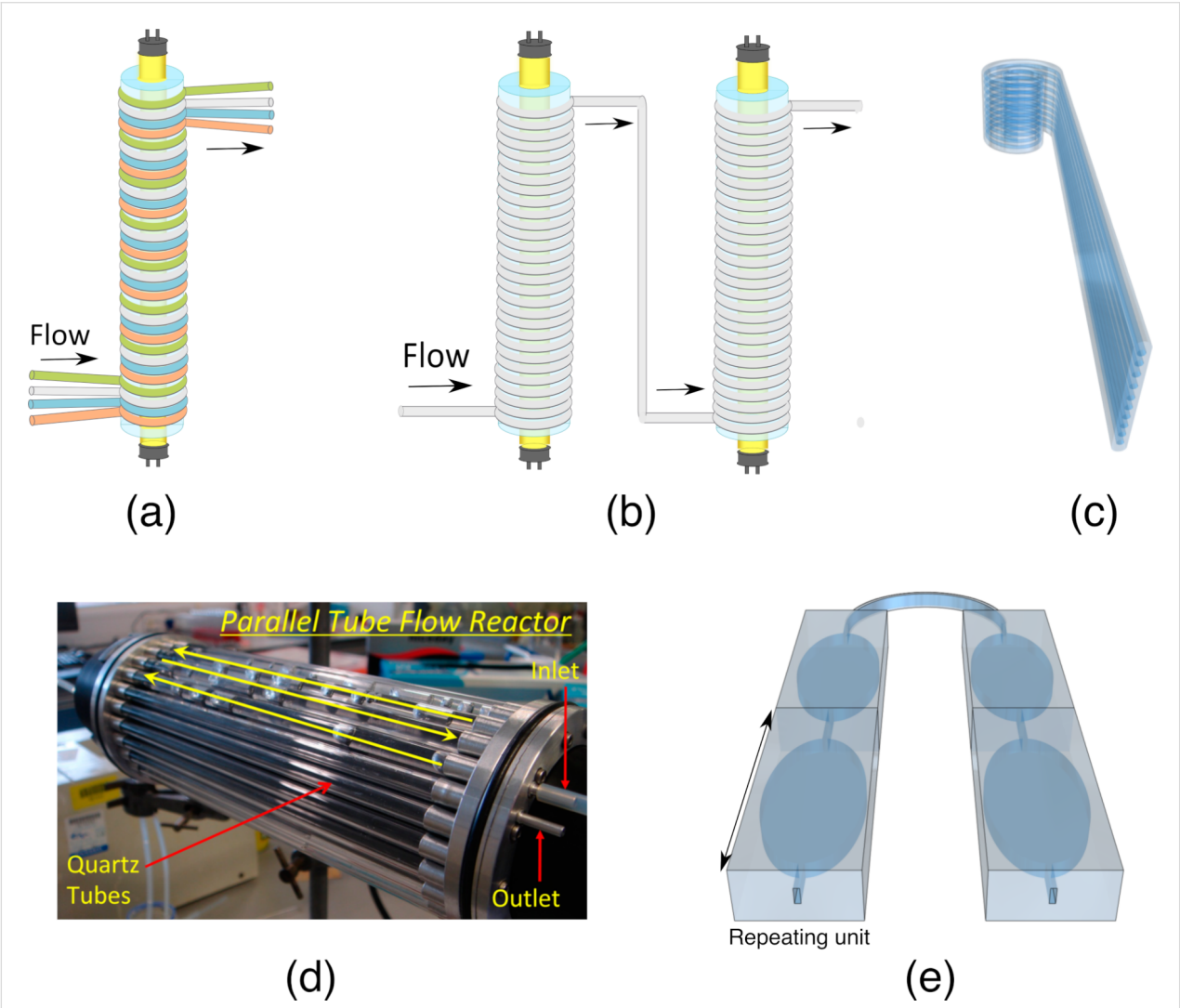

Figure 3: Benchmarked photoreactors: (a) Microcapillaries in parallel, (b) microcapillaries in series, (c) fluoropolymer microcapillary films, (d) firefly reactor (reprinted from [33], licensed under a Creative Commons Attribution 4.0 International license), and (e) internal and external numbering up of a microreactor unit. The image was drawn by the authors of this article to illustrate the microreactor structures reported in [34].

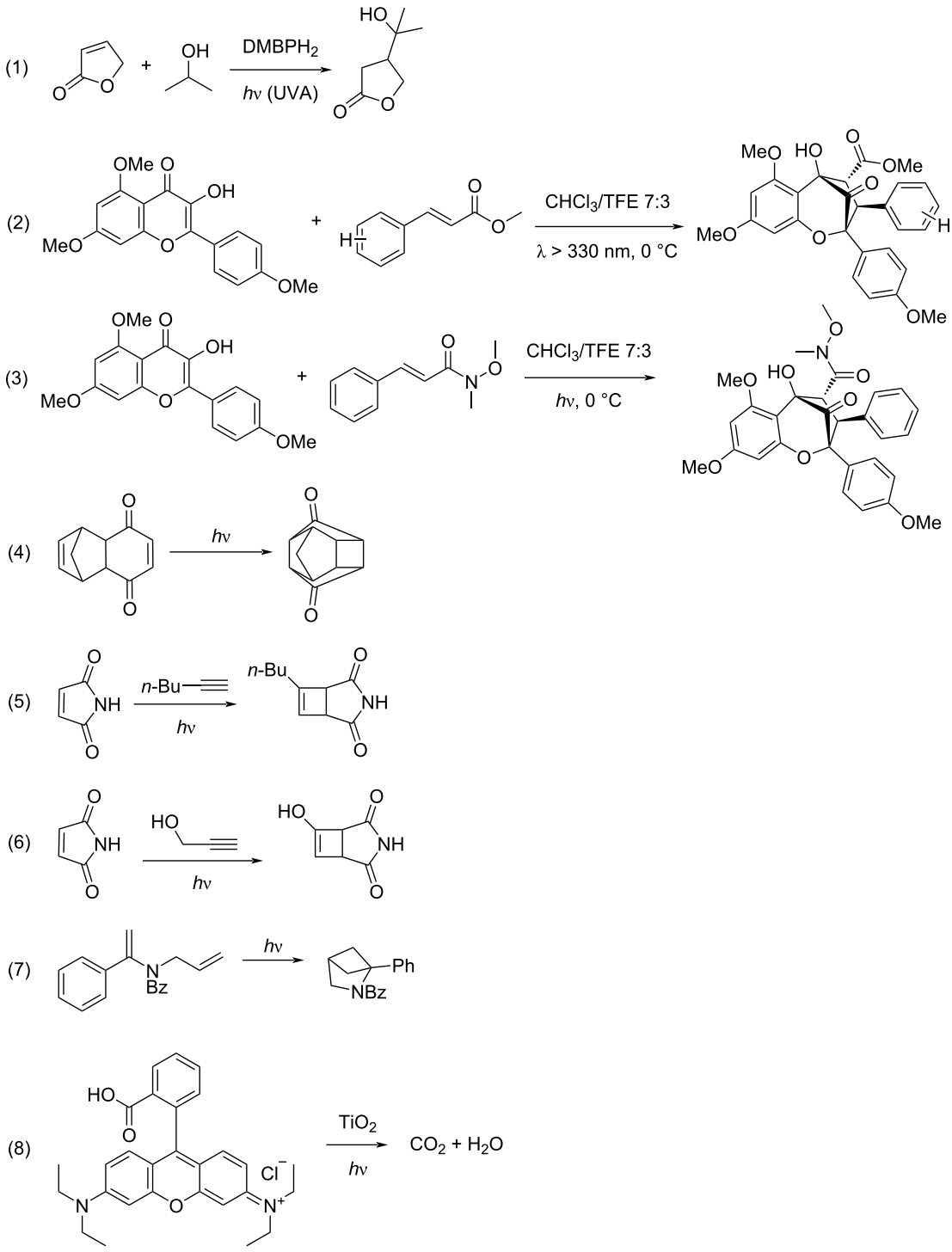

Figure 4: Photochemical reactions that are detailed in Table 1.

itations and resulted in a lower yield. Lower DMBP concentrations decreased the yield significantly, which decreased the PSTY values around 6-fold (data not shown). In another work, the same group reported the use of the same reaction in a commercial microchip (Micronit Microfluidics FC_R150.676.2) with an internal volume of 15 µm. This microchip was illuminated by 6 × 75 mW LEDs. The DMBP concentration was 6.7 mM, which resulted in around 95% light transmission through 150 µm channel depth of the microreactor [32]. This reactor had a PSTY of 0.57 mol·day^{-1}·kW^{-1} (Table 1, entry 3).

Table 1: Comparison of different reactors in terms of PSTY. τ is the residence time and C is the concentration of the reactant. STY and PSTY are calculated based on Equation 4 and 5, respectively.

entry	reactor type	*V* (mL)	τ (min)	reaction (see Figure 4)	lamp power (W)	*c* (mM)	yield	STY ($mmol \cdot L^{-1} \cdot min^{-1}$)	PSTY ($mol \cdot day^{-1} \cdot kW^{-1}$)	Ref.
1	microcapillary photoreactors (Figure 3a)	50.00	5.0	1	36.0	33.3	0.71	4.72	9.43	[31]
2			10.0				0.94	3.13	6.26	
3	commercial microchip	0.02	2.5	1	0.5	33.3	0.89	11.87	0.57	[32]
4	microcapillary photoreactors (Figure 3b)	37.50	35.0	2	450.0	120.0	0.61	2.09	0.25	[35]
5		37.50	35.0	3	450.0	120.0	0.35	1.20	0.14	
6		12.00	20.0	3	300.0	120.0	0.32	1.92	0.11	
7		3.50	30.0	3	150.0	120.0	0.36	1.44	0.05	
8	fluoropolymer microcapillary films (Figure 3c)	0.15	0.5	removal of indigo carmine dye	8.0	0.2	0.70	0.30	0.01	[33]
9	firefly reactor (Figure 3d)	120.00	76.0	4	3000.0	1000.0	0.88	11.58	0.67	[36]
10			151.0	4	1500.0	500.0	0.89	2.95	0.34	
11			227.0	4	3000.0	1000.0	0.89	3.92	0.23	
12			76.0	5, 6	3000.0	100.0	0.65	0.86	0.05	
13			1342.0	7	3000.0	400.0	0.86	0.26	0.01	
14	microchip (Figure 3e)	1.00	960.0	8	0.2	0.012	0.78	$9.74 \cdot 10^{-6}$	$7.01 \cdot 10^{-5}$	[34]
15		0.80	960.0				0.85	$1.06 \cdot 10^{-5}$	$6.12 \cdot 10^{-5}$	
16		0.50	960.0				0.86	$1.08 \cdot 10^{-5}$	$3.89 \cdot 10^{-5}$	
17		0.01	480.0				0.98	$2.46 \cdot 10^{-5}$	$1.77 \cdot 10^{-6}$	
18		0.02	240.0				0.97	$4.88 \cdot 10^{-5}$	$7.02 \cdot 10^{-6}$	
19		0.04	120.0				0.98	$9.76 \cdot 10^{-5}$	$2.81 \cdot 10^{-5}$	
20		0.06	60.0				0.98	$1.96 \cdot 10^{-4}$	$8.48 \cdot 10^{-5}$	

Although the same reaction and similar conversions were achieved in these two photomicroreactors [31,32], the PSTY was more than ten times lower in the microchip. This was potentially due to the difference in the volumes and the fraction of photons absorbed in two different photomicroreactors. These results illustrate that choosing a proper light source and adjusting the concentrations would improve the PSTY significantly, leading to an efficient scale-up of photomicroreactors.

In a previous study, a microcapillary reactor (1/6” OD, 3.5 mL reactor volume) that was wrapped around a metal halide UV lamp was scaled up by using several strategies together. Rather than splitting up the reaction medium into many photoreactors, the photoreactors were numbered up by adding them in series (Figure 3b). This allowed for a larger reactor volume with the same illumination. The throughput was increased by using a larger volumetric flow rate. Several [3 + 2] photocycloadditions were performed. While scaling up, the concentration of the reactants, the diameter of the tubes, and the number of the reactors were increased systematically. The throughput was increased around 20-fold by increasing the reactant concentration from 30 mM to 120 mM. The throughput was further increased by changing the diameter of the capillary from 1/6” to 1/8”. Finally, three reactors were connected in series, which resulted in a reactor volume of 37.5 ml. By using three reactors in series, with a larger capillary diameter, the throughput was increased from 0.14 g/L to 1.16 g/L. Similar yields were obtained in each step by adjusting the residence time [35]. The highest PSTY of this paper was calculated as 0.25 $mol \cdot day^{-1} \cdot kW^{-1}$ when a 37.5 mL reactor was used (Table 1, entry 4). The PSTY was decreased to 0.14 $mol \cdot day^{-1} \cdot kW^{-1}$ with a different reaction although the reaction conditions were the same (Table 1, entry 5). When smaller reactor volumes were used, the PSTY decreased further (Table 1, entries 5–7). The PSTY was expected to stay approximately the same when the reactors were connected in series since the lamp power and the throughput were increased at the same level. However, in Table 1, entries 5–7, in addition to using more reactors in series, the microcapillary diameter was also changed, which in turn changed the PSTY. The PSTY values of this paper were quite low, considering that the authors

followed a systematic way of scaling up by utilizing several strategies together. The low PSTY might be associated with the challenging syntheses chosen in the paper. Previously, the synthesis of rocaglate was reported with an even higher lamp power (450 W) in a Pyrex® test tube (16 × 100 mm) [37].

Fluoropolymer microcapillary films were suggested as another scale-up approach (Figure 3c). These microcapillary films were produced commercially by Lamina Dielectrics Ltd (UK). The internal diameters of the microcapillaries range from 10 μm to 1 mm. The microcapillary films are transparent to UV and visible light. Furthermore, they have a refractive index close to water (≈1.33), which makes them good candidates for photochemical reactors. In one study, those microcapillary films were used for the photodegradation of indigo carmine, diclofenac, and benzoylecgonine. The reactor volume was 0.15 mL [36]. The PSTY of the photodegradation of indigo carmine was calculated as 0.01 mol·day^{-1}·kW^{-1} (Table 1, entry 8). In another study, those microcapillary films were used to synthesize ascaridole, an antimalarial drug, from α-terpinene by utilizing singlet oxygen. The permeability of the fluoropolymer film to oxygen was utilized to supply oxygen to microcapillaries. The system was suggested to be used in combination with dangerous gases to ensure safe operational conditions. With the fluoropolymer microcapillaries, space time yields 20 times larger than in the corresponding bulk synthesis were obtained [38]. Although it was suggested that fluoropolymer films could easily be scaled up by numbering up, how the flow was distributed to the microcapillaries was not explained in those studies [36,38].

In another scale-up study, quartz tubes were assembled in series and placed axially around a high-power UV lamp, as shown in Figure 3d. The reactor had an internal volume of 120 mL. The photoreactor was enclosed with an annular metal cavity that reflected UV radiation back to the reactor and served as UV protection. However, the metal cavity caused overheating. Therefore, a cooling jacket around the metal cavity was implemented in the design, along with a fan to blow air through the space between the lamp and the quartz photoreactor tubes. The design was called firefly reactor. Various [2 + 2] cycloadditions were performed in this reactor. Although similar amounts of starting material were used, the residence time varied significantly among different photoreactions to achieve the same yield [33]. The highest PSTY was calculated as 0.67 mol·day^{-1}·kW^{-1} (Table 1, entry 9). This was the second-highest PSTY among the photoreactors compared in this paper. However, the PSTY ranged between 0.23 and 0.67 mol·day^{-1}·kW^{-1} (Table 1, entries 9–11), depending on the residence time, lamp power, and the initial reactant concentration, although the same reaction was used, and similar yields were obtained. Therefore, a higher residence time reduced the PSTY around three times since the yield did not improve further (Table 1, entries 9 and 11). When different reactions were used, the same reactor resulted in a PSTY of 0.01 and 0.05 mol·day^{-1}·kW^{-1} (Table 1, entries 9 and 11). This study demonstrated that the optimization of the process conditions and the kinetics of the selected reaction can lead to drastic changes in the PSTY.

de Sá et al. combined external and internal numbering up in meso- and microchemical reactors of various sizes (Figure 3e). Photocatalytic degradations of methylene blue, rhodamine B, and phenol with TiO_2 were performed. Multiple microreactor units were connected to each other to increase the volume of the reactor while keeping the benefits of a microreactor. The reaction mixture was fully recycled when it left the reactor. Therefore, the reactor was operated as a batch reactor. Due to the small characteristic length of the reactor, there were less mass and photon transfer limitations compared to a conventional batch reactor [34]. The numbering-up was more beneficial in terms of STY and PSTY compared to increasing the dimensions, as shown in Table 1 entries 14–20. Increasing the volume from 0.5 mL to 1 mL by increasing the dimensions decreased the STY by 10%, whereas this increased the PSTY by 45%. When scaling up a reactor by increasing its dimensions, the surface-to-volume ratio decreases. This explains why the STY decreases: since the illuminated catalyst area per volume decreases, this leads to an increase in the mass transfer limitations and in turn to a lower apparent reaction rate and productivity. The PSTY increased since the same lamp was used to illuminate a larger reactor volume. Increasing the volume of the reactor by numbering up increased the STY and the PSTY by 97 and 98%, respectively. This is due to the increased total irradiated area while keeping the same surface-to-volume ratio.

Tree-like structures (bifurcation configuration) have been used to distribute the flow to many channels in various fields of research. Su et al. applied this numbering up approach to a capillary multiphase photoreactor by using the photocatalytic oxidation of thiols to disulfides as a model reaction [9]. Two, four, and eight photomicroreactors, each having a 0.5 mm internal diameter and a 0.95 mL volume were connected in parallel by using T-junctions. The fluid is distributed in a tree-like structure. A stable Taylor flow was obtained. The standard deviation of the flow distribution was less than 10%. The relative deviations of the liquid flow rate and the yield in each channel were found to be less than 4% [9]. Such a tree-like structure was also utilized in the scale-up of a luminescent solar photomicroreactors, which was fabricated via 3D printing [39]. Luminescent solar concentrators have been used in photovoltaic cell research for a couple of decades [40]. Noël's group combined the use of luminescent solar concentrators with

microfluidics to harvest solar radiation into a narrow wavelength region and derive photochemical reactions [41-43]. By distributing the flow with a tree-like structure, the luminescent solar photomicroreactor was operated with 32 channels, with less than 10% standard deviation in the flow distribution [39].

Enlarging one dimension while keeping the rest of the dimensions constant is another scale-up strategy. This strategy has been applied in commercial Corning Advanced-Flow™ reactors. Heart shapes provide good mixing for the liquid and gas phases and enhance the mass transfer while using the space on the microreactor chip efficiently. A photo of a Corning reactor is given in the Mass Transport section. Corning is offering reactors with different internal volumes. The lab-scale reactor has an internal volume of 2.6 mL, whereas the G1 and G3 photoreactors have an internal volume of 9 mL and 60 mL, respectively. All Corning reactors have the same heart-shaped static mixers [44]. The photocatalytic oxidation of methionine was performed in the Corning laboratory reactor. Two LED panels coupled with heat exchangers were placed on both sides of the reactor. Flow was supplied with an HPLC pump. Full conversion was achieved with a residence time ranging from 0.6 min to 1.4 min. This reaction could be scaled up using other Corning reactors. For example, if the same conditions could be maintained in a Corning G3 reactor, this reaction would have a productivity of 100 mol/day [45]. The power consumption of the LEDs was not reported in the paper. Therefore, the PSTY could not be calculated.

Packed-bed structures are often used for mass transfer enhancement. Once the channel size is adjusted, translucent packed structures can be used as an alternative scale-up strategy to the numbering-up of microreactors. Claes et al. adjusted the size of the beads in a catalytic packed bed reactor so that several microchannels were created among the beads. Glass beads were coated with a TiO_2 photocatalyst. The photoreactor was illuminated with 192 LEDs that could provide 100 mW of power each. The distance between the LED board and the reactor was adjusted to give a uniform illumination, which resulted in a high light efficiency [15].

A novel approach to scale up microreactors is to use an aerosol photoreactor. In this reactor concept, micron-sized droplets are generated using a nebulizer. Each droplet works as a microreactor. The high surface area of the droplets enables fast mass transfer. As a result, aerosol photoreactors offer a great platform especially for gas–liquid or gas–liquid–solid photoreactions. When light hits a droplet, it is scattered. Therefore, the nature of the aerosol–light interactions enables good light distribution to all droplets. The reactor concept is easily scalable by simply increasing the number of nebulizers. An aerosol photoreactor called NebPhotOX has recently been operated several times and has been proved to work extremely efficient [46-48]. In that work, the liquid reactants were nebulized into a glass chamber that was wrapped with LED strips. A pneumatic nebulizer was used. The droplet diameter was reported by the nebulizer supplier as 6 μm for water-based solutions. The droplet size depends on the surface tension and viscosity of the liquid and the pressure of the gas. Therefore, it might be different for different solvents used in the photoreactor. Several singlet-oxygen-mediated photooxidation reactions were performed in the aerosol photoreactor. Singlet oxygen is a highly reactive state of oxygen, which can be formed by some photosensitizers or dyes when an appropriate light source is used. The authors performed an ene reaction of β-citronellol and Diels–Alder reactions of α-terpinene and (5-methylfuran-2-yl)methanol [46] as well as the synthesis of cyclopent-2-enones from furans [47] and the synthesis of diverse γ-lactam scaffolds [48]. Conversions larger than 90% were achieved for all reactions [46-48]. If the droplets are assumed to move with the gas, the residence time of the reactor would be around one minute. The PSTY of those papers could not be calculated, as the power consumption of the LEDs was not reported. Aerosol photoreactors are quite promising as they can solve the bottleneck of the photoreactor design, which is the distribution of the light efficiently in a large-scale reactor. Still, the light efficiency of aerosol reactors requires further work as it would depend on the droplet diameter, the aerosol number concentration, which is the total number of droplets per unit volume, and the light path of the reactor. The major drawback of the aerosol photoreactor are safety issues, especially for organic oxidation reactions. Spraying organics into air or oxygen could lead to explosions. Therefore, the lower and upper explosion limits for the several organic photooxidation reactions should be determined in order to ensure safe operating conditions.

Mass transport

The mass transport phenomena can be quantified by the characteristic mixing time and the overall volumetric mass transfer coefficient. The characteristic mixing time in conventional reactors depends on many parameters, such as the diffusivity, kinematic viscosity, reactor volume, stirrer speed, etc. For a laminar flow in microstructured reactors, the characteristic mixing time can be calculated by the Einstein–Smoluchovski equation (Equation 6). Due to the short diffusion distances, complete mixing can be achieved rapidly. That is the reason why microreactors are suitable for reactions with a high intrinsic reaction rate [11].

$$t_{\mathrm{m}} = \frac{L^2}{D} \tag{6}$$

where t_m is the characteristic mixing time, L is the diffusion path, and D is the molecular diffusivity.

The relative importance of the characteristic mixing time in microreactors to the characteristic reaction time is given by the second Damköhler number (Da_{II}, Equation 7). When Da_{II} is smaller than 1, the reaction is reaction-rate-limited. In this region, further mixing does not affect the reaction rate. When Da_{II} is around 1, the reaction is controlled by both the reaction rate and the mass transport. When Da_{II} is larger than 1, the reaction is mass-transport-limited. The residence time needs to be larger than the characteristic reaction time to achieve a complete conversion [11].

$$Da_{II} = \frac{\text{reaction rate}}{\text{diffusive mass transfer rate}} = \frac{t_m}{t_r} \quad (7)$$

where t_r is the characteristic reaction time, which can be loosely defined as the inverse of the reaction rate constant.

Many photoreactions are heterogeneous, which means that the reaction requires the presence of at least two phases. Heterogeneous reactions require either a solid photocatalyst in a liquid medium or gas and liquid phases as the reactants. The mass transport and mixing gain extra importance in such systems. The mass transport is usually represented by the ratio of catalyst surface area to the reaction volume in photocatalytic systems. The photocatalyst could either be mixed with the reactants and fed into the reactor (slurry systems) or immobilized on a reactor surface. Slurry reactors remain the most preferred photoreactors due to the excellent contact between the catalyst and the reactants [2]. The ratio of the catalyst surface area to the reaction volume is quite high in slurry systems. However, the catalyst needs to be separated from the reaction medium in such systems, which adds complexity and additional costs to the overall process. It is possible to avoid the catalyst separation step with immobilized systems. Although they eliminate the catalyst separation step, the design of efficient immobilized systems is also quite challenging and requires complex mathematical models for the calculation of the internal mass and light transfer limitations. The catalyst thickness should be adjusted so that all of the catalyst is utilized. The optimum catalyst thickness would depend on the interplay of many parameters, such as the porosity of the catalyst and the support, the flow rate of the reactants, the light distribution throughout the catalyst layer, and the reaction rate. Leblebici et al. [49] showed that increasing the flow rate of the reactants did not increase the apparent reaction rate for phenol degradation in an immobilized photoreactor. Increasing the flow rate would result in a higher driving force for the mass transfer when there are no internal mass transfer limitations. As a result, it was concluded that the internal mass transfer limitation of the catalyst coating limited the reaction rate. Therefore, increasing the catalyst layer does not necessarily increase the apparent reaction rate [49].

Structures are commonly used to alleviate the mass transport effects. Catalysts are usually coated on beads [15,50,51], monoliths [52-54], or foams [55]. Beads coated with catalyst are often used in packed bed photoreactors. Schematic representations of a packed bed photoreactor and a monolith are shown in Figure 5a and Figure 5b, respectively. The performance of a capillary photomicroreactor packed with TiO_2-coated glass beads were compared to a photomicroreactor having the walls coated with TiO_2. The degradation of methylene blue was chosen as a model reaction. Complete conversion was achieved within 20 s when glass beads were used. The maximum space time yield of the packed bed photomicroreactor was found to be 2322 $m^3 \cdot day^{-1} \cdot m^{-3}$. On the other hand, in the wall-coated photomicroreactor, the maximum space time yield was found to be 356 $m^3 \cdot day^{-1} \cdot m^{-3}$. The significant improvement in the space time yield was attributed to the larger ratio of the catalyst surface area to the reactor volume in the packed bed reactor as well as the flow perturbation that increased the mass transfer rate. In addition, the packed bed photomicroreactor showed a good durability. The reactor performance dropped 17% after 6 h of operation and remained stable for the next 19.5 h [51]. Similarly, glass beads coated with photocatalysts were proved to increase the photoreaction rate twice in a luminescent solar concentrator (LSC) photomicroreactor with capillary channels [50]. Azam et al. studied monolithic honeycomb structures coated with La/TiO_2 for hydrogen production. The photocatalytic activity was increased 1.8-fold in the monolithic photoreactor compared to the slurry photoreactor. The increased photocatalytic activity led to a 9-fold higher hydrogen production rate in the monolithic photoreactor. The main reasons for this increase was the high surface-area-to-volume ratio and better illumination of the monolithic photoreactor [56]. The monolithic photoreactor was shown to have a higher yield for the CO_2 photoreduction compared to a cell-type reactor that had no channels. This was associated with a better illumination efficiency and a higher catalytic surface area [57]. There are several commercial photoreactors that have been designed with static mixers to enhance the mass transfer, such as the HANU photoreactor and Corning Advanced-Flow™ reactors (Figure 5c and Figure 5d). The combination of an oscillatory flow with the static mixers of the HANU reactor (Figure 5c) enabled a stable suspension of the photocatalysts without clogging of the reactor channels [58]. Corning flow reactors are designed to provide good mixing for multiphase reactions with periodic heart-shaped static mixers (Figure 5d). Two-phase flow transitions from a Taylor flow to a stratified flow and further to a dispersed flow were investigated. The interfacial mass transfer

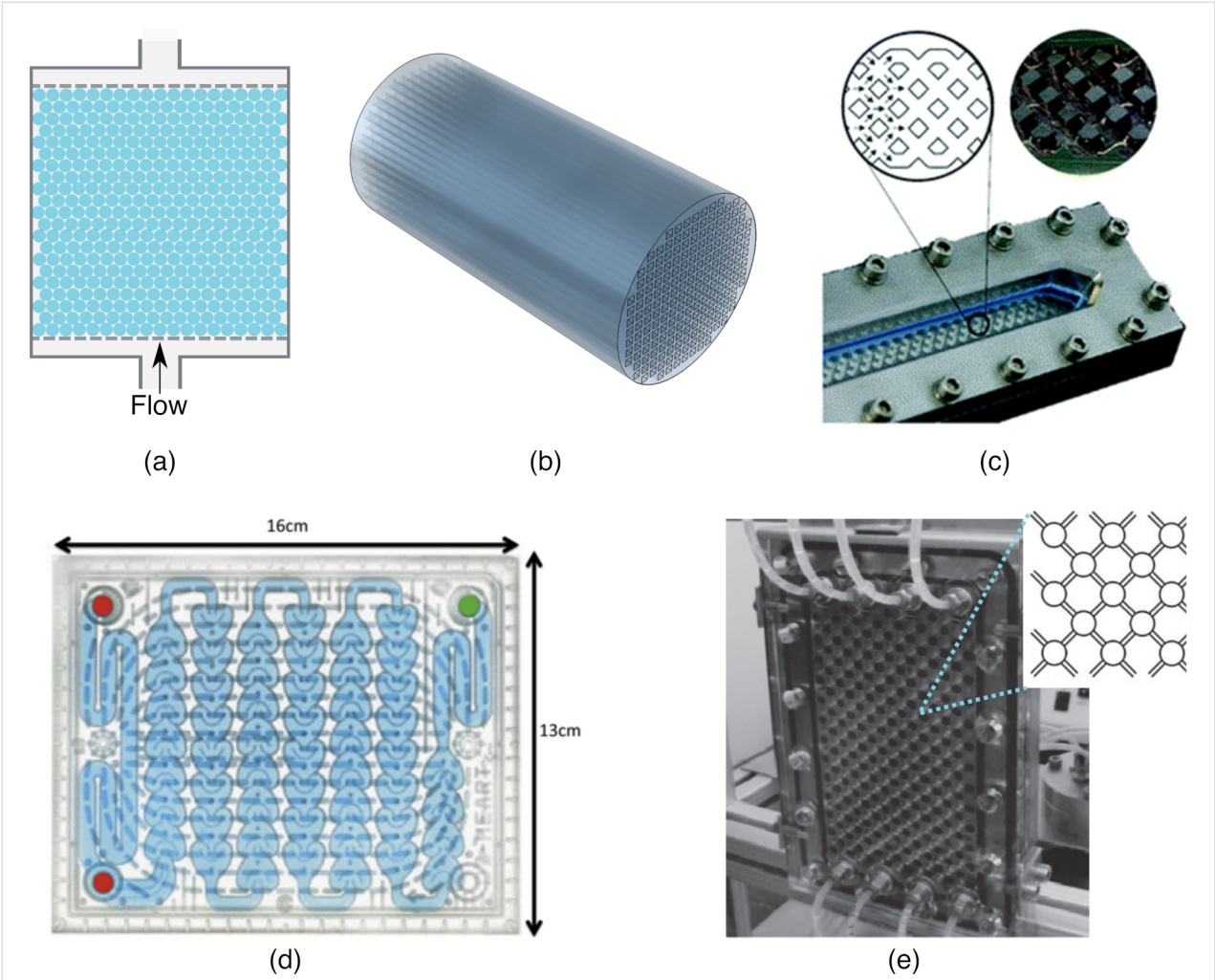

Figure 5: Structured reactors designed for enhancing the mass transfer: (a) Packed bed photoreactor, (b) monolith reactor, (c) HANU reactor (reprinted from [58] under a Creative Commons Attribution 3.0 Unported license), (d) commercial Corning Advanced-Flow™ reactor (reprinted from [44] under a Creative Commons Attribution 3.0 Unported license), and (e) NETmix reactor (reprinted with permission from [59], copyright 2013 Elsevier).

and phase transitions were shown to be driven by fluid–structure interactions on the milli scale. Therefore, this reactor design has a straightforward scalability with the same mass transfer characteristics by keeping the periodic heart-shaped static mixers [44].

The NETmix reactor (shown in Figure 5e) was originally developed by Brito Lopes et al. [60]. The NETmix reactor was coated with a TiO_2 photocatalyst for the removal of oxytetracycline (a pharmaceutical micropollutant) from urban wastewater. The effect of a catalyst-coated surface and the illumination mechanism were studied. When a larger surface area was coated with the photocatalysts, the photocatalyst reactivity was increased [61]. Marinho et al. compared the performance of the NETmix reactor with a monolithic reactor packed with translucent cellulose acetate monolithic structures. The front glass of the slab, the network of the channels, and the chambers imprinted in the back stainless steel slab of the NETmix reactor were coated with a thin-film photocatalyst (TiO_2-P25) by using a spray system. The catalyst reactivity in the NETmix reactor was 70 times higher than for the monolithic photoreactor [62].

When the reactions involve a gas phase, a Taylor flow, also known as a slug flow, is commonly utilized in microstructured reactors. Su et al. studied the intrinsic kinetics of the photocatalytic oxidation of thiophenol to phenyl disulfide using a Taylor flow in a microreactor that consists of a capillary tube. By varying the flow rate of the gas and liquid phase and comparing the oxygen concentration in the liquid phase with the equilibrium concentration without a reaction, the authors showed that mass transfer limitations were overcome in the microreactor [24].

Photon transport

A uniform light field is desired inside photoreactors. However, due to the exponential decay of the light intensity along the light path, having a uniform light field throughout the reactor usually means that light is wasted. On the other hand, if the utilization of all the light is desired, some of the reactors would be overilluminated, and the rest would be poorly illuminated. Reflective surfaces would eliminate this problem to some degree. Still, for an efficient photoreactor operation, the light source and intensity need to be properly coupled with the reactor geometry. While selecting the light source, the light spectrum and energy efficiency of the lamp and shape of the reactor should be considered. Ideally, the light source should emit light only at specific wavelengths that match the absorption spectrum of the photoactive molecule. In addition, the distance between the light source and the reactor should be taken into account while positioning the lamp. The irradiance pattern changes depending on the distance from the light source. At a long distance between the light source and the lamp, the irradiance decreases with the square root of the distance from a point light source according to the inverse square law (Equation 8).

$$E \propto \frac{1}{d^2} \tag{8}$$

where E is the irradiance and d is the distance between the object and the light path.

In the near field, the irradiance can be modeled with ray tracing algorithms or it can be measured experimentally with a near field goniophotometer. The far field for LEDs is usually assumed to start at a distance that is five times larger than the dimensions of the light source. In reality, the distance for the far field can go up to twenty times larger than the dimensions of the light source [63,64]. As mentioned in the previous section, just adjusting the irradiance can lead to a PSTY two orders of magnitude higher. Ziegenbalg et al. pointed out the importance of the geometrical compatibility between the light source and the photomicroreactor by investigating a glass microreactor coupled with organic light-emitting diodes. The authors showed that 63% of the photons were lost due to the mismatch between the reactor channels and the light source, whereas 17% of the photons were lost due to the spectra mismatch [65]. While designing light sources, heat generated by the light sources should be considered as well. Excess heat can lead to damages of the whole setup. In addition, the spectrum and the energy efficiency of the lamp can be affected by the temperature. For instance, the LED junction temperature affects the optical output power and spectrum of the LEDs and as a result decrease the efficiency of the LEDs [66].

LEDs are usually preferred to illuminate microstructured photoreactors due to their small size, monochromaticity, and adjustable power. LEDs are also the most efficient light sources in the visible range [67]. Roibu et al. designed LED boards consisting of narrow-viewing-angle LEDs for an optimal coupling between the light source and the photomicroreactor. The design of the two LED boards, which were called the channel configuration (CC) and the matrix configuration (MC), is shown in Figure 6a and Figure 6b. The distance between the adjacent LEDs was 8 mm. The irradiance values at different distances z between the tip of the LED and the surface of the reactor was modeled with a ray tracing algorithm. The results were validated by experimental measurements. For these LED boards, the optimum z value where a uniform light distribution can be obtained on the surface of the photomicroreactor was found to be 1.5 cm. The normalized irradiance value when z was 2 cm and 4 cm, respectively, is shown in Figure 6c–f. The most uniform irradiance was obtained with the CC array when z was 2 cm. The irradiance at the outer edges was lower compared to the central sections for the MC array. The irradiance became more homogenous at the central sections when z was increased to 4 cm. However, the overall uniformity decreased as the irradiance at the edges decreased even more. When the LEDs were configured in the same shape as the reactor, the energy efficiency was the highest [63].

As mentioned in the previous section, structures such as beads or monolith supports are frequently used to increase the mass transfer in photoreactors. Zhao et al. studied beads made of glass, zircon, or steel in a capillary-based photomicroreactor. Opaque packing (steel) decreased the conversion by 5-15%, depending on the flow rate. A material with a higher refractive index increased the conversion [50]. This is in line with the observations in the work of Cambié et al. [43]. Ramos et al. also confirmed that the utilization of a transparent packed material increased the apparent reaction rate by a 4-fold compared to an iron packing material [68]. Therefore, a translucent material should be preferred in photoreactors.

The photon flux received by the absorbing species needs to be determined accurately in order to characterize photochemical reactors. The calculation of the local volumetric rate of photon (or energy) absorption (LVRPA or LVREA) is the main aspect of the modeling of photoreactors. LVRPA represents the amount of photons absorbed per unit time and per unit reactor volume at different locations in the reactor. Then, the reaction rate at a given location can be related to the light field by using the quantum yield (Equation 9), where r is the reaction rate ($mol \cdot m^{-3} \cdot s^{-1}$), ϕ is the quantum yield ($mol \cdot mol \cdot photons^{-1}$), and LVRPA is local volumetric rate of photon absorption ($mol \cdot photon \cdot m^{-3} \cdot s^{-1}$). In order to obtain the average reaction

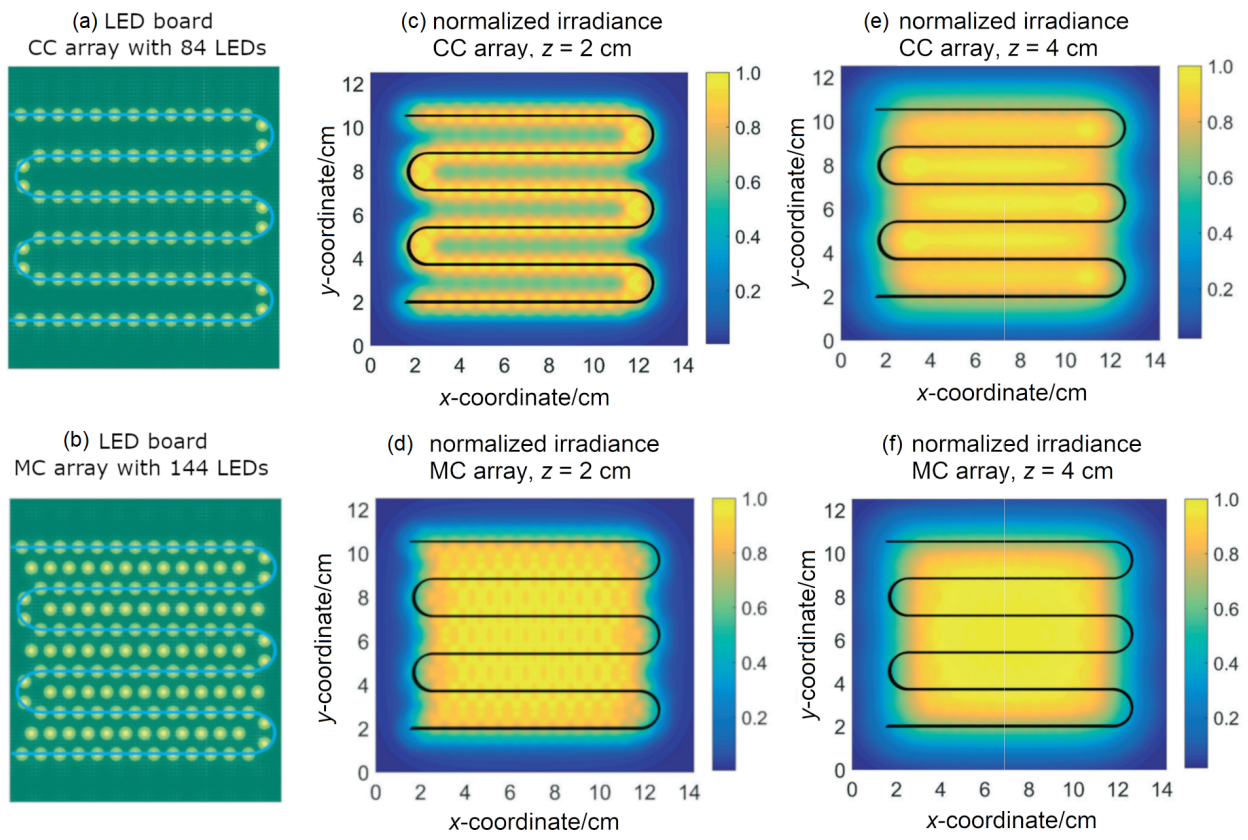

Figure 6: Comparison of the LED board designs of photomicroreactors: (a) CC array design, (b) MC array design. Normalized irradiance on a parallel plane placed at (c) z = 2 cm from a CC array, d) z = 2 cm from an MC array, e) z = 4 cm from a CC array, f) z = 4 cm from an MC array. The photomicroreactor channels are represented by the S-shaped blue and black lines. The photomicroreactor dimensions are not drawn to scale. Reprinted with permission from [63], copyright 2018 The Royal Society of Chemistry.

rate, both the concentration field and the light field inside the reactor need to be solved. The concentration field inside the reactor depends on the hydrodynamics. For ideal reactors (perfectly mixed or plug flow), the reaction rate would still be heterogeneous due to the attenuation of the light inside the reactor [4]. The light field in single phase for homogenous photoreactions can be easily predicted by the Beer–Lambert–Bouguer law (Equation 10).

$$-r = \phi \, \mathrm{LVRPA} \tag{9}$$

$$A = \log_{10} \frac{E}{E_0} = \varepsilon \cdot l \cdot C \tag{10}$$

where A is absorbance, E_0 is the incident irradiance ($\mathrm{W \cdot m^{-2}}$), E is the irradiance transmitted by the medium ($\mathrm{W \cdot m^{-2}}$), ε is the absorptivity ($\mathrm{m^2 \cdot mol^{-1}}$), l is the path length (m), and C is the concentration of the attenuating species ($\mathrm{mol \cdot m^{-3}}$).

Photoreactions are often heterogeneous, with solid particles in the reaction medium. In addition, some photoreactions contain a gas phase, which further complicates light field models. For heterogeneous photoreactions, the liquid reaction medium is usually transparent to light. Solid photocatalysts, on the other hand, are absorbing and scattering light. The scattering of light by a particle depends on the refractive index of the medium and the particle, the particle size, and the wavelength of light. The ratio of the diameter of the particle to the wavelength of the light is called the size parameter. The scattering phenomenon in a tubular reactor is depicted in Figure 7.

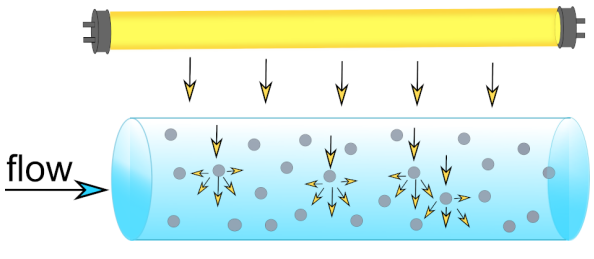

Figure 7: Illustration of the light scattering phenomenon inside a photocatalytic flow reactor.

The efficiency of the absorption in scattering media with respect to pure absorption situations is shown in Figure 8. The optical thickness is the natural logarithm of the ratio of the incident to the transmitted irradiance. The efficiency of the absorption process approaches 1 at a large optical thickness. For an optically thick medium, the mean free path of a photon becomes so short that the medium can be considered as a continuum with a constant optical thickness [69].

The scattering by a single particle is described by Mie's theory, who solved the Maxwell equations for a plane electromagnetic wave encountering a sphere. Mie's theory gives exact analytical solutions for all size parameters. Still, Rayleigh scattering is preferred for small size parameters. For large size parameters, ray tracing, which is also called geometric optics, is less computationally demanding and therefore more frequently used in this region. Once the scattering profile of a photocatalyst particle is obtained, the radiative transfer equation still needs to be solved to obtain the LVRPA value. The integro-differential nature of the equation makes it quite hard to obtain an analytical solution. Therefore, approximations, such zero reflectance [70], two flux [71], and six flux [72] were suggested to model the slurry photocatalytic systems. Among the simplified models, two flux gives a simple and still accurate solution of the radiative transfer equation in a scattering medium. The model assumes that the particles are purely backscattering the photon. The six flux model assumes that photons flow the six routes of the coordinate system. Therefore, it is more accurate. Six flux is slightly more complex than the two flux approximation, but it is still an analytical equation that can be easily calculated if the single scattering albedo is known. If the absorbance of the photocatalyst is known, the single scattering albedo can be obtained by using online tools that solve Mie's theory [73]. For solid photocatalysts, the absorbance is usually unknown. Therefore, the single scattering albedos for solid photocatalysts are usually obtained experimentally.

Scattering phenomena are seen in all dimensions while designing a photoreactor. Not only the structures in the photoreactors but also the reactor tubes would scatter light when a bundle of tubes is illuminated. In a previous study, three different configurations of tube bundles in a 20 mm tube photoreactor were studied. The tube bundle consisted of 31 tubes of a 3 mm outer diameter, 19 tubes of a 4 mm outer diameter, and 6 tubes of an 8 mm outer diameter. An array of 6 tubes resulted in the best performance. The authors concluded that the effectively illuminated surface area was of secondary importance in the design of the tube bundles [74]. Jacobs et al. used ray tracing to model a 3D-printed translucent monolith. The diameter (D), the number of channels, and the distance between the channels (L) were varied in the model. The optimal L/D ratio was found to be 2. Increasing the number of channels stacked upon each other up to 6 channels increased the amount of absorbed light and the PSTY, with the cost of increased

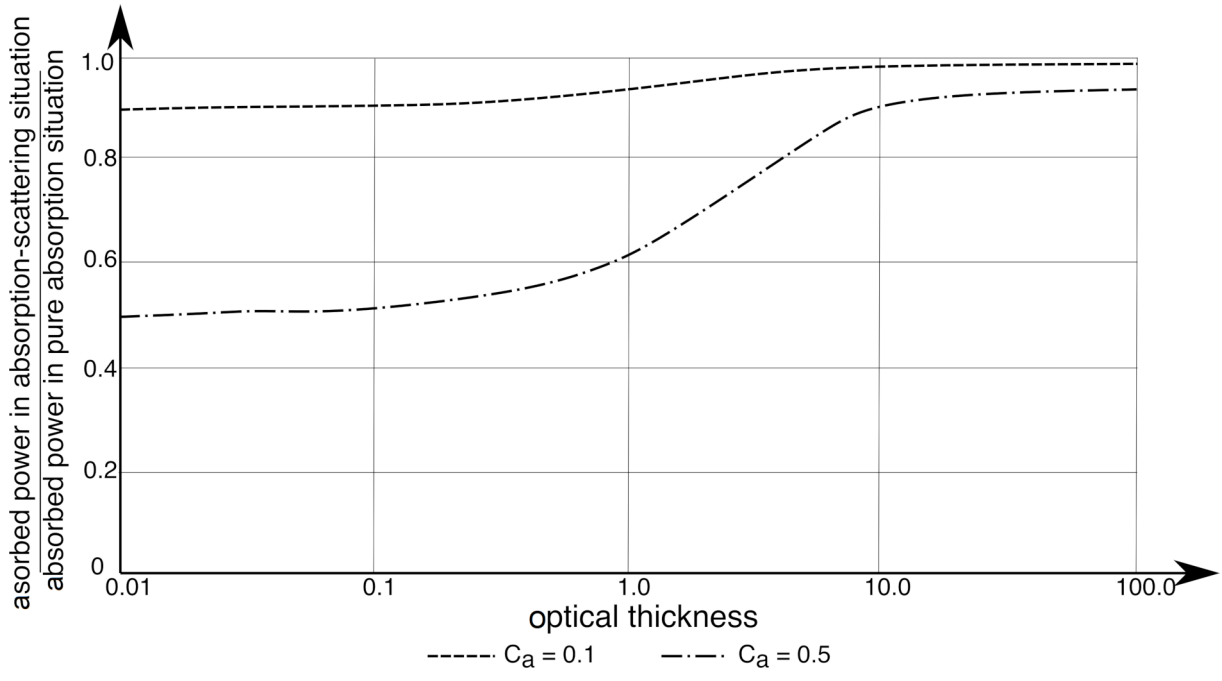

Figure 8: Efficiency of the absorption process in scattering situations with respect to pure absorption situations. The figure was redrawn from a paper by Spadoni et al. [69].

inhomogeneous irradiation. Since translucent monoliths do not have the disadvantages of an optical fiber reactor, they showed an improvement of seven orders of magnitude in terms of the PSTY compared to internally illuminated monoliths.

Gas–liquid reactions in photomicroreactors use the Taylor flow, which is characterized by the regularly sized bubbles surrounded by liquid slugs. The light distribution is affected by the presence of bubbles in the Taylor flow. In a recent study, a photochemical reaction model was developed to optimize the performance of reactors that use a Taylor flow in a serpentine-shaped photomicroreactor. The photon flux per liquid volume was shown to increase exponentially with the amount of gas inside the channels. The conversion was significantly affected by the liquid distribution inside the channels rather than the light scattering or the liquid mixing. In that work, an empirical formula was suggested for the prediction of the optical path length in gas–liquid flows [75]. The photon transport, together with the hydrodynamics in the commercially available Corning G1 Advanced-Flow^{TM} reactor (G1 AFR) was studied. A Corning AFR was shown in the previous section in Figure 5d. It was concluded that the photon flux per unit volume and the hydrodynamics did not depend on the gas content for a wide range of flow conditions, which showed the high flexibility of the AFR. In that work, an empirical formula was suggested for the optical path length [76].

The utilization of solar energy for photoreactions can significantly reduce the cost of the process. In order to use solar energy effectively, the use of luminescent solar concentrators (LSC) together with flow photochemistry is suggested. LSCs are devices in which luminophores, such as fluorescent dyes or quantum dots, are dispersed in a glass or polymeric material to capture the sunlight. The luminophore absorbs sunlight and can emit a specific wavelength of light. LCSs have often been coupled with photovoltaics. Cambié et al. embedded a microstructured photoreactor in a luminophore. The reactor was benchmarked with a [4 + 2] cycloaddition. Monte Carlo ray tracing simulations showed that the aspect ratio of the channels, the relative height of the channels compared to the device thickness, and the number of channels per unit area were the most important design parameters [41]. In a recent work, the efficiency of the photomicroreactors embedded in LSCs was demonstrated for many homogenous and heterogeneous photoreactions, which span the entire visible spectrum. An autonomous control system that changed the residence time based on the fluctuations of the solar light intensity was successfully operated [43]. These operations of photomicroreactors embedded in LSCs are quite promising since they have the potential to reduce the energy costs significantly.

Flow distribution and fabrication of microreactors

The homogenous distribution of fluids while numbering up microreactors is still one of the challenges when numbering up. A nonuniform flow distribution can cause a plethora of problems, such under- and overirradiation and a lower conversion. The maldistribution index (MI) is a common method to assess the flow distribution in internally scaled-up reactors [9,77-80]. It is defined as the relative standard deviation of the mass flow rate inside the microreactors or channels. This is shown in Equation 11.

$$\mathrm{MI} = \sqrt{\frac{1}{n-1}\sum_{i=1}^{\mathrm{n}}\left(\frac{q_i-\bar{q}}{\bar{q}}\right)^2}\cdot 100\% \qquad (11)$$

where n is the number of channels, q_i is the mass flow rate in a channel, and $\bar{\mathrm{q}}$ is the mean flow rate. A low MI indicates a uniform flow distribution.

Numerous distributors can be used to number up photochemical microreactors. These are not limited to the field of photochemistry, and inspiration can be found in the field of heat exchangers and other microreactors. These distributors are categorized and shown in Figure 9. When selecting a distributor to scale up (photo)chemical microreactors by numbering up, a careful consideration based on the flow rate as well as the amount of channels and phases that need to be distributed in the microreactors must be made.

The traditional manifolds, also known as consecutive manifolds, are one of the most used distributors for microreactor arrays due to the simplicity and well-known design rules. They are used for single-phase reactions at a low flow rate. Discrete methods are used to study the flow distribution and pressure drop in manifold systems. In these methods, a lattice network of resistances describes the system, which is analogous to electrical resistance networks. The flow rate is assumed to be linearly related to the pressure drop. The Darcy–Weisbach or Hagen–Poiseuille equation is used in combination with Kirchhoff's law to predict the flow rate in each channel [81-84]. A consecutive manifold is shown in Figure 9a. It is also possible to perform computational fluid dynamics (CFD) simulations to design a distributor. However, the resistance network models are usually preferred over CFD studies due to simplicity [85].

A bifurcation manifold is inspired by nature (e.g., trees, blood vessels, and lungs). The flow is divided by tree-like structures, as shown in Figure 9b. The same discrete methods of consecutive manifolds can be used to design a bifurcation distributor [83]. In contrast to the consecutive manifold, this distributor can

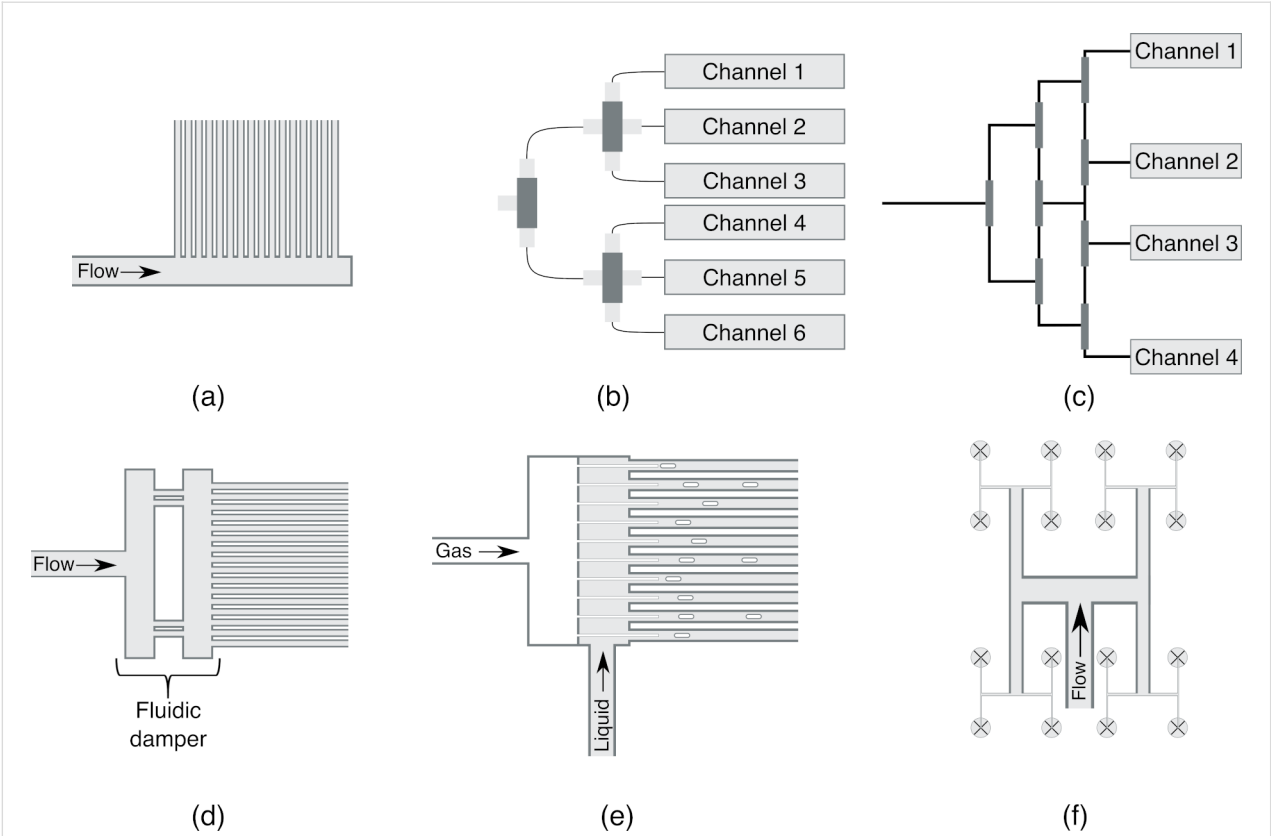

Figure 9: Different types of distributors: (a) Traditional or consecutive manifold, (b) bifurcation unit distributing flow to 6 microreactors (MR), (c) split-and-recombine, (d) distributor with fluidic damper, (e) needle distributor, and (f) fractal distributor (the channels are perpendicular to the plane of the paper and are depicted with an X).

be used to distribute the gas and liquid efficiently [9]. Furthermore, the homogeneity of the flow distribution does not change for different flow rates if all the channels have the same characteristic length [83]. However, when a part of the network clogs, all downstream microreactors will suffer from this. Nagaki et al. have developed a split-and-recombine bifurcation distributor to mitigate the aforementioned issue by recombining the flow after each level of distribution, as shown in Figure 9c [86].

When high flow rates are used in manifolds, the flow distribution will most likely not be uniform, due to the inertial force [87]. It is known that placing baffles or a fluidic damper, with protrusions or holes, increases the hydraulic resistance so that a uniform flow can be obtained. Park et al. developed a method to design distributors containing baffles to obtain a uniform flow while utilizing a high flow rate [87]. Furthermore, this design can be used when the system contains a large number of microreactors, which is not the case with bifurcation manifolds. This design type is shown in Figure 9d.

A different approach to distribute the fluid and gas over a stack of microreactors is to put needle-like structures inside the channels, as shown in Figure 9e. This distributor was able to distribute the flow over 357 channels with a MI lower than 3% [88,89]. Fractals are selfsimilar-repeating geometric structures that are invariant when scaling up or scaling down [90]. Mazur et al. obtained an MI of 1.63% when distributing a fluid with a fractal distributor over 64 channels at a Reynolds number of 10000, and thus making the fractal distributor an interesting option when picking a suitable distributor for the microreactor [91]. A method to optimize this type of distributor is presented in the work of Wang et al. They used the lattice Boltzmann method to optimize the shape of a fractal distributor to obtain a lower pressure drop [92]. The lattice Boltzmann method is an alternative to traditional CFD methods to calculate the flow field. A pressure drop reduction between 15.9% and 25.1% was obtained by shape optimizations, in which the T-junctions evolved into Y-junctions by the algorithm. The design of the fractal distributors is shown in Figure 9f. A comparison of the different distributors is shown in Table 2, and this Table can be used to select a suitable distributor.

The fabrication of these distributors and microreactors is not always straightforward due to the many available fabrication

Table 2: Comparison of different distributors.

type	phase	inlet liquid flow rate (mL/min)	Reynolds number inlet	number of microreactors fed	MI (%)	Ref.
consecutive manifold	liquid	0.01	0.1–10	10	0–16	[93]
consecutive manifold	gas–liquid	0.08–1.92	0–5	4	4.5	[94]
bifurcation	liquid	0.2–12	5–500	2–8	7–30	[77]
bifurcation	gas–liquid	0.6–5.6	5–200	8	1–10	[9]
split-and-recombine	liquid	3	200	5	1.8	[86]
manifold with fluidic damper	liquid	250	1485	625	1.2	[87]
needle distributor	gas–liquid	superficial velocity fluid 0.018–0.07 ms^{-1}	20–250	32–357	0.5–3	[88]
fractal distributor	liquid	2880	1000–100 000	16–64	0.84–3.04	[91]

techniques and material constraints. The photoreactor material needs to be transparent, which limits the materials. Furthermore, the small dimensions of the channels and shape also limit the fabrication methods.

Advanced fabrication methods, such as 3D printing, micromilling, laser microchanneling, photolithography, etching, hot embossing, and casting were covered in recent review papers [95-97]. The next section will give an overview on the materials that are commonly used for photomicroreactors, together with the advantages and disadvantages.

A popular material for the construction of photomicroreactors is PDMS, and the most common fabrication method to produce PDMS photoreactors consists of two parts: In the first part, a mold is created by 3D printing, soft lithography, milling, or by manually constructing it with objects. The second part consists of casting the PDMS in the mold and curing it. An advantage of PDMS is that it can be bonded to glass, silicon, and itself by treating the surface with oxygen plasma, which oxidizes the surface. This treatment allows the construction of complex geometries by stacking multiple pieces of PDMS. This material was used in the research of Cambié et al. to fabricate a photomicroreactor with 32 parallel channels and a bifurcated flow distributor. They performed the [4 + 2] cycloaddition of 9,10-diphenylanthracene (DPA) with singlet oxygen in acetonitrile [39]. Another example of the fabrication of a photomicroreactor is found in the work of Lamberti et al. in which they produced a microfluidic chip to degrade methylene blue utilizing TiO_2 as a photocatalyst [98]. Despite the fact that PDMS is utilized to fabricate photomicroreactors, there are some limitations to this material, which includes a limited resistivity against organic solvents and the absorption of small hydrophobic molecules [20,99]. This issue can be solved by coating the surface with a protective coating. Table 3 can be considered to help selecting a suitable material that is compatible with the common solvents used in photochemistry.

Table 3: Common solvents used in photochemistry and solvent resistance of PDMS, PMMA and glass.

	solvent resistance[a]		
	PDMS	PMMA	glass
water	+	+	+
acetonitrile	+	0	+
ethanol	0	0	+
tetrahydrofuran	–	–	+
benzene	–	–	+
toluene	–	–	+
acetone	0	–	+

[a]+: resistant, 0: swelling or cracking may occur after long-term exposure, –: immediate damage may occur.

Another polymer that can be used to fabricate photomicroreactors is PMMA. It is noteworthy that PMMA has similar properties and a wider variety of fabrication methods. However, it is not often used for the construction of photochemical reactors. This is due to the lower surface quality, which causes the scattering of the light, making them less transparent [100]. Nevertheless, in the work of Cambié et al., PMMA is used as a waveguide instead of PDMS since more light (40%) is directed to the reaction channel due to the higher refractive index (1.49 and 1.42 for PMMA and PDMS, respectively) [43,101,102]. Recently, a 3D printer was used to fabricate a microchannel from PMMA while incorporating a photoactive monomer, 4,7-distyrene-2,1,3-benzothiadiazole (BTZ), in the reactor structure [103]. This demonstrated that it is possible to directly manufac-

ture a photomicroreactor with 3D printing, allowing a high degree of design freedom. The direct manufacturing of a photomicroreactor has also been shown in the research of Guba et al. [104].

Glass is an excellent material due to the high optical transparence. The wavelength cutoff for quartz and borosilicate is 170 nm and 275 nm, respectively. Furthermore, glass is more resistant to high temperatures and inert to the majority of the solvents used in photochemistry, as shown in Table 3 [105]. Due to the more complex fabrication techniques for glass, it is more expensive and time-consuming to make a glass photomicroreactor. The most common fabrication methods are micromilling, photolithography, and wet etching. Takei at al. used a photomicroreactor with 16 channels created by photolithography and wet etching. The reaction zone was coated with TiO_2 to catalyze the synthesis of L-pipecolinic acid [16]. Usami et al. utilized a more exotic method to fabricate photoreactors, consisting of partially melting (sintering) glass beads to produce a highly interconnected transparent structure inside a cylinder. The photocatalytic degradation of 4-chlorophenol was performed in this reactor. Due to the high surface-to-volume ratio of the structure (6500 m^{-1}), there was a relative increase of 66% in the conversion compared to the reactor without this structure [106].

New techniques emerged to 3D-print complex glass microstructures, which are required to scale up repetitive structures. Kotz et al. presented a 3D printing method to fabricate microchannels with a characteristic length of 20 µm. Moreover, they showed the ability to 3D-print microchannels with a spherical, triangular, trapezoidal, and rectangular cross-section [107]. This allows the fabrication of complex geometries from glass necessary for the intensification of photochemical reactions.

Conclusion

When combined with a continuous flow mode, micro- and mesostructured photoreactors have the potential to enable efficient and safe operational conditions. As a result, there is a growing interest in micro- and mesostructured photoreactors, leading to a "renaissance" of photochemistry. In this paper, we have discussed the flow and light distribution and mass transport issues of these photoreactors. It was concluded that not only the reactor geometry but also the operational conditions, such as the concentration of the photoactive molecules and the reactants, the residence time, and the light intensity needed to be tuned for an efficient photoreactor operation. A proper coupling of the light source and the reactor geometry is one of the major hurdles of high-throughput photochemistry. It would be good to keep testing new reactor geometries in large scales where the photon flux, mass transfer characteristics, and flow dynamics are characterized. The technical challenges for different structured reactors differ widely. For example, aerosol photoreactors provide a great platform for multiphase reactions. However, if they are going to be used for photooxidations, the lower and upper explosion limits of aerosols should be studied further. For the photomicroreactors, the technical challenges lie in the distribution of light and flow to all units of the microreactors. Much work has been done on the design of flow distributors in two dimensions. However, more research needs to be done on the flow distribution in three dimensions. Different fabrication methods have different challenges. For example, 3D printing is currently limited to certain polymers and metals that are usually not chemically inert, not UV-transparent, or they cannot handle a high temperature and pressure. Utilizing 3D printing of glass in photochemistry would be a great contribution to this field.

Funding

Mumin Enis Leblebici thankfully acknowledges FWO-Flanders for a postdoctoral fellowship (39715).

ORCID® iDs

Emine Kayahan - https://orcid.org/0000-0002-5286-624X
Mathias Jacobs - https://orcid.org/0000-0002-9865-746X
Leen C.J. Thomassen - https://orcid.org/0000-0002-4970-7475
Simon Kuhn - https://orcid.org/0000-0002-2816-0060
M. Enis Leblebici - https://orcid.org/0000-0003-4599-9412

References

1. Pfoertner, K.-H.; Oppenlander, T. Photochemistry. *Ullmann's Encyclopedia of Industrial Chemistry*; Wiley-VCH: Weinheim, Germany, 2000.
2. Van Gerven, T.; Mul, G.; Moulijn, J.; Stankiewicz, A. *Chem. Eng. Process.* **2007,** *46,* 781–789. doi:10.1016/j.cep.2007.05.012
3. Turconi, J.; Griolet, F.; Guevel, R.; Oddon, G.; Villa, R.; Geatti, A.; Hvala, M.; Rossen, K.; Göller, R.; Burgard, A. *Org. Process Res. Dev.* **2014,** *18,* 417–422. doi:10.1021/op4003196
4. Loubière, K.; Oelgemöller, M.; Aillet, T.; Dechy-Cabaret, O.; Prat, L. *Chem. Eng. Process.* **2016,** *104,* 120–132. doi:10.1016/j.cep.2016.02.008
5. Boston, D. J.; Xu, C.; Armstrong, D. W.; MacDonnell, F. M. *J. Am. Chem. Soc.* **2013,** *135,* 16252–16255. doi:10.1021/ja406074w
6. Banerjee, A.; Yuhas, B. D.; Margulies, E. A.; Zhang, Y.; Shim, Y.; Wasielewski, M. R.; Kanatzidis, M. G. *J. Am. Chem. Soc.* **2015,** *137,* 2030–2034. doi:10.1021/ja512491v
7. Bhatta, S.; Nagassou, D.; Trelles, J. P. *Sol. Energy* **2017,** *142,* 253–266. doi:10.1016/j.solener.2016.12.031
8. Suresh, A. K.; Sharma, M. M.; Sridhar, T. *Ind. Eng. Chem. Res.* **2000,** *39,* 3958–3997. doi:10.1021/ie0002733
9. Su, Y.; Kuijpers, K.; Hessel, V.; Noël, T. *React. Chem. Eng.* **2016,** *1,* 73–81. doi:10.1039/c5re00021a
10. Sambiagio, C.; Noël, T. *Trends Chem.* **2020,** *2,* 92–106. doi:10.1016/j.trechm.2019.09.003

11. Su, Y.; Straathof, N. J. W.; Hessel, V.; Noël, T. *Chem. – Eur. J.* **2014,** *20,* 10562–10589. doi:10.1002/chem.201400283
12. Herrmann, J.-M. *Catal. Today* **1999,** *53,* 115–129. doi:10.1016/s0920-5861(99)00107-8
13. Kumar, A.; Gogate, P. R.; Pandit, A. B. *Ultrason. Sonochem.* **2007,** *14,* 538–544. doi:10.1016/j.ultsonch.2006.11.005
14. Shaban, Y. A.; El Sayed, M. A.; El Maradny, A. A.; Al Farawati, R. K.; Al Zobidi, M. I. *Chemosphere* **2013,** *91,* 307–313. doi:10.1016/j.chemosphere.2012.11.035
15. Claes, T.; Dilissen, A.; Leblebici, M. E.; Van Gerven, T. *Chem. Eng. J.* **2019,** *361,* 725–735. doi:10.1016/j.cej.2018.12.107
16. Takei, G.; Kitamori, T.; Kim, H. B. *Catal. Commun.* **2005,** *6,* 357–360. doi:10.1016/j.catcom.2005.02.010
17. Li, X.; Wang, H.; Inoue, K.; Uehara, M.; Nakamura, H.; Miyazaki, M.; Abe, E.; Maeda, H. *Chem. Commun.* **2003,** 964–965. doi:10.1039/b300765k
18. Braslavsky, S. E.; Braun, A. M.; Cassano, A. E.; Emeline, A. V.; Litter, M. I.; Palmisano, L.; Parmon, V. N.; Serpone, N. *Pure Appl. Chem.* **2011,** *83,* 931–1014. doi:10.1351/pac-rec-09-09-36
19. Janz, G. J.; Wait, S. C., Jr. *J. Chem. Phys.* **1955,** *23,* 1550–1551. doi:10.1063/1.1742359
20. Cambié, D.; Bottecchia, C.; Straathof, N. J. W.; Hessel, V.; Noël, T. *Chem. Rev.* **2016,** *116,* 10276–10341. doi:10.1021/acs.chemrev.5b00707
21. Roibu, A. *Characterization of Microstructured Reactions for Photochemical Transformations*. 2019.
22. Leblebici, M. E.; Stefanidis, G. D.; Van Gerven, T. *Chem. Eng. Process.* **2015,** *97,* 106–111. doi:10.1016/j.cep.2015.09.009
23. Aillet, T.; Loubière, K.; Dechy-Cabaret, O.; Prat, L. *Chem. Eng. Technol.* **2016,** *39,* 115–122. doi:10.1002/ceat.201500163
24. Su, Y.; Hessel, V.; Noël, T. *AIChE J.* **2015,** *61,* 2215–2227. doi:10.1002/aic.14813
25. Visan, A.; Rafieian, D.; Ogieglo, W.; Lammertink, R. G. H. *Appl. Catal., B* **2014,** *150–151,* 93–100. doi:10.1016/j.apcatb.2013.12.003
26. Satuf, M. L.; Macagno, J.; Manassero, A.; Bernal, G.; Kler, P. A.; Berli, C. L. A. *Appl. Catal., B* **2019,** *241,* 8–17. doi:10.1016/j.apcatb.2018.09.015
27. Li Puma, G.; Yue, P. L. *Ind. Eng. Chem. Res.* **2001,** *40,* 5162–5169. doi:10.1021/ie0010316
28. Lim, T. H.; Kim, S. D. *Chemosphere* **2004,** *54,* 305–312. doi:10.1016/s0045-6535(03)00753-7
29. Yatmaz, H. C.; Wallis, C.; Howarth, C. R. *Chemosphere* **2001,** *42,* 397–403. doi:10.1016/s0045-6535(00)00088-6
30. Hamill, N. A.; Weatherley, L. R.; Hardacre, C. *Appl. Catal., B* **2001,** *30,* 49–60. doi:10.1016/s0926-3373(00)00219-8
31. Yavorskyy, A.; Shvydkiv, O.; Hoffmann, N.; Nolan, K.; Oelgemöller, M. *Org. Lett.* **2012,** *14,* 4342–4345. doi:10.1021/ol301773r
32. Shvydkiv, O.; Yavorskyy, A.; Nolan, K.; Youssef, A.; Riguet, E.; Hoffmann, N.; Oelgemöller, M. *Photochem. Photobiol. Sci.* **2010,** *9,* 1601–1603. doi:10.1039/c0pp00223b
33. Elliott, L. D.; Berry, M.; Harji, B.; Klauber, D.; Leonard, J.; Booker-Milburn, K. I. *Org. Process Res. Dev.* **2016,** *20,* 1806–1811. doi:10.1021/acs.oprd.6b00277
34. de Sá, D. S.; Vasconcellos, L. E.; de Souza, J. R.; Marinkovic, B. A.; Del Rosso, T.; Fulvio, D.; Maza, D.; Massi, A.; Pandoli, O. *J. Photochem. Photobiol., A* **2018,** *364,* 59–75. doi:10.1016/j.jphotochem.2018.05.020
35. Yueh, H.; Gao, Q.; Porco, J. A., Jr.; Beeler, A. B. *Bioorg. Med. Chem.* **2017,** *25,* 6197–6202. doi:10.1016/j.bmc.2017.06.010
36. Reis, N. M.; Li Puma, G. *Chem. Commun.* **2015,** *51,* 8414–8417. doi:10.1039/c5cc01559f
37. Gerard, B.; Sangji, S.; O'Leary, D. J.; Porco, J. A. *J. Am. Chem. Soc.* **2006,** *128,* 7754–7755. doi:10.1021/ja062621j
38. Elvira, K. S.; Wootton, R. C. R.; Reis, N. M.; Mackley, M. R.; deMello, A. J. *ACS Sustainable Chem. Eng.* **2013,** *1,* 209–213. doi:10.1021/sc300093j
39. Zhao, F.; Cambié, D.; Janse, J.; Wieland, E. W.; Kuijpers, K. P. L.; Hessel, V.; Debije, M. G.; Noël, T. *ACS Sustainable Chem. Eng.* **2018,** *6,* 422–429. doi:10.1021/acssuschemeng.7b02687
40. Debije, M. G.; Verbunt, P. P. C. *Adv. Energy Mater.* **2012,** *2,* 12–35. doi:10.1002/aenm.201100554
41. Cambié, D.; Zhao, F.; Hessel, V.; Debije, M. G.; Noël, T. *Angew. Chem., Int. Ed.* **2017,** *56,* 1050–1054. doi:10.1002/anie.201611101
42. Cambié, D.; Zhao, F.; Hessel, V.; Debije, M. G.; Noël, T. *React. Chem. Eng.* **2017,** *2,* 561–566. doi:10.1039/c7re00077d
43. Cambié, D.; Dobbelaar, J.; Riente, P.; Vanderspikken, J.; Shen, C.; Seeberger, P. H.; Gilmore, K.; Debije, M. G.; Noël, T. *Angew. Chem., Int. Ed.* **2019,** *58,* 14374–14378. doi:10.1002/anie.201908553
44. Woitalka, A.; Kuhn, S.; Jensen, K. F. *Chem. Eng. Sci.* **2014,** *116,* 1–8. doi:10.1016/j.ces.2014.04.036
45. Emmanuel, N.; Mendoza, C.; Winter, M.; Horn, C. R.; Vizza, A.; Dreesen, L.; Heinrichs, B.; Monbaliu, J.-C. M. *Org. Process Res. Dev.* **2017,** *21,* 1435–1438. doi:10.1021/acs.oprd.7b00212
46. Ioannou, G. I.; Montagnon, T.; Kalaitzakis, D.; Pergantis, S. A.; Vassilikogiannakis, G. *ChemPhotoChem* **2017,** *1,* 173–177. doi:10.1002/cptc.201600054
47. Ioannou, G. I.; Montagnon, T.; Kalaitzakis, D.; Pergantis, S. A.; Vassilikogiannakis, G. *Org. Biomol. Chem.* **2017,** *15,* 10151–10155. doi:10.1039/c7ob02557b
48. Ioannou, G. I.; Montagnon, T.; Kalaitzakis, D.; Pergantis, S. A.; Vassilikogiannakis, G. *ChemPhotoChem* **2018,** *2,* 860–864. doi:10.1002/cptc.201800068
49. Leblebici, M. E.; Rongé, J.; Martens, J. A.; Stefanidis, G. D.; Van Gerven, T. *Chem. Eng. J.* **2015,** *264,* 962–970. doi:10.1016/j.cej.2014.12.013
50. Zhao, F.; Chen, Z.; Fan, W.; Dou, J.; Li, L.; Guo, X. *Chem. Eng. J.* **2020,** *389,* 124409. doi:10.1016/j.cej.2020.124409
51. Zhang, S.; Zhang, J.; Sun, J.; Tang, Z. *Chem. Eng. Process.* **2020,** *147,* 107746. doi:10.1016/j.cep.2019.107746
52. Lu, K.-T.; Nguyen, V.-H.; Yu, Y.-H.; Yu, C.-C.; Wu, J. C. S.; Chang, L.-M.; Lin, A. Y.-C. *Chem. Eng. J.* **2016,** *296,* 11–18. doi:10.1016/j.cej.2016.03.097
53. Ola, O.; Maroto-Valer, M.; Liu, D.; Mackintosh, S.; Lee, C.-W.; Wu, J. C. S. *Appl. Catal., B* **2012,** *126,* 172–179. doi:10.1016/j.apcatb.2012.07.024
54. Marinho, B. A.; Cristóvão, R. O.; Djellabi, R.; Loureiro, J. M.; Boaventura, R. A. R.; Vilar, V. J. P. *Appl. Catal., B* **2017,** *203,* 18–30. doi:10.1016/j.apcatb.2016.09.061
55. Hajiesmaili, S.; Josset, S.; Bégin, D.; Pham-Huu, C.; Keller, N.; Keller, V. *Appl. Catal., A* **2010,** *382,* 122–130. doi:10.1016/j.apcata.2010.04.044
56. Azam, M. U.; Tahir, M.; Umer, M.; Jaffar, M. M.; Nawawi, M. G. M. *Appl. Surf. Sci.* **2019,** *484,* 1089–1101. doi:10.1016/j.apsusc.2019.04.030

57. Tahir, M.; Amin, N. S. *Chem. Eng. J.* **2013,** *230,* 314–327. doi:10.1016/j.cej.2013.06.055
58. Rosso, C.; Gisbertz, S.; Williams, J. D.; Gemoets, H. P. L.; Debrouwer, W.; Pieber, B.; Kappe, C. O. *React. Chem. Eng.* **2020,** *5,* 597–604. doi:10.1039/d0re00036a
59. Fonte, C. M.; Leblebici, M. E.; Dias, M. M.; Lopes, J. C. B. *Chem. Eng. Res. Des.* **2013,** *91,* 2250–2258. doi:10.1016/j.cherd.2013.07.014
60. Brito Lopes, J. C.; dos S. da C. Laranjeira, P. E. M.; Dias, M. M. G. Q.; Martins, A. A. A. Network Mixer and Related Mixing Process. U.S. Patent 8,434,933 B2, May 7, 2013.
61. Espíndola, J. C.; Cristóvão, R. O.; Santos, S. G. S.; Boaventura, R. A. R.; Dias, M. M.; Lopes, J. C. B.; Vilar, V. J. P. *Sci. Total Environ.* **2019,** *681,* 467–474. doi:10.1016/j.scitotenv.2019.05.066
62. Marinho, B. A.; Cristóvão, R. O.; Djellabi, R.; Caseiro, A.; Miranda, S. M.; Loureiro, J. M.; Boaventura, R. A. R.; Dias, M. M.; Lopes, J. C. B.; Vilar, V. J. P. *J. Environ. Manage.* **2018,** *217,* 555–564. doi:10.1016/j.jenvman.2018.04.003
63. Roibu, A.; Morthala, R. B.; Leblebici, M. E.; Koziej, D.; Van Gerven, T.; Kuhn, S. *React. Chem. Eng.* **2018,** *3,* 849–865. doi:10.1039/c8re00165k
64. Moreno, I.; Sun, C.-C. *Opt. Express* **2008,** *16,* 1808–1819. doi:10.1364/oe.16.001808
65. Ziegenbalg, D.; Wriedt, B.; Kreisel, G.; Kralisch, D. *Chem. Eng. Technol.* **2016,** *39,* 123–134. doi:10.1002/ceat.201500498
66. Bürmen, M.; Pernuš, F.; Likar, B. *Meas. Sci. Technol.* **2008,** *19,* 122002. doi:10.1088/0957-0233/19/12/122002
67. Sender, M.; Ziegenbalg, D. *Chem. Ing. Tech.* **2017,** *89,* 1159–1173. doi:10.1002/cite.201600191
68. Ramos, B.; Couri, A. P.; Ookawara, S.; Teixeira, A. C. S. C. *ChemRxiv* **2018,** No. 6726395. doi:10.26434/chemrxiv.6726395.v1
69. Spadoni, G.; Bandini, E.; Santarelli, F. *Chem. Eng. Sci.* **1978,** *33,* 517–524. doi:10.1016/0009-2509(78)80012-8
70. Brucato, A.; Rizzuti, L. *Ind. Eng. Chem. Res.* **1997,** *36,* 4740–4747. doi:10.1021/ie960259j
71. Brucato, A.; Rizzuti, L. *Ind. Eng. Chem. Res.* **1997,** *36,* 4748–4755. doi:10.1021/ie960260i
72. Brucato, A.; Cassano, A. E.; Grisafi, F.; Montante, G.; Rizzuti, L.; Vella, G. *AIChE J.* **2006,** *52,* 3882–3890. doi:10.1002/aic.10984
73. http://www.philiplaven.com/mieplot.htm#Download%20MiePlot.
74. Denny, F.; McCaffrey, P.; Scott, J.; Peng, G.-D.; Amal, R. *Chem. Eng. Sci.* **2011,** *66,* 3641–3647. doi:10.1016/j.ces.2011.04.037
75. Roibu, A.; Van Gerven, T.; Kuhn, S. *ChemPhotoChem* **2020,** in press. doi:10.1002/cptc.202000065
76. Roibu, A.; Horn, C. R.; Van Gerven, T.; Kuhn, S. *ChemPhotoChem* **2020,** in press. doi:10.1002/cptc.202000066
77. Qiu, M.; Zha, L.; Song, Y.; Xiang, L.; Su, Y. *React. Chem. Eng.* **2019,** *4,* 351–361. doi:10.1039/c8re00224j
78. Schultes, M. *Ind. Eng. Chem. Res.* **2000,** *39,* 1381–1389. doi:10.1021/ie990437j
79. Yim, S. J.; Ramanjaneyulu, B. T.; Vidyacharan, S.; Yang, Y. D.; Kang, I. S.; Kim, D.-P. *Lab Chip* **2020,** *20,* 973–978. doi:10.1039/c9lc01099h
80. Ahn, G.-N.; Yu, T.; Lee, H.-J.; Gyak, K.-W.; Kang, J.-H.; You, D.; Kim, D.-P. *Lab Chip* **2019,** *19,* 3535–3542. doi:10.1039/c9lc00764d
81. Wang, J. *Chem. Eng. J.* **2011,** *168,* 1331–1345. doi:10.1016/j.cej.2011.02.050
82. Wang, J.; Wang, H. *Appl. Therm. Eng.* **2015,** *89,* 927–945. doi:10.1016/j.applthermaleng.2015.06.069
83. Amador, C.; Gavriilidis, A.; Angeli, P. *Chem. Eng. J.* **2004,** *101,* 379–390. doi:10.1016/j.cej.2003.11.031
84. Tondeur, D.; Fan, Y.; Commenge, J.-M.; Luo, L. *Chem. Eng. Sci.* **2011,** *66,* 2568–2586. doi:10.1016/j.ces.2011.03.003
85. Garciadiego Ortega, E.; Tsaoulidis, D.; Angeli, P. *Chem. Eng. J.* **2018,** *351,* 589–602. doi:10.1016/j.cej.2018.06.020
86. Nagaki, A.; Hirose, K.; Tonomura, O.; Taniguchi, S.; Taga, T.; Hasebe, S.; Ishizuka, N.; Yoshida, J.-i. *Org. Process Res. Dev.* **2016,** *20,* 687–691. doi:10.1021/acs.oprd.5b00414
87. Park, Y.-J.; Yu, T.; Yim, S.-J.; You, D.; Kim, D.-P. *Lab Chip* **2018,** *18,* 1250–1258. doi:10.1039/c8lc00004b
88. Meitzner, C.; Hilpmann, G.; Schäfer, T.; Haase, S.; Lange, M.; Hampel, U. *Chem. Eng. Technol.* **2017,** *40,* 2058–2066. doi:10.1002/ceat.201700125
89. Haase, S.; Bauer, T. *Chem. Eng. J.* **2011,** *176–177,* 65–74. doi:10.1016/j.cej.2011.01.104
90. Mandelbrot, B. B.; Wheeler, J. A. The Fractal Geometry of Nature. *American Journal of Physics.* 1983; pp 286–287. doi:10.1119/1.13295
91. Mazur, M.; Bhatelia, T.; Kuan, B.; Patel, J.; Webley, P. A.; Brandt, M.; Pareek, V.; Utikar, R. *Chem. Eng. Process.* **2019,** *143,* No. 107595. doi:10.1016/j.cep.2019.107595
92. Wang, L.; Fan, Y.; Luo, L. *Comput. Fluids* **2014,** *94,* 49–57. doi:10.1016/j.compfluid.2014.01.034
93. Renault, C.; Colin, S.; Orieux, S.; Cognet, P.; Tzédakis, T. *Microsyst. Technol.* **2012,** *18,* 209–223. doi:10.1007/s00542-011-1334-7
94. Al-Rawashdeh, M.; Fluitsma, L. J. M.; Nijhuis, T. A.; Rebrov, E. V.; Hessel, V.; Schouten, J. C. *Chem. Eng. J.* **2012,** *181–182,* 549–556. doi:10.1016/j.cej.2011.11.086
95. Das, S.; Srivastava, V. C. *Photochem. Photobiol. Sci.* **2016,** *15,* 714–730. doi:10.1039/c5pp00469a
96. Gale, B. K.; Jafek, A. R.; Lambert, C. J.; Goenner, B. L.; Moghimifam, H.; Nze, U. C.; Kamarapu, S. K. *Inventions* **2018,** *3,* No. 60. doi:10.3390/inventions3030060
97. Convery, N.; Gadegaard, N. *Micro Nano Eng.* **2019,** *2,* 76–91. doi:10.1016/j.mne.2019.01.003
98. Song, H.; Ismagilov, R. F. *J. Am. Chem. Soc.* **2003,** *125,* 14613–14619. doi:10.1021/ja0354566
99. Wang, Y.; Chen, S.; Sun, H.; Li, W.; Hu, C.; Ren, K. *Microphysiol. Syst.* **2018,** *2,* No. 6. doi:10.21037/mps.2018.08.02
100. Matellan, C.; del Río Hernández, A. E. *Sci. Rep.* **2018,** *8,* 6971. doi:10.1038/s41598-018-25202-4
101. Sultanova, N.; Kasarova, S.; Nikolov, I. *Acta Phys. Pol., A* **2009,** *116,* 585–587. doi:10.12693/aphyspola.116.585
102. van Lierop, B.; Castle, L.; Feigenbaum, A.; Boenke, A. *Polydimethylsiloxane;* Spectra for the Identification of Additives in Food Packaging; Springer Netherlands: Dordrecht, Netherlands, 1998; pp 396–400. doi:10.1007/978-94-011-5222-8_78
103. Zhakeyev, A.; Tobin, J.; Wang, H.; Vilela, F.; Xuan, J. *Energy Procedia* **2019,** *158,* 5608–5614. doi:10.1016/j.egypro.2019.01.579
104. Guba, F.; Tastan, Ü.; Gugeler, K.; Buntrock, M.; Rommel, T.; Ziegenbalg, D. *Chem. Ing. Tech.* **2019,** *91,* 17–29. doi:10.1002/cite.201800035
105. McMullen, J. P.; Jensen, K. F. *Annu. Rev. Anal. Chem.* **2010,** *3,* 19–42. doi:10.1146/annurev.anchem.111808.073718
106. Usami, H.; Ohta, K.; Inagawa, S. *J. Photochem. Photobiol., A* **2017,** *332,* 595–601. doi:10.1016/j.jphotochem.2016.10.005

107. Kotz, F.; Risch, P.; Helmer, D.; Rapp, B. E.
Adv. Mater. (Weinheim, Ger.) **2019,** *31,* No. 1805982.
doi:10.1002/adma.201805982

License and Terms

This is an Open Access article under the terms of the Creative Commons Attribution License (https://creativecommons.org/licenses/by/4.0). Please note that the reuse, redistribution and reproduction in particular requires that the authors and source are credited.

The license is subject to the *Beilstein Journal of Organic Chemistry* terms and conditions: (https://www.beilstein-journals.org/bjoc)

The definitive version of this article is the electronic one which can be found at: https://doi.org/10.3762/bjoc.16.202